ACCSCIENCE PUBLISHING

International Journal of BIOPRINTING

ACCSCIENCE PUBLISHING
Volume 10 Issue 2 (April 2024)
ISSN: 2424-8002 (Online) ISSN: 2424-7723 (Print)

ACCSCIENCE PUBLISHING

International Journal of Bioprinting

Print ISSN: 2424-7723

Online ISSN: 2424-8002

International Journal of Bioprinting is an international journal covering the technology, science and clinical application of the broadly defined field of Bioprinting. Bioprinting is defined as the use of 3D printing technology with materials that incorporate viable living cells or biological elements to produce tissue or biotechnological products. We are interested in the scientific topics spanning all stages of bioprinting process from concept creation to fabrication and beyond.

Scan to access website:

Scan to submit papers:

About the Publisher

AccScience Publishing is a publishing company based in Singapore. We publish a range of high-quality, open-access, peer-reviewed journals and books from a broad spectrum of disciplines.

Contact Us

Managing Editor
ijb.office@accscience.sg

AccScience Publishing
8 Burn Road, #15-03 Trivex, Singapore 369977.

Volume 10 Issue 2 • April 2024
ISSN 2424-7723 (print) ISSN 2424-8002 (online)

INTERNATIONAL JOURNAL OF BIOPRINTING

ACCSCIENCE PUBLISHING

Access Science Without Barriers

INTERNATIONAL JOURNAL OF BIOPRINTING

ISSN: 2424-7723 (print)
ISSN: 2424-8002 (online)

Editorial and Production Credits

Publisher: AccScience Publishing
Managing Editor: Cathy Huang
Editorial Assistant: Flora Kang
Production Editor: Puvanesswaray Ramakrishnan
Special Issue Commissioning Editors: Shirley Song, Terra Shi
Article Layout and Typeset: Bsmart Publishing (India)

For all advertising queries, contact ijb.office@accscience.sg.

Supplementary file

Supplementary files of articles can be obtained at https://accscience.com/journal/IJB/10/2.

International Journal of Bioprinting

Editorial Board

ACCSCIENCE PUBLISHING

Volume 10 | Issue 2 | April 2024 | Page 1 – 562 |

International Journal of Bioprinting

https://accscience.com/journal/IJB

CONTENTS

ACCSCIENCE PUBLISHING

International Journal of Bioprinting

REVIEW ARTICLE

2D/3D-printed PEDOT/PSS conductive hydrogel for biomedical sensors

Bin Huang[1], Zengjie Zhao[1], Yayu Zheng[1], Kaidi Xu[1], Dan Wang[1], Qingyuan Yang[1], Tingting Yang[1], Xiaojie Yang[2]*, and Huangqin Chen[1]*

[1]School of Stomatology and Ophthalmology, Hubei University of Science and Technology, Xianning City, Hubei Province, China

[2]School of Nuclear Technology and Chemistry & Biology, Hubei University of Science and Technology, Xianning City, Hubei Province, China

(This article belongs to the *Special Issue: Advances in 3D Printing of Hydrogels*)

Abstract

The integration of conductive hydrogels and advanced three-dimensional (3D) printing is a trigger of the development of biomedical sensors for healthcare diagnostics and personalized treatment. Poly(3,4-ethylenedioxythiophene):poly(styrene sulfonate) (PEDOT:PSS) is a versatile conductive hydrogel materials renowned for its exceptional conductivity and hydrophilicity, and 3D printing technology allows for precise and customized fabrication of electronic components and devices. In this review, we aim to explore the potential of 3D-printed PEDOT/PSS conductive hydrogel in the fabrication of biomedical sensors, with a focus on their distinct characteristics, application potential, and systematic classification. We also discuss the methods for fabricating PEDOT:PSS hydrogel electronic devices by employing 3D printing techniques, including extrusion-based 3D printing technology (fused deposition modeling, direct ink writing, and inkjet printing), powder-based 3D printing technology (selective laser sintering and selective laser melting), and photopolymerization-based 3D printing technology (stereolithography and digital light processing). The applications of 2D/3D-printed PEDOT:PSS hydrogels in biomedical sensors, such as strain sensors, pressure sensors, stretchable sensors, electrochemical sensors, temperature sensors, humidity sensors, and electrocardiogram sensor, are also summarized in this review. Finally, we provide insights into the development of 3D-printed PEDOT:PSS-based biomedical sensors and the innovative techniques for biomedical sensor integration.

Keywords: PEDOT:PSS; 3D printing; Conductive hydrogel; Biomedical sensor

***Corresponding authors:**
Xiaojie Yang
(mailyangxiaojie@126.com)

Huangqin Chen
(chenhuangqin79@163.com)

Citation: Huang B, Zhao Z, Zheng Y, et al. 2D/3D-printed PEDOT/PSS conductive hydrogel for biomedical sensors. *Int J Bioprint*. 2024;10(2):1725. doi: 10.36922/ijb.1725

Received: August 31, 2023
Accepted: October 26, 2023
Published Online: January 16, 2024

1. Introduction

Hydrogels are intricate three-dimensional (3D) polymer networks that form through chemical and/or physical crosslinking in an aqueous solution. They harbor vast potential in various domains, spanning from tissue engineering scaffolds to drug delivery carriers and biomedical devices. Hydrogels bear high resemblance to extracellular matrix for their exceptional capacity to absorb and retain water. They offer a stable micro-environment that allows cellular activities and facilitates tissue formation, all the while maintaining outstanding biocompatibility. Furthermore, these versatile materials display

biomimetic qualities and harbor anti-inflammatory, antioxidant, and even anticancer properties. The past studies on hydrogels are primarily focused on enhancing the mechanical properties of hydrogel, spawning several strategies that improve the mechanical performance of hydrogels, including topological crosslinking structures,[1] nanocomposite structures,[2] interpenetrating network structures,[3] strengthened hydrogen bonding,[4] and co-crosslinking structures.[5] In general, an effective approach should allow for the incorporation of stimulus-responsive functional groups into the hydrogel structure.[6] Nevertheless, achieving rapid stimulus responsiveness and novel functionality design while preserving high mechanical performance poses yet another challenge in the creation of smart hydrogel systems.

The introduction of this review expounds the distinctive attributes, potential applications, and classification of conductive hydrogels. Subsequently, we delve into a thorough examination of the recent advancements in poly(3,4-ethylenedioxythiophene):poly(styrene sulfonate) (PEDOT:PSS) conductive hydrogels fabricated by 3D printing technology. Within this context, we explore their significant roles in the realm of biomedicine sensors, including strain sensors, pressure sensors, stretchable sensors, electrochemical sensors, temperature sensors, humidity sensors, and electrocardiogram sensors. The paper is concluded with a summary of the existing challenges and the future prospects of PEDOT:PSS hydrogels, illuminating how 3D printing technology stands as a novel avenue for the fabrication of these remarkable materials (Figure 1). The principal aim of this review is to shed light on the promising trajectory of this evolving field, where science and technology converge to create transformative possibilities.

2. Characteristics and applications of conductive hydrogels

Conductive hydrogel is a novel composite hydrogel that combines a hydrophilic matrix with conductive fillers. It integrates the properties of both conductive materials and hydrogels, offering excellent electronic conduction

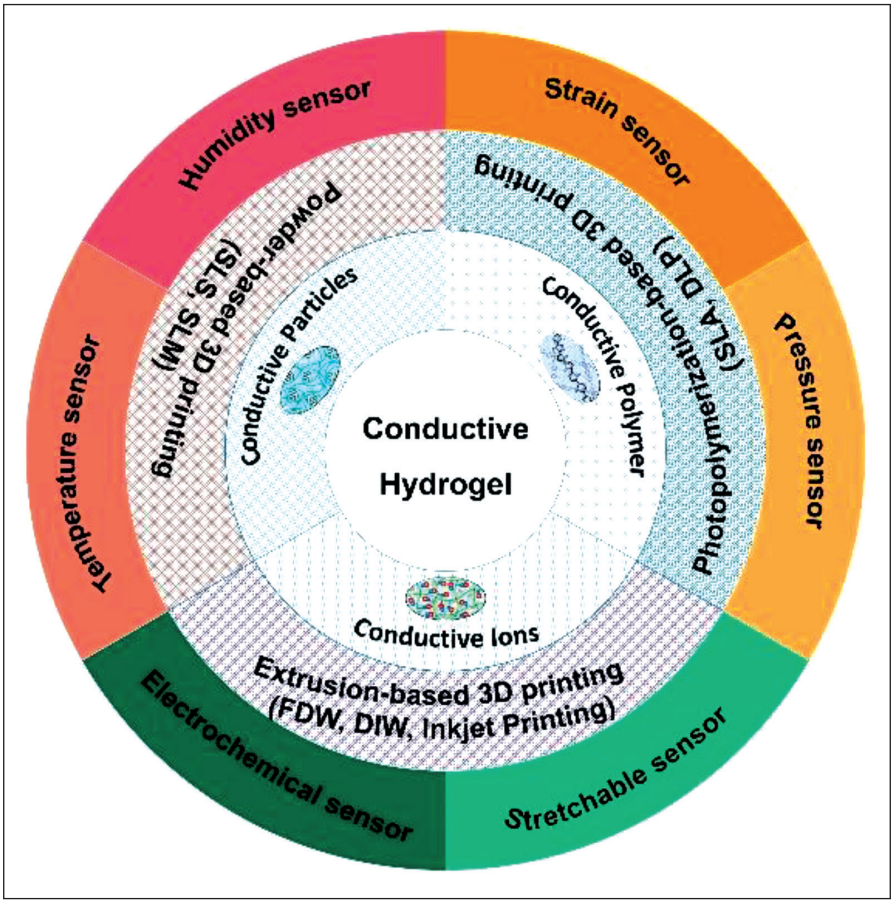

Figure 1. Application of conductive hydrogels in biomedical sensors.

and ion transport capabilities along with desirable biological features such as biocompatibility, adhesion, and antibacterial properties.[7] These remarkable attributes have bestowed conductive hydrogels a myriad of applications, encompassing drug delivery systems, tissue engineering, electronic skins, biosensors, supercapacitors, and flexible wearable electronic devices.[8] In addition, conductive hydrogels are poised to play a pivotal role in the realm of flexible and wearable electronic devices due to their inherent conductivity, enabling seamless integration with wearable technologies.[9] As a rising star in materials science, conductive hydrogels hold immense promise in reshaping the future of sensor industries and bridging the gap between electronic systems and biological entities. Their ongoing development promises to unlock innovative and cutting-edge applications, ushering in a new era of possibilities.

Over the past few decades, significant progress has been made in the development of various types of conductive hydrogels. These can generally be classified into three main categories, according to the different types of conductive media integrated into the hydrogel matrix. The first category involves incorporating conductive particles such as metal nanoparticles and carbon-based nanomaterials into the hydrogel to form electronically conductive hydrogels. In these hydrogels, conductivity arises from the directed movement of free electrons within these embedded conductive particles. This results in the formation of a percolating particle network, effectively enhancing both the electrical conductivity and mechanical properties of the hydrogel.[10] For example, the conductive hydrogel synthesized by oxidized tannic acid-modified AuNPs and chitosan hydrogel matrix with a dynamic Schiff base reaction shows electrical conductivity ranging from 1 to 1.4 mS/cm. It also effectively alleviates the irregular discharge of nerve cells in the intracerebral projection area, leading to improved motor function recovery and reduced histological neurodegeneration in rats with Parkinson's disease.[11] Regardless of these achievements, certain attributes of this material type limit its applications, such as the high cost of noble metal conductive materials. Additionally, metals are susceptible to corrosion in humid environments, and it thus leads to a degradation in the electrical performance of the conductive hydrogel biomaterials. Carbon-based nanomaterials, such as carbon nanotubes (CNTs), graphene oxide (GO), and carbon fibers, have emerged as highly promising conductive materials due to high electrical conductivity, environmental stability, and good biocompatibility,[12] making them excellent alternatives to metallic nanoparticles.[13] However, the low dispersibility in solution and high cost of CNTs and GO also limit their practical applications in large-scale production.

The second strategy entails the introduction of ionic species into the hydrogel network to synthesize conductive hydrogels, either during the gel synthesis process or through post-synthesis doping methods. The presence of conductive ions within the hydrogel establishes an interconnected pathway for the movement of charge carriers, facilitating their migration throughout the material. The conductive ions, acting as mobile charge carriers, enable the hydrogel to conduct electricity effectively and pave the way for applications in various fields, including flexible electronics, bioelectronics, and smart sensors, among others.

The third strategy involves introducing conductive polymer into a hydrogel matrix to obtain polymer electronic conductive hydrogel. Conductive polymers belong to a class of high polymers capable of generating a positive response to electric current signals and achieve electrical conductivity through their own conjugated structures or ionizable ions along the molecular chains. The recognition of this field's significance is evident from the 2000 Nobel Prize in Chemistry awarded in celebration of the birth and evolution of conductive polyacetylene. By linking the structural units within polymers, these materials can harness the π-π conjugated structure present within large molecular chains or utilize ionizable ions along the chains to facilitate the free movement of charge carriers. Consequently, they acquire electrical conductivity. In this strategy, the conductive properties of the polymer are retained within the hydrogel, rendering it an efficient solid-state conductor for electronic charge transport. Since the discovery of conductive polyacetylene, numerous other conductive polymer materials have been developed, including polyaniline, polypyrrole, and poly(3,4-ethylenedioxythiophene) (PEDOT). However, a noteworthy challenge arises with many conductive polymer materials. They tend to be challenging to dissolve, or in some cases, entirely insoluble in water due to their high molecular weights and the hydrophobic nature of their organic constituents. As a result, when attempting to prepare conductive hydrogels using the doping method, the solubility issue can lead to difficulties in achieving uniform incorporation of the conductive components into the hydrogel matrix. This non-uniform distribution within the gel structure significantly compromises the electrical conductivity of the conductive hydrogel.[14] The typical strategy for achieving water-soluble conductive polymers is to complex them with other hydrophilic molecules. For example, PEDOT, a derivative of polythiophene, is inherently insoluble in water due to its hydrophobic nature. However, PEDOT can be doped with hydrophilic poly(styrene sulfonate) (PSS) to form PEDOT:PSS electrostatic complex.[15] This

electrostatic interaction between PEDOT and PSS allows for the homogeneous dispersion of the complex in water, creating a stable and conductive aqueous solution. Its water solubility and compatibility with solution-based processing techniques make it an attractive choice for various applications, enabling the realization of cost-effective and scalable manufacturing processes. A solvent-free strategy using laser-based heating enhances the conductivity of PEDOT:PSS thin films up to three orders of magnitude.[16] Furthermore, laser-induced phase separation enhances aqueous stability of PEDOT:PSS which allows the transformation of PEDOT:PSS into water-stable hydrogels and maintains electrochemical properties even after 6 months in a physiological environment.[17]

Throughout the year, we have witnessed the rapid development of PEDOT:PSS from being a mere material to sophisticated sensors.[18] Various manufacturing processes, including coating, printing, and lithography, have made it possible to produce PEDOT:PSS nanowires with exceptional sensing capabilities. However, neat PEDOT:PSS lacks the flexibility and stretchability required for wearable electronic applications. Enhancing the mechanical flexibility of conductive polymers like PEDOT:PSS for wearable electronics has been achieved through methods such as polymerization directly on textiles, coating/dyeing, and printing.[19] These techniques involve combining PEDOT:PSS with commercially available polymers known for their high flexibility and stretchability, such as polyurethane. PEDOT-based conductive composite materials, whether in gel, fiber, or film form, have found extensive applications in strain, pressure, and temperature sensors within the realm of wearable bioelectronics.[20] This integration not only leverages the superior sensing properties of PEDOT:PSS but also ensures the necessary mechanical durability and adaptability required for wearable electronic applications. At present, PEDOT/PSS conductive hydrogels are regarded as promising materials, exhibiting advantages for application in sensors compared with other materials. However, there is a conspicuous dearth of comprehensive reports systematically summarizing the applications of 3D printing technology in the production of PEDOT:PSS conductive hydrogels for biosensors. Thus, in this context, we delve into the discussion of various 3D printing techniques employed in fabricating PEDOT:PSS hydrogel electronic devices. We also provide an overview of the progress made in the application of 3D-printed PEDOT:PSS hydrogels in biomedical sensors, including strain sensors, pressure sensors, stretchable sensors, electrochemical sensors, temperature sensors, humidity sensors, and electrocardiogram sensors.

3. 3D-printed PEDOT/PSS conductive hydrogel

3D printing technology, commonly referred to as additive manufacturing, offers distinct advantages for replicating natural tissue micro-structures and has gained prominence in recent years for the fabrication of conductive hydrogels. The method relies on layer-by-layer deposition of materials using methods such as heating and melting, laser sintering, or photopolymerization. These processes enable the design and fabrication of complex structures that are challenging to achieve through conventional manufacturing methods. Based on the different forming methods, 3D printing technology can be categorized into three main types (Table 1).

3.1. Extrusion-based 3D printing technology

Extrusion-based 3D printing technology represents a method for fabricating 3D objects, wherein materials are deposited layer by layer through an extrusion process. One of the most representative techniques in this category is fused deposition modeling (FDM), along with direct ink writing (DIW) and inkjet printing.

FDM stands out a popular and accessible 3D printing technique that employs a thermoplastic filament as the printing material. The filament is fed through a heated nozzle, where it undergoes melting and is then precisely deposited onto the build platform, layer by layer. It is worth noting that the reports on PEDOT:PSS materials being exclusively used with FDM technology for 3D printing are scarce. The majority of significant reports typically involve PEDOT:PSS material forming an active or functional layer on the substrate via FDM technology, often through methods like spray deposition or drop-casting.

DIW is another extrusion-based 3D printing method that finds particularly suitable for printing soft and bioactive materials such as hydrogels and living cells. In DIW, a viscous ink or bioink is directly extruded from a nozzle, enabling the precise deposition of material in a controlled manner. The resulting PEDOT:PSS-based supercapacitors exhibit exceptional energy storage performance, outstanding cyclic stability, and remarkable bending stability.[24,28,38] By incorporating various additives such as deep eutectic solvents,[39] glucose, and ascorbic acid,[40] or by combining with other materials like MXene[25] and carbon methyl cellulose,[41] the conductivity of PEDOT:PSS can be significantly enhanced. The introduction of thermally crosslinkable N-(hydroxymethyl)acrylamide segments[42] and the combination with graphene oxide (GO) nanosheets and anionic polyurethane,[43] or post-printing freeze-thawing treatment,[44] facilitated the development of flexible, tough, and stretchable PEDOT:PSS-based hydrogels. The organic electrochemical

Table 1. Classification of 3D printing technology of PEDOT:PSS-based conductive hydrogels

Classification	Component	Resolution	Properties	Application	References
FDW	CNTs, AgNW, and PEDOT:PSS	0.25 mm vertical resolution	Transmittance and sheet resistance	Bioelectronics	[21]
	Polydimethylsiloxane, PEDOT:PSS	0.1 to 0.16 mm at 0.02 mm intervals	Outstanding sensitivity, stable and repeatable operation	Flexible pressure sensor	[22]
	Poly(diallyldimethyl-ammonium chloride), PEDOT:PSS	3 pairs of digits having 9 mm length, 1 mm width	Easily distinguish the chemical fertility of soil samples without pre-treatment	Electronic tongue sensing device	[23]
DIW	PEDOT:PSS	Diameter: 1 mm Distance: 0.15 mm Speed: 3 mm/s Pressure: 20 psi	High energy storage performance and outstanding cycle stability	Flexible micro-supercapacitors	[24]
	(PEDOT:PSS)/MXene	Printing pressure: ~70 kPa Printing speed: 6 mm/s Needle diameter: 210 μm	Deliver exceptionally large areal capacitances, remarkable rate performance, and high cycling stability with thickness-independent capacitances	Flexible micro-supercapacitors	[25]
	PEDOT-graft-PLA copolymers	0.001 mm of maximum resolution, and a maximum pressure of 4 × 10^5 Pa. In this study, needles with an inner diameter of 0.2 and 0.3 mm were used.	The conductive and biocompatible printed patterns of PEDOT-g-PLA showed excellent cell growth and maturation of neonatal cardiac myocytes co-cultured with fibroblasts.	Bioelectronics	[26]
	Functionalized multi-walled CNTs, PEDOT:PSS		The sensitivity and selectivity to ammonia gas (NH_3) at room temperature	Room-temperature gas sensor	[27]
	PEDOT:PSS	High resolution Width: 500 μm Spacing: 700 μm Thickness: 6 μm	High cyclic and bending stability	Flexible all-solid-state micro-supercapacitors	[28]
	PEDOT:PSS	High resolution (~30 μm)	High resolution and high conductivity, while maintaining stable electrochemical properties	A cortex-wide neural interface	[29]
Inkjet printing	PEDOT:PSS, formamide, d-sorbitol, sodium dodecyl benzene sulfonate, and ethylene glycol	The drop spacing was 35 μm, and the printing height was 1.2 mm	High conductivity, stretching properties, as well as good biocompatibility	Stretchable transparent electrodes in optoelectronic devices	[30]

Continued

Table 1. ***Continued***

	Dihydrolevoglucosenone, glycerol carbonate, PEDOT:PSS	21 μm nozzle diameter, droplet spacing of 34 μm	Enhanced performance stability was observed under cyclic bending, thermal annealing, ultraviolet, or infrared exposure	Heterostructures and flexible electronics	[31]
	Co-solvents, a non-ionic surfactant, PEDOT:PSS	A single nozzle with diameter of 300 μm; the ejects dropped (volume = 15 nL) from 7 mm height	Good morphological, optical, and electrical properties	Devices containing high-efficiency printed organic light-emitting diodes	[32]
SLA	PEDOT:PSS, carbon black matrix	500 μm thickness, 250 μm inset windows, 300° circumferential nerve–electrode interface coverage	Enable rapid development of cost-effective functional stimulation devices targeting nerve bundles less than 1.0 mm in diameter	Cuff electrode shell design	[33]
	PEDOT:PSS, photocurable poly(ethylene glycol) diacrylate	Lateral resolution around 80 μm	Performances in biosensing for dopamine detection	Organic electrochemical transistors	[34]
DLP	Dye ((3)Rf*), the amine (TEA), poly(2-hydroxyethyl acrylate)/ PEDOT:PSS	Highest resolution between 20 and 100 μm	Significantly increase its mechanical modulus and electrical properties	Conductive scaffolds	[35]
	Si/PEDOT:PSS/PEG		Preserve a specific discharge capacity, structural integrity, and significantly high flexibility with an enhanced load	Free-standing electrode	[36]
	PEDOT:PSS-coated silver(I) selenide nanowires		The thermoelectric figure of merit of cured composite increased, with the highest at room temperature	Thermoelectric composites	[37]

Abbreviations: AgNW, silver nanowire; CNT, carbon nanotube; FDM; PEDOT, poly(3,4-ethylenedioxythiophene); PEG, polyethylene glycol; PLA, polylactic acid; PSS, poly(styrene sulfonate).

transistors, fabricated by integrating PEDOT:PSS with 3D printing techniques (FDM and DIW), demonstrate high transconductance, low operating voltage, and high current ON/OFF ratio. Moreover, the printed devices exhibit noteworthy sensitivity, stability, and robust behavior even after several measurement cycles.[45]

Within the domain of 3D inkjet printing, the printing material is precisely jetted from multiple small nozzles onto the build platform in a layer-by-layer fashion. The material droplets are rapidly cured or solidified to form the desired 3D object. In the realm of PEDOT:PSS-based bioelectronics, inkjet printing stands out as one of the most cost-effective techniques, offering substantial advantages such as digital design precision, non-contact deposition, and additive manufacturing versatility in additive manufacturing. Current research predominantly focuses on the development and optimization of PEDOT:PSS ink formulations. Secondary doping and post-treatments with formamide have been explored in an effort to enhance the film's conductivity. The addition of d-sorbitol plasticizer gives the PEDOT:PSS film the ability to tolerate cyclic tension.[30] Substituting dimethyl sulfoxide (DMSO) with bio-renewable solvents enhances jetting reliability and long-term stability, while concurrently improves the electrical properties of deposited PEDOT:PSS layers.[31] Surface modification of silicon substrates with (3-aminopropyl)triethoxysilane has been employed to enhance the adhesion of printed semiconductor layers.[34] Moreover, careful regulation of surface tension through the use of co-solvents and a non-ionic surfactant has led to the creation of films with favorable morphological, optical, and electrical properties, which are similar to those observed for the corresponding spin-coated layers.[32] Furthermore, a comprehensive exploration of factors

influencing PEDOT:PSS inkjet printing progress has been investigated. The results highlight that resolution, substrate treatment, and print head height are the most pivotal factors affecting printing quality.[46] The properties of the PEDOT:PSS-based temperature-sensitive layer have also been evaluated and analyzed, encompassing aspects like sensitivity,[47] time drift,[48] and mechanical flexibility.[49]

Electrohydrodynamic (EHD) printing technology, also known as electrohydrodynamic inkjet printing technology, is an innovative approach of inkjet printing. It distinguishes itself from conventional inkjet techniques, which rely on pressure or jetting force to control ink flow. Instead, EHD printing operates by applying an electric field to precisely regulate the movement and distribution of ink during the printing process. This groundbreaking technology seamlessly combines principles from both electrochemistry and printing, resulting in significantly enhanced precision and superior print quality. Typically, EHD jet printing operates in four jetting modes: dripping, micro-dripping, cone-jet, and multi-jet. When working with PEDOT:PSS, the cone-jet mode is typically the preferred choice.[50] To further improve PEDOT:PSS properties, silicon-based hardeners are used to enhance conductivity and solvent resistance,[51] while the incorporation of CNTs provides exceptional dimensional stability.[52] The addition of the surfactant Triton X-100 not only increases the conductivity of PEDOT:PSS films[53] but also optimizes surface tension, enabling multiple jetting modes.[54] In comparison to traditional EHD jet printing methods, when operating under similar printing conditions, the EHD jet printing method employing high-voltage electrostatic focusing lenses achieves higher resolution.[55] PEDOT:PSS prepared using the low-temperature cone-jet mode exhibits tunable conductive and thermal properties, making it potentially valuable for applications in flexible and wearable micro-devices.[56]

3.2. Powder-based 3D printing technology

The powder-based approach involves the utilization of powdered materials to achieve the layer-by-layer fabrication of 3D objects through selective sintering or melting processes. This technique encompasses two primary methodologies: selective laser sintering (SLS) and selective laser melting (SLM), both employing a heat source such as a laser or electron beam. SLS has shown remarkable potential in the production of medical devices, and SLS-based 3D-printed dosage forms hold the promise of revolutionizing the production of personalized drugs.[57] On the other hand, SLM technology excels at rapidly processing metal powder to obtain the necessary parts with outstanding metal structure performance and excellent metal thermal performance, making it indispensable for modern industrial revolution.[58] While SLS and SLM are highly effective technologies for working with powder materials, they are not particularly well-suited for use with hydrogels.

3.3. Photopolymerization-based 3D printing technology

Photopolymerization-based 3D printing falls under the umbrella of additive manufacturing techniques that utilize light-induced polymerization to create 3D objects layer by layer. These techniques rely on the solidification of liquid photopolymer resins when exposed to specific wavelengths of light. They offer precise control over geometry and are particularly suitable for producing intricate and finely detailed structures characterized by smooth surface finishes. The commonly photopolymerization-based 3D printing methods for constructing PEDOT:PSS-based conductive hydrogels are stereolithography (SLA) and digital light processing (DLP).

Renowned for its ability to produce high-resolution models and prototypes with intricate details, SLA employs an ultraviolet laser to selectively cure a liquid photopolymer resin layer by layer. Within the realm of conductive hydrogels, SLA technology has achieved success in fabricating such materials using a blend of PEDOT:PSS and polyethylene glycol diacrylate (PEGDA) as the photopolymerizable matrix.[59] The optimization of the photocurable resin's composition has been accomplished through three aspects: photoinitiator, surfactant, and filler concentrations. This optimization process has yielded printed objects possessing noteworthy electrical conductivity and mechanical properties.[60] Furthermore, the utilization of the PEGDA:PEDOT resin mixture is able to facilitate the rapid prototyping of 3D organic electrochemical transistors, highlighting the promising potential of this methodology for generating functional electronic devices with excellent sensing capabilities.[34]

Similar to SLA, DLP uses a digital light processor (DLP chip) to project an entire layer's image onto the liquid photopolymer resin, allowing for the simultaneous curing of the entire layer and thereby achieving faster printing speeds. Within DLP process, PEDOT:PSS plays a dual role: It expedites the photoinitiation process and imparts the resulting hydrogels with high conductivity and exceptional electrical stability.[35,61] The 3D-printed PEDOT:PSS-based electrodes developed via DLP maintain a notably high specific discharge capacity, accompanied by an extremely low-capacity fade, showcasing remarkable flexibility.[36] Incorporating PEDOT:PSS-coated silver selenide nanowires as a filler enhances the thermoelectric figure of merit and mechanical properties of the cured composite material.[37]

4. 2D/3D-printed PEDOT/PSS conductive hydrogel for biomedical sensors

In this section, we discuss the recent advances of 2D/3D-printed PEDOT/PSS conductive hydrogel for biomedical sensors, including strain sensors, pressure sensors, stretchable sensors, electrochemical sensors, temperature sensors, humidity sensors, and electrocardiogram sensors.

4.1. Strain sensor

The initial studies on PEDOT:PSS-based strain sensors primarily focused on optimizing ink formulations and conducting tests under various tensile conditions and strain histories.[62] These efforts aimed to highlight the correlation between electrical response, applied strain, time, and mechanical history. As the research progressed, attention shifted toward investigating the feasibility of printing conductive patterns on flexible polyimide film substrates using graphene/PEDOT:PSS multi-component ink materials.[63] The effect of different graphene doping amounts on composite ink performance and printing processes was thoroughly analyzed.

Subsequent research endeavors aimed to enhance specific characteristics of strain sensors. For instance, novel hybrid inks were developed by incorporating foam graphene foam/PEDOT:PSS hybrid ink using 2-propanol and ethylene glycol as solvents.[64] This innovation resulted in conductive patterns with a gauge factor of 4.3, rendering them suitable for low strain sensor applications. However, deposition of PEDOT:PSS thin films onto treated flexible substrate surfaces using inkjet printed technique achieves high gauge factors and showcases the materials potential in high-strain sensing applications[65] (Figure 2).

To minimize interference from skin deformation caused by skin-contact strain sensors, an ultra-thin strain sensor was developed using PEDOT:PSS inkjet-printed on polystyrene-polybutadiene-polystyrene nanosheets.[66] This sensor demonstrated the capability to accurately detect minor skin strains (approximately 2%), offering a new approach for precisely monitoring the movement of both human and artificial soft robotic skin.

In the pursuit of enhancing the gauge factor of piezoresistive strain sensors, a novel approach was employed, introducing a high resistive path perpendicular to the sensing direction, driven by phase separation of PEDOT:PSS polymer material.[67] Inspired by sesame candy, a PEDOT:PSS-based conductive nanocomposite with viscoelasticity was crafted through electrostatic/coordination interactions and hydrogen bonds.[68] This composite material was used to create epidermal electrodes and strain sensors for monitoring human electrocardiogram/electromyogram and movement signals.

In response to the challenge posed by the challenge of poor processability of conductive polymer PEDOT:PSS in solution, low electrical resistance PEDOT particles were first synthesized and applied via brush painting, enabling the fabrication of pH and strain sensors on hydrophobic surfaces such as 3D printable thermoplastics.[69]

Furthermore, a robust fluidic strain sensor was developed, using biocompatible PEDOT:PSS/multi-wall CNTs liquid.[70] This sensor had shown high linear response, minimal hysteresis, and stable response across a full humidity range and at temperatures between 20°C and 40°C. Additionally, it demonstrated good biocompatibility, as confirmed through cell viability assessment using human epidermal keratinocytes and human umbilical cord vascular endothelial cells.

4.2. Pressure sensor

The PEDOT:PSS hydrogel possesses exceptional electrical conductivity, inherent flexibility, and mechanical robustness. This unique combination of attributes empowers the hydrogel to adeptly convert mechanical pressure into electrical signals, allowing for precise and sensitive pressure detection.[71] By incorporating PEDOT:PSS hydrogel-based pressure sensors into robotic systems or interactive surfaces, it becomes possible to enhance the safety and precision of human–robot interactions. These sensors can detect changes in pressure distribution and intensity, enabling robots to respond intelligently to human touch and providing a more natural and intuitive user experience.[72] PEDOT:PSS hydrogel-based pressure sensors have gained substantial attention in the realm of wearable fields. They can be seamlessly integrated into clothing, gloves, or even attached directly to the skin, providing real-time pressure monitoring in various contexts. A commonly employed strategy involves combining PEDOT:PSS with polydimethylsiloxane, either by coating or drop-casting it onto 3D-printed polydimethylsiloxane sheets as the active layer, or formulating it as a composite electrode in conjunction with polydimethylsiloxane. These pressure sensors exhibit remarkable sensitivity and linearity, rendering them suitable for detecting diverse health signals such as wrist pulses, swallowing, and speech articulation[22,73,74] (Figure 3).

Another intriguing approach involves crafting pressure sensing patches by sandwiching conductive cotton fabric between two parallel electrodes.[75] In essence, this method entails mixing carbon-based paste with the organic conductor PEDOT-PSS to create a conductive nanocomposite solution. A nanofibrous and stretchable cotton fabric was then selected and immersed in the nanocomposite solution to serve as the pressure sensing layer. The resulting sensors, when tested, demonstrated the ability to record resistance variation as

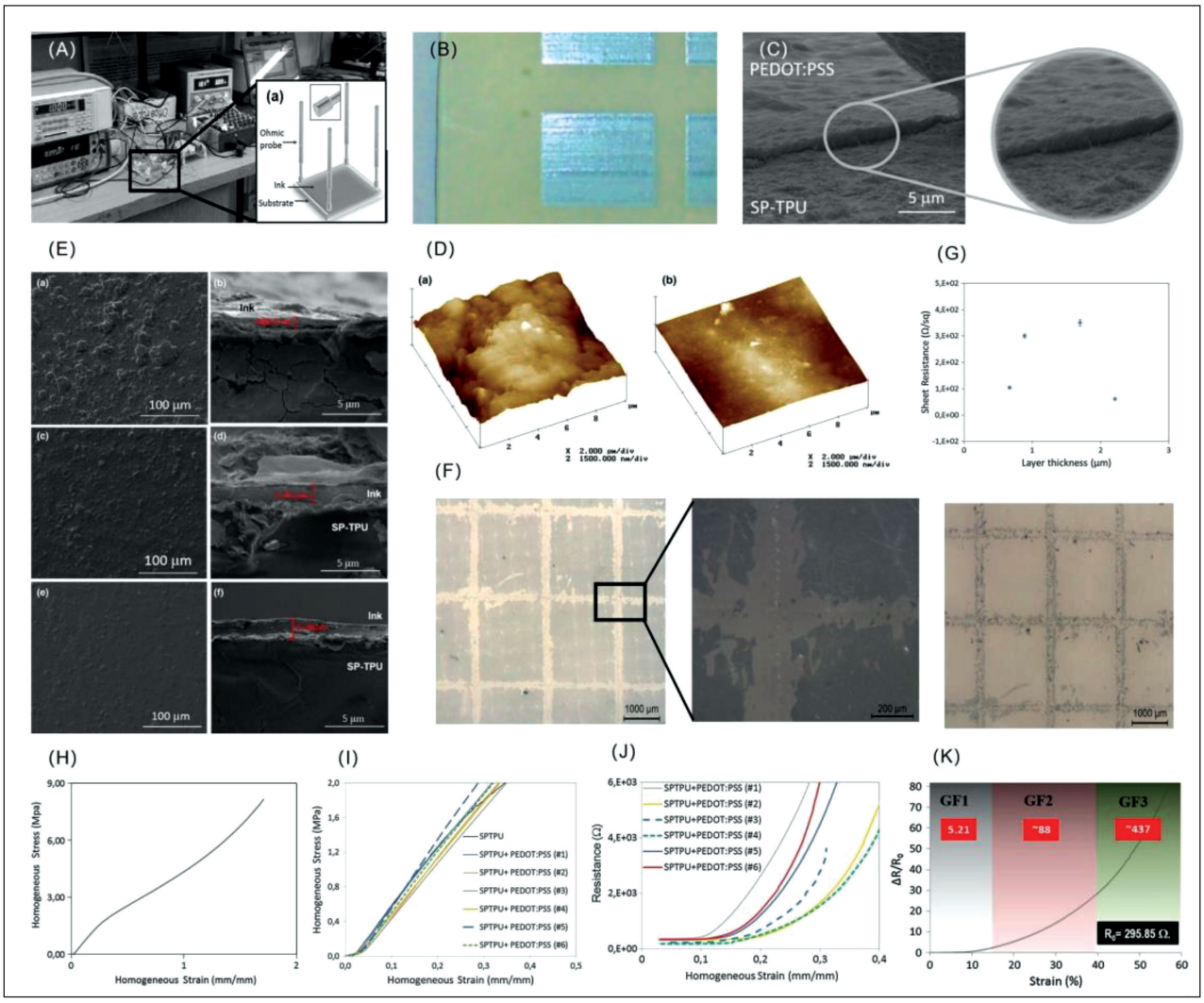

Figure 2. PEDOT:PSS-based strain sensor.[65] (A) Experimental test setup: sample assembly jig with four ohmic contact proven from the resistivity measurements system. (B) Image of the PEDOT:PSS ink printed on the SP-TPU substrate after annealing (at 80°C). (C) Detail of the interface between ink and the SP-TPU substrate. (D) Atomic force microscopy (AFM) topographic images of: (a) SP-TPU surface; (b) the printed SP-TPU surface with six layers of PEDOT. The image size is 10 µm × 10 µm. (E) Scanning electron microscopy (SEM) images of SP-TPU substrate with inkjet printed PEDOT:PSS ink: (a, b) top and fractured cross section surface, respectively, with five layers of ink; (c, d) top and fractured cross. (F) Optical microscopy (OM) images of the printed substrate after the cross-cut tape test: (a) remaining ink on the substrate; (b) detail of (a); (c) remaining ink on the adhesion tape. (G) Sheet resistance measurement, according to the PEDOT:PSS printed layer thickness. (H) Typical TPU stress versus strain curve. (I) Stress–strain curves of the SP-TPU substrate and stress–strain curves of SP-TPU substrate inkjet printed with 6 layers of PEDOT:PSS. (J) Electrical resistance versus homogeneous strain. (K) Resistance changes with strain for printed PEDOT:PSS ink over a SP-TPU substrate. Copyright © 2023 Springer Nature. Reprinted and modified with permission of Springer Nature.

small as 1 gram of weight. These findings underscore the successful application of this sensor for various scenarios necessitating extensive deployment of pressure mapping and force monitoring systems.

4.3. Stretchable sensor

The unique combination of electrical conductivity and mechanical flexibility makes PEDOT:PSS an ideal candidate for stretchable sensor applications. Traditional sensors often encounter challenges when subjected to mechanical deformation, as the strain can induce changes in electrical properties or even lead to sensor failure. The significance of PEDOT:PSS in stretchable devices lies in its ability to maintain electrical performance even under mechanical strain. Its inherent stretchability enables the creation of electronic circuits, sensors, and displays that can be bent, stretched, or conformed to various shapes without compromising functionality. This attribute is particularly crucial for applications in wearable electronics, soft robotics, and healthcare monitoring.

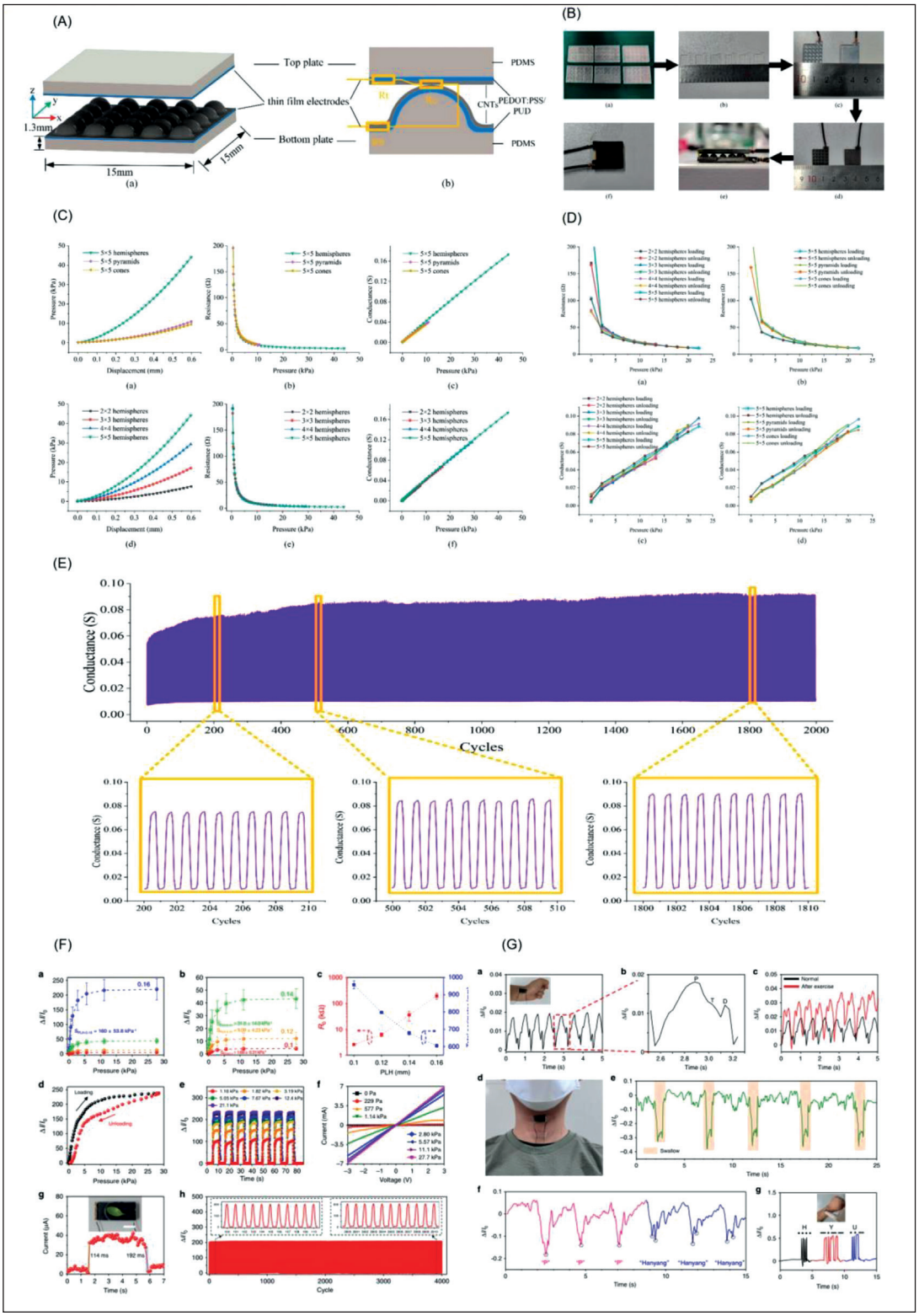

Figure 3. PEDOT:PSS-based pressure sensor.[22,73] (A) The proposed pressure sensor: (a) basic structure; (b) simplified sensor model. (B) Fabrication process of sensors. (C) Finite Element Method (FEM) results of the sensors with different micro-structures. (D) Static test results of sensors. (E) Durability test results. (F) Characterization of the sensing performance of a concentric circle pattern (CCP)-based pressure sensor. (G) Applications of the CCP-based pressure sensor with a 0.16 mm printing layer height (PLH) for human health monitoring. Copyright licensed under Creative Commons Attribution 4.0 license.

The printed PEDOT:PSS-based interconnects exhibit an impressive ability to withstand strains exceeding 100%, highlighting their robust mechanical flexibility.[76] The integration of PEDOT:PSS and a stretchable poly(2-hydroxyethyl acrylate-isobornyl acrylate) (PHI) structure has led to the creation of 3D-printed porous stereo structures characterized by well-interconnected, uniform networks. This innovative combination enhances storage modulus and conductivity, showcasing exceptional stability and durability even when subjected to substantial strains of up to 60%[77] (Figure 4). PEDOT:PSS-based sensors can also achieve elasticity by blending with the

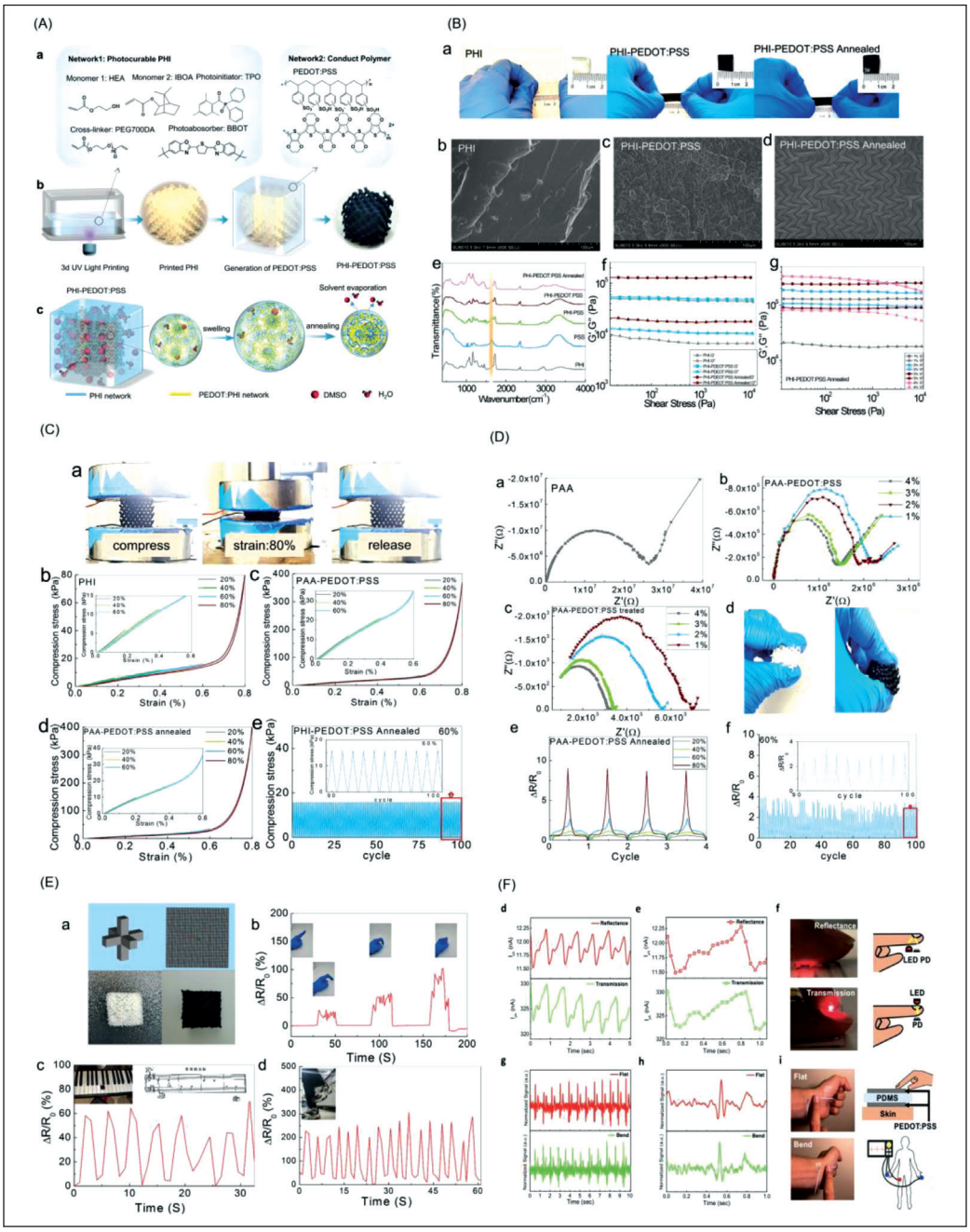

Figure 4. PEDOT:PSS-based stretchable sensor.[77,78] (A) Preparation route for PHI/PEDOT: PSS DN. (B) Properties of PHI, PHI/PEDOT: PSS and annealed PHI/PEDOT: PSS. (C) Compression curves. (D) Electrochemical impedance spectroscopy and its shape deformation under finger pressing. (E) Illustration of sensor design process and sensor output (dynamic test). (F) Representative applications of the printed stretchable PEDOT:PSS/PEO conductor for wearable electrocardiography (ECG) and photoplethysmography (PPG) sensors. Copyright © 2023 Elsevier. Reprinted and modified with permission of Elsevier. Copyright © 2023 Elsevier. Reprinted and modified with permission of Elsevier. Copyright © 2021 American Chemical Society. Reprinted and modified with permission of American Chemical Society.

soft polymer polyethylene oxide (PEO),[78] or printing on a thermoplastic polyurethane (TPU) substrate.[79] Thin films of PEDOT:PSS/PEO polymer can resist up to 50% tensile strain with minimal changes in electrical performance, while PEDOT:PSS/TPU polymer can achieve one-time stretching up to 40%, increasing the sheet resistance up to 214 Ohm/sq only. The integration of hydrogels and dielectric elastomer PEDOT:PSS composite materials combines the water-based flexibility and biocompatibility of hydrogels with the excellent conductivity and mechanical resilience of PEDOT:PSS composites, creating a new paradigm of stretchable electronics.[61]

The application of stretchable and conductive materials has revolutionized the field of sensors, especially in applications related to strain, pressure and force sensing. In strain sensing, the composition of PEDOT:PSS nanofibers with polyvinyl alcohol, coupled with a fusion of 3D printing and successive freeze-thawing, has given rise to a conducting polymer hydrogel strain sensor that exhibits both ultimate strain (300%) and negligible hysteresis (<1.5%).[80] Notably, these sensors show remarkable attributes, such as stretchability, linearity, cyclic stability, and robustness against mechanical twisting and pressing. By modulating micro-cracking patterns within carbon nanofiber-thin film sensors containing PEDOT:PSS by changing thickness, these sensors exhibit an extraordinary linear response to exceptional tensile strains, reaching up to 97% under a high measurement factor.[81] Introducing fiber-reinforced region within the PEDOT:PSS thin film proves to be an effective strategy in suppressing crack propagation in strain sensors. Even after subjecting the sensor to 1000 cyclic tests at a 50% tensile strain, its operational range remains robust at 70%.[82]

In addition to these advancements, coating the surface of acrylic polyurethane layers with a PEDOT:PSS film[83] or applying a mixture of PEDOT:PSS and polyurethane dispersion on the contact surface of polydimethylsiloxane plates[73] allows for the design and fabrication of flexible force sensors and flexible pressure sensors.

4.4. Electrochemical sensor

The remarkable electrical conductivity inherent in PEDOT:PSS hydrogels, coupled with their unique ability to retain ionic species and their compatibility with various electrode substrates, renders them effective in facilitating electron transfer and ion diffusion. This ensures precise and responsive electrochemical signal transduction. In the domain of medical diagnostics, PEDOT:PSS-based electrochemical sensors hold promise for rapid and reliable point-of-care testing.

Among various biosensing applications, glucose sensors based on PEDOT:PSS have gone through a remarkable metamorphosis in terms of sample type amenable for testing, i.e., from blood-based glucose measurement to saliva-based detection.[84] This transformation has been driven by the desire to make blood sugar monitoring more convenient and user-friendly, shifting away from invasive blood measurements that come with discomfort and inconvenience. In the realm of fabrication technology, the traditional screen printing technology[85] has evolved into the more precise and adaptable methods, such as inkjet printing.[86] Meanwhile, PEDOT:PSS modification has become a key strategy in the works involving sensor materials. On the one hand, enhancements in electrical conductivity and biocompatibility have paved the way for improved sensor performance and reliability.[87] On the other hand, the combination of glucose oxidase with biosensors has given rise to enzyme-based platforms, catapulting PEDOT:PSS-modified sensors into being applied in the realm of glucose oxidase-anchored enzyme biosensors[86] (Figure 5). Using appropriate surface immobilization strategies, these enzyme biosensors realize accurate and sensitive glucose measurements. This comprehensive exploration underscores the importance of PEDOT:PSS as a groundbreaking material for advancing glucose detection, providing a potential breakthrough for diabetes management and personalized medicine. Furthermore, a biosensor array has been developed, featuring PEDOT:PSS conductive polymer, silicone, activated carbon, and platinum nanoparticles. This array allows for the concurrent measurement of glucose, lactate, and neurotransmitters like glutamate in cell cultures over hours to days.[88] Notably, the application of this array offers a dynamic and longitudinal view on how neural cells respond to various drugs and environmental cues. It can be seamlessly integrated into micro-fluidic organ-on-a-chip platforms or as part of intelligent culture dish systems. This innovation enables real-time monitoring of multiple analytes, providing insights into cellular behavior and responses that are crucial for advancing our understanding of complex biological processes and drug interactions.

PEDOT:PSS sensors have proven versatile in detecting various cations and anions, such as sodium, potassium, calcium,[89] and chloride ions,[90] as well as in pH sensing.[45] The application of PEDOT:PSS in ulcer pH detection holds significant potential for advancing wound care. As chronic or infected wounds often exhibit pH variations outside the normal range, the PEDOT:PSS-based sensor provides clinicians with a valuable tool to assess wound healing progress and infection risk.[91] Additionally, their biocompatible nature ensures minimal adverse reactions when in contact with the wound environment. This

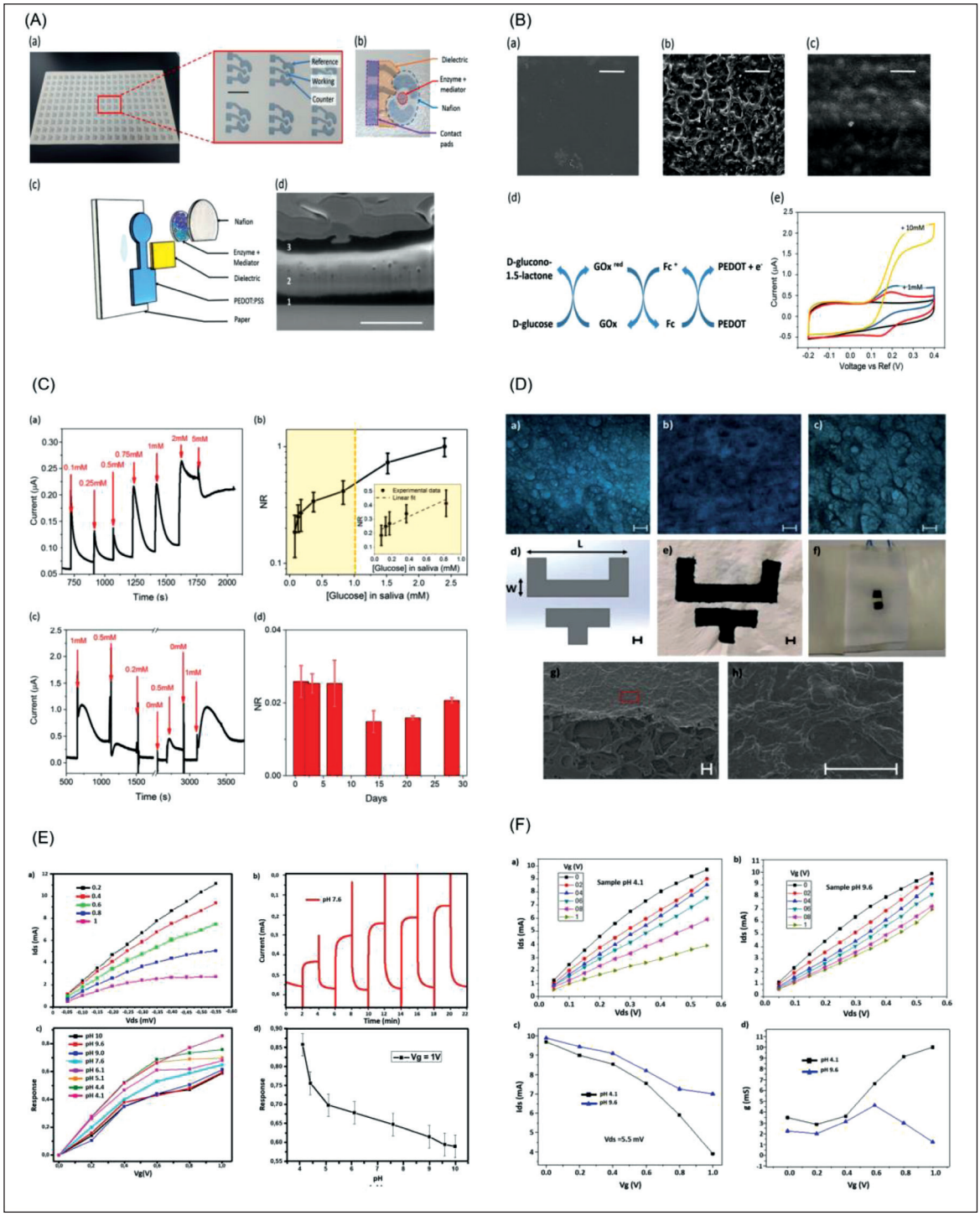

Figure 5. PEDOT:PSS-based electrochemical sensor.[86,91] (A) Glucose biosensors inkjet printed on paper with a loop on the device and their geometry or configuration. (B) Scanning electron microscopy (SEM) images of PEDOT:PSS film printed on paper, mechanism of the enzymatic reaction, and cyclic voltammetry (CV) curves of the biosensor. (C) Current-time characteristics of the sensor in response to different concentrations of glucose successively added into saliva. (D) Scaffold characterization. (E) Response of biocompatible organic electrochemical transistor (OECT) device using a 10^{-3} M NaCl solution. (F) Characteristic of OECT device on scaffold for human physiological sample at different gate voltages (Vg) and pH (4.1 and 9.6). Copyright © 2023 Springer Nature Limited. Reprinted and modified with permission of Springer. Copyright © 2023 IOP Publishing. Reprinted and modified with permission of IOP.

technology offers the potential to detect pH deviations indicative of complications, prompting timely interventions and personalized treatment strategies. It can also gauge the effectiveness of wound healing interventions, marking a substantial leap forward in patient care.

In addition to glucose and various ions, PEDOT:PSS-based organic electrochemical transistors have found application in detecting hydrogen peroxide. For instance, biocompatible electronic devices have been designed using conductive/semiconductive polymers in combination with the biologically active enzyme horseradish peroxidase.[92] These devices demonstrate excellent sensitivity and notable operational stability. Moreover, the incorporation of Prussian-blue nanoparticles, PEDOT:PSS, and water-soluble silkworm protein has been shown to result in a high-accuracy H_2O_2-selective organic–inorganic 3D heterointerface.[93] PSS and silkworm protein, acting as poly-anionic and poly-cationic charge compensating elements, generate a physical blockage effect, significantly enhancing the potential cycling and response stability of the sensing system. Furthermore, PEDOT:PSS-based biosensors have been tailored for detecting various analytes, such as triglyceride,[94] hydrazine,[95] human papillomavirus-related DNA,[96] psychoactive ingredient in cannabis,[97] and nicotine.[98]

4.5. Temperature sensor

By monitoring the changes in electrical resistance of the PEDOT:PSS layer in response to temperature fluctuations, the sensors can precisely and swiftly measure variations in body temperature. This conductivity-driven mechanism not only eliminates the need for complex circuitry but also enables real-time monitoring of body temperature without compromising user comfort.[99] The incorporation of GO endows the temperature sensor with better performance in terms of faster speed as well as shorter response and recovery times, as compared with commercial thermistors.[100] These sensors are integrated onto the electronic skins of a robotic hand, enabling robots to respond through temperature feedback. Furthermore, the introduction of a crosslinker (3-glycidoxypropyl)trimethoxysilane and fluorinated polymer passivation significantly improves the humidity stability and temperature sensitivity of the PEDOT:PSS-based film.[101] The integration of these printed sensors into flexible hybrid circuits creates a wireless temperature sensing platform, which enables stable real-time healthcare monitoring. Additionally, utilizing a hybrid composite of zinc oxide (ZnO) and PEDOT:PSS as the temperature-sensitive layer in flexible sensors yields a high sensitivity of up to 1.06%, with response and recovery times of 5 s and 12.7 s, respectively.[102] The incorporation of graphene nanoflakes and Co3O4 nanoparticles into PEDOT:PSS-based sensing electrodes affords these sensors with high-pressure sensitivity and high-temperature sensitivity simultaneously, with negligible interferences among these parameters[103] (Figure 6).

In addition to material doping to enhance sensor performance and the construction of multi-functional sensors, several studies have also focused on the substrate of printed temperature sensors. For instance, fabricating temperature sensors on pre-treated pure cotton fabric flexible substrates results in comfortable, skin-friendly wearable electronic products.[104] Fabricated by means of printing paper and PEDOT:PSS solution, paper-based temperature sensors boast significantly superior sensitivity, a desirable attribute enabling their integration into a body-attachable patches for a wearable thermometer.[105] These sensors can transfer signal results to smartphones via bluetooth, supporting their applications in a wide range of flexible electronics and healthcare scenarios.

Furthermore, studies have explored the alternatives or supplementary materials for PEDOT:PSS-based temperature sensors, a PEDOT-like self-doped conjugated polymer. These investigations have examined the electrical and morphological characteristics of both polymers and their blends for temperature sensing applications.[106] Research has also delved into silk-protein-based biodegradable temperature sensors, evaluating their temperature sensitivity, humidity stability, and biodegradability.[107] Additionally, a passive design of matrix sensor that achieves high sensor density for spatial temperature readings while maintaining a small array size has been proposed.[108] Collectively, these advancements highlight the potential for diverse applications and multi-functional capabilities of printed temperature sensors in fields ranging from flexible electronics to healthcare monitoring.

4.6. Humidity sensor

Humidity detection holds paramount significance within the realm of biomedical applications, exerting a far-reaching impact on critical aspects such as infection control in medical environments, optimal functionality of medical equipment, maintenance of pharmaceutical storage conditions, and assurance of a controlled environment for medical testing and diagnostics. Its integration into wearable electronic devices introduces a range of functionalities, including respiratory monitoring,[109] assurance of surgical mask integrity,[110] and diaper wetness alerts,[111] which are valuable in the healthcare domain. By serially connecting multiple interdigital transducer electrodes with PEDOT:PSS, methyl red, and GO as active sensing materials, humidity sensors can respond to much

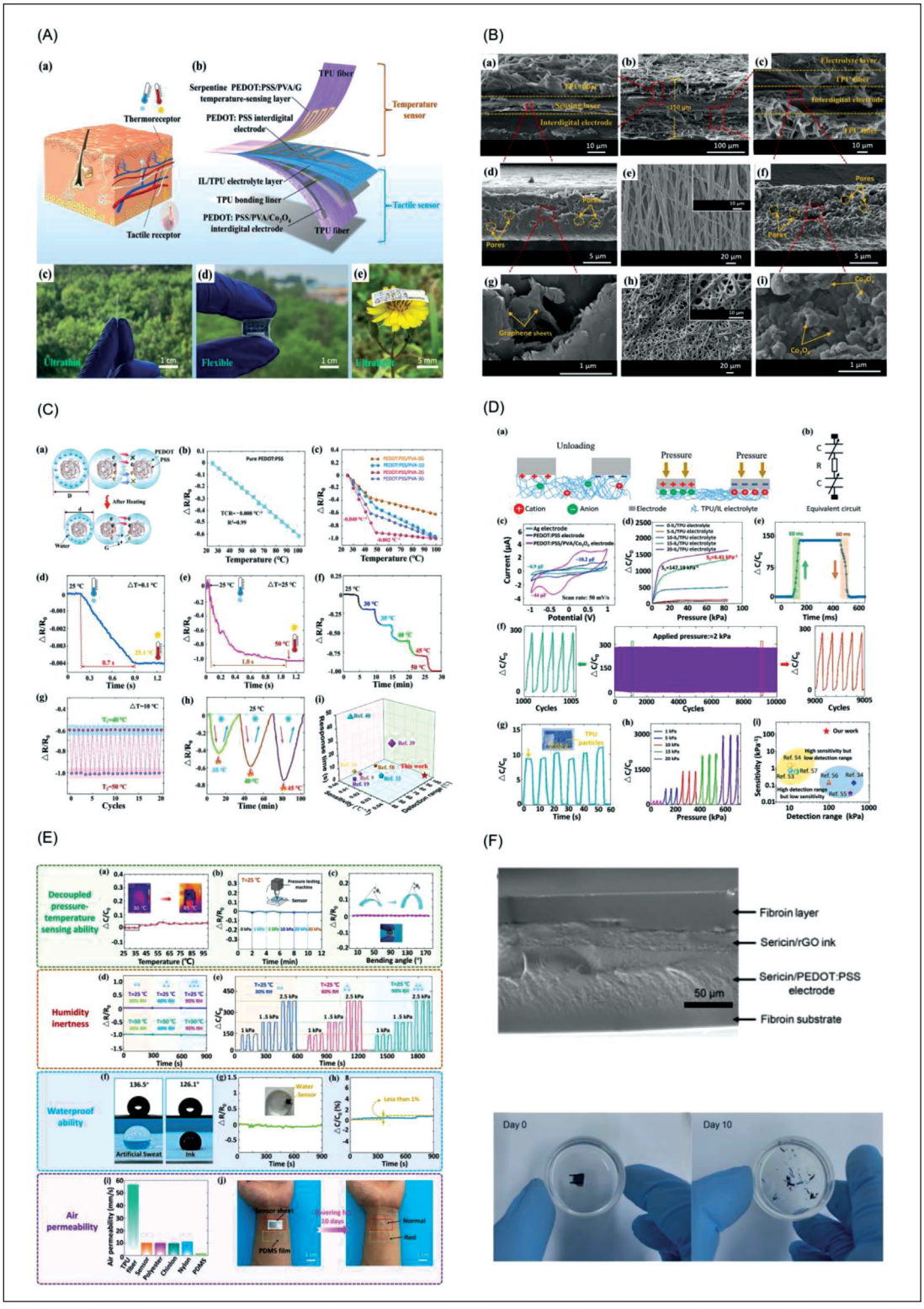

Figure 6. PEDOT:PSS-based temperature sensor.[103,107] (A) Structural design and photographs of the flexible all-nanofiber pressure–temperature sensor. (B) Morphology characterization of the all-nanofiber pressure–temperature sensor. (C) Working principle and performance evaluation of the temperature sensor. (D) Working principle and performance evaluation of the pressure sensor. (E) Stability test of the pressure–temperature sensor. (F) Photolithographically printed flexible silk/PEDOT:PSS temperature sensors. Copyright © 2023 Elsevier. Reprinted and modified with permission of Elsevier. Copyright © 2020 American Chemical Society. Reprinted and modified with permission of American Chemical Society.

wider range of relative humidity with high sensitivity[112] (Figure 7).

The unique approach of combining multiple transducers within a single sensing device facilitates the development of high-performance sensors and circumvents the limitations of single-transducer-based sensing devices. For instance, using both PEDOT:PSS and two-dimensional material molybdenum disulfide (MoS_2) nanosheets as active

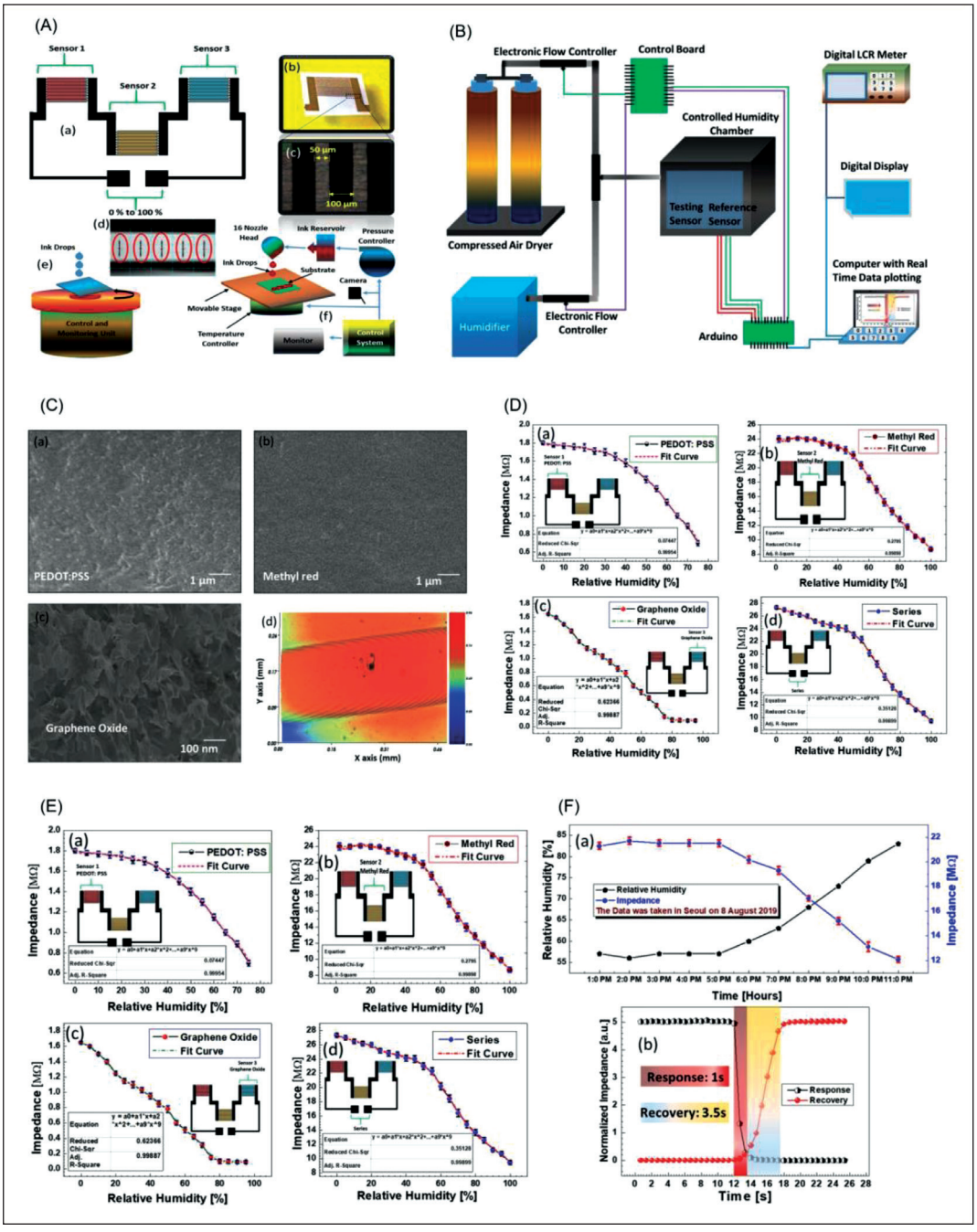

Figure 7. PEDOT:PSS-based humidity sensor.[112] (A) Schematic image of sensor, interdigital electrode, electrode fingers, and inkjet printer DMP-3000. (B) Schematic set-up for characterizing response versus relative humidity change in the tested sensors. (C) Surface morphology characterizations. (D) Impedance response of the sensors. (E) Stability responses at different humidity levels. (F) Real-time application and stability in the open natural environment: (a) impedance response data of the sensor in actual environment and its stability; (b) transient response and recovery time curves of the proposed humidity sensor. Copyright © © 2023 Springer Nature Limited. Reprinted and modified with permission of Springer Nature.

layers for two independent sensors on a single substrate, interconnected in a serial combination, it enables a single humidity sensing device with good properties, such as high sensitivity that exhibits exceptionally high sensitivity and responds to a wide range of relative humidity.[113] Integrating multiple sensors may address the limitations of separate sensors and at the same time combine their advantages. For instance, integrating strain and pH sensors with a humidity detector based on PEDOT:PSS into a single demonstrator enables simultaneous monitoring of multiple biomedical parameters.[114]

Furthermore, the synergistic use of various materials is also a common approach for developing multi-functional sensors. Printing commercial silver nanoparticle ink and PEDOT:PSS onto glossy inkjet photo paper allows the formation of an interdigitated electrode array and curved micro-ribbon, which enable concurrent measurement of relative humidity, temperature, as well as compression and tensile bending.[115]

4.7. Electrocardiogram sensor

As a critical tool used in healthcare sector, electrocardiography (ECG) provides a clear picture about cardiac activity. Commercially available Ag/AgCl electrodes are commonly used to capture ECG signals. However, they may cause skin irritation and lead to unreliable data during prolonged use. In contrast, PEDOT:PSS hydrogels offer a promising alternative due to their low electrode interface impedance and excellent biocompatibility.[116] ECG signals acquired with PEDOT:PSS electrodes closely resemble those obtained with commercial electrodes. Remarkably, these electrodes maintain their electrical properties and functionality even after several washing cycles when subjected to physical stretching.[117] In certain electrolyte conditions, the skin contact impedance and physiological signal extraction characteristics closely resemble those achieved with disposable gelled Ag/AgCl electrodes (rho >0.99). Therefore, PEDOT:PSS electrodes can potentially replace commercial electrodes in wearable devices for health monitoring under both static and dynamic conditions. In addition, the dual ionic and electronic conductivity properties of PEDOT:PSS endow the electrodes the ability to record ECG signals on dry skin conditions.[118] Signal amplification occurs when moisture evaporates from the skin or common emollients are applied, making the recorded ECG signals comparable to those obtained with copper-wired Ag/AgCl electrodes. This phenomenon may be attributed to PEDOT:PSS's ability to reduce contact impedance of dry electrodes.[119] Therefore, dry electrodes which are reusable, comfortable to use, and suitable for long-term measurements permit the collection of electrocardiograms comparable to those collected with gel-based electrodes in terms of quality. Additionally, textile electrodes coated with PEDOT:PSS via the layer-by-layer technique not only exhibit low impedance and excellent skin contact properties, but can also reliably detect high-quality heart rate signals in both wet and dry conditions and maintain stability through 20–30 wash cycles and 120–130 bending cycles.[120] The highly porous PEDOT:PSS hydrogels, formed through self-assembly on paper fibers, enable efficient electron transmission and substance diffusion.[121] They can function as low-impedance ECG electrodes and highly sensitive glucose sensors, providing simultaneous real-time monitoring of ECG and biochemical signals (glucose levels) in sweat during physical activity. 3D-printed PEDOT-based eutectogels, known for their flexibility, stretchability, strong adhesion, and excellent capacity as conformal electrodes, can continuously record epidermal physiological signals such as electrocardiograms and electromyograms over extended periods.[122] However, when prepared as concentric ring electrodes, silver electrodes provide a more stable response (fewer saturations and alterations) to intentionally induced subject movement, as compared with PEDOT:PSS concentric rings.[123] When PEDOT conductive polymer inks are added to thermoplastic styrene-ethylene-butylene-styrene elastomers for micro-extrusion 3D printing, the resulting PEDOT composites demonstrate conductivity and stretchability lower than those of silver micro-flakes and carbon black nanoparticles.[124] Although they exhibit unique properties due to their ionic conductivity, the application of PEDOT conductive polymers in ECG signal detection requires further exploration.

5. Recent advances of 3D-printed PEDOT/PSS conductive hydrogel for biomedical sensors

In summary, the recent advances of 3D-printed PEDOT/PSS conductive hydrogel for biomedical sensors are rooted in the development of strategies for fabricating PEDOT/PSS conductive hydrogels using 3D printing technology, allowing for the amalgamation of the conductivity of PEDOT with the water solubility and processability of PSS. This unique combination makes PEDOT:PSS an exceptional candidate for biomedicine sensors. The main achievements in this field are summarized in the following:

5.1. Fabrication methods: from traditional methods to 3D printing

The evolution of PEDOT:PSS-based sensor fabrication methods has traversed various stages. Initially, simple coating and spraying methods were employed to apply PEDOT:PSS onto substrates in the process of creating basic sensors. After gaining significant understanding

of the material's properties, researchers explored techniques such as screen printing, which allowed for controlled deposition of PEDOT:PSS patterns, enabling the fabrication of more intricate and tailored sensors. Coincidentally, the breakthrough occurred with the advent of 3D printing technology, which revolutionized the sensor fabrication process in a few ways: (i) allowing the deposition of PEDOT:PSS in controlled patterns and precise locations, (ii) fabricating sensors with improved spatial resolution, (iii) reducing waste, and (iii) allowing on-demand fabrication. Direct ink writing, inkjet printing, and DLP techniques have found promising applications in the realm of PEDOT:PSS-based sensors. These techniques enable the rapid creation of intricate sensor patterns with high resolution and versatility in design. As 3D printing technologies continue to evolve, it is expected that sensor performance, resolution, and complexity will continue to improve. Innovations in material formulations, ink development, and integration with emerging technologies like Internet of Things (IoT) and flexible electronics will likely drive the next wave of PEDOT:PSS-based sensor applications.

5.2. Substrate: from polymer to flexible paper

The substrate for PEDOT:PSS-based sensors has undergone notable evolution over time. In the early stages, conventional substrates like polyethylene terephthalate were commonly used. However, as the focus shifted toward creating flexible and wearable sensors, there was a transition to substrates that offered both hydrophilicity and flexibility. Hydrophilic and flexible paper-based substrates emerged as a preferred choice. This shift to paper substrates not only enhances the adaptability of the sensors for wearable applications but also aligns with the growing interest in eco-friendly and biodegradable materials. The utilization of paper substrates not only contributes to the comfort and conformance of the sensors to different surfaces but also reflects the broader trend of integrating sustainable materials into sensor fabrication processes. This evolution in substrate selection demonstrates the dynamic nature of PEDOT:PSS-based sensor technology, driven by the pursuit of enhanced functionality, comfort, and environmental consciousness.

5.3. Materials composition: from single to multi-component

The composition of PEDOT:PSS-based printing inks has also undergone substantial changes, evolving from single-component formulations to more sophisticated multi-component formulations. In the early stages, PEDOT:PSS with inherent conductivity was commonly used as the primary component for sensor fabrication. As the demand for improved sensor performance grew, there was a shift toward exploring and optimizing multi-component printing inks. This progression involved the incorporation of additional components, such as CNTs and graphene, to enhance various aspects of the sensors. The integration of CNTs into PEDOT:PSS formulations leads to the creation of composite inks that offer improved sensing repeatability and enhanced bending stability. These enhancements stem from the unique properties of CNTs, such as their excellent electrical conductivity and mechanical strength. Likewise, graphene/PEDOT:PSS composite inks have been developed to leverage the exceptional electrical, mechanical, and thermal properties of graphene. The synergistic effects of combining graphene with PEDOT:PSS contribute to sensors with enhanced sensitivity, response time, and stability. The shift from single-component to multi-component ink formulations highlights the drive to harness the strengths of various materials for optimized sensor performance. This evolution showcases the innovative approach in sensor development, where the judicious selection and combination of materials lead to sensors with advanced capabilities and improved reliability.

5.4. Function: from single function to multi-function

The functionalities of PEDOT:PSS-based sensors have undergone a remarkable evolution from singular capabilities to multi-functional versatility. Initially, these sensors started as single-purpose devices, such as pressure and strain sensors, providing specific insights into mechanical interactions. However, advancements in technology have driven a leap toward multi-functionality. From the early pressure and strain sensors, the field expanded to include stretchable versions of these sensors, enabling them to withstand deformation while retaining their sensing capabilities. This development marked a significant breakthrough in wearable and flexible electronics, allowing sensors to be seamlessly integrated into various applications. Furthermore, the expansion into multiple parameters has been a noteworthy trend. Sensors that were once limited to single measurements, such as temperature or humidity, have now evolved into dual-response sensors, simultaneously detecting both temperature and humidity changes. This expanded functionality is particularly useful in applications where correlated data provides a more comprehensive understanding of the environment. In the realm of biometric sensing, PEDOT:PSS-based sensors have exhibited a similar trend toward multi-functionality. Some sensors are engineered to simultaneously monitor multiple biochemical markers, enabling the comprehensive assessment of physiological conditions. For instance, sensors are designed to detect glucose, glutamate, and lactate simultaneously, enabling comprehensive metabolic insights. Moreover, the integration of different sensing modalities has led to the development of sensors capable

of capturing both physiological and biochemical signals. This is exemplified by sensors that can monitor both ECG signals and glucose levels in sweat during physical activities. Such multi-functional biosensors offer a holistic perspective, merging real-time physiological responses with biochemical variations.

6. Concluding remarks and prospects

PEDOT:PSS, a popular conducting polymer material, faces several challenges that limit its widespread use in various applications. The primary issues include the inconsistent conductivity of the material due to environmental sensitivity, instability, and aging of PEDOT:PSS over time, leading to decreased performance and reliability, difficulty in achieving uniform and defect-free film formation, low mechanical strength and flexibility, and interface incompatibility with certain substrates and interfaces in electronic devices. Addressing these limitations and challenges is essential to enhance the performance and applicability of PEDOT:PSS in areas such as energy storage devices, flexible electronics, and biosensors. Ongoing research focuses on improving stability, conductivity, mechanical properties, and interfacial compatibility of PEDOT:PSS materials to widen their practical utilization.

Looking ahead, the future of 3D-printed PEDOT:PSS hydrogel sensors holds promising prospects for further expanding their functionalities and applications. Regardless of these achievements, some challenges still remain. As technology continues to advance, several exciting directions emerge:

(1) *Enhanced sensing modalities*. Future PEDOT:PSS sensors are likely to encompass an even broader spectrum of sensing modalities. This may involve the integration of new materials, such as nanomaterials and biomolecules, to enable the detection of a wider range of analytes, including specific chemicals, ions, gases, and biomarkers.

(2) *Real-time monitoring*. The evolution of PEDOT:PSS sensors could lead to real-time, continuous monitoring of various parameters. This helps revolutionize the healthcare sector, enabling the constant tracking of health indicators and early disease detection, as well as improving patient outcomes and preventive care.

(3) *Wireless connectivity*. Incorporating wireless communication capabilities into PEDOT:PSS sensors may allow seamless data transmission to external devices or cloud platforms. This can facilitate remote monitoring, data analysis, and personalized feedback in real time.

(4) *Miniaturization and integration*. Advances in fabrication techniques could lead to smaller, more compact sensors that can be seamlessly integrated into a wide range of wearable devices, textiles, and even implantable medical devices.

(5) *Adaptive and self-powered sensors*. Future PEDOT:PSS sensors might harness energy from their surroundings or body movements, allowing them to operate autonomously and extend their operational lifetimes.

(6) *Smart environments and Internet of Things (IoT)*. As the IoT ecosystem expands, PEDOT:PSS sensors could play a pivotal role in creating smart environments. These sensors may contribute to data-driven decision-making in industries, such as agriculture, infrastructure monitoring, and urban planning.

(7) *Multi-parameter sensing*. The sensors capable of simultaneous detection of multiple parameters will become more refined, allowing for a comprehensive understanding of complex systems and environments.

(8) *Biocompatible and implantable sensors*. Advancements in biocompatible materials and fabrication techniques will enable the creation of PEDOT:PSS sensors for implantation within the body, providing real-time monitoring of health conditions and therapeutic responses.

(9) *Artificial intelligence integration*. Supported by artificial intelligence and machine learning algorithms, the PEDOT:PSS sensors will be able to process complex data patterns, thereby improving accuracy and providing predictive insights.

(10) *Environmental monitoring*. Environmental monitoring is an important element in the development of sustainable and smart cities, and thus, PEDOT:PSS sensors can play a role in this regard by monitor environmental factors, such as pollution, humidity, and temperature.

Acknowledgments

None.

Funding

This work was supported by the Xianning City Program of Science & Technology (No. 2022ZRKX051), Science Development Foundation of Hubei University of Science & Technology (No. BK202217, 2021F005, 2021ZX14), Special Fund for Medical Research of Hubei University of

Science and Technology (2022YKY14), and Special Fund of School of Stomatology and Ophthalmology of Hubei University of Science and Technology (2020WG01).

Conflict of interest

The authors declare no conflicts of interest.

Author contributions

Conceptualization: Xiaojie Yang, Bin Huang

Writing – original draft: Huangqing Chen, Yayu Zheng, Qingyuan Yang, Dan Wang

Writing – review & editing: Zengjie Zhao, Kaidi Xu, Tingting Yang

Ethics approval and consent to participate

Not applicable.

Consent for publication

Not applicable.

Availability of data

Not applicable.

References

1. Zhang X, Wang Y, Wu X, et al. A universal post-treatment strategy for biomimetic composite hydrogel with anisotropic topological structure and wide range of adjustable mechanical properties. *Biomater Adv*. 2022;133:112654. doi: 10.1016/j.msec.2022.112654

2. Han IK, Chung T, Han J, Kim YS. Nanocomposite hydrogel actuators hybridized with various dimensional nanomaterials for stimuli responsiveness enhancement. *Nano Converg*. 2019;6(1):18. doi: 10.1186/s40580-019-0188-z

3. Yumin A, Liguo D, Yi Y, Yongna J. Mechanical properties of an interpenetrating network poly(vinyl alcohol)/alginate hydrogel with hierarchical fibrous structures. *RSC Adv.* 2022;12(19):11632-11639. doi: 10.1039/d1ra07368k

4. Zhou T, Qiao Z, Yang M, et al. Hydrogen-bonding topological remodeling modulated ultra-fine bacterial cellulose nanofibril-reinforced hydrogels for sustainable bioelectronics. *Biosens Bioelectron.* 2023;231:115288. doi: 10.1016/j.bios.2023.115288

5. Chen ZY, Zhou RB, Wang RD, Su SL, Zhou F. Dual-crosslinked network of polyacrylamide-carboxymethylcellulose hydrogel promotes osteogenic differentiation in vitro. *Inj J Biol Macromol.* 2023;234:123788. doi: 10.1016/j.ijbiomac.2023.123788

6. Jiang Y, Wang Y, Li Q, Yu C, Chu W. Natural polymer-based stimuli-responsive hydrogels. *Curr Med Chem.* 2020;27(16):2631-2657. doi: 10.2174/0929867326666191122144916

7. Tang L, Wu S, Qu J, Gong L, Tang J. A review of conductive hydrogel used in flexible strain sensor. *Materials (Basel).* 2020;13(18):3947. doi: 10.3390/ma13183947

8. Walker BW, Lara RP, Mogadam E, Yu CH, Kimball W, Annabi N. Rational design of microfabricated electroconductive hydrogels for biomedical applications. *Prog Polym Sci.* 2019;92:135-157. doi: 10.1016/j.progpolymsci.2019.02.007

9. Chen Z, Chen Y, Hedenqvist MS, et al. Multifunctional conductive hydrogels and their applications as smart wearable devices. *J Mater Chem B.* 2021;9(11):2561-2583. doi: 10.1039/D0TB02929G

10. Zhang W, Feng P, Chen J, Sun Z, Zhao B. Electrically conductive hydrogels for flexible energy storage systems. *Prog Polym Sci.* 2019;88:220-240. doi: 10.1016/j.progpolymsci.2018.09.001

11. Xu J, Chen TY, Tai CH, Hsu SH. Bioactive self-healing hydrogel based on tannic acid modified gold nano-crosslinker as an injectable brain implant for treating Parkinson's disease. *Biomater Res.* 2023;27(1):8. doi: 10.1186/s40824-023-00347-0

12. Liu X, Miller AL, Park S, et al. Functionalized carbon nanotube and graphene oxide embedded electrically conductive hydrogel synergistically stimulates nerve cell differentiation. *ACS Appl Mater Inter.* 2017;9(17):14677-14690. doi: 10.1021/acsami.7b02072

13. Meng Z, Stolz RM, Mendecki L, Mirica KA. Electrically-transduced chemical sensors based on two-dimensional nanomaterials. *Chem Rev*. 2019;119(1):478-598. doi: 10.1021/acs.chemrev.8b00311

14. Gan D, Shuai T, Wang X, et al. Mussel-inspired redox-active and hydrophilic conductive polymer nanoparticles for adhesive hydrogel bioelectronics. *Nano-Micro Lett*. 2020;12(1):169. doi: 10.1007/s40820-020-00507-0

15. Lu B, Yuk H, Lin S, et al. Pure PEDOT:PSS hydrogels. *Nat Commun*. 2019;10(1):1043. doi: 10.1038/s41467-019-09003-5

16. Yun C, Han JW, Kim S, et al. Generating semi-metallic conductivity in polymers by laser-driven nanostructural reorganization. *Mater Horiz.* 2019;6(10):2143-2151. doi: 10.1039/C9MH00959K

17. Won D, Kim J, Choi J, et al. Digital selective transformation and patterning of highly conductive hydrogel bioelectronics by laser-induced phase separation. *Sci Adv*. 2022;8(23):eabo3209. doi: 10.1126/sciadv.abo3209

18. Zhang XS, Yang WT Zhang HN, Xie MG. PEDOT:PSS: From conductive polymers to sensors. *Nanotechnol Precis Eng,* 2021;4(4):045004. doi: 10.1063/10.0006866

19. Tseghai GB, Mengistie DA, Malengier B, Fante KA, Langenhove LV. PEDOT:PSS-based conductive textiles and their applications. *Sensors.* 2020;20(7):1881. doi: 10.3390/s20071881

20. Zhang WY, Su Z, Zhang XC, Wang WT, Li ZF. Recent progress on PEDOT-based wearable bioelectronics. *View*. 2022;3(5):20220030. doi: 10.1002/VIW.20220030

21. Falco A, Petrelli M, Bezzeccheri E,Abdelhalim A, Lugli P. Towards 3D-printed organic electronics: Planarization and spray-deposition of functional layers onto 3D-printed objects. *Org Electron.* 2016;39:340-347. doi: 10.1016/j.orgel.2016.10.027

22. Lee JH, So HY. 3D-printing-assisted flexible pressure sensor with a concentric circle pattern and high sensitivity for health monitoring. *Microsyst Nanoeng.* 2023;9:44. doi: 10.1038/s41378-023-00509-z

23. Da Silva TA, Braunger ML, Countinho MAN. 3D-printed graphene electrodes applied in an impedimetric electronic tongue for soil analysis. *Chemosensors.* 2019;7(4):50. doi: 10.3390/chemosensors7040050

24. Wu KB, Kim KW, Kwon JH, Kim JK, Kim SH, Moon HC. Direct ink writing of PEDOT:PSS inks for flexible micro-supercapacitors. *J Ind Eng Chem*. 2023;123:272-277. doi: 10.1016/j.jiec.2023.03.042

25. Li L, Meng J, Bao XR, Huang Y. Direct-ink-write 3D printing of programmable micro-supercapacitors from MXene-regulating conducting polymer inks. *Adv Energy Mater.* 2023;13 (9):2203683. doi: 10.1002/aenm.202203683

26. Dominguez-Alfaro A, Gabirondo E, Alegret N. 3D printable conducting and biocompatible PEDOT-graft-PLA copolymers by direct ink writing. *Macromol Rapid Comm.* 2021;42 (12):2100100. doi: 10.1002/marc.202100100

27. Thaibunnak A, Pakdee U. Pen-based writing of functionalized MWCNT-PEDOT:PSS ink on flexible substrate for application in ammonia gas sensor. *Suranaree J Sci Tech.* 2022;29(2).

28. Ovhal MM, Kumar N, Kang JW. 3D direct ink writing fabrication of high-performance all-solid-state micro-supercapacitors. *Mol Cryst Liq Cryst.* 2020;705(1):105-111. doi: 10.1080/15421406.2020.1743426

29. Zheng Y, Wang YD, Zhang F, et al. Coagulation bath-assisted 3D printing of PEDOT:PSS with high resolution and strong substrate adhesion for bioelectronic devices. *Adv Mater Technol-US.* 2022;7(7):2101514. doi: 10.1002/admt.202101514

30. Hou SY, Chen HQ, Lv D, et al. Highly conductive inkjet-printed PEDOT:PSS film under cyclic stretching. *ACS Appl Mater Interfaces.* 2023;15(23):28503-28515. doi: 10.1021/acsami.3c03378

31. Rivers G, Austin JS, He YF, et al. Stable large area drop-on-demand deposition of a conductive polymer ink for 3D-printed electronics, enabled by bio-renewable co-solvents. *Addit Manuf.* 2023;66:103452. doi: 10.1016/j.addma.2023.103452

32. Cinquino M, Prontera CT, Zizzari A, et al. Effect of surface tension and drying time on inkjet-printed PEDOT:PSS for ITO-free OLED devices. *J Sci-Adv Mater Dev.* 2022;7(1):100394. doi: 10.1016/j.jsamd.2021.09.001

33. Doering OM, Vetter C, Alhawwash A, Horn MR, Yoshida K. Durable scalable 3D SLA-printed cuff electrodes with high performance carbon plus PEDOT:PSS-based contacts. *Artif Organs.* 2022;46(10):2085-2096. doi: 10.1111/aor.14387

34. Bertana V, Scordo G, Parmeggiani M, et al. Rapid prototyping of 3D organic electrochemical transistors by composite photocurable resin. *Sci Rep.* 2020; 10(1):13335. doi: 10.1038/s41598-020-70365-8

35. Lopez-Larrea N, Gallastegui A, Lezama L, Criado-Gonzalez M, Casado N, Mecerreyes D. Fast visible-light 3D printing of conductive PEDOT:PSS hydrogels. *Macromol Rapid Comm.* 2023;26:2300229. doi: 10.1002/marc.202300229

36. Ye XL, Wang C, Wang L, Lu BH, Gao FL, Shao D. DLP printing of a flexible micropattern Si/PEDOT:PSS/PEG electrode for lithium-ion batteries. *Chem Comm.* 2022;58(55):7642-7645. doi: 10.1039/D2CC01626E

37. Park D, Lee S, Kim J. Thermoelectric and mechanical properties of PEDOT:PSS-coated Ag2Se nanowire composite fabricated via digital light processing based 3D printing. *Compos Commun.* 2022;30:101084. doi: 10.1016/j.coco.2022.101084

38. Hill IM, Hernandez V, Xu BH. Imparting high conductivity to 3D printed PEDOT:PSS. *ACS Appl Polym Mater*. 2023;5(6):3989-3998. doi: 10.1021/acsapm.3c00232

39. Aguzin A, Dominguez-Alfaro A, Criado-Gonzalez M, et al. Direct ink writing of PEDOT eutectogels as substrate-free dry electrodes for electromyography. *Mater Horiz.* 2023;10(7):2516-2524. doi: 10.1039/D3MH00310H

40. Greco G, Giuri A, Bagheri S, et al. Pedot:PSS/graphene oxide (GO) ternary nanocomposites for electrochemical applications. *Molecules.* 2023;28(7):2963. doi: 10.3390/molecules28072963

41. Bao P, Lu Y, Tao P, Liu B, Li J, Cui X. 3D printing PEDOT-CMC-based high areal capacity electrodes for Li-ion batteries. *Ionics.* 2021;27(7):2857-2865. doi: 10.1007/s11581-021-04063-4

42. Yu JW, Tian FJ, Wang W, et al. Design of highly conductive, intrinsically stretchable, and 3D printable PEDOT:PSS hydrogels via PSS-chain engineering for bioelectronics. *Chem Mater.* 2023;35(15):5936-5944. doi: 10.1021/acs.chemmater.3c00844

43. Kye MJ, Cho J, Yu HC, et al. "Drop-on-textile" patternable aqueous PEDOT composite ink providing highly stretchable and wash-resistant electrodes for electronic textiles. *Dyes Pigments.* 2018;155:150-158. doi: 10.1016/j.dyepig.2018.03.024

44. Liu J, Garcia J, Leahy LM, et al. 3D printing of multifunctional conductive polymer composite hydrogels. *Adv Funct Mater.* 2023;2214196. doi: 10.1002/adfm.202214196

45. Fan JX, Montemagno C, Gupta M. 3D printed high transconductance organic electrochemical transistors on flexible substrates. *Org Electron.* 2019;73:122-129. doi: 10.1016/j.orgel.2019.06.012

46. Buga C, Viana JC. Optimization of print quality of inkjet printed PEDOT:PSS patterns. *Flex Print Electron.* 2022;7(4):045004. doi: 10.1088/2058-8585/ac931e

47. Khalaf AM, Issa HH, Ramírez JL, Mohamed SA. All inkjet-printed temperature sensors based on PEDOT:PSS. *IEEE Access.* 2022;10:61094-61100. doi: 10.1109/ACCESS.2022.3176822

48. Wang XP, Mu BY, Zhang LW, Zhang X. Drift characteristic analysis of additive manufactured Ag NPs-PEDOT:PSS flexible temperature sensor. *Results Eng.* 2022;13:100384. doi: 10.1016/j.rineng.2022.100384

49. Khalaf AM, Ramirez JL, Mohamed SA, Issa H. Highly sensitive interdigitated thermistor based on PEDOT:PSS for human body temperature monitoring. *Flex Print Electron.* 2022;7(4):045012. doi: 10.1088/2058-8585/acaabc

50. Jung EM, Lee SW, Kim SH. Printed ion-gel transistor using electrohydrodynamic (EHD) jet printing process. *Org Electron.* 2018;52:123-129. doi: 10.1016/j.orgel.2017.10.013

51. Tang X, Kwon HJ, Ye HQ, et al. Enhanced solvent resistance and electrical performance of electrohydrodynamic jet printed PEDOT:PSS composite patterns: Effects of hardeners on the performance of organic thin-film transistors. *Phys Chem Chem Phys.* 2019;21(46):25690-25699. doi: 10.1039/C9CP04864B

52. Park SH, Kim J, Lee SY, et al. Organic thin-film transistors with sub-10-micrometer channel length with printed polymer/carbon nanotube electrodes. *Org Electron.* 2018;52:165-171. doi: 10.1016/j.orgel.2017.10.023

53. Lim S, Park SH, An TK, Lee HS, Kim SH. Electrohydrodynamic printing of poly(3,4-ethylenedioxythiophene):poly(4-styrenesulfonate) electrodes with ratio-optimized surfactant. *Rsc Adv.* 2016;6(3):2004-2010. doi: 10.1039/C5RA19462H

54. Park SH, Kim J, Park CE. Optimization of electrohydrodynamic-printed organic electrodes for bottom-contact organic thin film transistors. *Org Electron.* 2016;38:48-54. doi: 10.1016/j.orgel.2016.07.040

55. Chen J, Wu T, Zhang L, Tang C, Yang X. Flexible conductive patterns using electrohydrodynamic jet printing method based on high-voltage electrostatic focusing lens. *Int J Adv Manuf Technol.* 2023;127:4321-4329. doi: 10.1007/s00170-023-11833-z

56. Chang JK, He JK, Lei Q, Li D. Electrohydrodynamic printing of microscale PEDOT:PSS-PEO features with tunable conductive/thermal properties. *ACS Appl Mater Interfaces.* 2018;10(22):19116-19122. doi: 10.1021/acsami.8b04051

57. Balasankar A, Anbazhakan K, Arul V, et al. Recent advances in the production of pharmaceuticals using selective laser sintering. *Biomimetics.* 2023;8(4):330. doi: 10.3390/biomimetics8040330

58. Gao BW, Zhao HJ, Peng LQ, Sun Z. A review of research progress in selective laser melting (SLM). *Micromachines.* 2023;14(1):57. doi: 10.3390/mi14010057

59. Heo DN, Lee SJ, Timsina R, Qiu X, Castro NJ, Zhang LG. Development of 3D printable conductive hydrogel with crystallized PEDOT:PSS for neural tissue engineering. *Mater Sci Eng: C.* 2019;99:582-590. doi: 10.1016/j.msec.2019.02.008

60. Scordo G, Bertana V, Scaltrito L, et al. A novel highly electrically conductive composite resin for stereolithography. *Mater Today Commun.* 2019;19:12-17. doi: 10.1016/j.mtcomm.2018.12.017

61. Zhu H, Hu XC, Liu BH, Chen Z, Qu S. 3D printing of conductive hydrogel-elastomer hybrids for stretchable electronics. *ACS Appl Mater Interfaces.* 2021;13(49):59243-59251. doi: 10.1021/acsami.1c17526

62. Borghetti M, Serpelloni M, Sardini E. Mechanical behavior of strain sensors based on PEDOT:PSS and silver nanoparticles inks deposited on polymer substrate by inkjet printing. *Sensor Actuat A-Phys.* 2016;243:71-80. doi: 10.1016/j.sna.2016.03.021

63. Wuhao Z, Zhou P, Sun L, Liu L, Zhao MS, Yu H. Flexible wearable sensor based on graphene/PEDOT:PSS composite material. *Scientia Sinica Technologica.* 2019;49(7):851-860.

64. Saidina DS, Mariatti M, Zubir, SA, Fontana S, Hérold C. Performance of graphene hybrid-based ink for flexible

electronics. *J Mater Sci: Mater Electron.* 2019;30(22): 19906-19916.
doi: 10.1007/s10854-019-02357-y

65. Cruz S, Rocha LA, Viana JC. Piezo-resistive behaviour at high strain levels of PEDOT:PSS printed on a flexible polymeric substrate by a novel surface treatment. *J Mater Sci: Mater Electron.* 2017;28(3):2563-2573.
doi: 10.1007/s10854-016-5832-3

66. Tetsu Y, Yamagishi K, Kato A, et al. Ultrathin epidermal strain sensor based on an elastomer nanosheet with an inkjet-printed conductive polymer. *Appl Phys Express.* 2017;10(8):087201.
doi: 10.7567/APEX.10.087201

67. Kang TK. Inkjet printing of highly sensitive, transparent, flexible linear piezoresistive strain sensors. *Coatings.* 2021;11(1):51.
doi: 10.3390/coatings11010051

68. Li Z, Li YR, Wang ZW, et al. 3D-printable and multifunctional conductive nanocomposite with tunable mechanics inspired by sesame candy. *Nano Energy.* 2023;108:108116.
doi: 10.1016/j.nanoen.2023.108166

69. Lu Y, Yang HR, Diao YF, et al. Solution-processable PEDOT particles for coatings of untreated 3D-printed thermoplastics. *ACS Appl Mater Interfaces.* 2023;15(2):3433-3441.
doi: 10.1021/acsami.2c18328

70. Jabbar F, Soomro AM, Lee JW, et al. Robust fluidic biocompatible strain sensor based on PEDOT:PSS/CNT composite for human-wearable and high-end robotic applications. *Sens Mater.* 2020;32(12):4077-4093.
doi: 10.18494/SAM.2020.3085

71. Mirza F, Sahasrabuddhe RR, Baptist JR, Wijesundara MBJ, Lee WH, Popa D. Piezoresistive pressure sensor array for robotic skin. In: *Proceedings of the Sensors for Next-Generation Robotics III*, 98590K; 2016.
doi: 10.1117/12.2225411

72. Das SK, Baptist JR, Sahasrabuddhe R, Le WHH, Popa D. Package analysis of 3D-printed piezo-resistive strain gauge sensors. In: *Proceedings of the* Sensors for Next-Generation Robotics III, 985905; 2016.
doi: 10.1117/12.2224352

73. Shao YW, Zhang Q, Zhao Y, et al. Flexible pressure sensor with micro-structure arrays based on PDMS and PEDOT:PSS/PUD&CNTs composite film with 3D printing. *Materials.* 2021;14(21):6499.
doi: 10.3390/ma14216499

74. Karagiorgis X, Ntagios M, Skabara P, Dahiya R. Elastomeric foam-based soft capacitive pressure sensors using direct ink writing. *IEEE J Flex Electron.* 2023;2(2):175-182.
doi: 10.1109/JFLEX.2023.3264190

75. Khan S, Ali S, Khan A, Bermak A. Developing pressure sensors from impregnated textile sandwiched in inkjet-printed electrodes. *J Mater Sci: Mater Electron.* 2021;33(1):541-553.
doi: 10.1007/s10854-021-07325-z

76. Kraft U, Molina-Lopez F, Son D, Bao Z, Murmann B. Ink development and printing of conducting polymers for intrinsically stretchable interconnects and circuits. *Adv Electron Mater.* 2020;6(1):1900681.
doi: 10.1002/aelm.201900681

77. Cheng XY, Peng SQ, Wu LX, Sun QF. 3D-printed stretchable sensor based on double network PHI/PEDOT:PSS hydrogel annealed with cosolvent of H_2O and DMSO. *Chem Eng J.* 2023;470:144058.
doi: 10.1016/j.cej.2023.144058

78. Lo LW, Zhao JY, Wan HC, Wang Y, Chakrabartty S, Wang C. An inkjet-printed PEDOT:PSS-based stretchable conductor for wearable health monitoring device applications. *ACS Appl Mater Interfaces.* 2021;13(18):21693-21702.
doi: 10.1021/acsami.1c00537

79. Basak I, Nowicki G, Ruttens B, et al. Inkjet printing of PEDOT:PSS based conductive patterns for 3D forming applications. *Polymers.* 2020;12(12):2915.
doi: 10.3390/polym12122915

80. Shen ZQ, Zhang ZL, Zhang NB, et al. 2022. High-Stretchability, Ultralow-Hysteresis Conducting Polymer Hydrogel Strain Sensors for Soft Machines. *Adv Mater,* 34 (32):2203650.
doi: 10.1002/adma.202203650

81. Mousavi S, Thai MT, Amjadi M, et al. Unidirectional, highly linear strain sensors with thickness-engineered conductive films for precision control of soft machines. *J Mater Chem A.* 2022;10(26):13673-13684.
doi: 10.1039/D2TA02064E

82. Kim T, Kim D, Joo Y, Park J, Yoon J, Hong Y. Crack propagation design in transparent polymeric conductive films via carbon nanotube fiber-reinforcement and its application for highly sensitive and mechanically durable strain sensors. *Smart Mater Struct.* 2019;28(2):025008.
doi: 10.1088/1361-665X/aaf0e9

83. Shao YW, Zhao YL, Liu J, et al. Flexible force sensor with micro-pyramid arrays based on 3D printing. *IEEE Sens.* 2018;1-4.
doi: 10.1109/ICSENS.2018.8589555

84. Nair RR. Glucose sensing and hybrid instrumentation based on printed organic electrochemical transistors. *Flex Print Electron.* 2020;5(1):015001.
doi: 10.1088/2058-8585/ab63a0

85. Ramli NI, Abd-Wahab MF, Salim WWAW. Characterization of enzymatic glucose biosensor in buffer solution, in artificial saliva, and in potassium ferricyanide by linear sweep voltammetry. *AIP Conf Proc.* 2018;2031(1):020037.
doi: 10.1063/1.5066993

86. Bihar E, Wustoni S, Pappa AM, Salama KN, Baran D, Inal S. A fully inkjet-printed disposable glucose sensor on paper. *npj Flex Electron.* 2018;2(1):30.
doi: 10.1038/s41528-018-0044-y

87. Khan S, Ali S, Khan A, Wang B, Bermak A. Printing sensors on biocompatible substrates for selective detection of glucose. *IEEE Sens J.* 2021;21(4):4167-4175. doi: 10.1109/JSEN.2020.3032539

88. Nolan JK, Nguyen TNH, Le KVH, DeLong LE, Lee H. Simple fabrication of flexible biosensor arrays using direct writing for multianalyte measurement from human astrocytes. *SLAS Technol.* 2019;25(1):33-46. doi: 10.1177/2472630319888442

89. Majak D, Fan JX, Gupta M. Fully 3D printed OECT based logic gate for detection of cation type and concentration. *Sensor Actuat B-Chem.* 2019:286:111-118. doi: 10.1016/j.snb.2019.01.120

90. Nair RR. Organic electrochemical transistor on paper for the detection of halide anions in biological analytes. *Flex Print Electron.* 2020;5(4):045004. doi: 10.1088/2058-8585/abc9c9

91. Cavallo A, Losi P, Buscemi M, et al. Biocompatible organic electrochemical transistor on polymeric scaffold for wound healing monitoring. *Flex Print Electron.* 2022;7(3):035009. doi: 10.1088/2058-8585/ac84ec

92. Setti L, Fraleoni-Morgera A, Mencarelli I, Filippini A, Ballarin B, Di Biase M. An HRP-based amperometric biosensor fabricated by thermal inkjet printing. *Sensor Actuat B-Chem.* 2007;126(1):252-257. doi: 10.1016/j.snb.2006.12.015

93. Uzuncar S, Kac H, Ak M. Electro-templating of prussian blue nanoparticles in PEDOT:PSS and soluble silkworm protein for hydrogen peroxide sensing. *Talanta.* 2022;252: 123841. doi: 10.1016/j.talanta.2022.123841

94. Phongphut A, Sriprachuabwong C, Wisitsoraat A, Tuantranont A, Prichanont A, Sritongkham P. A disposable amperometric biosensor based on inkjet-printed Au/PEDOT-PSS nanocomposite for triglyceride determination. *Sensor Actuat B-Chem.* 2013;178:501-507. doi: 10.1016/j.snb.2013.01.012

95. Beduk T, Bihar E, Surya SG, Castillo AN, Inal S, Salama KN. A paper-based inkjet-printed PEDOT:PSS/ZnO sol-gel hydrazine sensor. *Sensor Actuat B-Chem.* 2020;306:127539. doi: 10.1016/j.snb.2019.127539

96. Zeng RJ, Wang WJ, Chen MM, et al. CRISPR-Cas12a-driven MXene-PEDOT:PSS piezoresistive wireless biosensor. *Nano Energy.* 2021;82:105711. doi: 10.1016/j.nanoen.2020.105711

97. Majak D, Fan JX, Kang S, Gupta M. Delta-9-tetrahydrocannabinol (Delta(9)-THC) sensing using an aerosol jet printed organic electrochemical transistor (OECT). *J Mater Chem B.* 2021;9(8):2107-2117. doi: 10.1039/D0TB02951C

98. Amr AGE, Kamel AH, Almehizia AA, Sayed AYA, Elsayed EA, Abd-Rabboh HSM. Paper-based potentiometric sensors for nicotine determination in smokers' sweat. *ACS Omega.* 2021;6(17):11340-11347. doi: 10.1021/acsomega.1c00301

99. Kuzubasoglu BA, Sayar E, Bahadir SK. Inkjet-printed CNT/PEDOT:PSS temperature sensor on a textile substrate for wearable intelligent systems. *IEEE Sens J.* 2021;21(12): 13090-13097. doi: 10.1109/JSEN.2021.3070073

100. Soni M, Bhattacharjee M, Ntagio M, Dahiya R. Printed temperature sensor based on PEDOT: PSS-graphene oxide composite. *IEEE Sens J.* 2020;20(14):7525-7531. doi: 10.1109/JSEN.2020.2969667

101. Wang YF, Sekine T, Takeda Y., et al. Fully printed PEDOT:PSS-based temperature sensor with high humidity stability for wireless healthcare monitoring. *Sci Rep.* 2020;10(1):2467. doi: 10.1038/s41598-020-59432-2

102. Aidit SN, Rezali FAM, Nor NHM, Yusoff N. Hydrothermal synthesis of zinc oxide/PEDOT:PSS composite for flexible temperature sensor application. *Flex Print Electron.* 2023;8(2):025008. doi: 10.1088/2058-8585/acd06e

103. Wang P, Yu W, Li GX, Meng C, Guo S. Printable, flexible, breathable and sweatproof bifunctional sensors based on an all-nanofiber platform for fully decoupled pressure-temperature sensing application. *Chem Eng J.* 2022;452:139174. doi: 10.1016/j.cej.2022.139174

104. Guo H, Song J, Zhang X. Research and fabrication and test of flexible temperature sensor based on fabric substrate. *Transduc Microsyst Technol.* 2022;41(6):86-89,93.

105. Lee JW, Choi Y, Jiang J, Yeom SH, Lee W, Ju BK. High sensitivity flexible paper temperature sensor and body-attachable patch for thermometers. *Sensor Actuat A-Phys.* 2020;313:112205. doi: 10.1016/j.sna.2020.112205

106. Roy AL, Beaumont C, Leclerc M. Evaluating polythiophenes as temperature sensing materials using combinatorial inkjet printing. *Flex Print Electron.* 2023;8(1):014002. doi: 10.1088/2058-8585/acc07f

107. Pradhan S, Yadavalli VK. Photolithographically printed flexible silk/PEDOT:PSS temperature sensors. *ACS Appl Electron Mater.* 2021;3(1):21-29. doi: 10.1021/acsaelm.0c01017

108. Bucher T, Huber R, Eschenbaum C, Mertens A, Lemmer U, Amrouch H. Printed temperature sensor array for high-resolution thermal mapping. *Sci Rep.* 2022;12(1):14231. doi: 10.1038/s41598-022-18321-6

109. Wang G, Zhang Y, Yang H. Fast-response humidity sensor based on laser printing for respiration monitoring. *RSC Adv.* 2020;10(15):8910-8916. doi: 10.1039/C9RA10409G

110. Galliani M, Ferrari LM, Ismailova E. Interdigitated organic sensor in multimodal facemask's barrier integrity and wearer's respiration monitoring. *Biosensors.* 2022;12(5):305. doi: 10.3390/bios12050305

111. Tekcin M, Sayar E, Yalcin MK. Wearable and flexible humidity sensor integrated to disposable diapers for wetness monitoring and urinary incontinence. *Electronics.* 2022;11(7):1025. doi: 10.3390/electronics11071025

112. Hassan G, Sajid M, Choi C. Highly sensitive and full range detectable humidity sensor using PEDOT:PSS, methyl red and graphene oxide materials. *Sci Rep.* 2019;9: 15227. doi: 10.1038/s41598-019-51712-w

113. Siddiqui GU, Sajid M, Ali J. Wide range highly sensitive relative humidity sensor based on series combination of MoS_2 and PEDOT:PSS sensors array. *Sensor Actuat B-Chem.* 2018;266:354-363. doi: 10.1016/j.snb.2018.03.134

114. Conti S, Nepa F, Pascoli SD. Hybrid flexible NFC sensor on paper. *IEEE J Flex Electron.* 2023;2(1):4-10. doi: 10.1109/JFLEX.2023.3238682

115. Barmpakos D, Tsamis C, Kaltsas G. Multi-parameter paper sensor fabricated by inkjet-printed silver nanoparticle ink and PEDOT:PSS. *Microelectron Eng.* 2020;225: 111266. doi: 10.1016/j.mee.2020.111266

116. Xu SY, Li TY, Ren HX, Mao X, Ye X, Liang B. PEDOT:PSS hydrogel based flexible electrodes for wearable ECG monitoring. *IEEE Sensors.* 2020;20242466.

117. Achilli A, Bonfiglio A, Pani D. Design and characterization of screen-printed textile electrodes for ECG monitoring. *IEEE Sens J.* 2018;18(10):4097-4107.

118. Sinha SK, Noh Y, Reljin N, et al. Screen-printed PEDOT:PSS electrodes on commercial finished textiles for electrocardiography. *ACS Appl Mater Interfaces.* 2017;9(43):37524-37528. doi: 10.1021/acsami.7b09954

119. Zalar P, Saalmink M, Raiteri D, van den Brand J, Smits ECP. Screen-printed dry electrodes: basic characterization and benchmarking. *Adv Eng Mater.* 2020;22(11):2000714. doi: 10.1002/adem.202000714

120. Shathi MA, Chen MZ, Khoso NA, Deb H, Ahmed A, Sai WS. All organic graphene oxide and Poly (3, 4-ethylene dioxythiophene) - Poly (styrene sulfonate) coated knitted textile fabrics for wearable electrocardiography (ECG) monitoring. *Synth Met.* 2020;263:116329. doi: 10.1016/j.synthmet.2020.116329

121. Li TY, Liang B, Ye ZC, et al. An integrated and conductive hydrogel-paper patch for simultaneous sensing of Chemical-Electrophysiological signals. *Biosens Bioelectron.* 2021;198:113855. doi: 10.1016/j.bios.2021.113855

122. Picchio ML, Gallastegui A, Casado N, et al. Mixed ionic and electronic conducting eutectogels for 3D-printable wearable sensors and bioelectrodes. *Adv Mater Technol.* 2022;7(10):2101680. doi: 10.1002/admt.202101680

123. Lidon-Roger JV, Prats-Boluda G, Ye-Lin Y, Garcia-Casado J, Garcia-Breijo E. Textile concentric ring electrodes for ECG recording based on screen-printing technology. *Sensors.* 2018;18(1):300. doi: 10.3390/s18010300

124. Pless CJ, Nikzad S, Papiano I, et al. Soft electronic block copolymer elastomer composites for multi-material printing of stretchable physiological sensors on textiles. *Adv Eng Mater.* 2023;9(5):2201173. doi: 10.1002/aelm.202201173

ACCSCIENCE PUBLISHING

International Journal of Bioprinting

REVIEW ARTICLE

DNA-functionalized hyaluronic acid bioink in cartilage engineering: a perspective

Mengmeng Li[1,2†], Yan Wu[1,2†], Miaomiao Wang[1,2†], Wencai Zhang[3*], Peiran Song[1,2*], and Jiacan Su[1,2,4*]

[1]Organoid Research Center, Institute of Translational Medicine, Shanghai University, Shanghai, China

[2]National Center for Translational Medicine (Shanghai) SHU Branch, Shanghai University, Shanghai, China

[3]Department of Orthopedics, First Affiliated Hospital, Jinan University, Guangzhou, China

[4]Department of Orthopedics, Xinhua Hospital Affiliated to Shanghai Jiao Tong University School of Medicine, Shanghai, China

(This article belongs to the *Special Issue: Application of 3D Bioprinting Materials: Hyaluronic Acid-Based Bioink*)

Abstract

Degenerative osteoarthritis, a common sequela of articular cartilage defect, significantly impacts the quality of life of millions of individuals worldwide. Three-dimensional (3D) bioprinting has emerged as an advanced tissue engineering strategy, offering precise spatial arrangements of cells, hydrogels, and bioactive cues. Hyaluronic acid (HA) is a crucial component of bioink designed for fabricating cartilage tissue. However, creating a bioink that closely mimics the cartilaginous extracellular matrix (ECM) still remains a challenge. HA hydrogels have limitations in recapitulating tunable mechanical properties, stimuli responsiveness, and flexibility in ligands' adhesion akin to those of native tissues. In recent years, DNA has emerged as a smart biomaterial that endows hydrogels with tunable properties and allows for precise structural customization of the hydrogels due to its unique programmability. Integrating reversible DNA linkages, reconfigurable DNA architectures, DNA plasmid, and targeted DNA aptamers into HA hydrogels allows them to respond to the extracellular environment and express desired molecules, making them ideal artificial ECMs for 3D bioprinting of cartilage tissue. This review targets this challenge by highlighting the characteristics of DNA moieties designed as reversible crosslinkers, responsive units, and adhesion ligands to functionalize HA hydrogels. Furthermore, we offer perspectives on how DNA-functionalized HA hydrogels can be harnessed to create dynamic and biomimetic bioink capable of recapitulating the more complex functions required for cartilage tissue engineering.

Keywords: Hyaluronic acid; DNA functionalization; Cartilage regeneration; Tissue engineering

†These authors contributed equally to this work.

***Corresponding authors:**
Wencai Zhang (wczhang@jnu.edu.cn)

Peiran Song (songpeiran@163.com)

Jiacan Su (drsujiacan@163.com)

Citation: Li M, Wu Y, Wang M, Zhang W, Song P, Su J. DNA-functionalized hyaluronic acid bioink in cartilage engineering: a perspective. *Int J Bioprint*. 2024;10(2):1814. doi: 10.36922/ijb.1814

Received: August 24, 2023
Accepted: November 21, 2023
Published Online: January 16, 2024

1. Introduction

Articular cartilage, a load-bearing connective tissue located at the bone interfaces, facilitates smooth and frictionless skeletal movements. However, cartilage defects due to traumatic injury or disease can lead to its degradation, resulting in widespread cartilage loss and potentially causing degenerative osteoarthritis.[1-3] Adopting different tissue engineering

strategies, incorporating stem cells, utilizing advanced engineering techniques, and creating scaffold designs are among the techniques aimed at creating biostructures that are optimally conducive to cartilage regeneration.[4-6] Among these approaches, three-dimensional (3D) bioprinting has emerged as a potent tool, enabling precise manipulation of the spatial arrangement of cells,[7-9] biomaterials,[10-12] and bioactive cues[13-15] within three dimensions, thus emulating the intricate structure of natural tissues. Considering the distinctive tissue architecture of articular cartilage, such as low cell density and lack of vasculature, much emphasis is being placed on the careful selection of polymeric biomaterials for cartilage tissue engineering, among which hyaluronic acid (HA)—a pivotal polysaccharide constituent of the cartilage ECM and synovial fluid—has gained prominence.[16-18] HA offers exceptional biocompatibility, biodegradability, and low immunogenicity, playing a crucial role in maintaining cartilage structural integrity through water retention and interactions with aggrecan and type II collagen.[19] Moreover, HA supplementation in patients with degenerative osteoarthritis promotes the production and retention of matrix components, contributing to cartilage homeostasis.[20-22] Although HA-based hydrogels possess appealing bioactive properties, they still have limitations in recapitulating tunable mechanical properties, stimuli responsiveness, and flexibility in ligands' adhesion akin to those of native tissues.

Regenerating cartilage tissue is a complex biological process involving intricate interactions between cells and bioactive factors within the matrix. The extracellular matrix (ECM) plays a pivotal role in the cellular microenvironment, encompassing organized, anisotropic, and dynamic structures that deliver essential physical and chemical cues through interactions with cells.[23-25] Constructing 3D structures that closely mimic the natural ECM is essential for cartilage tissue regeneration. The ideal HA-based bioink should possess tunable physical and chemical properties, resembling the elastic modulus and dynamic characteristics that respond to changes in the cellular metabolic microenvironment. Additionally, adhesive ligands, similar to those in the native ECM, should be incorporated into HA-based hydrogels to recognize and interact with cell for desired biological functions.

DNA, traditionally known for its role in storing, replicating, and transmitting genetic information within cells, has emerged as a versatile, non-genetic biomaterial for constructing or functionalizing hydrogels.[26,27] Notably, certain well-designed DNA hydrogels, such as those driven by DNAzyme catalysis,[26] light,[28] or magnetism,[29] could convert chemical energy, magnetic energy, or light energy into mechanical energy, and dynamically modulate the morphology and properties of the hydrogel network. DNA hydrogels offer unique programmability due to Watson–Crick base pairing, allowing the creation of precisely tailored structures, adjustable mechanical properties,[30,31] functional and targeted molecular recognition motifs,[28,32,33] stimuli responsiveness,[29,34-35] and exceptional biocompatibility.[36] The substantial transformation undergone by DNA-functionalized hydrogels is marked by the integration of DNA molecules as crosslinkers or functional components and their release with programmable, versatile, and responsive characteristics, making them well-suited for applications in bioprinting and tissue engineering. Initially, oligonucleotides were covalently attached to vinyl polymers, enabling self-assembly via complementary base pairing.[37] Subsequent advancements incorporated DNA as crosslinkers, leading to smart hydrogels. Notable milestones also include the development of a supramolecular peptide-DNA hydrogel, capable of retaining shape and preserving cell viability, for 3D bioprinting.[38] Another innovation is represented by a stimuli-responsive G-quadruplex-crosslinked pNIPAM hydrogel capable of reversible transitions.[39] In 2021, DNA aptamers were employed to functionalize bioink for 3D-printing cell-specific scaffold, which was utilized to promote cartilage formation.[40] A recent development involves a dynamic DNA-crosslinked matrix formed using a synthetic DNA library-based hydrogel with ultra-high-molecular-weight polymers.[41] This technology allows precise control over viscoelasticity, thermodynamics, and kinetics, mimicking living tissue properties. Although research on DNA-functionalized bioinks is in its early stages, these materials show great potential in constructing ideal artificial ECMs, enabling the formation of artificial cartilage tissues *in vitro* and facilitating advanced tissue regeneration *in vivo*. This review outlines the characteristics and functional mechanisms of DNA sequence moieties, including reversible DNA linkages, reconfigurable DNA architectures, DNA plasmid, and targeted DNA aptamers, that are ideal for functionalizing HA hydrogels to create dynamic bioinks for cartilage tissue engineering (Figure 1). With special emphasis, this review describes the current state of strategies used to functionalize hydrogels with DNA molecules, and exclusive advances of DNA-functionalized HA hydrogels as dynamic and smart bioinks for engineering cartilage tissue. Although DNA-functionalized bioinks are in their infancy, this review article aims to provide directions for guiding insightful research studies in this field.

2. Action of DNA moieties

2.1. DNA as a crosslinker

The intrinsic properties of DNA in encoding sequences and its highly accurate structural assembly are keys to

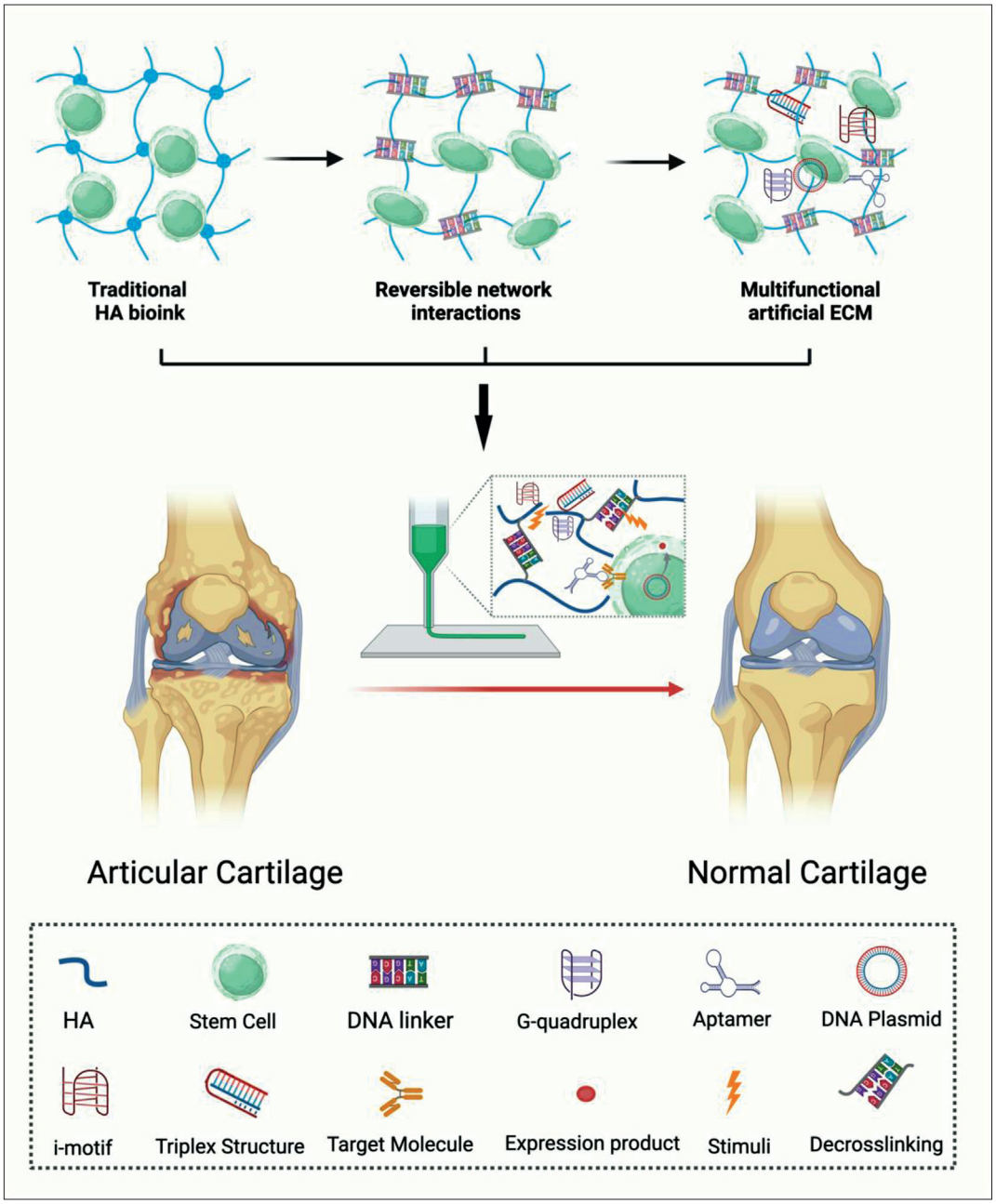

Figure 1. Schemvatic illustration of DNA-functionalized HA bioink for cartilage regeneration. Created using BioRender.com.

manipulating both the microscopic and macroscopic characteristics of DNA-based hydrogels. DNA hydrogels can be obtained through various gelation strategies, including chemical or physical crosslinking. Chemical crosslinking is involved in the formation of the intermolecular covalent bonds within DNA, establishing stable and irreversible connections that preserve the mechanical resilience, stability, and shape fidelity. On the other hand, physical crosslinking capitalizes on non-covalent bonds including hydrogen bonds between complementary DNA sequences, electrostatic interactions as well as metal–ion coordination for crosslinking purposes. These bonds offer a dynamic and adjustable nature to the structure.[42,43] When it comes to the fabrication of tunable DNA hydrogels, the gelation strategies can be categorized into three types: assembly guided by DNA sticky ends, assembly-induced enzymatically, and assembly based on hybridization chain reaction.

2.1.1. Assembly guided by DNA sticky ends

Sticky ends of a DNA molecule refer to the protruding parts of one strand beyond its complementary strand within the double helix. This structural characteristic allows the DNA chains to engage in hybridization, leveraging the principle of base pair complementarity. Based on this concept, a highly entangled 3D DNA hydrogel was fabricated through the self-assembly of short linear double-stranded DNA (dsDNA) units, each equipped with sticky ends[44] (Figure 2a). DNA hydrogels can also be fabricated via branched DNA gelation systems. The assembly of Y-shaped DNA units was accomplished by means of i-motif DNA structures forming at the sticky ends. As a consequence, the fabricated DNA hydrogels exhibited prompt responsiveness to alterations in environmental pH, enabling controlled encapsulation and release cargos.[45] DNA hydrogels with properties of thermal and enzymatic responsiveness can be hybridized via sticky ends that affix to two types of building blocks, such as linear double-stranded DNA and Y-shaped DNA. This adaptability of dynamic properties was achieved through precise modulation of the ratio of these constituent building blocks[46] (Figure 2b). This method relies on hybridization reactions between single-stranded DNA molecules with complementary sequences to create a 3D network structure. The core advantages of this method lie in its simplicity, speed, and controllability, which allow for adjustments in hydrogel porosity and stiffness through an alteration to the length, type, and concentration of DNA molecules. However, a drawback of this method is its reduced stability and responsiveness, marked by its susceptibility to factors such as nucleases and temperature fluctuations, which could lead to hydrogel disassembly or annealing.

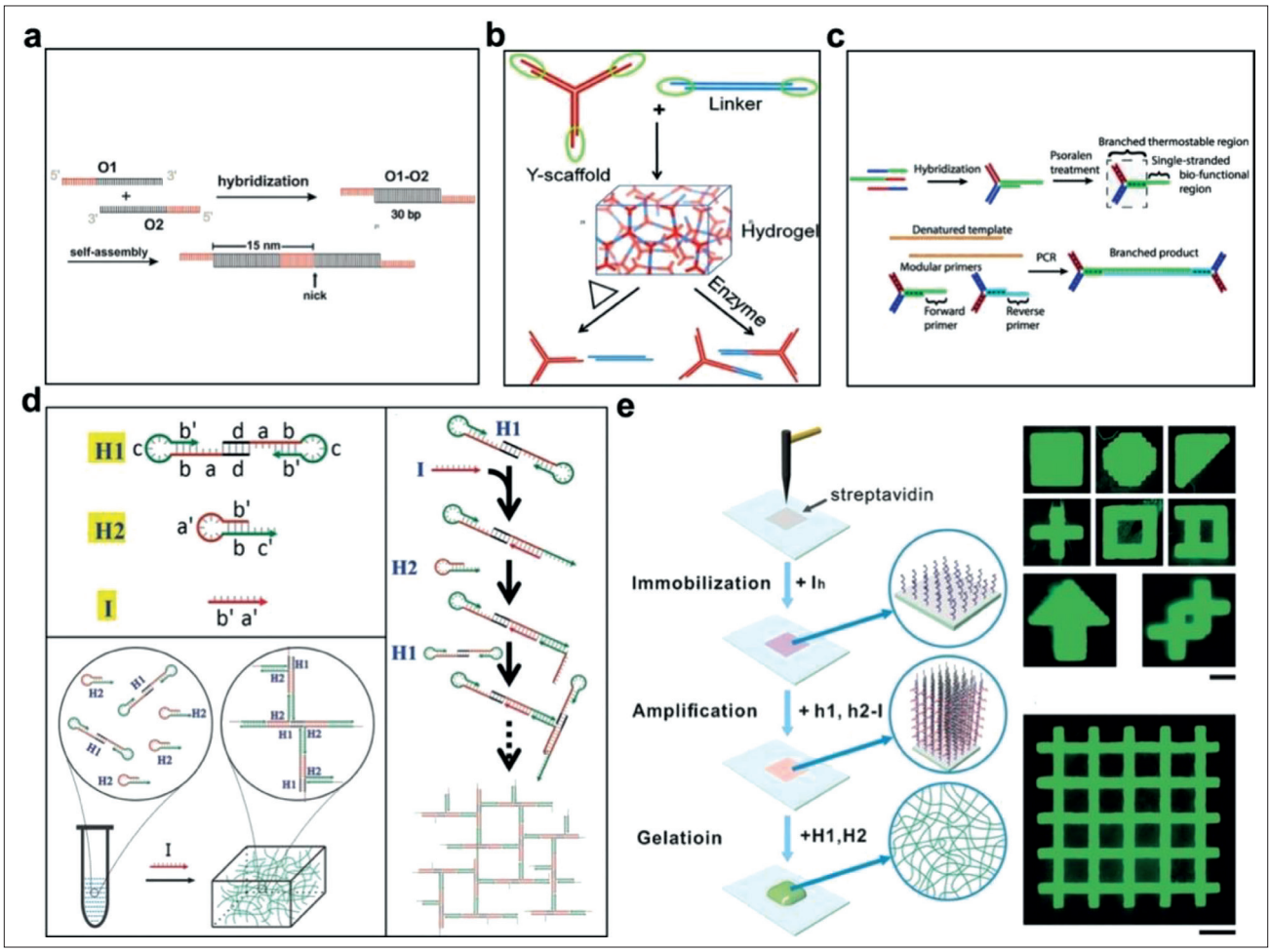

Figure 2. Assembly strategies of DNA hydrogels. (a) A pure DNA hydrogel formed by direct assembly of dsDNA monomers with sticky ends. Reprinted with permission from ref.[44] Copyright © 2014 Wiley. (b) Direct assembly of sticky ends of Y-scaffold and linkers for pure DNA hydrogel. Reprinted with permission from ref.[46] Copyright © 2011 Wiley. (c) DNA hydrogels by crosslinking and subsequent PCR primer extension. Reprinted with permission from ref.[48] Copyright © 2013 Wiley. (d) DNA initiator-triggered clamped hybridization chain reaction self-assembly process. Reprinted with permission from ref.[49] Copyright © 2017 Wiley. (e) Surface-initiated DNA hydrogel formation. Reprinted with permission from ref.[49] Copyright © 2017 Wiley.

2.1.2. Assembly induced enzymatically

Enzymes also play a pivotal role as essential molecular agents in facilitating the assembly of DNA hydrogels.[47] For example, by using Taq polymerase, coupled with a pair of thermostable Y-shaped DNA building blocks, thermostable DNA hydrogels could be synthesized via polymerase chain reaction (PCR)[48] (Figure 2c). Firstly, the DNA was crosslinked with psoralen and extended into a dumbbell shape. Subsequently, these oligonucleotides formed covalently interstranded, branched DNA nanostructures, highlighting the crucial role of polymerase enzymes in the efficient production of robust DNA hydrogels. The two Y-structured DNA units underwent psoralen treatment, resulting in crosslinked structures. These crosslinked entities served as modular primers for PCR.[48] Moreover, the utilization of T4 ligase-mediated reactions enables the effective crosslinking of branched X-, Y-, and T-shaped DNAs, resulting in the formation of an interconnected gel system.[47] The resulting DNA hydrogel leverages this enzyme-driven, ligase-mediated crosslinking mechanism under physiological conditions, showcasing its potential for applications such as controlled substance encapsulation. Different swelling profiles of DNA hydrogels can be achieved by adjusting the initial concentration and types of building blocks. This method employs reactions of enzymes such as ligases or polymerases to connect DNA molecules with different end sequences or branched structures to form a 3D network structure. The advantages of this method lie in its performance under physiological conditions and the ability to adjust crosslinking density and mechanical strength by selecting different enzyme types and concentrations. However, the drawbacks of this method include the complexity of hydrogel preparation process, which necessitates precise control of enzyme activity and reaction time, and the susceptibility to factors such as enzyme residues or inhibitors.

2.1.3. Assembly based on hybridization chain reaction

Hybridization chain reaction (HCR) is a unique, isothermal DNA strand displacement process involving two hairpin structures. It facilitates the formation of cross-opening polymer nucleic acid strands, acting as a versatile strategy to fabricate responsive hydrogels endowed with tunable characteristics. For example, DNA initiators, similar to catalysts in chemical synthesis or seeds in crystal growth, were employed to achieve precise temporal and spatial control in gelation process.[49] These initiators direct 3D self-assembly and clamped hybridization, yielding hydrogels with enhanced mechanical properties. Moreover, employing printed, surface-confined DNA initiators, these hydrogels can be patterned into two-dimensional shapes without external constraints to allow for the generation of hydrogels with precisely defined geometry, composition, and arrangement[49] (Figure 2d and e). Hydrogen bonds, rather than covalent bonds, provide major support to the HCR-mediated network in DNA gelation systems, which is endowed with a less rigid but dynamic structure. This method employs HCR between single-stranded DNA molecules with hairpin structures or initiator sequences to form long-chain polymers, which crosslink with polymer chains to create a 3D network structure. The advantages of this method encompass precise control over hydrogel patterns, shapes, responsiveness, and the ability to introduce various functional elements, but this method is tied a time-consuming hydrogel preparation process, which involves multiple reaction steps and purification, and it may be susceptible to impurities or non-specific hybridization.

2.2. DNA as functional units

Beyond their role as crosslinking agents, DNA-functionalized hydrogels can also incorporate reconfigurable DNA architectures and targeted DNA aptamers as responsive and recognition elements,[50,51] such as G-quadruplexes (G4), i-motifs, triplex nucleic acids, plasmid, and aptamers, which facilitate the intelligent and functional regulation of hydrogels. By incorporating different functional elements, DNA hydrogels can achieve structural regulation, molecular recognition, and functional display under different environmental conditions.

2.2.1. G-quadruplex

G-quadruplex and i-motif are both crosslinking modes induced by the secondary structure of DNA, depending on specific base pairing and structural conformation.[52] G-quadruplex is a four-stranded structure formed by guanine (G) bases of DNA. By regulating ion concentration and pH value, the physical and chemical properties of hydrogels can be controlled. Lu et al. explored a novel DNA hydrogel synthesized with acrylamide and G-rich nucleic acid. In the presence of K^+ ions, the nucleic acid crosslinkers formed G-quadruplex structures, enabling reversible hydrogel formation. Furthermore, the authors incorporated hemin into the G-quadruplex hydrogel, endowing it with catalytic activity similar to horseradish peroxidase. By modulating K^+ ions, krypto[2.2.2], temperature, and pH as stimulus factors, the authors could regulate the phase transitions of the hydrogel between solution, hydrogel, and solid states as well as the conductivity and spectral properties of polyaniline[39] (Figure 3a).

2.2.2. i-motif

i-motif is a special structure formed by the pairing of protonated cytosine and guanine under acidic conditions. It can regulate the structural changes of hydrogels[45] (Figure 3b). For example, the incorporation of i-motif structures at the sticky ends of the DNA strands facilitates the formation of DNA hydrogels that respond rapidly to pH

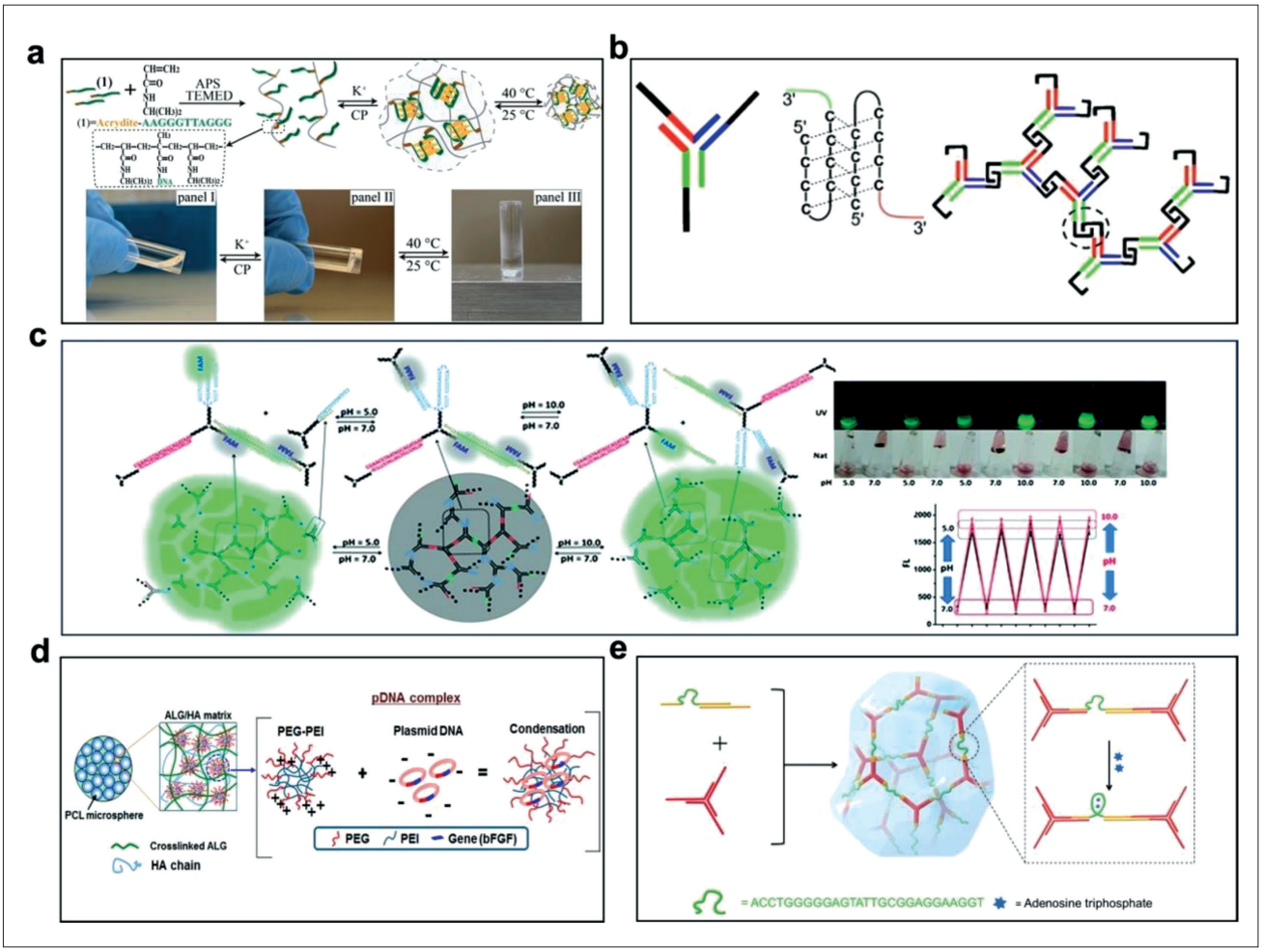

Figure 3. Hydrogels with functional DNA units. (a) Thermosensitive G-quadruplex-crosslinked copolymer hydrogel with reversible solution–hydrogel–solid transitions. Reprinted with permission from ref.[39] Copyright © 2015 Royal Society of Chemistry. (b) pH-responsive DNA hydrogel based on 3D assembly of Y-shaped DNA nanostructure with interlocking i-motif domains. Reprinted with permission from ref.[45] Copyright © 2009 Wiley. (c) pH-activated reversible DNA hydrogels based on triplex structures. Reprinted with permission from ref.[54] Copyright © 2018 Royal Society of Chemistry. (d) Plasmid-complex-encapsulated-loaded alginate/HA hydrogel for *bFGF* delivery. Reprinted with permission from ref.[56] Copyright © 2019 Royal Society of Chemistry. (e) ATP aptamer-modified linker and Y-scaffold DNA hydrogel with conformational transition and mechanical properties. Reprinted with permission from ref.[57] Copyright © 2018 MDPI.

fluctuations. These changes allow the hydrogel to capture and release cargo in a regulated manner. By integrating this i-motif sequence, which undergoes a pH-dependent conformational change, into the DNA hydrogel network, microscopic transitions occur, leading to significant changes in the mechanical properties of the hydrogel. Consequently, this strategy enables the reversible control of the hydrogel's mechanical strength, ranging from 250 Pa to 1000 Pa, proving beneficial for applications such as cell differentiation and tissue engineering.[53]

2.2.3. Triplex structures

The formation of triplex structures relies on the protonation of cytosine-guanine-cytosine (C-G-C+) and thymine-adenine-thymine (T-A-T) base triplets. By adjusting environmental conditions (such as pH), the morphology and properties of hydrogels can be controlled. The C-G-C+ triplexes are formed at a pH of 5.0 and disassemble at a pH of 7.0, while the T-A-T triplexes are formed at a pH of 7.0 and disassemble at a pH of 10.0. These triplex structures afford the DNA structures the ability to perform pH-regulated reversible self-assembly, which allows it to switch between gel and liquid phases[54] (Figure 3c).

2.2.4. DNA plasmid

Among its primary utilities, plasmids are instrumental in the field of recombinant DNA technology. This technique involves the integration of foreign DNA sequences into

plasmids, resulting in the formation of recombinant plasmids that can be introduced into host cells. This procedure requires the use of restriction enzymes to cleave DNA at specific sites, followed by the application of ligases to facilitate the fusion of DNA molecules. By harnessing these methodologies, researchers can construct plasmids containing precise DNA sequences. The inherent capacity of plasmid DNA to carry and independently replicate foreign DNA sequences establishes it as a fundamental tool in genetic engineering. In recent years, DNA plasmids have been introduced into hydrogel materials for tissue regeneration applications. For example, Wang et al. constructed two plasmids that encode mouse vascular endothelial growth factor (VEGF) and transforming growth factor-β1 (TGF-β1), respectively.[55] They combined these plasmids with arginine-modified chitosan (Arg-CS) to form Arg-CS/pDNA nanoparticles, which acted as gene carriers. Next, they incorporated these nanoparticles into a composite hydrogel prepared from N-carboxymethyl chitosan (NCMC) and sodium alginate (SA), forming a gene-activated matrix (GAM). This GAM could achieve long-term and sustained gene release and expression *in vitro* and *in vivo*.[55] Kim et al. combined plasmid DNA (pDNA) encoding mouse *bFGF* gene, which is a growth factor that can promote tissue regeneration, with polyethylenimine-grafted poly(ethylene glycol) (PEI-g-PEG) complex to form a nanoparticle carrier that can protect pDNA from degradation and enhance transfection efficiency.[56] They further loaded the nanoparticles into a mixture hydrogel of alginate (ALG) and hyaluronic acid (HA), which can solidify under mild conditions and release pDNA complex slowly[56] (Figure 3d).

2.2.5. Aptamers

Aptamers are oligonucleotide molecules with high affinity and specificity that are obtained by systematic evolution screening. They can interact with specific target molecules, making hydrogels targeted and specific[57] (Figure 3e). For instance, the adenosine triphosphate (ATP) aptamer, whose 3D structure is designed to precisely match the molecular structure of ATP, can be integrated into the linker DNA to regulate the mechanical properties of the hydrogel. When ATP is present, it is recognized and bound by the aptamer, causing a change in the 3D structure of the aptamer and subsequently forming a stable framework composed of two stacked G-quartets. The formation of this framework triggers a conformational change in the aptamer-DNA, thereby altering the physical properties of the DNA hydrogel, such as its mechanical strength. As a result of the specific interaction between ATP and its corresponding aptamer, the mechanical strength of the hydrogel increases from 204 Pa to 380 Pa. This regulatory mechanism can be achieved by changing the concentration of ATP in the hydrogel, thereby achieving fine control over the mechanical properties of the hydrogel.[57] Additionally, aptamers can be conjugated into DNA hydrogels as targeting recognition molecules to enable selective binding and internalization of target cells by the DNA nanohydrogels, thus achieving targeted gene delivery.

Cartilage ECM is characterized by its intricate structure and multifaceted functions, serving as a source of mechanical, chemical, and biological cues that orchestrate cell behaviors such as proliferation, differentiation, migration, and tissue formation.[58] Consequently, the properties of hydrogels, which act as synthetic ECMs, play a pivotal role in shaping cell functions during cartilage regeneration. Mechanical properties hold particular significance in the context of cartilage regeneration, as this tissue must endure varying loads and directions. Additionally, hydrogels possess the unique capacity to emulate the recognition attributes of natural ECM, which facilitates selective recruitment or release of cells and substances. Notably, the functionalization of hydrogels with DNA molecules allows them to mimic the characteristics of cartilage ECM, inducing differentiation of cells into chondrocytes and enhancing cartilage tissue support. This can be achieved through the introduction of reversible DNA crosslinking that enables the regulation of hydrogel mechanical properties in a reversible or even self-healing manner.[39,52] The incorporation of reconfigurable DNA structures further enhances hydrogel responsiveness, enabling adaptation to complex and dynamic microenvironments and regulation of cell behaviors and fate.[56,57,59] By enhancing the recognition properties of hydrogels, DNA aptamers represent an additional avenue for enabling the selective adsorption and release of target cells or molecules, thereby enhancing the efficiency and quality of cartilage regeneration.[60]

3. DNA-functionalized hyaluronic acid hydrogels

In comparison to pure DNA hydrogels, hybrid DNA hydrogels offer a broader spectrum of applications. Hybrid hydrogels constructed through DNA crosslinking not only retain the inherent biological functions of DNA but also preserve the structural integrity of hydrogels.[59] The energy necessary to break the bonds between complementary DNA base pairs is notably lower compared to the energy required for traditional polymer chains and crosslinking agents. The integration of customizable DNA into polymer gel systems imparts a degree of structural control and property modulation. HA is a linear high-molecular-weight polysaccharide comprising repeating disaccharide units composed of N-acetyl-D-glucosamine and D-glucuronide.

These units are connected by β-(1,3) and β-(1,4) glycosidic bonds. HA encompasses both polar segments with positive and negative charges, as well as non-polar portions lacking charge separation, which contribute to the formation of intermolecular linkages. The fundamental structure of HA consists of a continuous polymer chain covalently linking N-acetyl-D-glucosamine and D-glucuronic acid units.[58] The carboxyl group of glucuronic acid, primary and secondary hydroxyl groups, and N-acetyl group are the three functional groups involved in the chemical modification of HA.[61] To prepare DNA-conjugated HA, DNA strands can be post-modified onto HA by means of EDC-NHS chemistry, Michael addition, click chemistry, etc. to incorporate DNA molecules functionalized with handles like amino-DNA, thiol-DNA, and azide-DNA. The extent of DNA attachment via this approach is contingent on distinct reaction efficiencies and conditions.[59]

HA can be prepared as a derivative of DNA-crosslinked HA hydrogels by chemically modifying groups on the molecular chain. For example, HA reacts with maleic anhydride to form HA-Mal, which then forms a thioether bond with thiol groups in deprotected thiolated oligo-DNA. After mixing HA modified with two complementary single-stranded DNAs, the hybridized complementary strands serve as crosslinking points to form a hydrogel[62] (Figure 4a). Moreover, HA can be activated by EDC (1-ethyl-3-(3-dimethylaminopropyl) carbodiimide) and NHS (N-hydroxysuccinimide), which converted carboxylic acid groups on HA into highly active reaction intermediates that could react with amino-modified nucleic acids. By connecting amino-modified nucleic acids (3) and hairpins (5) to the HA skeleton, copolymers HA-(3) and HA-(5) are formed. Then, nucleic acid (3) in HA-(3) hybridized with equimolar amount of nucleic acid (4), generating crosslinked copolymer HA-(3)/(4). Hairpins (5) also participate in the HCR reaction, forming crosslinking units by complementary base-pairing with hairpins (4). These crosslinking units can stably connect the MOFzyme and the hydrogel. Moreover, hairpins contain the ZEN-

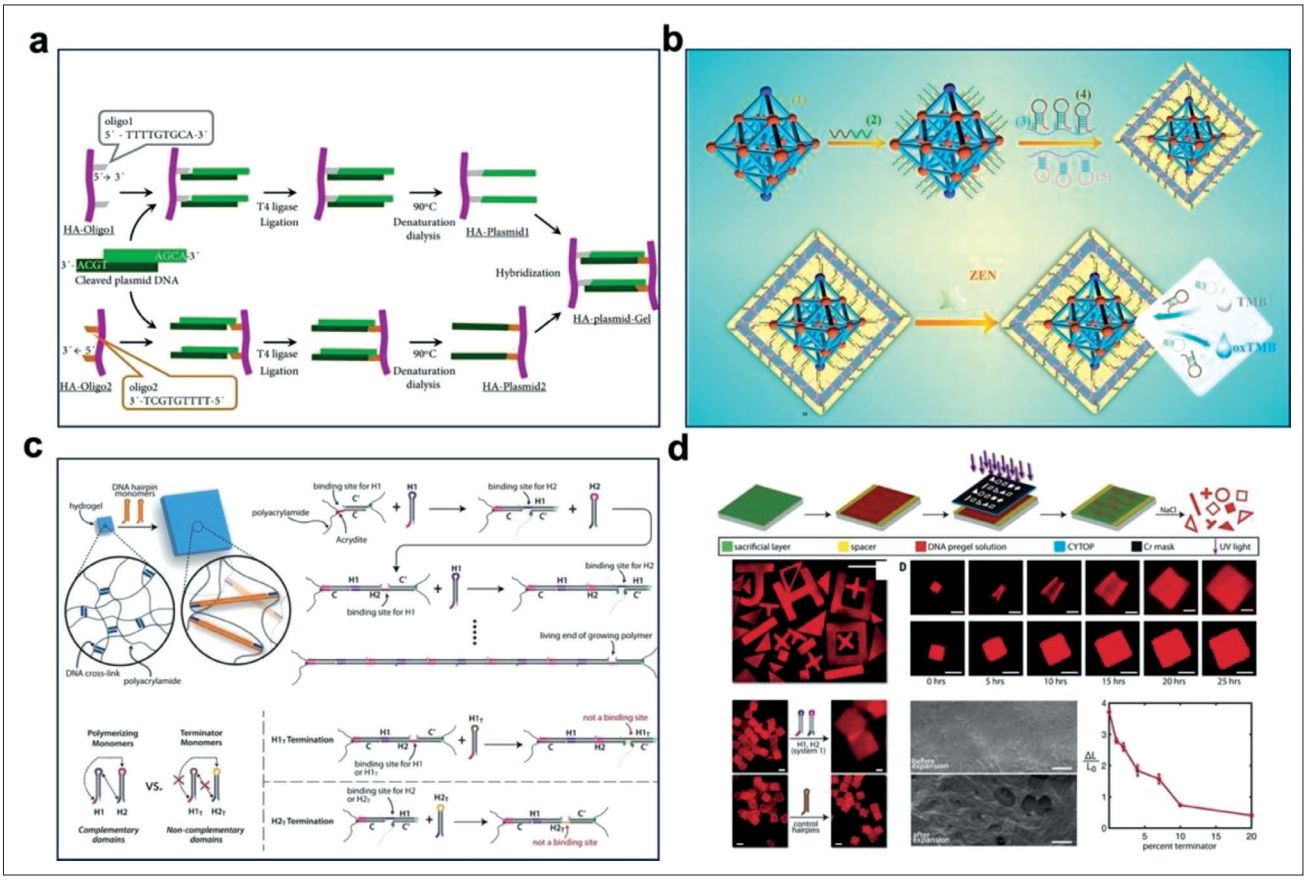

Figure 4. Hydrogels functionalized with DNA moieties. (a) Crosslinking of HA–DNA via cleaved plasmid DNA fragments. Reprinted with permission from ref.[62] Copyright © 2020 Hindawi. (b) DNA–HA hydrogel and bimetallic MOFzyme-based colorimetric aptasensor targeting zearalenone. Reprinted with permission from ref.[63] Copyright © 2022 Elsevier. (c) DNA-directed expansion of DNA-crosslinked polyacrylamide gels. Reprinted with permission from ref.[28] Copyright © 2017 AAAS. (d) Photopatterning and hydrogel expansion. Reprinted with permission from ref.[28] Copyright © 2017 AAAS.

specific aptamer sequence that binds to ZEN, if present, to cause a conformational change of hairpins (5) and trigger the disintegration of the hydrogel[63] (Figure 4b).

The DNA sequences within hybrid hydrogels can also be crosslinked using diverse strategies to attain reversible and mechanical control. For example, two types of functionalized single-stranded DNAs can be copolymerized with polymer monomers to form reversible DNA hybrid hydrogels by introducing R1 sequences complementary to the crosslinking chains.[64,65] In addition, the "hairpin structure" of DNA sequences is used to control the expansion and change shape of hybrid hydrogels. The hairpin structure refers to a structure composed of two complementary DNA fragments; one of which is a "polymerizing hairpin" used to introduce additional monomers and promote hydrogel expansion, while the other is a "terminator hairpin" that does not participate in further DNA crosslinking reactions and limits the expansion process of hydrogels. The final expansion size of hydrogels can be precisely controlled by adjusting the relative concentration of polymerizing and terminator hairpins[28] (Figure 4c and d).

The functionality of DNA hybrid hydrogels can be tailored by integrating specific DNA components, such as reconfigurable DNA architectures for environmental responsiveness, gene transfection, and DNA aptamers for molecular recognition[60,66] (Figure 5). For example, two types of polymer monomers (polyacrylamide chains) have been modified with predesigned hairpins and nucleic acid tethers, respectively. In the presence of a promoter, the hairpin structures hybridized with each other to form double-stranded DNA bridges that crosslinked the copolymer chains into a hydrogel. Notably, the hairpins contained caged sequences of anti-ATP or anti-cocaine aptamers, which could be unlocked by the formation of aptamer–ligand complexes. The nucleic acid tethers contained pH-sensitive duplex units, which could dissociate by forming i-motif structures under acidic conditions. These nucleic acid units provided stimuli-responsive functions to the hydrogel shells.[67] The unique

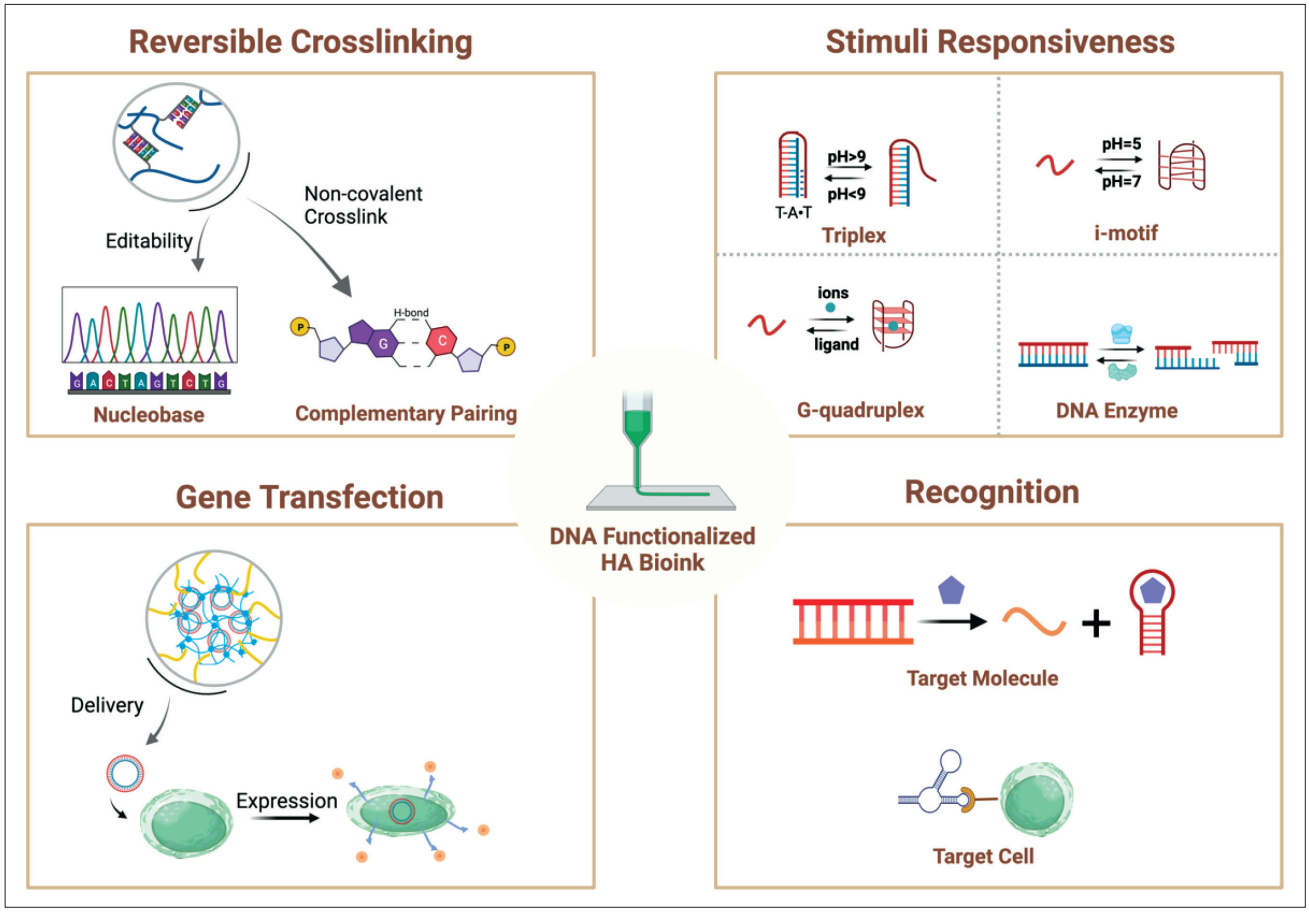

Figure 5. Advantages of DNA-functionalized HA bioink. Created using BioRender.com.

sequences and structures of these DNA elements can encode functional details, imbuing hydrogels with precise and tailored recognition and response to external stimuli. This inherent programmability of DNA affords researchers the flexibility to adeptly design and regulate smart hydrogel.[68] DNA-functionalized HA hydrogels combine the advantages of both HA and DNA as biomaterials for cartilage engineering. HA provides biocompatibility, biodegradability, and low immunogenicity, as well as mimics the natural component of cartilage ECM. DNA provides structural programmability, stimuli responsiveness, molecular recognition, and gene delivery functions, and enables precise control over the mechanical properties and degradation rate of the hydrogels. Therefore, DNA-functionalized HA hydrogels have the potential to serve as a versatile and intelligent bioink platform for 3D bioprinting of cartilage tissue.

4. Implications of advanced bioinks for cartilage engineering

Utilizing customizable structural configurations, DNA-functionalized hydrogels exhibit the ability to regulate cellular behavior and fate, providing essential physical, chemical, and biological cues necessary for cellular proliferation.[69,70] These functionalized hydrogels have broad application prospects in cartilage regeneration and can be classified, according to their modes of action, into different categories, such as cell protection, drug delivery, cell recruitment, gene transfection, and reversible mechanical regulation (Figure 6).

4.1. Cell protection

Certain DNA-functionalized hydrogel can serve as an ideal cell carrier, providing suitable mechanical support and

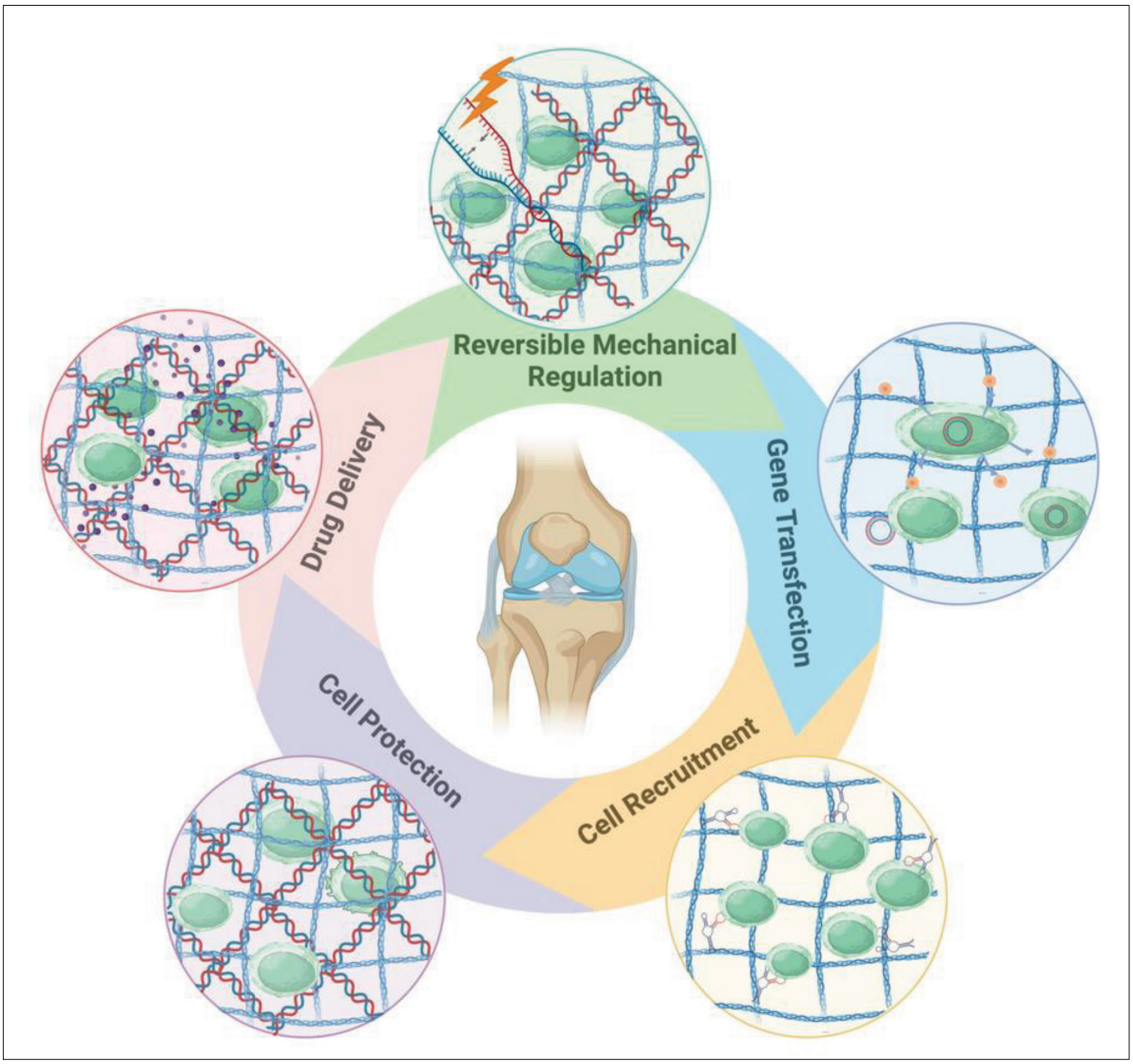

Figure 6. Overall concept map of the DNA-functionalized HA bioink in cartilage engineering. Created using BioRender.com.

biological protection, preventing cells from being damaged by shear forces or immune system during delivery. Yan et al. presented a DNA hydrogel-based delivery system for mesenchymal stem cells (MSCs) for severe osteoarthritis treatment in a rabbit model.[71] The DNA hydrogel matrix demonstrated effective shielding of encapsulated MSCs, which led to enhanced therapeutic outcomes in terms of cell transportation and cartilage regeneration. The hydrogel exhibited remarkable resistance against robust shear forces, thereby contributing to the successful improvement of MSC-mediated treatment[71] (Figure 7a and b). Another study showed that the rigidity of dsDNA and the soft protection of DNA supramolecular network in DNA hydrogel ensured the proliferation and differentiation of tendon stem/progenitor cells (TSPCs) by protecting them from external compression and sliding

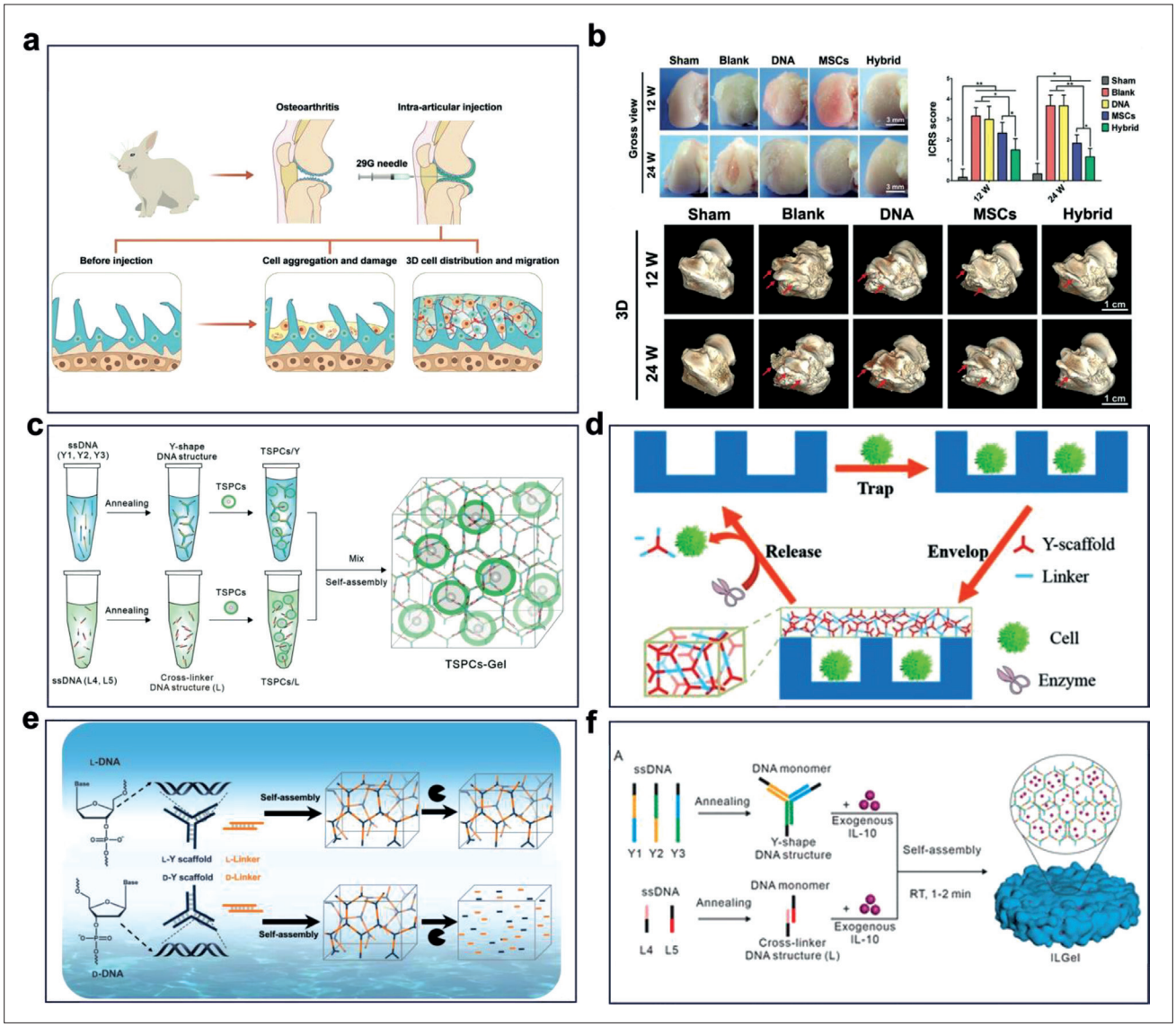

Figure 7. DNA hydrogels for the construction of tissue *in vitro*. (a) Anti-friction delivery system for MSCs to treat severe osteoarthritis. Reprinted with permission from ref.[71] Copyright © 2021 Wiley. (b) Assessment of DNA hydrogels in cartilage degeneration using macroscopic observations, ICRS score, and micro-computed tomography imaging after treatment. Reprinted with permission from ref.[70] Copyright © 2021 Wiley. (c) Schematic illustration of encapsulating tendon stem/progenitor cells (TSPCs) within DNA hydrogel. Reprinted with permission from ref.[72] Copyright © 2023 Wiley. (d) Cell encapsulation and release using microwells and DNA hydrogel with controlled restriction enzyme digestion. Reprinted with permission from ref.[73] Copyright © 2013 Wiley. (e) The L-DNA hydrogel self-assembles from L-Y scaffold and L-linker, which have a left-handed duplex structure, in contrast to the right-handed helical D-DNA. Reprinted with permission from ref.[75] Copyright © 2022 Wiley. (f) Sustained cytokine delivery with physically crosslinked DNA hydrogel. Reprinted with permission from ref.[77] Copyright © 2022 American Chemical Society.

shear.[72] Jin et al. encapsulated single cells in DNA hydrogel caps within PDMS (polydimethylsiloxane) microwells. After 24 h of culture, 98% of the cells remained viable. Using the restriction enzyme EcoR I could open the DNA hydrogel caps to release the encapsulated single cells on demand. Strategically, using specific restriction enzymes and digesting DNA hydrogel could precisely control the release of cells[73] (Figure 7d). In addition, researchers also prepared biostable and non-biodegradable DNA hydrogel networks by replacing natural D-type DNA with L-type DNA, which had better biostability and low inflammation response. In 3D cell culture and tissue engineering, L-DNA hydrogels can maintain uniform cell distribution, prevent degradation and remodeling of ECM, and provide an inert mechanical stimulation platform[74,75] (Figure 7e).

4.2. Drug delivery

The structure of DNA hydrogels can form hollow internal spaces, which provide a favorable environment for drug molecule encapsulation. Under electrostatic attraction, positively charged subunits can bind to DNA nanostructures. These characteristics are the prime factors prompting researchers to use nucleic acid nanostructures as carriers to deliver drugs to target cells. Notably, Chen et al. developed an injectable DNA hydrogel that could deliver dexamethasone and induce macrophages to polarize to M2 phenotype, in order to promote bone formation.[76] Li et al. also developed a physically crosslinked DNA hydrogel loaded with interleukin-10 as a soft bioscaffold,[77] which could gradually degrade or hydrolyze under physiological conditions, thereby continuously releasing cytokines for a long time (Figure 7f). In addition, Borum et al. effectively encapsulated MB-Dox conjugates within specific regions of DNA hydrogels.[78] Upon *in vivo* injection, these hydrogels undergo degradation initiated by nucleases present in bodily fluids, resulting in the gradual release of MB-Dox conjugates. Importantly, the rate of this release can be finely controlled by modulating the weight percentage of the hydrogel.[78]

4.3. Cell recruitment

Unlike inherent ECMs, traditional hydrogels generally lack bioactive groups serving as "baits" to attract cells. The integration of bait molecules into DNA-based hydrogels enables precise interactions between cell and matrices, thus verifying the presence of requisite cell surface markers. Mimicking the ECM requires the ability of the hydrogels to recognize specific cell types, which is the fundamental of tissue engineering.[51,79] Yao et al. constructed a DNA hydrogel using the double rolling circle amplification (RCA) method to achieve effective capture and enzymatically triggered release of bone marrow mesenchymal stem cells (BMSCs)[80] (Figure 8a). The introduced aptamer Apt19S exhibited a strong binding affinity toward the ALPL protein on the surface of BMSCs, achieving specific anchoring of BMSCs. By digesting the DNA network into fragments with the nucleic acid enzyme DNase I, BMSCs can be released in a concentration-dependent manner within tens of minutes. Moreover, Hu et al. employed DNA aptamer Apt19S was immobilized on the bilayer scaffold to recruit MSCs for articular cartilage and subchondral bone regeneration.[81] The inclusion of the stimulatory factor kartogenin (KGN) within the aptamer-functionalized gel layer enhanced the process of chondrogenic differentiation, guiding MSCs toward adopting a chondrocyte phenotype. In parallel, the aptamer-functionalized 3D graphene oxide-based biomineral framework (GBF) layer expedited the osteoblastic differentiation of MSCs, facilitating their transformation into osteoblasts[81] (Figure 8b). Except aptamer Apt19S, aptamer HM69 was also used to specifically recruit MSC. Yang et al. chemically combined the aptamer HM69 with decellularized cartilage ECM and subsequently blended it with gelatin methacrylate (GelMA) to produce a photo-crosslinkable bioink. The 3D-bioprinted scaffold can guide MSCs to move directionally to the site of cartilage injury *in situ*[82] (Figure 8c and d). Apart from cells, DNA hydrogels can also bind to and recruit exosomes. An exosome separation strategy based on a DNA network of polyvalent adaptors has been developed.[40] A DNA ultra-long single strand containing polyvalent adaptors was synthesized by enzyme-catalyzed RCA reaction. The DNA single strand was added to the biological system. The DNA chain containing polyvalent adaptors could capture exosomes through specific recognition of CD63 protein on exosomes.[40]

4.4. Gene transfection

Hydrogels can serve as an effective gene carrier for encapsulating and delivering different types of DNA molecules, such as plasmid DNA and siRNA, to damaged tissues.[55,56] Hydrogels can prevent plasmid DNA from being degraded or cleared by nucleases or the immune system and enhance the transfection efficiency of DNA molecules.[55,56] These functionalized hydrogels can also achieve long-term and sustained release of DNA molecules through the addition of degradable or cleavable crosslinkers or functional units, which enable the hydrogel to undergo structural changes or degradation according to environmental conditions or target molecules to release active DNA molecules.

4.5. Reversible mechanical regulation

One of the enduring challenges in tissue engineering is to construct artificial tissues with 3D arrangement of different types of living cells.[83] Li et al. showed that these hydrogels can be used for *in situ* multilayer 3D cell printing, which

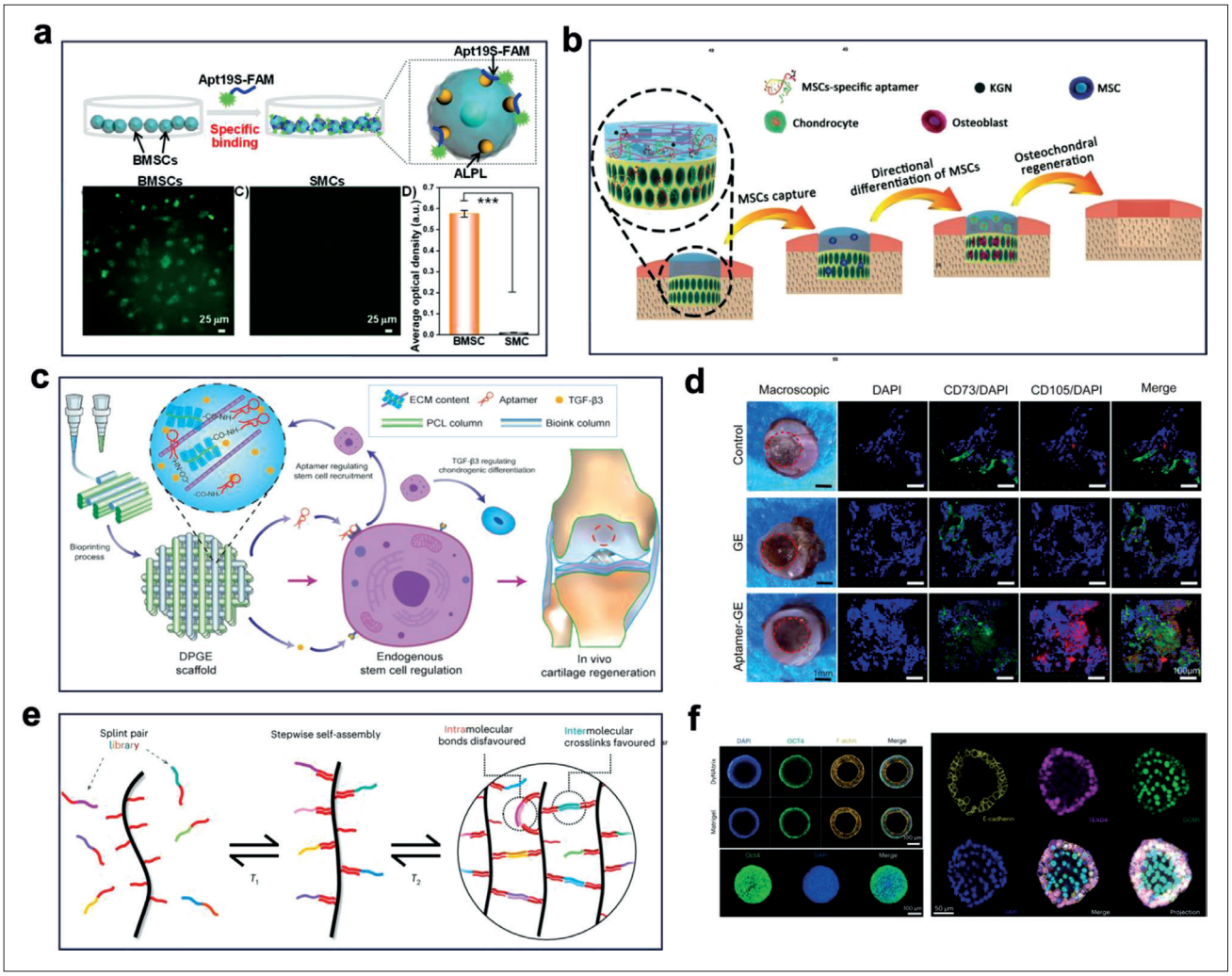

Figure 8. DNA-functionalized hydrogels for construction of tissue *in vitro*. (a) BMSCs recognition and binding by Apt19S-FAM, analysis of fluorescence microscopy, and quantitative assessment. Reprinted with permission from ref.[80] Copyright © 2022 American Chemical Society. (b) Aptamer-bilayer scaffold in osteochondral defect repair. Reprinted with permission from ref.[81] Copyright © 2017 Wiley. (c) Aptamer-based 3D-bioprinted scaffolds for enhanced cartilage regeneration. Reprinted with permission from ref.[82] Copyright © 2021 American Chemical Society. (d) *In vivo* macroscopic and confocal images of endogenous stem cell migration. Reprinted with permission from ref.[82] Copyright © 2021 American Chemical Society. (e) Polymer crosslinking scheme using a library of crosslinker splints to prevent intramolecular bond formation. Reprinted with permission from ref.[41] Copyright © 2023 Nature. (f) Confocal microscopy images of hiPSC cysts in DyNAtrix [+RGD] vs. Matrigel at day 7, and images of a trophoblast organoid in DyNAtrix [+RGD] stained for TEAD4, E-cadherin, GCM1, and DAPI (nuclei) at day 7. Reprinted with permission from ref.[41] Copyright © 2023 Nature.

creates structures with viable cells and normal functions. By mixing peptide–DNA conjugates (bioink A) and covalent DNA linkers (bioink B) in specific ratios, the hydrogel forms rapidly and possesses self-healing and high mechanical strength properties. It also responds to proteases and nucleases, allowing selective removal of hydrogel sections in the presence of cells. This advancement opens doors to fabricating precise 3D tissue structures with diverse cell arrangements.[84] Recently, Peng et al. developed a hydrogel named DyNAtrix, which consists of ultra-high-molecular-weight polymers and DNA crosslinkers.[41] The polymers are connected with DNA anchor chains, which can bind with DNA crosslinkers composed of two splints, forming a dynamic supramolecular network. By changing the sequence information of the overlap domain between the splints in the DNA crosslinkers, the mechanical, thermodynamic, and kinetic properties of the hydrogel can be systematically regulated to suit different cell and organoid culture needs. For instance, stress relaxation time from less than 1 s to several hours can be achieved by choosing different lengths of overlap domain. Thermally activated crosslinking at 37°C can be achieved by adding blocking strand. Controlled degradation of the hydrogel can be achieved by adding DNase I. Since the non-covalent

bonds between DNA crosslinkers are reversible, this hydrogel has good self-healing properties, which allows the hydrogel to be printed and reshaped without damaging cells. The authors successfully cultured human-induced pluripotent stem cells using DyNAtrix and observed their proliferation, morphogenesis, and differentiation in the hydrogel, which holds great potential in tissue engineering[41] (Figure 8e and f).

Taken together, the integration of DNA hybrid hydrogels into cartilage engineering holds immense promise for driving the field forward. These hydrogels offer precise control over cellular behaviors through customizable structures. This modulation capacity enables diverse applications, from shielding encapsulated cells from shear forces to enabling controlled cell release. Beyond cell encapsulation, DNA hybrid hydrogels function as versatile carriers delivering therapeutics, such as drugs, cytokines, and exosomes, to targeted sites in order to boost treatment effectiveness. However, several limitations surrounding the application of DNA-functionalized hydrogels in cartilage regeneration should be acknowledged: (i) impurities or non-specific hybridization, which leads to reduced stability and responsiveness of hydrogels; (ii) interference by enzyme residues or inhibitors, which makes the preparation process of hydrogels complex and uncontrollable; and (iii) rejection by the immune system or adverse reaction stemming from exogenous gene expression, which lowers biocompatibility and safeness of hydrogels. Nevertheless, by mimicking synthetic ECMs using specific aptamers, DNA-functionalized hydrogels facilitate cell-specific recruitment and differentiation, which are the core functions required by tissue engineering strategies. With their multifaceted capabilities, DNA hybrid hydrogels emerge as a dynamic toolset with transformative potential, poised to redefine cartilage engineering and tissue regeneration.

5. Conclusion

Hyaluronic acid is a prominent polysaccharide found in living tissues, possessing high potential for hydrogel fabrication due to its exceptional biocompatibility. Nevertheless, conventional crosslinking methods for HA, which often involve the use of chemical agents or the introduction of functional groups, limit the dynamic and adaptable characteristics of the resulting products. This renders them less than optimal for cartilage applications.[56] Conversely, DNA, as a biological macromolecule, exhibits enhanced biocompatibility and degradability. It offers exceptional structural programmability and multifunctionality, allowing for the customization of desired attributes, such as specific recognition, targeted specificity, and biocatalytic activity.[59] The inherent flexibility of DNA molecules empowers hydrogels with precise structural customization and the ability to fine-tune their physical and chemical properties. Recently, a review unveils the unprecedented prospects of DNA integration into dynamic supramolecular hydrogels in cartilage tissue engineering and illuminates the strategy of incorporating reconfigurable DNA building blocks into hyaluronic acid hydrogels, which serve as crosslinking nodes within network structures, with implications for advancing cartilage repair through the rational design of responsive smart hydrogels.[38]

The complex interplay between *in vivo* cell interactions and the ECM relies on the temporal dynamics and spatial definition of physical and chemical cues. This interaction replicates stem cell microenvironments and guides suitable cell phenotypes. Unlike conventional static hydrogels, dynamic DNA–HA hybrid hydrogels not only fulfill the biological and mechanical requirements of bioinks, but also exhibit *in situ* responsiveness to cellular signals and external stimuli. This attribute holds promise for simulating the physicochemical characteristics of chondrocyte ECMs.[85] Despite these advantages, several challenges remain in advancing the utilization of DNA–HA hybrid hydrogels for cartilage tissue regeneration. Variations in synthesis methodologies yield DNA hydrogels with distinct pharmacokinetics, suggesting varying anti-enzyme activities. Distinct stimuli should induce different kinetic behaviors in DNA hydrogels. However, comprehensive studies on the pharmacokinetics of DNA hydrogels are currently limited, possibly due to research limitations or insufficient focus on this area. In-depth kinetic inquiries will contribute to the informed design of DNA hydrogels for specific applications, fostering the development of controlled release hydrogels and tissue engineering advancements. With the continuous development of DNA nanotechnology, the structure and function of DNA-functionalized hydrogels will become more diverse and sophisticated to align with different biomedical needs. For example, increasing studies focus on exploring various DNA crosslinking strategies, optimizing the mechanical properties of DNA hydrogels, and achieving dynamic regulation of mechanical signals. Moreover, improving enzyme resistance and immune evasion abilities of DNA hydrogels, as well as controlling their degradation rate and products, are also important directions. Furthermore, by integrating different functional elements, such as nucleic acid aptamers, nucleases, gene carriers, and nanoparticles, more DNA-functionalized hydrogels can be developed as bioinks to construct organoids with complex structure and function. In summary, the convergence of DNA and HA presents an intriguing bioink platform, which has the potential to be widely applied in the field of cartilage repair.

Acknowledgment

None.

Funding

The work was supported by the Natural Science Foundation of Shanghai (22ZR1423400), National Natural Science Foundation of China (82230071, 82172098), and Shanghai Committee of Science and Technology (23141900600).

Conflict of interest

The authors declare no conflicts of interest.

Author contributions

Conceptualization: Mengmeng Li
Funding acquisition: Jiacan Su
Visualization: Yan Wu, Peiran Song
Writing – original draft: Mengmeng Li, Yan Wu, Miaomiao Wang, Peiran Song
Writing – review & editing: Wencai Zhang, Jiacan Su

Ethics approval and consent to participate

Not applicable.

Consent for publication

Not applicable.

Availability of data

Not applicable.

References

1. Costantini M, Idaszek J, Szöke K, et al. 3D bioprinting of BM-MSCs-loaded ECM biomimetic hydrogels for in vitro neocartilage formation. *Biofabrication*. 2016;8(3):035002.
doi: 10.1088/1758-5090/8/3/035002

2. Kesti M, Müller M, Becher J, et al. A versatile bioink for three-dimensional printing of cellular scaffolds based on thermally and photo-triggered tandem gelation. *Acta Biomater*. 2015;11:162-172.
doi: 10.1016/j.actbio.2014.09.033

3. Laomeephol C, Ferreira H, Kanokpanont S, Luckanagul JA, Neves NM, Damrongsakkul S. Osteogenic differentiation of encapsulated cells in dexamethasone-loaded phospholipid-induced silk fibroin hydrogels. *Biomater Transl*. 2022;3(3):213.
doi: 10.12336/biomatertransl.2022.03.005

4. Choi JR, Yong KW, Choi JY. Effects of mechanical loading on human mesenchymal stem cells for cartilage tissue engineering. *J Cell Physiol*. 2018;233(3):1913-1928.
doi: 10.1002/jcp.26018

5. Zhang H, Wu S, Chen W, Hu Y, Geng Z, Su J. Bone/cartilage targeted hydrogel: strategies and applications. *Bioact Mater*. 2023;23:156-169.
doi: 10.1016/j.bioactmat.2022.10.028

6. Hu Y, Zhang H, Wang S, et al. Bone/cartilage organoid on-chip: construction strategy and application. *Bioact Mater*. 2023;25:29-41.
doi: 10.1016/j.bioactmat.2023.01.016

7. Armstrong JP, Burke M, Carter BM, Davis SA, Perriman AW. 3D bioprinting using a templated porous bioink. *Adv Healthc Mater*. 2016;5(14):1724-1730.
doi: 10.1002/adhm.201600022

8. Xue X, Zhang H, Liu H, et al. Rational design of multifunctional CuS nanoparticle-PEG composite soft hydrogel-coated 3D hard polycaprolactone scaffolds for efficient bone regeneration. *Adv Funct Mater*. 2022;32(33):2202470.
doi: 10.1002/adfm.202202470

9. Sahranavard M, Sarkari S, Safavi S, Ghorbani F. Three-dimensional bio-printing of decellularized extracellular matrix-based bio-inks for cartilage regeneration: a systematic review. *Biomater Transl*. 2022;3(2):105.
doi: 10.12336/biomatertransl.2022.02.004

10. Nakamura M, Iwanaga S, Henmi C, Arai K, Nishiyama Y. Biomatrices and biomaterials for future developments of bioprinting and biofabrication. *Biofabrication*. 2010;2(1):014110.
doi: 10.1088/1758-5082/2/1/014110

11. Xue X, Hu Y, Wang S, Chen X, Jiang Y, Su J. Fabrication of physical and chemical crosslinked hydrogels for bone tissue engineering. *Bioact Mater*. 2022;12:327-339.
doi: 10.1016/j.bioactmat.2021.10.029

12. Chen W, Zhang H, Zhou Q, Zhou F, Zhang Q, Su J. Smart hydrogels for bone reconstruction via modulating the microenvironment. *Research*. 2023;6:0089.
doi: 10.34133/research.0089

13. Tamayol A, Najafabadi AH, Aliakbarian B, et al. Hydrogel templates for rapid manufacturing of bioactive fibers and 3D constructs. *Adv Healthc Mater*. 2015;4(14):2146-2153.
doi: 10.1002/adhm.201500492

14. Zhou Z, Cui J, Wu S, Geng Z, Su J. Silk fibroin-based biomaterials for cartilage/osteochondral repair. *Theranostics*. 2022;12(11):5103.
doi: 10.7150/thno.74548

15. Liu H, Su J. Organoid and organoid extracellular vesicles for osteoporotic fractures therapy: current status and future perspectives. *Interdiscip Med*. 2023;1(3):e20230011.
doi: 10.1002/INMD.20230011

16. Maturavongsadit P, Wu W, Fan J, Roninson IB, Cui T, Wang Q. Graphene-incorporated hyaluronic acid-based hydrogel as a controlled Senexin A delivery system. *Biomater Transl*. 2022;3(2):152.
doi: 10.12336/biomatertransl.2022.02.007

17. Yuan J, Maturavongsadit P, Zhou Z, et al. Hyaluronic acid-based hydrogels with tobacco mosaic virus containing cell adhesive peptide induce bone repair in normal and osteoporotic rats. *Biomater Transl*. 2020;1(1):89-98. doi: 10.3877/cma.j.issn.2096-112X.2020.01.009

18. Galarraga JH, Zlotnick HM, Locke RC, et al. Evaluation of surgical fixation methods for the implantation of melt electrowriting-reinforced hyaluronic acid hydrogel composites in porcine cartilage defects. *Int J Bioprinting*. 2023;9(5):493-509. doi: 10.18063/ijb.775

19. Ghorbani F, Ghalandari B, Khajehmohammadi M, et al. Photo-cross-linkable hyaluronic acid bioinks for bone and cartilage tissue engineering applications. *Int Mater Rev*. 2023;68(7):901-942. doi: 10.1080/09506608.2023.2167559

20. Hauptstein J, Böck T, Bartolf-Kopp M, et al. Hyaluronic acid-based bioink composition enabling 3D bioprinting and improving quality of deposited cartilaginous extracellular matrix. *Adv Healthc Mater*. 2020;9(15):2000737. doi: 10.1002/adhm.202000737

21. Xue X, Hu Y, Deng Y, Su J. Recent advances in design of functional biocompatible hydrogels for bone tissue engineering. *Adv Funct Mater*. 2021;31(19):2009432. doi: 10.1002/adfm.202009432

22. Wu S, Zhang H, Wang S, et al. Ultrasound-triggered in situ gelation with ROS-controlled drug release for cartilage repair. *Mater Horiz*. 2023;10:3507–3522. doi: 10.1039/D3MH00042G

23. Chen S, Chen X, Geng Z, Su J. The horizon of bone organoid: a perspective on construction and application. *Bioact Mater*. 2022;18:15-25. doi: 10.1016/j.bioactmat.2022.01.048

24. Jiang Y, Li J, Xue X, Yin Z, Xu K, Su J. Engineered extracellular vesicles for bone therapy. *Nano Today*. 2022;44:101487. doi: 10.1016/j.nantod.2022.101487

25. Wu S, Wu X, Wang X, Su J. Hydrogels for bone organoid construction: from a materiobiological perspective. *J Mater Sci Technol*. 2023;136:21-31. doi: 10.1016/j.jmst.2022.07.008

26. Li F, Tang J, Geng J, Luo D, Yang D. Polymeric DNA hydrogel: design, synthesis and applications. *Prog Polym Sci*. 2019;98:101163. doi: 10.1016/j.progpolymsci.2019.101163

27. Han Y, Cao L, Li G, Zhou F, Bai L, Su J. Harnessing nucleic acids nanotechnology for bone/cartilage regeneration. *Small*. 2023;19(37):2301996. doi: 10.1002/smll.202301996

28. Cangialosi A, Yoon C, Liu J, et al. DNA sequence–directed shape change of photopatterned hydrogels via high-degree swelling. *Science*. 2017;357(6356):1126-1130. doi: 10.1126/science.aan3925

29. Tang J, Yao C, Gu Z, Jung S, Luo D, Yang D. Super-soft and super-elastic DNA robot with magnetically driven navigational locomotion for cell delivery in confined space. *Angew Chem Int Ed Engl*. 2020;59(6):2490-2495. doi: 10.1002/anie.201913549

30. Wang S, Yue L, Shpilt Z, et al. Controlling the catalytic functions of DNAzymes within constitutional dynamic networks of DNA nanostructures. *J Am Chem Soc*. 2017;139(28):9662-9671. doi: 10.1021/jacs.7b04531

31. Bai L, Li M, Su J. A perspective on light-based bioprinting of DNA hydrogels for advanced bone regeneration: implication for bone organoids. *Int J Bioprinting*. 2023; 9(2):688. doi: 10.18063/ijb.688

32. Li C, Li H, Ge J, Jie G. Versatile fluorescence detection of microRNA based on novel DNA hydrogel-amplified signal probes coupled with DNA walker amplification. *Chem Commun*. 2019;55(27):3919-3922. doi: 10.1039/C9CC00565J

33. Sun S, Liu H, Hu Y, et al. Selection and identification of a novel ssDNA aptamer targeting human skeletal muscle. *Bioact Mater*. 2023;20:166-178. doi: 10.1016/j.bioactmat.2022.05.016

34. Lu S, Shen J, Fan C, Li Q, Yang X. DNA assembly- based stimuli-responsive systems. *Adv Sci*. 2021;8(13): 2100328. doi: 10.1002/advs.202100328

35. Li M, Yu B, Wang S, Zhou F, Cui J, Su J. Microenvironment-responsive nanocarriers for targeted bone disease therapy. *Nano Today*. 2023;50:101838. doi: 10.1016/j.nantod.2023.101838

36. Wei Y, Wang K, Luo S, et al. Programmable DNA hydrogels as artificial extracellular matrix. *Small*. 2022;18(36):2107640. doi: 10.1002/smll.202107640

37. Nagahara S, Matsuda T. Hydrogel formation via oligonucleotide hybridization in water-soluble vinyl polymers. *Polym Gels Netw*. 1996;4(2):111-127. doi: 10.1016/0966-7822(96)00001-9

38. Morgan FL, Moroni L, Baker MB. Dynamic bioinks to advance bioprinting. *Adv Healthc Mater*. 2020;9(15):1901798. doi: 10.1002/adhm.201901798

39. Lu CH, Guo W, Qi XJ, Neubauer A, Paltiel Y, Willner I. Hemin–G-quadruplex-crosslinked poly-N-isopropylacrylamide hydrogel: a catalytic matrix for the deposition of conductive polyaniline. *Chem Sci*. 2015;6(11):6659-6664. doi: 10.1039/C5SC02203G

40. Tang J, Jia X, Li Q, et al. A DNA-based hydrogel for exosome separation and biomedical applications. *Proc Natl Acad Sci USA*. 2023;120(28):e2303822120. doi: 10.1073/pnas.2303822120

41. Peng YH, Hsiao SK, Gupta K, et al. Dynamic matrices with DNA-encoded viscoelasticity for cell and organoid culture. *Nat Nanotechnol*. 2023;18:1463-1473.

doi: 10.1038/s41565-023-01483-3

42. Yang D, Hartman MR, Derrien TL, et al. DNA materials: bridging nanotechnology and biotechnology. *Acc Chem Res*. 2014;47(6):1902-1911. doi: 10.1021/ar5001082

43. Roh YH, Ruiz RC, Peng S, Lee, JB, Luo D. Engineering DNA-based functional materials. *Chem Soc Rev*. 2011;40(12): 5730-5744. doi: 10.1039/C1CS15162B

44. Nöll T, Schönherr H, Wesner D, Schopferer M, Paululat T, Nöll G. Construction of three-dimensional DNA hydrogels from linear building blocks. *Angew Chem Int Ed Engl*. 2014;126(32):8468-8472. doi: 10.1002/ange.201402497

45. Cheng E, Xing Y, Chen P, et al. A pH-triggered, fast-responding DNA hydrogel. *Angew Chem Int Ed Engl*. 2009;48(41):7660-7663. doi: 10.1002/anie.200902538

46. Xing Y, Cheng E, Yang Y, et al. Self-assembled DNA hydrogels with designable thermal and enzymatic responsiveness. *Adv Mater*. 2011;23(9):1117-1121. doi: 10.1002/adma.201003343

47. Um SH, Lee JB, Park N, Kwon SY, Umbach CC, Luo D. Enzyme-catalysed assembly of DNA hydrogel. *Nat Mater*. 2006;5(10):797-801. doi: 10.1038/nmat1741

48. Hartman MR, Yang D, Tran TN, et al. Thermostable branched DNA nanostructures as modular primers for polymerase chain reaction. *Angew Chem Int Ed Engl*. 2013;125(33):8861-8864. doi: 10.1002/ange.201302175

49. Wang J, Chao J, Liu H, et al. Clamped hybridization chain reactions for the self-assembly of patterned DNA hydrogels. *Angew Chem Int Ed Engl*. 2017;56(8):2171-2175. doi: 10.1002/anie.201610125

50. Ren J, Hu Y, Lu CH, et al. pH-responsive and switchable triplex- based DNA hydrogels. *Chem Sci*. 2015;6(7): 4190-4195. doi: 10.1039/C5SC00594A

51. Song P, Ye D, Zuo X, et al. DNA hydrogel with aptamer-toehold-based recognition, cloaking, and decloaking of circulating tumor cells for live cell analysis. *Nano Lett*. 2017;17(9):5193-5198. doi: 10.1021/acs.nanolett.7b01006

52. Chu B, Zhang D, Paukstelis PJ. A DNA G-quadruplex/i-motif hybrid. *Nucleic Acids Res*. 2019;47(22):11921-11930. doi: 10.1093/nar/gkz1008

53. Zhou X, Li C, Shao Y, Chen C, Yanga Z, Liu D. Reversibly tuning the mechanical properties of a DNA hydrogel by a DNA nanomotor. *Chem Commun*. 2016;52(70): 10668-10671. doi: 10.1039/C6CC04724F

54. Lu S, Wang S, Zhao J, Sun J, Yang X. A pH-controlled bidirectionally pure DNA hydrogel: reversible self-assembly and fluorescence monitoring. *Chem Commun*. 2018;54(36):4621-4624. doi: 10.1039/C8CC01603H

55. Wang L, Sun L, Gu Z, et al. N-carboxymethyl chitosan/sodium alginate composite hydrogel loading plasmid DNA as a promising gene activated matrix for in-situ burn wound treatment. *Bioact Mater*. 2022;15:330-342. doi: 10.1016/j.bioactmat.2021.12.012

56. Kim IG, Park MR, Choi YH, et al. Regeneration of paralyzed vocal fold by the injection of plasmid DNA complex-loaded hydrogel bulking agent. *ACS Biomater Sci Eng*. 2019;5(3):1497-1508. doi: 10.1021/acsbiomaterials.8b01541

57. Liu H, Cao T, Xu Y, Dong Y, Liu D. Tuning the mechanical properties of a DNA hydrogel in three phases based on ATP aptamer. *Int J Mol Sci*. 2018;19(6):1633. doi: 10.3390/ijms19061633

58. Sekar MP, Suresh S, Zennifer A, Sethuraman S, Sundaramurthi D. Hyaluronic acid as bioink and hydrogel scaffolds for tissue engineering applications. *ACS Biomater Sci Eng*. 2023;9(6):3134-3159. doi: 10.1021/acsbiomaterials.3c00299

59. Wang C, Zhang J. Recent advances in stimuli-responsive DNA-based hydrogels. *ACS Appl Bio Mater*. 2022;5(5): 1934-1953. doi: 10.1021/acsabm.1c01197

60. Kahn JS, Trifonov A, Cecconello A, Guo W, Fan C, Willner I. Integration of switchable DNA-based hydrogels with surfaces by the hybridization chain reaction. *Nano Lett*. 2015;15(11):7773-7778. doi: 10.1021/acs.nanolett.5b04101

61. Burdick JA, Prestwich GD. Hyaluronic acid hydrogels for biomedical applications. *Adv Mater*. 2011;23(12):H41-H56. doi: 10.1002/adma.201003963

62. Fujita S, Hara S, Hosono A, Sugihara S, Uematsu H, Suye SI. Hyaluronic acid hydrogel crosslinked with complementary DNAs. *Adv Polym Technol*. 2020;2020:1470819. doi: 10.1155/2020/1470819

63. Sun Y, Qi S, Dong X, Qin M, Zhang Y, Wang Z. Colorimetric aptasensor targeting zearalenone developed based on the hyaluronic acid-DNA hydrogel and bimetallic MOFzyme. *Biosens Bioelectron*. 2022;212: 114366. doi: 10.1016/j.bios.2022.114366

64. Liedl T, Dietz H, Yurke B, Simmel F. Controlled trapping and release of quantum dots in a DNA-switchable hydrogel. *Small*. 2007;3(10):1688-1693. doi: 10.1002/smll.200700366

65. Lin DC, Yurke B, Langrana NA. Inducing reversible stiffness changes in DNA-crosslinked gels. *J Mater Res*. 2005;20(6):1456-1464. doi: 10.1557/JMR.2005.0186

66. English MA, Soenksen LR, Gayet RV, et al. Programmable CRISPR-responsive smart materials. *Science*. 2019;365(6455):780-785.
doi: 10.1126/science.aaw5122

67. Liao WC, Lilienthal S, Kahn JS, et al. pH-and ligand-induced release of loads from DNA–acrylamide hydrogel microcapsules. *Chem Sci*. 2017;8(5):3362-3373.
doi: 10.1039/C6SC04770J

68. Du X, Bi Y, He P, Wang C, Guo W. Hierarchically structured DNA-based hydrogels exhibiting enhanced enzyme-responsive and mechanical properties. *Adv Funct Mater*. 2020;30(51):2006305.
doi: 10.1002/adfm.202006305

69. Gu Y, Distler ME, Cheng HF, Huang C, Mirkin CA. A general DNA-gated hydrogel strategy for selective transport of chemical and biological cargos. *J Am Chem Soc*. 2021;143(41):17200-17208.
doi: 10.1021/jacs.1c08114

70. Huang F, Chen M, Zhou Z, Duan R, Xia F, Willner I. Spatiotemporal patterning of photoresponsive DNA-based hydrogels to tune local cell responses. *Nat Commun*. 2021;12(1):2364.
doi: 10.1038/s41467-021-22645-8

71. Yan X, Yang B, Chen Y, et al. Anti-friction MSCs delivery system improves the therapy for severe osteoarthritis. *Adv Mater*. 2021;33(52):2104758.
doi: 10.1002/adma.202104758

72 Ge Z, Li W, Zhao R, et al. Programmable DNA hydrogel provides suitable microenvironment for enhancing TSPCS therapy in healing of tendinopathy. *Small*. 2023;19(32):2207231.
doi: 10.1002/smll.202207231

73. Jin J, Xing Y, Xi Y, et al. A triggered DNA hydrogel cover to envelop and release single cells. *Adv Mater*. 2013;25(34):4714-4717.
doi: 10.1002/adma.201301175

74. Zhou B, Yang B, Liu Q, et al. Effects of univariate stiffness and degradation of DNA hydrogels on the transcriptomics of neural progenitor cells. *J Am Chem Soc*. 2023;145(16): 8954-8964.
doi: 10.1021/jacs.2c13373

75. Yang B, Zhou B, Li C, et al. A biostable l-DNA hydrogel with improved stability for biomedical applications. *Angew Chem Int Ed*. 2023;134(30):e202202520.
doi: 10.1002/ange.202202520

76. Chen F, He Y, Li Z, et al. A novel tunable, highly biocompatible and injectable DNA-chitosan hybrid hydrogel fabricated by electrostatic interaction between chitosan and DNA backbone. *Int J Pharm*. 2021;606:120938.
doi: 10.1016/j.ijpharm.2021.120938

77. Li W, Wang C, Wang Z, et al. Physically cross-linked DNA hydrogel-based sustained cytokine delivery for in situ diabetic alveolar bone rebuilding. *ACS Appl Mater Interfaces*. 2022;14(22):25173-25182.
doi: 10.1021/acsami.2c04769

78. Borum RM, Moore C, Mantri, Y, Xu M, Jokerst JV. Supramolecular loading of DNA hydrogels with dye–drug conjugates for real-time photoacoustic monitoring of chemotherapy. *Adv Sci*. 2023;10(1):2204330.
doi: 10.1002/advs.202204330

79. Yao C, Zhu C, Tang J, Ou J, Zhang R, Yang D. T lymphocyte-captured DNA network for localized immunotherapy. *J Am Chem Soc*. 2021;143(46):19330-19340.
doi: 10.1021/jacs.1c07036

80. Yao C, Tang H, Wu W, et al. Double rolling circle amplification generates physically cross-linked DNA network for stem cell fishing. *J Am Chem Soc*. 2020;142(7): 3422-3429.
doi: 10.1021/jacs.9b11001

81. Hu X, Wang Y, Tan Y, et al. A difunctional regeneration scaffold for knee repair based on aptamer-directed cell recruitment. *Adv Mater*. 2017;29(15):1605235.
doi: 10.1002/adma.201605235

82. Yang Z, Zhao T, Gao C, et al. 3D-bioprinted difunctional scaffold for in situ cartilage regeneration based on aptamer-directed cell recruitment and growth factor-enhanced cell chondrogenesis. *ACS Appl Mater Interfaces*. 2021;13(20):23369-23383.
doi: 10.1021/acsami.1c01844

83. Seliktar D. Designing cell-compatible hydrogels for biomedical applications. *Science*. 2012;336(6085):1124-1128.
doi: 10.1126/science.1214804

84. Li C, Faulkner-Jones A, Dun AR, et al. Rapid formation of a supramolecular polypeptide–DNA hydrogel for in situ three-dimensional multilayer bioprinting. *Angew Chem Int Ed*. 2015;54(13):3957-3961.
doi: 10.1002/anie.201411383

85. Lewns FK, Tsigkou O, Cox LR, Wildman RD, Grover LM. Hydrogels and bioprinting in bone tissue engineering: creating artificial stem-cell niches for in vitro models. *Adv Mater*. 2023;35(52):2301670.
doi: 10.1002/adma.202301670

ACCSCIENCE PUBLISHING

International Journal of Bioprinting

REVIEW ARTICLE

Recent developments and challenges of 3D bioprinting technologies

Ximin Yuan[1,2], Zhenjia Wang[1,2], Lixin Che[3], Xushuai Lv[1,2], Jie Xu[1,2]*, Debin Shan[1,2], and Bin Guo[1,2]*

[1]State Key Laboratory of Advanced Welding and Joining, Harbin Institute of Technology, Harbin, Heilongjiang, China

[2]National Innovation Center for Advanced Medical Devices, Shenzhen, Guangdong, China

[3]Dalian Jiang Xiaolan Dental Clinic Co., Ltd, Dalian, Liaoning, China

(This article belongs to the *Special Issue: Advances in Bioprinting Technologies*)

Abstract

Three-dimensional (3D) bioprinting technologies play significant roles in various facets of the medical field, such as bioengineering, tissue repair, scaffolds, biomedical devices, and drug. As a versatile manufacturing technology, 3D bioprinting is able to overcome the constraints of other conventional methods and shows potential for future advancements in the field of biology. Nevertheless, the existing 3D bioprinting technologies still grapple with significant challenges in materials, equipment, and applications. Therefore, it is essential to select appropriate bioprinting method in alignment with the required application. In this review, we aim to cover the development, classification, and application of 3D bioprinting, with a particular emphasis on the fundamental printing principles. Additionally, we discuss the potential of 3D bioprinting in terms of materialization, structuralization, and functionalization, highlighting its prospective applications. We firmly believe that 3D printing technology will witness widespread adoption in the future, as it has the potential to address the limitations associated with multi-size, multi-material, multi-cell, and high-precision bioprinting.

Keywords: Tissue engineering; Scaffolds; Biomedical devices; Drug delivery

***Corresponding authors:**
Jie Xu
(xjhit@hit.edu.cn)

Bin Guo
(bguo@hit.edu.cn)

Citation: Yuan X, Wang Z, Che L, et al. Recent developments and challenges of 3D bioprinting technologies. *Int J Bioprint*. 2024;10(2):1752.
doi: 10.36922/ijb.1752

Received: September 3, 2023
Accepted: October 30, 2023
Published Online: January 27, 2024

1. Introduction

Three-dimensional (3D) bioprinting technology leverages customizable 3D models, software algorithms, and precision control molding methods to integrate cells, biomolecules, and biological scaffolds.[1] This innovative and multidisciplinary field unifies manufacturing principles with biomedical science to conceive and produce functional artificial organs, implants, and intricate 3D cellular structures.[2] Due to their capacity to fabricate intricate and personalized structures, 3D bioprinting technologies hold tremendous potential in medical applications. More importantly, 3D printing offers an effective solution, marked by its precision and customization capabilities, to address the distinct physiological variations and characteristics between individuals.[3] Thus, this technology finds utility in crafting medical innovations like customized implant stents, tissues, and organs, which can be tailored to individual needs, revolutionizing healthcare through personalized therapeutic solutions.[4] 3D bioprinting demonstrates its prowess

in producing limited-batch or large-scale personalized medical devices, expanding from its initial role in *in vitro* device production. Its applications are now rapidly growing to encompass individually customized permanent implants, clinical restorative interventions, and pioneering research endeavors in drug development.[5] 3D bioprinting technologies have emerged as promising tools for creating intricate 3D cell structures *in vitro*. However, there are several common misconceptions surrounding these technologies. Many people believe that 3D bioprinting can print any type of material and facilitate the production of transplantable organs, such as hearts, livers, kidneys, and lungs. In reality, the original vision of 3D bioprinting producing fully functional transplantable organs has not been realized, and significant hurdles remain to be overcome.[6] Organs are significantly more complex than commonly understood. Firstly, there is still much to uncover about the intricate biological processes involved in organ development. Secondly, reproducing the complex architecture of organs presents substantial manufacturing challenges.[7] For instance, despite their seemingly simple appearance, blood vessels comprise multiple layers with diverse cell structures, and they possess properties such as selective permeability, elasticity, and anticoagulation. These factors make it extremely challenging to bioprint fully functional blood vessels *in vitro* to replace damaged ones *in vivo*.

Contemporary research in the realm of 3D bioprinting primarily concentrates on establishing a 3D biological environment *in vitro* to mimic *in vivo* conditions, and encompasses endeavors like high-throughput drug screening, organogenesis, and the study of pathological mechanisms. It is crucial to recognize, however, that creating tissues or organs *in vitro* is incapable of fully addressing the escalating scarcity of transplantable organs. While it is feasible to manufacture cell-housing structures, these structures merely mimic the external appearance and form of internal tissues and organs. The cells within these constructs only exhibit fundamental collaborative functions, falling short of the intricate physiological operations showcased by real organs. This conundrum epitomizes the major challenge confronting 3D bioprinting technologies today.

This paper furnishes an overarching review of the evolution, categorization, and utilization of 3D bioprinting technologies, emphasizing the foundational principles of 3D printing. Additionally, we introduce biological materials that harmonize with 3D printing. However, the current research landscape predominantly encompasses a limited spectrum of biological materials, whereas human tissues and organs, for the most part, comprise intricate amalgamations of elements with specific biological and mechanical impacts. Gazing ahead, we engage in speculation concerning the potential evolution of 3D bioprinting technologies. Our projection envisions widespread adoption of these technologies across diverse domains, especially for the fabrication of individualized and heterogeneous intricate biological constructs. 3D bioprinting stands poised for applications spanning the generation of *in vitro* medical models, bespoke implantable devices, scaffolds for tissue engineering, and elaborate 3D cellular frameworks. Furthermore, it will wield a pivotal role in tailored diagnostics and therapeutics, customized medical equipment, regenerative medicinal interventions, and domains of investigation encompassing pathological and pharmacological inquiries, drug innovation, and biopharmaceutical sector. On the whole, the forthcoming horizons for 3D bioprinting technologies radiate promise and portend a revolution in the medical sector for years to come.

2. Overview of 3D bioprinting technologies

2.1. Research progress of 3D bioprinting at home and abroad

In recent times, the advancements in artificial organ 3D printing technology have garnered significant interest across diverse research fields. Numerous investigations have been undertaken in this domain. For example, Antezana et al. harnessed micro-stereolithography technology to fabricate scaffolds for tissues.[8] Jiang et al. devised a technique that incorporates graphene oxide (GO) and mesenchymal stem cells directly into gelatin methacryloyl (GelMA), forming biocompatible scaffolds for bone regenerative therapy.[9] Furthermore, through 3D bioprinting, the decellularized extracellular matrix (dECM) is freeze-dried and subsequently reconstituted, then amalgamated with gelatin, alginate, and cells, yielding a novel form of biological scaffold. The United States is actively playing a spearheading role in the research and development of 3D printing of artificial organs, and has initiated projects focusing on the crafting of 3D breast cancer tissue models, cell printing for wound healing, and the fusion of microliver simulations with cell constructs. Esteemed institutions such as the Massachusetts Institute of Technology (MIT) are at the forefront of this field, concentrating notably on cell 3D printing and organ bioprinting. Several medical research organizations and enterprises have also made significant strides utilizing 3D printing technology to fabricate human organs and tissues, including arteries, cardiac tissue, lungs, and kidneys. In addition, Koch et al. have corroborated the viability of 3D printing for tissue regeneration.[10] The rapidly evolving 3D printing technology for artificial organ in China has surpassed the global standards. Researchers from numerous Chinese universities and institutions have

achieved remarkable breakthroughs in this domain. At Tsinghua University, Sun et al. group produced animal hearts using cardiomyocytes and biomaterials. The printed cells demonstrated rhythmic beating, suggesting potential functionality of the printed organs. Furthermore, they 3D-printed stem cells extracted from amniotic fluid and incorporated bone differentiation factors to achieve activation. This innovation can address periodontal tissue defects. Following printing and cultivation, the product exhibited an organized structure with physiological functions. This team also pioneered essential bioprinting technology, resulting in novel biological patents for a precise stem cell culture system featuring biomimetic capabilities. China's rapid strides in the advancements of 3D printing technology for artificial organ have enabled its permeation into diverse applications, including medical implants. These advancements hold immense potential for the future of regenerative medicine and healthcare (Figure 1).

Leveraging strides in both life science and manufacturing, 3D printing has found wide-ranging applications within biomedical domains encompassing surgery, dentistry, tissue engineering, regenerative medicine, and pharmaceutical formulation.[11] Empowered by computer-assisted imaging, 3D bioprinting technology empowers the meticulous creation of tailored scaffolds that faithfully replicate the intricate 3D framework of impaired tissues and organs. These scaffolds, coupled with seed cells and scaffold materials, acquire biological functionality. As a result, 3D bioprinting has drawn substantial interest within the sphere.[12] In 1990, Chuck Hull first introduced the concept of 3D printing.[13] Since the 1990s, 3D printing technology has rapidly advanced. The initial 3D bioprinter was developed by Wilson and Boland.[14] In contrast to traditional flat printing, 3D printing entails the creation of 3D objects. It operates on the principles of additive manufacturing, where layers are progressively deposited to form a complex 3D structure. This diverges from conventional manufacturing methods like subtractive manufacturing and molding. As one of the disruptive technologies shaping the forthcoming economy and human existence, 3D printing seamlessly amalgamates diverse disciplines, including materials science, machinery manufacturing, information technology, electronics, and engineering design. It surmounts the limitations encountered by conventional manufacturing in dealing with intricate structures. 3D printing permits the production of tailored and personalized items, significantly improving

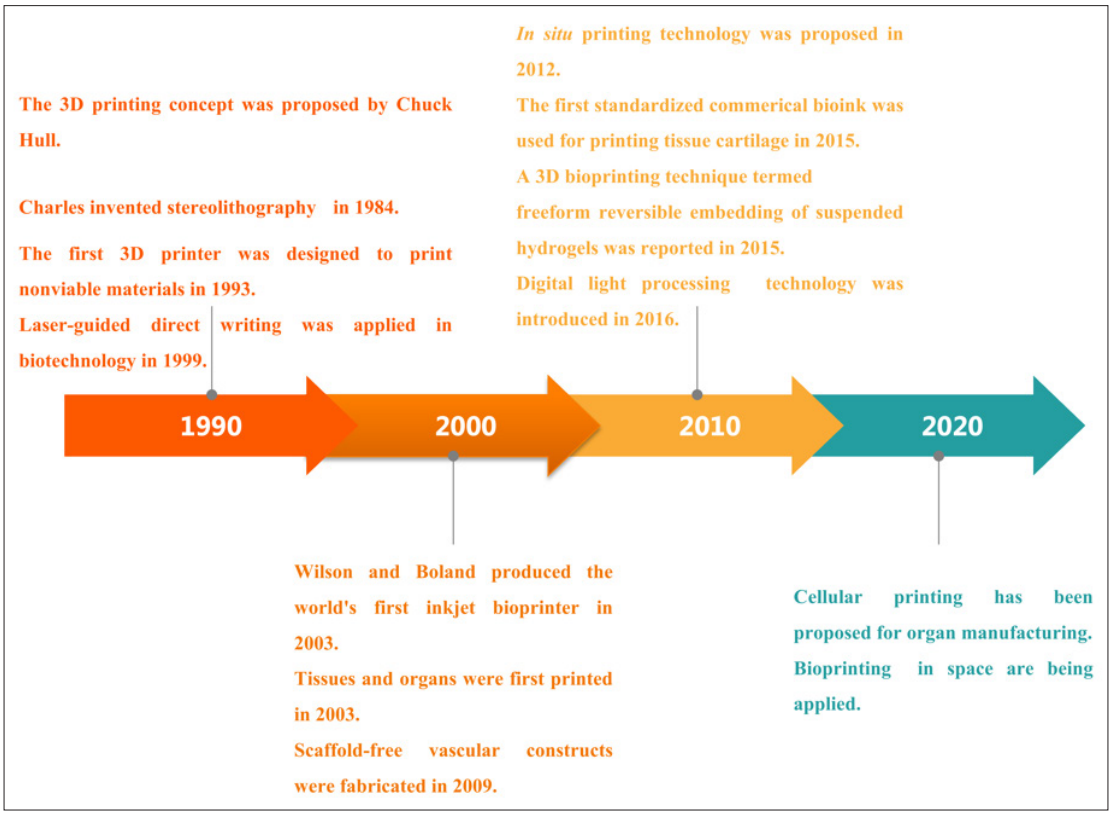

Figure 1. A timeline depicting the advancements of 3D bioprinting.

cost-efficiency and instigating a fresh industrial paradigm. Post-2020, numerous novel 3D bioprinting techniques have emerged, such as *in situ* printing, suspension printing, and digital light processing.[15] Presently, 3D printing boasts wide-ranging applications across domains such as biomedicine, aerospace, architectural design, cultural industries, industrial production, and military equipment.[16,17]

In this part, we present and compare four primary types of 3D bioprinting technologies, namely fused deposition modeling (FDM), direct ink writing (DIW), selective laser sintering (SLS), and digital light processing (DLP) (Table 1). Abbreviations: DLP, digital light processing; DIW, direct ink writing; FDM, fused deposition modeling; SLS, selective laser sintering.

2.2. Fused deposition modeling

Fused deposition modeling is a rapid prototyping process distinct from other techniques as it does not rely on lasers as a formative energy source. Instead, it involves the heating and liquefaction of diverse wire-like materials, such as engineering plastics including polylactic acid (PLA) and polycarbonate (PC), followed by layer-by-layer construction.[18,19] The formative sequence is described as follows (Figure 2A): Controlled by computer algorithms, the heating nozzle maneuvers within the *XY* plane in line with the cross-sectional outline of the desired product. Thermoplastic filament materials are fed into the heating nozzle via a wire feeding mechanism. Subsequently, these materials are heated, reaching a semi-liquid state within the nozzle, and then extruded. Upon extrusion, the material is selectively laid onto the work surface and rapidly cooled, yielding a slender profile with a designated thickness. After each cross-sectional layer is generated, the work surface is lowered, and the subsequent layer is deposited. This iterative process closely resembles the act of "drawing" the contour of the cross-section, culminating in the creation of a 3D product.[20] Nevertheless, it is crucial to acknowledge that FDM, as a molding technology, bears inherent merits and demerits in comparison to other molding techniques. Among its merits are elevated molding precision, robustness of the printed model, and an array of color choices. On the flip side, it harbors shortcomings, including a relatively coarse surface texture on the molded object.

2.3. Direct ink writing

Direct ink writing, also known as robocasting grouting, is a process involving the controlled extrusion of ink from a temperature-regulated barrel through a nozzle onto a substrate using either a screw extrusion or pneumatic pressure control system (Figure 2B). The ink is deposited in a layer-by-layer fashion based on the analysis of model slices and the generation of code. Key direct writing parameters (pressure, speed) and environmental factors (temperature, direct writing medium) significantly influence the process. It is crucial to appropriately match the ink with the corresponding direct writing parameters and environmental conditions to ensure structural stability. DIW displays three central attributes.[21,22] Firstly, it offers versatility in material selection, encompassing metals, ceramics, polymers, hydrogels, composites, and even biological cells. Secondly, the ink exhibits shear-thinning properties and notable viscoelasticity, enabling it to sustain a consistent form and layer stacking without collapsing post-extrusion. Thirdly, the ink boasts elevated solid content, thereby mitigating volume and shape alterations during subsequent processing. Ink solidification can be accomplished through solvents, temperature shifts, gelation, or direct writing media, among others. The rheological properties and solid content are contingent on the chosen solidification mechanism. Inks with slower curing rates require solid content with higher moduli to ensure proper solidification, whereas inks with quicker curing rates can tolerate with solid content of lower moduli.[23] However, DIW does come with certain constraints. Primarily, materials must be carefully designed to be compatible with direct writing inks and to flow seamlessly through the narrow nozzle, as clogging can occur otherwise. Secondly, the product's diameter is often confined by the nozzle's size, and the pattern deposited is restricted by

Table 1. Comparison of different 3D printing technologies

Methods	Materials	Fabrication mechanism	Typical resolution	Applications	Cost
FDM	Thermoplastics	Heating and extruding solid filament	50–100 μm	Blood vessel, tissue	+
DIW	Viscoelastic ink	Liquid ink is squeezed through the nozzle	1–250 μm	Organ, tissue	+
SLS	Polymers, ceramics, metals, and composites	Melt sintering	1–250 μm	Tooth, skeleton	++++
DLP	Optical crosslinking material	Optical crosslinking	50–200 μm	Organ, tissue, delivery	+++

the movement trajectory of the nozzle.[24] These limitations present challenges to the innovative application of DIW.

2.4. Selective laser sintering

Selective laser sintering is a 3D printing methodology that employs an infrared laser to fuse powder materials together. The process commences by depositing a layer of powder material using a powder roller (Figure 2C). Subsequently, the powder is heated to a temperature just below the sintering threshold by a temperature control mechanism within the printing apparatus. A laser beam is then directed onto the powder layer, elevating the temperature of the irradiated powder above its melting point. This triggers sintering, causing the powder particles to fuse and establish a bond with the previously consolidated layer beneath.[25] As each layer is sintered, the printing platform descends by a layer thickness, and the powder application system overlays a fresh layer of powder onto the platform. Subsequently, the laser beam is precisely controlled to irradiate the new layer for sintering. This cyclical procedure is reiterated layer by layer until the entire 3D object is successfully printed.

SLS demonstrates versatility in printing diverse materials, spanning polymers, ceramics, metals, and composite substances. Additionally, it facilitates the generation of intricate and distinct structures. The merits of SLS encompass a few crucial aspects[26]:

(i) SLS technology is compatible with a broad spectrum of materials, encompassing nylon, polystyrene, various polymers, metals like iron and titanium, alloys, ceramics, and coated sand. This material diversity facilitates the creation of diverse prototypes and components.

(ii) One notable advantage of SLS is its heightened manufacturing efficiency. Unlike certain additive manufacturing processes that fully melt the powder, SLS solely sinters it, thereby speeding up the production times. Furthermore, SLS demonstrates remarkable material utilization efficiency. Unfused powder can be reclaimed for use, minimizing material wastage and saving cost in comparison to other techniques.

(iii) Diverging from FDM and stereolithography processes, SLS does not necessitate auxiliary support structures. Unfused powder can inherently support the model's cavities and overhangs, negating the requirement for supplementary support design. This enables the direct fabrication of intricate prototypes and components. The versatility of SLS technology extends to an array of applications. Leveraging a variety of formable materials, sintered components are adaptable for multiple functions, including prototype design models, master dies for die casting, investment casting molds, and casting shells and cores.

Several technical limitations of SLS are depicted as follows[27]:

(i) Elevated raw material expenses and procurement costs: The materials employed in SLS, especially metal powders, can be costly. Additionally, sourcing and acquiring these materials can prove to be demanding and expensive.

(ii) Metal parts produced through SLS often exhibit unsatisfactory or limited mechanical properties, such as heightened porosity and suboptimal mechanical attributes. The joining of low-melting-point powder with high-melting-point powder results in reduced elongation and restricted suitability for manufacturing functional metal components.

(iii) Utilizing varied materials in SLS might necessitate supplementary and intricate auxiliary procedures. For instance, raw materials may need extensive pretreatment, including heating, which increases overall production time and expenses. Additionally, finishing surfaces may entail powder cleaning.

2.5. Digital light processing

Digital light processing is a technology harnessing digital processing to project image signals, yielding a final product. The DLP apparatus (depicted in Figure 2D) comprises a reservoir containing photopolymer, which can be solidified through ultraviolet light exposure at a specific wavelength. Positioned below the liquid reservoir is the DLP imaging system, with its imaging surface situated at the bottom. Through the curing of a thin layer of photopolymer possessing a predefined shape and thickness corresponding to the cross-sectional configuration extracted from prior slicing, a 3D structure is incrementally assembled layer by layer.[28] Above the liquid reservoir, a lifting mechanism elevates the cured resin, detaching it from the bottom surface and causing it to adhere to the lifting plate or the preceding mold's resin layer. This integration of projection mechanisms contributes to the compact sizing of the equipment, as the layer curing and forming function module is more compact. The molding traits of DLP technology are concisely summarized as follows[2,29]: (i) elevated curing speed due to heightened light efficiency at 405 nm; (ii) cost-effectiveness; (iii) high-resolution output; and (iv) enhanced reliability.

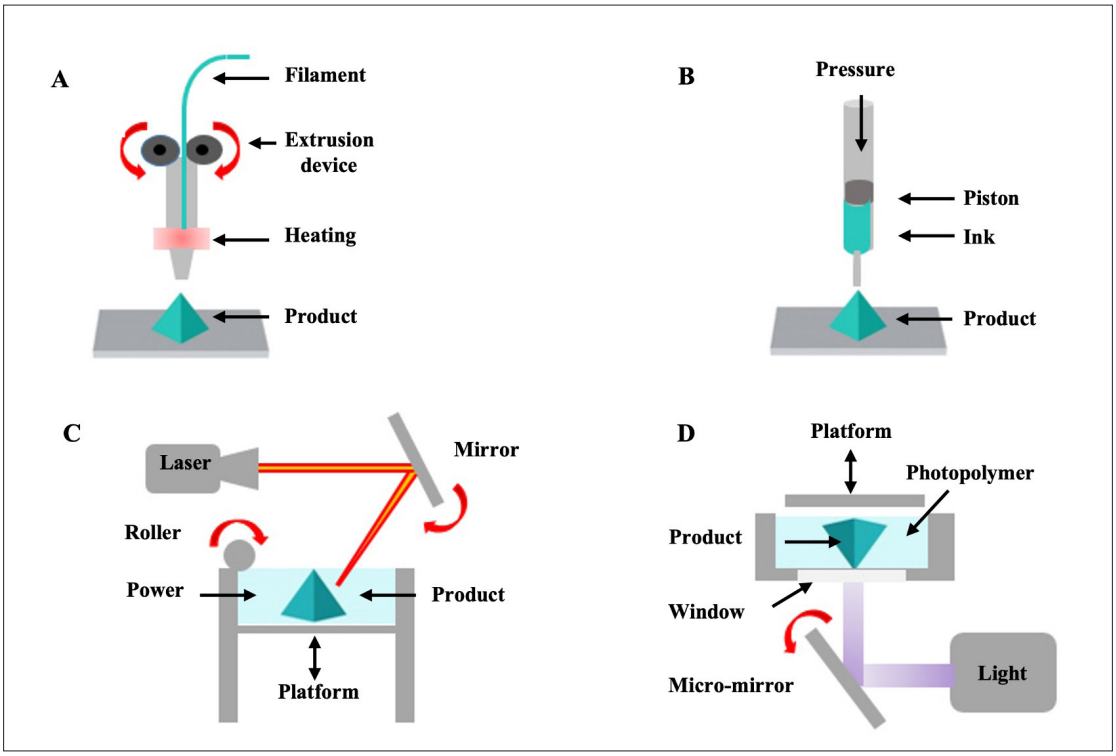

Figure 2. Schematic illustrations of different 3D printing technologies. (A) Fused deposition modeling; (B) direct ink writing; (C) selective laser sintering; (D) digital light processing.

However, DLP is not devoid of inherent drawbacks and disadvantages: (i) Post-printing, remnants of consumable resin may be left on the model's surface, necessitating subsequent cleaning and washing. (ii) The printing platform's dimensions are restricted, preventing the production of voluminous models. (iii) Resin is a chemical compound emitting a range of undesirable odors, containing trace toxins, and demanding a specific operating environment (Figure 2).

3. Materials for bioprinting

3.1. Biomedical polymer materials

Biomedical materials represent a distinct category of substances, either natural or synthetic, that are meticulously crafted to interact harmoniously with living systems. These materials find application in diverse medical contexts, encompassing disease diagnosis, treatment, the replacement of cells, tissues, and organs, as well as the stimulation of regenerative processes.[30,31] Medical polymer materials can be sorted into three primary categories: natural polymer materials, non-degradable polymer materials, and degradable polymer materials. In this segment, we delve into a more comprehensive exploration of each of these material categories.

Natural medical polymer materials are of organic origin and encompass substances like cellulose, chitin, and hyaluronic acid. For example, cellulose is as a macromolecular polysaccharide composed of glucose units.[32] It demonstrates insolubility in water and common organic solvents. Notably, cellulose is the primary constituent of plant cell walls and ranks as the most abundant polysaccharide in nature, contributing to over 50% of the carbon content in the plant realm. Cotton, characterized by a cellulose content approaching 100%, represents a pristine natural source of cellulose.[33] Broadly, wood harbors around 40–50% cellulose, 10–30% hemicellulose, and 20–30% lignin. Although cellulose itself is soluble in water, the substantial intermolecular hydrogen bonding it possesses obstructs its dissolution in both water and organic solvents. This solubility constraint restricts its utility in biomedical applications (Figure 3).[34]

Chitin, a polysaccharide sourced from the exoskeletons of marine crustaceans, manifests as a pale beige to white substance. It readily dissolves in concentrated hydrochloric acid, phosphoric acid, sulfuric acid, and acetic acid, yet it remains insoluble in alkaline solutions, various other organic solvents, and water. The versatility of chitin is showcased through its extensive application in diverse medical products. It finds utility in crafting an array of medical supplies, such as contact lenses, synthetic skin, sutures, artificial dialysis membranes, and prosthetic blood vessels (Figure 4).[35,36]

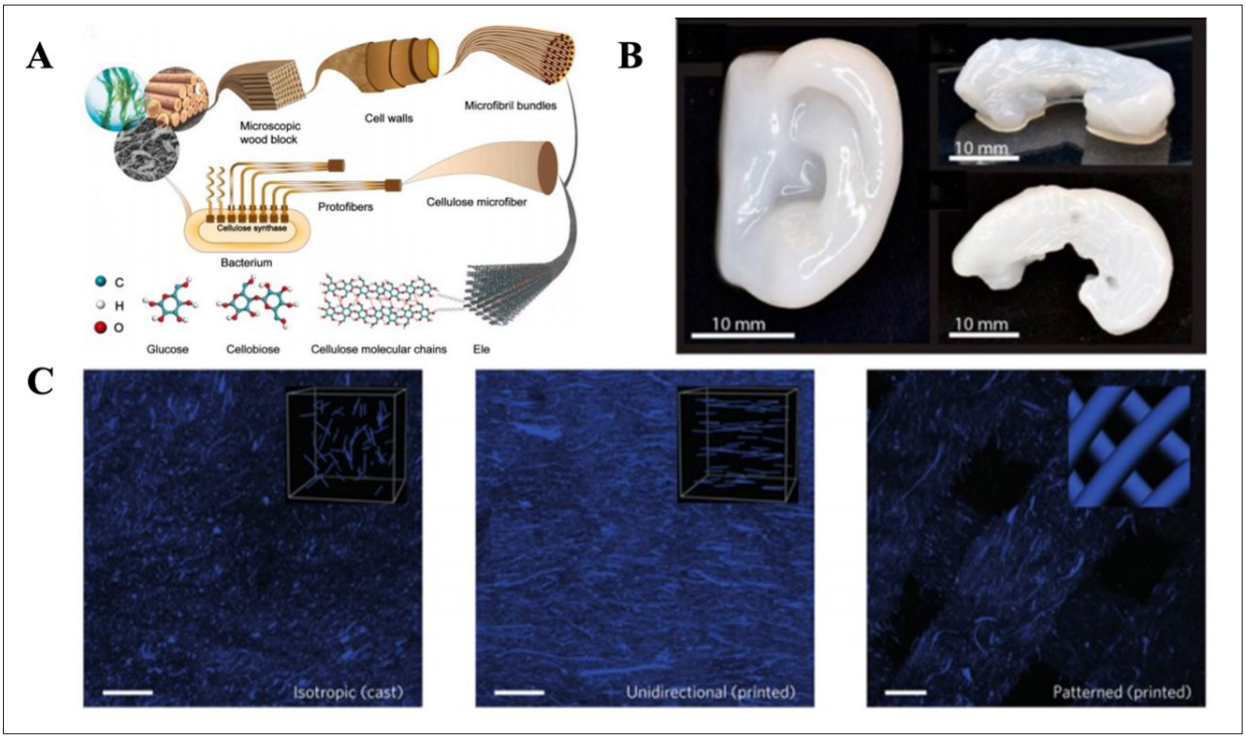

Figure 3. Cellulose material. (A) Schematic representation of the hierarchical structure of cellulose molecules from abundant sources.[32] Copyright © Elsevier 2022. Reprinted with permission of Elsevier. (B) 3D-printed cellulose nanofibrils resembling cartilage tissues of human ear.[33] Copyright © American Chemical Society 2015. Reprinted with permission of American Chemical Society. (C) Direct imaging of cellulose fibrils (stained blue) in isotropic, unidirectional and patterned samples; scale bar: 200 μm.[34] Copyright © Springer Nature 2016. Reprinted with permission of Springer Nature.

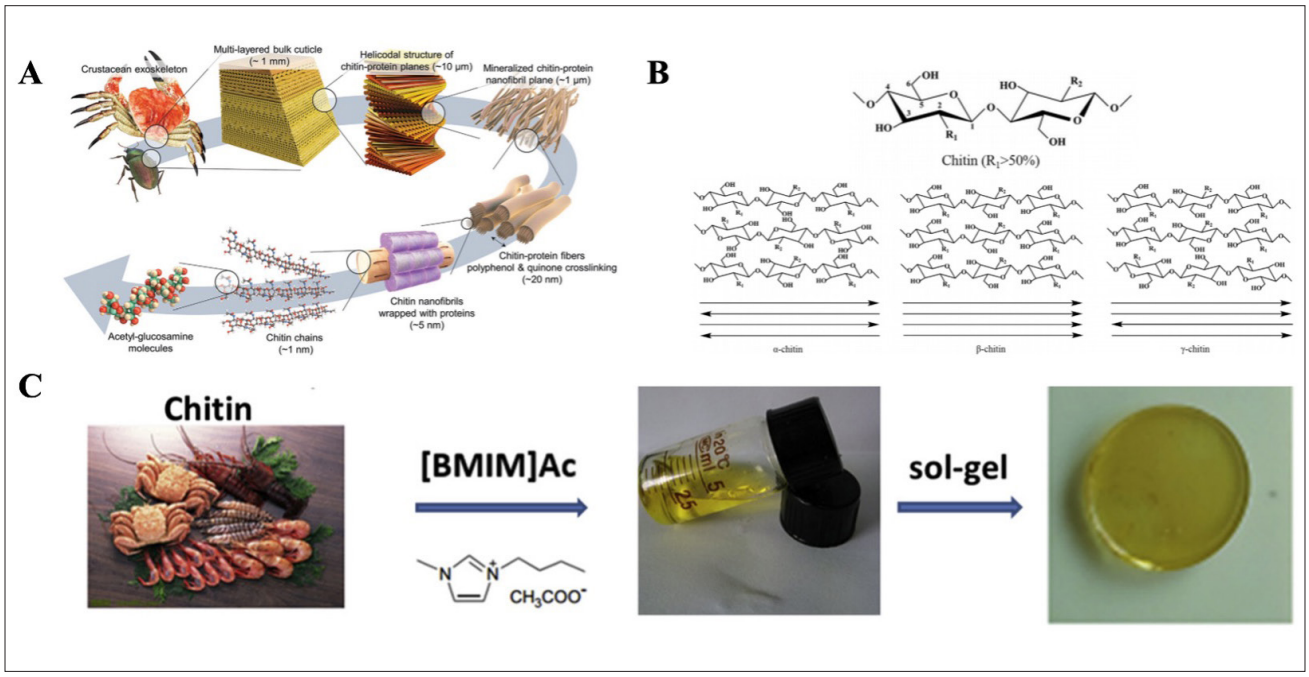

Figure 4. Chitin material. (A) Multi-scale structures of chitin in nature.[35] Copyright © John Wiley and Sons 2023. Reprinted with permission of John Wiley and Sons. (B) Chemical structures of chitin; arrangements of chitin molecules in α-chitin, β-chitin, and γ-chitin.[35] Copyright © John Wiley and Sons 2023. Reprinted with permission of John Wiley and Sons. (C) Preparation of chitin ionic liquid gel.[35,36] Copyright © Elsevier 2020. Reprinted with permission of Elsevier.

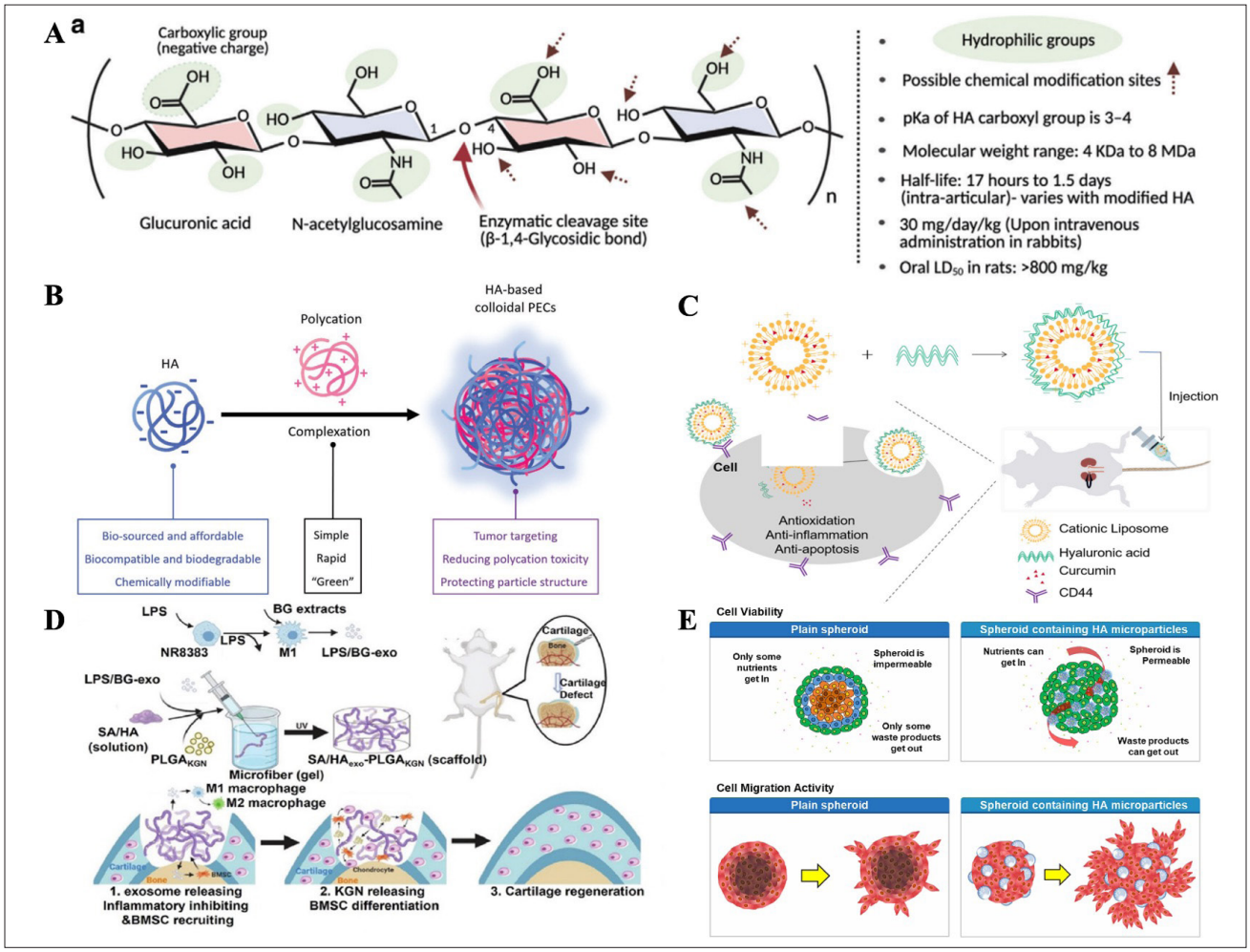

Figure 5. Hyaluronic acid (HA) material. (A) HA disaccharide unit chemical structure and its structural, physical, and biological properties.[37] Copyright © John Wiley and Sons 2023. Reprinted with permission of John Wiley and Sons. (B) Major applications of HA in biomedical fields.[37] (C) HA-coated liposome for targeted delivery of curcumin.[38,39] Copyright © John Wiley and Sons 2022. Reprinted with permission of John Wiley and Sons. Copyright © Elsevier 2023. Reprinted with permission of Elsevier. (D) Preparation of SA/HAexo-PLGAKGN scaffold and its biological function.[38,39] Copyright © John Wiley and Sons 2022. Reprinted with permission of John Wiley and Sons. Copyright © Elsevier 2023. Reprinted with permission of Elsevier. (E) Schematic illustration of forming HepaRG spheroids containing HA microparticles and evaluating cell viability and cell migration activity.[38,39] Copyright © John Wiley and Sons 2022. Reprinted with permission of John Wiley and Sons. Copyright © Elsevier 2023. Reprinted with permission of Elsevier.

Hyaluronic acid is an acidic mucopolysaccharide initially extracted from the vitreous body of bovine eyes.[37] Owing to its distinctive molecular structure and unique physical and chemical attributes, hyaluronic acid serves various pivotal physiological roles within the body. For instance, it functions in joint lubrication, the regulation of blood vessel wall permeability, and the modulation of proteins. Given its considerable clinical significance as a biochemical drug, hyaluronic acid has extensive applications in numerous types of eye surgeries, including lens implantation, corneal transplantation, and anti-glaucoma procedures.[38,39] Furthermore, it contributes to the treatment of arthritis and expedites wound healing (Figure 5).

Non-degradable polymer medical materials possess the capacity to maintain stability over extended periods within the physiological environment, resisting substantial degradation, crosslinking, or physical deterioration. These polymers showcase exceptional physical and mechanical attributes, which are pivotal for their swift integration into the medical domain. Several noteworthy non-degradable polymer medical materials include polyethylene, polypropylene, polyvinyl chloride, polyvinyl alcohol, and polymethyl methacrylate (Figure 6).

Polyethylene is a milky white thermoplastic resin polymerized from ethylene. It can be industrially produced from a mixture of the copolymer of ether and a small amount of α-olefin. Polyethylene is tasteless, odorless,

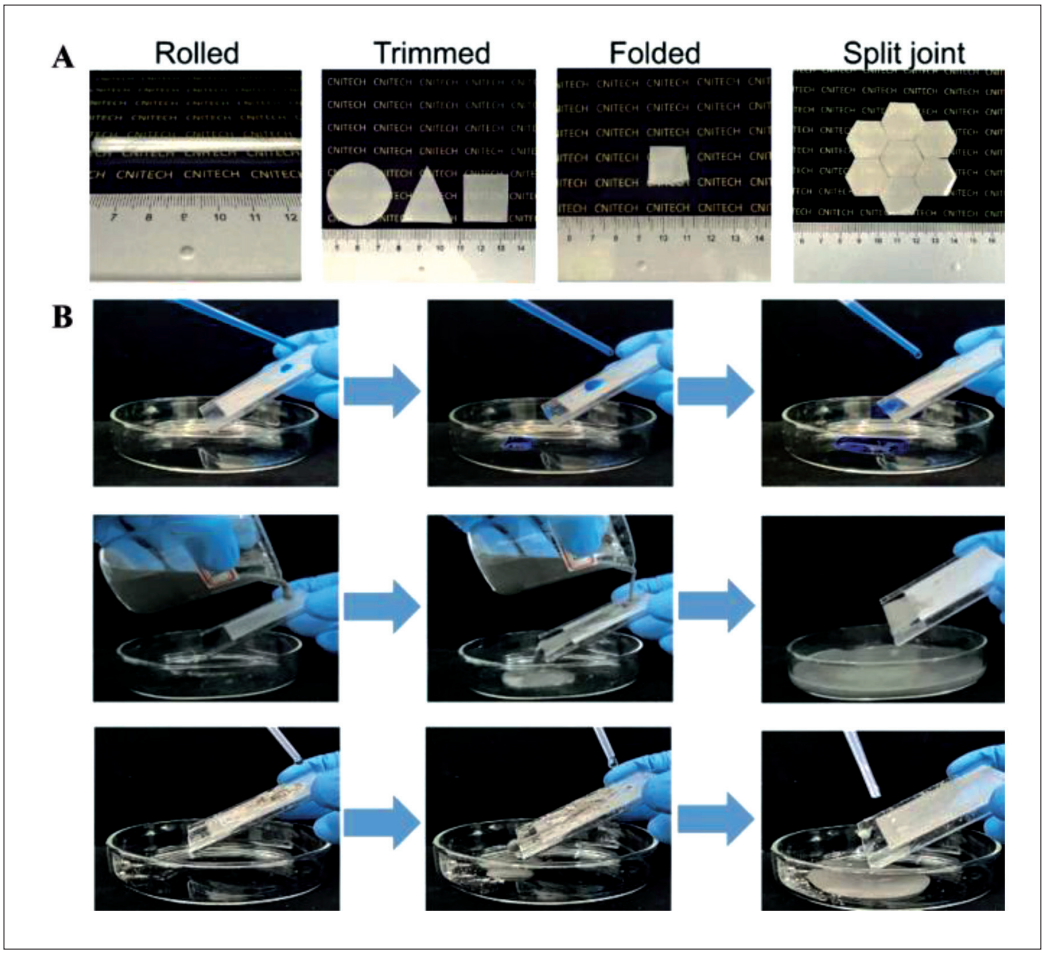

Figure 6. Polyethylene material. (A) Schematic representation of the methodology adopted for biomimetic porous high-density polyethylene/polyethylene-grafted-maleic anhydride scaffold development.[40] Copyright © Elsevier 2023. Reprinted with permission of Elsevier. (B) Porous high-density polyethylene scaffolds.[40] Copyright © Elsevier 2023. Reprinted with permission of Elsevier.

non-toxic, and wax-like in texture. It has excellent low-temperature resistance (the lowest operating temperature can reach -100 to -70°C), has good chemical stability, and is resistant to most acids and alkalis. Given its good biocompatibility, it is ideal for long-term implantation.[40] The fact that it can be preformed lends itself convenient for clinical use, and it can be thermally sculpted to meet clinical requirements. Polyethylene can be fastened with sutures, screws, and wires and is mainly used in jaw surface repairs, eyeball fillings, nose or cheek fillings, and ventilation medical devices.

Polypropylene is a polymer produced through addition polymerization of propylene. It is a white waxy material with transparency and lightness. Polypropylene is flammable, but it can resist the corrosion of acids, alkalis, salt solutions, and various organic solvents below 80°C.[41] Nevertheless, it will decompose under high temperature and oxidation. Polypropylene is a thermoplastic synthetic resin with excellent properties. It is a colorless, translucent, lightweight, general-purpose plastic with notable properties such as chemical resistance, heat resistance, electrical insulation, high mechanical strength, and good processability, including abrasion resistance.[42] In the medical field, the most common polypropylene medical products are medical non-woven fabrics. These fabrics are produced with special polypropylene material and warp knitting process, which have excellent thermal stability and abrasion resistance.[43] In addition, disposable medical products such as gloves, scotch tape, and medical tubing are also made of polypropylene.[44,45] Polypropylene is also used in hardware products due to its chemical stability, mechanical properties, and physiological safety. For example, it can be used as a flat artificial kidney splint. Polypropylene, whose surface has been treated with active agents, can also be used to produce artificial lungs (Figure 7).

Polyvinyl chloride (PVC) is a polymer formed through free radical polymerization under the action of light and heat. It is an amorphous white powder with a relative

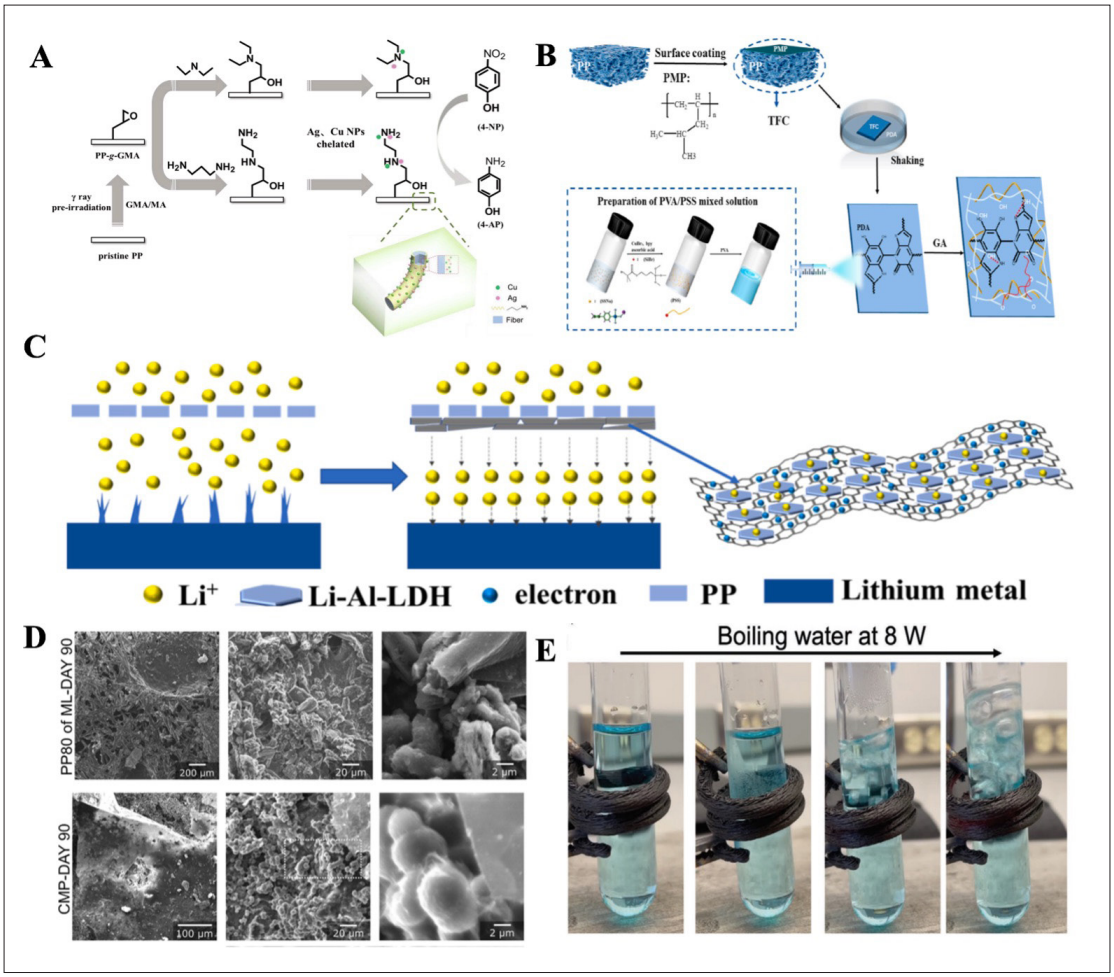

Figure 7. Polypropylene material. (A) Ag-Cu nanoparticles anchored on polypropylene (PP) nonwoven fabrics.[41] Copyright © Elsevier 2021. Reprinted with permission of Elsevier. (B) Schematic illustration of the preparation of PMP/PP TFC membrane and subsequent anticoagulant modification with PVA/PSS.[42] Copyright © Elsevier 2022. Reprinted with permission of Elsevier. (C) Schematic illustration of lithium deposition for cells using rGO/Li-Al-LDH@PP separators.[43] Copyright © Elsevier 2022. Reprinted with permission of Elsevier. (D) Scanning electron microscopy micrographs.[44,45] (E) Polypropylene-derived carbon can be employed as a heating element for boiling water at 8 W.[44,45] Copyright © Elsevier 2021. Reprinted with permission of Elsevier. Copyright © John Wiley and Sons 2023. Reprinted with permission of John Wiley and Sons.

density of about 1.4. PVC materials are widely used in the medical device industry, mainly because of their good physical properties, such as ease to manufacture, and good compatibility with intravenous fluids and blood. Commonly used PVC products in medical treatment contain dihexyl phthalate plasticizer. The function of dihexyl phthalate is to increase the elasticity of PVC products. As one of the most cost-effective and widely used plasticizers, dihexyl phthalate functions to make PVC soft and elastic. PVC is also the principal material used in disposable sterile medical devices, and medical products made of plasticized PVC were originally used to replace natural rubber and glass in medical devices, since plasticized PVC material is easier to sterilize, more transparent, more chemically stable, and cost-effective. Plasticized PVC products are easy to use, and because of their softness and elasticity, they can minimize damage to sensitive tissues and reduce discomfort to patients (Figure 8).

Polyvinyl alcohol (PVA) is a white, stable, non-toxic, water-soluble polymer. It usually exists in the form of a powder, flake, or flocculent solid produced through the polymerization and alcoholysis of vinyl acetate. PVA contains many alcohol groups, which give it polarity and the ability to form hydrogen bonds with water. Therefore, it is soluble in water. It is also soluble in hot hydroxyl solvents, such as glycerin and phenol, but insoluble in general organic solvents, such as methanol, benzene, acetone, and gasoline. PVA with a degree of alcoholysis of less than 95% can be dissolved in water at room temperature, while PVA with a degree of alcoholysis of more than 99.5% can only be dissolved in hot water above 95°C. PVA has been widely used in the field of biomedical engineering due to

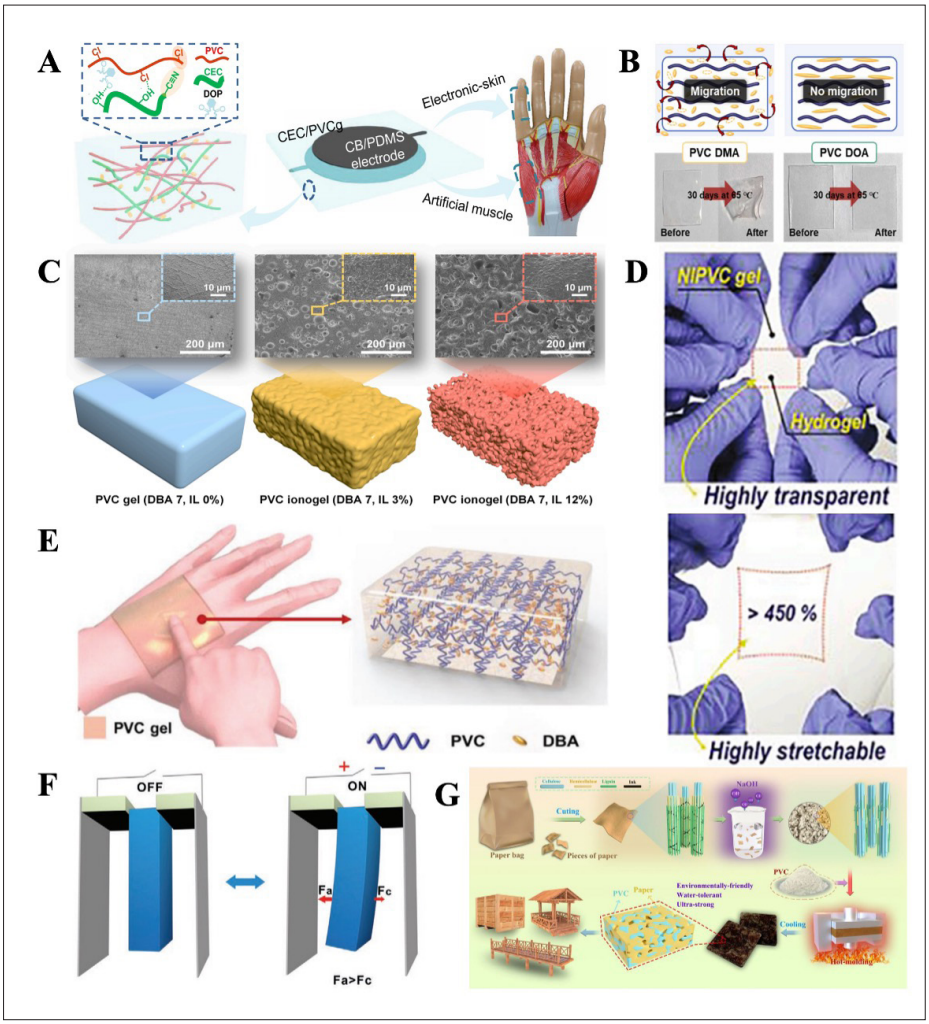

Figure 8. Polyvinyl chloride (PVC) material. (A) Schematic illumination of CEC/PVCg matrix for actuation and sensing applications.[46] Copyright © Springer Nature 2023. Reprinted with permission of Springer Nature. (B) Photograph of PVC DMA gel and PVC.[47] Copyright © Elsevier 2023. Reprinted with permission of Elsevier. (C) Microscopic morphology of PVC gel and PVC organic-ionogel.[48] Copyright © Elsevier 2023. Reprinted with permission of Elsevier. (D) Hydrogel-interconnected NIPVC gel being stretched by >450%.[49] Copyright © Elsevier 2022. Reprinted with permission of Elsevier. (E) Schematic of the PVC gel-based single layer TENG and 3D network structure of the PVC gel.[50] Copyright © John Wiley and Sons 2022. Reprinted with permission of John Wiley and Sons. (F) Schematic representation of the mechanism behind electric field-induced bending deformation of PVC gel.[51] Copyright © John Wiley and Sons 2022. Reprinted with permission of John Wiley and Sons. (G) Schematic of biocomposites preparation.[52] Copyright © Springer Nature 2023. Reprinted with permission of Springer Nature.

its water content, elastic modulus, low friction coefficient, high mechanical strength, rich pore structure, and good biocompatibility, which is equivalent to that of human tissue. PVA is also used in artificial cartilage, sustained drug release system, ophthalmology, artificial cell microencapsulation, anticoagulant materials, biomedical sponge, etc (Figure 9).

Polymethyl methacrylate (PMMA), commonly known as acrylic or plexiglass, is a polymer used as a substitute for glass by virtue of its high transparency, affordability, and ease of processing. In addition to possessing high mechanical strength and good moisture resistance, PMMA is lightweight and durable for a long time under humid conditions. It is also resistant to water-soluble inorganic salts and some dilute acids. PMMA has excellent anti-aging properties, biocompatibility, excellent optical properties, and high light transmittance.[57,58] Carbon fiber-reinforced PMMA composites exhibit superior flexural strength, modulus of rupture, and impact resistance compared to human skull materials, and play a vital role in protecting patients after skull defect repair.[59] Modified hydrophilic PMMA is widely used in ophthalmology, burn dressings, drug microcapsules, and other fields. In addition, PMMA

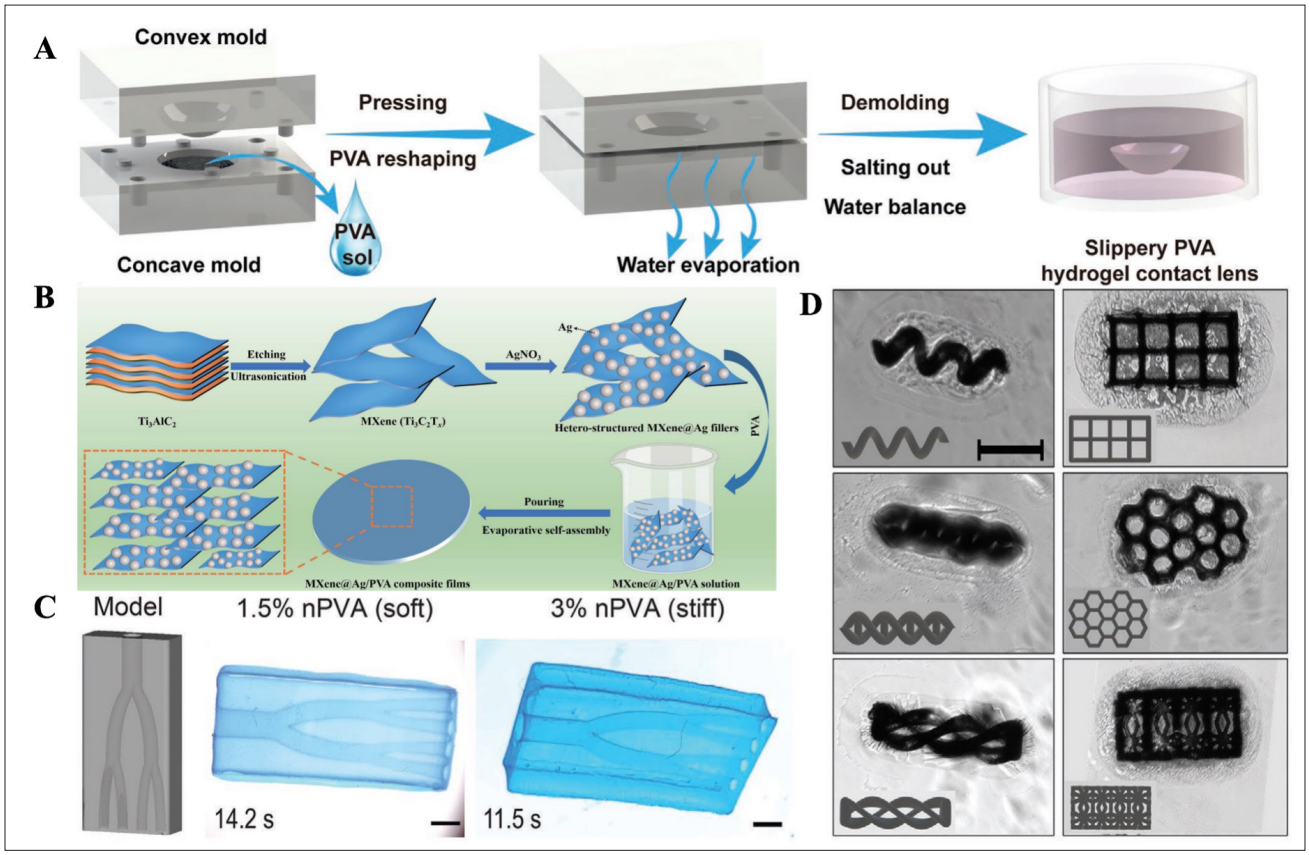

Figure 9. Polyvinyl alcohol (PVA) material. (A) A schematic illustration of the fabrication process of slippery PVA hydrogel contact lens using 3D-printed smooth molds.[53] Copyright © John Wiley and Sons 2023. Reprinted with permission of John Wiley and Sons. (B) Schematic illustration process for MXene@Ag/PVA composite films.[54] Copyright © Springer Nature 2023. Reprinted with permission of Springer Nature. (C) Computer-aided design (CAD) model (left) and stereomicroscopic images (right) of perfusable branch constructs fabricated via volumetric printing using a resin containing 1.5% nPVA and 3% nPVA within 14.2 and 11.5 s, respectively.[55] Copyright © John Wiley and Sons 2023. Reprinted with permission of John Wiley and Sons. (D) Optical images of different magnetic salted-out PVA microrobot structures immersed in acetone. Scale bar: 100 μm. The insets correspond to the designs used for printing the microstructures.[56] Copyright © John Wiley and Sons 2023. Reprinted with permission of John Wiley and Sons.

is the main polymer material used in the production of dialysis membranes for artificial kidneys (Figure 10).

Degradable polymer materials refer to synthetic polymers that can spontaneously degrade in a biological environment and produce non-toxic degradation products. These materials must meet specific requirements, such as not causing an immune or toxic reaction after entering the human body. In addition, the degradation time of the material must match the time for the material to function *in vivo*, with its eventual metabolism occurring outside the body. Degradation products of the material must also be non-toxic and non-immunogenic. Finally, the material must be easy to process. Polycaprolactone, poly(lactic-co-glycolic acid), and hydrogel are typical degradable polymer materials.

Polycaprolactone (PCL) is an organic polymer that appears as a white solid powder. It is soluble in organic solvents but insoluble in water. PCL has a low melting point, is biodegradable and biocompatible, and can be used in degradable plastics, medical and hygienic products, plastic materials, nanofiber spinning, plasticizers, etc.[65,66] Poly(lactic acid-co-glycolic acid) (PLGA) is produced by the random polymerization of two monomers, lactic acid and glycolic acid. It is a functional, degradable organic compound with excellent biocompatibility, non-toxicity, and film-forming ability. PLGA has a wide range of applications in medicine, medical engineering, and various modern industrial fields.[67] In the United States, PLGA has been certified by the U.S. Food and Drug Administration (FDA) and officially recognized as a pharmaceutical excipient by the United States Pharmacopoeia (Figure 11).[68]

3.2. Hydrogel materials

Hydrogels are potential materials providing a strong impetus behind the development of medical field. The 3D

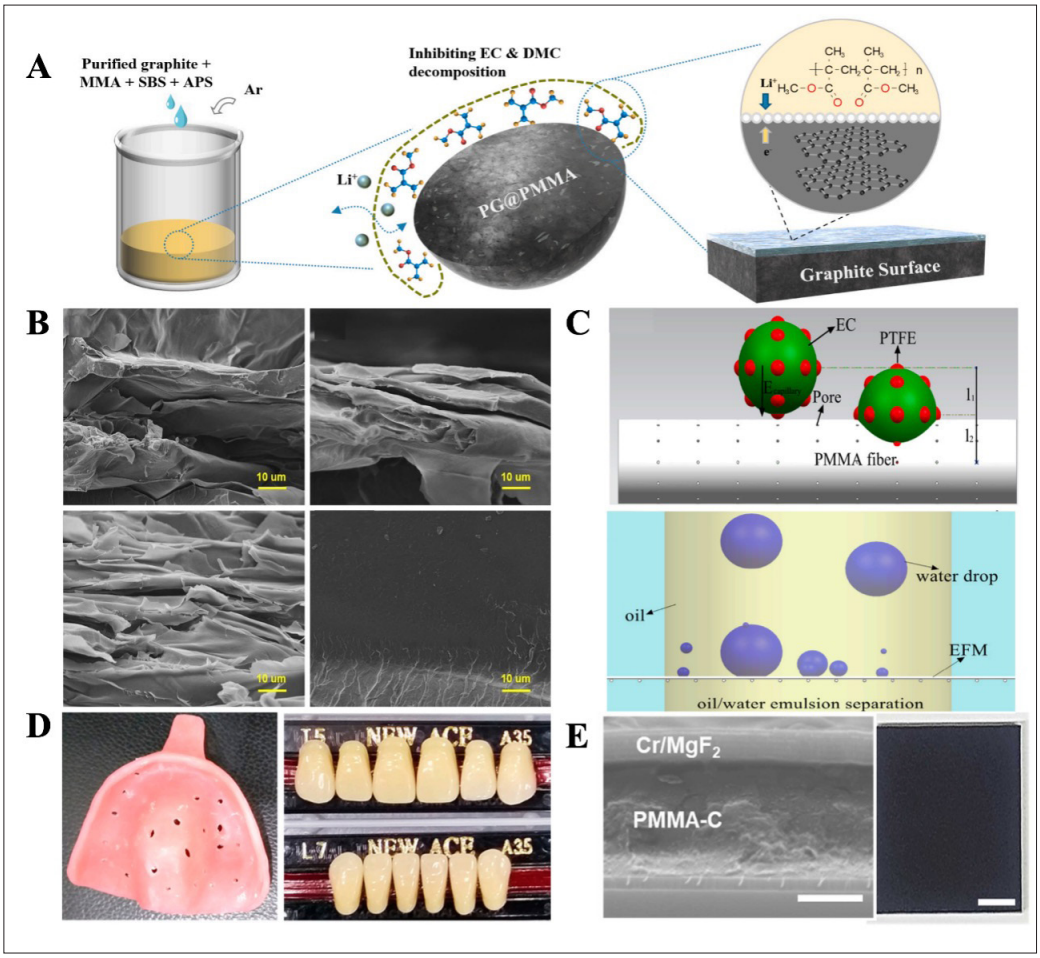

Figure 10. Polymethyl methacrylate (PMMA) material. (A) Schematic of the preparation and functional mechanism of PG@PMMA through emulsion polymerization.[60] Copyright © Elsevier 2023. Reprinted with permission of Elsevier. (B) Scanning electron microscopy (SEM) images of tensile fracture surface.[61] Copyright © Springer Nature 2023. Reprinted with permission of Springer Nature. (C) Electrospun PMMA fibers-based membrane achieving a full-particle size separation of oil-water emulsion.[62] Copyright © Elsevier 2023. Reprinted with permission of Elsevier. (D) Key applications of PMMA: secondary impression tray, acrylic artificial teeth, and denture with acrylic teeth.[63] (E) Cross-sectional SEM and digital camera images of the hybrid photothermal structure; scale bars: 1 μm and 0.5 cm, respectively.[64] Copyright © Elsevier 2023. Reprinted with permission of Elsevier.

network structure allows them to absorb large amounts of water, which causes expansion while maintaining the structure. The properties of hydrogels are dictated by their structure. Biocompatibility, biodegradability, and nanocomposite properties are the most common properties of hydrogels used in the medical field. Hydrogels boast a high resemblance to living tissue than any other synthetic biomaterial and are closer to the extracellular matrix (ECM) in nature.[75,76] Besides, hydrogels are able to reduce water absorption at the surrounding tissues, thereby improving the biological properties of the material.

Hydrogels can be classified according to their response to external stimuli. Traditional hydrogels are relatively insensitive, while environmentally sensitive hydrogels can detect small changes in the environment, which could lead to structural, chemical, and even genetic changes. Temperature-sensitive hydrogels, pH-sensitive hydrogels, light-sensitive hydrogels, and pressure-sensitive hydrogels are a few examples of sensitive hydrogels. Hydrogels have good scientific research and market application prospects due to their varied response properties to different environmental conditions.[77,78] Furthermore, hydrogels can be distinguished based on their network bonding. Physical hydrogels are generated by physical forces such as electrostatic interactions, hydrogen bonds, and chain entanglements, while chemical hydrogels are formed by crosslinking chemical bonds. Hydrogels can also be classified according to their synthetic materials, with synthetic polymer hydrogels and natural polymer hydrogels being the two main subcategories.

Hydrogel materials are biofunctional materials that share high level of similarity to living tissues by

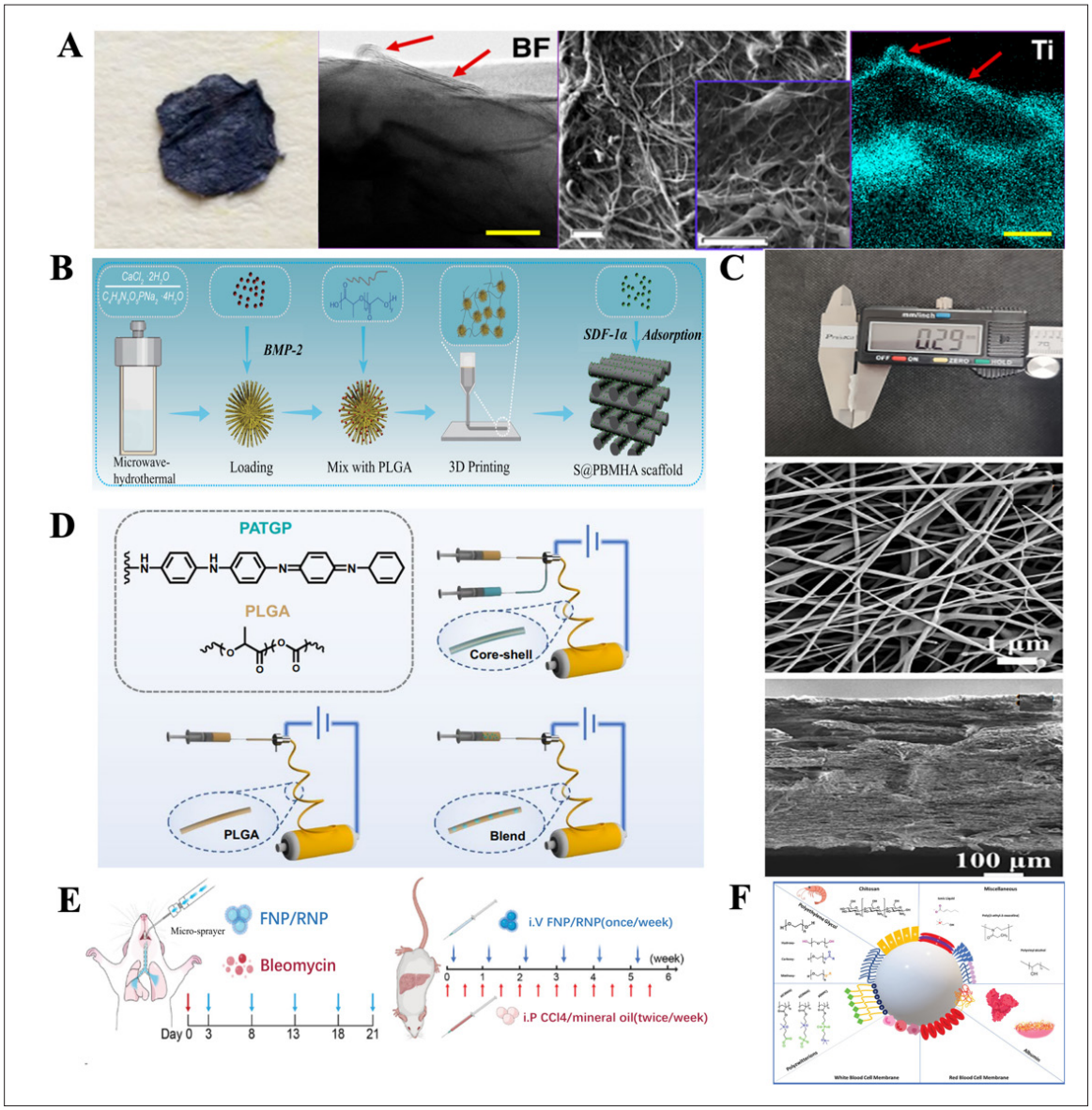

Figure 11. Polycaprolactone (PCL) and poly(lactic acid-co-glycolic acid) (PLGA) materials. (A) PCL electrospun nanofiber membranes with immobilized MXene; transmission electron microscopy image of the PCL-MX-2 sample (red arrows point to MXene flakes).[69] Copyright © American Chemical Society 2023. Reprinted with permission of American Chemical Society. (B) Schematic diagram of a composite scaffold of mesoporous hyaluronic acid (HA) microspheres loaded with BMP-2 and PLGA matrix.[70] Copyright © John Wiley and Sons 2023. Reprinted with permission of John Wiley and Sons. (C) Morphological images of fabricated electrospun PCL/polycarbosilane (PCS).[71] Copyright © Elsevier 2022. Reprinted with permission of Elsevier. (D) The preparation process of PLGA/PATGP core-shell nanofibers.[72] Copyright © Springer Nature 2022. Reprinted with permission of Springer Nature. (E) Fibroblast membrane-camouflaged nanoparticle (FNP) is supported by a PLGA-based nanoparticle cores.[73] Copyright © John Wiley and Sons 2022. Reprinted with permission of John Wiley and Sons. (F) Contemporary stealth surface modifications for improved PLGA particulate drug delivery.[74] Copyright © John Wiley and Sons 2022. Reprinted with permission of John Wiley and Sons.

virtue of their high water content, good water retention, good biocompatibility, and microstructure similar to ECM. Hydrogels are highly permeable to water-soluble metabolites, such as glucose, nutrients, and oxygen. Their ability to immobilize and release cells, genes, and drugs makes them versatile materials for biomedical applications, including drug delivery systems, ophthalmic materials, tissue engineering scaffolds, medical dressings, and cosmetics.

Hydrogels have good permeability to water-soluble small molecules and can release loaded substances continuously for a long time. This property enables hydrogels to be used as smart carriers in drug delivery systems for enhanced targeting efficacy. The vitreous body, situated between the

lens and the retina, is a clear gel composed of collagen and hyaluronic acid, making it a hydrogel tissue with sufficient strength and elastic functions. Hydrogels have been utilized to make artificial vitreous bodies for addressing conditions such as vitreous opacity and retinal detachment that can lead to vision loss. The hydrogel-based artificial vitreous body developed by Leone et al. using polyethylene glycol/polyvinylpyrrolidone exhibited viscoelasticity and effectively filled and smoothed the retina. Additionally, hydrogels are biocompatible and hydrophilic, and can swell up after water absorption without affecting their structural integrity. They can encapsulate bioactive factors, transmit signals to cells, and support cell culture.[79] As scaffold materials for tissue engineering, hydrogels can fill defect spaces and provide support structures for cell growth and function. Furthermore, neural progenitor cells can be cultured and expanded within hydrogels to create scaffolds for stem cell culture.[80] Traditional wound dressings such as gauze and cotton balls are clinically used because they can easily adhere to the wound. On the other hand, hydrogels emerge as a better option as they provide a high-humidity healing environment while continuously absorbing wound exudate. The transparency or translucence of hydrogel is another advantage, allowing wound monitoring, and the drug can be embedded in the hydrogel, so that the drug can be gradually and continuously released to the affected area to promote healing of the wound. Therefore, hydrogel dressings have become an increasingly important functional material in the field of skin repair and regeneration in recent years.[81] This is also marked by the important functions of hydrogels suitable for skin repair, such as oxygen permeability, physical barrier against bacteria, absorption of secretions and odor control, mitigation of inflammatory response and blood infiltration, inhibition of scar formation, and acceleration of wound healing. Hydrogels can be used as skin substitutes during wound healing, protecting the skin while preventing subsequent damage, promoting skin regeneration, and accelerating wound healing.[82] Taken together, hydrogels have great promise as potential material for facilitating effective wound healing and skin repair (Figure 12).

3.3. Biomedical ceramic materials

A biomedical ceramic is a specific type of ceramic designed for medical applications. They represent an important branch of biomaterials and are the first inorganic non-metallic materials used for the diagnosis, treatment, and regeneration of pathological human tissues and organs.[88] Initially, the materials for implantation into the human body for tissue replacement and repair were selected based on the criteria of non-biochemical reactivity and high stability, and this resulted in the first generation of bioceramics or bioinert ceramics. However, further research on the interaction of implant materials with the human body gave rise to the second-generation bioceramics, which have been developed into bioactive ceramics that can form biochemical bonds with tissues.[89] Porous calcium phosphate bioactive ceramics exhibit osteoinductivity, or the ability to induce bone tissue formation without the addition of growth factors or living cells, sparking research interest in materials for tissue regeneration. Biomaterials such as biomedical ceramics can adjust the biological effects of materials by controlling various parameters of the material, such as phase structure, chemical composition, mechanical properties, porous structure, and surface micro-nanostructure. This regulation can effectively control the directed differentiation and specific cell behavior of stem cells, regulate the growth of blood vessels, and promote the regeneration and repair of damaged tissues. A new generation of tissue-inducing biomaterials has been developed based on osteoinductive studies of porous calcium phosphate ceramics. These materials can stimulate self-healing functions, allowing regeneration of damaged tissue or organs after implantation.

Traditional belief suggests that non-living biomaterials cannot elicit tissue formation or organ regeneration. However, recent research developments challenge this notion by showing that tissues and organs can indeed arise from non-living substances. This perspective represents a significant departure from the established concept of biomaterials. Notably, research on biomedical calcium phosphate ceramics, which can induce bone tissue formation, has illuminated several novel approaches to tissue regeneration. These approaches propose utilizing non-living biomaterials implanted within the human body to stimulate the regeneration or formation of living tissues and organs. This innovative method is referred to as material-induced tissue regeneration.[95]

Biomedical ceramics have found extensive applications in medical field, including artificial bones, artificial joints, artificial tooth roots, bone filling materials, bone substitutes, tissue engineering scaffolds, artificial heart valves, artificial tendons, artificial blood vessels, artificial trachea, and prosthetic skin. This versatility has led to their integration into a wide range of prosthetic and medical devices. From a clinical perspective, the primary objective of utilizing biomedical ceramic materials is to replace damaged hard tissues like bone and dental tissue through transplantation techniques, addressing defects and providing mechanical support. Due to their remarkable physical and chemical similarity to natural hard tissues, biomedical ceramics have gained prominence in surgical applications, notably in the fields of dentistry and orthopedics. Alumina and zirconia ceramics are among the most notable biomedical ceramics,

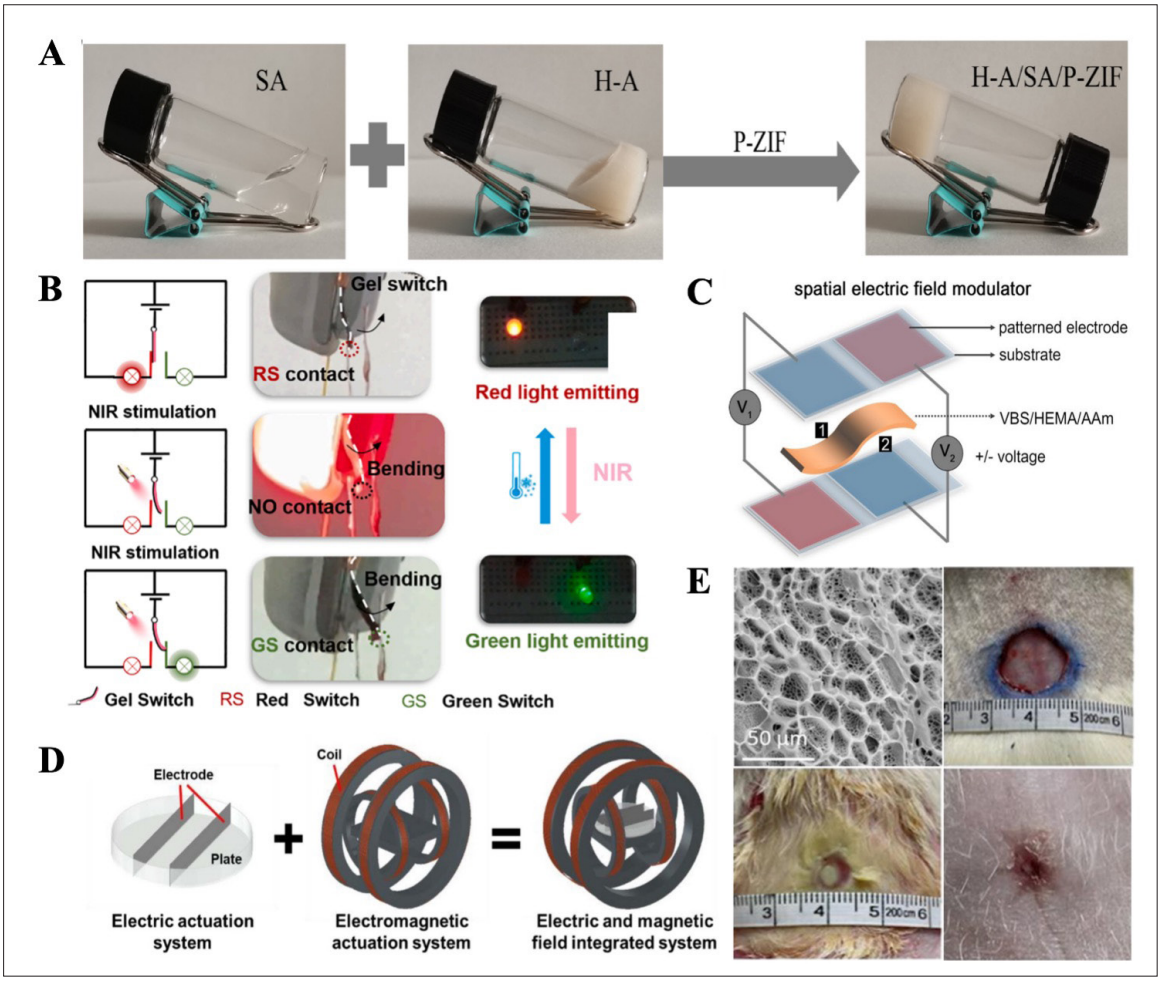

Figure 12. Hydrogel materials. (A) Photographs of sodium alginate(SA) solution, human-like collagen (H-A) solution, and formed hydrogel.[83] Copyright © Springer Nature 2023. Reprinted with permission of Springer Nature. (B) Schematic illustration and photos of the CNTs-Ecoflex0.1/PNIPAm0.5 as an electric switch to turn on/off red and green lights under NIR irradiation.[84] Copyright © Elsevier 2021. Reprinted with permission of Elsevier. (C) Schematic diagram of the positive and negative curvatures bending for electroactive hydrogel as a function of the separated electric field with a vertical electrode configuration.[85] Copyright © Springer Nature 2020. Reprinted with permission of Springer Nature. (D) The structure of the electric and magnetic field integrated systems.[86] Copyright © IOP 2020. Reprinted with permission of IOP. (E) Scanning electron microscopy images of microgel@PAM/CS hydrogels and typical macroscopic wound healing panorama on days 7, 11, and 15.[87] Copyright © American Chemical Society 2023. Reprinted with permission of American Chemical Society.

which are renowned for their exceptional mechanical properties. These materials can be fashioned into artificial implants, dental crowns, and patches, restoring the function of compromised tooth tissues. Additionally, they can be utilized to create artificial joints that replace damaged joints for restoring mobility and functionality. The continuously advancing biomedical ceramics preparation techniques have bequeathed ceramic artificial joints superior performance, as compared to traditional alloy materials, in replacement operations of joints, such as hip, knee, shoulder, elbow, and wrist. For instance, alumina-zirconia composite ceramic joints, often referred to as "powder pottery," have substantially improved wear resistance, chemical stability, and biocompatibility. They also emerge as a promising interface material for artificial joints, potentially surpassing both traditional alloy joints and conventional ceramic artificial joint materials (Figure 13).

Furthermore, hydroxyapatite and bioactive glass biomedical ceramic materials have gained significant attention in recent years. These materials find widespread use as coatings for metallic implants or as components in composite implants, such as bone screws, plates, and other orthopedic implants. These materials capitalize on their strong biocompatibility properties, leading to substantial improvements in the osseointegration capability of

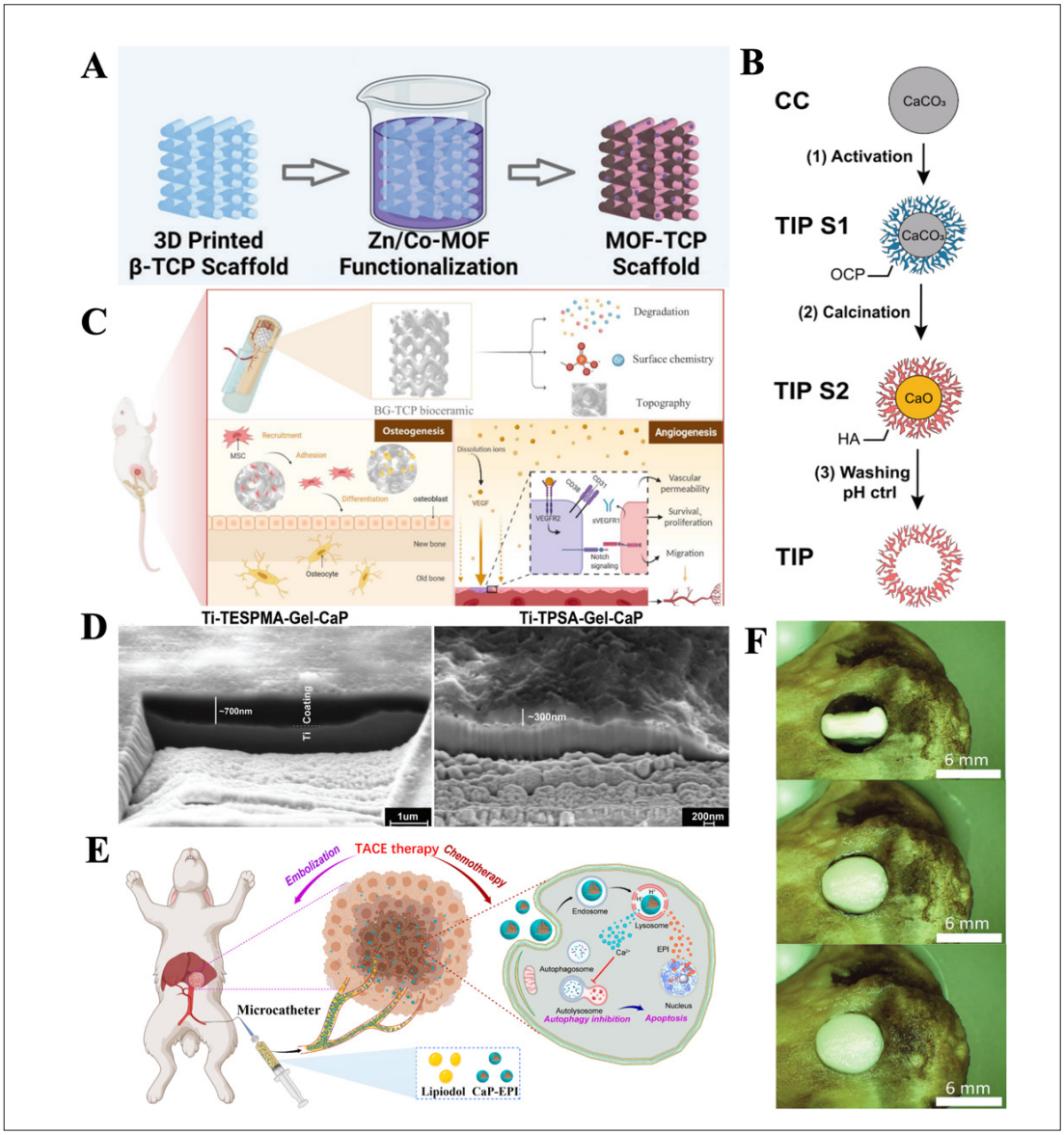

Figure 13. (A) Schematic diagrams of metal-organic framework tricalcium phosphate (MOF-TCP) scaffolds.[89] Copyright © John Wiley and Sons 2023. Reprinted with permission of John Wiley and Sons. (B) Schematic representation of the process for producing template inverted particle (TIP), an inorganic calcium phosphate microparticle.[90] Copyright © John Wiley and Sons 2023. Reprinted with permission of John Wiley and Sons. (C) BG-TCP bioceramic scaffolds promote bone regeneration through the regulation of angiogenesis and osteogenesis.[91] Copyright © Elsevier 2023. Reprinted with permission of Elsevier. (D) Focused ion beam scanning electron microscopy (FIB-SEM) images of Ti-TESPMA-Gel-CaP and Ti-TPSA-Gel-CaP.[92] Copyright © John Wiley and Sons 2023. Reprinted with permission of John Wiley and Sons. (E) Schematic diagram of EPI-loaded PAA/CaP (CaP-EPI) nanoparticles for transarterial chemoembolization (TACE) therapy.[93] Copyright © American Chemical Society 2023. Reprinted with permission of American Chemical Society. (F) Images of water-triggered, complete filling of a defect in chicken bone by using a pre-compressed biphasic calcium phosphate (BCP) ceramic sponge.[94] Copyright © John Wiley and Sons 2021. Reprinted with permission of John Wiley and Sons.

implants.[96] Their importance is growing across various applications, including fracture fixation repair, spinal fusion, alveolar bone elevation, mandibular reconstruction, and tooth root replacement. In cases of bone replacement and filling, porous biodegradable biomedical ceramics are employed, which are readily absorbed by the body after implantation. These ceramics stimulate bone tissue regeneration, expediting the recovery of bone tissue function. This category encompasses materials like porous hydroxyapatite ceramics, tricalcium phosphate ceramics, and more. Notably, these porous ceramic materials often serve as carriers for cells and factors used in bone tissue

Table 2. Comparison of different materials

Materials	Advantages	Disadvantages
Cellulose	Abundant in content	Poor solubility
Chitin	Abundant in content	Poor solubility
Hyaluronic acid	Good mechanical properties	The preparation process is intricate and costly
Polyethylene	High biocompatibility	Poor solubility
Polypropylene	Excellent electrical performance	Poor antioxidant
Polyvinyl chloride	Excellent electrical performance	Low biocompatibility
Polyvinyl alcohol	Excellent electrical performance	Poor fluidity
Polymethyl methacrylate	High biocompatibility	The preparation process is intricate and costly
Polycaprolactone	Excellent electrical performance	Poor solubility
Poly(lactic acid-co-glycolic acid)	High biocompatibility	The preparation process is intricate and costly
Hydrogels	High biocompatibility	Low biocompatibility
Biomedical ceramics	High biocompatibility	The preparation process is intricate and costly

engineering, significantly enhancing bone regeneration processes.[97] As 3D printing technology for biomedical ceramics continues to mature, the potential clinical applications for these materials are likely to expand further, opening up new avenues for innovation in the medical field (Table 2).

4. Applications of 3D bioprinting

As advancements in science and technology continue, organ transplantation has emerged as a lifeline for an increasing number of individuals facing organ failure and diagnosed with malignant tumors. However, the persistent shortage of donors has posed significant challenges for both patients and medical professionals. This scarcity has spurred the growth of underground and black-market organ trading. Recognizing the importance of addressing this concern, the Chinese government has resorted to scientific approach, placing significant emphasis on developing new technologies in the field of organ transplantation. Statistics reveal that out of the 1.5 million individuals in China afflicted with organ failure each year, only a fraction, roughly over 10,000 people, are qualified for organ transplantation. Unfortunately, many of the unselected individuals are left to face the increasing risk of organ deterioration or fatality while awaiting suitable donors.[98,99] In recent years, the advent of 3D printing technology has offered a potential solution to the grave challenges encountered in organ transplantation. The inception of 3D printing technology dated back to the mid-1990s. This technique involves methodologies such as photocuring and layering of materials to rapidly prototype a design. This emerging application technology relies on computer-generated 3D digital imaging and multi-level continuous printing techniques. 3D printing for artificial organs is rooted in this technology, which specifically utilizes living cells as raw materials to print functional living tissues. This approach can employ autogenic adult stem cells, which are induced to differentiate *in vitro*, as the foundation for printing functional organs or tissues. This can be achieved by *in vitro* and *in vivo* means, thus overcoming the challenge of organ scarcity by generating substitutes for malfunctioning organs or tissues.[100,101] In the realm of organ transplantation, this technique stands as a notable method for generating bone, artificial blood vessels, skin, vascular splints, heart tissue, and cartilage structures.

4.1. Artificial bone

The demand for personalized customized artificial bones in clinical applications is significant due to the irregular shapes of human bones and substantial variations in inter-individual anatomy.[102,103] Ma's work involves femtosecond laser-programmed 3D microrobotic prototype artificial musculoskeletal systems.[104] This approach utilizes two photosensitive materials sequentially built in predesigned structures, offering a general protocol for the direct printing of 3D microrobots composed of multiple materials. Huang et al. introduced a new surgical strategy for anterior fixation of unstable sacral fractures assisted by a minimally invasive subtropical approach using 3D printing.[105] This approach minimizes trauma and bleeding while addressing complex fractures. Strehin developed a chondroitin sulfate-polyethylene glycol (CS-PEG) adhesive hydrogel with versatile biomedical applications.[106] By functionalizing the carboxyl groups on the chondroitin sulfate (CS) chain with n-hydroxysuccinimide (NHS), adhesive hydrogels comprising biological and synthetic components were established. On the other hand, Dekali et al. reported a reproducible bioprinting process, followed by successful post-bioprinting chondrogenic differentiation using numerous human mesenchymal stem cell spheroids

encapsulated in xanthan alginate gel.[107] Liu et al. prepared PCL/SrHA composite scaffolds via 3D printing, which hold great promise as bone tissue engineering implant materials.[108] Another achievement was accomplished in the creation of a 3D-printed biodegradable scaffold for controlled release of deferoxamine, which is essential for angiogenesis and osteogenesis.[109] The scaffold's design aligns with bone development and remodeling through surface ammonolysis and layer-by-layer assembly techniques. The combination of 3D printing technology and digital design effectively enhances internal fixation and implantation outcomes for complex tibial plateau fractures (Figure 14).

4.2. Artificial blood vessels

In the modern context, the rising prevalence of cardiovascular and cerebrovascular diseases has heightened the clinical demand for vascular grafts. To meet this demand, 3D artificial organ technology is harnessed to fabricate blood vessels and vascular repair materials for transplantation. For instance, Gold et al. introduced a novel nanoengineered hydrogel bioink capable of 3D-printing anatomically accurate multicellular blood vessels by recreating the intricate physical and chemical microenvironment of the human vasculature.[110] A bioprinting strategy known as sequential printing in a reversible ink template (SPIRIT) was developed by Fang et al., which allows the generation of cardiac tissue and organoids through extensive stem cell proliferation and cardiac differentiation.[111] Moore et al. identified a subset of natural materials with the potential to produce durable, small-diameter vascular grafts, addressing a critical need for cardiovascular treatments.[112] As part of the effort to meet the growing demand for grafts, Silbermann et al. introduced a method

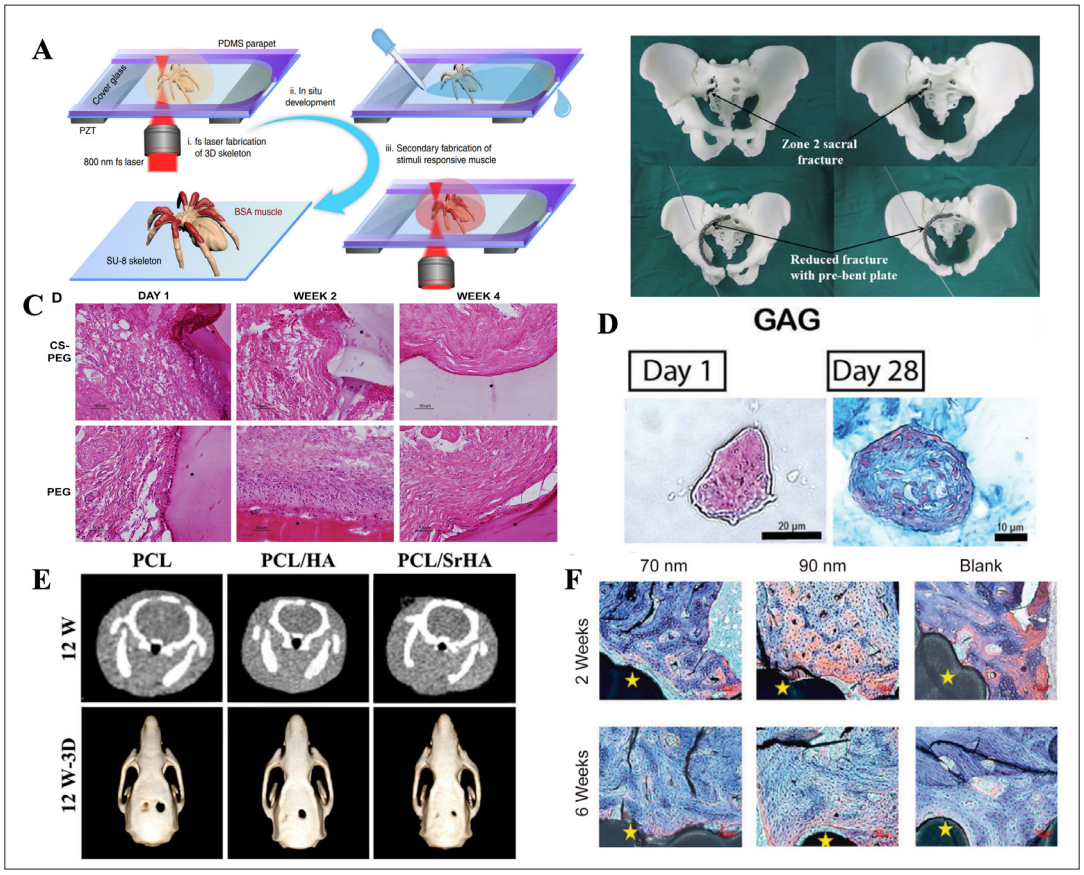

Figure 14. Artificial bone. (A) Schematic illustration for the femtosecond laser programmable fabrication of the musculoskeletal systems.[104] Copyright © Springer Nature 2020. Reprinted with permission of Springer Nature. (B) Simulated anterior plate fixation on a 3D-printed sacral fracture model.[105] Copyright © Elsevier 2021. Reprinted with permission of Elsevier. (C) Hematoxylin–eosin staining of CS-PEG and PEG gels after subcutaneous injection in a rat model.[106] Copyright © Elsevier 2010. Reprinted with permission of Elsevier. (D) Chondrogenic differentiation after the bioprinting process was confirmed with the assessment of GAG deposition in cells cultured in chondrogenic media for 28 days (GAG is stained blue in Alcian blue staining), as compared to no deposition at day 1, before the differentiation process commenced.[107] Copyright © John Wiley and Sons 2023. Reprinted with permission of John Wiley and Sons. (E) Microcomputed tomography images and 3D reconstruction images of Sprague-Dawley rats' skull defects after treatment with different 3D-printed scaffolds for 12 weeks.[108] Copyright © Elsevier 2019. Reprinted with permission of Elsevier. (F) The staining image showed that the new bone matured after 4 and 8 weeks of implantation.109 Copyright © Elsevier 2019. Reprinted with permission of Elsevier.

to enhance engineered cardiac tissue prepared from differentiated induced pluripotent stem cells (iPSCs) and ECM-based hydrogels in a fully biocompatible manner.[113] On the other hand, Mark et al. pioneered the assembly of hundreds of thousands of organ-building blocks into living matrices with high cell density.[114] Embedded 3D bioprinting introduces perfusable vascular channels, resulting in perfused cardiac tissue that fuses and beats synchronously over a 7-day period. Besides, Song et al. utilized a femtosecond laser beam loaded on a spatial light modulator (SLM) through pre-designed computer-generated holograms (CGHs) to modulate into a gap-ring Bessel beam, subsequently fabricating artificial blood vessels (Figure 15).[114]

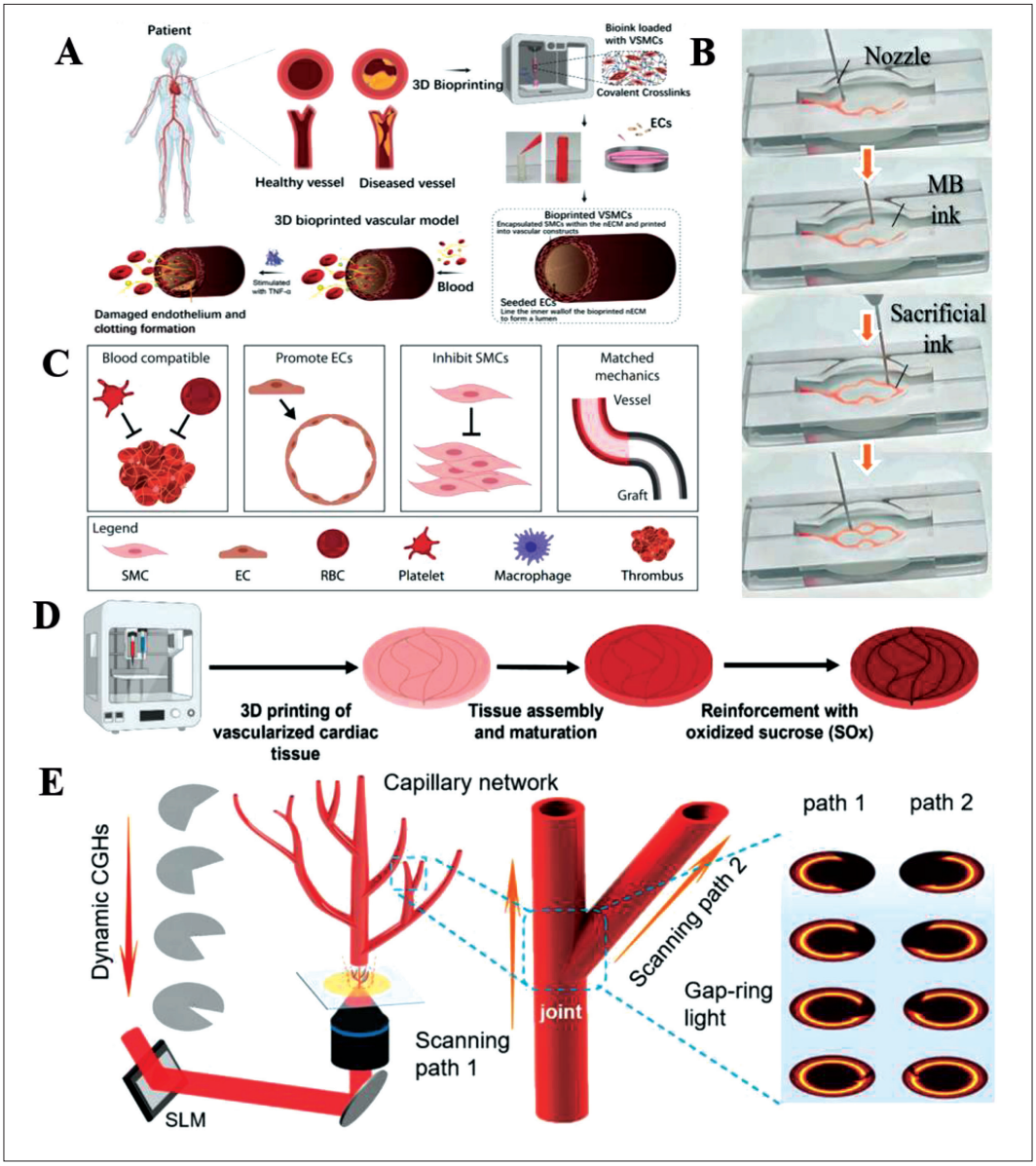

Figure 15. Artificial blood vessel. (A) Fabrication of 3D vascular model.[110] Copyright © John Wiley and Sons 2021. Reprinted with permission of John Wiley and Sons. (B) An image sequence showing the embedded printing of a branched vascular network within the micro-based biphasic (MB) bioink-based suspension medium.[111] Copyright © John Wiley and Sons 2023. Reprinted with permission of John Wiley and Sons. (C) Criteria for the rational design of artificial blood vessels. Abbreviations: EC, endothelial cell; EG, endothelial glycocalyx; RBC, red blood cell; SMC, smooth muscle cell.[112] Copyright © Elsevier 2022. Reprinted with permission of Elsevier. (D) Reinforcing 3D-printed vascularized cardiac tissue.[113] Copyright © John Wiley and Sons 2023. Reprinted with permission of John Wiley and Sons. (E) A conceptual schematic showing the rapid preparation of complex biomimetic microtube networks by a dynamic holographic processing method.[114] Copyright © John Wiley and Sons 2023. Reprinted with permission of John Wiley and Sons.

4.3. Artificial organ

The integration of precision medicine approach into 3D printing of human organs was first proposed by Radenkovic et al.[115] This concept involves seeding cells with optimal resolution, ensuring their viability during printing, employing compatible printers, and ultimately implanting the fabricated organs into patients. For instance, creating artificial livers involves emulating hepatic lobule structure to manufacture hepatic units, the fundamental components of liver structure and function. Yuan et al. presented a robust gelatin-based hydrogel with remarkable toughness and biocompatibility, which can be directly sutured to severed tendons of adult rabbits, rapidly promoting tendon differentiation and recovery to the initial state within 8 weeks.[116] In another study, Wang et al. developed a clinical-grade bioartificial liver (BAL) device utilizing human induced hepatocytes (hiHeps) produced under Good Manufacturing Practice (GMP) conditions.[117] Meanwhile, Liu et al. successfully repaired a skull model with a sagittal suture defect.[118] Several studies have proposed techniques based on 3D printing for facilitating artificial organ creation. John et al. reported a method for creating aligned cardiac tissue using anisotropic organ building blocks bioprinted from human-induced pluripotent stem cell-derived cardiomyocytes.[119] This approach enables high cell density and intricate cell arrangements, which are critical determinants for functional cardiac tissue creation. On the other hand, Noor et al. presented a simple technique for 3D printing thick, vascularized, perfusable cardiac patches tailored to a patient's immune, cellular, biochemical, and anatomical attributes.[120] Mathematical modeling of oxygen delivery further improved vascular structure, and the elongated cardiomyocytes in these patches exhibited abundant actin striations (Figure 16).

4.4. Skin repair

Researchers have explored various ECMs in the context of 3D printing technology for skin applications. This approach aims to optimize the natural properties and activity of skin, allowing for effective repair of damaged skin post-transplantation and seamless integration between printed and normal skin. Wu et al. utilized three distinct skin cell types—keratinocytes, melanocytes, and fibroblasts from different donors—to create a 3D-colored human skin structure that closely resembles the complex pigmentation of the donors.[121] This innovation has enabled the development of *in vitro* 3D skin constructs with coloration, serving purposes such as toxicology testing and basic cell biology research. Hakimi et al. introduced a handheld skin printer capable of on-site fabrication of biomaterial and skin tissue sheets featuring varied homogeneity and structural composition.[122] Precise sheet formation was achieved by synchronizing the delivery flow rates of bioink and crosslinker solutions, along with the speed at which a pair of rollers actively moved the cartridge across the surface. Additionally, Kim et al. presented a novel printing platform for the creation of mature, perfusable vascularized 3D human skin equivalents, encompassing epidermis, dermis, and subcutaneous tissue.[123] This advancement holds potential for offering an enhanced *in vitro* platform for pathology research and the investigation of dermatological mechanisms. The application of 3D bioprinting in regenerative medicine provides a flexible tool to address these challenges. For instance, Cubo utilized this technique to print two layers of human skin using bioinks containing human plasma, primary human fibroblasts, and keratinocytes obtained from skin biopsies.[124] This highlights the potential of 3D bioprinting in generating skin constructs for various applications, ranging from regenerative medicine to dermatological research.

Ma et al. employed "cell writing" bioprinting technology to create a functional skin substitute, supplied with blood vessels, based on a biomimetic multicellular system.[125] This system, encompassing SS-containing constructs, showcased an unprecedented blend of vascularized skin-like structure and the capacity to induce vascularization. It demonstrated remarkable angiogenic activity both *in vitro* and *in vivo*. This investigation offers insights into crafting biomimetic multicellular structures with angiogenesis-inducing attributes, which can aid in regenerating vascularized complex and layered tissues. Zhang et al. developed a swift and straightforward method to directly process adipose tissue into microfragmented adipocyte ECM.[126] This matrix was harnessed as the primary component of bioinks for fabricating biomimetic multilayered implants via 3D bioprinting. This approach accelerates the production of bioprinted skin substitutes and holds promise for treating full-thickness skin defects. Puchett et al. showcased newly formulated inks and the capability to generate comprehensive skin models through an open-source printer.[127] Through immunostaining and electron microscopy, they demonstrated that the bioprinted skin displayed all the characteristics of human skin at both molecular and macromolecular levels. This underscores the potential of bioprinting to create highly authentic skin models for various applications (Figure 17).

4.5. Stomatology

Mouthwash tools are made of a variety of materials, including alloys, biochemical ceramics, and photosensitive resins. Alloys are predominantly used in 3D printing for creating toothed belts, dental bridges, metal inner crowns, and other components. Laser sintering is sometimes employed in tooth restoration. Ceramic 3D printing is used to repair damaged oral tools and restore gear components, especially for backlash correction, and is

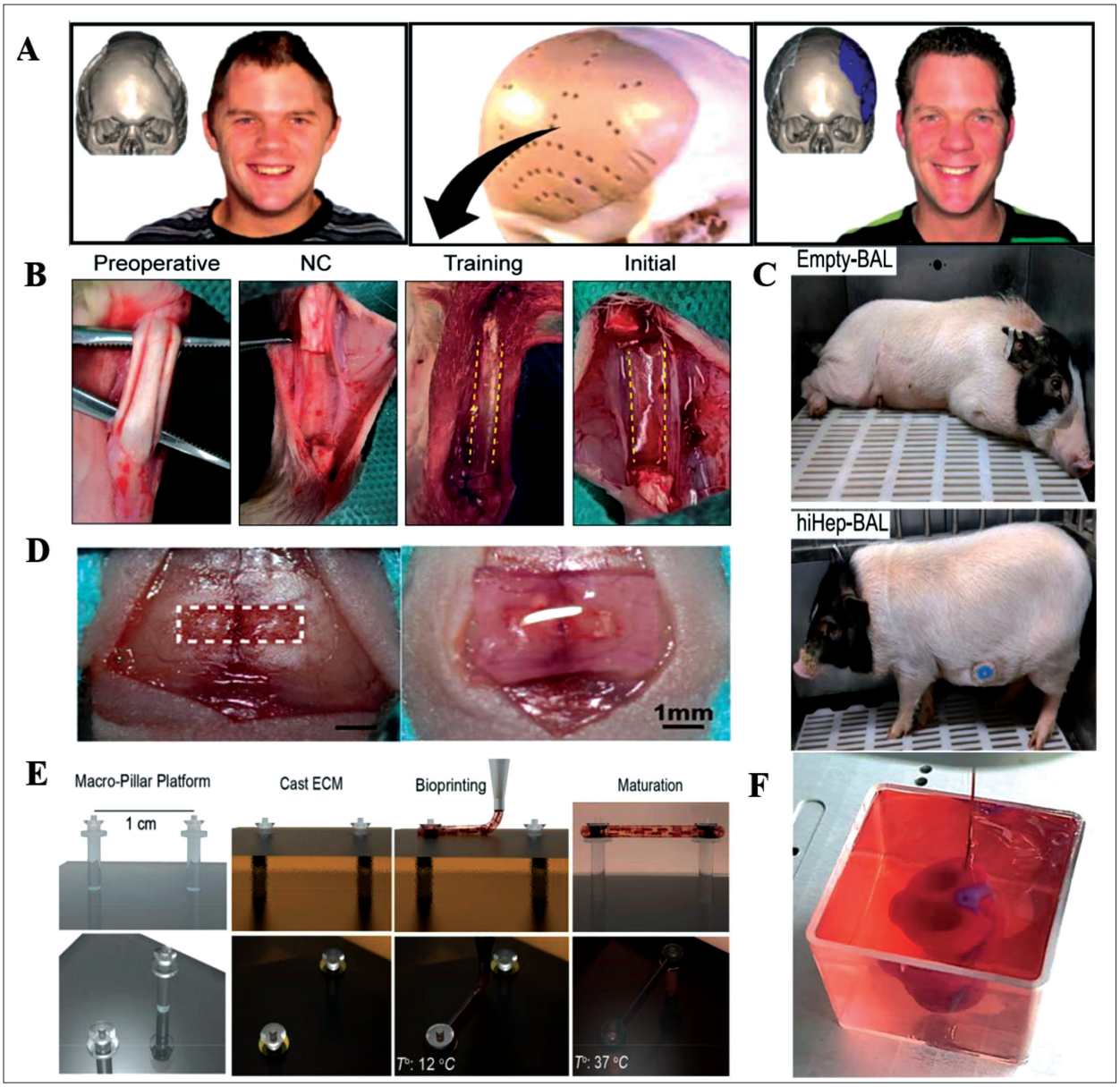

Figure 16. Artificial organ. (A) 3D-printed custom-made skull implant produced by Xilloc B.V. was used to treat a left-skull deformity acquired after multiple surgeries and resorption of transplanted bones.[115] Copyright © Elsevier 2016. Reprinted with permission of Elsevier. (B) Intraoperative images of *in vivo* tendon repair experiments.[116] Copyright © John Wiley and Sons 2023. Reprinted with permission of John Wiley and Sons. (C) Miniature pigs treated with empty-BAL or hiHep-BAL.[117] Copyright © Elsevier 2023. Reprinted with permission of Elsevier. (D) Photographs showing a critical-sized skull defect (4 × 1 mm) in the nude mice and the transplantation of biomimetic periosteum.[118] Copyright © John Wiley and Sons 2023. Reprinted with permission of John Wiley and Sons. (E) Schematic overview of the bioprinting process used to generate aligned cardiac macrofilaments on macropillars.[119] Copyright © John Wiley and Sons 2022. Reprinted with permission of John Wiley and Sons. (F) A printed heart within a support bath.120 Copyright © John Wiley and Sons 2019. Reprinted with permission of John Wiley and Sons.

often performed together with β-tricalcium phosphate and apatite, which share structural similarity to teeth.[128,129] Polymer materials, specifically photosensitive resin, are employed in mouthwash tools, often combined with anodized aluminum oxide and zirconia-mounted ceramics in printed joints.

Han et al. developed a particle-based bioink called demineralized dentin matrix (DDM) with improved 3D printing capabilities.[130] Cytocompatibility tests demonstrated that this bioink preserved the viability of dental pulp stem cells (DPSCs) at over 95%. Furthermore, DPSCs displayed enhanced odontogenic differentiation

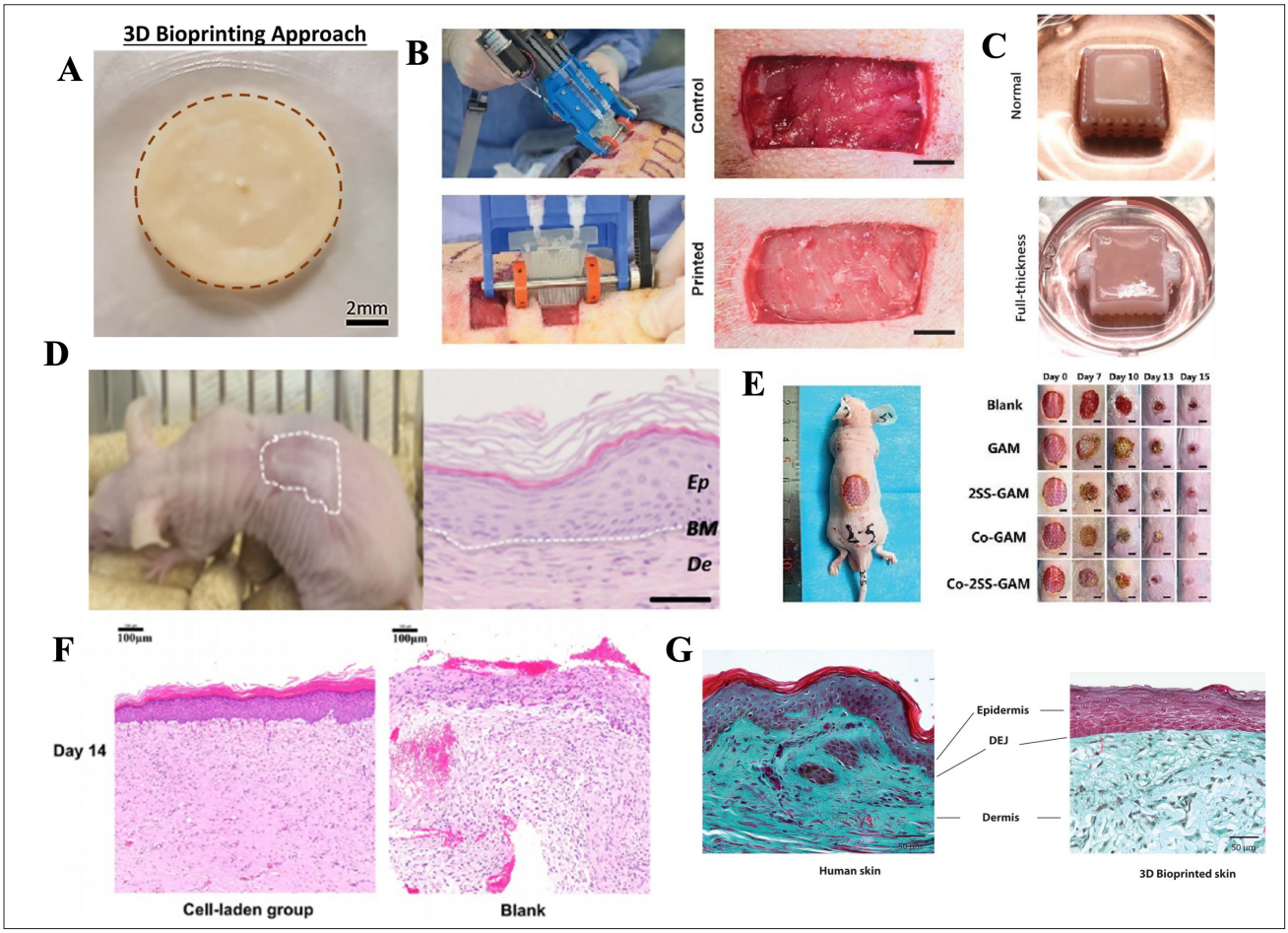

Figure 17. Skin repair. (A) 3D-bioprinted pigmented human skin constructs with uniform skin pigmentation.[121] Copyright © IOP 2018. Reprinted with permission of IOP. (B) *In situ* 3D printing in the field of skin repair.[122] Copyright © Royal Society of Chemistry 2018. Reprinted with permission of Royal Society of Chemistry. (C) A 3D skin equivalent composed of dermis and epidermis (normal) and a perfusable and vascularized 3D skin equivalent composed of hypodermis, dermis, and epidermis.[123] Copyright © John Wiley and Sons 2019. Reprinted with permission of John Wiley and Sons. (D) Histological analysis, performed 8 weeks post-grafting, of bioprinted human skin grafted to immunodeficient mice.[124] Copyright © IOP 2018. Reprinted with permission of IOP. (E) Induction of skin tissue regeneration in nude mice.[125] Copyright © John Wiley and Sons 2021. Reprinted with permission of John Wiley and Sons. (F) Representative hematoxylin–eosin staining images of biomimetic multilayer implants on day 14, which accelerated wound healing in a murine model of a full-thickness skin defect.[126] Copyright © American Chemical Society 2023. Reprinted with permission of American Chemical Society. (G) Histological and morphological characterization of bioprinted skin.[127] Copyright © John Wiley and Sons 2017. Reprinted with permission of John Wiley and Sons.

with increasing DDM particle concentration. Ahmadinejad et al. created composite materials, such as PCL/45S5 bioglass (BG), and 3D-printed scaffolds using PCL/HA.[131] These structures were evaluated separately for dentin and pulp tissue regeneration. Their findings indicate that PCL/BG and PCL/HA scaffolds exhibit the potential to enhance human dental pulp stem cell (hDPSC) adhesion and odontogenic differentiation, contributing to dental tissue regeneration.

Lin et al. conducted research involving the incorporation of varying concentrations of calcium silicate (CS) within a GelMA matrix.[132] They utilized bioprinting to create scaffolds loaded with hDPSCs, aiming to assess their potential to promote tooth formation. The outcomes revealed that CS/GelMA scaffolds not only improved the physical and chemical attributes of hDPSCs but also exhibited enhanced tooth generation capabilities when compared to GelMA scaffolds. These findings suggest that CS/GelMA scaffolds hold promise as cell-loaded materials for future clinical applications and dentin regeneration. In the work by Wang et al., bilayer scaffolds supported by gingival fibroblasts and composed of collagen and strontium-

doped calcium silicate (SrCS) were fabricated.[133] Achieved through 3D printing, these cell-supported collagen/SrCS bilayer scaffolds demonstrated the potential to promote bone regeneration in the context of osteoporosis, while also enhancing osteogenesis. This approach is particularly relevant for periodontal regeneration. Kim et al. evaluated the effects of biocomposites incorporated with bioactive cells, bone-derived dECM, and calcium phosphate ceramics on osteogenic and odontogenic differentiation of hDPSCs.[134] The hDPSC-loaded biocomposite was implanted into the subcutaneous region of mice, leading to significant osteogenic/odontogenic heterotopic hard tissue formation after 8 weeks. Yang et al. designed 3D-bioprinted biomimetic periodontal modules using GelMA/dECM cell-loaded bioinks.[22] These modules exhibited high integrity and substantially enhanced the regeneration of periodontal tissues in Beagle hybrid models. Notably, they facilitated the development of well-aligned periodontal fibers, anchoring structures at the bone-ligament interface, and highly mineralized alveolar bone (Figure 18).

4.6. Cellular printing

Cell printing pertains to incorporating living cells in biomaterials, like hydrogels, for generating bioinks. These

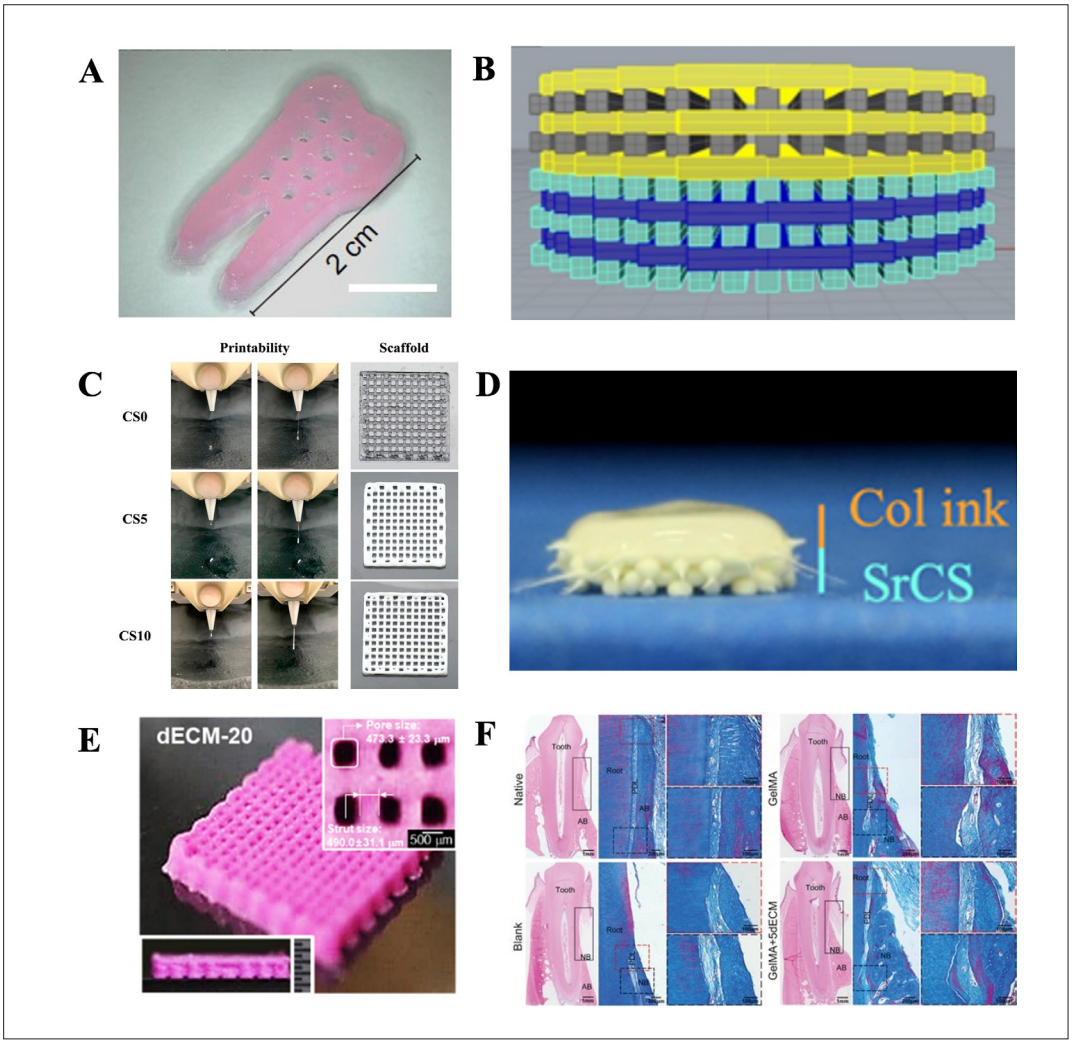

Figure 18. Stomatology. (A) Fabrication result of tooth-shaped hydrogel construct printed with DPSC-laden DDM particle bioink (10% w/v).[130] (B) Morphological characterization of the 3D-printed PCL/BG and PCL/HyA bilayer scaffolds CAD models of the scaffolds.[131] Copyright © MDPI 2021. Reprinted with permission of MDPI. (C) Printability test of CS/GelMa bioinks and the images of the fabricated 3D scaffolds.[132] Copyright © MDPI 2021. Reprinted with permission of MDPI. (D) Side-view images of the Collagen bioink/SrCS bilayer scaffolds.[133] Copyright © MDPI 2021. Reprinted with permission of MDPI. (E) Optical for 3D printing dECM-20 biocomposite.[134] Copyright © John Wiley and Sons 2022. Reprinted with permission of John Wiley and Sons. (F) Periodontal regeneration induced by the 3D-bioprinted periodontal module.[22] Copyright © John Wiley and Sons 2023. Reprinted with permission of John Wiley and Sons.

bioinks are then used in 3D printing to construct organs or organ prototypes. This approach finds extensive utility in tissue repair, which is instrumental for unraveling tissue development mechanisms and facilitating drug screening. Hydrogels, formulated from hydrophilic polymers such as alginate, gelatin, and GelMA, undergo crosslinking through various mechanisms, such as thermal entanglement, molecular self-assembly, electrostatic interactions, ionic bonding, and chemical reactions. Cui et al. introduced an innovative technique employing 3D cell printing technology to establish a method for addressing volumetric muscle loss using dECM bioink.[135] This technique facilitated the generation of volumetric muscle structures utilizing cell-loaded dECM bioinks with the aid of a particle-based printing approach. The outcomes underscore the potential of 3D cell printing in conjunction with tissue-derived bioinks for effectively generating biomimetic engineered muscles, thus enhancing the treatment of volumetric muscle loss injuries. Proposed by Ribezzi et al., a groundbreaking approach termed embedded extrusion volume printing, which encompasses polymer extrusion bioprinting and layerless ultrafast volumetric bioprinting, allows for the spatial arrangement of various inks and cell types, opening up new avenues for producing biologically functional regenerative grafts.[136] Moreover, this approach holds promise in developing engineered living systems and models for metabolic diseases.

Ali et al. devised a kidney-specific microenvironment for kidney tissue bioprinting using a photo-crosslinked kidney ECM-derived bioink called KdECMMA.[137] The resulting bioprinted kidney constructs exhibit both structural and functional traits akin to native kidney tissue. The utility of tissue-specific ECM-derived bioinks was demonstrated in cell-based bioprinting, promoting cell maturation and eventual tissue formation. Singh et al. utilized coaxial 3D cell printing technology to craft microfluidic hollow tubes, comprising tubular/vascular renal parenchyma composed of tubular epithelial cells and endothelial cells.[138] They developed a hybrid bioink that can create the microenvironment of vascularized native kidney tissue. With rapid crosslinking properties, this hybrid bioink optimizes cell function and retains the predefined hollow tube architecture, which holds promise for applications in regenerative medicine. On the other hand, Kim et al. innovatively modified the 3D cell printing process to yield *in situ* uniaxial alignment and microtopography.[139] Leveraging 3D printing technology, they successfully generated cell-based dECM structures imbued with distinct topographical cues. This approach's potential extension to various musculoskeletal tissues like tendons and ligaments could lead to the development of *in vitro* tissue-on-a-chip models for drug screening and developmental studies. Abate's team introduced a novel microfluidic technique named high-resolution single-cell printing.[140] This technique utilizes a highly miniaturized microfluidic sorter within Bioprine to precisely print individual cells from a mixture of multiple candidates. Achieving precision at ~10 μm and a speed of ~100 Hz, this approach has notable implications for bioprinting applications requiring single-cell precision.

This technology overcame the limitations of traditional tissue engineering methods with low spatial resolution and allows for precise control of cell distribution. In the "cell printing" process, cells (or cell aggregates) and a sol gel (precursor of hydrogel) are simultaneously placed in the printhead of a printer. The deposition positions of cell-containing droplets are controlled by a computer, and printing is done point by point at specified locations. After printing one layer, another layer is printed on top, and this layer-by-layer process continues to create a 3D multicellular/gel system.

Compared to traditional tissue engineering techniques like "cell-scaffold" methods, cell printing offers several advantages: (i) simultaneous construction of biologically active 2D or 3D "multi-cell/material" systems; (ii) accurate deposition of different types of cells in spatiotemporal manner; and (iii) creation of a 3D microenvironment for cells.

Furthermore, cell printing is a high-throughput cell arrangement technology that is entirely computer-controlled and can be developed into a technique for *in situ* operations within an organism. This technology finds applications in tissue engineering, development of cell-based sensors, modeling in drug metabolism kinetics, and drug screening (Figure 19).

5. Discussion

3D bioprinting technology can meet personalized, small-batch, and large-scale medical needs. It has been widely used in the field of *in vitro* medical device manufacturing and is currently being extended to personalized permanent implants, clinical prosthetics, and drug development trials. However, with the expansion of the application of 3D bioprinting technology in the field of biomedicine, problems such as low printing throughput, standardization of preparations, and specialization have become key constraints restricting the application of this technology. In addition to adopting the core technology of traditional 3D printing, all manufacturing processes must be able to satisfy biological and medical standards, as well as preserve cell activity and tissue function. This required extensive experimentations to optimize the integration of biomaterials, cells, and growth factors for 3D bioprinting

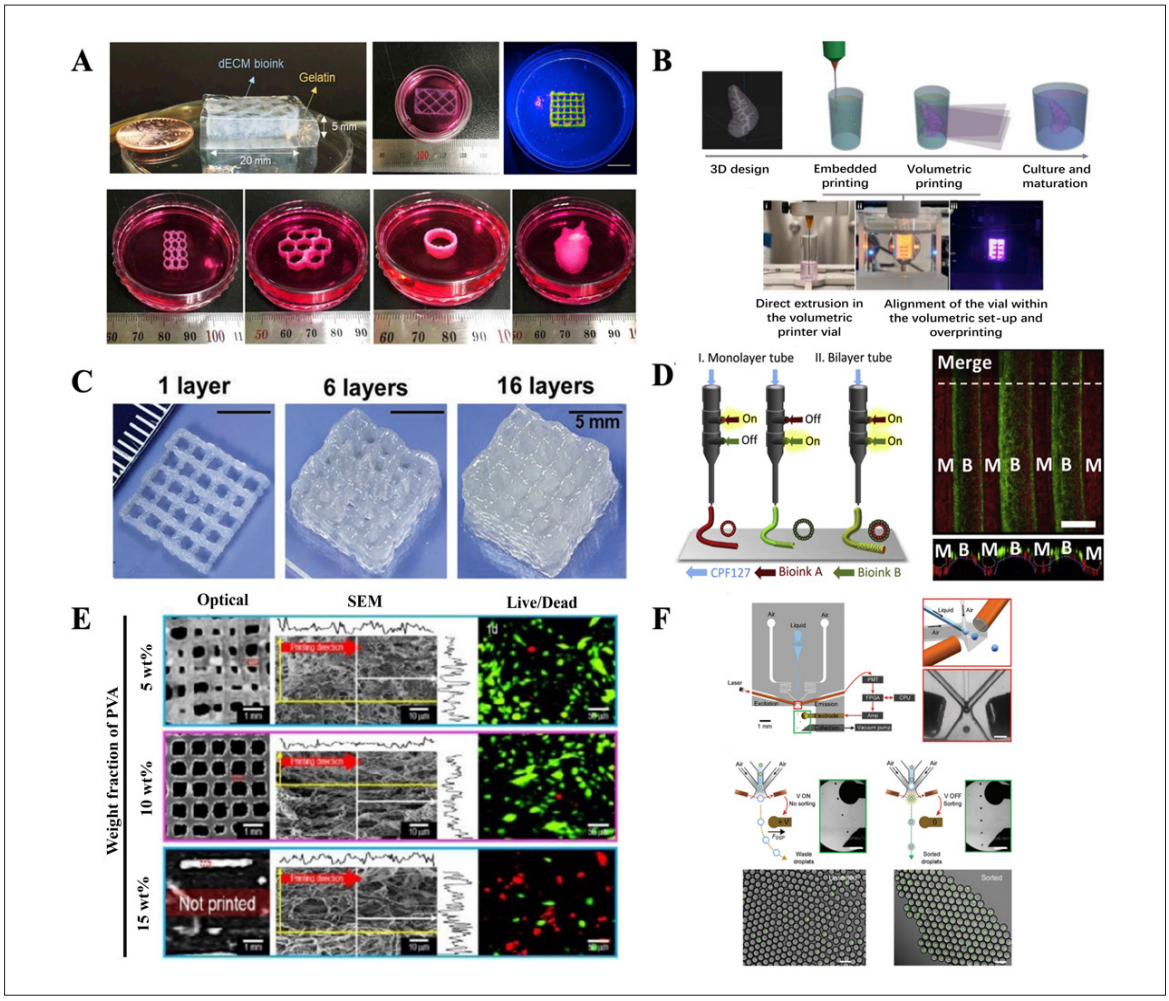

Figure 19. Cellular printing. (A) 3D cell printing of large-volume tissue constructs with a granule-based printing reservoir.[135] Copyright © Elsevier 2019. Reprinted with permission of Elsevier. (B) Sequential steps of embedded extrusion volumetric printing.[136] Copyright © John Wiley and Sons 2023. Reprinted with permission of John Wiley and Sons. (C) Printing code and gross images of the printed KdECMMA-based constructs.[137] Copyright © John Wiley and Sons 2019. Reprinted with permission of John Wiley and Sons. (D) Coaxial printing of monolayer and bilayer structures in complex hollow tubes.[138] Copyright © Elsevier 2020. Reprinted with permission of Elsevier. (E) Optical, scanning electron microscopy, and live/dead images of the structures printed using the dECM-MA-based bioinks.[139] Copyright © Elsevier 2020. Reprinted with permission of Elsevier. (F) High-definition single-cell printing printhead design and operation.[140] Copyright © John Wiley and Sons 2020. Reprinted with permission of John Wiley and Sons.

each organ. Despite that, some specific limitations of bioprinting should be acknowledged.

5.1. Methods

Extrusion printing poses a considerable hurdle to sustaining cell viability. When printing involves cells, the chief detriment to cellular integrity arises from the shear forces induced by liquid flow during the printing process. Furthermore, the diminutive caliber of the nozzle markedly exacerbates cellular impairment. Consequently, the extrusion printing approach encounters challenges in concurrently attaining optimal cell vitality and precise printing. Altering the nozzle diameter entails trade-offs: increasing it compromises printing resolution, whereas decreasing it compromises printing accuracy, thus jeopardizing cell viability. Conversely, light-assisted methodologies sidestep the nozzle structure, effectively managing both cell vitality and printing precision. Nonetheless, it is important to note that light exposure also influences cell activity, necessitating judicious control of light parameters for optimal outcomes.

5.2. Materials

Modifying crosslinked materials presents a pivotal approach within the realm of light-assisted molding. This technique, known as crosslinking molding, involves the fixation and shaping of printed materials through precise temperature regulation, chemical treatments, ultraviolet

irradiation, and similar methods, all aimed at achieving the desired form. However, these crosslinking methodologies encounter a significant challenge, notably the potential to induce harm to cellular structures, proteins, and other sensitive materials. Presently, the prevailing strategy involves scaffold crosslinking employing substances like alginate, followed by cell cultivation atop the scaffold. Within the domain of bioprinting, conventional 3D printing materials are inadequate, thereby underscoring the ongoing necessity for innovative material development to address this predicament.

5.3. High throughput

The term "high throughput" denotes the capability to concurrently print multiple materials. It is important to note that different biological tissues own a diverse array of components, including cell types, proteins, and growth factors. Thus, this necessitates a more broadened scope of materials for printing, including those with intricate compositions and structures. As such, this constitutes a remarkably intricate precision-centric printing technology. Presently, extrusion printing employs a multi-nozzle structure to simultaneously print various materials; however, this approach struggles to maintain precise control over accuracy. In contrast, light-assisted printing lacks an efficient means to seamlessly switch between a multitude of printing materials, thus posing a limitation to its versatility.

5.4. Printing cost

The cost implications stem from two principal facets: the expense associated with printing equipment and the outlay for printing materials. In terms of equipment, extrusion printing equipment emerges as the more economical choice. Nevertheless, it harbors intrinsic constraints such as subpar resolution, compromised cell vitality, compatibility with a restricted spectrum of applicable materials, as well as susceptibility to issues like nozzle clogs and pipeline contamination. Separately, light-assisted printing demands a higher initial investment for equipment and entails greater technical complexity. In addition to the primary printing apparatus, supplementary equipment such as temperature and humidity control systems, monitoring devices, and other support structures also contribute to the overall cost.

Regarding printing supplies, when it comes to cell-loaded printing, an assortment of cultured cell materials like serum and media are requisite. The delicate nature of cells makes them susceptible to premature demise, thereby exacerbating the depletion of consumables. Moreover, the field of bioprinting is currently marked by a protracted return-on-investment timeline. This is particularly evident in the context of tissue engineering, where the application of bioprinting remains primarily confined to research and development, with only a scant number of tangible product-level applications thus far.

5.5. Multi-technology integration

The four printing technologies highlighted in section 2 exhibit distinct strengths and weaknesses. However, the existing literature has yet to yield reports that comprehensively amalgamate these various technologies for simultaneous application. The prospect of employing diverse methods tailored to specific organs is compelling, given the intricate nature of biological tissue. The multifaceted structure of biological tissue necessitates distinct preparation methods for varying components. The challenge lies in seamlessly harmonizing disparate realization methods to achieve a unified and cohesive approach. Currently, the integration of these methods remains a formidable task, one that demands innovative solutions to bridge the gap between the intricacies of tissue structure and the practicalities of printing technologies.

6. Outlooks

With the advances in 3D bioprinting and deepening crossover of different disciplines, the potential for revolutionary strides within *in vitro* living system engineering becomes increasingly plausible. Technological trends signify a shift from employing singular structural materials to harnessing functional and biological materials, underpinned by the scientific groundwork laid by 3D bioprinting. Concomitantly, progress in cell technology and biological materials furnishes the essential building blocks. The crux of this transformative evolution lies in 3D bioprinting as a pivotal manufacturing technique. Notably, the fusion of micro-nanotechnology and microfluidic chip technology has the capacity to engender sophisticated bionic bioreactors for cultivating living systems and living mechanical devices. Collectively, these developments hold the promise of catalyzing paradigmatic shifts within the realm of *in vitro* living system engineering.

6.1. 3D printing of tissues and organs

Indeed, 3D bioprinting represents a pivotal avenue for surmounting the challenges of organ transplantation in the future. It emerges as a crucial approach in addressing the persistent scarcity of donor organs. Anchored in an interdisciplinary convergence encompassing biology, materials science, chemistry, computer science, and various other fields, 3D bioprinting stands as a profound synthesis. This amalgamation of disciplines facilitates the fabrication of human tissues and organs, thereby offering a transformative solution to the critical donor shortfall in organ transplantation. By harnessing the power of 3D bioprinting, the prospect of manufacturing functional

human organs emerges as a promising trajectory that could revolutionize the field of organ transplantation.

Currently, the field of organ fabrication through 3D bioprinting is still in its nascent stages, with numerous underlying mechanisms yet to be fully elucidated. While successful achievements have been made in printing simpler tissues such as cartilage and skin, considerable limitations persist when attempting to print organs with intricate functionalities, such as liver, heart, and kidneys. Presently, the focus lies in reproducing the structural form of the organ, but the replication of complex physiological functions remains an ongoing challenge. Aspects like blood circulation, efficient oxygen and nutrient delivery to tissues, and timely elimination of metabolic waste prove intricate to replicate. Consequently, achieving artificial organs that emulate the capabilities of natural tissues and organs necessitates the convergence of 3D bioprinting with microfluidic technology, organ chips, and other related approaches. This underscores the requirement for continued exploration and research by numerous scholars in the quest to develop functional artificial organs.

6.2. Drug screening

Absolutely, 3D bioprinting technology holds immense potential in the realm of drug screening. As 3D bioprinting techniques advance, so does the refinement of 3D cell culture methods, subsequently catalyzing the development of sophisticated *in vitro* drug screening models. This technology transcends the limitations of traditional single-layer cell cultures, offering the capability to intricately mimic the microenvironment and material structure of cells within the body. This heightened fidelity in cell culture facilitates more accurate and intuitive representations of physiological conditions, culminating in optimal conditions for drug screening and the mitigation of treatment-related risks, particularly in the context of cancer. By harnessing the power of 3D bioprinting, the landscape of drug screening is significantly enhanced, enabling researchers to explore and assess potential treatments with heightened precision and reliability.

Indeed, the *in vitro* tumor models engendered through 3D bioprinting technology offer a remarkable advancement in accurately emulating the human physiological context. These models intricately replicate the dynamic spread of tumor cells within the human body, enhancing the efficacy of drug screening procedures. The progression of research in this field has even extended to encompass the intricate microenvironment existing within tumors.

While these achievements signify notable strides, it is crucial to acknowledge that the journey toward transformative breakthroughs in cancer treatment and the fabrication of artificial organs is far from concluded. The complexities inherent in cancer, along with the multifaceted intricacies of organ functionality, present formidable challenges that necessitate continued dedication, interdisciplinary collaboration, and innovative approaches. Nonetheless, the fusion of 3D bioprinting and advanced biomedical research positions us on a promising trajectory, guiding us toward future breakthroughs that hold the potential to reshape the landscape of cancer treatment and organ manufacturing.

6.3. Construction of *in vitro* physiological system

Microphysiological systems, also commonly known as organ-on-a-chip platforms, are *in vitro* constructs that emulate the interconnections between diverse human tissues and organs. Each of these systems is meticulously fashioned to replicate both the configuration and functionality of a distinct human organ or internal organ section. These constructs are interconnected through microfluidic networks. Their capabilities encompass the emulation and examination of interactions, such as those of drug–cell, cell–cell, and organ–organ, within an *in vitro* setting, demonstrating an exceptional level of physiological fidelity.

Microphysiological systems span a spectrum of technological domains, including microfluidic chips, stem cell biology, 3D microarchitectures/matrices, engineering of multicellular systems, diverse bioassay methodologies, database tools, and computational models catering to singular or multiple organ systems. The paradigm of microphysiological systems is poised to bring about a paradigm shift in fundamental biology, physiology, pharmacology, toxicology, and medical research. The emphasis of microphysiological systems should be on devising tools that are physiologically relevant, straightforward, reproducible, and economical, thereby benefiting the entire scientific community.

6.4. Transition from structural to functional bioprinting

3D bioprinting is an advanced technology that combines biological materials with biocompatible scaffold materials to create biological tissues or organs with specific structures and functions. In this field, there are several challenges, and one of them is the transition from structural to functional bioprinting.

Potential solutions to achieve this transition include:

(i) *Cell viability and differentiation.* The structures created through 3D printing may have adverse effects on cell viability and differentiation. Solutions involve improving the formulation of bioinks to enhance cell

viability and utilizing biofeedback mechanisms to guide cell differentiation.

(ii) *Structural complexity.* Creating biologically complex tissues is a challenge. Using multi-material printing and scaffold melting techniques can enable the fabrication of more intricate structures.

(iii) *Biocompatibility.* Printed materials must be compatible with the human body and not trigger immune responses. Researchers have been developing novel bioinks to enhance biocompatibility.

(iv) *Functionality.* Structured biological tissues must perform specific physiological functions. This may require consideration of the tissue's microstructure and tissue engineering parameters during the design process to ensure it possesses the desired functionality.

6.5. Embedded bioprinting

Embedded 3D bioprinting refers to the 3D printing technology where biological materials are directly embedded into living tissues to repair, enhance, or augment the functionality of biological organisms. This is a field with enormous potential but also faces future opportunities and challenges.

Embedded 3D bioprinting enables the customization of biological tissues and organs according to the individual patient's needs, epitomizing the concept of personalized medicine. This technology can be used for tissue repair, organ regeneration, and treatment of various diseases and injuries. Embedded 3D bioprinting can also be employed to create microtissue models with specific cell types and functions, suitable for drug screening and disease research. Devices for embedded 3D bioprinting can be utilized to produce wearable sensors, implantable medical devices, and smart health monitoring systems. If successful, embedded 3D bioprinting holds the potential to address long-standing issues in the medical field, such as organ transplantation.

However, it also presents several challenges:

(i) *Material selection and compatibility.* The biological materials used in printing must be compatible with the host tissue to prevent immune rejection. Nevertheless, finding suitable bioinks and scaffold materials remains a challenge.

(ii) *Cell survival and differentiation.* During the embedding process, cells need to survive and adapt to their new environment. However, ensuring cell survival and differentiation is a complex issue.

(iii) *Structural stability.* The structures created through embedded 3D bioprinting must remain stable and can interact with surrounding tissues. Addressing issues related to structural stability and interaction is crucial.

6.6. Artificial food

3D-printed artificial food is a field full of potential, offering many opportunities, but this rising domain also faces some challenges. The following are the future prospects and challenges of 3D-printed artificial food.

3D-printed food can be customized according to individual health needs and taste preferences, providing more personalized nutritional solutions. A more efficient production process is employed to produce 3D-printed food, thereby reducing food waste and the demand for land and water resources. This technology can be used to create new food textures, shapes, and tastes, driving food innovation. 3D printing of food is regarded as a rapid food production process that can efficiently overcome any food shortage situations.

However, there are still some challenges facing this particular segment of 3D printing. Developing materials suitable for 3D printing of food while considering food safety, taste, and texture is a complex challenge. Ensuring the safety of 3D-printed food is a critical issue that needs to be addressed by a strict adherence to the prevailing food manufacturing and hygiene standards. Currently, 3D printing of food is a relatively costly endeavor; therefore, improvements in production efficiency to reduce costs and achieve scalability are required. In addition, the use of sustainable materials and production methods must be considered to minimize the environmental impact arising from the 3D printing process of food.

7. Conclusion

In summary, 3D bioprinting technology is widely used in the medical field and has unique advantages in the field of organ reconstruction, including the production of simulated medical models and biomedical devices. This technique has garnered enormous attention, which has promoted the unprecedented development of a growing number of promising biomolecular materials. At present, 3D bioprinting technology is still unable to build organs and tissues that can be directly used for transplantation. In fact, several challenges should be surmounted in the process of continuously optimizing the current bioprinting techniques, such as strengthening immune response, affording capacity to vascularize, enabling multi-tissue printing, and allowing bionic structure formation, which are also viewed as opportunities for further improving the techniques. We believe that in the near future, bioprinting can achieve more profound breakthroughs in artificial organ preparation, which

directly contributes to the development of organ transplantation and personalized medicine.

Acknowledgments

None.

Funding

This work was supported by Heilongjiang Province Key Research and Development Program Under Grant (2022XJ03C07).

Conflict of interest

The authors declare no conflicts of interest.

Author contributions

Conceptualization: Ximin Yuan, Lixin Che, Xushuai Lv
Writing – original draft: Ximin Yuan, Zhenjia Wang,
Writing – review & editing: Jie Xu, Debin Shan, Bin Guo

Ethics approval and consent to participate

Not applicable.

Consent for publication

Not applicable.

Availability of data

Not applicable.

References

1. Lu YQ, Xu J, Su Y, et al. A biocompatible double-crosslinked gelatin/sodium alginate/dopamine/quaterniazed chitosan hydrogel for wound dressings based on 3D bioprinting technology. *Int J Bioprint*. 2023;9(2):439-452. doi: 10.18063/ijb.v9i1.689
2. Ding YW, Zhang XW, Mi CH, Qi XY, Zhou J, Wei DX. Recent advances in hyaluronic acid-based hydrogels for 3D bioprinting in tissue engineering applications. *Smart Mater Med*. 2022;4:59-68. doi: 10.1016/j.smaim.2022.07.003
3. Khalaf AT, Wei YY, Wan J, et al. Bone tissue engineering through 3D bioprinting of bioceramic scaffolds: a review and update. *Life*. 2022;12(6):903-930. doi: 10.3390/life12060903
4. Wang PP, Sun LJ, Li CC, et al. Study on drug screening multicellular model for colorectal cancer constructed by three-dimensional bioprinting technology. *Int J Bioprint*. 2023;9(3) 379-398. doi: 10.18063/ijb.694
5. Neufeld L, Yeini E, Pozzi S, et al. 3D bioprinted cancer models: from basic biology to drug development. *Nat Rev Cancer*. 2022;22(12):679-692. doi: 10.1038/s41568-022-00514-w
6. Chae S, Cho DW. Three-dimensional bioprinting with decellularized extracellular matrix-based bioinks in translational regenerative medicine. *MRS Bullet*. 2022;47(1):70-79. doi: 10.1557/s43577-021-00260-8
7. Muskan, Gupta D, Negi NP. 3D bioprinting: printing the future and recent advances. *Bioprinting*. 2022;27:e00211. doi: 10.1016/j.bprint.2022.e00211
8. Antezana PE, Municoy S, Álvarez-Echazú MI, et al. The 3D bioprinted scaffolds for wound healing. *Pharmaceutics*, 2022;14(2):464-509. doi: 10.3390/pharmaceutics14020464
9. Jiang Y, Zhou DZ, Yang B. 3D bioprinted GelMA/GO composite induces osteoblastic differentiation. *J Biomater Appl*. 2022;37(3):527-537. doi: 10.1177/08853282221098235
10. Koch L, Michael S, Reimers K, Strauß S, Vogt PM, Chichkov B. Bioprinting for skin. In: *3D Bioprinting and Nanotechnology in Tissue Engineering and Regenerative Medicine*. Elsevier;2022(9):397-425. doi: 10.1016/B978-0-12-824552-1.00011-6
11. McMillan A, McMillan N, Gupta N, Kanotra SP, Salem AK. 3D bioprinting in otolaryngology: a review. *Adv Healthc Mater*. 2023;3268-3284. doi: 10.1002/adhm.202203268
12. Shen MK, Wang LL, Gao Y, et al. 3D bioprinting of in situ vascularized tissue engineered bone for repairing large segmental bone defects. *Mater Today Bio*. 2022;16 100382. doi: 10.1016/j.mtbio.2022.100382
13. Prabhakaran P, Palaniyandi T, Kanagavalli B, et al. Prospect and retrospect of 3D bio-printing. *Acta Histochem*. 2022;124(7):151932. doi: 10.1016/j.acthis.2022.151932
14. Banerjee D, Singh YP, Datta P, et al. Strategies for 3D bioprinting of spheroids: a comprehensive review. *Biomaterials*. 2022;291:121881. doi: 10.1016/j.biomaterials.2022.121881
15. Blevins KM, Danilkowicz RM, Fletcher AN, Allen NB, Johnson LG, Adams SB. In situ 3D bioprinting of musculoskeletal tissues in orthopedic surgery. *J 3D Print Med*. 2022;6(1):25-36. doi: 10.2217/3dp-2021-0022
16. Mohammadrezaei D, Moghimi N, Vandvajdi S, Powathil G, Hamis S, Kohandel M. Predicting and elucidating the post-printing behavior of 3D printed cancer cells in hydrogel structures by integrating in-vitro and in-silico experiments. *Sci Rep*. 2023;13(1):1211-1223. doi: 10.1038/s41598-023-28286-9

17. Alheib O, da Silva LP, Youn YH, Kwon IK, Reis RL, Correlo VM. 3D bioprinting of gellan gum-based hydrogels tethered with laminin-derived peptides for improved cellular behavior. *J Biomed Mater Res Part A*. 2022;110(10): 1655-1668.
doi: 10.1002/jbm.a.37415

18. Lovecchio J, Cortesi M, Zani M, Govoni M, Dallari D, Giordano E. Fiber thickness and porosity control in a biopolymer scaffold 3D printed through a converted commercial FDM device. *Materials*. 2022;15(7):2394-2403.
doi: 10.3390/ma15072394

19. Koch F, Thaden O, Conrad S, et al. Mechanical properties of polycaprolactone (PCL) scaffolds for hybrid 3D-bioprinting with alginate-gelatin hydrogel. *J Mech Behav Biomed Mater.* 2022;130:105219.
doi: 10.1016/j.jmbbm.2022.105219

20. Soni VK, Sinha SK, Sharma HK. A review on 3D bioprinting materials and technique. *J Phase Change Mater.* 2022;2(2):7-24.
doi: 10.58256/jpcm.v2i2.26

21. Kantaros A. 3D printing in regenerative medicine: technologies and resources utilized. *Int J Mol Sci.* 2022;23(23): 14621-14633.
doi: 10.3390/ijms232314621

22. Yang XT, Ma Y, Wang XT, et al. A 3D-bioprinted functional module based on decellularized extracellular matrix bioink for periodontal regeneration. *Adv Sci.* 2023;10(5): 5041-5058.
doi: 10.1002/advs.202205041

23. Zhang W, Ye WB, Yan YF. Advances in photocrosslinkable materials for 3D bioprinting. *Adv Eng Mater.* 2022;24(1): 663-675.
doi: 10.1002/adem.202100663

24. Zhu J, Wu PW, Chao YH, et al. Recent advances in 3D printing for catalytic applications. *Chem Eng J.* 2022;433:134341.
doi: 10.1016/j.cej.2021.134341

25. Vrana NE, Gupta S, Mitra K, et al. From 3D printing to 3D bioprinting: the material properties of polymeric material and its derived bioink for achieving tissue specific architectures. *Cell Tissue Bank.* 2022;27:417-440.
doi: 10.1007/s10561-021-09975-z

26. Jandyal A, Chaturvedi I, Wazir I, Raina A, Haq MIU. 3D printing–A review of processes, materials and applications in industry 4.0. *Sustain Operation Comput*. 2022;3:33-42.
doi: 10.1016/j.susoc.2021.09.004

27. Yap YL, Toh W, Giam A, et al. Topology optimization and 3D printing of micro-drone: numerical design with experimental testing. *Int J Mech Sci.* 2023;237:107771.
doi: 10.1016/j.ijmecsci.2022.107771

28. Tao J, Zhu SY, Liao XY, et al. DLP-based bioprinting of void-forming hydrogels for enhanced stem-cell-mediated bone regeneration. *Mater Today Bio*. 2022;17:100487.
doi: 10.1016/j.mtbio.2022.100487

29. Daikuara LY, Chen XF, Yue ZL, et al. 3D bioprinting constructs to facilitate skin regeneration. *Adv Funct Mater.* 2022;32(3):5080-5103.
doi: 10.1002/adfm.202105080

30. Noroozi R, Shamekhi MA, Mahmoudi R, et al. In vitro static and dynamic cell culture study of novel bone scaffolds based on 3D-printed PLA and cell-laden alginate hydrogel. *Biomed Mater*. 2022;17(4):045024.
doi: 10.1088/1748-605x/ac7308

31. Wang YM, Xu XY, Chen XY, Li JS. Multifunctional biomedical materials derived from biological membranes. *Adv Mater.* 2022;34(46):7406-7432.
doi: 10.1002/adma.202107406

32. Cheng W, Zhu Y, Jiang GY, et al. Sustainable cellulose and its derivatives for promising biomedical applications. *Prog Mater Sci*. 2023;138:101152.
doi: 10.1016/j.pmatsci.2023.101152

33. Markstedt K, Mantas A, Tournier I, Avila HM, Hagg D, Gatenholm P. 3D bioprinting human chondrocytes with nanocellulose–alginate bioink for cartilage tissue engineering applications. *Biomacromolecules*. 2015;16(5):1489-1496.
doi: 10.1021/acs.biomac.5b00188

34. Sydney Gladman A, Matsumoto EA, Nuzzo RG, Mahadevan L, Lewis JA. Biomimetic 4D printing. *Nat Mater.* 2016;15(4):413-418.
doi: 10.1038/nmat4544

35. Lee S, Hao LT, Park J, Oh DX, Hwang DS. Nanochitin and nanochitosan: chitin nanostructure engineering with multiscale properties for biomedical and environmental applications. *Adv Mater.* 2023;35(4):3325-3360.
doi: 10.1002/adma.202203325

36. Deng LZ, Zhang LM. Rheological characteristics of chitin/ionic liquid gels and electrochemical properties of regenerated chitin hydrogels. *Colloids Surf A: Physicochem Eng Asp.* 2020;586:124220.
doi: 10.1016/j.colsurfa.2019.124220

37. Kotla NG, Mohd Isa IL, Larrañaga A, et al. Hyaluronic acid-based bioconjugate systems, scaffolds, and their therapeutic potential. *Adv Healthc Mater.* 2023;2203104.
doi: 10.1002/adhm.202203104

38. Le HV, Cerf DL. Colloidal polyelectrolyte complexes from hyaluronic acid: preparation and biomedical applications. *Small*. 2022;18(51):4283-4308.
doi: 10.1002/smll.202204283

39. Park KH, Ryu B, Song JJ, et al. Hyaluronic acid microparticles for effective spheroid culture and transplantation in liver tissue. *Chem Eng J.* 2023;464:142666.
doi: 10.1016/j.cej.2023.142666

40. Chen QX, Lu YH, Zhang JP, et al. Flexible structural polyethylene films for dynamically tunable energy harvesting from the sun and outer space. *Nano Energy*. 2023;114:108610.
doi: 10.1016/j.nanoen.2023.108610

41. Zhang XQ, Shen RF, Guo XJ, et al. Bimetallic Ag-Cu nanoparticles anchored on polypropylene (PP) nonwoven fabrics: superb catalytic efficiency and stability in 4-nitrophenol reduction. *Chem Eng J.* 2021;408:128018. doi: 10.1016/j.cej.2020.128018

42. Wang LW, Liu Y, Han Q, Lin HB, Liu F. A novel poly (4-methyl-1-pentene)/polypropylene (PMP/PP) thin film composite (TFC) artificial lung membrane for enhanced gas transport and excellent hemo-compatibility. *J Membr Sci.* 2022;649:120359. doi: 10.1016/j.memsci.2022.120359

43. Yang L, Sheng L, Gao XX, et al. rGO/Li-Al-LDH composite nanosheets modified commercial polypropylene (PP) separator to suppress lithium dendrites for lithium metal battery. *Electrochim Acta*. 2022;430:141073. doi: 10.1016/j.electacta.2022.141073

44. Pasternak G, Ormeno-Cano N, Rutkowski P. Recycled waste polypropylene composite ceramic membranes for extended lifetime of microbial fuel cells. *Chem Eng J.* 2021;425:130707. doi: 10.1016/j.cej.2021.130707

45. Smith P, Obando AG, Griffin A, Robertson M, Bounds E, Qiang Z. Additive manufacturing of carbon using commodity polypropylene. *Adv Mater.* 2023;35(17): 8029-8040. doi: 10.1002/adma.202208029

46. Huang JJ, Zhang XD, Liu RX, Ding YH Guo DJ. Polyvinyl chloride-based dielectric elastomer with high permittivity and low viscoelasticity for actuation and sensing. *Nat Commun.* 2023;14(1):1483-1492. doi: 10.1038/s41467-023-37178-5

47. Park H, Oh SJ, Kim M, et al. Plasticizer structural effect for sustainable and high-performance PVC gel-based triboelectric nanogenerators. *Nano Energy*. 2023;114:108615. doi: 10.1016/j.nanoen.2023.108615

48. He QS, Zhong QY, Sun Z, et al. Highly stretchable, repeatable, and easy-to-prepare ionogel based on polyvinyl chloride for wearable strain sensors. *Nano Energy*. 2023;113:108535. doi: 10.1016/j.nanoen.2023.108535

49. Choi DS, Bae JW, Lee SH, et al. Emotion-interactive empathetic transparent skin cushion with tailored frequency-dependent hydrogel–plasticized nonionic polyvinyl chloride interconnections. *Chem Eng J.* 2022;442:136142. doi: 10.1016/j.cej.2022.136142

50. Park H, Oh SJ, Kim D, et al. Plasticized PVC-gel single layer-based stretchable triboelectric nanogenerator for harvesting mechanical energy and tactile sensing. *Adv Sci.* 2022;9(22):1070-1078. doi: 10.1002/advs.202201070

51. Liu ZW, Li BB, Liu YD, Liang YR. Integrated bending actuation and the self-sensing capability of poly (vinyl chloride) gels with ionic liquids. *Adv Funct Mater.* 2022;32(35):4259-4270. doi: 10.1002/adfm.202204259

52. Ye HR, Jiang JX, Yang Y, et al. Ultra-strong and environmentally friendly waste polyvinyl chloride/paper biocomposites. *Adv Compos Hybrid Mater.* 2023;6(2):81-92. doi: 10.1007/s42114-023-00664-x

53. Liu DS, Cao YF, Jiang P, et al. Tough, transparent, and slippery PVA hydrogel led by syneresis. *Small*. 2023;19(14): 6819-6829. doi: 10.1002/smll.202206819

54. Li MK, Sun YY, Feng DY, Ruan KP, Liu X, Gu JW. Thermally conductive polyvinyl alcohol composite films via introducing hetero-structured MXene@ silver fillers. *Nano Res.* 2023;16(5):7820-7828. doi: 10.1007/s12274-023-5594-1

55. Qiu W, Gehlen J, Bernero M, et al. A synthetic dynamic polyvinyl alcohol photoresin for fast volumetric bioprinting of functional ultrasoft hydrogel constructs. *Adv Funct Mater.* 2023;33(20):14393-14403. doi: 10.1002/adfm.202214393

56. Sanchis-Gual R, Ye H, Ueno T, et al. 3D printed template-assisted casting of biocompatible polyvinyl alcohol-based soft microswimmers with tunable stability. *Adv Funct Mater.* 2023;2212952. doi: 10.1002/adfm.202212952

57. Wei Y, Baskaran N, Wang HY, Su YC, Nabilla SC, Chung RJ. Study of polymethylmethacrylate/tricalcium silicate composite cement for orthopedic application. *Biomed J.* 2023;46(3):100540-100549. doi: 10.1016/j.bj.2022.05.005

58. Wang Z, Yuh SJ, Renaud-Charest E, et al. Cervical spine reconstruction with chest tube technique after metastasis resection: a single-center experience. *World Neurosurg.* 2022;157:e49-e56. doi: 10.1016/j.wneu.2021.09.088

59. Jian L. Effect of sizing agent on interfacial properties of carbon fiber-reinforced PMMA composite. *Compos Adv Mater.* 2021;30:2633366X20978657. doi: 10.1177/2633366x20978657

60. Da HR, Pan SS, Li J, et al. Greatly recovered electrochemical performances of regenerated graphite anode enabled by an artificial PMMA solid electrolyte interphase layer. *Energy Stor Mater.* 2023;56:457-467. doi: 10.1016/j.ensm.2023.01.038

61. Duan YX, Yang HB, Liu K, et al. 2023, Cellulose nanofibril aerogels reinforcing polymethyl methacrylate with high optical transparency, *Advanced Composites and Hybrid Materials*, Vol. 6 (3):123-134. doi: 10.1007/s42114-023-00700-w

62. Hu Y, Lin XY, Liu DT, et al. Electrospun polymethyl methacrylate fibers-based membrane with heterogeneous structure achieving a full-particle size separation of oil-water emulsion. *J Membr Sci.* 2023;680:121716. doi: 10.1016/j.memsci.2023.121716

63. Zafar MS. Prosthodontic applications of polymethyl methacrylate (PMMA): an update. *Polymers*. 2020;12(10):2299-2333. doi: 10.3390/polym12102299

64. Kwak G, Jeong YS, Kim SW, et al. Hybrid photothermal structure based on Cr-MgF2 solar absorber/PMMA-graphene heat reservoir for enhanced thermoelectric power generation. *Nano Energy*. 2023;110:108352. doi: 10.1016/j.nanoen.2023.108352

65. Backes EH, Harb SV, Beatrice CAG, et al. Polycaprolactone usage in additive manufacturing strategies for tissue engineering applications: a review. *J Biomed Mater Res Part B: Appl Biomater.* 2022;110(6): 1479-1503. doi: 10.1002/jbm.b.34997

66. Yang YT, Wu HC, Fu QL, et al. 3D-printed polycaprolactone-chitosan based drug delivery implants for personalized administration. *Mater Des.* 2022;214:110394. doi: 10.1016/j.matdes.2022.110394

67. Singh AP, Prakash O, Kumar S, Shukla A, Maiti P. Poly (lactic acid-co-glycolic acid) as sustained drug delivery vehicle for melanoma therapy. *Mater Today Commun.* 2022;31:103661. doi: 10.1016/j.mtcomm.2022.103661

68. Lin JL, Huang JC, Wu J, Tang B, Li CB, Xiao HJ. Poly (lactic acid-co-glycolic acid)-based celecoxib extended-release microspheres for the local treatment of traumatic heterotopic ossification. *J Biomater Appl.* 2022;36(8): 1458-1468. doi: 10.1177/08853282211056937

69. Diedkova K, Pogrebnjak AD, Kyrylenko S, et al. Polycaprolactone–MXene nanofibrous scaffolds for tissue engineering. *ACS Appl Mater Interfaces*. 2023;15(11): 14033-14047. doi: 10.1021/acsami.2c22780

70. Wei JW, Xia X, Xiao SQ, et al. Sequential dual-biofactor release from the scaffold of mesoporous HA microspheres and PLGA matrix for boosting endogenous bone regeneration. *Adv Healthc Mater.* 2023;624-637. doi: 10.1002/adhm.202300624

71. Li PF, Ruan LM, Jiang GH, et al. Design of 3D polycaprolactone/ε-polylysine-modified chitosan fibrous scaffolds with incorporation of bioactive factors for accelerating wound healing. *Acta Biomater.* 2022;152: 197-209. doi: 10.1016/j.actbio.2022.08.075

72. Huang YQ, Du ZY, Li K, et al. ROS-scavenging electroactive polyphosphazene-based core–shell nanofibers for bone regeneration. *Adv Fiber Mater.* 2022;4(4):894-907. doi: 10.1007/s42765-022-00153-8

73. Long Q, Liu ZH, Shao QW, et al. Autologous skin fibroblast-based PLGA nanoparticles for treating multiorgan fibrosis. *Adv Sci.* 2022;9(21):856-869. doi: 10.1002/advs.202200856

74. Sheffey VV, Siew EB, Tanner EEL, Eniola-Adefeso O. PLGA's plight and the role of stealth surface modification strategies in its use for intravenous particulate drug delivery. *Adv Healthc Mater.* 2022;11(8):1536-1569. doi: 10.1002/adhm.202101536

75. Liu JJ, Qu SX, Suo ZG, Yang W. Functional hydrogel coatings. *Natl Sci Rev.* 2021;8(2):nwaa254. doi: 10.1093/nsr/nwaa254

76. Sun X, Yao FL, Li JJ. Nanocomposite hydrogel-based strain and pressure sensors: a review. *J Mater Chem A*. 2020;8(36):18605-18623. doi: 10.1039/d0ta06965e

77. Shen ZQ, Zhang ZL, Zhang NB, et al. High-stretchability, ultralow-hysteresis conductingpolymer hydrogel strain sensors for soft machines. *Adv Mater.* 2022;34(32): 3650-3657. doi: 10.1002/adma.202203650

78. Mandal A, Clegg JR, Anselmo AC, Mitragotri S. Hydrogels in the clinic. *Bioeng Transl Med.* 2020;5(2):e10158. doi: 10.1002/btm2.10158

79. Unagolla JM, Jayasuriya AC. Hydrogel-based 3D bioprinting: a comprehensive review on cell-laden hydrogels, bioink formulations, and future perspectives. *Appl Mater Today*. 2020;18:100479. doi: 10.1016/j.apmt.2019.100479

80. Ye WL, Yang Z, Cao FY, et al. Articular cartilage reconstruction with TGF-β1-simulating self-assembling peptide hydrogel-based composite scaffold. *Acta Biomater.* 2022;146:94-106. doi: 10.1016/j.actbio.2022.05.012

81. Sharma A, Panwar V, Mondal B, et al. Electrical stimulation induced by a piezo-driven triboelectric nanogenerator and electroactive hydrogel composite, accelerate wound repair. *Nano Energy*. 2022;99:107419. doi: 10.1016/j.nanoen.2022.107419

82. Peng W, Li D, Dai KL, et al. Recent progress of collagen, chitosan, alginate and other hydrogels in skin repair and wound dressing applications. *Int J Biol Macromol.* 2022;208:400-408. doi: 10.1016/j.ijbiomac.2022.03.002

83. Li N, Liu W, Zheng XY, et al. Antimicrobial hydrogel with multiple pH-responsiveness for infected burn wound healing. *Nano Res.* 2023;23(6):1-10. doi: 10.1007/s12274-023-5751-6

84. Li HJ, Liang Y, Gao GR, et al. Asymmetric bilayer CNTs-elastomer/hydrogel composite as soft actuators with sensing performance. *Chem Eng J.* 2021;415:128988. doi: 10.1016/j.cej.2021.128988

85. Choi MY, Shin Y, Lee HS, Kim SY, Na JH. Multipolar spatial electric field modulation for freeform electroactive hydrogel actuation. *Sci Rep.* 2020;10(1): 2482-2489. doi: 10.1038/s41598-020-59318-3

86. Kim DI, Song S, Jang S, et al. Untethered gripper-type hydrogel millirobot actuated by electric field and magnetic field. *Smart Mater Struct.* 2020;29(8):085024. doi: 10.1088/1361-665x/ab8ea4

87. Peng XW, Peng Q, Wu M, et al. A pH and temperature dual-responsive microgel-embedded, adhesive, and tough hydrogel for drug delivery and wound healing. *ACS Appl Mater Interfaces*. 2023;15(15):19560-19573. doi: 10.1021/acsami.2c21255

88. Youness RA, Tag El-deen DM, Taha MA . A review on calcium silicate ceramics: properties, limitations, and solutions for their use in biomedical applications. *Silicon*. 2023;15(6):2493-2505. doi: 10.1007/s12633-022-02207-3

89. Shu CQ, Qin C, Chen L, et al. Metal-organic framework functionalized bioceramic scaffolds with antioxidative activity for enhanced osteochondral regeneration. *Adv Sci.* 2023;10(13):6875-6888. doi: 10.1002/advs.202206875

90. Kost J, Huwyler J, Puchkov M. Calcium phosphate microcapsules as multifunctional drug delivery devices. *Adv Funct Mater.* 2023;202303333. doi: 10.1002/adfm.202303333

91. Li M, Jiang JW, Liu WB, et al. Bioadaptable bioactive glass-β-tricalcium phosphate scaffolds with TPMS-gyroid structure by stereolithography for bone regeneration. *J Mater Sci Technol.* 2023;155:54-65. doi: 10.1016/j.jmst.2023.01.025

92. Feng YHZ, Wu D, Knaus J, et al. A bioinspired gelatin–amorphous calcium phosphate coating on titanium implant for bone regeneration. *Adv Healthc Mater.* 2023; 3411-3423. doi: 10.1002/adhm.202203411

93. Yuan G, Xu YN, Bai XP, et al. Autophagy-targeted calcium phosphate nanoparticles enable transarterial chemoembolization for enhanced cancer therapy. *ACS Appl Mater Interfaces*. 2023;15(9):11431-11443. doi: 10.1021/acsami.2c18267

94. Zhang YG, Li JP, Soleimani M, et al. Biodegradable elastic sponge from nanofibrous biphasic calcium phosphate ceramic as an advanced material for regenerative medicine. *Adv Funct Mater.* 2021;31(40):2911-2923. doi: 10.1002/adfm.202102911

95. Bartmański M, Rościszewska M, Wekwejt M, Ronowska A, Nadolska-Dawidowska M, Mielewczyk-Gryń A. Properties of new composite materials based on hydroxyapatite ceramic and cross-linked gelatin for biomedical applications. *Int J Mol Sci.* 2022;23(16):9083-9097. doi: 10.3390/ijms23169083

96. Vaiani L, Boccaccio A, Uva AE, et al. Ceramic materials for biomedical applications: an overview on properties and fabrication processes. *J Funct Biomater.* 2023;14(3):146-167. doi: 10.3390/jfb14030146

97. Rieu J, Goeuriot P. Ceramic composites for biomedical applications. *Clin Mater.* 1993;12(4):211-217. doi: 10.1016/0267-6605(93)90075-I

98. Swarte JC, Li YN, Hu SX, et al. Gut microbiome dysbiosis is associated with increased mortality after solid organ transplantation. *Sci Transl Med.* 2022;14(660):eabn7566. doi: 10.1126/scitranslmed.abn7566

99. Duneton C, Winterberg PD, Ford ML. Activation and regulation of alloreactive T cell immunity in solid organ transplantation. *Nat Rev Nephrol.* 2022;18(10):663-676. doi: 10.1038/s41581-022-00600-0

100. Xu KL, Han Y, Huang YY, Wei P, Yin J, Jiang JY. The application of 3D bioprinting in urological diseases. *Mater Today Bio*. 2022;100388. doi: 10.1016/j.mtbio.2022.100388

101. Zennifer A, Manivannan S, Sethuraman S, Kumbar SG, Sundaramurthi D. 3D bioprinting and photocrosslinking: emerging strategies & future perspectives. *Biomater Adv.* 2022;134:112576-112599. doi: 10.1016/j.msec.2021.112576

102. Bose S, Roy M, Bandyopadhyay A. Recent advances in bone tissue engineering scaffolds. *Trends Biotechnol.* 2012;30(10):546-554. doi: 10.1016/j.tibtech.2012.07.005

103. Bose S, Vahabzadeh S, Bandyopadhyay A. Bone tissue engineering using 3D printing. *Mater Today*. 2013;16(12):496-504. doi: 10.1016/j.mattod.2013.11.017

104. Ma ZC, Zhang YL, Han B, et al. Femtosecond laser programmed artificial musculoskeletal systems. *Nat Commun.* 2020;11(1):4536-4545. doi: 10.1038/s41467-020-18117-0

105. Huang HJ, Xing WR, Zeng CJ, Huang WH. Pararectus approach combined with three-dimensional printing for anterior plate fixation of sacral fractures. *Injury.* 2021;52(10):2719-2724. doi: 10.1016/j.injury.2020.03.049

106. Strehin I, Nahas Z, Arora K, Nguyen T, Elisseeff J. A versatile pH sensitive chondroitin sulfate-PEG tissue adhesive and hydrogel. *Biomaterials*. 2010;31(10):2788-2797. doi: 10.1016/j.biomaterials.2009.12.033

107. Decarli MC, Seijas-Gamardo A, Morgan FLC, et al. Bioprinting of stem cell spheroids followed by post-printing chondrogenic differentiation for cartilage tissue engineering. *Adv Healthc Mater.* 2023;2203021. doi: 10.1002/adhm.202203021

108. Liu DH, Nie W, Li DJ, et al. 3D printed PCL/SrHA scaffold for enhanced bone regeneration. *Chem Eng J.* 2019;362:269-279. doi: 10.1016/j.cej.2019.01.015

109. Yan YF, Chen H, Zhang HB, et al. Vascularized 3D printed scaffolds for promoting bone regeneration. *Biomaterials*. 2019;190:97-110. doi: 10.1016/j.biomaterials.2018.10.033

110. Gold KA, Saha B, Pandian NKR, et al. 3D bioprinted multicellular vascular models. *Adv Healthc Mater.* 2021;10(21):1141-1154. doi: 10.1002/adhm.202101141

111. Fang YC, Guo YH, Wu BY, et al. Expanding embedded 3D bioprinting capability for engineering complex organs with freeform vascular networks. *Adv Mat.* 2023;35(22): 5082-5096. doi: 10.1002/adma.202205082

112. Moore MJ, Tan RP, Yang NJ, Rnjak-Kovacina J, Wise SG. Bioengineering artificial blood vessels from natural materials. *Trends Biotechnol.* 2022;40(6):693-707. doi: 10.1016/j.tibtech.2021.11.003

113. Silberman E, Oved H, Namestnikov M, Shapira A, Dvir T. Post-maturation reinforcement of 3d-printed vascularized cardiac tissues. *Adv Mater.* 2023;2302229. doi: 10.1002/adma.202302229

114. Song BW, Wang CW, Fan SY, et al. Rapid construction of 3D biomimetic capillary networks with complex morphology using dynamic holographic processing. *Adv Funct Mater.* 2023;2305245. doi: 10.1002/adfm.202305245

115. Radenkovic D, Solouk A, Seifalian A. Personalized development of human organs using 3D printing technology. *Med Hypotheses*. 2016;87:30-33. doi: 10.1016/j.mehy.2015.12.017

116. Yuan XM, Zhu Z, Xia PC, et al. Tough gelatin hydrogel for tissue engineering. *Adv Sci.* 2023;2301665. doi: 10.1002/advs.202301665

117. Wang YF, Zheng Q, Sun Z, et al. Reversal of liver failure using a bioartificial liver device implanted with clinical-grade human-induced hepatocytes. *Cell Stem Cell*. 2023;30(5):617-631. doi: 10.1016/j.stem.2023.03.013

118. Liun C, Lou YT, Sun ZY, et al. 4D printing of personalized-tunable biomimetic periosteum with anisotropic microstructure for accelerated vascularization and bone healing. *Adv Healthc Mater.* 2023;12(22):2202868. doi: 10.1002/adhm.202202868

119. Ahrens JH, Uzel SGM, Skylar-Scott M, et al. Programming cellular alignment in engineered cardiac tissue via bioprinting anisotropic organ building blocks. *Adv Mater.* 2022;34(26):217-227. doi: 10.1002/adma.202200217

120. Noor N, Shapira A, Edri R, Gal I, Wertheim L, Dvir T. 3D printing of personalized thick and perfusable cardiac patches and hearts. *Adv Sci.* 2019;6(11):344-353. doi: 10.1002/advs.201900344

121. Ng WL, Qi JTZ, Yeong WY, Naing MW. Proof-of-concept: 3D bioprinting of pigmented human skin constructs. *Biofabrication*. 2018;10(2):025005. doi: 10.1088/1758-5090/aa9e1e

122. Hakimi N, Cheng R, Leng L, et al. Handheld skin printer: in situ formation of planar biomaterials and tissues. *Lab Chip*. 2018;18(10):1440-1451. doi: 10.1039/c7lc01236e

123. Kim BS, Gao G, Kim JY, Cho DW. 3D cell printing of perfusable vascularized human skin equivalent composed of epidermis, dermis, and hypodermis for better structural recapitulation of native skin. *Adv Healthc Mater.* 2019; 8(7):1019-1029. doi: 10.1002/adhm.201801019

124. Cubo N, Garcia M, Cañizo JFD, Velasco D, Jorcano JL. 3D bioprinting of functional human skin: production and in vivo analysis. *Biofabrication*. 2016;9(1):015006. doi: 10.1088/1758-5090/9/1/015006

125. Ma J, Qin C, Wu JF, et al. 3D printing of strontium silicate microcylinder-containing multicellular biomaterial inks for vascularized skin regeneration. *Adv Healthc Mater.* 2021;10(16):523-536. doi: 10.1002/adhm.202100523

126. Zhang DQ, Lai LY, Fu HJ, Fu Q, Chen ML. 3D-bioprinted biomimetic multilayer implants comprising microfragmented adipose extracellular matrix and cells improve wound healing in a murine model of full-thickness skin defects. *ACS Appl Mater Interfaces*. 2023;15:29713-29728. doi: 10.1021/acsami.2c21629

127. Pourchet LJ, Thepot A, Albouy M, et al. Human skin 3D bioprinting using scaffold-free approach. *Adv Healthc Mater.* 2017;6(4):1101-1107. doi: 10.1002/adhm.201601101

128. Bose S, Darsell J, Kintner M , Hosick H, Bandyopadhyay A. Ore size and pore volume effects on alumina and TCP ceramic scaffolds. *Mater Sci Eng C*. 2003;23:479-486. doi: 10.1016/s0928-4931(02)00129-7

129. Bose S, Ke D, Sahasrabudhe H, Bandyopadhyay A. Additive manufacturing of biomaterials. *Prog Mater Sci.* 2018;93:45-111. doi: 10.1016/j.pmatsci.2017.08.003

130. Han J, Jeong W, Kim MK, Nam SH, Park EK, Kang HW. Demineralized dentin matrix particle-based bio-ink for patient-specific shaped 3D dental tissue regeneration. *Polymers*. 2021;13(8):1294-1307. doi: 10.3390/polym13081294

131. Nejad ZM, Zamanian A, Saeidifar M, Vanaei HR, Amoli MS. 3D bioprinting of polycaprolactone-based scaffolds for pulp-dentin regeneration: investigation of physicochemical and biological behavior. *Polymers*. 2021;13(24):4442-4455. doi: 10.3390/polym13244442

132. Lin YT, Hsu YT, Liu YW, Kao CT, Huang TH. Bidirectional differentiation of human-derived stem cells induced by biomimetic calcium silicate-reinforced gelatin methacrylate bioink for odontogenic regeneration. *Biomedicines*. 2021;9(8):929-945. doi: 10.3390/biomedicines9080929

133. Wang CY, Chiu YC, Lee AKX, Lin YA, Lin PY, Shie MY. Biofabrication of gingival fibroblast cell-laden collagen/strontium-doped calcium silicate 3D-printed bi-layered scaffold for osteoporotic periodontal regeneration. *Biomedicines*. 2021;9(4):431-448.
doi: 10.3390/biomedicines9040431

134. Kim D, Lee H, Lee GH, Hoang TH, Kim HR, Kim GH. Fabrication of bone-derived decellularized extracellular matrix/ceramic-based biocomposites and their osteo/odontogenic differentiation ability for dentin regeneration. *Bioeng Transl Med*. 2022;7(3):e10317.
doi: 10.1002/btm2.10317

135. Choi YJ, Jun YJ, Kim DY, et al. A 3D cell printed muscle construct with tissue-derived bioink for the treatment of volumetric muscle loss. *Biomaterials*. 2019;206:160-169.
doi: 10.1016/j.biomaterials.2019.03.036

136. Ribezzi D, Gueye M, Florczak S, et al. Shaping synthetic multicellular and complex multimaterial tissues via embedded extrusion-volumetric printing of microgels. *Adv Mater*. 2023;2301673.
doi: 10.1002/adma.202301673

137. Ali M, Pr AK, Yoo JJ, Zahran F, Atala A, Lee SJ. A photo-crosslinkable kidney ECM-derived bioink accelerates renal tissue formation. *Adv Healthc Mater*. 2019;8(7):992-1001.
doi: 10.1002/adhm.201800992

138. Singh NK, Han W, Nam SA, et al. Three-dimensional cell-printing of advanced renal tubular tissue analogue. *Biomaterials*. 2020;23(2):119734-119748.
doi: 10.1016/j.biomaterials.2019.119734

139. Kim W, Lee H, Lee J, et al. Efficient myotube formation in 3D bioprinted tissue construct by biochemical and topographical cues. *Biomaterials*. 2020;230:119632-119647.
doi: 10.1016/j.biomaterials.2019.119632

140. Zhang PF, Abate AR. High-definition single-cell printing: cell-by-cell fabrication of biological structures. *Adv Mater*. 2020;32(52):5346-5354.
doi: 10.1002/adma.202005346

ACCSCIENCE PUBLISHING

International Journal of Bioprinting

REVIEW ARTICLE

3D bioprinting of anisotropic filler-reinforced polymer nanocomposites: Synthesis, assembly, and multifunctional applications

Yun Wu[1†], Sayan Ganguly[2,3†], and Xiaowu Shirley Tang[2,3*]

[1]College of Textile Science and Engineering, Jiangnan University, Wuxi, Jiangsu Province, China

[2]Department of Chemistry & Waterloo Institute for Nanotechnology, University of Waterloo, Waterloo, Ontario, Canada

[3]Centre for Eye and Vision Research Limited, Hong Kong

(This article belongs to the *Special Issue: Convergence of 3D Bioprinting and Nanotechnology*)

Abstract

Bioprinting is a novel technique with a wide range of potential uses, including the fabrication of functioning tissue constructs for use in the biomedical sectors. It is a revolutionary method for high-throughput manufacturing that automates fine control over manufactured structures. Bioink refers to the solution of biomaterials usually encapsulating cells used in the bioprinting process; this bioink often encapsulates the appropriate cell types. In order to create the ultimate architecture, this bioink should solidify during or shortly after bioprinting. Bioinks can be developed from either all-natural or all-synthetic biomaterials, or a blend of the two. Cell aggregation can occasionally be used as a bioink without addition of any biomaterials, in bioprinting process. To bioprint functional tissues and organs, an optimal bioink should possess mechanical, rheological, and biological characteristics mimicking those of the target tissues. For attaining physicomechanical properties, anisotropic fillers are commonly added in bioink formulations. In this review, we provide an in-depth discussion of various anisotropic fillers used in bioprinting and their fabrication techniques, and outline their multifunctional applicability in biomedical and environmental areas. Given the steady growth of bioprinting market, we also present the global scenario of the bioprinting market and their techno-commercial orientations.

Keywords: 3D printing; Cell-laden scaffolds; Bioink; Biofabrication; Bioprinting; Commercialization

†These authors contributed equally to this work.

***Corresponding author:**
Xiaowu Shirley Tang
(tangxw@uwaterloo.ca)

Citation: Wu Y, Ganguly S, Tang XS. 3D bioprinting of anisotropic filler-reinforced polymer nanocomposites: Synthesis, assembly, and multifunctional applications. *Int J Bioprint*. 2024;10(2):1637.
doi: 10.36922/ijb.1637

Received: August 19, 2023
Accepted: October 19, 2023
Published Online: February 5, 2024

1. Introduction

Three-dimensional (3D) bioprinting is a groundbreaking technology that holds great significance in tissue engineering. It enables the precise fabrication of intricate 3D structures by depositing biomaterials, cells, and bioactive factors layer by layer. One of the main benefits of 3D bioprinting is its ability to precisely control the spatial arrangement of components within the fabricated constructs. This level of control enables the creation of biomimetic tissue architectures, encompassing intricate vasculature networks and

multicellular arrangements, which are critical for the proper functioning of tissues. By mimicking the native tissue microenvironment, 3D-bioprinted constructs have the potential to exhibit enhanced functionality and promote more accurate tissue replication.[1] This technology has far-reaching implications in regenerative medicine, as it offers the possibility of creating personalized tissues and organs tailored to individual patient needs. Moreover, 3D bioprinting enables the fabrication of tissue models for drug screening and disease research, providing a platform for more accurate and efficient preclinical studies. Overall, 3D bioprinting represents a transformative approach in tissue engineering with the potential to revolutionize regenerative medicine and address the growing demand for tissue-engineered therapies.

Anisotropic filler (AF)-reinforced polymer nanocomposites (PNCs) are a type of material that merges polymer matrices with fillers that have directional properties.[2] Fillers like carbon nanotubes (CNT), graphene, nanocellulose, or aligned nanofibers are usually used to give nanocomposites anisotropic properties. Incorporating anisotropic fillers into polymer matrices can affect their mechanical, electrical, thermal, cell behavior, and other functional properties in specific directions.[3] The production of AF-PNCs involves various techniques, such as electrospinning, self-assembly, templating, and other fabrication methods. Nanocomposites have numerous applications in various fields, including aerospace, automotive, electronics, energy, and biomedical engineering.[4] Their anisotropic properties can be utilized to enhance performance and functionality in specific directions.

The integration of 3D bioprinting and nanocomposites holds great significance and potential in tissue engineering and beyond. The mechanical properties of 3D-printed constructs can be significantly enhanced by incorporating nanoscale fillers into the bioink or polymer matrix,[5] resulting in increased strength and structural integrity. Nanocomposites can be designed to have specific biological functions, allowing for the precise release of bioactive molecules that can affect cellular behavior and promote tissue regeneration.[6] By incorporating functional elements that possess unique properties, such as electrical conductivity or magnetic responsiveness, it becomes possible to create multifunctional tissues and bioelectronic devices. In essence, the combination of 3D bioprinting and nanocomposites offers a promising avenue for the creation of tailored tissue constructs that possess enhanced mechanical, biological, and functional characteristics.[7]

The distinctive aspect of this review article is its exclusive amalgamation of methodologies, focus on anisotropic fillers, and investigation of multifaceted applications. The objective of the current discussion is to provide an overview of the synergistic potential between the fields of 3D bioprinting and AF-PNC, along with its innovative perspectives. Secondly, the article concentrates on several different types of AFs, the application of which in 3D bioprinting provides distinctive prospects, despite the extensive research conducted on nanocomposites with isotropic fillers. This review aims to enhance the current knowledge base in the specialized area of AF-PNCs through an analysis of synthesis techniques, dispersion strategies, and resultant properties. Finally, this article delves into the multifaceted applications of 3D-bioprinted AF-PNCs, which extend beyond the conventional mechanical improvements commonly attributed to such materials. The prospective applications of the subject matter in the application of tissue engineering, drug delivery systems, and bioelectronic devices are also discussed.

2. Overview of 3D printing techniques

3D printing, a subset of additive manufacturing (AM), constructs 3D structures layer by layer from a variety of materials, including plastics, metal, and polymers.[8-10] It possesses several advantages, in terms of cost-efficiency, ease of operation, and mass production availability, as compared to traditional manufacturing procedures.[11] However, 3D printing is difficult since it typically involves a process of trial and error in order to determine the combination of components (material, printer, process parameters, and post-processing) that can generate the desired result. On the other hand, with the exception of fibrous reinforcements, it is extremely challenging for manufacturers to manage the distribution or placement of fillers inside polymeric frameworks.[12]

3D printing applications include not only manufacture of clothing and toys as well as construction, but also biomedicine like fabrication of cartilage, ears, and skin. Non-living constructs are fabricated as 3D-printed objects to serve as space-filling or structural prostheses in medical applications.[13] However, replacement of injured organs is the final goal of tissue engineering.[14] Bioprinting can be used to create organ-mimetic scaffolds, which precisely deposit bioinks to fabricate tissue-mimetic structures. The 3D environment promotes cell–cell and cell–extracellular matrix (ECM) interactions which are not available in plate-culturing conditions.[15-17]

The four main 3D bioprinting techniques are inkjet-based, laser-assisted, light-induced, and microextrusion-based printing (Figure 1).[18-22] The main features of the four categories, including operation principle, resolution, ink materials, and cell viability, are summarized in Table 1.

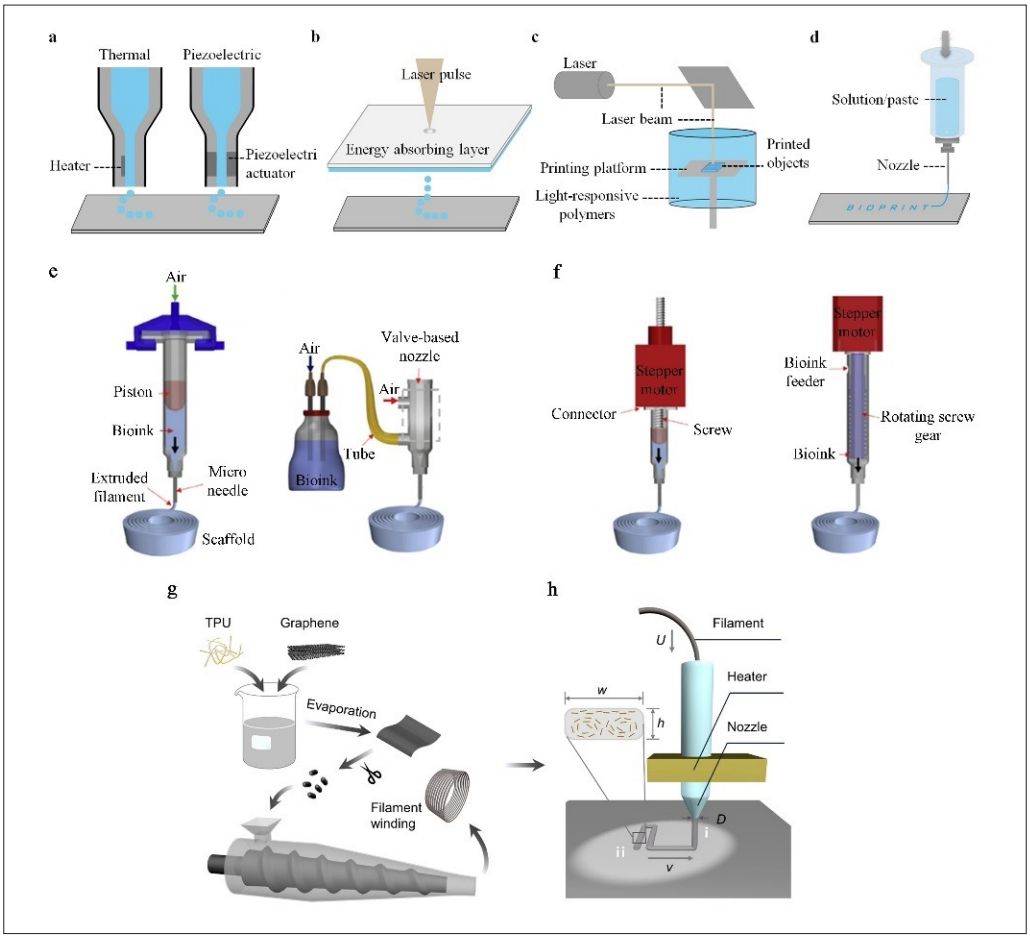

Figure 1. Schematic illustrations of the four 3D printing strategies: (a) inkjet-based, (b) laser-assisted, (c) light-induced, and (d) extrusion-based. Schematic illustrations of (e) pneumatic and (f) mechanical-driven extrusion-based printing. Reproduced from ref.[14] Schematic illustration of (g) graphene/TPU filament production and (h) conventional FDM method for printing graphene/TPU composites. Reproduced with the permission from ref.[22] Copyright © 2021 American Chemical Society.

Inkjet bioprinting is the simplest and least expensive strategy, producing small volumes of droplets at about 1 to 100 picoliters to a printing platform via piezoelectric actuators.[8] It has been discovered that interactions between adjacent droplets and droplets-substrate affect the spatial resolution. However, the main limitation of this approach is the restricted materials choice and low cell viability. The ink's viscosity should be maintained at a low level of 3.5–12.0 mPa·s, which however limits its use to constructing two-dimensional (2D) tissues such as skin and cartilage.[14]

Laser-assisted bioprinting (LAB) is renowned for its ability to deposit bioinks composed of cells, nucleic acids, or peptides.[23] LAB is carried out by shining a laser on the bioinks. It is capable of working with inks with viscosities between 1 and 300 mPa·s and encapsulating cell with concentrations of up to 10^8 cells/mL. A needle-free system that can eliminate needle clogging and high spatial resolution are major advantages of this technique. The fact that the materials must rapidly crosslink to prevent cellular gravitational settling during long printing processes is an important consideration for LAB.

Light-induced bioprinting, also known as stereolithography (SLA), was developed in the 1980s.[19] In SLA, a focal point of light is moved with scanning mirrors, and the light-sensitive liquid inks are crosslinked on the building stage. After curing each layer, the build stage gets lower in the ink solution so that further crosslinking can take place. The stage's lowering height is set to less than the curing depth, thus giving a high level of integrity between each layer.[24] Traditional SLA has a maximum resolution of about 25 μm. The newly-developed high-definition SLA and μ-SLA have high resolution of up to several micrometers.[8] Furthermore, the needle-free system, like LAB, avoids the occurrence of needle clogging.

Microextrusion-based bioprinting is a technique that extrudes ink through the needle and controls its

Table 1. Comparison of the four bioprinting approaches

Specification	Inkjet	Laser-assisted	Light-induced	Microextrusion-based	Ref
Principle	Electrical heating or piezoelectric actuation	Applying an energized pulsed laser on target or ribbons and being deposited over metal substrates.	UV-initiated curing of the liquid photo-responsive materials on the build stage	Extrusion of pre-gel solution through a needle and build up layer-by-layer	[29-39]
Resolution	85–300 μm	> 5 μm	> 25 μm	100 μm–10 mm	
Gelation	Fast; chemical crosslinking.	Fast; chemical, photo-crosslinking	Fast; chemical, photo-crosslinking	Medium; chemical crosslinking, shear-thinning, temperature	
Dispensing speed	Fast (1–10,000 droplets/s)	Medium-fast (200–1600 mm/s)	Fast, chemical crosslinking	Slow (10 μm–50 mm/s)	
Material viscosity	3.5–12 mPa·s	1–300 mPa·s	1–300 mPa·s	30–6 × 10^7 mPa·s	
Cell density	Low (<10^6 cells/mL)	Medium, 10^8 cells/mL	Medium, 10^8 cells/mL	High, cell spheroids	
Cell viability	>85%	>95%	>90%	40–80%	
Advantages	• Low-cost, simple system • High resolution • Fast printing speed • High cell viability	• High resolution • High cell viability • Good vertical fidelity	• Low cost • High resolution • Fast bioprinting speeds • High cell viability • Fair vertical fidelity	• Bioinks with wide range of viscosity • High cell density • Simple system • Multiple composition • Feasibility	
Disadvantages	• Limited availability of bioinks with low to medium viscosities • Low cell density • Mostly applied to 2D	• Complex system • Expensive • Medium bioprinting speed • Medium on cell density	• Moderately complex system • Bioink limited to photo-polymerization crosslinking • Medium on cell density	• Low to moderate cell viability • Slow bioprinting speed • Moderate resolution	

movement with a three-axis motion control system to build 3D layer objects. In the traditional extrusion-based printing technique, the plastic filament is extruded through a high-temperature extruder, and the melted plastic solidified once extruded and quickly bound to the previous layers.[25] Microextrusion bioprinter with syringes was created based on the general concept of fused deposition modeling (FDM) printer. This strategy is very popular in tissue engineering owing to its advantages such as ease of operation, availability of inks with a wide range of viscosities, multiple crosslinking methods, and high cell loading density.[26-28] To create 3D architectures, biomaterials are loaded into the syringe and extruded via a pneumatical (Figure 1e) or mechanical-driven (Figure 1f) system.[14] Inks with a viscosity between 30 mPa·s and 60 kPa·s can be readily extruded via a pneumatic system, whereas high-viscosity bioinks of greater than 60 kPa·s can be better extruded via a mechanically driven system. A systematic consideration should be given to the pressure, movement speed, extrusion flow rates, needle size, and layer heights in order to ensure an optimal resolution.

Inspired by the concept of using a coaxial spinneret to fabricate hollow nanofilaments in electrospinning, coaxial needles were first adopted by Ozbolat et al. in 3D bioprinting to fabricate micro-fluidic channels.[40-42] The bioink is injected through the exterior needle, while the crosslinking agent is extruded through the interior needle, leaving stand-alone perfusable vessels. The commonly used bioink and crosslinking agent for coaxial printing are alginate composite and $CaCl_2$ solution.[41,43,44] Sacrificial bioprinting, a "removable" bioink deposited in a matrix via microextrusion bioprinting which was followed by matrix curing and sacrificial ink removal,[45,46] was first demonstrated by Wu et al.[47] This method could be utilized for fabricating 3D interconnected wall-less channels. Similar to sacrificial bioprinting, embedded extrusion bioprinting was developed to fabricate heterogeneous complex 3D tissue with biomaterials in high resolution,[48,49] where the bioinks are extruded into a supporting matrix, composed of elastomer,[48] viscous oil,[50] granular gel suspension,[51] or self-healing hydrogels,[52] which is removed afterward.

The supporting bath material should, in general, behave like Bingham plastic that is rigid at low shear forces but flexible when it reaches high shear stresses.[27,49] Suitable yield stress smooths needle movement and supports printed constructions. Supporting bath yield

stress is usually one order of magnitude lower than ink yield stress to prevent filament breaking and enable fine filament deposition.[50] Ink and supporting bath should have equal viscosity, osmolality, and density to increase print resolution. Supporting bath material and ink with a weak interfacial tension prevents printed structures from deforming. Microparticle size also affects extruded filament surface shape in granular supporting bath. Microparticle "spurs" link filaments.[50] In comparison to larger granular gels, smaller and more uniform microgel supporting media exhibit higher-resolution structures due to their lower stiffness, viscosity, and yielding stress.

3. Rheological aspects of 3D-printed composites

Previous studies suggest that bioinks must meet certain chemical and physicochemical requirements to print high-resolution constructs and provide a cell-friendly environment. Rheological property, which describes material's flow and deformation under stress, is the main factor affecting its printability and fidelity. Microextrusion-based bioprinting is widely studied due to its broad viscosity range processability, ease of use, multimaterial printing possibility, and high cell loading density; therefore., this review will discuss the required rheological properties for microextrusion-based bioprinting.

In microextrusion-based printing, bioink undergoes high shear strains during extrusion and rests after deposition. Viscosity, dynamic modulus, yield stress, and elastic recovery are used to characterize the process; extrudability, printability, and shape fidelity affect tissue construct feasibility; printability describes bioink's ability to be extruded, form filaments, and stack up to create constructs, while printing fidelity refers to the filaments' shape retention and is usually assessed by filament diameter, uniformity, and gravity resistance.

3.1. Shear thinning and its impact in bioprinting

Viscosity decreases with increasing shear rate in shear-thinning materials. Due to their unique properties and potential to fabricate complex biological structures, these materials have garnered interest in 3D bioprinting. Effects of shear-thinning materials on 3D bioprinting, bioink formulation, and printed constructs are described as follows:

- *Printability and precise deposition:* Shear-thinning behavior allows bioinks to flow easily through the printing nozzle, allowing precise layer deposition. Under shear stress, viscosity decreases, ensuring smooth flow and accurate cell and biomaterial placement for high-resolution printed structures.
- *Structural support:* Shear-thinning materials can support printing. The bioink's viscosity can be adjusted to maintain structural integrity during layer-by-layer printing by changing the shear rate. Printing delicate scaffolds or complex anatomical structures requires structural support.
- *Cell viability and biofunctionality*: Shear-thinning materials can be biocompatible and promote cell survival, proliferation, and differentiation.[53] The controlled decrease in viscosity during printing reduces shear stress and mechanical damage to encapsulated cells, preserving their viability and functionality; therefore, living cells can be added to bioink to create functional tissues and organs.
- *Complex tissue architecture:* Shear-thinning materials can create complex tissue architectures with precise microstructure control. The bioink's ability to flow and conform to intricate geometries allows it to create vascular networks, heterogeneous tissue structures, and biochemical cue gradients. Biomimetic tissues that mimic native tissue organization can be created.

Bioinks should have shear-thinning behavior and a viscosity suitable for extrusion to optimize flow during printing and stability after deposition. To achieve the desired viscosity profile, rheological characterization helps determine the bioink composition, including biomaterials, crosslinkers, and additives. The printed structure is also required to solidify via a crosslinking mechanism, such as physical crosslinking (temperature or pH changes), chemical crosslinking (reactive groups), or light-mediated crosslinking (photoinitiators). Additionally, the bioinks should be compatible with encapsulated cells for high cell viability and functionality. Cell adhesion, proliferation, and differentiation should be supported by the bioink composition while minimizing cytotoxicity and inflammatory responses. These interactions depend on biomaterials, growth factors, and cell-encapsulation methods.

3.2. Viscoelasticity

Viscoelasticity is a fundamental characteristic of materials in demonstrating both elastic and viscous behaviors, significantly impacting the printed constructs' structural integrity, cell viability, and functionality.[54] The present section delves into the influence of viscoelasticity on the process of bioprinting and deliberates on its effects on the formulation of bioink, printing parameters, and the potential applications of tissue engineering.[55] The general method for determining a fluid's viscosity involves placing the sample in the annulus of a series

of concentric cylinders. Fluid should be sheared between cylinders, and the torque exerted on the inner, stationary cylinder by the outer, rotating cylinder is measured.[56] Non-Newtonian fluids are those that follow this relationship and can be further classified as either pseudoplastic ($n = 1$) or dilatant ($n > 2$) fluids. Pseudoplastic fluids (sometimes called shear-thinning fluids) have high viscosities at low shear strengths but lower values as the shear force is increased. On the other hand, a dilatant (also known as a shear-thickening fluid) acts in the opposite way.[57] A shear pressure versus shear rate diagram is used to compare and contrast Newtonian and non-Newtonian liquids. Some non-Newtonian fluids also behave like solids when they are moved. This is considered a factor of time because flow causes the rearrangement of fluid molecules,[58] a reaction defining the characteristic of viscoelasticity, which can happen to both solids and liquids. Viscoelastic materials are polymers and predominantly biological materials, manifesting qualities in the zone between those of an elastic material and a viscous material.

4. Different types of AF-based 3D prints

In spite of its widespread adoption and user-friendliness, microextrusion-based 3D printing technique has numerous drawbacks that prevent it from fulfilling its potential as an environment-friendly alternative to conventional production techniques. For example, the mechanical property of 3D-printed parts is commonly poorer than that of samples fabricated via traditional methods. It is anticipated that polymer/nanofillers would display enhanced characteristics, particularly at low weight percentage of filler under which the influence of mechanical reinforcing will be the most obvious.[59]

4.1. Clay/polymer nanocomposites

Due to its layered structure, thermal stability, rheology, mechanical strength, and absorption and adsorption capacity, clay, such as phyllosilicate, laponite, and montmorillonite, has great potential in tissue engineering.[60-63] However, the incorporation of nanoclays into the polymer feedstock filament is still challenging due to the high viscosity of the raw material melt, which is detrimental to the processability of the material and the establishment of printed objects. For example, when laponite is dispersed in water, sodium ions dissociate from individual platelets, resulting in negatively charged face, while the hydroxide ions dissociate at the rim, leaving the rim slightly positively charged.[8] The charge distribution drives the self-assembly of laponite platelets via electrostatic interactions to form gel, which shows typical characteristics of "thixotropic" and "shear-thinning" behavior.[8]

At present, studies on the addition of non-rubber polymer/clay composites in FDM that has demonstrated greater attributes remain scarce. Weng et al. used melt intercalation method to prepare acrylonitrile butadiene styrene (ABS) containing modified montmorillonite.[64] Adding 5 wt% of the modified montmorillonite enhanced the tensile strength of 3D-printed and molded ABS samples by 43% and 28.9%, respectively. It was discovered that the incorporation of the modified montmorillonite resulted in a significant rise in elastic strength, toughness, and dynamic mechanical modulus, while simultaneously leading to a reduction in thermal expansion ratio and weight loss. The developed ABS nanocomposites with improved mechanical and thermal characteristics are therefore good candidates for FDM 3D printing. Additionally, the large and highly charged plane surface of montmorillonite is beneficial for the adsorption of bioactive molecules. In addition to being biocompatible, it promotes cell proliferation and attachment, and induces osteogenesis of the encapsulated stem cells.[65] Poly (lactic acid) (PLA) is another widely used material in filament compounding, ranking among the top five in terms of both market value and volume, alongside ABS.[66] Paspali et al. prepared PLA/clay nanocomposite strands to determine how the composition affects the physical properties of the printed specimens and delineate the effect of clay intercalation level on the physical properties.[67] In another research, the production of biocompatible polymer nanocomposite was revealed. Using a single screw extruder nanomixer, the ink was manufactured by mechanically combining polycaprolactone (PCL), montmorillonite, and hydroxyapatite.[68]

4.2. Graphene/polymer nanocomposites

Hierarchically coordinated pattern engineering has been made possible by the attention paid to carbon-based nanomaterials during the past two decades. These nanomaterials include fullerene, carbon nanotubes (CNT), graphene and its derivatives, nanodiamonds, and carbon dots reinforcements.[69] Its unusual atomic structure and electron distribution provide graphene exceptional specific surface areas, thermal and electrical conductivity, mechanical properties, optoelectronic behaviors, carrier mobility, and chemical stability.[47]

Recent research has discovered that graphenic filler increases polymeric mechanical properties because a single graphene layer's Young's modulus is 1 TPa, which is 200 times the breaking strength of steel.[70] In order to generate graphene-based polymer nanocomposites, various manufacturing procedures, such as melt mixing, solvent-aided casting/coating methods, electrospinning, and so on, are utilized. Moreover, the basic dispersion

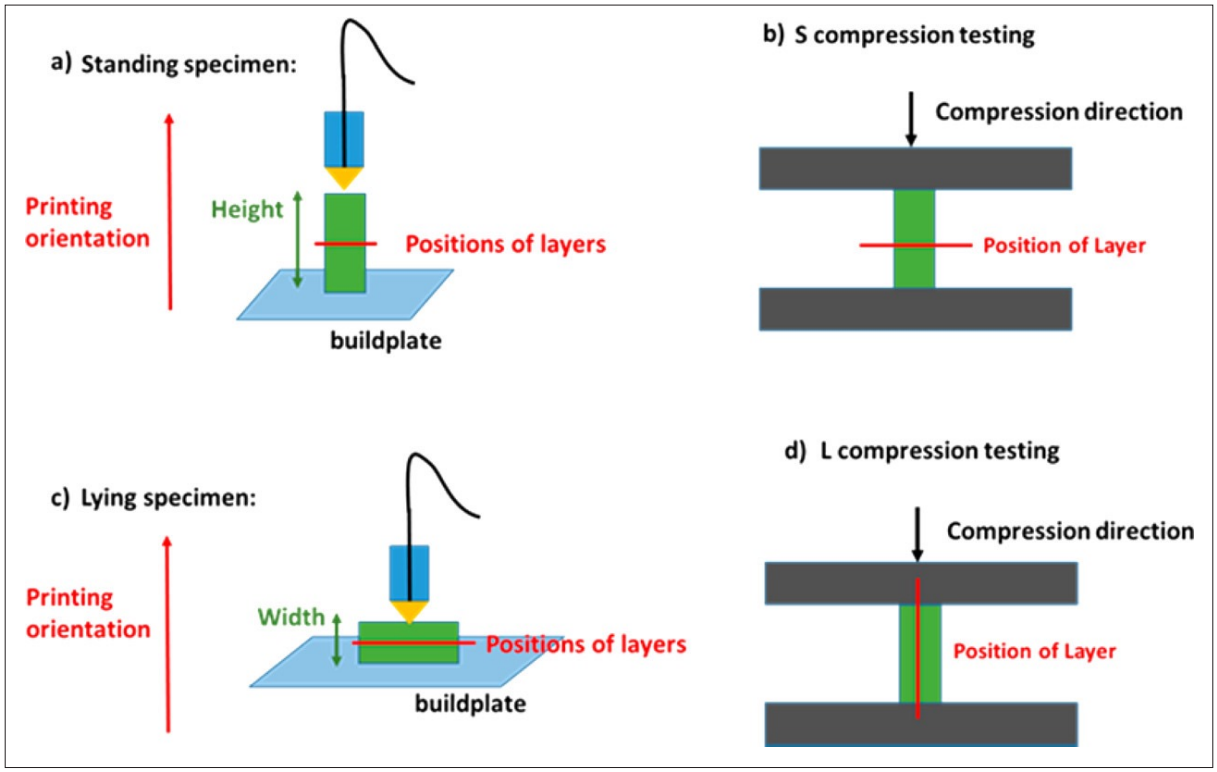

Figure 2. Diagrammatic representations of (a) 3D printing standing specimens, (b) S compression illustration, (c) 3D printing lying specimens, and (d) L compression test. Reproduced with the permission from ref.[79] Copyright © 2017 American Chemical Society.

efficiency is significantly reduced by phase separation and graphene agglomeration in the polymer matrix, but this could be overcome by adding graphene derivatives.[71-75] The use of 3D printing and graphene or its derivatives allows rapid prototyping and manufacture of 3D systems with appropriate properties and functionality.[76] In most cases, printing complex 3D designs with less than 5% graphene improves their properties, processing time, and cost. FDM is an effective way to build complex structures from graphene-based polymer nanocomposites, according to Wei et al.[77] Guo et al. also reported the creation of an asymmetrically aligned structure printed with thermoplastic polyurethane (TPU)/graphene composites.[22] The through-plane thermal conductivity of the printed vertically aligned framework is shown to be up to 12 $W \cdot m^{-1} \cdot K^{-1}$ at 45 wt%. This is approximately eight times higher than the through-plane thermal conductivity (TC) of a laterally printed construct and outperforms several of the conventional particulate composite structures (Figure 1g and h). Similar kind of phenomenon also has been reported elsewhere.[78] Furthermore, Chen et al. discovered that the attributes of the printed structure differed depending on printing orientation (Figure 2).[79] The printed structures are biocompatible with NIH/3T3 fibroblasts, making them promising tissue engineering scaffolds. Other studies show that most graphene and its derivatives are cytocompatible *in vitro* and *in vivo*, suggesting their potential in tissue engineering and regenerative medicine. However, concentration, geometry, size, and surface functionality of 2D nanomaterials affect biocompatibility. Nanoscale graphene derivatives, especially tubular ones like single-walled CNTs (SWCNTs) in the 10–100 nm size range, may cause cytotoxicity and inflammation.[46]

4.3. Carbon nanotubes/polymer composites

Since the popularization by Iijima, CNTs have been widely employed to build multifunctional polymer composites because of its outstanding electrical, thermal, and mechanical characteristics.[80] Polymer nanocomposites achieve electrical conduction via inter-aggregate conductance, field emission, and electron tunneling. Either the particles make contact with one another, creating a conductive effect, or the electrons "tunnel" from one CNT to another, creating a conductive effect. This assembly of CNTs results in a percolated network of continuous conductivity. Above a certain critical CNT concentration, it is feasible to develop a percolated network.[81] Conversely, a quasi-dispersion of CNTs can potentially lead to higher electrical conductivity.[82] However, the aggregation of CNTs might clog the nozzles in microextrusion-based printing.

By optimizing the size of the conductive fillers and printing variables, such as temperature, movement speed, and retention time, the nozzle jamming can be controlled.[83] Gonzalez et al. conducted research on a mixture of multiwalled carbon nanotubes (MWCNTs), poly(ethylene glycol) dimethacrylate (PEGDA), and poly(ethylene glycol) methyl ether methacrylate (PEGMEMA).[84] The desired CNT distribution was achieved by first sonicating a mixture containing PEGMEMA and CNTs, and then high-shear mixing the slurry following the addition of PEGDA resin and photoinitiator. Additionally, recent research has also investigated the application of CNT in tissue engineering applications. Shin et al. found that adding small amount of CNTs (3 mg/mL) in GelMA increased the compressive modulus from 10 kPa to 32 kPa and influenced the hydrogel pore size without changing the porosity.[85,86]

4.4. MXenes-based composites

To create a flexible, self-standing polymer composite, Li et al. combined the advanced polymer binder jet printing method (Figure 3a) with novel 2D $Ti_3C_2T_x$ MXene.[87] The negative electrostatic charge of the MXene, in conjunction with dependable ink deposition technique, makes it possible for ultra-high concentrations of MXene ink to be expelled without any clumping or other issues.[88] Due to its dissolvability in water and compatibility with biological systems, poly(vinyl alcohol) (PVA) was selected as the basis for the polymer. Rheological studies revealed that the ink continued to act as a liquid and exhibited good shear-thinning behavior. This, in turn, made it possible to print a PVA construct that was both consistent and devoid of voids.

In another research, aqueous 3D-printable MXene/polyethylene oxide (PEO) inks were developed for liquid deposition modeling 3D printing.[89] The hydrogen bonding among MXenes and PEO in an aqueous system endows hybrid ink with thixotropy behavior, thus enabling printing. Electromagnetic interference (EMI) shielding performance was investigated in the printed semi-transparent samples. In addition, extremely anisotropic thermal properties may be achieved by the 3D printing technique. Yuan et al. conceived the idea for an intelligent EMI shielding switch, which allowed them to concurrently achieve the electromagnetic shielding and transmitting functionalities in one piece.[90]

Basara et al. engineered human cardiac patching using aerosol jet-printed 2D titanium carbide ($Ti_3C_2T_x$) MXene-PEG hybrids.[91] Aerosol jet printing is a type of additive manufacturing enabling to print nanomaterial-based inks on curved surfaces at a spatial precision.[92] The nanoink is volatilized with the help of an ultrasonic atomizer and guided to the deposition head, where it is aerodynamically focused by a concentric sheath gas flow. This process is depicted in Figure 3b. The fabricated electroconductive cardiac patches illustrated enhanced alignment of human-induced cardiomyocytes (iCMs) from pluripotent stem cells. They also evaluated the cytotoxic effects of the MXene-PEG hybrid hydrogel on iCMs for a period of 7 days. Further, they analyzed the protein production, gene function, and Ca^{2+} flow intensity and transmission.

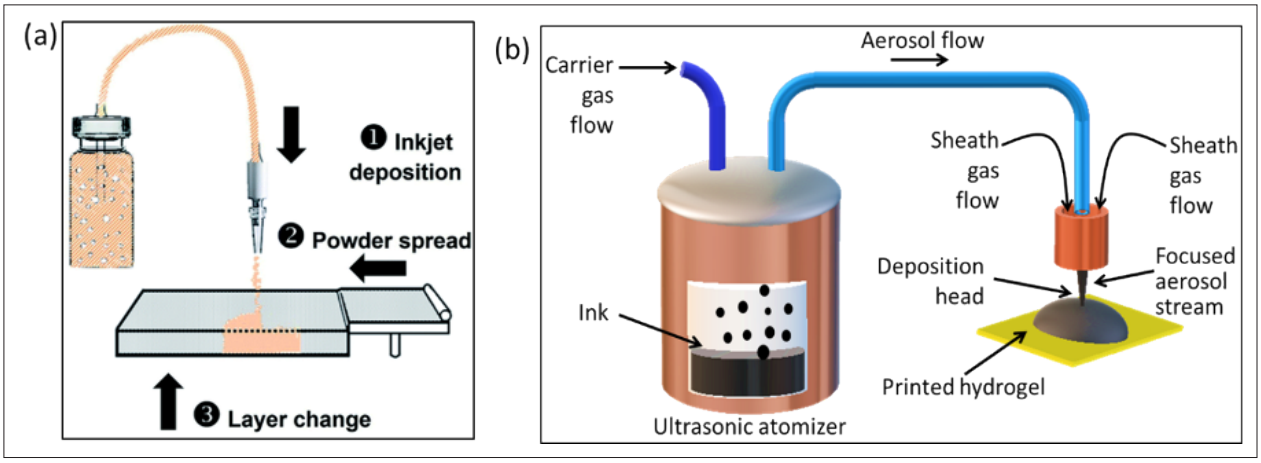

Figure 3. (a) Schematic illustration of binder jet printing process. An inkjet setup was created by connecting an MXene ink supply to a peristaltic pump and a print nozzle. A uniform coating of PVA powder was applied to the print stage by a roller and then spread there. Reproduced with the permission from ref.[87] Copyright © 2022 Royal Society of Chemistry. (b) Schematic illustration of ultrasonic atomizer and printer deposition head. In the ultrasonic atomizer (left), ultrasonication aerosolizes ink and an inert carrier gas flow (N_2) presses the ink vial, forcing the aerosolized ink and inert gas flow toward the deposition head. In the deposition head (right), an annular inert gas sheath (N_2) focuses aerosolized ink flow and directs it to the substrate through a nozzle.

According to the results of this work, a composite hydrogel made of MXene and PEG shows potential as an electroactive scaffold for the treatment of heart damage.

4.5. Biofiber-based composites

Biomass can completely decompose in the soil without generating harmful chemicals.[93] Low cost, availability, degradability, widespread accessibility, light weight, acceptable tensile stiffness, and diminished healthcare implications are all benefits of lignocellulosic fibers.[94] Therefore, natural fibers (e.g., from poplar wood or other biopolymers) are commonly incorporated into polymer matrix to develop hybrid biocomposites with high stiffness, light weight, biodegradability, and recyclability.[95] In addition to being low-cost, degradable, widely accessible, and light weight, lignocellulosic fibers have appropriate tensile stiffness and do not cause profound healthcare implications.[94]

Biorefinery lignin derived from *Pinus radiata* was blended with polyhydroxybutyrate composites and melt-extruded to form composite filaments.[96] The rheology findings show that adding lignin as fillers at a weight-to-weight ratio of 20% caused a change in the melt viscosity and made the material suitable for 3D printing. Zhao et al. prepared poplar/PLA composites with variable sized poplar fiber mesh.[97] As poplar fibers shrank, poplar/PLA tensile strength increased from 34 to 54 MPa. Composites made from shorter poplar fibers showed more compact fracture surfaces and fewer voids. Liu et al. synthesized PLA composites with sugarcane bagasse.[98] Adding sugarcane bagasse to PLA lowered tensile and flexural strength but enhanced flexural modulus in printed samples. In another study, two types of polyethylene were mixed with thermal–mechanical pulp fibers to make biocomposites.[93] The hydrophilic character of thermal–mechanical pulp fibers was changed by enzymatically grafting hydrophobic compounds (octyl gallate and lauryl gallate). Ethylene filaments with low melt flow index have low void percentage and thickness variability. The morphologies, mechanical properties, crystallization properties, and heat resistance of 3D-printed materials were also studied. This research shows that biocomposites can be made from massive amounts of residual lignin.

5. Engineering strategies for filler alignment in bioprinting

Tissue engineering is a multidisciplinary biomedical engineering field that integrates biological science and engineering.[99] It represents a new approach to constructing artificial tissues for clinical studies, translation, and drug delivery since the patient-specific autologous cell-incorporated scaffold generated through this approach shows no adverse response.[100-102] Engineered human organ-mimicking scaffolds can be produced using bioprinting strategy. Unlike current intraoperative procedures, 3D printing can generate customized devices with exceptional accuracy. Thus, most 3D printing-related biomedical applications include the production of non-living structures, such as gadgets used in orthopedics, surgical equipment, and osteonecrosis implants.[103] In order to improve the functionality and viability of bioprinted constructions, controlled filler orientation is crucial since it mimics the natural structure of tissues and organs. Many tissues including muscles, skin, vessel, and nerves exhibit parallel alignment in the arrangement of cells and ECM. For example, the cytoskeletons and nuclei of tenocytes are elongated along the direction of parallel-aligned collagen fibers in tendon.[104] The alignment of cells plays a significant role in the cell functions; for instance, the alignment of cardiac cells is fundamental to heart contraction.[105] In addition, radially alignment of tissue is observed in cornea, meniscus, dura mater, etc.[106] To simulate human tissue and engineer tissue or organ for replacement, developing controlled anisotropic scaffolds is therefore vital as the matrix microenvironment is responsible for cellular behaviors including attachment, movement, proliferation, and differentiation *in vivo*.[107,108] Anisotropic topographies have a significant impact on how cells behave in terms of both morphology and function, particularly fibroblasts, osteoblasts, neurons, and mesenchymal stem cells (MSCs).[108] The transverse or longitudinal topological signals in anisotropic scaffold could be sensed by cells and guide cellular fate by modulating cell growth and differentiation, which in turn regulates tissue regeneration and their microenvironment.[104]

Cell adhesion that regulates the signal transmission between cell membrane and ECM during adhesion and migration can be modulated via the nano- or micro-scale topographies in the anisotropic scaffolds.[108,109] Cell movement is usually influenced by several factors including durotaxis, haptotaxis, chemotaxis, galvanotaxis, and mechanotaxis.[107] Among these, mechanotaxis is of great importance in regulating cell fate. Research has explored the mechanical feedback to cells. Cells sense the internal matrix stiffness and external mechanical loads and transduce the mechanical signal into physiological responses to guide cell growth and differentiation.[110] As substrate stiffness increases, 3T3 fibroblasts become less motile while spreading more widely, an indication of the significant role that substrate stiffness plays in tissue regeneration by influencing cell behavior and cellular fate. Stiffer ones are prone to guide cells to produce stress fibers and enter cell cycle, increasing cell traction, spreading, and proliferation. In contrast to stiffer ones, softer substrates promote cell secretory activity. The cellular response to

substrate stiffness in some representative tissues has been investigated.[104] Therefore, by controlling the alignment of AFs, the scaffold exhibits anisotropic mechanical properties, thus regulating cellular behaviors. For instance, human umbilical vein endothelial cells (HUVECs) are found to align themselves along the direction of fibers. Additionally, aligning the conductive fillers increases the possibility of filler connections, which help establish conductive network and promote cell growth in scaffolds, such as cardiac tissues.[111]

Filler alignment is a complex problem warranting a solution by means of novel technical approaches. There are a number of intriguing approaches for achieving exact filler orientation, including the use of external stimuli like magnetic and electric fields, the optimization of nozzle design, gradient printing, and multimaterial extrusion. Researchers can use external magnetic fields to precisely move and align fillers in bioink that contains magnetic nanomaterials.[112] This method provides interesting new opportunities for the printing of highly shaped tissues by allowing for dynamic control over filler orientation both during and after the printing process. Pardo et al. suggested that magnetically assisted 3D bioprinting and matrix-assisted 3D bioprinting be used together to make high-resolution hybrid composites that can not only copy the anisotropy of native tissues but also allow for remote control of tissue constructs as they mature.[114] For this purpose, bioinks made of gelatin-methacryloyl (GelMA), short magnetically responsive microfibers (sMRFs), and human adipose-derived stem cells (hASCs) were extruded into fibrillar cellulose nanocrystals (CNCs)-based baths while low-strength magnetic fields were applied. This produced high-resolution constructs with controlled anisotropic architectures.

In the quest for filler alignment, electric fields are another potent instrument. Electrostatic forces can be used to direct and orient charged fillers within the bioink.[113] It is feasible to engineer tissues with desired qualities by aligning charged fillers to form structures using controlled electric fields. Moreover, shear forces within the printing nozzle can be manipulated to achieve filler alignment. With optimized nozzle design, bioprinters may generate controlled shear pressures on the bioink during extrusion.[115] Mechanically enforcing filler alignment along the shear direction paves the way for highly anisotropic design. By adjusting the filler content or bioink properties, gradient printing is a flexible method. Fillers position themselves as bioink moves from one area to another, creating structures with acceptable orientation gradients. This method is applicable to the development of multilayered, complex tissues.[116] Bioprinters with dual or multinozzle systems provide finer control over filler alignment than those with single-material extrusion capability. By extruding multiple materials at once, each with its own unique properties, scientists may design structures with precisely controlled filler orientation.[117] This method is perfect for fabricating composite tissues and scaffolds with tailored architectural properties. In smart rheological control, the viscosity and shear-thinning behavior of the bioink are adjusted for optimal performance. By fine-tuning these characteristics, we can improve the bioink's ability to aid with filler alignment during printing. Rheological optimization keeps the filler oriented while the bioink flows smoothly.

Filler alignment can be stabilized through post-printing crosslinking techniques. After bioprinting, the structure can be treated with UV radiation, chemical crosslinkers, or enzymatic reactions.[118] The fillers can be permanently fixed in their preferred orientation using any one of these treatments to enhance the structure's durability.

The combination of smart rheological control, real-time monitoring, and post-printing crosslinking has placed us closer to realizing the full potential of bioprinting in regenerative medicine and tissue engineering. However, recreating the organization of ECM and the cell patterns of anisotropic tissues in bioengineered constructs is still a major problem in the realm of biofabrication.

6. Applications of 3D-printed polymer composites for biomedical applications

To demonstrate the applicability of bioprinting in tissue engineering, most studies focused on developing bioink materials because cell-friendly environment is one of the most important factors influencing its feasibility.[119,120] Additionally, AF-PNCs are under investigation as the orientation of the AF has significant influence on the cellular behaviors.

6.1. Skin tissue

Skin is the largest organ of human body and composed of multilayered structures, including epidermis, dermis, and hypodermis, and various cell types, such as keratinocytes, fibroblasts, and melanocytes.[121] Artificial skins can not only serve as skin grafts for wound healing but also experimental platform to investigate its permeability and inflammatory response during the transdermal and topical drug formulation development and screening. The development of techniques has allowed for the highly accurate and complex 3D bioprinting of multistratified skin tissue that closely resembles natural skin.

Cubo et al. fabricated a human plasma-derived bi-layered skin.[122] To replicate the structure of natural skin, they printed the dermis with fibroblasts-laden fibrin

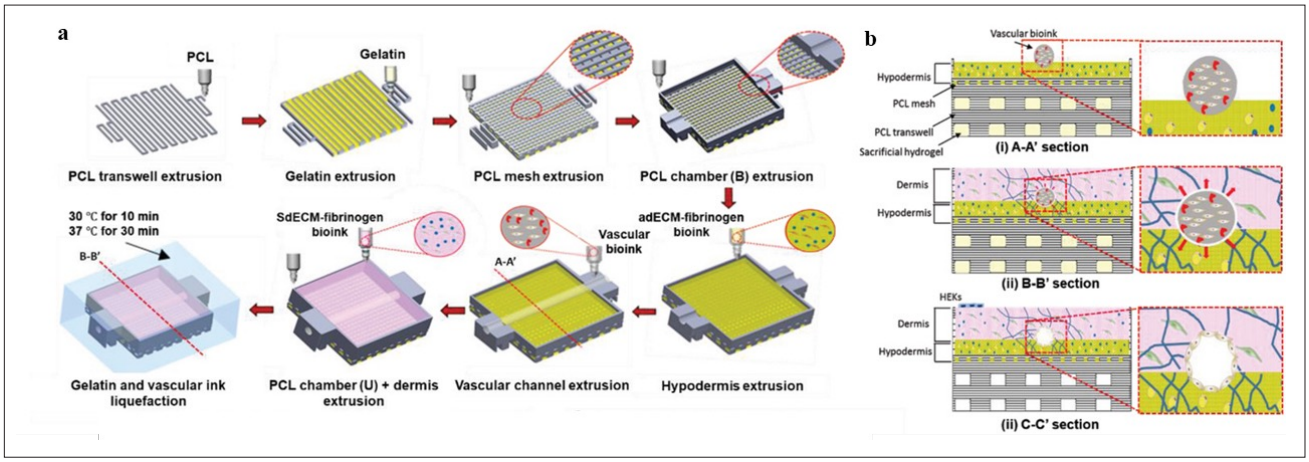

Figure 4. (a) Schematic representation of the fabricated artificial skin with microstructure and (b) the cross-sectional views. Reproduced with the permission from ref.[123] Copyright © 2018 John Wiley & Sons, Inc.

hydrogel and then deposited a second confluent monolayer of hydrogels encapsulating keratinocytes. Both *in vitro* and *in vivo* experiments were conducted on the artificial skin through histological and immunohistological methods. The encapsulated cells exhibited high cell viability, and the *in vivo* differentiation property of the skin, which grafted onto the back of mice, was examined. Orthkeratotic stratum corneum was generated, implying stratification and terminal differentiation of the printed skin. The fast fabrication speed, together with the high resemblance to the natural human skin, corroborates the application of microextrusion-based bioprinting in fabricating artificial skin. Kim et al. replicated skin anatomy by constructing vascularized dermis and hypodermis and the topical epidermal layer via extrusion (Figure 4a and b).[123] The functional biomarkers in each compartment, such as filaggrin, laminin, keratin 10, fibronectin, collagen type I, and CD31, were examined and expressed in specific regions, indicating the successful formation of matured skin. The bioengineered vessel provided nutrition and oxygen and promoted the physiological interaction with epidermis during the differentiation of keratinocyte, presenting a novel strategy used to fabricate physiologically human-mimetic skin that serves as a more reliable experimental platform for evaluating the cytotoxicity of drug and cosmetic and investigating skin-related diseases.

Skin tissues are anisotropic with varied mechanical characteristics depending on their location. Flexible anisotropic electronic skin was engineered by Pei et al. via 3D printing strategy. The strong shear and tensile stress generated at the nozzle walls assisted the alignment of the ionic salt-montmorillonite (IS-MMT) in poly (vinylidene fluoride) (PVDF) inks along the printing path, thereby constructing a desirable anisotropic artificial skin. The oriented IS-MMT in turn facilitates PVDF dipoles alignment, which greatly improved the piezoelectric properties of electronic skin.[124] Lackner et al. fabricated anisotropic structures, composed of nanocellulose and alginate, with gradient mechanical properties. Controlling the fiber orientation through the printing path allowed for fine-tuning of the mechanical performance. The engineered structure could be applied to the production of different tissues, such as skin, cartilage, and cardiovascular tissues.[125]

6.2. Cartilage tissues

Cartilage is an avascular tissue containing only 10–15% of chondrocytes, which justifies its limited self-regenerative capability.[126] Several techniques have been developed to repair defective cartilage, but the repaired cartilage exhibits fibrocartilaginous phenomena and is not able to withstand the intense mechanical pressure.[127] Therefore, it is crucial to regenerate cartilage-like tissue endowed with mechanical property that can induce chondrogenesis and replace damaged cartilage.

Antich et al. deposited PLA with superior mechanical strength in grid-like structure to support hyaluronic acid-based hydrogel. They mixed hyaluronic acid and alginate and discovered that adding hyaluronic acid increased the expression of chondrogenic gene markers.[128] Schipani et al. fabricated anisotropic articular cartilage constructs with interpenetrating network composed of alginate and GelMA.[129] The constructs are soft in compression and stiff in tension, which simulated human cartilage. In addition, the bioprinted artificial articular cartilage promoted chondrogenesis, and the encapsulated bone marrow-derived stromal cells produced hyaline-like

cartilage matrix. By adding anisotropic fillers, such as nanocellulose, into alginate solution, the printability of the bioink was significantly improved.[130,131] The nanocellulose-incorporated bioink exhibited enhanced cell spreading, proliferation, and ECM formation, demonstrating its great potential in 3D printing of living tissue and organs. Researchers have also demonstrated that the anisotropic gradient-structured cartilage exhibited better cartilage repair effect both *in vivo* and *in vitro* as the anisotropic structure can provide desirable mechanical characteristics and signaling pathway required for chondrogenic differentiation.[132,133] To closely resemble the anisotropic heterogeneous multilayered structure of natural cartilage, a novel strategy combining microfluidic and 3D printing technique to construct engineered zonal cartilage was developed.[134,135] The technology relies on a microfluidic printing head connected to a coaxial needle extruder to print muscle precursor cells onto hydrogel fibers in a high-resolution 3D bioprinting process. The advanced approach enables the deposition of chemical, physical, and biological cues, making it possible to fabricate scaffolds with exceptionally high shape fidelity and cell viability. Zone-specific matrix was observed after human articular chondrocytes and human bone marrow-derived mesenchymal stem cells were cultured for 3 weeks *in vitro*.[134]

6.3. Bone tissues

Bone is one of the rigid body tissues and composed of two main components, i.e., collagen and calcium phosphate. Bone tissue constructs that are hierarchically porous are helpful for vascularization and cell proliferation.[136] To treat bone defects, tough but light, biocompatible substitutes endowed with the capability of preventing any allergic reactions are required. Traditional fabrication methods, such as freeze-casting, foam replica, high-pressure pressing, and injection molding, cannot control the porous structure, but the recently developed 3D printing techniques could overcome the limitations to fabricate customized scaffolds.

As one of the main bone components, calcium phosphate supports osteoblast adhesion, proliferation, and osteoinduction. Additionally, it regenerates bone marrow stromal cells to induce bone formation.[137] Besides calcium phosphate, other nanomaterials, such as silicate nanoplatelets and hydroxyapatite, are commonly used in bone tissue engineering. Nyberg et al. fabricated PCL scaffolds functionalized with tricalcium phosphate, hydroxyapatite, or decellularized bone matrix and co-cultured with adipose-derived stromal/stem cells.[138] The addition of minerals increased the viscosity of the PCL melts. By tuning the 3D printing parameters, the porosity and the strut thickness of the engineered constructs were optimized to provide sufficient strength and induce the osteoinductive effect as well.

Byambaa et al. fabricated pyramidal microstructured bone-like tissue constructs that mimic the architecture of natural bone tissue.[139] Rapidly degradable GelMA hydrogel encapsulated with HUVECs and human mesenchymal stem cells (hMSCs) was printed in the center of the construct, which was surrounded by gelatin methacryloyl (GelMA)/silicate nanoplatelets hydrogel (Figure 5a). The vessel was formed via the degradation of GelMA overtime (Figure 5b). The encapsulated hMSCs and HUVECs could migrate and proliferate in the constructs, and the hMSCs promoted vasculogenesis. In addition, hMSCs in silicate nanoplatelets hydrogels differentiated into osteoblasts. Chiesa et al. also developed vascularized bone model with controlled pore geometry, size, and interconnectivity by printing gelatin-nanohydroxyapatite hydrogel in a supporting bath composed of Pluronic F127 (Figure 5c–f).[140] A wood-pile scaffold was first printed and kept in the supporting bath. Gelatin was crosslinked with genipin, followed by removing sacrificial materials. Cylinders with a diameter of 4 mm were cut from the scaffolds for further investigation, including pore connectivity, compressive modulus, osteogenic differentiation, and vascularization. The engineered bone model exhibited robust vascularization and HUVECs-supported osteogenesis, indicating that vascularized bone model could be readily fabricated via 3D bioprinting.

6.4. Cardiac tissues

Similar to chondrocytes, cardiomyocytes have limited regenerative capacity. This signals a crucial need to regenerate cardiac tissues. The cardiomyocytes are aligned in cardiac tissues to execute spontaneous, synchronous, and rhythmic contractions. The hierarchical property of native myocardium and complicated blood vessels are the main challenges in fabricating cardiac tissues.[141]

Lee et al. had attempted to fabricate a model of left ventricle of human heart via embedded printing.[27] Collagen was crosslinked by changing the pH of supporting bath, and the geometry could be maintained for over 28 days. Cell viability achieved 96%, and the ventricular contraction was noticed after 4 days of culturing. Moreover, wall thickening, an evidence of ventricular contraction, was observed during peak systole. They also printed a functional robust tri-leaflet heart valve that was mounted to a pulsatile pump. Cyclical opening and closing of the valve leaflets were observed under the pulsatile flow. Further, a monolayer of HUVECs was formed on the leaflets. However, the limitation of this study is that the cell density was too low to mimic the real tissue as it requires

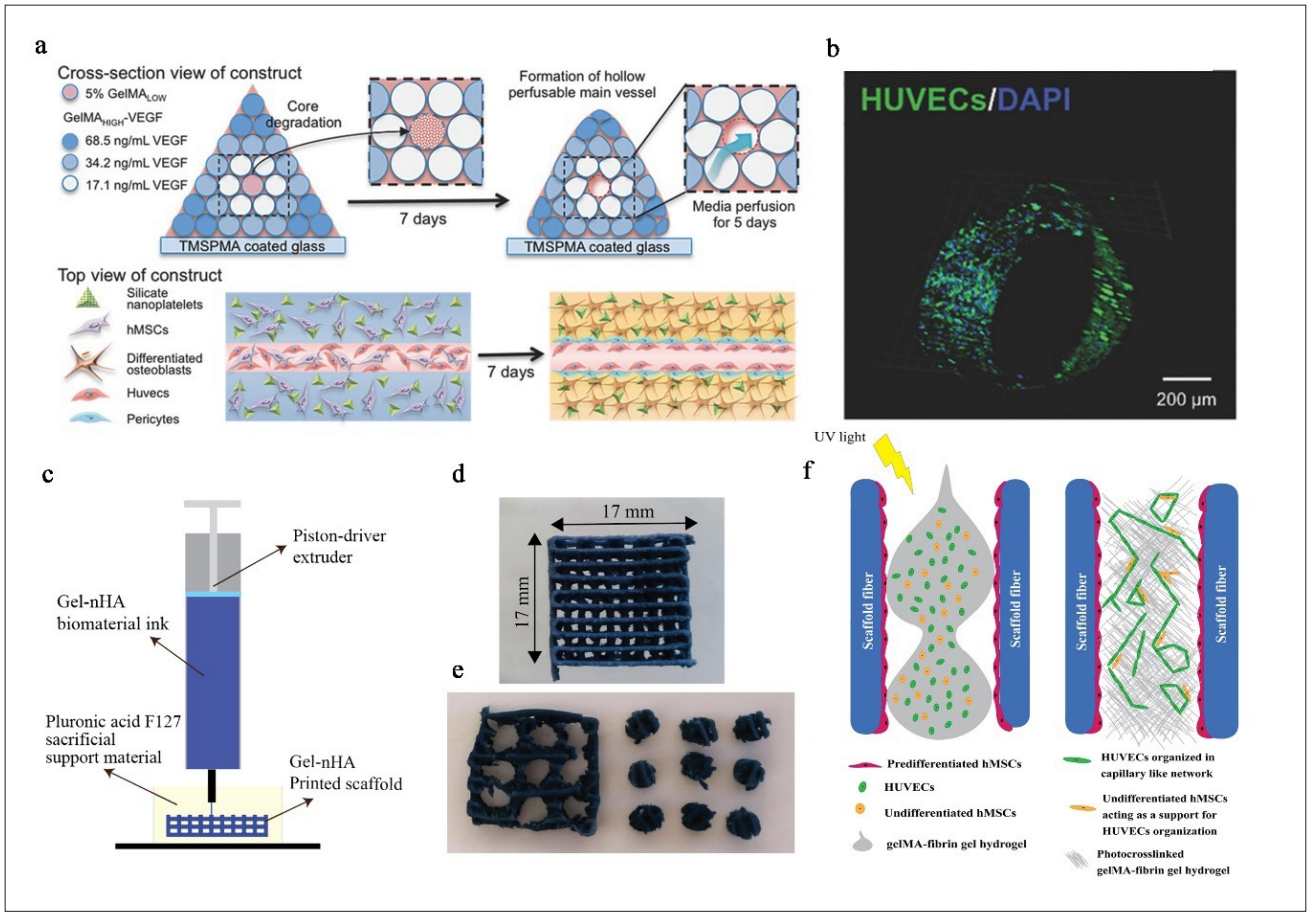

Figure 5. (a) Schematic illustration of the fabricated bone tissue constructs. The engineered structures were cultured in static condition for 7 days, and the core GelMA degraded within this period. Osteoinductive medium was perfused through the perfusable lumen for 5 days followed by static culture for 9 days. (b) The confocal image of the HUVEC-lined lumen structure. Reproduced with the permission from ref.[139] Copyright © 2017 John Wiley & Sons, Inc. (c) Schematic illustration of the 3D bioprinting technique for printing bone model into supporting bath. (d) The printed genipin-gelled wood-pile structured scaffolds. (e) 4 mm cylinder cores (bottom middle). (f) The fabrication process of vascularized bone construct. Reproduced with the permission from ref.[140] Copyright © 2023 IOP Publishing.

billions of cells to create a cardiac tissue at human scale. Skylar-Scott et al. fabricated vascularized cardiac tissues by embedded printing sacrificial gelatin into dense cardiac organoids building blocks containing induced pluripotent stem cells (iPSC)-derived cardiac myocytes and primary cardiac fibroblasts.[45] The building blocks exhibited self-healing and viscoplastic behavior, allowing the recovery of the organoids and the support of sacrificial ink which was removed afterward. Pervasive sarcomeric architecture was generated, and contractility increased over 20 times during the culturing period for 8 days. Despite the synchronous beating of cardiac tissue for over a week, sufficient cell maturation and microvascular formation could still unachievable. Therefore, fabricating anisotropic cardiac tissues is the next step to enhance tissue function.

The human-mimetic cardiac tissues with vasculature regenerated by researchers in human scale lack conductivity, a vital property that encourages cell–cell communication and signal delivery in cardiac tissue. Electrical stimulation improved tissue regeneration when applied on rats with sciatic nerve crush injuries, and it also improved the contractile behavior of engineered cardiac tissue that had high levels of cardiac troponin-I and connexin-43.[142] Conductive polymers, like polypyrrole and polyaniline, are utilized to guide cellular activities. These materials have been demonstrated to enhance proliferation and aid in the differentiation of neural and cardiac stem cells.[142,143] Conductive nanomaterials with high conductivity and mechanical strength, like gold nanowires, graphene, reduced graphene oxide(rGO), and CNTs, are excellent candidates for cardiac tissue engineering.[144-146] For example, Shin et al. engineered myocardial microenvironment containing CNTs, GO, or rGO and compared their corresponding structural

organization and cellular functionality. CNT-containing constructs exhibited desired electrical conductivity, native heart tissue-like mechanical property, and enhanced gene expression, suggesting that CNTs are preferred in regenerating cardiac tissues.[147] Zhu et al. incorporated gold nanorod into GelMA/alginate bioink to print layered constructs to address the problems of poor conductivity of the existing artificial cardiac tissue and inefficient cardiac cell communication via electrical coupling.[148] Cardiac fibroblasts (CFs) were co-cultured with cardiomyocytes as CFs are important in essential physiological activities, but CFs tend to over-proliferate, breaking the initial cardiomyocytes-to-CFs ratio. The conductive gold nanorod could help balance the growth and proliferation between cardiomyocytes and CFs. In addition, gold nanorods promoted synchronized contraction of the cardiac tissue. This study implies that the gold nanorods nanocomposite bioink shows great potential in fabricating conductive cardiac tissue, which could be used for drug screening and implantation. Further, not only cardiac tissues but also other electrogenic tissues, such as brain tissue, could be regenerated via this technique. Notably, the length of the nanowire should be larger than the average wall thickness of the hydrogel pore in order for cells on either side to interact with each other and increase their electrical signal transmission.[144]

6.5. Vessel tissues

Bioprinting has not yet produced functional large-scale tissues with physiological heterogeneity that perfectly simulate the morphological, biochemical, and physiological characteristics. This is primarily caused by the complexity of human tissue and organs, particularly the vasculature which includes millimeter-scale arteries and micrometer-scale capillaries.[149] The artificial vessel permits the exchange of vital nutrients and metabolic waste products but prevents the exchange of immunogenic molecules.[150] When creating large tissues, a vascular network is necessary to support cell survival because the distance at which oxygen and nutrient can diffuse is only 100–200 μm.[151] Blood compatibility is also important. The vessels can be modified through the creation of bioactive antithrombotic surface, surface passivation, and surface endothelialization to eliminate thrombosis in the vessels.[150] Additionally, since endothelial layers are inherently anti-thrombogenic and hemocompatible, a layer of endothelial cells would inhibit thrombus formation.[152] Strategies, such as incorporation of angiogenic growth factor and co-culturing with pericytes and smooth muscle cells (SMCs), have been devised to promote the vascularization of the scaffold.[153] Additionally, sacrificial materials, such as Pluronic F127 and gelatin, were blended with polymers, followed by washing, leaving microporous network inside the scaffold.[154,155] These approaches show success in forming microvascular networks. However, the fabrication of perfusable vascularized tissue still remains challenging.

To this end, two bioprinting techniques—indirect and direct bioprinting—have been developed to fabricate perfused vasculature.[156] Sacrificial materials are deposited into a cell-laden crosslinkable supporting bioink in indirect bioprinting. The sacrificial materials are removed after printing through temperature-induced phase transition under mild condition, forming a perfused open lumen, which is infused with endothelial cells to realize the endothelialization of the microchannels.[45-47] For example, Kolesky et al.[46] were successful in creating microvascular networks using Pluronic F127 which liquefies at 4°C to produce mirochannels within a covalently crosslinked hydrogel matrix. By employing this strategy, multilayered vascularized tissue structures with multiple cells types and ECM were constructed. Human neonatal dermal fibroblasts and 10T1/2 cells were encapsulated in GelMA while HUVECs were suspended in fugitive Pluronic F127. It was noticed that on day 7, cells in the bioink have comparable cell viability to cells cultured in medium, indicating that the bioinks and bioprinting are not harmful to cells.[46] The strategy was adopted by Noor et al. to fabricate thick, perusable vascularized cardiac patches (Figure 6a). iPSC-derived cardoimyocytes were blended with decellularized ECM (dECM), and iPSC-derived endothelial cell was mixed with gelatin, serving as a sacrificial bioink. A customized vascularized patch has been successfully created with high cell viability. After 7 days, a continuous layer of endothelial cells was formed on the inner side of the lumen (~300 μm in diameter), as shown in Figure 6b. Moreover, *in vivo* test revealed that the printed lumen remained in rat, and the encapsulated cells were elongated and aligned, showing that 3D bioprinting may be used for engineering vascularized tissues that mimic biological matrix.[88]

Apart from the vasculature embedded within a hydrogel matrix, stand-alone vascular structure can be fabricated through direct bioprinting strategy, including coaxial and embedded bioprinting. A vessel phantom was created by coaxially printing cell-laden bioinks in the shell and sacrificial ink in the core, followed by forming a confluent monolayer of cells.[157]

Alginate is the most commonly used material in fabricating hollow fibers as it could be readily *in situ* crosslinked with $CaCl_2$ solution which is injected through the core nozzle. For example, Dolati et al.[158] used alginate and MWCNTs hybrid bioink as the shell material and $CaCl_2$ as the core materials to construct vascular conduits. The addition of CNTs had a significant effect on the

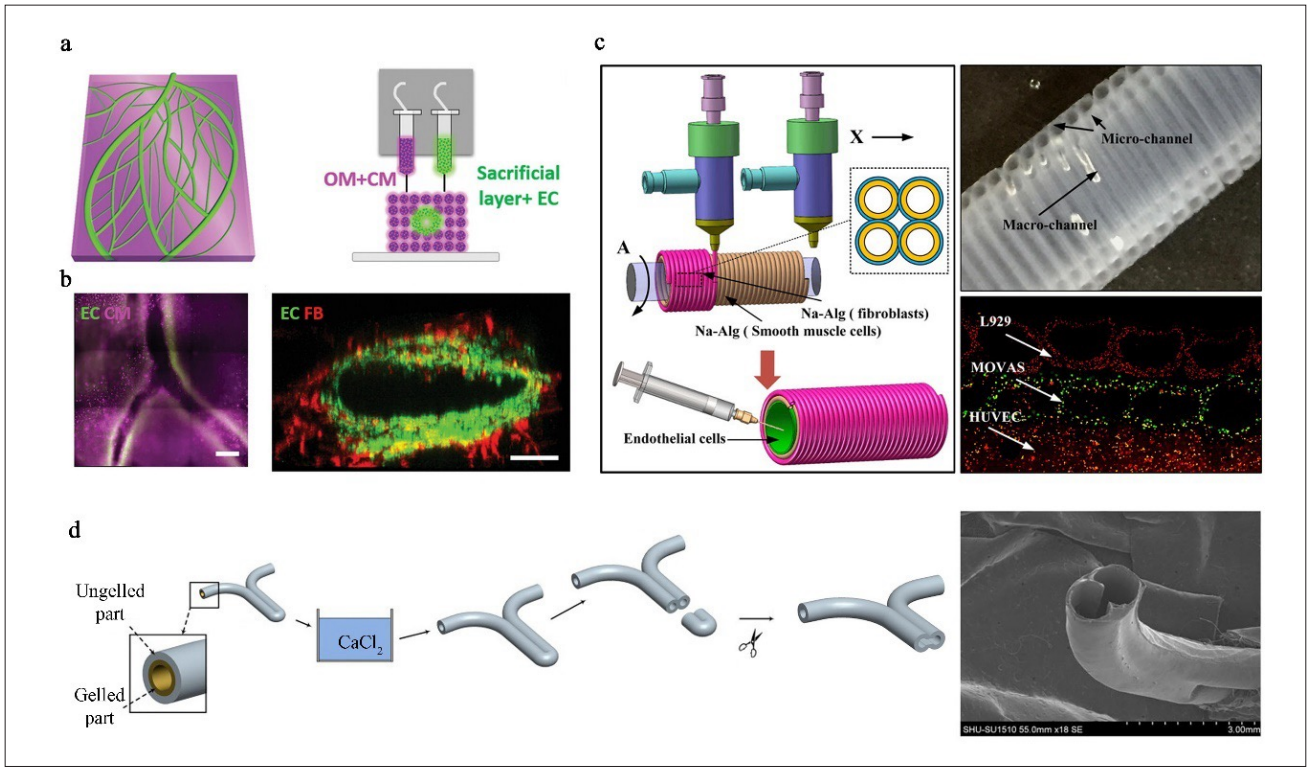

Figure 6. Bioprinting perfused vasculature. (a) Schematic illustration of cardiac patch model and the printing process concept. (b) A continuous layer of endothelial cells (ECs) inside the printed blood vessels and the cross-sectional view of lumen. Reproduced with the permission from ref.[88] Copyright © 2019 John Wiley & Sons, Inc. (c) Schematics of a rotated rod template used in coaxial printing of bioinks (left). A picture of a double-layer vessel-like structure (top right). Fluorescent image of three cell lines-encapsulated vessels (bottom right). Reproduced with the permission from ref.[156] Copyright © 2017 American Chemical Society. (d) The fabrication process of branched micro-channels generated via coaxial printing (left). Scanning electron microscopy (SEM) image of double-channel part of Y-shaped microchannels after trimming (right). Reproduced with the permission from ref.[161] Copyright © 2016 AIP.

physical properties of the vessels, including stiffness, elastic modulus, vascular shrinkage rate, and liquid adsorption capacity. Further, the cell viability was not influenced by MWCNTs in the short term, but the cell viability, cellular motility, and the generation of ECM were reduced in the long term due to CNT-induced toxicity.[158,159] Other researchers have found that the cell viability in the hollow structure was higher than that in constructs without microchannels, indicating the importance of vessels and nutrients delivery in large-scale organ models.[41] Additionally, co-culturing HUVECs and MSCs in the bioprinted constructs promoted cell function of HUVECs, including proliferation, protein expression, and angiogenesis.[43] Gelatin is another kind of sacrificial material which can be injected through the inner nozzle as it can be easily liquefied and removed by increasing temperature. Shao et al. prepared GelMA bioinks encapsulated with tissue cells that were extruded through the outer nozzle onto a cooling platform allowing the thermo-crosslinking of gelatin.[160] The printed stacked vessels constructs were then permanently UV-crosslinked. Different from the previous published methods that endothelial cells were seeded by perfusion post-printing, HUVECs were mixed with gelatin in this study and printed in the core of extruded filaments. Endothelial cells deposit and adhere to inner wall of the microchannels during static culture period. Gelatin was then dissolved to obtain vascular channels. Endothelial cells proliferated over the culturing time and spread and formed a layer on the inner side of the vascular channels. Moreover, angiogenic sprouts were observed in the bioprinted constructs, further suggesting its *in vivo* application.

The coaxial bioprinting approach can also be used in conjunction with a rotated rod to create hierarchical architectures as shown in Figure 6c.[156] However, one main challenge of this strategy is to fabricate interconnected branched vessels.[157] Li et al. developed a novel method to engineer branched micro-channel via partial crosslinking and trimming (Figure 6d).[161] The patency of branched vessels was confirmed by injecting cell media, and the fibroblasts were found to maintain high viability and proliferate after being cultured for 6 days. Moreover, vessels

created using this method can be used as a disease model to study how vessel morphology affects blood flow and clogging. Carotid bifurcation construct in centimeter scale with good interconnectivity was successfully printed by Wu et al.[162] They also fabricated multisegment hollow tube models with different moduli via a customized dual-syringe system. The engineered vessels could withstand pulsatile flow over 863,000 cycles, implying its excellent mechanical integrity and feasibility for diagnostic applications.

Besides the aforementioned tissues, other organs and tissues, such as liver,[163-165] muscle,[166-168] and neuronal tissues,[169-171] have been investigated. With the advancement of the bioprinting strategies, multiscale tissue constructs with vasculature or neuron, large-scale biomimetic tissue constructs, or anisotropic tissue models have been successfully created. Nevertheless, instead of creating entire organs that accurately recreate the anatomy and physiology of the organ, which is the next step of 3D bioprinting development, the focus of current research lies primarily on tissue organization and concept demonstration. Although most research mentioned in this review investigated the biocompatibility and bioactivity of the bioinks, the degradation profiles and their *in vivo* response also need to be characterized for future clinical trials. In summary, it is anticipated that 3D bioprinting will facilitate the development of the field of regenerative medicine.

7. Applications of 3D-printed polymer composites for environmental treatment

In the past decades, 3D bioprinting has been widely applied in tissue engineering and regenerative medicine. Meanwhile, the microorganisms-encapsulated bioinks are developed to broaden its applications in energy and environmental science, covering photosynthesis, biofuel production, and bioremediation, such as wastewater treatment and air purification, but the relevant studies remain scarce.[172-174] For example, techniques such as ion exchange, adsorption, and flocculation-precipitation have been widely used to treat water polluted by heavy metals, dye, and antibiotics.[175-177] However, the main issue of wastewater treatment strategies is the secondary pollution; therefore, biological wastewater treatment that involves microorganisms to reduce the negative impact on environment is an alternative.

Several groups use algae, plant cells, yeast, and bacteria to bioprint live materials for use in the field environmental science. For instance, Balasubramanian et al. printed mono- or multilayered microalgal cell-encapsulated alginate on bacterial cellulose/$CaCl_2$ substrate.[172] The microalgae *Chlamydomonas reinhardtii* can grow photoautotrophically and chemotropically on agar or bacterial cellulose substrate, which provides carbon, and they can survive in the alginate matrix for at least 3 days without nutrients. The regenerative and reusable microalgal cells could also make new bioinks. The bioprinted constructs stuck stably to the cellulose substrate and did not release microalgae after being immersed in water, suggesting its use in environmental remediation. Qian et al. constructed microporous structures using bacteria that transform carbon into useful compounds in their ink.[178] The freeze-dried *Saccharomyces cerevisiae* yeast cells in the bioink make the PEGDA and nanocellulose hybrid mix thicker and thinner. The cells inside the non-sterile capsules worked for 4 months, suggesting that they could be used as a biocatalyst for bioremediation (Figure 7a–c). Seidel et al. demonstrated that plant cells were compatible with bioprinting process and exhibited high viability and metabolic activity, showing potential application in environmental science.[179] The fabricated microporous 3D grid constructs with immobilized plant cells remained stable under culture conditions, allowing long-term control of mass transfer and diffusion paths of substrates.

3D-bioprinted living bioremediation materials can be utilized for different purposes. Schaffner et al. created functional structures using *Pseudomonas putida* in a hydrogel made of hyaluronic acid, κ-carrageenan, and fumed silica.[180] The hydrogel's bacterial metabolism and growth were studied, and the inks were found to support bacterial growth. Various forms were 3D-bioprinted, and bacteria were properly placed to immobilize and localize. The released and immobilized bacteria of the printed structures turned toxic phenol into biomass. Additionally, printed constructs can be easily isolated from the environment and recycled multiple times, minimizing secondary contamination. Similarly, Liu et al. immobilized laccase to fabricate constructs for the degradation of phenolic compounds.[181] The engineered laccase-laden constructs exhibited good stability and reusability.

Deng et al. fabricated "living filter" for bioremediation via 3D bioprinting.[182] The hierarchical frameworks were assembled with conductive bacterial "cable" produced by a coaxial microfluidic device (Figure 7d). The bioink was composed of living catalyst, *Shewanella loihica* PV-4, alginate, and GO. The *S. loihica* metabolized GO to rGO, contributing to the electrical connection of adjacent cells and expansion of the extracellular electron transfer surface area (Figure 7e). The biocatalytic ability of *S. loihica* guaranteed the reduction of heavy metal ions to solid nanoparticles. Moreover, Cr (VI) treatment efficiency in the hierarchical frameworks was much higher than that in the bulk counterpart due to the enhanced mass/charge transport (Figure 7f). This implies that biological

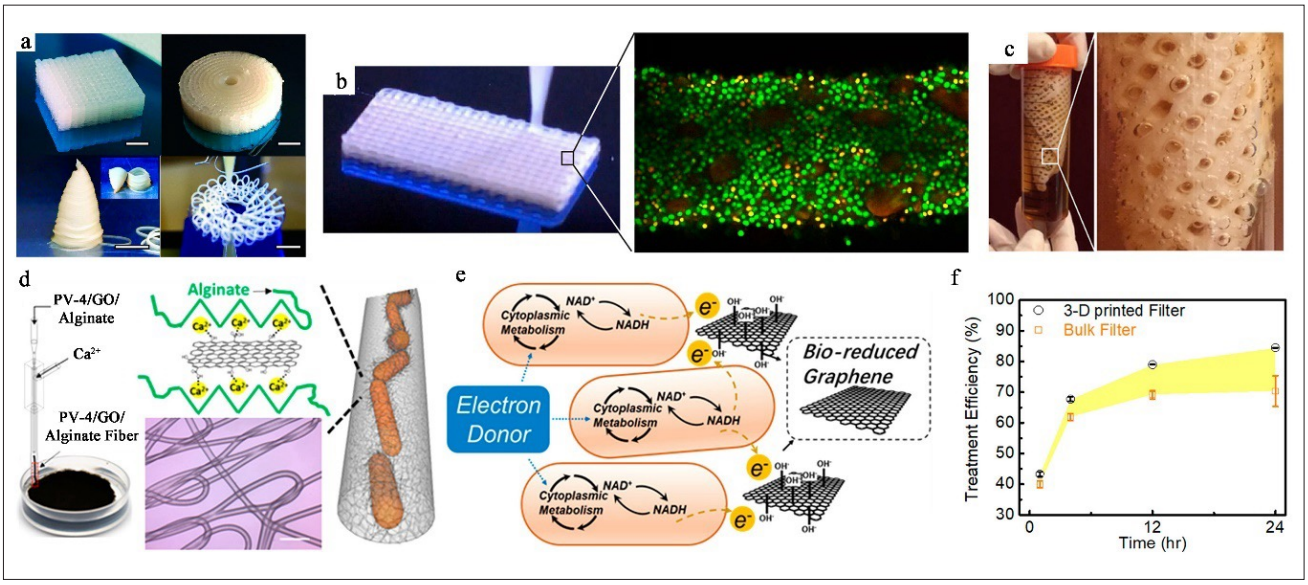

Figure 7. (a) Images of the 3D-printed complex constructs. Scale bars = 5 mm. (b) Image of the printing process and live-dead staining image of the printed thin filament (green: live; red: dead). (c) Photographs of the printed grid in medium releasing CO_2. Reproduced with the permission from ref.[178] Copyright © 2019 American Chemical Society. (d) Schematic illustration of the engineered conductive bacterial "cable." (e) Schematic illustration of the bioreduction of GO to rGO by the metabolism of *S. loihica*. (f) The comparison of Cr (VI) treatment efficiency between bioprinted hierarchical frameworks and bulk counterpart. Reproduced with the permission from ref.[182] Copyright © 2020 American Chemical Society.

species combined with 3D bioprinting strategy show great potential in environmental applications.

8. 3D bioprinting and its techno-commercial alignment

Tissue engineering and regenerative medicine have benefited greatly from the advancements in 3D bioprinting, which have made it possible to construct and imitate biological microenvironments ranging from molecular to macroscopic scale. Multiple methods for the biofabrication of tissue constructs are now available, owing to recent developments in 3D bioprinting technology. Innovative technologies that build 3D cell microenvironments can be used to fabricate artificial tissues and improve our knowledge of cellular interactions and tissue creation. It is indeed a challenge to design a completely closed bioprinting system that incorporates printing and post-printing operations such as *in vitro* culture and the development of new tissue. Such a platform would be needed for the technology to reach its full potential. Despite these setbacks, the bioprinting industry has seen the emergence of new players and the forging of new alliances. A brief information of some bioprinting companies which are playing pivotal role in medical industries is shown in Figure 8.

There are two primary obstacles that need to be taken into consideration before further exploring the prospects offered by bioprinting. To begin generating functioning organoids or tissue models/substitutes, it is necessary to first address hurdles such as the advancement of cell culture systems, the creation of cell/tissue-specific bioinks, and the development of bioprinting technology. Moreover, it is crucial to establish a uniform and detailed set of rules for bioprinting projects. Industrial bioink manufacturing, bioprinting workflow, and post-printing culture techniques should all be standardized by bioprinting firms as a result of this rule. Furthermore, this policy should consider the unique characteristics of each patient to ensure that the final bioprinted items are effective for people of varied backgrounds, ages, and genders. The field of bioprinting has recently seen some significant advances in terms of governing policies. On May 10, 2016, the Food and Drug Administration announced regulations for 3D-printed pharmaceutical products, marking a significant step forward in their therapeutic uses.

9. Summary and future perspectives

3D printing has revolutionized manufacturing technology in the past years, paving the way to new possibilities and reshaping the field in a comprehensive manner. Compared to conventional production processes, additive manufacturing has some shortcomings and problems. Choice of materials, production time, low mechanical

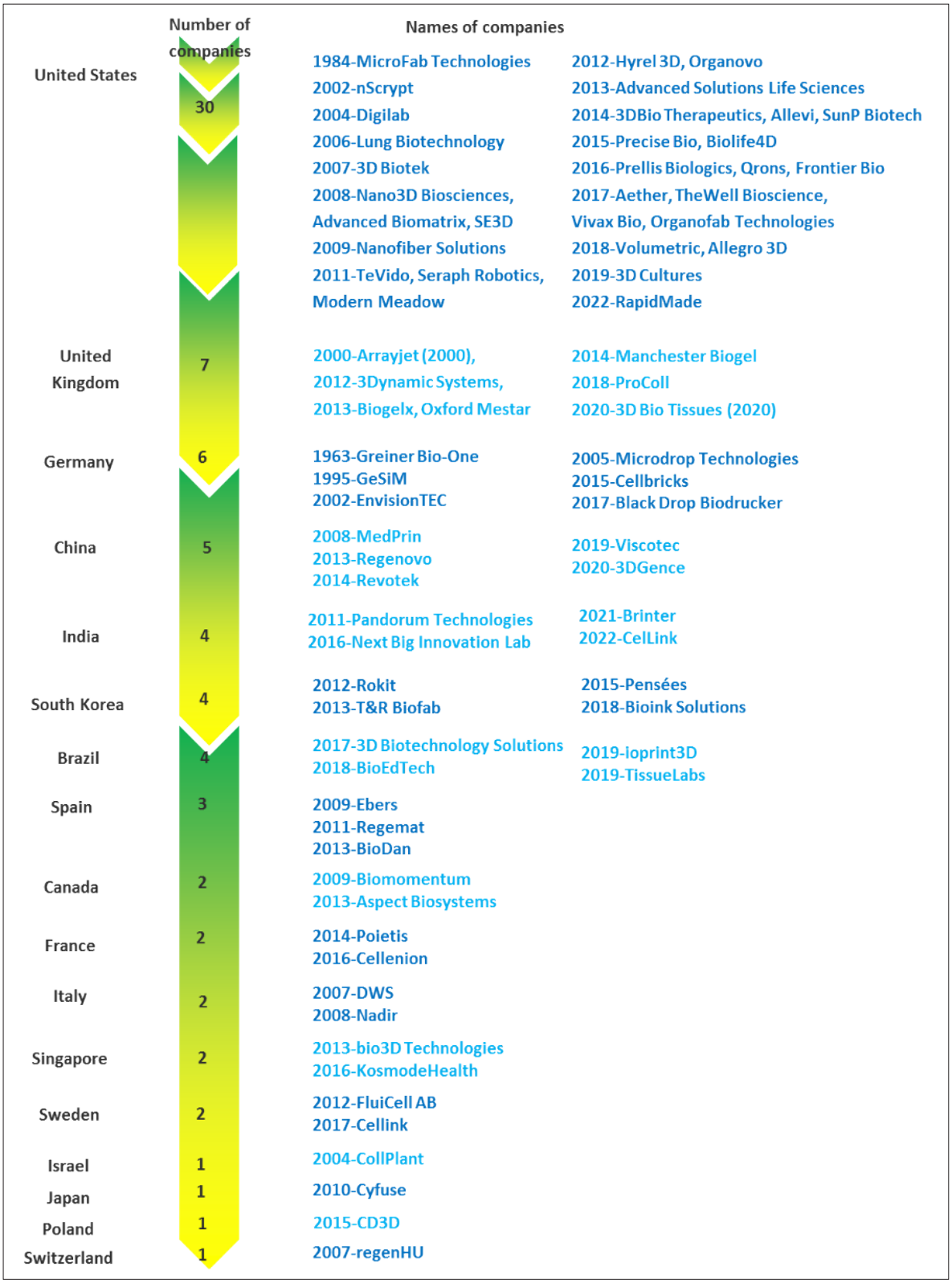

Figure 8. Some notable bioprinting companies in different countries.

characteristics, defect generation, limitation of geometrical consistency after extrusion, layered visual appeal, and overall cost-effectiveness are some of the challenges in 3D printing. However, researchers are now able to create goods with precise mechanical qualities because of recent advancements in AM. Materials made from matrix composites have recently attracted increasing interest due to their outstanding mechanical and thermoelectric characteristics. The majority of the difficulties encountered by AM approaches stem from the processes themselves. For example, the FDM technique is by far the most widely used method. The simultaneous heating and cooling that occurs during the FDM extrusion and multilayer deposition processes is the foremost contributing factor to void generation. This results in the formation of anisotropic structures and a reduction in the material's mechanical property. Because of the fluctuating temperature gradient that occurs during curing, the vertical and horizontal directed characteristics may take on different values. It is possible that the printed part will exhibit anisotropic behavior. During production process, other methods also confront the same problems in processing speed and anisotropic characteristics.

The utilization of AM technology has grown, despite the various hurdles and limitations it has faced. Scientists are striving to improve 3D printing technologies by addressing the limitations in traditional production processes. Researchers now have greater flexibility to examine and manage product features and performance linked to their functional use thanks to the development of polymer composites, which opens up a new arena for advanced materials. Likewise, industrial and commercial players should embrace the scientifically created 3D printing-based polymer matrix composites with open arms, as this innovation will not grow without the collaborative efforts of academics and industry in research and development. In order to solve the obstacles and to increase industrial competitiveness, a wide range of multidisciplinary research must be conducted to expedite the revolution of 3D printing-based production and inspection methods. Moreover, the combination of many types of 3D printing methods has the potential to solve current printing problems, which are related to the substances and variables. Besides, effective multimaterial constructs can be developed by adhering to a combination of a variety of printing concepts.

Acknowledgments

None.

Funding

Not applicable.

Conflict of interest

The authors declare no conflicts of interest.

Author contributions

Conceptualization: Yun Wu, Sayan Ganguly, Xiaowu Shirley Tang

Writing – original draft: Yun Wu, Sayan Ganguly

Writing – review & editing: Yun Wu, Sayan Ganguly, Xiaowu Shirley Tang

Ethics approval and consent to participate

Not applicable.

Consent for publication

Not applicable.

Availability of data

Not applicable.

References

1. Leberfinger AN, Dinda S, Wu Y, et al. Bioprinting functional tissues. *Acta Biomater.* 2019;95, 32-49.

2. Dutton S, Kelly D, Baker A. *Composite Materials for Aircraft Structures*. Reston: AIAA; 2004.
doi: 10.2514/4.861680

3. Clyne TW, Hull D. *An Introduction to Composite Materials*. Cambridge: Cambridge University Press; 2019.
doi: 10.1017/9781139050586

4. Chang JH, An YU. Nanocomposites of polyurethane with various organoclays: thermomechanical properties, morphology, and gas permeability. *J Polym Sci B Polym Phys*. 2002;40(7):670-677.
doi: 10.1002/polb.10124

5. Ramanathan T, Abdala A, Stankovich S, et al. Functionalized graphene sheets for polymer nanocomposites. *Nat Nanotechnol*. 2008;3(6):327-331.
doi: 10.1038/nnano.2008.96

6. Potts JR, Dreyer DR, Bielawski CW, Ruoff RS. Graphene-based polymer nanocomposites. *Polymer*. 2011; 52(1):5-25.
doi: 10.1016/j.polymer.2010.11.042

7. Lavrador P, Esteves MR, Gaspar VM, Mano JF. Stimuli-responsive nanocomposite hydrogels for biomedical applications. *Adv Funct Mater*. 2021;31(8):2005941.
doi: 10.1002/adfm.202005941

8. Guvendiren M, Molde J, Soares RM, Kohn J. Designing biomaterials for 3D printing. *ACS Biomater Sci Eng*. 2016;2(10):1679-1693.
doi: 10.1021/acsbiomaterials.6b00121

9. Gungor-Ozkerim PS, Inci I, Zhang YS, Khademhosseini A, Dokmeci MR. Bioinks for 3D bioprinting: an overview. *Biomater Sci*. 2018;6(5):915-946. doi: 10.1039/C7BM00765E

10. Armstrong JP, Burke M, Carter BM, Davis SA, Perriman AW. 3D bioprinting using a templated porous bioink. *Adv Healthc Mater*. 2016;5(14):1724-1730. doi: 10.1002/adhm.201600022

11. Holmström J, Partanen J, Tuomi J, Walter M. Rapid manufacturing in the spare parts supply chain: alternative approaches to capacity deployment. *J Manuf Technol Manag*. 2010;21(6):687-697. doi: 10.1108/17410381011063996

12. Kalsoom U, Nesterenko PN, Paull B. Recent developments in 3D printable composite materials. *RSC Adv*. 2016;6(65):60355-60371. doi: 10.1039/C6RA11334F

13. Mythri G, Kavitha K, Kumar MR, Jagadeesh Singh SD. Novel mucoadhesive polymers – a review. *J Appl Pharm Sci*. 2011;1(8):37-42.

14. Gao G, Kim BS, Jang J, Cho D-W. Recent strategies in extrusion-based three-dimensional cell printing toward organ biofabrication. *ACS Biomater Sci Eng*. 2019;5(3):1150-1169. doi: 10.1021/acsbiomaterials.8b00691

15. Kang H-W, Lee SJ, Ko IK, Kengla C, Yoo JJ, Atala A. A 3D bioprinting system to produce human-scale tissue constructs with structural integrity. *Nat Biotechnol*. 2016;34(3):312-319. doi: 10.1038/nbt.3413

16. Mazzocchi A, Devarasetty M, Huntwork R, Soker S, Skardal A. Optimization of collagen type I-hyaluronan hybrid bioink for 3D bioprinted liver microenvironments. *Biofabrication*. 2018;11(1):015003. doi: 10.1088/1758-5090/aae543

17. Isaacson A, Swioklo S, Connon CJ. 3D bioprinting of a corneal stroma equivalent. *Exp Eye Res*. 2018;173:188-193. doi: 10.1016/j.exer.2018.05.010

18. Liu W, Heinrich MA, Zhou Y, et al. Extrusion bioprinting of shear-thinning gelatin methacryloyl bioinks. *Adv Healthc Mater*. 2017;6(12):1601451. doi: 10.1002/adhm.201601451

19. Scott EA, Stano A, Gillard M, Maio-Liu AC, Swartz MA, Hubbell JA. Dendritic cell activation and T cell priming with adjuvant-and antigen-loaded oxidation-sensitive polymersomes. *Biomaterials*. 2012;33(26):6211-6219. doi: 10.1016/j.biomaterials.2012.04.060

20. Mueller J, Skylar-Scott M, Visser C, Lewis JA. Voxelated soft matter via multimaterial multinozzle 3D printing. *Nature*. 2019;575(7782):330-335. doi: 10.1038/s41586-019-1736-8

21. Krishtul S, Baruch L, Machluf M. Processed tissue-derived extracellular matrices: tailored platforms empowering diverse therapeutic applications. *Adv Funct Mater*. 2020;30(18):1900386. doi: 10.1002/adfm.201900386

22. Guo H, Zhao H, Niu H, et al. Highly thermally conductive 3D printed graphene filled polymer composites for scalable thermal management applications. *ACS Nano*. 2021;15(4):6917-6928. doi: 10.1021/acsnano.0c10768

23. Matai I, Kaur G, Seyedsalehi A, McClinton A, Laurencin CT. Progress in 3D bioprinting technology for tissue/organ regenerative engineering. *Biomaterials*. 2020;226:119536. doi: 10.1016/j.biomaterials.2019.119536

24. Vikram SA, Hasan DAM, Wang S, et al. The adoption of three-dimensional additive manufacturing from biomedical material design to 3D organ printing. *Appl Sci*. 2019;9(4):811. doi: 10.3390/app9040811

25 Fedorovich NE, Alblas J, de Wijn JR, Hennink WE, Verbout AJ, Dhert WJA. Hydrogels as extracellular matrices for skeletal tissue engineering: state-of-the-art and novel application in organ printing. *Tissue Eng*. 2007;13(8):1905-1925. doi: 10.1089/ten.2006.0175

26. Miri AK, Mirzaee I, Hassan S, et al. Effective bioprinting resolution in tissue model fabrication. *Lab Chip*. 2019;19(11):2019-2037. doi: 10.1039/c8lc01037d

27. Lee A, Hudson A, Shiwarski D, et al. 3D bioprinting of collagen to rebuild components of the human heart. *Science*. 2019;365(6452):482-487. doi: 10.1126/science.aav9051

28. Mehrotra S, Moses JC, Bandyopadhyay A, Mandal BB. 3D printing/bioprinting based tailoring of in vitro tissue models: recent advances and challenges. *ACS Appl Bio Mater*. 2019;2(4):1385-1405. doi: 10.1021/acsabm.9b00073

29. Jin Y, Liu C, Chai W, Compaan A, Huang Y. Self-supporting nanoclay as internal scaffold material for direct printing of soft hydrogel composite structures in air. *ACS Appl Mater Interfaces*. 2017;9(20):17456-17465. doi: 10.1021/acsami.7b03613

30. García-Villén F, Ruiz-Alonso S, Lafuente-Merchan M, et al. Clay minerals as bioink ingredients for 3D printing and 3D bioprinting: application in tissue engineering and regenerative medicine. *Pharmaceutics*. 2021;13(11):1806. doi: 10.3390/pharmaceutics13111806

31. Zhou Y, LaChance AM, Smith AT, Cheng H, Liu Q, Sun L. Strategic design of clay-based multifunctional materials: from natural minerals to nanostructured membranes. *Adv Funct Mater*. 2019;29(16):1807611. doi: 10.1002/adfm.201807611

32. Ahlfeld T, Cidonio G, Kilian D, et al. Development of a clay-based bioink for 3D cell printing for skeletal application. *Biofabrication*. 2017;9(3):034103. doi: 10.1088/1758-5090/aa7e96

33. Cidonio G, Glinka M, Kim YH, et al. Nanoclay-based 3D printed scaffolds promote vascular ingrowth ex vivo and generate bone mineral tissue in vitro and in vivo. *Biofabrication*. 2020;12(3):035010. doi: 10.1088/1758-5090/ab8753

34. Leu Alexa R, Ianchis R, Savu D, et al. 3D printing of alginate-natural clay hydrogel-based nanocomposites. *Gels*. 2021;7(4):211. doi: 10.3390/gels7040211

35. Habib A, Khoda B. Development of clay based novel hybrid bio-ink for 3D bio-printing process. *J Manuf Process*. 2019;38:76-87. doi: 10.1016/j.jmapro.2018.12.034

36. Cui ZK, Kim S, Baljon JJ, Wu BM, Aghaloo T, Lee M. Microporous methacrylated glycol chitosan-montmorillonite nanocomposite hydrogel for bone tissue engineering. *Nat Commun*. 2019;10(1):1-10. doi: 10.1038/s41467-019-11511-3

37. Ding F, Liu J, Zeng S, et al. Biomimetic nanocoatings with exceptional mechanical, barrier, and flame-retardant properties from large-scale one-step coassembly. *Sci Adv*. 2017;3(7):e1701212. doi: 10.1126/sciadv.1701212

38. Sun L, Parker ST, Syoji D, Wang X, Lewis JA, Kaplan DL. Directnarker ST, Syoji D, adv.1701212nal mechanical, barrier, and flame-retardan*Adv Healthc Mater*. 2012;1(6):729-735. doi: 10.1002/adhm.201200057

39. Michna S, Wu W, Lewis JA. Concentrated hydroxyapatite inks for direct-write assembly of 3-D periodic scaffolds. *Biomaterials*. 2005;26(28):5632-5639. doi: 10.1016/j.biomaterials.2005.02.040

40. Zhang T, Yan KC, Ouyang L, Sun W. Mechanical characterization of bioprinted in vitro soft tissue models. *Biofabrication*. 2013;5(4):045010. doi: 10.1088/1758-5082/5/4/045010

41. Gao G, He Y, Fu J-z, Liu A, Ma L. Coaxial nozzle-assisted 3D bioprinting with built-in microchannels for nutrients delivery. *Biomaterials*. 2015;61:203-215. doi: 10.1016/j.biomaterials.2015.05.031

42. Ozbolat IT, Peng W, Ozbolat V. Application areas of 3D bioprinting. *Drug Discov Today*. 2016;21(8):1257-1271. doi: 10.1016/j.drudis.2016.04.006

43. Jia W, Gungor-Ozkerim PS, Zhang YS, et al. Direct 3D bioprinting of perfusable vascular constructs using a blend bioink. *Biomaterials*. 2016;106:58-68. doi: 10.1016/j.biomaterials.2016.07.038

44. Florczyk SJ, Simon MH, Juba D, et al. A bioinformatics 3D cellular morphotyping strategy for assessing biomaterial scaffold niches. *ACS Biomater Sci Eng*. 2017;3(10):2302-2313. doi: 10.1021/acsbiomaterials.7b00473

45. Skylar-Scott MA, Uzel SG, Nam LL, et al. Biomanufacturing of organ-specific tissues with high cellular density and embedded vascular channels. *Sci Adv*. 2019;5(9): eaaw2459. doi: 10.1126/sciadv.aaw2459

46. Kolesky DB, Truby RL, Gladman AS, Busbee TA, Homan KA, Lewis JA. 3D bioprinting of vascularized, heterogeneous cellgh cellular density and em*Adv Mater*. 2014;26(19):3124-3130. doi: 10.1002/adma.201305506

47. Wu W, DeConinck A, Lewis JA. Omnidirectional printing of 3D microvascular networks. *Adv Mater*. 2011;23(24):H178-H183. doi: 10.1002/adma.201004625

48. Bhattacharjee T, Zehnder SM, Rowe KG, et al. Writing in the granular gel medium. *Sci Adv*. 2015;1(8):e1500655. doi: 10.1126/sciadv.1500655

49. Hinton TJ, Jallerat Q, Palchesko RN, et al. Three-dimensional printing of complex biological structures by freeform reversible embedding of suspended hydrogels. *Sci Adv*. 2015;1(9):e1500758. doi: 10.1126/sciadv.1500758

50. O'Bryan CS, Bhattacharjee T, Hart S, et al. Self-assembled micro-organogels for 3D printing silicone structures. *Sci Adv*. 2017;3(5):e1602800. doi: 10.1126/sciadv.1602800

51. Choi Y-J, Jun Y-J, Kim DY, et al. A 3D cell printed muscle construct with tissue-derived bioink for the treatment of volumetric muscle loss. *Biomaterials*. 2019;206:160-169. doi: 10.1016/j.biomaterials.2019.03.036

52. Jeon O, Lee YB, Jeong H, Lee SJ, Wells D, Alsberg E. Individual cell-only bioink and photocurable supporting medium for 3D printing and generation of engineered tissues with complex geometries. *Mater Horiz*. 2019;6(8):1625-1631. doi: 10.1039/c9mh00375d

53. Ouyang L. Pushing the rheological and mechanical boundaries of extrusion-based 3D bioprinting. *Trends Biotechnol*. 2022;40(7):P891-902. doi: 10.1016/j.tibtech.2022.01.001

54. Siacor FDC, Chen Q, Zhao JY, et al. On the additive manufacturing (3D printing) of viscoelastic materials and flow behavior: from composites to food manufacturing. *Addit Manuf*. 2021;45:102043. doi: 10.1016/j.addma.2021.102043

55. Golzar H, Wu Y, Ganguly S, Tang XS. Micro-extrusion 3D printing of articular cartilage substitutes with a multizonal structure using hydrophilic and rapidly curing silicone-based ink materials. *Addit Manuf*. 2023;73:103691. doi: 10.1016/j.addma.2023.103691

56. Dealy J, Tee T, Petersen J. A concentric-cylinder rheometer for polymer melts. In: Vallet G, Meskat W, eds. *Rheological Theories Measuring Techniques in Rheology Test Methods in Rheology Fractures Rheological Properties of Materials Rheo-Optics Biorheology*. Heidelberg: Steinkopff; 1975:466-474. doi: 10.1007/978-3-662-41458-3_69

57. Tang S, Richardson BM, Anseth KS. Dynamic covalent hydrogels as biomaterials to mimic the viscoelasticity of soft tissues. *Prog Mater Sci*. 2021;120:100738. doi: 10.1016/j.pmatsci.2020.100738

58. Shitikova MV, Krusser AI. Models of viscoelastic materials: a review on historical development and formulation. In: Giorgio I, Placidi L, Barchiesi E, Abali BE, Altenbach H, eds. *Theoretical Analyses, Computations, and Experiments of Multiscale Materials: A Tribute to Francesco dell'Isola*. Cham: Springer Nature; 2022: 285-326. doi: 10.1007/978-3-031-04548-6

59. Pirani SI, Krishnamachari P, Hashaikeh R. Optimum loading level of nanoclay in PLA nanocomposites: impact on the mechanical properties and glass transition temperature. *J Thermoplast Compos Mater*. 2014;27(11):1461-1478. doi: 10.1177/0892705712473627

60. Skylar-Scott MA, Mueller J, Visser CW, Lewis JA. Voxelated soft matter via multimaterial multinozzle 3D printing. *Nature*. 2019;575(7782):330-335. doi: 10.1038/s41586-019-1736-8

61. Ganguly S, Das P, Das TK, et al. Acoustic cavitation assisted destratified clay tactoid reinforced in situ elastomer-mimetic semi-IPN hydrogel for catalytic and bactericidal application. *Ultrason Sonochem*. 2020;60:104797. doi: 10.1016/j.ultsonch.2019.104797

62. Ganguly S, Das NC. Water uptake kinetics and control release of agrochemical fertilizers from nanoclay-assisted semi-interpenetrating sodium acrylate-based hydrogel. *Polym Plast Technol and Eng*. 2017;56(7):744-761. doi: 10.1080/03602559.2016.1233268

63. Ganguly S, Das TK, Mondal S, Das NC. Synthesis of polydopamine-coated halloysite nanotube-based hydrogel for controlled release of a calcium channel blocker. *RSC Adv*. 2016;6(107):105350-105362. doi: 10.1039/C6RA24153K

64. Weng Z, Wang J, Senthil T, Wu L. Mechanical and thermal properties of ABS/montmorillonite nanocomposites for fused deposition modeling 3D printing. *Mater Des*. 2016;102:276-283. doi: 10.1016/j.matdes.2016.04.045

65. Cui ZK, Kim S, Baljon JJ, Wu BM, Aghaloo T, Lee M. Microporous methacrylated glycol chitosan-montmorillonite nanocomposite hydrogel for bone tissue engineering. *Nat Commun*. 2019;10(1):3523. doi: 10.1038/s41467-019-11511-3

66. Ganguly S, Das P. Synthesis and production of polylactic acid (PLA). In: Parameswaranpillai J, Siengchin S, Salim NV, George JJ, Poulose A, eds. *Polylactic Acid-Based Nanocellulose and Cellulose Composites*. Boca Raton: CRC Press; 2022: 29-50. doi: 10.1201/9781003160458

67. Paspali A, Bao Y, Gawne DT, Piestert F, Reinelt S. The influence of nanostructure on the mechanical properties of 3D printed polylactide/nanoclay composites. *Compos B Eng*. 2018;152:160-168. doi: 10.1016/j.compositesb.2018.07.005

68. Abdul Haq RH, Wahab MS, Wahid MU. Fused deposition modeling of PCL/HA/MMT biocompatible polymer nano-composites. In: Öchsner A, Altenbach H, eds. *Machining, Joining and Modifications of Adv Mater*. Singapore: Springer; 2016: 23-32. doi: 10.1007/978-981-10-1082-8

69. Mohan VB, Lau KT, Hui D, Bhattacharyya D. Graphene-based materials and their composites: a review on production, applications and product limitations. *Compos B Eng*. 2018;142:200-220. doi: 10.1016/j.compositesb.2018.01.013

70. Terrones M, Martín O, González M, et al. Interphases in graphene polymer, esb.2018.01.013 review on production, applications*Adv Mater*. 2011;23(44):5302-5310. doi: 10.1002/adma.201102036

71. Ganguly S. Preparation/processing of polymer-graphene composites by different techniques. In: Rahaman M, Nayak L, Hussein IA, Das NC, eds. *Polymer Nanocomposites Containing Graphene*. USA: Elsevier; 2022: 45-74. doi: 10.1016/B978-0-12-821639-2.00015-X

72. Zaman A, Orasugh JT, Banerjee P, et al. Facile one-pot in-situ synthesis of novel graphene oxide-cellulose nanocomposite for enhanced azo dye adsorption at optimized conditions. *Carbohydr Polym*. 2020;246:116661. doi: 10.1016/j.carbpol.2020.116661

73. Ganguly S, Mondal S, Das P, et al. An insight into the physico-mechanical signatures of silylated graphene oxide in poly (ethylene methyl acrylate) copolymeric thermoplastic matrix. *Macromol Res*. 2019;27:268-281. doi: 10.1007/s13233-019-7039-y

74. Du J, Cheng HM. The fabrication, properties, and uses of graphene/polymer composites. *Macromol Chem Phys*. 2012;213(10(10ol1060-1077. doi: 10.1002/macp.201200029

75. Dai JF, Wang GJ, Ma L, Wu C-K. Surface properties of graphene: relationship to graphene-polymer composites. *Rev Adv Mater Sci*. 2015;40(1):60-71.

76. Khezri B, Villa K, Novotný F, Sofer Z, Pumera M. Smartdust 3Dla K, Novotný F, . 00029 of graphene/polymer composites. e oxide in poly (ethylene*Small*. 2020;16(33):2002111. doi: 10.1002/smll.202002111

77. Wei X, Li D, Jiang W, et al. 3D printable graphene composite. *Sci Rep*. 2015;5(1):1-7. doi: 10.1038/srep11181

78. Chen S, Wu Q, Mishra C, et al. Thermal conductivity of isotopically modified graphene. *Nat Mater*. 2012;11(3):203-207. doi: 10.1038/nmat3207

79. Chen Q, Mangadlao JD, Wallat J, De Leon A, Pokorski JK, Advincula RC. 3D printing biocompatible polyurethane/poly

(lactic acid)/graphene oxide nanocomposites: anisotropic properties. *ACS Appl Mater Interfaces*. 2017;9(4):4015-4023. doi: 10.1021/acsami.6b11793

80. Iijima S. Helical microtubules of graphitic carbon. *Nature*. 1991;354(6348):56-58. doi: 10.1038/354056a0

81. Stauffer D, Aharony A. *Introduction to Percolation Theory*. London: Taylor & Francis; 2018. doi: 10.1201/9781315274386

82. Pang H, Xu L, Yan DX, Li Z-M. Conductive polymer composites with segregated structures. *Prog Polym Sci*. 2014;39(11):1908-1933. doi: 10.1016/j.progpolymsci.2014.07.007

83. Gnanasekaran K, Heijmans T, Van Bennekom S, et al. 3D printing of CNT-and graphene-based conductive polymer nanocomposites by fused deposition modeling. *Appl Mater Today*. 2017;9:21-28. doi: 10.1016/j.apmt.2017.04.003

84. Gonzalez G, Chiappone A, Roppolo I, et al. Development of 3D printable formulations containing CNT with enhanced electrical properties. *Polymer*. 2017;109:246-253. doi: 10.1016/j.polymer.2016.12.051

85. Shin SR, Bae H, Cha JM, et al. Carbon nanotube reinforced hybrid microgels as scaffold materials for cell encapsulation. *ACS Nano*. 2012;6(1):362-272. doi: 10.1021/nn203711s

86. Lee J, Manoharan V, Cheung L, et al. Nanoparticle-based hybrid scaffolds for deciphering the role of multimodal cues in cardiac tissue engineering. *ACS Nano*. 2019;13(11):12525-12539. doi: 10.1021/acsnano.9b03050

87. Li T, Chen T, Shen X, Shi HH, Jabaria E, Naguib HE. A binder jet 3D printed MXene composite for strain sensing and energy storage application. *Nanoscale Adv*. 2022;4(3):916-925. doi: 10.1039/D1NA00698C

88. Noor N, Shapira A, Edri R, Gal I, Wertheim L, Dvir T. 3D printing of personalized thick and perfusable cardiac patches and hearts. *Adv Sci*. 2019;6(11):1900344. doi: 10.1002/advs.201900344

89. Hong SY, Sun Y, Lee J, et al. 3D printing of free-standing $Ti_3C_2T_x$/PEO architecture for electromagnetic interference shielding. *Polymer*. 2021;236:124312. doi: 10.1016/j.polymer.2021.124312

90. Yuan W, Liu H, Wang X, Huang L, Yin F, Yuan Y. Conductive MXene/melamine sponge combined with 3D printing resin base prepared as an electromagnetic interference shielding switch. *Compos Part A Appl Sci Manuf*. 2021;143:106238. doi: 10.1016/j.compositesa.2020.106238

91. Basara G, Saeidi-Javash M, Ren X, et al. Electrically conductive 3D printed Ti3C2Tx MXene-PEG composite constructs for cardiac tissue engineering. *Acta Biomater*. 2020;139:179-189. doi: 10.1016/j.actbio.2020.12.033

92. Wilkinson N, Smith M, Kay R, Harris RA. A review of aerosol jet printing—a non-traditional hybrid process for micro-manufacturing. *Int J Adv Manuf Technol*. 2019;105(11):4599-4619. doi: 10.1007/s00170-019-03438-2

93. Filgueira D, Holmen S, Melbø JK, Moldes D, Echtermeyer AT, Chinga-Carrasco G. 3D printable filaments made of biobased polyethylene biocomposites. *Polymers*. 2018;10(3):314. doi: 10.3390/polym10030314

94. Liu R, Chen Y, Cao J. Effects of modifier type on properties of in situ organo-montmorillonite modified wood flour/poly (lactic acid) composites. *ACS Appl Mater Interfaces*. 2016;8(1):161-168. doi: 10.1021/acsami.5b07989

95. Yang Z, Bi H, Bi Y, Rodrigue D, Xu M, Feng X. Comparison between polyethylene glycol and tributyl citrate to modify the properties of wood fiber/polylactic acid biocomposites. *Polym Compos*. 2019;40(4):1384-1394. doi: 10.1002/pc.24872

96. Vaidya AA, Collet C, Gaugler M, Lloyd-Jones G. Integrating softwood biorefinery lignin into polyhydroxybutyrate composites and application in 3D printing. *Mater Today Commun*. 2019;19:286-296. doi: 10.1016/j.mtcomm.2019.02.008

97. Zhao X, Tekinalp H, Meng X, et al. Poplar as biofiber reinforcement in composites for large-scale 3D printing. *ACS Appl Bio Mater*. 2019;2(10):4557-4570. doi: 10.1021/acsabm.9b00675

98. Liu H, He H, Peng X, Huang B, Li J. Three,He H, Peng X,021/acsabm.9b00675omposites for large-scale 3D printing. and application in 3D printing. c acid biocomposites. . lastic matrix. ation. l*Polym Adv Technol*. 2019;30(4):910-922. doi: 10.1002/pat.4524

99. Jang J, Yi H-G, Cho D-W. 3D printed tissue models: present and future. *ACS Biomater Sci Eng*. 2016;2(10):1722-1731. doi: 10.1021/acsbiomaterials.6b00129

100. Mohan TS, Datta P, Nesaei S, Ozbolat V, Ozbolat IT. 3D coaxial bioprinting: process mechanisms, bioinks and applications. *Prog Biomed Eng*. 2022;4(2):022003. doi: 10.1088/2516-1091/ac631c

101. Li W, Hu X, Yang S, et al. A novel tissue-engineered 3D tumor model for anti-cancer drug discovery. *Biofabrication*. 2018;11(1):015004. doi: 10.1088/1758-5090/aae270

102. Bhise NS, Ribas J, Manoharan V, et al. Organ-on-a-chip platforms for studying drug delivery systems. *J Control Release*. 2014;190:82-93. doi: 10.1016/j.jconrel.2014.05.004

103. Murphy SV, De Coppi P, Atala A. Opportunities and challenges of translational 3D bioprinting. *Nat Biomed Eng*. 2020;4(4):370-380. doi: 10.1038/s41551-019-0471-7

104. Yi B, Xu Q, Liu W. An overview of substrate stiffness guided cellular response and its applications in tissue regeneration. *Bioact Mater*. 2022;15:82-102. doi: 10.1016/j.bioactmat.2021.12.005

105. Xia H, Chen Q, Fang Y, et al. Directed neurite growth of rat dorsal root ganglion neurons and increased colocalization with Schwann cells on aligned poly(methyl methacrylate) electrospun nanofibers. *Brain Res*. 2014;1565:18–27. doi: 10.1016/j.brainres.2014.04.002

106. Lu K, Qian Y, Gong J, et al. Biofabrication of aligned structures that guide cell orientation and applications in tissue engineering. *Bio-Des Manuf*. 2021;4:258-277. doi: 10.1007/s42242-020-00104-5

107. Shin YM, Yang HS, Chun HJ. Directional cell migration guide for improved tissue regeneration. *Adv Exp Med Biol*. 2020;1249:131-140. doi: 10.1007/978-981-15-3258-0_9

108. Ballester-Beltran J, Biggs M, Dalby MJ, Salmerón-Sánchez M, Leal-Egaña A. Sensing the differences: the influence of anisotropic cues on cell behavior. *Front Mater*. 2015;2:39. doi: 10.3389/fmats.2015.00039

109. Zhuo Y, Choi JS, Martin T, Yu H, Harley BA, Cunningham BT. Quantitative analysis of focal adhesion dynamics using photonic resonator outcoupler microscopy (PROM). *Light Sci Appl*. 2018;7(1):9. doi: 10.1038/s41377-018-0001-5

110. Bowers DT, Brown JL. Nanofibers as bioinstructive scaffolds capable of modulating differentiation through mechanosensitive pathways for regenerative engineering. *Regen Eng Transl Med*. 2019;5:22-29. doi: 10.1007/s40883-018-0076-9

111. Wang S, Ameli A, Shaayegan V, et al. Modelling of rod-like fillers' rotation and translation near two growing cells in conductive polymer composite foam processing. *Polymers*. 2018;10(3):261. doi: 10.3390/polym10030261

112. Volpi M, Paradiso A, Costantini M, Święszkowski W. Hydrogel-based fiber biofabrication techniques for skeletal muscle tissue engineering. *ACS Biomater Sci Eng*. 2022;8(2):379-405. doi: 10.1021/acsbiomaterials.1c01145

113. Kim WJ, Jang CH, Kim GH. A myoblast-laden collagen bioink with fully aligned Au nanowires for muscle-tissue regeneration. *Nano Lett*. 2019;19(12):8612-8620. doi: 10.1021/acs.nanolett.9b03182

114. Pardo A, Bakht SM, Gomez-Florit M, et al. Magnetically-assisted 3D bioprinting of anisotropic tissue-mimetic constructs. *Adv Funct Mater*. 2022;32(50):2208940. doi: 10.1002/adfm.202208940

115. Zhang S, Chen X, Shan M, et al. Convergence of 3D bioprinting and nanotechnology in tissue engineering scaffolds. *Biomimetics*. 2023;8(1):94. doi: 10.3390/biomimetics8010094

116. Shin J, Lee Y, Li Z, Hu J, Park SS, Kim K. Optimized 3D bioprinting technology based on machine kearning: a review of recent trends and advances. *Micromachines*. 2022;13(3):363. doi: 10.3390/mi13030363

117. Quan Z, Wu A, Keefe M, et al. Additive manufacturing of multi-directional preforms for composites: opportunities and challenges. *Mater Today*. 2015;18(9):503-512. doi: 10.1016/j.mattod.2015.05.001

118. Rajabi M, McConnell M, Cabral J, Azam Ali M. Chitosan hydrogels in 3D printing for biomedical applications. *Carbonhydr Polym*. 2021;260:117768. doi: 10.1016/j.carbpol.2021.117768

119. Xu W, Molino BZ, Cheng F, et al. On low-concentration inks formulated by nanocellulose assisted with gelatin methacrylate (GelMA) for 3D printing toward wound healing application. *ACS Appl Mater Interfaces*. 2019;11(9):8838-8848. doi: 10.1021/acsami.8b21268

120. Wang X, Zhang X, Dai X, et al. Tumor-like lung cancer model based on 3D bioprinting. *3 Biotech*. 2018;8(12):1-9. doi: 10.1007/s13205-018-1519-1

121. Vijayavenkataraman S, Lu W, Fuh J. 3D bioprinting of skin: a state-of-the-art review on modelling, materials, and processes. *Biofabrication*. 2016;8(3):032001. doi: 10.1088/1758-5090/8/3/032001

122. Cubo N, Garcia M, Del Canizo JF, Velasco D, Jorcano JL. 3D bioprinting of functional human skin: production and in vivo analysis. *Biofabrication*. 2016;9(1):015006. doi: 10.1088/1758-5090/9/1/015006

123. Kim BS, Gao G, Kim JY, Cho D-W. 3D cell printing of perfusable vascularized human skin equivalent composed of epidermis, dermis, and hypodermis for better structural recapitulation of native skin. *Adv Healthc Mater*. 2019;8(7):1801019. doi: 10.1002/adhm.201801019

124. Pei H, Jing J, Chen Y, Guo J, Chen N. 3D printing of PVDF-based piezoelectric nanogenerator from programmable metamaterial design: Promising strategy for flexible electronic skin. *Nano Energy*. 2023;109:108303. doi: 10.1016/j.nanoen.2023.108303

125. Lackner F, Knechtl I, Novak M, et al. 3D-printed anisotropic nanofiber composites with Gradual mechanical properties. *Adv Mater Technol*. 2023;8(10):2201708. doi: 10.1002/admt.202201708

126. Markstedt K, Mantas A, Tournier I, Ávila HM, Hägg D, Gatenholm P. 3D bioprinting human chondrocytes with nanocellulose–alginate bioink for cartilage tissue engineering applications. *Biomacromolecules*. 2015;16(5):1489-1496. doi: 10.1021/acs.biomac.5b00188

127. Rathan S, Dejob L, Schipani R, Haffner B, Möbius ME, Kelly DJ. Fiber reinforced cartilage ECM functionalized bioinks for functional cartilage tissue engineering. *Adv Healthc Mater*. 2019;8(7):1801501. doi: 10.1002/adhm.201801501

128. Acedo CA, de Vicente J, González GJ, Chocarro C. Bio-inspired hydrogel composed of hyaluronic acid and alginate as a potential bioink for 3D bioprinting of articular cartilage engineering constructs. *Acta Biomater*. 2020;106:114-123. doi: 10.1016/j.actbio.2020.01.046

129. Schipani R, Scheurer S, Florentin R, Critchley SE, Kelly DJ. Reinforcing interpenetrating network hydrogels with 3D printed polymer networks to engineer cartilage mimetic composites. *Biofabrication*. 2020;12(3):035011. doi: 10.1088/1758-5090/ab8708

130. Müller M, Öztürk E, Arlov Ø, Gatenholm P, Zenobi-Wong M. Alginate sulfate–nanocellulose bioinks for cartilage bioprinting applications. *Ann Biomed Eng*. 2017; 45:210-223. doi: 10.1007/s10439-016-1704-5

131. Markstedt K, Mantas A, Tournier I, Ávila HM, Hägg D, Gatenholm P. 3D bioprinting human chondrocytes with nanocellulose–alginate bioink for cartilage tissue engineering applications. *Biomacromolecules*. 2015;16(5):1489-1496. doi: 10.1021/acs.biomac.5b00188

132. Sun Y, Wu Q, Zhang Y, Dai K, Wei Y. 3D-bioprinted gradient-structured scaffold generates anisotropic cartilage with vascularization by pore-size-dependent activation of HIF1α/FAK signaling axis. *Nanomedicine*. 2021;37:102426. doi: 10.1016/j.nano.2021.102426

133. Sun Y, You Y, Jiang W, Wang Bo, Wu Q, Dai K. 3D bioprinting dual-factor releasing and gradient-structured constructs ready to implant for anisotropic cartilage regeneration. *Sci Adv*. 2020;6(37):eaay1422. doi: 10.1126/sciadv.aay1422

134. Idaszek J, Costantini M, Karlsen TA, et al. 3D bioprinting of hydrogel constructs with cell and material gradients for the regeneration of full-thickness chondral defect using a microfluidic printing head. *Biofabrication*. 2019;11(4): 044101. doi: 10.1088/1758-5090/ab2622

135. Costantini M, Testa S, Mozetic P, et al. Microfluidic-enhanced 3D bioprinting of aligned myoblast-laden hydrogels leads to functionally organized myofibers in vitro and in vivo. *Biomaterials*. 2017;131:98-110. doi: 10.1016/j.biomaterials.2017.03.026

136. Li X, Yuan Y, Liu L, et al. 3D printing of hydroxyapatite/tricalcium phosphate scaffold with hierarchical porous structure for bone regeneration. *Bio-Des Manuf*. 2020;3(1):15-29. doi: 10.1007/s42242-019-00056-5

137. Samavedi S, Whittington AR, Goldstein AS. Calcium phosphate ceramics in bone tissue engineering: a review of properties and their influence on cell behavior. *Acta Biomater*. 2013;9(9):8037-8045. doi: 10.1016/j.actbio.2013.06.014

138. Nyberg E, Rindone A, Dorafshar A, Grayson WL. Comparison of 3D-printed poly-ε-caprolactone scaffolds functionalized with tricalcium phosphate, hydroxyapatite, bio-oss, or decellularized bone matrix. *Tissue Eng Part A*. 2017;23(11-12):503-514. doi: 10.1089/ten.TEA.2016.0418

139. Byambaa B, Annabi N, Yue K, et al. Bioprinted osteogenic and vasculogenic patterns for engineering 3D bone tissue. *Adv Healthc Mater*. 2017;6(16):1700015. doi: 10.1002/adhm.201700015

140. Chiesa I, De Maria C, Lapomarda A, et al. Endothelial cells support osteogenesis in an in vitro vascularized bone model developed by 3D bioprinting. *Biofabrication*. 2020;12(2):025013. doi: 10.1088/1758-5090/ab6a1d

141. Roy A, Saxena V, Pandey LM. 3D printing for cardiovascular tissue engineering: a review. *Mater Technol*. 2018;33(6): 433-442. doi: 10.1080/10667857.2018.1456616

142. Jin G, Li K. The electrically conductive scaffold as the skeleton of stem cell niche in regenerative medicine. *Mater Sci Eng C*. 2014;45:671-681. doi: 10.1016/j.msec.2014.06.004

143. Borriello A, Guarino V, Schiavo L, Alvarez-Perez MA, Ambrosio L. Optimizing PANi doped electroactive substrates as patches for the regeneration of cardiac muscle. *J Mater Sci Mater Med*. 2011;22(4):1053-1062. doi: 10.1007/s10856-011-4259-x

144. Dvir T, Timko BP, Brigham MD, et al. Nanowired three-dimensional cardiac patches. *Nat Nano*. 2011;6(11):720-725. doi: 10.1038/nnano.2011.160

145. Liu W, Zhao L, Wang C, Zhou J. Conductive nanomaterials for cardiac tissues engineering. *Eng Regener.* 2020;1:88-94. doi: 10.1016/j.engreg.2020.09.001

146. Ashtari K, Nazari H, Ko H, et al. Electrically conductive nanomaterials for cardiac tissue engineering. *Adv Drug Deliv Rev*. 2019;144:162-179. doi: 10.1016/j.addr.2019.06.001

147. Lee J, Manoharan V, Cheung L, et al. Nanoparticle-based hybrid scaffolds for deciphering the role of multimodal cues in cardiac tissue engineering. *ACS Nano*. 2019;13(11):12525-12539. doi: 10.1021/acsnano.9b03050

148. Zhu K, Shin SR, van Kempen T, et al. Gold nanocomposite bioink for printing 3D cardiac constructs. *Adv Funct Mater*. 2017;27(12):1605352. doi: 10.1002/adfm.201605352

149. Tomasina C, Bodet T, Mota C, Moroni L, Camarero-Espinosa S. Bioprinting vasculature: materials, cells and emergent techniques. *Materials*. 2019;12(17):2701. doi: 10.3390/ma12172701

150. Wu J, Hu C, Tang Z, Yu Q, Liu X, Chen H. Tissue-engineered vascular grafts: balance of the four major requirements. *Colloid Interface Sci Commun*. 2018;23:34-44. doi: 10.1016/j.colcom.2018.01.005

151. Moroni L, Burdick JA, Highley C, et al. Biofabrication strategies for 3D in vitro models and regenerative medicine. *Nat Rev Mater*. 2018;3(5):21-37. doi: 10.1038/s41578-018-0006-y

152. Piterina AV, Cloonan AJ, Meaney CL, et al. ECM-based materials in cardiovascular applications: inherent healing potential and augmentation of native regenerative processes. *Int J Mol Sci*. 2009;10(10):4375-4417. doi: 10.3390/ijms10104375

153. Heinrich MA, Liu W, Jimenez A, et al. 3D bioprinting: from benches to translational applications. *Small*. 2019;15(23):1970126. doi: 10.1002/smll.201805510

154. Sasmal P, Datta P, Wu Y, Ozbolat IT. 3D bioprinting for modeling vasculature. *Microphysiol Syst*. 2018;2:4. doi: 10.21037/mps.2018.10.02

155. Lee J, Kim G. Three-dimensional hierarchical nanofibrous collagen scaffold fabricated using fibrillated collagen and pluronic F-127 for regenerating bone tissue. *ACS Appl Mater Interfaces*. 2018;10(42):35801-35811. doi: 10.1021/acsami.8b14088

156. Gao Q, Liu Z, Lin Z, et al. 3D bioprinting of vessel-like structures with multilevel fluidic channels. *ACS Biomater Sci Eng*. 2017;3(3):399-408. doi: 10.1021/acsbiomaterials.6b00643

157. Gao G, Park JY, Kim BS, Jang J, Cho D-W. Coaxial cell printing of freestanding, perfusable, and functional in vitro vascular models for recapitulation of native vascular endothelium pathophysiology. *Adv Healthc Mater*. 2018;7(23):1801102. doi: 10.1002/adhm.201801102

158. Dolati F, Yu Y, Zhang Y, De Jesus AM, Sander EA, Ozbolat IT. In vitro evaluation of carbon-nanotube-reinforced bioprintable vascular conduits. *Nanotechnology*. 2014;25(14):145101. doi: 10.1088/0957-4484/25/14/145101

159. Zhang Y, Yu Y, Dolati F, Ozbolat IT. Effect of multiwall carbon nanotube reinforcement on coaxially extruded cellular vascular conduits. *Mater Sci Eng C*. 2014;39:126-133. doi: 10.1016/j.msec.2014.02.036

160. Shao L, Gao Q, Xie C, Fu J, Xiang M, He Y. Directly coaxial 3D bioprinting of large-scale vascularized tissue constructs. *Biofabrication*. 2020;12(3):035014. doi: 10.1088/1758-5090/ab7e76

161. Li S, Liu Y, Li Y, Liu C, Sun Y, Hu Q. A novel method for fabricating engineered structures with branched micro-channel using hollow hydrogel fibers. *Biomicrofluidics*. 2016;10(6):064104. doi: 10.1063/1.4967456

162. Wu Y, Chee AJ, Golzar H, Yu ACH, Tang XS. Embedded 3D printing of ultrasound-compatible arterial phantoms with biomimetic elasticity. *Adv Funct Mater*. 2022;32:2110153. doi: 10.1002/adfm.202110153

163. Wu Y, Lin ZYW, Wenger AC, Tam KC, Tang XS. 3D bioprinting of liver-mimetic construct with alginate/cellulose nanocrystal hybrid bioink. *Bioprinting*. 2018;9:1-6. doi: 10.1016/j.bprint.2017.12.001

164. Wu Y, Wenger A, Golzar H, Tang XS. 3D bioprinting of bicellular liver lobule-mimetic structures via microextrusion of cellulose nanocrystal-incorporated shear-thinning bioink. *Sci Rep*. 2020;10(1):1-12. doi: 10.1038/s41598-020-77146-3

165. Nguyen DG, Funk J, Robbins JB, et al. Bioprinted 3D primary liver tissues allow assessment of organ-level response to clinical drug induced toxicity in vitro. *PLoS One*. 2016;11(7):e0158674. doi: 10.1371/journal.pone.0158674

166. Zhuang P, An J, Chua CK, Tan LP. Bioprinting of 3D in vitro skeletal muscle models: a review. *Mater Des*. 2020;193:108794. doi: 10.1016/j.matdes.2020.108794

167. Fan T, Wang S, Jiang Z, et al. Controllable assembly of skeletal muscle-like bundles through 3D bioprinting. *Biofabrication*. 2021;14(1):015009. doi: 10.1088/1758-5090/ac3aca

168. Choi YJ, Kim TG, Jeong J, *et al.*, 2016, 3D cell printing of functional skeletal muscle constructs using skeletal muscle-derived bioink. *Adv Healthc Mater*. 2016;5(20):2636-2645. doi: 10.1002/adhm.201600483

169. Ma X, Wang M, Ran Y, et al. Design and fabrication of polymeric hydrogel carrier for nerve repair. *Polymers*. 2022;14(8):1549. doi: 10.3390/polym14081549

170. Lozano R, Stevens L, Thompson BC, et al. 3D printing of layered brain-like structures using peptide modified gellan gum substrates. *Biomaterials*. 2015;67:264-273. doi: 10.1016/j.biomaterials.2015.07.022

171. Yu X, Zhang T, Li Y. 3D printing and bioprinting nerve conduits for neural tissue engineering. *Polymers*. 2020;12(8):1637. doi: 10.3390/polym12081637

172. Balasubramanian S, Yu K, Meyer AS, Karana E, Aubin-Tam M-E. Bioprinting of regenerative photosynthetic living materials. *Adv Func Mater*. 2021;31(31):2011162. doi: 10.1002/adfm.202011162

173. Zhang Y, Hsu H-H, Wheeler JJ, Tanga S, Jiang X. Emerging investigator series: emerging biotechnologies in wastewater treatment: from biomolecular engineering to multiscale integration. *Environ Sci: Water Res Technol*. 2020;6(8):1967-1985. doi: 10.1039/D0EW00393J

174. Hsu L, Jiang X. 'Living' inks for 3D bioprinting. *Trends Biotechnol*. 2019;37(8):795-796. doi: 10.1016/j.tibtech.2019.04.014

175. Liu J, Chen Y, Jiang S, et al. Rapid removal of Cr (III) from high-salinity wastewater by cellulose-g-poly-(acrylamide-co-sulfonic acid) polymeric bio-adsorbent. *Carbohydr Polym*. 2021;270:118356.
doi: 10.1016/j.carbpol.2021.118356

176. Gao X, Guo C, Hao J, Zhao Z, Long H, Li M. Adsorption of heavy metal ions by sodium alginate based adsorbent-a review and new perspectives. *Int J Biol Macromol*. 2020;164:4423-4434.
doi: 10.1016/j.ijbiomac.2020.09.046

177. Yusoff NHM, Teo L-RI, Phang SJ, Wong V-L, Cheah KH, Lim S-S. Recent advances in polymer-based 3D printing for wastewater treatment application: an overview. *Chem Eng J*. 2022;429:132311.
doi: 10.1016/j.cej.2021.132311

178. Qian F, Zhu C, Knipe JM, et al. Direct writing of tunable living inks for bioprocess intensification. *Nano Lett*. 2019;19(9):5829-5835.
doi: 10.1021/acs.nanolett.9b00066

179. Seidel J, Ahlfeld T, Adolph M, et al. Green bioprinting: extrusion-based fabrication of plant cell-laden biopolymer hydrogel scaffolds. *Biofabrication*. 2017;9(4): 045011.
doi: 10.1088/1758-5090/aa8854

180. Schaffner M, Rühs PA, Coulter F, Kilcher S, Studart AR. 3D printing of bacteria into functional complex materials. *Sci Adv*. 2017;3(12):eaao6804.
doi: 10.1126/sciadv.aao6804

181. Liu J, Shen X, Zheng Z, et al. Immobilization of laccase by 3D bioprinting and its application in the biodegradation of phenolic compounds. *Int J Biol Macromol*. 2020;164: 518-525.
doi: 10.1016/j.ijbiomac.2020.07.144

182. Deng P, Sheng W, Xu A, et al. Bottom-up construction of electrochemically active living filters: from graphene oxide mediated formation of bacterial cables to 3D assembly of hierarchical architectures. *ACS Appl Mater Interfaces*. 2020;3(11):7376-7381.
doi: 10.1021/acsabm.0c01172

ACCSCIENCE PUBLISHING

International Journal of Bioprinting

REVIEW ARTICLE

Advances in tissue engineering and 3D bioprinting for corneal regeneration

Tamás Monostori[1,2,3], Diána Szűcs[1,2,3], Borbála Lovászi[1,2,3], Lajos Kemény[3,4], and Zoltán Veréb[1,3*]

[1]Regenerative Medicine and Cellular Pharmacology Laboratory (HECRIN), Department of Dermatology and Allergology, Faculty of Albert Szent-Györgyi Medical School, University of Szeged, Szeged, Hungary

[2]Doctoral School of Clinical Medicine, University of Szeged, Szeged, Hungary

[3]Centre of Excellence for Interdisciplinary Research, Development and Innovation, University of Szeged, Szeged, Hungary

[4]Hungarian Centre of Excellence for Molecular Medicine-USz Skin Research Group, University of Szeged, Szeged, Hungary

Abstract

Blindness resulting from corneal damage affects millions of people worldwide. The scarcity of corneal donors adds a layer of complexity to patient treatment. Consequently, exploring artificial cornea substitutes has become imperative in the realm of clinical research. Scientific advancements have ushered in a plethora of innovative solutions, including keratoprostheses or decellularized cornea scaffolds. The development of three-dimensional (3D) printing has further expanded the horizons of research in this field, delving into the feasibility of bioprinted corneas and yielding numerous promising outcomes. However, the manufacturing of corneal products via 3D printing poses a substantial challenge, demanding a meticulous selection of materials and techniques to ensure the transparency and preservation of the optical and mechanical properties of the artificial cornea. In the review, we present the artificial cornea substitutes. Additionally, we aim to provide a concise overview of the 3D printing techniques and materials applicable to corneal bioprinting.

Keywords: Cornea; Blindness; Artificial cornea; 3D printing; Stem cells

***Corresponding author:**
Zoltán Veréb
(vereb.zoltan@med.u-szeged.hu)

Citation: Monostori T, Szűcs D, Lovászi B, Kemény L, Veréb Z. Advances in tissue engineering and 3D bioprinting for corneal regeneration. *Int J Bioprint*. 2024;10(2):1669
doi: 10.36922/ijb.1669

Received: August 23, 2023
Accepted: October 31, 2023
Published Online: January 16, 2024

1. Introduction

Corneal blindness constitutes a significant global health challenge, with multifaceted etiologies including infections, scarring, and corneal dystrophy. Corneal transplants are undertaken for various reasons, with bullous keratopathy emerging as the predominant indication in developed countries, while infections and scarring are more prevalent causes in developing countries.[1]

As per the World Health Organization (WHO), the global population of blind individuals stands at 45 million, a figure that may escalate rapidly given the rise in life expectancy.[2] A study conducted in the United Kingdom between 2008 and 2011 revealed a breakdown of corneal transplant indications, with keratoconus accounting for 27.4%, Fuchs' dystrophy for 25.8%, cataract-caused endothelial dysfunction for 21%, infections

for 9.5%, ulcerative keratitis for 2.6%, and injuries for 2.4%.[3] Subsequently, a separate study conducted between August 2012 and August 2013 highlighted a substantial global demand for corneal transplants, estimating that 12.7 million individuals across 131 countries awaited this procedure.[4] In stark contrast, the annual incidence of corneal transplants in the United States is limited to 40,000.[5]

The treatment landscape is significantly challenged by the pronounced disjunction between the number of patients awaiting transplantation and the limited availability of cornea donors. This stark demand has prompted intensive research and development efforts in the realm of artificial cornea and cornea replacement products, which must meet stringent criteria.[6] Even when a suitable cornea donor is identified, the healing process may face impediments due to immune response-driven rejection.[5] The evolving landscape of science and medicine has ushered in myriad possibilities in the field of corneal research. The contemporary medical arena increasingly embraces personalized therapies, a trend underscored by the advent of translational biomedicine. A noteworthy surge in possibilities, such as the adoption of three-dimensional (3D) bioprinting, is reshaping the field. Traditional surgical approaches for reconstructing various tissues and organs confront formidable challenges owing to the distinctive functions of these tissues. To overcome these limitations, there has been a discernible escalation in research dedicated to the application of 3D printing techniques.

In corneal tissue engineering, in addition to 3D printing, nanotechnology offers a new avenue thanks to recent physical and chemical breakthroughs. These advancements enable the creation of specialized surfaces that facilitate cell adhesion and proliferation, establishing unique microenvironments to enhance nutrient supply. By incorporating various nanomaterials into hydrogels, it becomes possible to influence the physical and mechanical properties of the gel, including gelation. Nanoliposomes, when combined with stem cells in the gel, can mediate active substances, facilitating cell differentiation, reducing inflammation, and enhancing wound healing. The promising properties and versatile applications of nanomaterials hold potential for the future of corneal tissue engineering and regenerative medicine. However, it is important to note that the application of this technology in this field is still in the early stages of research.[5]

In 3D bioprinting for regenerative medicine, we are already witnessing promising results that allow for the printing of tissues with complex structures. Consequently, 3D bioprinting presents a new opportunity in personalized medicine for corneal replacement, addressing the challenge of donor shortage.[7]

2. The structure of the cornea

The cornea, a thin and transparent membrane, serves two primary functions: protecting the interior of the eye and facilitating light refraction. Optically, it is responsible for two-thirds of light refraction. The structural composition of the cornea involves various cell types, including epithelial cells, keratocytes, stromal cells, and corneal endothelial cells. In addition, extracellular components such as collagen or glycosaminoglycans (GAG) contribute to its composition.

The cornea is anatomically divided into five principal layers: epithelium, Bowman's membrane, stroma, Descemet's membrane, and endothelium (Figure 1). In terms of structure, the epithelial layer has a thickness of 5–7 cells, comprising three cell types: surface epithelial cells, stem cells, and basal cells. These cells collectively form a uniform layer with a thickness of 50 μm. Notably, corneal epithelial cells differentiate from limbal epithelial stem cells (LESCs) and do not undergo keratinization.[8] Following the epithelial layer, Bowman's membrane, characterized by an acellular structure, is constructed from a disordered multitude of collagen fibers. The stroma, which represents the thickest layer and constitutes roughly 90% of the total corneal thickness, plays an essential role in providing mechanical strength and critical optical properties. Structurally, it comprises approximately 200–250 parallel collagen fibers. Similar to Bowman's layer, Descemet's membrane is also acellular, composed of collagen, laminin, and fibronectin. The last layer of the cornea is the endothelial layer, semi-permeable to water and nutrients. Due to this property, the endothelial layer ensures fluid flow for the stroma. However, it is noteworthy that the number of cells forming the endothelial layer decreases with aging, and the proliferation capacity of these cells is significantly lower in the adult cornea.[9,10]

In addition to the well-established five layers, a sixth layer was recently discovered in 2013 by Dua and his colleagues.[11,12] Termed pre-Descemet's or Dua's layer, this membrane is located anterior to Descemet's layer. Dua's layer is a thin membrane primarily composed of type IV collagen, with a thickness ranging from 6 to 15 μm. The collagen fibers within this layer are organized into 5–8 layers.[8,9,11]

3. Cells of the cornea

3.1. Corneal epithelium

The corneal epithelium acts as a physical barrier, consisting of three different cell types: surface squamous

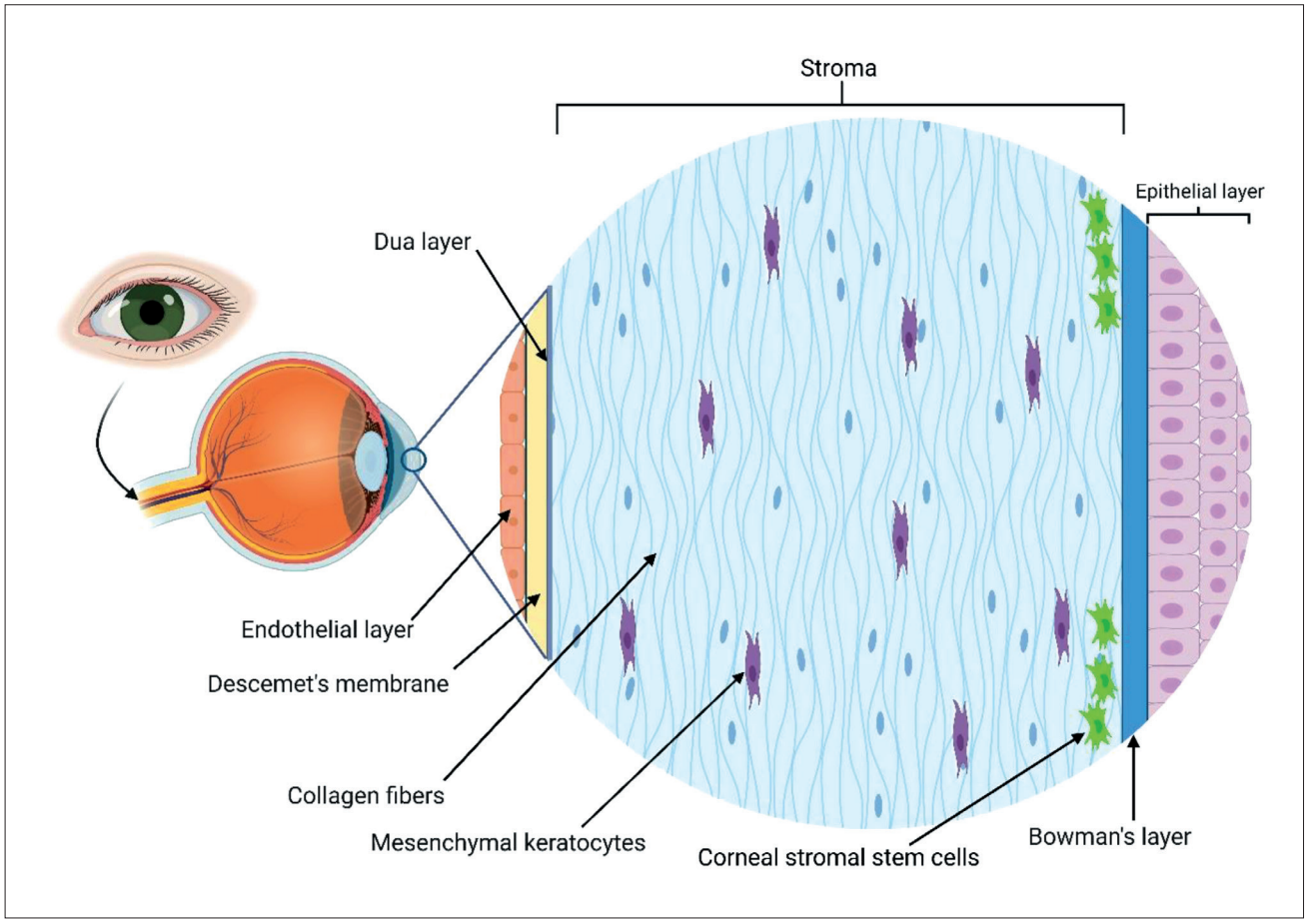

Figure 1. Structure of the cornea.

cells, suprabasal cells, and basal columnar cells located in the lower part of the epithelium. The upper three layers are comprised of differentiated surface squamous cells, covered with microvilli that significantly increase the surface of the squamous cell layer and facilitate contact with the thin tear layer protecting the cornea. The middle layer is composed of suprabasal cells, often referred to as Wing cells due to their wing-like shape.[13,14] Compared to squamous cells, suprabasal cells are flatter and more spread out, exhibiting elongated nuclei, with many vacuoles found in proximity to the squamous cell nucleus.[14] These cells divide relatively rarely, migrate toward the upper layer, and differentiate into squamous cells. The lowest layer of the epithelium is formed by basal cells in a single layer. These cells carry out essential tasks such as replacing suprabasal cells and secreting matrix factors that make up the lamina basalis and stroma. Basal cells are also responsible for the assembly of hemidesmosomes. These functions may play a role in cell migration during wound healing.[13] During eye development, the cornea's epithelium originates from the surface epidermal ectoderm.[4]

3.2. Keratocytes

The keratocytes residing in the cornea are situated amidst the collagen fibers comprising the stoma, originating from mesenchymal cells. Within this collagenous matrix, keratocytes form a unified network, interconnecting with neighboring cells in a dendritic manner. These cells contain crystals and proteins that contribute to the cornea's transparency. Play an important role in corneal wound healing and scarring, keratocytes exhibit two phenotypes. One phenotype is characterized as regenerative or repair-oriented, while the other promotes cell death. During the phenotypic transformation, cells deviate from their resting state. The regenerative phenotype facilitates wound healing through fibrotic scarring and tissue repair. However, it is noteworthy that scarring adversely affects corneal transparency.[13,15]

3.3. Corneal endothelium

The endothelium, constituting the cornea's innermost layer, comprises a single layer of cells located posterior to Descemet's membrane. Comprising squamous cells that

have undergone terminal differentiation, the endothelial layer lacks regenerative capacity. These cells fulfill crucial roles, including maintaining corneal transparency, supplying nutrients to the cornea, and ensuring hydration by permitting the passage of water into the stroma. Additionally, their pivotal function extends to preventing overhydration of the stroma through active transport mechanisms. This dual role is vital in preserving the organized structure of collagen fibers within the stroma, which is essential for facilitating light transmission and upholding corneal transparency. The endothelium and stroma are formed during eye development from the periocular mesenchyme—also known as periocular neural crest cells.[4,16-18]

3.4. Limbal epithelial stem cells

Adult limbal epithelial stem cells (LESCs) are located in the peripheral limbus, playing a pivotal role in the renewal of the corneal epithelium, specifically in the continuous replacement of the upper 4–6 layers, predominantly composed of squamous cells. These LESCs are located in the basal layer of the limbal epithelium, forming distinctive niches. Despite their essential function, it is noteworthy that the proliferation potential of these stem cells is extremely low. The potential loss or damage of these stem cells can occur due to various factors such as physical, chemical, or thermal impact, genetic diseases, or infections. Consequently, limbal stem cell deficiency triggers neovascularization and angiogenesis in the conjunctiva, leading to vision loss. To address this, clinically cultured LESCs are employed as a therapeutic strategy. These cultured cells are transplanted into the patient's cornea, and it is important to note that LESCs can be derived from either autologous or allogeneic sources.[19]

3.5. Corneal stromal stem cells

Corneal stromal stem cells (CSSCs) represent another crucial cell type within the cornea, specifically located in the limbal stoma. Functioning as mesenchymal progenitors of keratocytes, these cells contribute to wound healing and regeneration, essential processes for maintaining corneal transparency. The therapeutic potential of CSSCs extends to applications in artificial tissue replacement.[20] Notably, CSSCs demonstrate the capability to produce matrix components resembling the composition of the collagen matrix present in the stroma. In research endeavors, it was observed that stromal stem cells, when cultured on nanorods arranged in parallel, generated a collagen layer mirroring the structure and composition of the natural stroma.[21] These findings suggest that CSSCs hold promise for *in vitro* production of stroma-like tissue. Such advancements could open avenues for replacing the stroma in transplantation procedures.

4. Extracellular matrix proteins in the cornea

A crucial determinant of achieving optimal visual acuity is the correct composition, structure, and interplay of the extracellular matrix (ECM) situated within the cornea, forming what is known as the corneal stroma (Table 1). An illustrative instance of this is the organized network of keratocytes within the stroma, situated amidst collagen fibers and layers. This arrangement serves as a cornerstone for one of the main functions of the stroma, specifically imparting mechanical strength to the cornea while significantly contributing to its transparency.

The primary constituent of the ECM is collagen, accompanied by various leucine-rich proteoglycans.[22] The collagen matrix forming the corneal stroma incorporates diverse collagen types, including type I, type IV, type V, and type VIII. Unlike collagen layers in other connective tissues, the corneal collagen matrix is notably thinner, a characteristic that contributes to corneal transparency. The collagen fibers within the cornea serve as pivotal load-bearing elements, enduring tensile and compressive forces generated by intraocular pressure and external impacts to safeguard inner ocular tissues. This robust strength of collagen fibers is attributed to their rope-like structure and the different lateral orientations of the layers. Dermatan sulfate-containing proteoglycans in the stroma prevent the adhesion of neighboring collagen fibers.[9] Among the collagens, type I collagen prevails in abundance throughout the human body, with exceptions such as the eye's vitreous body or brain. Conversely, type V collagen is notably more abundant in the cornea. This collagen variant, characterized by its small fibrillar structure, plays an important role in fiber formation. The stroma layers mainly consist of type I and type V collagens, with an estimated count of approximately 250–300 layers enveloping the entire cornea. The distribution of particular collagen types may vary depending on the cornea's structure and condition. Given that type I and type V collagens collectively contribute to corneal transparency, any changes in their distribution or ratio can affect this transparency. For example, structural changes in type I collagen resulting from corneal wounds or scarring may lead to a decrease in transparency.[16]

Type VII collagen assumes a significant role in facilitating adhesion between the epithelial layer and the stroma, as well as in fiber fixation and wound healing. Unlike the previously discussed collagens, type VIII and type XII collagens lack the ability to independently form fibers. Nevertheless, they can engage in interactions with other collagen types, actively participating in fiber formation.[23,24]

Table 1. Proteins in the extracellular matrix of the cornea

Cornea layers	Extracellular matrix component	References
Epithelium	Very scanty or relatively no extracellular matrix	[96-103]
Epitope base membrane	Type I collagen	
	Type IV collagen	
	Laminin	
	Fibronectin	
	Fibrin	
	Proteoglycans	
Bowman's membrane	Type I collagen	
	Type III collagen	
	Type IV collagen	
	Fibronectin	
Stroma	Type I collagen	
	Type III collagen	
	Type V collagen	
	Fibronectin	
	Proteoglycans	
	Elastin	
Dua's layer	Type I collagen	
	Type IV collagen	
	Type V collagen	
	Type VI collagen	
	Fibronectin	
	Proteoglycans	
Descemet's membrane	Type I collagen	
	Type IV collagen	
	Type VIII collagen	
Endothelium	Very scanty or relatively no extracellular matrix	

In the fibrillogenesis process of the cornea, the longitudinal and linear growth of collagen fibers plays an important role in ensuring the formation of the eye's structural integrity. Significantly, inhibiting the lateral growth of fibers, which prevents the formation of thick fibers, is crucial for maintaining corneal transparency.[25] Proteoglycans contribute to this process during fibrillogenesis and matrix formation. Notably, research has underscored the substantial role played by proteoglycans containing keratan sulfate and dermatan sulfate in shaping the cornea's collagen structure and organizing the matrix, thereby contributing to corneal transparency.[16,26]

The predominant portion of proteoglycans present in the corneal stroma belongs to a small family of leucine-rich proteoglycans. These proteoglycans engage in binding with collagen fibrils, profoundly influencing the arrangement of collagen fibers within the stroma. Beyond their structural role, these proteoglycans play a significant regulatory role in cell adhesion, proliferation, and migration within the cornea. Consequently, they exert influence over cellular responses during the wound-healing process.[27]

5. Artificial corneas and corneal regeneration

Artificial cornea replacement products must adhere to a myriad of specifications to closely emulate the native cornea. From a manufacturing standpoint, these artificial corneas should be cost-effective, ensuring high-quality production, and designed for ease of mass production. On the medical front, crucial prerequisites include transparency and a sufficiently porous structure that facilitates the supply of nutrients and oxygen to the surrounding tissues. In

addition, the optical properties of these products must closely align with those of the native cornea while also demonstrating resilience to withstand transplantation and mitigate the risk of eliciting autoimmune reactions from the recipient's body.

5.1. Keratoprostheses

Blindness resulting from disease or corneal damage constitutes a significant global health concern affecting millions of individuals. Corneal transplantation, or keratoplasty, stands as the primary method for addressing corneal blindness. However, the scarcity of suitable donors poses a considerable challenge in caring for affected patients. Consequently, biomimetic substitutes that emulate the cornea have gained increasing prominence.

Artificial corneas, known as keratoprostheses, are laboratory-manufactured products comprising both synthetic and biological materials. These substitutes offer many advantages, including enhanced biocompatibility that mitigates the risk of rejection. Adhering to strict manufacturing regulations ensures the sterility of keratoprostheses, minimizing the risk of infections during implantation, which could potentially lead to further corneal damage. Notably, keratoprostheses exhibit reduced light scattering owing to their unique properties.[28]

The evolution of these products over the years reflects substantial advancements. Early keratoprostheses had a more artificial effect than the current, more advanced artificial corneas. The center of the early versions of these products featured a rigid, poly(methyl methacrylate) (PMMA) optical element attached by synthetic or alternative materials. However, challenges in patient implantation arose due to potential immune responses triggered by certain materials. Research suggests that porous materials such as Teflon, poly(2-hydroxyethyl methacrylate), or Dacron (polyethylene terephthalate [PET]) facilitate the integration of implants into the host body, potentially addressing these challenges.[29]

However, these prostheses come with inherent limitations and disadvantages, partly stemming from the structure and material composition of the implants. The typical hardness and relative rigidity of these materials can induce discomfort upon implantation in the patient's eyes, potentially causing damage to the surrounding healthy tissue. Another disadvantage is the restricted vision often experienced post-keratoplasty, a consequence of the material used for implant fixation. The choice of fixation material may compromise corneal transparency. Given the implantation of artificial materials, the transplantation process becomes more complicated than allografts, with the need for two surgical procedures in many cases, thereby elevating the risk of infections.[7]

5.2. Amniotic membrane

In addition to keratoprostheses, the amniotic membrane (AM) stands out as one of the most commonly used corneal substitutes. Derived from the placenta, the amniotic membrane is typically 0.02–0.5 mm thick and devoid of blood vessels and nerves. Structurally, the AM consists of three layers: the epithelial layer, the vascular stroma, and the basement membrane. Both the basement membrane and the stroma are rich in collagen, fibronectin, and laminin. The membrane serves multifaceted functions, promoting the migration of epithelial cells, orchestrating the organization of collagen fibers, and concurrently inhibiting neovascularization and fibrosis.[30]

Several studies have explored the applicability of the amniotic membrane, including research conducted by Rohaina et al.[31] In their study, the amnion was combined with stem cells for epithelial replacement, revealing enhanced post-operative transparency of the implanted AM attributed to reduced neovascularization. These findings suggest that the AM holds promise as a corneal substitute in corneal reconstruction surgeries.

Efforts have also been directed toward enhancing the stability and durability of the membrane by incorporating additional scaffolds, often involving various nanomaterials and nanofibers. However, the use of such supporting elements introduces uncertainties, including uncontrolled degradation, tissue interaction, and potential cytotoxicity. Despite these challenges, the use of AM is not without disadvantages, encompassing limitations such as the restricted number of available donors, difficulties in isolation from the placenta, and the inherent risks of infections that could be transmitted through transplantation.[32,33]

5.3. Corneal bioscaffolds

The development of artificial tissue production has presented a new opportunity to address the shortage of cornea donors. One approach involves combining real tissue with an artificial scaffold crafted from biomaterial. In comparison to keratoprostheses, these products may offer greater ease in terms of biocompatibility. Careful consideration of the chosen scaffold material and its preparation is crucial during the planning of these substitutes to ensure resulting tissue closely mimics native tissue.[32]

Another alternative involves using decellularized corneal stroma of animal origin, providing a potential remedy for the donor shortage. The effectiveness of using these scaffolds for stroma reconstruction is heightened

when the epithelium and endothelium are well-preserved. However, animal-derived products introduce limitations and disadvantages, including the necessity for extensive donor screening to detect various pathogens.[34] An additional disadvantage lies in the potential immune response triggered by residual cellular elements within the foreign tissue, which may lead to rejection.[7] Moreover, remnants of substances used in the decellularization process, such as Triton X-100, formic acid, sodium dodecyl sulfate, and dispase, may possess toxicity post-implantation.[28] Subsequently, these stroma substitutes undergo recellularization with various cell types using diverse techniques.

The shortage of donors has spurred the development of numerous techniques to meet the demand for artificial corneas. A notable example is the porcine collagen-based cornea pioneered by Xeroudaki et al. This approach utilized highly pure, medical-grade collagen extracted from pig skin, effectively replacing a segment of the stroma in a thin layer. The outcomes of their study reveal the successful survival, proliferation, and migration of cells within this layer. The surgical procedures utilizing this method are characterized by rapid regeneration, resulting in a transparent cornea. Impressively, over the examined 6-month period, the prepared implant retained its original morphology and successfully replaced the surgically affected part of the stroma.[35]

5.4. Tissue bioprinting

3D bioprinting emerges as a potential solution to address the biocompatibility challenges associated with artificial corneas and alleviate the demand stemming from the scarcity of donors. Leveraging 3D design programs and bioprinting technologies facilitates the creation of complex shapes using a variety of materials. A key advantage of 3D bioprinting, distinguishing it from existing methods, lies in its high-quality spatial resolution and the extensive array of available hydrogel materials and compatible cell types. The flexibility of various printing techniques allows for tailored approaches, enabling the selection of the most suitable method for the specific challenge at hand. 3D bioprinting enables the precise recreation of the cornea's different layers and anatomical features. This capability ensures high-fidelity reproducibility, allowing for the creation of corneal replacements with exceptional precision and accuracy for multiple patients.[5]

In the realm of the cornea, 3D bioprinting offers the capacity to create multicellular, multi-layered structures and easily print curved surfaces. This capacity is instrumental in fulfilling the crucial requirement for artificial corneas to resemble the native tissue. Furthermore, these properties significantly contribute to both the optical and mechanical properties of the final product. 3D bioprinting not only enables the modeling of individual corneal components but also paves the way for creating multi-component systems, facilitating the comprehensive recreation of the entire cornea. The potential to generate complex systems holds significant promise for drug development and toxicological studies, offering an alternative to conventional animal models and the less effective two-dimensional cell cultures employed thus far.[7,36]

The matrix, essential for cell adhesion and proliferation during tissue printing, can be provided by either natural materials (gelatin, collagen, laminin, cellulose) or artificial polymers (poly(ethylene glycol) diacrylate [PEGDA], poly(caprolactone) [PCL], poly(ethylene glycol) [PEG]).[34,37,38] Natural polymers possess numerous advantageous properties that can be easily adapted to the specific tissue and cell type to be printed.[39] However, it is crucial during printing to select materials that do not impede the proliferation and migration of cells.[40] In the design of bioprinting, careful consideration of certain properties of the polymer—such as viscosity, gelation time, or concentration—is necessary to establish an environment conducive to the cells in contact with the printed tissue.[38,40]

One disadvantage of these polymers is their mechanical sensitivity in many cases, a limitation that can be mitigated by mixing them with other materials to improve their physical properties.[41] For example, constructs made of alginate may readily disintegrate in a calcium-free environment and dissolve in the surrounding liquid. In contrast, gelatin scaffolds exhibit sensitivity to temperature changes, softening at room temperature and liquefying at around 37°C.

In the case of natural polymers, a cross-linking agent is used to address this issue, fostering bonds between the polymer chains. Cross-linking can be achieved through physical means (UV, blue light), chemical processes (divalent cations, pH change), or biological mechanisms—with the help of enzymes. The resulting cross-linked structure forms a semi-permeable system that facilitates the permeation of metabolites, nutrients, and oxygen. This permeability is essential for sustaining cell viability and the functionality of the 3D-printed tissue.[38]

In addition, the decellularized extracellular matrix holds great potential as a natural polymer for bioprinting. In this realm, the research conducted by Kim et al.[42] provides great novelty and promising results in the development of corneal analogs. The group formulated a decellularized ECM-based hydrogel derived from corneal tissue, cross-linked with a ruthenium and sodium persulfate-containing photoinitiator.

An important property of their hydrogels is the utilization of visible light for cross-linking, thereby safeguarding cells from damage inherent in common UV cross-linking methods. Moreover, the hydrogel can undergo gelation regardless of pH conditions, facilitating easier handling. The resultant scaffold exhibited commendable physio-mechanical properties, maintaining the printed shape of the cornea. After 30 min of saline washing to eliminate the yellow color of ruthenium, the scaffold retained 94% transparency and remained transparent after 10 days. Human trabecular meshwork stem cells (hTMSCs) mixed into the corneal dECM hydrogel demonstrated 90% viability even 48 h after printing. Notably, cornea-specific gene upregulation was observed in the cells, and immunostaining revealed collagen production. Zhang et al.[43] utilized cornea-derived dECM (CECM) and GelMA-based hydrogel for DLP-printed cornea structures. *In vitro* employed human corneal fibroblasts, while *in vivo* testing utilized rabbit models. Rheological tests demonstrated excellent physio-mechanical properties of their cornea scaffold, exhibiting stability and resistance to various forces and near-complete transparency. The CECM/GelMA hydrogel exhibited only 17% water loss after 4 h of air drying compared to pure GelMA (31%). Cell viability gradually increased during the 14-day culture period, indicating cell proliferation within the hydrogel, with observed migration toward inner areas. The CECM/GelMA hydrogel provided an optimal microenvironment to the cells, leading to a gradual increase in collagen, lumican, and ALDH3A1 production, as observed through immunostaining. In an *in vivo* rabbit model, the implanted CECM/GelMA hydrogel did not induce inflammation or rejection, and increased re-epithelialization was observed around the wound, resulting in a healing rate of 93.5% at 28 days after surgery.

Another significant category of polymers applicable to tissue printing comprises synthetic polymers, often preferred over biopolymers due to their mechanical strength and non-immunogenic properties.[38,44] Typically produced through chemical reactions, these materials are transformed into hydrogels using the inverse dispersion technique.[39] However, a disadvantage of synthetic polymers is their reliance on organic solvents and high temperatures for 3D printing, potentially compromising the biological activity of cells and various active substances and factors incorporated into the hydrogels.[38,45,46] Consequently, synthetic polymers find greater utility in constructing the frames of printed structures.

6. Type of printing methods

The primary challenge in constructing complex structures lies in the necessity for scaffolds to incorporate multiple cell types. One solution to this issue is the utilization of 3D fabric printing. Currently, several 3D printing techniques are available in the market, such as methods based on inkjet, extrusion, or light. The selection among these methods hinges on the specific characteristics of the intended sample, considering both their advantages and disadvantages. Depending on the type of printer used, the scaffold or printing mold can have a positive or negative pattern, and it is even possible to print without a mold using materials with special properties, such as poloxamer (Figure 2).

6.1. Material extrusion methods

Material extrusion-based printers can be categorized into two types based on the method used to dispense the material for printing: pneumatic (utilizing compressed air) and mechanical material extrusion. In both methods, printing is executed by one or more fixed print heads positioned above a printing table movable in three dimensions (X, Y, and Z directions). Pneumatic systems may exhibit less direct control over material flow due to the delay introduced by gas volume compression. Conversely, mechanically operated systems employ a screw-controlled piston in the syringes, making them more suitable for printing high-viscosity hydrogels. Continuous material flow must be carefully maintained in both types. Hydrogels used in this technique must undergo cross-linking during or after printing, achieved through physical or chemical methods. This technique is versatile, allowing the printing of various tissues, including the cornea. Material extrusion facilitates fast and cost-effective printing. A range of starting materials, including hydrogel containing different cell types, dECM, and synthetic polymer fibers, can be used for scaffolds. However, material extrusion techniques have drawbacks. Inadequate and excessive pressure application and overly swift movement of the printing table can disrupt the continuity of the print pattern, resulting in lower resolution and slower printing speeds compared to other methods. Attention must be given to the viscosity of the hydrogel, as excessive viscous hydrogels can lead to print head clogging. Moreover, cellular viability during cellular printing using material extrusion may be lower due to the high pressure and shearing forces applied to the cells, in contrast to other techniques.[6,36,47-50]

6.2. Inkjet printing

Within the inkjet printing technique, six methods can be distinguished: piezoelectric, thermal, electrostatic, electrohydrodynamic, microvalve-based, and acoustic. Material jetting offers the advantages of computer-controlled droplet formation with high precision and resolution, enabling control over the placement

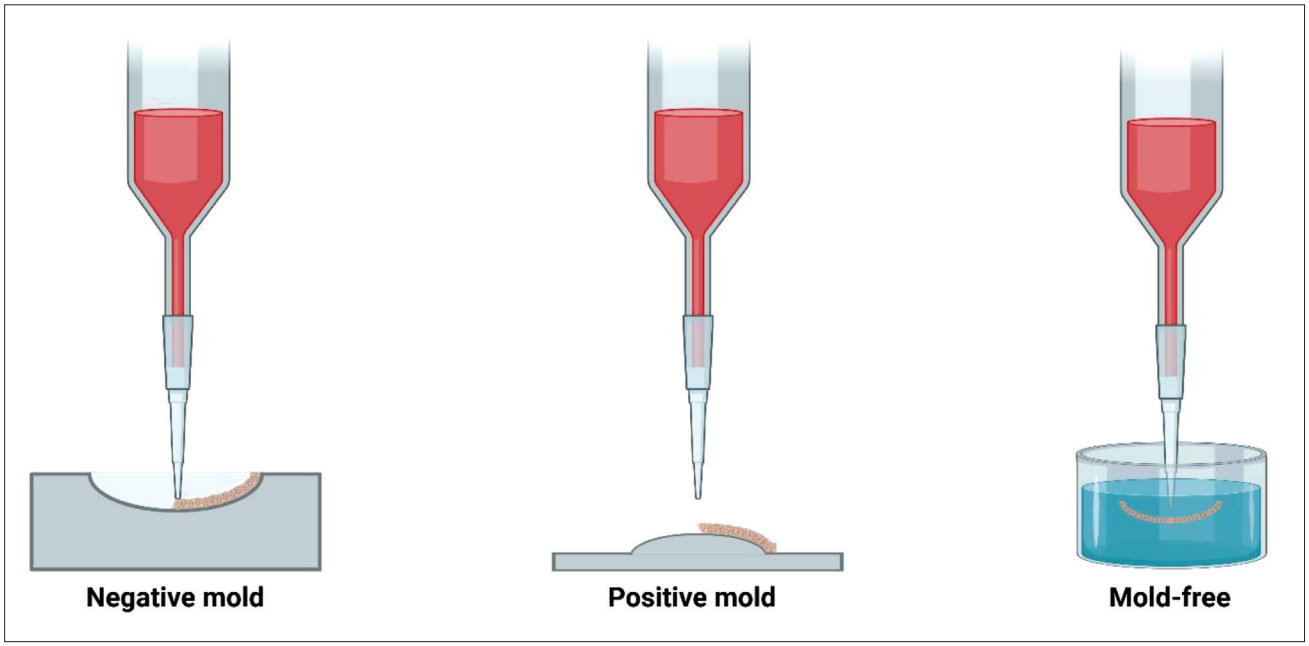

Figure 2. Types of mold used in corneal bioprinting.

of individual droplets in the scaffold. The difference among these techniques lies in the methods used for droplet production, such as a heat actuator in thermal inkjet printing, a pressure plate in electrostatic inkjet printing, and an electric field in electrohydrodynamic printing. Each technique has its drawbacks. In thermal inkjet printing, the hydrogel must be subjected to high temperatures (200–300°C) for droplet formation, which can potentially harm the cells inside the print head and inactivate biologically active proteins in the hydrogel. Maintaining appropriate viscosity is another challenge, as overly viscous materials may not form droplets effectively and can clog the print head, while excessively thin hydrogel may flow out of the print head without proper binding. Certain types of 3D printing methods may be suitable for corneal printing, such as the reactive inkjet method (RIJ) based on inkjet technology. Duffy et al.[51] utilized RIJ to construct a cornea based on poly-ε-lysine and gellan gum hydrogel. This inkjet printing method employs two print heads, each containing different components of the hydrogel. While each component is inactive on its own, their simultaneous printing on a special substrate results in binding through physical or chemical reactions *in situ*.[36,47,51-53]

6.3. Light-based methods

Among the 3D printing methods using light, two categories can be distinguished: laser-induced forward printing (LIFT) and methods based on resin polymerization. LIFT uses laser pulses—collimated, monochromatic light beams—to print individual bioink droplets. The equipment consists of a laser passing through a focusing system, heating a quartz glass plate coated with an absorption metal layer (such as gold) at a specific point. The opposite side of the plate contains a hydrogel coating. The laser induces the formation of droplets at a designated point, which then lands on a surface equipped with a receiving substrate. One advantage of this technique is the absence of print head clogging, allowing for a wide viscosity range during printing. High cell density can be achieved without compromising cell viability. However, the disadvantage is the potential introduction of particles from the metal layer into the sample during printing, and the method incurs a high material cost. This technique is applicable for printing various tissues and organs, including the cornea. Techniques based on the resin polymerization method include stereolithography (SLA), digital light processing (DLP), and two-photon polymerization (2PP). In these methods, a photoactive or light-binding bioresin is used and bound layer by layer with an LED or laser-based light source. SLA and DLP are very similar, with SLA employing a UV laser or visible light source focused on a movable platform to bind the bioresin through laser scanning. In contrast, DLP focuses the image of the pattern to be printed in the resin using a complex mirror system, allowing for the creation of entire layers at once. Two-photon polymerization is a method in which a resin molecule absorbs two photons.

This resin is composed of two special components (a positive and negative tone resin). Printing is accomplished using a femtosecond near-infrared (NIR) laser source and a glass plate situated at the bottom of the resin bath. In contrast to cellular printing, laser techniques are primarily used for scaffolds, given that the unbound resin from the printed sample is dissolved using solvents that can be harmful to cells. However, the advantage lies in the capability of these techniques to swiftly and economically produce substantial quantities of constructs.[36,52,54-57]

In addition to potentially harmful solvent and resin-based techniques, many water-soluble, less, or non-cytotoxic photoinitiators can be used in corneal bioprinting with common hydrogels. For instance, Irgacure and LAP (lithium phenyl-2,4,6-trimethylbenzoylphosphinate) are commonly used in the photocuring of acrylate and methacrylate-based hydrogels. Studies have demonstrated that a low concentration of LAP exhibits enhanced cytocompatibility and improved physio-mechanical properties in printed constructs compared to Irgacure 2959.[58] Cytotoxicity tends to escalate with the initiator concentration and exposure to cross-linking UV light.[59] Barroso et al.[60] also used LAP as a photoinitiator for printing a methacrylated silk fibroin-based bioink (SilkMA) in artificial corneal research. Their study revealed that LAP-cured SilkMA exhibited good viability, and metabolic activity increased over the 14-day observation period. The prepared hydrogel could be cured with neutral pH and low-energy UV light or through lithography-based printing. In another study, He et al.[61] prepared PEGDA-GelMA hydrogel with LAP as a photoinitiator, successfully printed with cells using the DLP method. Cells demonstrated proliferation in the hydrogel 6 days after printing with approximately 90% viability. Additionally, numerous photoinitiators can facilitate cross-linking via visible light, such as Eosin Y, riboflavin, or ruthenium (as mentioned in Zhang et al.[43]). These methods represent viable alternatives in light-based bioprinting with high biocompatibility, as measured using MTT or Live/Dead assay.[58]

7. Hydrogels and scaffolds for corneal bioprinting

7.1. Alginic acid

Alginic acid, commonly known as alginate, is a polysaccharide extracted from brown algae. Its versatile applications extend across industries, including textiles, pharmaceuticals, and food, where it serves as a thickener, gelling agent, and emulsifier marked as E400. Another common form is sodium alginate, the sodium salt of alginic acid. Cross-linking of alginate is typically achieved with divalent cations such as calcium (Ca^{2+}), magnesium (Mg^{2+}), or barium (Ba^{2+}). This binding method allows reversible cross-linking, as the cations are released from the cross-linked alginate in a cross-linker-free environment. In addition to cationic cross-linking, alginic acid exhibits excellent cross-linking through enzymatic and photoactive compounds. While alginate-bound cells can be efficiently recovered, and cells remain viable for weeks in alginate scaffolds, there are disadvantages. Cells enclosed in alginate hydrogel tend to maintain a spherical shape due to encapsulation, and they may exhibit lower proliferation and differentiation rates.[38,44,62]

7.2. Gelatin

Gelatin, derived from collagen through the partial hydrolysis of its tertiary structure, is a protein that originates from various sources, such as pork, calf, or fish, each with slightly different properties. Gelatin-based hydrogels are renowned for their excellent biocompatibility and biodegradability, making them a commonly used hydrogel component in 3D printing. Gelatin-based hydrogels maintain cell viability and differentiation potential, which are important factors when working with stem cells. One disadvantage of using gelatin lies in its thermosensitive property, wherein its cross-linked structure becomes unstable and liquefies under physiological conditions above 20°C, such as the standard human body temperature of 37°C.[38,44] To address this, improving the mechanical properties of gelatin-based hydrogels is necessary and can be achieved by incorporating other polymers, such as chitosan, collagen, or alginate, into the gelatin matrix.[38,63] Alternatively, chemical modifications on gelatin, such as methacrylation, result in the formation of gelatin methacrylamide (GelMA). The addition of a photoinitiator to GelMA allows photopolymerized using UV light.[64]

7.3. Collagen

Collagen, an important component of ECM, is widely used in clinical settings as a tissue replacement and regenerative material, as well as in 3D bioprinting due to its excellent mechanical and degradable properties. This ECM protein is abundantly present in the connective tissues of many organisms, with the primary sources for laboratory uses being animals like calves, pigs (skin and bone), or marine animals.[65]

In the context of tissue printing, collagen stands out as an excellent hydrogel material due to its scaffold structure. The porous structure of collagen facilitates the diffusion

of nutrients and growth factors within the hydrogel.[66] Its degradation characteristics are contingent on chemical and thermal conditions: for instance, it resists dissolution in acidic solvents (e.g., acetic acid) and maintains stability when stored at a low temperature (2–8°C). Under physiological conditions, preventing fibrillogenesis (neutralized pH, 37°C) ensures gel formation occurs within hours. Despite its numerous advantages, collagen does have notable disadvantages, including low stiffness and short duration of maintained stability.[62]

However, the utilization of animal-derived collagens in humans carries the risk of provoking unwanted immune responses, which, in some cases, can be severe. In addition, the use of collagens sourced from various tissues poses a potential risk of transmitting infections and pathogens.[67] In an experiment conducted by Cooperman and Michaeli on volunteers, employing high-purity dermal calf collagen resulted in side effects in 3% of patients (2 out of 61), highlighting the immunogenic nature of animal-derived proteins.[68] To address this, recombinant collagens present a viable solution. Various host organisms, such as mammalian cells, yeasts, and bacteria (e.g., *Escherichia coli*), are suitable for collagen production, each capable of producing collagen in different quantities. Notably, hydroxylated full-length collagen can only be produced with transfected mammalian cells. Nonetheless, it is completely equivalent to tissue collagen.[69]

7.4. Hyaluronic acid

Hyaluronic acid (HA) is a naturally occurring glycosaminoglycan, characterized by the repetition of disaccharide units (glucuronate and N-acetylglucosamine). For applications in tissue printing, HA can undergo chemical modifications, resulting in derivatives such as sodium hyaluronate, tyramine-substituted HA, and thiolated hyaluronic acid.[62] Found in various tissues (e.g., skin, cartilage), HA serves as an excellent scaffold in bioprinting.[32] The development of stable HA hydrogels can be achieved through cross-linking with hydrazone, employing a two-component system that promotes rapid gel formation and embeds cells within the hydrogel matrix. In the context of cornea, HA promotes cell migration and tissue regeneration.[70,71]

7.5. Other materials

Silk fibrin, a high-molecular-weight substance derived from the cocoon of the *Bombyx mori* silkworm, exhibits low immunogenicity, favorable mechanical properties, and a controllable degradation rate. The incorporation of this material into hydrogels improves the mechanical properties of scaffolds, a critical requirement for a corneal scaffold. This augmentation promotes stromal cell proliferation while maintaining the transparency of the printed pattern. The application of silk fibrin in 3D bioprinting and cornea reconstruction has been extensively explored by researchers. Investigations into combining silk fibrin with other materials, such as PEG or RGD peptides, have been conducted to enhance cell adhesion. The outcomes of these studies consistently reveal an enhancement in the adhesion of specific cell types.[30,32,72,73]

Chitosan, an amino polysaccharide derived from chitin found in shellfish, insects, and fungi, stands as a widely used natural biopolymer with numerous positive attributes, such as biocompatibility or biodegradability. These characteristics make it well-suited for applications in wound healing and 3D bioprinting. The stability of chitosan can be enhanced through cross-linking; without this process, chitosan would undergo rapid degradation, particularly under acidic pH conditions.[39,65,74] The incorporation of chitosan into scaffolds promotes cell adhesion, proliferation, and differentiation, and remarkably, only minor rejection incidents were observed post-transplantation.[75]

Fibronectin is a multi-domain glycoprotein capable of binding to numerous ECM components, playing an important role in establishing the cell–ECM connection through cell surface integrins. Synthesized by diverse cell types, fibronectin has significant involvement in various physiological processes, including blood clot formation and the regulation of cell migration. Moreover, its contributions extend to embryonic development and tissue regeneration.[39,76]

A key component of the lamina basalis, laminin, forms a thin, sheet-like structure through a heterotrimer comprising α, β, and γ polypeptide chains. These polypeptides, structurally arranged in a cross-shaped configuration connected by disulfide bonds, contribute to lamini's vital roles in cellular processes such as adhesion, migration, and differentiation.[39,76,77]

7.6. Combined materials for enhanced properties

Beyond various standalone hydrogel and scaffold materials, composite hydrogels offer the unique benefit of combining and enhancing the desirable properties of multiple components. This allows for tailoring physical and mechanical properties such as water retention, flexibility, and optical properties to a greater extent. Notably, chitosan serves as an excellent hydrogel base material due to its biocompatibility, solubility, antimicrobial properties, and biodegradability. However, its standalone mechanical properties often fell short. Tayebi et al.[78] addressed this limitation by incorporating chitosan nanoparticles into

composite membranes alongside chitosan and PCL. The resulting hydrated membranes exhibited increased flexibility and ease of handling, with the 50% nanoparticles and 25% PCL composition demonstrating near transparency comparable to the acellular stroma.

In an effort to improve the properties of chitosan, Ulag et al.[79] incorporated polyvinyl alcohol (PVA), a widely-used synthetic polymer in biomedicine that is known for its utility as a carrier material due to its physio-mechanical properties. Employing an aluminum mold shaped like a cornea, the hydrogel was printed using the extrusion method without the use of a cross-linking material. Although the prepared composite gel was completely transparent, measured transmittance indicated values between 49% and 56%. Importantly, the scaffold perfectly retained the shape of the cornea post-printing. Chen et al.[80] developed a composite hydrogel using type 1 collagen, chitosan, and sodium hyaluronate (NaHA). The study explored the effect of the ratio of individual components on transmittance and water content within the prepared hydrogels. Notably, the hydrogels containing 0.5 and 0.9 (wt)% NaHA exhibited a transmittance of 95%. *In vitro* cytocompatibility studies and *in vivo* rabbit experiments revealed that the hydrogel composed of 20% collagen, 10% chitosan, and 0.5% NaHA proved to be the most efficacious, maintaining transparency even 5 months post-implantation.

8. Stem cells in cornea bioprinting

There are two main categories of stem cells: embryonic stem cells (ESCs) and adult stem cells. In addition, induced pluripotent stem cells (iPSCs) represent another category created through the dedifferentiation of somatic cells.[81] Adult stem cells include mesenchymal stem cells, which can be sourced from diverse tissues such as corneal stroma (CS-MSC), bone marrow (BM-MSC), adipose tissue (AD-MSC), umbilical cord (UC-MSC), placenta (P-MSC), and dental pulp.[82] Mesenchymal stem cells exhibit the ability to differentiate into multiple cell types under *in vitro* conditions, such as adipocytes, chondrocytes, osteocytes, and cardiomyocytes. These cells, characterized by exceptionally high immune tolerance and the capacity to exert an anti-inflammatory effect through their immunomodulation function, find application in allografts. This usage serves to reduce the likelihood of rejection and contributes to expedited wound healing.[83,84]

The use of stem cells in bioprinting stands as a widespread practice in regenerative medicine research, facilitating the production of various implants and tissue models[85] (Figure 3). The 3D printing technique orchestrates the arrangement of cells, multiple factors, and active substances into complex 3D structures. The construction of the scaffolds involves three main steps. Firstly, data pertaining to the organs and tissues slated for printing are collected to facilitate the selection of appropriate models and materials. Secondly, a computer model is generated based on this data, and the corresponding printing code is written. The final step involves the physical construction of the structure through 3D printing.[86]

During the design and material selection phases, an important consideration is ensuring that the bioprinted scaffold effectively provides the appropriate supply of nutrients and oxygen for the diverse cell types encapsulated within the hydrogel.

These bioprinted tissue models serve as valuable tools in elucidating the behavior of immobilized stem cells within different matrix materials. Examining cell functions post-bioprinting yields invaluable insights into the impact of processes during 3D printing on cellular behavior. A comprehensive understanding of these dynamics is essential not only for the success of future bioprinting endeavors but also for their widespread applications.[87]

9. Pre-clinical and clinical studies with bioprinted cornea

Many clinical solutions are currently available to restore the epithelial layer of the cornea, and it is even possible to replace the endothelial layer through endothelial keratoplasty (e.g., Descemet stripping endothelial keratoplasty [DSEK]).[88] However, only three therapies exist for replacing the stroma, which constitutes about 90% of the cornea. These options include the transplantation of the entire cornea from a human donor (penetrating keratoplasty), the partial transplantation of the stroma in a deeper layer (deep anterior lamellar keratoplasty), or the transplantation in a less deep layer (anterior lamellar keratoplasty)[89] (Figure 4). However, these surgical solutions pose a considerable risk of scarring, rejection, and infection.

In recent years, owing to technological advancements, numerous new techniques have been explored in the quest to develop corneal substitutes, among which 3D printing has emerged as a notable contender. The advent of 3D printing introduces possibilities for regenerative medicine and drug testing. Consequently, the growing interest in personalized medicine finds additional avenues, positioning itself as an excellent model for research. The application of this technology in ophthalmic contexts holds promise for advancing clinical practices, enriching medical education, and presenting a cost-effective solution for corneal transplants.[90]

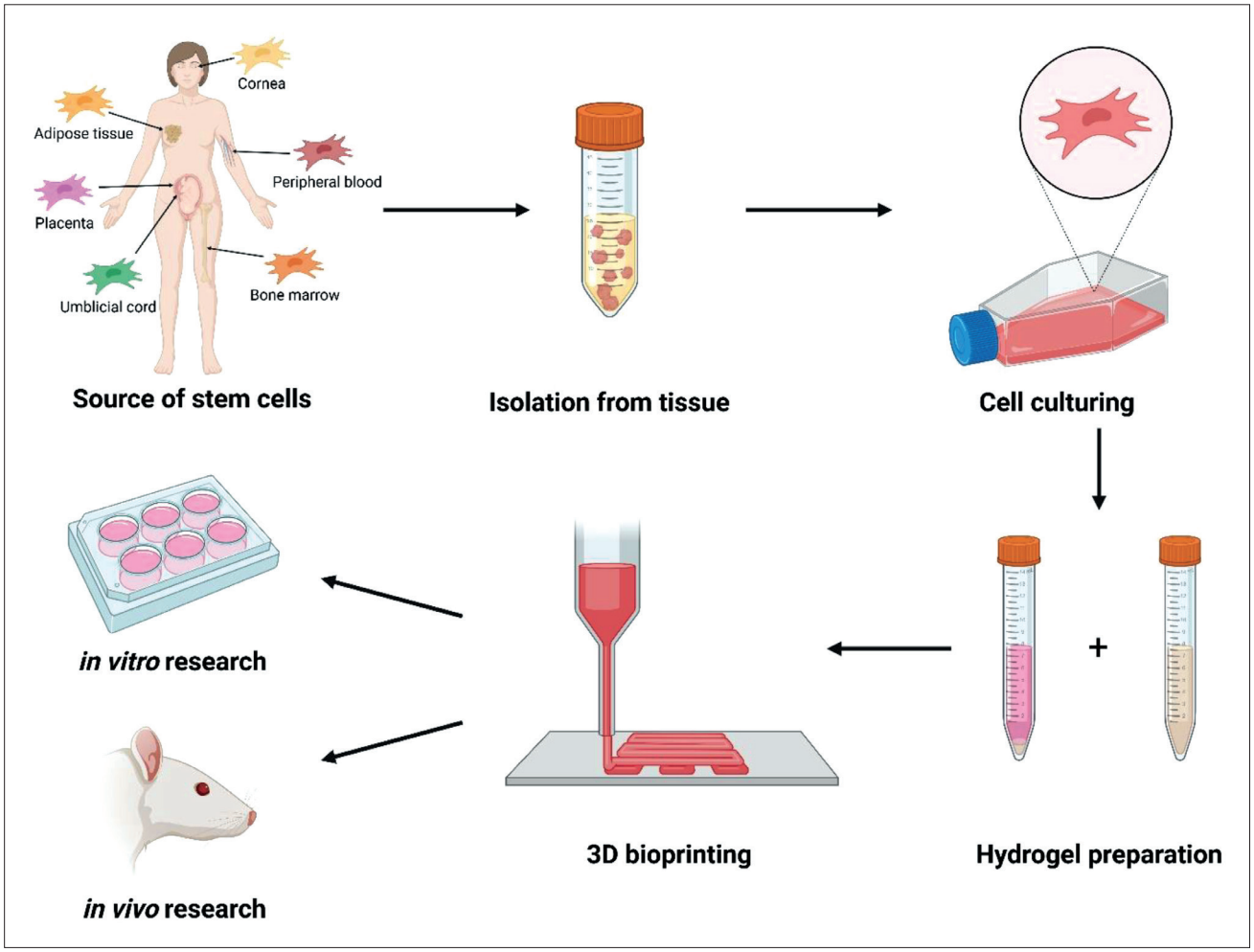

Figure 3. Stem cells in bioprinting: the processes from isolation to research experiments.

In this context, however, a method for the clinical replacement of the stroma with bioprinted artificial cornea substitutes remains elusive. A substantial portion of the current research is situated within the phases of *in vitro* studies and *in vivo* animal experiments, with only a handful of methodologies progressing to the clinical trial phase. Throughout these investigations, the overarching objective is to create a viable cornea capable of replacing either the cornea organ or specific components thereof[91] (Table 2). The integration of 3D bioprinting, coupled with the biotinylation of individual matrix components (such as fibronectin), has gained prominence in research endeavors. These techniques aim to fabricate implants that closely mimic native tissue.[92] Notably, several research groups have achieved success in generating 3D bioprinted constructs, marking a significant stride toward the development of products applicable to corneal reconstruction (Table 3).

For example, Isaacson et al. successfully applied 3D printing to fabricate a stroma with a scaffold composed of biotin-containing sodium alginate and methacrylated type I collagen.[6] In the study, they utilized extrusion-based bioprinting to craft the artificial stroma, embedding human keratocyte cells in an alginate/methacrylated type I collagen hydrogel for their 3D-printed construct.[6] In another study, Sorkio et al. explored the utilization of biotinylated human and recombinant materials for constructing artificial corneas. Employing human embryonic stem cell-derived limbal epithelial stem cells (hESC-LESCs) and human adipose tissue-derived stem cells (hASCs), they utilized laser-assisted bioprinting (LASP) to create an artificial cornea model. The hydrogel matrix for hESC-LESCs comprised human recombinant laminin and type I collagen, while for hASCs, a hydrogel consisting of type 1 collagen, EDTA, thrombin, and plasma was employed. While the results from their artificial cornea

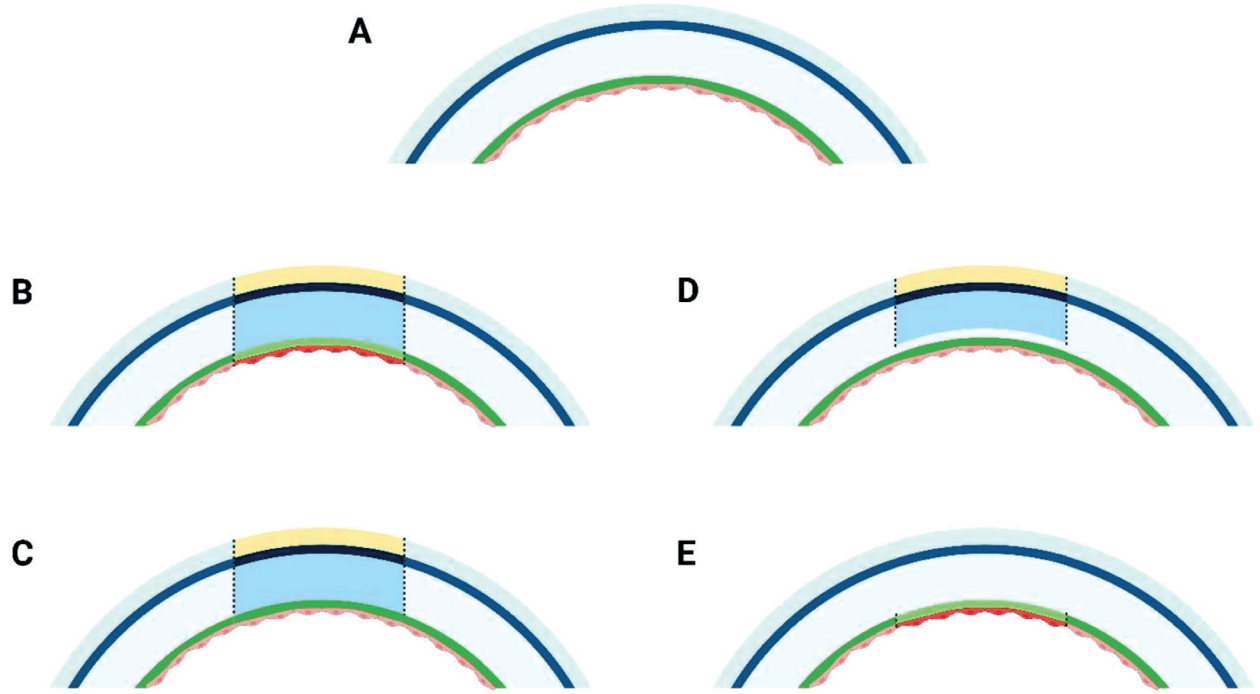

Figure 4. Types of keratoplasty. (A) Structure of healthy cornea, (B) penetrating keratoplasty, (C) deep anterior lamellar keratoplasty, (D) anterior lamellar keratoplasty, and (E) Descemet stripping endothelial keratoplasty.

model are very promising, further functional studies are imperative.[57] Alternatively, Campos et al. utilized inkjet-based bioprinting to create a stroma-like construct from a hydrogel containing type I collagen/agarose and human keratocytes.[93]

Goran et al. employed human BM-MSCs, AD-MSCs, and CS-MSCs in their investigation of corneal replacement. The potential of femtosecond laser-assisted intrastromal keratoplasty using 3D-printed constructs was also explored, using porcine eyes as a model. Alginate-nanocellulose hydrogel, with or without the addition of type 1 collagen, served as the matrix. Individual MSC hydrogels were printed through an extrusion-based method and cultured *in vitro* for 14 days. The viability of cells within the fabricated constructs was assessed through Live/Dead staining, PrestoBlue assay, lactate dehydrogenase (LDH) cytotoxicity test, and immunostaining. Additionally, the physio-mechanical properties of the artificial cornea were examined. Notably, the cells demonstrated resilience during the bioprinting process, and they exhibited the ability to produce ECM and other biomolecules, such as pigment epithelium-derived factor (PEDF). The findings from the study hold significant implications for the advancement of 3D-bioprinted corneas and their potential clinical applications.[94]

10. Future perspectives

Considering the substantial clinical unmet medical need, there exists a high probability that an artificial cornea produced using 3D bioprinting will be among the first to receive approval from regulatory bodies such as the Food and Drug Administration (FDA) or European Medicines Agency (EMA). The technological background is secure, and notably, unlike other tissues and organs, the cornea lacks blood vessels, thereby reducing the engineering and technological challenge. However, achieving optical perfection is paramount for vision improvement, necessitating a tissue that can sustain and regenerate itself over the long term, making cellular components a primary focus. Addressing this focus presents a significant challenge, notably in ensuring sufficient cellular resources for autologous procedures. The scarcity of donor numbers exacerbates this challenge. In regions with inadequate donor availability, 3D printing technology emerges as a viable alternative, even if economically costlier than utilizing a cadaver cornea. Given the trends observed in recent years, it is anticipated that the cost of a 3D tissue-printed cornea will soon align with or even surpass the economic feasibility of traditional alternatives, providing a considerable stimulus to this field. However, it is crucial

Table 2. Tissue engineering approaches for corneal replacement

Corneal replacement	Clinical status	Biopolymer used	Results	References
Full thickness cornea	*In vitro* study and *in vivo* experiment on rabbit	Acellular porcine cornea	Fully transparent; suture retention (5 Newton) near to NPC (6 Newton); tier resistance (3.42 Newton) lower than NPC (5.35 Newton); cell-loaded APC repaired alkali corneal burn on rabbit	[91,104]
Full thickness cornea	Animal model: pig	Collagen-chitosan hydrogels	Fully transparent after transplantation; visible light transmittance (>90%) better than native human cornea (~80%); light scatter lower than the human cornea; 100% suturable	[91,105]
Full thickness cornea	*In vitro* study	Fibrin-agarose hydrogels	Different cells proliferate in hydrogel; epithelial cells formed normal, several-layer epithelia; high expression of vimentin and cytokeratin; similar structure to the native cornea by SEM	[91,106]
Full thickness cornea	Phase I clinical trial: human	Cross-linked recombinant human type III collagen	10 patients (8 male, 2 female); 500 μm thick biosynthetic corneal scaffold; sutures were removed 6.5 weeks after implantation; no pain or discomfort; complete epithelization in about 2.5 months	[91,107]
	4 years of follow-up		Optical clarity was higher (95.1%) than human cornea (>87%); water content 91.5% (cornea: 78%); no significant biodegradation; mechanical strength was lower than the cornea; tensile strength: 0.286 MPa (cornea: 3.81 MPa); modulus: 1.749 MPa (cornea: 3–13 MPa); only 1 rejection was reported	[91,108]
Epithelial tissue	*In vitro* study and Clinical study with 4 human patients	Heat-sensitive cell culture for tissue-engineered oral mucosal epithelial cell sheets	Directly transplantation without suture; re-epithelization within 1 week; transparent during 14-month follow-up; no complication	[91,109]
	Animal model: rabbit	Automated cell culture system for epithelial sheet scaffold preparation	Cell viability 93.6%, growth in multilayer; culturing time: 2 weeks; 10 times medium change with an automated system; fully transparent sheet 1 week after transplantation; no adverse effect	[91,110]
Epithelial tissue	*In vitro* study	Silk foil with pattern	Silk produced by *Bombyx mori* on a patterned silicon layer; HCLEs had better culturing conditions on silk sheets; better vinculin and actin production	[91,111]
Epithelial tissue	*In vitro* study	Rat-tail Type I collagen hydrogel	Cells seeded on cell-loaded hydrogel with crypted surface; cells were able to proliferate; 7 layers produced by cells; different epithelial markers expressed	[91,112]
Epithelial tissue	*In vitro* study	Rat-tail Type I collagen hydrogel	Cell-embedded in compressed collagen hydrogel; morphology similar to the amniotic membrane observed with SEM; the gel was mechanically dense and strong; the peripheral region showed more proliferative capacity than the central; higher cytokeratin and collagen expression than on amniotic membrane	[91,113]
Epithelial tissue	*In vitro* study	Chemically cross-linked collagen hydrogel	80–90% transmittance of dendrimer cross-linked collagen; modulus: 1.4–5.3 MPa (in the range of natural human cornea); cells proliferated in hydrogel and remained viable	[91,114]

(Continued)

Table 2. *(Continued)*

Epithelium and anterior stroma	Animal model: pig	Collagen-copolymer	Robust, suturable scaffold; refractive index: 1.343 (human tier film: 1.336); optically clear; good glucose permeability; intraocular pressure after surgery: 10–16 Hgmm (10–13 Hgmm before surgery)	[91,115]
Epithelium and anterior stroma	Animal model: pig	Cross-linked recombinant human Type I and Type III collagen	Type III collagen gels were more transparent (87–92%) than human cornea (87%) depending on cross-linker concentration; refractive index (1.3451 to 1.3552) lower than human cornea (1.373 to 1.380); fully biocompatible *in vitro*; promoted regeneration of cells and nerves *in vivo*	[91,116]
Stroma	*In vitro* study	Magnetically oriented collagen/proteoglycan hydrogels	Oriented collagen sheets prepared HDFs colonized the gel successfully; collagen concentration (2 mg/mL) was very low compared to native cornea; concentrated scaffold was not transparent but was improved by proteoglycans; cells could align to the orientation of collagen gel	[91,117]
		Magnetically oriented Rat tail type I collagen	Non-cytotoxic; cells could penetrate and remodel scaffold; cells in gel had aligned multilayered structures; cells produce collagen in the matrix but degrade the original scaffold	[91,118]
Stroma	*In vitro* study	Bovine collagen film	Scaffold size showed a 10% decrease during 4 weeks of culture; fibroblast cells flattened after 1 week of culturing on film and formed multilayer; cells penetrated the film itself; surface roughness: 0.987 nm (cornea: 1.197 nm)	[91,119]
Stroma	*In vitro* and *in vivo* study	Gelatin hydrogels	4-week follow-up; *in vivo*, cells expressed more vimentin than *in vitro*; precursor in gel had better results on collagen and vimentin expression; gelatin in gel promotes only ECM production; ECM and vimentin production arise from host species, not from transplanted cells	[91,120]
Stroma	*In vitro* study	Surface patterned silk foil	Silk film was fully transparent; cells aligned to the circular pattern of silk film; proliferation was lower than on TCP; cell density was higher on patterned silk than on flat silk film; high expression of type V collagen and vimentin; films stackable to create 3D structures	[73,91]
Stroma	*In vitro* study	Silk foil with porous and patterned surface	RGD functionalized silk films; cells do not grow to confluent without RGD; cell morphology was more elongated on the patterned surface; cells proliferate more on patterned/porous silk film with RGD RGD content results in stronger expression of ECM; stacked silk films had good transparency	[91,121,122]
Endothelium	*In vitro* and *in vivo* study on cat model	Decellularized amniotic membrane	Cells formed a confluent monolayer on dAC; dAC and cell-loaded dAC were transplanted into cats; inflammation in the cell-loaded group decreased more; cell-loaded dAC group had less or no opaque cornea; cell morphology on dAC was similar to normal culture	[91,123]

(Continued)

Table 2. *(Continued)*

Endothelium	*In vitro* and *in vivo* experiments on rabbit model	Decellularized human Descemet's membrane	HCECs seeded on decellularized membrane; cell morphology and structure were similar to normal cornea; different grafting methods examined in *ex vivo*; transparency and edema healed better in cell-loaded membranes *in vivo*; the preserved sclerocorneal button is not suitable for grafting; younger cell donors are better for cell loading	[91,124]
Endothelium	*In vitro* study	Gelatin hydrogel	The gelatin hydrogel sheet had almost 100% transparency; tensile strength: 2–3.5 MPa (depending on cross-linking time); good diffusion properties for cell carrier application; morphology of HCECs on gelatin sheet similar to *in vivo*	[91,125]
Endothelium	*In vitro* study	Dense collagen hydrogel	Easy handle acellular RAFTs; HCECs formed a monolayer on RAFT; high viability over 14 days; immunostaining showed that cells keep their functional phenotype	[91,126]

Abbreviations: APC: acellular porcine cornea; dAC: decellularized amniotic membrane; ECM: extracellular matrix, HCLEs: human corneal-limbal epithelial cells; HCECs: human corneal endothelial cells; HDF: human dermal fibroblast; NPC: nature porcine cornea; RAFT: Real Architecture For 3D Tissues; RGD: arginyl-glycyl-aspartic acid; SEM: scanning electron microscopy; TCP: tissue culture plastic.

Table 3. Established 3D-bioprinted constructs until 2023

Corneal layer	Bioink	Printing technique	Cell type	**Result**	***In vivo* results**	**Reference**
Epithelial tissue	Methacrylated gelatin bioink; methacrylated gelatin in the form of a dome	Extrusion	Human corneal epithelial cells	Transparent gel	No data	[127,128]
	Sodium alginate, gelatin, and type I collagen	Extrusion	Human corneal epithelial cells	Good transparency, high cell viability after bioprinting, Production of degradation-controllable systems using sodium citrate	No	[50,90]
Stroma	Methacrylate gelatin bioink	Extrusion	Human corneal stromal keratocytes	High mechanical strength, good transparency, low metabolic activity of cells	No	[90,127,129]
	Alginate type I collagen bioink	Extrusion	Human corneal stromal keratocytes	Transparent gel, high cell viability after plucking. Creation of optimal curvature	No	[6,90,127]
	Methacrylated gelatin bioink, reinforced with PEG-PCL fibers	Extrusion	Rat limbal stromal stem cells	Cell viability is good after printing, and the construction is transparent.	No data	[127,130]
	Type I collagen and agarose bioink	Drop-on-demand	Human corneal stromal keratocytes	Transparent gel	No	[90,93,127]
	Matrigel Type I collagen bioink; Laminin-type IV collagen on a carrier base	Laser	Human limbal epithelial cells + adipose-derived stem cells	Highly transparent, high cell viability	No	[57,90,127]

(Continued)

Table 3. *(Continued)*

Stroma	Corneal origin decellularizes ECM bioink	Extrusion	Turbinate-derived mesenchymal stem cells by keratocyte induction	Good transparency, keratocytes activated after transplantation	Rabbit	[90,127,131,132]
	Alginate-nanocellulose-type I collagen hydrogel	Extrusion	Human adipose tissue-, bone marrow-, and corneal stroma-derived mesenchymal stem cells	Good transparency, High viability, ECM production	No	[94]
Endothelium	Gelatin-RGD bioink; amniotic membrane decellularizes ECM	Extrusion	Human corneal endothelial cells	No data	Rabbit	[90,127,133]

Abbreviations: ECM: extracellular matrix; PCL: poly(caprolactone); PEG: poly(ethylene glycol); RGD: arginyl-glycyl-aspartic acid.

to acknowledge the overarching challenge that currently there are no medical devices or Good Manufacturing Practice (GMP)-certified tissue printers capable of mass-producing artificial tissues with the requisite clinical and therapeutic quality. Consequently, only a fraction of the localized and personalized therapeutic needs are presently met. These challenges underscore the need for continued advancements in technology and regulatory frameworks to fully realize the potential of 3D bioprinting in meeting broader clinical demands for corneal regeneration.

11. Conclusion

Studies revealed that 3D bioprinting holds significant promise in advancing regenerative medicine research. Among the myriad printing techniques available, extrusion processes predominate in research owing to their relative cost-effectiveness. However, despite notable progress, tissue printing with 3D bioprinting remains in its nascent phases. While the majority of research focuses on developing stromal substitutes, promising results are also emerging in the reconstruction of the epithelial and endothelial layers.

Materials utilized in bioprinting must meet stringent criteria, encompassing bifunctionality, stability, and the ability to foster appropriate biochemical and physiological interactions with cells. Equally critical is the requirement that these materials do not induce autoimmune reactions in the body. Frequently, 3D-printed cornea analogs are limited to using only one or two cell types and can successfully print in only one or two layers. Consequently, artificial corneas fall short of wholly resembling native tissue. An additional important consideration before clinical application revolves around the challenges of vascularization and the implantation of artificially produced tissue.[95] These issues are pervasive not only in artificial corneas but also in the exploration of other tissue types and organs using 3D printing, such as the skin or liver, underscoring the complexity of the field.[36,39]

To date, stem cells or progenitor cells are the most commonly utilized cell types in research, primarily due to their expansive differentiation potential and wound-healing capabilities. The immunomodulation effect exhibited by these cells further positions them to potentially mitigate inflammation during transplantation.

The future commercialization of 3D-bioprinted tissues necessitates the consideration of additional criteria, including the control of production processes, standardization of protocols, cost-effectiveness, and the logistics of manufactured products. For biological products, challenges related to storage and potential ethical considerations await resolution. However, ongoing research, in parallel with the development of 3D-bioprinted tissues *in vitro* and further investigations into *in vivo* applications, will collectively contribute to the advancement of 3D bioprinting for clinical use.[90]

Acknowledgments

All figures were generated using Biorender (www.app.biorender.com).

Funding

This work was supported by the National Research, Development, and Innovation Office (NKFI PD 132570, awarded to Z.V.). Z.V. was also the recipient of the Bolyai János Postdoctoral Fellowship (BO/00190/20/5), funded by the New National Excellence Program of the Hungarian Ministry for Innovation and Technology through the National Research Development and Innovation Fund. Projects TKP2021-EGA-28 and TKP2021-EGA-32 were carried out with support from the Ministry of Innovation

and Technology of Hungary through the National Research, Development and Innovation Fund, financed under the TKP2021-EGA funding scheme. The funders played no role in study design, data collection, analysis, publishing decisions, or manuscript preparation.

Conflict of interest

The authors declare no conflicts of interest.

Author contributions

Conceptualization: Tamás Monostori, Zoltán Veréb
Funding acquisition: Zoltán Veréb
Supervision: Zoltán Veréb
Writing – original draft: Tamás Monostori
Writing – review & editing: Diána Szűcs, Borbála Lovászi, Lajos Kemény, Zoltán Veréb

Ethics approval and consent to participate

Not applicable.

Consent for publication

Not applicable.

Availability of data

Not applicable.

References

1. Zare M, Javadi MA, Einollahi B, et al. Changing indications and surgical techniques for corneal transplantation between 2004 and 2009 at a tertiary referral center. *Middle East Afr J Ophthalmol*. 2012;19(3):323-329. doi: 10.4103/0974-9233.97941
2. Pandey AK, Mudgil N, Wadgave Y, Mishra SS. Corneal transplantation during COVID-19 pandemic: need for special considerations-A live review. *AIMS Public Health*. 2021;8(2):186-195. doi: 10.3934/publichealth.2021014
3. Gaum L, Reynolds I, Jones MN, Clarkson AJ, Gillan HL, Kaye SB. Tissue and corneal donation and transplantation in the UK. *Br J Anaesth*. 2012;108(Suppl 1): i43-47. doi: 10.1093/bja/aer398
4. Hatou S, Shimmura S. Review: corneal endothelial cell derivation methods from ES/iPS cells. *Inflamm Regen*. 2019;39:19. doi: 10.1186/s41232-019-0108-y
5. Orash Mahmoud Salehi A, Heidari-Keshel S, Poursamar SA, et al. Bioprinted membranes for corneal tissue engineering: a review. *Pharmaceutics*. 2022;14(12):2797. doi: 10.3390/pharmaceutics14122797
6. Isaacson A, Swioklo S, Connon CJ. 3D bioprinting of a corneal stroma equivalent. *Exp Eye Res*. 2018;173:188-193. doi: 10.1016/j.exer.2018.05.010
7. Zhang B, Xue Q, Li J, et al. 3D bioprinting for artificial cornea: challenges and perspectives. *Med Eng Phys*. 2019;71: 68-78. doi: 10.1016/j.medengphy.2019.05.002
8. Sridhar MS,. Anatomy of cornea and ocular surface. *Indian J Ophthalmol*. 2018;66(2):190-194. doi: 10.4103/ijo.IJO_646_17
9. Meek KM, Knupp C. Corneal structure and transparency. *Prog Retin Eye Res*. 2015;49:1-16. doi: 10.1016/j.preteyeres.2015.07.001
10. Mobaraki M, Soltani M, Zare Harofte S, et al. Biodegradable nanoparticle for cornea drug delivery: focus review. *Pharmaceutics*. 2020;12(12). doi: 10.3390/pharmaceutics12121232
11. Dua HS, Faraj LA, Branch MJ, et al. The collagen matrix of the human trabecular meshwork is an extension of the novel pre-Descemet's layer (Dua's layer). *Br J Ophthalmol*. 2014;98(5):691-697. doi: 10.1136/bjophthalmol-2013-304593
12. Ruan Y, Jiang SB, Musayeva A, Pfeiffer N, Gericke A. Corneal epithelial stem cells-physiology, pathophysiology and therapeutic options. *Cells*. 2021;10(9). doi: 10.3390/cells10092302
13. Secker GA, Daniels JT. Limbal epithelial stem cells of the cornea. In: Melton D, Cowan CA, eds. *StemBook*. Cambridge (MA): Harvard Stem Cell Institute; 2008. doi: 10.3824/stembook.1.48.1
14. Collin HB, Ratcliffe J, Collin SP. The functional anatomy of the cornea and anterior chamber in lampreys: insights from the pouched lamprey, Geotria australis (Geotriidae, Agnatha). *Front Neuroanat*. 2021;15:786729. doi: 10.3389/fnana.2021.786729
15. West-Mays JA, Dwivedi DJ. The keratocyte: corneal stromal cell with variable repair phenotypes. *Int J Biochem Cell Biol*. 2006;38(10):1625-1631. doi: 10.1016/j.biocel.2006.03.010
16. Massoudi D, Malecaze F, Galiacy SD. Collagens and proteoglycans of the cornea: importance in transparency and visual disorders. *Cell Tissue Res*. 2016;363(2):337-349. doi: 10.1007/s00441-015-2233-5
17. Zavala J, Lopez Jaime GR, Rodriguez Barrientos CA, Valdez-Garcia J. Corneal endothelium: developmental strategies for regeneration. *Eye (Lond)*. 2013;27(5):579-588. doi: 10.1038/eye.2013.15
18. Sie NM, Yam GH, Soh YQ, et al. Regenerative capacity of the corneal transition zone for endothelial cell therapy. *Stem Cell Res Ther*. 2020;11(1):523. doi: 10.1186/s13287-020-02046-2

19. Saghizadeh M, Kramerov AA, Svendsen CN, Ljubimov AV. Concise review: stem cells for corneal wound healing. *Stem Cells*. 2017;35(10):2105-2114. doi: 10.1002/stem.2667

20. Hertsenberg AJ, Shojaati G, Funderburgh ML, Mann MM, Du Y, Funderburgh JL. Corneal stromal stem cells reduce corneal scarring by mediating neutrophil infiltration after wounding. *PLoS One*. 2017;12(3):e0171712. doi: 10.1371/journal.pone.0171712

21. Hertsenberg AJ, Funderburgh JL. Stem cells in the cornea. *Prog Mol Biol Transl Sci*. 2015;134:25-41. doi: 10.1016/bs.pmbts.2015.04.002

22. Espana EM, Birk DE. Composition, structure and function of the corneal stroma. *Exp Eye Res*. 2020;198:108137. doi: 10.1016/j.exer.2020.108137

23. Gipson IK, Spurr-Michaud SJ, Tisdale AS. Anchoring fibrils form a complex network in human and rabbit cornea. *Invest Ophthalmol Vis Sci*. 1987;28(2):212-220.

24. Gipson IK, Spurr-Michaud S, Tisdale A, Keough M. Reassembly of the anchoring structures of the corneal epithelium during wound repair in the rabbit. *Invest Ophthalmol Vis Sci*. 1989;30(3):425-434.

25. Chen S, Mienaltowski MJ, Birk DE. Regulation of corneal stroma extracellular matrix assembly. *Exp Eye Res*. 2015;133:69-80. doi: 10.1016/j.exer.2014.08.001

26. Michelacci YM,. Collagens and proteoglycans of the corneal extracellular matrix. *Braz J Med Biol Res*. 2003;36(8):1037-1046. doi: 10.1590/s0100-879x2003000800009

27. Tanihara H, Inatani M, Koga T, Yano T, Kimura A. Proteoglycans in the eye. *Cornea*. 2002;21(7 Suppl):S62-69. doi: 10.1097/01.ico.0000263121.45898.d2

28. Holland G, Pandit A, Sanchez-Abella L, et al. Artificial cornea: past, current, and future directions. *Front Med (Lausanne)*. 2021;8:770780. doi: 10.3389/fmed.2021.770780

29. Ilhan-Sarac O, Akpek EK. Current concepts and techniques in keratoprosthesis. *Curr Opin Ophthalmol*. 2005;16(4):246-250. doi: 10.1097/01.icu.0000172829.33770.d3

30. Lin L, Jin X,. The development of tissue engineering corneal scaffold: which one the history will choose? *Ann Eye Sci*. 2018;3(1):6. doi: 10.21037/aes.2018.01.01

31. Rohaina CM, Then KY, Ng AM, et al. Reconstruction of limbal stem cell deficient corneal surface with induced human bone marrow mesenchymal stem cells on amniotic membrane. *Transl Res*. 2014;163(3):200-210. doi: 10.1016/j.trsl.2013.11.004

32. Ahearne M, Fernandez-Perez J, Masterton S, Madden PW, Bhattacharjee P. Designing scaffolds for corneal regeneration. *Adv Funct Mater.* 2020;30(44). doi: 10.1002/adfm.201908996

33. Liu JB, Lawrence BD, Liu AH, Schwab IR, Oliveira LA, Rosenblatt MI. Silk fibroin as a biomaterial substrate for corneal epithelial cell sheet generation. *Invest Ophthalmol Vis Sci*. 2012;53(7):4130-4138. doi: 10.1167/iovs.12-9876

34. Hussain Z, Pei RJ. Scaffold-free and scaffold-based cellular strategies and opportunities for cornea tissue engineering. *Prog Biomed Eng.* 2021;3(3). doi: 10.1088/2516-1091/ac12d7

35. Xeroudaki M, Thangavelu M, Lennikov A, et al. A porous collagen-based hydrogel and implantation method for corneal stromal regeneration and sustained local drug delivery. *Sci Rep*. 2020;10(1):16936. doi: 10.1038/s41598-020-73730-9

36. Szucs D, Fekete Z, Guba M, et al. Toward better drug development: three-dimensional bioprinting in toxicological research. *Int J Bioprint*. 2023;9(2):663. doi: 10.18063/ijb.v9i2.663

37. Goh KL, Holmes DF. Collagenous extracellular matrix biomaterials for tissue engineering: lessons from the common sea urchin tissue. *Int J Mol Sci*. 2017;18(5). doi: 10.3390/ijms18050901

38. Wang X. Advanced polymers for three-dimensional (3D) organ bioprinting. *Micromachines (Basel)*. 2019;10(12). doi: 10.3390/mi10120814

39. Guba M, Szűcs D, Kemény L, Veréb Z. Mesterséges bőrszövetek a kutatásban és a gyógyításban. *Orvosi Hetilap*. 2022;163(10):375-385. doi: 10.1556/650.2022.32330

40. Angelats Lobo D, Ginestra P. Cell bioprinting: the 3D-bioplotter case. *Materials (Basel)*. 2019;12(23). doi: 10.3390/ma12234005

41. Elsawy MM, de Mel A,. Biofabrication and biomaterials for urinary tract reconstruction. *Res Rep Urol*. 2017;9:79-92. doi: 10.2147/RRU.S127209

42. Kim H, Kang B, Cui XL, et al. Light-activated decellularized extracellular matrix-based bioinks for volumetric tissue analogs at the centimeter scale. *Adv Funct Mater.* 2021;31(32). doi: 10.1002/adfm.202011252

43. Zhang MS, Yang F, Han DB, et al. 3D bioprinting of corneal decellularized extracellular matrix: GelMA composite hydrogel for corneal stroma engineering. *Int J Bioprint*. 2023;9(5):474-492. doi: 10.18063/ijb.774

44. Lei M, Wang X. Biodegradable polymers and stem cells for bioprinting. *Molecules*. 2016;21(5). doi: 10.3390/molecules21050539

45. Tao O, Kort-Mascort J, Lin Y, et al. The applications of 3D printing for craniofacial tissue engineering. *Micromachines (Basel)*. 2019;10(7). doi: 10.3390/mi10070480

46. Aljohani W, Ullah MW, Zhang X, Yang G. Bioprinting and its applications in tissue engineering and regenerative medicine. *Int J Biol Macromol*. 2018;107(Pt A):261-275. doi: 10.1016/j.ijbiomac.2017.08.171

47. Borovjagin AV, Ogle BM, Berry JL, Zhang J. From microscale devices to 3D printing: advances in fabrication of 3D cardiovascular tissues. *Circ Res*. 2017;120(1):150-165. doi: 10.1161/CIRCRESAHA.116.308538

48. Ozbolat IT, Hospodiuk M,. Current advances and future perspectives in extrusion-based bioprinting. *Biomaterials*. 2016;76:321-343. doi: 10.1016/j.biomaterials.2015.10.076

49. Derakhshanfar S, Mbeleck R, Xu K, Zhang X, Zhong W, Xing M. 3D bioprinting for biomedical devices and tissue engineering: a review of recent trends and advances. *Bioact Mater*. 2018;3(2):144-156. doi: 10.1016/j.bioactmat.2017.11.008

50. Wu Z, Su X, Xu Y, Kong B, Sun W, Mi S. Bioprinting three-dimensional cell-laden tissue constructs with controllable degradation. *Sci Rep*. 2016;6:24474. doi: 10.1038/srep24474

51. Duffy GL, Liang H, Williams RL, Wellings DA, Black K. 3D reactive inkjet printing of poly-varepsilon-lysine/gellan gum hydrogels for potential corneal constructs. *Mater Sci Eng C Mater Biol Appl*. 2021;131:112476. doi: 10.1016/j.msec.2021.112476

52. Dzobo K, Thomford NE, Senthebane DA, et al. Advances in regenerative medicine and tissue engineering: innovation and transformation of medicine. *Stem Cells Int*. 2018;2018:2495848. doi: 10.1155/2018/2495848

53. Turnbull G, Clarke J, Picard F, et al. 3D bioactive composite scaffolds for bone tissue engineering. *Bioact Mater*. 2018;3(3):278-314. doi: 10.1016/j.bioactmat.2017.10.001

54. Keriquel V, Oliveira H, Remy M, et al. In situ printing of mesenchymal stromal cells, by laser-assisted bioprinting, for in vivo bone regeneration applications. *Sci Rep*. 2017;7(1):1778. doi: 10.1038/s41598-017-01914-x

55. Varkey M, Visscher DO, van Zuijlen PPM, Atala A, Yoo JJ. Skin bioprinting: the future of burn wound reconstruction? *Burns Trauma*. 2019;7:4. doi: 10.1186/s41038-019-0142-7

56. Bose S, Ke D, Sahasrabudhe H, Bandyopadhyay A. Additive manufacturing of biomaterials. *Prog Mater Sci*. 2018;93:45-111. doi: 10.1016/j.pmatsci.2017.08.003

57. Sorkio A, Koch L, Koivusalo L, et al. Human stem cell based corneal tissue mimicking structures using laser-assisted 3D bioprinting and functional bioinks. *Biomaterials*. 2018;171:57-71. doi: 10.1016/j.biomaterials.2018.04.034

58. Zennifer A, Manivannan S, Sethuraman S, Kumbar SG, Sundaramurthi D. 3D bioprinting and photocrosslinking: emerging strategies & future perspectives. *Biomater Adv*. 2022;134:112576. doi: 10.1016/j.msec.2021.112576

59. Tomal W, Ortyl J. Water-soluble photoinitiators in biomedical applications. *Polymers*. 2020;12(5):1079. doi: 10.3390/polym12051073

60. Barroso IA, Man K, Hall TJ, et al. Photocurable antimicrobial silk-based hydrogels for corneal repair. *J Biomed Mater Res Part A*. 2022;110(7):1401-1415. doi: 10.1002/jbm.a.37381

61. He BB, Wang J, Xie MT, et al. 3D printed biomimetic epithelium/stroma bilayer hydrogel implant for corneal regeneration. *Bioact Mater*. 2022;17:234-247. doi: 10.1016/j.bioactmat.2022.01.034

62. Caliari SR, Burdick JA. A practical guide to hydrogels for cell culture. *Nat. Methods*. 2016;13(5):405-414. doi: 10.1038/Nmeth.3839

63. Liu F, Chen QH, Liu C, et al. Natural polymers for organ 3D bioprinting. *Polymers*. 2018;10(11):1278. doi: 10.3390/Polym10111278

64. Ning LQ, Chen XB. A brief review of extrusion-based tissue scaffold bio-printing. *Biotechnol J*. 2017;12(8):1600671. doi: 10.1002/Biot.201600671

65. Bhardwaj N, Chouhan D, Mandal BB. Tissue engineered skin and wound healing: current strategies and future directions. *Curr Pharm Des*. 2017;23(24):3455-3482. doi: 10.2174/1381612823666170526094606

66. Chan EC, Kuo SM, Kong AM, et al. Three dimensional collagen scaffold promotes intrinsic vascularisation for tissue engineering applications. *PLoS One*. 2016;11(2):e0149799. doi: 10.1371/journal.pone.0149799

67. Furtado M, Chen L, Chen Z, Chen A, Cui W. Development of fish collagen in tissue regeneration and drug delivery. *Engineered Regeneration*. 2022. 3(3): 217-231. doi: 10.1016/j.engreg.2022.05.002

68. Cooperman L, Michaeli D. The immunogenicity of injectable collagen. II. A retrospective review of 72 tested and treated patients. *J Am Acad Dermatol*. 1984;10(4):647-651. doi: 10.1016/S0190-9622(84)80272-8

69. Olsen D, Yang CL, Bodo M, et al. Recombinant collagen and gelatin for drug delivery. *Adv Drug Deliv Rev*. 2003;55(12):1547-1567. doi: 10.1016/j.addr.2003.08.008

70. Nicholas MN, Jeschke MG, Amini-Nik S. Methodologies in creating skin substitutes. *Cell Mol Life Sci*. 2016;73(18):3453-3472. doi: 10.1007/s00018-016-2252-8

71. Koivusalo L, Kauppila M, Samanta S, et al. Tissue adhesive hyaluronic acid hydrogels for sutureless stem cell delivery

and regeneration of corneal epithelium and stroma. *Biomaterials*. 2019;225:119516.
doi: 10.1016/j.biomaterials.2019.119516

72. Donderwinkel I, van Hest JCM, Cameron NR. Bio-inks for 3D bioprinting: recent advances and future prospects. *Polym Chem*. 2017;8(31):4451-4471.
doi: 10.1039/c7py00826k

73. Lawrence BD, Marchant JK, Pindrus MA, Omenetto FG, Kaplan DL. Silk film biomaterials for cornea tissue engineering. *Biomaterials*. 2009;30(7):1299-1308.
doi: 10.1016/j.biomaterials.2008.11.018

74. Yang JZ, Zhang YS, Yue K, Khademhosseini A. Cell-laden hydrogels for osteochondral and cartilage tissue engineering. *Acta Biomater.* 2017;57:1-25.
doi: 10.1016/j.actbio.2017.01.036

75. Li Z, Ramay HR, Hauch KD, Xiao D, Zhang M. Chitosan-alginate hybrid scaffolds for bone tissue engineering. *Biomaterials*. 2005;26(18):3919-3928.
doi: 10.1016/j.biomaterials.2004.09.062

76. Schoen F, Mitchell R. Tissues, the extracellular matrix, and cell–biomaterial interactions. In: Ratner BD, Hoffman Allan S, Schoen FJ, Lemons JE, eds. *Biomaterials Science.* 3rd ed. Oxford, UK; Waltham, USA: Academic Press; 2013:452-474.
doi: 10.1016/B978-0-08-087780-8.00039-5

77. Francisco AT, Mancino RJ, Bowles RD, et al. Injectable laminin-functionalized hydrogel for nucleus pulposus regeneration. *Biomaterials*. 2013;34(30):7381-7388.
doi: 10.1016/j.biomaterials.2013.06.038

78. Tayebi T, Baradaran-Rafii A, Hajifathali A, et al. Biofabrication of chitosan/chitosan nanoparticles/polycaprolactone transparent membrane for corneal endothelial tissue engineering. *Sci Rep*. 2021;11(1):7060.
doi: 10.1038/S41598-021-86340-W

79. Ulag S, Ilhan E, Sahin A, et al. 3D printed artificial cornea for corneal stromal transplantation. *Eur Polym J.* 2020;133:109744.
doi: 10.1016/j.eurpolymj.2020.109744

80. Chen JS, Li QH, Xu JT, et al. Study on biocompatibility of complexes of collagen-chitosan-sodium hyaluronate and cornea. *Artif Organs*. 2005;29(2):104-113.
doi: 10.1111/j.1525-1594.2005.29021.x

81. Si ZZ, Wang X, Sun CH, et al. Adipose-derived stem cells: sources, potency, and implications for regenerative therapies. *Biomed Pharmacother.* 2019;114:108765.
doi: 10.1016/J.Biopha.2019.108765

82. Rodriguez-Fuentes DE, Fernandez-Garza LE, Samia-Meza JA, Barrera-Barrera SA, Caplan AI, Barrera-Saldaña HA. Mesenchymal stem cells current clinical applications: a systematic review. *Arch Med Res*. 2021;52(1):93-101.
doi: 10.1016/j.arcmed.2020.08.006

83. Irvine SA, Venkatraman SS. Bioprinting and differentiation of stem cells. *Molecules*. 2016;21(9):1188.
doi: 10.3390/molecules21091188

84. Tasnim N, De la Vega L, Anil Kumar S, et al. 3D bioprinting stem cell derived tissues. *Cell Mol Bioeng*. 2018;11(4):219-240.
doi: 10.1007/s12195-018-0530-2

85. Cui H, Nowicki M, Fisher JP, Zhang LG. 3D bioprinting for organ regeneration. *Adv Healthc Mater*. 2017;6(1).
doi: 10.1002/adhm.201601118

86. He P, Zhao J, Zhang J, et al. Bioprinting of skin constructs for wound healing. *Burns Trauma*. 2018;6:5.
doi: 10.1186/s41038-017-0104-x

87. Tasoglu S, Demirci U. Bioprinting for stem cell research. *Trends Biotechnol*. 2013;31(1):10-19.
doi: 10.1016/j.tibtech.2012.10.005

88. Goncalves ED, Campos M, Paris F, Gomes JAP, de Farias CC. Bullous keratopathy: etiopathogenesis and treatment. *Arq Bras Oftalmol*. 2008;71(6 Suppl):61-64.
doi: 10.1590/s0004-27492008000700012

89. Matthyssen S, Van den Bogerd B, Ni Dhubhghaill S, Koppen C, Zakaria N. Corneal regeneration: a review of stromal replacements. *Acta Biomater.* 2018;69:31-41.
doi: 10.1016/j.actbio.2018.01.023

90. Ruiz-Alonso S, Villate-Beitia I, Gallego I, et al. Current insights into 3D bioprinting: an advanced approach for eye tissue regeneration. *Pharmaceutics*. 2021;13(3).
doi: 10.3390/pharmaceutics13030308

91. Ghezzi CE, Rnjak-Kovacina J, Kaplan DL. Corneal tissue engineering: recent advances and future perspectives. *Tissue Eng Part B Rev*. 2015;21(3):278-287.
doi: 10.1089/ten.TEB.2014.0397

92. Mobaraki M, Abbasi R, Omidian Vandchali S, Ghaffari M, Moztarzadeh F, Mozafari M. Corneal repair and regeneration: current concepts and future directions. *Front Bioeng Biotechnol*. 2019;7:135.
doi: 10.3389/fbioe.2019.00135

93. Campos DFD, Rohde M, Ross M, et al. Corneal bioprinting utilizing collagen-based bioinks and primary human keratocytes. *J Biomed Mater Res Part A*. 2019;107(9):1945-1953.
doi: 10.1002/jbm.a.36702

94. Boix-Lemonche G, Nagymihaly RM, Niemi EM, et al. Intracorneal implantation of 3D bioprinted scaffolds containing mesenchymal stromal cells using femtosecond-laser-assisted intrastromal keratoplasty. *Macromol Biosci*. 2023;23(7):e2200422.
doi: 10.1002/mabi.202200422

95. Murphy SV, De Coppi P, Atala A. Opportunities and challenges of translational 3D bioprinting. *Nat Biomed Eng*. 2020;4(4):370-380.
doi: 10.1038/s41551-019-0471-7

96. Blackburn BJ, Jenkins MW, Rollins AM, Dupps WJ. A review of structural and biomechanical changes in the

cornea in aging, disease, and photochemical crosslinking. *Front Bioeng Biotechnol*. 2019;7:66.
doi: 10.3389/fbioe.2019.00066

97. Benzvi A, Rodrigues MM, Krachmer JH, Fujikawa LS. Immunohistochemical characterization of extracellular-matrix in the developing human cornea. *Curr Eye Res*. 1986;5(2):105-117.
doi: 10.3109/02713688609015099

98. Millin JA, Golub BM, Foster CS. Human basement membrane components of keratoconus and normal corneas. *Invest Ophthalmol Vis Sci*. 1986;27(4):604-607.

99. Torricelli AA, Singh V, Santhiago MR, Wilson SE. The corneal epithelial basement membrane: structure, function, and disease. *Invest Ophthalmol Vis Sci*. 2013;54(9): 6390-6400.
doi: 10.1167/iovs.13-12547

100. Newsome DA, Foidart JM, Hassell JR, Krachmer JH, Rodrigues MM, Katz SI. Detection of specific collagen types in normal and keratoconus corneas. *Invest Ophthalmol Vis Sci*. 1981;20(6):738-750.

101. Tsuchiya S, Tanaka M, Konomi H, Hayashi T. Distribution of specific collagen types and fibronectin in normal and keratoconus corneas. *Jpn J Ophthalmol*. 1986;30(1):14-31.

102. Dua HS, Faraj LA, Said DG, Gray T, Lowe J. Human corneal anatomy redefined: a novel pre-Descemet's layer (Dua's layer). *Ophthalmology*. 2013;120(9):1778-1785.
doi: 10.1016/j.ophtha.2013.01.018

103. Tamura Y, Konomi H, Sawada H, Takashima S, Nakajima A. Tissue distribution of type VIII collagen in human adult and fetal eyes. *Invest Ophthalmol Vis Sci*. 1991;32(9): 2636-2644.

104. Luo H, Lu Y, Wu T, Zhang M, Zhang Y, Jin Y. Construction of tissue-engineered cornea composed of amniotic epithelial cells and acellular porcine cornea for treating corneal alkali burn. *Biomaterials*. 2013;34(28):6748-6759.
doi: 10.1016/j.biomaterials.2013.05.045

105. Rafat M, Li F, Fagerholm P, et al. PEG-stabilized carbodiimide crosslinked collagen-chitosan hydrogels for corneal tissue engineering. *Biomaterials*. 2008;29(29):3960-3972.
doi: 10.1016/j.biomaterials.2008.06.017

106. Alaminos M, Del Carmen Sanchez-Quevedo M, Munoz-Avila JI, et al. Construction of a complete rabbit cornea substitute using a fibrin-agarose scaffold. *Invest Ophthalmol Vis Sci*. 2006;47(8):3311-3317.
doi: 10.1167/iovs.05-1647

107. Fagerholm P, Lagali NS, Merrett K, et al. A biosynthetic alternative to human donor tissue for inducing corneal regeneration: 24-month follow-up of a phase 1 clinical study. *Sci Transl Med*. 2010;2(46):46ra61.
doi: 10.1126/scitranslmed.3001022

108. Fagerholm P, Lagali NS, Ong JA, et al. Stable corneal regeneration four years after implantation of a cell-free recombinant human collagen scaffold. *Biomaterials*. 2014;35(8):2420-2427.
doi: 10.1016/j.biomaterials.2013.11.079

109. Nishida K, Yamato M, Hayashida Y, et al. Corneal reconstruction with tissue-engineered cell sheets composed of autologous oral mucosal epithelium. *N Engl J Med*. 2004;351(12):1187-1196.
doi: 10.1056/Nejmoa040455

110. Kobayashi T, Kan K, Nishida K, Yamato M, Okano T. Corneal regeneration by transplantation of corneal epithelial cell sheets fabricated with automated cell culture system in rabbit model. *Biomaterials*. 2013;34(36):9010-9017.
doi: 10.1016/j.biomaterials.2013.07.065

111. Lawrence BD, Pan Z, Liu AH, Kaplan DL, Rosenblatt MI. Human corneal limbal epithelial cell response to varying silk film geometric topography in vitro. *Acta Biomater*. 2012;8(10):3732-3743.
doi: 10.1016/j.actbio.2012.06.009

112. Levis HJ, Massie I, Dziasko MA, Kaasi A, Daniels JT. Rapid tissue engineering of biomimetic human corneal limbal crypts with 3D niche architecture. *Biomaterials*. 2013;34(35):8860-8868.
doi: 10.1016/j.biomaterials.2013.08.002

113. Mi SL, Chen B, Wright B, Connon CJ. Ex vivo construction of an artificial ocular surface by combination of corneal limbal epithelial cells and a compressed collagen scaffold containing keratocytes. *Tissue Eng Part A*. 2010;16(6):2091-2100.
doi: 10.1089/ten.tea.2009.0748

114. Duan X, Sheardown H. Dendrimer crosslinked collagen as a corneal tissue engineering scaffold: mechanical properties and corneal epithelial cell interactions. *Biomaterials*. 2006;27(26):4608-4617.
doi: 10.1016/j.biomaterials.2006.04.022

115. Li FF, Carlsson D, Lohmann C, et al. Cellular and nerve regeneration within a biosynthetic extracellular matrix for corneal transplantation. *Proc Natl Acad Sci USA*. 2003;100(26):15346-15351.
doi: 10.1073/pnas.2536767100

116. Liu W, Merrett K, Griffith M, et al. Recombinant human collagen for tissue engineered corneal substitutes. *Biomaterials*. 2008;29(9):1147-1158.
doi: 10.1016/j.biomaterials.2007.11.011

117. Torbet J, Malbouyres M, Builles N, et al. Orthogonal scaffold of magnetically aligned collagen lamellae for corneal stroma reconstruction. *Biomaterials*. 2007;28(29):4268-4276.
doi: 10.1016/j.biomaterials.2007.05.024

118. Builles N, Janin-Manificat H, Malbouyres M, et al. Use of magnetically oriented orthogonal collagen scaffolds for hemi-corneal reconstruction and regeneration. *Biomaterials*. 2010;31(32):8313-8322.
doi: 10.1016/j.biomaterials.2010.07.066

119. Crabb RA, Chau EP, Evans MC, Barocas VH, Hubel A. Biomechanical and microstructural characteristics of a

collagen film-based corneal stroma equivalent. *Tissue Eng*. 2006;12(6):1565-1575.
doi: 10.1089/ten.2006.12.1565

120. Mimura T, Amano S, Yokoo S, et al. Tissue engineering of corneal stroma with rabbit fibroblast precursors and gelatin hydrogels. *Mol Vis*. 2008;14:1819-1828.

121. Wu J, Rnjak-Kovacina J, Du Y, Funderburgh ML, Kaplan DL, Funderburgh JL. Corneal stromal bioequivalents secreted on patterned silk substrates. *Biomaterials*. 2014;35(12):3744-3755. doi: 10.1016/j.biomaterials.2013.12.078

122. Gil ES, Mandal BB, Park SH, Marchant JK, Omenetto FG, Kaplan DL. Helicoidal multi-lamellar features of RGD-functionalized silk biomaterials for corneal tissue engineering. *Biomaterials*. 2010;31(34):8953-8963. doi: 10.1016/j.biomaterials.2010.08.017

123. Fan T, Ma X, Zhao J, et al. Transplantation of tissue-engineered human corneal endothelium in cat models. *Mol Vis*. 2013;19:400-407.

124. Honda N, Mimura T, Usui T, Amano S. Descemet stripping automated endothelial keratoplasty using cultured corneal endothelial cells in a rabbit model. *Arch Ophthalmol*. 2009;127(10):1321-1326. doi: 10.1001/archophthalmol.2009.253

125. Watanabe R, Hayashi R, Kimura Y, et al. A novel gelatin hydrogel carrier sheet for corneal endothelial transplantation. *Tissue Eng Part A*. 2011;17(17-18):2213-2219. doi: 10.1089/ten.TEA.2010.0568

126. Levis HJ, Peh GSL, Toh KP, et al. Plastic compressed collagen as a novel carrier for expanded human corneal endothelial cells for transplantation. *PLoS One*. 2012;7(11):e50993. doi: 10.1371/journal.pone.0050993

127. Fuest M, Yam GHF, Mehta JS, Duarte Campos DF. Prospects and challenges of translational corneal bioprinting. *Bioengineering*. 2020;7(3):71. doi: 10.3390/bioengineering7030071

128. Zhang B, Xue Q, Hu HY, et al. Integrated 3D bioprinting-based geometry-control strategy for fabricating corneal substitutes. *J Zhejiang Univ Sci B*. 2019;20(12):945-959. doi: 10.1631/jzus.B1900190

129. Bektas CK, Hasirci V. Cell loaded 3D bioprinted GelMA hydrogels for corneal stroma engineering. *Biomater Sci*. 2020;8(1):438-449. doi: 10.1039/c9bm01236b

130. Kong B, Chen Y, Liu R, et al. Fiber reinforced GelMA hydrogel to induce the regeneration of corneal stroma. *Nat Commun*. 2020;11(1):1435. doi: 10.1038/S41467-020-14887-9

131. Kim H, Park MN, Kim J, Jang J, Kim H-K, Cho D-W. Characterization of cornea-specific bioink: high transparency, improved in vivo safety. *J Tissue Eng*. 2019;10. doi: 10.1177/2041731418823382

132. Kim H, Jang J, Park J, et al. Shear-induced alignment of collagen fibrils using 3D cell printing for corneal stroma tissue engineering. *Biofabrication*. 2019;11(3). doi: 10.1088/1758-5090/Ab1a8b

133. Kim KW, Lee SJ, Park SH, Kim JC. Ex vivo functionality of 3D bioprinted corneal endothelium engineered with ribonuclease 5-overexpressing human corneal endothelial cells. *Adv Healthc Mater*. 2018;7(18):e1800398. doi: 10.1002/adhm.201800398

ACCSCIENCE PUBLISHING

International Journal of Bioprinting

REVIEW ARTICLE

Decellularized extracellular matrix for three-dimensional bioprinted *in vitro* disease modeling

Mihyeon Bae[1,2†], Joeng Ju Kim[1,2†], Jongmin Kim[1,2], and Dong-Woo Cho[1,2*]

[1]Department of Mechanical Engineering, Pohang University of Science and Technology (POSTECH), Pohang, Kyungbuk, Republic of Korea

[2]POSTECH-Catholic Biomedical Engineering Institute, POSTECH, Pohang, Kyungbuk, Republic of Korea

(This article belongs to the *Special Issue: Fine-tuned Hydrogels for 3D Bioprinting*)

Abstract

Precise *in vitro* models in tissue engineering have attracted the attention of researchers seeking to understand physiological consequences from native tissues as well as the mechanism of diseases *in vitro*. To construct delicate native tissue-like *in vitro* models, a proper combination of biomimetic materials and a biofabrication strategy is required. Conventional biomaterials, such as collagens, laminins, and synthetic polymers, have been widely adapted in tissue recapitulation; however, they lack tissue specificity in the context of biophysical properties and native-like extracellular matrix composition. The lack of tissue specificity accounts for the pathophysiological discrepancy between preclinical model and actual human patient. Thus, biomaterials should be improved for attaining physiological similarity between disease models and patients. Additionally, a biofabrication technique is essential for building mature cellular or tissue structures with a sophisticated bioassembly process. Among the biofabrication techniques, bioprinting stands as a promising approach for constructing three-dimensional (3D) cellular structures using specific cell types and biomaterials. Combining multifunctional bioinks and bioprinting is expected to enhance tissue specificity with regard to structural recapitulation. From this viewpoint, decellularized extracellular matrix (dECM) bioink has been increasingly used to achieve tissue specificity and manufacturability in 3D bioprinting. Progress in this domain requires the clarification of tissue-specific decellularization method and the development of a proper 3D bioprinting method, in conjunction with the improvement of the compatibility between dECM and bioprinting. In this review, we introduce the production methods and characteristics of dECM in the context of tissue specificity and examine state-of-the-art dECM-incorporated 3D-bioprinted *in vitro* models for disease investigation. We also recommend a strategy for improving dECM for use in therapeutic studies based on simulations of the pathophysiological microenvironment.

Keywords: Decellularized extracellular matrix; Bioink; 3D bioprinting; *In vitro* model; Biomaterial

†These authors contributed equally to this work.

***Corresponding author:**
Dong-Woo Cho
(dwcho@postech.ac.kr)

Citation: Bae M, Kim JJ, Kim J, Cho D-W. Decellularized extracellular matrix for three-dimensional bioprinted *in vitro* disease modeling. *Int J Bioprint*. 2024;10(2):1970.
doi: 10.36922/ijb.1970

Received: October 6, 2023
Accepted: November 3, 2023
Published Online: January 16, 2024

1. Introduction

Modeling human tissues *in vitro* has contributed to advancements in biology, pharmacology, physiology, and medicine field.[1,2] The rapid development of human tissue

models has ushered in the advent of three-dimensional (3D) *in vitro* models, which enable 3D cell–cell, cell–tissue, and tissue–tissue interactions.[3] The 3D *in vitro* model has attained a swift advancement under the expectation that the system can imitate complex physiology via the recapitulation of interactions in the body not found in animal models or non-physiological models.[4] In particular, *in vitro* disease models that recapitulate specific features of patients are widely adopted in the study of disease mechanisms and pharmaceutical development. A precisely designed 3D *in vitro* model should contain cells and extracellular matrix (ECM) in the right composition, as well as microstructure of the tissues or organs. Therefore, applying an appropriate biofabrication strategy together with a combination of biomaterials can help establish *in vitro* models with proper physiological reliability.

Biomaterials are used in *in vitro* models as essential scaffolds for tissue analogs.[4] Various biomaterials, including nature-derived ECM and synthetic materials,[5] have been employed to build *in vitro* models over the past decades. These biomaterials are closely related to the regulation of cellular behavior.[6] In particular, the interaction of nature-derived ECMs with cells has been elucidated and compared with synthetic biomaterials.[7] Since, however, the conventional natural biomaterials, such as collagens, laminins, and fibronectins, are chemically less complex than ECM of native tissues,[8] it is rather challenging to investigate their exact cellular behavior related to tissue specificity. Thus, it is necessary to develop more native tissue-like biomaterials for enhancing cell–ECM interactions in *in vitro* models.

Additionally, biofabrication methods (e.g., photolithography, bioprinting, organoid formation) have been used in attempts to reconstruct the 3D physiological structure of native tissues.[9,10] The physiological structure of each tissue is closely related to the essential role of the organ. For example, a tubular-like and perfusable structure is the key feature of vascular tissues.[11] In addition, epithelial tissues have layered structures composed of several cell sheets,[11] and muscular tissues have bundle structures that can contract and expand.[12] Thus, recapitulation of innate features of tissues is essential for elucidating the tissue–tissue interactions in organisms. However, photolithography-based models are simplified into almost two-dimensional (2D) structures, and traditional organoid generation is restricted owing to the lack of spatiotemporal regulation of cells and ECM placement in the context of bioengineered design.

Therefore, native tissue-derived biomaterials and spatial-controllable biofabrication methods have been suggested to improve the level of tissue recapitulation. First, for the biomaterials, it is technically difficult to recapitulate whole proteins in the native tissues with chemically designed hydrogels. In particular, each tissue has a specific protein composition and specific mechanical properties; thus, full reproduction of the ECM composition with synthetic materials is difficult. From this viewpoint, the decellularized extracellular matrix (dECM)-based hydrogel is a favorable material to satisfy the requirements of tissue recapitulation.[13,14] Fabrication of a dECM essentially involves the reduction of cellular components and preservation of proteins—particularly the ECM; thus, it is advantageous for maintaining tissue specificity.[15] Through the use of tissue-specific decellularization methods, various dECMs have been developed from organs such as the brain, cornea, bone, skin, and liver. The developed dECMs exhibit tissue-specific biochemical and mechanical properties. For example, Han et al. investigated the direct differentiation potential of adult stem cells in a dECM bioink.[16] Because of their multipotency, the adult stem cells differentiated into the targeted tissues, including those of liver, skin, cornea, and heart, depending on the bioinks used. The Matrisome and ATLAS databases indicate tissue-specific functions of ECMs with regard to organ homeostasis and maturation, respectively.[17,18] Collectively, the role of ECMs in simulating tissue function has been profoundly elucidated using dECMs.

In terms of biofabrication, 3D bioprinting is useful for fabricating various structures with a high manufacturing degree of freedom. 3D bioprinting is a layer-by-layer fabrication method for obtaining tissue analogs via additive manufacturing, by employing biomaterials, cells, and other biological components, such as growth factors.[19] The notable advantage of 3D bioprinting, compared to traditional photolithography or organoid formation, is its enhanced prowess in recapitulating 3D physiological structures.[20] Various 3D bioprinting methods, such as extrusion-based, inkjet-based, and laser-assisted, can be selected by users in considerations with the materials, precision level, and designed structure.[21-24] Extrusion-based bioprinting employs pneumatic or mechanical pressure with shear-thinning biomaterials such as hydrogels or thermoplastics.[22,25] It is compatible with a wide range of printing materials, as most shear-thinning materials, including cell-laden hydrogels, can be adopted. In addition, extrusion-based bioprinting yields low thermal stress during the fabrication process, which is favorable for high cellular viability. However, shear stress due to highly viscous material and nozzle clogging due to cell clusters can damage cells. Inkjet-based bioprinting employs electrohydrodynamic drop-on-demand control.[23,26] It is advantageous in terms of fabrication speed, but it has limited control precision owing to non-uniform droplet formation. On the other hand, laser-

assisted bioprinting enables high control precision and is not constrained by viscosity or clogging issues, as it is a nozzle-free method; however, the cellular viability is unstable because of heat generation.[27] In summary, it is necessary to select the suitable bioprinting methods according to designed tissue models.

Owing to the technical advantages of dECM bioink and 3D bioprinting, dECM-incorporated 3D bioprinting has contributed to the fabrication of precise *in vitro* models, marked by the recapitulation of microphysiological features of native tissues. Since the development of 3D-bioprinted tissue analogs with dECM bioink by Pati et al.,[28] tissue models bioprinted with dECM have emerged as platforms for drug testing owing to their interactions with drugs and disease factors, as well as the recapitulation of tissue-specific pathophysiology. However, despite the prospects of harmonizing dECM with 3D bioprinting, it is necessary to further investigate dECM bioinks for building reliable *in vitro* models. The bioprinting process has been significantly improved to build precise structures and adopt various materials, whereas dECM bioink has many uncertain features that require investigations, such as protein composition, quality control, safety issues, and mechanical properties, which limit the improvement of *in vitro* models and reliability under native tissue condition.

Thus, this review focuses on the unmet needs of dECM bioinks from the viewpoint of enhancing the utility of *in vitro* models for drug testing by incorporating 3D bioprinting. First, we describe the components, functions, and fabrication methods of dECMs to elucidate their physiology. We then discuss the use of 3D bioprinting technology and dECM, along with their applicability to *in vitro* modeling. Finally, we address the state of the art in the realm of 3D models bioprinted with dECM, with special emphasis on their medical applications, such as disease mechanism study and drug testing. In addition, we discuss the limitations of the 3D models bioprinted with dECM for medical use, along with the relevant improvement strategies (Figure 1).

2. Decellularized extracellular matrix: key macromolecules for recapitulating tissue-specific microenvironment

Decellularized extracellular matrix plays the fundamental role of preserving the original protein composition of its native tissue.[14,15] Therefore, the macromolecular composition of the dECM and strategies for preserving ECM proteins have to be elucidated. In this review, we focus on ECM proteins rather than carbohydrates or adipose tissue because of the primary function of ECM proteins as structural supports. In this section, we introduce the composition of ECM proteins with respect to the original tissues, the decellularization methods for the tissues, and the function of dECM in tissue engineering.

2.1. Composition of decellularized extracellular matrix

The ECMs have different mechanical and biological characteristics depending on their protein compositions and types. They can be roughly categorized into two types of macromolecules: fibrous proteins, including collagens and elastin; and glycoproteins, including proteoglycans and laminin.[29] The tissue-specific microstructure and biological functions of an ECM are manifested by a combination of fibrous proteins, glycoproteins, and ECM-associated proteins. A dECM preserves the ECM composition, which

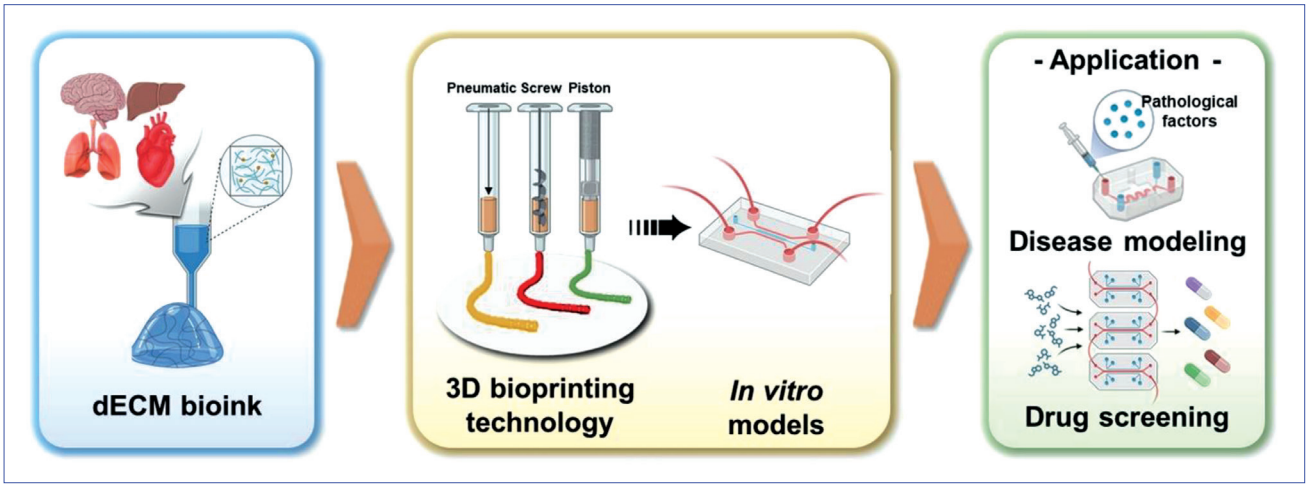

Figure 1. Schematic of *in vitro* model fabrication using dECM bioinks and 3D bioprinting and its applications. Abbreviations: dECM, decellularized extracellular matrix.

recapitulates the physiological features of the tissue and organ (Figure 2).

2.1.1. Fibrous proteins

Fibrous proteins refer to a combination of polypeptide chains that exist in elongated structures or sheet forms in tissues.[30,31] They include collagens, elastin, keratin, and fibrin. A major characteristic of polypeptide chains is that they regulate the mechanical properties of tissues depending on the combination type. Collagen is the most abundant protein in mammalian tissues and organs, constituting 25–35% of the entire body.[32] It is composed of polypeptides, and thus far, 28 types of collagens made up of different polypeptide composition have been discovered. Collagen regulates the mechanical stiffness and structure of tissues with a level of mineralization. Furthermore, in the presence of collagens, elastin maintains its tissue form.[33] This is particularly important because elastin is associated with tissue resilience after stretching or contraction. Conversely, keratin is composed of a monomer bundle that forms the hair, nails, and outer skin of vertebrates.[34] It is viscoelastic and protects epithelial cells from external stress. Similarly, fibrin is a type of fibrous protein that attaches to cells in the ECM and is related to the maintenance of the vascular structure in the body. Overall, fibrous proteins are highly relevant to the regulation and protection of tissue and organ microstructures.

2.1.2. Glycoproteins

Glycoproteins are formed by the covalent combination of amino acid side chains with monosaccharides, disaccharides, or oligosaccharides.[35] They are highly relevant to the maintenance of cohesive networks in tissues by connecting structural proteins. This protein type includes fibronectin, laminin, and matricellular glycoproteins. Fibronectin predominantly combines with integrin to maintain the structure of the membrane, and attaches to collagen, fibrin, and heparan sulfate proteoglycans. Through its combination with other ECM proteins, fibronectin regulates cell attachment, growth, migration, and differentiation. Laminin is one of the representative proteins of the basal lamina, a layer of the basement membrane. It is also relevant to cellular behavior in that it mediates cell–cell interactions through receptors on cell surfaces (e.g., integrin). Laminin is composed of three types of chains (i.e., alpha, beta, gamma) and is expressed in 14 combinations in the body. Collectively, the various glycoprotein subtypes regulate cell–ECM crosstalk by incorporating cell surface receptors, for diverse functions including cellular maturation and survival.

2.2. Physiological roles of tissue-specific extracellular matrix

The human body comprises various organs, each of which has a different ECM composition from that of the other organs.[36] Thus, dECM derived from an organ-specific

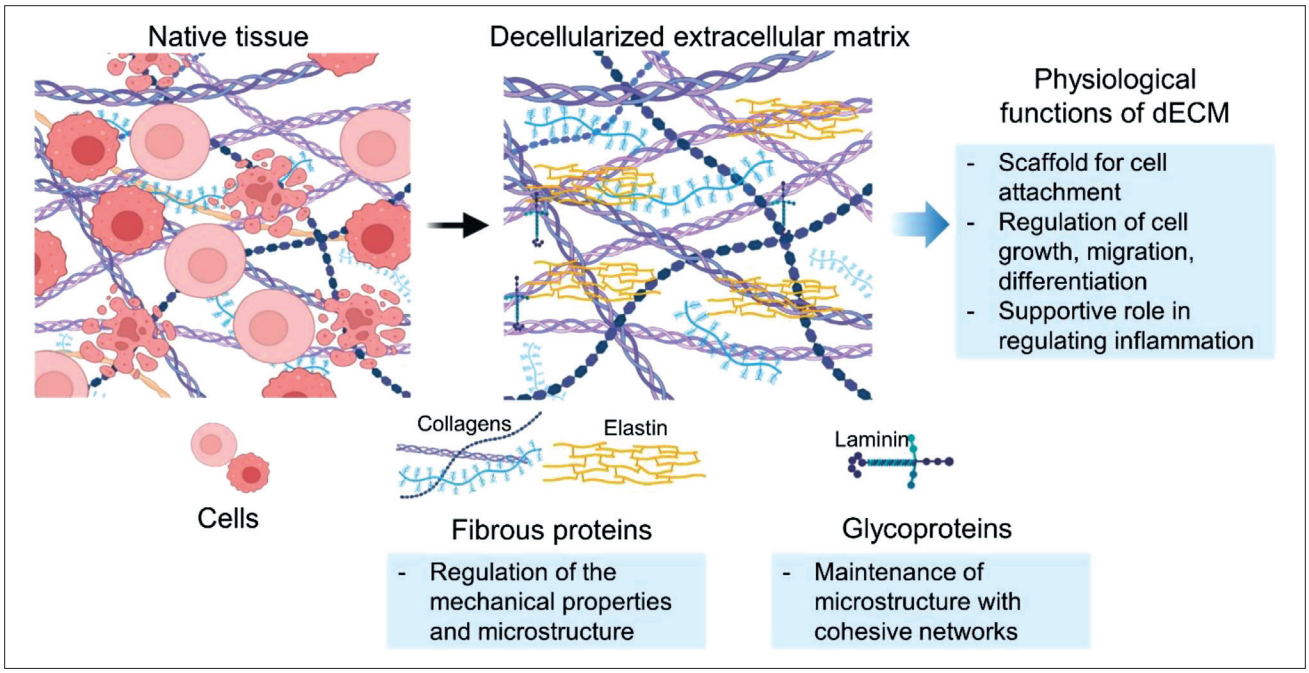

Figure 2. Schematic of protein composition of extracellular matrix (ECM) before and after decellularization. Abbreviations: dECM, decellularized extracellular matrix.

ECM composition exhibits tissue specificity.[37] The dECM provides a tissue-specific microenvironment containing various receptors and growth factors.[15] Moreover, tissue-specific dECMs directly transmit special chemical signals, such as cytokines and growth factors, to surrounding cells, inducing cell growth and tissue-specific cellular responses.[38]

The differences in properties between the dECMs of different organs affect the spatial distribution of cell surface receptors that regulate cell morphology and behavior.[39] Furthermore, dECMs regulate organ-specific cell proliferation, migration, and behavior by participating in tissue polarization and transmission of mechanical forces, and serve as a structural support for cells.[40] Additionally, specific components of the dECM are involved in organ development and maturation.[41] For example, laminin promotes cell adhesion and migration, and fibronectin is essential for heart, lung, and kidney formation and maturation.[41,42] The tissue specificity of the dECM can be applied to 3D-bioprinted organ mimicry and development of disease models that recapitulate actual pathophysiology.[43] The pathological dysfunction in ECM induces disorder in various tissues, such as brain, liver, and lung. Here, we briefly review the ECM composition in the tissues of central nervous system, cardiac tissues, liver tissues, and tissues of respiratory system, as well as the role of ECM proteins. The main tissue-specific ECM compositions are summarized in Table 1.

2.2.1. Extracellular matrix in central nervous system

The nervous system is a sophisticated network of neurons and glia cells.[44] ECM is an important constituent of the network, accounting for 10–20% of the volume of the nervous system. For the central nervous system (CNS), the main components are the basement membrane and perineural nets, including the neural interstitial matrix.[45] The basement membrane is a thin membrane and an interface that separates astrocytic attachment and perivascular mesenchymal tissue.[46] It provides a barrier, which is called the blood–brain barrier (BBB), setting apart the neural tissues and the vascular structure to protect the neural tissue from external pathogen. In addition, the basement membrane is essential for neural cell attachment and differentiation during the developmental process. The basement membrane consists of laminin, nidogen, collagens, fibronectin, and glycans, which are essential for the maintenance of barrier integrity. The perineuronal net is composed of various chondroitin sulfate proteoglycans (CSPGs), such as neurocan, veriscan, brevican, and aggrecan,[47] which primarily regulate neural plasticity of the perineuronal nets. For example, CSPGs in the nets regulate excitatory and inhibitory signal balance. Among these CSPGs, brevicans interact with tenascin-R and regulate synaptic plasticity.[48] Another feature of the CNS is the neural interstitial matrix, which is located between neurons and glial cells.[49]

Table 1. Main composition and role of tissue-specific extracellular matrix

Tissue	Main components of ECM	Role of each ECM
Central nervous system	Laminin/Nidogen	Basement membrane, neural cell attachment, regulation of neural differentiation
	Fibronectin	Perineuronal nets, structural support, oligodendrocyte differentiation
	Type IV collagen	Perineuronal nets, structural support, neural cell migration support
	CSPGs	Perineuronal nets, regulation of signal balance between excitatory and inhibitory signals
Cardiac tissue	Fibronectin	Regulation of cardiac cellular polarity
	Type IV collagen	Mechanical support to cardiac cells
	Proteoglycans	Regulation of cardiac cellular differentiation
Liver	Types I and III collagen	Maintenance of structure
	Fibrillin	Regulation of elasticity and flexibility
	Hyaluronic acid	Filling gaps in tissue
	Proteoglycans	Regulation of gas exchange between cells
Respiratory system	Types I, III, and IV collagen	Maintenance of organelle formation
	Glycosaminoglycans	Responsible for gas exchange
	Hyaluronic acid	Filling gaps in tissue
	Proteoglycans	Formation of gel state in tissue
	Elastin	Providing elasticity and flexibility

Abbreviations: CSPGs, chondroitin sulfate proteoglycans; ECM, extracellular matrix.

A dysfunction in the matrix could lead to neurological pathology in the brain. For example, a breach in the basement membrane compromises the BBB integrity, thereby inducing neuroinflammation, ischemia, and edema. In the case of a brain tumor, the levels of hyaluronic acid, collagens, and CSPGs are upregulated owing to tumor cell proliferation.[50,51] Thus, understanding the native brain-like ECM is key to elucidating the pathological mechanism of brain disease.

2.2.2. Extracellular matrix in cardiac tissue

Cardiac tissue is composed of a sophisticated ECM network that includes fibrous proteins and non-fibrous proteins. The spatial matrix is categorized as a basement membrane with a pericellular matrix and an interstitial matrix, which provide physical strength to determine plasticity of cardiac tissue.[52,53] The basement membrane in cardiac tissue regulates cardiac cellular polarity and differentiation with fibronectin, type IV collagen, laminin, and various proteoglycans. In addition, the interstitial matrix of cardiac tissue provides mechanical support to the cells. The heart is developed with a collagen network and a combination of proteoglycans from embryonic stage. The changes in ECM composition from the embryonic stage to the fetal stage[54] lead to the formation of a cardiac-specific structure[55] by promoting cardiac cell proliferation and formation of a layered structure.

Adult heart, which is formed with mature cardiac tissue, may be vulnerable to pathological factors and events, such as fibrosis. Under the circumstance of fibrosis, the elevated secretion of cytokines as well as thrombospondin, collagen, and osteoglycin drives the scar formation. Adult cardiac tissues are rarely regenerated in the pathological state; thus, the role of the ECM in regeneration and treatment must be elucidated. In particular, it is important to decipher the life stage of cardiac ECM in various environments that allow reconstruction of cardiac tissues using *in vitro* models.[52,56]

2.2.3. Extracellular matrix in liver tissues

Although ECM constitutes a small amount in liver tissue,[57] this component is an important ingredient for the formation of complex tissue structures and various cells that constitute the liver scaffold.[58] The ECM of the liver consists of several major components.

Collagen is one of the most abundant components of the liver ECM, mainly consisting of type I and III collagens. It provides strength and structure to liver tissue and supports the arrangement of liver cells and blood vessels.[59] Fibrillin that exists between collagen fibers plays an important role in regulating the elasticity and flexibility of liver tissue.[60] As one of the gel-like ECM components of the liver, hyaluronic acid fills gaps between tissues.[60] Proteoglycans combine with hyaluronic acid to form a gel in the ECM and regulate gas exchange with cells.[61] The liver ECM maintains the structure of liver tissue by supporting and fixing liver cells and blood vessels.[62] It also contributes to the regulation of signaling and cell–cell interactions necessary for liver function.[62]

In the case of liver fibrosis, which is a typical liver disease, the ECM components of a fibrotic liver are similar to those of a normal liver, but their volume is increased by a factor of approximately 3 to 5 times.[63] Therefore, changes in the ECM are closely linked to structural distortion and other important mechanisms such as liver cell regeneration and vascular redistribution.[64] In addition to fibrous deposits, these mechanisms have severe consequences for liver function. If fibrosis progresses, cirrhosis occurs, in which most of the vascular spaces become interconnected.[59] Recently, attempts have been made to treat fibrotic liver by inducing changes in the ECM composition and reducing its absolute amount.[65] As such, the composition of the liver-specific ECM plays an important role in the overall metabolism of liver tissue and is an important trigger and therapeutic target for liver disease; hence, it must be considered in studies on liver disease.

2.2.4. Extracellular matrix in tissues of respiratory system

In the respiratory system, the ECM is an important component, equipped with various physiological functions, of respiratory tissues.[66] The ECM of respiratory tissues is composed of several components, such as collagen, glycosaminoglycans (GAGs), hyaluronic acid, proteoglycans, and elastin. Among these, collagen is the most abundant and includes mainly types I, III, and IV.[67] Collagen provides tissue with strength and structure and plays a role in maintaining the formation and function of lung organelles.[68] GAGs have important roles in gas exchange and gas transport. Hyaluronic acid fills the gaps between mucous membranes and tissues in the respiratory tract and facilitates gas exchange.[69] On the other hand, proteoglycans regulate gas exchange within the ECM and form the gel state of the tissue,[70] whereas elastin provides elasticity and assists in transporting gases and maintaining the flexibility of respiratory tissues.[71] In short, the major functions of ECM in respiratory tissues are to significantly expand the gas exchange area, provide structural support necessary for gas transport, maintain elasticity, and assist with repetitive contraction and relaxation of respiratory tissues.[70] Besides, it regulates the behavior of immune cells and molecules and regulates the immune responses associated with respiratory infections and inflammation.[70]

Chronic inflammation is a hallmark in the typical respiratory diseases including chronic obstructive

pulmonary disease (COPD), acute respiratory distress syndrome (ARDS), and asthma.[72] Under chronic inflammation, ECM components are altered, causing mechanical stress, which leads to the release of contractile agonists and attenuates fiber remodeling.[73] Ultimately, the structure of the respiratory tissue is altered, narrowing the airways and irreversibly damaging lung function.[73] Bronchodilators and steroids are mainly used to relieve the symptoms of respiratory diseases but are not fundamental treatments; thus, this underscores the urgency in developing fundamental treatments that can abrogate changes in the composition of the ECM.[74] In summary, ECM composition distinctive to the respiratory tissues is implicated in the regulation of gas exchange, immune response, and progression of respiratory disease, underlining more in-depth, comprehensive investigations into ECM composition in relation to disease mechanisms.

2.3. Applicability of decellularized extracellular matrix

The dECM is an important biomaterial used in tissue engineering and has pharmaceutical potential.[75] Representative dECM functions include the provision of tissue-specific microenvironments, pharmaceutical potential, and usability as bioink for 3D bioprinting.[15,28,76] Because the dECM originally contains most of the ECM of an organ, it provides signals for cell survival, function maintenance, and differentiation.[77] It also acts as a substrate for cell–cell interactions and regulates cell behavior.[78] Additionally, dECM bioink plays important roles in pharmaceutical potential, such as drug screening and therapy.[79] Finally, dECMs can be used as a hydrogel bioink for 3D bioprinting to fabricate 3D cell-containing structures with optimized microenvironments.[28] The primary applications of the dECM are explained in further detail in the following subsections.

2.3.1. Potential of decellularized extracellular matrix in drug testing and development

Biomaterials, including scaffolds that can guide and support cells, are required for building platforms for drug testing.[80] The dECM contains most of the components of numerous biomaterials, such as collagen and laminin, which are often used for organ/tissue formation and maintenance.[13] Therefore, dECM bioink has considerable potential across various areas of drug development and therapeutic applications. The dECMs can help create a microenvironment similar to that of each organ to support cells and enhance cell proliferation.[41] Moreover, in response to physiological changes or damage caused by multiple external stimuli, dECM-mediated stress regulates cell proliferation and phenotypes to maintain tissue homeostasis.[41] Additionally, patient-derived dECM can be utilized to create a disease-specific microenvironment, which can be employed to develop disease-specific tissue models.[81] By virtue of these functions, dECMs are used to build platforms that can respond to a variety of stimuli for investigations of disease mechanisms and potential treatments, and evaluation of the safety and efficacy of new drugs. In fact, many platforms for specific organs have been created, and some have been commercialized.

The potential of dECMs for use in drug testing and development has been validated for various tissues and organs, including periodontal tissue,[82] cornea,[83] and orthopedic tissue.[84] For example, Yang et al. developed a dental follicle-derived dECM and mixed it with methacrylate gelatin to create a hybrid bioink.[82] Hybrid bioinks are used to fabricate *in vitro* periodontal constructs via digital light processing-based 3D bioprinting. The dECM, which contains dental follicular cells, optimized the structural characteristics of the periodontal tissue and maximized the physiological response in toxicology research. Kim et al. fabricated an *in vitro* corneal construct using gelatinized cornea-derived dECM (Co-dECM) and confirmed the construct delivered satisfactory therapeutic outcomes.[83] The gelatinized Co-dECM was suitable for simulating the corneal microenvironment and could be applied to precise drug screening and testing. Chae et al. developed a tendon-derived dECM and bone-derived dECM, and fabricated a tendon–bone interface (TBI) structure containing cells from each dECM bioink via extrusion-based 3D bioprinting.[84] Through the reproduction of the TBI gradient with structural integrity using dECM bioinks, the success probability of rotator cuff tear treatment was significantly increased. Additionally, by reproducing TBI gradients more precisely, the likelihood of success in drug screening and discovery can be significantly increased.

As such, dECMs have huge potential in drug screening and discovery for various organs. However, it is not known exactly which components of the dECM mimic the microenvironment of each organ and enable the potential in drug screening and discovery.[15] Thus, analytical methods such as proteomics are being used to determine the overall components of the dECM of each organ and the specific components that contribute to this particular potential.[16,85] Additionally, the components of dECMs derived from different organs are distinct, implying that an organ-derived dECM can recapitulate the specific microenvironment of the corresponding organ. Therefore, to fabricate an organ-specific platform, a dECM derived from the same organ should be used.[16] In the future, to use dECMs for the fabrication of more diverse organ platforms and realize their potential for drug screening and discovery,

it will be necessary to attempt decellularization for various organs that have not yet been developed and consider adjusting the decellularization process to ensure that the manufactured dECM bioink generates ECM with the same components for each batch.[86]

2.3.2. Usability as bioink for 3D bioprinting

Three-dimensional bioprinting uses biological materials, including cells, as bioinks to create specific cell structures.[28] This technology enables the fabrication of structures with controlled biomechanical properties, including fine-tuned cells and biomaterials, thereby enabling the manufacture of various *in vitro* models and implanted structures for tissue regeneration.[75] Three-dimensional bioprinting methods can be categorized into laser-assisted, inkjet, and extrusion-based bioprinting.[87] Conventionally, extrusion-based bioprinting has been widely used to fabricate layered structures with cells.[28] In 3D bioprinting, the required printing material is referred to as a bioink, which is a polymer solution containing living cells.[88] A bioink is primarily a hydrogel material that must have sufficient mechanical properties to maintain the shape of its structure after printing and spraying.[89]

Owing to the capability of dECMs to form tissue-specific microenvironments, there have been even further developments of dECM bioinks for various organs recently, and printability tests have been conducted to confirm that the bioinks could be used for 3D bioprinting.[88] The dECM bioinks can serve as a support structure and cell delivery carrier in the printing process and should be compliant with 3D bioprinting in terms of mechanical properties, printability, and biocompatibility.[89] Moreover, they can protect cells from external stimuli, such as shear stress and temperature changes, that occur during the printing process.[89] Each dECM bioink preserves its ECM components and provides an organ-specific environment for organ-derived cells, improving biocompatibility and cell function compared to those provided by other hydrogels, such as collagen and hyaluronic acid.[28] Additionally, dECM bioink can simulate the pathophysiological microenvironment better than other hydrogels.[81] For example, Kim et al. succeeded in fabricating a precise *in vitro* model of diabetes via 3D bioprinting using a visceral adipose tissue-derived dECM (vadECM) bioink.[81] The vadECM bioink proved superior to other hydrogels in simulating diabetes.

Taken together, the complex tissue-specific composition of the dECM bioink provides excellent biochemical function, biocompatibility, and a pathophysiological environment. Therefore, it is widely used as an effective bioink for the fabrication of various organ-mimicking models and disease models via 3D bioprinting.

2.4. Troubleshooting issues related to dECM bioink in 3D bioprinting

Compared to other biomaterials, dECM bioink provides a tissue-specific microenvironment by preserving its own biochemical composition of native tissue. Despite that, the dECM must be improved with regard to safety, mechanical properties, and fabrication yield to develop safer and more sophisticated dECM bioink-based *in vitro* models for drug screening and discovery. In this section, we discuss considerations for improving dECM bioink in the context of safety and fabrication usability.

2.4.1. Immunogenicity of dECM bioink

Animal tissue is the most widely used source of dECM bioink, encompassing porcine, bovine, and murine tissues.[90] These animal-derived tissue sources are easy to acquire for experiments and produce sufficient quantities and various types of dECMs; however, animal-related pathological factors, such as viruses, antigens, or bacteria, are safety concerns in the dECM application with human cells. For example, all mammalian tissues, except those of primates, have a carbohydrate antigen called the alpha-gal epitope on the cell surface, which induces immune rejection and inflammation in human tissues.[91,92] In addition, some animal-specific viruses are not known to be safe in reaction with human cells.[93] Porcine endogenous retrovirus (PERV) is a porcine genome-encoded virus that can infect human cells.[94] Another concern regarding the immunogenicity of the dECM is the adverse effects of the residual detergent. The residual detergent can destroy the intracellular microstructure and affect the permeability of the adapted cell membrane in the dECM.[95] Thus, if the immune cells that are employed in the dECM are activated because of immunogenicity in the dECM, the basal immune reaction elicited from the cells *in vitro* is not reflective of the health status; therefore, the unintended cytotoxic reactivity restricts the study concerning a disease.[96,97] Therefore, the decellularization process should include proper immunogen removal for the safe applications of dECM. However, if the immunogen removal process is too violent, the dECM can lose its protein composition and microstructure, affecting the tissue specificity. Therefore, it is necessary to discuss the reliable standard for immunogenicity lessening and the similarity to the native tissue in the context of biochemical features.[98,99] The concern about the immunogenicity of dECM can be traced to the regulatory issues stemming from the approvals by US Food and Drug Administration (FDA). Currently, one of the FDA's regulatory criteria for approving medical devices is a detection level of <0.5 EU/mL for endotoxins.[100] Another criterion for immunogen removal is that the residual DNA level must be <50 ng/mg for dry products.[101] In view of these criteria, production

guidelines for the preparation of dECMs for use in clinical study, covering topics such as biocompatibility, viruses, and bacterium, should be discussed.

2.4.2. Fabrication issue of dECM bioink

Different tissues and organs in the human body have different mechanical properties. For example, the brain and other soft tissue have low mechanical stiffness, whereas the bone has high mechanical stiffness. Cells also exhibit different behaviors, including differentiation and proliferation, depending on the stiffness of the cultured substrate. Therefore, simulation of specific mechanical properties in biomaterial for recapitulating native tissue is essential for predicting cellular behavior and fabricating artificial tissue models. One of the advantages of dECM bioinks is that their mechanical properties can be changed by adjusting the concentration of dried dECM; however, the adjustability of mechanical properties by changing the dECM concentration is limited owing to the solubility of the dECM. In addition, with a low-viscosity dECM bioink, it is difficult to maintain the structure during the fabrication process, whereas a high-viscosity bioink can induce nozzle clogging in 3D bioprinting and affect the cell growth and morphology. Thus, it is necessary to adjust the mechanical properties of the dECM so that it has similar stiffness to native tissue with sufficient printability. Currently, various supporting materials have been adapted to overcome mechanical weakness,[102,103] including gelatin methacryloyl (GelMA), poly(ethylene glycol)-diacrylate (PEG-DA), vitamin B2, and other crosslinkers, which induce rapid crosslinking under external stimuli such as light or chemical treatment. With supporting crosslinkers, the tuned mechanical properties allow free fabrication before crosslinking, which can prevent nozzle clogging in the 3D printer and reduce the shear-stress effect on cellular viability. In addition, it is favorable to recapitulate the stiffness of native tissue after crosslinking. For example, a spinal cord-derived dECM is conducive for neural stem cell adhesion and differentiation; however, it is easily degradable and thus requires mechanical-property tailoring. He et al. developed a spinal cord dECM with GelMA to tune and support the mechanical properties until neural stem cells were sufficiently differentiated.[104] In addition to GelMA, biocompatible polymers such as PEG-DA can be applied to regulate the mechanical properties. Shin et al. developed a PEG-DA-incorporated cardiac dECM to recapitulate the moduli of cardiac tissues. They found that the compressive modulus of PEG-DA/dECM could be tuned by regulating the concentration of PEG-DA. The enhanced bioink is favorable for maintaining the shape fidelity and adaptability of the printed construct.[105] Additionally, sacrificial materials allow the formation of complex tissue structures in conjunction with dECMs. For example, Pluronic F-127 (PF-127) is a type of hydrophilic detergent material that forms a solid gel structure at 37°C but forms a liquid below the gel point. It can be washed with water or a medium and thus can be applied to form a sacrificial structure, such as the hollow structure of a vessel. Gao et al. developed vascular models based on a vascular dECM together with calcium-PF-127 (CPF-127).[106] The usage of CPF-127 allowed the formation of a hollow structure, and by regulating the printing speed, atherosclerotic models were developed to study the vascular disease pathologies.[106] As such, incorporation with supportive biomaterial can improve not only the mechanical properties of the printed structure but also the fabrication freedom for the complex structure.

3. Decellularization and evaluation methodologies

Decellularization is an important procedure for clearing cellular components from the tissue while preserving only the ECM.[13] The decellularization method needs to be optimized depending on the tissue and organ, because mechanical stiffness and protein compositions vary between tissues. This section introduces different decellularization approaches and the optimization steps for specific tissues, as well as methods for evaluating the acquired dECMs.

3.1. Physical treatment

The purpose of physical treatment in decellularization is to destroy cellular membranes and achieve cellular dissolution.[107] Physical treatment is available in different forms, including chopping, repeated freeze–thaw cycles, and sonication. The conditions of these physical treatments should be adapted differently according to tissue characteristics. For example, in the case of extremely soft tissues (e.g., the brain and peripheral nerves), the inner structure of the ECM could be destroyed if the tissues are chopped into excessively small pieces.[108,109] In the case of retina, the ECM ultrastructure can be damaged in freeze–thaw processes because of ice crystal growth.[110,111] Conversely, cartilage and bone decellularization requires mechanical destruction to generate small pieces, such that the cellular membrane can be destroyed and the cells removed from the tissue.[112,113] Therefore, a suitable physical treatment is essential in pre-treatments for decellularization to effectively remove cellular components and maintain the ultrastructure of the tissue, depending on the density, mechanical stiffness, and protein/lipid composition. However, a single physical treatment is inadequate for sufficiently cleaving the cellular components; therefore, a combination of physical and chemical treatments is

required. The suitable physical treatment methods and precautions for different tissue types are summarized in Table 2.

3.2. Chemical treatment

The principle of chemical treatment in decellularization lies in dissolving various intracellular and extracellular connections and destroying cellular membranes, a step instrumental for the elimination of nuclear and cellular components.[101,114] In this section, we introduce representative solutions for decellularization, including ionic/nonionic detergents, enzymes, and acids/bases.

Detergents for decellularization can be categorized into ionic and nonionic detergents. The histological features of decellularized tissues are strongly affected by the type of detergent.[101,115] Ionic detergents, such as sodium dodecyl sulfate (SDS) and sodium deoxycholate, solubilize cell membranes and remove cellular components. These detergents are effective in the clearance of cytoplasmic components but can also damage essential ECM proteins, such as collagen and glycosaminoglycans (GAGs). By contrast, nonionic detergents, such as Triton X-100, disrupt lipidic interactions on cell membranes, including lipid–protein and lipid–lipid interactions.[115,116] They are relatively gentle compared to ionic detergents; therefore, they can be applied to thin and soft tissues. However, they may also disrupt the fibrous matrix network because of disconnection of the protein–lipid network. Therefore, nonionic and ionic detergents can be used together in compensatory methods for preserving proteins and preventing their denaturation.

The properties of the decellularized tissues can differ depending on the detergent type. For example, a nonionic detergent-treated decellularized urinary bladder matrix retains its fibrous network, whereas an ionic detergent-treated one will contain an irregular fraction of the protein network. However, the double-stranded deoxyribonucleic acid (DNA) fraction was higher under nonionic conditions than after being exposed to ionic detergent treatment.[117] Conversely, in the case of eye tissue, decellularized corneal hydrogels have different light transmittances, depending on the type of detergent used.[118,119] Therefore, the type of detergent for decellularization should be selected based on the target tissue type and the need to eliminate cellular component.

Enzymatic methods are used specifically to remove membrane surface allergens and cellular components (e.g., DNA, ribonucleic acid (RNA)). Examples of enzymes that can be used for decellularization include nucleases, lipase proteases, and alpha-galactosidase.[37,91,120] Nucleases can disconnect ribonucleotide or deoxyribonucleotide chains to make fractions that could then be washed away with detergents or solutions. Proteases (e.g., trypsin) break peptide bonds in proteins and destroy the microstructure of native tissue, thereby allowing decellularization solution to permeate the tissue's ultrastructure. The strong penetration effect of proteases underpins the success of the primary stage of decellularization; however, prolonged treatment induces protein loss, which decreases yield. Alpha-galactosidase can be additionally used for cleaving alpha-gal epitopes—a range of representative antigenic carbohydrate molecules in mammalian tissue—that are capable of inducing xenorejection in human transplants and inflammatory response in human-derived immune cells with immunoglobulin G (IgG).

Acid and base solutions can be utilized to hydrolyze the cellular membrane and dissolve the cytoplasm, supporting the cleavage of nuclear components (e.g., DNA, RNA) in cells.[121,122] Furthermore, these solutions can sterilize dECMs by lysing microorganisms during the fabrication process. Examples of acids used in decellularization include peracetic, acetic, and sulfuric acids; these three acids are widely used for decellularization to eliminate cellular membranes and cell organelles. On the other hand, base solutions disassemble extracellular biomolecules and remove cellular components between ECM structures; however, they cut off the fibril structures of fibrous proteins, inducing a transmutation of the mechanical properties of the ECMs.

Collectively, a proper combination of chemical decellularization processes, including detergent-based, enzymatic, and acid–base decellularization approaches, is necessary for eliminating cellular components while preserving essential proteins. Furthermore, treatment

Table 2. Physical treatments for decellularization and corresponding caveats for different tissue types

Physical treatment	Applicable tissues	Caveats
Chopping into small pieces	Brain, lung, skin, kidney	Obstruction to slurry formation due to small pieces
Freeze–thaw cycles	Adipose tissues, lung, cornea	Incomplete isolation of cellular component
Hydrostatic pressurization	Cardiac tissue, vessel, bone	Not suitable for soft tissue due to aggressive destruction of ECM structure
Mechanical agitation	Brain, adipose tissue, skin	Low-agitation RPM for soft tissue; high agitation RPM for hard tissue

Abbreviations: ECM, extracellular matrix; RPM, revolutions per minute.

time and chemical concentration should be optimized in an effort to preserve the ECM molecules. In particular, decellularization methods should be tissue-specific because tissues and organs have different mechanical stiffnesses, as well as protein and lipid compositions. A list of tissue-specific chemical decellularization methods is summarized in Table 3.

3.3 Evaluation of decellularized extracellular matrix

After decellularization, the acquired dECM should be evaluated with regard to the level of cellular removal, preservation of the ECM, and physical properties of the dECM. These parameters mirror the success rate of recapitulating the native tissue using the dECM. First, the residual cellular components can be evaluated according to the DNA fragment concentration in the dECM. The residual nucleic components are regarded as pathogenic factors in the adapting human cells. The nucleic acids can be analyzed by several methods, including hematoxylin staining, DAPI staining, Picogreen, TUNEL, and DNA kit analysis.[15,123,124] Among them, stained image-based analysis is favorable for macroscopically checking the remnant cellular components in the dECM. Meanwhile, optical absorbance-based analysis, such as Picogreen and DNA kit analysis, is necessary for quantitatively measuring remnant nucleic components. Thus, evaluation of cellular components should be conducted in both image-based and quantitative analyses.

The main purpose of decellularization is to preserve ECM components of the native tissue. The residual ECMs can be roughly classified as collagens, adhesive proteins, and GAGs. The degree of preservation of the ECM is currently a nonstandard yardstick for assessing the utility of a decellularization method. For example, a decellularized human brain contains a GAGs concentration similar to that of native human brain,[125] and the collagen content in decellularized porcine skin is 121% the amount in its native counterpart.[126] The residual ECM concentration can exceed the ECM concentration of the native tissue, because other components are removed; therefore, the ratio of remnant ECM to total mass is relatively higher in decellularized specimens. Thus, a proper standard is needed to assess the decellularization process from the viewpoint of preserving the dECM.

Furthermore, the tissue specificity of preserved ECMs can be evaluated. Toward this end, proteomics analysis can be conducted to determine the detailed composition of proteins and their physiological roles in the tissue.[127] Prior to proteomic analysis, the acquired dECM is solubilized and subjected to characterization by means of liquid chromatography/mass spectrometry (LC-MS). Through LC-MS, the protein profile of the dECM, as well as its relative intensity in the solubilized dECM, can be obtained. The characterized proteins can be categorized in Matrisome to delineate the interaction between ECM and

Table 3. Chemical treatment methods for decellularization of different tissues

Tissue/Organ type	Chemical combination	Chemical solution	Ref.
Brain	Ionic/Nonionic detergent, enzyme, acid	0.2% SDS, 0.2% Triton X-100, 50 U/mL DNase, 0.1% Peracetic acid	141
	Lysis buffer, enzyme	1% SDC, 40 U/mL DNase	131
	Nonionic detergent, enzyme, acid, base	1–3% Triton X-100, 0.05% Trypsin-EDTA, 0.1% Ammonium hydroxide	85
Cornea	Ionic/nonionic detergent	0.1–1% SDS, 1% Triton X-100	242
	Lysis buffer, enzyme	0.5 –4% Sodium deoxycholate, 1 mg/mL DNase	243
	Ionic detergent, enzyme	0.1% SDS, 4 mg/mL Dispase II,	244
Skin	Nonionic detergent, acid, enzyme	1% Triton X-100, 0.25% Trypsin, 1 mM EDTA, 30 U/ml DNase, 0.1% peracetic acid	126
	Ionic/Nonionic detergent, enzyme, acid	0.1% SDS, 0.26% EDTA, 0.69% Tris	245
Cardiac/Vessel	Ionic/Nonionic detergent, enzyme, acid	1% Triton X-100, 0.02% EDTA, RNase A 20 mg/mL, DNase I 0.2 mg/mL, 0.1% SDS, 0.05% trypsin, 0.02% EDTA	246
	Ionic/Nonionic detergent, acid	1% SDS, 1% Triton X-100, 0.1% peracetic acid	247
	Zwitterionic detergent, acid	8 mM CHAPS, 25 mM EDTA	248
Adipose tissue	Lysis buffer, enzyme	10 mM Tris, 5 mM EDTA, 0.25% trypsin, DNase, RNase, lipase,	249
	Solvent, enzyme	Isopropanol, DNase	250
Cartilage	Enzyme, acid	0.1% w/v EDTA, 3.5% phenylmethyl sulfonyl fluoride	251
	Ionic detergent, enzyme	2% SDS, 0.5 mg/mL DNase, 50 μg/mL RNase, 0.02% EDTA	252

cells in the tissue.[17] Details concerning ECM composition are available in a number of databases, such as the Human Protein Atlas,[18] PANTHER,[128] and MatrisomeDB.[129] Analysis of dECM protein composition data available on these databases could shed light on the similarity between human-derived ECM and other species-derived ECM, and the physiologic effect of each protein on cell behavior.

The physical properties of the dECM are also important for assessing the recapitulation of native tissue properties or intended mechanical properties from an engineering viewpoint. To investigate the mechanical properties of the dECM, several methods can be used, such as scanning electron microscopy, rheological analysis, and stress–strain analysis. The type of analysis is dictated by the target organ. For example, stiff tissues such as bone and cartilage require mechanical analyses, such as tensile and compressive tests.[130] Rheological analysis of soft tissues, including the brain, liver, and pancreas, is required to find out the tissue's stiffness, which is a determinant for selecting a suitable condition for cellular differentiation.[131-133] In addition, the dECM concentration in the solubilization process affects the stiffness of the hydrogel. Thus, it is necessary to have a complete picture of the physical properties and the stiffness of the target organs before adjustment can be conducted by controlling the concentration of dECM.

4. Application of tissue-derived decellularized extracellular matrix to disease modeling by 3D bioprinting

Under the current state of technology, fabricating disease models that perfectly mimic the function of an actual human organ and its pathological mechanism is still not possible,[134] posing a major challenge to the fabrication of 3D-bioprinted models. Nonetheless, accumulating evidence has proved that disease models generated by 3D bioprinting with dECM bioinks can simulate the microenvironments of organs. The human body consists of eight systems, with each made of various tissues.[135] In this review, we focus on the models that mimic nervous, cardiovascular, liver, and respiratory tissues, and their similarity in biological function to actual organs. Moreover, the disease models for these tissues are discussed. Table 4 summarizes the *in vitro* models made with dECM bioinks.

4.1. Nervous tissue-derived decellularized extracellular matrix

The nervous system encompasses both the central and peripheral nervous systems, which are constituted by tissues and organs such as brain, spinal cord, and peripheral neural networks.[136] The nervous system

Table 4. Summary of various in vitro models based on dECM bioinks

Target tissue/ organ	Bioinks	Cell type	Target disease	Ref.
Brain tumor	Porcine brain-derived dECM	Patient-derived glioblastoma	Glioblastoma	[141]
Brain	Porcine brain-derived dECM	Human neural stem cells	Traumatic brain injury	[253]
Sciatic nerve	Porcine sciatic nerve-derived dECM	No cells encapsulated (host tissue integration)	Peripheral nerve injury	[254]
Sciatic Nerve	Rat sciatic nerve-derived dECM	Rat Schwann cells	Peripheral nerve injury (*in vitro* evaluation)	[255]
Artery	Porcine aortic tissue	Human umbilical vein endothelial cells, human coronary artery smooth muscle cells, human dermal fibroblasts, human monocytes	Atherosclerosis	[106]
Heart/Cardiac tissues	Human omenta	Cardiomyocytes and endothelial cells differentiated from human-induced pluripotent stem cells (iPSCs)	Heart regeneration	[256]
Liver	Liver-derived dECM-based hybrid bioink	Human hepatocarcinoma cells	Liver epithelial-to-mesenchymal transition process	[184]
Liver	Gelatin, liver-derived dECM	Human hepatocytes, human umbilical vein endothelial cells, human hepatic stellate cells	Liver fibrosis	[186]
Airway	Airway mucosa-derived dECM, Matrigel	Human dermal microvascular endothelial cells, human lung fibroblasts, human tracheal epithelial cells	Asthma	[215]
Trachea	Tracheal mucosa-derived dECM, vascular-derived dECM	Bronchial/Tracheal epithelial cells, human umbilical vein endothelial cells, human eosinophil cells, human monocytes	Tracheal inflammatory disease	[216]

Abbreviation: dECM, decellularized extracellular matrix.

regulates bodily functions, including motor, cognitive, and autonomic functions, through signal processing between neurons. Damages to the nervous system are accompanied by ultimate apoptosis of neurons and the inevitable deterioration of the aforementioned functions. Typically, it is challenging to treat neural diseases, which also induce permanent disorders affecting the patients throughout their lifetime. Therefore, neurological studies are focused on elucidating disease mechanisms and exploring therapeutic solutions. To support these studies, models that delicately simulate neural tissues are required.

The brain is composed of multilayered structures and several types of neural cells, such as neurons, astrocytes, and microglia. Ever since Lancaster et al. developed brain organoids with complex layers and cellular compositions, various studies on brain tissue formation have been performed.[85,125,137] Matrigel, one of the most widely used materials in organ fabrication, is a non-neuronal matrix that generally lacks brain-specific proteins essential to the brain developmental process. In addition, traditional neural culture platforms (e.g., *in vitro* 2D cell culture) are not capable of simulating the sophisticated structure of the brain—particularly the neural-network model and vascularized units. Moreover, the neural cell behavior depends on the culture environment, including the mechanical stiffness of the substrate and ECM structures[138,139]; for example, the neuroinflammatory responses from glial cells are more intense on a 2D substrate than in the native tissue. Thus, conventional neural cell culture models differ from the native brain, which can be an obstacle for elucidating the neural physiology.

To offset the limitations in fabrication, brain decellularized extracellular matrix (BdECM) has been applied, in combination with 3D bioprinting, to *in vitro* brain modeling including brain cancer modeling. The major features of cancer are uncontrolled cell proliferation, increased angiogenesis, and chemotherapy resistance.[140] The origin of cancer should be ideally studied using preclinical models for patient-specific cancer therapy. Under the impact of mutations in relevant genes, tumorigenesis is particularly vulnerable to the effects of cell–ECM crosstalk. For example, brain glioblastoma (GBM) manifests varying levels of chemoresistance to therapies in different patients, thus requiring patient-specific anticancer therapy, such as a combination of medication and radiotherapy. The features of GBM are related to the hypoxic core in necrotizing zones. A hypoxic-core-formed GBM model has been developed using 3D bioprinting (Figure 3A),[141,142] and the hypoxic core has been simulated using a computer-aided design (CAD) program, with a focus on the oxygen diffusion gradient. Based on the simulation, GBM cells encapsulated in BdECM bioink at the core of the model were printed, and endothelial cells were printed using BdECM bioink at the outer ring of the core to recapitulate angiogenesis in the cancer model. The printed GBM with animal-derived BdECM effectively exhibited the chemoradiotherapy sensitivity seen in the cancer cells. For example, the GBM printed with BdECM had an upregulated expression in angiogenesis markers (e.g., serine hydroxymethyltransferase 2 [SHMT2], SRY-box transcription factor 2 [SOX2], vascular endothelial growth factor A [VEGFA], and nestin [NES]) and exhibited higher radiotherapy resistance compared with the model printed with collagen only. Collectively, experimental evidence confirmed that BdECM-based models possess the features of a patient-specific cancer therapy model and can sufficiently recapitulate cancer–ECM interaction effect.

Another application of dECMs in nervous system disease research is creating motor neuron models for neuromuscular disease study. Motor neurons in the CNS connect to skeletal muscle fibers to control muscular motion. However, aging process drives the degradation of multiple motor systems, thereby inducing neuromuscular diseases such as amyotrophic lateral sclerosis and myasthenia gravis. These neurodegenerative diseases have yet to be fully elucidated, and satisfactory clinical outcomes cannot be effectively achieved with drug treatments.[143-145] An *in vitro* neuromuscular model suitable for neuromuscular disease mechanism study and drug testing stands as an ideal avenue for circumventing the limitations inherent in animal models. A neuromuscular model should contain native-like long nerve bundles as well as muscular bundles, which are capable of recapitulating signal transduction between neurons and muscles. Kong et al. developed 3D-bioprinted neuromuscular junction (NMJ) models with a porcine spinal cord-derived dECM (CNSdECM) (Figure 3B) by building 3D-printed pillar with poly(ethylene-co-vinyl acetate) (PEVA) to induce mechanical stimulation of muscle cells for forming myotubes.[146] The muscle cells were encapsulated in a skeletal muscular dECM (MdECM), and induced pluripotent stem cell (iPSC)-derived motor neurons were encapsulated in the CNSdECM. Then, a cell-laden MdECM was printed in a belt shape for a muscular module beside the printed pillar to induce mechanical extension of the muscle cells and provide structural stability. In addition, the cell-laden CNSdECM was printed after 4 days of maturation of the muscular module and was connected to the muscular models as a neural module. Thus, the printed muscular module and neural module were connected to form an NMJ. The physiological synchronization of connected modules was confirmed with the presence electrophysiological signal transduction. The NMJ model is favorable for maintaining a long-term culture of the NMJ module, which allows degenerative disease modeling.

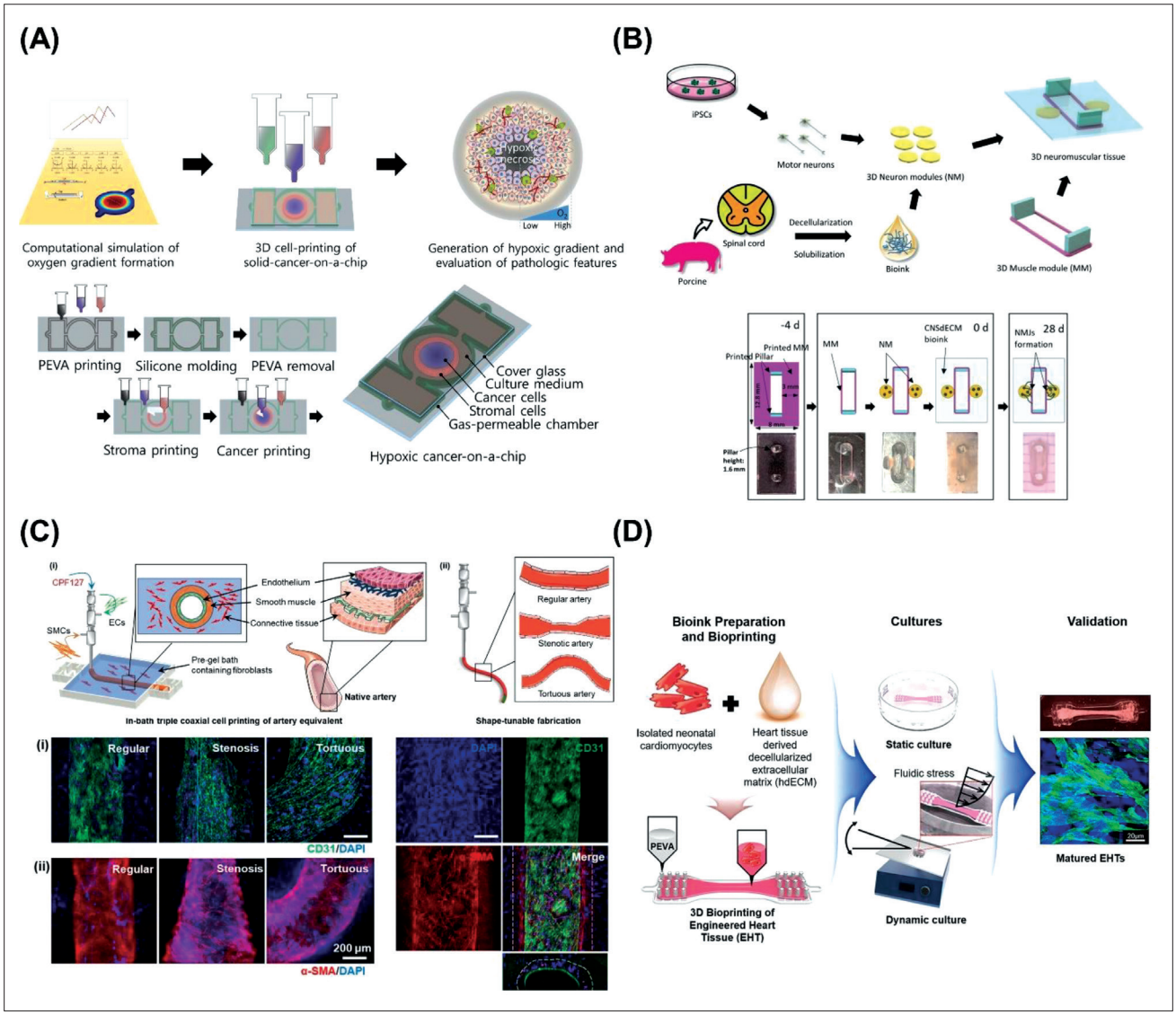

Figure 3. Examples of neural and cardiovascular models 3D-bioprinted with decellularized extracellular matrix (dECM). (A) 3D-bioprinted glioblastoma (GBM) on a chip. (B) PNSdECM-based 3D-bioprinted neuromuscular models. (C) Atherosclerosis disease model containing coaxial-printed vessels. (D) 3D-bioprinted cardiac tissue model incorporated with external stimuli. (Reproduced with permission from[106,142,146,162])

The neuromuscular model requires vascularization and regulation of the muscle bundle direction. Kim et al. built 3D NMJ models with endothelial spheroids by developing a methacrylate MdECM for recapitulating the mechanical stiffness of muscle tissues and applying electric field-assisted bioprinting to uniaxially align muscles in a bundle.[147] In addition, they used microdroplet-based spheroid-forming bioprinting (MDS-Printing) for generating endothelial cell spheroids. The co-printed endothelial cell spheroids and muscle fibers exhibited increased crosstalk related to myogenesis and vascularization, as compared to a simply mixed culture model. Moreover, when motor neuron spheroids were co-cultured with the endothelial spheroid-incorporated muscle chip, the NMJ was effectively activated with upregulated expression of growth factors and neuronal genes. These results indicate the crosstalk between vascularization and NMJ formation.

As such, neural models 3D-bioprinted with dECM are highly favorable for building 3D physiological structures. Notably, the dECM-based models can recapitulate the native tissue microenvironment, which directly affects cellular behavior. For example, brain cancer cells in the non-neuronal matrix (e.g., collagens) exhibited varying levels of chemosensitivity to therapies. In the case of a

nerve bundle, the CNSdECM can support neurons more as they grow and secret new ECMs, as opposed to Matrigel, which is degradable and not able to maintain the structural integrity. Moreover, 3D bioprinting-based models have the advantage of realizing the engineered design of the tissue analog, which is similar to the native tissue structure. Conventional methods are limited to building 2D structures and structures naturally generated from cellular differentiation. The 3D bioprinting structure in adherence with the engineer's design, which is intended to enhance the physiological resemblance to native tissues, is feasible. However, the current nervous system models require improvement with regard to precise control of neuronal direction and maturation. The technical limitations can be overcome by applying various 3D bioprinting methods and incorporating nervous tissue-specific dECMs and specific components of the dECM.[85,148] For example, the BBB—a brain-specific vascular structure—plays an essential role in the CNS as an innate barrier with selective permeability to prevent penetration of foreign material.[149] Owing to the tightly impregnable layer of endothelial cells in the BBB, most drug molecules as well as pathological factors cannot penetrate into the neural tissue. Thus, it is necessary to develop BBB-incorporated neural tissue models (i.e., neurovascular unit models), which can be utilized in studies for deciphering the penetration mechanism, and to identify a proper strategy for transporting drugs to the brain. For this, a vascular structure can be added to the *in vitro* neural model via 3D bioprinting. 3D bioprinting has potential for building various tubular structures for vessels and adapting different cell types for reconstructing complex organ systems. Thus, 3D-bioprinted neurovascular unit models, integrating the BBB and neural tissues, should be constructed to aid elucidation of the crosstalk between neural cells and BBB.[150]

Furthermore, additional bioreaction can support the recapitulation of the complex structure of central nervous tissue, such as the aligned neural network. The directionally controlled neural network is important for elucidating neural signal transduction in the CNS. In addition, 3D-bioprinted neural models incorporated with electrical sensors and reactors, such as microelectrode arrays, can widen the applicability of *in vitro* models in the context of healthy and pathological signal transduction in the CNS.[151]

4.2. Cardiovascular tissue-derived decellularized extracellular matrix

Cardiovascular disease (CVD) is a chronic and difficult-to-cure illness with the highest mortality rate in the world.[152,153] The cardiovascular system consists of the heart, arteries, veins, and capillaries that circulate blood throughout the body.[154] The vascular conduits and contractile tissues are interconnected with high complexity and heterogeneity. The vascular network delivers oxygen, nutrients, metabolites, and blood. Arteries transport oxygen-rich blood from the heart to other organs, whereas veins deliver metabolites to organs and tissues such as kidney and liver. Capillaries are also involved in substance transport, mediated by diffusion through thin endothelia. The heart acts as a pump to induce blood flow. Thus, any disruptions to the structural integrity and functions of cardiovascular tissue place an obstacle to substance circulation in the body.[155] One of the most prominent conditions associated with CVDs is atherosclerosis, which occurs as a result of plaque formation in the arterial walls due to high cholesterol and triglyceride levels. The development of atherosclerosis is also closely related to the alterations in hemodynamics, which can be affected by changes in vascular geometry.

Numerous experimental cardiac tissue models are available for clarifying the mechanisms behind cardiac diseases. Generally constructed on Transwell inserts, traditional *in vitro* 2D vessel models, which belong to the category of cardiac tissue models, allow for the observation of material penetration from one side to other side in the endothelial layer.[156] These models have contributed to our understanding of transport through the endothelium. Additionally, 2D cardiac models have been used to investigate cardiac myocyte behavior in cellular models.[157] However, the limited geometry of the models constrains their usefulness in the delineation of vascular and cardiac physiology, which are related to the geometry and mechanical properties of cardiac tissue. Furthermore, the hemodynamic mechanism in vessels has not been sufficiently elucidated from the viewpoint of biomechanical-therapeutic interplay. Thus, the mimicking potential of conventional microfluidic vascular models is limited to the recapitulation of various vascular geometries, which is not feasible for clarifying CVD mechanism. To overcome this limitation, recapitulation of 3D geometry has attracted attention. For example, Gao et al. suggested the use of vascular tissue-derived dECM (VdECM)-based arteries in atherosclerosis modeling (Figure 3C).[106] The VdECM has shown favorable effects on the angiogenesis and proliferation of endothelial cells by supporting the expression of cell–ECM attachment factors (e.g., vascular endothelial [VE]-cadherin, integrin beta-1), as reported in various studies. By capitalizing on these vascular-related advantages, Gao et al. developed a vessel structure using triple coaxial printing with VdECM.[106] To simulate the heterogeneity of the arterial structure, smooth muscles cells (SMCs) and endothelial cells (ECs) were employed in the triple coaxial printing. The geometry of the three-layered artery is adjustable; modifications can give rise to regular,

stenotic, and tortuous arteries. These arteries are able to recapitulate the pathophysiologic facets of atherosclerosis, such as inflammatory stimuli, hyperlipidemia, and turbulent flow. Thus, 3D bioprinting is a useful approach to building various tubular structures for models mimicking hemodynamically regulated pathological conditions. These models can be adapted for drug screening and disease prediction in models created with patient-derived cells.

Possessing microstructure of cardiac tissue, which is essential for understanding cardiac physiology, is another strength of 3D *in vitro* cardiac models. Cardiotoxicity is commonly cited as the one of the major reasons for drug failure. Among post-approval drugs, 45% have been withdrawn owing to cardiotoxicity.[158] In addition, the physiology of the animal heart differs from that of the human heart. For example, the resting heart rate of humans is between 60 and 100 bpm; in comparison, the animal models for clinical experiments (e.g., mice, rabbits, and dogs) have much higher heart rates, measuring 120–500 ppm.[159] Thus, a humanized cardiac model is indispensable for assessing drug toxicity in the context of human physiology. From this viewpoint, a cardiac dECM can simulate the sophisticated cardiac ECM network, and 3D bioprinting can aid in forming specific cardiac microstructures.[160,161] Das et al. bioprinted cardiac tissue models with a heart dECM (hdECM).[162] Cardiomyocytes in the hdECM differentiated into cells with a stretched morphology, whereas the cells in the collagen exhibited irregular morphologies. In particular, upregulated expression of heart-specific proteins in the bioprinted cardiac tissue indicated that the dECM and bioprinted models had enhanced tissue-specific characteristics.

As such, bioprinted cardiovascular models can be used in disease mechanism investigations and drug testing. To build more reliable cardiac tissue models, additional biological strategies can be applied to bioprinted models. The bioprinted cardiovascular models can be improved by tuning the mechanical properties of the bioink to match the native tissue's properties and by enhancing maturation orchestrated by external stimuli.[163] To simulate heart-specific mechanical stiffness, dECM bioink can be modified with biocompatible polymers. Shin et al. developed tuned cardiac dECM bioink with laponite and PEG-DA.[105] The biomaterials incorporated with dECM bioink exhibited a higher compressive modulus and stable shape fidelity. This tuning strategy can extend the application of cardiac dECMs to various disease conditions, facilitating the fabrication of healthy and fibrotic heart models. In addition, applying external stimuli to the cardiac models can enhance maturation. The commonly used cell sources are derived from iPSCs or animal-derived cells, which are immature cells that do not fully recapitulate cardiac functionality. Electrical stimuli are used because they affect the heart rate.[164] Bouchard et al. reported that maturation of human iPSC-derived cardiomyocytes in fibrin hydrogel can be accelerated using electromechanical signals.[165] In summary, engineered cardiovascular models can be improved with tunable dECMs and bioprinting, and their maturation can be induced with external stimuli. These cardiovascular models can be applied to various CVDs.

4.3. Liver tissue-derived decellularized extracellular matrix

The representative organs of the digestive system are stomach, liver, and intestine,[166] among which the liver plays an important role in regulating the overall metabolism, including blood sugar control, and processing and storage of body substances.[166] Additionally, the liver makes and stores various nutrients necessary for the body, such as proteins, participates in carbohydrate, fat, hormone, vitamin, and mineral metabolism, and detoxifies harmful substances.[167] However, diverse as these functions are, the list of known liver diseases, such as hepatitis, liver cancer, and alcoholic and non-alcoholic fatty liver disease, is similarly varied.[168] Particularly, fibrosis and cirrhosis may develop in the liver, resulting in homeostasis disruption and organ failure.[169] Fibrosis occurs only in certain organs, such as liver, lungs, and heart.[170] Since liver transplantation is the only feasible treatment for severe liver damage, it is essential to develop new therapies and *in vitro* models to test these therapies.[166] Additionally, simulating various liver functions *in vitro* has important implications for tissue engineering, liver regenerative medicine, and drug development.[75]

The traditional *in vitro* liver modeling entails the step of culturing liver cells in two dimensions,[171] which can be conducted with sandwich culturing of hepatocytes or different co-culture methods involving multiple cell types.[172] These traditional *in vitro* liver models are relatively simple in design, allow for adjustment of experimental conditions, and are convenient for operation during experiments. They are also used for evaluating drug metabolism and toxicity and for early assessment of drug effectiveness and safety. However, the 2D culture is faced with challenges in mimicking hepatic sinusoid heterogeneity, cell density under *in vivo* condition, and liver circulation.[173] To solve these problems, various 3D *in vitro* liver models have been developed. To create a successful 3D *in vitro* liver model, it is important to mimic a liver-specific sinusoidal structure with functional maturity.[174] The sinusoids are composed of various cells, including liver sinusoidal endothelial cells, hepatocytes, hepatic stellate cells, and Kupffer cells.[175] There are two fluidic channels consisting of the above-mentioned cells in the sinusoids within the 3D microenvironment of the ECM.[176] Various approaches have been attempted to simulate the

complex structure of the liver and its cell configurations *in vitro*. Several microfabrication techniques, such as photolithography and etching, have been used to replicate the complex physiological structure of the liver and to control its function.[177,178] An *in vitro* model integrated with a multilayered structure composed of various liver cells has been reported,[179] and a more advanced *in vitro* liver model containing sinusoidal structure that allows fluid flow has also been developed.[180]

However, the existing models cannot recapitulate the interactions between blood vessels and immune cells in the liver, rendering simulation of complex metabolic pathways and modeling of various liver diseases difficult. Additionally, co-culturing various liver cells on a single platform and reproducing a liver-specific microenvironment is challenging. Therefore, to create a liver-specific microenvironment, liver-derived dECM (LdECM) has recently been used as a bioink for 3D bioprinting.[181] Unlike conventional manufacturing methods, 3D bioprinting is suitable for positioning multiple cells and fabricating complex liver structures on one platform, which is able to simulate cell–cell interactions.[182] Thus, 3D-bioprinted models can reproduce the complex 3D structure and microenvironment of liver tissue, more closely reflecting actual liver pathophysiology and increasing the reliability and utility of research results. These models can also contribute to a better understanding of the mechanisms behind the development and progression of liver disease and the development of treatment and prevention strategies.[183] The significance of the *in vitro* liver models created by 3D bioprinting using LdECM bioink is detailed in the following.

Kang et al. prepared an LdECM-based hybrid bioink by mixing various hydrogels, including gelatin and alginate, with LdECM.[184] Human hepatocarcinoma cells (HepG2) were mixed with this hybrid bioink, and the mixture was then used in extrusion-based bioprinting to fabricate liver tissue in hexagonal pattern (Figure 4A).[184] The hybrid

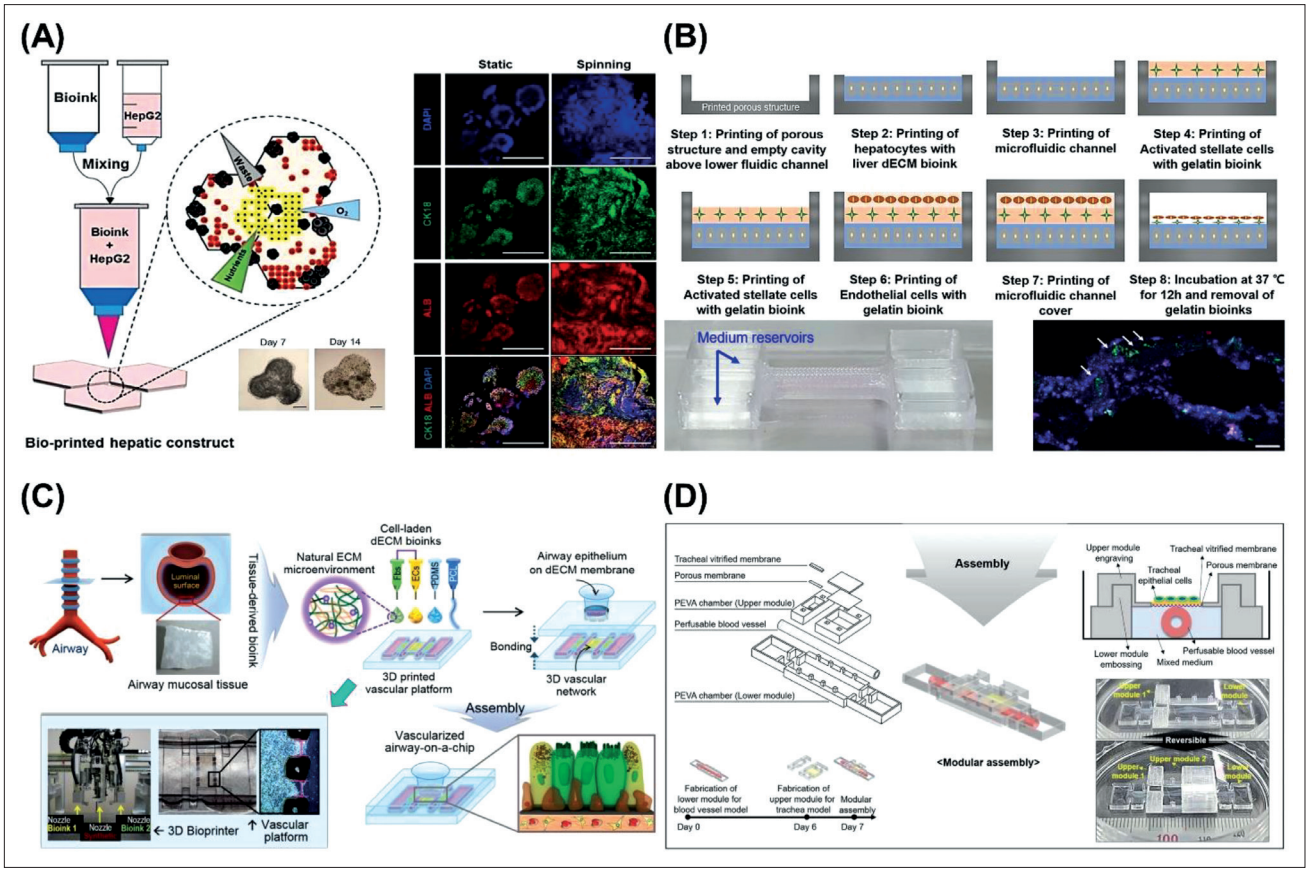

Figure 4. Examples of *in vitro* liver and respiratory models and their applications. (A, B) Fabrication of *in vitro* liver model using extrusion-based 3D bioprinting with (A) LdECM-based hybrid bioink and (B) LdECM bioink, and simulation of fibrosis in this model. (C, D) Fabrication of airway-on-a-chip and *in vitro* tracheal model using extrusion-based 3D bioprinting with mucosa-derived dECM: (C) fabrication of airway-on-a-chip and its application as an asthma model, and (D) fabrication of *in vitro* tracheal model and its application as an inflammatory respiratory disease model. (Reproduced with permission from[184,186,215,216])

bioink and spinning conditions helped generate liver spheroids and improve certain functions of the spheroids, such as albumin secretion. Additionally, a liver injury model was created via treatment with transforming growth factor-beta (TGF-beta), an inducer of epithelial-to-mesenchymal transition. The cells were treated with N-acetylcysteine (NAC), a therapeutic agent, to confirm the function of the model and its potential as a platform for drug testing. The model contained a hexagonal structure featuring a liver-specific microenvironment, mimicking a complex 3D liver structure. Furthermore, because of the spinning conditions, the model allowed fluid flow and could deliver sufficiently accurate data after drug screening. However, the cell sources that can be employed to create this 3D model are rather limited, and the model features an exceedingly simple structure that could not effectively mimic sinusoidal structures. Furthermore, inducing blood flow and tissue crosstalk within the model is difficult due to the absence of vascular mimetic structure.

Lee et al. were the first to develop an LdECM bioink, in which they encapsulated various hepatic cells, and with which they fabricated a normal *in vitro* model using extrusion-based 3D bioprinting.[181,185] Based on the normal liver model fabrication technology, an *in vitro* liver fibrosis model was created via the encapsulation of activated stellate cells, which are liver-inducing factors, in gelatin to induce liver fibrosis (Figure 4B).[186] A model was created using most of the cell types constituting the sinusoid structure, and a multilayered sinusoidal structure was fabricated by extrusion-based 3D bioprinting using the gelatin bioink as the sacrificial material. Additionally, a microfluidic channel was incorporated into the model; therefore, it was possible to simulate blood flow in a sinusoidal structure. Hallmarks of liver fibrosis, such as collagen accumulation, apoptosis, and liver fibrosis-specific marker expression, were conspicuously featured in this model. The model created in this study is significant as it was able to mimic most liver functions by precisely expressing the sinusoidal structure and liver-specific microenvironment, and it could be employed as a liver fibrosis model. Since the progression of liver fibrosis requires crosstalk among multiple organs, this *in vitro* liver model is unable to recapitulate the interactions between the specific tissues and organs. Nevertheless, this study successfully created a drug testing platform for liver fibrosis, paving the way for further research and development of drugs for liver diseases.

Although liver models that successfully simulate many functions of the liver *in vitro* have been developed using 3D bioprinting and various hydrogels, including LdECM, there are still many areas that require improvement in terms of fabrication and application. Recently, Taymour et al. developed a practical co-culture system featuring independently adjustable sections for various cell types via core-shell bioprinting.[187] Although multiple types of cells that constitute the liver were successfully arranged on one platform in three dimensions to mimic the liver's microenvironment, they were faced with the constraints in creating an intact liver-specific structure. In particular, current 3D bioprinting technology is limited to implementing complex vascular mimetics in various sizes, including cells, on one platform; therefore, producing a perfect sinusoid structure is not feasible using this technology.[184] Additionally, to implement the pathophysiological mechanisms of various liver diseases in these models, crosstalk between liver and different organ compartments via vascular mimetics is essential. Therefore, the development of 3D bioprinting technology that allows for the versatile fabrication of functional vascular mimetics of various sizes at the desired locations within *in vitro* models is necessary.[188]

Owing to the variations in genetics and lifestyle, the types and manifestations of liver diseases vary among patients, accentuating the needs for personalized 3D-bioprinted liver models tailored to the clinical requirements of patients.[189] Thus, a 3D bioprinting technique that can create liver models stably using patient-specific or individualized liver-derived stem cells is urgently needed to accurately simulate the mechanism of occurrence and progression of liver disease in each case. Yang et al. have attempted in creating a liver structure using hepatorganoids via 3D bioprinting technology, and various research teams have fabricated liver models using liver cell lines and primary cells.[190] However, liver models 3D-bioprinted with liver-derived cells obtained from patients are hitherto unavailable.[191] Thus, there is an urgent need to develop a 3D-bioprinted liver model using liver-derived cells. These personalized models may contribute to the development of personalized treatment and prevention strategies.

The liver functions in a dynamic environment.[192] Therefore, to simulate the functions of a real liver, it is necessary to develop a chamber that mimics blood flow, fluid dynamics, mechanical stress, etc., and combine it with a 3D-printed liver model. In addition to reproducing the structure and functions of the liver, the 3D-bioprinted model must be able to mimic the biochemical reactions of the liver.[191] To achieve this, analysis of multi-omics data, including those pertaining to RNA, proteins, and metabolites, is required to help understand the complex physiological responses of liver models. Shinozawa et al. recently developed a high-fidelity *in vitro* model using human pluripotent stem cell-derived organoids for the purpose of studying drug-induced liver injury.[193]

Additionally, many research teams have created high-fidelity liver models, which enable accurate and rapid drug screening.[191] However, these models do not recapitulate the liver-specific microenvironment. Therefore, hydrogels such as dECM bioink that can simulate liver microenvironment while maintaining high fidelity are promising ingredients for making liver models. Additionally, automated bioprinting technologies and advanced control systems must be introduced to increase efficiency and improve result consistency.

4.4. Respiratory tissue-derived decellularized extracellular matrix

Nasal meatus, airways, trachea, and lung are the representative tissues and organs of the respiratory system,[194] whose most important function is to facilitate the exchange of oxygen and carbon dioxide.[195] Respiratory diseases include infectious diseases (e.g., pneumonia[196]), airway-related diseases (e.g., asthma, COPD[197]), and malignant tumors.[194] Chronic respiratory diseases can develop into fibrosis, leading to organ failure.[198] Since there is no perfect treatment for these diseases, it is necessary to develop new treatments for respiratory diseases and efficient *in vitro* respiratory models for research and drug testing.[199]

The development of conventional *in vitro* respiratory model entails a step of culturing respiratory cells in two dimensions.[200] For example, this can be achieved with co-culturing methods of respiratory epithelial cell lines and endothelial cells, or air–liquid interface (ALI) culture methods.[200] These traditional *in vitro* models are relatively easy to set up, and the experimental conditions are easy to control. They are also relatively inexpensive compared with other models and are suitable for conducting basic research on respiratory system function and physiology.[200] However, the 2D culture is unable to produce 3D structure and to simulate the functional interactions of the lung; additionally, it faces challenges in reproducing complex physiological functions, such as gas exchange and respiratory movements.[201] Additionally, it does not sufficiently mimic the role of the immune system and inflammatory response.[201] To address these issues, various 3D *in vitro* respiratory models have been created. An effective *in vitro* respiratory model should possess multilayer structure made of the epithelium, basement membrane, and endothelium, and should be able to carry out the repetitive contraction and relaxation for gas exchange.[195,202] Air and blood flows are also important features of the model.[203] To incorporate these features in the model, flexible biomaterials must be used in the fabrication of the *in vitro* model.[204] The characteristics mentioned above reflect the requirements to realize the generation of complex structure seen in the respiratory system and the *in vitro* configurations of various respiratory cells for creating the models. Previous studies have demonstrated using Transwell and *in vitro* models to generate air–liquid interface (ALI) models, which possess multilayered structures composed of various alveolar cells on one platform.[205-208] Of particular importance, several studies have created models that simultaneously mimic repetitive breathing motion as well as blood and air flow, using flexible biomaterials and by means of photolithography-based microfabrication.[209,210]

The *in vitro* respiratory models should not only mimic structural features, but also reproduce the interactions between immune cells and microbial ecosystem in the respiratory system. However, the existing, conventional models have limitations in portraying interplay between the microenvironment of respiratory system and the external environment.[211,212] These models are also not useful for studying pathophysiological mechanisms behind the pathogenesis of asthma and COPD. Therefore, *in vitro* models are urgently needed for therapy testing and disease investigation.[213,214] One solution is to use airway-derived dECM as a bioink for 3D bioprinting to mimic the airway-specific microenvironments and pathophysiological environments of airway diseases.[88] Unlike conventional manufacturing methods, 3D bioprinting is suitable for precise airway simulation because it can manufacture multilayered cellular structures and simultaneously enable fluid and air flows on a single platform.[215,216] This allows 3D-bioprinted models to precisely reproduce the complex 3D structure and microenvironment of the airway, more closely reflecting the pathophysiology of various respiratory diseases and making research results more realistic.[217] In particular, it can more effectively mimic the role of the immune system and inflammatory response, enabling a better understanding of the mechanisms of progression of respiratory diseases and the development of treatment strategies.[218]

The importance of 3D bioprinting is exemplified by an *in vitro* respiratory model fabricated through 3D bioprinting using airway-derived dECM bioink. Park et al. developed a tracheal mucosa-derived dECM (tmdECM) bioink, in which they encapsulated epithelial cells and fibroblasts, and with which they fabricated an *in vitro* normal vascularized airway model by means of extrusion-based 3D bioprinting (Figure 4C).[215] Additionally, an *in vitro* asthma model has been created by treating a normal model with interleukin-13 (IL-13), an asthma-inducing factor.[219] To create a vascular part, 3D bioprinting was utilized to fabricate a vascular scaffold incorporating vascular cells. After undergoing a maturation process, the scaffold was induced to generate microvessels,

thereby successfully forming a vascular network where microvessels are interconnected. An *in vitro* vascularized airway model containing a multilayered cell structure was successfully fabricated after integrating the epithelial and vascular parts. Judging based on the functional activation of the cells constituting the models, tmdECM is more suitable than Matrigel, which is widely used in fabricating *in vitro* respiratory models, for simulating the airway-specific microenvironment.[205] Moreover, asthma-specific features were well expressed in the disease model, as confirmed by the secretion of inflammatory cytokines. This study is significant because it used a tmdECM bioink and 3D bioprinting to create a model that precisely features the airway-specific microenvironment and mimics the functions of most airways, and showed that the model is applicable for investigating asthma, which is an airway-specific disease. However, the model has limitations in that it does not have an airflow structure, and the inflammatory response cannot be precisely simulated owing to the absence of inflammatory cells. Nevertheless, this study showcases a pioneering *in vitro* model that features an airway-specific microenvironment and can aid the development of new asthma therapies and related research.

Nam et al. fabricated tmdECM and VdECM bioinks, in which they encapsulated epithelial and endothelial cells, and with which they fabricated normal *in vitro* tracheal models using extrusion-based 3D bioprinting (Figure 4D).[216] They developed cylindrical airway vascular structures via coaxial bioprinting using a sacrificial layer. This printing method is suitable for reproducing normal vascular structures because it can mimic the shapes of real vascular structures and adjust the structure's diameter.[220] A module containing tracheal epithelial cells was combined with this vascular structure to create the resultant *in vitro* tracheal model. In this model, tracheal epithelial cells formed an epithelial barrier, and treatment with IL-13 induced an inflammatory response. In particular, immune cell transmigration and infiltration occurred in the monocyte/macrophage lineage cells that flowed with the media through the blood vessels. This is representative of the airway immune response to exposure to an inflammatory environment.[221] In this study, a trachea-specific microenvironment was precisely created using tmdECM, VdECM bioink, and advanced 3D bioprinting. Additionally, the inflammatory mechanism in the 3D-bioprinted cylindrical matured vascular structure could be precisely simulated by flushing immune cells with medium. However, this structure did not possess trachea-specific microbial composition and was unable to simulate air flow, which is the main function of the trachea. Nevertheless, this study developed an advanced *in vitro* model that reflects the airway-specific microenvironment and overall tracheal multilayer structure. Moreover, because of the inclusion of a vascular structure, it is possible for the model to be connected with other organs of the respiratory system and contribute to the overall research related to tracheal disease.

While numerous models have been created using 3D bioprinting and diverse hydrogels, such as airway-derived dECMs, to effectively replicate numerous aspects of the respiratory system *in vitro*, several areas still require further improvement and practical implementation. Recently, Park et al. demonstrated the swift production of a multilayer structure of the respiratory system using extrusion-based 3D bioprinting.[222] The recent 3D-bioprinted respiratory models focus on featuring the simulation of more complex respiratory structures using various respiratory cells and the integration of different cell types to realistically mimic physiological characteristics.[223] However, the current 3D bioprinting technology is not capable of rapid creation of a respiratory structure encompassing cells and an airflow passage on one single platform and has limited strength in simulating respiratory function, including gas exchange.[224] Additionally, since most respiratory diseases have a fundamental link with the immune system, including an etiological connection with microorganisms, it becomes evident that a 3D bioprinting technology that can integrate immune cells and microbial composition to build a model is urgently needed.[224] Recently, Cho et al. developed a blood-lymphatic-integrated *in vitro* model using 3D bioprinting and successfully implemented the vascular system and immune system on one platform.[225] However, there has yet to be an attempt to combine respiratory cells within a lung model; thus, it is necessary to secure cell lines that can be used for 3D bioprinting and develop technology that can produce a model in one step in a short time.[224]

Additionally, more precise recapitulation of the microenvironment in respiratory models is warranted. In particular, the respiratory system functions in a dynamic environment.[226] To reflect this, Sengupta et al. have recently created a model equipped with electro-pneumatic devices and used elastic silicone to observe physiological responses on the platform under changing pressure conditions.[227] Nevertheless, to simulate a dynamic environment, a bioreactor that can mimic gas dynamics and control pressure and can reproduce various dynamic characteristics of the respiratory system and realistic chest movements must be developed in the future. Combining the bioreactor with a 3D-printed airway model can create a microenvironment that better resembles the actual respiratory system. To more accurately mimic pulmonary function, it is essential to incorporate methods such as sensors for real-time assessment of functional respiration, gas exchange, and mucosal movement into the bioreactor. With the real-time evaluation results, operational errors of

bioreactor can be minimized, allowing for generation of results that are highly reflective of the actual situation of respiratory system.

5. Conclusions and future perspectives

To create 3D structure and to simulate pathology-specific microenvironment in a disease model, it is important to select appropriate biomaterials and model manufacturing methods.[88] From this perspective, the combination of dECM as a biomaterial and 3D bioprinting as a manufacturing method is currently a promising approach to fabricate disease models.[87] First, 3D bioprinting can be used to process various cells and biomaterials that constitute organs into shapes suitable for creating pathophysiological structures.[228] 3D bioprinting can create *in vitro* and *in vivo* models that precisely mimic the structures and functions of human organs via the spatial placement of cell-containing bioink. To maximize the advantages of 3D bioprinting, it is important to select an appropriate biomaterial that can create the microenvironment of the disease model.[229] Therefore, employing dECM as a bioink to reproduce the ECM composition specific to a given organ has considerable potential for simulating the pathophysiological microenvironment of a disease.[229] 3D-bioprinted disease models created with dECM bioinks have demonstrated the potential for pathophysiological mechanism studies, tissue regeneration, and drug screening for various diseases.[228] However, widespread application of 3D bioprinting using dECM bioinks is limited by several challenges.[15] Some of these challenges associated with dECM and 3D bioprinting for the fabrication of various disease models are discussed as follows. Approaches to overcome these problems are also proposed. Additionally, ethical and legal issues related to 3D bioprinting and dECM bioink are briefly addressed.

Biomaterials suitable for 3D bioprinting must possess specific physical properties to ensure mechanical stability of the printed structure. In the case of hydrogels, for example, their restricted crosslinking limits their applicability as bioinks.[230] Therefore, to have a high degree of freedom in 3D bioprinting, it is necessary to develop advanced biomaterials with controllable physical properties through the chemical or physical treatment of conventional biomaterials. Regarding dECM, its important property is that it can simulate an organ-specific microenvironment.[229] However, despite their biochemical superiority, dECM bioinks have insufficient mechanical properties to fabricate various structures with high resolution.[15] One possible supportive method that addresses this limitation is the integration of a hydrogel with a polymer, such as polycaprolactone (PCL) and polyethylene-vinyl acetate (PEVA), to enhance structural integrity; however, plastic scaffolds may limit the usage of printed analogs in the context of native tissue substitutes.[88,231] Nonetheless, augmenting dECM bioink with other hydrogels is considered a reasonable strategy for improving the printability of the bioink through the improvement of its physical properties, and there are attractive methods for accomplishing this integration.[232,233] For example, Ali et al. improved the physical properties of a bioink using a methacrylated-dECM bioink and applied it to kidney regeneration,[232] whereas Kim et al. developed a light-activated dECM bioink and successfully fabricated centimeter-scale structures using extrusion-based 3D bioprinting.[233] These methods, which leverage the advantage of dECM bioink, can be used to fabricate stable 3D structures to improve their mechanical properties while maintaining their characteristics essential for creating tissue-specific microenvironment.

To maximize the utilization of the enhanced dECM bioink through the previously mentioned methods in various applications, the versatility of 3D bioprinting technology itself is essential. To develop more diverse disease models and to fabricate large-volume structures for tissue regeneration, it is necessary to improve fabrication technology, in terms of fabrication time and precision, using advanced dispensers and nozzles.[234] These requirements can be fulfilled by adopting a combination of existing 3D bioprinting technologies.[234] For example, Brassard et al. successfully generated macroscale tissue blocks using a combination of extrusion-based and inkjet bioprinting techniques.[234] Moreover, it is difficult to accurately control the printing conditions of a conventional 3D bioprinting system in real time, such as temperature and humidity, setting the stage for problems in the precision of structure manufacturing using dECM.[235] Therefore, it is necessary to establish a printability database for dECM bioinks and to apply real-time automatic control to printing systems.

Other challenges related to dECM bioinks include reproducibility and standardization issues.[15] The toxicity of agents used for decellularization and incomplete cell removal have also emerged as additional problems.[88] The dECM is an attractive biomaterial for tissue regeneration and disease models because it can be used to create tissue-specific microenvironments.[229] However, the dECM composition changes slightly from batch to batch, resulting in functional differences.[88] To address this problem, standardization of the material preparation process is required. There is a method for decellularizing large amounts of tissue to produce large amounts of dECM at once and mixing it.[13] A thorough analysis of all components of each organ-derived dECM lays a foundation for the quantitative standardization of their composition, which is instrumental for the creation of a more potent and uniform biological material. Furthermore, animal-derived dECM

should be subjected to immunogen removal to enhance biocompatibility.[98]

The use of toxic chemicals in the aforementioned decellularization and crosslinking processes gives rise to problems regarding cell survival and tissue necrosis, while incomplete cell removal following the decellularization process causes heterogeneous immune responses.[88] To address these problems, it is necessary to fundamentally analyze the effect of decellularization and crosslinking processes on ECM composition. Most current decellularization processes use a variety of toxic chemicals, which are detrimental to the preservation of the unique ECM composition; therefore, improved decellularization technology is required.[88] To avert this problem, Topuz et al. used supercritical carbon dioxide ($scCO_2$) in the decellularization process to minimize changes to the ECM composition.[236] Moreover, an advanced rapid detection method to determine whether residual toxic and cellular components remain in the dECM should be developed, and a standardized quality control protocol should be conducted in order to resolve this issue.

Proper resolution of the aforementioned issues could facilitate the utilization of dECM for the production of more precise normal and disease models and the process of tissue regeneration for various organs. Medical products for skin regeneration have already been developed using skin-derived dECM, such as AlloDerm® (BioHorizons) and Oasis® (Smith & Nephew).[237,238] A hydrogel bioink called deCelluid™ (T&R Biofab), which is applicable to 3D bioprinting and created from bone-derived dECM, has also been developed.[84] However, only dECMs applicable to the fabrication of a limited selection of organ models have been commercialized, and clinical cases describing the application of these dECMs remain scanty.[88] Therefore, it is necessary to standardize and commercialize dECM bioinks for a wider range of organs and to conduct more clinical trials to validate their reliability.

Finally, ethical and legal issues need to be addressed for more efficient use of 3D bioprinting and dECM bioink. 3D bioprinting and dECM bioink have the potential to overcome various ethical issues that fall within the realms of indiscriminate animal testing, clinical trials, and organ transplantation. At present, however, there has been no in-depth discussion regarding the ethical and legal issues related to 3D bioprinting and dECM bioink. Aside from the problems with printing technology, issues concerning biology, bioethics, and philosophy are catching our attention since a variety of human and animal derivatives, including cells, are employed in the process of 3D bioprinting.[239] Some of these ethical and legal issues associated with 3D bioprinting and dECM bioinks that are currently emerging are discussed as follows.

The source of biomaterials and dECM bioink applied in 3D bioprinting is an important ethical consideration. In compliance with ethical regulations, clarifications on how human or animal tissues and cells are obtained and used are needed. This may cover a wide range of aspects, such as tissue and cell donation procedure, consent giving, and protection of personal data. Additionally, research and complete verification of the safety and hazards of the biomaterials used are required. The use of unidentified materials or techniques that pose a risk to patients should be avoided. In the case of 3D bioprinting, digital 3D models should be treated as personalized human data; thus, the protection of human identifiable information must be considered under the context of privacy laws. Additionally, when cells and tissues are obtained from patients or donors, informed consent must be obtained.

Furthermore, ethics committee approval for conducting research or clinical trials involving dECM bioinks is required, and there is a need to harmonize these protocols globally. Currently, there are no unified regulations in this regard; thus, a set of comprehensive unified regulations should be drafted and officiated as soon as possible to protect the safety of research participants and ensure the compliance to the bioethical principles.[240] For reference, the European Medicines Agency regulates several tissue-engineered products as advanced therapy medicinal products (ATMPs) under the Gene Therapy Act.[241] Because the central idea of combining 3D bioprinting technology with dECM bioink serves the similar purposes as the production of ATMPs, unified regulations on this matter can be formulated in reference to the relevant acts. Additionally, to ensure that products stemming from the combination of 3D bioprinting and dECM bioink are safe, efficacious, and of good quality, protocols concerning the production, marketing, and utilization of dECM bioink must be set in compliance with local laws and regulations. Furthermore, it is important to note that commercial use of relevant technologies and dECM bioink may give rise to intellectual property infringement issues. Thus, caution must be exercised with regard to the development and sale of bioinks, and the patents and copyrights of established inventions must always be respected.

In conclusion, 3D bioprinting using dECM bioink is expected to achieve wide-scale application for the development of various intractable disease models and personalized models through the simulation of organ-specific microenvironments. Additionally, this technique is anticipated to be applicable to the fabrication of artificial organs for organ transplantation.

Acknowledgments

We extend our appreciation to BioRender (https://biorender.com/), with which we used to create schematics used in this paper.

Funding

This work was supported by the Korean Fund for Regenerative Medicine funded by Ministry of Science and ICT, and Ministry of Health and Welfare (22A0106L1, Republic of Korea), and was supported by the Alchemist Project (20012378, Development of Meta Soft Organ Module Manufacturing Technology without Immunity Rejection and Module Assembly Robot System) funded by the Ministry of Trade, Industry & Energy (MOTIE, Republic of Korea).

Conflict of interest

The authors declare no conflicts of interest.

Author contributions

Conceptualization: Mihyeon Bae, Joeng Ju Kim, Dong-Woo Cho
Writing – original draft: Mihyeon Bae, Joeng Ju Kim
Writing – review & editing: Jongmin Kim, Dong-Woo Cho

Ethics approval and consent to participate

Not applicable.

Consent for publication

Not applicable.

Availability of data

Not applicable.

References

1. Nikolic M, Sustersic T, Filipovic N. In vitro models and on-chip systems: biomaterial interaction studies with tissues generated using lung epithelial and liver metabolic cell lines. *Front Bioeng Biotechnol.* 2018;6:120. doi: 10.3389/fbioe.2018.00120
2. Rothbauer M, Rosser JM, Zirath H, Ertl P. Tomorrow today: organ-on-a-chip advances towards clinically relevant pharmaceutical and medical in vitro models. *Curr Opin Biotechnol.* 2019;55:81-86. doi: 10.1016/j.copbio.2018.08.009
3. Wang YI, Carmona C, Hickman JJ. Multiorgan microphysiological systems for drug development: strategies, advances, and challenges. *Adv Healthc Mater.* 2018;7(2):1701000. doi: 10.1002/adhm.201701000
4. Wikswo JP. The relevance and potential roles of microphysiological systems in biology and medicine. *Exp Biol Med.* 2014;239(9):1061-1072. doi: 10.1177/1535370214542068
5. Shyam R, Reddy LVK, Palaniappan A. Fabrication and characterization techniques of in vitro 3D tissue models. *Int J Mol Sci.* 2023;24(3):1912. doi: 10.3390/ijms24031912
6. Bae M, Yi H-G, Jang J, Cho D-W. Microphysiological systems for neurodegenerative diseases in central nervous system. *Micromachines.* 2020;11(9):855. doi: 10.3390/mi11090855
7. Brovold M, Almeida JI, Pla-Palacín I, et al. Naturally-derived biomaterials for tissue engineering applications. *Novel Biomater Regen Med.* 2018:421-449. doi: 10.1007/978-981-13-0947-2_23
8. Joyce K, Fabra GT, Bozkurt Y, Pandit A. Bioactive potential of natural biomaterials: identification, retention and assessment of biological properties. *Signal Transduct Target Ther.* 2021;6(1):122. doi: 10.1038/s41392-021-00512-8
9. Groll J, Boland T, Blunk T, et al. Biofabrication: reappraising the definition of an evolving field. *Biofabrication.* 2016;8(1):013001. doi: 10.1088/1758-5090/8/1/013001
10. Moroni L, Burdick JA, Highley C, et al. Biofabrication strategies for 3D in vitro models and regenerative medicine. *Nat Rev Mater.* 2018;3(5):21-37. doi: 10.1038/s41578-018-0006-y
11. Devillard CD, Marquette CA. Vascular tissue engineering: challenges and requirements for an ideal large scale blood vessel. *Front Bioeng Biotechnol.* 2021;9:721843. doi: 10.3389/fbioe.2021.721843
12. Cesare G. Muscle tissue engineering. Nukavarapu SP, Freeman JW, Laurencin CT, eds. *Regenerative Engineering of Musculoskeletal Tissues and Interfaces.* Amsterdam, Netherlands: Elsevier; 2015:239-268. doi: 10.1016/C2014-0-02826-2
13. Zhang X, Chen X, Hong H, Hu R, Liu J, Liu C. Decellularized extracellular matrix scaffolds: recent trends and emerging strategies in tissue engineering. *Bioact Mater.* 2022;10:15-31. doi: 10.1016/j.bioactmat.2021.09.014
14. Kim BS, Kim H, Gao G, Jang J, Cho D-W. Decellularized extracellular matrix: a step towards the next generation source for bioink manufacturing. *Biofabrication.* 2017;9(3):034104. doi: 10.1088/1758-5090/aa7e98
15. Kim BS, Das S, Jang J, Cho D-W. Decellularized extracellular matrix-based bioinks for engineering tissue-and organ-specific microenvironments. *Chem Rev.* 2020;120(19):10608-10661. doi: 10.1021/acs.chemrev.9b00808

16. Han W, Singh NK, Kim JJ, et al. Directed differential behaviors of multipotent adult stem cells from decellularized tissue/organ extracellular matrix bioinks. *Biomaterials*. 2019;224:119496.
doi: 10.1016/j.biomaterials.2019.119496

17. Hynes RO, Naba A. Overview of the matrisome—an inventory of extracellular matrix constituents and functions. *Cold Spring Harb Perspect Biol.* 2012;4(1):a004903.
doi: 10.1101/cshperspect.a004903

18. Uhlén M, Fagerberg L, Hallström BM, et al. Tissue-based map of the human proteome. *Science*. 2015;347(6220):1260419.
doi: 10.1126/science.1260419

19. Murphy SV, Atala A. 3D bioprinting of tissues and organs. *Nat. Biotechnol.* 2014;32(8):773-785.
doi: 10.1038/nbt.2958

20. Tan B, Gan S, Wang X, Liu W, Li X. Applications of 3D bioprinting in tissue engineering: advantages, deficiencies, improvements, and future perspectives. *J Mater Chem B*. 2021;9(27):5385-5413.
doi: 10.1039/D1TB00172H

21. Kačarević ŽP, Rider PM, Alkildani S, et al. An introduction to 3D bioprinting: possibilities, challenges and future aspects. *Materials*. 2018;11(11):2199.
doi: 10.3390/ma11112199

22. Zhang YS, Haghiashtiani G, Hübscher T, et al. 3D extrusion bioprinting. *Nat Rev Methods Primers*. 2021;1(1):75.
doi: 10.1038/s43586-021-00073-8

23. Li X, Liu B, Pei B, et al. Inkjet bioprinting of biomaterials. *Chem Rev.* 2020;120(19):10793-10833.
doi: 10.1021/acs.chemrev.0c00008

24. Guillotin B, Souquet A, Catros S, et al. Laser assisted bioprinting of engineered tissue with high cell density and microscale organization. *Biomaterials*. 2010;31(28): 7250-7256.
doi: 10.1016/j.biomaterials.2010.05.055

25. Ramesh S, Harrysson OL, Rao PK, et al. Extrusion bioprinting: recent progress, challenges, and future opportunities. *Bioprinting*. 2021;21:e00116.
doi: 10.1016/j.bprint.2020.e00116

26. Binder KW, Allen AJ, Yoo JJ, Atala A. Drop-on-demand inkjet bioprinting: a primer. *Gene Ther Regul.* 2011;6(01):33-49.
doi: 10.1142/S1568558611000258

27. Ventura RD. An overview of laser-assisted bioprinting (LAB) in tissue engineering applications. *Med Lasers*. 2021;10(2):76-81.
doi: 10.25289/ML.2021.10.2.76

28. Pati F, Jang J, Ha D-H, et al. Printing three-dimensional tissue analogues with decellularized extracellular matrix bioink. *Nat Commun*. 2014;5(1):3935.
doi: 10.1038/ncomms4935

29. Hubmacher D, Apte SS. The biology of the extracellular matrix: novel insights. *Curr Opin Rheumatol.* 2013;25(1):65.
doi: 10.1097/BOR.0b013e32835b137b

30. Huggins ML. The structure of fibrous proteins. *Chem Rev.* 1943;32(2):195-218.
doi: 10.1021/cr60102a002

31. Parry DA, Squire JM. *Fibrous Proteins: Structures and Mechanisms*. New York City, USA: Springer; 2017.
doi: 10.1007/978-3-319-49674-0

32. Linsenmayer T. Collagen. In: Hay ED, ed. *Cell Biology of Extracellular Matrix*. 2nd ed. New York, NY: Springer; 1991:7-44.
doi: 10.1007/978-1-4615-3770-0

33. Kristensen J, Karsdal M. Elastin. Karsdal MA, eds. *Biochemistry of Collagens, Laminins, and Elastin: Structure, Function, and Biomarkers*. Cambridge, Massachusetts, USA: Elsevier; 2016.
doi: 10.1016/C2015-0-05547-2

34. Rouse JG, Van Dyke ME. A review of keratin-based biomaterials for biomedical applications. *Materials*. 2010;3(2):999-1014.
doi: 10.3390/ma3020999

35. Kwiatkowska D, Kwiatkowska-Korczak J. Adhesive glycoproteins of the extracellular matrix. *Postepy Hig Med Dosw.* 1999;53(1):55-74.

36. Bonnans C, Chou J, Werb Z. Remodelling the extracellular matrix in development and disease. *Nat Rev Mol Cell Biol.* 2014;15(12):786-801.
doi: 10.1038/nrm3904

37. Mendibil U, Ruiz-Hernandez R, Retegi-Carrion S, Garcia-Urquia N, Olalde-Graells B, Abarrategi A. Tissue-specific decellularization methods: rationale and strategies to achieve regenerative compounds. *Int J Mol Sci.* 2020;21(15):5447.
doi: 10.3390/ijms21155447

38. Bowers SL, Banerjee I, Baudino TA. The extracellular matrix: at the center of it all. *J Mol Cell Cardiol.* 2010;48(3): 474-482.
doi: 10.1016/j.yjmcc.2009.08.024

39. Das S, Gao G, Lee JY, Jang J, Cho D-W. Decellularized tissue matrix-based 3D tissue modeling. In: Cho D-W, ed. *Biofabrication and 3D Tissue Modeling*. Burlington House, Piccadilly, London: The Royal Society of Chemistry; 2019.
doi: 10.1039/9781788012683-00148

40. Brown BN, Badylak SF. Extracellular matrix as an inductive scaffold for functional tissue reconstruction. *Transl Res.* 2014;163(4):268-285.
doi: 10.1016/j.trsl.2013.11.003

41. Song JJ, Ott HC. Organ engineering based on decellularized matrix scaffolds. *Trends Mol Med.* 2011;17(8):424-432.
doi: 10.1016/j.molmed.2011.03.005

42. Sakai T, Larsen M, Yamada KM. Fibronectin requirement in branching morphogenesis. *Nature*. 2003;423(6942):876-881. doi: 10.1038/nature01712

43. Hwang DG, Choi Y-m, Jang J. 3D bioprinting-based vascularized tissue models mimicking tissue-specific architecture and pathophysiology for in vitro studies. *Front Bioeng Biotechnol.* 2021;9:685507. doi: 10.3389/fbioe.2021.685507

44. Barros CS, Franco SJ, Müller U. Extracellular matrix: functions in the nervous system. *Cold Spring Harb Perspect Biol.* 2011;3(1):a005108. doi: 10.1101/cshperspect.a005108

45. Lau LW, Cua R, Keough MB, Haylock-Jacobs S, Yong VW. Pathophysiology of the brain extracellular matrix: a new target for remyelination. *Nat Rev Neurosci.* 2013;14(10):722-729. doi: 10.1038/nrn3550

46. Choi BH. Role of the basement membrane in neurogenesis and repair of injury in the central nervous system. *Microsc Res Tech*. 1994;28(3):193-203. doi: 10.1002/jemt.1070280304

47. Fawcett JW, Oohashi T, Pizzorusso T. The roles of perineuronal nets and the perinodal extracellular matrix in neuronal function. *Nat Rev Neurosci.* 2019;20(8):451-465. doi: 10.1038/s41583-019-0196-3

48. Bekku Y, Saito M, Moser M, et al. Bral2 is indispensable for the proper localization of brevican and the structural integrity of the perineuronal net in the brainstem and cerebellum. *J Comp Neurol.* 2012;520(8):1721-1736. doi: 10.1002/cne.23009

49. Ricks CB, Shin SS, Becker C, Grandhi R. Extracellular matrices, artificial neural scaffolds and the promise of neural regeneration. *Neural Regen Res.* 2014;9(17):1573. doi: 10.4103/1673-5374.141778

50. Sood D, Tang-Schomer M, Pouli D, et al. 3D extracellular matrix microenvironment in bioengineered tissue models of primary pediatric and adult brain tumors. *Nat Commun.* 2019;10(1):4529. doi: 10.1038/s41467-019-12420-1

51. Henke E, Nandigama R, Ergün S. Extracellular matrix in the tumor microenvironment and its impact on cancer therapy. *Front Mol Biosci.* 2020;6:160. doi: 10.3389/fmolb.2019.00160

52. Silva AC, Pereira C, Fonseca ACR, Pinto-do-Ó P, Nascimento DS. Bearing my heart: the role of extracellular matrix on cardiac development, homeostasis, and injury response. *Front Cell Dev Biol.* 2021;8:621644. doi: 10.3389/fcell.2020.621644

53. Rienks M, Papageorgiou A-P, Frangogiannis NG, Heymans S. Myocardial extracellular matrix: an ever-changing and diverse entity. *Circ Res.* 2014;114(5):872-888. doi: 10.1161/CIRCRESAHA.114.302533

54. Lockhart M, Wirrig E, Phelps A, Wessels A. Extracellular matrix and heart development. *Birth Defects Res, Part A*. 2011;91(6):535-550. doi: 10.1002/bdra.20810

55. Buijtendijk MF, Barnett P, van den Hoff MJ. Development of the human heart. *Am J Med Genet, Part C*. 2020;184(1):7-22. doi: 10.1002/ajmg.c.31778

56. Park H-J, De Jesus Morales KJ, Bheri S, Kassouf BP, Davis ME. Bidirectional relationship between cardiac extracellular matrix and cardiac cells in ischemic heart disease. *Stem Cell*. 2021;39(12):1650-1659. doi: 10.1002/stem.3445

57. Bedossa P, Paradis V. Liver extracellular matrix in health and disease. *J Pathol.* 2003;200(4):504-515. doi: 10.1002/path.1397

58. Martinez-Hernandez A, Amenta PS. Morphology, localization and origin of the hepatic extracellular matrix. In: Zern MA, Reid L, eds. *Extracellular Matrix: Chemistry, Biology, and Pathobiology with Emphasis on the Liver.* New York, NY: Marcel Dekker; 1993:255-327. doi: 10.1007/BF01606580

59. Rojkind M, Giambrone M-A, Biempica L. Collagen types in normal and cirrhotic liver. *Gastroenterology*. 1979;76(4):710-719. doi: 10.1016/S0016-5085(79)80170-5

60. Martinez-Hernandez A. The hepatic extracellular matrix. I. Electron immunohistochemical studies in normal rat liver. *Lab Invest.* 1984;51(1):57-74. https://europepmc.org/article/med/6376944

61. Schuppan D. Structure of the extracellular matrix in normal and fibrotic liver: collagens and glycoproteins. *Semin Liver Dis.* 1990;10(1):1-10. doi: 10.1055/s-2008-1040452

62. Wells RG. The role of matrix stiffness in regulating cell behavior. *Hepatology*. 2008;47(4):1394-1400. doi: 10.1002/hep.22193

63. Gressner A. Hepatic fibrogenesis: the puzzle of interacting cells, fibrogenic cytokines, regulatory loops, and extracellular matrix molecules. *Z Gastroenterol.* 1992;30:5-16.

64. McGuire RF, Bissell DM, Boyles J, Joseph Roll F. Role of extracellular matrix in regulating fenestrations of sinusoidal endothelial cells isolated from normal rat liver. *Hepatology*. 1992;15(6):989-997. doi: 10.1002/hep.1840150603

65. Tan Z, Sun H, Xue T, et al. Liver fibrosis: therapeutic targets and advances in drug therapy. *Front Cell Dev Biol.* 2021;9:730176. doi: 10.3389/fcell.2021.730176

66. Hussey GS, Dziki JL, Badylak SF. Extracellular matrix-based materials for regenerative medicine. *Nat Rev Mater.* 2018;3(7):159-173.

doi: 10.1038/s41578-018-0023-x

67. de Hilster RHJ, Sharma PK, Jonker MR, et al. Human lung extracellular matrix hydrogels resemble the stiffness and viscoelasticity of native lung tissue. *Am J Physiol.* 2020;318(4):L698-L704. doi: 10.1152/ajplung.00451.2019

68. Silver FH, Birk DE. Molecular structure of collagen in solution: comparison of types I, II, III and V. *Int J Biol Macromol.* 1984;6(3):125-132. doi: 10.1016/0141-8130(84)90052-7

69. Lever R, Page C. Glycosaminoglycans, airways inflammation and bronchial hyperresponsiveness. *Pulmon Pharmacol Therap.* 2001;14(3):249-254. doi: 10.1006/pupt.2001.0296

70. Burgstaller G, Oehrle B, Gerckens M, White ES, Schiller HB, Eickelberg O. The instructive extracellular matrix of the lung: basic composition and alterations in chronic lung disease. *Eur Respir J.* 2017;50(1):1601805. doi: 10.1183/13993003.01805-2016

71. Shifren A, Mecham RP. The stumbling block in lung repair of emphysema: elastic fiber assembly. *Proc Am Thorac Soc.* 2006;3(5):428-433. doi: 10.1513/pats.200601-009AW

72. Kranenburg AR, Willems-Widyastuti A, Mooi WJ, et al. Enhanced bronchial expression of extracellular matrix proteins in chronic obstructive pulmonary disease. *Am J Clin Pathol.* 2006;126(5):725-735. doi: 10.1309/JC477FAEL1YKV54W

73. Salazar LM, Herrera AM. Fibrotic response of tissue remodeling in COPD. *Lung.* 2011;189:101-109. doi: 10.1007/s00408-011-9279-2

74. Chakir J, Shannon J, Molet S, et al. Airway remodeling-associated mediators in moderate to severe asthma: effect of steroids on TGF-β, IL-11, IL-17, and type I and type III collagen expression. *J Allergy Clin Immunol.* 2003;111(6):1293-1298. doi: 10.1067/mai.2003.1557

75. Huang D, Gibeley SB, Xu C, et al. Engineering liver microtissues for disease modeling and regenerative medicine. *Adv Funct Mater.* 2020;30(44):1909553. doi: 10.1002/adfm.201909553

76. Parmaksiz M, Dogan A, Odabas S, Elçin AE, Elçin YM. Clinical applications of decellularized extracellular matrices for tissue engineering and regenerative medicine. *Biomed Mater.* 2016;11(2):022003. doi: 10.1088/1748-6041/11/2/022003

77. Mouw JK, Ou G, Weaver VM. Extracellular matrix assembly: a multiscale deconstruction. *Nat Rev Mol Cell Biol.* 2014;15(12):771-785. doi: 10.1038/nrm3902

78. Choudhury D, Tun HW, Wang T, Naing MW. Organ-derived decellularized extracellular matrix: a game changer for bioink manufacturing? *Trends Biotechnol.* 2018;36(8):787-805. doi: 10.1016/j.tibtech.2018.03.003

79. Park W, Gao G, Cho D-W. Tissue-specific decellularized extracellular matrix bioinks for musculoskeletal tissue regeneration and modeling using 3D bioprinting technology. *Int J Mol Sci.* 2021;22(15):7837. doi: 10.3390/ijms22157837

80. Heath DE. A review of decellularized extracellular matrix biomaterials for regenerative engineering applications. *Regen Eng Transl Med.* 2019;5:155-166. doi: 10.1007/s40883-018-0080-0

81. Kim JJ, Park JY, Nguyen VVT, et al. Pathophysiological reconstruction of a tissue-specific multiple-organ on-a-chip for Type 2 diabetes emulation using 3D cell printing. *Adv Funct Mater.* 2023;33(22):2213649. doi: 10.1002/adfm.202213649

82. Yang X, Ma Y, Wang X, et al. A 3D-bioprinted functional module based on decellularized extracellular matrix bioink for periodontal regeneration. *Adv Sci.* 2022;10(5):2205041. doi: 10.1002/advs.202205041

83. Kim H, Jang J-H, Han W, et al. Extracellular matrix-based sticky sealants for scar-free corneal tissue reconstruction. *Biomaterials.* 2023;292:121941. doi: 10.1016/j.biomaterials.2022.121941

84. Chae S, Yong U, Park W, et al. 3D cell-printing of gradient multi-tissue interfaces for rotator cuff regeneration. *Bioact Mater.* 2023;19:611-625. doi: 10.1016/j.bioactmat.2022.05.004

85. Cho A-N, Jin Y, An Y, et al. Microfluidic device with brain extracellular matrix promotes structural and functional maturation of human brain organoids. *Nat Commun.* 2021;12(1):4730. doi: 10.1038/s41467-021-24775-5

86. Giobbe GG, Crowley C, Luni C, et al. Extracellular matrix hydrogel derived from decellularized tissues enables endodermal organoid culture. *Nat Commun.* 2019;10(1):5658. doi: 10.1038/s41467-019-13605-4

87. Mandrycky C, Wang Z, Kim K, Kim D-H. 3D bioprinting for engineering complex tissues. *Biotechnol Adv.* 2016;34(4):422-434. doi: 10.1016/j.biotechadv.2015.12.011

88. Abaci A, Guvendiren M. Designing decellularized extracellular matrix-based bioinks for 3D bioprinting. *Adv Healthc Mater.* 2020;9(24):2000734. doi: 10.1002/adhm.202000734

89. De Santis MM, Alsafadi HN, Tas S, et al. Extracellular-matrix-reinforced bioinks for 3D bioprinting human tissue. *Adv Mater.* 2021;33(3):2005476. doi: 10.1002/adma.202005476

90. de Paula AGP, de Lima JD, Bastos TSB, et al. Decellularized extracellular matrix: the role of this complex biomaterial in regeneration. *ACS Omega.* 2023;8(25):22256-22267. doi: 10.1021/acsomega.2c06216

91. Wu L-C, Kuo Y-J, Sun F-W, et al. Optimized decellularization protocol including α-Gal epitope reduction for fabrication of an acellular porcine annulus fibrosus scaffold. *Cell Tissue Bank*. 2017;18:383-396. doi: 10.1007/s10561-017-9619-4

92. Stahl EC, Bonvillain RW, Skillen CD, et al. Evaluation of the host immune response to decellularized lung scaffolds derived from α-Gal knockout pigs in a non-human primate model. *Biomaterials*. 2018;187:93-104. doi: 10.1016/j.biomaterials.2018.09.038

93. Warren CJ, Sawyer SL. Identifying animal viruses in humans. *Science*. 2023;379(6636):982-983. doi: 10.1126/science.ade6985

94. Denner J. Porcine endogenous retroviruses and xenotransplantation, 2021. *Viruses*. 2021;13(11):2156. doi: 10.3390/v13112156

95. Naso F, Gandaglia A. Can heart valve decellularization be standardized? A review of the parameters used for the quality control of decellularization processes. *Front Bioeng Biotechnol.* 2022;10:830899. doi: 10.3389/fbioe.2022.830899

96. Rocha DN, Ferraz-Nogueira JP, Barrias CC, Relvas JB, Pêgo AP. Extracellular environment contribution to astrogliosis—lessons learned from a tissue engineered 3D model of the glial scar. *Front Cell Neurosci.* 2015;9:377. doi: 10.3389/fncel.2015.00377

97. Galarza S, Crosby AJ, Pak C, Peyton SR. Control of astrocyte quiescence and activation in a synthetic brain hydrogel. *Adv Healthc Mater.* 2020;9(4):1901419. doi: 10.1002/adhm.201901419

98. Kasravi M, Ahmadi A, Babajani A, et al. Immunogenicity of decellularized extracellular matrix scaffolds: a bottleneck in tissue engineering and regenerative medicine. *Biomater Res.* 2023;27(1):1-24. doi: 10.1186/s40824-023-00348-z

99. Chakraborty J, Roy S, Ghosh S. Regulation of decellularized matrix mediated immune response. *Biomater Sci.* 2020;8(5):1194-1215. doi: 10.1039/C9BM01780A

100. Jiang Y, Li R, Han C, et al. Extracellular matrix grafts: from preparation to application. *Int J Mol Med.* 2021;47(2):463-474. doi: 10.3892/ijmm.2020.4818

101. Gilpin A, Yang Y. Decellularization strategies for regenerative medicine: from processing techniques to applications. *Biomed Res Int.* 2017;2017:9831534. doi: 10.1155/2017/9831534

102. Basara G, Ozcebe SG, Ellis BW, Zorlutuna P. Tunable human myocardium derived decellularized extracellular matrix for 3D bioprinting and cardiac tissue engineering. *Gels*. 2021;7(2):70. doi: 10.3390/gels7020070

103. Jang J, Kim TG, Kim BS, Kim S-W, Kwon S-M, Cho D-W. Tailoring mechanical properties of decellularized extracellular matrix bioink by vitamin B2-induced photo-crosslinking. *Acta Biomater.* 2016;33:88-95. doi: 10.1016/j.actbio.2016.01.013

104. He W, Wang H, Zhang X, et al. Construction of a decellularized spinal cord matrix/GelMA composite scaffold and its effects on neuronal differentiation of neural stem cells. *J Biomater Sci.* 2022;33(16):2124-2144. doi: 10.1080/09205063.2022.2102275

105. Shin YJ, Shafranek RT, Tsui JH, Walcott J, Nelson A, Kim D-H. 3D bioprinting of mechanically tuned bioinks derived from cardiac decellularized extracellular matrix. *Acta Biomater.* 2021;119:75-88. doi: 10.1016/j.actbio.2020.11.006

106. Gao G, Park W, Kim BS, et al. Construction of a novel in vitro atherosclerotic model from geometry-tunable artery equivalents engineered via in-bath coaxial cell printing. *Adv Funct Mater.* 2021;31(10):2008878. doi: 10.1002/adfm.202008878

107. Rabbani M, Zakian N, Alimoradi N. Contribution of physical methods in decellularization of animal tissues. *J Med Signals Sens.* 2021;11(1):1-11. https://doi.org/10.4103/jmss.JMSS_2_20

108. DeQuach JA, Yuan SH, Goldstein LS, Christman KL. Decellularized porcine brain matrix for cell culture and tissue engineering scaffolds. *Tiss Eng Part A*. 2011;17(21-22):2583-2592. doi: 10.1089/ten.tea.2010.0724

109. Gregory E, Baek IH, Ala-Kokko N, et al. Peripheral nerve decellularization for in vitro extracellular matrix hydrogel use: a comparative study. *ACS Biomater Sci Eng.* 2022;8(6):2574-2588. doi: 10.1021/acsbiomaterials.2c00034

110. Kim J, Park JY, Kong JS, Lee H, Won JY, Cho D-W. Development of 3D printed Bruch's membrane-mimetic substance for the maturation of retinal pigment epithelial cells. *Int J Mol Sci.* 2021;22(3):1095. doi: 10.3390/ijms22031095

111. Kundu J, Michaelson A, Talbot K, Baranov P, Young MJ, Carrier RL. Decellularized retinal matrix: natural platforms for human retinal progenitor cell culture. *Acta Biomater.* 2016;31:61-70. doi: 10.1016/j.actbio.2015.11.028

112. Lee J, Hong J, Kim W, Kim GH. Bone-derived dECM/alginate bioink for fabricating a 3D cell-laden mesh structure for bone tissue engineering. *Carbohydr Polym.* 2020;250:116914. doi: 10.1016/j.carbpol.2020.116914

113. Sun Y, Yan L, Chen S, Pei M. Functionality of decellularized matrix in cartilage regeneration: a comparison of tissue versus cell sources. *Acta Biomater.* 2018;74:56-73. doi: 10.1016/j.actbio.2018.04.048

114. Gilbert TW, Sellaro TL, Badylak SF. Decellularization of tissues and organs. *Biomaterials*. 2006;27(19):3675-3683. doi: 10.1016/j.biomaterials.2006.02.014

115. Neishabouri A, Soltani Khaboushan A, Daghigh F, Kajbafzadeh A-M, Zolbin MM. Decellularization in tissue engineering and regenerative medicine: evaluation, modification, and application methods. *Front Bioeng Biotechnol.* 2022;10:805299. doi: 10.3389/fbioe.2022.805299

116. Ketchedjian A, Jones AL, Krueger P, et al. Recellularization of decellularized allograft scaffolds in ovine great vessel reconstructions. *Ann Thorac Surg.* 2005;79(3):888-896. doi: 10.1016/j.athoracsur.2004.09.033

117. White LJ, Taylor AJ, Faulk DM, et al. The impact of detergents on the tissue decellularization process: a ToF-SIMS study. *Acta Biomater.* 2017;50:207-219. doi: 10.1016/j.actbio.2016.12.033

118. Pellegata AF, Asnaghi M, Stefani I, et al. Detergent-enzymatic decellularization of swine blood vessels: insight on mechanical properties for vascular tissue engineering. *Biomed Res Int.* 2013;2013:918753. doi: 10.1155/2013/918753

119. Fernández-Pérez J, Ahearne M. The impact of decellularization methods on extracellular matrix derived hydrogels. *Sci Rep.* 2019;9(1):14933. doi: 10.1038/s41598-019-49575-2

120. Yang B, Zhang Y, Zhou L, et al. Development of a porcine bladder acellular matrix with well-preserved extracellular bioactive factors for tissue engineering. *Tissue Eng Part C.* 2010;16(5):1201-1211. doi: 10.1089/ten.tec.2009.0311

121. Poornejad N, Schaumann LB, Buckmiller EM, et al. The impact of decellularization agents on renal tissue extracellular matrix. *J Biomater Appl.* 2016;31(4):521-533. doi: 10.1177/0885328216656099

122. Choi JS, Kim BS, Kim JY, et al. Decellularized extracellular matrix derived from human adipose tissue as a potential scaffold for allograft tissue engineering. *J Biomed Mater Res Part A*. 2011;97(3):292-299. doi: 10.1002/jbm.a.33056

123. Narciso M, Otero J, Navajas D, Farré R, Almendros I, Gavara N. Image-based method to quantify decellularization of tissue sections. *Int J Mol Sci.* 2021;22(16):8399. doi: 10.3390/ijms22168399

124. Dimou Z, Michalopoulos E, Katsimpoulas M, et al. Evaluation of a decellularization protocol for the development of a decellularized tracheal scaffold. *Anticancer Res.* 2019;39(1):145-150. doi: 10.21873/anticanres.13090

125. Jin Y, Lee JS, Kim J, et al. Three-dimensional brain-like microenvironments facilitate the direct reprogramming of fibroblasts into therapeutic neurons. *Nat Biomed Eng.* 2018;2(7):522-539. doi: 10.1038/s41551-018-0260-8

126. Kim BS, Kwon YW, Kong J-S, et al. 3D cell printing of in vitro stabilized skin model and in vivo pre-vascularized skin patch using tissue-specific extracellular matrix bioink: a step towards advanced skin tissue engineering. *Biomaterials*. 2018;168:38-53. doi: 10.1016/j.biomaterials.2018.03.040

127. Byron A, Humphries JD, Humphries MJ. Defining the extracellular matrix using proteomics. *Int J Exp Pathol.* 2013;94(2):75-92. doi: 10.1111/iep.12011

128. Mi H, Muruganujan A, Thomas PD. PANTHER in 2013: modeling the evolution of gene function, and other gene attributes, in the context of phylogenetic trees. *Nucleic Acids Res.* 2012;41(D1):D377-D386. doi: 10.1093/nar/gks1118

129. Shao X, Taha IN, Clauser KR, Gao YT, Naba A. MatrisomeDB: the ECM-protein knowledge database. *Nucleic Acids Res.* 2020;48(D1):D1136-D1144. doi: 10.1093/nar/gkz849

130. Chen Y-W, Lin Y-H, Lin T-L, Lee K-XA, Yu M-H, Shie M-Y.3D-biofabricated chondrocyte-laden decellularized extracellular matrix-contained gelatin methacrylate auxetic scaffolds under cyclic tensile stimulation for cartilage regeneration. *Biofabrication*. 2023;15(4):045007. doi: 10.1088/1758-5090/ace5e1

131. Simsa R, Rothenbücher T, Gürbüz H, et al. Brain organoid formation on decellularized porcine brain ECM hydrogels. *PLoS One*. 2021;16(1):e0245685. doi: 10.1371/journal.pone.0245685

132. Ijima H, Nakamura S, Bual R, Shirakigawa N, Tanoue S. Physical properties of the extracellular matrix of decellularized porcine liver. *Gels*. 2018;4(2):39. doi: 10.3390/gels4020039

133. Goh S-K, Bertera S, Olsen P, et al. Perfusion-decellularized pancreas as a natural 3D scaffold for pancreatic tissue and whole organ engineering. *Biomaterials*. 2013;34(28):6760-6772. doi: 10.1016/j.biomaterials.2013.05.066

134. Mironov V, Visconti RP, Kasyanov V, Forgacs G, Drake CJ, Markwald RR. Organ printing: tissue spheroids as building blocks. *Biomaterials*. 2009;30(12):2164-2174. doi: 10.1016/j.biomaterials.2008.12.084

135. Chen X, Zhang YS, Zhang X, Liu C. Organ-on-a-chip platforms for accelerating the evaluation of nanomedicine. *Bioact Mater.* 2021;6(4):1012-1027. doi: 10.1016/j.bioactmat.2020.09.022

136. Brodal P. *The Central Nervous System: Structure and Function*. Oxford, England: Oxford University Press; 2004. https://global.oup.com/academic/product/the-central-nervous-system-9780190228958?cc=kr&lang=en&

137. Lancaster MA, Renner M, Martin C-A, et al. Cerebral organoids model human brain development and microcephaly. *Nature*. 2013;501(7467):373-379. doi: 10.1038/nature12517

138. Saha K, Keung AJ, Irwin EF, et al. Substrate modulus directs neural stem cell behavior. *Biophys J*. 2008;95(9):4426-4438. doi: 10.1529/biophysj.108.132217

139. Yi B, Xu Q, Liu W. An overview of substrate stiffness guided cellular response and its applications in tissue regeneration. *Bioact Mater.* 2022;15:82-102. doi: 10.1016/j.bioactmat.2021.12.005

140. Portenoy RK. Cancer pain: pathophysiology and syndromes. *Lancet*. 1992;339(8800):1026-1031. doi: 10.1016/0140-6736(92)90545-e

141. Yi H-G, Jeong YH, Kim Y, et al. A bioprinted human-glioblastoma-on-a-chip for the identification of patient-specific responses to chemoradiotherapy. *Nat Biomed Eng.* 2019;3(7):509-519. doi: 10.1038/s41551-019-0363-x

142. Park W, Bae M, Hwang M, Jang J, Cho D-W, Yi H-G. 3D cell-printed hypoxic cancer-on-a-chip for recapitulating pathologic progression of solid cancer. *JoVE.* 2021;(167):e61945. doi: 10.3791/61945

143. Slanzi A, Iannoto G, Rossi B, Zenaro E, Constantin G. In vitro models of neurodegenerative diseases. *Front Cell Dev Biol.* 2020;8:328. doi: 10.3389/fcell.2020.00328

144. Cetin S, Knez D, Gobec S, Kos J, Pišlar A. Cell models for Alzheimer's and Parkinson's disease: at the interface of biology and drug discovery. *Biomed Pharmacother.* 2022;149:112924. doi: 10.1016/j.biopha.2022.112924

145. Osaki T, Shin Y, Sivathanu V, Campisi M, Kamm RD. In vitro microfluidic models for neurodegenerative disorders. *Adv Healthc Mater.* 2018;7(2):1700489. doi: 10.1002/adhm.201700489

146. Kong JS, Huang X, Choi YJ, et al. Promoting long-term cultivation of motor neurons for 3D neuromuscular junction formation of 3D in vitro using central-nervous-tissue-derived bioink. *Adv Healthc Mater.* 2021;10(18):2100581. doi: 10.1002/adhm.202100581

147. Kim W, Kim G. Bioprinting 3D muscle tissue supplemented with endothelial-spheroids for neuromuscular junction model. *Appl Phys Rev.* 2023;10(3):031410. doi: 10.1063/5.0152924

148. Lee SJ, Esworthy T, Stake S, et al. Advances in 3D bioprinting for neural tissue engineering. *Adv Biosyst.* 2018;2(4):1700213. doi: 10.1002/adbi.201700213

149. Daneman R, Prat A. The blood–brain barrier. *Cold Spring Harb Perspect Biol.* 2015;7(1):a020412. doi: 10.1101/cshperspect.a020412

150. Potjewyd G, Moxon S, Wang T, Domingos M, Hooper NM. Tissue engineering 3D neurovascular units: a biomaterials and bioprinting perspective. *Trends Biotechnol.* 2018;36(4):457-472. doi: 10.1016/j.tibtech.2018.01.003

151. Mossink B, Verboven AH, van Hugte EJ, et al. Human neuronal networks on micro-electrode arrays are a highly robust tool to study disease-specific genotype-phenotype correlations in vitro. *Stem Cell Rep.* 2021;16(9):2182-2196. doi: 10.1016/j.stemcr.2021.07.001

152. Nabel EG. Cardiovascular disease. *N Engl J Med.* 2003;349(1):60-72. doi: 10.1056/NEJMra035098

153. Wilkins E, Wilson L, Wickramasinghe K, et al. *European Cardiovascular Disease Statistics 2017*. Brussels, Belgium: European Heart Network; 2017. https://researchportal.bath.ac.uk/en/publications/european-cardiovascular-disease-statistics-2017

154. Zhang WJ, Liu W, Cui L, Cao Y. Tissue engineering of blood vessel. *J Cell Mol Med.* 2007;11(5):945-957. doi: 10.1111/j.1582-4934.2007.00099.x

155. Abramson DI. *Blood Vessels and Lymphatics*. Cambridge, Massachusetts, USA: Elsevier; 2013. doi: 10.1016/C2013-0-12391-4

156. Bogseth A, Ramirez A, Vaughan E, Maisel K. In vitro models of blood and lymphatic vessels—connecting tissues and immunity. *Adv Biol.* 2023;7(5):2200041. doi: 10.1002/adbi.202200041

157. Abdelsayed G, Ali D, Malone A, et al. 2D and 3D in-vitro models for mimicking cardiac physiology. *Appl Eng Sci.* 2022;12:100115. doi: 10.1016/j.apples.2022.100115

158. Ferri N, Siegl P, Corsini A, Herrmann J, Lerman A, Benghozi R. Drug attrition during pre-clinical and clinical development: understanding and managing drug-induced cardiotoxicity. *Pharmacol Ther.* 2013;138(3):470-484. doi: 10.1016/j.pharmthera.2013.03.005

159. Ho D, Zhao X, Gao S, Hong C, Vatner DE, Vatner SF. Heart rate and electrocardiography monitoring in mice. *Curr Protoc Mouse Biol.* 2011;1(1):123-139. doi: 10.1002/9780470942390.mo100159

160. Wolfe JT, He W, Kim M-S, et al. 3D-bioprinting of patient-derived cardiac tissue models for studying congenital heart disease. *Front Cardiovasc Med.* 2023;10:1162731. doi: 10.3389/fcvm.2023.1162731

161. Faulkner-Jones A, Zamora V, Hortigon-Vinagre MP, et al. A bioprinted heart-on-a-chip with human pluripotent stem cell-derived cardiomyocytes for drug evaluation. *Bioengineering*. 2022;9(1):32. doi: 10.3390/bioengineering9010032

162. Das S, Kim S-W, Choi Y-J, et al. Decellularized extracellular matrix bioinks and the external stimuli to enhance cardiac

tissue development in vitro. *Acta Biomater.* 2019;95:188-200. doi: 10.1016/j.actbio.2019.04.026

163. Min S, Cho S-W. Engineered human cardiac tissues for modeling heart diseases. *BMB Rep.* 2023;56(1):32. doi: 10.5483/BMBRep.2022-0185

164. Eng G, Lee BW, Protas L, et al. Autonomous beating rate adaptation in human stem cell-derived cardiomyocytes. *Nat Commun.* 2016;7(1):10312. doi: 10.1038/ncomms10312

165. Ronaldson-Bouchard K, Ma SP, Yeager K, et al. Advanced maturation of human cardiac tissue grown from pluripotent stem cells. *Nature*. 2018;556(7700):239-243. doi: 10.1038/s41586-018-0016-3

166. Lasli S, Kim HJ, Lee K, et al. A human liver-on-a-chip platform for modeling nonalcoholic fatty liver disease. *Adv Biosyst.* 2019;3(8):1900104. doi: 10.1002/adbi.201900104

167. Ozougwu JC. Physiology of the liver. *Int J Res Pharm Biosci.* 2017;4(8):13-24.

168. Bellentani S. The epidemiology of non-alcoholic fatty liver disease. *Liver Int.* 2017;37:81-84. doi: 10.1111/liv.13299

169. Friedman SL. Liver fibrosis–from bench to bedside. *J Hepatol.* 2003;38:38-53. doi: 10.1016/S0168-8278(02)00429-4

170. Border WA, Noble NA. Transforming growth factor β in tissue fibrosis. *N Engl J Med.* 1994;331(19):1286-1292. doi: 10.1056/NEJM199411103311907

171. Yanni SB, Augustijns PF, Benjamin DK, Brouwer KLR, Thakker DR, Annaert PP. In vitro investigation of the hepatobiliary disposition mechanisms of the antifungal agent micafungin in humans and rats. *Drug Metab Dispos.* 2010;38(10):1848-1856. doi: 10.1124/dmd.110.033811

172. LeCluyse EL, Audus KL, Hochman JH. Formation of extensive canalicular networks by rat hepatocytes cultured in collagen-sandwich configuration. *Am J Physiol: Cell Physiol.* 1994;266(6):C1764-C1774. doi: 10.1152/ajpcell.1994.266.6.C1764

173. De Graaf IA, Olinga P, De Jager MH, et al. Preparation and incubation of precision-cut liver and intestinal slices for application in drug metabolism and toxicity studies. *Nat. Protoc.* 2010;5(9):1540-1551. doi: 10.1038/nprot.2010.111

174. Du Y, Li N, Yang H, et al. Mimicking liver sinusoidal structures and functions using a 3D-configured microfluidic chip. *Lab Chip*. 2017;17(5):782-794. doi: 10.1039/C6LC01374K

175. Vollmar B, Menger MD. The hepatic microcirculation: mechanistic contributions and therapeutic targets in liver injury and repair. *Physiol Rev.* 2009;89(4):1269-1339. doi: 10.1152/physrev.00027.2008

176. Wisse E, De Zanger R, Charels K, van der Smissen P, McCuskey RS. The liver sieve: considerations concerning the structure and function of endothelial fenestrae, the sinusoidal wall and the space of Disse. *Hepatology*. 1985;5(4):683-692. doi: 10.1002/hep.1840050427

177. Berger DR, Ware BR, Davidson MD, Allsup SR, Khetani SR. Enhancing the functional maturity of induced pluripotent stem cell–derived human hepatocytes by controlled presentation of cell–cell interactions in vitro. *Hepatology*. 2015;61(4):1370-1381. doi: 10.1002/hep.27621

178. Petronis S, Eckert K-L, Gold J, Wintermantel E. Microstructuring ceramic scaffolds for hepatocyte cell culture. *J Mater Sci: Mater Med.* 2001;12:523-528. doi: 10.1023/A:1011219729687

179. Rennert K, Steinborn S, Gröger M, et al. A microfluidically perfused three dimensional human liver model. *Biomaterials*. 2015;71:119-131. doi: 10.1016/j.biomaterials.2015.08.043

180. Yamada M, Utoh R, Ohashi K, et al. Controlled formation of heterotypic hepatic micro-organoids in anisotropic hydrogel microfibers for long-term preservation of liver-specific functions. *Biomaterials*. 2012;33(33): 8304-8315. doi: 10.1016/j.biomaterials.2012.07.068

181. Lee H, Chae S, Kim JY, et al. Cell-printed 3D liver-on-a-chip possessing a liver microenvironment and biliary system. *Biofabrication*. 2019;11(2):025001. doi: 10.1088/1758-5090/aaf9fa

182. Carvalho V, Gonçalves I, Lage T, et al. 3D printing techniques and their applications to organ-on-a-chip platforms: a systematic review. *Sensors*. 2021; 21(9):3304. doi: 10.3390/s21093304

183. Mazzocchi A, Soker S, Skardal A. 3D bioprinting for high-throughput screening: drug screening, disease modeling, and precision medicine applications. *Appl Phys Rev.* 2019;6(1):011302. doi: 10.1063/1.5056188

184. Kang HK, Sarsenova M, Kim D-H, et al. Establishing a 3D in vitro hepatic model mimicking physiologically relevant to in vivo state. *Cells*. 2021;10(5):1268. doi: 10.3390/cells10051268

185. Lee H, Han W, Kim H, et al. Development of liver decellularized extracellular matrix bioink for three-dimensional cell printing-based liver tissue engineering. *Biomacromolecules*. 2017;18(4):1229-1237. doi: 10.1021/acs.biomac.6b01908

186. Lee H, Kim J, Choi Y, Cho D-W. Application of gelatin bioinks and cell-printing technology to enhance cell delivery capability for 3D liver fibrosis-on-a-chip development. *ACS Biomater Sci Eng.* 2020;6(4):2469-2477.

doi: 10.1021/acsbiomaterials.9b01735

187. Taymour R, Kilian D, Ahlfeld T, Gelinsky M, Lode A. 3D bioprinting of hepatocytes: core–shell structured co-cultures with fibroblasts for enhanced functionality. *Sci Rep.* 2021;11(1):5130.
doi: 10.1038/s41598-021-84384-6

188. Wang T, Du Z, Zhu F, et al. Comorbidities and multi-organ injuries in the treatment of COVID-19. *Lancet*. 2020;395(10228):e52.
doi: 10.1016/S0140-6736(20)30558-4

189. Sahlman P, Nissinen M, Puukka P, et al. Genetic and lifestyle risk factors for advanced liver disease among men and women. *J Gastroenterol Hepatol.* 2020;35(2):291-298.
doi: 10.1111/jgh.14770

190. Yang H, Sun L, Pang Y, et al. Three-dimensional bioprinted hepatorganoids prolong survival of mice with liver failure. *Gut*. 2021;70(3):567-574.
doi: 10.1136/gutjnl-2019-319960

191. Jin B, Liu Y, Du S, Sang X, Yang H. Current trends and research topics regarding liver 3D bioprinting: a bibliometric analysis research. *Front Cell Dev Biol.* 2022;10:1047524.
doi: 10.3389/fcell.2022.1047524

192. Deng J, Wei W, Chen Z, et al. Engineered liver-on-a-chip platform to mimic liver functions and its biomedical applications: a review. *Micromachines*. 2019;10(10):676.
doi: 10.3390/mi10100676

193. Shinozawa T, Kimura M, Cai Y, et al. High-fidelity drug-induced liver injury screen using human pluripotent stem cell–derived organoids. *Gastroenterology*. 2021;160(3):831-846.e10.
doi: 10.1053/j.gastro.2020.10.002

194. Man WH, de Steenhuijsen Piters WA, Bogaert D. The microbiota of the respiratory tract: gatekeeper to respiratory health. *Nat Rev Microbiol.* 2017;15(5):259-270.
doi: 10.1038/nrmicro.2017.14

195. Comroe JH. The lung. *Sci Am.* 1966;214(2):56-71.
https://jstor.org/stable/24931268

196. Mccracken Jr GH. Diagnosis and management of pneumonia in children. *Pediatr Infect Dis J*. 2000;19(9):924-928.
doi: 10.1097/00006454-200009000-00036

197. Bateman ED, Reddel HK, van Zyl-Smit RN, Agusti A. The asthma–COPD overlap syndrome: towards a revised taxonomy of chronic airways diseases? *Lancet Respir Med.* 2015;3(9):719-728.
doi: 10.1016/S2213-2600(15)00254-4

198. Flume PA, Van Devanter DR. State of progress in treating cystic fibrosis respiratory disease. *BMC Med.* 2012;10(1):88.
doi: 10.1186/1741-7015-10-88

199. Antonelli M, Conti G, Bufi M, et al. Noninvasive ventilation for treatment of acute respiratory failure in patients undergoing solid organ transplantation: a randomized trial. *JAMA*. 2000;283(2):235-241.
doi: 10.1001/jama.283.2.235

200. Cidem A, Bradbury P, Traini D, Ong HX. Modifying and integrating in vitro and ex vivo respiratory models for inhalation drug screening. *Front Bioeng Biotechnol.* 2020;8:581995.
doi: 10.3389/fbioe.2020.581995

201. Baldassi D, Gabold B, Merkel OM. Air–liquid Interface cultures of the healthy and diseased human respiratory tract: promises, challenges, and future directions. *Adv Nanobiomed Res.* 2021;1(6):2000111.
doi: 10.1002/anbr.202000111

202. Zheng F, Fu F, Cheng Y, Wang C, Zhao Y, Gu Z. Organ-on-a-chip systems: microengineering to biomimic living systems. *Small*. 2016;12(17):2253-2282.
doi: 10.1002/smll.201503208

203. Horváth L, Umehara Y, Jud C, Blank F, Petri-Fink A, Rothen-Rutishauser B. Engineering an in vitro air-blood barrier by 3D bioprinting. *Sci Rep.* 2015;5(1):7974.
doi: 10.1038/srep07974

204. Osório LA, Silva E, Mackay RE. A review of biomaterials and scaffold fabrication for organ-on-a-chip (OOAC) systems. *Bioengineering*. 2021;8(8):113.
doi: 10.3390/bioengineering8080113

205. Humayun M, Chow C-W, Young EW. Microfluidic lung airway-on-a-chip with arrayable suspended gels for studying epithelial and smooth muscle cell interactions. *Lab Chip*. 2018;18(9):1298-1309.
doi: 10.1039/C7LC01357D

206. Benam K H, Villenave R, Lucchesi C, et al. Small airway-on-a-chip enables analysis of human lung inflammation and drug responses in vitro. *Nat Methods*. 2016;13(2):151-157.
doi: 10.1038/nmeth.3697

207. Sellgren KL, Butala EJ, Gilmour BP, Randell SH, Grego S. A biomimetic multicellular model of the airways using primary human cells. *Lab Chip*. 2014;14(17):3349-3358.
doi: 10.1039/C4LC00552J

208. Nalayanda DD, Puleo C, Fulton WB, Sharpe LM, Wang T-H, Abdullah F. An open-access microfluidic model for lung-specific functional studies at an air-liquid interface. *Biomed Microdevices*. 2009;11:1081-1089.
doi: 10.1007/s10544-009-9325-5

209. Douville NJ, Zamankhan P, Tung Y-C, et al. Combination of fluid and solid mechanical stresses contribute to cell death and detachment in a microfluidic alveolar model. *Lab Chip*. 2011;11(4):609-619.
doi: 10.1039/C0LC00251H

210. Huh D, Matthews BD, Mammoto A, Montoya-Zavala M, Hsin HY, Ingber DE. Reconstituting organ-level lung functions on a chip. *Science*. 2010;328(5986):1662-1668.
doi: 10.1126/science.1188302

211. Bennet TJ, Randhawa A, Hua J, Cheung KC. Airway-on-a-chip: designs and applications for lung repair and disease. *Cells*. 2021;10(7):1602. doi: 10.3390/cells10071602

212. Higham A, Bostock D, Booth G, Dungwa JV, Singh D. The effect of electronic cigarette and tobacco smoke exposure on COPD bronchial epithelial cell inflammatory responses. *Int J Chronic Obstruct Pulm Dis*. 2018;13:989-1000. doi: 10.2147/COPD.S157728

213. de Boer JD, Majoor CJ, van't Veer C, Bel EHD, van der Poll T. Asthma and coagulation. *Blood*. 2012;119(14):3236-3244. doi: 10.1182/blood-2011-11-391532

214. Guo R, Pittler M, Ernst E. Herbal medicines for the treatment of COPD: a systematic review. *Eur Respir J*. 2006;28(2):330-338. doi: 10.1183/09031936.06.00119905

215. Park JY, Ryu H, Lee B, et al. Development of a functional airway-on-a-chip by 3D cell printing. *Biofabrication*. 2018;11(1):015002. doi: 10.1088/1758-5090/aae545

216. Nam H, Choi Y-m, Cho S, et al. Modular assembly of bioprinted perfusable blood vessel and tracheal epithelium for studying inflammatory respiratory diseases. *Biofabrication*. 2022;15(1):014101. doi: 10.1088/1758-5090/ac93b6

217. Gu Z, Fu J, Lin H, He Y. Development of 3D bioprinting: from printing methods to biomedical applications. *Asian J Pharm Sci*. 2020;15(5):529-557. doi: 10.1016/j.ajps.2019.11.003

218. Chen EP, Toksoy Z, Davis BA, Geibel JP. 3D bioprinting of vascularized tissues for in vitro and in vivo applications. *Front Bioeng Biotechnol*. 2021;9:664188. doi: 10.3389/fbioe.2021.664188

219. Kuperman DA, Huang X, Koth LL, et al. Direct effects of interleukin-13 on epithelial cells cause airway hyperreactivity and mucus overproduction in asthma. *Nat Med*. 2002;8(8):885-889. doi: 10.1038/nm734

220. Gao G, Lee JH, Jang J, et al. Tissue engineered bio-blood-vessels constructed using a tissue-specific bioink and 3D coaxial cell printing technique: a novel therapy for ischemic disease. *Adv Funct Mater*. 2017;27(33):1700798. doi: 10.1038/nm734

221. Luster AD, Alon R, von Andrian UH. Immune cell migration in inflammation: present and future therapeutic targets. *Nat Immunol*. 2005;6(12):1182-1190. doi: 10.1038/ni1275

222. Park JH, Ahn M, Park SH, et al. 3D bioprinting of a trachea-mimetic cellular construct of a clinically relevant size. *Biomaterials*. 2021;279:121246. doi: 10.1016/j.biomaterials.2021.121246

223. Nizamoglu M, Joglekar MM, Almeida CR, et al. Innovative three-dimensional models for understanding mechanisms underlying lung diseases: powerful tools for translational research. *Eur Respir Rev*. 2023;32(169). doi: 10.1183/16000617.0042-2023

224. Barreiro Carpio M, Dabaghi M, Ungureanu J, et al. 3D bioprinting strategies, challenges, and opportunities to model the lung tissue microenvironment and its function. *Front Bioeng Biotechnol*. 2021;9:773511. doi: 10.3389/fbioe.2021.773511

225. Cho WW, Ahn M, Kim BS, et al. Blood-lymphatic integrated system with heterogeneous melanoma spheroids via in-bath three-dimensional bioprinting for modelling of combinational targeted therapy. *Adv Sci*. 2022;9(29): 2202093. doi: 10.1002/advs.202202093

226. Alencar AM, Arold SP, Buldyrev SV, et al. Dynamic instabilities in the inflating lung. *Nature*. 2002;417(6891): 809-811. doi: 10.1038/417809b

227. Sengupta A, Roldan N, Kiener M, et al. A new immortalized human alveolar epithelial cell model to study lung injury and toxicity on a breathing lung-on-chip system. *Front Toxicol*. 2022;4:840606. doi: 10.3389/ftox.2022.840606

228. Yi H-G, Kim H, Kwon J, et al. Application of 3D bioprinting in the prevention and the therapy for human diseases. *Signal Transduction Targeted Ther*. 2021;6(1):177. doi: 10.1038/s41392-021-00566-8

229. Vanaei S, Parizi MS, Vanaei S, Salemizadehparizi F, Vanaei HR. An overview on materials and techniques in 3D bioprinting toward biomedical application. *Eng Regener*. 2021;2:1-18. doi: 10.1016/j.engreg.2020.12.001

230. Malda J, Visser J, Melchels FP, et al. 25th anniversary article: engineering hydrogels for biofabrication. *Adv Mater*. 2013;25(36):5011-5028. doi: 10.1002/adma.201302042

231. Khoshnood N, Zamanian A. A comprehensive review on scaffold-free bioinks for bioprinting. *Bioprinting*. 2020;19:e00088. doi: 10.1016/j.bprint.2020.e00088

232. Ali M, Pr AK, Yoo JJ, Zahran F, Atala A, Lee SJ. A photo-crosslinkable kidney ECM-derived bioink accelerates renal tissue formation. *Adv Healthc Mater*. 2019;8(7):1800992. doi: 10.1002/adhm.201800992

233. Kim H, Kang B, Cui X, et al. Light-activated decellularized extracellular matrix-based bioinks for volumetric tissue analogs at the centimeter scale. *Adv Funct Mater*. 2021;31(32):2011252.

doi: 10.1002/adfm.202011252

234. Brassard JA, Nikolaev M, Hübscher T, Hofer M, Lutolf MP. Recapitulating macro-scale tissue self-organization through organoid bioprinting. *Nat Mater.* 2021;20(1):22-29. doi: 10.1038/s41563-020-00803-5

235. Lee VK, Dai G. Three-dimensional bioprinting and tissue fabrication: prospects for drug discovery and regenerative medicine. *Adv Healthc Technol*. 2015;2015:23-35. doi: 10.2147/AHCT.S69191

236. Topuz B, Günal G, Guler S, Aydin HM. Use of supercritical CO2 in soft tissue decellularization. *Methods Cell Biol*. 2020;157:49-79. doi: 10.1016/bs.mcb.2019.10.012

237. Mostow EN, Haraway GD, Dalsing M, Hodde JP, King D. Effectiveness of an extracellular matrix graft (OASIS Wound Matrix) in the treatment of chronic leg ulcers: a randomized clinical trial. *J Vasc Surg.* 2005;41(5):837-843. doi: 10.1016/j.jvs.2005.01.042

238. Wainwright D. Use of an acellular allograft dermal matrix (AlloDerm) in the management of full-thickness burns. *Burns*. 1995;21(4):243-248. doi: 10.1016/0305-4179(95)93866-I

239. Kirillova A, Bushev S, Abubakirov A, Sukikh G. Bioethical and legal issues in 3D bioprinting. *Int J Bioprint.* 2020;6(3). doi: 10.18063/ijb.v6i3.272

240. Jessop ZM, Al-Sabah A, Gardiner MD, Combellack E, Hawkins K, Whitaker IS. 3D bioprinting for reconstructive surgery: principles, applications and challenges. *J Plast Reconstr. Aesthetic Surg.* 2017;70(9):1155-1170. doi: 10.1016/j.bjps.2017.06.001

241. Salmikangas P, Schuessler-Lenz M, Ruiz S, et al. Marketing regulatory oversight of advanced therapy medicinal products (ATMPs) in Europe: the EMA/CAT perspective. *Regul Aspects Gene Ther Cell Ther Prod.* 2015:103-130. doi: 10.1007/978-3-319-18618-4_6

242. Shafiq MA, Gemeinhart RA, Yue BY, Djalilian AR. Decellularized human cornea for reconstructing the corneal epithelium and anterior stroma. *Tissue Eng Part C.* 2012;18(5):340-348. doi: 10.1089/ten.tec.2011.0072

243. Polisetti N, Schmid A, Schlötzer-Schrehardt U, et al. A decellularized human corneal scaffold for anterior corneal surface reconstruction. *Sci Rep.* 2021;11(1):1-15. doi: 10.1038/s41598-021-82678-3

244. Gonzalez-Andrades M, de la Cruz Cardona J, Ionescu AM, Campos A, del Mar Perez M, Alaminos M. Generation of bioengineered corneas with decellularized xenografts and human keratocytes. *Invest Ophthalmol Visual Sci.* 2011;52(1):215-222. doi: 10.1167/iovs.09-4773

245. Ventura RD, Padalhin AR, Park CM, Lee BT. Enhanced decellularization technique of porcine dermal ECM for tissue engineering applications. *Mater Sci Eng C*. 2019;104:109841. doi: 10.1016/j.msec.2019.109841

246. Funamoto S, Nam K, Kimura T, et al. The use of high-hydrostatic pressure treatment to decellularize blood vessels. *Biomaterials*. 2010;31(13):3590-3595. doi: 10.1016/j.biomaterials.2010.01.073

247. Jang J, Park H-J, Kim S-W, et al. 3D printed complex tissue construct using stem cell-laden decellularized extracellular matrix bioinks for cardiac repair. *Biomaterials*. 2017;112: 264-274. doi: 10.1016/j.biomaterials.2016.10.026

248. Quint C, Kondo Y, Manson RJ, Lawson JH, Dardik A, Niklason LE. Decellularized tissue-engineered blood vessel as an arterial conduit. *Proc Natl Acad Sci.* 2011;108(22): 9214-9219. doi: 10.1073/pnas.1019506108

249. Flynn L. The use of decellularized adipose tissue to provide an inductive microenvironment for the adipogenic differentiation of human adipose-derived stem cells. *Biomaterials*. 2010;31(17):4715-4724. doi: 10.1016/j.biomaterials.2010.02.046

250. Banyard DA, Sarantopoulos C, Tassey J, et al. Preparation, characterization, and clinical implications of human decellularized adipose tissue extracellular matrix. In: Duscher D, Shiffman MA, eds. *Regenerative Medicine and Plastic Surgery*. Cham: Springer; 2019:71-89. doi: 10.1007/978-3-030-19962-3_6

251. Kang H, Peng J, Lu S, et al. In vivo cartilage repair using adipose-derived stem cell-loaded decellularized cartilage ECM scaffolds. *J Tissue Eng Regener Med.* 2014;8(6): 442-453. doi: 10.1002/term.1538

252. Elder BD, Kim DH, Athanasiou KA. Developing an articular cartilage decellularization process toward facet joint cartilage replacement. *Neurosurgery*. 2010;66(4):722-727. doi: 10.1227/01.NEU.0000367616.49291.9F

253. Bae M, Ko MK, Jin Y, et al. Neural stem cell delivery using brain-derived tissue-specific bioink for recovering from traumatic brain injury. *Biofabrication*. 2021;13(4): 044110. doi: 10.1088/1758-5090/ac293f

254. Min K, Kong JS, Kim J, et al. Three-dimensional microfilament printing of a decellularized extracellular matrix (dECM) bioink using a microgel printing bath for nerve graft fabrication and the effectiveness of dECM graft combined with a polycaprolactone conduit. *ACS Appl Biomater.* 2022;5(4):1591-1603.

doi: 10.1021/acsabm.1c01142

255. Chen C-C, Yu J, Ng H-Y, et al. The physicochemical properties of decellularized extracellular matrix-coated 3D printed poly (ε-caprolactone) nerve conduits for promoting Schwann cells proliferation and differentiation. *Materials*. 2018;11(9):1665.
doi: 10.3390/ma11091665

256. Noor N, Shapira A, Edri R, Gal I, Wertheim L, Dvir T. 3D printing of personalized thick and perfusable cardiac patches and hearts. *Adv Sci.* 2019; 6(11):1900344.
doi: 10.1002/advs.201900344

ACCSCIENCE PUBLISHING

International Journal of Bioprinting

REVIEW ARTICLE

Potential of bioprinted intestine-on-chip models in advancing understanding of human coronavirus infections and drug screening

Min-Hyeok Kim[1], Jeeyeon Lee[2], Chwee Teck Lim[2,3,4], and Sungsu Park[1,5]*

[1]School of Mechanical Engineering, Sungkyunkwan University (SKKU), Suwon, Republic of Korea

[2]Institute for Health Innovation and Technology (iHealthtech), National University of Singapore, Singapore

[3]Department of Biomedical Engineering, National University of Singapore, Singapore

[4]Mechanobiology Institute, National University of Singapore, Singapore

[5]Department of Biophysics, Institute of Quantum Biophysics (IQB), Sungkyunkwan University (SKKU), Suwon, Republic of Korea

(This article belongs to the *Special Issue: Role of 3D Printing Processes in Medicine*)

Abstract

Human coronaviruses, including severe acute respiratory syndrome coronavirus 2 (SARS-CoV-2), contribute to both respiratory and gastrointestinal symptoms, necessitating a comprehensive approach to studying viral pathogenesis. In this context, bioprinted intestine-on-chip models offer a cutting-edge technology for closely replicating the tissue architecture and microenvironment of the human intestine, providing valuable insights into viral dynamics and host responses. Integration of intestinal organoids with organoid-on-chip technology enhances the accuracy of modeling SARS-CoV-2 infection by means of improving cellular differentiation and virus-binding receptor expression. Furthermore, bioprinting technology allows for automated fabrication, enabling high-throughput drug screening on the intestine-on-chip platform. These advancements in bioprinted intestine-on-chip models hold immense promise for advancing our understanding of coronavirus infection in the gut and accelerating drug development, ultimately contributing to improved patient outcomes and public health measures.

Keywords: Intestine; Bioprinting; Organ-on-chip; Coronavirus; Drug screening

***Corresponding author:**
Sungsu Park
(nanopark@skku.edu)

Citation: Kim M-H, Lee J, Lim CT, Park S. Potential of bioprinted intestine-on-chip models in advancing understanding of human coronavirus infections and drug screening. *Int J Bioprint*. 2024;10(2):1704.
doi: 10.36922/ijb.1704

Received: August 29, 2023
Accepted: November 9, 2023
Published Online: January 23, 2024

1. Introduction

Human coronaviruses, including severe acute respiratory syndrome coronavirus 2 (SARS-CoV-2), lead to a spectrum of respiratory illnesses, ranging from mild cold-like symptoms to severe diseases like severe acute respiratory syndrome (SARS), Middle East respiratory syndrome (MERS), and coronavirus disease 2019 (COVID-19). Besides respiratory manifestations, these viruses can also induce gastrointestinal symptoms, such as diarrhea, nausea, and vomiting (Figure 1). Understanding the mechanisms and consequences of gut infection holds direct clinical implications, offering valuable insights for targeted interventions to alleviate gastrointestinal distress, curb transmission through fecal shedding, and address potential long-term gut-related

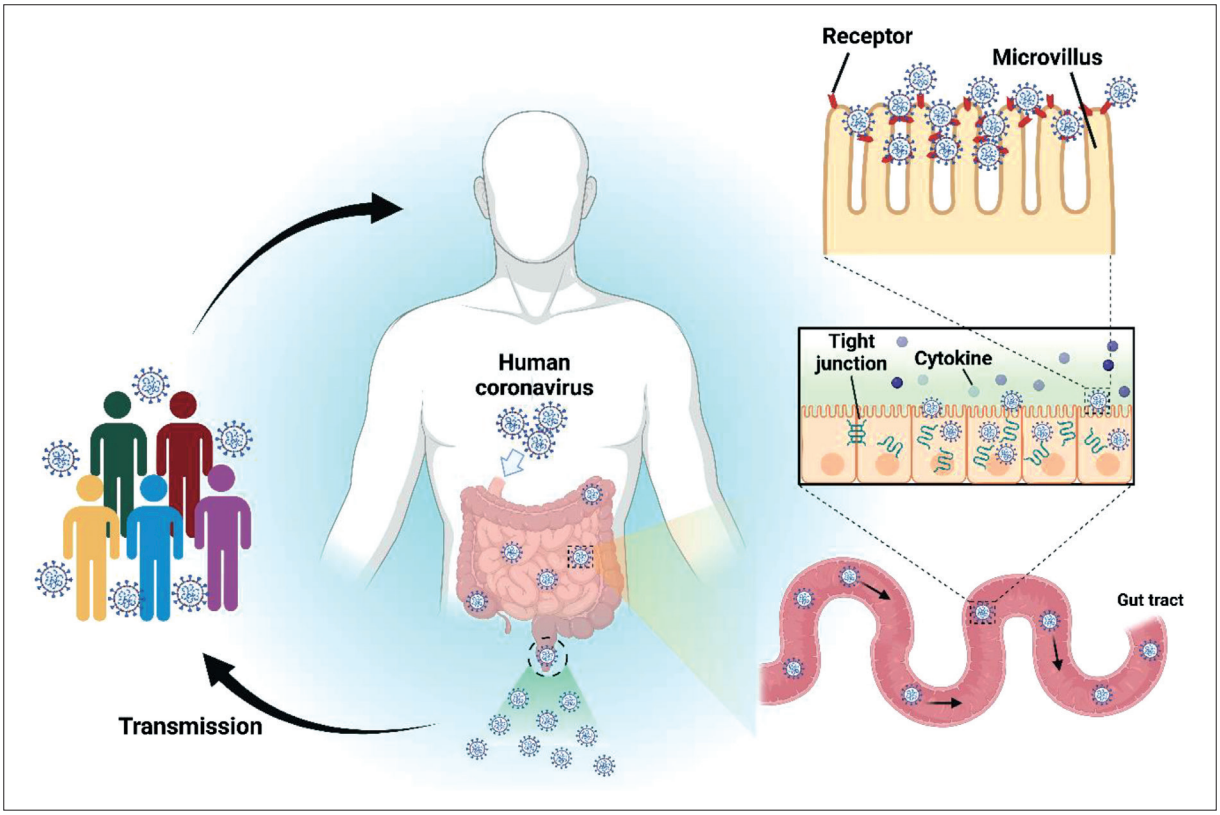

Figure 1. Illustration of the multifaceted impacts following intestinal human coronavirus (HCoV) infection. Tight junction disruption and inflammatory responses emerge as central precursors to a range of intestinal symptoms. The abundance of HCoV-binding receptors in the human gut facilitates virus propagation and fecal-to-oral transmission. This illustration was generated using Biorender.com.

complications. Thus, comprehensive research into human coronavirus infections necessitates a holistic approach, as solely focusing on respiratory aspects may overlook critical dimensions of the disease. By exploring the gut, researchers can enhance their understanding of the virus' multi-organ involvement and systemic effects, contributing to a more comprehensive knowledge base.

Intestinal organoids and intestine-on-chip models have emerged as powerful tools to bridge the gap between traditional cell culture and animal models, facilitating targeted investigations into the gut-related aspects of human coronavirus infections. Yet, the incorporation of bioprinted intestine-on-chip models, which offer precise three-dimensional (3D) tissue structures closely resembling the native intestine, remains underexplored in coronavirus research. Utilizing bioprinted intestine-on-chip models represents a significant advancement in the field of human coronavirus research and drug screening, offering innovative and precise methods for studying infection mechanisms and evaluating potential treatments. These sophisticated 3D tissue structures closely mimic the native intestine's architecture, enabling the replication of the complex microenvironment necessary for accurate virus–host interaction studies. Additionally, the integration of high-throughput screening approaches with intestine-on-chip technology holds great promise for drug discovery and development, enabling efficient and scalable investigations of potential therapeutics. By employing bioprinted intestine-on-chip models, researchers can gain invaluable insights into human coronavirus infections in the intestinal context, shedding light on viral pathogenesis, host responses, and the impact of the gut microenvironment. This knowledge can inform the development of preventive strategies, therapeutic interventions, and public health measures to mitigate the impact of fecal-to-oral transmission and enhance patient outcomes in the face of human coronavirus infections.

Numerous review articles have addressed the utilization of bioprinting technology in intestine research, covering topics ranging from gut–brain interactions to gastrointestinal cancers.[1,2] A subset of these reviews also discuss bioprinting's broader application in countering infectious diseases.[3,4] Yet, a distinct gap exists: the focused exploration of bioprinted intestine models tailored for viral diseases, particularly concerning human coronaviruses. Our review is uniquely poised to bridge this gap.

Table 1. Summary of characteristics of cutting-edge *in vitro* intestine models

Model	Cell source	Standardized initiation/ culture protocol	Physical features	High throughput	Handling difficulty	Cell differentiation	Formation of villi structure
Intestinal organoid	Primary cells, stem cells[101]	Well established[14]	Presence of 3D architecture, no perfusion[102]	Available[84]	Relatively easy (expect microinjection)[19,26,103]	Possible[15,18]	Self-formed[18]
Intestine-on-chip	Cell lines, primary cells, stem cells, organoid-derived cells[43]	Varies depending on chip design[104]	Presence of perfusion, exposure to mechanical cues, presence of 3D architecture[102]	Available, depending on chip design[87-89]	Varies depending on chip design[43]	Possible[50-55]	Self-formed or artificially formed[56,72]
Bioprinted intestine	Cell lines, primary cells, stem cells[1,81,83]	Varies depending on bioink composition and bioprinting method[105]	Diverse 3D structures and cell compositions, wide selection of materials and printing methods[106,107]	Available[108]	Difficult to optimize printing condition[105]	Possible[1,81,83]	Artificially formed[82,109]

In this paper, we emphasize the transformative potential of bioprinted gut chip models for understanding viral infections and fortifying our arsenal against human coronaviruses. Starting with an overview of the human coronavirus, we review its intimate interactions with the intestine. Subsequently, we evaluate contemporary *in vitro* human intestinal models, focusing on the strengths and limitations of bioprinted iterations for studying enteric coronavirus (Table 1). Our narrative is structured to illuminate current research gaps, which could be addressed through the advancements in bioprinted intestine-on-chips. Ultimately, we envision that with continued exploration, these models can be pivotal in reshaping our perception of gut-centric coronavirus infections, catalyzing the advent of innovative therapeutic solutions for global public health.

2. Human coronaviruses

Coronaviruses are named for the crown-like spikes on their surface and belong to the family Coronaviridae. There are seven known strains of coronaviruses that can infect humans: human coronavirus-229E (HCoV-229E), HCoV-OC43, HCoV-NL63, HCoV-HKU1, SARS-CoV, Middle East respiratory syndrome coronavirus (MERS-CoV), and SARS-CoV-2.[5] Some strains such as HCoV-229E are believed to cause the common cold and can cause mild to moderate respiratory illness, while some other stains such as SARS-CoV-2 can cause severe respiratory illness that has led to a significant number of deaths worldwide.

Human coronavirus infections have been observed to manifest not just in respiratory symptoms, but also in the gastrointestinal system.[6] For instance, a significant proportion, between 25% and 38%, of patients infected with HCoV-229E, -OC43, -NL63, and -HKU1 have exhibited gastrointestinal symptoms.[7] In a similar vein, another study highlighted that out of 47 patients with MERS-CoV, many reported symptoms like diarrhea (26%), vomiting (21%), and abdominal pain (17%).[8] Furthermore, it is noteworthy that the gut is not merely a site for symptomatic manifestation but also plays a pivotal role in the potential transmission of the virus.[9] For instance, human coronaviruses, including the widely studied SARS-CoV-2, have been identified in fecal samples, suggesting the presence of viable virus particles.[10] This underscores the possibility that infected individuals can shed the virus through their stool, which in turn raises concerns about transmission via the fecal-oral route, potentially through contaminated food, water, or surfaces, as illustrated in Figure 1.

Exploring the relationship between human coronaviruses and the gut is critical because the gut microbiome and immune response have a major impact on viral infection. For example, the gut microbiome can potentially influence the invasion and replication of SARS-CoV-2 by downregulating angiotensin-converting enzyme 2 (ACE2), a key regulator of innate immunity and the microbiome.[11-13] Such in-depth studies could contribute significantly to the development of targeted therapies, immunomodulatory approaches, and personalized treatments, which are essential in the fight against viral diseases. In addition, understanding the role of the gut in human coronavirus transmission and evolution has broad implications for vaccine effectiveness. Vaccines primarily target the spike protein of the virus, which is essential for respiratory infection, but investigating the involvement of the gut can provide insights into whether vaccines

also provide protection against intestinal infection and potential fecal shedding. This valuable knowledge can guide vaccine development and strategies to improve overall vaccine efficacy.

3. Utilization of intestinal organoid in studying human coronavirus infection

3.1. Intestinal organoids

Intestinal organoids, which are 3D structures derived from human intestinal stem cells, provide a physiologically-relevant representation of the intestinal epithelium. These organoids were among the first successfully established, and their development has paved the way for the establishment of protocols for other organoid types and yielded remarkable findings in the field of intestinal research.[14] One of the key advantages of intestinal organoids is their composition, which includes multi-potent tissue-specific stem cells and differentiated daughter cell types.[15] Moreover, under certain culture conditions, intestinal organoids are capable of virtually indefinite propagation.[16,17] Additionally, these organoids recapitulate the *in vivo* tissue architecture, displaying multiple cell type heterogeneity and interactions in an *in vitro* setting (Figure 2A).[14] When fully developed, human intestinal organoids can form crypt and villi domains that house intestinal stem cells, progenitors, and differentiated enterocytes.[18] The high-throughput scalability and physiological relevance of intestinal organoids make them valuable tools for studying disease phenotypes and screening potential drug candidates.[14,19,20]

Given their advantages, intestinal organoids have been extensively utilized to model pathogen–host interactions in the human intestine with various types of pathogens.[21,22] For example, Heo et al. established an infection model of the protozoan parasite *Cryptosporidium* using human small intestinal organoids.[23] Bartfeld et al. successfully

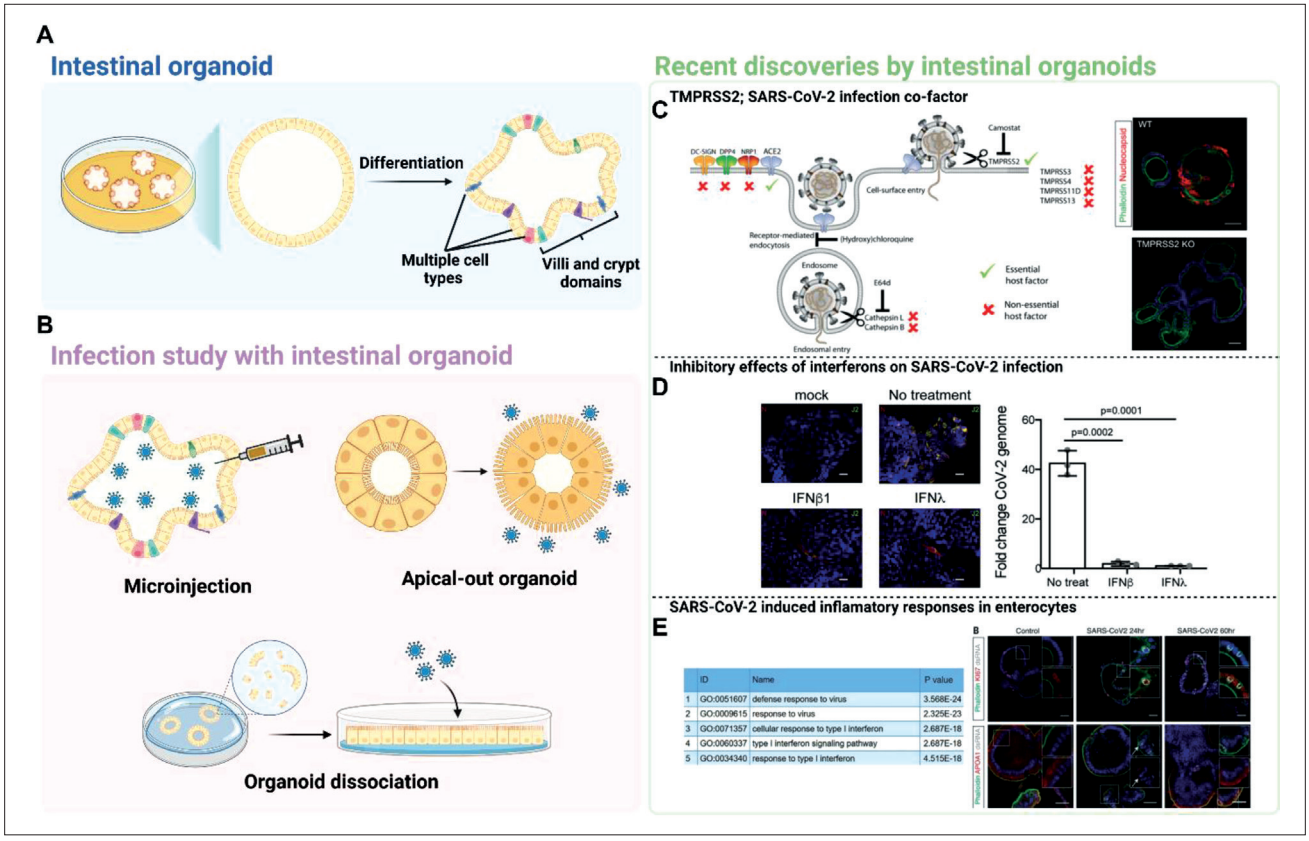

Figure 2. Employing intestinal organoids to investigate HCoV infection in the intestinal context. (A) Well-developed intestinal organoids mirror the complexity of *in vivo* intestinal structures, encompassing distinct cell types and architectural features such as crypt and villi domains (created with Biorender.com). (B) The versatility of organoid systems facilitates the exploration of pathogen–host dynamics using techniques like microinjection, apical-out organoid assays, and organoid dissociation approaches (created with Biorender.com). Studies employing intestinal organoids have (C) elucidated the role of TMPRSS2 as a co-factor in SARS-CoV-2 infection (reprinted under the terms of the Creative Commons CC-BY license),[33] (D) probed the impact of interferons on restraining SARS-CoV-2 infection (reprinted under the terms of the Creative Commons CC-BY-NC-ND license),[32] and (E) unveiled inflammatory responses triggered by SARS-CoV-2 infection (licensed under a Creative Commons Attribution 4.0 International (CC BY 4.0) license and reprinted with permission granted by American Association for the Advancement of Science).[30]

induced intestinal inflammation using the pathogenic bacterium *Helicobacter pylori* in human intestinal organoids.[24] Additionally, since the infection behavior of intestinal pathogens is often determined by the polarity of intestinal cells, the ability of intestinal organoids to exhibit clear cell polarization is highly useful in discerning these differences, particularly in terms of apical or basolateral infection sites.[22,25]

In some cases, experiments involving organoids may require microinjection, which presents certain limitations such as extensive labor, difficulties in controlling injection doses, and low-throughput.[26] To overcome these challenges, alternative techniques have been developed, such as apical-out organoids and organoid-derived monolayers (Figure 2B). Apical-out organoids are formed by dissolving the surrounding matrix of the organoids, which is then resuspended in a culture medium and transferred to low-attachment surface culture platforms, resulting in the formation of apical-out intestinal organoids, where the apical microvilli face outward.[27] Organoid-derived monolayers, on the other hand, involve the enzymatic dissociation of 3D organoids into fragments or single cells, which are then seeded on traditional two-dimensional (2D) platforms like flat plastic surfaces or transwells. These monolayers of organoid-derived cells allow easier access to the apical side of cells and enable straightforward microscopic analysis due to their flat 2D cell layer.[26] These techniques have been effectively used to study pathogen–human intestine interactions.[28]

3.2. Intestinal organoids for human coronavirus infection

Intestinal organoids have also been instrumental in studying viral infections, providing new insights into behaviors of various viruses.[22] For example, human intestinal organoids revealed that respiratory adenovirus serotypes predominantly infect intestinal goblet cells, contrasting with human enteric adenovirus strains that infect enterocytes.[29] Thus, by infecting intestinal organoids with human coronaviruses, researchers can investigate the mechanisms of viral entry, replication, and pathogenesis specifically in the gut. This approach allows for the examination of the viral life cycle and the identification of potential targets for intervention or therapeutics that can disrupt gut infection.

In the early stages of the COVID-19 pandemic, our understanding of SARS-CoV-2 infection in the human intestine was limited. Later on, studies using human intestinal organoids demonstrated that both SARS-CoV and SARS-CoV-2 could readily infect enterocytes within the organoids, leading to the production of infectious viral particles.[30] These findings were further supported by studies using bat and human intestinal organoids infected with SARS-CoV-2.[31] Subsequent studies using intestinal organoids have contributed additional insights into SARS-CoV-2 infection. Combined experiments using cell lines and intestinal organoids revealed that type I and III interferons play a role in controlling SARS-CoV-2 infection in human intestinal epithelial cells.[32] Moreover, transmembrane serine protease 2 (TMPRSS2) has been identified as a mediator of virus entry in intestinal organoids.[33,34] Furthermore, the application of single-cell RNA-sequencing (scRNA-seq) analysis to SARS-CoV-2-infected intestinal organoids revealed the induction of pro-inflammatory pathways and interferon-mediated signaling.[35] These findings shed light on the host response to viral infection within the intestinal organoids and provide valuable insights into the mechanisms underlying SARS-CoV-2 pathogenesis in the intestine (Figure 2C–E).[35]

While numerous studies have focused on modeling intestinal SARS-CoV-2 infections using intestinal organoids, there is a lack of organoid models for other human coronavirus strains. SARS-CoV and MERS-CoV infections have been modeled with human intestinal organoids.[30,36] However, only a few organoid models have been reported for other strains, and most of the studies have utilized human airway organoids to recapitulate infection.[37-40] As seen during the SARS, MERS, and COVID-19 pandemics, the lack of pan-coronavirus antivirals significantly contributes to the vulnerability of public health systems. To address this, it is crucial to develop organoid models that can simulate infections in other organs, such as the intestine, with different coronavirus strains. For instance, Calistri et al. demonstrated that MEDS433, a human dihydroorotate dehydrogenase inhibitor, could inhibit the replication of SARS-CoV-2 and other strains, such as HCoV-229E, using kidney organoids.[41] Similarly, employing other strains in organoid models may provide new insights into intestinal HCoV infection.

4. Intestine-on-chip for studying human coronavirus infection

4.1. Intestine-on-chip

Organ-on-chip platforms, also known as microphysiological systems, are innovative tools that aim to replicate the structure and function of human organs in a controlled laboratory environment.[42,43] These platforms integrate microfluidics and cell culture techniques to create dynamic, miniaturized models of organs, allowing for detailed studies of organ-level physiology and interactions with various stimuli (Figure 3A).

Intestine-on-chip platforms are a specific type of organ-on-chip system designed to replicate the structure

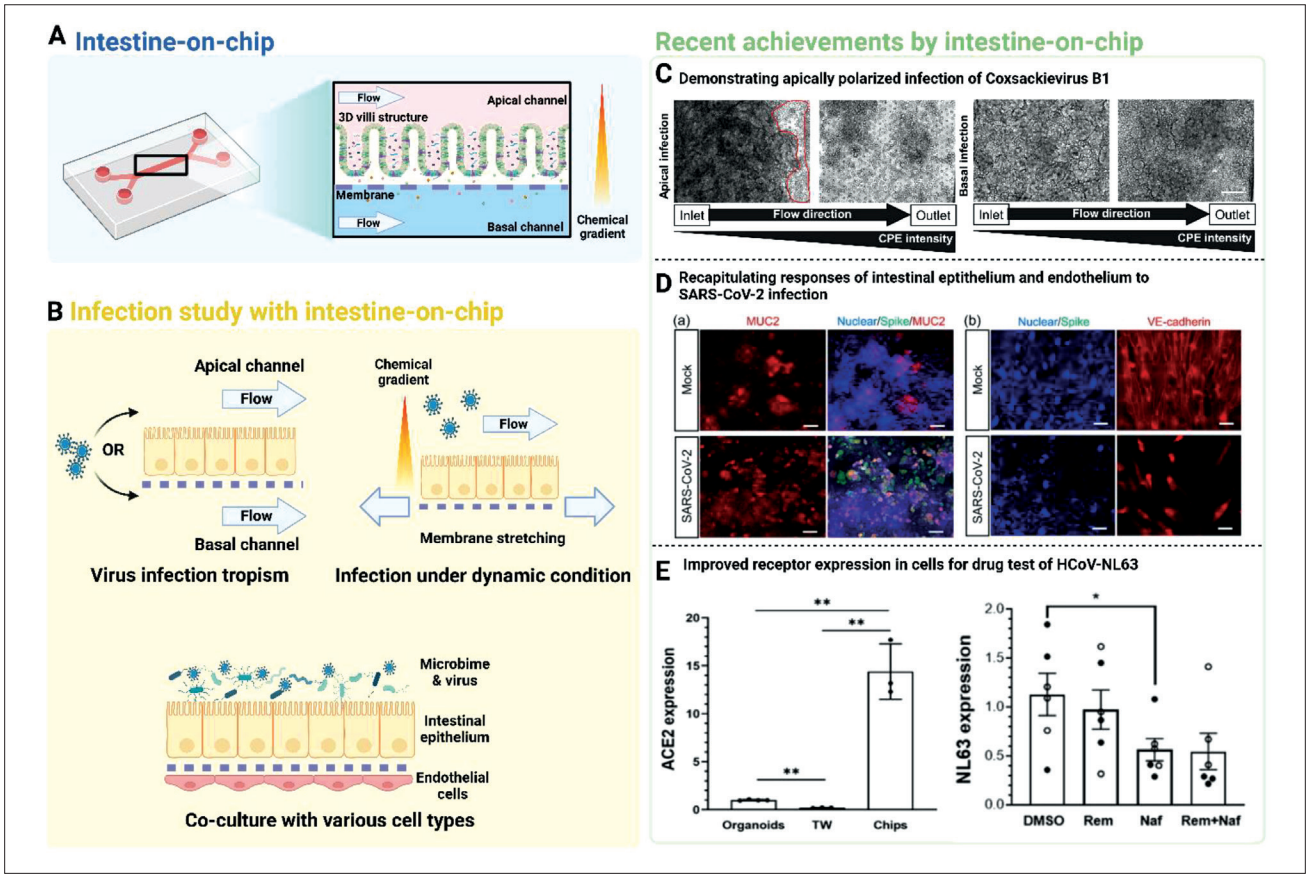

Figure 3. Advancing intestinal HCoV infection studies through intestine-on-chip models. (A) The intestine-on-chip platform cultivates gut epithelial cells within dynamic environments, faithfully emulating the intricate conditions of the human gut *in vivo*. This setup integrates continuous perfusion, 3D villi architecture, and chemical gradients (created with Biorender.com). (B) Leveraging these attributes, diverse scenarios of viral infection can be simulated, offering insights into the complexities of infection dynamics (created with Biorender.com). Applications of intestine-on-chip for virus studies include (C) the observation of apical polarization of Coxsackievirus B1 infection within the intestine-on-chip (reprinted under the Creative Commons CC0 public domain dedication),[66] (D) recapitulation of the responses of intestinal epithelial and endothelial cells to SARS-CoV-2 infection (reprinted with permission granted by 2020 Science China Press; published by Elsevier B.V. and Science China Press),[69] as well as (E) modeling and treatment of HCoV infection in the gut using HCoV-NL63-infected intestine-on-chip setups (reprinted under the terms of the Creative Commons CC-BY license).[67]

and function of the human intestine.[44] These platforms utilize microfluidic channels lined with intestinal epithelial cells and supporting cell types to recreate the complex architecture and physiological conditions of the intestinal tissue. By employing microfluidic-based systems, intestine-on-chip models offer several advantages. They can mimic the dynamic flow of fluids, facilitate nutrient transport, and simulate peristalsis-like movements, providing a more physiologically-relevant and controlled environment for studying the interactions between pathogens and gut epithelium. By recreating the microenvironment of the human intestine, intestine-on-chip models enable the study of various aspects, such as pathogen entry, epithelial response, immune interactions, and potential therapeutic interventions. The ability to simulate these interactions in a controlled and dynamic manner enhances our understanding of intestinal infections and aids in the development of targeted strategies for prevention and treatment.

One important consideration when establishing an interaction model between the human intestine and pathogens on an intestine-on-chip is the 3D architecture present in the human intestine. The human intestine features villi structures, which are finger-like projections that increase the surface area of the intestinal epithelium to maximize nutrient absorption efficiency.[44,45] Between each villus lies the crypt domain, which consists of multi-potent stem cells and Paneth cells; the other upper villi domains consist of other functionally differentiated epithelial cells, such as absorptive enterocytes, goblet cells, and enteroendocrine cells.[46,47] This differentiation between the crypt and the tip of the villi leads to environmental variations that can affect pathogen–intestine interactions.

For example, the pH and oxygen gradients generated along the crypt–villus connection give rise to different microbial compositions and distributions at the crypt and the villus tip, resulting in locally different signaling outcomes and physiology.[48] Introducing villi structures to *in vitro* platforms induces significant changes in the physiological traits of cultured epithelial cells, ultimately impacting pathogen–host cell interactions. We have previously shown that gut epithelial cells cultured on 3D villi protect themselves against the bacterial pathogen *Salmonella typhimurium* infections through increased production of mucin 17 (MUC17), which is not observed in 2D cultured cells.[49] By incorporating 3D villi structures into intestine-on-chip models, researchers can better mimic the physiological characteristics of the human intestine and gain insights into the complex interactions between pathogens and the intestinal epithelium.

Mechanical stress is pivotal in replicating the dynamics of pathogen infections on an intestine-on-chip platform. The gastrointestinal tract is continuously subjected to a myriad of mechanical forces, such as strains and shear stress due to gut motility. Such forces have profound implications on the physiology and functionality of *in vitro* intestinal epithelial cells.[50-55] Influences extend to aspects like mucus secretion, barrier fortitude, cytoskeletal arrangement, mitochondrial operations, drug processing, and the development of microvilli—all of which can potentially modulate pathogen–host dynamics. For instance, Kim et al. exposed gut epithelial cells to mechanical stimuli, encompassing cyclic strain and fluidic shear. This exposure culminated in the emergence of villi structures, creating an environment that mirrored *in vivo* gut conditions.[56] Capitalizing on this device with primary human cells, they further unveiled that an upsurge in certain microbiome metabolites heightens the human susceptibility to infections from enterohemorrhagic *Escherichia coli* (EHEC).[57] Such revelations underscore the value of the intestine-on-chip approach, asserting its capability to emulate a setting where bacterial interactions with intestinal epithelial cells are physiologically akin to real-life scenarios.

In the future, intestine-on-chip platforms incorporated with multiple cell types, including epithelial cells, immune cells, and microbiota, hold promise for investigating host–pathogen interactions, understanding the effects of parasitic infections on barrier integrity and immune responses, and exploring the modulation of the gut microbiota during infection.

4.2. Intestine-on-chip for human coronavirus infection

Organ-on-chip platforms have been extensively used to study viral infections in various human organs.[58,59] Liver-on-chip models have been used to investigate hepatitis B virus life cycle and immune responses,[60] while kidney distal tubule-on-chip models have been utilized to explore renal dysfunction induced by Pseudorabies virus.[61] In light of the ability of SARS-CoV-2 to infect multiple organs and cause diverse symptoms,[62] organ-on-chip models have been employed to replicate SARS-CoV-2 infection in relevant human tissues. Lung-on-chip models demonstrated the efficacy of remdesivir in inhibiting viral replication and preserving alveolar barrier integrity,[63] while liver-on-chip models shed light on liver pathophysiology in COVID-19 patients.[64] Additionally, organ-on-chip models have been utilized to study other human coronavirus infections such as HCoV-NL63 and its impact on endothelial barrier function, VE–cadherin junctions, and pro-inflammatory cytokine levels.[65] These findings highlight the immense potential of organ-on-chip models in advancing our understanding of viral infections in the intestine and other organs.

Intestine-on-chip models have shown promising potential in studying viral infections in the intestinal context, although the number of studies remains limited (Figure 3B). Villenave et al. conducted an investigation using a human gut-on-chip model infected with Coxsackie B1 virus, an enterovirus strain, revealing polarized infection dynamics (Figure 3C).[66] The study demonstrated that viral infection primarily occurred on the apical side of polarized intestinal epithelial cells, while the basolateral side exhibited reduced viral titers, diminished cytopathic effects, and delayed caspase-3 activation. Notably, virus release and cytokine release were predominantly observed on the apical side, underscoring the relevance of the intestine-on-chip model for studying viral behaviors and infection mechanisms in the intestinal context.

Although the number of studies incorporating human coronavirus strains in intestine-on-chip models remains limited, recent efforts have aimed to fill this gap (Figure 3D and E). Bein et al. infected an intestine-on-chip model with HCoV-NL63, a surrogate for SARS-CoV-2, and tested drug candidates while assessing their effects on the inflammatory responses induced by infection.[67] They also demonstrated a significant increase in the expression of ACE2, the binding receptor for SARS-CoV-2, in intestine-on-chip conditions, which closely resembles the *in vivo* environment for viral infection.[68] Similarly, Guo et al. infected an intestine-on-chip model with SARS-CoV-2 and employed transcriptomic analysis to investigate abnormal RNA and protein metabolism, as well as activated immune responses in intestinal epithelial and endothelial cells following infection.[69] These studies illustrate the ongoing progress in utilizing intestine-on-chip models for studying viral infections, including those caused by

human coronaviruses, and highlight their potential for advancing our understanding of intestinal viral infections. Furthermore, the abundance of coronavirus receptors in the intestine facilitates the infection of other coronavirus strains. For instance, aminopeptidase N, the binding receptor for HCoV-229E,[70] is abundantly expressed on the microvilli of intestinal epithelium.[71] Studies have reported significantly increased aminopeptidase activity in intestine-on-chip conditions.[72,73] Hence, intestine-on-chip models offer a robust platform for investigating the infection of various coronavirus strains. Further advancements in intestine-on-chip technology hold great promise for enhancing our understanding of intestinal viral infections and aiding in the development of targeted strategies for prevention and treatment. The integration of more complex physiological features and the ability to investigate viral behaviors and host–pathogen interactions in a controlled and physiologically-relevant environment offer valuable opportunities for studying intestinal viral infections in a more accurate and effective manner.

4.3. Intestinal organoid-on-chip for coronavirus research

Researchers have been exploring more advanced technologies to closely mimic *in vivo* organ environments. One promising approach is the combination of organoids with organ-on-chip models, referred to as organoid-on-chip. Organ-on-chip platforms provide precise control over the tissue microenvironment found in the human body, while organoids leverage the intrinsic developmental programs of self-organizing stem cells to replicate the key structural and functional properties of their *in vivo* counterparts, including the formation of various functionally differentiated cells specific to the organ of interest.[74] This integration of organoids and organ-on-chip technology offers several significant advantages. Organoids, due to their stem cell maintenance, can be expanded indefinitely, making them an invaluable source of untransformed primary cells for organ-on-chip studies.[75]

Intestinal organoid-on-chip models have demonstrated significant potential in studying the human intestine. Workman et al. demonstrated that it is feasible to culture intestinal organoid-derived cells on a micro-engineered chip, which develops villi-like projections and elicits biological responses to inflammatory cytokines.[76] Kasendra et al. reported that organoid-derived cell culture on an intestine-on-chip more closely resembled the transcriptomic profile of the *in vivo* intestine compared to that of the initial organoid culture.[77] This approach has also been employed to investigate intestinal metabolism and drug transport.[78] Moreover, the morphogenesis of villi-like projections in intestinal organoid-on-chip models has been studied at the molecular level.[79] Additionally, successful co-culture systems of intestinal epithelial cells and microbiome isolated from human stool samples have been established using intestinal organoid-on-chip models.[80]

Given the limited availability of viral infection models using intestine-on-chip, particularly in the context of human coronavirus infection, the integration of intestinal organoids with organ-on-chip technology presents a promising opportunity (Figure 4). Notably, ACE2 expression has been shown to be significantly higher in intestine-on-chip models using intestinal organoid-derived primary cells than in 2D or initial organoid cultures.[67] Furthermore, the expression of the intestinal stem cell marker leucine-rich repeat-containing G-protein coupled receptor 5 (LGR5) was found to be lower in the intestine organoid-on-chip condition than in 2D and initial organoid cultures.[67] Therefore, culturing organoid-derived cells on intestine-on-chip is perhaps a more accurate approach to modeling SARS-CoV-2 infection in that ACE-2 expression and cell differentiation more closely resembled the *in vivo* condition. Thus, intestinal organoid-on-chip better replicates virus-binding receptor expression and cell differentiation observed in the *in vivo* intestinal environment.

5. Bioprinted intestine-on-chips for coronavirus research and drug screening

5.1. Bioprinted intestine for coronavirus research

Bioprinting, a cutting-edge technology, allows the precise deposition of cells and biomaterials to create complex 3D tissue structures, closely mimicking the native tissue architecture. In the context of studying human coronaviruses, bioprinting offers a powerful tool to replicate the complex microenvironment of the human intestine, enabling more physiologically-relevant investigations into viral dynamics, host responses, and therapeutic interventions. For example, bioprinting has demonstrated great potential in generating 3D intestinal models composed of human primary intestinal epithelial cells and myofibroblasts that exhibit polarized epithelium with tight junctions, specialized epithelial cell types, and functional cytochrome P450 (CYP450) enzymes. These advanced 3D intestinal tissues develop physiological barrier function, distinguish between high- and low-permeability compounds, and possess functional transporters for drug absorption and distribution. This model holds promise in enhancing safety and efficacy prediction in drug development, particularly for absorption, distribution, metabolism, and excretion (ADME)/toxicity studies.[81]

One innovative approach employed an optimized bioink formulation and printing parameters to produce

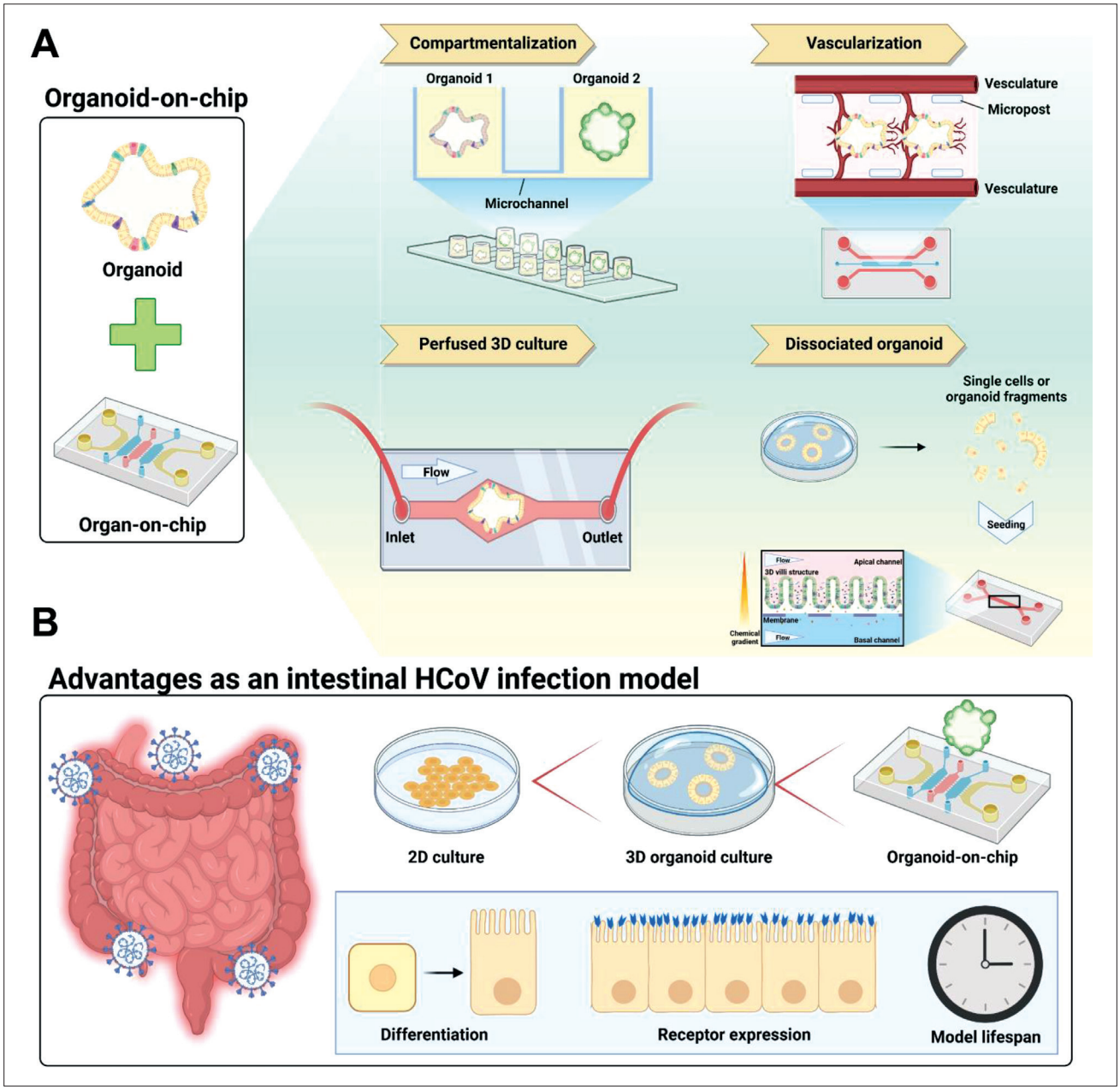

Figure 4. Synergistic strategies and advantages of merging intestinal organoids and organ-on-chip platforms for HCoV infection investigations. (A) The fusion of organoids and organ-on-chip technology gives rise to organoid-on-chip configurations, enhancing physiological fidelity. Within microfluidic systems under continuous perfusion, a diverse array of organoids can be mono-/co-cultured, while organ-on-chip setups enable the creation of vascularized organoid models. (B) Within the context of intestinal organoid-on-chip, cells derived from dissociated intestinal organoids serve as a pivotal source, faithfully emulating the human gut environment. This integrated model facilitates streamlined cell differentiation, heightened expression of virus-binding receptors, and extended cellular viability through continuous perfusion. This illustration was created with Biorender.com.

fibroblast-laden crypt-villus structures, faithfully replicating the intestinal tissue's 3D complexity. This process, based on digital light projection stereolithography (DLP-SLA), demonstrated excellent cell viability, accurate spatial resolution, and high printing throughput, representing a robust biofabrication approach that yields functional gut mucosa tissues compatible with conventional testing techniques. These biofabricated gut mucosa tissues can serve as advanced *in vitro* models for studying human coronaviruses, providing valuable insights into viral pathogenesis and host responses.[82] In another groundbreaking study, a customized DLP-SLA

3D bioprinting system was adapted to work with reduced bioink volumes and environmental control, allowing the fabrication of cell-laden structures resembling the intestinal mucosa in a single printing step. The resulting intestinal tissues closely mimic the 3D architecture of the small intestine, including villi and crypts, with both the epithelial and stromal compartments faithfully represented. These integrated intestinal models offer a promising platform to study viral–host interactions, viral dynamics within the gut, and the influence of the gut microenvironment on viral infectivity and pathogenesis.[82] With ongoing research and innovation in bioprinting technologies, the field is continuously advancing to address challenges in recapitulating the human intestinal system more accurately. Recently, tissue-specific biomaterials, such as colon-derived decellularized extracellular matrix (colon dECM), have been utilized in novel bioprinting strategies to create perfusable tubular models that spontaneously mimic the 3D morphogenesis of human intestinal epithelium. These innovative bioprinted models offer an unprecedented platform to study potential drug-induced toxicity on the human intestinal tissue and to create co-culture models with commensal microbes and immune cells for future therapeutic investigations.[83]

5.2. Bioprinted intestine-on-chip for high-throughput drug screening

High-throughput screening techniques are essential for drug development and discovery in the modern era.[84-87] Organ-on-chip technology has emerged as a powerful tool for understanding human physiology and various diseases. While significant advancements have been made in the field, the advances in automating high-throughput screening approaches in organ-on-chip models still lag behind the developments of other *in vitro* models. This is due to additional considerations such as device design, fabrication, maintenance, and operation.

Most studies utilizing organ-on-chip systems have focused on single or a few organ units per platform, limiting throughput.[87] Fortunately, recent studies have proposed scalable designs with increased throughput. Beaurivage et al. developed an intestine-on-chip model for high-throughput disease modeling and drug discovery.[88] Their platform consisted of 40 individual intestine-on-chip units, each featuring three lanes of channels in a single layer, with an intestinal tubule in the middle channel and two side media channels. Perfused culture was achieved through periodic tilting of the platform. Additionally, an automated multichannel impedance spectrometer designed for use with the platform measured transepithelial electrical resistance (TEER) at different time points. In a more recent study, Azizgolshani et al. created a high-throughput organ-on-chip platform capable of generating more complex tissue structures, with 96 chips per platform, enabling real-time measurement of barrier function, oxygen concentration, and renal transport.[89]

A pivotal advantage of 3D printing lies in its ability to create a wide array of high-throughput systems swiftly and automatically with varying designs. Mazrouei et al. demonstrated this potential by employing bioprinting to generate a range of custom-designed organ-on-chip-like platforms, integrating human colon cancer cells. These platforms have proven effective for conducting 3D cell model analysis and exploring cellular responses to therapeutic interventions (Figure 5A).[90] Moreover, recent advancements in bioprinting technology have paved the way for complete automation of the organ-on-chip process, from fabrication to data analysis. To illustrate, Lind et al. harnessed multi-material 3D printing to produce a heart-on-chip system that incorporated a built-in sensor for gauging the contractile strength of cardiac muscles.[91] Notably, the sensor itself was created via 3D printing during the fabrication phase. More recently, Trampe et al. developed a bioink containing sensor nanoparticles for monitoring oxygen in bioprinted cell-laden structures (Figure 5B).[92] These instances underscore the substantial potential of bioprinting technology in streamlining the creation of multifaceted devices encompassing cellular components and sensors. Ultimately, this progress holds the promise of revolutionizing drug screening and advancing coronavirus research through intestine-on-chip models.

5.3. Studying multi-organ interactions using bioprinted intestine-on-chip

The human intestine plays a pivotal role in upholding our well-being by serving as a vital communicator with distal organs. For instance, perturbations in the integrity of the intestinal barrier have been linked to chronic liver disease, diabetes, and obesity.[93] Numerous diseases progress via intricate multi-organ interactions. Consequently, it is plausible that an intestinal coronavirus infection could potentially trigger aberrations in other organs.

The concept of multi-organ-on-chip (MOC) involves the integration of cells from diverse organs or tissues within a single platform, thereby emulating multi-organ interplay. Notable endeavors have employed such platforms to replicate and study the impacts of intestinal pathogens on interconnected organs. For instance, we have previously emulated kidney damage induced by shiga toxin-producing *E. coli* through an intestine-kidney-on-chip setup.[94] This design encompasses distinct intestine and kidney modules, enabling an examination of antibiotic treatments' effects on each organ during infection. Leveraging the modular nature of this setup, our findings

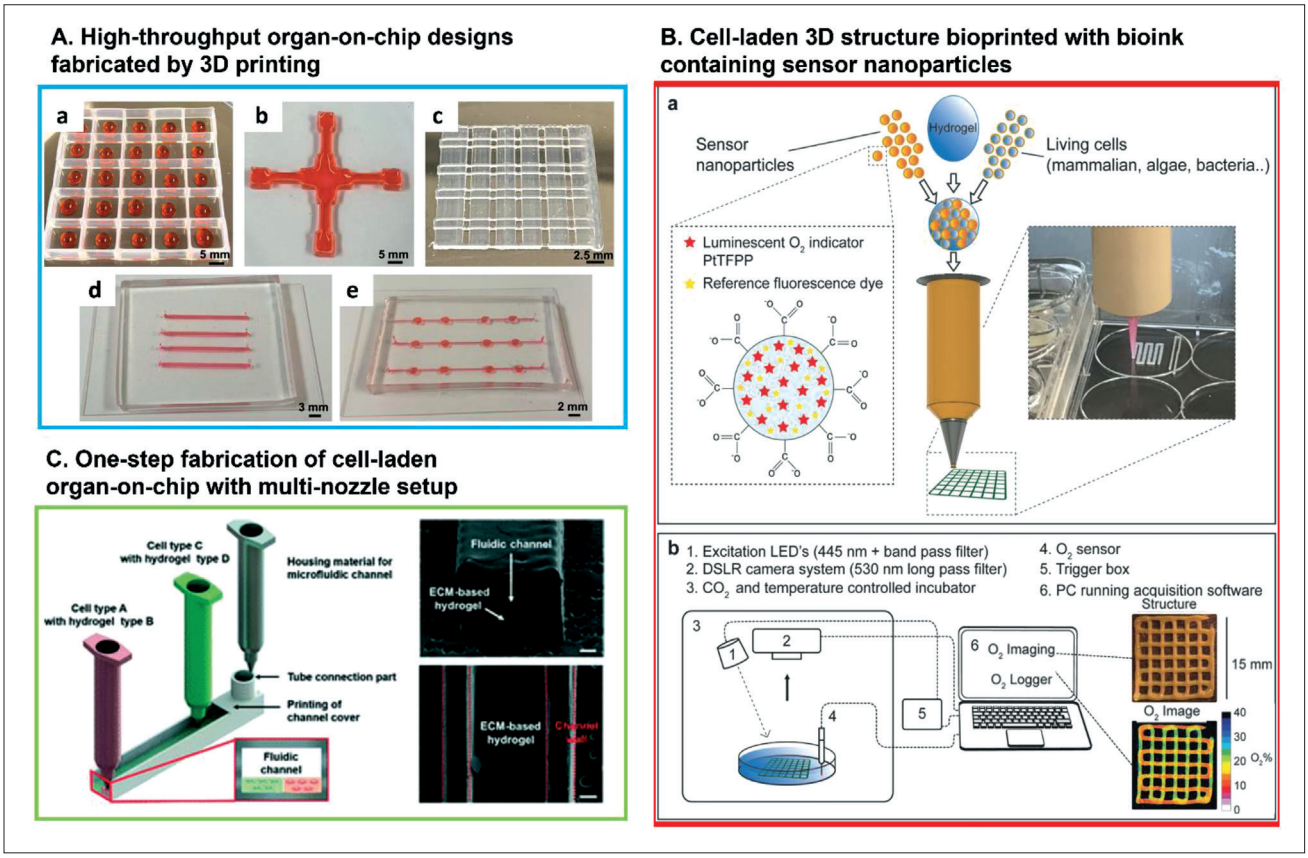

Figure 5. Progress in bioprinting innovations toward developing bioprinted intestine-on-chip models in coronavirus research and drug evaluation. (A) Utilization of bioprinting techniques for constructing high-throughput organ-on-chip platforms (reprinted under the terms of the Creative Commons CC-BY license).[90] (B) Bioprinting of cell-laden structure with bioink containing sensor nanoparticles (reprinted with permission granted by John Wiley & Sons).[92] (C) One-step fabrication of cell-laden organ-on-chip featuring multiple cell types with multi-nozzle bioprinting (reprinted under the terms of the Creative Commons CC-BY license).[99]

showcased that gentamicin mitigated shiga toxin-induced renal damage, while ciprofloxacin amplified such damage despite reduced infection levels in the intestine.

Bioprinting technology has been harnessed to simulate intricate interactions between multiple organs within organ-on-chip platforms. Skardal et al. pioneered the adaptation of bioprinting, utilizing organoid-laden bioinks to mimic the interplay between the liver, heart, and lungs.[95] Their system encompassed separate organ modules, interconnected through external devices and an intricate network of tubes. While modular strategies in multi-organ systems allow individual organ analysis, the fusion of organoids with organ-on-chip technology imparts enhanced physiological relevance. Nonetheless, the creation of distinct organ modules through separate bioprinting processes, along with the relatively large system size, posed hindrances to practical utility. Recent advancements have seen the fabrication of MOC platforms using various 3D printing techniques, such as the DLP-SLA method.[96,97]

Given the intricacy and multifaceted considerations of multi-organ systems, the throughput of these platforms varies based on their nature.[98] Direct 3D printing of MOC platforms enables automated mass production, thereby elevating throughput. An illustrative example is the work by Lee et al., who achieved one-step fabrication of cell-laden organ-on-chip systems using extrusion-based bioprinting equipped with multiple printing nozzles (Figure 5C).[99] This innovative approach involved loading two distinct cell types into separate cartridges alongside bioinks, while another cartridge held poly caprolactone for chip material. This strategy facilitated concurrent cell seeding during chip fabrication. In the context of modular MOC, this technique allows the simultaneous creation of multiple cell-laden organ modules, offering immense potential for replicating and studying multi-organ diseases induced by intestinal pathogens using MOC setups.

Although bioprinted intestine models are undoubtedly promising, they come with notable challenges that need

addressing. The accuracy of cell placement in these models is vital for mimicking the native environment, highlighting the importance of bioprinting resolution.[100] Additionally, the choice of bioink is crucial, with the need for optimal balance in biocompatibility, structural properties, and biodegradability. Even though the bioink domain is rapidly evolving, standardizing protocols remains a challenge. The bioprinting method selected also has its trade-offs: while DLP-SLA is efficient for mass production, it might struggle with multiple materials, unlike extrusion-based methods which offer material versatility but might be less efficient for bulk production. In essence, while bioprinted intestine-on-chip models have potential, they demand careful consideration and custom strategies to navigate their inherent complexities.

6. Conclusion

In the early stages of the pandemic, our comprehension of human coronaviruses was constrained by the limitations of the available models. Although cell line-based systems, organoids, and intestine-on-chip platforms provided valuable insights, they each had inherent challenges. Notably, while organoid technology unveiled key interactions of SARS-CoV-2 within the human intestine, the broader applications for other coronaviruses remained limited, often being studied in specialized settings, such as human airway organoids.

Bioprinting technology presents a novel avenue that addresses many of these challenges. It facilitates the creation of intricate 3D tissue structures that closely mirror native tissue architecture, especially the signature crypt-villus layout of the intestine. By merging the strengths of traditional models and rectifying their drawbacks, bioprinted intestinal models stand at the cusp of a new research frontier. They possess the potential to more authentically recapitulate the human intestine's 3D intricacies, allowing for a more grounded exploration of virus–host interactions and the influence of the gut environment on viral dynamics.

In conclusion, the integrated application of organoids, bioprinting, and organ-on-chip can redefine our approach to understanding coronaviruses. With bioprinted intestine-on-chip models at the forefront, we are poised to gain a holistic view of viral pathogenesis, steering the course for the development of tailored antiviral solutions.

Acknowledgments

None.

Funding

This work was supported by both the SKKU Global Research Platform Research Fund (Sungkyunkwan University, 2022; No. RS-2023-00218543) and the National Research Foundation of Korea (NRF) grants funded by the Korea government (MSIT; No. RS-2023-00242443).

Conflict of interest

The authors declare no conflicts of interest.

Author contributions

Conceptualization: Min-Hyeok Kim, Sungsu Park, Chwee Teck Lim
Visualization: Min-Hyeok Kim
Writing – original draft: Min-Hyeok Kim, Jeeyeon Lee
Writing – review & editing: Min-Hyeok Kim, Sungsu Park

Ethics approval and consent to participate

Not applicable.

Consent for publication

Not applicable.

Availability of data

Not applicable.

References

1. Han H, Jang J. Recent advances in biofabricated gut models to understand the gut-brain axis in neurological diseases. *Front Med Technol*. 2022;4:931411. doi: 10.3389/fmedt.2022.931411
2. Prashantha K, Krishnappa A, Muthappa M. 3D bioprinting of gastrointestinal cancer models: a comprehensive review on processing, properties, and therapeutic implications. *Biointerphases*. 2023;18(2):020801. doi: 10.1116/6.0002372
3. Zimmerling A, Chen X. Bioprinting for combating infectious diseases. *Bioprinting*. 2020;20:e00104. doi: 10.1016/j.bprint.2020.e00104
4. Yi H-G, Kim H, Kwon J, Choi Y-J, Jang J, Cho D-W. Application of 3D bioprinting in the prevention and the therapy for human diseases. *Signal Transduct Target Ther*. 2021;6(1):177. doi: 10.1038/s41392-021-00566-8
5. V'kovski P, Kratzel A, Steiner S, Stalder H, Thiel V. Coronavirus biology and replication: implications for SARS-CoV-2. *Nat Rev Microbiol*. 2021;19(3):155-170. doi: 10.1038/s41579-020-00468-6
6. Luo X, Zhou G-Z, Zhang Y, Peng L-H, Zou L-P, Yang Y-S. Coronaviruses and gastrointestinal diseases. *Mil Med Res*. 2020;7(1):49. doi: 10.1186/s40779-020-00279-z
7. Vabret A, Dina J, Gouarin S, et al. Human (non-severe acute respiratory syndrome) coronavirus infections in hospitalised

children in France. *J Paediatr Child Health*. 2008;44(4): 176-181.
doi: 10.1111/j.1440-1754.2007.01246.x

8. Assiri A, Al-Tawfiq JA, Al-Rabeeah AA, et al. Epidemiological, demographic, and clinical characteristics of 47 cases of Middle East respiratory syndrome coronavirus disease from Saudi Arabia: a descriptive study. *Lancet Infect Dis*. 2013;13(9):752-761.
doi: 10.1016/S1473-3099(13)70204-4

9. Guo M, Tao W, Flavell RA, Zhu S. Potential intestinal infection and faecal–oral transmission of SARS-CoV-2. *Nat Rev Gastroenterol Hepatol*. 2021;18(4):269-283.
doi: 10.1038/s41575-021-00416-6

10. Chen Y, Chen L, Deng Q, et al. The presence of SARS-CoV-2 RNA in the feces of COVID-19 patients. *J Med Virol*. 2020;92(7):833-840.
doi: 10.1002/jmv.25825

11. Zhang F, Lau RI, Liu Q, Su Q, Chan FKL, Ng SC. Gut microbiota in COVID-19: key microbial changes, potential mechanisms and clinical applications. *Nat Rev Gastroenterol Hepatol*. 2023;20(5):323-337.
doi: 10.1038/s41575-022-00698-4

12. Hashimoto T, Perlot T, Rehman A, et al. ACE2 links amino acid malnutrition to microbial ecology and intestinal inflammation. *Nature*. 2012;487(7408):477-481.
doi: 10.1038/nature11228

13. Viana SD, Nunes S, Reis F. ACE2 imbalance as a key player for the poor outcomes in COVID-19 patients with age-related comorbidities – role of gut microbiota dysbiosis. *Ageing Res Rev*. 2020;62:101123.
doi: 10.1016/j.arr.2020.101123

14. Taelman J, Diaz M, Guiu J. Human intestinal organoids: promise and challenge. *Front Cell Dev Biol*. 2022;10:854740.
doi: 10.3389/fcell.2022.854740

15. Zachos NC, Kovbasnjuk O, Foulke-Abel J, et al. Human enteroids/colonoids and intestinal organoids functionally recapitulate normal intestinal physiology and pathophysiology. *J Biol Chem*. 2016;291(8):3759-3766.
doi: 10.1074/jbc.R114.635995

16. Sato T, Vries RG, Snippert HJ, et al. Single Lgr5 stem cells build crypt-villus structures in vitro without a mesenchymal niche. *Nature*. 2009;459(7244):262-265.
doi: 10.1038/nature07935

17. Sato T, Stange DE, Ferrante M, et al. Long-term expansion of epithelial organoids from human colon, adenoma, adenocarcinoma, and Barrett's epithelium. *Gastroenterology*. 2011;141(5):1762-1772.
doi: 10.1053/j.gastro.2011.07.050

18. Onozato D, Ogawa I, Kida Y, et al. Generation of budding-like intestinal organoids from human induced pluripotent stem cells. *J Pharm Sci*. 2021;110(7):2637-2650.
doi: 10.1016/j.xphs.2021.03.014

19. Zhao Z, Chen X, Dowbaj AM, et al. Organoids. *Nat Rev Methods Primers*. 2022;2(1):94.
doi: 10.1038/s43586-022-00174-y

20. Frum T, Spence JR. hPSC-derived organoids: models of human development and disease. *J Mol Med*. 2021;99(4): 463-473.
doi: 10.1007/s00109-020-01969-w

21. Puschhof J, Pleguezuelos-Manzano C, Martinez-Silgado A, et al. Intestinal organoid cocultures with microbes. *Nat Protoc*. 2021;16(10):4633-4649.
doi: 10.1038/s41596-021-00589-z

22. Crawford SE, Ramani S, Blutt SE, Estes MK. Organoids to dissect gastrointestinal virus–host interactions: what have we learned? *Viruses*. 2021;13(6):999.
doi: 10.3390/v13060999

23. Heo I, Dutta D, Schaefer DA, et al. Modelling cryptosporidium infection in human small intestinal and lung organoids. *Nat Microbiol*. 2018;3(7):814-823.
doi: 10.1038/s41564-018-0177-8

24. Bartfeld S, Bayram T, van de Wetering M, et al. In vitro expansion of human gastric epithelial stem cells and their responses to bacterial infection. *Gastroenterology*. 2015;148(1):126-136.e6.
doi: 10.1053/j.gastro.2014.09.042

25. Aguirre Garcia M, Hillion K, Cappelier J-M, Neunlist M, Mahe MM, Haddad N. Intestinal organoids: new tools to comprehend the virulence of bacterial foodborne pathogens. *Foods*. 2022;11(1):108.
doi: 10.3390/foods11010108

26. Aguilar C, Alves da Silva M, Saraiva M, Neyazi M, Olsson IAS, Bartfeld S. Organoids as host models for infection biology – a review of methods. *Exp Mol Med*. 2021;53(10): 1471-1482.
doi: 10.1038/s12276-021-00629-4

27. Co JY, Margalef-Català M, Monack DM, Amieva MR. Controlling the polarity of human gastrointestinal organoids to investigate epithelial biology and infectious diseases. *Nat Protoc*. 2021;16(11):5171-5192.
doi: 10.1038/s41596-021-00607-0

28. Han X, Mslati MA, Davies E, Chen Y, Allaire JM, Vallance BA. Creating a more perfect union: modeling intestinal bacteria-epithelial interactions using organoids. *Cell Mol Gastroenterol Hepatol*. 2021;12(2):769-782.
doi: 10.1016/j.jcmgh.2021.04.010

29. Holly MK, Smith JG. Adenovirus infection of human enteroids reveals interferon sensitivity and preferential infection of goblet cells. *J Virol*. 2018;92(9):e00250-18.
doi: 10.1128/JVI.00250-18

30. Lamers MM, Beumer J, van der Vaart J, et al. SARS-CoV-2 productively infects human gut enterocytes. *Science*. 2020;369(6499):50-54.
doi: 10.1126/science.abc1669

31. Zhou J, Li C, Liu X, et al. Infection of bat and human intestinal organoids by SARS-CoV-2. *Nat Med*. 2020;26(7):1077-1083. doi: 10.1038/s41591-020-0912-6

32. Stanifer ML, Kee C, Cortese M, et al. Critical role of type III interferon in controlling SARS-CoV-2 infection in human intestinal epithelial cells. *Cell Rep*. 2020;32(1):107863. doi: 10.1016/j.celrep.2020.107863

33. Beumer J, Geurts MH, Lamers MM, et al. A CRISPR/Cas9 genetically engineered organoid biobank reveals essential host factors for coronaviruses. *Nat Commun*. 2021;12(1):5498. doi: 10.1038/s41467-021-25729-7

34. Zang R, Castro MFG, McCune BT, et al. TMPRSS2 and TMPRSS4 promote SARS-CoV-2 infection of human small intestinal enterocytes. *Sci Immunol*. 2020;5(47):eabc3582. doi: 10.1126/sciimmunol.abc3582

35. Triana S, Metz-Zumaran C, Ramirez C, et al. Single-cell analyses reveal SARS-CoV-2 interference with intrinsic immune response in the human gut. *Mol Syst Biol*. 2021;17(4):e10232. doi: 10.15252/msb.202110232

36. Zhou J, Li C, Zhao G, et al. Human intestinal tract serves as an alternative infection route for Middle East respiratory syndrome coronavirus. *Sci Adv*. 2017;3(11):eaao4966. doi: 10.1126/sciadv.aao4966

37. Wang Y, Li P, Lavrijsen M, et al. Immunosuppressants exert differential effects on pan-coronavirus infection and distinct combinatory antiviral activity with molnupiravir and nirmatrelvir. *United European Gastroenterol J*. 2023;11(5):431-447. doi: 10.1002/ueg2.12417

38. Li J, Wang Y, Solanki K, et al. Nirmatrelvir exerts distinct antiviral potency against different human coronaviruses. *Antiviral Res*. 2023;211:105555. doi: 10.1016/j.antiviral.2023.105555

39. Li P, Wang Y, Lamers MM, et al. Recapitulating infection, thermal sensitivity and antiviral treatment of seasonal coronaviruses in human airway organoids. *eBioMedicine*. 2022;81:104132. doi: 10.1016/j.ebiom.2022.104132

40. Hashimoto R, Tamura T, Watanabe Y, et al. Evaluation of broad anti-coronavirus activity of autophagy-related compounds using human airway organoids. *Mol Pharmaceutics*. 2023;20(4):2276-2287. doi: 10.1021/acs.molpharmaceut.3c00114

41. Calistri A, Luganini A, Mognetti B, et al. The new generation hDHODH inhibitor MEDS433 hinders the in vitro replication of SARS-CoV-2 and other human coronaviruses. *Microorganisms*. 2021;9(8):1731. doi: 10.3390/microorganisms9081731

42. Kim M-H, van Noort D, Sung JH, Park S. Organ-on-a-chip for studying gut-brain interaction mediated by extracellular vesicles in the gut microenvironment. *Int J Mol Sci*. 2021;22(24):13513. doi: 10.3390/ijms222413513

43. Leung CM, de Haan P, Ronaldson-Bouchard K, et al. A guide to the organ-on-a-chip. *Nat Rev Methods Primers*. 2022;2(1):33. doi: 10.1038/s43586-022-00118-6

44. Xian C, Zhang J, Zhao S, Li X-G. Gut-on-a-chip for disease models. *J Tissue Eng*. 2023;14:20417314221149882. doi: 10.1177/20417314221149882

45. Fois CAM, Le TYL, Schindeler A, et al. Models of the gut for analyzing the impact of food and drugs. *Adv Healthc Mater*. 2019;8:1900968. doi: 10.1002/adhm.201900968

46. Ensari A, Marsh MN. Exploring the villus. *Gastroenterol Hepatol Bed Bench*. 2018;11:181-190.

47. Parker A, Maclaren OJ, Fletcher AG, et al. Cell proliferation within small intestinal crypts is the principal driving force for cell migration on villi. *FASEB J*. 2017;31:636-649. doi: 10.1096/fj.201601002

48. Sommer F, Bäckhed F. Know your neighbor: microbiota and host epithelial cells interact locally to control intestinal function and physiology. *BioEssays*. 2016;38:455-464. doi: 10.1002/bies.201500151

49. Kim SH, Chi M, Yi B, et al. Three-dimensional intestinal villi epithelium enhances protection of human intestinal cells from bacterial infection by inducing mucin expression. *Integr Biol*. 2014;6:1122-1131. doi: 10.1039/C4IB00157E

50. Fois CAM, Schindeler A, Valtchev P, Dehghani F. Dynamic flow and shear stress as key parameters for intestinal cells morphology and polarization in an organ-on-a-chip model. *Biomed Microdevices*. 2021;23:55. doi: 10.1007/s10544-021-00591-y

51. Delon LC, Guo Z, Oszmiana A, et al. A systematic investigation of the effect of the fluid shear stress on Caco-2 cells towards the optimization of epithelial organ-on-chip models. *Biomaterials*. 2019;225:119521. doi: 10.1016/j.biomaterials.2019.119521

52. Chi M, Yi B, Oh S, Park D-J, Sung JH, Park S. A microfluidic cell culture device (μFCCD) to culture epithelial cells with physiological and morphological properties that mimic those of the human intestine. *Biomed Microdevices*. 2015;17:58. doi: 10.1007/s10544-015-9966-5

53. Gayer CP, Basson MD. The effects of mechanical forces on intestinal physiology and pathology. *Cell Signal*. 2009;21:1237-1244. doi: 10.1016/j.cellsig.2009.02.011

54. Feaugas T, Sauvonnet N. Organ-on-chip to investigate host-pathogens interactions. *Cell Microbiol*. 2021;23:e13336. doi: 10.1111/cmi.13336

55. Grassart A, Malardé V, Gobaa S, et al. Bioengineered human organ-on-chip reveals intestinal microenvironment and mechanical forces impacting shigella infection. *Cell Host Microbe*. 2019;26:435-444.e4. doi: 10.1016/j.chom.2019.08.007

56. Kim HJ, Huh D, Hamilton G, Ingber DE. Human gut-on-a-chip inhabited by microbial flora that experiences intestinal peristalsis-like motions and flow. *Lab Chip*. 2012;12(12):2165-2174. doi: 10.1039/C2LC40074J

57. Tovaglieri A, Sontheimer-Phelps A, Geirnaert A, et al. Species-specific enhancement of enterohemorrhagic E. coli pathogenesis mediated by microbiome metabolites. *Microbiome*. 2019;7(1):43. doi: 10.1186/s40168-019-0650-5

58. Wang Y, Wang P, Qin J. Human organoids and organs-on-chips for addressing COVID-19 challenges. *Adv Sci*. 2022;9(10):2105187. doi: 10.1002/advs.202105187

59. Tang H, Abouleila Y, Si L, et al. Human organs-on-chips for virology. *Trends Microbiol*. 2020;28(11):934-946. doi: 10.1016/j.tim.2020.06.005

60. Ortega-Prieto AM, Skelton JK, Wai SN, et al. 3D microfluidic liver cultures as a physiological preclinical tool for hepatitis B virus infection. *Nat Commun*. 2018;9(1):682. doi: 10.1038/s41467-018-02969-8

61. Wang J, Wang C, Xu N, Liu Z-F, Pang D-W, Zhang Z-L. A virus-induced kidney disease model based on organ-on-a-chip: pathogenesis exploration of virus-related renal dysfunctions. *Biomaterials*. 2019;219:119367. doi: 10.1016/j.biomaterials.2019.119367

62. Han Y, Yang L, Lacko LA, Chen S. Human organoid models to study SARS-CoV-2 infection. *Nat Methods*. 2022;19(4):418-428. doi: 10.1038/s41592-022-01453-y

63. Zhang M, Wang P, Luo R, et al. Biomimetic human disease model of SARS-CoV-2-induced lung injury and immune responses on organ chip system. *Adv Sci*. 2021;8(3):2002928. doi: 10.1002/advs.202002928

64. Deguchi S, Kosugi K, Hashimoto R, et al. Elucidation of the liver pathophysiology of COVID-19 patients using liver-on-a-chips. *PNAS Nexus*. 2023;2(3):pgad029. doi: 10.1093/pnasnexus/pgad029

65. Lu RXZ, Lai BFL, Rafatian N, et al. Vasculature-on-a-chip platform with innate immunity enables identification of angiopoietin-1 derived peptide as a therapeutic for SARS-CoV-2 induced inflammation. *Lab Chip*. 2022;22(6):1171-1186. doi: 10.1039/D1LC00817J

66. Villenave R, Wales SQ, Hamkins-Indik T, et al. Human gut-on-a-chip supports polarized infection of Coxsackie B1 virus in vitro. *PLOS ONE*. 2017;12(2):e0169412. doi: 10.1371/journal.pone.0169412

67. Bein A, Kim S, Goyal G, et al. Enteric coronavirus infection and treatment modeled with an immunocompetent human intestine-on-a-chip. *Front Pharmacol*. 2021;12:718484. doi: 10.3389/fphar.2021.718484

68. Hikmet F, Méar L, Edvinsson Å, Micke P, Uhlén M, Lindskog C. The protein expression profile of ACE2 in human tissues. *Mol Syst Biol*. 2020;16(7):e9610. doi: 10.15252/msb.20209610

69. Guo Y, Luo R, Wang Y, et al. SARS-CoV-2 induced intestinal responses with a biomimetic human gut-on-chip. *Sci Bull*. 2021;66(8):783-793. doi: 10.1016/j.scib.2020.11.015

70. Yeager CL, Ashmun RA, Williams RK, et al. Human aminopeptidase N is a receptor for human coronavirus 229E. *Nature*. 1992;357(6377):420-422. doi: 10.1038/357420a0

71. Tobey N, Heizer W, Yeh R, Huang T-I, Hoffner C. Human intestinal brush border peptidases. *Gastroenterology*. 1985;88(4):913-926. doi: 10.1016/S0016-5085(85)80008-1

72. Shim K-Y, Lee D, Han J, Nguyen N-T, Park S, Sung JH. Microfluidic gut-on-a-chip with three-dimensional villi structure. *Biomed Microdevices*. 2017;19(2):37. doi: 10.1007/s10544-017-0179-y

73. Tan H-Y, Trier S, Rahbek UL, Dufva M, Kutter JP, Andresen TL. A multi-chamber microfluidic intestinal barrier model using Caco-2 cells for drug transport studies. *PLOS ONE*. 2018;13(5):e0197101. doi: 10.1371/journal.pone.0197101

74. Park SE, Georgescu A, Huh D. Organoids-on-a-chip. *Science*. 2019;364(6444):960-965. doi: 10.1126/science.aaw7894

75. Hofer M, Lutolf MP. Engineering organoids. *Nat Rev Mater*. 2021;6(5):402-420. doi: 10.1038/s41578-021-00279-y

76. Workman MJ, Gleeson JP, Troisi EJ, et al. Enhanced utilization of induced pluripotent stem cell–derived human intestinal organoids using microengineered chips. *Cell Mol Gastroenterol Hepatol*. 2018;5(4):669-677.e2. doi: 10.1016/j.jcmgh.2017.12.008

77. Kasendra M, Tovaglieri A, Sontheimer-Phelps A, et al. Development of a primary human small intestine-on-a-chip using biopsy-derived organoids. *Sci Rep*. 2018;8(1):2871. doi: 10.1038/s41598-018-21201-7

78. Kasendra M, Luc R, Yin J, et al. Duodenum intestine-chip for preclinical drug assessment in a human relevant model. *eLife*. 2020;9:e50135. doi: 10.7554/eLife.50135

79. Shin W, Hinojosa CD, Ingber DE, Kim HJ. Human intestinal morphogenesis controlled by transepithelial morphogen gradient and flow-dependent physical cues

in a microengineered gut-on-a-chip. *iScience*. 2019;15: 391-406.
doi: 10.1016/j.isci.2019.04.037

80. Jalili-Firoozinezhad S, Gazzaniga FS, Calamari EL, et al. A complex human gut microbiome cultured in an anaerobic intestine-on-a-chip. *Nat Biomed Eng*. 2019;3(7):520-531.
doi: 10.1038/s41551-019-0397-0

81. Madden LR, Nguyen TV, Garcia-Mojica S, et al. Bioprinted 3D primary human intestinal tissues model aspects of native physiology and ADME/Tox functions. *iScience*. 2018;2: 156-167.
doi: 10.1016/j.isci.2018.03.015

82. Torras N, Zabalo J, Abril E, Carré A, García-Díaz M, Martínez E. A bioprinted 3D gut model with crypt-villus structures to mimic the intestinal epithelial-stromal microenvironment. *Biomater Adv*. 2023;153:213534.
doi: 10.1016/j.bioadv.2023.213534

83. Han H, Park Y, Choi Y-M, et al. A bioprinted tubular intestine model using a colon-specific extracellular matrix bioink. *Adv Healthc Mater*. 2022;11(2):2101768.
doi: 10.1002/adhm.202101768

84. Lampart FL, Iber D, Doumpas N. Organoids in high-throughput and high-content screenings. *Front Chem Eng*. 2023;5:1120348.
doi: 10.3389/fceng.2023.1120348

85. Szymański P, Markowicz M, Mikiciuk-Olasik E. Adaptation of high-throughput screening in drug discovery—toxicological screening tests. *Int J Mol Sci*. 2012;13(1):427-452.
doi: 10.3390/ijms13010427

86. Bajorath J. Integration of virtual and high-throughput screening. *Nat Rev Drug Discov*. 2002;1(11):882-894.
doi: 10.1038/nrd941

87. Probst C, Schneider S, Loskill P. High-throughput organ-on-a-chip systems: current status and remaining challenges. *Curr Opin Biomed Eng*. 2018;6:33-41.
doi: 10.1016/j.cobme.2018.02.004

88. Beaurivage C, Naumovska E, Chang YX, et al. Development of a gut-on-a-chip model for high throughput disease modeling and drug discovery. *Int J Mol Sci*. 2019;20(22):5661.
doi: 10.3390/ijms20225661

89. Azizgolshani H, Coppeta JR, Vedula EM, et al. High-throughput organ-on-chip platform with integrated programmable fluid flow and real-time sensing for complex tissue models in drug development workflows. *Lab Chip*. 2021;21(8):1454-1474.
doi: 10.1039/D1LC00067E

90. Mazrouei R, Velasco V, Esfandyarpour R. 3D-bioprinted all-inclusive bioanalytical platforms for cell studies. *Sci Rep*. 2020;10(1):14669.
doi: 10.1038/s41598-020-71452-6

91. Lind JU, Busbee TA, Valentine AD, et al. Instrumented cardiac microphysiological devices via multimaterial three-dimensional printing. *Nat Mater*. 2017;16(3):303-308.
doi: 10.1038/nmat4782

92. Trampe E, Koren K, Akkineni AR, et al. Functionalized bioink with optical sensor nanoparticles for O2 imaging in 3D-bioprinted constructs. *Adv Funct Mater*. 2018;28(45):1804411.
doi: 10.1002/adfm.201804411

93. Vancamelbeke M, Vermeire S. The intestinal barrier: a fundamental role in health and disease. *Expert Rev Gastroenterol Hepatol*. 2017;11(9):821-834.
doi: 10.1080/17474124.2017.1343143

94. Lee Y, Kim M-H, Alves DR, et al. Gut–kidney axis on chip for studying effects of antibiotics on risk of hemolytic uremic syndrome by shiga toxin-producing escherichia coli. *Toxins*. 2021;13(11):775.
doi: 10.3390/toxins13110775

95. Skardal A, Murphy SV, Devarasetty M, et al. Multi-tissue interactions in an integrated three-tissue organ-on-a-chip platform. *Sci Rep*. 2017;7(1):8837.
doi: 10.1038/s41598-017-08879-x

96. Goldstein Y, Spitz S, Turjeman K, et al. Breaking the third wall: implementing 3D-printing techniques to expand the complexity and abilities of multi-organ-on-a-chip devices. *Micromachines*. 2021;12(6):627.
doi: 10.3390/mi12060627

97. Díaz Lantada A, Pfleging W, Besser H, et al. Research on the methods for the mass production of multi-scale organs-on-chips. *Polymers*. 2018;10(11):1238.
doi: 10.3390/polym10111238

98. Picollet-D'hahan N, Zuchowska A, Lemeunier I, Le Gac S. Multiorgan-on-a-chip: a systemic approach to model and decipher inter-organ communication. *Trends Biotechnol*. 2021;39:788-810.
doi: 10.1016/j.tibtech.2020.11.014

99. Lee H, Cho D-W. One-step fabrication of an organ-on-a-chip with spatial heterogeneity using a 3D bioprinting technology. *Lab Chip*. 2016;16(14):2618-2625.
doi: 10.1039/C6LC00450D

100. Zandrini T, Florczak S, Levato R, Ovsianikov A. Breaking the resolution limits of 3D bioprinting: future opportunities and present challenges. *Trends Biotechnol*. 2023;41(5): 604-614.
doi: 10.1016/j.tibtech.2022.10.009

101. Tian C-m, Yang M-f, Xu H-m, et al. Stem cell-derived intestinal organoids: a novel modality for IBD. *Cell Death Discov*. 2023;9(1):255.
doi: 10.1038/s41420-023-01556-1

102. van Berlo D, Nguyen VVT, Gkouzioti V, Leineweber K, Verhaar MC, van Balkom BWM. Stem cells, organoids, and organ-on-a-chip models for personalized in vitro drug testing. *Curr Opin Toxicol*. 2021;28:7-14.
doi: 10.1016/j.cotox.2021.08.006

103. Kim J, Koo B-K, Knoblich JA. Human organoids: model systems for human biology and medicine. *Nat Rev Mol Cell Biol*. 2020;21(10):571-584.
doi: 10.1038/s41580-020-0259-3

104. Piergiovanni M, Leite SB, Corvi R, Whelana M. Standardisation needs for organ on chip devices. *Lab Chip*. 2021;21(15):2857-2868.
doi: 10.1039/D1LC00241D

105. Kesti M, Fisch P, Pensalfini M, Mazza E, Zenobi-Wong M. Guidelines for standardization of bioprinting: a systematic study of process parameters and their effect on bioprinted structures. *BioNanoMaterials*. 2016;17(3-4):193-204.
doi: 10.1515/bnm-2016-0004

106. Ren Y, Yang X, Ma Z, et al. Developments and opportunities for 3D bioprinted organoids. *Int J Bioprint*. 2021; 7(3):364.
doi: 10.18063/ijb.v7i3.364

107. Ashammakhi N, Ahadian S, Xu C, et al. Bioinks and bioprinting technologies to make heterogeneous and biomimetic tissue constructs. *Mater Today Bio*. 2019;1:100008.
doi: 10.1016/j.mtbio.2019.100008

108. Mazzocchi A, Soker S, Skardal A. 3D bioprinting for high-throughput screening: drug screening, disease modeling, and precision medicine applications. *Appl Phys Rev*. 2019;6(1):011302.
doi: 10.1063/1.5056188

109. Kim W, Kim G. Intestinal villi model with blood capillaries fabricated using collagen-based bioink and dual-cell-printing process. *ACS Appl Mater Interfaces*. 2018;10(48): 41185-41196.
doi: 10.1021/acsami.8b17410

ACCSCIENCE PUBLISHING

International Journal of Bioprinting

REVIEW ARTICLE

Optimizing cell deposition for inkjet-based bioprinting

Wei Long Ng[1]*, Viktor Shkolnikov[2]*

[1]Singapore Centre for 3D Printing (SC3DP), School of Mechanical and Aerospace Engineering, Nanyang Technological University, Singapore

[2]HP Inc., 1501 Page Mill Road, Palo Alto, California, United States of America

(This article belongs to the *Special Issue: Special Issue of International Journal of Bioprinting in the BDMC 2023 Conference*)

Abstract

Although inkjet-based bioprinting enables precise drop-on-demand cell deposition within three-dimensional (3D) tissue constructs and facilitates critical cell–cell and cell–matrix interactions, it faces challenges such as poor cell homogeneity and low cell viability. To date, there is a lack of comprehensive review papers addressing the optimization of cell deposition in inkjet-based bioprinting. This review aims to fill that gap by providing an overview of various critical aspects in bioprinting, ranging from bio-ink properties to the impact of printed droplets. The bio-ink section begins by exploring how cells influence the physical properties of bio-inks and emphasizes the significance of achieving cell homogeneity within bio-inks to ensure consistent and reliable printing. The discussion then delves into inkjet-based printing chambers (thermal and piezoelectric), the effect of shear stress on printed cells, droplet formation dynamics, the influence of polymer-based and cell-laden droplets on the underlying substrate surface, and the dynamics of droplet impact. Beyond droplet formation and impact, the review highlights the importance of biophysical and biological cues within 3D hydrogel matrices for cell proliferation and differentiation. Finally, the paper highlights current and potential applications, with a specific focus on skin and lung tissue engineering using inkjet-based bioprinting techniques, and provides insights into the emerging role of machine learning in optimizing the cell deposition process for inkjet-based bioprinting.

Keywords: 3D bioprinting; Biofabrication; Inkjet bioprinting; Cells; Bio-inks; Machine learning

***Corresponding authors:**
Wei Long Ng
(ng.wl@ntu.edu.sg)

Viktor Shkolnikov
(viktors@hp.com)

Citation: Ng WL, Shkolnikov V. Optimizing cell deposition for inkjet-based bioprinting. *Int J Bioprint*. 2024;10(2):2135. doi: 10.36922/ijb.2135

Received: October 29, 2023
Accepted: January 2, 2024
Published Online: February 5, 2024

1. Introduction

The field of bioprinting has sparked a profound and ever-growing interest due to its potential to fabricate complex three-dimensional (3D) cell-laden structures in a highly repeatable and scalable manner.[1-3] The convergence of engineering, materials science, and biology has ushered into a new era of possibilities, where fabrication of functional 3D tissue constructs becomes a reality. 3D bioprinting techniques can be categorized into three distinct classifications, namely jetting-based,[4-8] extrusion-based,[9-14] and vat photopolymerization-based bioprinting.[15,16] Each bioprinting technique has its specific

advantages and limitations; the choice of bioprinting technique is dependent on the specific goals of the research or application.

Inkjet-based bioprinting is one of the pioneering 3D printing technologies that facilitate cell deposition for fabrication of 3D tissues or organs, whereby the printing of collagen and fibronectin for life science applications was first demonstrated using a HP thermal inkjet printer in 1988.[17] To date, it has emerged as an important technique in the rapidly evolving landscape of biotechnology and regenerative medicine for manipulating, patterning, and assembling of biologically relevant materials (cells, biomolecules, and biomaterials) in the form of ejected droplets to achieve specific biological functions in a drop-on-demand (DOD) manner (Figure 1). The DOD inkjet-based bioprinting can be categorized as thermal inkjet (TIJ) or piezo inkjet (PIJ) bioprinting. TIJ bioprinting uses thermal energy to create vapor bubbles within the print chamber; the generated force from the rapid expansion of the vapor bubble expels tiny droplets of bio-ink from the nozzle onto an underlying substrate. In contrast, PIJ bioprinting uses piezo actuator to induce mechanical deformation of the print chamber, which generates pressure waves and ejects droplets from the nozzle. This cutting-edge approach facilitates DOD deposition of living cells and biomaterials in a layer-by-layer fabrication approach with unparalleled precision and control.

One of the key challenges in harnessing the full potential of inkjet bioprinting lies in optimizing cell deposition to ensure cell homogeneity and high cell viability during the printing process. This review paper explores the critical importance of optimizing cell deposition in inkjet bioprinting, delving into various important considerations, such as bio-ink formulation, printing chamber design and operation, droplet formation, droplet impact, and 3D hydrogel matrix. By addressing these fundamental aspects, researchers can unlock the true potential of cell deposition for inkjet-based bioprinting.

2. Properties of cell-laden bio-inks

2.1. Influence of cells on physical properties of bio-inks

In general, cell-laden bio-inks can be classified into three distinct groups based on the cell volume fraction, denoted

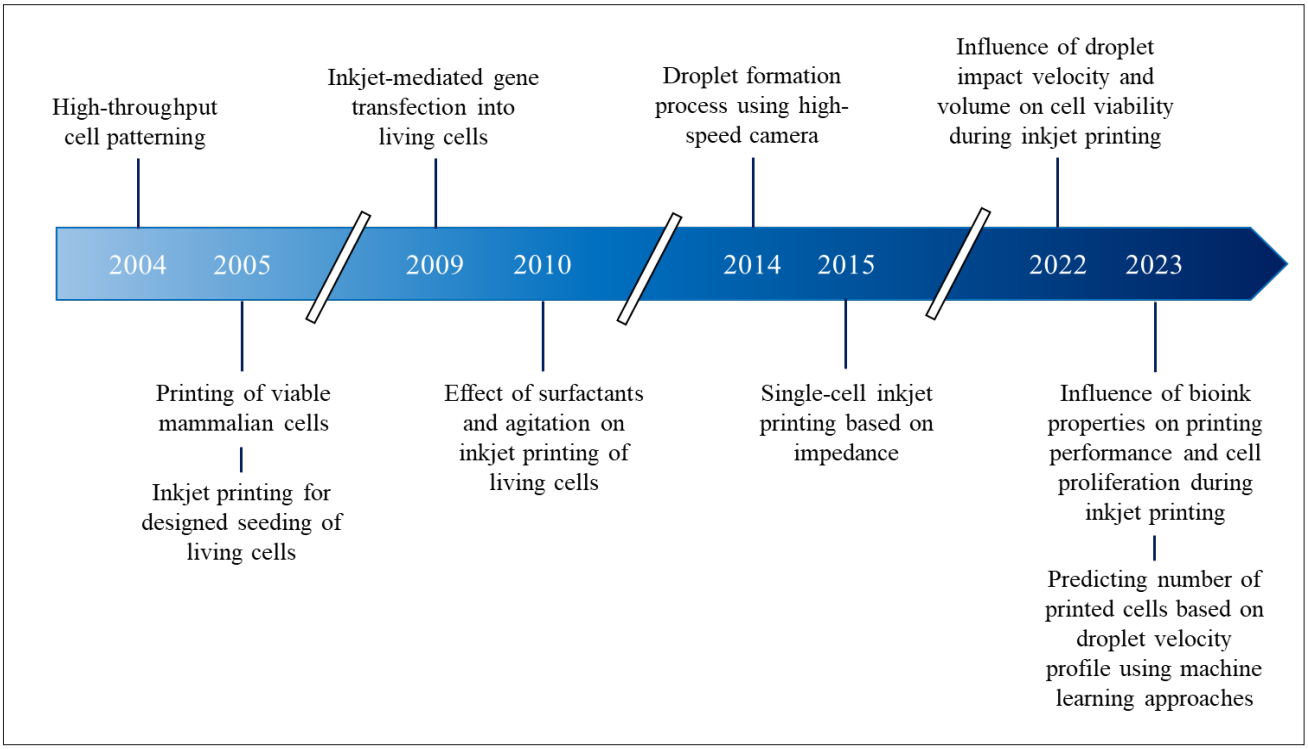

Figure 1. Advancements in cell deposition for inkjet-based bioprinting. Pioneering studies encompass various aspects such as high-throughput cell patterning,[18] printing of viable cells,[19] and pre-defined deposition of living cells.[20] The application of inkjet printing technology for cell transfection was successfully demonstrated,[21] and the effect of surfactants and agitation on cell homogeneity within the bio-ink was evaluated.[22] Furthermore, high-speed imaging was employed to investigate the droplet formation process,[23] and a separate study has demonstrated single-cell inkjet printing.[24] High-speed imaging technique also played a critical role in analyzing the influence of droplet impact velocity and droplet volume on cell viability,[25] as well as employing machine learning approaches to predict the number of printed cells during inkjet bioprinting process based on droplet velocity profiles.[26]

as ϕ.[27] These groups are characterized as follows: dilute bio-inks (with $\phi \leq 2\%$), semi-dilute bio-inks (within $2\% \leq \phi \leq 25\%$), and concentrated bio-inks (with $\phi > 25\%$). The typical diameter of mammalian cells is ~16 μm, and when the cell concentrations are 1, 10, and 120 million cells/mL, this corresponds to volume fractions of 0.21%, 2.15%, and 25.74%, respectively.[28] The introduction of cells into the suspension leads to an increase in the effective (shear) viscosity. Typically, an increase in the cell concentration resulted in higher viscosity and slightly higher density but lower surface tension (Figure 2a).[23] Depending on the cell type, cells can be modeled as rigid spheres or deformable viscous spheres with a surface tension originating from the cell membrane.

Several models have been proposed to describe the effective viscosity of a suspension of spheres. The simplest is Einstein's model, which is expressed as:

$$\eta = \eta_0 (1 + 2.5\phi) \quad \text{(I)}$$

This model is valid for very dilute suspensions of rigid spheres ($\phi < 0.01$), where ϕ represents the viscosity of the pure solvent.[29] The model was extended to account for viscous spheres with internal viscosity η_s and can be expressed as:[30]

$$\eta = \eta_0 \left(1 + 2.5\phi \left(\frac{\eta_s + 0.4\eta_0}{\eta_s + \eta_0} \right) \right) \quad \text{(II)}$$

The model is also applicable for dilute suspensions and assumes that the cell membrane's surface tension is sufficient to maintain the cell's mostly spherical shape. The parameter η_s represents the cytoplasmic viscosity, which typically ranges from 1 to 1000 Pa·s for mammalian cells

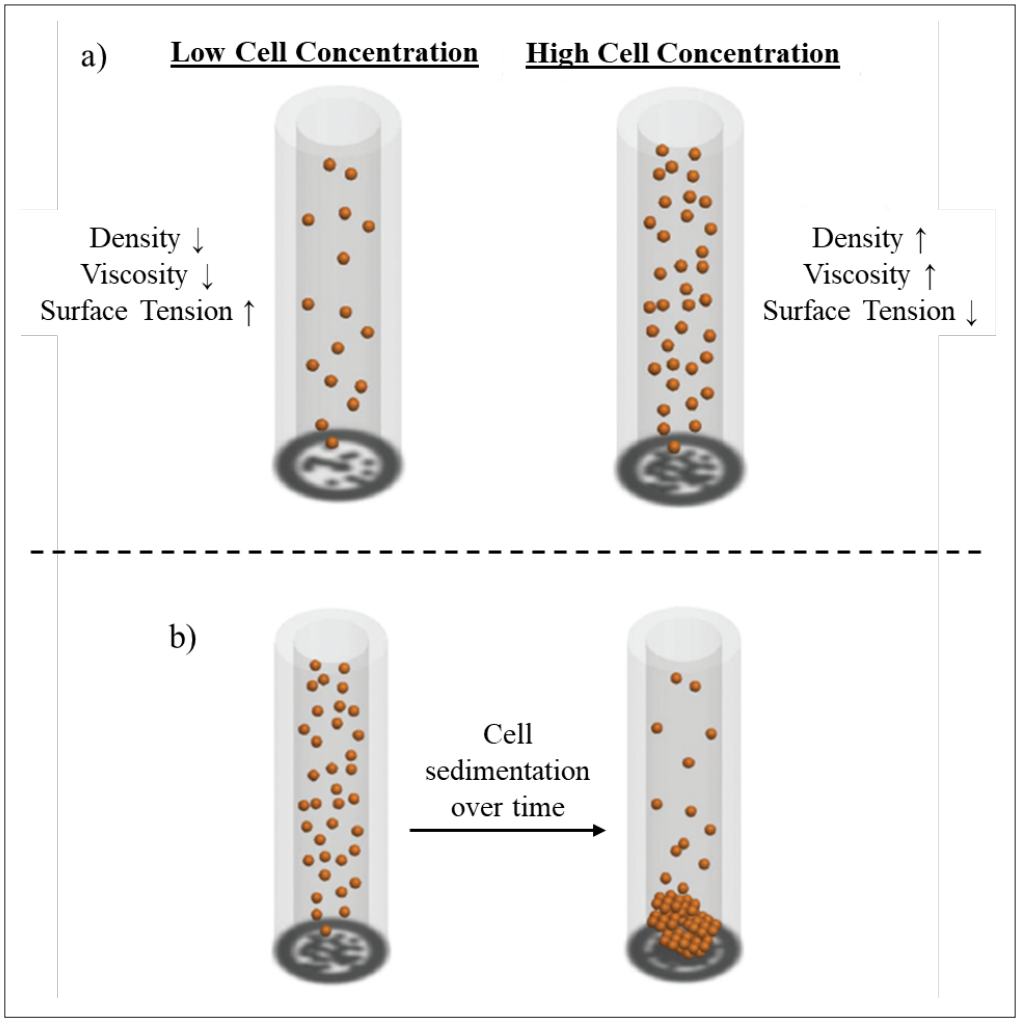

Figure 2. Schematic diagram illustrating the influence of cell concentration on the physical characteristics of bio-inks.

and varies by cell type.[31] The model was further extended to describe viscosity in concentrated solutions with the following equation:[32]

$$\phi = 1 - \left(\frac{\eta_0}{\eta}\right)^{2/5} \left(\frac{2.5\eta_s + \eta_0}{2.5\eta_s + \eta}\right) \quad \text{(III)}$$

This model is only valid where cell membrane surface tension is sufficient to keep the cell mostly spherical. A different model for viscosity of a concentrated suspension of poly-dispersed spheres has been proposed.[28]

$$\phi = 1 - \left(\frac{\eta_0}{\eta}\right)^{2/5} \left(\frac{\eta_s - \eta}{\eta_s - \eta_0}\right) \quad \text{(IV)}$$

Notably, this model does not explicitly account for size polydispersity. For high-volume fraction cell suspensions, a more comprehensive model of model treats the suspension as a viscoelastic fluid.[33] The viscous response is attributed to the cytoplasmic viscosity and the viscous contribution of the cell membrane, while the elastic response is attributed to the cell membrane's ability to reversibly restore the cell to a spherical morphology. In situations where cells at high volume fractions tend to aggregate, these aggregates also exhibit viscoelastic behavior, contributing to the overall viscoelastic response of the suspension. This behavior can be modeled by the semi-empirical Mooney equation:

$$\eta = \eta_0 exp\left(\frac{K_1 \gamma^{-\beta} \phi}{1 - K_2 \frac{\sigma}{D} \phi}\right) \quad \text{(V)}$$

In this equation, K_1 and K_2 are fitting parameters that consider cell shape and the degree of cell aggregation; $\dot{\gamma}$ represents the fluid shear rate, β is the shear flow index; σ is the effective cell membrane thickness, and D is the average cell diameter. Typically, K_1, K_2, and β are determined experimentally by measuring the complex viscosity as a function of shear rate in a rheometer.

The presence of particles (including cells) in high concentration (>0.5% *v*/*v*) decreases surface tension, and surface tension decreases asymptotically with increasing particle loading. However, in practical bio-inks, other substances including peptides, proteins, and cellular debris have a substantially dominating effect of lowering the surface tension. Thus, in practice, surface tension of bio-inks is determined empirically. By understanding the influence on cells on the physical properties of the bio-inks, one can formulate a cell-laden bio-ink of high printability.

2.2. Cell homogeneity within bio-inks

Cell sedimentation is a common occurrence in most inkjet bioprinting systems, primarily caused by the influence of gravitational forces on the freely suspended cells. The uniformity of cell distribution within the printing cartridge changes with time as these suspended cells settle to the bottom of the bio-ink reservoir, resulting in cell inhomogeneity in the printing output (Figure 2b). A research study has investigated the impact of cell sedimentation on the bioprinter's output and has highlighted the issue of inconsistent printing output over time.[34] As time progresses, the concentration of localized cells at the bottom of the reservoir increases significantly, which can lead to problems such as nozzle clogging and highly unstable droplet ejection. Consequently, this results in a decline in overall printing reliability and quality.

The cell homogeneity within the bio-inks can be examined by recording real-time video of the sedimentation process and calculating the cell sedimentation velocity using sophisticated optical set-ups. The theoretical values for cell sedimentation velocity can be determined using Stokes' law, defined as follows:

$$v = \frac{(\rho_p - \rho_f) g D_C^2}{18\mu} \quad \text{(VI)}$$

where v represents the sedimentation velocity, g is the gravitational acceleration, D_c is the cell diameter, ρ_p and ρ_f are the densities of particles and the fluid, respectively, and μ is the fluid viscosity.[35] As the distance between neighboring cells decreases, the cells start adhering to each other and form larger cell aggregates, which can exceed the nozzle diameter and result in nozzle clogs and unstable droplet ejection. Additionally, interactions such as van der Waals forces between the inner surfaces of the printing cartridge and the suspended cells can cause cells to adhere to the walls; this is especially important in constrictions in the print cartridge, where the adhered cells can grow into larger cell aggregates and clog the constriction.[36,37] These floating cells are then attracted to the adhered cells, contributing to the growth of larger cell aggregates near the constriction at the bottom of the printing cartridge.

To counter cell sedimentation and minimize cell adhesion and aggregation along the cartridge's constricted regions, an inert polyvinylpyrrolidone (PVP)-based bio-ink can be used to pre-coat the printing cartridge.[38] Other strategies to mitigate cell sedimentation and aggregation include active stirring and modifying the bio-ink properties to achieve neutral buoyancy.[39] It is important to note that while active stirring can be effective in reducing

cell sedimentation, it has been reported to significantly reduce cell viability from approximately 99% to around ~75% after 50 min of stirring.[40] Therefore, this approach may not be suitable for certain types of cells that are more sensitive to mechanical stresses.

3. Printing chamber

It is crucial to address the design and operation of the print chamber in bioprinting, as it has significant impact on various factors, including cell viability, number of dispensed cells, and post-dispense cell phenotype. Specifically, we discuss the design and operation of TIJ print chambers, PIJ print chambers, the cellular behavior under shear forces, and the conditions experienced by cells within these print chambers. This is essential for ensuring successful and effective bioprinting processes and the fabrication of 3D-bioprinted tissue constructs.

3.1. Overview of thermal and piezo printing chambers

The TIJ printing chamber typically comprises an ink supply inlet, a thin film resistor, and a nozzle, serving as the outlet for the ink (as shown in Figure 3). In its usual operation, a sub 40 V voltage pulse (1–10 μs) is applied across the resistor. This pulse results in the rapid heating of the resistor surface, with a heat flux of the order of GW/m^2 and at a rate of ~10^8 K/s, raising the temperature to around 300°C.[41,42] The primary purpose of this process is to induce uniform nucleation at the surface of the resistor.[43]

The resistor vaporizes only a tiny portion of the ink above it, typically between 20 and 100 nm (equivalent to 0.1% of the chamber height), forming numerous small vapor bubbles. Importantly, this heating process does not lead to a temperature excursion or significantly impact the cells within the chamber. These small vapor bubbles rapidly coalesce into one large vapor bubble,[44] with the pressure inside the bubble reaching several MPa.[45] As this vapor bubble rapidly expands, it imparts momentum on the surrounding liquid.

The liquid column on the inlet side of the TIJ resistor, which includes the cell reservoir, has a much larger mass than the downstream column (the outlet or nozzle side). Consequently, the downstream liquid is accelerated to a much larger velocity than the upstream column, ultimately ejecting the liquid out of the nozzle. After ejection, the vapor within the vapor bubble condenses, causing the bubble to collapse. The capillary pressure created by the resulting meniscus pulls new liquid into the printing chamber, preparing it for another dispense cycle. The duration of the dispense cycle is determined by the time it takes for the meniscus to draw new liquid into the chamber, typically lasting between 20 and 1000 μs.

The lifetime of the print chamber is influenced by several factors, including cavitation and kogation at the resistor surface, as well as cell lysis. In TIJ cavitation, the collapsing vapor bubble generates a shock wave toward the resistor, inducing stresses in the resistor material. This cyclic stress can lead to material fatigue and damage to

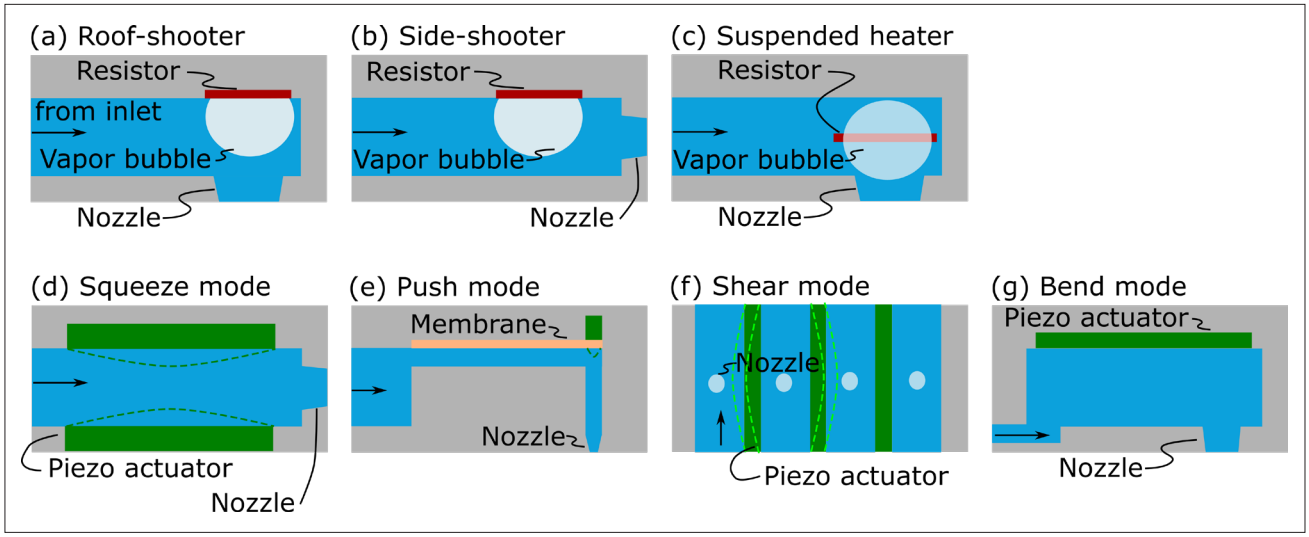

Figure 3. Schematic cross sections of typical thermal (a–c) and piezo (d–g) inkjet print chamber designs. Thermal inkjet designs vary in the position of the heating element (resistor) relative to the location of the nozzle. This is mainly dictated by the fabrication methodology. Piezo inkjet designs vary in chamber geometry, position and design of the piezo actuator, and presence of axillary components such as membranes. As deflection of the fluid due to the piezo element is typically smaller than that of a vapor bubble, piezo inkjet (PIJ) chambers are typically larger than their inkjet counterparts, leading to lower nozzle density on the print die. For PIJ, dashed lines depict exaggerated deformation of the piezo element during printing.

the resistor surface. In TIJ kogation, the resistor pyrolyzes a small portion of the ink on the resistor surface.[46] This process degrades the heat transfer between the resistor's surface and the liquid above it, affecting surface roughness, bubble nucleation, and ultimately vapor bubble generation. When cells lyse in the print chamber, the resulting sticky debris, believed to be nucleic acid material, adheres to the chamber walls and promotes the adhesion of other cells to the walls. The presence of debris on the chamber walls also alters the wetting properties of the walls and affects the rate of refill, potentially changing the achievable dispense frequencies. Notably, debris-induced cell adhesion can lead to the formation of cell clumps, preventing chamber refill and resulting in the failure of the print chamber.

Piezo inkjet printing chamber typically consists of an ink supply inlet, a piezo element, and a nozzle, through which the ink exits the chamber (Figure 3). The ink is expelled from the printing chamber through mechanical deformation caused by a piezo element. The displacement of the print chamber by the piezo element is usually much smaller than the deformation of the liquid caused by vapor bubble. To counteract this, the print chamber can be designed with a larger area. Typically, the print chamber has a length ranging from 5 to 20 mm and a cross-sectional area of 10,000 to 50,000 μm^2. The channel material is often made of silicon, brass, or graphite, and the nozzle typically has a diameter in the range of 18 to 50 μm.[47]

During standard operation, a 40 V pulse (10 μs) is applied to the piezo element. Initially, this pulse causes the piezo element to contract, increasing the height of the print chamber by ~20 nm. This action draws liquid into the chamber and generates a negative pressure wave of around 100 kPa. This negative pressure wave propagates upstream into the ink reservoir. As the reservoir is significantly larger than the channel, the pressure wave reflects toward the nozzle, transforming into a positive pressure wave. Simultaneously, the piezo element returns to its original size, creating a positive pressure pulse. In an acoustically tuned channel, these two pressure pulses combine, working in tandem to eject the ink out of the nozzle for the printing process.

3.2. Effect of shear on printed cells

The impact of mechanical shear stress on biological cells over an extended duration can result in changes to their phenotype and viability, and in severe cases, lead to cell lysis. When it comes to typical cell handling procedures, such as pipetting, cells are subjected to shear stress levels ranging from 1 to 10 Pa for durations of 1 to 10 ms. Conversely, different stages of inkjet bioprinting expose cells to much higher shear stress levels, reaching as high as 500 Pa but only for a very brief period of ~ 100 μs. A probability model for cell survival as a function of shear stress (τ), time in shear (t), critical shear stress (τ_c),and several fitting parameters has been proposed; it can be expressed as:[48-50]

$$p_s = k(\tau - \tau_c)^a t^b \quad \text{(VII)}$$

Here, the critical shear stress represents the maximum stress that cells can endure without showing a noticeable decrease in viability over an extended period. This model, with laminar shear of $k = 1$, $a = -1$, $b = -0.5$, has shown good agreement with experimental data for erythrocytes (red blood cells).[48] It is important to note that erythrocytes have unique properties, such as their discoid shape and the absence of nuclei, which may make them not perfectly representative of other mammalian cells. Nonetheless, there are numerous advanced models available to assess the viability of erythrocytes under shear stress due to the significant interest in modeling and developing devices like cardiac assist systems and other blood-contacting devices. A recent paper has also provided a detailed review of more advanced models of hemolysis, which could beneficial for numerical simulations and modeling purposes.[51]

There is a scarcity of data regarding the probability of cell survival as a function of shear stress and exposure time for various mammalian cells. To address this knowledge gap, additional data points have been provided to offer insights into the conditions that different cells can endure without experiencing a loss of viability or a change in phenotype (Table 1). Embryonic stem cells were found to be sensitive to shear stress, as exposure to a low shear stress of 1 Pa for 24 h led to cell differentiation.[52] Similarly, hybridoma cells experienced an increase in lactate dehydrogenase release into the medium when subjected to a shear stress as low as 0.16 Pa for up to 15 h.[53] The response to shear stress is highly dependent on the cell type, as well as the level of shear stress and the duration of exposure. The leukocytes and erythrocytes typically experience shear stresses of 1.5 Pa in arterial circulation and 0.1–0.6 Pa in venous circulation.[54,55] In some cases, these cells can be exposed to shear stresses of up to 300 Pa for short periods near the walls of large blood vessels and in the heart.[54] While exposing erythrocytes to shear stresses of 450–560 Pa for milliseconds can induce hemolysis,[56,57] some studies have shown that these cells can withstand shear stresses as high as 4000 Pa for 10 μs.[58,59] It was found that the response of baby hamster kidney cells (BHK-21/C13) to shear stress varies with the duration of exposure. These cells experienced a decrease in viability after 2 h of exposure to a shear stress on the order of 10 Pa.[60] However, the cells withstood shear stresses as high as 80 Pa without significant loss of viability when exposed to shear stress for under 1 h, although there were changes in cell morphology.[60]

In a more detailed study, the viability of different cell types, including primary cells, immortalized cell lines,

Table 1. Summary of cellular response to shear stress

Cells	Duration	Shear stress	Response	References
Embryonic stem cells	24 h	1 Pa	Cell differentiation	[52]
Hybridoma cells	Up to 15 h	0.16 Pa	Increase in lactate dehydrogenase release	[53]
Erythrocytes	Milliseconds	450–560 Pa	Hemolysis	[56,57]
Erythrocytes	10 μs	Up to 4000 Pa	Normal	[58,59]
BHK-21/C13 cells	2 h	10 Pa	Decrease in viability	[60]
BHK-21/C13 cells	<1 h	Up to 80 Pa	Changes in cell morphology, but no significant loss of viability	[60]
Erythrocytes & leukocytes	Milliseconds	30–90 Pa	Low decrease in viability	[61]
Primary human breast cells (HMEC) and primary human prostate epithelial cells (PrEC)	Milliseconds	30–90 Pa	Substantial loss of viability	[61]

*A typical shear stress of order 300 Pa is obtained for a characteristic time of 10^{-5} s based on the typical print chamber and ink properties.

transformed cell lines, and metastatic derivatives, was investigated under shear stress conditions ranging from 30 to 90 Pa and lasting for milliseconds.[61] The decrease in cell viability varied significantly depending on the cell state and its state; both erythrocytes and leukocytes, which are blood cells, showed relatively low decrease in viability under shear stress. In contrast, non-blood primary cells, specifically primary human breast cells (HMEC) and primary human prostate epithelial cells (PrEC), experienced a substantial loss of viability, with some cases showing viability as low as 2% of the total population. Non-transformed cell lines were found to be more sensitive to shear stress compared to cancer cell lines.[61] This sensitivity was influenced by whether the cells had undergone a transformation process. Cells transformed via specific methods such as myc/PI3K or H-ras exhibited higher resistance to fluid shear stress compared to wild-type PrEC cells and isogenic immortalized, non-transformed controls. It was also found that the resistance of cells to fluid shear stress was not strongly correlated with their cell size or cell cycle state. Instead, it was highly dependent on the extracellular calcium concentration.[61] The composition of the bio-ink used in bioprinting played a significant role in influencing cell viability under shear stress conditions. Using a calcium-free bio-ink led to a notable reduction in cell viability, even at low shear stress levels of 50 Pa with a 10 ms exposure to shear.[61] These findings emphasize the importance of cell type, transformation state, and bio-ink composition during cell printing. Understanding these factors is crucial for maintaining cell viability and ensuring the success of bioprinting applications.

The primary function of the print chamber is to provide the necessary momentum for ejection of a precise volume of fluid droplets from the chamber. Several factors come into play to achieve this, including overcoming the fluid's inertia, accelerating the droplets, and dealing with viscous resistance in the nozzle. The dynamic pressure $\left(p_d \sim \frac{1}{2}\rho u^2\right)$ is associated with overcoming the inertia of the fluid; unsteady pressure $\left(p_a \sim \rho L_n \frac{du}{dt}\right)$ and capillary pressure $(p_c \sim 2\sigma\cos\theta / R_n)$ are responsible for accelerating the droplet; the viscous pressure $(p_v \sim 8\eta L_n u / R_n^2)$ is associated with overcoming the viscous resistance in the nozzle. Here a ρ, μ, η, and σ are the fluid density, droplet velocity, dynamic viscosity, and surface tension, respectively; R_n is the nozzle diameter, L_n is the characteristic length scale, and $\frac{du}{dt}$ is the change in fluid velocity with respect to time.[62] For most bioprinting applications, these typically are ρ = 1000 kg/m^3, η = 1 mPa·s, and σ = 0.07 N/m for pure aqueous solutions; R_n = 15 μm, L_n = 50 μm, and characteristic time scale of ejection is in the order of 10 μs to generate a droplet velocity of 5 m/s. The order of magnitude of the pressures in the print chamber required to eject a drop can be deduced from these values: p_d = 13 kPa, p_a = 25 kPa, p_c = 9 kPa, p_v = 9 kPa, which is equivalent to a total pressure of 56 kPa for successful ejection of a drop. Understanding these pressure considerations is essential for the design and operation of print chambers in bioprinting to ensure the precise and controlled ejection of fluid droplets.

From the typical print chamber and ink properties, a typical shear stress of order 300 Pa is obtained for a characteristic time of 10^{-5} s. A previous study investigated cell exposure to similar shear stress magnitudes but for 100 times longer.[61] Assuming a power law viability vs. shear time model of cell viability (Equation VII), and a shear

time coefficient of ~ 0.5 as that for erythrocytes, minimal damage to mammalian cells with inkjet dispensing is expected. For TIJ-based printers, little change in viability or functionality has been experimentally confirmed, for example, for neural cells dispensed by HP 51626a cartridge[63] and more recently for variety of mammalian cells by specialized HP cell dispense cartridges.[25] For PIJ printers, minimal changes to RNA expression post dispense were observed for mouse embryonic stem cells.[64] These findings highlight the complex and cell type-dependent nature of cellular responses to shear stress. Understanding these responses is crucial for bioprinting, where cells are exposed to shear stress during dispensing, to ensure cell viability and phenotype preservation.

4. Droplet formation

The presence of particles, such as cells, in bio-inks can affect the jet break-up and droplet formation. For mammalian cell sizes of ~16 μm and typical bio-ink cell concentrations of 10^5–10^7 cells/mL, the particle volume fractions, ϕ, range between 0.02% and 2.15%. Jet break-up for low ϕ suspensions $(\phi < 10\%)$ is similar to that of simple Newtonian bio-inks, with the exception that individual particles can be captured in the droplet tail, which leads to new modes of satellite drop formation.[65] For higher ϕ suspensions, presence of large number of particles in the droplet tail results in thick cone-like structures. These structures are similar to beads-on-string structures found in the jets of dilute polymer-based bio-inks.

The presence of particles suppresses the formation of satellite droplets, and the satellite droplets that do form are usually larger and fewer in number. This is advantageous for bioprinting as this leads to better cell placement and accuracy as well as to reduction in evaporation and thus change in cell media composition. Thinning of the droplet tail slows down as particle concentration increases, and this can be attributed to the increasing effective viscosity as a function particle concentration.[66] The length of the droplet tail at rupture decreases with increasing particle concentration due to the action of discrete particles. Specifically, the particles trapped in the tail induce another axis of curvature perpendicular to the original axis of the column as the tail narrows to the size comparable to the particle diameter and thus encourages the breakup of the liquid column.[66]

5. Droplet impact

Droplet impact behavior is influenced by a variety of factors, including fluid properties (density, viscosity, and surface tension), impact conditions (impact velocity, and drop size), and the characteristics of the substrate surface (advancing contact angle, surface roughness, and temperature, stiffness). In the context of bioprinting, precise cell placement is crucial, and different droplet impact regimes have varying degrees of suitability for this purpose. There are six primary regimes of droplet impact on dry surfaces: deposition, prompt splash, corona splash, receding breakup, partial rebound, and rebound (Figure 4).[67,68] In the deposition regime, the droplet deforms upon impact but remains on the surface throughout the entire process without breaking apart. This is the most favorable regime for bioprinting applications as it allows for high cell placement accuracy. Additionally, the lower surface-to-volume ratio results in a reduced rate of evaporation and minimal changes in media concentration. In the prompt splash regime, droplets are generated directly at the contact line during the initial spreading phase when the lamella has a high radial (outward) velocity. The characteristics of the surface, particularly its roughness, influence the formation of droplets. In the corona splash regime, droplets are formed around the rim of a bowl-like shape (corona), often at a distance from the impact surface. This phenomenon is common for droplet impacting liquid films and is a significant consideration for bioprinting applications. The receding breakup regime is primarily controlled by surface wetting, especially the dynamic contact angle. As the liquid retracts from the maximum spreading radius, droplets are left behind on the surface when the dynamic contact angle decreases to zero. In the partial rebound regime, part of the initial droplet remains attached on the surface while the remaining part rebounds off the surface. In the complete rebound regime, the entire droplet rebounds from the surface. Both rebound regimes occur only when the droplet recedes after spreading. The droplet receding process is influenced by the maximum spreading diameter and the receding contact angle. Partial rebound typically occurs for low values of the dynamic receding contact angle, while complete rebound occurs for high values of the dynamic receding contact angle.

In bioprinting process, droplets of bio-inks are typically dispensed in a layer-by-layer manner on top of other cells in media. Hence, it is important to consider droplet impact on a liquid surface, which can be modeled as a small pool of liquid. Two regimes of droplet impact on liquid surfaces have been reported: splashing regime, and a combined regime of bouncing, floating, and coalescing.[69] In the splashing regime, the droplet collides with the surface of the target liquid, and a flared film of liquid is thrown upward and outward from the periphery of the colliding region. This regime has a similar morphology to the corona splash regime

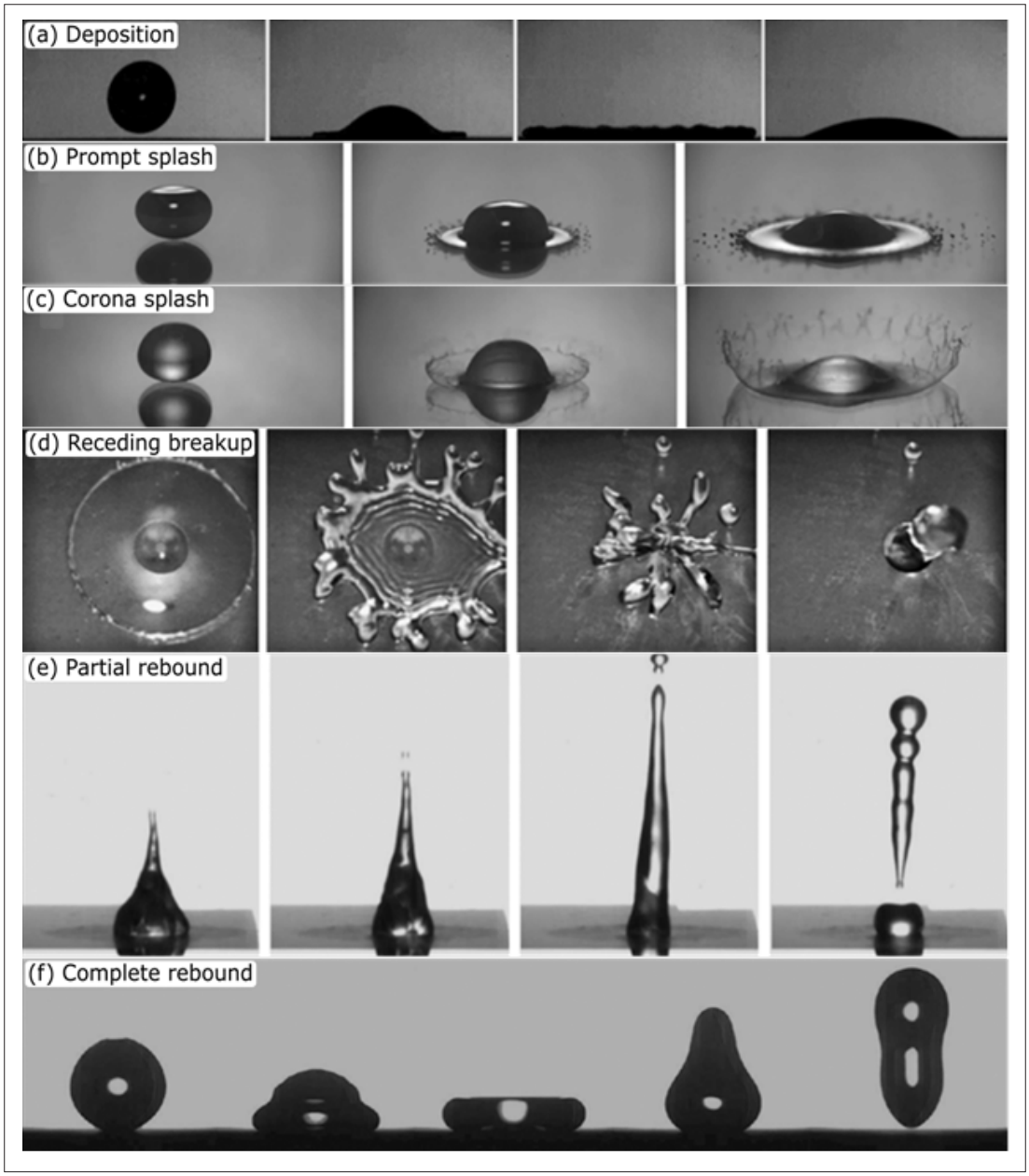

Figure 4. Droplet impact regimes on dry solid surfaces. (a) In the deposition regime, the droplet deforms and remains on the surface. This is the desirable regime for bioprinting applications. (b) The prompt splash regime is characterized by formation of small droplets at the contact line as the droplet spreads. (c) The corona splash regime is characterized by formation of a bowl-shaped thin liquid film, later forming a corona with small droplets detaching from its rim. Similar morphology is observed for impacts on liquid films. (d) In the receding breakup regime, droplets break up and are left behind the receding lamella during the retraction phase of the droplet impact. (e) In the partial rebound regime, part of the droplet remains on the surface. (f) In complete rebound regime, the entire droplet rebounds during the retraction phase of the droplet impact with the entire droplet leaving the substrate. Adapted with permission from ref.[68]

for droplet impact onto solid surfaces. This flared film contains primarily the liquid from the impacting drop as well as some of the target liquid. A capillary wave train often propagates through the film and is always perpendicular to the target surface. The top of the film also breaks up into jets and small droplets, forming an appearance of a crown. This large increase in surface-to-volume ratio (relative to the original drop) promotes rapid evaporation. Meanwhile, a cavity begins to develop below the original free liquid surface. The cavity enlarges until it quickly takes the shape of a hemisphere, and the crown wall simultaneously begins to subside and

becomes thicker. The expanding cavity can displace cells in the target fluid, reducing accuracy of cell placement. The cavity stops its downward penetration into the fluid, and subsequently, the capillary waves from the crown spread into the cavity and distort its shape. At this point, the cavity begins to close from the bottom and decrease its penetration into the fluid while its radial dimension (width) does not change significantly. A central jet then emerges and grows upward. It then breaks up with a droplet at its very tip, and the remnants of the jet fall toward the target surface.[70]

It is somewhat debated if the combined regime of bouncing, floating, and coalescing should be classified as separate regimes or as separate stages of a single regime.[69-72] In this regime, the target liquid and the cells deposited in it are substantially less disturbed. The most striking characteristic of this regime is droplet bouncing, which unfortunately reduces the cell placement accuracy. As a droplet approaches the target liquid surface, a thin film of gas prevents the droplet from touching the surface and the droplet bounces upward.[71] In the floating regime, the droplet is also prevented from touching the target liquid by a thin gas film. However, instead of bouncing upward, it travels laterally and skates on the gas film over the target fluid. In the coalescing regime, the droplet penetrates the gas film, touches the target liquid, and coalesces with it. The transition between bouncing, floating to the coalescing regime is dependent on the relative importance of inertia to surface tension (as the droplet needs to have enough inertia to break through the gas film), gas mean-free path, and gas viscosity.[73] The bouncing, floating, and partial coalescing can coexist as one regime and can proceed as a cascade whereby each step generates a smaller droplet.[70] In this case, the droplet first bounces, then floats after losing some momentum, and lastly coalesces partially with the target fluid after losing more momentum. However, the resulting daughter droplet has enough momentum to bounce and repeat the cascade.

Splashing and formation of thin lamella, as found in the many droplet impact regimes, dramatically increases the surface to volume ratio of the liquid, as well as produce high liquid velocity relative to the surrounding air, and so can dramatically increase evaporation rates. This accelerated evaporation leads to increases in concentration of reagents in the bio-ink which, if not accounted for, can adversely affect the resulting cell viability. Most dramatically, at low dispense flow rates, the cell media may completely evaporate, resulting in high vitality loss. Typically, bio-inks are isosmotic prior to dispense, and due to evaporation, they will become hyperosmotic post dispense, lowering cell viability. This can be mitigated, for example, by dispensing cells onto cell layers saturated with isosmotic media, or by co-dispensing hypoosmotic media (from a separate print chamber) along with the cells to maintain the correct osmolality. Similarly, it is also important to compensate for the change in concentration of other reagents in the bio-ink, such as signaling molecules.

5.1. Polymer-based droplet impact on media

The addition of polymers to bio-inks can improve bioprinting performance, decreasing splashing, improving cell placement accuracy, and increasing cell viability. Polymer-based solutions can be modeled either as a power-law fluid, a yield-stress fluid, or a viscoelastic fluid. With these non-Newtonian fluids, it is difficult to predict droplet impact behavior, as the fluid viscosity will vary both spatially and temporally as a function of the local shear rate. For a power-law fluid, the effective viscosity $\mu_{eff} = K(\partial u / \partial y)^{n-1}$, where K is the flow consistency index and n is the flow behavior index; $n < 1$ for shear-thinning fluids; and $n > 1$ for shear-thickening fluids. Shear thinning is typically attributed to breakdown of structure formed by interacting particles in the fluid (e.g., cells, polymer chains), and shear-thickening behavior is attributed to jamming of these particles induced by the flow.[74] It was observed that increasing the flow behavior index n for a shear-thinning fluid (0.125–0.75 wt.% xanthan gum-based solutions) increases the maximum spreading diameter.[75] This is counterintuitive as lower n leads to lower viscosity for high velocity gradients (as can be seen in the beginning of the impact) and thus lower viscous dissipation of the initial kinetic energy, and so should lead to a larger spreading diameter. It may be that the average apparent viscosity, which is governed by the flow consistency index K, has a more significant effect on the maximum spreading diameter.[76] Furthermore, the dimensionless retraction rate decreases with the flow consistency index K.[76]

Low concentration polyethylene oxide (PEO) solutions (in the order of 100 ppm) form a class of viscoelastic bio-inks. These solutions have a reduced tendency for drop rebound on impact with hydrophobic surfaces, thus improving cell placement accuracy.[77,78] As these solutions have a similar surface tension and shear viscosity as the base solvent, it is speculated that the reduction of rebound was due to the increase in elongational viscosity of the solution due to the presence of PEO.[76] It appears that the droplet behavior is due to the energy dissipation caused by the stretching of the polymer molecules by a combination of hydrodynamic and surface forces during the droplet retraction phase.[76] However, suppression of prompt splash is observed in dilute (0.01 wt.%) 18 MDa polyacrylamide viscoelastic solutions, and this is attributed to the elastic forces of the fluid.[79] The mechanism behind this phenomena appears to

be that when the surface tension is insufficient to maintain the integrity of the droplet or lamella, elastic forces pull the attached fingers and droplets back to the main body of the lamella, preventing droplet ejection and inhibiting prompt splash phenomena.[79] A study investigated the influence of inert PVP-based bio-inks for cell printing; the experimental results indicated that an increase in the viscosity of the bio-ink facilitated the deposition of droplets onto a wetted substrate surface without causing splashing. This, in turn, greatly enhanced the precision of the primary droplet deposition.[80] Further analysis revealed that cell-laden bio-inks with higher viscosity demonstrated higher measured average cell viability. This can be attributed to the presence of polymer within the printed droplets, which provided cushioning effect during droplet impact on the substrate, dissipating more energy. Consequently, this improvement in energy dissipation enhanced the average cell viability, even when subjected to higher droplet impact velocities, and maintained the proliferation potential of the printed cells.[80]

5.2. Cell-laden droplet impact on media

Typical bio-inks have low cell loading ($\phi < 0.01$) and therefore exhibit droplet impact behavior similar to that of simple Newtonian fluids described above. At higher cell loading (e.g., $>10^7$ cells/mL for 20 μm diameter cells, ($\phi > 0.04$), the bio-ink exhibits shear-thinning properties, and the drop impact behavior is still qualitatively similar to a Newtonian fluid with a corresponding equivalent viscosity.[75,81] The maximum spreading diameter of a shear-thinning fluid after impact was well predicted by the models for simple Newtonian fluids using a viscosity given by the average of the infinite shear viscosity and the zero-shear viscosity.[82] The transition between droplet spreading and splashing for neutrally buoyant particles on a hydrophilic surface is dependent on both Reynolds number and Weber number, and particle loading.[83] Splashing is undesirable as it decreases cell placement accuracy. For low particle loading, droplet spreading occurs for $We^{1/2}\ Re^{1/4} < 350$ and splashing occurs above this threshold. Here, $Re = \frac{\rho V d}{\eta}$ and $We = \frac{\rho V^2 d}{\gamma}$, and ρ and η are the fluid density and viscosity, V is its characteristic velocity, d is the characteristic length scale, typically the diameter of the jet, nozzle, or droplet, and γ is the surface tension. This threshold decreases to ~150, for particle loading between 0.1 and 0.5. For high cell loading ($\phi \sim 0.5$), cells spread uniformly into a disk left behind on the droplet, on hydrophobic surfaces.[84]

Droplet impact can have significant influence on cell viability. A numerical model for single-cell dispensing and associated stresses on the cell within a droplet was reported.[85] The cell was modeled as a viscoelastic fluid inside a simple Newtonian droplet impacting a pool of target simple Newtonian liquid. Droplet impact was categorized into four stages. In the first stage, the droplet dynamics are mainly controlled by inertia effects. In this stage, the droplet touches the target liquid and forms a liquid neck at the interface, which spreads laterally due to surface tension forces. This slows down the droplet considerably. The deceleration of the fluid at the former bottom of the droplet, combined with the capillary forces at the top of the droplet stretch the cell into an ellipsoid shape, with the major axis parallel to the former target fluid–gas interface. The characteristic time scale for this stage is $d/2u$. For the second stage, the stress and deformation of the cell are governed by interfacial flow. The droplet penetrates deeper into the target liquid and decelerates further. The interfacial force at the upper portion of the droplet increases the pressure in the surrounding liquid, driving the liquid droplet downward to form a small crater similar to the simple (empty) droplet impact into a target fluid described above. During this period, the von Mises stress in the cell increases the most, peaks, and then declines. The stress scales as $\sqrt{\sigma\mu_c / d_c}$, where μ_c is the cell's shear modulus (in the order of 10 kPa for mammalian cells), and d_c is the diameter of the cell. For a cell of 15 μm diameter, and a solution with a surface tension of 50 mN/m, this gives a stress of order 7 kPa. This stage lasts for order $\sqrt{\rho d^3 / 8\sigma}$. For a typical inkjet aqueous droplet of 30 μm diameter, this stage lasts for order 8 μs. This condition is near the threshold for survivability for mammalian cells, and therefore, most cell damage likely occurs during this stage. Substituting this scaling into $p_s = k(\tau - \tau_c)^a t^b$ (Equation VII) and assuming $\tau \gg \tau_c$ and $k = 1$, $a = -1$, $b = -0.5$, the probability of cell survival at this stage scales as:

$$p_s \sim \left(\frac{d_c}{\mu_c}\right)^{1/2} \left(\frac{8}{\sigma\rho d^3}\right)^{1/4} \quad \text{(VIII)}$$

In the third stage, the interfacial forces cause the crater to close, and the cell undergoes damped spheroid oscillations. This stage lasts for order $\sqrt{\rho d^3 / 8\sigma}$, and the cell experiences a shear stress of less than order $\sqrt{\rho d_c^2 / \mu_c}$ during this time. The final stage is governed by the interaction between viscous dissipation and interfacial tension. Here, the cell further relaxes toward its resting shape, and the stress on the cell is significantly less than in the other stages. This stage lasts on the order of the viscocapillary timescale, ud/σ. It is worth noting that a study has demonstrated that

an increase in cell concentration results in reduced impact velocity of the ejected droplets, ultimately enhancing the viability of the printed cells and eliminating the occurrence of droplet splashing.[25]

6. Applications

6.1. Incorporating biophysical and biological cues within 3D hydrogel matrices

The utilization of inkjet bioprinting offers a valuable method for precise DOD deposition of cell-laden droplets and manipulation of desired cell density by controlling the number of cell-laden droplets at specific locations. A printable bio-ink has stringent requirements for its physical properties in terms of viscosity, surface tension, and density; the printed cells are usually encapsulated within low-viscosity bio-inks with viscosities ranging from 3 to 10 mPa·s.[86] Various hydrogel-based bio-inks are employed for diverse bioprinting applications; the hydrogel-based bio-ink comprises a 3D polymeric network with a significant water content and provides a 3D microenvironment that closely mimics the natural extracellular matrix (ECM).[87] The biomimetic 3D microenvironment plays a critical role in providing the necessary signals and guiding cellular responses to facilitate proper tissue development and function;[88-90] some important considerations for fabricating such biomimetic 3D microenvironment include the incorporation of biophysical (porosity/pore size and mechanical) and biological (growth factors) cues within the 3D hydrogel matrices.

In the context of 3D hydrogel matrices used in *in vitro* tissue engineering, a significant concern revolves around the limited porosity of most hydrogels. This limited porosity can constrain the mobility and spreading of encapsulated cells. To address these limitations, PVP macromolecule-based bio-ink was used to modulate the collagen fibrillogenesis process and fabricate 3D hierarchical porous collagen-based hydrogel constructs.[91] Increasing the number of printed PVP droplets led to the formation of thicker collagen fibers and larger pore sizes within the 3D collagen matrices. This effect occurred because an increased PVP concentration has a more pronounced excluded volume effect (EVE) on the surrounding collagen fibrils during the fibrillogenesis process (Figure 5). Additionally, the study noted a slower growth rate for the human skin fibroblasts within 3D collagen matrices with larger pore sizes, aligning with findings from previous studies that indicated that larger pores generally lead to a reduction in cell proliferation rates.[92,93] Further analysis also revealed that 3D collagen matrices with larger pore sizes exhibited higher fibronectin deposition.

Another study has suggested the utilization of porous hydrogels created from aqueous two-phase systems (ATPS), which consist of photocrosslinkable gelatin methacryloyl (GelMA) and dextran.[94] The phase behavior, either monophasic or biphasic, can be adjusted by controlling the pH and dextran concentration. The manipulation of these two parameters leads to the development of hydrogels with three distinct microstructures: homogeneous nonporous (NOP), regular disconnected pores (RDP), and bicontinuous interconnected pores (ICP). Notably, the sizes of the pores in the latter two types of hydrogels can be finely tuned within the range of 4–100 μm by adjusting the pH and dextran concentration, ensuring a high level of reproducibility in the microstructure. Various types of cells including human bone marrow-derived mesenchymal stem cells (hMSC), human periodontal ligament fibroblasts (hPDLF), and human neuroblastoma (hNB) cells were used to investigate how the microenvironment influences cellular behavior. The ICP hydrogels, with the largest pore sizes ranging from 40 to 60 μm, facilitated a more homogeneous distribution of cells and the formation of a dense network of cell-to-cell connections for both hMSC and hPDLF. In contrast, hNB cells maintained their characteristic rosette-like organization with minimal or no spreading, even in the presence of interconnected pores within the hydrogels.[94] Another work delved into the impact of 3D matrix stiffness on potential alterations in the morphology of stem cells and their subsequent differentiation capabilities.[95] By combining thermo-responsive agarose hydrogels with collagen type I, it was possible to enhance the mechanical stiffness and precision of the contours in printed constructs compared to pure collagen hydrogels, which are commonly used as the standard materials for differentiating hMSC into osteogenic lineages. The hMSC exhibited the highest degree of spreading and branching when encapsulated within the softest 3D hydrogels, whereas those encapsulated within the rigid 3D matrix maintained a spherical morphology. Although further analysis revealed that the stiffness of the 3D hydrogel has no significant effect on calcium accumulation as indicated by Alizarin Red staining or alkaline phosphatase (ALP) activity, there was an increase in the expression of osteogenic genes (*COL1* and *RUNX2*) in the softer 3D matrix. As a result, the study concluded that the preferable conditions for hMSC osteogenic differentiation were found in less stiff agarose-collagen hydrogels that did not hinder cell spreading and branching.

To date, there are limited studies that investigated the influence of growth factor patterning within 3D matrix.[96] This is a key research area that is valuable for translating 3D growth factor patterning into potential *in vivo* applications. A study utilized inkjet bioprinting to

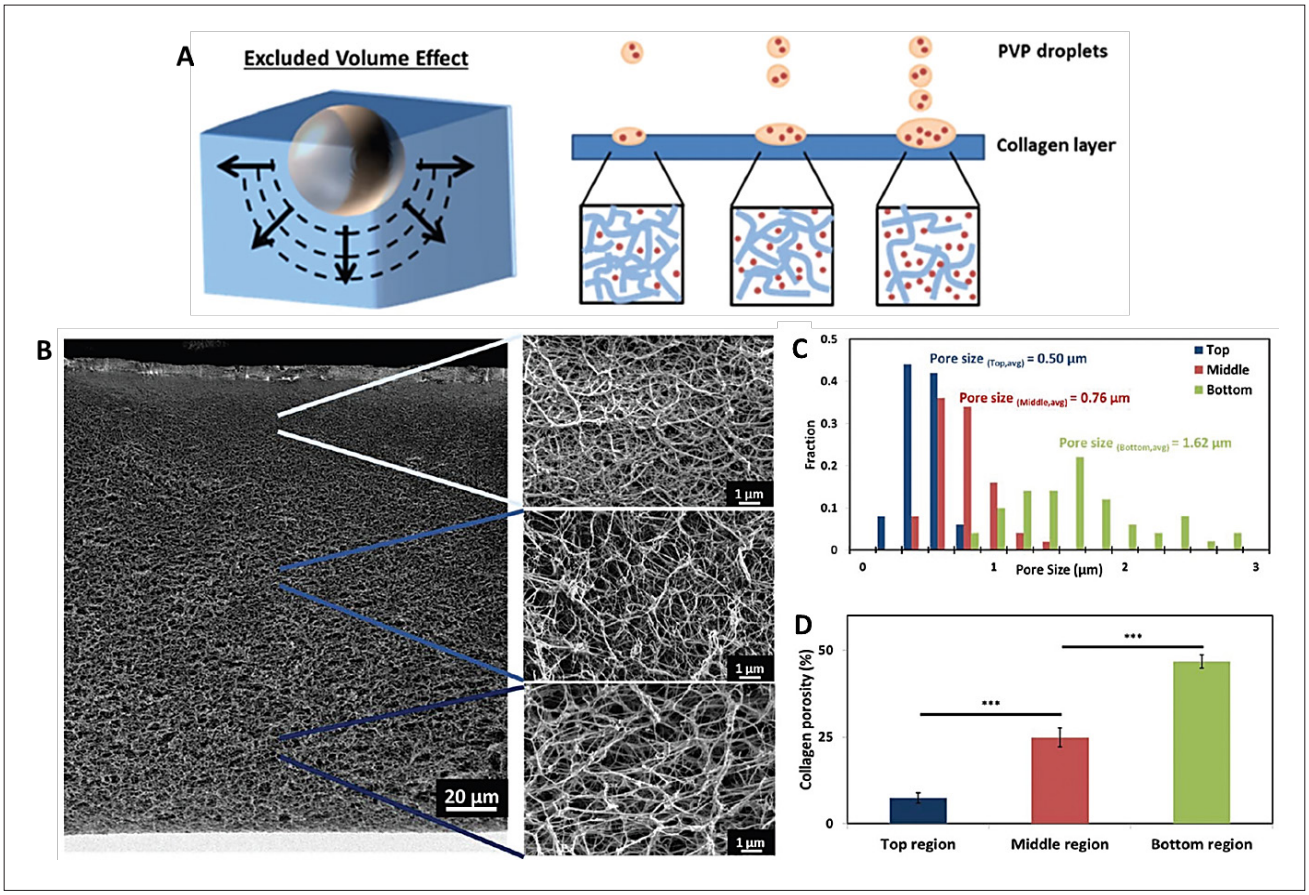

Figure 5. (A) Effect of varying polyvinylpyrrolidone (PVP) concentration on the collagen microstructure; an increase in the number of PVP droplets on the same spot resulted in a more pronounced excluded volume effect (EVE) on the adjacent collagen fibrils. (B) Representative field emission scanning electron microscopy (FE-SEM) images of bioprinted 3D hierarchical porous collagen-based structures. Examination of (C) pore size and (D) porosity in collagen-based structures fabricated via bioprinting across three distinct regions. Adapted with permission from ref.[91]

pattern bone morphogenetic protein-2 (BMP-2) and its inhibitor (noggin) within 3D microporous scaffolds;[96] the mouse C2C12 progenitor cells exhibited a dose-dependent differentiation toward an osteoblastic fate in response to the BMP-2 patterns. Notably, the precision in spatially confining osteoblastic differentiation at the boundary between adjacent BMP-2 and noggin patterns improved as compared to patterns without noggins. Moreover, the patterns of bone formation observed *in vivo* closely resembled the spatially patterned osteoblastic differentiation responses observed *in vitro*. In another study, inkjet bioprinting was employed to deposit DLL1 proteins, which act as Notch activators, within a 3D matrix to create an artificial stem cell niche in dystrophic muscle.[97] Subsequently, the bioprinted DLL1 construct was transplanted into the dystrophic muscle of *mdx/scid* mice, leading to enhanced cell engraftment and noticeable progress in muscle regeneration within 10 days after transplantation (Figure 6). The hypothesis behind this approach is that the precise arrangement of DLL1 proteins contributes to the maintenance of stem cell characteristics and enhances the proliferation of both resident and transplanted stem cells. Additionally, the activation of the Notch pathway is expected to have an antiapoptotic effect, thereby promoting increased cell survival. Another study showcased a multi-component inkjet bioprinting method that enables precise customization of the biochemical properties of each individual layer of the printed hydrogel with an exceptional resolution of 50 µm.[98] This customization involves controlling the distribution of platelet-derived growth factor (PDGF-BB) within the starPEG-heparin hydrogel structures. The findings revealed that hMSC exhibited migration in response to the PDGF-BB gradient. In the presence of PDGF-BB, the cells began adhering to the hydrogel network and exhibited an elongated cell morphology within a 3-week period. Conversely, there was minimal cell migration or noticeable changes in cell morphology in hydrogels lacking PDGF-

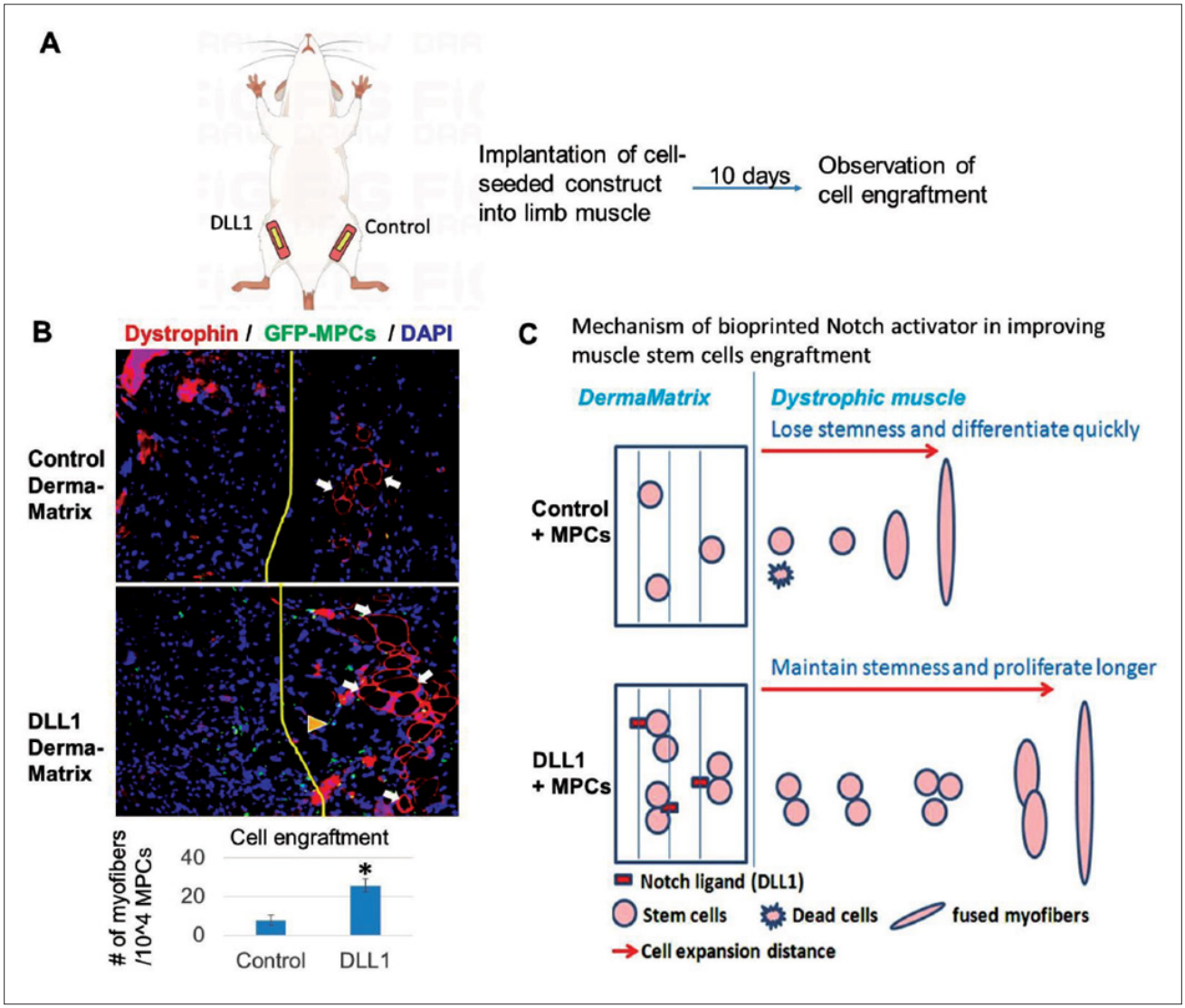

Figure 6. Implantation of muscle progenitor cells labeled with green fluorescent protein (GFP-MPC) seeded into DLL1-DermaMatrix constructs resulted in enhanced cell engraftment in *mdx/scid* mice. (A) A schematic representation of the *in vivo* experiment illustrating the implantation of 3D constructs into mice, both in the control group and the DLL1 group. (B) The muscle tissue implanted with MPC-seeded DLL1-DermaMatrix constructs exhibited improved cell engraftment compared to the control group. More GFP-positive MPCs are visible (indicated by yellow arrow), as well as dystrophin-positive myofibers (indicated by white arrows) in DLL1-DermaMatrix construct group. (C) A proposed mechanism for the enhanced engraftment of muscle stem cell through the bioprinting of a Notch activator within a 3D construct, which acts as a niche for stem cells. Adapted from ref.[97]

BB under similar culture conditions. These outcomes underscore the pivotal role of PDGF-BB in governing hMSC migration and morphogenesis.

6.2. Fabricating complex 3D tissue constructs

Inkjet bioprinting plays a crucial role in the progress of tissue engineering and regenerative medicine by enabling the fabrication of complex 3D tissue constructs at high resolution and repeatability. This technique achieves this by depositing cell-laden droplets with remarkable accuracy at pre-defined positions via a layer-by-layer fabrication approach. Notably, inkjet bioprinting holds significant potential for fabrication of thinner 3D tissue constructs, opening up numerous possibilities in research areas such as skin[99-105] and alveolar lung.[106-108] The subsequent sections offer an in-depth discussion of the application of inkjet bioprinting in the fabrication of various types of tissues.

6.2.1. Skin

Although the fabrication of tissue-engineered skin constructs may appear straightforward, replicating the intricate 3D structure of native skin necessitates precise

cell and biomaterial patterning to enable vital cell–cell and cell–biomaterial interactions.[109] Human skin comprises two distinct regions: the upper epidermal and lower dermal layers, separated by a basement membrane. The upper epidermal region is characterized by densely packed keratinocytes, forming stratified cell layers with increasing differentiation toward the skin's surface. Proliferating keratinocytes near the epidermal–dermal junction gradually move upward, undergoing sequential differentiation to form fully stratified keratinocyte layers over a 2-week period. In contrast, the dermal region comprises collagen fibers and relatively lower fibroblast density (ranging from 0.2 to 2.0 × 10^5 fibroblasts/cm^3).[110] These dermal fibroblasts play a crucial role in secreting essential extracellular matrix proteins (such as collagen I and IV, laminin, fibronectin, and elastin) and growth factors that facilitate cell–ECM and cell–cell interactions. The epidermal–dermal junction comprises melanocytes and basal keratinocytes, with an approximate ratio of 1:20, and a minimum density of 1.0 × 10^4 melanocytes/cm^2 is necessary to restore skin pigmentation in tissue-engineered skin constructs.[103]

Numerous studies on the field of skin bioprinting have been conducted over the years, and the morphological analysis of the 3D-bioprinted skin constructs has shown high degree of similarities to native human skin. Additionally, recent advancements in this field include the fabrication of full-thickness skin constructs,[100-102] the restoration of skin pigmentation,[103,104] and the incorporation of hair follicles.[105] A full-thickness skin constructs comprise both the epidermal and dermal layers. One of the initial attempts at inkjet bioprinting of full-thickness human skin constructs involved printing keratinocytes and fibroblasts embedded within collagen layers to form distinct epidermal and dermal layers in the multi-layered skin constructs.[100] This study successfully demonstrated the feasibility of creating multi-layered skin cell–hydrogel composites on non-planar surfaces. Both the keratinocytes and fibroblasts exhibited normal proliferation within the multi-layer constructs after printing.

Subsequently, efforts were made to enhance the maturation and stratification of 3D-bioprinted full-thickness skin constructs by culturing them at air–liquid interface (ALI).[101] During the ALI culture period, the bioprinted skin tissue became progressively more translucent, indicating the formation of a stratum corneum through terminal differentiation of keratinocytes. The fully matured skin tissue exhibited 3 to 7 distinct cell layers in the epidermis, and the presence of tight junctions between the keratinocytes suggested the formation of a well-developed barrier with extensive cell–cell contacts, like what is observed *in vivo*.[101] However, it was noted that the ordered stratification and keratinization of the epidermal region remained incomplete due to the use of immortalized keratinocytes, which may lead to the gradual loss of cell phenotype and function.

Another work aimed to introduce microvasculature into the full-thickness human skin tissue constructs to enhance wound healing. The construct consisted of neonatal human dermal fibroblast (NHDF), human dermal microvascular endothelial cells (HMVEC), and neonatal human epidermal keratinocytes (NHEK).[102] Subsequently, it was implanted in an athymic nude mouse model to assess its integration with the host tissue and the wound healing process. Microvessels were found in the surrounding mouse tissue on day 14, likely due to the recruitment of the human endothelial cells from the bioprinted skin constructs, leading to graft–host anastomoses. Moreover, there was a notable improvement in wound contraction, up to 10%, compared to control groups.[102]

Another study has demonstrated uniform patterning of epidermal cells (keratinocytes and melanocytes) over the upper surface of 3D-bioprinted dermal tissue constructs.[103] Each droplet containing melanocytes is encircled by droplets containing keratinocytes, forming a repetitive 3 × 3 array to mimic functional epidermal melanin units. This approach enables the uniform distribution of printed cells in a controlled manner, a significant improvement over the manual casting approach. The human skin constructs (containing keratinocytes, melanocytes, and fibroblasts) were cultured in an ALI environment for a duration of 4 weeks in both the 3D bioprinting and manual casting groups. The matured 3D-bioprinted skin constructs exhibited consistent skin pigmentation, whereas the manually cast skin constructs displayed uneven pigmentation with the presence of dark-pigmented spots (Figure 7).[103]

In a recent study, an innovative technique for the scalable and automated preparation of hair microgel using inkjet bioprinting method was presented.[105] Hair follicle germs (HFGs) encapsulated within collagen exhibited higher hair-inducing activity compared with HFGs without collagen. To create hair microgels, two collagen droplets containing mesenchymal and epithelial cells were positioned side by side, and the cell traction forces caused these pairs of microgel beads to contract spontaneously during culture and form the hair microgel. When transplanted onto the back skin of mice, it was reported that these hair microgels effectively regenerated hair follicles and shafts. The inkjet bioprinting method offers a distinct advantage in accurately depositing various types of skin cells, facilitating essential interactions between these cells and their surrounding biomaterials. This precise

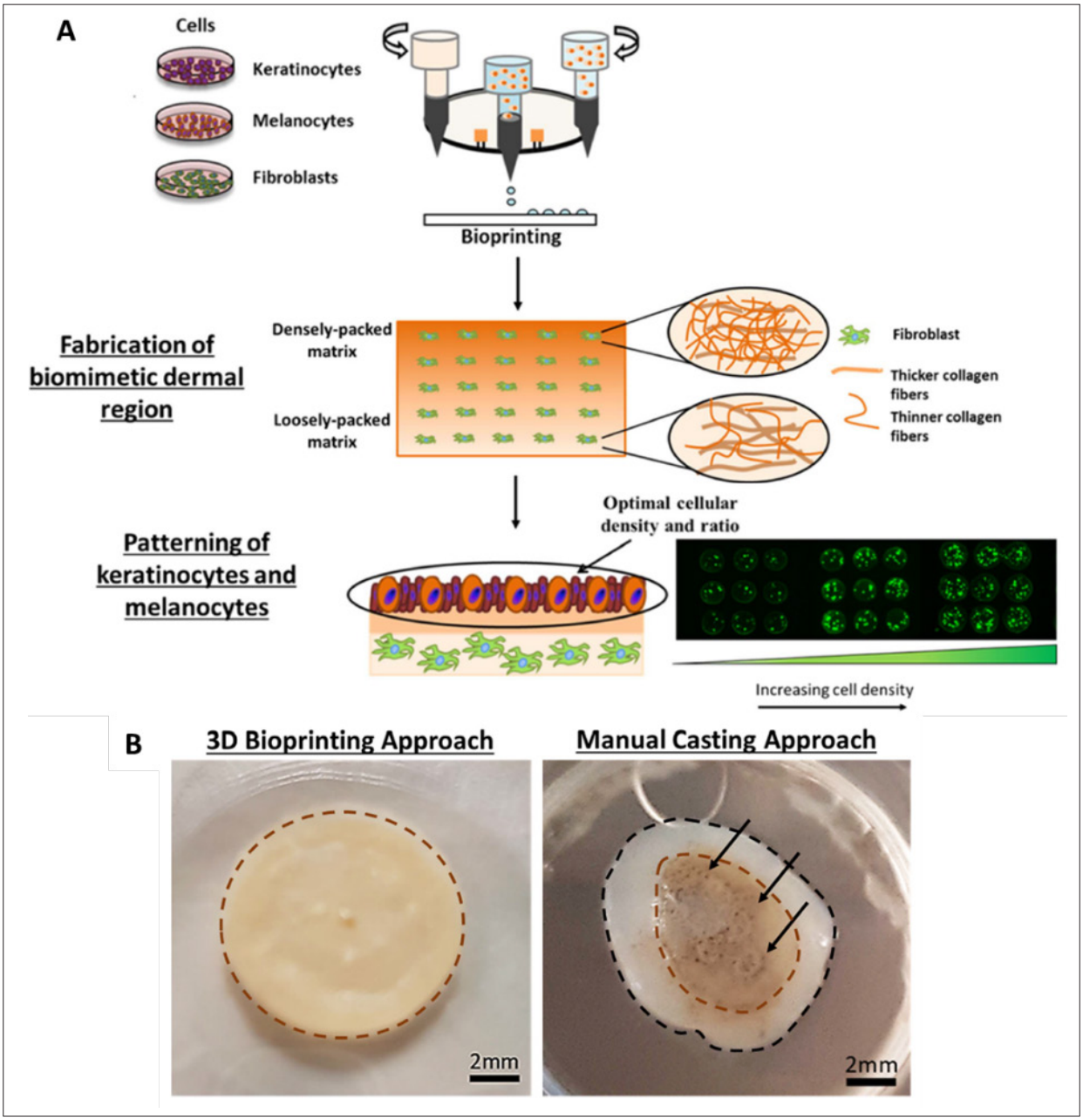

Figure 7. (A) Illustration depicting a two-step bioprinting approach for the design and fabrication of 3D-pigmented human skin constructs—fabrication of biomimetic 3D hierarchical porous collagen-based dermal region followed by precise patterning of epidermal cells (keratinocytes and melanocytes) at the optimal density over the collagen-based dermal constructs. (B) Representative images of 3D-pigmented human skin constructs fabricated via two distinct approaches. (Left) 3D-bioprinted pigmented human skin constructs with uniform pigmentation, enclosed within the brown dotted line. (Right) Manually cast 3D-pigmented human skin constructs with uneven pigmentation and presence of dark-pigmented spots, as indicated by the black arrows. The pigmented area is enclosed within the brown dotted line, while the non-pigmented area is delineated by the black dotted line. Scale bar: 2 mm. Adapted with permission from ref.[103]

approach leads to the development of *in vitro* skin tissue constructs with a certain degree of functionalities.

6.2.2. Lung

A typical pair of human lungs contain ~300 million alveoli, that covers a total surface area of ~140 m^2.[111] The alveoli represent the primary functional and structural units within the lung parenchyma; they feature a thin tissue barrier (~0.6–2 μm in thickness) that separates the airspace surface from the interior of capillaries. This air–blood barrier primarily serves to facilitate gas exchange through diffusion, allowing for the uptake of oxygen and removal of

carbon dioxide.[112] The air–blood barrier comprises of type I and type II alveolar epithelial cells (AECs), macrophages, and pulmonary endothelial cells. Type I AECs are flat, thin cells that line the alveolar walls, covering about 95% of the alveolar surface. They establish functional tight junctions that protect against inhaled toxins, particles, or microorganisms while regulating gaseous exchange.[113] Type II AECs are cuboidal cells responsible for synthesizing and secreting pulmonary surfactant, which regulates alveolar surface tension. Additionally, they serve as progenitor cells for type I AECs in case of injury.[114] Macrophages play a vital role in clearing apoptotic cells and cellular debris, as well as participating in immunological responses.[115] Endothelial cells form the lining of the pulmonary artery and its branches, each ~500 μm diameter, and play a crucial role in maintaining vascular homeostasis.[116] In the lung, extracellular matrices (ECMs) are typically found in the basement membranes and interstitial spaces, and the alveolar fibroblasts, primarily located in interstitial spaces, are responsible for ECM production and serve as effector cells during injury.[117]

The utilization of inkjet bioprinting has enabled precise deposition of various alveolar lung cells to create ultra-thin 3D-bioprinted alveolar lung constructs with ~10 μm thickness. These constructs more accurately replicate the structure, morphology, and functions of *in vitro* lung tissue compared to conventional two-dimensional (2D) cell culture models. One of the earliest works on 3D alveolar lung bioprinting demonstrated the production of a simplified air–blood barrier model. It included type II alveolar epithelial cells (A549), endothelial cells (EA.hy926), and extracellular matrix (Matrigel) in specific regions, produced in a consistent and fully-automated manner.[106] In contrast to manual techniques, this method allows for automated and reproducible fabrication of thinner and more uniform cell layers, an important requirement for an optimal air–blood barrier model.

Subsequently, another study demonstrated 3D bioprinting of triple-layered human alveolar lung models.[107] In each distinct layer, A549 human lung epithelial cells, EA.hy926 human endothelial cells, and MRC5 human lung fibroblasts were patterned to mimic the spatial arrangement of native lung alveolar cells. The use of ALI culture condition mimics the native air–blood barrier environment, resulting in increased expression of pro-SPC (AT-2) and pan-cytokeratin (epithelial cell) biomarkers compared to traditional liquid–liquid interface. It also reduced the overall thickness of the 3D-bioprinted human alveolar lung models to around ~8–10 μm.[107]

Another study demonstrated the fabrication of 3D alveolar lung model using four different human alveolar cell lines: type I and II alveolar cells (NCI-H1703 and NCI-H441), lung fibroblasts (MRC5), and lung microvascular endothelial cells (HULEC-5a). Drop-on-demand inkjet bioprinting enables high-resolution deposition of multiple types of alveolar cells to replicate the intricate microarchitecture and morphologies of native alveolar lung, resulting in a three-layered biomimetic alveolar lung model with an unprecedented thickness of ~10 μm.[108] The precise spatial arrangement of cells is critical for the physiological interactions between cell–cell and cell–matrix. Quantitative real-time polymerase chain reaction (qPCR) tests were conducted to measure representative gene levels and cellular functions. The 3D-bioprinted alveolar lung tissues demonstrated enhanced barrier integrity, with elevated mRNA levels for tight junction and adherence junction proteins (ZO-1, occludin, and E-cadherin), ion channel proteins (epithelial sodium channels: α-ENaCs, β-ENaCs, and Na^+/K^+ transporting ATPase subunit α1: ATP1A1), and surfactant proteins (SP-A and SP-B) (Figure 8). The results indicated that the 3D-structured model better recapitulates the structure, morphology, and functions of the lung tissue when compared to both conventional 3D cell culture models and 3D non-structured models consisting of a homogeneous mixture of alveolar cells and collagen.[108]

7. Outlook

7.1. Machine learning

The use of machine learning has garnered significant attention in recent years owning to its superior ability to identify and model intricate relationships among various factors in extensive, multi-factor datasets.[118] Machine learning has the potential to enhance the bioprinting process from the initial pre-printing phase to final post-printing phase, by offering a simplified empirical model of the complex multi-factor bioprinting process and improving the existing workflow.[119] Some potential applications of machine learning include annotating various 3D tissues at the pre-printing phase, optimizing printing parameters or bio-ink composition based on the printability constraints for each bioprinting technique during the printing phase, and characterizing the printed constructs (including assessing cell viability) at the post-printing phase.[119]

To date, machine learning has been integrated into several studies, such as optimization of droplet formation,[120-122] or even prediction of the number of printed cell during the inkjet-based bioprinting processes.[26] Various printing parameters such as applied voltages, bio-ink properties, and print-head design in inkjet-based bioprinting influence the droplet formation regime, size, and velocity. A research group employed

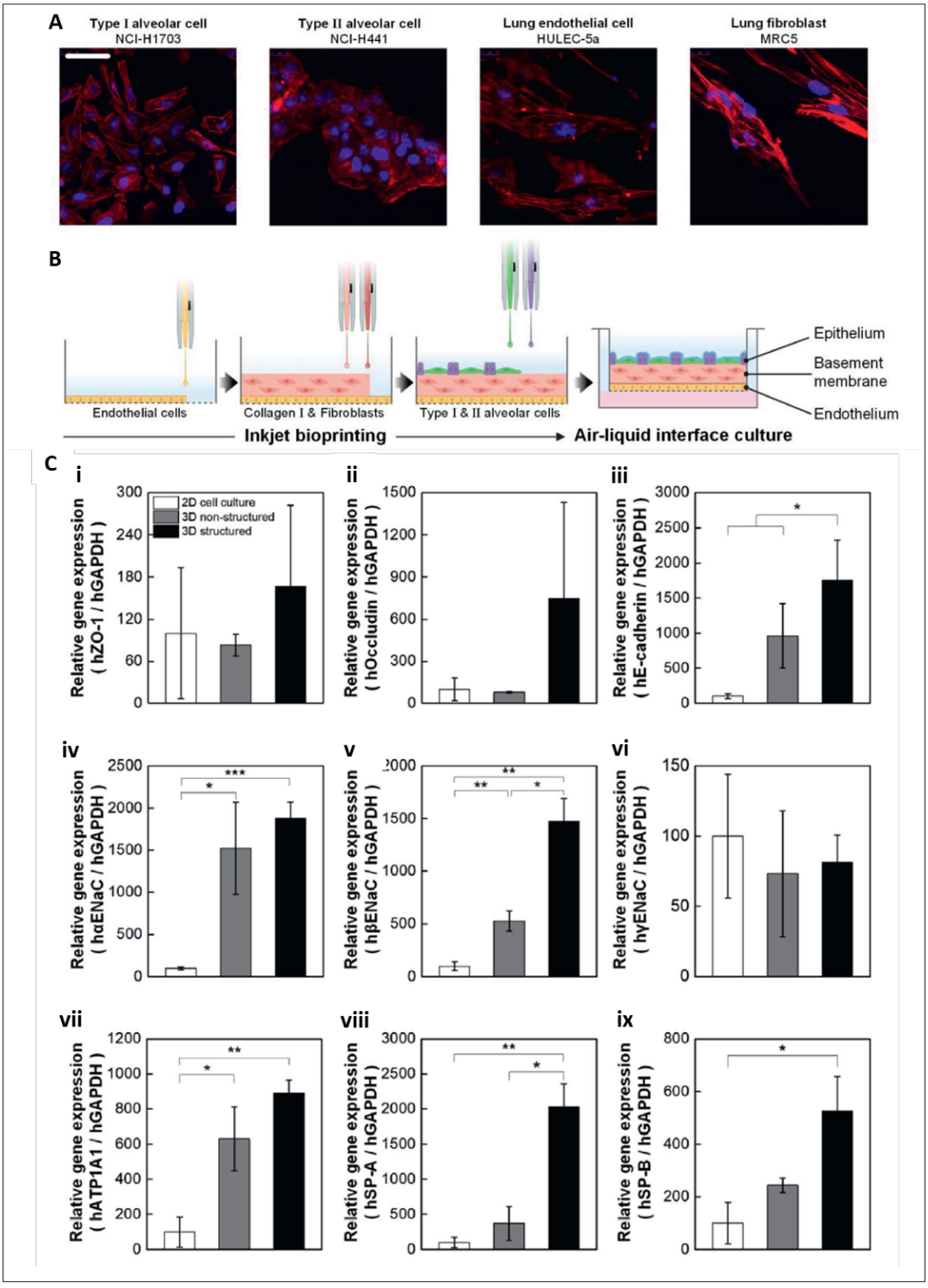

Figure 8. (A) Fabrication of 3D alveolar barrier models using type I alveolar cells (NCI-H1703), type II alveolar cells (NCI-H441), lung endothelial cells (HULEC-5a), and lung fibroblasts (MRC5). Scale bar: 50 μm. (B) Schematic diagram of inkjet bioprinting process for fabrication of 3D alveolar barrier model in a layer-by-layer manner. (C) Comparison of representative alveolar gene expression profiles between conventional and 3D inkjet-bioprinted structured models. Relative mRNA expression was measured via qPCR for 2D cell culture, 3D non-structured, and 3D-structured models using specific markers involved in (i–iii) intercellular junction formation, (iv–vi) epithelial ion channels and ion transport, and (vii–ix) pulmonary surfactant secretion. Each expression levels were normalized by the level of 2D cell culture models. Adapted from ref.[108]

high-speed cameras to capture the droplet formation process for various bio-inks with distinct fluid properties, like viscosity and surface tension, under varying applied voltages. Machine learning was then applied to reduce the formation of satellite droplets, minimize droplet size, and increase droplet velocity using a multi-objective optimization design method for piezoelectric printing using fully connected neural networks.[120] Another study explored the influence of various factors such as polymer concentration, excitation voltage, dwell time, and rise time on droplet volume and velocity during piezoelectric bioprinting.[121] An optical system was employed to capture images of the droplet formation and the trajectories of droplets in flight, enabling the training of various predictive models for estimating droplet volume and velocity.[122] Similarly, high-speed images of the droplet trajectories were captured, and the droplet velocity profile was utilized to predict the number of printed cells within each ejected primary droplet.[26] The optimization of cell printing is crucial for creating *in vitro* 3D tissue constructs in a scalable and reproducible manner.

7.2. Multi-modal bioprinting

Creating biomimetic human-scale tissues or organs solely through inkjet-based bioprinting poses a huge challenge, mainly due to the difficulty of printing large-sized tissue constructs. Each bioprinting approach (jetting-based, extrusion-based, and vat photopolymerization-based) comes with its own set of strengths and limitations, encompassing factors such as operational simplicity, bio-ink requirements, printing speed, and resolution.

An early exploration into multi-modal bioprinting systems involved employing an inkjet bioprinting/electrospinning system to fabricate cartilage-like constructs.[123] The inkjet bioprinting process posed limitations in shape fidelity due to the low mechanical strength of the printed bio-inks, making them unsuitable for load-bearing tissues. To overcome this, an inkjet bioprinting/electrospinning approach was adopted to create flexible nanofibrous mats of electrospun synthetic polymer with inkjet-bioprinted chondrocyte cells in a layer-by-layer deposition manner. Histological analysis of the resulting constructs demonstrated *in vitro* and *in vivo* deposition of both type II collagen and glycosaminoglycans, indicating the formation of cartilage-like tissues.

Another study employed an inkjet/melt extrusion printing approach to pattern arrays of cellular spheroids within printed polymeric microchamber templates for the fabrication of stratified articular cartilage constructs.[124] Mesenchymal stromal cells and chondrocytes were patterned within pre-printed microchambers using inkjet bioprinting, while melt extrusion-printed microchambers guided spheroid growth and fusion. The research indicated that creation of articular cartilage tissues with native-like collagen fiber orientations could be achieved by cultivating tissue spheroids within the microchamber system. This approach was further extended to produce large cartilage constructs (50 mm × 50 mm), whose compressive modulus increased by 50-fold after an 8-week culture, along with a stratified collagen network comprising dense collagen fibrils near the tissue surface and thinner fibrils within the core.[125]

Utilizing complementary bioprinting techniques, such as inkjet and extrusion-based bioprinting, offers several advantages, including scalability for larger constructs and enhanced mechanical properties. Inkjet-based bioprinting excels in high-resolution cell printing, while extrusion-based bioprinting enables the deposition of materials at high-throughput rates. Hence, the integration of these techniques facilitates the scalable production of large 3D tissue constructs. Moreover, a broader range of bio-inks becomes accessible by combining complementary inkjet and extrusion-based bioprinting techniques to fabricate 3D tissue constructs with increased complexities. The inkjet-based bioprinting provides precise control over the spatial arrangement of cells within the constructs, while extrusion-based bioprinting enables the deposition of materials with improved mechanical properties. This collaboration results in 3D tissue constructs that not only exhibit improved overall mechanical properties but also maintain intricate spatial control over the printed cells. The synergy of complementary bioprinting techniques empowers researchers to leverage the unique strengths of each method, effectively addressing limitations and pushing the boundaries of bioprinting technology. This advancement holds great promise for the fabrication of complex, functional tissues and organs with applications spanning from regenerative medicine to personalized healthcare.

8. Concluding remarks

Inkjet-based bioprinting offers an attractive approach for tissue engineering and regenerative medicine applications by enabling the precise deposition of sub-nanoliter droplets at pre-defined positions in a contactless, DOD manner. Our discussion begins with an examination of how cells influence the physical characteristics of bio-inks and the importance of achieving cell homogeneity within these bio-inks. Moving forward, we delve into the thermal and piezo printing chambers, unveiling their significant roles in shaping the printing process. We also highlight the impact of shear stress on printed cells, a critical process

that affects the cell viability and cell phenotype. Next, we provide in-depth discussion on the droplet formation process, dynamics of both polymer-based and cell-laden droplet impact on media. This discussion underscores their pivotal role in achieving successful cell deposition. Furthermore, we emphasize the critical significance of 3D hydrogel matrices, elucidating their critical role in providing a conducive microenvironment for printed cells to adhere, proliferate, and differentiate. Lastly, we take a glimpse into the promising future of inkjet-based bioprinting, particularly in the fields of skin and lung tissue engineering. We also consider the potential integration of machine learning to enhance the precision and efficiency of inkjet-based bioprinting and the development of complementary bioprinting technologies to fabricate larger tissue constructs with increased complexities in a scalable manner. In summary, our comprehensive review has unveiled the multifaceted aspects of inkjet-based bioprinting, emphasizing its potential to revolutionize tissue engineering and regenerative medicine while also paving the way for advanced, machine learning-driven optimization of the cell deposition process.

Acknowledgments

Wei Long Ng would like to acknowledge support from NTU Presidential Postdoctoral Fellowship.

Funding

This work is supported and funded by NTU Presidential Postdoctoral Fellowship and HP Inc.

Conflict of interest

Viktor Shkolnikov is an employee of HP Inc. and may own stock as part of the standard compensation package.

Author contributions

Conceptualization: Wei Long Ng, Viktor Shkolnikov
Visualization: Wei Long Ng, Viktor Shkolnikov
Writing – original draft: Wei Long Ng, Viktor Shkolnikov
Writing – review & editing: Wei Long Ng, Viktor Shkolnikov

Ethics approval and consent to participate

Not applicable.

Consent for publication

Not applicable.

Availability of data

Not applicable.

References

1. Ng WL, Chua CK, Shen Y-F. Print me an organ! Why we are not there yet. *Prog Polym. Sci*. 2019;97:101145. doi: 10.1016/j.progpolymsci.2019.101145
2. Sun W, Starly B, Daly AC, et al. The bioprinting roadmap. *Biofabrication*. 2020;12(2):022002. doi: 10.1088/1758-5090/ab5158
3. Levato R, Jungst T, Scheuring RG, Blunk T, Groll J, Malda J, et al. From shape to function: The next step in bioprinting. *Adv Mater.* 2020;32(12):1906423. doi: 10.1002/adma.201906423
4. Gudapati H, Dey M, Ozbolat I. A comprehensive review on droplet-based bioprinting: past, present and future. Biomaterials. *Biomaterials*. 2016;102:20-42. doi: 10.1016/j.biomaterials.2016.06.012
5. Ng WL, Yeong WY, Naing MW. Microvalve bioprinting of cellular droplets with high resolution and consistency. *Proc Int Conf Prog Addit Manuf*. 2016;397-402. doi: 10.3850/2424-8967_V02-236
6. Ng WL, Lee JM, Yeong WY, Naing MW. Microvalve-based bioprinting – process, bio-inks and applications. *Biomaterials. Sci.* 2017;5(4):632-647. doi: 10.1039/C6BM00861E
7. Koch L, Deiwick A, Franke A, et al. Laser bioprinting of human induced pluripotent stem cells—the effect of printing and biomaterials on cell survival, pluripotency, and differentiation. *Biofabrication*. 2018;10(3):035005, 1-21. doi: 10.1088/1758-5090/aab981
8. Kotlarz M, Ferreira AM, Gentile P, Russell SJ, Dalgarno K. Droplet-based bioprinting enables the fabrication of cell–hydrogel–microfibre composite tissue precursors. *Bio-Des Manuf.* 2022;5(3):512-528. doi: 10.1007/s42242-022-00192-5
9. Ng WL, Yeong WY, Naing MW. Potential of bioprinted films for skin tissue engineering. P*roceedings of the 1st International Conference on Progress in Additive Manufacturing*. 2014;441-446. doi: 10.3850/978-981-09-0446-3_065
10. Ozbolat IT, Hospodiuk M. Current advances and future perspectives in extrusion-based bioprinting. *Biomaterials.* 2016;76:321-343. doi: 10.1016/j.biomaterials.2015.10.076
11. Ng WL, Yeong WY, Naing MW. Development of polyelectrolyte chitosan-gelatin hydrogels for skin bioprinting. *Procedia CIRP*. 2016; 49:105-112. doi: 10.1016/j.procir.2015.09.002
12. Zhuang P, Ng WL, An J, Kai Chua C, Tan LP. Layer-by-layer ultraviolet assisted extrusion-based (UAE) bioprinting of hydrogel constructs with high aspect ratio for soft tissue engineering applications. *PLoS One*. 2019;14(6):e0216776. doi: 10.1371/journal.pone.0216776

13. Liu S, Zhang H, Ahlfeld T, et al. Evaluation of different crosslinking methods in altering the properties of extrusion-printed chitosan-based multi-material hydrogel composites. *Bio-Des Manuf*. 2023;6(2):150-173. doi: 10.1007/s42242-022-00194-3

14. WL Ng, Yeong WY, Naing MW. Polyelectrolyte gelatin-chitosan hydrogel optimized for 3D bioprinting in skin tissue engineering. *Int J Bioprint*. 2016;2(1):53-62. doi: 10.18063/IJB.2016.01.009

15. Ng WL, Lee JM, Zhou M, et al. Vat polymerization-based bioprinting–process, materials, applications and regulatory challenges. *Biofabrication*. 2020;12(2):022001. doi: 10.1088/1758-5090/ab6034

16. Li W, Mille LS, Robledo JA, Uribe T, Huerta V, Zhang YS. Recent advances in formulating and processing biomaterial inks for vat polymerization-vased 3D printing. *Adv Healthc Mater*. 2020;9(15):2000156. doi: 10.1002/adhm.202000156

17. Klebe RJ. Cytoscribing: A method for micropositioning cells and the construction of two-and three-dimensional synthetic tissues. *Exp Cell Res*. 1988;179(2):362-373. doi: 10.1016/0014-4827(88)90275-3

18. Roth EA, Xu T, Das M, Hickman JJ, Boland T. Inkjet printing for high-throughput cell patterning. *Biomaterials*. 2004;25(17):3707-3715. doi: 10.1016/j.biomaterials.2003.10.052

19. Xu T, Jin J, Gregory C, Hickman JJ, Boland T. Inkjet printing of viable mammalian cells. *Biomaterials*. 2005;26(1):93-99. doi: 10.1016/j.biomaterials.2004.04.011

20. Nakamura M, Kobayashi A, Takagi F, et al. Biocompatible inkjet printing technique for designed seeding of individual living cells. *Tissue Eng*. 2005;11(11-12):1658-1666. doi: 10.1089/ten.2005.11.1658

21. Xu T, Rohozinski J, Zhao W, Moorefield EC, Atala A, Yoo JJ. Inkjet-mediated gene transfection into living cells combined with targeted delivery. *Tissue Eng Part A*. 2009;15(1):95-101. doi: 10.1089/ten.tea.2008.0095

22. Parsa S, Gupta M, Loizeau F, Cheung KC. Effects of surfactant and gentle agitation on inkjet dispensing of living cells, *Biofabrication*. 2010;2(2):025003.

23. Xu C, Zhang M, Huang Y, Ogale A, Fu J, Markwald RR. Study of droplet formation process during drop-on-demand inkjetting of living cell-laden bioink. *Langmuir*. 2014;30(30):9130-9138. doi: 10.1021/la501430x

24. Schoendube J, Wright D, Zengerle R, Koltay P. Single-cell printing based on impedance detection. *Biomicrofluidics*. 2015;9(1).

25. Ng WL, Huang X, Shkolnikov V, et al. Controlling droplet impact velocity and droplet volume: Key factors to achieving high cell viability in sub-nanoliter droplet-based bioprinting. *Int J Bioprint*. 2022;8(1):424. doi: 10.18063/ijb.v8i1.424

26. Huang X, Ng WL, Yeong WY. Predicting the number of printed cells during inkjet-based bioprinting process based on droplet velocity profile using machine learning approaches. *J Intell Manuf*. 2023;1-16. doi: 10.1007/s10845-023-02167-4

27. Rutgers IR. Relative viscosity of suspensions of rigid spheres in newtonian liquids. *Rheol Acta*. 1962;2(3):202-210. doi: 10.1007/BF01983952

28. Hsueh C, Wei W. Analyses of effective viscosity of suspensions with deformable polydispersed spheres. *J Phys D: Appl Phys*. 2009;42(7):075503. doi: 10.1088/0022-3727/42/7/075503

29. A. Einstein. Eine neue bestimmung der Moleküldimensionen. *Annalen der Physik*. 1906;324(2):289-306. doi: 10.1002/andp.19063240204

30. Taylor GI. The viscosity of a fluid containing small drops of another fluid, proceedings of the royal society of london. Series A. *Containing Pap of a Math & Phys Character*. 1932;138(834):41-48. doi: 10.1098/rspa.1932.0169

31. Wang K, Sun X, Zhang Y, et al. Characterization of cytoplasmic viscosity of hundreds of single tumour cells based on micropipette aspiration. *R Soc Open Sci*. 2019;6(3):181707. doi: 10.1098/rsos.181707

32. Phan-Thien N, Pham D. Differential multiphase models for polydispersed suspensions and particulate solids. *J Nonnewton Fluid Mech*. 1997;72(2-3):305-318. doi: 10.1016/S0377-0257(97)90002-1

33. Shi Y, Ryu DD, Ballica R. Rheological properties of mammalian cell culture suspensions: Hybridoma and HeLa cell lines. *Biotechnol Bioeng*. 1993;41(7):745-754. doi: 10.1002/bit.260410709

34. Pepper ME, Seshadri V, Burg TC, Burg KJL, Groff RE. Characterizing the effects of cell settling on bioprinter output. *Biofabrication*. 2012;4(1):011001. doi: 10.1088/1758-5082/4/1/011001

35. Wang Z, Belovich JM. A simple apparatus for measuring cell settling velocity. *Biotechnol Progr*. 2010;26(5):1361-1366. doi: 10.1002/btpr.432

36. Sendekie ZB, Bacchin P. Colloidal jamming dynamics in microchannel bottlenecks. *Langmuir*. 2016;32(6):1478-1488. doi: 10.1021/acs.langmuir.5b04218

37. Dersoir B, de Saint Vincent MR, Abkarian M, Tabuteau H. Clogging of a single pore by colloidal particles. *Microfluid Nanofluid*. 2015;19(4):953-961. doi: 10.1007/s10404-015-1624-y

38. Ng WL, Yeong WY, Naing MW. Polyvinylpyrrolidone-based bio-ink improves cell viability and homogeneity during drop-on-demand printing. *Materials*. 2017;10(2):190, 1-12. doi: 10.3390/ma10020190

39. Xu H, Liu J, Zhang Z, et al. Cell sedimentation during 3D bioprinting: a mini review. *Bio-Des Manuf*. 2022;5(3): 617-626.
doi: 10.1007/s42242-022-00183-6

40. Liu J, Shahriar M, Xu H, Xu C. Cell-laden bioink circulation-assisted inkjet-based bioprinting to mitigate cell sedimentation and aggregation. *Biofabrication*. 2022;14(4):045020.
doi: 10.1088/1758-5090/ac8fb7

41. Allen RR, Meyer JD, Knight WR. Thermodynamics and hydrodynamics of thermal ink jets. *Hewlett-Packard J*. 1985;36(5):21-27
doi: hparchive.com/Journals/HPJ-1985-05.pdf

42. Morita N, Hiratsuka M, Hamazaki T, et al. Pulse and temperature control of thermal ink jet printheads without a heater passivation layer. *J Imaging Sci Technol*. 2008;52(2):20503-1-20503-5.
doi: 10.2352/J.ImagingSci.Technol.(2008)52:2(020503)

43. Skripov VP. *Metastable Liquids*. New York: Wiley;1974.

44. Okuyama K, Tsukahara S, Morita N, Iida Y. Transient behavior of boiling bubbles generated on the small heater of a thermal ink jet printhead. *Exp Therm Fluid Sci*. 2004;28(8):825-834.
doi: 10.1016/j.expthermflusci.2003.12.018

45. Meyer J. Bubble Growth and Nucleation Properties in Thermal Ink-jet Printing Technology. *Digest of Technical Papers - SID International Symposium*. 1986; (17) 101-104.

46. Chang L. Effects of kogation on the operation and lifetime of bubble jet thin-film devices. *Denshi Shashin Gakkaishi(Electrophotography)*. 1989;28(1):2-8.
doi: 10.11370/isjepj.28.2

47. Wijshoff H. The dynamics of the piezo inkjet printhead operation. *Phys Rep*. 2010;491(4-5):77-177.
doi: 10.1016/j.physrep.2010.03.003

48. Sharp MK, Mohammad SF. Scaling of hemolysis in needles and catheters, *Ann Biomed Eng*. 1998;26:788-797.
doi: 10.1114/1.65

49. Grigioni M, Daniele C, Morbiducci U, D'Avenio Giuseppe, Di Benedetto G, Barbaro V. The power-law mathematical model for blood damage prediction: analytical developments and physical inconsistencies. *Artif Organs*. 2004;28(5):467-475.
doi: 10.1111/j.1525-1594.2004.00015.x

50. Grigioni M, Morbiducci U, D'Avenio G, Di Benedetto G, Del Gaudio C. A novel formulation for blood trauma prediction by a modified power-law mathematical model. *Biomech Model Mechanobio*. 2005;4:249-260.
doi: 10.1007/s10237-005-0005-y

51. Faghih MM, Sharp MK. Modeling and prediction of flow-induced hemolysis: A review. *Biomech Model Mechanobio*. 2019;18:845-881.
doi: 10.1007/s10237-019-01137-1

52. Stolberg S, McCloskey KE. Can shear stress direct stem cell fate? *Biotechnol Progr*. 2009;25(1):10-19.
doi: 10.1002/btpr.124

53. Smith C, Greenfield P, Randerson D. Shear sensitivity of three hybridoma cell lines in suspension culture. *Mod Apr Anim cell tech*. 1987;316-327.
doi: 10.1016/B978-0-408-02732-8.50027-4

54. Malek AM, Alper SL, Izumo S. Hemodynamic shear stress and its role in atherosclerosis. *Jama*. 1999;282(21): 2035-2042.
doi: 10.1001/jama.282.21.2035

55. Reneman RS, Hoeks AP. Wall shear stress as measured in vivo: consequences for the design of the arterial system. *Med Biol Eng Comput*. 2008;46:499-507.
doi: 10.1007/s11517-008-0330-2

56. Williams A, Hughes D, Nyborg W. Hemolysis near a transversely oscillating wire. *Sci*. 1970;169(3948):871-873.
doi: 10.1126/science.169.3948.871

57. Rooney JA. Hemolysis near an ultrasonically pulsating gas bubble. *Sci*. 1970;169(3948):869-871.
doi: 10.1126/science.169.3948.869

58. Forstrom RJ. *A New Measure of Erythrocyte Membrane Strength: The Jet Fragility Test*. [PhD thesis]. Minnesota: University of Minnesota; 1969

59. Blackshear PL. Hemolysis at prosthetic surfaces. In: Hair ML, ed. *Chemistry of Biosurfaces*. New York: Marcel Dekker; 1972: 523-561.

60. Kretzmer G, Schügerl K. Response of mammalian cells to shear stress. *Appl Microbiol Biotechnol*. 1991;34:613-616.
doi: 10.1007/BF00167909

61. Barnes JM, Nauseef JT, Henry MD. Resistance to fluid shear stress is a conserved biophysical property of malignant cells. *PloS one*. 2012;7(12):e50973.
doi: 10.1371/journal.pone.0050973

62. Lohse D. Fundamental fluid dynamics challenges in inkjet printing. *Annu Rev Fluid Mech*. 2022;54:349-382.
doi: 10.1146/annurev-fluid-022321-114001

63. Xu T, Gregory CA, Molnar P, Cui X. Viability and electrophysiology of neural cell structures generated by the inkjet printing method. *Biomaterials*. 2006;27(19):3580-3588.
doi: 10.1016/j.biomaterials.2006.01.048

64. Yumoto M, Hemmi N, Sato N, et al. Evaluation of the effects of cell-dispensing using an inkjet-based bioprinter on cell integrity by RNA-seq analysis. *Sci Rep*. 2020;10(1):7158.
doi: 10.1038/s41598-020-64193-z

65. Furbank RJ, Morris JF. An experimental study of particle effects on drop formation. *Phys Fluids*. 2004;16(5): 1777-1790.
doi: 10.1063/1.1691034

66. Furbank RJ, Morris JF. Pendant drop thread dynamics of particle-laden liquids. *Int J Multiphase Flow*. 2007;33(4): 448-468.
doi: 10.1016/j.ijmultiphaseflow.2006.02.021

67. Rioboo R, Tropea C, Marengo M. Outcomes from a drop impact on solid surfaces. *Atomization Sprays*. 2001;11(2).
doi: 10.1615/AtomizSpr.v11.i2.40

68. Liu Y, Yan X, Wang Z. Droplet dynamics on slippery surfaces: small droplet, big impact. *Biosurface and Biotribology*. 2019;5(2):35-45.
doi: 10.1049/bsbt.2019.0004

69. Rein M. Phenomena of liquid drop impact on solid and liquid surfaces. *Fluid Dyn Res*. 1993;12(2):61-93.
doi: 10.1016/0169-5983(93)90106-K

70. Fedorchenko AI, Wang A-B. On some common features of drop impact on liquid surfaces. *Phys Fluids*. 2004;16(5): 1349-1365.
doi: 10.1063/1.1652061

71. Zou J, Wang PF, Zhang TR, Fu Xin, Ruan X. Experimental study of a drop bouncing on a liquid surface. *Phys Fluids*. 2011;23(4).
doi: 10.1063/1.3575298

72. Leng LJ. Splash formation by spherical drops, *J Fluid Mech*. 2001;427:73-105.
doi: 10.1017/S0022112000002500

73. Bach GA, Koch DL, Gopinath A. Coalescence and bouncing of small aerosol droplets. *J Fluid Mech*. 2004;518:157-185.
doi: 10.1017/S0022112004000928

74. Frith WJ, d'Haene P, Buscall R, Mewis J. Shear thickening in model suspensions of sterically stabilized particles. *J Rheol*. 1996;40(4):531-548.
doi: 10.1122/1.550791

75. German G, Bertola V. Impact of shear-thinning and yield-stress drops on solid substrates. *J Phys Condens Matter* 2009;21(37):375111.
doi: 10.1088/0953-8984/21/37/375111

76. Bertola V, Marengo M. Single drop impacts of complex fluids: a review. In: Ferrari M, Liggieri L, Miller R, eds. *Drops and Bubbles in Contact with Solid Surfaces*. Florida, United States: Taylor & Francis(CRC Press); 2012: 267-298.

77. Bergeron V, Bonn D, Martin JY, Vovelle L. Controlling droplet deposition with polymer additives. *Nature*. 2000;405(6788):772-775.
doi: 10.1038/35015525

78. Bergeron V. Designing intelligent fluids for controlling spray applications. *C R Phys*. 2003;4(2):211-219.
doi: 10.1016/S1631-0705(03)00043-4

79. Vega E, Castrejón-Pita A. Suppressing prompt splash with polymer additives. *Exp Fluids*. 2017;58(5):57.
doi: 10.1007/s00348-017-2341-y

80. Ng WL, Huang X, Shkolnikov V, Suntornnond R. Polyvinylpyrrolidone-based bioink: Influence of bioink properties on printing performance and cell proliferation during inkjet-based bioprinting. *Bio-Des Manuf*. 2023;6: 676-690.
doi: 10.1007/s42242-023-00245-3

81. Guémas M, Marín ÁG, Lohse D. Drop impact experiments of non-Newtonian liquids on micro-structured surfaces. *Soft Matter*. 2012;8(41):10725-10731.
doi: 10.1039/C2SM26230D

82. An SM, Lee SY. Maximum spreading of a shear-thinning liquid drop impacting on dry solid surfaces. *Exp Therm Fluid Sci*. 2012;38:140-148.
doi: 10.1016/j.expthermflusci.2011.12.003

83. Nicolas M. Spreading of a drop of neutrally buoyant suspension. *J Fluid Mech*. 2005;545:271-280.
doi: 10.1017/S0022112005006944

84. Chen X, O'Mahony AP, Barber T. Spreading behavior of cell-laden droplets in 3D bioprinting process. *J Appl Phys* 2023;133(1).
doi: 10.1063/5.0130063

85. He P, Liu Y, Qiao R. Fluid dynamics of the droplet impact processes in cell printing. *Microfluid Nanofluid*. 2015;18: 569-585.
doi: 10.1007/s10404-014-1470-3

86. Suntornnond R, Ng WL, Huang X, Ethan Yeowa CH, Yee Yeong Wai. Improving printability of hydrogel-based bio-inks for thermal inkjet bioprinting applications via saponification and heat treatment process. *J Mater Chem B*. 2022;10(31):5989-6000.
doi: 10.1039/D2TB00442A

87. Ng WL, Lee JM, Zhou M, Yeong WY. Hydrogels for 3-D bioprinting-based tissue engineering. In: Narayan R, ed. *Rapid Prototyping of Biomaterials*. Chapel Hill, NC: Elsevier; 2020: 183-204.

88. Tibbitt MW, Anseth KS. Hydrogels as extracellular matrix mimics for 3D cell culture. *Biotechnol Bioeng*. 2009;103(4):655-663.
doi: 10.1002/bit.22361

89. Blache U, Ford EM, Ha B, et al. Engineered hydrogels for mechanobiology. *Nat Rev Methods Primers*. 2022;2(1):98.
doi: 10.1038/s43586-022-00179-7

90. Loh QL, Choong C. Three-dimensional scaffolds for tissue engineering applications: role of porosity and pore size, *Tissue Eng Part B: Reviews*. 2013;19(6):485-502.
doi: 10.1089/ten.teb.2012.0437

91. Ng WL, Goh MH, Yeong WY, Naing MW. Applying Macromolecular Crowding to 3D Bioprinting: Fabrication of 3D Hierarchical Porous Collagen-based Hydrogel Constructs. *Biomater Sci*. 2018;6(3):562-574.
doi: 10.1039/C7BM01015J

92. Kumbar SG, Nukavarapu SP, James R, Nair LS, Laurencin CT. Electrospun poly(lactic acid-co-glycolic acid) scaffolds for skin tissue engineering. *Biomaterials*. 2008;29(30): 4100-4107.
doi: 10.1016/j.biomaterials.2008.06.028

93. Lien S-M, Ko L-Y, Huang T-J. Effect of pore size on ECM secretion and cell growth in gelatin scaffold for articular cartilage tissue engineering. *Acta Biomater*. 2009;5(2): 670-679.
doi: 10.1016/j.actbio.2008.09.020

94. Ben Messaoud G, Aveic S, Wachendoerfer M, et al. 3D printable gelatin methacryloyl (GelMA)-dextran aqueous two-phase system with tunable pores atructure and aize enables physiological behavior of embedded cells In Vitro. *Small*. 2023;2208089.
doi: 10.1002/smll.202208089

95. Duarte Campos DF, Blaeser A, Buellesbach K, et al. Bioprinting organotypic hydrogels with improved mesenchymal stem cell remodeling and mineralization properties for bone tissue engineering. *Adv Healthc Mater*. 2016;5(11):1336-1345.
doi: 10.1002/adhm.201501033

96. Cooper GM, Miller ED, DeCesare GE, et al. Inkjet-based biopatterning of bone morphogenetic protein-2 to spatially control calvarial bone formation. *Tissue Eng Part A*. 2010;16(5):1749-1759.
doi: 10.1089/ten.tea.2009.0650

97. Sun Z, Yue X, Liu L, et al. Bioprinted Notch ligand to function as stem cell niche improves muscle regeneration in dystrophic muscle. *Int J Bioprint*. 2023;9(3):711.
doi: 10.18063/ijb.711

98. Zimmermann R, Hentschel C, Schrön F, et al. High resolution bioprinting of multi-component hydrogels. *Biofabrication*. 2019;11(4):045008.
doi: 10.1088/1758-5090/ab2aa1

99. Ng WL, Wang S, Yeong WY, Naing MW. Skin bioprinting: Impending reality or fantasy? *Trends Biotechnol*. 2016;34 (9):689 - 699.
doi: 10.1016/j.tibtech.2016.04.006

100. Lee W, Debasitis JC, Lee VK, et al. Multi-layered culture of human skin fibroblasts and keratinocytes through three-dimensional freeform fabrication. *Biomaterials*. 2009;30(8):1587-1595.
doi: 10.1016/j.biomaterials.2008.12.009

101. Lee V, Singh G, Trasatti JP, et al. Design and fabrication of human skin by three-dimensional bioprinting. *Tissue Eng Part C: Methods*. 2013;20(6):473-484.
doi: 10.1089/ten.tec.2013.0335

102. Yanez M, Rincon J, Dones A, De Maria C, Gonzales R, Boland T. In vivo assessment of printed microvasculature in a bilayer skin graft to treat full-thickness wounds. *Tissue Eng Part A*. 2015;21(1-2):224-233.
doi: 10.1089/ten.tea.2013.0561

103. Ng WL, Tan ZQ, Yeong WY, Win Naing M. Proof-of-concept: 3D bioprinting of pigmented human skin constructs. *Biofabrication*. 2018;10(2):025005, 1-13.
doi: 10.1088/1758-5090/aa9e1e

104. Min D, Lee W, Bae IH, Lee TR, Croce P, Yoo S-S. Bioprinting of biomimetic skin containing melanocytes. *Exp Dermatol*. 2018;27(5):453-459.
doi: 10.1111/exd.13376

105. Nanmo A, Yan L, Asaba T, Wan L, Kageyama T, Fukuda J. Bioprinting of hair follicle germs for hair regenerative medicine. *Acta Biomater*. 2023;165:50-59.
doi: 10.1016/j.actbio.2022.06.021

106. Horváth L, Umehara Y, Jud C, Blank F, Petri-Fink A, Rothen-Rutishauser B. Engineering an in vitro air-blood barrier by 3D bioprinting. *Sci Rep*. 2015;5:7974, 1-8.
doi: 10.1038/srep07974

107. Ng WL, Ayi TC, Liu Y-C, Sing SL, Yeong WY, Tan B-H. Fabrication and characterization of 3D bioprinted triple-layered human alveolar lung models. *Int J Bioprint*. 2021;7(2):332.
doi: 10.18063/ijb.v7i2.332

108. Kang D, Park JA, Kim W, et al. All-inkjet-printed 3D alveolar barrier model with physiologically relevant microarchitecture. *Adv Sci*. 2021;8(10):2004990.
doi: 10.1002/advs.202004990

109. Ng WL, Yeong WY. The Future of Skin Toxicology Testing - 3D bioprinting meets microfluidics. *Int J Bioprint*. 2019;5(2.1):237.
doi: 10.18063/ijb.v5i2.1.237

110. El-Ghalbzouri A, Gibbs S, Lamme E, Van Blitterswijk CA, Ponec M. Effect of fibroblasts on epidermal regeneration. *Br J Dermatol*. 2002;147(2):230-243.
doi: j.1365-2133.2002.04871.x

111. Hoet PHM, Brüske-Hohlfeld Irene, Salata OV Nanoparticles–known and unknown health risks. *J Nanobiotechnol*. 2004;2(1):12, 1-15.
doi: 10.1186/1477-3155-2-12

112. Habib RH, Chalker RB, Suki B, Jackson AC. Airway geometry and wall mechanical properties estimated from subglottal input impedance in humans. *J Appl Physiol*. 1994;77(1):441-451.
doi: 10.1152/jappl.1994.77.1.441

113. Crandall ED, Matthay MA. Alveolar epithelial transport: basic science to clinical medicine. *Am J Respir Crit Care Med*. 2001;163(4):1021-1029.
doi: 10.1164/ajrccm.163.4.2006116

114. Fehrenbach H. Alveolar epithelial type II cell: defender of the alveolus revisited. *Respir Res*. 2001;2(1):33-46.
doi: 10.1186/rr36

115. Hussell T, Bell TJ. Alveolar macrophages: plasticity in a tissue-specific context. *Nat Rev Immunol*. 2014;14(2):81-93.
doi: 10.1038/nri3600

116. Comhair SA, Xu W, Mavrakis L, Aldred MA, Asosingh K, Erzurum SC. Human primary lung endothelial cells in culture. *Am J Respir Cell Mol Biol*. 2012;46(6):723-730. doi: 10.1165/rcmb.2011-0416TE

117. White ES. Lung extracellular matrix and fibroblast function. *Ann Am Thorac Soc*. 2015;12(Suppl 1):S30-S33. doi: 10.1513/AnnalsATS.201406-240MG

118. LeCun Y, Bengio Y, Hinton G. Deep learning. *Nature*. 2015;521(7553):436-444. doi: 10.1038/nature14539

119. Ng WL, Chan A, Ong YS, Chua CK. Deep learning for fabrication and maturation of 3D bioprinted tissues and organs. *Virtual Phys Prototyp*. 2020;15(3):340-358. doi: 10.1080/17452759.2020.1771741

120. Shi J, Song J, Song B, Lu WF. Multi-objective optimization design through machine learning for drop-on-demand bioprinting. *Engr*. 2019;5(3):586-593. doi: 10.1016/j.eng.2018.12.009

121. Wu D, Xu C. Predictive modeling of droplet formation processes in inkjet-based bioprinting. *J Manuf Sci Eng*. 2018;140(10):101007. doi: 10.1115/1.4040619

122. Ogunsanya M, Isichei J, Parupelli SK, Desai SS, Cai Yi. In-situ droplet monitoring of inkjet 3D printing process using image analysis and machine learning models. *Procedia Manuf*. 2021;53:427-434. doi: 10.1016/j.promfg.2021.06.045

123. Xu T, Binder KW, Albanna MZ, et al. Hybrid printing of mechanically and biologically improved constructs for cartilage tissue engineering applications. *Biofabrication*. 2012;5(1):015001, 1-10. doi: 10.1088/1758-5082/5/1/015001

124. Daly AC, Kelly DJ. Biofabrication of spatially organised tissues by directing the growth of cellular spheroids within 3D printed polymeric microchambers. *Biomaterials*. 2019;197:194-206. doi: 10.1016/j.biomaterials.2018.12.028

125. Dufour A, Gallostra XB, O'keeffe C, et al. Integrating melt electrowriting and inkjet bioprinting for engineering structurally organized articular cartilage. *Biomaterials*. 2022;283:121405. doi: 10.1016/j.biomaterials.2022.121405

ACCSCIENCE PUBLISHING

International Journal of Bioprinting

RESEARCH ARTICLE

Effect of lattice type on biomechanical and osseointegration properties of 3D-printed porous Ti6Al4V scaffolds

Jiantao Liu[1], Kao Wang[2], Runqing Wang[3], Zhanhai Yin[1], Xiaoling Zhou[1], Aofei Xu[4], Xiwei Zhang[4], Yiming Li[4], Ruiyan Wang[4], Shuyuan Zhang[4], Jun Cheng[5], Weiguo Bian[1], Jia Li[1], Zhiwei Ren[1], Mengyuan Sun[1], Yin Yang[6]*, Dezhi Wang[7]*, and Jing Ren[1]*

[1]Department of Orthopedics, the First Affiliated Hospital of Xi'an Jiaotong University, Xi'an, Shaanxi, China

[2]Medical School of Yan'an University, Yanan, Shaanxi, China

[3]Lanzhou University, Lanzhou, Gansu, China

[4]Xi'an Jiaotong University, Xi'an, Shaanxi, China

[5]Shaanxi Key laboratory of Biomedical Metal Materials, Northwest Institute for Nonferrous Metal Research, Xi'an, Shaanxi, China

[6]Department of Orthopedics, Xi'an Central Hospital, Xi'an, Shaanxi, China

[7]Anesthesiology Department, Honghui Hospital, Xi'an Jiaotong University, Xi'an, Shaanxi, China

(This article belongs to the *Special Issue: Advancements in 3D Bioprinting Applied to Musculoskeletal Tissues*)

Abstract

Porous structure is an efficient tool for optimizing the elastic modulus and osseointegration properties of titanium alloy materials. However, the investigations on pore shape remain scarce. In this study, we created porous Ti6Al4V scaffolds with a pore size of 600 μm but different lattices (cubic pentagon, diamond, cuboctahedron). The mechanical and biological properties of the scaffolds were investigated in static simulation analysis, *in vitro* mechanical compression test, computational fluid dynamics, as well as cell and animal experiments. The results demonstrated that the calculated yield strength difference between the three Ti6Al4V porous scaffolds was negligible, at approximately 140 MPa, allowing them to match the strength requirements of human bones. The diamond scaffold has the lowest calculated elastic modulus (11.6 GPa), which is conducive for preventing stress shielding. The shear stress was largely concentrated in the diamond scaffold, and the stress range of 120–140 MPa accounted for the greatest share. The mouse MC3T3-E1 cells were found to attach to all three scaffolds, with the diamond scaffold displaying a higher degree of cell adherence. There was more proliferating cells on the diamond and cubic pentagon scaffolds than on the cuboctahedron scaffolds ($P < 0.05$). The diamond scaffold exhibited the highest alkaline phosphatase activity and calcium salt accumulation in cell differentiation tests. Besides, the expression of osteogenic genes on the diamond scaffold was higher than that on the cuboctahedron scaffold, the cubic pentagon scaffold displaying the lowest expression. The *in vivo* studies revealed that all three scaffolds fused well with the surrounding bone and that there was no loosening or movement of the prosthesis. Micro-computed tomography, corroborated by the staining results of hard tissues, revealed that the level of new bone formation was the highest in the diamond scaffold, followed by the cuboctahedron scaffold ($P < 0.05$). Taken together, the diamond scaffold is comparatively better at

***Corresponding authors:**
Yin Yang
(yydcotor@126.com)

Dezhi Wang
(derver8479@sina.com)

Jing Ren
(674909042@qq.com)

Citation: Liu J, Wang K, Wang R, et al. Effect of lattice type on biomechanical and osseointegration properties of 3D-printed porous Ti6Al4V scaffolds. *Int J Bioprint*. 2024;10(2):1698.
doi: 10.36922/ijb.1698

Received: August 28, 2023
Accepted: October 24, 2023
Published Online: January 8, 2024

optimizing the elastic modulus and osseointegration properties of titanium alloy materials, and thus is a preferred choice for porous design.

Keywords: Titanium; Porous structure; Lattice; Biomechanics; Osseointegration

1. Introduction

Due to the superior mechanical and biological qualities, titanium alloy implants are commonly utilized for the replacement and restoration of bone abnormalities.[1,2] In clinical settings, however, prostheses experience issues such as loosening and displacement,[3-5] which were caused by the faults of titanium alloy material with a high elastic modulus[6,7] and biological inertness.[8,9] High elastic modulus leads to "stress shielding" effect, which results in excessive tension on the local cortical bone and insufficient stress on the underlying bone tissue, hence causing osteolysis.[10,11] Titanium alloy materials are biologically inert, marked by their lack of osteoinducibility, which makes osseointegration after implantation difficult, and poor osseointegration performance.[12,13] In recent years, plasma sandblasting, spraying, acid etching, micro-arc oxidation, and dealloying have been utilized to alter the surface of titanium alloy materials, enhancing their osseointegration characteristics to certain degree.[14-16] However, this approach does not efficiently reduce the elastic modulus of titanium alloy materials and cannot prevent stress shielding. To optimize the elastic modulus and osseointegration performance of titanium alloy materials, several researchers have developed a porous technique.[17-19] The porous titanium alloy material has the following advantages over the dense solid: (i) The porous structural design not only satisfies the mechanical strength needs of the to-be-replaced bone tissue but also reduces the elastic modulus to accomplish biomechanical adaptation, thereby successfully reducing or eliminating the "stress shielding" phenomena.[20] (ii) Not only does the porous structure promote the adhesion, proliferation, and differentiation of human cells, but it also improves the movement of body fluids and nutrients. It encourages new bone tissue to grow into the pores so that the implant can develop a biological fixation between the bone and the implant, thus enhancing its osseointegration performance.

Casting, solid foam, and organic foam-impregnated foam sintering are used to create porous structures, but they are associated with some drawbacks, such as the inability to manage porosity and pore size and the instability of mechanical properties.[21,22] Due to the continuous advances in additive manufacturing technology in recent years, the design and preparation of porous titanium alloy scaffolds with various structures become achievable by using computer-aided design software and three-dimensional (3D) printing technology.[23-26] Numerous researchers have examined porosity and pore size to identify a porous structure suitable for improving the biomechanical and osseointegration capabilities of titanium alloy materials.[27-32] Zaharin *et al.*[33] conducted mechanical tests on Ti6Al4V regular porous scaffolds with varying porosity and discovered that the yield strength and elastic modulus of the scaffolds decreased with the increase in porosity, allowing them to better meet the mechanical requirements of human bones within a certain range. Taniguchi *et al.*[34] conducted animal tests using Ti6Al4V scaffolds with pore sizes of 300 μm, 600 μm, and 900 μm and a porosity of 65% and discovered that the porous structure with a 600 μm diameter was more favorable to bone development. After conducting *in vitro* cell assays and *in vivo* animal studies involving Ti6Al4V porous structures with actual pore sizes of around 400 μm, 600 μm, and 800 μm, Ran *et al.*[32] found that Ti6Al4V porous structures with a pore size of 600 μm demonstrated superior osseointegration performance. It has been demonstrated that titanium alloy porous scaffolds with 60–70% porosity and 500–700 μm pore diameter have good elastic modulus and osseointegration performance; however, the role of pore shape has never been investigated.

Currently, some researchers are focusing on the impact of pore shape variations on the mechanical properties of titanium porous alloy scaffolds.[35] Chen *et al.* reviewed various lattice types of porous structures and opined that different lattice types could reduce the elastic modulus of Ti6Al4V implants and partially meet their mechanical requirements.[36] Nonetheless, investigations on pore form are often restricted to mechanical aspects, and little is known about their osseointegration properties. Analysis using computational fluid dynamics (CFD) revealed that alterations in pore shape would affect the permeability and shear stress of porous titanium alloy scaffolds.[37-39] Different shear stresses would certainly alter the osseointegration performance of porous scaffolds, as it has been demonstrated that cells can sense the surrounding mechanical environment and regulate their own cellular behavior.[40-42] In this study, three types of pore shapes—diamond lattice, cubic pentagon lattice, and cuboctahedron lattice—were constructed in order to elucidate further the effect of pore shape on the mechanical and biological aspects of titanium alloy porous scaffolds. All of them have a 66% porosity and a pore size of 600 μm. Using the selective laser melting (SLM) technique, a porous Ti6Al4V scaffold was created. Static simulation analysis, *in vitro* mechanical compression test, CFD, *in vitro* cell experiments, and *in vivo*

experiments were performed to investigate the effect of unit cell structure on the mechanical and biological properties of porous titanium alloy scaffolds. This paper also presents feedback and theoretical guidance for optimizing the biological and mechanical properties of titanium alloy implants.

2. Methods and materials

2.1. Design of porous scaffolds with different lattices

2.1.1. Cubic pentagon lattice

The construction of a cubic pentagon consists of eight pentagons and four quadrilaterals. These polygons are interconnected by a spatial structure known as cubic pentagon lattice (CPL). The diameter of the connecting rod is represented by d_1. The unit cell was encased in a box with dimensions a_1, and the dimensions of the box were defined as the dimensions of the CPL unit cell. The CPL pore size (D_1) was established as the diameter of a ball tangent to the CPL (Figure 1A). The relation of the porosity P_1, d_1, and a_1 was calculated by a fitting technique. As a result, the porosity of the unit cell was given as Equation I.

$$P_1 = -290.84\left(\frac{d_1}{a_1}\right)^2 - 55.109\left(\frac{d_1}{a_1}\right) + 102.33 \quad \text{(I)}$$

If P_1 is set to 66%, d_1/a_1 will be 0.27. The relation between d_1, D_1, and a_1 can be expressed as (II).

Table 1. The parameters for the three lattice structures

Type of lattice	Unite cell size (mm)	Diameter of the rod (μm)	Designed porosity (%)	Designed pore size (μm)
CPL	1.18	363	66	600
Diamond	0.76	200	66	600
Cuboctahedron	0.946	245	66	600

$$D_1 = \frac{\sqrt[3]{2}}{4}a_1 - d_1 \quad \text{(II)}$$

In addition, we set the pore size to 600 μm. Each parameter was computed and displayed in Table 1. The demand models are illustrated in Figure 1B.

2.1.2. Diamond lattice structure

The unit cell of the diamond lattice consists of 4 four-rod components. Each four-rod element consists of four rods with an angle of 109.47° between each pair. The unit cell was encased in a box with dimensions of a_2, and the dimensions of the box were defined as the dimensions of the diamond unit cell. Moreover, the pore size (D_2) of the unit cell was defined as the diameter of a ball tangent to the unit cell (Figure 1A). The relationship of the pore size (D_2), size of the unit cell (a_2), and diameter of the rod (d_2) is expressed in Equation III.

$$D_2 = \frac{\sqrt{6}}{3}a_2 - d_2 \quad \text{(III)}$$

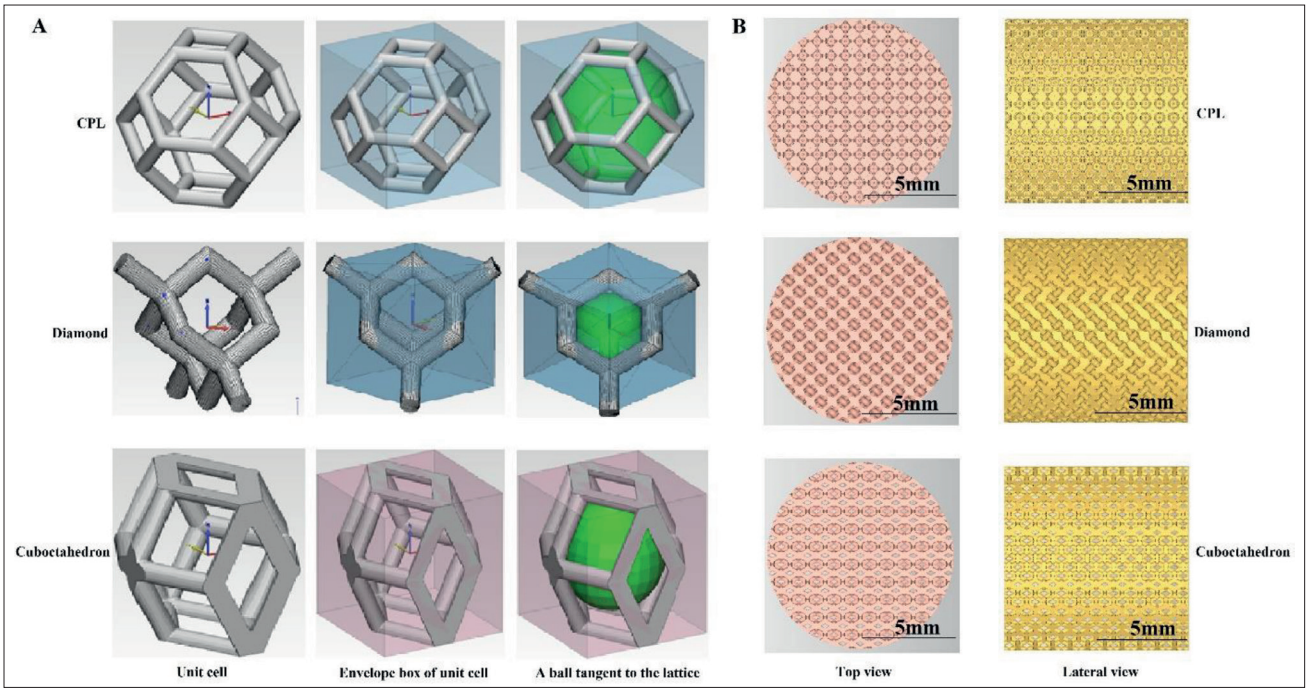

Figure 1. Design of different lattices. (A) Schematic diagram of the construction of the three lattices. (B) 3D models of porous scaffolds were generated based on three different unit cell structures.

If D_2 is equal to 600 μm, d_2 is equal to 300 μm, then a_2 will be 1.102 mm. In addition, the relationship between P_2, d_2, and a_2 was computed using a fitting approach. Porosity of unit cell is expressed in Equation IV.

$$P_2 = -318.17\left(\frac{d_2}{a_2}\right)^2 + 96.185 \quad \text{(IV)}$$

Both porosity (P_2) and pore size (D_2) are the import parameters on our software. Therefore, the diameter of the rod is variable. In this study, the demand porosity and pore size were 66% and 600 μm, respectively. Finally, the parameters of the diamond lattice were calculated, as illustrated in Table 1. The demand models are depicted in Figure 1B.

2.1.3. Cuboctahedron lattice

The unit cell of the cuboctahedron lattice structure is displayed in Figure 1A. Its dimensions mirrored those of the envelope box. Additionally, the pore size (D_3) was determined as the diameter of the unit cell's inner ball. The relation of the porosity P_3, d_3, and a_3 was calculated using a fitting technique. Porosity of the unit cell is expressed in Equation V.

$$P_3 = -247.39\left(\frac{d_3}{a_3}\right)^2 - 83.911\left(\frac{d_3}{a_3}\right) + 104.95 \quad \text{(V)}$$

where a_3 represents the size of the unit cell, and d_3 denotes the size of the rod. If P_3 is set to 66%, d_3/a_3 will be 0.26. The relation between d_3, D_3, and a_3 is expressed in Equation VI.

$$D_3 = \frac{\sqrt[3]{5}}{5}a_3 - d_3 \quad \text{(VI)}$$

We also set the pore size D_3 to 600 μm. Each parameter was computed, as depicted in Table 1. The demand models are illustrated in Figure 1B.

2.2. Fabrication and test of the porous Ti6Al4V scaffold

The designed 3D models of the different unit cell structures were fabricated into Ti6Al4V scaffolds by means of selective laser melting (A320, BLT, China) (Figure 2). To maximize the processing precision, we configured the printing parameters as follows: 80 W laser power, 200 mm/s scanning speed, 60 μm pitch, and 20 μm powder thickness. After spraying gold on the scaffolds, we observed the surface morphology of the scaffolds

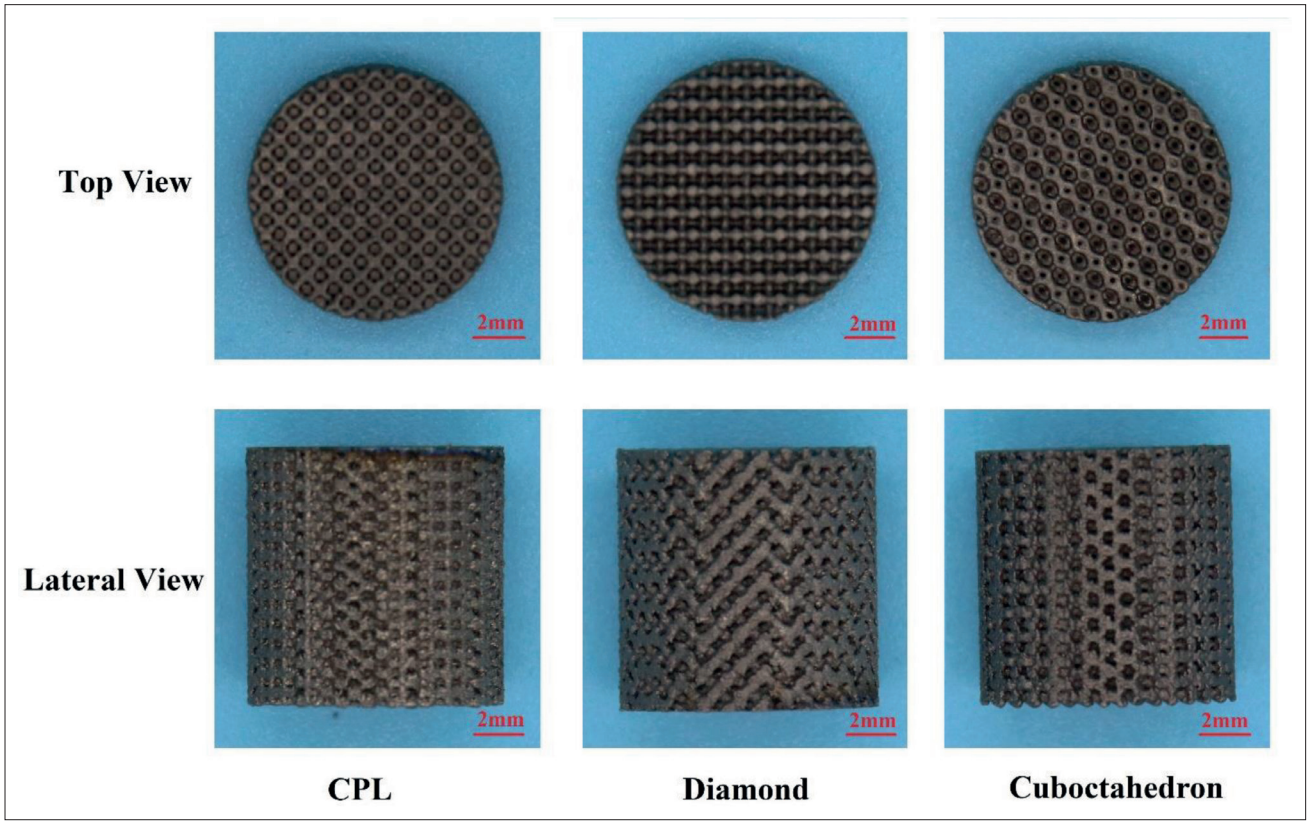

Figure 2. Ti6Al4V porous scaffolds (Φ10 mm × 10 mm) with three different unit cell structures fabricated by SLM technique.

Table 2. Parameters of the model

Experimental type	Type of lattice	Partition grid type	Number of grids (10^4)
Compression test	CPL	C3D4	619
	Diamond	C3D4	835
	Cuboctahedron	C3D4	839
CFD	CPL	C3D4	666
	Diamond	C3D4	873
	Cuboctahedron	C3D4	1096

and measured the real pore size and rod diameter using scanning electron microscopy (SEM). Simultaneously, the scaffolds were scanned with micro-computed tomography (micro-CT; voltage 155 kV, current 120 μA, resolution 17 μm, projection number 1440, integration time 500 ms). Then, the VG Studio MAX3.5 software (Volume Graphics, Germany) was employed to redevelop the 3D structure of the scaffold, and the internal structure of the scaffold was analyzed. The real porosity of the porous Ti6Al4V scaffolds was determined using the dry weight method. In other words, under typical air pressure, the porous scaffolds of each group were in dry state. The actual porosity of the scaffolds was computed using the following formulas once the actual weight of the scaffolds was determined (Equations VII and VIII):

$$\rho_0 = \frac{m}{V_0} \quad \text{(VII)}$$

$$P = \left(1 - \frac{\rho_0}{\rho}\right) \quad \text{(VIII)}$$

where ρ_0 represents the apparent density (g/cm^3), and m denotes the actual weight (g) of the porous titanium alloy scaffold. V_0 denotes the volume of the porous titanium alloy scaffold in its natural state (cm^3), P shows the actual porosity of the porous titanium alloy scaffold, and ρ represents the theoretical density of Ti6Al4V material (4.5 g/cm^3).

2.3. Compressive mechanical testing

Static simulation analysis was employed to test the compressive mechanical properties of porous Ti6Al4V scaffolds with different unit cell structures (Φ10 mm × 10 mm). Importing 3D models of scaffolds with various unit cell configurations into the Hypermesh program and using the surface deviation function to mesh the models is a unique procedure (Figure 3A). The mesh parameters are illustrated in Table 2. After using the cleanup function and cleanup tools to repair the mesh, the .inp format file was exported. Ti6Al4V material properties (Poisson's ratio of 0.376 and elastic modulus of 110 GPa) were assigned to the model after the saved files were imported into the Abaqus software. The bottom end of the model was held in place, while the higher end was subjected to the displacement load. The stress–strain curve was plotted based on the measured data. According to the slope of the elastic deformation zone in the stress–strain curve, we estimated the elastic modulus of the scaffold, drew a straight line using the elastic deformation stage, and then translated the line by 0.2%. The intersection point obtained was the yield strength. In order to test the actual mechanical properties of titanium alloy porous scaffolds with different lattice structures, mechanical compression tests were carried out *in vitro*. During the experiment, the porous scaffolds with different lattice structures (diameter 10 mm, height 10 mm) were placed on the universal test machine (C43.104, MTS Ltd., China) to make the long axis of the scaffolds consistent with the direction of the application force (Figure 3B). The load device drops at a constant speed of 1 mm/min. According to the software equipped with the loading system, the stress–strain curve was drawn (Figure 3C), and the yield strength and elastic modulus of the scaffolds were calculated (Table 4).

2.4. Computational fluid dynamics analysis

Utilizing computational fluid dynamics (CFD), the hydrodynamic properties of porous scaffolds with different unit cell types were analyzed. The scaffold model (Φ10 mm × 3 mm) was a hard, inflexible body (see Table 2 for specific parameters). The fluid used was an incompressible and homogeneous tissue fluid with a temperature of 37°, a viscosity coefficient (η) of 3.20×10^{-3} Pa·s, and a density (ρ) of 1060 kg/m^3. In order to avoid the influence of the fluid domain boundary on the experimental structure, the fluid domain size was Φ10 mm × 5 mm, and the porous model was positioned at the center of the fluid domain model. We defined the fluid inlet surface, the outlet surface, and the inner wall of the scaffold (Figure 3D). The fluid domain and rigid surface satisfied the no-slip condition, and the normal and tangential vectors at the fluid–solid interface were both zero. The fluid entered the fluid channel at a flow rate of 0.1 mm/s from the intake surface. The outlet surface of the fluid channel is the fluid outlet, which is defined as the free boundary condition, i.e., the pressure is 0 MPa. We investigated the specific surface area of the scaffold (Equation IX) in addition to the fluid flow velocity through the porous scaffold and the shear stress created on the scaffold's inner wall. In addition, the permeability of the scaffold was determined using the Darcy formula (Equation X).[43]

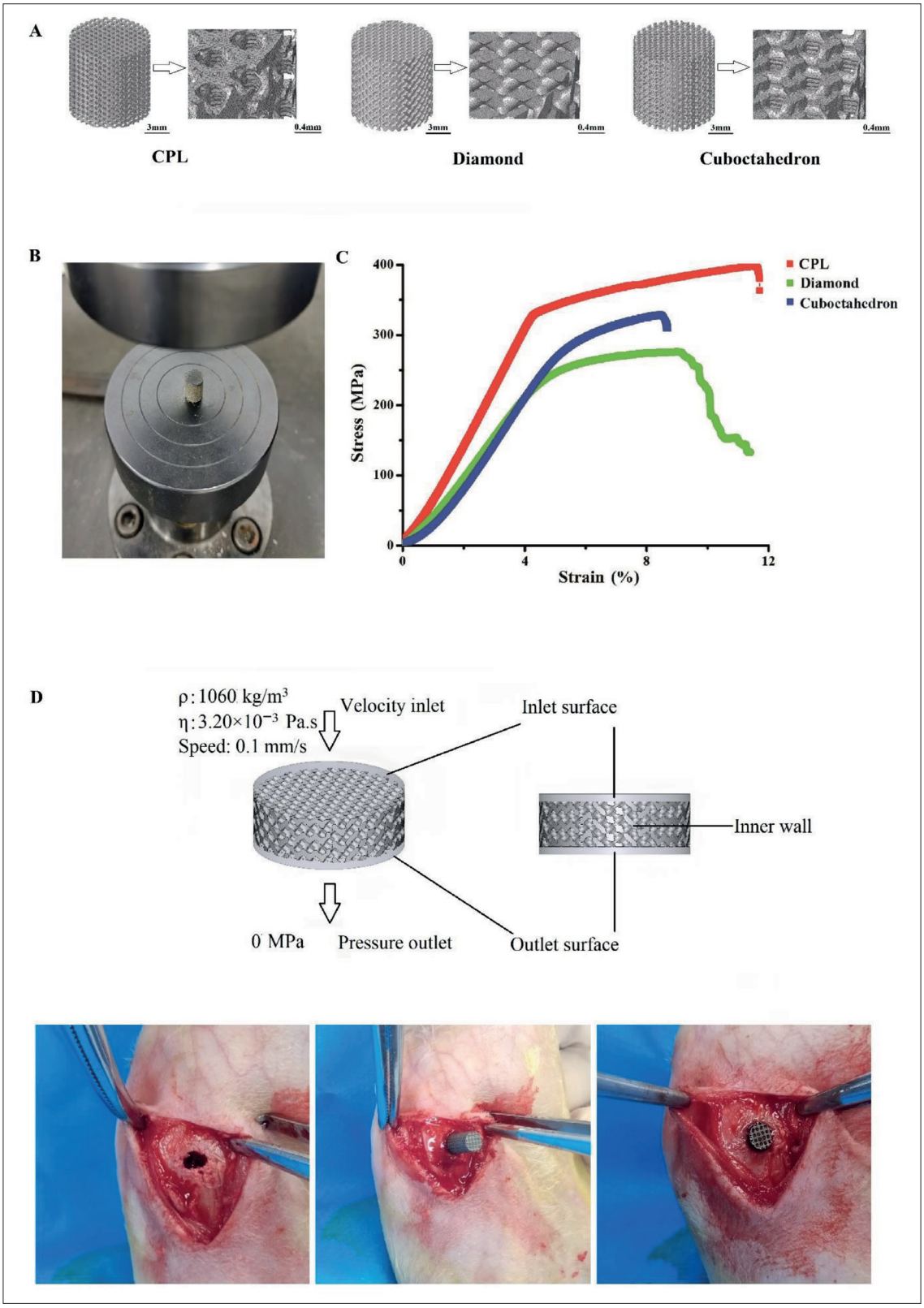

Figure 3. Experimental techniques. (A) Gridded 3D model of mechanical compression test; (B) *in vitro* compression test of porous titanium alloy scaffolds; (C) stress–strain curves of porous titanium alloy scaffolds under compression At panel (D), insert a space between the number and the unit.*in vitro*; (D) schematic diagram of the CFD; (E) surgical procedure of scaffold implantation in rabbits.

$$\delta = \frac{S}{V_s} \quad \text{(IX)}$$

$$K = \frac{uL}{A}\frac{Q}{\Delta p} \quad \text{(VI)}$$

where δ represents the specific surface area; S denotes the internal surface area and refers to the interface between solid and pore in the porous structure; V_S shows the volume of the porous structure; L represents the thickness of the scaffold; u denotes the dynamic viscosity of the fluid; A represents the cross-sectional area of the scaffold; Δp shows the pressure gradient when the fluid passes through the scaffold at the flow rate Q; and K is the permeability.

2.5. *In vitro* cell experiments

2.5.1. Scaffold processing

Ti6Al4V porous scaffolds (Φ10 mm × 3 mm) with various unit cells were pickled (2% HF, ultrasonic pickling for 5 min) to eliminate powder residue, followed by sonication (KQ5200DE, Kunshan Ultrasonic Instrument Co., LTD., China) with deionized water, acetone, 95% ethanol, and deionized water for 30 min in each liquid or solution. The scaffolds were then wrapped with sterile gauze and then subjected to sterilization at high temperature (121°C, 90 min). Finally, the sterilized scaffolds were dried in air and subsequently placed in sterile tubes for further cell experiments.

2.5.2. Cell adhesion

In the logarithmic phase of growth, mouse pre-osteoblasts MC3T3-E1 cells (5×10^4/ml) were seeded into 24-well plates containing Ti6Al4V scaffolds at 1 ml per well, and scaffolds of each unit cell were set up in triplicate. The cells were grown for 3 h under preset conditions (37°, 95% relative humidity, 5% CO_2). The number of adherent cells was quantitatively and qualitatively determined using CCK8 kit (Beyotime, Shanghai, China) and acridine orange staining (Source Leaf Biology, Shanghai, China), respectively. Similarly, Ti6Al4V scaffolds seeded with MC3T3-E1 cells (5×10^4/ml) were cultured in 24-well plates, and the culture medium (α-MEM medium, 10% fetal bovine serum, 1% streptomycin) was changed every 2 days. After 3 days of culture, phalloidin/DAPI staining (Yeasen, Shanghai, China) and scanning electron microscopy (SEM) were employed to further observe the cell adhesion status.

Table 3. Sequences of upper and lower primers for RT-PCR

Gene	Forward primers	Reverse primers
ALP	5'-GGCACCTGCCT-TACCAACTCT-3'	5'-GTTGTGGTGTAGCTGG-CCCTTA-3'
OCN	5'-ACAG-GCTTCCTAGAACAAG-GGC-3'	5'-AAGAACTCAAACATAC-GGGCAA-3'
Runx2	5'-ATGACACTGC-CACCTCTGACTTCT-3'	5'AGGGATGAAATGCTTGG-GAACT-3'
GAP-DH	5'-CCTCGTCCCGTAG-ACAAAATG-3'	5'-TGAGGTCAATGAAGGG-GTCGT-3'

2.5.3. Cell proliferation

Similar to the cell adhesion experiment, mouse MC3T3-E1 cells at a concentration of 2×10^4/ml were seeded onto 24-well plates containing Ti6Al4V scaffolds. After 5 days of incubation, a CCK8 assay was performed to measure cell growth.

2.5.4. Cell differentiation

Ti6Al4V scaffolds seeded with mouse MC3T3-E1 cells (5×10^4/ml) were grown in 24-well plates containing α-MEM medium supplemented with 10% fetal bovine serum and 1% penicillium–streptomycin. The following day, the medium was changed to an induction medium (α-MEM medium, 10% fetal bovine serum, 1% streptomycin, 10 nmol/l dexamethasone, 10 mmol/l β-glycerophosphoid sodium, 50 μg/ml vitamin C), and the medium was replaced after every 3 days. Each experiment required three copies of the porous Ti6Al4V scaffold for each type of unit cell. Alkaline phosphatase (ALP) activity was determined after 7 and 14 days of culture using an ALP kit, and the expression of osteogenesis-related genes (*ALP*, *OCN*, *Runx2*) was determined using reverse-transcription polymerase chain reaction (RT-PCR). Primer sequences are listed in Table 3. After 30 days of culture, 10% cetylpyridinium chloride was employed to dissolve the calcium salt deposited, and the optical density (OD) value was measured using a microplate reader at the wavelength of 590 nm.

2.6. *In vivo* animal experiments

2.6.1. Surgical procedure

Twenty healthy adult male New Zealand rabbits (2 kg) were divided into four groups at random. Via the auricular vein, pentobarbital sodium (30 mg/kg) was injected to induce anesthesia. After preparing the skin, the surgical region was cleansed three times with iodophor, and then the skin and fascia were sliced to expose the lateral epicondyle of the femur. With a 3.0 Kirschner wire and a manual grinding drill, a circular hole with a diameter of 4 mm and a depth of 10 mm was created perpendicular to the lateral epicondyle of the femur. After washing and sterilizing, Ti6Al4V scaffolds of four different unit cell types (Φ4 mm × 10 mm) were implanted into the femurs of four groups of rabbits, one scaffold per femur (Figure 3E). After the wound was treated with iodophor and saline, 2-0 silk thread was used to close the wound layer by layer. After surgery, all animals received injectable penicillin (10,000 U) for 3 days to prevent infection.

2.6.2. X-ray examination

At 3 months post-operatively, the bilateral femurs were inspected by anteroposterior and lateral X-rays to monitor the healing of the scaffold and the surrounding bone and to determine whether there was scaffold loosening and displacement.

2.6.3. Micro-CT analysis

Three months following surgery, the animals were euthanized with severe anesthesia, and femoral specimens containing Ti6Al4V scaffolds were obtained from the femurs. Micro-CT scan was performed (voltage 155 kV, current 120 μA, resolution 17 μm, projection number 1440, integration time 500 ms). The scanned data were imported into the VG Studio MAX3.5 computer-aided design software (Volume Graphics, Germany) for 3D reconstruction and data analysis. The region of interest (ROI) consists of two parts: the inner component refers to the scaffold, while the outer part refers to the 500 μm annular area surrounding the scaffold. The ratio of bone volume to space volume (BV/TV) indicates the quantity of bone development.

2.6.4. Histological evaluation

The femurs of the sacrificed animals were preserved with 4% paraformaldehyde (Sigma, USA). Gradient alcohol was used for dehydration, while methyl methacrylate was used for embedding. The embedded specimens were sectioned using a LeicaSP1600 slicer, and the sections were then affixed to the resin slide. The sections were processed with sandpaper of sizes 300, 800, and 1200 in succession until the desired thickness was achieved, and there were no visible scratches on the surface of the section under a microscope. Goldner dyed the produced sections of hard tissue, which he then viewed and photographed under a light microscope.

2.7. Statistical analysis

The data are expressed as mean ± standard deviation (S.D.). One-way analysis of variance (ANOVA) was utilized to evaluate the differences between groups. $P < 0.05$ was considered statistically significant.

3. Results

3.1. Characteristics of porous Ti6Al4V scaffolds with different lattices

The SEM images of the porous Ti6Al4V scaffolds with various types of unit cells are shown in Figure 4A. All scaffolds exhibited acceptable processing accuracy, consistent pore size distribution, and size uniformity, and no evident titanium powder deposition or pore obstruction was detected. A micro-CT scan of the scaffolds (Figure 4B) revealed that the internal connectivity of the scaffold was satisfactory and the connecting rod diameter was homogeneous. Also, no unfavorable events, such as a fracture or powder deposition, were observed. We investigated the real porosity, pore size, and connecting rod diameter of the 3D-printed titanium alloy scaffold (Figure 4C). The actual porosity (CPL 64.8%, diamond 65.1%, cuboctahedron 64.9%) and pore size (CPL 589 μm, diamond 592 μm, cuboctahedron 591 μm) of the processed scaffold were smaller than those of the intended models. However, the difference was not statistically significant. The actual diameter of the connecting rods (CPL 371 μm, diamond 205 μm, cuboctahedron 252 μm) is slightly larger than that of the models. The real structure of Ti6Al4V scaffolds with varied unit cells fabricated using the SLM technique corresponded well to the 3D models.

3.2. Compressive mechanical properties

According to the von Mises stress distribution of Ti6Al4V porous scaffolds with different unit cells (Figure 5A), the stress at the center of the scaffolds was slightly greater than that in the periphery, but the overall distribution was relatively uniform, and there was no obvious point of stress concentration. According to the stress–strain curve (Figure 5B) based on static simulation analysis, the load of the three types of scaffolds increased linearly with increasing deformation in the initial stage, which corresponded to the elastic deformation zone. The calculated and tested elastic modulus and yield strength are shown in Table 4. According to the results, though the calculated mechanical properties of the porous titanium alloy scaffolds were different from those tested by compression, they can still meet the mechanical requirements of human bones. In addition, the Ti6Al4V scaffold with a diamond lattice has the lowest elastic modulus of the three scaffolds and can better prevent the stress shielding effect.

3.3. Specific surface area and permeability

The movement of tissue fluid via the scaffold was visualized using CFD simulations (Figure 6A). The tissue fluid mass flow rate through the outflow surface of the scaffold is depicted in Figure 6E. The volume of tissue fluid moving through the cross-section per unit time of the diamond scaffold was much greater than that of the CPL and cuboctahedron unit cells. In addition, the specific surface area and permeability of the various unit cell architectures were computed (Table 5). At the same porosity and pore size, the specific surface area of CPL (17.2 mm^{-1}) is bigger than that of cuboctahedron (13.9 mm^{-1}), while diamond (10 mm^{-1}) has the smallest specific surface area. However, the average flow rate (diamond 0.88 mm/s, cuboctahedron 0.87 mm/s, CPL 0.75 mm/s) and permeability (diamond 0.72×10^{-10} m^2, cuboctahedron 0.24×10^{-10} m^2, CPL 0.18 $\times 10^{-10}$ m^2) revealed the opposite trend, that the diamond scaffold exhibited the best diffusion effect of cells and tissue fluid, followed by the cuboctahedron scaffold.

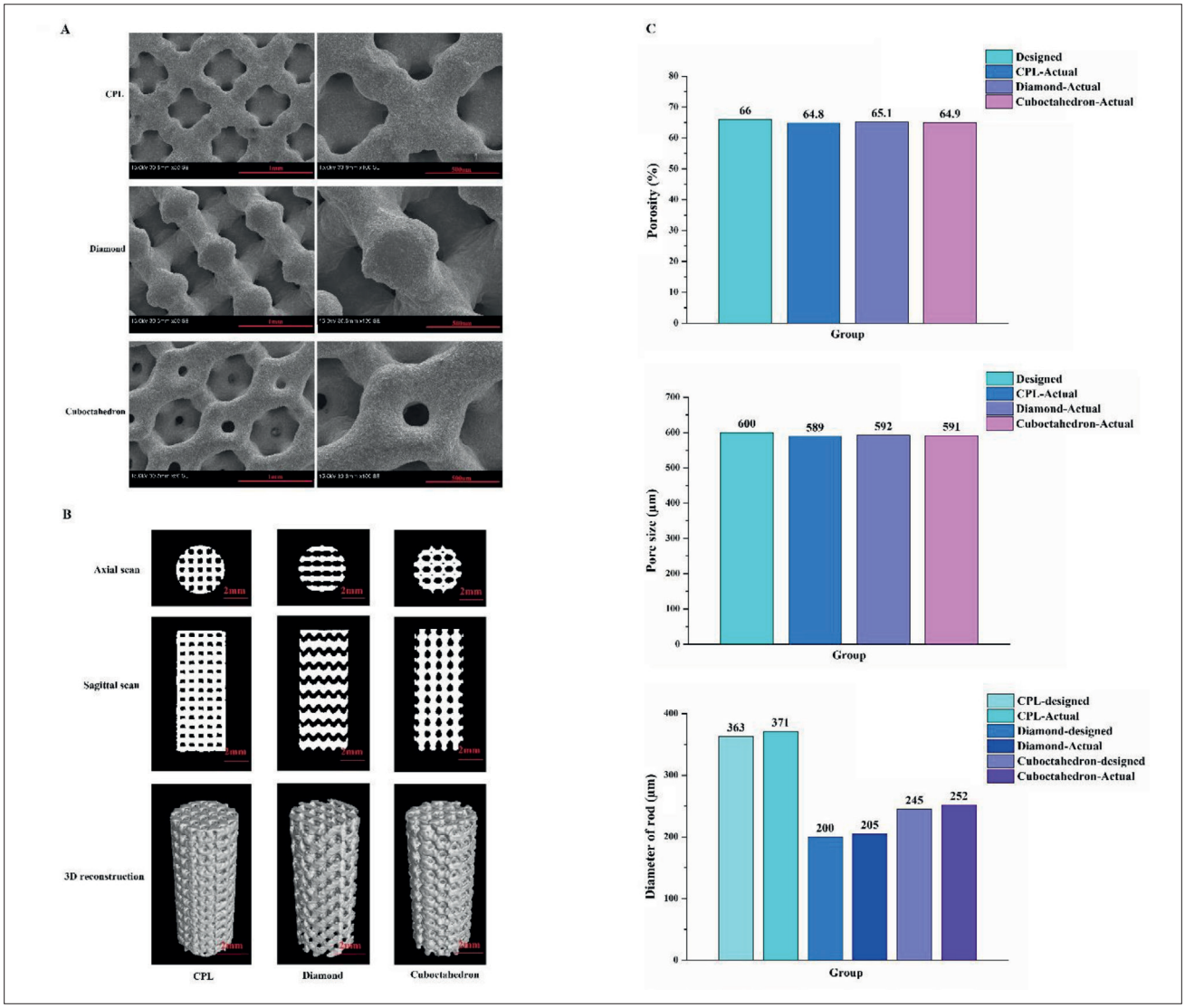

Figure 4. Characteristics of porous Ti6Al4V scaffolds. (A) The surface structures of the scaffolds were observed using SEM; (B) micro-CT scanning of the scaffolds; (C) the actual porosity, pore diameter, and rod diameter of the scaffolds were compared with the designed values.

3.3. Shear stress distribution

Figure 6B depicts the shear stress cloud diagram produced by the tissue fluid moving through the scaffold's inner wall. Inside the scaffold, the shear stress was evenly distributed, and there were no highly concentrated areas of stress. A comparative examination of the overall scaffold's average shear stress (Figure 6D) showed that the shear stress of the three scaffolds are significantly different ($P < 0.05$): cuboctahedron scaffold (108.2 ± 1.1 MPa) > CPL scaffold (97.5 ± 1.3 MPa) > diamond scaffold (87.6 ± 1.3 MPa). A further analysis of the distribution range of shear stress on the scaffold (Figure 6C) revealed that

Table 4. Mechanical properties of titanium alloy scaffolds with different lattice structures

Lattice	Elastic modulus—Calculated (GPa)	Yield strength—Calculated (MPa)	Elastic modulus—Test (GPa)	Yield strength—Test (MPa)
CPL	18.049	143.35	7.070 ± 1.477	398.33 ± 2.89
Diamond	11.635	138.52	5.360 ± 1.057	286.67 ± 16.07*
Cuboctahedron	17.689	135.18	7.043 ± 1.076	323.33 ± 2.89*

* $P < 0.05$, compared with CPL porous titanium alloy scaffold.

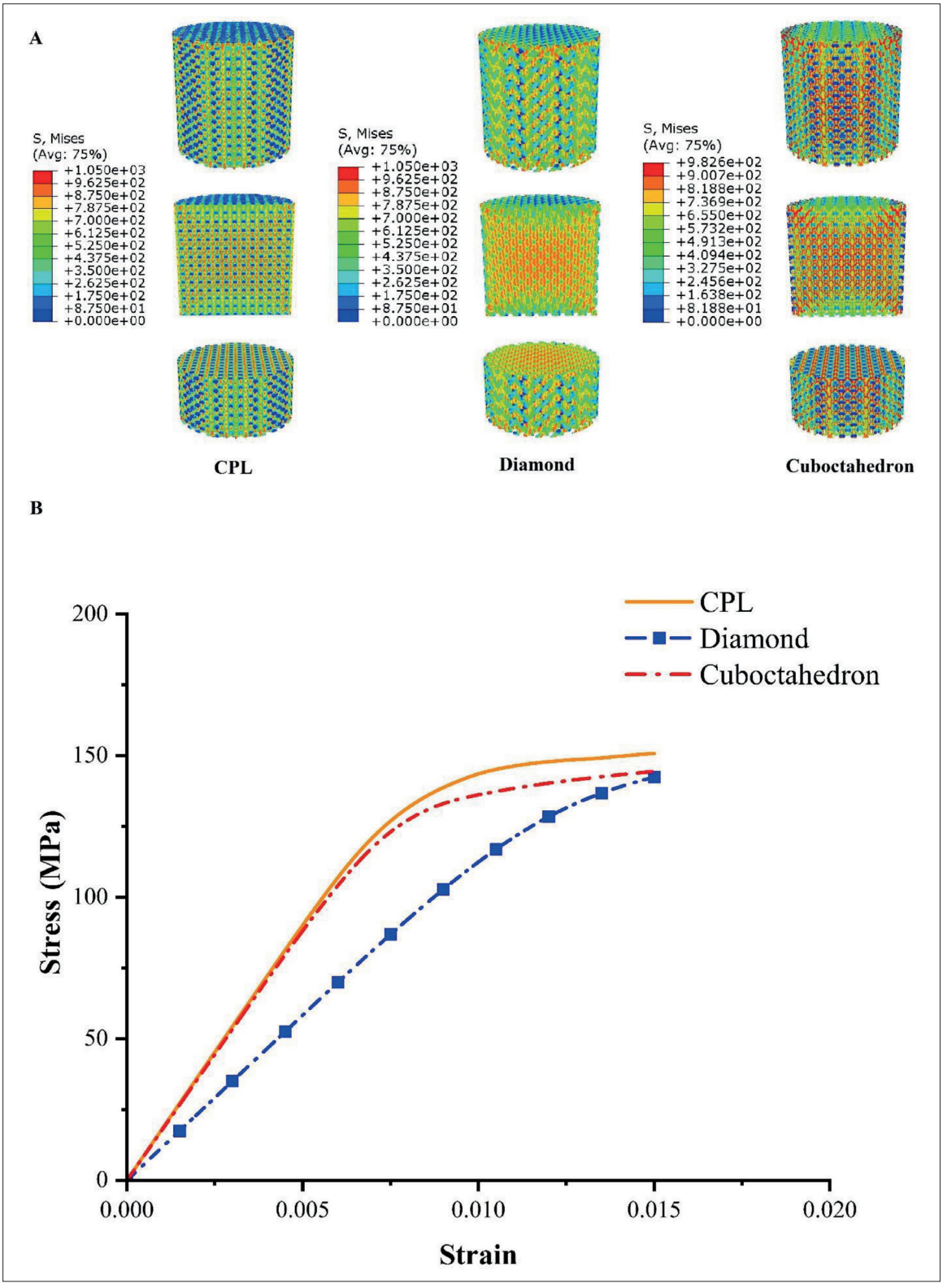

Figure 5. Mechanical compression test results. (A) Von Mises stress distribution of porous scaffolds with different unit cell types, and (B) stress–strain curves of three kinds of porous scaffolds by finite element analysis.

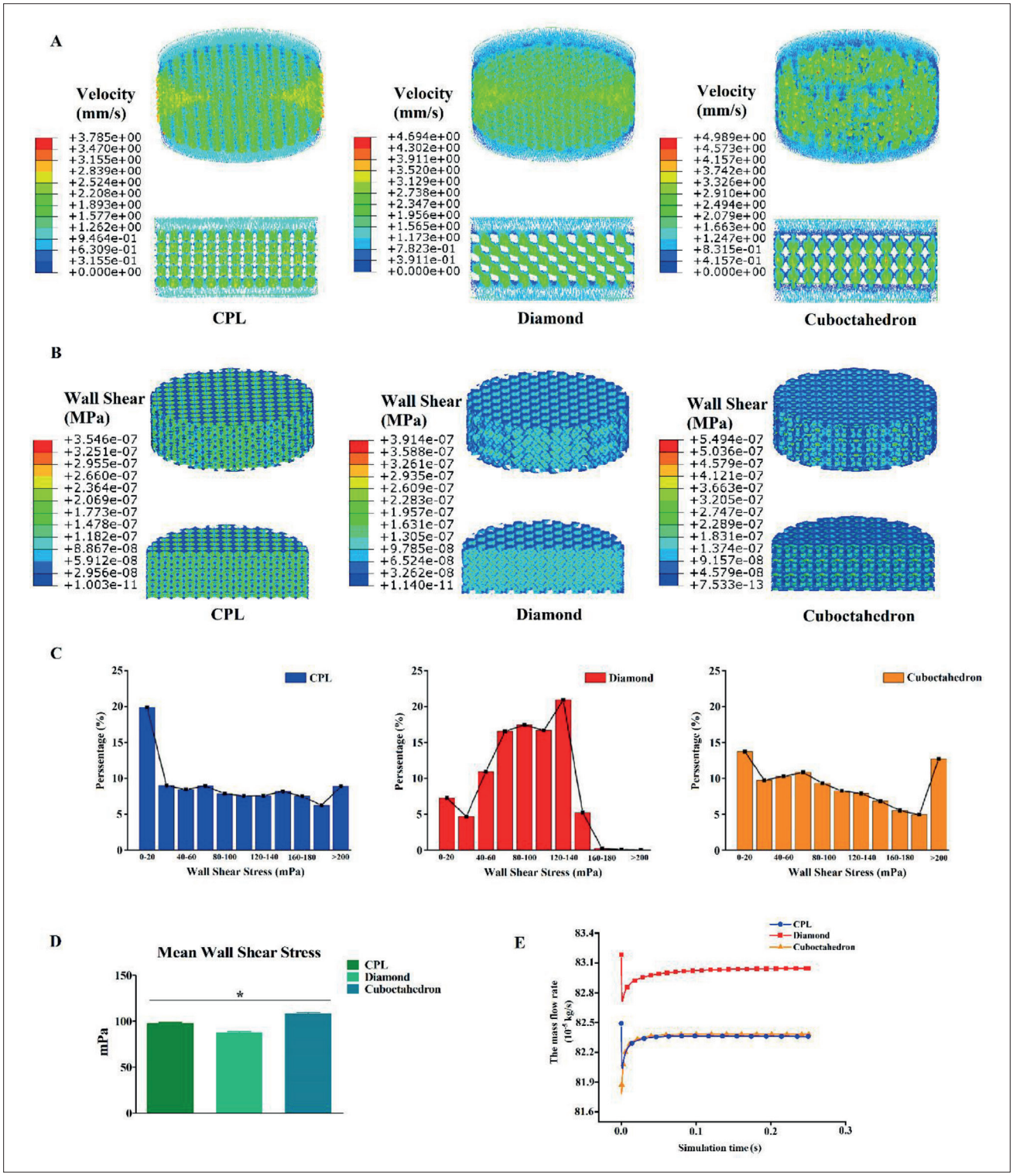

Figure 6. CFD simulation results. (A) A visual representation of tissue fluid traveling through the scaffold in the simulation, where the direction of the streamlines shows the flow direction of tissue fluid and the color denotes the flow rate. A color closer to red indicates a greater flow rate. (B) The shear stress nephrogram of the scaffolds. The closer the color is to the red, the greater the shear stress is. (C) Diagram illustrating the shear stress distribution of the scaffolds. According to its shear stress, each grid element of the scaffold was separated into a certain stress range and then categorized. The percentage of this shear stress range was calculated by dividing the number of grid elements in each stress range by the total number of grid elements. (D) Comparison of average shear stress of the scaffolds. *$P < 0.05$. (E) The flow of tissue fluid through the outlet surface.

Table 5. Calculated specific surface area and permeability values

Lattice	S (mm^2)	V_S (mm^3)	(mm^{-1})	V_{max} (mm/s)	V_{mean} (mm/s)	(Pa)	K (10^{-10}m^2)
CPL	287.8366	75.0299	17.16	3.789	0.7499	5.2229	0.1755
Diamond	867.1071	86.6514	10.01	4.694	0.8782	2.5574	0.7197
Cuboctahedron	1125.7823	81.1718	13.87	4.989	0.8730	4.4625	0.2391

Note: δ represents the specific surface area; S represents the internal surface area and refers to the interface between solid and pore in the porous structure; V_S depicts the volume of the porous structure; V_{max} represents the maximum flow velocity; V_{mean} is the average flow velocity; Δp is the pressure gradient when the fluid passes through the scaffold; and K is the permeability.

although the distribution range of shear stress of CPL and cuboctahedron scaffolds was relatively broad (0 to >200 MPa), the recorded shear stress of the scaffolds mostly falls within the range of 0–20 MPa, whereas the shear stress distribution range of the diamond scaffold was more concentrated (0–180 MPa), with the majority of the recorded values falling within the range of 120–140 MPa. It is evident that the variation of unit cells has a significant impact on the value and distribution of shear stress in scaffolds. Through their shear stress distribution analysis of porous scaffolds using CFD, Omar *et al.*[38] and Li *et al.*[52] found that the value is in the tens of millipascals (MPa), consistent with our experimental results, indicating that the simulation analysis has a good authenticity.

3.4. Cell adhesion and proliferation

After 3 h of co-culture with mouse MC3T3-E1 cells, acridine orange staining revealed a substantial level of cell attachment in Ti6Al4V scaffolds with various unit cells (Figure 7A). CCK8 assay results revealed that the number

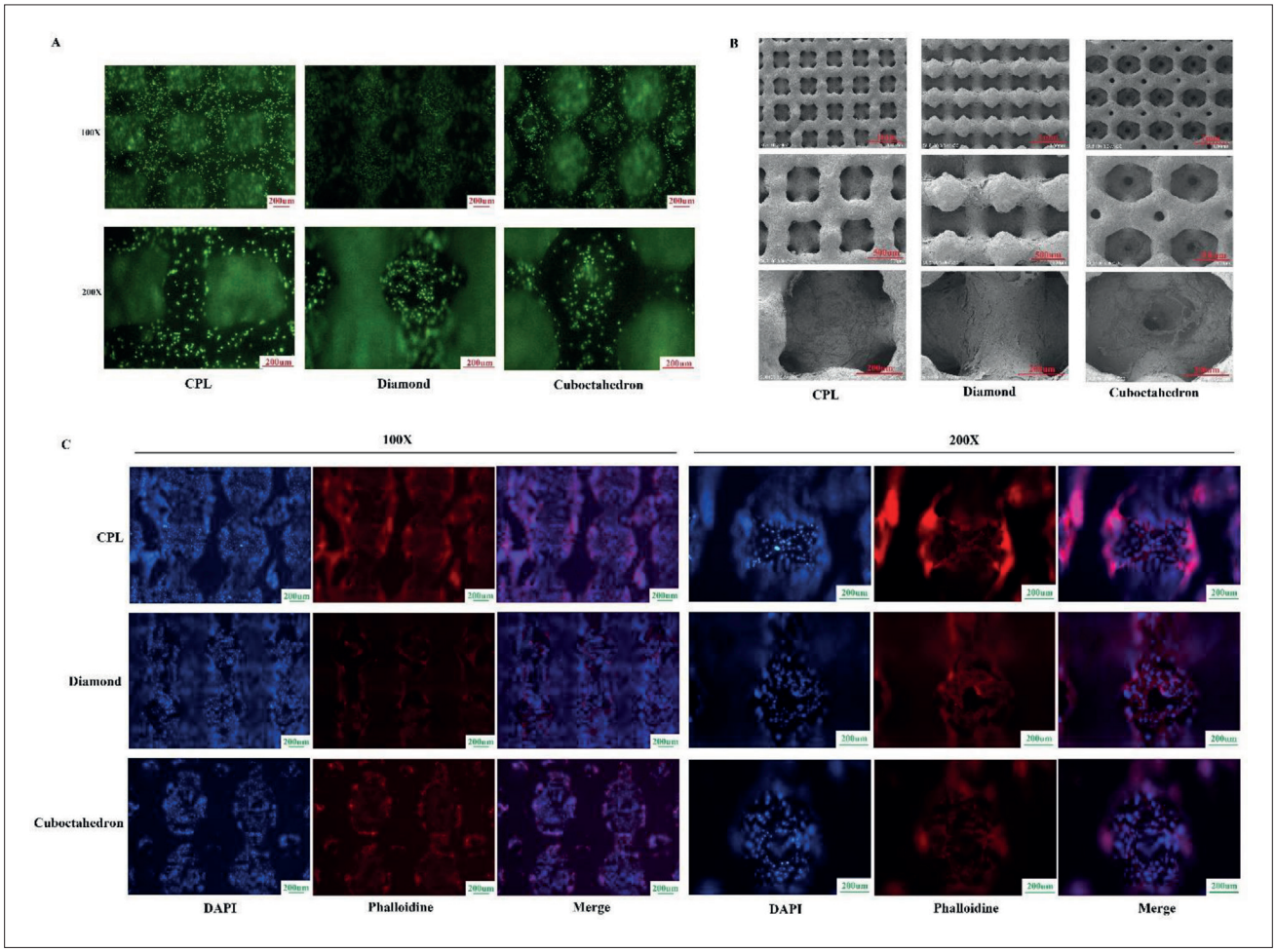

Figure 7. Cell adhesion assay. (A) Acridine orange staining was performed qualitative determination of the number of cell adhesions. (B) SEM. (C) DAPI/phalloidin staining was performed to determine the level of adherence of MC3T3-E1 cells.

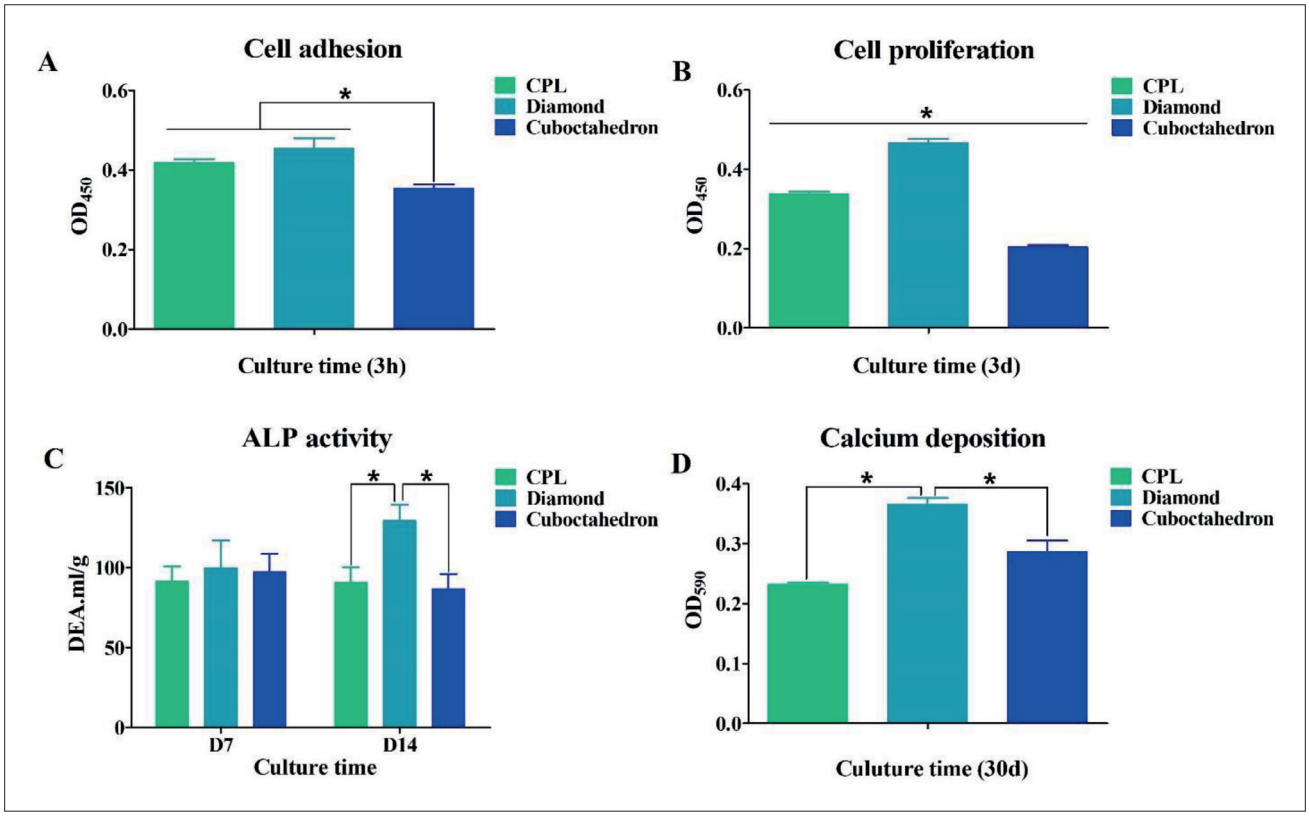

Figure 8. Results of cell experiments. (A) Quantitative analysis of cell adhesion density; (B) quantitative analysis of cell proliferation; (C) quantitative analysis of ALP activity; (d) quantitative analysis of calcium deposition. *$P < 0.05$.

of adhered cells in diamond and CPL scaffolds was greater than that in cuboctahedron scaffold ($P < 0.05$, Figure 8A). Mice MC3T3-E1 cells adhered well to the three Ti6Al4V scaffolds after 3 days of culture, as determined by SEM. A significant number of pseudopodia expanded while the cells linked into sheets. Phalloidin/DAPI staining revealed that the oval nucleus (blue fluorescence) and reticular actin skeleton (red fluorescence) of MC3T3-E1 cells on the three Ti6Al4V scaffolds were clearly visible, demonstrating excellent cell adhesion capabilities. Cell proliferation assay demonstrated that there was a significant difference in the number of MC3T3-E1 cells among the three scaffolds after 3 days of culture ($P < 0.05$). The highest number of MC3T3-E1 cells was seen on the diamond scaffold, followed by the CPL scaffold (Figure 8B).

3.5. Cell differentiation

ALP activity and calcium deposit levels are significant indications of osteogenic differentiation (Figure 8C and D). At 7 days after induction, the ALP activity of diamond scaffolds was slightly higher than that of CPL and cuboctahedron scaffolds, but there was no statistically significant difference between the three scaffolds ($P > 0.05$). Nevertheless, with the extension of the differentiation period (14 days), the ALP activity of diamond scaffolds dramatically increased, which was significantly higher than that of CPL and cuboctahedron scaffolds ($P < 0.05$). At 7 and 14 days, there was no significant change in ALP activity between CPL and cuboctahedron scaffolds ($P > 0.05$). In addition, calcium deposit increased considerably in the diamond scaffold, as compared with the other two scaffolds ($P < 0.05$). Although the amount of calcium salt deposited on the cuboctahedron scaffold was more than that on the CPL scaffold, there was no discernible difference between the two ($P > 0.05$). The expression of osteogenesis-related genes was analyzed to further assess the benefits and drawbacks of various unit cell scaffolds in promoting the osteogenic differentiation of MC3T3-E1 cells (Figure 9). There were substantial changes in *ALP* and *OCN* gene expression of MC3T3-E1 cells on the three scaffolds after 7 days of culture ($P < 0.05$), according to the results. The cuboctahedron scaffold demonstrated the highest *ALP* expression, while the diamond scaffold demonstrated the highest *OCN* expression. Although there was no significant difference in *Runx2* gene expression between cuboctahedron and diamond scaffolds ($P > 0.05$), their expression levels still dwarfed the expression level in CPL scaffold ($P < 0.05$). The expression of *ALP* and *Runx2* genes

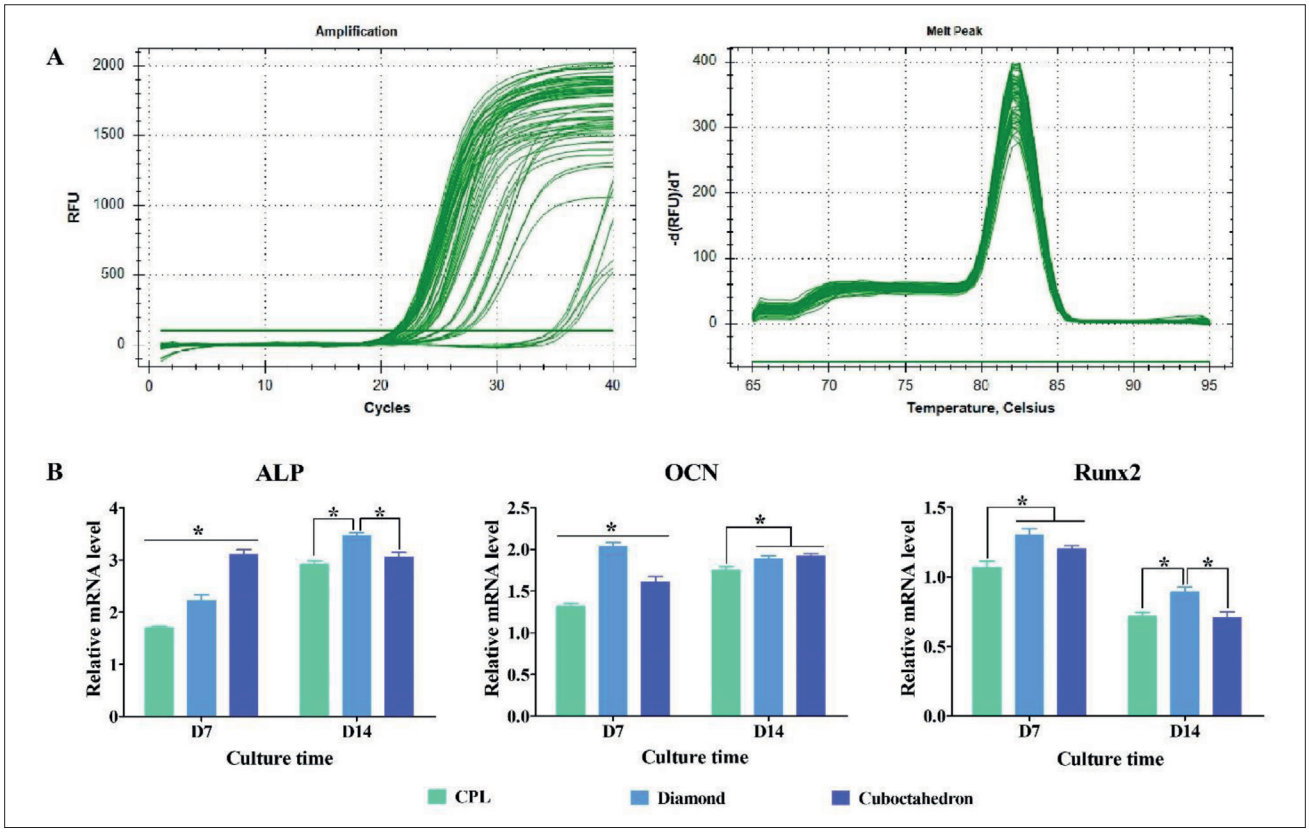

Figure 9. Results of RT-PCR. (A) *Runx2* gene amplification and melting curve during RT-PCR; (B) quantitative analysis of osteogenesis-related gene expression. *$P < 0.05$.

in diamond scaffold was considerably higher than that in CPL and cuboctahedron scaffolds ($P < 0.05$). Although *OCN* gene expression in diamond scaffold was substantially higher than that in CPL scaffold ($P < 0.05$), there was no statistical difference in *OCN* expression level between diamond and cuboctahedron scaffolds ($P > 0.05$). These findings showed that the diamond scaffold promotes osteogenic differentiation of MC3T3-E1 cells more effectively.

3.7. X-ray and micro-CT

Three months after surgery, all scaffolds had successfully fused with the surrounding bone, and no loosening or displacement was noted (Figure 10A). According to the 3D reconstruction of micro-CT of the femoral specimens (Figure 10B), new bone growth was found at the perimeter and inside the three scaffolds, with the periphery showing a greater amount of new bone formation compared with the interior. New bone formation outside and within the scaffold was separately quantified (Figure 10C). The results demonstrated that the BV/TV of new bone within the 500 μm ring area surrounding the three scaffolds did not differ significantly ($P > 0.05$), even though the BV/TV ratio of new bone within the scaffold was significantly different ($P < 0.05$). We found that the diamond scaffold achieved the highest level of new bone formation (23.7%), followed by the cuboctahedron scaffold (22.1%). Taken together, the diamond unit cell was more conducive to bone ingrowth into scaffolds.

3.8. Goldner staining

After 3 months, we stained the hard tissue sections with Goldner dye and found a significant portion of newly formed bone in and around the three scaffolds (Figure 10D). The area of newly formed bone in the diamond scaffold was much larger than those in the CPL and cuboctahedron scaffolds, confirming that the diamond unit cells were more favorable to bone growth while having the same porosity and pore size.

4. Discussion

In recent years, 3D-printed porous titanium alloy scaffolds have been utilized extensively for the repair and regeneration of bone deformities, leveraging the advantages of additive manufacturing technology.[44-46] However, the biomechanical and osseointegration capabilities of porous titanium alloy scaffolds vary greatly because of differences in porosity, pore size, and pore shape.[47,48] Numerous studies have

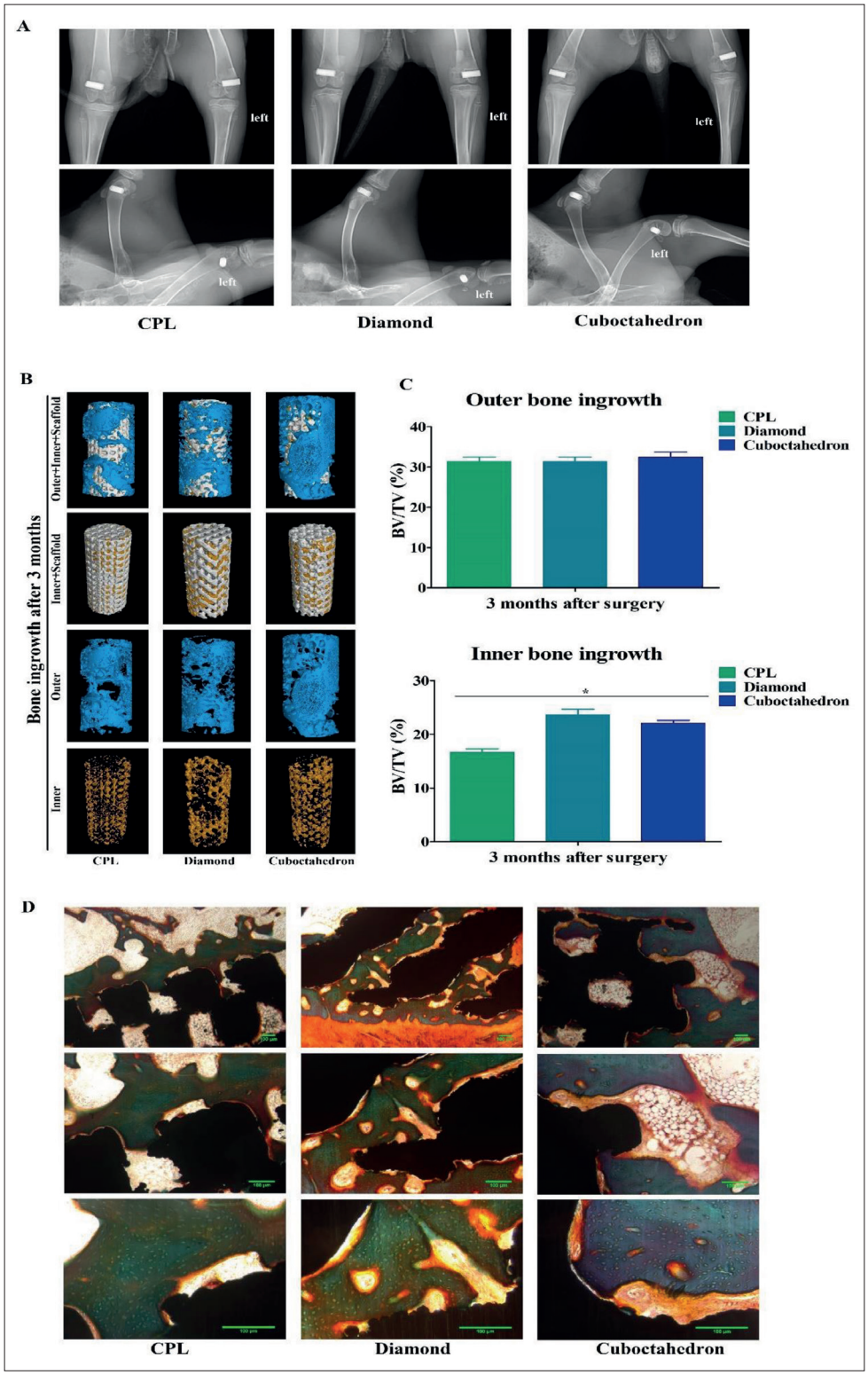

Figure 10. Results from animals experiments. (A) Animals were subjected to an X-ray evaluation of the surgical site three months after surgery. (B) Micro-CT 3D reconstruction was performed on femoral samples. Yellow indicates the new bone within the scaffold; blue represents the new bone in a 500 μm ring surrounding the scaffold; and white represents the titanium alloy scaffold. (C) Quantitative analysis (BV/TV) of new bone formation within and outside the three scaffolds. *$P < 0.05$ compared with each other. (D) Goldner staining of hard tissue sections. The newly formed mineralized bone is depicted in turquoise, the osteoid in orange, and the titanium alloy scaffold in black.

demonstrated that titanium porous alloy scaffolds with a porosity of 60–70% and a pore diameter of 500–700 μm have good mechanical and biological capabilities, although the aforementioned research has given insufficient attention to pore shape. In light of this, computer-aided software was utilized in this experiment to create porous scaffold models with 66% porosity, 600 μm pore size, and three lattice geometries of CPL, diamond, and cuboctahedron, which were then processed using SLM technology into Ti6Al4V scaffolds. The results of SEM and micro-CT scans revealed that 3D-printed Ti6Al4V scaffolds had uniform pore distribution, good internal connectivity, and no evident powder deposition or pore blockage. The actual porosity, pore diameter, and rod diameter of the three scaffolds closely matched their designed values. It can be demonstrated that the SLM technique has good processing precision and can produce the correct Ti6Al4V scaffolds with varying pore types, which is consistent with previous results in the literature.[49,50]

Biomechanical adaptation is a prerequisite for the use of porous titanium alloy scaffolds in bone defect healing. Not only must the yield strength match the load-bearing criteria, but the elastic modulus must also be comparable to that of human bone (3–30 GPa for cortical bone and 0.02–3 GPa for cancellous bone),[51] so as to avoid the stress shielding effect. The static simulation analysis revealed that the yield strength of Ti6Al4V porous scaffolds with CPL, diamond, and cuboctahedron lattice elements is approximately 140 MPa, which is quite different from the compression test result. The discrepancy can be justified by a fabrication error in SLM, which leads to a difference between the diameter of the connecting rod of the porous structure and the theoretical designed value. In addition, simulation analysis is a theoretical calculation of the mechanical properties of the scaffolds using the finite element analysis method, and the reliability of the results is related to the type, number of grid units, and material attribute assignment. Therefore, the simulation analysis results can only be used as a supplement to the research on the mechanical properties of the porous scaffolds, and the *in vitro* mechanical test data should still be used as the standard. According to the literature, the yield strength of human cortical bone is 109.6 ± 4.7 MPa, and the yield strength of cancellous bone is 55.3±8.6 MPa, demonstrating that Ti6Al4V scaffolds with three pore shapes can acquire the strength requirements of the human body when the porosity is 66% and the pore diameter is 600 μm. In addition, we evaluated the elastic modulus of the three types of porous scaffolds, and the results demonstrated that their calculated elastic modulus decreased to 83.6–89.5% when compared to the elastic modulus (110 GPa) of the dense solid titanium alloy material, which better met the modulus requirements of human cortical bone. However, the diamond scaffold has the lowest elastic modulus (calculated: 11.6 GPa, test: 5.360 ± 1.057 GPa), which resembles to that of human cancellous bone, thus lending itself to better prevention of osteolysis caused by stress shielding of cancellous bone. Overall, the diamond scaffold offers superior mechanical properties to those of the CPL and cuboctahedron scaffolds.

On the premise of meeting the mechanical qualities of human bones, how to create porous titanium alloy scaffolds that integrate more effectively with the surrounding bone has always been a topic of intense research. Li *et al.*[52] conducted a hydrodynamic investigation on porous scaffolds with various pore sizes and discovered that the permeability of scaffolds increased with the porosity, and the porous scaffolds with a pore size of 800 μm experienced the highest shear stress. Li *et al.*[53] simulated the fluid characteristics of two shapes of unit cells (octet truss and rhombic dodecahedron) with different strut sizes and discovered that the unit cell shape and strut size significantly determined and influenced other physical parameters and flow properties of porous scaffolds. Li *et al.*[54] used CFD to analyze the fluid characteristics of five different unit cell types of porous scaffolds and discovered that different unit cells could directly lead to diverse fluid properties of porous implants. Porosity, pore size, and pore shape have a significant effect on the fluid dynamics of porous scaffolds, and the fluid dynamics influence the delivery of nutrients and the shear stress of the scaffold wall. Relevant research has demonstrated that nutrition transport and shear stress are crucial for cell adhesion, proliferation, and differentiation[55-57].

The present study investigated the fluid dynamics of three pore forms (CPL, diamond, and cuboctahedron) with identical porosity and pore size. The results demonstrated that the diamond scaffold had superior permeability and average flow rate compared to the cuboctahedron and CPL scaffolds. Therefore, diamond scaffold is comparatively better than others in nutrient transport, which is a crucial aspect of cell proliferation. *In vitro* investigations with mouse MC3T3-E1 cells revealed that the number of cells proliferating on diamond scaffolds was much higher than that on CPL and cuboctahedron scaffolds after 3 days of culture, confirming the results of the fluid simulation analysis. Shear stress study revealed that the average shear stress on the walls of the three types of scaffolds differed significantly ($P < 0.05$), the diamond scaffold displaying the smallest average shear stress, while the cuboctahedron scaffold the largest. Nevertheless, based on the proportion diagram of shear stress distribution, the diamond scaffold with a shear stress of 120–140 MPa accounted for the biggest part, whereas the other two scaffolds had the

largest proportion of shear stress at 0–20 MPa. Therefore, despite the fact that the average shear stress of the diamond scaffold is lower than that of the CPL and cuboctahedron scaffolds, the diamond scaffold has a more concentrated shear stress distribution and is more effective in promoting cell differentiation. ALP activity and calcium deposition on the diamond scaffold were considerably more pronounced than those on the other two groups 14 and 30 days after induction, showing that the diamond scaffold was more favorable to fostering osteoblast development. The results demonstrated that with the same porosity and pore size, the CPL scaffold had a greater specific surface area than the cuboctahedron scaffold, while the diamond scaffold had the smallest specific surface area. Theoretically, a larger specific surface area endows more space for cell adhesion. However, there are some discrepancies between our *in vitro* cell tests and theoretical prediction. After 3 h of culture, the number of adhered cells on the diamond scaffolds was only marginally higher than that on the CPL scaffolds ($P > 0.05$) but significantly higher than that on the cuboctahedron scaffold ($P < 0.05$). Despite the bigger specific surface area, the lower permeability of CPL scaffold limits the cells from entering the scaffold for adherence, explaining the insignificant difference in cell adherence between the two scaffolds.

In a study about local curvature and pore shape, Bael *et al.*[58] determined that obtuse angles were more likely to obstruct cells than acute angles. According to Urda *et al.*,[59] straight edges and convex surfaces in pore structure are detrimental to cell development. Huang *et al.*[27] discovered that the porous titanium alloy scaffold with dodecahedron unit cell exhibited superior osseointegration performance after studying the osseointegration performance of titanium alloy scaffolds with two unit cells (diamond and rhombic dodecahedron). Xu *et al.*[23] compared the osseointegration properties of two unit cells (a hollow hexagonal prism and a hollow triangular prism) through animal experiments. They found that a hollow hexagonal prism had more new bone ingrowths. Changes in pore shape have a significant effect on the osseointegration efficiency of porous titanium alloy scaffolds.

In this study, the effects of the three pore configurations on the adhesion, proliferation, and differentiation of MC3TE-E1, a mouse osteoblast precursor cell line, were compared. Staining with acridine orange revealed that a substantial percentage of MC3T3-E1 cells adhered to the three titanium alloy scaffolds. The percentage of MC3T3-E1 cells attached to scaffolds can be ranked in the following order: diamond > CPL > cuboctahedron. Using SEM and phalloidin/DAPI labeling, it was determined that MC3T3-E1 cells adhered well to all three scaffolds, with no significant differences between them. Different types of unit cell structures in porous titanium alloy scaffolds can impact the number of adhered cells but have minimal effect on the state of cell adhesion. The growth of MC3T3-E1 cells on the cuboctahedron scaffolds was the lowest after 3 days of culture. Cuboctahedrons did not demonstrate evident advantages in terms of specific surface area and permeability, which are linked to additional space and nutrients for cell proliferation. ALP activity detection is useful for assessing the functional condition of osteoblasts. At the earliest stage of differentiation, we found no statistically significant variation in ALP activity between titanium alloy scaffolds with different pore shapes ($P > 0.05$). At 14 days, the ALP activity of the diamond scaffold was substantially greater than that of CPL and cuboctahedron ($P < 0.05$). Mineralized nodules are the ultimate manifestation of the osteogenic phenotype of osteoblasts *in vitro*, as well as a sign of mineralized matrix development. The mineralized nodules could be dissolved by 10% cetyl pyridine chloride, and the absorbance value was proportional to the calcium ion content. After the dissolution of mineralized nodules, the diamond scaffold exhibited the highest OD value, which was much higher than those of CPL and cuboctahedron scaffolds ($P < 0.05$).

Consistent with the results of our fluid simulation research, it can be extrapolated that the diamond scaffold has a greater influence on inducing osteogenic differentiation of MC3T3-E1 cells. To further elucidate the aforementioned impacts, the expression levels of osteogenesis-related genes, namely *ALP*, *Runx2*, and *OCN*, were measured quantitatively. In the process of bone matrix mineralization, OCN expression is the primary indication of osteogenic differentiation, and Runx2 is one of the most significant transcription factors for osteoblast differentiation. The results demonstrated that the expression of osteogenic genes on the diamond scaffold was superior to that on the cuboctahedron scaffold, while expression was lowest on the CPL scaffold. We expected that the diamond porous titanium alloy scaffold would promote osteogenic differentiation more effectively. The lateral femoral epicondyle of rabbits was implanted with three types of Ti6Al4V scaffolds with various unit cells. Three months after feeding, an X-ray inspection revealed that all scaffolds had successfully fused with the surrounding bone, and there was no evidence of prosthesis loosening or displacement. Micro-CT 3D reconstruction also confirmed the creation of new bone inside and around the scaffold. Quantitative research revealed that the amount of new bone surrounding the three scaffolds did not differ significantly; however, the amount of new bone inside the scaffolds is ranked in this order: diamond > cuboctahedron > CPL, and the difference was statistically significant ($P < 0.05$). Titanium alloys are inert materials and do not release

any active molecules to promote the growth of surrounding bone after implantation in animals. Theoretically, the growth environments around titanium alloy scaffolds with different lattices are identical, rationalizing the same degree of new bone formation around the scaffolds. In the current study, however, porous scaffolds with different lattices have different fluid dynamics. These attributes were the source of variations in shear stress and nutrient transport inside the scaffolds, which resulted in large differences in the bone growth microenvironment inside the scaffolds, and ultimately led to varying amount of inner bone ingrowth. Goldner staining revealed the presence of new bone formation in and around the three scaffolds, with the diamond scaffold exhibiting the highest level of new bone growth. Collectively, the cell and animal studies showed that the diamond scaffold has the best osseointegration performance, followed by the cuboctahedron scaffold.

This study is not without limitation. In the present study, due to a lack of funding, we were only able to compare the biomechanical and osseointegration properties of three types of porous titanium alloys, without including all the unit cell types previously reported.

5. Conclusion

In this study, three types of Ti6Al4V porous scaffolds with distinct lattices were designed and fabricated using computer-aided software and SLM technology, and their biomechanical and osseointegration properties were systematically investigated using static simulation analysis, *in vitro* mechanical test, CFD, and cell and animal experiments. The main conclusions based on the findings of this study are as follows:

(i) A porous Ti6Al4V scaffold with 66% porosity and 600 μm pore size, as well as CPL, diamond, and cuboctahedron unit cells, can be precisely produced utilizing computer-aided software and SLM technology.

(ii) Under the circumstance of identical porosity and pore size of porous Ti6Al4V scaffolds, the change in pore shape has a significant effect on yield strength, elastic modulus, permeability, shear stress, and specific surface area.

(iii) The diamond porous Ti6Al4V scaffold with 66% porosity and 600 μm pore size has superior biomechanical and osseointegration properties compared to the CPL and cuboctahedron scaffolds, making it an excellent option for optimizing the elastic modulus and osseointegration properties of titanium alloy implants.

Acknowledgments

We want to express our special thanks to Suzhou Yunjing Metal Technology Co., LTD. for their assistance in the processing of titanium alloy scaffolds and to the Animal Center of Xi'an Jiaotong University, which provided us with the required experimental animals.

Funding

This work was financially supported by Key Research and Development Plan of Shaanxi Province-General Project (2022GY-390), Health and Family Planning Commission of Shaanxi Province (2022E001), General Cultivation Project of Xi'an Municipal Health Commission (2022ms02), Shaanxi Natural Science Basic Research Foundation (2021JM-276), Key Research and Development Program of Shaanxi (2023-YBGY-488), and National Natural Science Foundation of China (52271249).

Conflict of interest

The authors declare they have no competing interest.

Author contributions

Conceptualization: Yin Yang, Dezhi Wang, Jing Ren
Data curation: Jiantao Liu, Kao Wang, Xiaoling Zhou, Aofei Xu, Xiwei Zhang, Yiming Li, Ruiyan Wang, Shuyuan Zhang
Formal analysis: Jiantao Liu, Kao Wang, Xiaoling Zhou, Aofei Xu, Xiwei Zhang, Yiming Li, Ruiyan Wang, Shuyuan Zhang
Funding acquisition: Jiantao Liu, Yin Yang, Jing Ren, Jun Cheng
Investigation: Aofei Xu, Xiwei Zhang, Yiming Li, Ruiyan Wang, Shuyuan Zhang
Methodology: Jun Cheng, Weiguo Bian, Jia Li, Zhiwei Ren, Mengyuan Sun
Project administration: Jiantao Liu, Kao Wang, Runqing Wang, Zhanhai Yin
Software: Runqing Wang, Zhanhai Yin
Writing – original draft: Jiantao Liu, Kao Wang
Writing – review & editing: Yin Yang, Jing Ren

Ethics approval and consent to participate

All experimental animals in this study were used in strict adherence to the code for animal use, and the experiments were approved by the Ethics Committee of Xi'an Jiaotong University (No. 2022056).

Consent for publication

Not applicable.

Availability of data

The data used in this work, including 3D model of the porous scaffold, can be obtained from the corresponding authors upon reasonable request.

References

1. Neto MQ, Radice S, Hall DJ, et al. Microstructure and electrochemical behavior of contemporary Ti6Al4V implant alloys. *J Bio Tribocorros*. 2022;8(1). doi: 10.1007/s40735-021-00623-3
2. Xi D, Wong L. Titanium and implantology: A review in dentistry. *J Biol Regul Homeost Agents*. 2021;35(1 Suppl. 1):63-72. doi: 10.3390%2Fma15093150
3. Gkiatas I, Sharma AK, Driscoll DA, McLawhorn AS, Chalmers BP, Sculco PK. Nonconcentric and irregular dislocations of total hip arthroplasties: Radiographic analysis and review of the literature. *J Emerg Med*. 2021;60(4): 451-459. doi: 10.1016/j.jemermed.2020.11.023
4. Liu T, Hua X, Yu W, et al. Long-term follow-up outcomes for patients undergoing primary total hip arthroplasty with uncemented versus cemented femoral components: A retrospective observational study with a 5-year minimum follow-up. *J Orthop Surg Res*. 2019;14(1):371. doi: 10.1186/s13018-019-1415-3
5. Raja BS, Gowda A, Singh S, Ansari S, Kalia RB, Paul S. Comparison of functional outcomes and complications of cemented vs uncemented total hip arthroplasty in the elderly neck of femur fracture patients: A systematic review and meta-analysis. *J Clin Orthop Trauma*. 2022;29:101876. doi: 10.1016%2Fj.jcot.2022.101876
6. Bittredge O, Hassanin H, El-Sayed MA, et al. Fabrication and optimisation of Ti-6Al-4V lattice-structured total shoulder implants using laser additive manufacturing. *Materials (Basel)*. 2022;15(9). doi: 10.3390/ma15093095
7. Ito K, Mori Y, Kamimura M, et al. Beta-type TiNbSn alloy plates with low Young modulus accelerates osteosynthesis in *Rabbit Tibiae*. *Clin Orthop Relat Res*. 2022;480(9):1817-1832. doi: 10.1097/corr.0000000000002240
8. Lei P, Qian H, Zhang T, et al. Porous tantalum structure integrated on Ti6Al4V base by laser powder bed fusion for enhanced bony-ingrowth implants: In vitro and in vivo validation. *Bioact Mater*. 2022;7:3-13. doi: 10.1016/j.bioactmat.2021.05.025
9. Li L, Li Y, Yang L, et al. Polydopamine coating promotes early osteogenesis in 3D printing porous Ti6Al4V scaffolds. *Ann Transl Med*. 2019;7(11):240. doi: 10.21037/atm.2019.04.79
10. Meena VK, Kalra P, Sinha RK. Finite element study on the influence of pore size and structure on stress shielding effect of additive manufactured spinal cage. *Comput Methods Biomech Biomed Engin*. 2022;25(5):566-577. doi: 10.1080/10255842.2021.1970142
11. Al-Tamimi AA. 3D topology optimization and mesh dependency for redesigning locking compression plates aiming to reduce stress shielding. *Int J Bioprint*. 2021;7(3):339. doi: 10.18063/ijb.v7i3.339
12. Han X, Ma J, Tian A, et al. Surface modification techniques of titanium and titanium alloys for biomedical orthopaedics applications: A review. *Colloids Surf B Biointerfaces*. 2023;227:113339. doi: 10.1016/j.colsurfb.2023.113339
13. Xia C, Ma X, Zhang X, et al. Enhanced physicochemical and biological properties of C/Cu dual ions implanted medical titanium. *Bioact Mater*. 2020;5(2):377-386. doi: 10.1016/j.bioactmat.2020.02.017
14. Wang Q, Zhou P, Liu S, et al. 2020, Multi-scale surface treatments of titanium implants for rapid osseointegration: A review. *Nanomaterials (Basel)*, 10(6). doi: 10.3390%2Fnano10061244
15. Wang L, Zhou W, Yu Z, et al. An in vitro evaluation of the hierarchical micro/nanoporous structure of a Ti3Zr2Sn3Mo25Nb alloy after surface dealloying. *ACS Appl Mater Interfaces*. 2021;13(13):15017-15030. doi: 10.1021/acsami.1c02140
16. Wang R, Ni S, Ma L, Li M. Porous construction and surface modification of titanium-based materials for osteogenesis: A review. *Front Bioeng Biotechnol*. 2022; 10:973297. doi: 10.3389%2Ffbioe.2022.973297
17. Liverani E, Rogati G, Pagani S, Brogini S, Fortunato A, Caravaggi P. Mechanical interaction between additive-manufactured metal lattice structures and bone in compression: Implications for stress shielding of orthopaedic implants. *J Mech Behav Biomed Mater*. 2021;121:104608. doi: 10.1016/j.jmbbm.2021.104608
18. Arabnejad S, Johnston B, Tanzer M, Pasini D. Fully porous 3D printed titanium femoral stem to reduce stress-shielding following total hip arthroplasty. *J Orthop Res*. 2017; 35(8):1774-1783. doi: 10.1002/jor.23445
19. Yao YT, Yang Y, Ye Q, et al. Effects of pore size and porosity on cytocompatibility and osteogenic differentiation of porous titanium. *J Mater Sci Mater Med*. 2021;32(6):72. doi: 10.1007/s10856-021-06548-0
20. Cuan-Urquizo E, Silva RG. Fused filament fabrication of cellular, lattice and porous mechanical metamaterials: A review. *Virtual Phys Prototyp*. 2023;1(18):e2224300. doi: 10.1080/17452759.2023.2224300

21. Yan L, Wu J, Zhang L, Liu X, Zhou K, Su B. Pore structures and mechanical properties of porous titanium scaffolds by bidirectional freeze casting. *Mater Sci Eng C Mater Biol Appl.* 2017;75:335-340. doi: 10.1016/j.msec.2016.12.044

22. Dziaduszewska M, Zielinski A. Structural and material determinants influencing the behavior of porous ti and its alloys made by additive manufacturing techniques for biomedical applications. *Materials (Basel).* 2021;14(4). doi: 10.3390/ma14040712

23. Xu Z, Zhang Y, Wu Y, et al. In vitro and in vivo analysis of the effects of 3D-printed porous titanium alloy scaffold structure on osteogenic activity. *Biomed Res Int.* 2022;2022:8494431. doi: 10.1155/2022/8494431

24. Wang H, Su K, Su L, Liang P, Ji P, Wang C. Comparison of 3D-printed porous tantalum and titanium scaffolds on osteointegration and osteogenesis. *Mater Sci Eng C Mater Biol Appl.* 2019;104:109908. doi: 10.1016/j.msec.2019.109908

25. Yang J, Li Y, Shi X, et al. Design and analysis of three-dimensional printing of a porous titanium scaffold. *BMC Musculoskelet Disord.* 2021;22(1):654. doi: 10.1186/s12891-021-04520-1

26. Afrouzian A, Groden CJ, Field DP, Bose S, Bandyopadhyay A. Additive manufacturing of Ti-Ni bimetallic structures. *Mater Des.* 2022;215. doi: 10.1016%2Fj.matdes.2022.110461

27. Huang G, Pan ST, Qiu JX. The osteogenic effects of porous Tantalum and Titanium alloy scaffolds with different unit cell structure. *Colloids Surf B Biointerfaces.* 2022;210:112229. doi: 10.1016/j.colsurfb.2021.112229

28. Ciliveri S, Bandyopadhyay A. Influence of strut-size and cell-size variations on porous Ti6Al4V structures for load-bearing implants. *J Mech Behav Biomed Mater.* 2022;126:105023. doi: 10.1016/j.jmbbm.2021.105023

29. Deng F, Liu L, Li Z, Liu J. 3D printed Ti6Al4V bone scaffolds with different pore structure effects on bone ingrowth. *J Biol Eng.* 2021;15(1):4. doi: 10.1186/s13036-021-00255-8

30. Lei H, Yi T, Fan H, et al. Customized additive manufacturing of porous Ti6Al4V scaffold with micro-topological structures to regulate cell behavior in bone tissue engineering. *Mater Sci Eng C Mater Biol Appl.* 2021;120:111789. doi: 10.1016/j.msec.2020.111789

31. Suresh S, Sun CN, Tekumalla S, Rosa V, Ling Nai SM, Wen Wong RC. Mechanical properties and in vitro cytocompatibility of dense and porous Ti-6Al-4V ELI manufactured by selective laser melting technology for biomedical applications. *J Mech Behav Biomed Mater.* 2021;123:104712. doi: 10.1016/j.jmbbm.2021.104712

32. Ran Q, Yang W, Hu Y, et al. Osteogenesis of 3D printed porous Ti6Al4V implants with different pore sizes. *J Mech Behav Biomed Mater.* 2018;84:1-11. doi: 10.1016/j.jmbbm.2018.04.010

33. Zaharin HA, Abdul RA, Azam FI, et al. Effect of unit cell type and pore size on porosity and mechanical behavior of additively manufactured Ti6Al4V scaffolds. *Materials (Basel).* 2018;11(12). doi: 10.3390%2Fma11122402

34. Taniguchi N, Fujibayashi S, Takemoto M, et al. Effect of pore size on bone ingrowth into porous titanium implants fabricated by additive manufacturing: An in vivo experiment. *Mater Sci Eng C Mater Biol Appl.* 2016;59:690-701. doi: 10.1016/j.msec.2015.10.069

35. Lu Y, Cheng L, Yang Z, Li J, Zhu H. Relationship between the morphological, mechanical and permeability properties of porous bone scaffolds and the underlying microstructure. *PLoS One.* 2020;15(9):e238471. doi: 10.1371%2Fjournal.pone.0238471

36. Chen H, Han Q, Wang C, Liu Y, Chen B, Wang J. Porous scaffold design for additive manufacturing in orthopedics: A review. *Front Bioeng Biotechnol.* 2020;8:609. doi: 10.3389/fbioe.2020.00609

37. Li X, Wang Y, Zhang B, et al. The design and evaluation of bionic porous bone scaffolds in fluid flow characteristics and mechanical properties. *Comput Methods Programs Biomed.* 2022;225:107059. doi: 10.1016/j.cmpb.2022.107059

38. Omar AM, Hassan MH, Daskalakis E, et al. Geometry-based computational fluid dynamic model for predicting the biological behavior of bone tissue engineering scaffolds. *J Funct Biomater.* 2022;13(3). doi: 10.3390/jfb13030104

39. Chao L, Jiao C, Liang H, Xie D, Shen L, Liu Z. Analysis of mechanical properties and permeability of trabecular-like porous scaffold by additive manufacturing. *Front Bioeng Biotechnol.* 2021;9:779854. doi: 10.3389%2Ffbioe.2021.779854

40. Zhang C, Zhu H, Ren X, et al. Mechanics-driven nuclear localization of YAP can be reversed by N-cadherin ligation in mesenchymal stem cells. *Nat Commun.* 2021;12(1):6229. doi: 10.1038/s41467-021-26454-x

41. Zhang Z, Sha B, Zhao L, et al. Programmable integrin and N-cadherin adhesive interactions modulate mechanosensing of mesenchymal stem cells by cofilin phosphorylation. *Nat Commun.* 2022;13(1):6854. doi: 10.1038/s41467-022-34424-0

42. De Belly H, Paluch EK, Chalut KJ. Interplay between mechanics and signalling in regulating cell fate. *Nat Rev Mol Cell Biol.* 2022;23(7):465-480. doi: 10.1038/s41580-022-00472-z

43. Truscello S, Kerckhofs G, Van Bael S, Pyka G, Schrooten J, Van Oosterwyck H. Prediction of permeability of regular scaffolds for skeletal tissue engineering: A combined computational and experimental study. *Acta Biomater.* 2012;8(4):1648-1658. doi: 10.1016/j.actbio.2011.12.021

44. Winther NS, Jensen CL, Jensen CM, et al. Comparison of a novel porous titanium construct (Regenerex(R)) to a well proven porous coated tibial surface in cementless total knee arthroplasty - A prospective randomized RSA study with two-year follow-up. *Knee.* 2016;23(6): 1002-1011.
doi: 10.1016/j.knee.2016.09.010

45. Arts M, Torensma B, Wolfs J. Porous titanium cervical interbody fusion device in the treatment of degenerative cervical radiculopathy; 1-year results of a prospective controlled trial. *Spine J.* 2020;20(7):1065-1072.
doi: 10.1016/j.spinee.2020.03.008

46. Ibhadode O, Zhang Z, Sixt J, et al. Topology optimization for metal additive manufacturing: current trends, challenges, and future outlook. *Virtual Phys Prototyp.* 2023;1(18):e2181192.
doi: 10.1080/17452759.2023.2181192

47. Ahmadi SM, Yavari SA, Wauthle R, et al. Additively manufactured open-cell porous biomaterials made from six different space-filling unit cells: The mechanical and morphological properties. *Materials (Basel).* 2015;8(4):1871-1896.
doi: 10.3390%2Fma8041871

48. Hedayati R, Sadighi M, Mohammadi-Aghdam M, et al. Mechanics of additively manufactured porous biomaterials based on the rhombicuboctahedron unit cell. *J Mech Behav Biomed Mater.* 2016;53:272-294.
doi: 10.1016/j.jmbbm.2015.07.013

49. Matena J, Petersen S, Gieseke M, et al. SLM produced porous titanium implant improvements for enhanced vascularization and osteoblast seeding. *Int J Mol Sci;* 2015;16(4):7478-7492.
doi: 10.3390%2Fijms16047478

50. Gogolewski D, Kozior T, Zmarzly P, Gogolewski D. Morphology of models manufactured by SLM technology and the Ti6Al4V titanium alloy designed for medical applications. *Materials (Basel).* 2021;14(21).
doi: 10.3390/ma14216249

51. Ataee A, Li Y, Brandt M, Wen C. Ultrahigh-strength titanium gyroid scaffolds manufactured by selective laser melting (SLM) for bone implant applications. *Acta Materialia.* 2018;158:15.
doi: 10.3390%2Fjfb14030125

52. Li JL, Guo D, L J, et al. Irregular pore size of degradable bioceramic Voronoi scaffolds prepared by stereolithography: Osteogenesis and computational fluid dynamics analysis. *Mater Des.* 2022;224:111414.
doi: 10.1016/j.matdes.2022.111414

53. Li J, Chen D, Luan H, Zhang Y, Fan Y. Numerical evaluation and prediction of porous implant design and flow performance. *Biomed Res Int.* 2018;2018:1215021.
doi: 10.1155%2F2018%2F1215021

54. Li J, Chen D, Fan Y, Evaluation and prediction of mass transport properties for porous implant with different unit cells: A numerical study. *Biomed Res Int.* 2019;2019:3610785.
doi: 10.1155/2019/3610785

55. Porter B, Zauel R, Stockman H, Guldberg R, Fyhrie D. 3-D computational modeling of media flow through scaffolds in a perfusion bioreactor. *J Biomech.* 2005;38(3):543-549.
doi: 10.1016/j.jbiomech.2004.04.011

56. Cartmell SH, Porter BD, Garcia AJ, Guldberg RE. Effects of medium perfusion rate on cell-seeded three-dimensional bone constructs in vitro. *Tissue Eng.* 2003;9(6):1197-1203.
doi: 10.1089/10763270360728107

57. Raimondi MT, Boschetti F, Falcone L, et al. Mechanobiology of engineered cartilage cultured under quantified fluid-dynamic environment. *Biomechan Model Mechanobiol.* 2002;1(1):14.
doi: 10.1007/s10237-002-0007-y

58. Van Bael S, Chai YC, Truscello S, et al. The effect of pore geometry on the in vitro biological behavior of human periosteum-derived cells seeded on selective laser-melted Ti6Al4V bone scaffolds. *Acta Biomater.* 2012;8(7):2824-2834.
doi: 10.1016/j.actbio.2012.04.001

59. Rudrich U, Lasgorceix M, Champion E, et al. Pre-osteoblast cell colonization of porous silicon substituted hydroxyapatite bioceramics: Influence of microporosity and macropore design. *Mater Sci Eng C Mater Biol Appl.* 2019;97:510-528.
doi: 10.1016/j.msec.2018.12.046

ACCSCIENCE PUBLISHING

International Journal of Bioprinting

RESEARCH ARTICLE

Building a degradable scaffold with 3D printing using Masquelet technique to promote osteoblast differentiation and angiogenesis in chronic tibial osteomyelitis with bone defects

Fan Liu, Chaohan Wu, Xinhui Wang, Rongkang Guo, Tianhua Dong, and Tao Zhang*

Department of Emergency Trauma Center, The Third Hospital of Hebei Medical University, Shijiazhuang, Hebei, China

Abstract

The aim of this study was to investigate the use of three-dimensional (3D) printing technology to create a biodegradable scaffold loaded with WNT5A protein and assess its impact on chronic tibial osteomyelitis with bone defects (CTO&BD), focusing on osteoblast differentiation and angiogenesis. We extracted RNA from peripheral blood of healthy individuals and CTO&BD patients for sequencing, followed by differential expression and functional enrichment analysis. Network analysis was performed to identify core genes associated with CTO&BD and construct a protein–protein interaction network. Using Masquelet technique, we fabricated a 3D-printed biodegradable scaffold (G40T60@WNT5A) and conducted various experiments, including rheological testing, printability evaluation, Fourier-transform infrared spectroscopy, X-ray diffraction, scanning electron microscopy analysis, as well as mechanical and degradation performance assessments. In *in vivo* experiments, we observed the formation of induced membranes in a CTO&BD rat model implanted with the scaffold. *In vitro* experiments involved the assessment of scaffold toxicity on rat bone marrow mesenchymal stem cells and umbilical vein endothelial cells, as well as the influence on osteoblast differentiation and angiogenesis. Molecular biology techniques were used to analyze gene and protein expression levels. We discovered for the first time that WNT5A may play a crucial role in CTO&BD. The biodegradable scaffold prepared by 3D printing (G40T60@WNT5A) exhibited excellent biocompatibility *in vitro*. This scaffold significantly promoted the formation of induced membranes in CTO&BD rats and further enhanced osteoblast differentiation and angiogenesis. In conclusion, this study utilized innovative 3D printing technology to fabricate the G40T60@WNT5A scaffold, confirming its potential application in the treatment of CTO&BD, particularly in promoting osteoblast differentiation and angiogenesis. This research provides new methods and theoretical support for the treatment of bone defects.

Keywords: 3D printing; WNT5A; Chronic tibial osteomyelitis; Bone defect; Osteogenic differentiation; Scaffold transplantation

***Corresponding author:**
Tao Zhang
(zt50500@hebmu.edu.cn)

Citation: Liu F, Wu C, Wang X, Guo R, Dong T, Zhang T. Building a degradable scaffold with 3D printing using Masquelet technique to promote osteoblast differentiation and angiogenesis in chronic tibial osteomyelitis with bone defects. *Int J Bioprint*. 2024;10(2):1461. doi: 10.36922/ijb.1461

Received: August 7, 2023
Accepted: October 10, 2023
Published Online: January 9, 2024

1. Introduction

Chronic osteomyelitis is a serious complication of orthopedic surgery.[1] After the surgery, the severe damage to the periosteum at the lesion caused by inflammation weakens the ability to form bone, leading to bone necrosis and long-segment bone defects.[2] Chronic osteomyelitis presents with extensive scarring, sinuses, necrotic bone, and dead spaces. Adding to the severity of the condition is the poor local blood circulation, which restricts antimicrobial drugs to reach the affected area, thereby promoting bacterial growth and subsequently leading to recurrent infections. Thus, these issues pose a challenge in clinical practice.[3-5] Chronic osteomyelitis usually occurs in adults and is typically secondary to open bone injuries or bone reconstruction surgery.[6,7]

In 1965, Gavriil Ilizarov proposed a theory known as "tension-stress principle," based on which the Ilizarov technique for bone sliding was conceptualized, which has been the preferred method for treating tibial bone defects and nonunion since then.[8-11] Surgical debridement and bone grafting are conventional approaches for treating chronic osteomyelitis with bone defects. However, for patients with longer defect lengths, the difficulty in bone reconstruction is increased due to significant bone loss, resulting in often unsatisfactory patient outcomes.[12] The Masquelet technique could produce a satisfactory induced membrane when bone cement is placed on the infection-free surgical area, targeting bone defects caused by thorough debridement and various factors.[13,14] Moreover, the implantation of autologous bone has relatively fewer limitations in terms of length, which gives it a significant advantage over other techniques when dealing with large segmental bone defects. The implantation of autologous bone also enhances patients' medical experience and facilitates nursing care and rehabilitation.[14-16] However, several limitations of using traditional Masquelet technique in bone cement filling should be acknowledged. In the traditional *in vivo* shaping method, the bone defect is filled with bone cement before it solidifies and wraps around the fracture ends for natural solidification. The solidification process is started during the second stage surgery once the bone cement becomes firmly connected to the bone ends; however, given its relatively large size, removal of the bone cement would introduce damages to the induced membrane and the interface between the bone cement and bone tissue, thus affecting fracture healing in the second-stage bone grafting. Additionally, the heat released during the solidification process of the bone cement can also damage adjacent bone and tissues.[17,18]

With the increasing application of three-dimensional (3D) printing in orthopedics, this technology provides a platform for improving the compatibility of prostheses with bone defects and enabling the restoration of bone stability.[19-21] Varying degrees of bone defects are the frequently encountered challenges in bone joint remodeling surgeries. Nevertheless, 3D-printed models could help restore the anatomical structure of bone joints and assist surgeons to better understand the 3D morphology of bone joints, in addition to other apparent advantages such as increased efficiency and stability of prosthetic matching and reduced surgical difficulty.[22] Besides, surgeons may formulate treatment plans, perform surgical rehearsal, and conduct evaluation using these models. Therefore, 3D printing stands as an obvious solution in the creation of customized prosthetics in the case of significant bone defects.[23] Recently, owing to their favorable biocompatibility and bioactivity, there has been growing interest in biodegradable materials, which are used to promote bone tissue regeneration and repair. Biodegradable polymers have been widely applied in various functions, such as drug delivery,[24] biomedicine,[25] 3D printing,[26] food packaging,[27] enzyme immobilization, tissue engineering scaffolds, nanotechnology, and technological applications.[28] Biodegradable polymers can be generally classified into two categories: synthetic polymers and natural polymers.[29] Synthetic polymers are compatible with the human body, can undergo biodegradation, and can be easily transformed into different 3D structures. On the other hand, natural polymers can be metabolized into utilizable metabolites or easily cleared by the kidneys. A few noteworthy advantages of biodegradable polymers include reduced inflammatory reactions, non-toxicity, and the ability to degrade enzymatically in the body.[30] He *et al.* discovered that 3D-printed biodegradable PU/PAAM/Gel hydrogel scaffolds exhibit high flexibility and adaptive capacity for irregular defects, making them suitable for non-load-bearing bone regeneration.[31] Chen *et al.* found that 3D-printed scaffolds can direct extracellular matrix/stromal stem cells for bone and cartilage defect regeneration.[32]

According to previous research, WNT5A is closely related to osteogenic differentiation. Some studies have reported that microvesicles derived from adipocytes could inhibit osteogenic differentiation by secreting miR-148a, which targets and regulates the Wnt5a/Ror2 pathway.[33-36] In addition, it was found that activation of Wnt5a could mediate the mechanical stretch-induced osteogenic differentiation of mesenchymal stem cells.[37] WNT5A is also associated with angiogenesis. Research has found that antagonizing the Wnt/β-catenin signaling pathway could inhibit endothelial cell proliferation, tube formation, and migration as well as induce endothelial cell apoptosis, thereby suppressing endothelial cell angiogenesis.[38]

In this study, we investigated the application of Masquelet technique and 3D printing technology in the context osteogenic differentiation and angiogenesis. Preliminary findings suggest that utilizing the Masquelet technique and preparing a degradable WNT5A-loaded scaffold G40T60 through 3D printing could facilitate the formation of the induced membrane in rats with chronic tibial osteomyelitis and tibial bone defects (CTO&BD), thus promoting osteoblast differentiation and angiogenesis. The findings also underscored the potential of Masquelet technique combined with 3D printing as a promising treatment modality for CTO&BD, and showed that WNT5A may be a potential therapeutic target in CTO&BD. The purpose of this study is to explore and develop an advanced bone repair technique for the treatment of CTO&BD, using a 3D-printed biodegradable WNT5A-loaded scaffold constructed based on the Masquelet technique to promote healing. This innovative technology has substantial clinical value in the arena of bone healing. Relative to other 3D-printed scaffolds, induced membranes created through bioengineering approach combined with Masquelet technique have superior quality and are of favorable sizes, which are distinct technical and biomechanical attributes. This technique can effectively treat orthopedic diseases, such as CTO&BD, that pose challenges in clinical treatment. Leveraging advanced technologies such as 3D printing and bioengineering may offer new avenue for addressing critical issues in current orthopedic treatments, thereby helping to improve patient's quality of life and life expectancy.

2. Materials and methods

2.1. Clinical specimen collection

Ten healthy individuals and 10 patients with chronic osteomyelitis with bone defects were recruited in this study. Peripheral blood samples were collected from the human participants, under the approval of the Ethics Committee of The Third Hospital of Hebei Medical University (Ethics Committee number: Ke-2022-104-1). Peripheral blood mononuclear cells were isolated from the samples using heparinized tubes. Fresh peripheral blood (2–5 ml) in each tube was centrifuged at 400 × *g* at room temperature. Afterward, 2 ml of the upper layer of plasma was discarded, followed by a top-up with an equal amount of phosphate-buffered saline (PBS). Five milliliters of single-nucleus isolation buffer (1:1) (bio-processing system, #25610) were added to a 15-ml centrifuge tube. Then, 5 ml of diluted whole blood was slowly added to the tube containing the single-nucleus isolation buffer. The suspension was centrifuged at room temperature for 20 min with a speed that ensures a smooth descent of the rotor. Specifically, the deceleration was set to "no break" (DECEL: set to slow). The cell layer in which peripheral blood mononuclear cells (PBMCs) reside is white.[39,40]

2.2. RNA extraction and sequencing

Total RNA was separated from peripheral blood samples using Trizol reagent (15596026, Invitrogen, CA, USA). RNA sample concentrations and purities were measured using a NanoDrop™ 2000 spectrophotometer (1011U; NanoDrop, USA). The total RNA samples that meet the following criteria are used for subsequent experiments: RNA integrity number (RIN) ≥7.0 and 28S:18S ratio ≥1.5.

The sequencing library was generated and sequenced by CapitalBio Technology (Beijing, China). Each sample used for sequencing contained 5 μg of RNA. The Ribo-Zero™ Magnetic Kit (MRZE706, Epicentre Technologies, Madison, WI, USA) was used to remove ribosomal RNA (rRNA) from total RNA. NEB Next Ultra RNA Library Prep Kit (#E7775, NEB, USA) was used for Illumina sequencing library construction. Then, in NEB Next First Strand Synthesis Reaction Buffer (5×), the RNA fragment was broken into fragments of approximately 300 base pairs (bp) in length. Reverse transcription primers and random primers were used to synthesize the first and second strands of cDNA in the reaction buffer of deoxyuridine triphosphate (dUTP) mix (10×) for the second strand synthesis reaction. The ends of cDNA fragments were repaired through the addition of polyA tails and the ligation of sequencing adaptors. After ligating Illumina sequencing adapters, the second strand of cDNA was digested using USER Enzyme (#M5508, NEB, USA) to construct a strand-specific library. The library DNA was amplified, purified, and enriched through PCR. Then, the libraries were assessed by Agilent 2100 and quantified using the KAPA Library Quantification Kit (KK4844, KAPA Biosystems, USA). Finally, paired-end sequencing was performed on the NextSeq CN500 (Illumina, USA) sequencer.[41,42]

2.3. Quality control of sequencing data and alignment to reference genome

Fast Quality Control (FastQC) software v0.11.8 was used to check the quality of the paired-end reads on the raw sequencing data. Raw data were processed using Cutadapt software 1.18, which removed the Illumina sequencing adapters and poly(A) tail sequences. Reads with an N content exceeding 5% were removed using a Perl script. Reads with a 70% base quality above 20 were extracted using FASTX Toolkit software 0.0.13. The paired-end sequences were repaired using BBMap software. Finally, the filtered high-quality reads fragments were aligned to the mouse reference genome using hisat2 software (0.7.12).[41,42]

2.4. Bioinformatics analysis

Differential gene expression analysis of mRNA was based on mRNA read count using the "edgeR" package in R language, with the criteria of $|\log2FC| > 1$ and $P < 0.05$ for differential gene selection. The target genes for

transcription factors were predicted through the TTRUST website; binding sites for transcription factors and target genes through the JASPAR website; genes involved in E3 ubiquitin ligase activity through the browser database; and potential ubiquitination sites for genes through the BioGRID database. STRING database was used for analyzing protein–protein interaction (PPI) among genes, while Cytoscape 3.5.1 software was used to visualize the PPI network. Kyoto Encyclopedia of Genes and Genomes (KEGG) pathway enrichment analysis on differentially expressed genes was performed using the "ClusterProfiler" package in R software. A significance level of P <0.05 was considered statistically significant.

2.5. Screening of differential gene expression

Differential gene expression analysis of mRNA was performed using the "edgeR" package in R language, based on read count numbers derived from mRNA. The criteria for selecting differentially expressed genes were set as |log2FC| >0.5 and P <0.05. The "ggplot2" package in R was used to create volcano plots and boxplots of differentially expressed genes. Additionally, the "heatmap" package in R was used to generate heat maps of differential gene expression.[42,43]

2.6. GO and KEGG functional enrichment analyses

Functional enrichment analysis on differentially expressed genes was performed. The "ClusterProfiler" R package was used for Gene Ontology (GO) enrichment analysis, which performs GO functional enrichment analysis at three levels—biological process (BP), cellular component (CC), and molecular function (MF). KEGG pathway analysis was performed using the PANTHER database (http://pantherdb.org/), with a significance threshold of P <0.05, and the results were then visualized using the ImageGP website.[44]

2.7. Machine learning algorithms for screening CTO&BD-related genes

Two machine learning algorithms were applied to screen the candidate genes for CTO&BD. Least absolute shrinkage and selection operator (LASSO) is a regression method used for variable selection to improve prediction accuracy and a regression technique used for variable selection and regularization to enhance statistical models' prediction accuracy and interpretability. Random forest (RF), which has no restrictions on variable conditions, has the advantages of better accuracy, sensitivity, and specificity. It could be used to predict continuous variables and provide predictions with no apparent changes. The R packages "glmnet" and "randomForest" were used for performing LASSO regression and RF analysis.[45-49]

2.8. PPI analysis

Protein–protein interaction analysis was performed using sequences of differentially expressed genes available from the STRING database(https://cn.string-db.org/cgi/), with the species set to human. The analyzed results were imported into Cytoscape 3.6.0 software for visualization, and the top 30 nodes in the PPI network were ranked based on their degree values.[50,51]

2.9. Preparation of brackets

A 12% w/v gelatin solution was prepared by adding gelatin powder to distilled water, followed by homogenization at 65°C for 15 min to make an aqueous gelatin solution. The beta-tricalcium phosphate (β-TCP) powder and gelatin solution were mixed in different ratios to prepare scaffolds (G80T20, gelatin:β-TCP, 80:20; G60T40, gelatin:β-TCP, 60:40; G40T60, gelatin:β-TCP, 40:60), followed by stirring at 60°C for 2 h. Brackets in various sizes were printed using a 3D bioprinting system, with a speed of 300 mm/min and a syringe size of 21 G. Each of the brackets had a thickness of 500 μm and a spacing of 700 μm. After bioprinting, the samples were cross-linked in 25% glutaraldehyde vapor at room temperature for 24 h. Unreacted aldehyde groups were capped with a 0.1 M glycine solution.[42]

2.10. Rheological testing

The rheology of composite hydrogel scaffolds comprising gelatin and β-TCP was tested using a rheometer (MARS 40; Haake, Germany) with parallel plates (diameter: 60 mm). The viscosity and storage modulus (G') at 25°C were measured, and the gel point at a heating rate of 1°C/min from 25 to 45°C was determined.[52]

2.11. Printability assessment

The printability of hydrogels prepared was evaluated with the aid of optical imaging. The bioprinting conditions for composite hydrogels, despite the different mixing ratios, remained the same, while the optimal pressure for each ratio was determined to ensure uniform extrusion.[52]

2.12. Fourier-transform infrared spectroscopy, X-ray diffraction, and scanning electron microscopy

To analyze the physical characteristics of the G40T60 bracket, attenuated total reflection infrared spectroscopy (ATR-IR; ALPHA, Bruker, Belgium) was used to analyze the spectral range of β-TCP in the wavelength region of 400–4000 cm^{-1} with a resolution of 2 cm^{-1}. The sample's crystal and amorphous phase regions were verified using an X-ray diffractometer (SmartLab; Rigaku Corporation, Japan) with an X-ray diffraction (XRD) working power of 9 kW and using a field emission scanning electron microscope (FE-SEM; Nova Nano SEM 200; FEI Corporation, USA). Before the scanning electron microscopy (SEM) analysis,

the sample was heated for 3 min using a sputter coating device (SCD 005; BAL-TEC, Liechtenstein) at a current of 30 mA.[52]

2.13. Mechanical experiment

The G40T60 bracket was placed on a load cell with a capacity of 500 N on a universal testing machine (EZ Test; SHIMADZU, Japan). The compressive strength of the bracket was measured at a crosshead speed of 5 mm/min. The compressive strength of five samples for each proportion was determined for the measurements of mean and standard deviation.[52]

2.14. Degradation experiment

β-TCP was incubated in PBS at 37°C for 4 weeks; the PBS was replaced every 3 days. After incubation, the samples were dried using a freeze-dryer (TFD8503; Yixin Laboratory Co., Ltd., China) for 14 or 28 days. The degradation value (W_d [%]) was calculated using Equation I:

$$W_d(\%) = \frac{W_{before} - W_{after}}{W_{before}} \times 100 \quad \text{(I)}$$

where W_{before} and W_{after} are the weights of the sample before and after degradation, respectively (n = 3).[52]

2.15. Embedding WNT5A in a 3D-printed scaffold

A 3D bioprinting system was utilized to print the scaffold, with the following settings: speed = 300 mm/min, syringe size = 21 G, bracket thickness = 500 μm, and spacing = 700 μm. After bioprinting, the sample was cross-linked at room temperature in 25% glutaraldehyde vapor for 24 h, resulting in a 3D-printed scaffold loaded with WNT5A (WNT5A final concentration of 500 μg/ml). Unreacted aldehyde groups were capped with a 0.1 M glycine solution.[52]

2.16. Cell culture and identification

Bone marrow mesenchymal stem cells (BMSCs) from healthy rats (catalog number: CP-M131, Procell, China) were cultured in α-MEM medium (catalog number: SH30265.01, HyClone, Thermo Fisher Scientific, USA) supplemented with 15% fetal bovine serum (FBS; catalog number: 10091148, Thermo Fisher Scientific, USA) and 100 U/ml penicillin–streptomycin solution (catalog number: 10378016, Thermo Fisher Scientific, USA). The culture was incubated at 37°C in a 5% CO_2 environment.

The BMSCs identification process started with the preparation of a single cell suspension (1×10^6/ml) after washing the cells with PBS. Various fluorescently labeled antibodies were added to different groups, including CD44-FTITC (MA5-17522, Thermo Fisher Scientific), CD90-PE (ab33694, Abcam, UK), CD45-FITC (ab33916, Abcam, UK), CD34-PE (ab223930, Abcam, UK), and IgG (ab150165, Abcam, UK). After incubation at 4°C for 30 min, unbound antibodies were washed away with PBS. The cells successfully targeted by the labeled antibodies were analyzed by means of flow cytometry. To study the differentiation of BMSCs into osteoblasts, adipocytes, and chondrocytes, an array of approaches including reagent kit (PD-003/4/5, Procell), Alizarin red staining (ARS), oil red O staining, and Alcian blue staining were used to observe the osteogenic, adipogenic, and chondrogenic differentiation abilities of BMSCs. The above methods confirmed the osteogenic, adipogenic, and chondrogenic differentiation capacity of the BMSCs used in this study (Figure S1A in Supplementary File), and they showed high expression of CD44 and CD90 but no expression of CD45 and CD34 (Figure S1B in Supplementary File), making them suitable for use in the subsequent experiments.

The rat umbilical vein endothelial cells (UVECs) (catalog number: CP-R232, Procell, China) was cultured in endothelial cell medium (ECM; 1001, Wegene, China) supplemented with 5% fetal bovine serum, 1% v/v penicillin/streptomycin, and 1% endothelial cell growth supplement (ECGS; KGY1052, Kaiji, China). The cells were incubated at 37°C in a 5% CO_2 environment. UVECs from the second to the fifth passages were used for subsequent experiments to investigate their cellular functions.[53-55]

2.17. Testing of 3D scaffold cytotoxicity

2.17.1. Cell adhesion and cell morphology detection

To investigate the cell viability and adhesion of BMSCs and UVECs on the scaffold, we used the LIVE/DEAD Viability/Cytotoxicity Assay Kit (Invitrogen, USA) for detection. The sample was washed once with PBS after removing the culture medium. A dye solution containing 4 ml of calcein-AM and 2 ml of homodimer-10 was added to each sample. After being left for reaction at 37°C for 30 min, the scaffold was washed with PBS. The live and dead cells on the scaffold were observed under a fluorescence microscope (Eclipse Ti, Nikon, Japan), and the cell morphology on the scaffold was examined using FE-SEM.

In addition, the scaffolds cultivated for 4 and 7 days were washed twice with PBS, for 5 min each time, and then chemically fixed with a 2.5% glutaraldehyde solution. Then, the cells were dehydrated in a gradient series of ethanol solutions (50%, 75%, 85%, 95%, and 100%), taking 10 min for incubation in each ethanol solution. After dehydration, the bracket was air-dried and coated with gold through a sputtering deposition for 3 min at 30 mA. Finally, the gold-plated bracket was observed using SEM.[52]

2.17.2. CCK-8 cell proliferation assay

BMSCs were seeded at a density of 1×10^4 cells/well in a 48-well plate coated with scaffolds. On the 4th, 7th, and 10th

days of cultivation, fresh medium containing 10% CCK8 (CA1210, Solarbio) was added to the 48-well plate. The plate was then incubated under light-shielding conditions for 1 h. Subsequently, the absorbance of the supernatant culture medium in a 96-well plate (100 μl per well) was measured at 450 nm using a microplate spectrophotometer (Bio-Tek, UK).[55]

2.18. CTO&BD rat model construction

Twenty-four Sprague-Dawley rats (male, 7 weeks old, weighing 250–300 g) were purchased from Beijing Vital River Laboratory Animal Technology Co., Ltd. (strain code: 101, Beijing, China). The rats were housed in an SPF-level animal laboratory maintained at a humidity of 60% to 65% and a temperature of 22 to 25°C. They were given *ad libitum* food and water under a 12-h light/dark cycle. After a week of adaptation feeding, the health status of the rats was observed before the experiment commenced. All animal experiments have been approved by the Animal Ethics Committee of the Third Hospital of Hebei Medical University (No. KSD2022-033-1), and all animal experiments in this study comply with the local principles for the management and use of experimental animals.

Under general anesthesia, the eccentric exercise of the triceps surae in the rat's leg was performed 3 times a week for 1 h each time (30 stimuli per minute) to induce Achilles tendinitis and tendon disorders, which are equivalent to tendinopathy. After 3 weeks, a longitudinal incision was made on the lateral side of the rat's left thigh skin, followed by dissection of the skin and subcutaneous tissue, blunt separation of fascia and muscle, and exposure of the femur. A 6-hole steel plate was placed on the outer side of the femur, and one screw was inserted into the distal and proximal ends after adjusting the position. We found that the length of the bone section in the steel plate was 0.5 cm using a sterile stainless steel ruler. The steel plate was secured with toothed forceps at the proximal and distal ends and partially cut through with an electric oscillating saw (leaving approximately 1/5 of the bone closest to the steel plate). Then, a diamond saw blade was used to cut through the remaining bone in the proximal and distal regions of the bone section. The bone section was removed, and a pre-prepared G40T60@WNT5A scaffold was placed in the bone defect area.

The G40T60@WNT5A scaffold was secured with 2-0 sutures to prevent displacement. In the control group, WNT5A, in a concentration equal to that of G40T60@WNT5A, was applied to the corresponding defect area to build a CTO&BD model.[56] The rats were randomly divided into four groups, each consisting of six rats: (i) PBS group, in which an animal received only a PBS injection of equal volume; (ii) G40T60 group, in which a scaffold was applied to each animal; (iii) WNT5A group, in which an animal received only an injection of WNT5A in a concentration equal to that of G40T60@WNT5A; (iv) G40T60@WNT5A group, in which G40T60@WNT5A scaffold was transplanted to the defect site of each animal. The final concentration of WNT5A is 500 μg/ml. After 2 weeks of treatment, the rats were euthanized. The skin over the original surgical incision on the left thigh was cut open to expose the muscle and fascial tissues, and the induced membrane formed on the surface of the scaffold was removed.

2.19. Induction of osteoblast differentiation and identification of osteoblasts

BMSCs were cultivated with induced membrane. An osteogenic induction medium comprising of 10 mM β-glycerophosphate, 100 nM dexamethasone, and 50 mg/ml ascorbic acid-2-phosphate in the BMSCs culture medium was prepared. The culture medium should be replaced every 3 days during the induction of BMSCs osteogenic differentiation. Cells were obtained after using GelMA lysis reagent kit (EFL-GM-LS-001, Suzhou, China) and trypsin (R001100, Thermo Fisher Scientific) to degrade the hydrogel.

2.19.1. Alkaline phosphatase staining

Alkaline phosphatase (ALP) staining was performed using an ALP staining kit (40749ES60, Yeasen, China), following the manufacturer's instructions for detection. Fixed with 4% paraformaldehyde for 7 days, the BMSCs were washed with PBS and stained for 30 min. Stained cells were imaged using a microscope (IX73, OLYMPUS, Japan). Meanwhile, we evaluated the ALP activity of the cell lysates of BMSCs using ALP activity assay kit (MAK411, Sigma-Aldrich). After being incubated with p-nitrophenyl phosphate solution, the absorbance of the cell lysates was measured at 520 nm using a microplate spectrophotometer (Bio-Tek, Thermo Fisher Scientific, USA) to determine the ALP activity.

2.19.2. Alizarin red S staining

The calcium deposited in the BMSCs induced for 21 days was stained with Alizarin red S (ARS) solution. BMSCs were fixed with 4% paraformaldehyde and stained with ARS solution (PH 1354, PHYGENE, China) at room temperature for 30 min, followed by PBS washing. The stained cells were then imaged using an inverted microscope (IX73, OLYMPUS). The calcium deposits stained with 10% cetylpyridinium chloride (CPC, C0732, Sigma-Aldrich) were dissolved in a microplate spectrophotometer at 562 nm to measure the absorbance, which helps gauge the degree of mineralization.[55]

2.20. Transwell, scratch assay, and tube formation assay

First, the migration of UVECs was assessed through Transwell experiments. UVECs, co-cultured and trypsinized, were resuspended and then seeded on the apical chamber of 8.0 μm Transwell inserts (BDFalcon™, USA) at a density of 2×10^5/insert. The induced membrane was placed in the sub-chamber. After 24 h, the cells were fixed with 4% paraformaldehyde for 30 min and then stained with 0.1% crystal violet. Imaging of migrating cells was performed using a microscope (IX73, OLYMPUS).

Scratch assay was used to detect the migration of UVECs. UVECs were seeded at a density of 2×10^5 cells/well in a 12-well plate and allowed to grow until 100% confluence. Scratch, measuring approximately 600 μm in width, was made on monolayers after 3 h of nutrient deprivation. Cells were incubated at 37°C and 5% CO_2 with different induced membranes (i.e., induced membranes were soaked in serum-free culture medium for 72 h) for 12 h. Then, the cells were imaged using a microscope (IX73, OLYMPUS). The relative closure degree of quantified scratches was measured using ImageJ software.

The tube-forming ability of UVECs was also assessed. After being thawed overnight on ice, the UVECs in a 48-well plate were added with 250 μl of Matrigel (BD Biosciences, USA) and incubated at 37°C for 30 min to allow gel formation. The UVECs were inoculated at a concentration of 2.5×10^4/cell in Matrigel and treated with different elution media. Subsequently, the cells were incubated at 37°C in 5% CO_2 for 6 h. Then, the cells were imaged using a microscope (IX73, OLYMPUS),[55] while quantitative analysis was performed using ImageJ software.

2.21. Hematoxylin and eosin staining

The extracted induced membrane was fixed with 4% formaldehyde, and after 24 h of fixation, paraffin embedding and slicing were performed. The routine hematoxylin and eosin (H&E) staining was carried out. Briefly, after being subjected to gradient alcohol dehydration, the slides were stained in hematoxylin for 3 min, and then rinsed with tap water. Next, 0.5% hydrochloric acid alcohol differentiation solution was applied for 10 s, and then the slides were rinsed with water. Counterstaining with bluing solution was performed for 10 min, and then the slides were stained with eosin solution for 5 min. Subsequently, routine dehydration, application of coverslips, and ultimately sealing with neutral gum were performed. The slides were observed under an optical microscope (XP-330, Shanghai Bingyu Optical Instrument Co., Ltd., Shanghai, China). In particular, the cells, fibrous tissue, and microvessels in the induced membrane were observed.[57,58]

2.22. Double immunofluorescence

The cells were fixed with 4% paraformaldehyde at room temperature for 15 min, and then washed twice with PBS. The cells were permeabilized with 0.5% Triton X-100 (P0096, Beyotime, China) for 10 min. Then, the cells were incubated overnight at 4°C with primary antibodies: sheep anti-OPN (ab11503, 1:200, Abcam, UK) and rabbit anti-RUNX2 (#12556, 1:6400, CST, USA). After washing the slides 3 times with PBS, the slides were incubated with Alexa Fluor 488-conjugated secondary antibody (ab150129/ab150077, 1:200, Abcam, UK) for 1 h. Then, the slides were washed 3 times with PBS and stained with DAPI (10 μg/ml; D3571, Thermo Fisher, USA) at room temperature for 10 min. The slides were stored at 4°C and then observed using a fluorescent microscope (IMT-2, Olympus).[59]

2.23. RT-qPCR

Total cellular RNA was extracted using Trizol (Catalog #: 16096020, Invitrogen, USA). The purity and concentration of the obtained RNA were assessed by measuring the absorbance of the solution at 260 and 280 nm by means of spectrophotometry. The A_{260}/A_{280} ratio of the sample should be ≥1.8. To obtain cDNA, reverse transcription was performed using the Reverse Transcription Kit (Catalog number: 11483188001, Roche, Switzerland). Reaction conditions were set as follows: 42°C for 15 min (reverse transcription reaction); 85°C for 5 s (reverse transcriptase inactivation reaction). The reverse-transcribed cDNA was diluted to 50 ng/μl for subsequent fluorescence quantitative polymerase chain reaction (PCR). PCR was performed using the LightCycler 480 SYBR Green I Master under the following conditions: initial denaturation at 95°C for 10 min, followed by denaturation at 95°C for 15 s, annealing at 60°C for 20 s, and extension at 72°C for 20 s, for a total of 40 cycles. With *Gapdh* as the internal reference, 2-ΔΔCt method was employed. 2-ΔΔCt represents the fold change in expression of the target gene in the experimental group compared to the control group,[60] and the formula is given in Equation II:

$$\Delta\Delta Ct = \Delta Ct\ experimental\ group - \Delta Ct\ control\ group \quad \text{(II)}$$

where $\Delta Ct = Ct$ (target gene) $- Ct$ (reference gene). The experiment was repeated 3 times. The primer sequences can be found in **Table S1** (Supplementary File).

2.24. Western blot

Total protein was extracted from tissues or cells using efficient RIPA lysis buffer (C0481, Sigma-Aldrich, USA) containing 1% proteinase inhibitor and 1% phosphatase inhibitor (ST019-5mg, Beyotime, Shanghai, China), in strict adherence to the manufacturer's instructions. After 15 min of cracking at 4°C, the suspension was centrifuged at 15,000 r/

min for 15 min. The supernatant was extracted, and the BCA assay kit (23227, TH&Ermo, USA) was used to determine the protein concentration of each sample. Quantification was performed by adding a 5× loading buffer (P0015, Beyotime, China)—the volume of which is subjected to the concentration of protein—followed by protein separation through polyacrylamide gel electrophoresis. The proteins were then transferred to a PVDF membrane (IPVH00010, Millipore, Billerica, MA, USA), which was then blocked at room temperature with 5% bovine serum albumin for 1 h. After adding antibodies such as rabbit anti-RUNX2 (#12556, 62 kDa, 1:1000, CST, USA), mouse anti-ALPL (#4747, 80 kDa, 1:1000, CST, USA), rabbit anti-GAPDH (#92310, 37 kDa, 1:1000, CST, USA), rabbit anti-Angiopoietin 1 antibody (ab8451, 1:1000, Abcam, UK), mouse anti-Pecam1 (CD31) antibody (ab9498, 1:1000, Abcam, UK), and rabbit anti-VCAM1 antibody (ab134047, 1:1000, Abcam, UK), the membranes were incubated overnight at 4°C. The next day, the membrane was washed with TBST for 5 min for 3 times. Then, the membrane was incubated with HRP-conjugated goat anti-rabbit IgG (1:2000, ab205718, Abcam, UK) or goat anti-mouse IgG (1:2000, ab6789, Abcam, UK) at room temperature for 1.5 h. After incubation, the membrane was washed with TBST for 5 min for 3 times. Then, developing solution (NCI4106, Pierce, Rockford, IL, USA) was added to the membrane. The ImageJ software was used for protein quantification analysis, which is based on the ratio of the grayscale value of each protein to the grayscale value of the internal reference GAPDH.[61] Each experiment was repeated 3 times.

2.25. Statistical analysis

The data was analyzed using SPSS 21.0 (IBM, USA) software. The measurement data was expressed as mean ± standard deviation. Normality and homogeneity of variance tests were conducted. If the data followed a normal distribution and exhibited homogeneity of variance, *t*-tests were used for between-group comparisons. For multiple group comparisons, one-way analysis of variance (ANOVA) was used, followed by *post hoc* tests using Tukey's method. Repeated-measures ANOVA combined with *post hoc* tests using Tukey's method was conducted for analyzing comparisons between different time points within groups. $P < 0.05$ indicates that the difference is statistically significant.

3. Results

3.1. Seventy-nine candidate genes related to CTO&BD were identified through transcriptome sequencing of clinical samples

First, high-throughput sequencing was performed on peripheral blood samples collected from healthy volunteers and patients with CTO&BD. The differential analysis identified 79 differentially expressed genes (DEGs), as shown in the heat map and volcano plot (Figure 1A and B). Among them, 53 genes were significantly upregulated, and 26 were significantly downregulated.

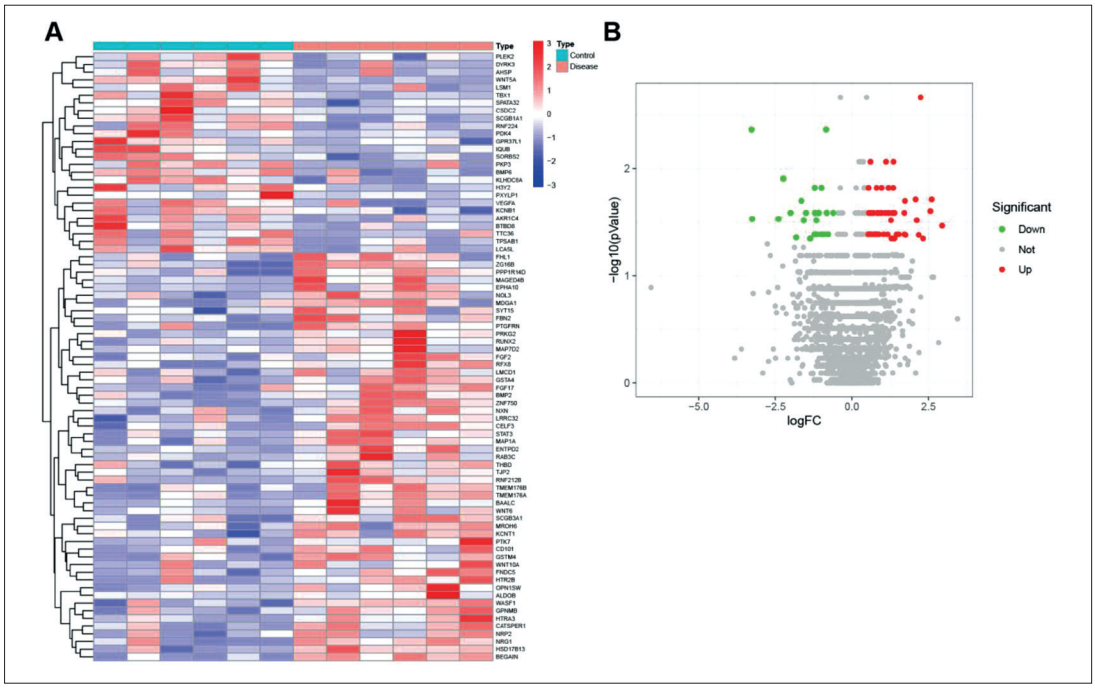

Figure 1. Screening of CTO&BD-related differentially expressed genes. (A) Heat map showing differential expression of genes of healthy volunteers and CTO&BD patients analyzed by high-throughput sequencing. Control group: $n = 6$, disease group: $n = 6$. (B) Volcano plot showing differential expression of genes of healthy volunteers and CTO&BD patients analyzed by high-throughput sequencing. Red represents upregulated genes, green represents downregulated genes, and gray represents genes with no differential expression.

3.2. Osteogenic differentiation and angiogenesis may be involved in the progression of CTO&BD

Next, functional enrichment analysis of GO and KEGG was conducted for the 79 DEGs. First, the GO functional analysis results indicated that 1317 DEGs were mainly enriched in BP in terms of positive regulation of endothelial cell proliferation (GO:0001938), cell fate commitment (GO:0045165), mesenchyme development (GO:0060485), and mesenchymal cell differentiation (GO:0048762), among others. In CC, they were mainly enriched in adherens junction (GO:0005912), lamellipodium (GO:0030027), GABA-ergic synapse (GO:0098982), and semaphorin receptor complex (GO:0002116), among others. In MF, they are mainly enriched in receptor-ligand activity (GO:0048018), signaling receptor activator activity (GO:0030546), cytokine activity (GO:0005125), and growth factor activity (GO:0008083), among others (Figure 2A and B). Based on the GO functional enrichment analysis results above, DEGs were mainly involved in biological processes such as cell proliferation, stromal stem cell development, and differentiation, with activity related to receptor ligands, cytokines, and growth factors.

In addition, KEGG pathway analysis revealed that DEGs were mainly enriched in signaling pathways such as angiogenesis, Alzheimer's disease-presenilin pathway, Cadherin signaling pathway, Wnt signaling pathway, and TGF-beta signaling pathway (Figure 2C). Literature reports indicate that vasculogenesis is closely related to osteogenesis, bone repair, and regeneration. Stimulating vasculogenesis could enhance the osteogenic differentiation potential of BMSCs, and activation of the Wnt/β-catenin signaling pathway could promote osteogenic differentiation and vasculogenesis.[62-64]

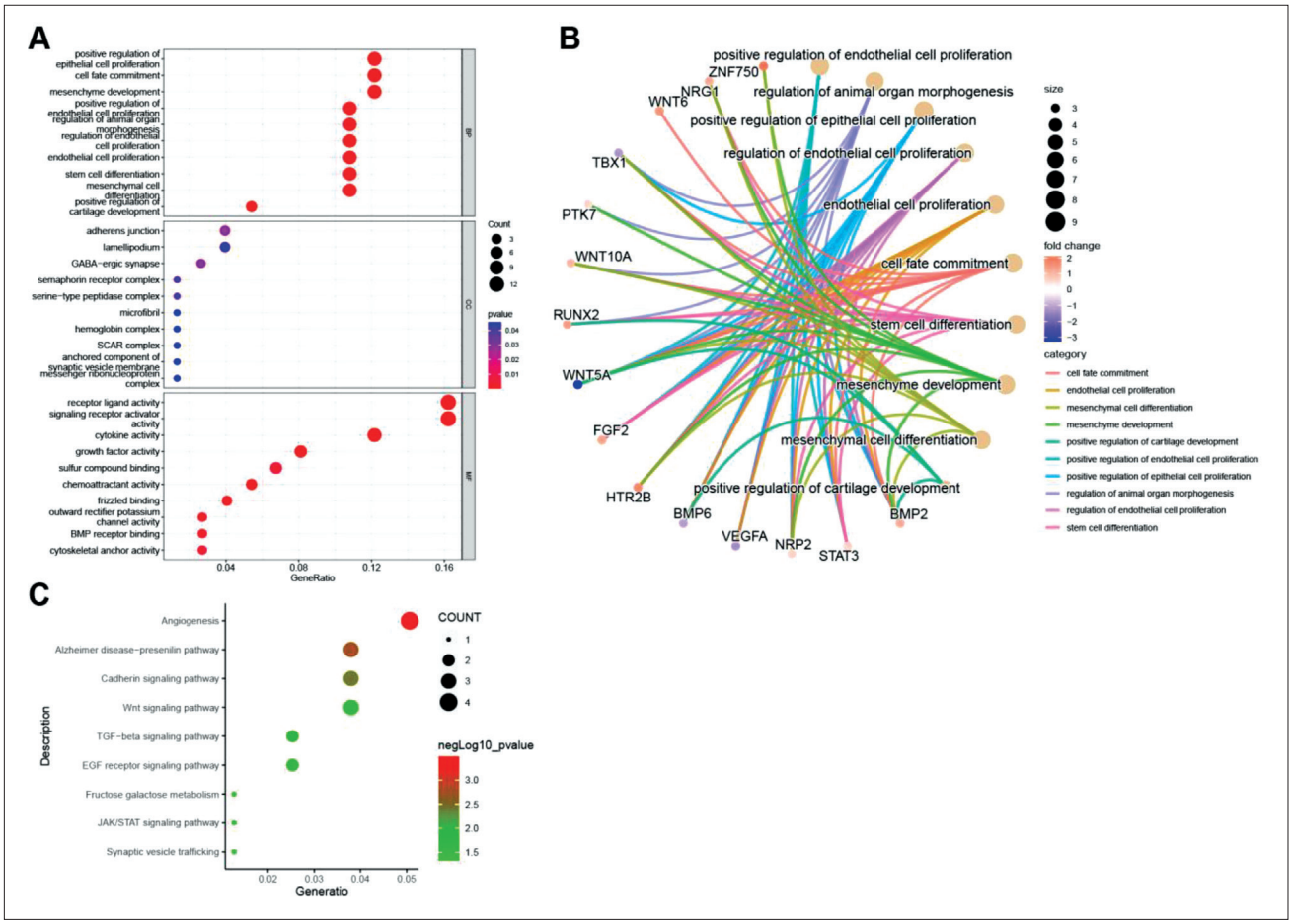

Figure 2. Enrichment analysis of differentially expressed genes (DEGs) in GO and KEGG terms. (A) Bubble plot showing the enrichment of DEGs in biological process (BP, top), cellular component (CC, middle), and molecular function (MF, bottom) categories based on GO analysis. The size of the circles denotes the number of enriched genes, and the change of color from blue to red indicates the decreasing *P* value. (B) Circular plot showing the enrichment of DEGs in the main BP pathways. (C) Enrichment analysis of DEGs in KEGG pathways. The size of the circles denotes the number of enriched genes, and the change of color from green to red indicates the decreasing *P* value.

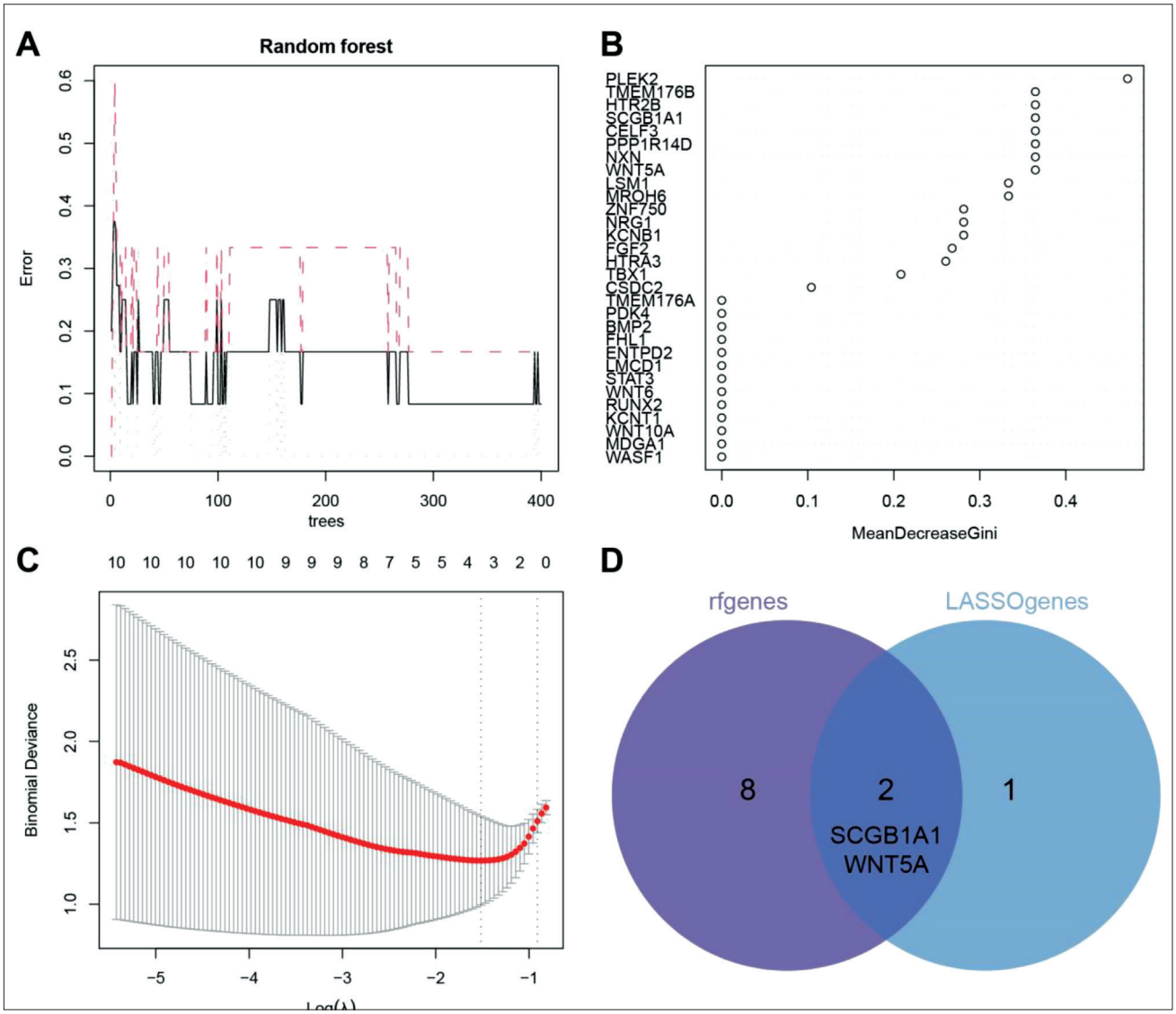

Figure 3. Selection of disease-related genes using random forest and LASSO regression analysis. (A) Cross-validation error curve of random forest analysis. The *x*-axis represents the number of trees, and the *y*-axis represents the cross-validation error. The lines of three different colors represent the errors of different groups. The black line represents the error of all samples, the red line represents the error of the disease group, and the green line represents the error of the control group. (B) Bubble plot ranking genes based on their importance calculated by the RF algorithm. The plot shows the top 30 genes based on importance. (C) Cross-validation error curve of LASSO regression. The *x*-axis represents log(λ) values, and the *y*-axis represents binomial deviance. The upper part of the plot shows the number of genes retained for each log(λ) value used in the calculation. The dotted line represents the log(λ) value corresponding to the optimal binomial deviance and the number of retained genes. (D) Venn diagram showing the intersection of disease-related genes selected by random forest and LASSO regression analysis.

In light of this, we speculate that osteogenic differentiation and vascular formation may be involved in the progression of CTO&BD.

3.3. Machine learning filters vital candidate genes for CTO&BD

Further, candidate disease feature genes were obtained through machine learning algorithms. We first conducted random forest analysis on the DEGs and obtained 10 disease-associated genes (*PLEK2*, *TMEM176B*, *HTR2B*, *SCGB1A1*, *CELF3*, *PPP1R14D*, *NXN*, *WNT5A*, *LSM1*, and *MROH6*) based on their gene importance ranking (Figure 3A and B). LASSO regression analysis identified three disease-associated genes (*SCGB1A1*, *BEGIN*, and *WNT5A*) (Figure 3C). Then, we derived the critical disease-specific genes SCGB1A1 and WNT5A from the overlapping zone of the genes obtained from both machine learning algorithms (Figure 3D). Therefore, we speculate that *SCGB1A1* and *WNT5A* may be essential candidate genes that regulate CTO&BD progression.

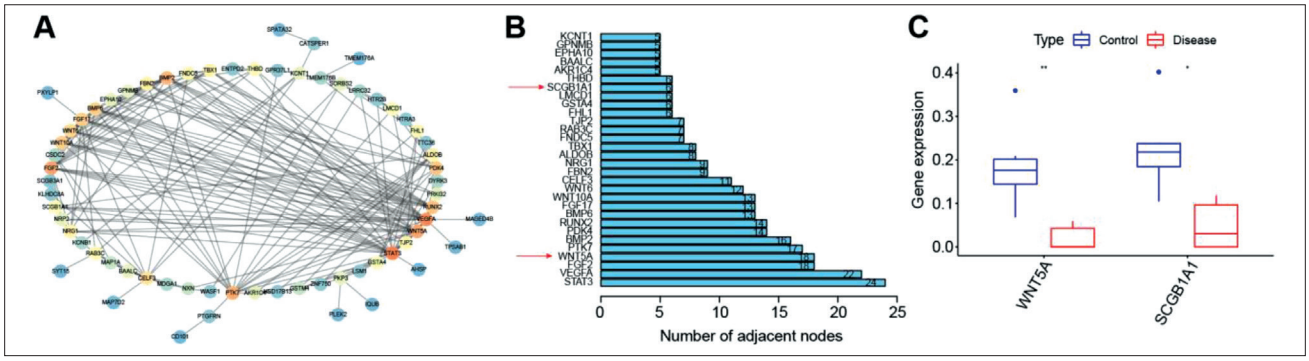

Figure 4. Selection of critical factors in CTO&BD. (A) Protein–protein interaction (PPI) network of proteins encoded by differentially expressed genes. Nodes represent proteins, and different colors represent degree values, with colors changing from blue to red indicating the increasing degree values. Edges represent the interactions between proteins. (B) Bar graph showing the top 30 genes ranked by the degree values. The red arrow points to SCGB1A1 and WNT5A. (C) Box plot showing the differential expression of *SCGB1A1* and *WNT5A* in high-throughput sequencing analysis. Control group: $n = 6$, disease group: $n = 6$. $^{*}P < 0.05$, $^{**}P < 0.01$ compared to the control group.

3.4. Bioinformatics screening identified WNT5A as the key factor of CTO&BD

Next, we imported the proteins encoded by the DEGs obtained from high-throughput sequencing into the String database for PPI network analysis. The PPI network relationships were visualized using Cytoscape software (Figure 4A). The degree values of each protein in the PPI network were calculated and sorted. It was found that both SCGB1A1 and WNT5A were among the top 30 proteins in the degree ranking. The degree value of WNT5A (18) was much higher than that of SCGB1A1 (6) (Figure 4B). Differential analysis results of high-throughput sequencing showed that WNT5A and SCGB1A1 were downregulated in CTO&BD, and the differential expression of WNT5A was more significant (Figure 4C). According to published literature, deferoxamine induces Wnt5a expression to promote osteogenic differentiation, while overexpression of miR-148a inhibits osteogenic differentiation by suppressing the Wnt5a/Ror2 pathway. Transcriptional activation of Wnt5a in fibroblasts could promote VEGF-independent angiogenesis.[33,65,66] Therefore, WNT5A may be essential in regulating osteogenesis and angiogenesis processes in CTO&BD.

3.5. Printability assessment of 3D-printed biodegradable brackets

To evaluate the printability and mechanical properties of gelatin/β-TCP composite hydrogel, we first analyzed its rheological data. For 3D bioprinting, hydrogels must have shear-thinning and dilution properties. According to the shear rate measurements of viscosity, all groups showed shear-thinning behavior, confirming that the hydrogel is a deformable material (Figure 5A). To evaluate the mechanical properties of hydrogels based on the proportion of β-TCP, G' was measured during the frequency sweep process. With the increase of β-TCP content, the G' value also increased, indicating that the stiffness of the hydrogel also increased (Figure 5B). We conducted an analysis of the hydrogel's gelation point in relation to its temperature to determine the stability of the material for bioprinting applications. The four groups were all in a gel state below 31°C, and the addition of β-TCP had no significant effect on the printability of the hydrogel at room temperature (Figure 5C). Gels, G80T20, G60T40, and G40T60 displayed uniform compression at pressures of 230, 360, 380, and 430 kPa, respectively, as observed optically (Figure 5D). As the content of β-TCP increases, higher pressure is required to obtain uniform chains. The pressure required for bioprinting material extrusion depends on the material's stiffness. Therefore, the G40T60 hydrogel, which had the highest hardness, required a higher pressure. Under the microscope, the observation of the composite scaffold prepared under optimized pressure confirmed a strut thickness of 500 μm (Figure 5E).

3.6. The chemical composition, crystallinity, surface morphology, compressive strength, and degradation characteristics of the scaffolds were characterized

We further characterized the scaffolds' chemical composition, crystallinity, surface morphology, compressive strength, and degradation properties. Figure 6A shows the composite scaffold's Fourier-transform infrared (FTIR) spectra cross-linked with 2.5% glutaraldehyde, which confirmed the presence of collagen and β-TCP in the scaffold and stable interactions between these components. The XRD pattern of the scaffold is shown in Figure 6B. At $2\theta = 20–25°$, gelatin exhibits a large and broad peak, indicating the presence of the peak β-TCP in the amorphous region of the gelatin phase in all composite scaffolds. With an increase in the gelatin amount, the intensity of these peaks decreases due to an increase in amorphous gelatin. The surface morphology of the freeze-dried scaffold is shown in Figure 6C. We found

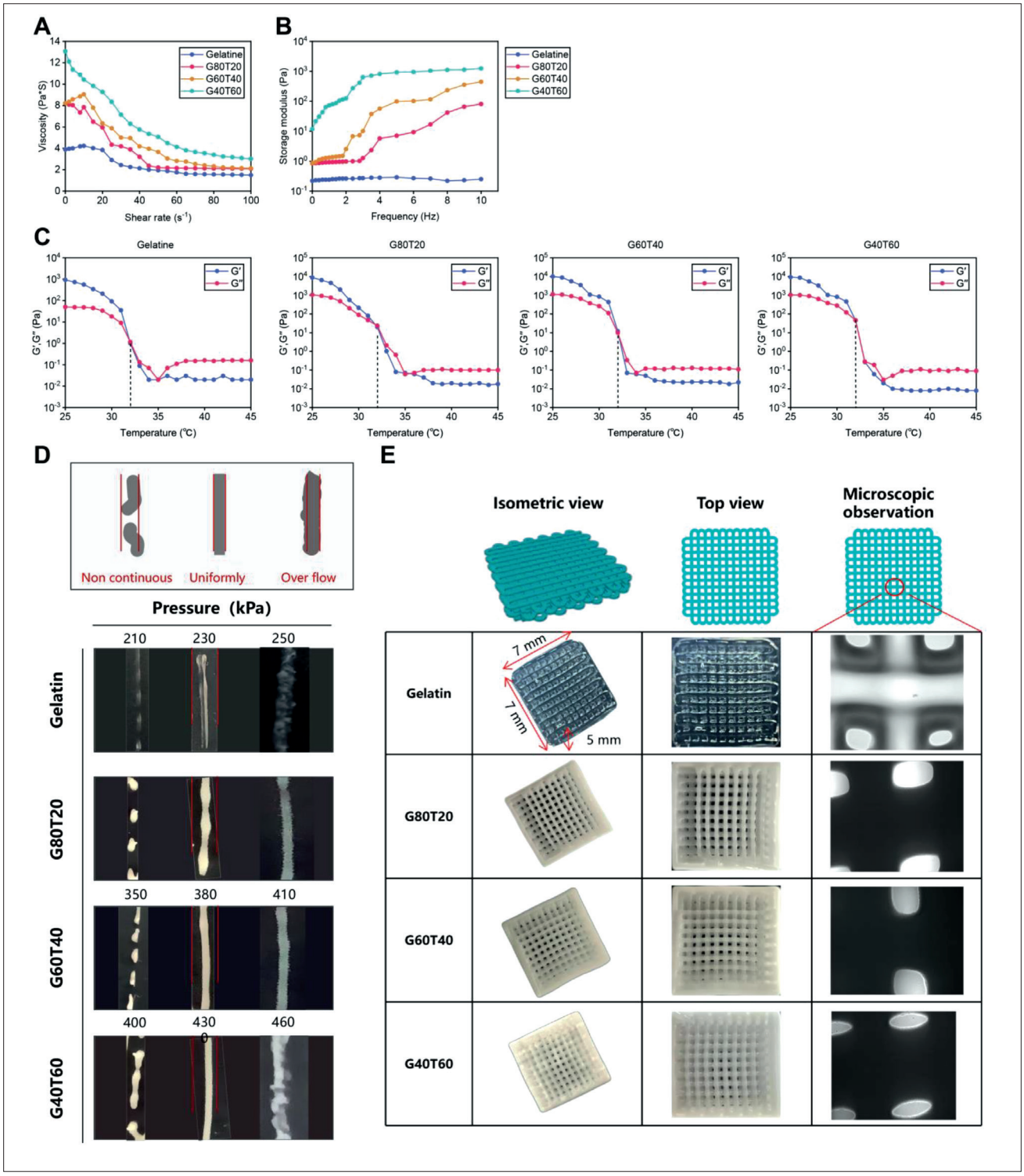

Figure 5. Fabrication of 3D-printed scaffolds. (A) Detection of shear rate viscosity behavior. (B) Detection of shear storage modulus at varying frequencies. (C) Detection of gelation temperature. (D) Evaluation of extrusion uniformity. (E) Representative views of the 3D-printed objects.

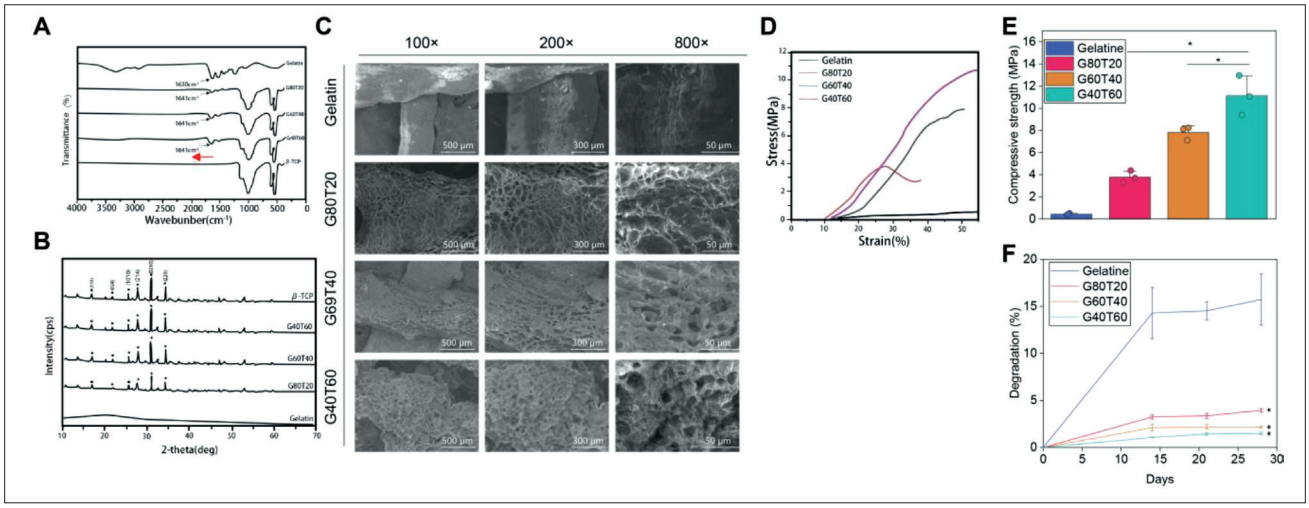

Figure 6. Characterization of 3D-printed scaffolds. (A) Fourier-transform infrared spectroscopy (FTIR) of the scaffold. (B) X-ray diffraction (XRD) pattern of the scaffold. (C) Scanning electron microscopy (SEM) images of the scaffold. (D) Stress–strain curve. (E) Compressive strength of the scaffold with different proportions of β-tricalcium phosphate. (F) Degradation of gelatin/β-tricalcium phosphate scaffold at 37°C in phosphate-buffered saline. *$P < 0.05$; the experiment was repeated 3 times.

that the collagen matrix formed an interconnected porous structure in the scaffold, and the β-TCP nanoparticles were uniformly distributed in the collagen phase. After the freeze-drying process, the scaffold made of gelatin did not retain its shape, but the addition of nanoparticles helped maintain the uniform structure of the chains. Compression testing analyzed the mechanical performance of the printed scaffolds' (Figure 6D and E). The results showed that the average compressive strength of the gelatin group was the lowest (0.4 ± 0.14 MPa), while the compressive strengths of G80T20, G60T40, and G40T60 were 4.12 ± 0.22, 8.41 ± 1.41, and 11.45 ± 1.96 MPa, respectively. The degradation of samples was measured for 4 weeks in PBS, and the freeze-dried samples were weighed to obtain the W_d value (Figure 6F). The results indicated that the scaffold containing only gelatin degraded, while the degradation rate of the gelatin/β-TCP composite scaffold decreased with an increase in β-TCP content.

Therefore, it is evident that the degradation rate of the composite scaffold can be manipulated by preselecting the proportion of its constituent components.

3.7. G40T60 has good biocompatibility

To investigate the biocompatibility of the scaffolds, we first assessed the attachment and viability of fluorescently stained BMSCs and tested them on scaffolds synthesized in various ratios. After incubating for 24 h and 72 h in G80T20, G60T40, and G40T60, we confirmed through fluorescence microscopy that the majority of live cells (green) were attached to the scaffolds in the group with the highest β-TCP ratio, G40T60. It is known that unreacted aldehyde groups generated by crosslinking methods could lead to toxicity. However, we confirmed through live/dead imaging of cell viability that the inhibition reaction of glycine was successful, resulting in almost no observed dead cells (in red), indicating that the scaffold is not at all cytotoxic (Figure 7A). The morphology and migration of BMSCs on the scaffold were evaluated by SEM (Figure 7B).

After 4 days of cultivation in G80T20, G60T40, and G40T60 at 37°C, every cell exhibited a round shape. However, after 7 days, we found filamentous projections growing from the pre-osteoblasts attached to the scaffold surface. After co-culturing the scaffolds with BMSCs, cell proliferation was assessed at different time points. The CCK8 assay was used to measure cell proliferation on the scaffolds. The results showed that the absorbance was measured after 4, 7, and 10 days of incubation, and the G40T60 group had the highest proliferation rate (Figure 7C). Cell proliferation was increasing until the 7th day, but showed sign of reduction on the 10th day. This proliferation reduction could be explained by cell differentiation.

The above results indicated that G40T60 could promote cell proliferation in the first 10 days and promote BMSCs differentiation after 10 days, demonstrating the excellent biocompatibility of G40T60. Therefore, the G40T60 scaffold was chosen for further investigation.

3.8. G40T60@WNT5A promoted the formation of induced membranes in CTO&BD rats, promoting osteogenic differentiation

During the bone formation phase, the BMSCs in the bone marrow gradually differentiate into osteoblasts. Osteoblasts secrete some collagen fibers around themselves, promoting

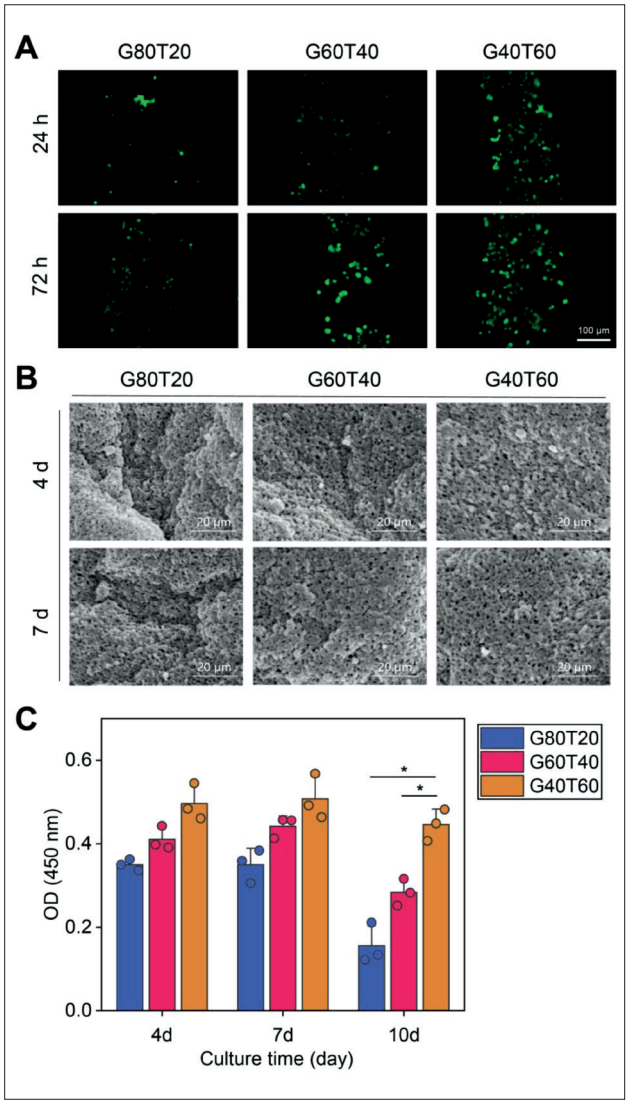

Figure 7. Biocompatibility evaluation of G40T60@WNT5A. (A) Fluorescence microscopic observation of cell viability (red/green staining). (B) Scanning electron microscopy (SEM) observation of BMSCs morphology and migration on the scaffold (scale bar: 20 μm). (C) CCK8 assay for cell proliferation. *$P < 0.05$; the experiment was repeated 3 times.

calcium deposition on the collagen fibers. Meanwhile, osteoblasts further transform into osteocytes.[67] There have been studies showing that WNT5A could directly or indirectly promote the osteogenic differentiation of BMSCs.[68]

To further investigate the effect of WNT5A-loaded G40T60 on the osteogenic differentiation of BMSCs, we co-cultured BMSCs with each group and then observed the effect of each group's treatment on the osteogenic differentiation of BMSCs. Following the ALP staining and ARS staining on the 7th and 21st days, respectively, to induce BMSCs osteogenic differentiation, compared with the PBS group, the G40T60 and WNT5A groups displayed significant ALP and ARS staining intensity, indicating that G40T60 and WNT5A significantly promoted BMSCs osteogenic differentiation. Furthermore, BMSCs osteogenic differentiation was significantly enhanced in the G40T60@WNT5A group, as compared with the G40T60 and WNT5A groups (Figure 8A and B).

Furthermore, using RT-qPCR and Western blot, we were able to detect the expression levels of osteogenic differentiation markers, such as Runx2, Osterix, Alpl, Opn, and Ocn, in BMSCs. The results showed that the expression levels of osteogenic differentiation markers in the G40T60 and WNT5A groups were significantly increased compared to the PBS group. Moreover, compared with the G40T60 and WNT5A groups, the expression levels of osteogenic differentiation markers in the G40T60@WNT5A group were significantly elevated (Figure 8C and D). H&E staining was used to examine the formation of induced membranes. The results showed that the G40T60@WNT5A group contained many cells and formed abundant parallel fibrous tissue with the scaffold (as indicated by the arrows in the image). The microvascular network was also highly developed. The number of cells and microvessel count in the G40T60 and WNT5A groups were lower than in the G40T60@WNT5A group. No significant microvessel formation was observed in the PBS control group (Figure 8E).

The above results indicated that after G40T60 was loaded with WNT5A, it could significantly promote the osteogenic differentiation of BMSCs.

3.9. Induced membrane formed by G40T60@WNT5A scaffold could promote angiogenesis in CTO&BD rats

Next, we continued to investigate whether the induced membrane formed by G40T60@WNT5A could promote angiogenesis in CTO&BD rats. Firstly, we detected the migration of UVECs in each group using the Transwell assay. The results showed that the G40T60 group exhibited a significant increase in cell migration compared to the PBS group. Compared with the PBS group, the WNT5A group exhibited significantly increased cell migration, indicating that G40T60 and WNT5A could significantly promote UVECs differentiation. Compared with the WNT5A group, the G40T60@WNT5A group showed increased cell migration in UVECs. The above results indicated that WNT5A tethered to the scaffold could enhance cell migration efficiency (Figure 9A). The scratch assay results were consistent with those of the Transwell chamber assay (Figure 9B). Compared to the control group, the migration distance of UVECs in the G40T60@WNT5A group was much longer.

Next, the angiogenic ability of UVECs in different groups was observed under an optical microscope. The

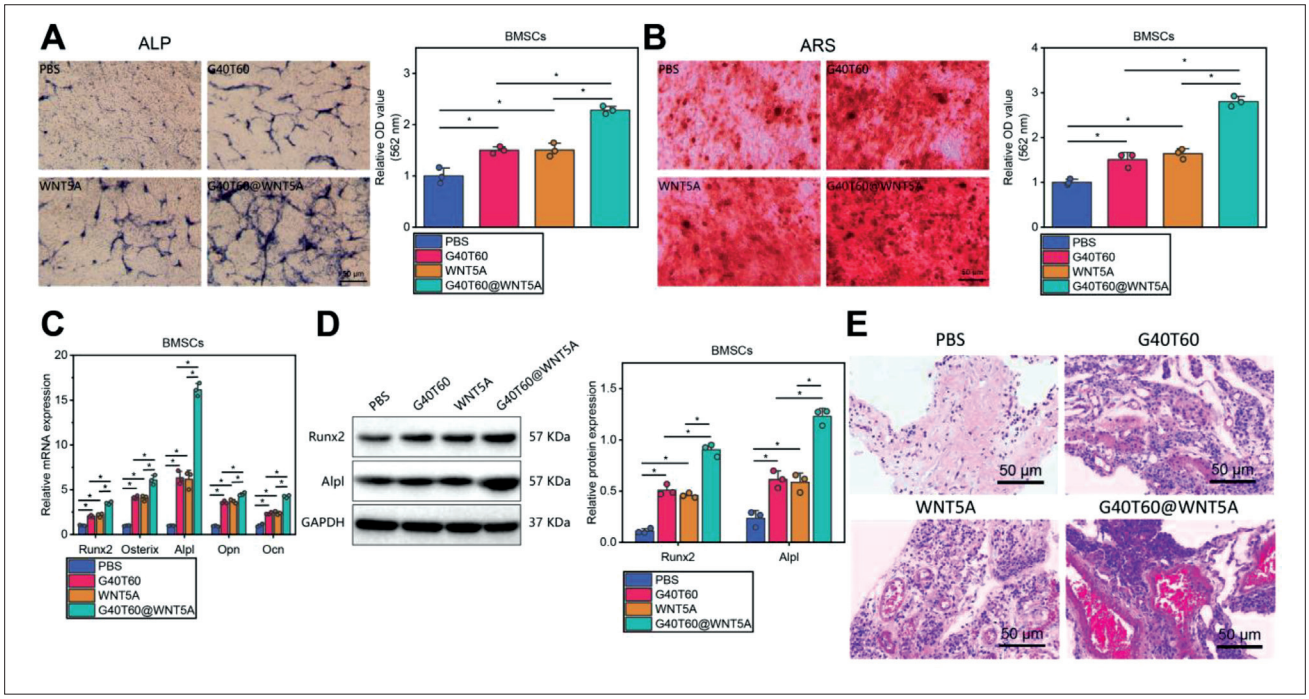

Figure 8. Influence of the induced membrane loaded with WNT5A on osteogenic differentiation and neovascularization in CTO&BD rat model (A) Alkaline phosphatase (ALP) staining for evaluating ALP activity of BMSCs in each group (scale bar: 400 μm). (B) Alizarin red S (ARS) staining for evaluating osteogenic differentiation of BMSCs in each group (scale bar: 200 μm). (C, D) RT-qPCR and Western blot analysis of gene and protein expression levels of osteogenic markers (Runx2, Osterix, Alpl, Opn, and Ocn) in BMSCs of each group. (E) Hematoxylin and eosin (H&E) staining for staining the induced membrane formed, with arrows indicating the formation of fibrous tissue (scale bar: 100 μm). * indicates comparison between two groups; the cell experiment was repeated 3 times.

results showed that the angiogenic ability of cells in the G40T60 group was significantly increased compared to the PBS group. Compared to the PBS group, the WNT5A group showed significantly increased angiogenic ability, indicating that G40T60 and WNT5A could significantly promote angiogenesis in UVECs. Additionally, compared to the WNT5A group, the G40T60@WNT5A group further enhanced the angiogenic ability of UVECs. The above results indicated that WNT5A attached to the scaffold harbors the capability to increase angiogenesis (Figure 9C–E). Finally, we assessed the gene expression levels of the key angiogenic factors, namely *Ang*, *Pecam1*, and *Vcam1*, in the UVECs of each group using RT-qPCR. The mRNA quantification results of these genes showed a significant increase in the levels of *Ang*, *Pecam1*, and *Vcam1* in UVECs cells in the G40T60@WNT5A group after treatment compared to the other control groups (Figure 9F). Western blot analysis also revealed a significant increase in the protein levels of *Ang*, *Pecam1*, and *Vcam1* in UVECs cells treated with G40T60@WNT5A compared to other control groups (Figure 9G). These findings suggested that the induced membrane formed by G40T60@WNT5A in CTO&BD rats promotes neovascularization.

4. Discussion

In this study, bioinformatics analysis revealed that WNT5A may be a critical factor in the progression of CTO&BD. Induction of Wnt5a expression has been reported to promote mesenchymal stem cell osteogenic differentiation and bone formation, as well as enhance osteoblast function in mice.[33-36,69] In addition, Pkn3 promotes the activation of Wnt5a signaling, promoting bone resorption. This pathway may be a therapeutic target for bone-related diseases, such as osteoporosis and rheumatoid arthritis.[70,71]

We obtained the G40T60@WNT5A scaffold by incorporating WNT5A into a 3D-printed biodegradable scaffold and demonstrated its excellent biocompatibility through *in vitro* cell experiments. The construction of 3D-printed scaffolds is under rapid development, and the application of 3D-printed scaffolds has been extensively reported. 3D printing has become an essential manufacturing process in skeletal engineering because it could control the volume geometry and internal structure of tissue scaffolds.[72,73] Developing optimal 3D scaffolds for bone defect repair has always been the focus of the advances in bioprinting methods. At present, the available technologies could afford cellular function, vitality, and mechanical

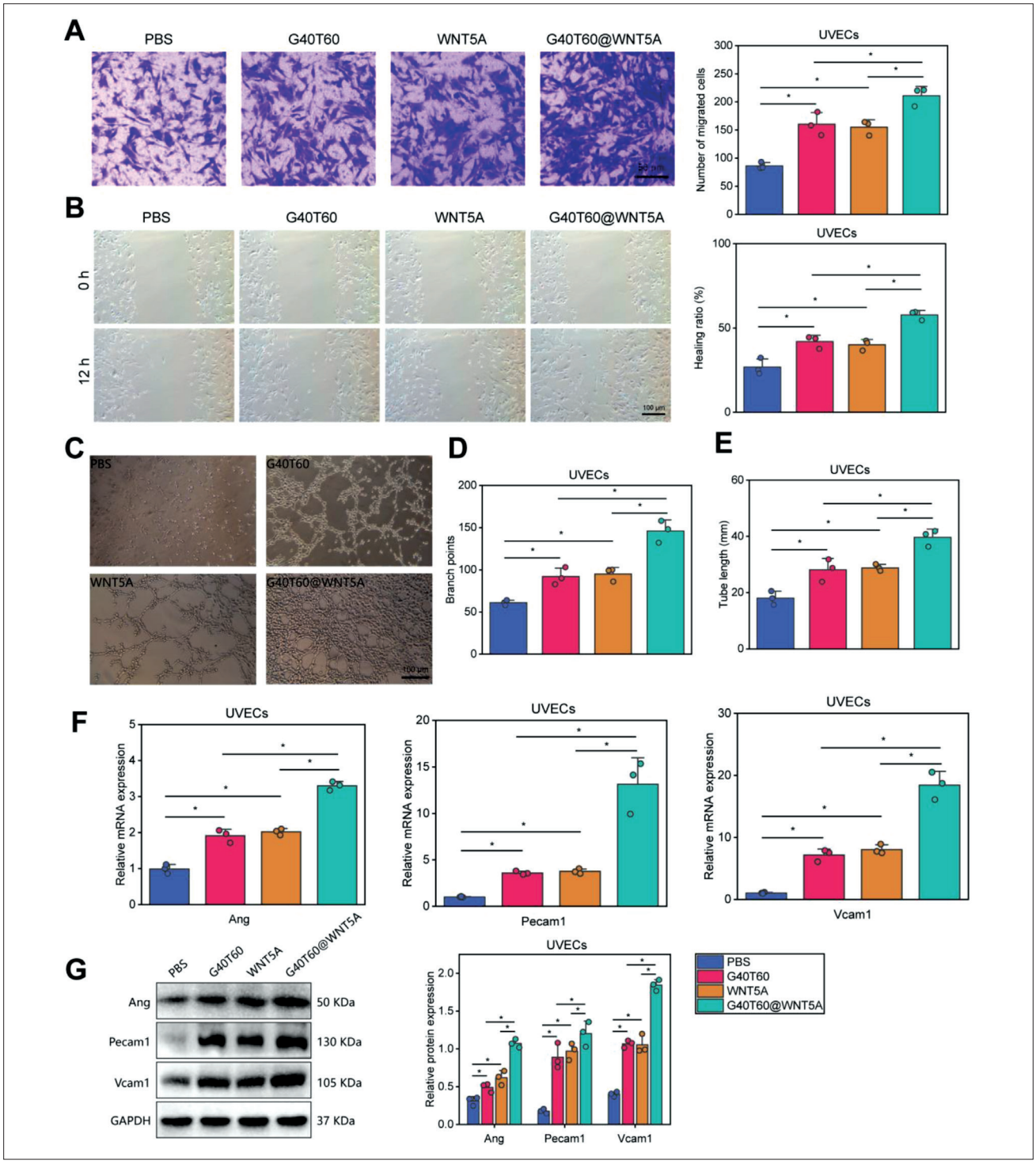

Figure 9. Influence of the induced membrane loaded with WNT5A on osteogenic differentiation and neovascularization in CTO&BD rat model. (A) Transwell assay for assessing the migration of UVECs in each group (scale bar: 200 μm). (B) Scratch assay for measuring the migration distance of UVECs in each group (scale bar: 400 μm). (C) Optical microscopic observation of the angiogenic ability of UVECs in each group (scale bar: 400 μm). (D) Branch points of tube formed by UVECs in each group. (E) Total length of tube formed by UVECs in each group. (F) RT-qPCR analysis of gene expression levels of angiogenesis-related factors (*Ang*, *Pecam1*, and *Vcam1*) in UVECs of each group. (G) Western blot and quantitative analysis of *ANG*, *PECAM1*, and *VCAM1* protein expression. **P* <0.05 between the two groups; the cell experiment was repeated 3 times.

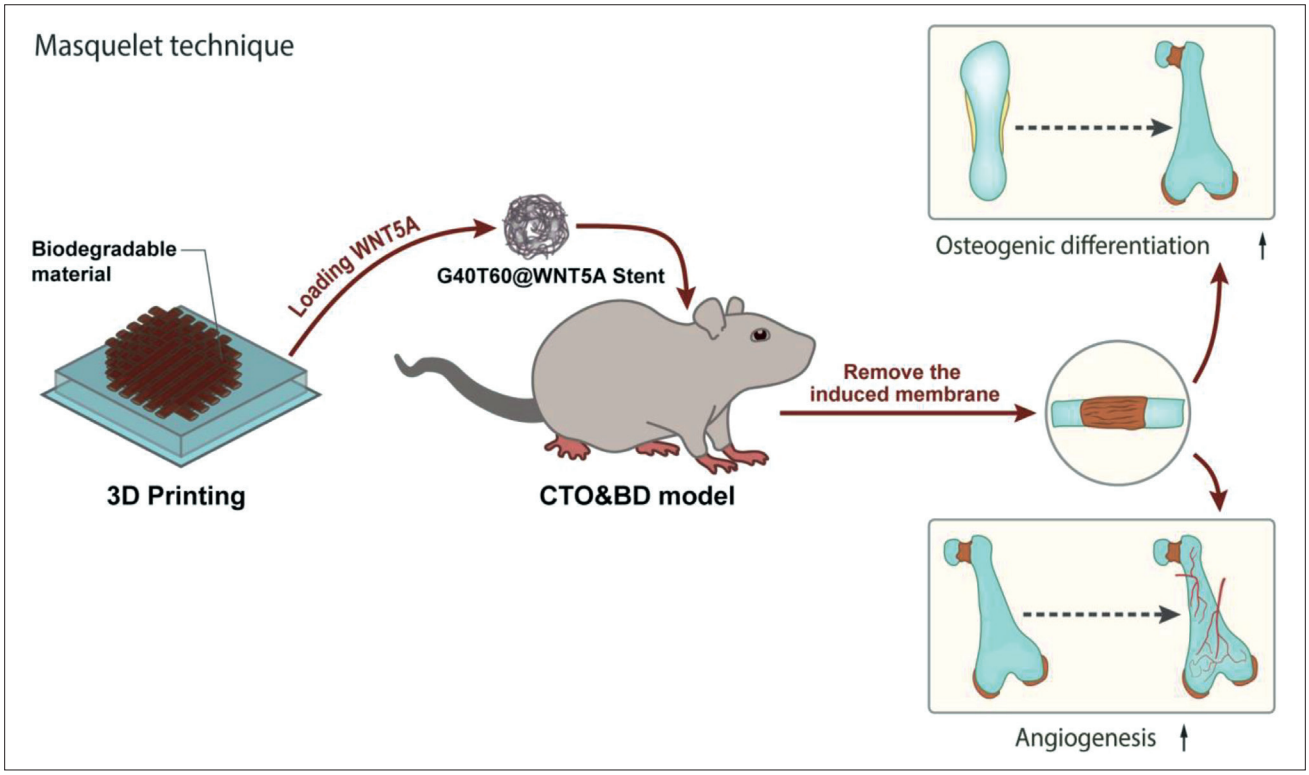

Figure 10. Mechanism behind of the therapeutic effect of a degradable WNT5A-loaded scaffold fabricated using Masquelet technique on CTO&BD by virtue of the scaffold's capacity in promoting osteogenic differentiation and angiogenesis.

integrity to 3D-printed constructs.[74] Consistent with our research findings, studies have found that 3D-printed scaffolds could direct the extracellular matrix/stromal stem cells for bone and cartilage defect regeneration.[23,32,75] In addition, according to a previous report, 3D-printed bioresorbable hydrogel scaffolds, which have high flexibility and adaptability and could be used for non-load-bearing bone regeneration, were successfully created.[31]

We confirmed that the G40T60@WNT5A scaffold could significantly promote the formation of induced membranes in a CTO&BD rat model we constructed, in which the scaffold was transplanted. The result indicated that the WNT5A-loaded, degradable G40T60 scaffold fabricated by 3D printing could promote the formation of induced membrane in a CTO&BD rat, thus facilitating osteogenic differentiation and angiogenesis. Our research is consistent with other studies, demonstrating that 3D-printed scaffolds significantly enhance bone regeneration in animal models.[32] Furthermore, 3D-printed biodegradable scaffolds have been demonstrated to promote collagen synthesis and induce membrane formation, vascularization, and osteogenesis, significantly promoting maxillofacial regeneration.[76] In addition, a few studies reported that 3D-printed degradable scaffolds in a rabbit femur cortical bone defect model delivered promising outcomes, in terms of safety during *in vivo* surgery, biodegradation, and ability to induce bone formation after membrane formation.[77,78]

We extracted the rat's induced membrane and co-cultured it with BMSCs and UVECs. The results showed that the membrane induced by the G40T60@WNT5A scaffold significantly promoted osteogenic differentiation and angiogenesis. The result indicated that 3D-printed degradable scaffolds could promote the formation of induced membrane in CTO&BD rat model, which stimulates osteogenic differentiation and vascular neogenesis. Another study has attempted to analyze the effects of a 3D-printed hydroxyapatite gel (HAP-GEL) scaffold combined with BMSCs and human umbilical vein endothelial cells (HUVECs) on repairing rabbit cranial defects, and found that the 3D-printed scaffold and the combination of BMSCs and HUVECs exhibited good osteogenic ability and biocompatibility and showed excellent results in repairing rabbit cranial defects.[79] In a study regarding the synergistic effects of co-cultivation of endothelial cells and matrix cells on 3D-printed calcium silicate-doped β-TCP scaffolds, which promote vascularization and bone formation, significantly enhanced bone formation was noted in 3D-printed porous β-TCP

and calcium silicate scaffolds co-cultured with HUVECs and BMSCs.[80]

5. Conclusion

WNT5A is a positive regulatory factor in osteoblast differentiation and angiogenesis. In this study, the degradable G40T60 scaffolds loaded with WNT5A were prepared based on Masquelet technique and using 3D printing, and we showed that they could promote the formation of induced membranes and thus facilitate osteoblast differentiation and angiogenesis in CTO&BD rats (Figure 10). This study proposes a new method for treating CTO&BD. The degradable G40T60@WNT5A scaffold we constructed using 3D printing based on the Masquelet technique successfully promoted the differentiation of osteoblasts and neovascularization in rats. This research provides a new perspective for treating chronic bone defects and has significant clinical relevance by effectively improving the quality of life for patients.

However, several limitations of this study should be acknowledged. Firstly, the experiments were conducted only in a rat model, and thus, further investigations are required for corroborating the clinical application of the scaffolds in humans. Secondly, due to cost and technological limitations, a degradable scaffold was used in this study, and the degradation rate and biocompatibility of the material need further optimization. In addition, CTO&BD is typically a chronic inflammatory process accompanied by bone destruction caused by bacterial infection; therefore, the antimicrobial properties of the G40T60@WNT5A scaffold should also be evaluated. Furthermore, this study requires further investigations into the specific mechanisms behind the role of *WNT5A* gene in osteoblast differentiation and neovascularization, as well as its interactions with other related factors. In future, it is necessary to further refine the treatment plan adopted in this study by optimizing degradation rate, improving biocompatibility of the scaffold material, and strengthening antimicrobial properties of the scaffold. Additionally, more genes and molecular mechanisms related to the development of CTO&BD, which have implications on the treatment, should be identified.

In summary, this study offers new directions to improve the treatment strategies for CTO&BD patients. Besides, the scaffolds we fabricated in this work will find broader applications in the field of orthopedics.

Acknowledgments

None.

Funding

This study was supported by Hebei Provincial Health and Health Commission Key Science and Technology Research Program (20210120, 20221202), Hebei Provincial Department of Finance Funding for Prevention and Treatment of Geriatric Diseases, and 2022 Government-funded Clinical Medicine Excellence Training Program Leader Project.

Conflict of interest

The authors declare no conflicts of interest.

Author contributions

Conceptualization: Tao Zhang
Data curation: Tao Zhang
Formal analysis: Xinhui Wang
Investigation: Rongkang Guo
Methodology: Tianhua Dong, Fan Liu
Visualization: Rongkang Guo, Xinhui Wang
Writing – original draft: Fan Liu, Chaohan Wu
Writing – review & editing: Tao Zhang, Fan Liu

Ethics approval and consent to participate

Peripheral blood samples were collected with the approval of the Ethics Committee of the Third Hospital of Hebei Medical University (Ethics Committee number: Ke-2022-104-1). All animal experiments have been approved by the Animal Ethics Committee of the Third Hospital of Hebei Medical University (No. KSD2022-033-1), and all animal experiments in this study comply with the local principles for the management and use of experimental animals. Subjects obtained their informed consent prior to participation in this study.

Consent for publication

Consent for publication was obtained from the participants.

Availability of data

The data that support the findings of this study are available on request from the corresponding author.

References

1. Montanaro L, Speziale P, Campoccia D, et al. Scenery of Staphylococcus implant infections in orthopedics. *Future Microbiol*. 2011;6(11):1329-1349. doi: 10.2217/fmb.11.117

2. Claro T, Widaa A, O'Seaghdha M, et al. *Staphylococcus aureus* protein A binds to osteoblasts and triggers signals that weaken bone in osteomyelitis. *PLoS One*. 2011;6(4):e18748. doi: 10.1371/journal.pone.0018748

3. McNally MA, Ferguson JY, Lau AC, et al. Single-stage treatment of chronic osteomyelitis with a new absorbable, gentamicin-loaded, calcium sulphate/hydroxyapatite biocomposite: A prospective series of 100 cases. *Bone Joint J*. 2016;98-B(9):1289-1296.
doi: 10.1302/0301-620X.98B9.38057

4. Bury DC, Rogers TS, Dickman MM. Osteomyelitis: Diagnosis and treatment. *Am Fam Physician*. 2021;104(4):395-402.

5. Hofmann SR, Kapplusch F, Girschick HJ, et al. Chronic recurrent multifocal osteomyelitis (CRMO): Presentation, pathogenesis, and treatment. *Curr Osteoporos Rep*. 2017;15(6):542-554.
doi: 10.1007/s11914-017-0405-9

6. Conterno LO, Turchi MD. Antibiotics for treating chronic osteomyelitis in adults. *Cochrane Database Syst Rev*. 2013;(9):CD004439.
doi: 10.1002/14651858.CD004439.pub3

7. Leerling AT, Clunie G, Koutrouba E, Dekkers OM, Appelman-Dijkstra NM, Winter EM. Diagnostic and therapeutic practices in adult chronic nonbacterial osteomyelitis (CNO). *Orphanet J Rare Dis*. 2023;18(1):206.
doi: 10.1186/s13023-023-02831-1

8. Guo B, Zhao W, Wu H, et al. Ilizarov metatarsal bone lengthening in treatment of diabetic foot ulcer complicated with chronic osteomyelitis of metatarsal head. *Zhongguo Xiu Fu Chong Jian Wai Ke Za Zhi*. 2020;34(8):1000-1004.
doi: 10.7507/1002-1892.201911070

9. Chou PH, Lin HH, Su YP, Chiang CC, Chang MC, Chen CM. Staged protocol for the treatment of chronic femoral shaft osteomyelitis with Ilizarov's technique followed by the use of intramedullary locked nail. *J Chin Med Assoc*. 2017;80(6):376-382.
doi: 10.1016/j.jcma.2017.01.001

10. Kliushin NM, Burnashov SI, Mekki WA, Leonchuk DS, Sudnitsyn AS. Treatment of postoperative tibial chronic osteomyelitis using bone transport techniques; an observational study. *J Clin Orthop Trauma*. 2021;24:101652.
doi: 10.1016/j.jcot.2021.101652

11. Xiang F, Fan W, Liang J, Yang Y. Ilizarov technique in treating chronic osteomyelitis of the tibia with severe malformation and skin canceration: A case report. *Asian J Surg*. 2023;46(5):2231-2232.
doi: 10.1016/j.asjsur.2022.11.117

12. Sergi CM, Miller E, Demellawy DE, Shen F, Zhang M. Chronic recurrent multifocal osteomyelitis. A narrative and pictorial review. *Front Immunol*. 2022;13:959575.
doi: 10.3389/fimmu.2022.959575

13. Masquelet A, Kanakaris NK, Obert L, Stafford P, Giannoudis PV. Bone repair using the Masquelet technique. *J Bone Joint Surg Am*. 2019;101(11):1024-1036.
doi: 10.2106/JBJS.18.00842

14. Careri S, Vitiello R, Oliva MS, Ziranu A, Maccauro G, Perisano C. Masquelet technique and osteomyelitis: Innovations and literature review. *Eur Rev Med Pharmacol Sci*. 2019;23(2 Suppl):210-216.
doi: 10.26355/eurrev_201904_17495

15. Klein C, Monet M, Barbier V, et al. The Masquelet technique: Current concepts, animal models, and perspectives. *J Tissue Eng Regen Med*. 2020;14(9):1349-1359.
doi: 10.1002/term.3097

16. Khaled A, El-Gebaly O, El-Rosasy M. Masquelet-Ilizarov technique for the management of bone loss post debridement of infected tibial nonunion. *Int Orthop*. 2022;46(9):1937-1944.
doi: 10.1007/s00264-022-05494-y

17. Zhang L, Lu C, Lv Y, Wang X, Guo S, Zhang H. Three-dimensional printing-assisted Masquelet technique in the treatment of calcaneal defects. *Orthop Surg*. 2021;13(3):876-883.
doi: 10.1111/os.12873

18. Wu Y, Shi X, Zi S, et al. The clinical application of customized 3D-printed porous tantalum scaffolds combined with Masquelet's induced membrane technique to reconstruct infective segmental femoral defect. *J Orthop Surg Res*. 2022;17(1):479.
doi: 10.1186/s13018-022-03371-3

19. Liu X, Liu Y, Lu W, et al. Combined application of modified three-dimensional printed anatomic templates and customized cutting blocks in pelvic reconstruction after pelvic tumor resection. *J Arthroplasty*. 2019;34(2):338-345.e1.
doi: 10.1016/j.arth.2018.10.001

20. Vasiliadis AV, Koukoulias N, Katakalos K. From three-dimensional (3D)- to 6D-printing technology in orthopedics: Science fiction or scientific reality?. *J Funct Biomater*. 2022;13(3):101. Published 2022 Jul 21.
doi: 10.3390/jfb13030101

21. Li B, Zhang M, Lu Q, et al. Application and development of modern 3D printing technology in the field of orthopedics. *Biomed Res Int*. 2022;2022:8759060.
doi: 10.1155/2022/8759060

22. Xu L, Qin H, Tan J, et al. Clinical study of 3D printed personalized prosthesis in the treatment of bone defect after pelvic tumor resection. *J Orthop Translat*. 2021;29:163-169.
doi: 10.1016/j.jot.2021.05.007

23. Ganguly P, Jones E, Panagiotopoulou V, et al. Electrospun and 3D printed polymeric materials for one-stage critical-size long bone defect regeneration inspired by the Masquelet technique: Recent advances. *Injury*. 2022;53(Suppl 2):S2-S12.
doi: 10.1016/j.injury.2022.02.036

24. George A, Shah PA, Shrivastav PS. Natural biodegradable polymers based nano-formulations for drug delivery: A review. *Int J Pharm*. 2019;561:244-264.
doi: 10.1016/j.ijpharm.2019.03.011

25. Ulery BD, Nair LS, Laurencin CT. Biomedical applications of biodegradable polymers. *J Polym Sci B Polym Phys*. 2011;49(12):832-864. doi: 10.1002/polb.22259

26. Feng Y, Zhu S, Mei D, et al. Application of 3D printing technology in bone tissue engineering: A review. *Curr Drug Deliv*. 2021;18(7):847-861. doi: 10.2174/1567201817999201113100322

27. Gumienna M, Górna B. Antimicrobial food packaging with biodegradable polymers and bacteriocins. *Molecules*. 2021;26(12):3735. doi: 10.3390/molecules26123735

28. Stroganov V, Al-Hussein M, Sommer JU, Janke A, Zakharchenko S, Ionov L. Reversible thermosensitive biodegradable polymeric actuators based on confined crystallization. *Nano Lett*. 2015;15(3):1786-1790. doi: 10.1021/nl5045023

29. Liu X, Holzwarth JM, Ma PX. Functionalized synthetic biodegradable polymer scaffolds for tissue engineering. *Macromol Biosci*. 2012;12(7):911-919. doi: 10.1002/mabi.201100466

30. Asghari F, Samiei M, Adibkia K, Akbarzadeh A, Davaran S. Biodegradable and biocompatible polymers for tissue engineering application: A review. *Artif Cells Nanomed Biotechnol*. 2017;45(2):185-192. doi: 10.3109/21691401.2016.1146731

31. He M, Hou Y, Zhu C, et al. 3D-printing biodegradable PU/PAAM/Gel hydrogel scaffold with high flexibility and self-adaptibility to irregular defects for nonload-bearing bone regeneration. *Bioconjug Chem*. 2021;32(8):1915-1925. doi: 10.1021/acs.bioconjchem.1c00322

32. Chen P, Zheng L, Wang Y, et al. Desktop-stereolithography 3D printing of a radially oriented extracellular matrix/mesenchymal stem cell exosome bioink for osteochondral defect regeneration. *Theranostics*. 2019;9(9):2439-2459. doi: 10.7150/thno.31017

33. Duan DY, Tang J, Tian HT, Shi YY, Jia J. Adipocyte-secreted microvesicle-derived miR-148a regulates adipogenic and osteogenic differentiation by targeting Wnt5a/Ror2 pathway. *Life Sci*. 2021;278:119548. doi: 10.1016/j.lfs.2021.119548

34. Park HW, Kim YC, Yu B, et al. Alternative Wnt signaling activates YAP/TAZ. *Cell*. 2015;162(4):780-794. doi: 10.1016/j.cell.2015.07.013

35. Zhang X, Chang M, Wang B, Liu X, Zhang Z, Han G. YAP/WNT5A/FZD4 axis regulates osteogenic differentiation of human periodontal ligament cells under cyclic stretch. *J Periodontal Res*. 2023;58(5):907-918. doi: 10.1111/jre.13143

36. Chen Y, Chen Q, Zhong M, Xu C, Wu Y, Chen R. miR-637 inhibits osteogenic differentiation of human intervertebral disc cartilage endplate stem cells by targeting WNT5A. *J Invest Surg*. 2022;35(6):1313-1321. doi: 10.1080/08941939.2022.2050857

37. Gu Q, Tian H, Zhang K, et al. Wnt5a/FZD4 mediates the mechanical stretch-induced osteogenic differentiation of bone mesenchymal stem cells. *Cell Physiol Biochem*. 2018;48(1):215-226. doi: 10.1159/000491721

38. Chen Y, Zhang Y, Deng Q, et al. Inhibition of Wnt inhibitory factor 1 under hypoxic condition in human umbilical vein endothelial cells promoted angiogenesis in vitro. *Reprod Sci*. 2016;23(10):1348-1358. doi: 10.1177/1933719116638174

39. Yan J, Dennin RH. High homologous nucleotide to GBV-C was amplified from DNA of MT2 and HeLa cells and PBMC of human and chimpanzee. *Acta Pharmacol Sin*. 2001;22(4):320-326.

40. Grievink HW, Luisman T, Kluft C, Moerland M, Malone KE. Comparison of three isolation techniques for human peripheral blood mononuclear cells: Cell recovery and viability, population composition, and cell functionality. *Biopreserv Biobank*. 2016;14(5):410-415. doi: 10.1089/bio.2015.0104

41. Hashimoto S, Noguchi E, Bando H, et al. Neoantigen prediction in human breast cancer using RNA sequencing data. *Cancer Sci*. 2021;112(1):465-475. doi: 10.1111/cas.14720

42. Li XN, Wang ZJ, Ye CX, Zhao BC, Li ZL, Yang Y. RNA sequencing reveals the expression profiles of circRNA and indicates that circDDX17 acts as a tumor suppressor in colorectal cancer. *J Exp Clin Cancer Res*. 2018;37(1):325. doi: 10.1186/s13046-018-1006-x

43. Zhang Z, Jia H, Gu T, et al. RNA sequencing and bioinformatics analysis of the long noncoding RNA-mRNA network in colorectal cancer. *J Cell Biochem*. 2018;119(12):9957-9966. doi: 10.1002/jcb.27319

44. Wan J, Liu B. Construction of lncRNA-related ceRNA regulatory network in diabetic subdermal endothelial cells. *Bioengineered*. 2021;12(1):2592-2602. doi: 10.1080/21655979.2021.1936892

45. Zhou Y, Shi W, Zhao D, Xiao S, Wang K, Wang J. Identification of immune-associated genes in diagnosing aortic valve calcification with metabolic syndrome by integrated bioinformatics analysis and machine learning. *Front Immunol*. 2022;13:937886. doi: 10.3389/fimmu.2022.937886

46. Yang C, Delcher C, Shenkman E, Ranka S. Machine learning approaches for predicting high cost high need patient expenditures in health care. *Biomed Eng Online*. 2018;17(Suppl 1):131. doi: 10.1186/s12938-018-0568-3

47. Ellis K, Kerr J, Godbole S, Lanckriet G, Wing D, Marshall S. A random forest classifier for the prediction of energy expenditure and type of physical activity from wrist and hip accelerometers. *Physiol Meas*. 2014;35(11):2191-2203.

doi: 10.1088/0967-3334/35/11/2191

48. Zhang M, Zhu K, Pu H, et al. An immune-related signature predicts survival in patients with lung adenocarcinoma. *Front Oncol*. 2019;9:1314. doi: 10.3389/fonc.2019.01314

49. Alderden J, Pepper GA, Wilson A, et al. Predicting pressure injury in critical care patients: A machine-learning model. *Am J Crit Care*. 2018;27(6):461-468. doi: 10.4037/ajcc2018525

50. Li J, Liu C, Chen Y, et al. Tumor characterization in breast cancer identifies immune-relevant gene signatures associated with prognosis. *Front Genet*. 2019;10:1119. doi: 10.3389/fgene.2019.01119

51. Zhu M, Ye M, Wang J, Ye L, Jin M. Construction of potential miRNA-mRNA regulatory network in COPD plasma by bioinformatics analysis. *Int J Chron Obstruct Pulmon Dis*. 2020;15:2135-2145. doi: 10.2147/COPD.S255262

52. Jeong JE, Park SY, Shin JY, et al. 3D printing of bone-mimetic scaffold composed of gelatin/β-tri-calcium phosphate for bone tissue engineering. *Macromol Biosci*. 2020;20(12):e2000256. doi: 10.1002/mabi.202000256

53. Jin J, Ou Q, Wang Z, et al. BMSC-derived extracellular vesicles intervened the pathogenic changes of scleroderma in mice through miRNAs. *Stem Cell Res Ther*. 2021;12(1):327. doi: 10.1186/s13287-021-02400-y

54. Lou Z, Peng Z, Wang B, Li X, Li X, Zhang X. miR-142-5p promotes the osteoclast differentiation of bone marrow-derived macrophages via PTEN/PI3K/AKT/FoxO1 pathway. *J Bone Miner Metab*. 2019;37(5):815-824. doi: 10.1007/s00774-019-00997-y

55. Li R, Zhou C, Chen J, et al. Synergistic osteogenic and angiogenic effects of KP and QK peptides incorporated with an injectable and self-healing hydrogel for efficient bone regeneration. *Bioact Mater*. 2022;18:267-283. doi: 10.1016/j.bioactmat.2022.02.011

56. Messner K, Wei Y, Andersson B, Gillquist J, Räsänen T. Rat model of Achilles tendon disorder. A pilot study. *Cells Tissues Organs*. 1999;165(1):30-39. doi: 10.1159/000016671

57. Wu J, Pan X, Fu H, et al. Effect of curcumin on glycerol-induced acute kidney injury in rats. *Sci Rep*. 2017;7(1):10114. doi: 10.1038/s41598-017-10693-4

58. Wang C, Liang C, Ma J, et al. Co-exposure to fluoride and sulfur dioxide on histological alteration and DNA damage in rat brain. *J Biochem Mol Toxicol*. 2018;32(2). doi: 10.1002/jbt.22023

59. Xu Y, Zhou J, Liu C, et al. Understanding the role of tissue-specific decellularized spinal cord matrix hydrogel for neural stem/progenitor cell microenvironment reconstruction and spinal cord injury. *Biomaterials*. 2021;268:120596. doi: 10.1016/j.biomaterials.2020.120596

60. Zhou W, Zhou Y, Chen X, et al. Pancreatic cancer-targeting exosomes for enhancing immunotherapy and reprogramming tumor microenvironment. *Biomaterials*. 2021;268:120546. doi: 10.1016/j.biomaterials.2020.120546

61. Wu Q, Yi X. Down-regulation of long noncoding RNA MALAT1 protects hippocampal neurons against excessive autophagy and apoptosis via the PI3K/Akt signaling pathway in rats with epilepsy. *J Mol Neurosci*. 2018;65(2):234-245. doi: 10.1007/s12031-018-1093-3

62. Shen J, Sun Y, Liu X, et al. EGFL6 regulates angiogenesis and osteogenesis in distraction osteogenesis via Wnt/β-catenin signaling. *Stem Cell Res Ther*. 2021;12(1):415. doi: 10.1186/s13287-021-02487-3

63. He X, Liu W, Liu Y, et al. Nano artificial periosteum PLGA/MgO/Quercetin accelerates repair of bone defects through promoting osteogenic - angiogenic coupling effect via Wnt/β-catenin pathway. *Mater Today Bio*. 2022;16:100348. doi: 10.1016/j.mtbio.2022.100348

64. Wu M, Chen F, Liu H, et al. Bioinspired sandwich-like hybrid surface functionalized scaffold capable of regulating osteogenesis, angiogenesis, and osteoclastogenesis for robust bone regeneration. *Mater Today Bio*. 2022;17:100458. doi: 10.1016/j.mtbio.2022.100458

65. Baschant U, Rauner M, Balaian E, et al. Wnt5a is a key target for the pro-osteogenic effects of iron chelation on osteoblast progenitors. *Haematologica*. 2016;101(12):1499-1507. doi: 10.3324/haematol.2016.144808

66. Wan X, Guan S, Hou Y, et al. FOSL2 promotes VEGF-independent angiogenesis by transcriptionnally activating Wnt5a in breast cancer-associated fibroblasts. *Theranostics*. 2021;11(10):4975-4991. doi: 10.7150/thno.55074

67. Clarke B. Normal bone anatomy and physiology. *Clin J Am Soc Nephrol*. 2008;3(Suppl 3):S131-S139. doi: 10.2215/CJN.04151206

68. Yang T, Zhang J, Cao Y, et al. Wnt5a/Ror2 mediates temporomandibular joint subchondral bone remodeling. *J Dent Res*. 2015;94(6):803-812. doi: 10.1177/0022034515576051

69. Brun J, Fromigué O, Dieudonné FX, et al. The LIM-only protein FHL2 controls mesenchymal cell osteogenic differentiation and bone formation through Wnt5a and Wnt10b. *Bone*. 2013;53(1):6-12. doi: 10.1016/j.bone.2012.11.020

70. Uehara S, Udagawa N, Mukai H, et al. Protein kinase N3 promotes bone resorption by osteoclasts in response to Wnt5a-Ror2 signaling. *Sci Signal*. 2017;10(494):eaan0023. doi: 10.1126/scisignal.aan0023

71. Uehara S, Udagawa N, Kobayashi Y. Regulation of osteoclast function via Rho-Pkn3-c-Src pathways. *J Oral Biosci*. 2019;61(3):135-140.
doi: 10.1016/j.job.2019.07.002

72. Wang Z, Wang Y, Yan J, et al. Pharmaceutical electrospinning and 3D printing scaffold design for bone regeneration. *Adv Drug Deliv Rev*. 2021;174:504-534.
doi: 10.1016/j.addr.2021.05.007

73. Wang S, Zhao S, Yu J, Gu Z, Zhang Y. Advances in translational 3D printing for cartilage, bone, and osteochondral tissue engineering. *Small*. 2022;18(36):e2201869.
doi: 10.1002/smll.202201869

74. Zhang L, Yang G, Johnson BN, Jia X. Three-dimensional (3D) printed scaffold and material selection for bone repair. *Acta Biomater*. 2019;84:16-33.
doi: 10.1016/j.actbio.2018.11.039

75. Xu J, Ji J, Jiao J, et al. 3D Printing for bone-cartilage interface regeneration. *Front Bioeng Biotechnol*. 2022;10:828921.
doi: 10.3389/fbioe.2022.828921

76. Chang PC, Lin ZJ, Luo HT, et al. Degradable RGD-functionalized 3D-printed scaffold promotes osteogenesis. *J Dent Res*. 2021;100(10):1109-1117.
doi: 10.1177/00220345211024634

77. Wu N, Liu J, Ma W, et al. Degradable calcium deficient hydroxyapatite/poly(lactic-glycolic acid copolymer) bilayer scaffold through integral molding 3D printing for bone defect repair. *Biofabrication*. 2021;13(2).
doi: 10.1088/1758-5090/abcb48

78. Yang Y, Chu L, Yang S, et al. Dual-functional 3D-printed composite scaffold for inhibiting bacterial infection and promoting bone regeneration in infected bone defect models. *Acta Biomater*. 2018;79:265-275.
doi: 10.1016/j.actbio.2018.08.015

79. Wang H, Fan HX, Cheng HZ, Li R, Geng HX. Shanghai Kou Qiang Yi Xue. 2021;30(1):28-32.

80. Deng Y, Jiang C, Li C, et al. 3D printed scaffolds of calcium silicate-doped β-TCP synergize with co-cultured endothelial and stromal cells to promote vascularization and bone formation. *Sci Rep*. 2017;7(1):5588.
doi: 10.1038/s41598-017-05196-1

ACCSCIENCE PUBLISHING

International Journal of Bioprinting

RESEARCH ARTICLE

3D bioprinting of adhesive, anti-bacterial alginate/polyacrylamide-based customized boluses using digital light processing for radiotherapy applications

Ying Lu[1,2], Xiaomin Zhang[3], Youjie Rong[3], Yannan Xu[2,4], Xiaohong Yao[3], Guobao Pang[2], Qinying Shi[2,4], Xiaobo Huang[3]*, Meiwen An[1]*, and Jianbo Song[2]*

[1]Biomedical Engineering Department, College of Biomedical Engineering, Taiyuan University of Technology, Taiyuan, Shanxi, China

[2]Radiation Therapy Center, Shanxi Bethune Hospital, Shanxi Academy of Medical Sciences, Tongji Shanxi Hospital, Third Hospital of Shanxi Medical University, Taiyuan, Shanxi, China

[3]Materials Science and Engineering Department, School of Materials Science and Engineering, Taiyuan University of Technology, Taiyuan, Shanxi, China

[4]Shanxi Provincial Key Laboratory for Translational Nuclear Medicine and Precision Protection, Taiyuan, Shanxi, China

Abstract

Boluses are a type of materials used to enhance skin dose during the treatment of superficial lesions. However, the current commercially available boluses cannot fully conform to irregular skin surfaces due to their uniform thickness, thereby compromising the efficacy of radiotherapy. Three-dimensional (3D) bioprinting boasts a huge potential in the creation of customized boluses, but the use of this technique is limited by shortcomings of the prevailing materials, such as their indirect printability and substance rigidity. As a potential substitute, hydrogels possessing a tensile modulus comparable to that of skin tissue are optimal candidates for customizing boluses. In this study, we developed a photocurable bioink for multifunctional boluses using digital light processing (DLP). Alginate, acrylamide, polyethylene glycol diacrylate, lithium phenyl-2,4,6-trimethylbenzoylphosphinate, and protocatechuic acid were synergistically combined to fabricate the bioink. The bolus printed using this bioink was endowed with enhanced toughness, superior adhesion, tissue equivalence, anti-dehydration and anti-bacterial properties, as well as excellent biocompatibility and radiation performance. In conclusion, the DLP-based 3D bioprinting of the proposed bioink can provide an avenue for obtaining personalized boluses in radiotherapy treatment of superficial tumors.

Keywords: Photocurable 3D bioprinting; Composite gel; Multifunctional bolus; Radiotherapy

***Corresponding authors:**
Xiaobo Huang
(huangtyut@163.com)
Meiwen An
(anmeiwen@tyut.edu.cn)
Jianbo Song
(jianbo2611@sxmu.edu.cn)

Citation: Lu Y, Zhang X, Rong Y, et al. 3D bioprinting of adhesive, anti-bacterial alginate/polyacrylamide-based customized boluses using digital light processing for radiotherapy applications. *Int J Bioprint*. 2024;10(2):1589. doi: 10.36922/ijb.1589

Received: August 12, 2023
Accepted: October 13, 2023
Published Online: January 9, 2024

1. Introduction

Radiotherapy plays a crucial role in the therapeutic management of tumors. The build-up effect of high-energy radiation is advantageous in depositing high doses in deep

tissues[1,2]. When dealing with superficial lesions, it is necessary to use boluses with a suitable thickness, which are a class of materials applied on patients, to increase the skin dose and bolster therapeutic outcomes[3,4].

Despite being widely used in clinical practice, commercial sheet boluses often fail to establish perfect skin contact in complex and irregular regions, resulting in the formation of air gaps between the bolus and skin[5]. The air gaps have a detrimental impact on the surface dose, particularly in light of the growing utilization of advanced radiotherapy technologies, such as volume-modulated arc therapy (VMAT) and intensity-modulated radiation therapy (IMRT)[6,7]. Therefore, to achieve better treatment outcome, customized boluses that can precisely conform to any skin contour are urgently required.

At present, various materials are known to have been printed in the construction of customized boluses[3,8-11]. Polylactic acid (PLA) and acrylonitrile butadiene styrene (ABS) are two commonly employed materials that can be directly printed; however, their rigidity may cause discomfort to patients with sensitive skin[12-14]. Silicone rubber is often used as a filling material by virtue of its excellent biocompatibility and chemical stability[15,16]; however, it exhibits a density of 1.1–1.2 g/cm^3, which presents a density difference when compared to human tissue. Recently, Kong *et al.* have fabricated a bolus using hydrogel as the filling material[17]. Although the structural and physical properties of hydrogels resemble those of human soft tissue, several disadvantages have deterred us from using hydrogels to prepare boluses. Firstly, the application of hydrogel to skin may leave a gap between them. Secondly, the hydrogel is prone to water loss and deformation. Finally, reports have shown that approximately 85% of cancer patients developed dermatitis in hydrogel-exposed areas that are susceptible to bacterial infection[18,19]. This points to a critical shortcoming of the hydrogels available on the current market, i.e., the lack of anti-bacterial activity, which renders them ineffective in preventing radiation dermatitis. Nevertheless, the development of a bioink with superior properties such as mechanical strength (excellent adhesiveness), anti-hydration, and biocompatibility remains a challenge.

In light of these challenges, three-dimensional (3D) bioprinting stands out as an important method for enhancing the properties of printed materials. A 3D bioprinting approach appropriate for processing bolus must possess three crucial features, namely swift printing speed, moderate printing size, and overall printing precision. Extrusion and inkjet printing methods employ a nozzle to dispense the polymers to the intended position and then harden them through a curing process. However, the use of point-to-point printing leads to a slow printing speed, significantly hampering the manufacturing efficiency of customized boluses[20,21]. On the other hand, vat photopolymerization-based bioprinting can selectively solidify polymers directly from a liquid tank while conducting the patterning and curing processes simultaneously[22]. As one of the photocurable 3D printing technologies, digital light process (DLP) has attracted wide attention on the grounds of its layer-by-layer molding method and rapid printing speed. Various medical devices can be manufactured using DLP printing[1-3]. Therefore, among various 3D bioprinting methods, the DLP technique that utilizes layer photocuring appears to be the most suitable technology for printing customized boluses.

In recent years, natural polyphenols, such as tannic acid, gallate, and protocatechuic acid (PA), have gained increasing attention due to their ability to endow hydrogels with anti-oxidative, anti-bacterial, and anti-inflammatory effects[23,24]. In this study, we incorporated PA into an alginate (ALG) and acrylamide (AM) double network (DN) using a glycerin/water solvent to create a composite bioink for creating personalized multifunctional bolus. The designed bioink is compatible with DLP printing, which offers faster building speed and higher manufacturing accuracy. Our constructed gel features a DN structure that exhibits excellent mechanical properties and has superior adhesion to the skin surface. Moreover, it is an organic gel that exhibits superior stability and anti-dehydration properties. Given the excellent biocompatibility and anti-bacterial properties it possesses, radiation-induced dermatitis can be mitigated to a certain extent. This study presents an innovative preparation method for radiotherapy bolus and opens up new avenues for the application of multifunctional gels.

2. Materials and methods

2.1. Materials

The commercial bolus (Klarity, China) was utilized as control in this study. ALG, AM, PA, and polyethylene glycol dimethacrylate (PEGDA, MW = 575) were procured from Shanghai MACKLIN Co., Ltd. Glycerol (GLY) was obtained from Tianjin Fengchuan Chemical Reagent Technology Co., Ltd. Live/Dead staining kit and cytoskeleton staining kit were obtained from Invitrogen and Sigma, respectively. Lithium phenyl-2,4,6-trimethylbenzoylphosphinate (LAP) was provided by Jiangyin StemEasy. The chemicals employed in this experiment were of analytical grade and did not require further purification, while deionized water was utilized throughout the experiments.

2.2. Preparation of gels

To prepare the bioink, a solution consisting of water and GLY was used to dissolve ALG and AM (20 wt%)

powders. Subsequently, PA, PEGDA (0.2 mol% of AM), LAP (0.1 wt%), and tartrazine (Tar; 0.0035 wt%) were gradually added under stirring to create the gel precursors. Subsequent procedures were carried out in the absence of light due to the high photosensitivity of the initiator. A series of water-to-glycerol ratios, i.e., 50%, 70%, and 80%, were tested to investigate their impact on the bioink, while different concentrations of ALG (0.5 wt%, 1 wt%, and 2 wt%) were examined to assess their influence on the mechanical properties of the resulting gel. Additionally, three distinct concentrations of PA (0.5 wt%, 3 wt%, and 6 wt%) were prepared to evaluate its anti-bacterial and adhesive properties. All bioinks were stored away from light.

To investigate the effect of different components on the properties of the hydrogel, five hydrogel samples were fabricated and labeled as PAM (polyacrylamide), PAM/ALG, PAM/ALG/PA, PAM/ALG/PA (GW), and PAM/ALG/PA/Tar (GW), in which GW denotes that the hydrogel was formed in glycerol-water (GW) binary solvent.

2.3. Physicochemical properties

2.3.1. Structural characterization

To assess the impact of ALG and PA on gel microstructure, composite gels were subjected to freeze-drying and subsequently coated with gold/palladium. The cross-sectional morphology of the gels was examined using a scanning electron microscope (SEM; JSM-7001F, JEOL, Japan). To investigate the structure of the composite gel, Fourier-transform infrared spectroscopy (FTIR) spectra (Bruker Daltonics, Bremen, Germany) were obtained at 22°C over a range of 500 to 4000 cm^{-1}.

2.3.2. Photoresponsive performance

The photocuring time of the bioink was determined using a rheometer (MCR 702 Anton Paar) equipped with an optics attachment (405 nm). The bioink was loaded onto a parallel plate with a gap size of 200 μm. An ultraviolet light with an intensity of 2 mW/cm^2 was used to illuminate the plate window, and the time required for photocuring was measured.

Additionally, a rheometer was employed to quantify the viscosity of the solution. The gel's viscosity was assessed at ambient temperature by rotating it at a rate of 2 revolutions per second using a 25 mm parallel plate clamp. Moreover, a sweep test was conducted with an angular frequency of 6 rad/s to monitor the temporal evolution of both loss modulus and storage modulus for gels.

2.3.3. Mechanical properties

The mechanical properties of the gels were evaluated using a universal testing machine (RGM-2010, Reger, China). Tensile tests were performed on the gel samples, with height and diameter measuring 10 mm and 18 mm, respectively. The compression speed was set at 5 mm/min. To ensure accuracy and repeatability, all samples were tested in triplicate under consistent conditions.

The elastic modulus of the gels was determined by calculating the stress–strain curve within a strain range of 5% to 10%. Additionally, tensile-adhesion tests were cyclically performed on porcine skin to evaluate the repeatability of the gel's adhesive properties. Adhesion strength was calculated as the maximum force divided by bonded area.

2.4. Biological properties

2.4.1. Evaluation of anti-bacterial efficacy

To assess the anti-bacterial efficacy of the specimens against *Staphylococcus aureus* (ATCC6538), quantitative evaluations were performed using both Live/Dead staining assay and spread plate analysis. The bacteria were cultured in a sterile liquid medium consisting of 1 g peptone, 0.5 g beef extract, and 0.5 g NaCl in 100 mL deionized water. A bacterial suspension of 1×10^6 CFU mL^{-1} was then incubated with the gels in a 24-well plate. Subsequently, the treated bacterial suspension was diluted to 1×10^3 CFU mL^{-1}, then the diluted bacterial suspension (80 μL) was spread onto agar medium and incubated for 24 h, followed by colony counting on the agar plate to determine anti-bacterial efficacy. The tests were conducted in triplicate to ensure reliability.

2.4.2. Cell viability and proliferation

NIH-3T3 cells (mouse embryonic fibroblast, ATCC CRL-1658) were employed to evaluate the cytocompatibility of the composite gel. Initially, the gels were prepared in 24-well plate and subsequently diluted gel leaching were co-cultured with cells (at a density of 2×10^4 cells per well) for 1, 3, and 5 days. Fifty microliter of a solution containing live/dead fluorescent dyes (0.5 μL mL^{-1} calcein AM and 2 μL mL^{-1} ethylenediamine homodimer (EthD-1)) was added to the slides, followed by a 40-min staining process in the dark. Following washing with phosphate-buffered saline, confocal laser scanning microscopy (CLSM) was utilized to capture images of green viable cells and red non-viable cells.

Furthermore, the cytocompatibility of the composite gels was assessed by means of the 3-(4,5-dimethylthiazol-2-yl)-2,5-diphenyl tetrazolium bromide (MTT) assay. The experiments were carried out in triplicate. The process entails inoculating 1 mL of cell suspension containing 2×10^4 cells onto a well of 24-well plate, followed by addition of different gels. After co-culturing for 1, 3, and 5 days, a mixture of 900 μL Dulbecco's Modified Eagle Medium (DMEM) and 100 μL of a 5 mg/mL MTT solution was

added to each well. The cells were incubated in the dark for 4 h. Subsequently, the supernatant was aspirated, and the resulting crystals were dissolved in 1 mL of dimethyl sulfoxide (DMSO). The absorbance of the solution was measured at 492 nm using a microplate reader (Infinite F50, TECAN).

2.5. Stability test

The cured gel was subjected to an environment with a temperature range of 22–26°C and a humidity level between 40% and 60%. Computed tomography (CT) imaging was performed using Philips CT scanner to evaluate the homogeneity of the gels. The CT scanner was configured with acquisition parameters: energy at 120 kV, current at 350 mA, and a slice thickness of 3 mm. The images were subsequently imported into Monaco treatment planning system (TPS), where Hounsfield units (HU) and relative density (RD) values were obtained from five 1 × 1 cm^2 regions of interest located in the central axial CT slice of the gels. Changes in shape were observed at various time points (0 h, 15 h, and 1 week) through CT imaging. The selected time points for observation were based on the practical application scenario of personalized boluses, which typically involve a maximum usage of 5 h per week over a duration of 3 weeks.

2.6. Radiological evaluation

A DLP projector (405 nm, Nova Bene 4, China) was utilized for printing our composite bioink, which comprises of ALG (0.5 wt%), AM (20 wt%), PEGDA (0.2 mol% of AM), LAP (0.1 wt%), GLY (30 wt%), and Tar (0.0035 wt%) based on mechanical and adhesive testing. The printer's G-code was generated through the use of commercial software, with printing parameters set to a thickness of 100 μm, five base layers, and a curing time of 9 s. After printing, the constructs were briefly rinsed with water to eliminate unreacted solution. Subsequently, the models underwent post-curing in a specialized box to enhance their internal structural stability and reinforce their printed form.

To assess the accuracy of the DLP system in utilizing bioink, gel cuboid arrays were printed orthogonally to the build platform. Two cuboid boluses (5 cm × 10 cm × 0.5 cm) were designed using CAD software, and the printing accuracy was assessed by calculating the deviation between the printed and intended dimensions. The gel can be used to prepare bolus for head radiotherapy.

The moldability of the gel was confirmed through CT imaging of a Rando phantom, wherein an artificial gross tumor volume (GTV) was initially defined below the skin surface in no-bolus CT images with a reconstruction thickness of 1 mm. A planning target volume (PTV) was generated by expanding a 3 mm margin around the GTV, while ensuring it remained on the patient's surface. A virtual bolus with a thickness of 5 mm was generated in the Monaco TPS to achieve the desired dose coverage of the PTV. During plan optimization, the PTV served as the objective structure, while rings surrounding it were utilized to restrict doses outside its boundaries. The target volume, achieving 95% coverage, was normalized to the prescribed dose following optimization. Subsequently, the virtual bolus was converted into a standard tessellation language (STL) file using MIM. The STL file was subsequently subjected to smoothing using 3D-matic software in order to eliminate CT slicing artifacts, and the resultant smoothed file was printed utilizing a DLP printer. Subsequently, CT images of the phantom were acquired using both the printed and commercial boluses. IMRT/VMAT plans were then generated for each type of bolus, including virtual ones, while adhering to identical dose constraints. A total prescription of 60 Gy was administered to the PTV for 30 consecutive days, with dose distribution calculated using the Monte Carlo algorithm for planning purposes. Subsequently, maximum gaps between skin and commercial/3D-printed boluses were investigated.

2.7. Statistical analysis

Statistical analyses were conducted using SPSS (version 19.0), with a significance threshold of $P < 0.05$.

3. Results and discussion

3.1. System design

The gel designed for bolus application is illustrated in Figure 1A. The DLP-based 3D bioprinting technique employs a blue light (405 nm) to activate the photoinitiator LAP, leading to the generation of free radicals that initiate the breaking of C=C double bonds in AM and PEGDA[25,26]. This process results in the formation of a crosslinking network and solidification of the bioink into a desired pattern. Figure 1B illustrates the formation of DN hybrid gels, which results from the interpenetration of a chemically crosslinked network and a physically crosslinked network. The former is synthesized through acrylamide polymerization with PEGDA and entanglement with ALG, where PEGDA serves as a crosslinker to facilitate covalent network formation. The second crosslinking network is built with the hydrogen bonds provided by PA, ALG, PAM, and GLY. The hydrogen bonds endowed the gel with enhanced tensile and adhesive properties. These intermolecular forces endow the gel with superior tensile strength and adhesive properties.

3.2. Structure of the gels

SEM images of the freeze-dried gels are presented in Figure 2A, revealing interconnected and porous structures. The gel without ALG displayed a loosely arranged network structure, whereas the inclusion of ALG led to a more

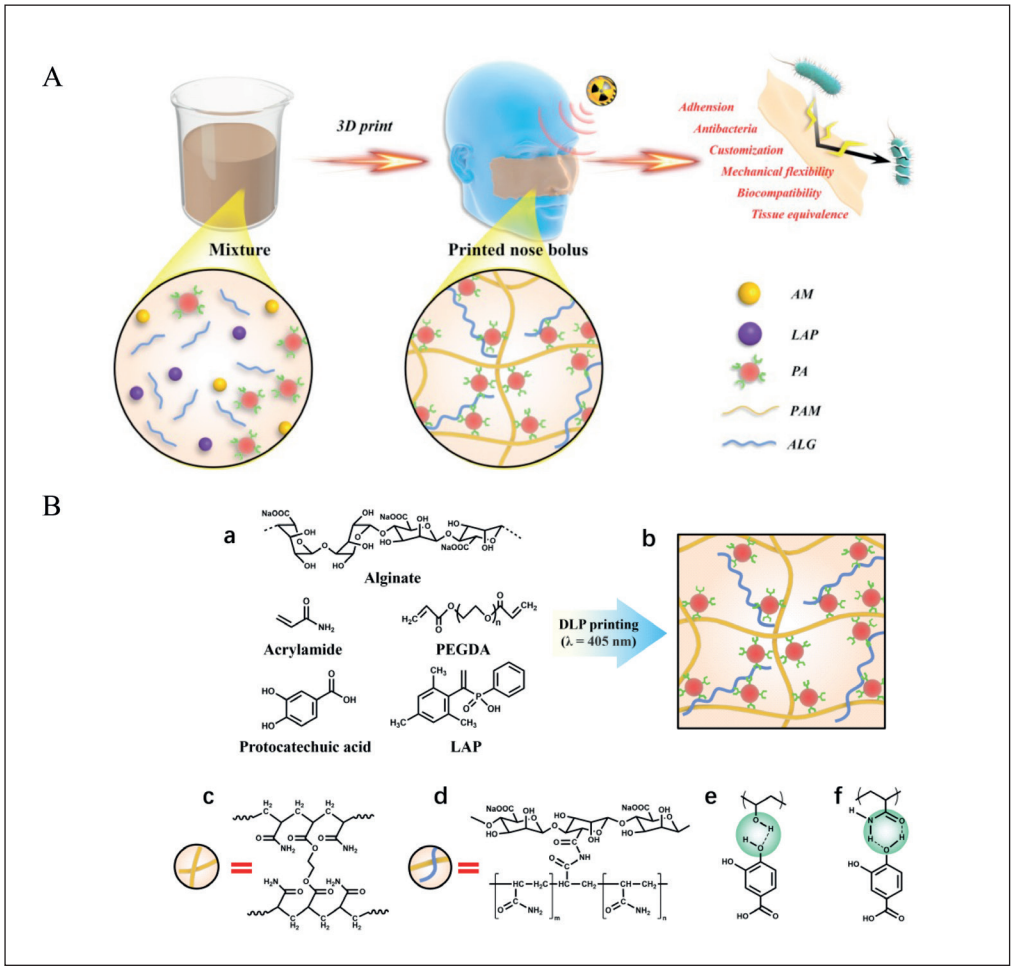

Figure 1. (A) Schematic of design strategy for the 3D bioprinting of multifunctional hydrogel bolus. (B) Formation of DN hybrid hydrogels. Abbreviations: ALG, alginate; AM, acrylamide; LAP, lithium phenyl-2,4,6-trimethylbenzoylphosphinate; PA, protocatechuic acid; PAM, polyacrylamide.

compact network structure characterized by smaller pore size and thinner pore walls. Additionally, the incorporation of PA resulted in gels with denser and more uniform pores, which are advantageous for enhancing their mechanical properties.

The FTIR spectra of the gels are presented in Figure 2B. In the PAM gel, the peaks at 1662 cm^{-1} and 1615 cm^{-1} corresponded to C=O stretching and N-H bending, respectively[27,28]. The crosslinking with ALG and PA led to the changes in intensity and peak position of C=O and N-H bonds, which are indicative of the interactions among the large-molecule ALG, small-molecule PA, and PAM. Compared to the hydrogel, the gel prepared using a binary solvent of GW shows that the presence of GLY enhanced the peak intensity, indicating its bridging effect within the system, which weakens interactions among network chains. Additionally, the peak observed at 1036 cm^{-1} corresponded to the C=O stretching vibration of glycerol's intrinsic molecular chain.

3.3. Photoresponsive performance

Rapid photocurability and favorable fluidity are two essential prerequisites for pre-hydrogels used in DLP printing[25,29,30]. AM is selected due to its inherent properties, including the photopolymerization of C=C groups triggered by light and high transparency. Under photo irradiation with an intensity of 2 mW/cm^2, the C=C double bonds in the gel underwent polymerization.

Other compounds in the photocuring ink also play an important role in influencing the polymerization efficiency. Specifically, the incorporation of GLY and PA can reduce photocuring time to as short as 5 s, thereby enhancing the speed of 3D bioprinting (Figure 3A). It is widely acknowledged that a photopolymerization time of less than 10 s falls within an acceptable range for DLP printing[31]. The reduction in photocuring time can be attributed to the hydrogen bonds which decrease the intermolecular distance and compact the network structure of the gel. Furthermore, based on our previous research, Tar plays

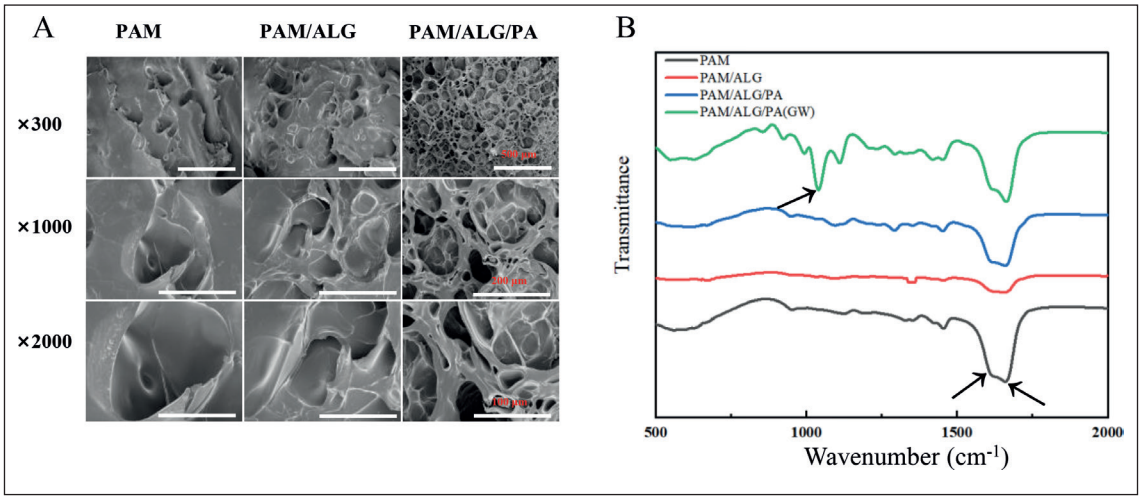

Figure 2. Effect of alginate and protocatechuic acid on the structural properties of freeze-dried hydrogels. (A) Scanning electron microscopy (SEM) images. (B) Fourier-transform infrared spectroscopy (FTIR) image. Abbreviations: ALG, alginate; PA, protocatechuic acid; PAM, polyacrylamide.

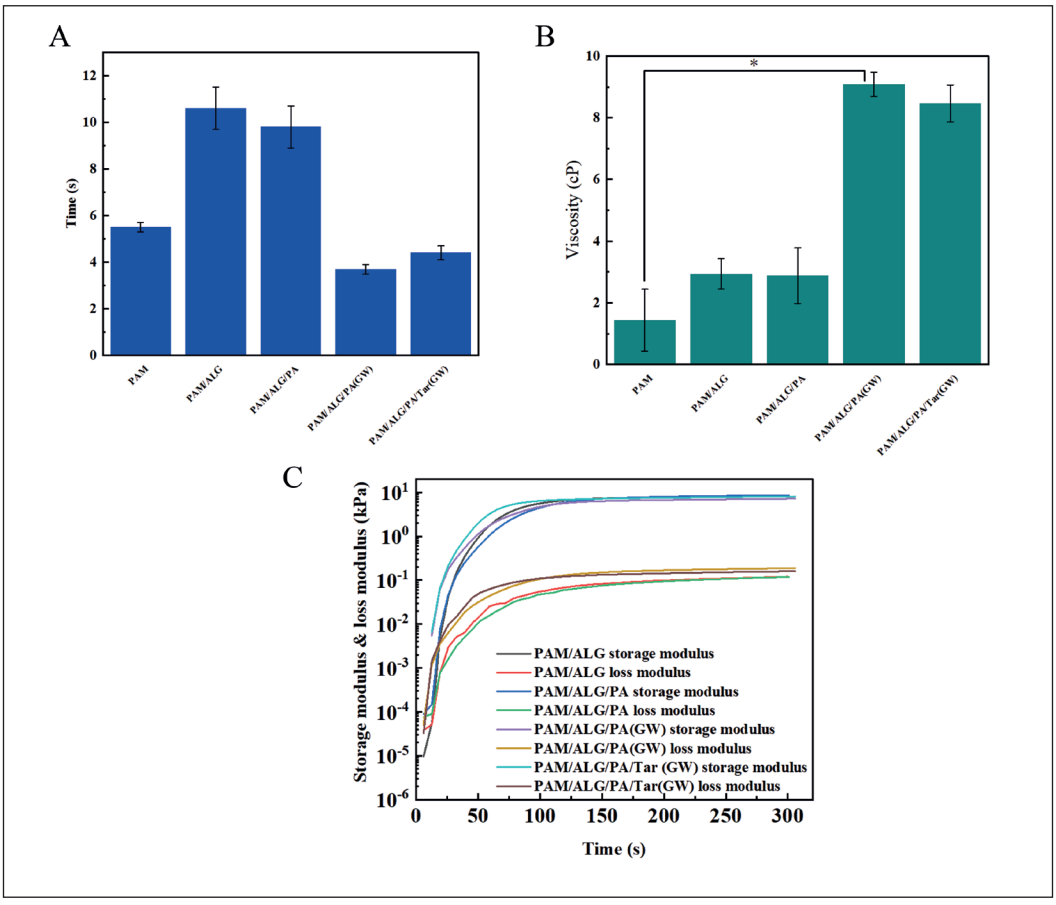

Figure 3. Photoresponse performance. (A) Photocuring time for different hydrogels. (B) Viscosity of different hydrogels. (C) Rheological testing results for different hydrogels.

a significant role in enhancing the printing resolution of the gel[32,33]. After being added to the gel, Tar retains its photoresponsive characteristics that could still satisfy the fundamental requirements of DLP printing.

To ensure precise printing and prevent excessive crosslinking, the photopolymer should possess low viscosity and fluidity[34,35]. Figure 3B displays the varying viscosities of different gels, with all solutions exhibiting

a preferable viscosity below 10 cp for DLP printing. The addition of GLY, which can form hydrogen bonds with water molecules, significantly increased the viscosity of the gels, while their excellent fluidity was preserved for DLP printing. The rheological test results showed that the storage modulus of each gel group consistently exceeded the loss modulus (Figure 3C), indicating their elastic flow properties under external forces. The majority of photosensitive resins utilized in DLP printing exhibit a viscosity range between 100 mPa·s and 300 mPa·s. Caprioli *et al.* reported that when the viscosity exceeds 1×10^3 mPa·s, effective ink printing cannot be achieved[36]. In this study, the photocurable ink is of low viscosity (<10 mPa·s), which favorably contributes to the performance of DLP printing.

3.4. Mechanical properties of the gels

The compressive test is a critical method for evaluating the mechanical performance of gels. The elongation and elastic modulus of the composite gels are presented in Figure 4A and B. Test samples were fabricated using a designed ink via DLP printing technique. Specifically, using a constant concentration of AM (20 wt%) and PEGDA (molar ratio of AM:PEGDA = 500:1), which was determined to be an appropriate crosslinker concentration for successful printing and optimal toughness, we initially evaluated the influence of ALG on the mechanical performance of gels (Figure S1 in Supplementary File). The ALG functioned by providing physical entanglement and covalent bonding within the PAM network, resulting in significant improvements to the gel's mechanical properties, including elastic modulus and elongation.

We further investigated the impact of PA on the adhesive performance of gels (Figure S2 in Supplementary File), which was attributed to its ability to introduce hydrogen bonds into the system. Initially, an increase in PA concentration led to a corresponding increase in modulus. However, at higher concentrations, the modulus was decreased due to the strong quenching effect of PA on radicals. This can be explained by the fact that in a dual network hydrogel, covalent crosslinking acts as a

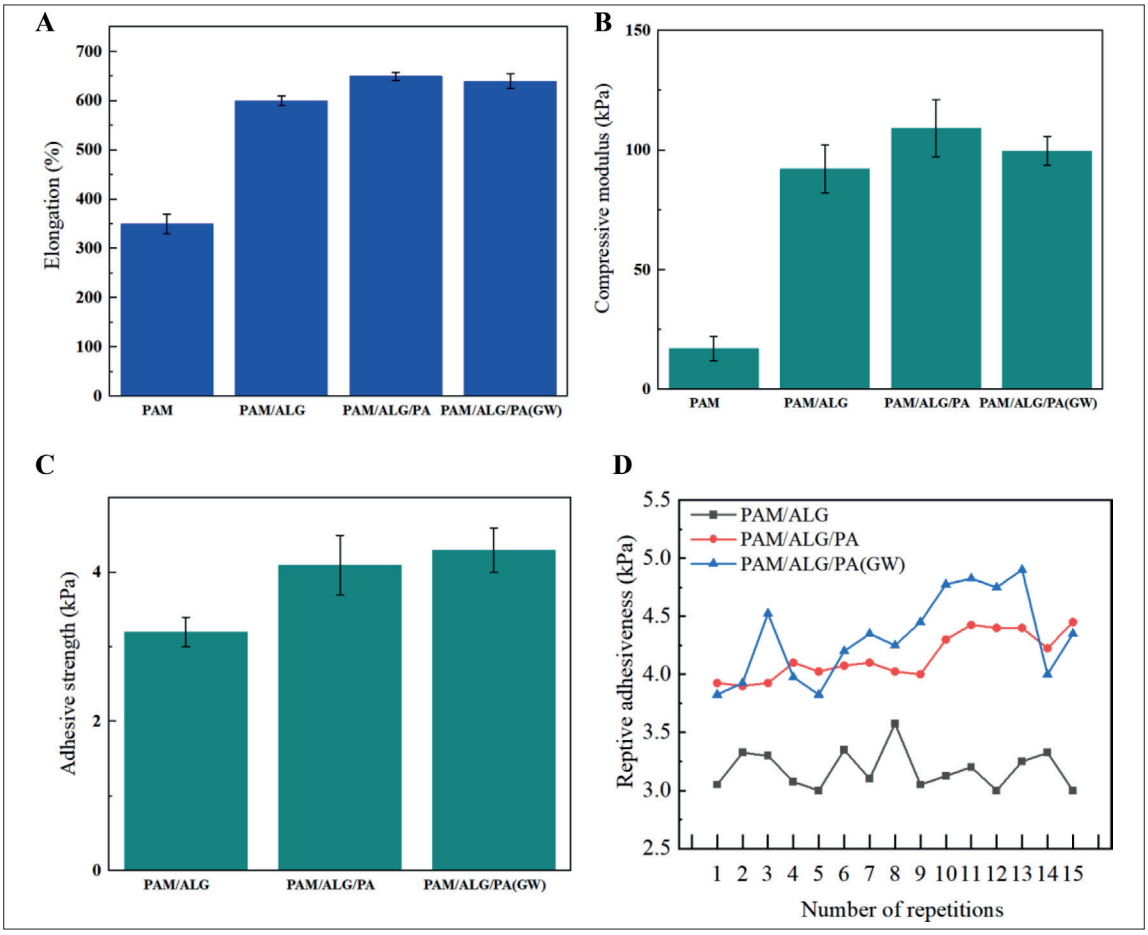

Figure 4. (A) Elongation of different hydrogels. (B) Elastic modulus of different hydrogels. (C) Adhesion strength of different hydrogels. (D) Repetitive adhesiveness of different hydrogels.

"rigid bridging" mechanism contributing to stiffness, while hydrogen bonding serves as a "flexible bridging" mechanism contributing to toughness. These two types of crosslinking are mutually restrictive. When covalent crosslinking dominates over hydrogen bonding, the rigid bridging overpowers the flexible bridging, resulting in a harder and more brittle gel. Subsequently, we conducted further investigations into the impact of GLY on gels (Figure S3 in Supplementary File). In a solvent system comprising glycerol and water, GLY formed hydrogen bonds with the catechol groups of PA, thereby impeding interactions between PA and free radicals and resulting in a reduction in the elastic modulus of printed gels.

3.5. Adhesive properties of the gel

Figure 4C depicts the results of adhesive properties of the gels. The gels incorporated with ALG, PA, and GLY exhibited repetitive adhesion behavior, which marks the potential for daily radiotherapy applications (Figure 4D). The adhesion of gels to various substrates was improved through the addition of ALG, which can be attributed to the formation of hydrogen bonds between ALG and PAM molecules. Similarly, the addition of PA enhances the adhesion of PAM/ALG gel by promoting hydrogen bonding among PA, ALG, and PAM molecules. PA is a polyphenolic compound abundant in catechol groups, which can be extracted from various natural sources and has been extensively applied in the field of biomedicine. One of its remarkable features lies in the reversible hydrogen bonding ability mediated by the catechol groups, endowing it with gel adhesion property[37,38]. This known characteristic has been capitalized upon in the fabrication of DN gels utilizing PA. The conventional method involves immersing the gel in a PA solution, which results in the formation of hydrogen bonds between PA and the polymer matrix, improving the mechanical properties of the DN gels. However, this approach often leads to gel heterogeneity. To circumvent this problem, we opted for the direct printing of composite gels that contain PA. This approach offers several advantages, including precise control over the distribution of PA within the gel and a more homogeneous incorporation of PA throughout the gel network. Additionally, the incorporation of PA allows for the fabrication of intricate gel structures with customized mechanical properties. The direct printing of composite gels containing PA represents a significant advancement in this field, offering a more efficient and versatile approach to preparing PA-based DN gels.

3.6. Biological properties

The anti-bacterial property of gels is critical for their use as radiotherapy bolus, given that up to 85% of cancer patients develop dermatitis in the irradiated areas[39].

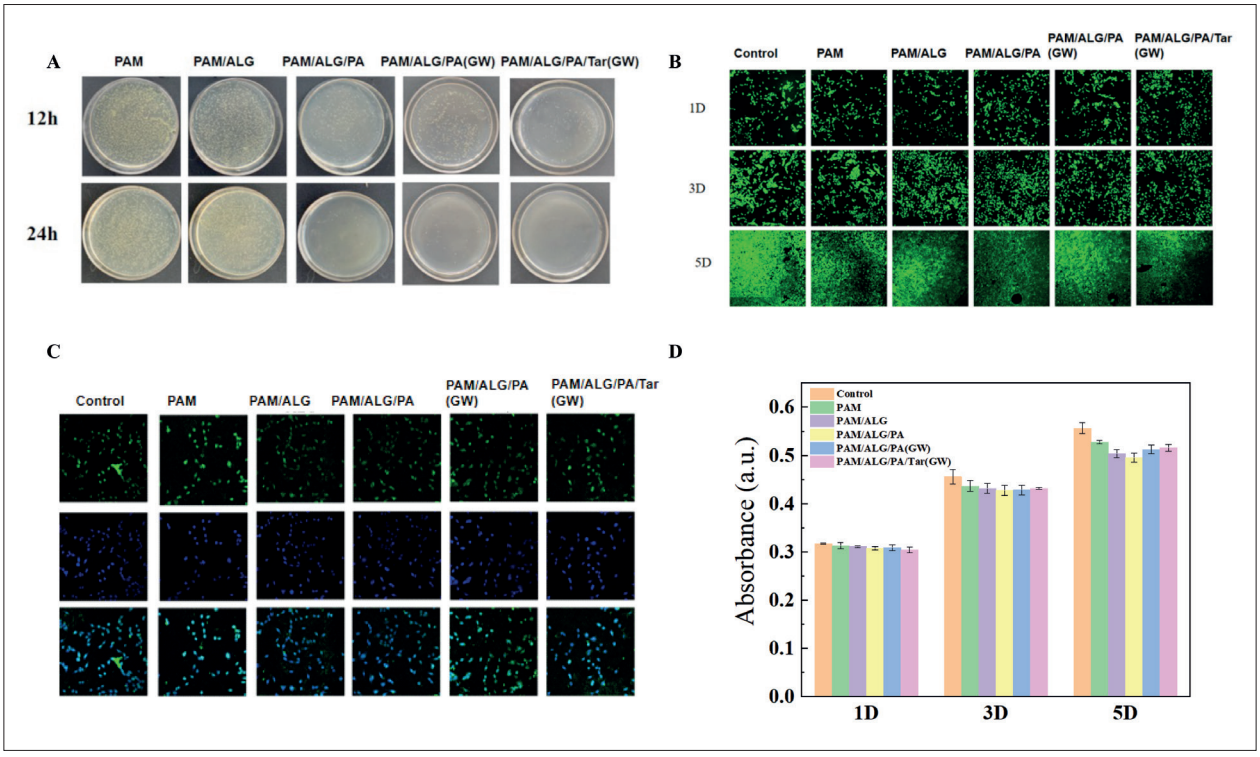

Figure 5. (A) Anti-bacterial performance (on *S. aureus*) of the designed gels. (B) Live/Dead staining of fibroblasts after incubation for 1, 3, and 5 days. (C) Cytoskeleton of fibroblasts. (D) MTT assay of fibroblasts after incubation for 1, 3, and 5 days.

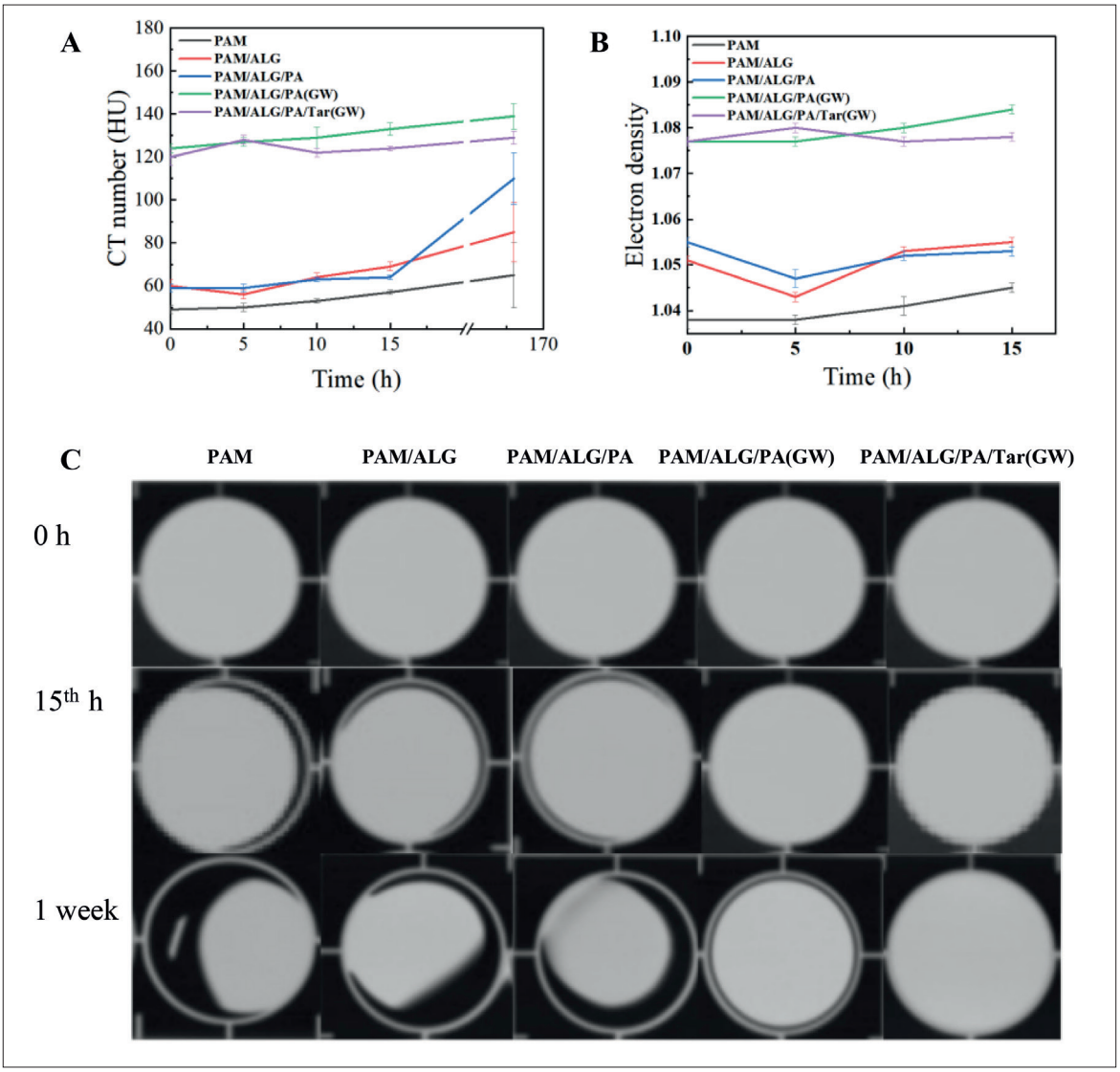

Figure 6. (A) CT number of different hydrogels over time. (B) ED number of different hydrogels time. (C) Stability of hydrogels over time.

In this context, a TPU-PAM gel developed by Hou *et al.* demonstrated promising and long-lasting anti-bacterial properties. However, the fact that the gel is not suitable for personalized 3D bioprinting limits its potential applications. The anti-bacterial efficacy of the designed gels was assessed by examining the formation of bacterial colonies (*S. aureus*) on agar plates, as shown in Figure 5A. The results revealed that the agar plates of PEGDA and ALG groups were almost entirely covered with bacterial colonies, indicating that samples without PA lacked anti-bacterial activity. However, the addition of PA resulted in a significant reduction in bacterial colony count, with the resulting gel demonstrating over 95% anti-bacterial activity. These findings emphasize the anti-bacterial properties of gels containing PA, which is rich in phenolic hydroxyl groups, contributing to the potent anti-bacterial effects against various bacterial strains. The possible mechanism for this activity is attributed to the presence of catechol structures within PA molecules, which can form complexes with iron ions and deprive microorganisms of essential elements necessary for their growth[33].

To assess the biocompatibility of the customized bolus, NIH-3T3 cells were cultured on the gels. After 3 or 5 days of incubation, a Live/Dead staining test was performed to evaluate cell viability, and a cytoskeletal staining was conducted to examine the cellular morphology. Few dead cells were observed in all samples, with their gel surfaces exhibiting robust proliferation of green-stained living cells over time; no significant difference was observed between the gels after 3 and 5 days of incubation, indicating that

the designed gel exhibited non-toxicity and is suitable for applications involving skin contact (Figure 5B). Furthermore, F-actin staining was used to determine their biocompatibility (Figure 5C). The MTT assay results depicted in Figure 5D demonstrate that there was no significant deviation in cell viability among the gels throughout the culture period, thus further validating their biocompatibility.

3.7. Stability of gel

Hydrogels are generally prone to water loss, which greatly affects their stability and performance. To overcome this issue, GLY was employed as a partial substitute for water in the gel formulation, which gave rise to an organic photosensitive gel with anti-dehydration properties[40]. The variations in CT number and electron density (ED) for different gels over time are illustrated in Figure 6A and B, respectively. Figure S4 (Supplementary File) displays the changes of mass density (MD) with time for different hydrogels. The initial mean values of composite gel's HU and relative RD were 127 ± 2 HU and 1.077 ± 0.001, respectively. No significant differences were observed in the initial 15 h for gels containing GLY. The results of RD measurements also confirmed the tissue equivalence of the composite gel. Furthermore, the gel demonstrated minimal moisture loss and maintained its structural integrity within a humidity range of 40% to 60% (Figure 6C). Conversely, the control groups without GLY experienced significant shrinkage (an approximate reduction from 1/3 to 1/2) within a mere 15 h, underscoring the pivotal role of GLY in water conservation. This phenomenon can be ascribed to the intermolecular interactions between GLY and water, where GLY forms hydrogen bonds with water molecules, thereby hindering the evaporation of water.

The gels exhibit excellent anti-dehydration properties, which make them highly promising materials for applications in the field of radiotherapy. It should be noted that increasing the concentration of GLY decreases the rate of water loss, and the content of GLY has a strong influence on the changes in HU and ED over time. Besides, the need for special storage conditions is obviated if the gels contain GLY.

3.8. Radiological properties

To evaluate the dimensional accuracy of DLP printing, a caliper with a resolution of 0.1 mm was used to measure the actual size of a printed gel and determine deviations (Table 1). The results indicate that the maximum measured differences between the designed and printed dimensions of the products were less than 1 mm on average, demonstrating the effectiveness of the printing method in producing structures with high shape fidelity requirements. Boluses for head radiotherapy are shown in Figure S5 (Supplementary File).

Table 1. Summary of the thickness and width of designed and printed rectangular boluses

Sample	Length (cm)	Width (cm)	Thickness (cm)
Design	5	5	0.5
Rectangle 1	5.1	4.9	0.5
Rectangle 2	5	5	0.5

A nose bolus composed of the composite gel was fabricated via DLP printing. Axial CT images demonstrated that the printed bolus can effectively eliminate air gaps, ensuring adequate dose coverage in the build-up region. In contrast, the use of commercial bolus resulted in air gap formation (as depicted in Figure 7), with approximately 15% of slices exhibiting air gaps larger than 5 mm. The printed bolus exhibited a close conformity to the intended design, as demonstrated in Figure 7 and the dose volume histogram (DVH) curves for all plans shown in Figure S6 (Supplementary File). DVH analysis indicated that 3D-printed bolus significantly enhanced D95% (dose covering 95% of volume) for PTV, compared with commercial bolus. Table 2 presents detailed dosimetric comparisons between the printed bolus and the control group. The use of both 3D-printed and commercial boluses resulted in improved dose coverage compared to the group without using boluses. The 3D-printed and virtual boluses exhibited superior performance in terms of target conformity indices (CI) and homogeneity indices (HI) for IMRT and VMAT plans compared to commercial boluses.

In this study, the utilization of soft gel material for direct printing of bolus significantly simplified the production process. The exceptional conformity to clinical model is an attribute that makes gel bolus a potential tool in addressing current clinical challenges associated with commercial boluses in radiotherapy. Moreover, the DVH curves indicated that the gel possessed near-water equivalent dosimetric transmission and exhibited dose distributions in accordance with virtual boluses, thereby eliminating the need for multiple rounds of CT scanning.

4. Conclusion

In summary, this study introduced a DN gel that can be fabricated into a customized bolus for radiotherapy in treating superficial tumors. Specifically, by formulating a photocurable ink consisting of acrylamide as the monomer, PEGDA as the crosslinker, LAP as the photoinitiator, and PA as an anti-bacterial agent in a glycerol-water system, we printed a gel-based bolus via DLP printing technology. The designed material is compatible with photocurable 3D bioprinting, allowing for personalized customization and eliminating gaps commonly encountered in the

Table 2. Comparison of planning target volume's parameters among different permutations of IMRT and VMAT plans

	D_{min} (cGy)	D_{mean} (cGy)	D_{max} (cGy)	CI	HI	V_{95} (%)	D_{95} (cGy)
Printed-IMRT	6128.6	6234.5	6537.6	0.30	1.04	99.49	6101.8
Printed-VMAT	6143.7	6237.5	6616.5	0.29	1.04	99.56	6120.8
Commercial-IMRT	6022.1	6136.1	6757.1	0.27	1.24	90.66	5194.9
Commercial-VMAT	6066.6	6154.7	6584.5	0.26	1.17	91.40	5458.7
Virtual-IMRT	6121.3	6234.8	6564.8	0.28	1.05	98.29	6080.0
Virtual-VMAT	6120.4	6219.4	6554.1	0.30	1.05	98.37	6081.4
Nobolus-IMRT	5701.1	6106.0	7113.8	0.31	1.21	80.01	5328.1
Nobolus-VMAT	5805.7	6175.9	6904.2	0.33	1.18	84.37	5519.8

Abbreviations: CI, conformity index; D_{95}, dose covering 95% of volume; HI, homogeneity index; V_{95}, volume covering 95% of dose.

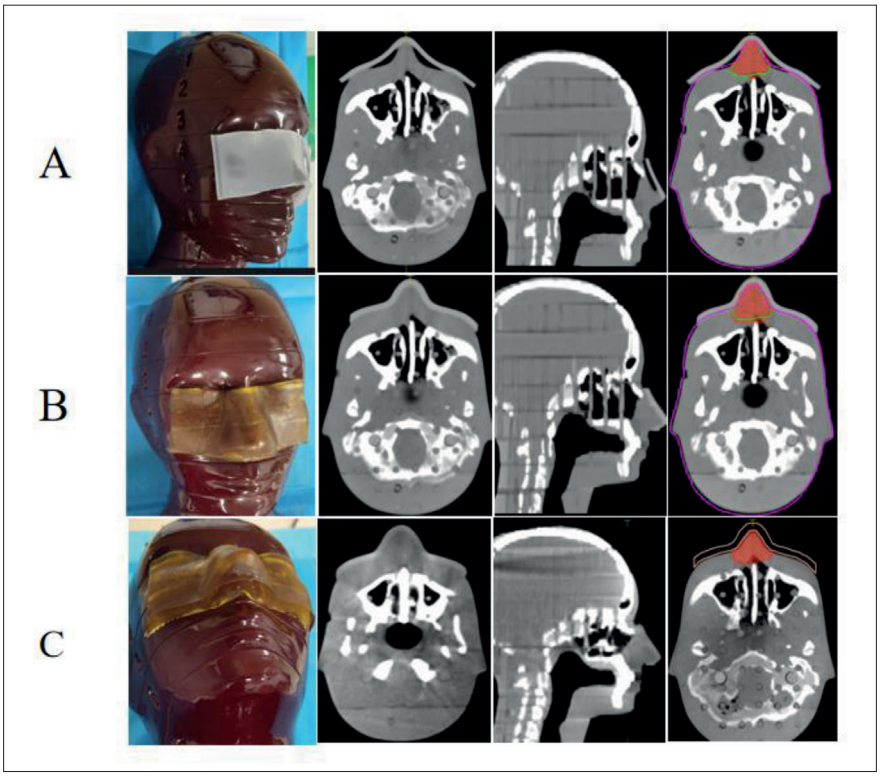

Figure 7. Accurate positioning of the bolus on phantom. The top and middle rows show the computed tomography (CT) slice images and corresponding prescription dose distribution of volume-modulated arc therapy (VMAT) plan with commercial and 3D-printed bolus, respectively. The bottom row shows the cone beam computed tomography (CBCT) slice images with 3D-printed bolus, and the dose distribution of VMAT plan with virtual bolus.

application of traditional boluses. Additionally, the elastic modulus of printed gel was similar to that of human skin (ranging from 5 kPa to 140 MPa)[41], indicating that the printed get is compatible with the patient's body. The gel constructed in this study possessed a DN structure, which endowed the gel with desirable mechanical properties and the ability to adhere to the skin surface. Moreover, compared to hydrogels, the gel exhibited superior stability, better control over water loss, and radiological properties that closely resemble to those of the skin. In addition, its biocompatibility and potent anti-bacterial properties have contributed significantly to the prevention of radiation-induced dermatitis. In conclusion, this study demonstrated the potential efficacy of 3D-printed gel-based boluses

in enhancing treatment outcomes for superficial tumors, providing a reference for the implementation of personalized medical devices in the field of radiotherapy.

Acknowledgments

None.

Funding

The authors wish to express their gratitude for the support received from the Fundamental Research Program of Shanxi Province (Number: 20210302123416), the National Natural Science Foundation of China (Number: 31870934), and the Central Leading Science and Technology Development Foundation of Shanxi Province (Number: YDZJSX20231A064).

Conflict of interest

The authors declare no conflicts of interest.

Author Contributions

Conceptualization: Xiaobo Huang, Jianbo Song, Meiwen An
Formal analysis: Xiaohong Yao
Investigation: Guobao Pang, Yannan Xu, Qinying Shi
Methodology: Youjie Rong, Xiaomin Zhang
Writing – original draft: Ying Lu
Writing – review & editing: Jianbo Song, Meiwen An
All authors have approved the final version of the manuscript.

Ethics approval and consent to participate

Not applicable.

Consent for publication

Not applicable.

Availability of data

Data used in this work are available from the corresponding author upon reasonable request.

References

1. Pugh R, Lloyd K, Collins M, et al. The use of 3D printing within radiation therapy to improve bolus conformity: A literature review. *J Radiother Pract*. 2017;16(3):319–325.
doi: 10.1017/s1460396917000115

2. Wang X, Wang X, Xiang Z, et al. The clinical application of 3D-printed boluses in superficial tumor radiotherapy. *Front Oncol*. 2021;11:698773.
doi: 10.3389/fonc.2021.698773

3. Lu Y, Song J, Yao X, et al. 3D printing polymer-based bolus used for radiotherapy. *Int J Bioprint*. 2021;7(4):414.
doi: 10.18063/ijb.v7i4.414

4. Aras S, Tanzer I O, Ikizceli T. Dosimetric comparison of superflab and specially prepared bolus materials used in radiotherapy practice. *Eur J Breast Health*. 2020;16(3):167–170.
doi: 10.5152/ejbh.2020.5041

5. Robar JL, Moran K, Allan J, et al. Intrapatient study comparing 3D printed bolus versus standard vinyl gel sheet bolus for postmastectomy chest wall radiation therapy. *Pract Radiat Oncol*. 2018;8(4):221–229.
doi: 10.1016/j.prro.2017.12.008

6. Khan Y, Villarreal-Barajas JE, Udowicz M, et al. Clinical and dosimetric implications of air gaps between bolus and skin surface during radiation therapy. *J Cancer Ther*. 2013;04(07):1251–1255.
doi: 10.4236/jct.2013.47147

7. Zheng Q, Zhao L, Wang J, et al. High-strength and high-toughness sodium alginate/polyacrylamide double physically crosslinked network hydrogel with superior self-healing and self-recovery properties prepared by a one-pot method. *Colloids Surf A: Physicochem Eng Asp*. 2020;589:124402.
doi: 10.1016/j.colsurfa.2019.124402

8. Al-Sudani TA, Biasi G, Wilkinson D, et al. eXaSkin: A novel high-density bolus for 6MV X-rays radiotherapy. *Phys Med*. 2020;80:42–46.
doi: 10.1016/j.ejmp.2020.09.002

9. Obeid JP, Gutkin PM, Lewis J, et al. Volumetric modulated arc therapy and 3-dimensional printed bolus in the treatment of refractory primary cutaneous gamma delta lymphoma of the bilateral legs. *Pract Radiat Oncol*. 2019;9(4):220–225.
doi: 10.1016/j.prro.2019.02.016

10. Baltz GC, Chi PM, Wong PF, et al. Development and validation of a 3D-printed bolus cap for total scalp irradiation. *J Appl Clin Med Phys*. 2019;20(3):89–96.
doi: 10.1002/acm2.12552

11. Zhao Y, Moran K, Yewondwossen M, et al. Clinical applications of 3-dimensional printing in radiation therapy. *Med Dosim*. 2017;42(2):150–155.
doi: 10.1016/j.meddos.2017.03.001

12. Park SY, Choi CH, Park JM, et al. A patient-specific polylactic acid bolus made by a 3D printer for breast cancer radiation therapy. *PLoS One*. 2016;11(12):e0168063.
doi: 10.1371/journal.pone.0168063

13. Park JW, Yea JW. Three-dimensional customized bolus for intensity-modulated radiotherapy in a patient with Kimura's disease involving the auricle. *Cancer Radiother*. 2016;20(3):205–209.
doi: 10.1016/j.canrad.2015.11.003

14. Ricotti R, Ciardo D, Pansini F, et al. Dosimetric characterization of 3D printed bolus at different infill percentage for external photon beam radiotherapy. *Phys Med*. 2017;39:25–32.
doi: 10.1016/j.ejmp.2017.06.004

15. Chiu T, Tan J, Brenner M, et al. Three-dimensional printer-aided casting of soft, custom silicone boluses (SCSBs) for head and neck radiation therapy. *Pract Radiat Oncol*. 2018;8(3):e167–e174.
doi: 10.1016/j.prro.2017.11.001

16. Park JM, Son J, An HJ, et al. Bio-compatible patient-specific elastic bolus for clinical implementation. *Phys Med Biol*. 2019;64(10):105006.
doi: 10.1088/1361-6560/ab1c93

17. Kong Y, Yan T, Sun Y, et al. A dosimetric study on the use of 3D-printed customized boluses in photon therapy: A hydrogel and silica gel study. *J Appl Clin Med Phys*. 2019;20(1):348–355.
doi: 10.1002/acm2.12489

18. Zasadzinski K, Spalek MJ, Rutkowski P. Modern dressings in prevention and therapy of acute and chronic radiation dermatitis-A literature review. *Pharmaceutics*. 2022;14(6).
doi: 10.3390/pharmaceutics14061204

19. Zhao M, Wang C, Xie J, et al. Eco-friendly and scalable synthesis of fullerenols with high free radical scavenging ability for skin radioprotection. *Small*. 2021;17(37):e2102035.
doi: 10.1002/smll.202102035

20. Fu Z, Naghieh S, Xu C, et al. Printability in extrusion bioprinting. *Biofabrication*. 2021;13(3).
doi: 10.1088/1758-5090/abe7ab

21. Ng WL, Huang X, Shkolnikov V, et al. Polyvinylpyrrolidone-based bioink: influence of bioink properties on printing performance and cell proliferation during inkjet-based bioprinting. *Bio-Des Manuf*. 2023;6:676–690.
doi: 10.1007/s42242-023-00245-3

22. Xu X, Awad A, Robles-Martinez P, et al. Vat photopolymerization 3D printing for advanced drug delivery and medical device applications. *J Control Release*. 2021;329:743–757.
doi: 10.1016/j.jconrel.2020.10.008

23. Braghiroli FL, Amaral-Labat G, Boss AFN, et al. Tannin gels and their carbon derivatives: A review. *Biomolecules*. 2019;9(10):587.
doi: 10.3390/biom9100587

24. Mortezaee K, Najafi M, Farhood B, et al. Resveratrol as an adjuvant for normal tissues protection and tumor sensitization. *Curr Cancer Drug Targets*. 2020;20(2):130–145.
doi: 10.2174/1568009619666191019143539

25. Zhou LY, Fu J, He Y. A review of 3D printing technologies for soft polymer materials. *Adv Funct Mater*. 2020;2000187.
doi: 10.1002/adfm.202000187

26. Mau R, Nazir J, John S, et al. Preliminary study on 3D printing of PEGDA hydrogels for frontal sinus implants using digital light processing (DLP). *Curr Dir Biomed Eng*. 2019;5(1):249–252.
doi: 10.1515/cdbme-2019-0063

27. Zhang B, Li S, Hingorani H, et al. Highly stretchable hydrogels for UV curing based high-resolution multimaterial 3D printing. *J Mater Chem B*. 2018;6(20):3246–3253.
doi: 10.1039/c8tb00673c

28. Sun JY, Zhao X, Illeperuma WR, et al. Highly stretchable and tough hydrogels. *Nature*. 2012;489(7414):133–136.
doi: 10.1038/nature11409

29. Huang B, Hu R, Xue Z, et al. Continuous liquid interface production of alginate/polyacrylamide hydrogels with supramolecular shape memory properties. *Carbohydr Polym*. 2020;231:115736.
doi: 10.1016/j.carbpol.2019.115736

30. Dávila JL, d'Ávila MA. Rheological evaluation of laponite/alginate inks for 3D extrusion-based printing. *Int J Adv Manuf Technol*. 2018;101(1–4):675–686.
doi: 10.1007/s00170-018-2876-y

31. Xiang Z, Li N, Rong Y, et al. 3D-printed high-toughness double network hydrogels via digital light processing. *Colloids Surf A: Physicochem Eng Asp*. 2022;639:128329.
doi: 10.1016/j.colsurfa.2022.128329

32. Li N, Xiang Z, Rong Y, et al. 3D printing tannic acid-based gels via digital light processing. *Macromol Biosci*. 2022;22(4):e2100455.
doi: 10.1002/mabi.202100455

33. Zhu L, Rong Y, Wang Y, et al. DLP printing of tough organogels for customized wearable sensors. *Eur Polym J*. 2023;187:111886.
doi: 10.1016/j.eurpolymj.2023.111886

34. Zhu W, Ma X, Gou M, et al. 3D printing of functional biomaterials for tissue engineering. *Curr Opin Biotechnol*. 2016;40:103–112.
doi: 10.1016/j.copbio.2016.03.014

35. Axpe E, Oyen M. Applications of alginate-based bioinks in 3D bioprinting. *Int J Mol Sci*. 2016;17(12):1976.
doi: 10.3390/ijms17121976

36. Caprioli M, Roppolo I. 3D-printed self-healing hydrogels via Digital Light Processing. *Nat Commun*. 2021;12(1):2462.
doi: 10.1038/s41467-021-22802-z

37. Guo J, Suma T, Richardson JJ, et al. Modular assembly of biomaterials using polyphenols as building blocks. *ACS Biomater Sci Eng*. 2019;5(11):5578–5596.
doi: 10.1021/ acsbiomaterials.8b01507

38. Lee J, Yeo M, Kim W, et al. Development of a tannic acid cross-linking process for obtaining 3D porous cell-laden collagen structure. *Int J Biol Macromol*. 2018;110:497–503.
doi: 10.1016/j.ijbiomac.2017.10.105

39. Fischer N, Seo EJ, Efferth T. Prevention from radiation damage by natural products. *Phytomedicine*. 2018;47: 192–200.
doi: 10.1016/j.phymed.2017.11.005

40. Wang J, Liu X, Wang Y, et al. Casein micelles embedded composite organohydrogel as potential wound dressing. *Int J Biol Macromol*. 2022;211:678–688.
doi: 10.1016/j.ijbiomac.2022.05.081

41. Kalra A, Lowe A, Al-Jumaily AM. Mechanical behaviour of skin: A review. *J Material Sci Eng*. 2016;5: 254.
doi: 10.4172/2169-0022.1000254

ACCSCIENCE PUBLISHING

International Journal of Bioprinting

RESEARCH ARTICLE

Preparation of tunable hollow composite microfibers assisted by microfluidic spinning and its application in the construction of *in vitro* neural models

Jingyun Ma[1]*, Wei Li[1,2], Lingling Tian[2], and Xinghua Gao[2]*

[1]Ningbo Institute of Innovation for Combined Medicine and Engineering, The Affiliated Lihuili Hospital of Ningbo University, Ningbo, Zhejiang, China

[2]Materials Genome Institute, Shanghai University, Shanghai, China

(This article belongs to the *Special Issue: Advancements in 3D Printing, Microfluidics, and Their Integrated Applications*)

Abstract

Microfluidic spinning, which has recently emerged as an important approach to processing hydrogels, can handle the flow in the fluid channel and generate microfibers in a controlled and mild manner, and therefore, it is suitable for cell loading, long-term culture, and tissue engineering. In this study, we utilized three-dimensional (3D) printing technology to prepare microfluidic chip templates with different microchannel heights in a one-step manner and obtained microfluidic spinning and microfiber assembly microchips. Hollow calcium alginate (CaA)/gelatin methacrylate (GelMA) composite microfibers were successfully prepared using a microfluidic spinning microchip combined with different fluid-injection strategies. The obtained hollow microfibers had one, two, or three lumens, and different inclusions could be added to the fiber walls. Hollow microfibers with a single lumen were used to load human umbilical vein endothelial cells (HUVECs) and exhibited good cell compatibility and barrier functions. We constructed a neural model based on the HUVEC-loaded hollow microfibers using a customized 3D printer. Using this established neural model, we induced the neural differentiation of rat adrenal medullary pheochromocytoma cells (PC12) using nerve growth factor. Axonal length, tubulin expression, and related gene (*GAP-43* and *TH*) expression in PC12 cells were assessed. The current findings underscore the potential of utilizing microfluidic spinning in *in vitro* blood–brain barrier simulation, neuropharmaceutical and toxin evaluation, and brain-on-a-chip construction.

Keywords: Microfluidic spinning; Hollow microfiber; 3D bioprinting; PC12 cells; Neural differentiation

***Corresponding authors:**

Xinghua Gao
(gaoxinghua@t.shu.edu.cn)

Jingyun Ma
(majingyun198401@126.com)

Citation: Ma J, Li W, Tian L, Gao X. Preparation of tunable hollow composite microfibers assisted by microfluidic spinning and its application in the construction of *in vitro* neural models. *Int J Bioprint*. 2024;10(2):1797.
doi: 10.36922/ijb.1797

Received: September 11, 2023
Accepted: November 7, 2023
Published Online: January 11, 2024

1. Introduction

Microfibers possess several desirable features, such as large specific surface areas, excellent mechanical properties, and good biocompatibility.[1,2] In particular, its structural characteristics allow for effective material exchange and mechanical support, making it an ideal three-dimensional (3D) carrier for cells or tissues, and it is increasingly being

used in fields such as tissue engineering and biomedical research.[3] Microfibers are similar, in terms of form and structure, in most tissues and organs of living organisms, such as the myocardium,[4] nerve bundles,[5,6] and other luminal structures (e.g., blood vessels,[7,8] pulmonary bronchi,[9] and intestinal cavities[10]). Thus, microfibers can be used to reconstruct biomimetic tissues and organs *in vitro*. Furthermore, through microfiber assembly, more functional 3D biomimetic bodies can be formed, thereby providing new models for disease model construction, drug evaluation, and personalized diagnosis.

Commonly used preparation methods for microfibers include melting, electrospinning, and wet spinning.[10-14] Owing to the presence of high-temperature and high-pressure environments, volatile organic solvents, and high shear stress during the melt-spinning and electrospinning processes, which can affect cell viability, prepared microfibers cannot be directly used for cell encapsulation and are often prepared as thin membrane materials for cell adhesion and growth.[15] However, wet spinning, especially microfluidic spinning technology developed from microfluidic technology, has become the primary method for preparing cell-loaded microfiber scaffolds because of its mild reaction conditions, accurate and controllable operation, and the use of biogel materials with good biological properties.[16] In addition, microfluidic spinning forms a coaxial laminar flow by injecting sample and sheath flow solutions with a certain viscosity into microchannels, which further undergo chemical or physical crosslinking in the preparation of microfibers.[17] Functional microfibers with various special morphologies and components can be obtained by adjusting the number of flow channels and injection strategies, particularly hollow microfibers with tubular structures, which is beneficial for 3D cell culture and tissue biomimetics.[18-23] For examples, based on a microfluidic platform with an attached photopolymerization device, Aykar et al. prepared poly(ethylene glycol diacrylate) (PEGDA)-based hollow fibers as self-standing microvessels with biocompatibility/cytocompatibility.[24] Also, Lee et al. reported 3D artificial microvessels based on HIVE-78 cell-encapsulated hollow alginate microfibers and co-cultured with smooth muscle cells (HIVS-125).[25] Zhao et al. prepared grooved microfibers by co-spinning sodium alginate (NaA) with GelMA, and the muscle cells grown on the microfibers showed good viability and ordered alignment.[26] The proposed method has the potential to replicate various arranged microstructures *in vivo*, such as nerve bundles and blood vessels.

Cell-loaded microfibers have been prepared using synthetic or natural polymer materials. Ionic crosslinking of NaA and calcium chloride ($CaCl_2$) is often adopted in microfluidic spinning to prepare microfibers; however, the surface of CaA microfibers lacks the cell adhesion sites of cultured cells, hindering the diffusion and migration of encapsulated cells.[27,28] Recently, GelMA has received increasing attention in the field of tissue engineering.[29,30] GelMA is a synthetic polymer material obtained from the reaction between gelatin and methacrylic anhydride. The principle behind GelMA-forming hydrogel is that, under ultraviolet (UV) irradiation, the unstable C=C bonds in the GelMA molecule break, producing active free radicals, and after the induction of the photoinitiator, a hydrogel with a network structure is formed.[31] As a substitute for gelatin, GelMA is commendable for its biocompatibility, which is far superior to that of other synthetic materials, and its ability to simulate the extracellular matrix.[32-34] In GelMA hydrogels loaded with cells, researchers observed high cell viability (>80%) and the formation of vascular networks.[35] The excellent biocompatibility of the GelMA hydrogel and its ability to rapidly solidify *in situ* promote its application in the construction of cells/tissues *in vitro*, especially in vascular tissue engineering.[36,37] In addition to GelMA, RGD-modified alginate is also suitable for vascular endothelial cell culture, yielding effects similar to that of GelMA, but comparatively, GelMA material is more readily available.[38]

In recent years, the accelerated population aging has significantly raised the prevalence of Parkinson's and Alzheimer's diseases.[39,40] Since there are no drugs available to reverse the axonal damage causing these degenerative diseases of the nervous system, rebuilding nerve axons *in vitro* emerges as a feasible strategy. Toward this end, a pathological/physiological model built with an assembly of microfibers and microchips is required to observe cell growth, perform functional testing in a 3D environment *in vitro*, offer a platform to study the mechanism of disease occurrence, and conduct drug evaluations.

In this study, we prepared a microfluidic spinning microchip template and microfiber assembly microchip template with different channel heights using 3D printing technology in one step and then prepared a microfluidic spinning microchip and microfiber assembly microchip using the polydimethylsiloxane (PDMS) molding method. Hollow calcium alginate (CaA)/GelMA composite microfibers with different numbers of cavities were prepared using a microfluidic spinning microchip and various flow strategies. The composition and structure of the microfibers were characterized using infrared spectroscopy and scanning confocal microscopy. Then, human umbilical vein endothelial cells (HUVECs) were seeded and cultured in CaA/GelMA composite hollow microfiber tube walls, and biomarkers related to vascular endothelialization were characterized. Finally,

by assembling HUVECs-loaded hollow microfiber microchips, an *in vitro* neural differentiation model, capable of detecting axonal growth and related gene expression in PC12 cells under the action of nerve growth factor (NGF), was constructed. This model is expected to provide a new platform for studying the development of neurological diseases and evaluating drugs, and to offer an avenue for personalized diagnosis.

2. Materials and methods

2.1. Materials

NaA, GelMA (90%), calcium chloride dihydrate ($CaCl_2 \cdot 2H_2O$), chitosan (η > 400 mPa·s), polystyrene microspheres (PS microspheres; 5 μm, ex/em: 400/450 nm), and polystyrene microspheres (PS microspheres; 5 μm, ex/em: 488/518 nm) were purchased from Shanghai Aladdin Biochemical Technology Co., Ltd. (Shanghai, China). Pluronic® F-127 (PF-127), 2-hydroxy-4'-(2-hydroxyethoxy)-2-methylphenylacetone (I2959, 98%), acetic acid, isopropanol, dimethyl sulfoxide (DMSO), and 4', 6-diamino-2-phenylindole dihydrochloride (DAPI) were purchased from Sigma (Shanghai, China). The 3D printing resin, containing methacrylate monomers, methyl oligomers, and photoinitiators, was purchased from Shenzhen Mofang Materials Technology Co., Ltd. Shenzhen, China. Sylgard 184 PDMS was purchased from Dow Corning (Midland, America). Fetal bovine serum (FBS), horse serum, Roswell Park Memorial Institute Medium 1640 (1640 medium), and double antibiotic solution containing penicillin and streptomycin were purchased from Gibco Grand Island, America. Endothelial cell culture medium, supplemented with FBS, double antibiotic solution containing penicillin and streptomycin, and endothelial cell growth additive, was purchased from ScienCell, San Diego, America. CellTracker Green CMFDA, propidium iodide, Alexa Fluor® 488 phalloidin, and Alexa Fluor 568 Dextran (10 kDa) were purchased from Life Invitrogen Carlsbad, America. Rabbit anti-von Willebrand factor (vWF), rabbit anti-β-Tubulin, goat anti-rabbit IgG 568, blocking buffer, and antibody diluent were all purchased from Abcam, Cambridge, England. Nerve growth factor was purchased from R&D Systems (Minneapolis, America).

2.2. Fabrication and characterization of microchip

According to the device manual, a 3D printing device (nanoArch® SI40, BMF Material Technology Inc., Shenzhen, China) was used to prepare microfluidic chip templates. There exist two types of templates: microfluidic spinning and microfiber assembly microchip templates. We prepared two templates as described previously.[41,42] Solidworks software was used to design the chip templates. BMF_3Dslice software was used to slice and import images to the computer connected to the 3D printer. The platform lifting distance was adjusted according to the number of images and the required accuracy, and the splicing mode was selected to print the photosensitive resin chip template. Subsequently, the PDMS monomer and initiator were evenly mixed in a 10:1 (v/v) solution and poured onto a resin template. Bubbles were removed under vacuum, and the PDMS prepolymer was cured at 80°C for 1 h. Subsequently, a PDMS layer with microchannels was obtained by peeling off the template. For the microfluidic spinning microchip, irreversible sealing was required, that is, oxygen plasma surface treatment was performed on two PDMS layers with the same structure for alignment and sealing to obtain the final microfluidic spinning microchip. The microfiber assembly microchip did not require sealing and was sterilized as a backup. The dimensions of the template and the microfluidic chip were measured using an inverted fluorescence microscope (IX-73, Olympus, Tokyo, Japan) or a stylus profilometer (AlphaStep D-300 Stylus Profile, KLA, Milpitas, America).

2.3. Preparation and characterization of composite hollow microfibers

NaA, GelMA, I2959, $CaCl_2 \cdot 2H_2O$, and PF-127 were all dissolved in deionized water and sterilized for future use. A 20% w/v PF-127 solution was used as the core flow, a mixture of 0.8% w/v NaA, 5% w/v GelMA, and 0.5% w/v photoinitiator I2959 was used as the sample flow, and a 4% (w/v) $CaCl_2$ solution was used as the sheath flow. The core, sample, and sheath flows were injected into the microchannels of the microfluidic spinning microchip using a microinjection pump (Harvard, Holliston, America). A UV device emitting rays at a wavelength of 365 nm was fixed above the microchip outlet position, and the microfibers were collected in a $CaCl_2$ solution tank. To determine the composition of the composite microfibers, we characterized the composition of GelMA, a mixture of CaA and GelMA, and the prepared CaA/GelMA microfibers using Fourier transform infrared (FTIR) spectroscopy (Thermo Fisher Scientific, Waltham, America). To investigate the effect of flow rate on the diameter of microfibers and facilitate the observation of the morphology of hollow microfibers, we mixed blue fluorescent PS microspheres (5 μm, ex/em: 400/450 nm) and green fluorescent PS microspheres (5 μm, ex/em: 488/518 nm) at a concentration of 0.1 mg/mL into the sample solution and injected them into the corresponding microchannels. The flow velocity rates for core flow, sample flow, and sheath flow were 5–100, 50–110, and 120–200 μL/min, respectively.

2.4. Microfiber assembly and diffusion experiment

In this study, we used a self-made 3D printing device[41] to print CaA/GelMA hollow composite microfibers onto a microfiber assembly microchip. Afterward, 100 μL NaA/GelMA mixed solution was added into the rectangular middle chamber of the microfiber assembly microchip to cover the composite microfiber. Subsequently, by adding $CaCl_2$ solution and applying UV light at a wavelength of 365 nm for 60 s, the assembly of composite microfibers in the microfiber assembly microchip was achieved. During the preparation of microfibers, Alexa Fluor 568 Dextran (10 kDa) was added to the core flow with a final concentration of 100 μg/L. After the microfibers were generated, they were immediately printed onto the microfiber assembly microchip, and the diffusion of the fluorescent dyes at different times in the assembly system was imaged using an inverted fluorescence microscope (IX-73, Olympus, Tokyo, Japan). In addition, to characterize the pores in the microfibers in the assembly system, blue fluorescent PS microspheres (0.1 mg/mL) were added to the inlet of the assembled fibers, and their tracks were tracked using an inverted fluorescence microscope.

2.5. Cell culture

HUVECs used in this study were donated by Prof. Wang Li (Fudan University). PC12 cells were purchased from the Cell Bank/Stem Cell Bank of the Chinese Academy of Sciences (ATCC Source). The HUVECs were cultured in endothelial cell culture medium supplemented with 1% v/v double antibiotic solution containing penicillin and streptomycin, 1% v/v endothelial cell growth additive, and 5% v/v FBS. PC12 cells were cultured in RPMI 1640 medium supplemented with 1% v/v double antibiotic solution containing penicillin and streptomycin, 5% v/v horse serum, and 10% v/v FBS. Cells were cultured in an incubator maintained at 37°C with a concentration of 5% CO_2, and passaged every 2 days.

2.6. Preparation of cell-loaded microfibers

The HUVECs were digested using 0.25% trypsin-EDTA and resuspended in a mixed NaA/GelMA solution to obtain a density of 2×10^5/mL. To encapsulate cells, a mixture of PF-127 solution and NaA/GelMA was filtered using a 0.22 μm sterile membrane before the operation. The $CaCl_2$ solution was high-pressure sterilized, and the spinning device was pre-disinfected with UV light for 30 min. After production was completed, the cell-loaded microfibers were transferred to a complete cell culture medium containing a 0.1% w/v chitosan solution (filtered for sterilization) for further cultivation, and the medium was changed every 2 days.

2.7. Cell tracing and staining

To track the HUVECs and their position in the microfibers, according to a previous study,[43] Cell Tracker Green CMFDA was used to label HUVECs. The cells were cultured for 7 days, during which fluorescence images of the cells were obtained using a laser scanning confocal microscope (FV3000, Olympus, Tokyo, Japan). For cell viability testing, the cell-loaded microfibers prepared using the above method were stained with propidium iodide on the 1st and 7th days. According to the instructions, Alexa Fluor 488 phalloidin was used to characterize the F-actin of HUVECs in microfibers and plates. In addition, immunofluorescence staining was used to detect the expression of vWF in HUVECs in hollow composite microfibers and plates. Cells were fixed at room temperature in 4% paraformaldehyde for 10 min. The cells were then soaked in 0.1% Triton X100 for 3–5 min and then in a blocking buffer for 1 h. Afterward, rabbit anti-vWF was added (diluted 1:100) and incubated overnight at 4°C. Finally, the secondary antibody (diluted 1:100) was added, the cells were incubated for 1 h, and the cell nuclei were stained with DAPI for 10 min. Fluorescent images of the cells were captured using a laser scanning confocal microscope.

2.8. Neural model construction and differentiation evaluation

The CaA/GelMA hollow composite microfibers loaded with HUVECs were 3D-printed onto a sterilized microfiber assembly microchip. The PC12 cells were resuspended in a NaA/GelMA mixture solution. The resultant cell suspension was added to the middle chamber of the microfiber assembly microchip, and 100 μL of the cell suspension was added to completely cover the composite microfibers, which were cured by the addition of $CaCl_2$ solution and UV light for 60 s to complete the assembly. In a previous study,[44] neural differentiation induction experiments were performed on PC12 cells, which were stimulated using a complete medium with 100 ng/mL NGF. There were three groups in this experiment: NGF- HUVEC- group, NGF+ HUVEC- group, and NGF+ HUVEC+ group. Among them, the NGF- HUVEC- group was the negative control group in which the assembled composite microfibers were not loaded with HUVECs, and NGF was not added to the system. In the NGF+ HUVEC- group, the microfibers were not loaded with HUVECs, and NGF was added to the hollow microfiber in PF-127 solution and continuously applied to the system after microfiber assembly. In the NGF+ HUVEC+ group, the microfibers were loaded with HUVEC cells, and NGF was added to hollow microfiber in PF-127 solution and continuously applied to the system after microfiber assembly. After 7 days of culture, PC12 cells were stained for F-actin, and the differentiation of PC12 cells was assessed by measuring the axon length on day 7 under a microscope. Tubulin III expression in PC12 cells was detected by means of immunofluorescence staining, and all images were acquired using laser confocal

microscopy. Quantitative polymerase chain reaction (qPCR) assays for growth cone marker growth-associated protein 43 (GAP-43) and sympathetic marker tyrosine hydroxylase (TH) of neural-associated mRNAs were performed. The primer sequences are as follows:

- GAP-43: 5'-CGACAGGATGAGGGTAAAGAA-3' (forward)
  5'-GACAGGAGAGGAAACTTCAGAG-3' (reverse)
- TH: 5'-GTGAACCAATTCCCCATGTG-3' (forward)
  5'-CAGTACCGTTCCAGAAGCTG-3' (reverse)
- GAPDH: 5'-TCCAGTATGACTCTACCCACG-3' (forward)
  5'-CACGACATACTCAGCACCAG-3' (reverse)

2.9. Statistical analysis

In this work, all experiments were performed at least three times. All data are presented as mean ± standard deviation (SD), unless otherwise stated. Results are considered statistically significant when p <0.05, as determined by Student's t-test. Data processing of the FTIR spectra was performed using Origin software. The cross-sectional area of the microfibers, number of cells in the microfibers, and axon length in the fluorescence images and 3D videos were analyzed using ImageJ software, an inverted fluorescence microscope, and confocal microscope self-contained software. Analysis of qPCR outputs was performed using the Lightcycle 96 (Roche) self-contained software.

3. Results and discussion

3.1. Design and preparation of microfluidic spinning microchip

In this study, we employed a microfluidic spinning strategy to fabricate CaA/GelMA microfibers with a hollow structure, and the microfluidic spinning microchip was designed according to a previous report.[41] The resin templates were prepared using 3D printing technology, as shown in Figure 1A$_1$. The microchip resin template was fixed on glass using an AB adhesive to ensure that the template was not bent or deformed. The resin template consists of 9 microchannels distributed in a symmetric structure, named M_I (2 microchannels), M_{II} (2 microchannels), M_{III} (2 microchannels), M_{IV} (2 microchannels), and M_V (1 microchannel) in order, where the design height of M_{III} and M_V is 0.21 mm, and the actual measured height is 0.16 ± 0.02 mm; for M_{II} and M_{IV}, a design height of 0.45 mm and an actual measurement height of 0.41 ± 0.02 mm were used; these 7 microchannels converge at the J_1 position, at a similar height as M_{II} and M_{IV}. The design height of M_I and the outlet is 0.63 mm, with the actual measurement height being 0.62 ± 0.01 mm, M_I with confluence point J_1 converging again at the J_2 position, and J_2 position being connected to the outlet with a height similar to that of M_I and the outlet. Resin templates with different channel heights can be prepared by one-step 3D printing. The generated template exhibits exceptional attributes, such as smooth surface, clear microchannels, minimum difference between the actual printing height and the design height, and high fineness, which are the most sought-after characteristics in the preparation of in microfluidic spinning chips.

After the resin template was cleaned and silanized, the PDMS layer was obtained by the PDMS molding method. One PDMS layer was perforated and plasma-sealed with another identical PDMS layer to obtain a microfluidic spinning microchip, as shown in the inset of Figure 1A$_2$. The transparent PDMS material of the microfluidic spinning chip also provided favorable conditions for observing the fluid flow in the microchannel under a microscope. To prepare CaA/GelMA microfibers with hollow structures, as shown in Figure 1A$_2$, we injected $CaCl_2$ solution as a sheath flow in channel M_I, sample solutions containing NaA, GelMA, and the photoinitiator in channels M_{II} and M_{IV}, and core flow solution in M_V. The transient ionic crosslinking of NaA and $CaCl_2$ was used to form hollow microfibers, and CaA/GelMA microfibers were obtained after crosslinking was induced by a second UV exposure (**Figure S1** in Supplementary File). Procedurally, the spinning process involves two crosslinking reactions: ionic crosslinking and UV crosslinking. The first step of ionic crosslinking was achieved by the rapid formation of a calcium-alginate hydrogel via an ion-exchange reaction of NaA and calcium ions.[26] This step is crucial as it encapsulates the prepolymer of GelMA and the photoinitiator I2959, enabling the second step of photocrosslinking. Under UV light irradiation at a wavelength of 365 nm, the photoinitiator I2959 underwent a cleavage reaction to form reactive radicals, and the GelMA-containing photosensitive groups underwent a polymerization reaction to form GelMA hydrogels.[45] To facilitate the observation of the morphology and structure of the hollow fibers, we added PS microspheres with a diameter of 5 μm each to the sample solution, and the particles in the walls of the hollow microfiber tubes could be viewed under the microscope, as shown in the inset of Figure 1A$_2$.

3.2. Manufacturing and characterization of composite hollow microfibers

Using this fast and efficient microfluidic spinning method, the material selection, concentration, and flow rates of the sample, sheath, and core flow solutions were optimized. The effects of the different sheath and sample flow rates on the

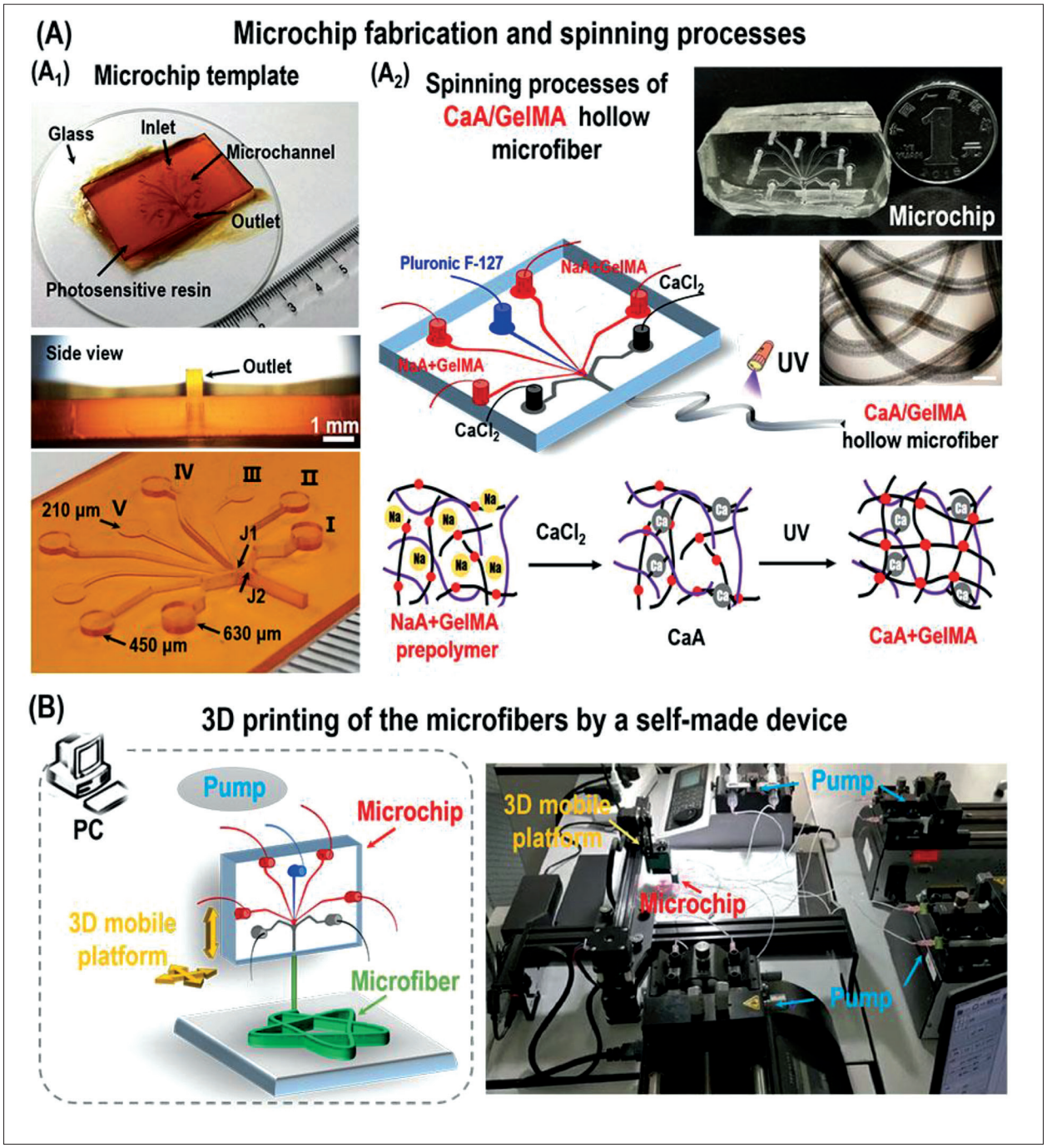

Figure 1. (A) Microchip fabrication and spinning processes. (A_1) Images of the resin template of the microfluidic spinning microchip prepared by 3D printing technology. (A_2) Schematic diagram of the processes of microfluidic spinning to prepare hollow CaA/GelMA microfibers. The inset illustrates images of the microfluidic spinning microchip and hollow microfibers, in which PS microspheres with a diameter of 5 μm each were added to the core flow. (B) Schematic diagram of 3D printing of the microfibers by a self-made device.

cross-sectional areas of the microfibers were investigated. As shown in Figure 2A, when the sheath flow rate was 160 μL/min and the sample flow rate was increased from 50 to 110 μL/min, the microfiber cross-sectional area increased with the increase of the sample flow rate. In contrast, as shown in Figure 2B, when the sample flow rate was 80 μL/min, the sheath flow rate increased from 120 to 200 μL/min, and the microfiber cross-sectional area decreased with an increase in the sheath flow rate. This situation is similar to findings reported in previous studies.[26,46] However, it is

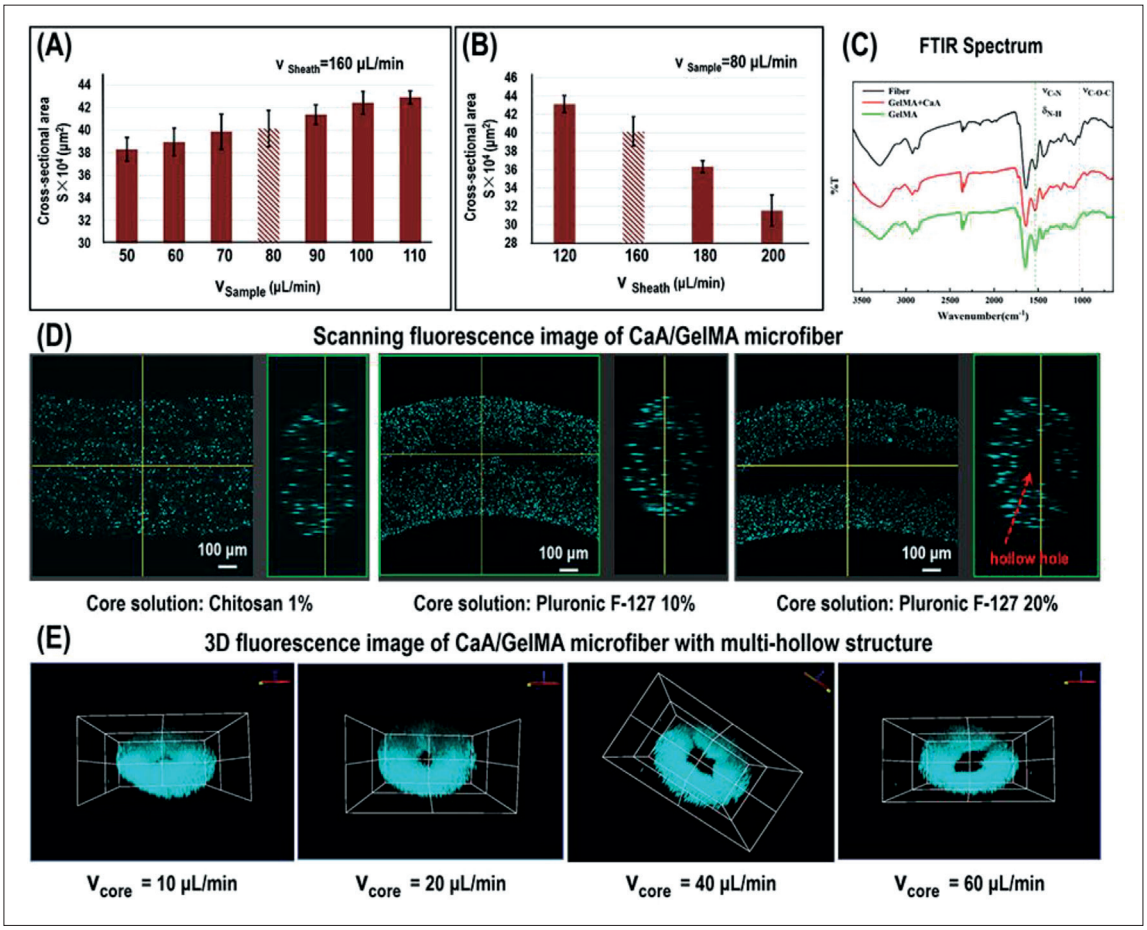

Figure 2. Manufacturing and characterization of composite hollow microfibers. (A) Histogram of the cross-sectional area of composite microfiber under different sample flow rates (n = 6). Data are expressed as mean ± SD. (B) Histogram of the cross-sectional area of composite microfiber under different sheath flow rates (n = 6). Data are expressed as mean ± SD. (C) FTIR Spectrum of GelMA, the mixture of CaA and GelMA (CaA+GelMA), and the prepared microfiber. (D) Fluorescence images of composite hollow microfibers with different core flow solutions. Scale bar = 100 μm. (E) 3D views of composite hollow microfibers with different core flow rates. Blue fluorescent PS microspheres were added to the sample flow for fluorescence photography.

worth noting that when the sample and sheath flow rates were too high or low, the formation of microfibers was difficult to maintain. When the flow rate is too low, the fluid will fluctuate owing to the limitation of the perfusion equipment; the microfibers cannot flow out of the channel quickly after formation and can easily accumulate at the outlet, leading to channel blockage and fiber deformation. When the flow rate is high, the sample flow and sheath laminar flow instability led to an uneven fiber morphology, and fast flow rate increased the sample flow consumption and waste. Therefore, after comparing the morphology of the microfibers at different flow rates, the optimal conditions for the rate of sample and sheath flows were determined to be 80 μL/min for the sample flow and 160 μL/min for the sheath flow. The optimal compositions for preparing the sample and sheath flows of the composite microfibers are 0.8% w/v NaA, 5% w/v GelMA, and 0.5% I2959 prepolymer solution for preparing the sample flow solution or 4% w/v $CaCl_2$ solution for preparing the sheath flow solution.

In addition, the compositions of the composite microfibers were characterized using FTIR spectroscopy, as shown in Figure 2C. Pure GelMA (GelMA), a mixture of GelMA and CaA (CaA+GelMA), and the prepared composite microfibers (fibers) were analyzed. The characteristic peak related to N-H bending vibration and C-N stretching vibration in GelMA occurred at about 1550 cm^{-1} wave number, and due to the stretching of C-O-C, the characteristic peak of CaA occurred at about 1030 cm^{-1} wave number, while the characteristic peaks of fibers containing CaA and GelMA occurred at 1030 cm^{-1} and 1550 cm^{-1}, respectively, a finding consistent with previous reports.[26,47] This confirmed that the microfibers contained GelMA.

In addition, we examined the effects of the core solution material selection, concentration, and flow rate on the preparation of composite hollow microfibers. The core solution, as the occupancy fluid of hollow microfibers, is generally selected as a substance with high viscosity that does not react with the sample solution; polyvinyl alcohol[41] and PF-127[8] are commonly used. In this study, for biocompatibility and stability reasons, we chose chitosan and PF-127 as the core solutions, which can stabilize the CaA gel so that it does not easily dissolve and degrade; of note, PF-127 is suitable for spinning systems by virtue of good biocompatibility and adjustable viscosity. We added fluorescent PS microspheres to the sample solution in order to perform fluorescence photography of the confocal microscope, and the structure of the microfibers is shown in Figure 2D. When the core flow was 1% chitosan solution, no hollow structure was formed inside the microfiber; when the core flow was 10% PF-127, the hollow pores were generated inside the microfiber, but the homogeneity was poor and the hollow pores were discontinuous; when 20% PF-127 solution was used as the core solution, the hollow pores were obvious and the hollow structure of the microfiber was stable. Therefore, 20% PF-127 solution was selected as the core solution. Subsequently, when the sample flow (80 μL/min) and sheath flow (160 μL/min) rates were kept constant, the core flow rate was changed to prepare hollow microfibers. When the core flow rate was increased from 10 to 60 L/min, the hollow pores of the composite microfibers gradually became obvious (Figure 2E). Among them, the flow rate of 20 μL/min promoted the formation of microfiber hollow structure with a regular circular cavity. When the flow rate was less than 10 μL/min, the cavities were small and irregular. In contrast, when the flow rate was between 40 and 60 μL/min, the cavity structure flattened, becoming elliptical and larger but remaining incomplete. This may be due to the fact that the core flow rate was too high for the whole system, which squeezed the sheath and sample flows, pushing them closer to the wall of the microchannel. This leads to thinner liquid flows, causing the deformation of the hollow microfibers and the formation of incomplete lumen. A core flow rate of 20 μL/min was chosen for subsequent experiments to ensure the stable formation of hollow composite microfibers and the integrity of the lumen. Under these optimized conditions, the flow was stable throughout the continuous spinning process, and the prepared hollow microfibers had a distinct and complete lumen structure, thereby confirming the controllability and stability of the microfluidic spinning strategy used in these experiments.

3.3. Preparation and characterization of multi-hollow composite microfibers

Based on the above results, we further prepared multi-hollow CaA/GelMA composite microfibers by adjusting the perfusion fluid strategy. While keeping the sheath flow and sample flow unchanged, the core flow was changed from M_V to M_{III} and the number of core flows was increased from one to two to facilitate the preparation of double-lumen hollow CaA/GelMA composite microfibers, as shown in Figure 3A and **Video S1** (Supplementary File). In addition, by adding different types of fluorescent PS microspheres, such as blue fluorescent PS microspheres and green fluorescent PS microspheres, to the sample solution of M_{II} and M_{IV}, two types of double-lumen hollow CaA/GelMA composite microfibers with different inclusions were obtained, as shown in Figure 3B and **Video S2** (Supplementary File). This type of microfiber with different contents holds application potential for 3D co-culture, 3D biomanufacturing, and multi-tissue simulation in complex systems. Furthermore, by applying core flow to both channels M_V and M_{III} and further increasing the number of core flows, three more complex three-lumen hollow CaA/GelMA composite microfibers could be prepared, as shown in Figure 3C and **Video S3** (Supplementary File). In theory, one can continue to increase the number of fluid channels and set up more complex fluid infusion strategies to prepare more complex multi-lumen hollow microfibers. However, increasing the number and type of fluids would further complicate the microfluidic spinning chip and encumber the peripheral fluid-driven devices, adversely affecting the preparation of the microfluidic spinning microchip and the stability of the fluid perfusion system.

3.4. Hollow composite microfibers for the 3D culture of HUVECs

In the above-mentioned experiment, PS microspheres were added to the sample solution to assist with microfiber loading. These microspheres had a diameter of 5 μm each, similar to the cell diameter (~10 μm). Since it is not difficult to prepare cell-loaded hollow microfibers using the hollow microfiber preparation method mentioned above, we loaded HUVECs into the CaA/GelMA hollow composite microfibers to explore the feasibility of using them as cell scaffolds to achieve microvascularization. The HUVECs were stained with Cell Tracker Green CMFDA for microfluidic spinning. The resulting hollow microfibers are shown in Figure 4A. After HUVECs-loaded hollow microfiber was incubated in the culture medium for 7 days, propidium iodide staining was performed to assess cell viability. The cell viability rate of HUVECs-loaded hollow microfiber, measuring approximately 90%, was significantly higher than that of the HUVEC-loaded CaA microfibers (Figure 4A). This was because the

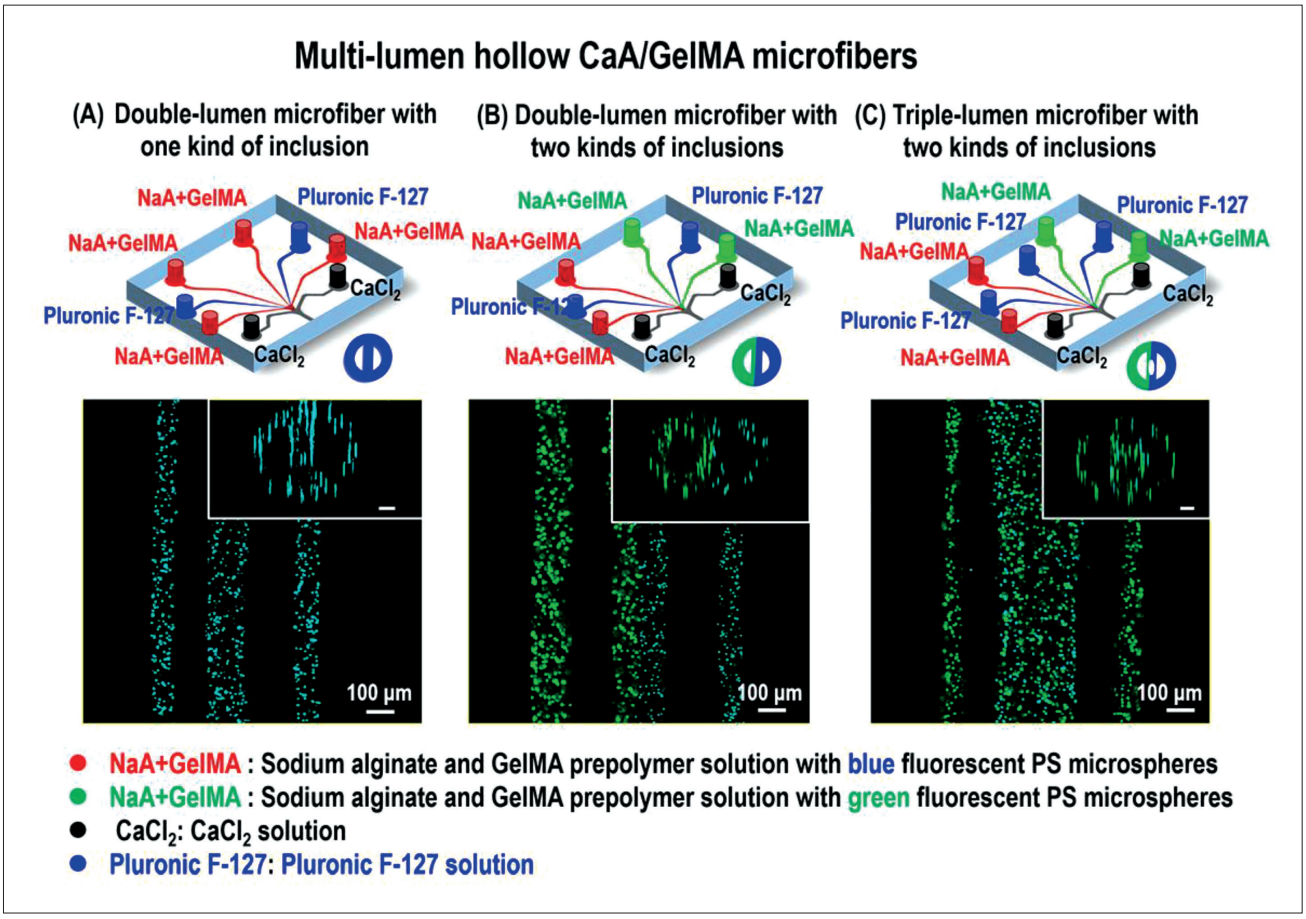

Figure 3. Perfusion fluid strategy and characterization of multi-lumen hollow CaA/GelMA composite microfibers. (A) CaA/GelMA double-lumen microfiber with one kind of inclusion. (B) CaA/GelMA double-lumen microfiber with two kinds of inclusions. (C) CaA/GelMA triple-lumen microfiber with two kinds of inclusions. Scale bar = 100 μm.

GelMA hydrogel was compounded in the microfiber.[48] As a substitute for gelatin, GelMA has been widely used as a scaffold material for vascular tissues in 3D cultures and vascular construction.[33,48,49] Owing to its excellent biocompatibility and rapid UV curing processability, it is also applied in 3D bioprinting.

In addition, we observed the morphology and protein expression of the HUVECs in the hollow composite microfibers using fluorescence staining. F-actin is a cytoskeletal protein commonly used to characterize cell morphology and can be characterized by staining with Alexa Fluor 488-labeled phalloidin. We stained the F-actin of HUVECs cultured in composite microfibers for 7 days and compared the morphology of HUVECs cultured on the plates. The high-magnification laser confocal microscopy images (Figure 4B and D) reveal that HUVECs cultured in composite microfibers have an enhanced 3D morphology and a tendency to extend, closely resembling the morphology of real living cells. Moreover, the morphology of HUVECs cultured on the plates tended to flatten. The vWF is a protein synthesized and secreted by vascular endothelial cells and megakaryocytes and a marker of vascular endothelialization. We characterized vWF in HUVECs cultured in composite microfibers for 7 days and compared the expression of vWF in HUVECs cultured on a plate. The high-magnification laser confocal microscopy images (Figure 4C and E) show that HUVECs cultured in composite microfibers exhibited a positive expression of vWF, which was brighter than that in HUVECs cultured in two-dimensional culture.

3.5. Assembly of hollow composite microfibers and construction of neural model

To further expand the application of hollow microfibers and make them convenient for the construction of various types of disease/physiological models, we realized the 3D printing of hollow composite microfibers using a 3D printing platform built in the laboratory (Figure 1B).[41] The fluorescence images of 3D-printed hollow microfiber are

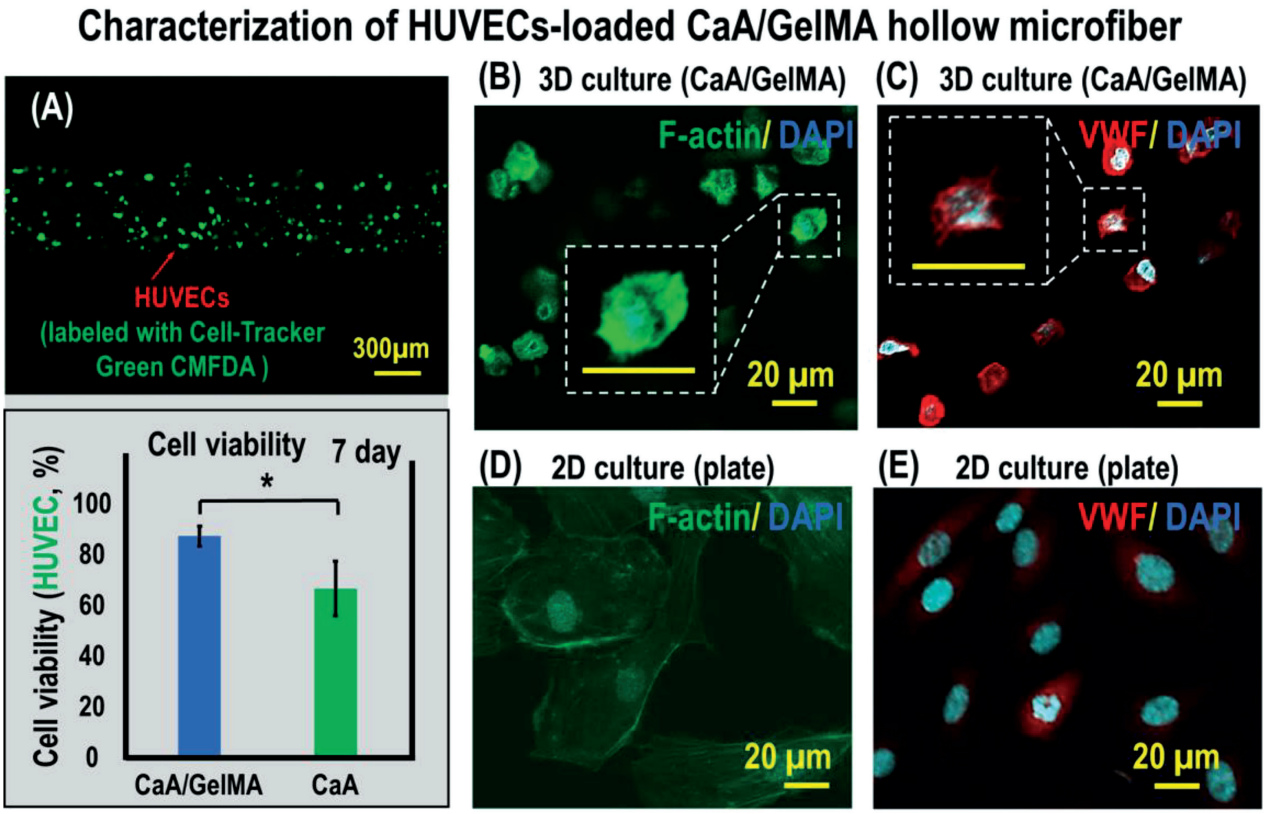

Figure 4. Characterization of HUVECs-loaded CaA/GelMA hollow microfiber. (A) Confocal images of HUVECs cultured in CaA/GelMA microfiber (green: Cell Tracker Green CMFDA) and cell viability histograms (n = 4). Data are expressed as mean ± SD. Student's t-tests were performed for data analysis. *$p < 0.05$. (B, D) F-actin staining images of HUVECs cultured in composite microfiber and plate. Green: F-actin; blue: DAPI; scale bar = 20 μm. (C, E) vWF staining images of HUVECs cultured in composite microfiber and plate. Red: vWF; blue: DAPI; scale bar = 20 μm.

shown in Figure 5A. Accordingly, we printed HUVECs-loaded hollow microfibers onto a microfiber assembly microchip consisting of one inlet, one outlet, a microfiber fixation channel, and a rectangular-area cell culture chamber, as shown in Figure 5B. The microfiber assembly microchip allowed the assembly of composite microfibers and was designed with a microchip channel width of 1000 μm and a rectangular area of 7.5 cm × 1.5 cm. To verify the ability of the hollow pipeline to transport liquid after hollow fiber assembly, we added an aqueous solution containing blue fluorescent PS microspheres dropwise at the inlet of the microfiber assembly microchip. The flow of the microspheres was video-recorded with the aid of fluorescence microscopy, as shown in Figure 5C and **Video S4** (Supplementary File). It can be seen that the microspheres can easily enter the hollow and roll continuously, which further proves the existence of hollow fiber pores and the patency of the duct.

To construct neural models using hollow microfibers, we used the pheochromocytoma cell line PC12 cells. PC12 cells are a validated neuronal cell model widely used to study neuronal differentiation. PC12 cells undergo neural differentiation in response to NGF and exhibit typical neural phenotypes and axonal growth. NGF is a biologically active protein, with a molecular weight of 26.5 kDa. To verify the ability of this protein to diffuse into the lumen of the hollow microfibers, we used 10 kDa Alexa Fluor 568 dextran as a fluorescent dye. During microfiber preparation, dextran at a final concentration of 100 μg/L was added to the core solution. After the microfibers were prepared, they were immediately printed onto the assembly microchip. Subsequently, NaA and GelMA were added to the assembly microchip for ionic crosslinking and UV light crosslinking, and real-time images were taken using an inverted fluorescence microscope to observe the dye molecules (Figure 6A). The fluorescently labeled dextran, a large-molecule fluorescent dye, could diffuse over time in the hollow microfibers without HUVECs, but the concentration gradient of the dye between the inside and the outside of the microfibers diminished after approximately 2 h. In contrast, in the HUVECs-loaded

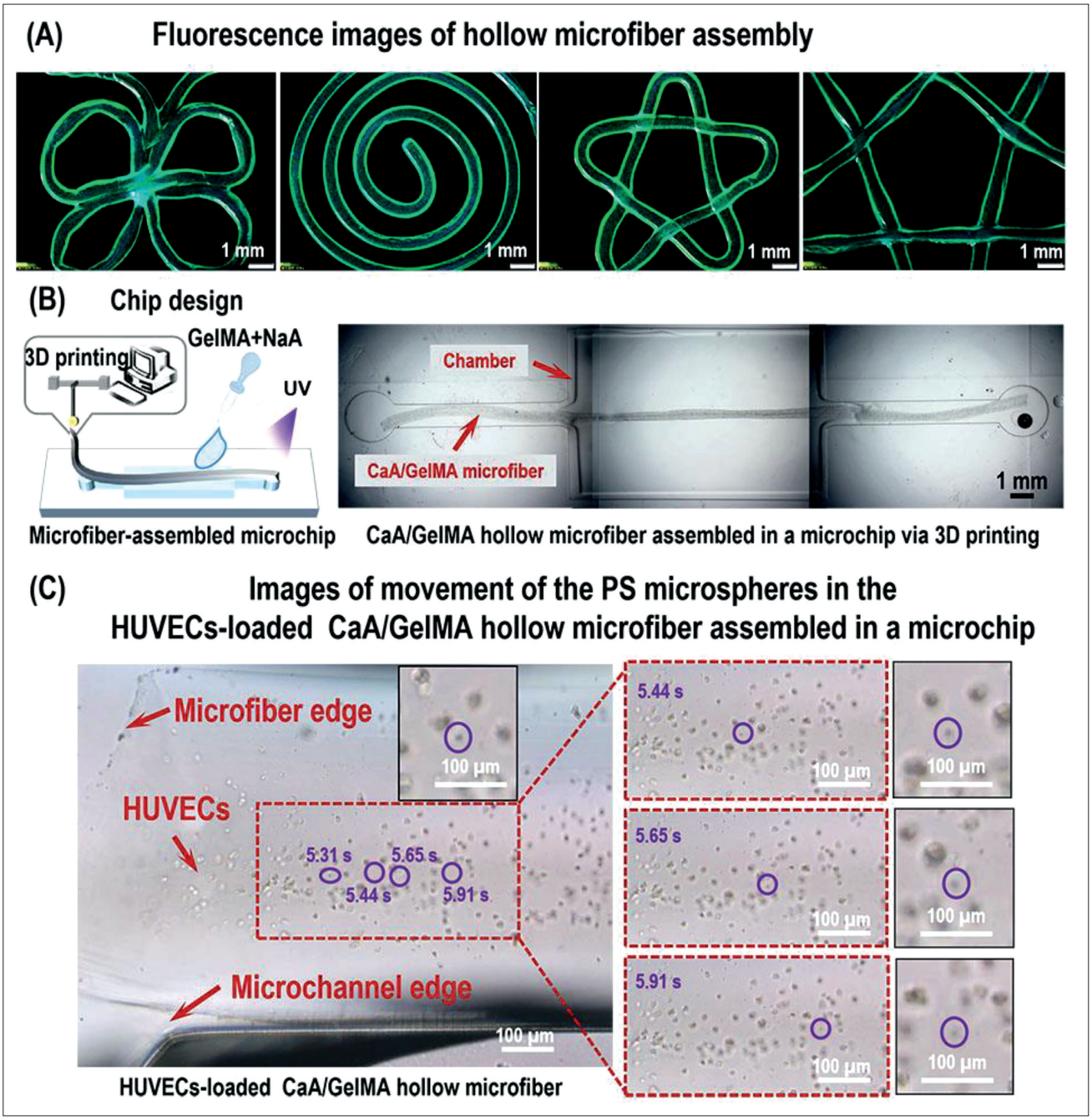

Figure 5. Hollow microfiber assembly and PS microspheres movement in the hollow microfibers. (A) Fluorescence images of 3D-printed hollow microfibers. Scale bar = 1 mm. (B) Hollow microfiber assembly in a microfiber assembly microchip. Scale bar = 1 mm. (C) Real-time images of PS microspheres movement in hollow microfibers. Scale bar = 100 μm.

hollow microfibers, the HUVECs posed an occupancy and barrier effect, blocking the diffusion of fluorescent dye molecules. In view of this, we added NGF to the hollow microfiber and adopted a continuous mode of NGF addition to the assembly microchip to induce PC12 cell differentiation in the construction of the neural model. A schematic representation of the constructed neural model is shown in Figure 6B.

For this HUVEC-loaded hollow microfiber-based neural model, we performed experiments in which we applied a permutation of NGF stimulation (labeled as NGF+) and HUVEC loading (labeled as HUVEC+) to the

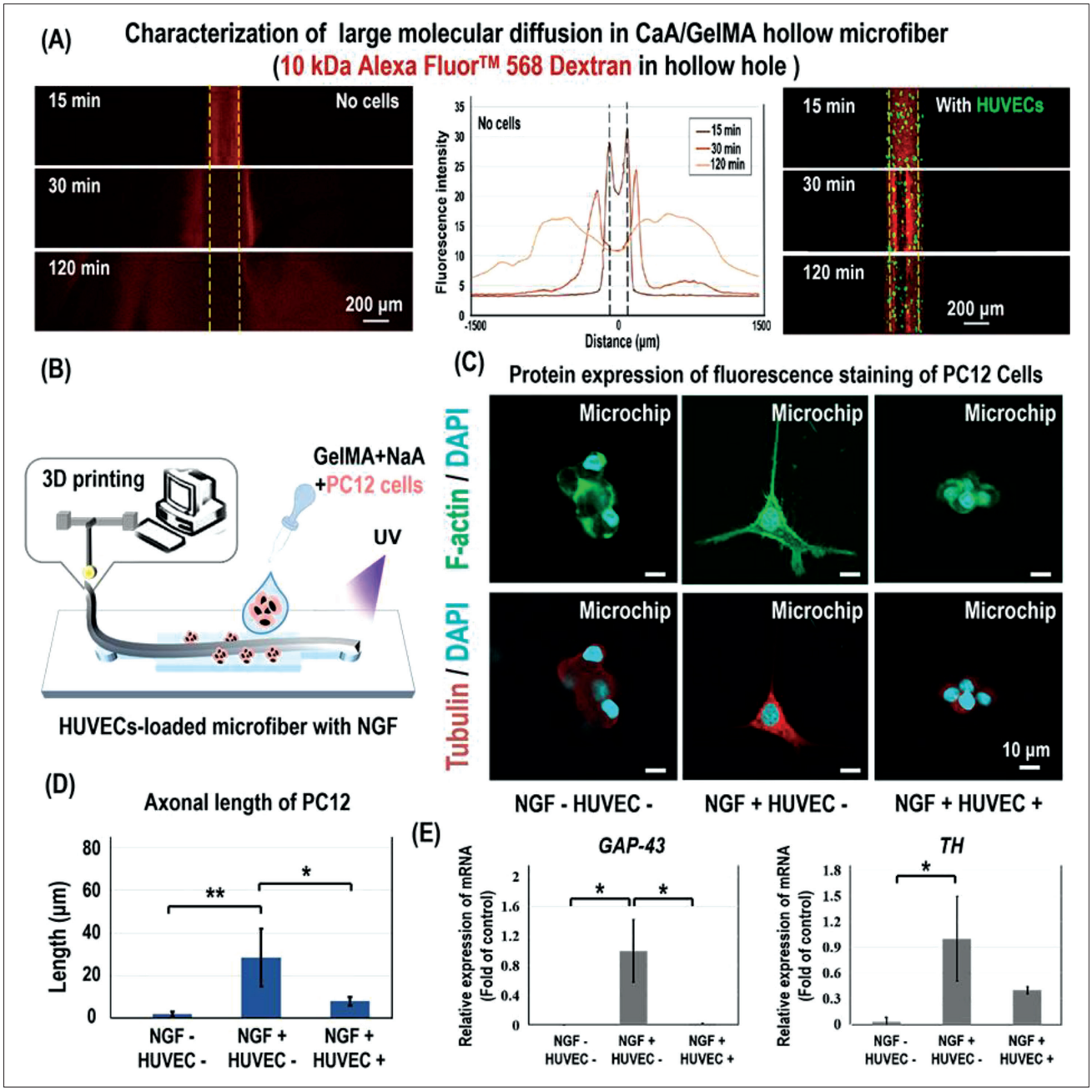

Figure 6. Assembly of hollow composite microfibers and construction of neural model. (A) The diffusion images of Alexa Fluor 568 dextran (10 kDa) in hollow microfibers. Scale bar = 200 μm. (B) Schematic diagram of the constructed neural model. (C) F-actin and tubulin fluorescence staining images of PC12 cells under different conditions for 7 days. (D) Histograms of the axonal length of PC12 under different conditions for 7 days (n = 6). Data are expressed as mean ± SD. Student's t-tests were performed for data analysis. $^{*}p < 0.05$; $^{**}p < 0.01$. (E) Histograms of *GAP-43* and *TH* gene expression in PC12 for 3 days under different conditions. In the gene expression experiment, a treatment of 100 ng/mL NGF was used, and *GAPDH* was used as the housekeeping gene (n = 3). Data are expressed as mean ± SD. Student's t-tests were performed for data analysis. $^{*}p < 0.05$.

microfibers, creating three groups, namely NGF- HUVEC- group (negative control group), NGF+ HUVEC- group, and NGF+ HUVEC+ group. After 7 days of treatment, F-actin and neuron-associated protein β-microtubulin III (tubulin) were fluorescently stained, and the axon lengths of the cells were measured according to the results of cell staining, as shown in Figure 6C and D. Following the addition of NGF, PC12 cells exhibited increased axon length, indicating that they underwent neural differentiation. Meanwhile, in the HUVEC+ group, axon length was significantly

reduced compared to that in HUVECs, consistent with the results of the diffusion experiments, where the presence of HUVECs would, to some extent, block the entry of NGF into the 3D culture microenvironment of PC12 cells, leading to reduced differentiation. To further verify this result, we examined the gene expression of *GAP-43* and *TH* using real-time qPCR. The results showed that *GAP-43* was obviously expressed in NGF+ HUVEC- group, but not detected in NGF- HUVEC- group and NGF+ HUVEC+ (Ct > 40) (Figure 6E). Also, the expression level of *TH* gene in NGF+ HUVEC+ group was significantly lower than that in NGF+ HUVEC- group, and no *TH* gene was detected in NGF- HUVEC- group, which indirectly reflected the barrier effect of vascular endothelium. Moreover, it is possible to construct an experimental neural model by assembling cell-loaded hollow microfibers in a microchip, thereby realizing the 3D culture of neural-related cells. The HUVECs-loaded hollow fibers, which possess barrier effect, hold application potential in *in vitro* blood–brain barrier simulation, neuropharmaceutical and toxin evaluation, and brain-on-a-chip construction.

4. Conclusion

In this study, we used 3D printing technology to prepare microchip templates and obtain microfluidic chips, which allowed the successful manufacture of CaA/GelMA composite microfibers with different numbers of hollow lumens using microfluidic spinning microchips coupled with different flow injection strategies. The compositions and structures of the composite microfibers were characterized using FTIR spectroscopy and scanning confocal microscopy. HUVECs were seeded and cultured in CaA/GelMA composite hollow microfiber tube walls, and the cell viability and expression of related biomarkers of vascular endothelialization were assessed. Finally, by assembling HUVEC-loaded hollow microfibers into assembly microchips, an *in vitro* neural differentiation model, capable of detecting axonal length, tubulin, and related gene (*GAP-43* and *TH*) expression in PC12 under the action of NGF, was constructed. This model is expected to provide a new platform for investigating the occurrence and development of neurological diseases and evaluating new drugs and toxins, with promising applications in *in vitro* blood–brain barrier simulation and organ-on-a-chip construction.

Acknowledgments

None.

Funding

This work was supported by the Ningbo Natural Science Foundation (grant no. 2022J252) and Ningbo Medical and Health Leading Academic Discipline Project (grant no. 2022-F04).

Conflict of interest

The authors declare no conflicts of interest.

Author contributions

Conceptualization: Jingyun Ma, Xinghua Gao
Formal analysis: Wei Li, Lingling Tian
Funding acquisition: Jingyun Ma
Investigation: Wei Li, Lingling Tian
Supervision: Jingyun Ma, Xinghua Gao
Visualization: Xinghua Gao
Writing – original draft: Lingling Tian, Jingyun Ma
Writing – review & editing: Jingyun Ma, Xinghua Gao

Ethics approval and consent to participate

Not applicable.

Consent for publication

Not applicable.

Availability of data

The data that support the findings of this study are available from the corresponding author upon reasonable request.

References

1. Colosi C, Shin SR, Manoharan V, et al. Microfluidic bioprinting of heterogeneous 3D tissue constructs using low-viscosity bioink. *Adv Mater.* 2016;28(4):677-684. doi: 10.1002/adma.201503310

2. Xiao Y, Yang C, Guo B, et al. Bioinspired strong and tough organic–inorganic hybrid fibers. *Small Struct.* 2023;4(10):2300080. doi: 10.1002/sstr.202300080

3. Shao L, Gao Q, Xie C, Fu J, Xiang M, He Y. Bioprinting of cell-laden microfiber: can it become a standard product? *Adv Healthc Mater.* 2019;8(9):1900014. doi: 10.1002/adhm.201900014

4. Zhang YS, Arneri A, Bersini S, et al. Bioprinting 3D microfibrous scaffolds for engineering endothelialized myocardium and heart-on-a-chip. *Biomaterials.* 2016;110:45-59. doi: 10.1016/j.biomaterials.2016.09.003

5. Jiao J, Wang F, Huang J-J, et al. Microfluidic hollow fiber with improved stiffness repairs peripheral nerve injury through non-invasive electromagnetic induction and controlled release of NGF. *Chem Eng J.* 2021;426:131826. doi: 10.1016/j.cej.2021.131826

6. Chen S, Wu C, Liu A, et al. Biofabrication of nerve fibers with mimetic myelin sheath-like structure and aligned fibrous niche. *Biofabrication.* 2020;12(3):035013. doi: 10.1088/1758-5090/ab860d

7. Guo Y, Yan J, Xin JH, et al. Microfluidic-directed biomimetic Bulbine torta-like microfibers based on inhomogeneous viscosity rope-coil effect. *Lab Chip.* 2021;21(13):2594-2604. doi: 10.1039/d1lc00252j

8. Bosch-Rue E, Delgado LM, Gil FJ, Perez RA. Direct extrusion of individually encapsulated endothelial and smooth muscle cells mimicking blood vessel structures and vascular native cell alignment. *Biofabrication.* 2020;13(1):015003. doi: 10.1088/1758-5090/abbd27

9. Yao K, Li W, Li K, et al. Simple fabrication of multicomponent heterogeneous fibers for cell co-culture via microfluidic spinning. *Macromol Biosci.* 2020;20(3):1900395. doi: 10.1002/mabi.201900395

10. Liu Y, Xu P, Liang Z, et al. Hydrogel microfibers with perfusable folded channels for tissue constructs with folded morphology. *RSC Adv.* 2018;8(42):23475-23480. doi: 10.1039/c8ra04192j

11. Tian L, Ma J, Li W, Zhang X, Gao X. Microfiber fabricated via microfluidic spinning toward tissue engineering applications. *Macromol Biosci.* 2023;23(3):2200429. doi: 10.1002/mabi.202200429

12. Song S, Zhou J, Wan J, et al. Three-dimensional printing of microfiber- reinforced hydrogel loaded with oxymatrine for treating spinal cord injury. *Int J Bioprint.* 2023;9(3):1-14. doi: 10.18063/ijb.692

13. Liu X, Yue T, Kojima M, Huang Q, Arai T. Bio-assembling and bioprinting for engineering microvessels from the bottom up. *Int J Bioprint.* 2021;7(3):3-17. doi: 10.18063/ijb.v7i3.366

14. Xiao Y, Yang C, Zhai X, et al. Bioinspired tough and strong fibers with hierarchical core–shell structure. *Adv Mater Interfaces.* 2022;10(2):2201962. doi: 10.1002/admi.202201962

15. Cheng J, Jun Y, Qin J, Lee S-H. Electrospinning versus microfluidic spinning of functional fibers for biomedical applications. *Biomaterials.* 2017;114:121-143. doi: 10.1016/j.biomaterials.2016.10.040

16. Nguyen TPT, Tran BM, Lee NY. Microfluidic approach for the fabrication of cell-laden hollow fibers for endothelial barrier research. *J Mater Chem B.* 2018;6(38):6057-6066. doi: 10.1039/c8tb02031k

17. Yu Y, Shang L, Guo J, Wang J, Zhao Y. Design of capillary microfluidics for spinning cell-laden microfibers. *Nat Protoc.* 2018;13(11):2557-2579. doi: 10.1038/s41596-018-0051-4

18. Sun J, Chen J, Liu K, Zeng H. Mechanically strong proteinaceous fibers: engineered fabrication by microfluidics. *Engineering.* 2021;7(5):615-623. doi: 10.1016/j.eng.2021.02.005

19. Yu Y, Wei W, Wang Y, Xu C, Guo Y, Qin J. Simple spinning of heterogeneous hollow microfibers on chip. *Adv Mater.* 2016;28(31):6649-6655. doi: 10.1002/adma.201601504

20. Feng F, He J, Li J, Mao M, Li D. Multicomponent bioprinting of heterogeneous hydrogel constructs based on microfluidic printheads. *Int J Bioprint.* 2019;5(2):39-48. doi: 10.18063/ijb.v5i2.202

21. Abrishamkar A, Nilghaz A, Saadatmand M, Naeimirad M, deMello AJ. Microfluidic-assisted fiber production: potentials, limitations, and prospects. *Biomicrofluidics.* 2022;16(6):061504. doi: 10.1063/5.0129108

22. Du XY, Li Q, Wu G, Chen S. Multifunctional micro/nanoscale fibers based on microfluidic spinning technology. *Adv Mater.* 2019;31(52):1903733. doi: 10.1002/adma.201903733

23. Filippi M, Buchner T, Yasa O, Weirich S, Katzschmann RK. Microfluidic tissue engineering and bio-actuation. *Adv Mater.* 2022;34(23):2108427. doi: 10.1002/adma.202108427

24. Aykar SS, Reynolds DE, McNamara MC, Hashemi NH. Manufacturing of poly(ethylene glycol diacrylate)-based hollow microvessels using microfluidics. *RSC Adv.* 2020;10(7):4095-4102. doi: 10.1039/c9ra10264g

25. Lee KH, Shin SJ, Park Y, Lee S-H. Synthesis of cell-laden alginate hollow fibers using microfluidic chips and microvascularized tissue-engineering applications. *Small.* 2009;5(11):1264-1268. doi: 10.1002/smll.200801667

26. Zhao M, Liu H, Zhang X, Wang H, Tao T, Qin J. A flexible microfluidic strategy to generate grooved microfibers for guiding cell alignment. *Biomater Sci.* 2021;9(14):4880-4890. doi: 10.1039/d1bm00549a

27. Liu H, Wang Y, Yu Y, Chen W, Jiang L, Qin J. Simple fabrication of inner chitosan-coated alginate hollow microfiber with higher stability. *J Biomed Mater Res B Appl Biomater.* 2019;107(8):2527-2536. doi: 10.1002/jbm.b.34343

28. Lee KY, Mooney DJ. Alginate: properties and biomedical applications. *Prog Polym Sci.* 2012;37(1):106-126. doi: 10.1016/j.progpolymsci.2011.06.003

29. Wu Z, Cai H, Ao Z, Xu J, Heaps S, Guo F. Microfluidic printing of tunable hollow microfibers for vascular tissue engineering. *Adv Mater Technol.* 2021;6(8):2000683. doi: 10.1002/admt.202000683

30. Patil P, Szymanski JM, Feinberg AW. Defined micropatterning of ECM protein adhesive sites on alginate microfibers for engineering highly anisotropic muscle cell bundles. *Adv Mater Technol.* 2016;1(4):1600003. doi: 10.1002/admt.201600003

31. Pei Z, Gao M, Xing J, et al. Experimental study on repair of cartilage defects in the rabbits with GelMA-MSCs scaffold prepared by three-dimensional bioprinting. *Int J Bioprint.* 2023;9(2):176-196.
doi: 10.18063/ijb.v9i2.662

32. Chen Z, Lv Z, Zhang Z, Zhang Y, Cui W. Biomaterials for microfluidic technology. *Mater Futures.* 1(1):012401.
doi: 10.1088/2752-5724/ac39ff

33. Xie R, Zheng W, Guan L, Ai Y, Liang Q. Engineering of hydrogel materials with perfusable microchannels for building vascularized tissues. *Small.* 2020;16(15):1902838.
doi: 10.1002/smll.201902838

34. Volpi M, Paradiso A, Costantini M, Święszkowski W. Hydrogel-based fiber biofabrication techniques for skeletal muscle tissue engineering. *ACS Biomater Sci Eng.* 2022;8(2):379-405.
doi: 10.1021/acsbiomaterials.1c01145

35. Bertassoni LE, Cecconi M, Manoharan V, et al. Hydrogel bioprinted microchannel networks for vascularization of tissue engineering constructs. *Lab Chip.* 2014;14(13):2202-2211.
doi: 10.1039/c4lc00030g

36. Klotz BJ, Gawlitta D, Rosenberg A, Malda J, Melchels FPW. Gelatin-methacryloyl hydrogels: towards biofabrication-based tissue repair. *Trends Biotechnol.* 2016;34(5):394-407.
doi: 10.1016/j.tibtech.2016.01.002

37. Gauvin R, Chen YC, Lee JW, et al. Microfabrication of complex porous tissue engineering scaffolds using 3D projection stereolithography. *Biomaterials.* 2012;33(15):3824-3834.
doi: 10.1016/j.biomaterials.2012.01.048

38. Wei D, Sun J, Bolderson J, et al. Continuous fabrication and assembly of spatial cell-laden fibers for a tissue-like construct via a photolithographic-based microfluidic chip. *ACS Appl Mater Interfaces.* 2017;9(17):14606-14617.
doi: 10.1021/acsami.7b00078

39. Nisbet RM, Gotz J. Amyloid-beta and tau in Alzheimer's disease: novel pathomechanisms and non-pharmacological treatment strategies. *J Alzheimers Dis.* 2018;64(s1):S517-S527.
doi: 10.3233/JAD-179907

40. Sveinbjornsdottir S. The clinical symptoms of Parkinson's disease. *J Neurochem.* 12016;39(Suppl 1):318-324.
doi: 10.1111/jnc.13691

41. Li W, Yao K, Tian L, Xue C, Zhang X, Gao X. 3D printing of heterogeneous microfibers with multi-hollow structure via microfluidic spinning. *J Tissue Eng Regen Med.* 2022;16(10):913-922.
doi: 10.1002/term.3339

42. Tan J, Sun X, Zhang J, et al. Exploratory evaluation of EGFR-targeted anti-tumor drugs for lung cancer based on lung-on-a-chip. *Biosensors (Basel).* 2022;12(8):618.
doi: 10.3390/bios12080618

43. Yang X, Li K, Zhang X, et al. Nanofiber membrane supported lung-on-a-chip microdevice for anti-cancer drug testing. *Lab Chip.* 2018;18(3):486-495.
doi: 10.1039/c7lc01224a

44. Sun X, Li W, Gong X, et al. Investigating the regulation of neural differentiation and injury in PC12 cells using microstructure topographic cues. *Biosensors (Basel).* 2021;11(10):399.
doi: 10.3390/bios11100399

45. Yue K, Trujillo-de Santiago G, Alvarez MM, Tamayol A, Annabi N, Khademhosseini A. Synthesis, properties, and biomedical applications of gelatin methacryloyl (GelMA) hydrogels. *Biomaterials.* 2015;73:254-271.
doi: 10.1016/j.biomaterials.2015.08.045

46. Tian Y, Wang J, Wang L. Microfluidic fabrication of bioinspired cavity-microfibers for 3D scaffolds. *ACS Appl Mater Interfaces.* 2018;10(35):29219-29226.
doi: 10.1021/acsami.8b09212

47. Tian L, Shi J, Li W, Zhang Y, Gao X. Hollow microfiber assembly-based endocrine pancreas-on-a-chip for sugar substitute evaluation. *Adv Healthc Mater.* 2023: 2302104.
doi: 10.1002/adhm.202302104

48. Zuo Y, He X, Yang Y, et al. Microfluidic-based generation of functional microfibers for biomimetic complex tissue construction. *Acta Biomater.* 2016;38:153-162.
doi: 10.1016/j.actbio.2016.04.036

49. Shi X, Ostrovidov S, Zhao Y, et al. Microfluidic spinning of cell-responsive grooved microfibers. *Adv Funct Mater.* 2015;25(15):2250-2259.
doi: 10.1002/adfm.201404531

ACCSCIENCE PUBLISHING

International Journal of Bioprinting

RESEARCH ARTICLE

Decellularized porcine kidney-incorporated hydrogels for cell-laden bioprinting of renal cell carcinoma model

Miaoben Wu[1,2†], Hangyu Zhou[2†], Jingying Hu[2], Zonghuan Wang[3], Yongqi Xu[2], Yibing Wu[1], Yang Xiang[1], Jun Yin[4], Peng Wei[1], Kailei Xu[5,6*], and Tiantian Ren[7*]

[1]Department of Plastic and reconstructive surgery, The First Affiliated Hospital of Ningbo University, Ningbo, Zhejiang, China

[2]Health Science Center, Ningbo University, Ningbo, Zhejiang, China

[3]Department of Medical Research Center, the First Affiliated Hospital of Ningbo University, Ningbo, Zhejiang, China

[4]The State Key Laboratory of Fluid Power and Mechatronic Systems, School of Mechanical Engineering, Zhejiang University, Hangzhou, Zhejiang, China

[5]Center for Medical and Engineering Innovation, Central Laboratory, The First Affiliated Hospital of Ningbo University, Ningbo, Zhejiang, China

[6]Key Laboratory of Precision Medicine for Atherosclerotic Diseases of Zhejiang Province, Ningbo, Zhejiang, China

[7]Department of Trauma Surgery, The First Affiliated Hospital of Ningbo University, Ningbo, Zhejiang, China

(This article belongs to the *Special Issue: 3D Bioprinting for Tumor Modeling*)

†These authors contributed equally to this work.

***Corresponding authors:**
Tiantian Ren
(fyyrentiantian@nbu.edu.cn)

Kailei Xu
(xukailei@zju.edu.cn)

Citation: Wu M, Zhou H, Hu J, et al. Decellularized porcine kidney-incorporated hydrogels for cell-laden bioprinting of renal cell carcinoma model. *Int J Bioprint*. 2024;10(2):1413.
doi: 10.36922/ijb.1413

Received: July 29, 2023
Accepted: October 18, 2023
Published Online: January 12, 2024

Abstract

More than 90% of kidney cancers are attributed to renal cell carcinoma (RCC), which is however highly resistant to traditional chemotherapy. The challenges met in treating RCC signify an imperative to accelerate the development of new and effective drugs. Preclinical testing has served as a foundation for evaluating potential effectiveness of new drugs, but this endeavor is deeply restricted by the current generation of *in vitro* two-dimensional culture models, which cannot accurately mimic the tumor microenvironment (TME). Therefore, new *in vitro* three-dimensional (3D) cell culture models that can better mimic the components and architecture of TME have been developed for preclinical testing, but only a few existing 3D cell culture models can simulate the TME of RCC, representing a limitative obstacle impeding the development of novel drugs for RCC. In this study, we prepared a bioink by mixing porcine kidney decellularized extracellular matrix (dECM) powders with gelatin methacryloyl (GelMA) to bioprint an *in vitro* 3D cell culture model for RCC. We found that GelMA stability, mechanical properties, and printability were all significantly improved following the addition of the dECM powder. Moreover, cell cultures using ACHN cells suggested that kidney dECM powders significantly improved the cellular proliferation and metastasis via upregulation of markers related to epithelial–mesenchymal transition, along with activation of several cancer progression-related signaling pathways. More importantly, ACHN cells also demonstrated higher resistance to sunitinib under the stimulation of kidney dECM, indicating that GelMA-kidney dECM hydrogels may be an appropriate preclinical model to be used for building an *in vitro* RCC platform for drug screening and development.

Keywords: Tumor microenvironment; Gelatin methacrylate; 3D culture; Tumor model; Drug screening

1. Introduction

The incidence of kidney cancer has continuously increased worldwide over the past decades.[1] Around 90% of kidney cancers are classified as renal cell carcinoma (RCC), a highly deadly urological cancer originating from the proximal tubular epithelial cells in the renal cortex.[2] More than 140,000 RCC-related deaths and 342,000 cases are recorded each year globally.[3] Advanced RCC cases have a 5-year survival rate of only 11.7%.[4] In addition, 30% of RCC patients have metastatic disease at initial presentation, and 30% of patients who experience complete resection suffer from RCC recurrence.[5] More importantly, all RCC subtypes are largely nonresponsive to traditional chemo- and radiotherapies.[4,6]

The tumor microenvironment (TME) comprises tumor cells and their stromal microenvironment, including various growth factors, cytokines, immune cells, stem cells, fibroblasts, and extracellular matrix (ECM).[7] The TME has been found to be one of the major factors influencing the efficiency of chemotherapy.[8,9] Non-cancer cells such as immune cells and fibroblasts have been shown to enhance RCC cellular proliferation, invasion, drug resistance, and angiogenesis.[10,11] Composed of mainly proteins and polysaccharides, ECM is the non-cellular component of the TME secreted by cells for its biochemical and structural support. The ECM has been shown to not only provide structural support for cell growth but also play a critical role in controlling cell differentiation, migration, and morphogenesis, which are critical pathological events occurring in the TME during the course of tumorigenesis.[12] Collagen, the main component of the ECM, has been proven to enhance the invasion of RCC cells.[13] Other ECM components, including hyaluronic acid, laminin, versican, and fibronectin, have also been found to promote cancer development and metastasis.[14-18] Therefore, mimicking the biochemical properties of the ECM and creating a more biomimetic culture model for RCC have become important research goals, which are instrumental for facilitating RCC-related drug development.[19-21]

In the recent years, the application of two-dimensional (2D) cultures has become widely accepted for biological investigations. However, they do not realistically recapitulate the nature of the TME and lack cell–cell/matrix interactions.[22] As a result of these limitations, various types of three-dimensional (3D) culture models were developed to study the complexity of the TME in RCC.[23] Spherical cancer and hydrogel-based culture models are now frequently used for 3D cultures of RCC cells.[24,25] Nevertheless, the failure to realistically simulate the TME of RCC implies that these models are also unable to yield accurate results in drug screening and assessment, and the positive drug testing outcome stemming from *in vitro* testing with these models is not necessarily commensurate with the efficacy of the drugs used in clinical treatment.[26,27] The decellularized extracellular matrix (dECM) is a biomaterial formed from tissues via the removal of immunogenic cellular components. This material has been used in tissue engineering,[28] since dECM can preserve the active components of the ECM and effectively reduce immune rejection while being well-tolerated by heterogeneous hosts.[29] For these reasons, dECM was also used to construct *in vitro* TME models to closely recapitulate dynamic cancer cell–ECM interactions. However, we cannot overlook the shortcomings of dECM, such as the uncontrollable degradation and its difficulty in forming hydrogel, which limit its wider application in 3D bioprinting and tissue engineering despite its structure being better able to mimic the TME.

In this study, we prepared porcine kidney-derived dECM powders and mixed them with gelatin methacryloyl (GelMA) to enhance dECM biological properties and printability. The mixture was then further used to construct a 3D cell culture model, which is able to better stimulate the RCC TME. GelMA is produced via the partial hydrolysis of native collagen, which is a potential 3D cell culture biomaterial for mimicking the TME since it retains most of the biological properties of collagen.[30] The degree of dECM decellularization, particle size, and GelMA material properties in dECMs of different concentrations were analyzed. The cells of ACHN, an RCC cell line, were further encapsulated in GelMA-based precursors and bioprinted into a nephron structure used for evaluating the effects of kidney dECM powders on cellular behaviors.

2. Materials and methods

2.1. Materials

Methacrylic anhydride (M102519) and gelatin (G108395) were obtained from Aladdin (China). Sodium dodecyl sulfate (SDS; L3771-500G) was obtained from Sigma (Germany). The Matrigel (356234) was purchased from Corning (Corning, NY). Polydimethylsiloxane (PDMS) was obtained from Sylgard (USA). The lithium phenyl-2,4,6-trimethylbenzoylphosphinate (LAP) was obtained from Engineering For Life (China). ACHN cells (CL-0021) were obtained from Procell (China). Dulbecco's modified Eagle medium (DMEM; C11995500BT), 0.25% trypsin-EDTA (25200056), and penicillin/streptomycin (15140122) were obtained from Gibco (USA). Cell counting kit-8 (CCK-8; C0038) was obtained from Beyotime (China).

Paraformaldehyde (PFA; P1110), 4,6-diamidino-2-phenylindole (DAPI, C0060), phalloidin-FITC (CA1660), and phosphate-buffered saline (PBS; P1020) were all obtained from Beijing Solarbio (China). The primary antibodies used including GAPDH (5174S), CD44 (3578S), CDH1 (3195S), vimentin (5741S), and CDH2 (13116S) were obtained from Cell Signaling Technology (USA), and the secondary antibody (ab150077) was obtained from Abcam (UK). All primers were synthesized by Beijing Tsingke Biotech (China). Power SYBR Green PCR Master Mix (4367659) and TRIzol (15596018) were obtained from Thermo Fisher Scientific (USA). FastKing gDNA Dispelling RT SuperMix kits (KR118) and DNA extraction kits (DP304) were obtained from Beijing TIANGEN (China). Fetal bovine serum (FSP500) was obtained from Shanghai ExCell Bio (China). BCA Protein Assay kits (23225) were obtained from Thermo Fisher Scientific (MA, USA).

2.2. Decellularization of kidney samples

The kidney samples used in the experiments were derived from Chinese Middle White Pig, which was purchased from Central Fresh Market (Ningbo, China). The decellularization method was adapted from a previously published method.[31] Briefly, fresh kidney samples were first cut into small pieces, washed with deionized water, stirred in 2% Triton X-100 solution for 24 h (changed every 12 h), and soaked in 0.1% SDS for 48 h (changed every 12 h). Finally, the samples were washed with deionized water for 24 h before being stored at −80°C.

2.3. DNA extraction

The DNA from fresh and decellularized samples was extracted using a DNA extraction kit with all procedures stipulated in the product's protocol. Briefly, the samples were lysed with a tissue homogenizer (TISS-BAS1C24, Jingxin, China), then washed with buffers and extracted using spin columns. The concentration of extracted DNA was determined using Nanodrop™ 2000 Spectrophotometer (Thermo Fisher Scientific, USA).

2.4. Scanning electron microscopy

Decellularized kidney samples were ground to powder using a tissue homogenizer (TISS-BAS1C24, Jingxin, China) and sputter-coated with gold on a sample holder for 1 min by a sputter coater (Supro Instrument, USA), and finally imaged (n = 6 images at different spots per group) using a scanning electron microscope (SEM; Phenom Pro, Phenom, Netherlands).

2.5. Western blotting

For Western blotting, fresh and decellularized samples were lysed with RIPA buffer and centrifuged at 12,000 rpm. The supernatant was then collected, and the protein concentrations were measured using a BCA Protein Assay Kit I adherence with the manufacturer's protocol. An aliquot of total protein was separated by polyacrylamide gel electrophoresis under reducing conditions and was then transferred onto a polyvinylidene fluoride (PVDF) membrane. The membrane was then blocked with blocking buffer for 2 h before being incubated overnight at 4°C with primary antibodies (GAPDH, 1:1000). Next, the membranes were incubated with the anti-rabbit secondary antibodies (1:5000) at room temperature for 1 h and finally visualized with ChemiDoc MP Imaging System (BIO-RAD, USA).

2.6. Hematoxylin–eosin staining

Fresh and decellularized samples were first fixed with 4% PFA, dehydrated with ethanol, mounted in paraffin, and then cut into section with a thickness of 10 μm using a microtome (Leica, Germany). Sections were then stained with hematoxylin and eosin (H&E). Briefly, the sections were first baked for 30 min at 60°C, deparaffinized with xylene, and then washed with ethanol. Next, the sections were stained with hematoxylin solution for 10 min, differentiated with a differentiation solution for 3 min, and washed with deionized water three times. The sections were then re-dyed with eosin Y solution for 1 min, cleared with xylene, and sealed with resin. Finally, the samples were imaged using a microscope (DMi1, Leica Microsystems, Germany).

2.7. GelMA synthesis

GelMA used in this study was synthesized based on a previously published protocol.[32,33] Briefly, gelatin, Na_2CO_3, and $NaHCO_3$ were dissolved at 50°C for 3 h until complete dissolution. Then, 2.5 wt% methacrylic anhydride was added to the dissolved gelatin solution for GelMA synthesis to achieve a degree of methacryloyl substitution (DMS) of 30%. After continuous stirring in the dark for 3 h, five times of deionized water was used to dilute the sample and dialyzed for 3 days with water change every 8 h. Finally, the synthesized GelMA were frozen overnight, freeze-dried for 3 days, and stored at -20°C for the later experimentation.

2.8. Hydrogel preparation

The 10 wt% GelMA was prepared with a fully supplemented DMEM containing 0.5% LAP. Various amounts of kidney dECM powders were added separately to GelMA precursors to obtain 1 wt%, 2 wt%, and 3 wt% of 10% GelMA-kidney solutions; hereafter, these are called the 10% GelMA-1% Kidney, 10% GelMA-2% Kidney, and 10% GelMA-3% Kidney solutions, respectively. Each precursor solution was photo-crosslinked using 405 nm ultraviolet (UV) light (10 W/cm^2) for 1.5 min in a disc-like PDMS

model with 8 mm inner diameter and 2 mm thickness for compressive and swelling tests.

2.9. Rheological analysis

The rheological properties of GelMA solutions with or without dECM powders (n = 3) were measured with a rheometer (Thermo Scientific, USA). Rotational shear thinning tests were then performed under increasing shear rates (0.1 to 100 1/s) in 5 min at 20°C. The effect of a temperature change (i.e., 4–35°C) on GelMA precursor viscosity was determined under a constant shear rate of 1/s over 30 min. In addition, the storage (G') and loss (G") modules of GelMA-based precursors were further evaluated to investigate the effect of a temperature change (i.e., 4–35°C) under 1 Pa constant shear stress and 1 Hz frequency.

2.10. Swelling test

All groups of disc-like GelMA samples (n = 5 per group) were soaked in DMEM medium and incubated at cell culture condition (37°C and 5% CO_2) for 5 days. The diameter of disc hydrogels was then determined with a digital micrometer (Deli, China) at multiple time points, i.e., 0, 0.5, 1.5, 4, 6, 24, 48, 72, and 120 h, and normalized to the diameter at 0 h to calculate the scaled diameter values.

2.11. Compressive test

Compressive test was performed to detect the compressive modulus of all GelMA groups (n = 5 per group) with a universal tester (Shimadzu, Japan). All samples were compressed at 0.5 mm/min rate to a strain of 50%. The linear region slope on the beginning of the stress–strain curve was used to calculate the compressive modulus.

2.12. Filament fusion test

The effect of kidney dECM powder on GelMA printability was evaluated in a filament fusion test, which was conducted in accordance with the procedures adapted from a previously published method.[34,35] The test entails using a square pattern with increasing filament-to-filament distance (1.5 to 4 mm with 0.5 mm increments). The 10% GelMA-1% Kidney, 10% GelMA-2% Kidney, and 10% GelMA-3% Kidney bioinks were printed at 20°C. High-resolution camera (ZK4A08MTP, SANOTID, China) was used to capture the image of the printed patterns immediately (n = 5 pattern printed per group). The pore area index (PAI) was calculated using Equation I:

$$PAI = \frac{A_t - A_a}{A_a} \times 100\% \quad (1)$$

where A_t is the theoretical area of pores, and A_a is the actual area of pores. A_a was determined using NIH ImageJ. For an ideal square pore, PAI should be 0, and $A_t = A_a$, indicating that there has no material spreading.

2.13. Cubic ratio measurement

A mesh structure was printed using 10% GelMA-1% Kidney, 10% GelMA-2% Kidney, and 10% GelMA-3% Kidney under 20°C (n = 50 per group). High-resolution camera was used to capture the images for the pore structure of printed pattern immediately (n = 50 pores counted per group). Cubic ratio (Pr) was then calculated using Equation II:

$$\mathrm{Pr} = \frac{L^2}{16A} \quad (II)$$

where L and A represent the perimeter and area of the square pore shape, respectively, which were determined using NIH ImageJ. Ideally, the Pr value of a perfect square morphology should be 1, and the higher the Pr value is, the better the bioink gelation degree is.

2.14. Material spreading index measurement

The material spreading index measurement was performed by printing with different nozzle sizes (i.e., 20G to 28G) using the 10% GelMA-1% Kidney, 10% GelMA-2% Kidney, and 10% GelMA-3% Kidney samples (n = 10 images per group) at constant temperature of 20°C. The material spreading index was calculated using Equation III:

$$Material\,spreading\,index = \frac{D_a}{D_n} \quad (III)$$

where D_n indicates the nozzle inner diameter, and D_a indicates the diameter of the extrusion filament measured using NIH ImageJ.

2.15. Cell cultures

ACHN cells were grown with complete DMEM medium containing 10% fetal bovine serum and 1% penicillin/streptomycin, and were maintained in 5% CO_2 at 37°C. Cells within passages of 10 were used for following experiments.

2.16. Development of cell-laden RCC model

At 70–80% confluence, ACHN cells were detached using 0.25% trypsin-EDTA, followed by resuspending in different groups of GelMA precursors. The final cellular concentration was 1×10^6 cells/mL. A nephron model for ACHN cell culture was printed using LB119 3D bioprinter (MEDPRIN, China). Cellular suspensions with different groups of GelMA precursors were loaded to a 1 mL sterile syringe, printed to a nephron structure, as shown in **Figure S1** (Supplementary File), with a nozzle of 24G at 20°C, and photo-crosslinked with 405 nm UV light (10 W/cm^2) for 1.5 min. ACHN cells with concentration of 1×10^6 cells/mL were also mixed with Matrigel or 10% GelMA-2% Kidney and added into PDMS models (8 mm inner diameter, 2 mm thickness). The Matrigel samples were incubated for 30 min at 37°C to form Matrigels, and 10% GelMA-2% Kidney was photo-crosslinked using 405 nm UV light (10 W/cm^2) for 90 s. All cell-laden models were placed into

24-well plates, cultured for 7 days, and the medium was changed every other day.

2.17. Cellular proliferation measurement

The effect of porcine kidney-derived dECM on ACHN cell proliferation was analyzed using CCK-8 assays on days 1, 3, 5, and 7 for all bioprinted nephron models. Samples from all groups were transferred to new culture plates and incubated with CCK-8 working solution (10% v/v) that dissolved with the fully supplemented DMEM for 1.5 h. Finally, the absorbance of the incubated medium was read at 450 nm. The cellular proliferation rate at each time point was then determined using the absorbance value of day 1 as the baseline.

2.18. Cellular morphology staining

The cellular morphology of ACHN cells in all bioprinted nephron models was fixed with 4% PFA and stained with phalloidin on day 5. Samples were incubated with 0.5% Triton X-100 for 15 min, phalloidin working solution (1:200) for 40 min, and DAPI solution for 10 min in the dark. Finally, the samples were washed with PBS and imaged (n = 6 images at different spots per group) using a confocal microscopy.

2.19. RNA extraction

Total RNA samples from all bioprinted nephron models and casted models were lysed with TRIzol, followed by mixing with chloroform, washing with isopropanol and ethanol, and dissolved with DEPC water, and the final RNA concentration was determined with Nanodrop™ 2000 Spectrophotometer (Thermo Fisher Scientific, USA).

2.20. Real-time quantitative polymerase chain reaction

The complementary DNA (cDNA) was reverse-transcribed with a HiScript® III All-in-one RT SuperMix kit, according to the product's protocol. Real-time polymerase chain reaction (RT-PCR; Roche, Switzerland) was used to analyze the relative gene expression. To perform RT-PCR, cDNA (50 ng), specific primers (Table 1), and SYBR Master Mix were mixed to a total reaction volume of 10 μL.

2.21. RNA sequencing and data analysis

Transcriptome sequencing and analysis were conducted by OE Biotech Co., Ltd. (China). The RNA integrity was assessed using an Agilent 2100 Bioanalyzer (Agilent Technologies, USA). Libraries were sequenced on an Illumina NovaSeq 6000 platform, and 150 bp paired-end reads were generated, with approximately 50 raw reads generated for each sample. Principal component analysis was performed using R version 3.2.0 to evaluate the biological duplication of samples. Differential expression analysis was performed using DESeq2. P value <0.05 and Log2FC >1 or Log2FC <-1 were set as the thresholds to identify significantly differentially expressed genes (DEGs). Gene Ontology (GO) pathway enrichment analysis of DEGs was performed to screen for significantly enriched terms. Gene set enrichment analysis (GSEA) was performed using GSEA software.

2.22. Immunofluorescence staining

All bioprinted nephron models were fixed on day 5 using 4% PFA at room temperature, washed in PBS three times, permeabilized with 0.2% Triton X-100 for 30 min, and blocked with 5% bovine serum albumin for 1 h. Primary antibodies (1:200) targeting CD44, TWIST, vimentin, CDH2, and CDH1 were added to the samples and incubated at room temperature for 2 h. Afterward, the samples was washed with PBS thrice, and then stained with secondary antibodies (1:200) for 1 h and DAPI for 5 min. Secondary antibody assay was also performed, where secondary antibody was directly stained after blocking,

Table 1. Sequences of primers used in this study

Primer	Forward sequence (5'-3')	Reverse sequence (5'-3')
GAPDH	TGTAGTTGAGGTCAATGAAGGG	ACATCGCTCAGACACCATG
Slug	CGAACTGGACACACATACAGTG	CTGAGGATCTCTGGTTGTGGT
Snail	GGCTGCTACAAGGCCAT	GCACTGGTACTTCTTGACATCT
MMP2	TACAGGATCATTGGCTACACACC	GGTCACATCGCTCCAGACT
MMP9	TGTACCGCTATGGTTACACTCG	GGCAGGGACAGTTGCTTCT
CD44	TGAAGATGAAAGAGACAGACACC	CTGGTTCTGTTTTGTGTGGTC
TWIST	ACTGTCCATTTTCTCCTTCTCTG	ATGTCCGCGTCCCACTA
ZEB1	GATGATGAATGCGAGTCAGATGC	ACAGCAGTGTCTTGTTGTTGT
SOX2	CTTGACCACCGAACCCAT	GTACAACTCCATGACCAGCTC
OCT4	CCAAGGAATAGTCTGTAGAAGTGC	TGCATGAGTCAGTGAACAGG
NANOG	CCTTCTGCGTCACACCATT	AACTCTCCAACATCCTGAACC

followed by DAPI staining. All samples were imaged (n = 6 images at different spots per group) immediately using confocal microscopy to avoid fluorescence quenching, and ImageJ was used to determine the fluorescence intensity.

2.23. Evaluation of the resistance to sunitinib

We further evaluated the resistance of ACHN cells in all groups to exogenous sunitinib, an anti-kinase cancer treatment drug. To do so, GelMA samples from all groups were cultured for 5 days, and 2D cells, which were used as control, were seeded with a concentration of 50,000 cells/well after 4 days of hydrogel culture. All groups (n = 5) were then cultured with 10 μM sunitinib using dimethylsulfoxide (DMSO) as the vehicle. Cell viability was determined with CCK-8 assays after 72 h of drug exposure, and viability was calculated by evaluating sample absorbance relative to vehicle absorbance for all groups.

2.24. Statistical analysis

Unless otherwise mentioned, all results were analyzed using GraphPad version 8.02. All experiments were performed in triplicate. Data are expressed as mean ± standard deviation. Student's t-tests and analysis of variance (ANOVA) were performed to evaluate the statistical significance of differences in group means for all data. A P value of <0.05 indicates significant difference (*P <0.05, ** P <0.01, ***P <0.001).

3. Results

3.1 Characterization of GelMA with dECM powders

First, porcine kidney tissues were sliced into tiny fragments, decellularized for 3 days, ground into powder, and imaged by means of SEM before mixing with GelMA (Figure 1A). The degree of decellularization was then assessed via DNA concentration measurements, Western blotting, and H&E staining. As shown in Figure 1B, the control sample without showing sign of decellularization had a significantly higher DNA concentration than decellularized samples. Similar results were also observed for GAPDH protein, as visualized using Western blotting (Figure 1C). H&E staining images depicted in Figure 1D show that the cytoplasm and nucleus were almost completely removed, while the ECM was preserved in most decellularized samples. dECM powders were further mixed with 10% GelMA precursors as shown in Figure 1E, where different concentrations of dECM were added. Here, the precursor solutions with higher dECM concentration were obviously more viscous, a finding consistent with rheological evaluation. Moreover, the viscosity of GelMA solution significantly increased with dECM concentration (Figure 1G).

Viscosity under various shear rate was also determined for all precursor solutions. Here, the dECM exerted a limited influence on GelMA shear-thinning (Figure 1H), but its addition increased the gelation temperature to 25°C (Figure 1I). The appearance of the GelMA hydrogel at different dECM concentrations is shown in Figure 1F. It is evident that the hydrogel samples became much less transparent after more dECM powder was added. The mechanical properties of all hydrogel compositions were evaluated using compressive tests. In this study, the Young's modulus for 10% GelMA, 10% GelMA-1% Kidney, 10% GelMA-2% Kidney, and 10% GelMA-3% Kidney samples was 19.77 ± 1.05 kPa, 20.46 ± 3.32 kPa, 39.51± 4.71 kPa, and 58.03 ± 8.65 kPa, respectively. These results indicate that the Young's modulus had a positive correlation with increasing dECM concentration (Figure 1J). The stability of all hydrogel compositions was then analyzed with a swelling test (Figure 1K and L), where the 10% GelMA, 10% GelMA-1% Kidney, and 10% GelMA-2% Kidney samples had a similar swelling rate, which was however significantly lower than the rate of 10% GelMA-3% Kidney sample.

3.2. Printability of GelMA with dECM powders

To further analyze the influence of dECM on GelMA properties, we then assessed the printability of the 10% GelMA, 10% GelMA-1% Kidney, 10% GelMA-2% Kidney, and 10% GelMA-3% Kidney samples. All compositions were printed with designated patterns to determine the impact of dECM powders on pore closure and filament fusion (Figure 2A). The PAI for each was then quantified (Figure 2B), and we found that the inclusion of an increasing amount of dECM powder significantly improved the PAI for all pore sizes, indicating a more stable structure was formed. On the other hand, the results on material spreading index and cubic ratio (Figure 2C–F) attested that the dECM powders were able to better enhance GelMA printability.

Subsequently, to further demonstrate the effect of dECM powders on printability, all samples were utilized to 3D-print more intricate structures, including a 15-layer thin-wall (0.4 mm) tube (diameter = 3.5 mm, and height = 10 mm), a five-layer Chinese knot (10 × 10 × 1 mm^3), and a ten-layer cubic (7 × 7 × 4 mm^3). A high-resolution camera was utilized to capture the images of the top, side, and zoom-up views of each of these structures (Figure 3), which portrayed the positive influence of dECM inclusion on GelMA printability.

3.3 Effect of kidney dECM on morphology, proliferation, and gene expression of ACHN cells

Next, the effect of dECM powder on RCC cellular behavior was assessed in a series of tests run on ACHN cells cultured in the bioprinted nephron structure. The ACHN cellular morphology was evaluated using phalloidin staining on days 1, 3, 5, and 7 for all hydrogel compositions

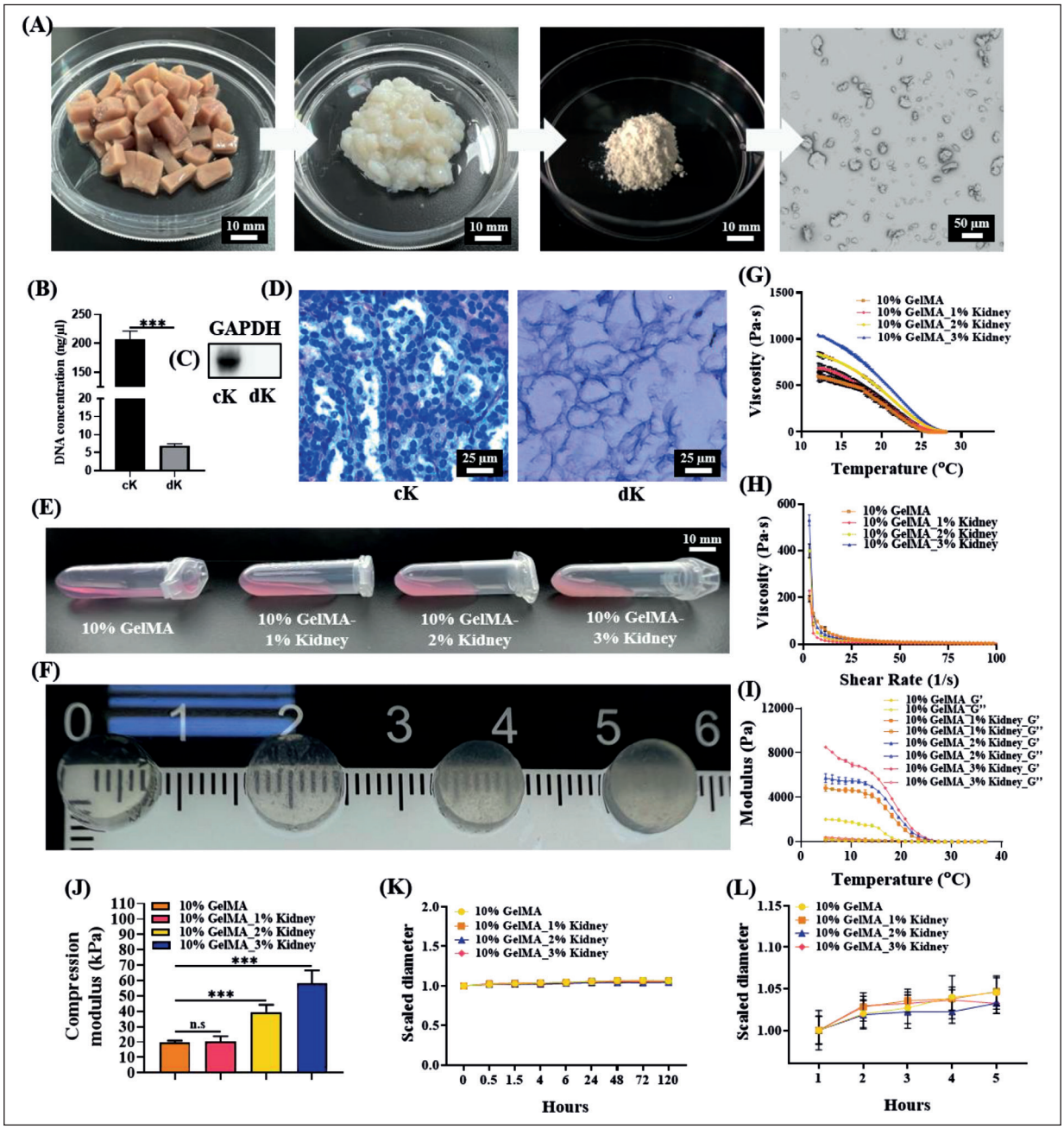

Figure 1. Material characterizations of GelMA-kidney hydrogels. (A) The decellularization process of porcine kidney and powder size evaluation; (B) DNA concentration of decellularized kidney and fresh kidney; (C) Western blotting of GAPDH for decellularized kidney and fresh kidney; (D) H&E staining for decellularized kidney and fresh kidney; (E) Appearance of the GelMA-kidney precursors in 2 mL tubes. (F) Appearance of the GelMA-kidney hydrogels after crosslinking; (G) Viscosities of the precursors at various temperatures; (H) Precursor viscosities under various shear stress; (I) Precursor storage and loss modulus under various temperature conditions; (J) Hydrogel compressive modulus; (K, L) Hydrogel stability determined with swelling tests.

(Figure 4A). The inclusion of dECM powder successfully supported the ACHN growth throughout culturing, and ACHN aggregated to form cellular spheroids rather than a spindle structure, as it did in 2D culture.

The CCK-8 assays were used to determine the cellular proliferation of ACHN on days 1, 3, 5, and 7 (Figure 4B). The ACHN cells in 10% GelMA-3% Kidney showed the lowest proliferation rate throughout the culture period, especially from days 1 to 5. The inclusion of 1% and 2% dECM powder had no significant influence on ACHN cellular growth from days 1 to 5 compared to 10% GelMA, while the 10% GelMA-2% Kidney sample had the highest

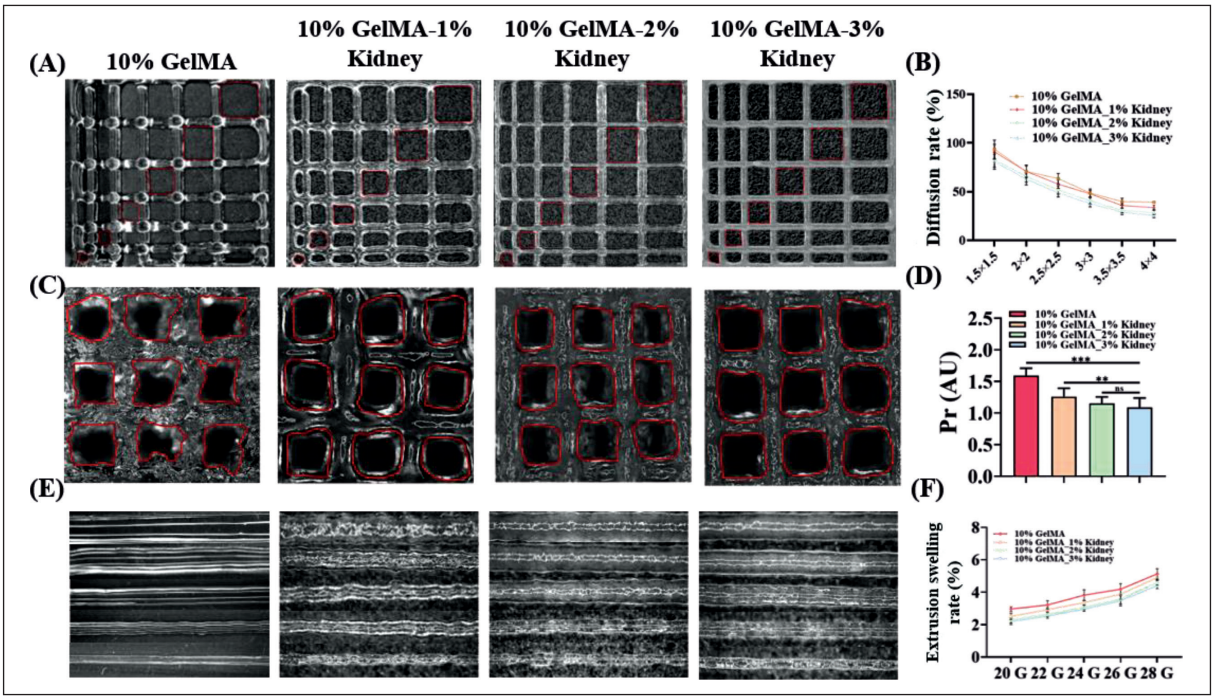

Figure 2. Printability analysis of GelMA mixed with dECM powders. (A, B) Filament fusion and pore area index; (C, D) Cubic ratio analysis; (E, F) Material spreading index measurement. Abbreviation: Pr, cubic ratio.

proliferation rate on day 7, indicating that kidney dECM powder has a positive influence on ACHN cellular proliferation if administered at a concentration of 2%.

The effects of kidney dECM powder on the gene expression of ACHN cells were analyzed by evaluating in the bioprinted 10% GelMA and 10% GelMA-2% Kidney samples for epithelial–mesenchymal transition (EMT) markers, including *Slug*, *Snail*, *MMP2*, *MMP9*, *ZEB1*, *CD44*, and *TWIST*, as well as cancer stem cell (CSC) markers, including *Nanog*, *Sox2*, and *Oct4*. As shown in Figure 4C, ACHN cells grown in the 10% GelMA-2% Kidney sample had the highest EMT-related and CSC-related marker expression relative to other groups, especially with respect to *Slug*, *MMP9*, *TWIST*, and *Nanog*, which were significantly upregulated by 21.40-, 38.13-, 20.42-, and 32.78-folds, respectively. The cells grown in the 10% GelMA-1% Kidney sample also showed significantly higher gene expression levels of these genes compared to 10% GelMA, but were still lower than cells grown in the 10% GelMA-2% Kidney sample. ACHN cells in 10% GelMA-3% Kidney sample had much lower gene expression compared with cells grown in the 10% GelMA-1% Kidney and 10% GelMA-2% Kidney samples. Moreover, the expression of several genes, including *Snail*, *ZEB1*, and *Sox2*, was downregulated compared with cells grown in 10% GelMA. To further explore the benefits of the 3D-bioprinted renal cancer models in this study, the EMT-related marker expression in bioprinted 10% GelMA-2% Kidney sample was also compared with Matrigel and casted 10% GelMA-2% Kidney samples (**Figure S2A–J** in Supplementary File). The ACHN cells in 10% GelMA-2% Kidney sample demonstrated significantly higher expression for all EMT-related marker genes, expect for *MMP2*, compared with other two groups, suggesting that the nephron model developed could serve a potential platform for renal cancer research in future.

Taken together, these results suggested that the inclusion of kidney dECM powders could promote ACHN cellular proliferation and EMT- and CSC-related gene expression in a concentration-dependent manner. Of note, the inclusion of 2% dECM powder outperformed the 1% dECM powder in terms of the parameters mentioned above, but an increase to 3% could lead to an opposite effect.

3.4. Effect of kidney dECM on ACHN transcriptional profiling

Global transcriptome profiling was performed by means of RNA sequencing (RNAseq). Specifically, the RNA extracted from the ACHN cells cultured in 10% GelMA and 10% GelMA-2% Kidney samples was subjected to sequencing as part of the effort to study the influences of kidney dECM on the transcriptional characteristics of renal cancer cells. The principal component analysis showed that ACHN cells under the stimulation of kidney dECM showed a strongly altered transcriptional profile. Several cancer-related or prognostic genes, including *UNX1-IT1*, *HIF1A-AS2*,

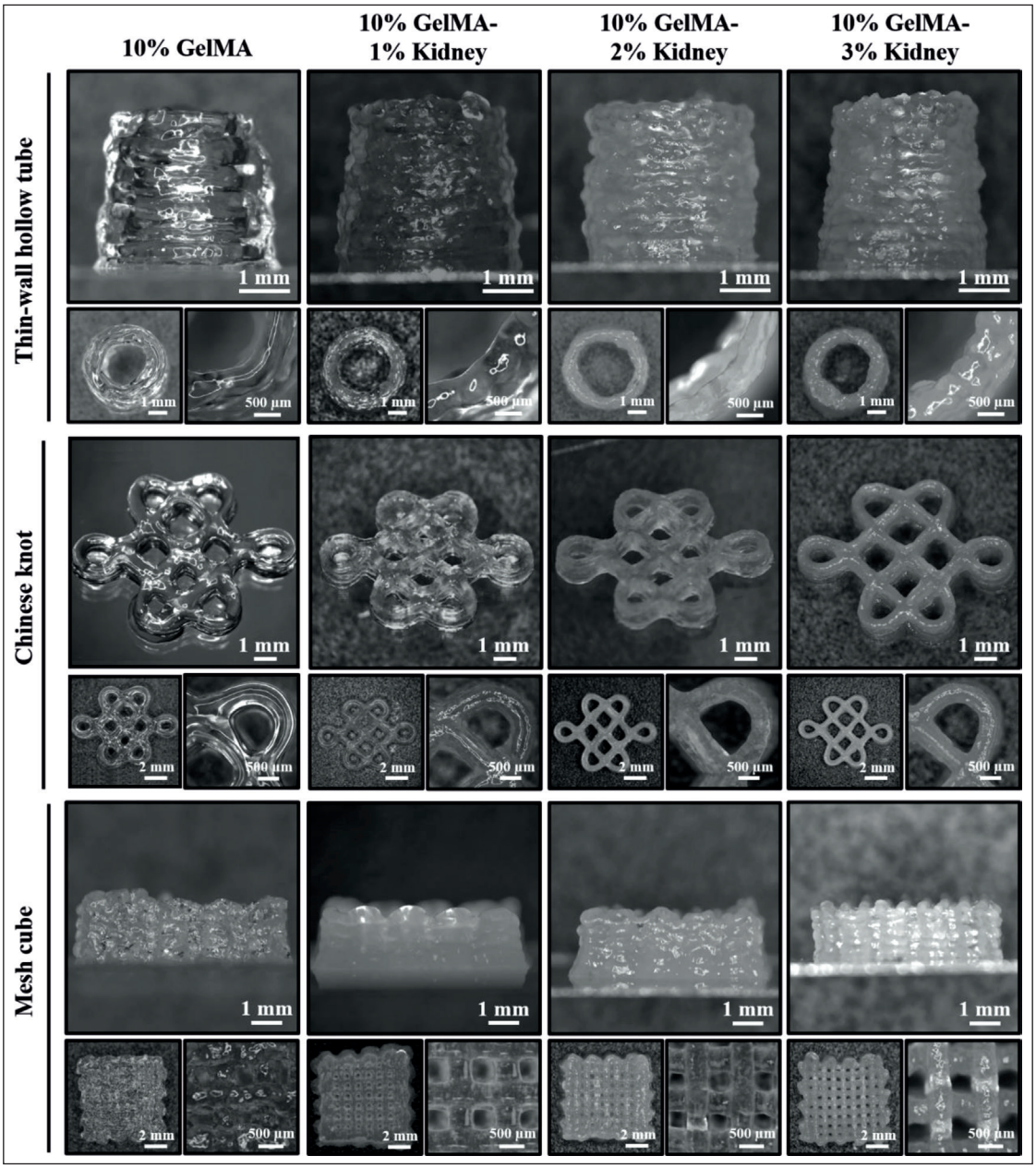

Figure 3. Extrusion printing of complicated structures using various concentrations of GelMA-Kidney bioink.

P2RX6, *ADIRF-AS1*, and *SGK2* (Figure 5A), were found to be significantly upregulated in response to stimulation by kidney dECM.

Additionally, GO enrichment analysis was performed using RNAseq results to study the changes in genes implicated in the molecular functioning, biological processes, and cellular components of ACHN cells (Figure 5B). ACHN cells in 10% GelMA-2% Kidney sample were found to be enriched with GO terms involved in the following specific terms within the biological process category: cell–cell interactions, cellular growth, and cellular migration. The cells were also found to be enriched with GO terms involved in the cellular component category, such as basement membrane and extracellular region, indicating that ACHN cells under the stimulation of kidney dECM could facilitate ECM remodeling. Separately, enriched GO terms involved in molecular functions included collagen binding, laminin binding, fibronectin binding, and integrin binding, suggesting that the presence of dECM facilitated the cell–matrix binding process.

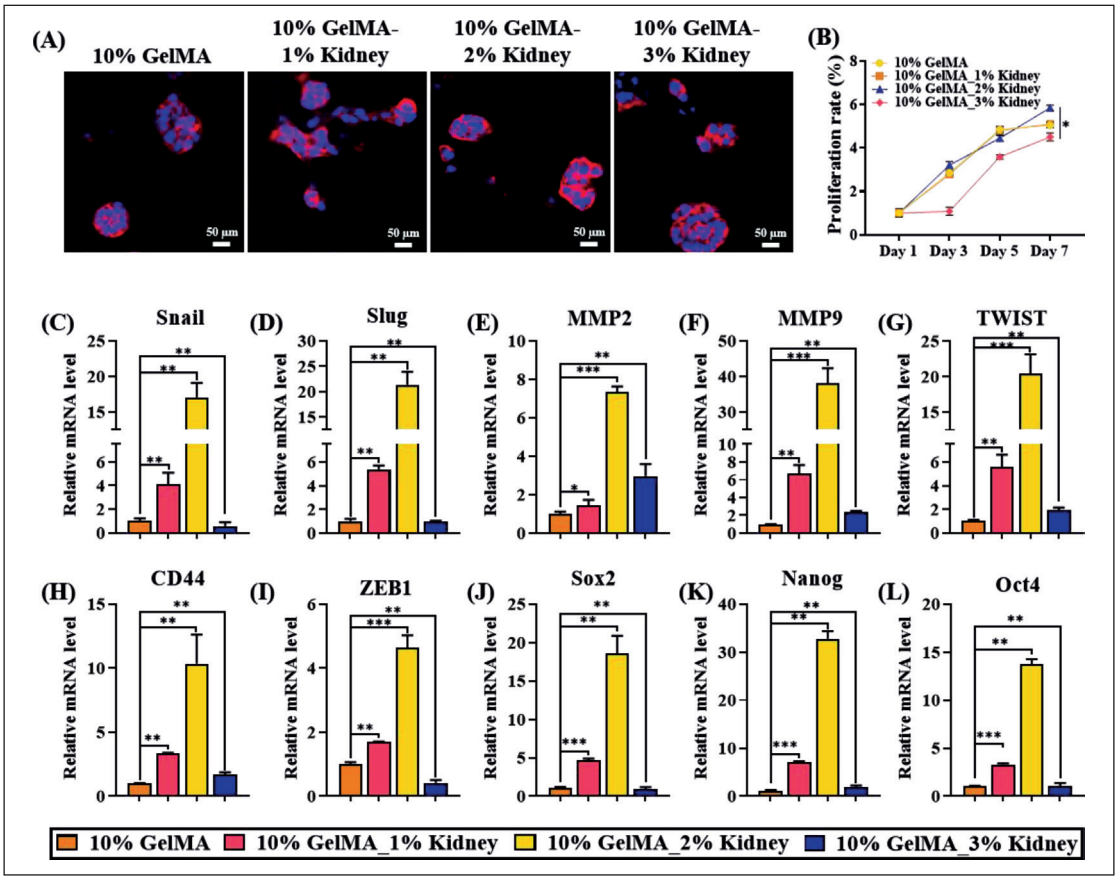

Figure 4. Biocompatibility tests of GelMA-Kidney hydrogel. (A) ACHN cellular morphology; (B) ACHN cellular proliferation; (C–L) Expression levels of an array of EMT-related markers in ACHN cells in various concentrations of GelMA-Kidney hydrogels.

Next, Kyoto Encyclopedia of Genes and Genomes (KEGG) enrichment analysis was also conducted to analyze changes in signaling pathways of ACHN cells grown in 10% GelMA-2% Kidney cultures (Figure 5C). We identified several signaling pathways related to cancer development, including the VEGF (hsa04370), PPAR (hsa03320), PI3K-Akt (hsa04151), HIF-1 (hsa04066), and TGF-beta (hsa04350).

3.5. Expression of EMT-related protein

To examine the effect of kidney dECM powder on ACHN behavior, we evaluated the effect of the 10% GelMA-2% Kidney on EMT-related protein expression. Specifically, we tested for vimentin, TWIST, CD44, CDH1, and CDH2, by immunofluorescence staining on day 5 of the 10% GelMA-2% Kidney treatment (Figure 6A). The result for secondary antibody assay is shown in **Figure S2K** (Supplementary File), where no positive staining was observed, indicating the genuine positivity in the fluorescence images. We found that the protein expression of vimentin, TWIST, CD44, and CDH2 was upregulated in the 10% GelMA-2% Kidney culture compared to the 10% GelMA control, while CDH1 was downregulated. This observation was further verified by the quantification of immunofluorescence intensity using NIH ImageJ (Figure 6B–F). Here, the expression of vimentin, TWIST, CD44, CDH1, and CDH2 was up- or downregulated by 2.53-, 1.52-, 2.00-, 0.71-, and 2.11-folds, respectively.

3.6. ACHN drug resistance

Finally, the effect of dECM powders on ACHN drug resistance was evaluated by assessing the resistance of the cells toward sunitinib on day 5 (**Figure S2** in Supplementary File). The cellular viabilities of the 2D, 10% GelMA, and 10% GelMA-2% Kidney cultures were 36.40% ± 1.08%, 40.19% ± 7.02%, and 46.41% ± 4.93%, respectively. ACHN cells cultured in GelMA-based hydrogels all showed significantly higher chemoresistance compared with 2D cell cultures. Moreover, the inclusion of 2% kidney dECM powder significantly promoted cellular viability compared to 10% GelMA, suggesting that kidney dECM powder can enhance the drug resistance of ACHN cells.

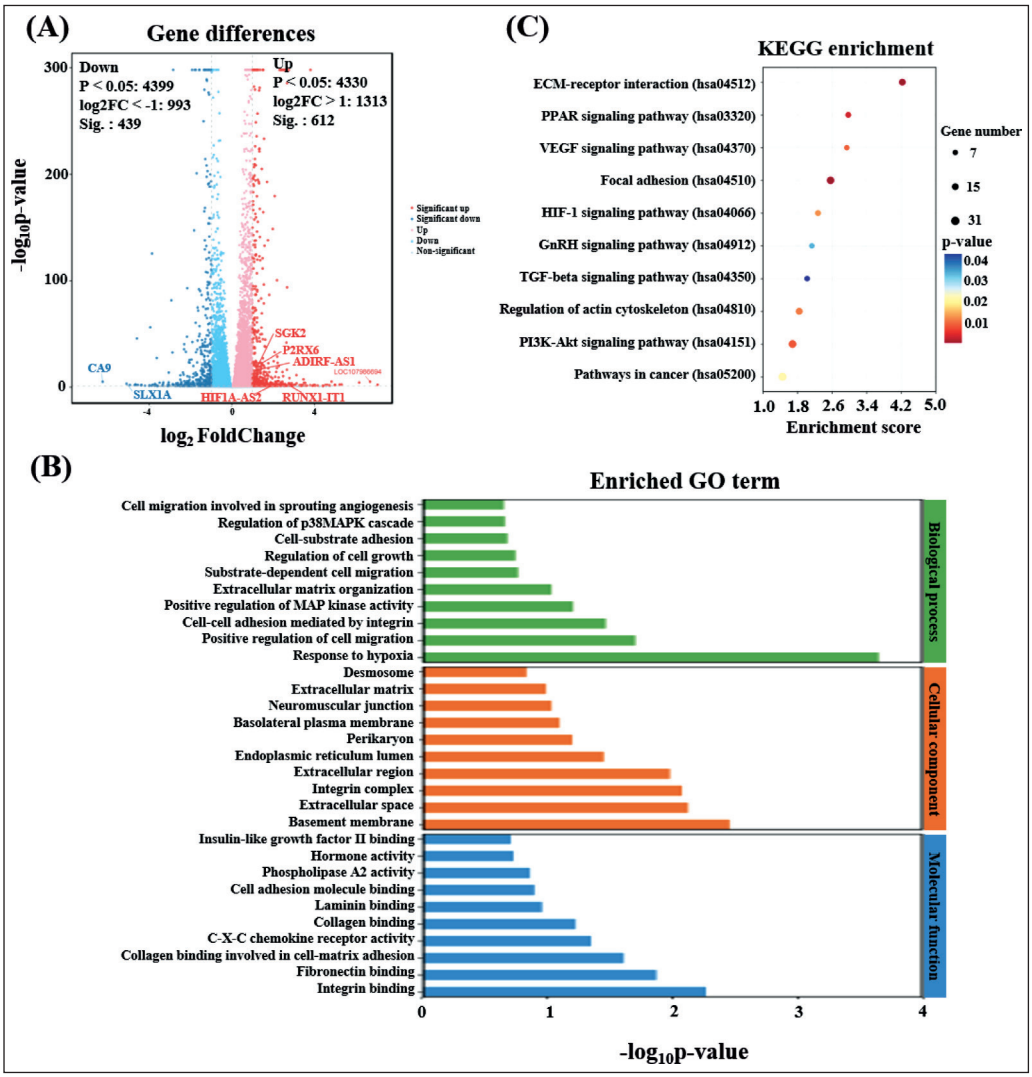

Figure 5. Transcriptional profiles for ACHN cells in GelMA-based samples. (A) Volcano plot; (B) GO terms enriched in ACHN cells; (C) KEGG terms enriched in ACHN cells.

4. Discussion

3D cell culture models have been widely used in RCC research. At present, however, few models can closely recapitulate cell–matrix interactions or be used for accurate drug assessment. In this study, we prepared a novel 3D cell culture substrate for RCC cells by mixing porcine kidney-derived dECM powders with GelMA. GelMA is a bioink commonly used in 3D bioprinting for tissue engineering since it maintains the desirable bioactive characteristics of collagen. Although collagen is a major ECM component found in the RCC stroma,[13] numerous other ECM components also play significant roles affecting RCC progression. Therefore, biochemical components of GelMA were supplemented with kidney dECM powder in this study to enrich treatments so as to better simulate the TME of RCC and promote printability.

Here, 10% GelMA was mixed with various concentrations of kidney dECM powders, and the resulting samples were systematically analyzed. We found that their material properties were significantly changed, and their mechanical properties and stability were all significantly improved following the addition of dECM powder. The mechanical behavior of a hybrid hydrogel mainly depends on the interactions between additives or fillers and gel matrix.[36] In this study, the dECM powders were found to disperse well and restrict the growth of microcracks in GelMA. This in turn led to increases in the compressive modulus and stability.[37] Similar results have also been observed in GelMA mixed with tofu powders[38] or decellularized bone powders[39] used for bone regeneration.

Next, treatments including GelMA mixed with dECM powders were further used to culture ACHN cells to examine

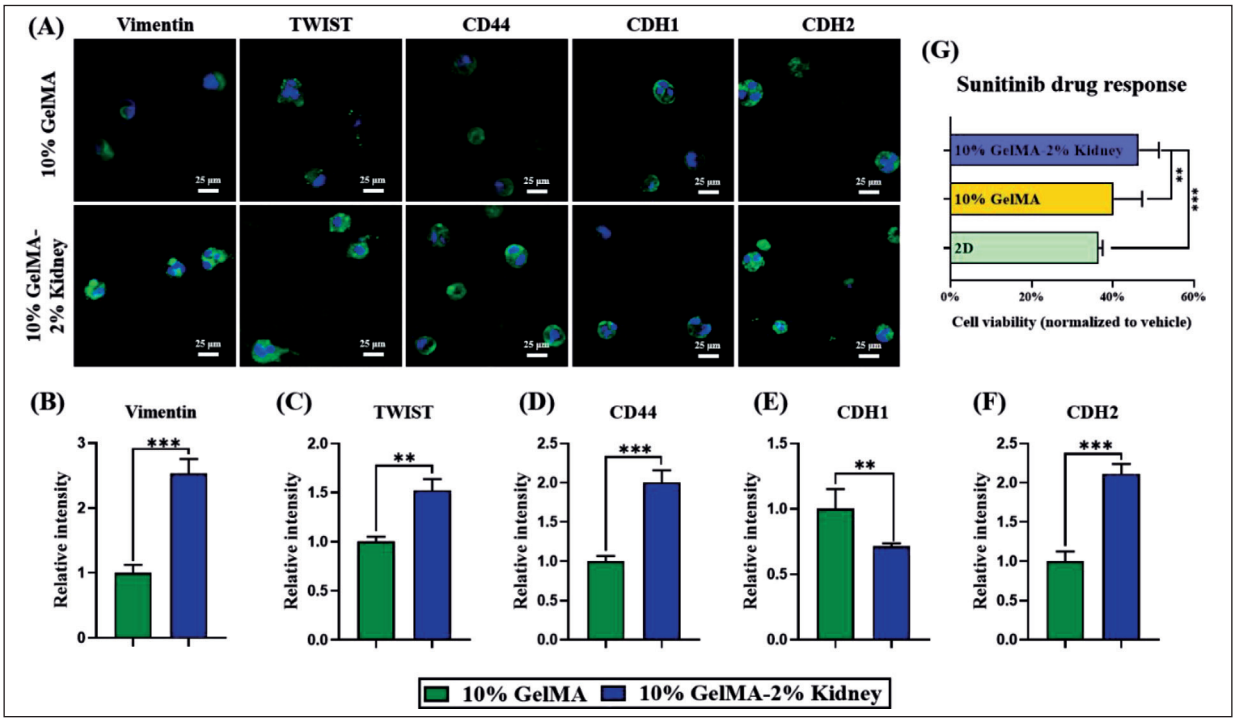

Figure 6. Immunofluorescence staining and semi-quantification. (A) Immunofluorescence images for CD44, vimentin, TWIST, CDH2, and CDH1 proteins of ACHN cells. (B–F) Semi-quantification analysis of CD44, vimentin, TWIST, CDH2, and CDH1 proteins. (g) Responses of ACHN cells to sunitinib in 2D, 10% GelMA, and 10% GelMA-2% Kidney.

the impact of RCC cellular metastasis at the molecular level. These analyses involved immunofluorescence staining and RT-qPCR of key EMT-related markers, including Slug, Snail, MMP2, MMP9, CD44, ZEB1, TWIST, CDH2, CDH1, and vimentin. EMT is one of the most crucial steps in the RCC metastatic process, where the renal epithelial cells acquire the phenotypical characteristics of mesenchymal cells and show enhanced cellular migration, invasion, plasticity, and chemoresistance.[40] RCC originates from the epithelial cells of the kidney, and the EMT process can promote the migration and metastasis of RCC cells.[41,42] Our findings showed that the expression of *Snail* and *Slug* gene was increased in ACHN cells assigned to the 10% GelMA-2% Kidney treatment compared to other groups. The Snail family transcription factors have been recognized as important mediators of EMT since they regulate the expression of several other EMT-related markers, including CDH1, MMPs, and vimentin.[43] Higher *Snail* expression has been found to be correlated with worse disease-free and disease-specific survival of RCC patients[43] and may also be an independent adverse prognostic biomarker for the recurrence and survival of patients with localized clear cell RCC after nephrectomy.[44] We also found that ACHN cells had higher *TWIST* expression when cultured with the 10% GelMA-2% Kidney sample. TWIST is a key transcription factor that confers tumor cells with CSC-like characteristics and is also associated with higher tumor grades; for this reason, it may be a valuable therapeutic marker for targeted therapies of RCC.[45,46] The 10% GelMA-2% Kidney sample also showed higher *MMP2* and *MMP9* gene expression compared with other groups, a fact that is consistent with the finding that the overexpression of Snail family can promote matrix metallopeptidase (MMP) expression in RCC.[43] MMPs play important roles in tumorigenesis and cancer cell progression since they degrade the main components of the ECM and facilitate RCC cellular metastasis.[47,48] The gene and protein expression of other EMT-related markers, including CD44, vimentin, and ZEB1, was also upregulated in ACHN cells exposed to the 10% GelMA-2% Kidney solution; each of these has also been significantly correlated with RCC metastasis, survival, and recurrence.[49-53] The cadherin switch refers to the upregulation of *CDH2* expression and the downregulation of *CDH1* expression, which was observed for ACHN cells cultured in 10% GelMA-2% Kidney via immunofluorescence staining and has been found to associate with metastasis and poor prognosis.[54,55] Given that culturing in 10% GelMA-2% Kidney significantly promoted ACHN metastasis, it was then used in the experiments for the 3D bioprinting of nephron.

The RNAseq was performed for ACHN cells cultured with 10% GelMA-2% Kidney as well as a 10% GelMA control culture. These results showed that *RUNX1*-

IT1, *P2RX6*, *SGK2*, *HIF1A-AS2*, and *ADIRF-AS1* were significantly upregulated. RUNX1 is a transcription factor that is critical for hematopoiesis and has been reported to be involved in diverse developmental processes, including cell differentiation, proliferation, and apoptosis.[56] *RUNX1* was upregulated in RCC tissues relative to normal tissues, and high *RUNX1* expression leads to significantly poorer clinical survival compared to patients with low expression.[56,57] Moreover, the inhibition of RUNX1 in RCC cells can reduce cellular proliferation and viability.[57] P2RX6 belongs to the family of P2X receptors, which are ATP-gated ion channels that mediate rapid and selective permeability to cations. It has been found that the RCC tissues express significantly higher levels of P2RX6, which modulate Ca^{2+}-mediated p-ERK1/2/MMP9 signaling to increase RCC cell migration and invasion.[58] The SGKs participate in the regulation of diverse cellular processes, including osmoregulation, cell survival, sodium homeostasis, cell proliferation, and invasion.[59] The SGK family comprises three members—SGK1, SGK2, and SGK3—with SGK2 being more highly expressed in the liver, kidney, and brain.[60] The upregulation of SGK2 has been shown to promote RCC progression by mediating the phosphorylation of ERK1/2/AKT/PKB, indicating that SGK2 could be a potential prognostic marker for RCC patients.[61] Furthermore, KEGG enrichment analysis showed that ACHN cells were enriched in the VEGF, HIF-1, and TGF-beta signaling pathways, all of which were significantly correlated with RCC progression and chemotherapy resistance.[62,63]

3D bioprinting technique has been widely applied in the development of tumor models for investigation purposes.[64] For instance, our group has successfully created prostate cancer models for the investigation of cell–cell interaction and drug resistance,[65] and also summarized the application of 3D bioprinting in urological diseases.[66] Other research groups have also demonstrated that 3D-bioprinted tumor models for cholangiocarcinoma[67] and liver cancer[68] provide platforms for more accurately assessing drug effectiveness.

The cancer cells in 3D-bioprinted tumor model were commonly laden in thin filaments with grid structure, and all cells were in homogeneous contact with culture media, a growth pattern different from that in mold-casted tumor models (which were commonly solid cylinder or cube-like), where cells at varying locations in the tumor model manifest different cellular behavior. The TME is a complicated structure, containing growth factors, extracellular matrix, and non-cancer cells. Fortunately, 3D bioprinting is capable of simulating the TME architecture in a co-culture model by printing various types of cells in precise location. The bioink and nephron model developed in this study provide potential platform that could be further modified for cell-laden bioprinting of different cells (like fibroblasts, immune cells, and endothelial cells) for kidney cancer cell co-culture in the future.

5. Conclusion

In this study, we developed a 3D cell culture substrate for ACHN cellular growth by mixing 10% GelMA with various concentrations of kidney dECM powders, including 1 wt%, 2 wt%, and 3 wt%, to mimic the ECM components in the TME of RCC. The GelMA stability, mechanical properties, and printability were significantly improved with the increase of dECM concentrations. Furthermore, RNAseq results demonstrated that the 10% GelMA-2% Kidney treatment could significantly enhance cellular growth and metastasis, a finding in concordance with the results of PCR and immunofluorescence staining of EMT-related markers. In addition, we found that the 10% GelMA-2% Kidney treatment could significantly promote the resistance of ACHN cells toward sunitinib, suggesting that the 10% GelMA-2% Kidney treatment is a potential preclinical RCC model for *in vitro* drug screening and development.

Acknowledgments

None.

Funding

This study was partly funded by the National Natural Science Foundation of China (Grant No. 12202387), the Natural Science Foundation of Zhejiang Province (Grant No. BY23H180015), the Natural Science Foundation of Ningbo (Grant Nos. 2022J216, 2022J212), the Foundation of Ningbo Science and Technology Bureau (Grant No. 2023Z193), Ningbo Medical Science and Technology Program (Grant No. 2020Y73), and the Zhejiang Medical Science and Technology Project (Grant No. 2020KY825).

Conflict of interest

The authors declare that they have no financial and personal relationships with other people or organizations that can inappropriately influence our work, and there is no professional or other personal interest of any nature or kind in any product, service, and/or company that could be construed as influencing the position of the authors in this paper.

Author contributions

Conceptualization: Kailei Xu
Formal analysis: Miaoben Wu, Hangyu Zhou, Jingying Hu, Zonghuan Wang

Funding acquisition: Yibing Wu, Yang Xiang, Peng Wei
Investigation: Miaoben Wu, Hangyu Zhou, Jingying Hu, Zonghuan Wang, Yongqi Xu
Methodology: Jun Yin, Kailei Xu, Tiantian Ren, Yongqi Xu
Writing – original draft: Miaoben Wu
Writing – review & editing: Jun Yin, Kailei Xu, Tiantian Ren

Ethics approval and consent to participate

Not applicable.

Consent for publication

Not applicable.

Availability of data

The data that support the findings of this study are available from the corresponding author upon reasonable request.

References

1. Capitanio U, Bensalah K, Bex A, et al. Epidemiology of renal cell carcinoma. *Eur Urol.* 2019;75(1):74-84. doi: 10.1016/j.eururo.2018.08.036
2. Siegel RL, Miller KD, Fuchs HE, Jemal A. Cancer statistics, 2022. *CA Cancer J Clin.* 2022;72(1):7-33. doi: 10.3322/caac.21708
3. Safiri S, Kolahi AA, Mansournia MA, et al. The burden of kidney cancer and its attributable risk factors in 195 countries and territories, 1990-2017. *Sci Rep.* 2020;10(1):13862. doi: 10.1038/s41598-020-70840-2
4. Makhov P, Joshi S, Ghatalia P, et al. Resistance to systemic therapies in clear cell renal cell carcinoma: Mechanisms and management strategies. *Mol Cancer Therap.* 2018;17(7): 1355-1364. doi: 10.1158/1535-7163.MCT-17-1299
5. Nerich V, Hugues M, Paillard MJ, et al. Clinical impact of targeted therapies in patients with metastatic clear-cell renal cell carcinoma. *Onco Targets Ther.* 2014;7:365-374. doi: 10.2147/OTT.S56370
6. Goyal R, Gersbach E, Yang XJ, Rohan SM. Differential diagnosis of renal tumors with clear cytoplasm: Clinical relevance of renal tumor subclassification in the era of targeted therapies and personalized medicine. *Arch Pathol Lab Med.* 2013;137(4):467-480. doi: 10.5858/arpa.2012-0085-RA
7. Hui L, Chen Y. Tumor microenvironment: Sanctuary of the devil. *Cancer Lett.* 2015;368(1):7-13. doi: 10.1016/j.canlet.2015.07.039
8. Jonasch E, Walker CL, Rathmell WK. Clear cell renal cell carcinoma ontogeny and mechanisms of lethality. *Nat Rev Nephrol.* 2021;17(4):245-261. doi: 10.1038/s41581-020-00359-2
9. Vuong L, Kotecha RR, Voss MH, Hakimi AA. Tumor microenvironment dynamics in clear-cell renal cell carcinoma. *Cancer Discov.* 2019;9(10):1349-1357. doi: 10.1158/2159-8290.CD-19-0499
10. Meszaros M, Yusenko M, Domonkos L, Peterfi L, Kovacs G, Banyai D. Expression of TXNIP is associated with angiogenesis and postoperative relapse of conventional renal cell carcinoma. *Sci Rep.* 2021;11(1):17200. doi: 10.1038/s41598-021-96220-y
11. Li S, Huang C, Hu G, et al. Tumor-educated B cells promote renal cancer metastasis via inducing the IL-1β/HIF-2α/ Notch1 signals. *Cell Death Dis.* 2020;11(3):163. doi: 10.1038/s41419-020-2355-x
12. Frantz C, Stewart K, Weaver V. The extracellular matrix at a glance. *J Cell Sci.* 2010;123:4195-4200. doi: 10.1242/jcs.023820
13. Majo S, Courtois S, Souleyreau W, Bikfalvi A, Auguste P. Impact of extracellular matrix components to renal cell carcinoma behavior. *Front Oncol.* 2020;10:625. doi: 10.3389/fonc.2020.00625
14. Afify A, Purnell P, Nguyen L. Role of CD44s and CD44v6 on human breast cancer cell adhesion, migration, and invasion. *Exp Mol Pathol.* 2009;86(2):95-100. doi: 10.1016/j.yexmp.2008.12.003
15. Theocharis A. Versican in health and disease. *Connect Tissue Res.* 2008;49(3):230-234. doi: 10.1080/03008200802147571
16. Marinkovich M. Tumour microenvironment: Laminin 332 in squamous-cell carcinoma. *Nat Rev Cancer.* 2007;7(5): 370-380. doi: 10.1038/nrc2089
17. Astrof S, Hynes R. Fibronectins in vascular morphogenesis. *Angiogenesis.* 2009;12(2):165-175. doi: 10.1007/s10456-009-9136-6
18. Hielscher A, Ellis K, Qiu C, Porterfield J, Gerecht S. Fibronectin deposition participates in extracellular matrix assembly and vascular morphogenesis. *PloS One.* 2016;11(1): e0147600. doi: 10.1371/journal.pone.0147600
19. Unal A, West J. Synthetic ECM: Bioactive synthetic hydrogels for 3D tissue engineering. *Bioconjug Chem.* 2020;31(10):2253-2271. doi: 10.1021/acs.bioconjchem.0c00270
20. Kabirian F, Mozafari M. Decellularized ECM-derived bioinks: Prospects for the future. *Methods (San Diego, Calif.).* 2020;171:108-118. doi: 10.1016/j.ymeth.2019.04.019
21. Fontana F, Marzagalli M, Sommariva M, Gagliano N, Limonta P. In vitro 3D cultures to model the tumor microenvironment. *Cancers (Basel).* 2021;13(12).

doi: 10.3390/cancers13122970

22. Habanjar O, Diab-Assaf M, Caldefie-Chezet F, Delort L. 3D cell culture systems: Tumor application, advantages, and disadvantages. *Int J Mol Sci.* 2021;22(22). doi: 10.3390/ijms222212200

23. Monteiro M, Gaspar V, Ferreira L, Mano J. Hydrogel 3D in vitro tumor models for screening cell aggregation mediated drug response. *Biomater Sci.* 2020;8(7):1855-1864. doi: 10.1039/c9bm02075f

24. Pan T, Fong EL, Martinez M, et al. Three-dimensional (3D) culture of bone-derived human 786-O renal cell carcinoma retains relevant clinical characteristics of bone metastases. *Cancer Lett.* 2015;365(1):89-95. doi: 10.1016/j.canlet.2015.05.019

25. Maliszewska-Olejniczak K, Brodaczewska KK, Bielecka ZF, et al. Development of extracellular matrix supported 3D culture of renal cancer cells and renal cancer stem cells. *Cytotechnology.* 2019;71(1):149-163. doi: 10.1007/s10616-018-0273-x

26. Liu K, Cui JJ, Zhan Y, et al. Reprogramming the tumor microenvironment by genome editing for precision cancer therapy. *Mol Cancer.* 2022;21(1):98-121. doi: 10.1186/s12943-022-01561-5

27. Nallasamy P, Nimmakayala RK, Parte S, Are AC, Batra SK, Ponnusamy MP. Tumor microenvironment enriches the stemness features: The architectural event of therapy resistance and metastasis. *Mol Cancer.* 2022;21(1):225-250. doi: 10.1186/s12943-022-01682-x

28. Zhang X, Chen X, Hong H, Hu R, Liu J, Liu C. Decellularized extracellular matrix scaffolds: Recent trends and emerging strategies in tissue engineering. *Bioact Mater.* 2022;10:15-31. doi: 10.1016/j.bioactmat.2021.09.014

29. Zhang W, Du A, Liu S, Lv M, Chen S. Research progress in decellularized extracellular matrix-derived hydrogels. *Regen Ther.* 2021;18:88-96. doi: 10.1016/j.reth.2021.04.002

30. Yue K, Trujillo-de Santiago G, Alvarez M, Tamayol A, Annabi N, Khademhosseini A. Synthesis, properties, and biomedical applications of gelatin methacryloyl (GelMA) hydrogels. *Biomaterials.* 2015;73:254-271. doi: 10.1016/j.biomaterials.2015.08.045

31. Wang F, Zhang R, Gao N, et al. Coagulation-anticoagulation-regulable and tough extracellular matrix hydrogels. *Compos Part B: Eng.* 2022;239: 109938. doi: 10.1016/j.compositesb.2022.109938

32. Yin J, Yan M, Wang Y, Fu J, Suo H. 3D bioprinting of low-concentration cell-laden gelatin methacrylate (GelMA) bioinks with a two-step cross-linking strategy. *ACS Appl Mater Interfaces.* 2018;10(8):6849-6857. doi: 10.1021/acsami.7b16059

33. Li Y, Mao Q, Yin J, Wang Y, Fu J, Huang Y. Theoretical prediction and experimental validation of the digital light processing (DLP) working curve for photocurable materials. *Addit Manuf.* 2021;37. doi: 10.1016/j.addma.2020.101716

34. Habib A, Sathish V, Mallik S, Khoda B. 3D printability of alginate-carboxymethyl cellulose hydrogel. *Materials (Basel).* 2018;11(3). doi: 10.3390/ma11030454

35. Ouyang L, Yao R, Zhao Y, Sun W. Effect of bioink properties on printability and cell viability for 3D bioplotting of embryonic stem cells. *Biofabrication.* 2016; 8(3):035020. doi: 10.1088/1758-5090/8/3/035020

36. Ljungberg N, Bonini C, Bortolussi F, Boisson C, Heux L, Cavaille JY. New nanocomposite materials reinforced with cellulose whiskers in atactic polypropylene effect of surface and dispersion characteristics. *Biomacromolecules.* 2005;6:2732-2739. doi: 10.1021/bm050222v

37. Shin MK, Spinks GM, Shin SR, Kim SI, Kim S. Nanocomposite hydrogel with high toughness for bioactuators. *Adv Mater.* 2009;21:1712-1715. doi: 10.1002/adma.200802205

38. Huang K, Gu Z, Wu J. Tofu-incorporated hydrogels for potential bone regeneration. *ACS Biomater Sci Eng.* 2020;6(5): 3037-3045. doi: 10.1021/acsbiomaterials.9b01997

39. Gao C, Sow WT, Wang Y, et al. Hydrogel composite scaffolds with an attenuated immunogenicity component for bone tissue engineering applications. *J Mater Chem B.* 2021;9(8):2033-2041. doi: 10.1039/d0tb02588g

40. Dongre A, Weinberg RA. New insights into the mechanisms of epithelial-mesenchymal transition and implications for cancer. *Nat Rev Mol Cell Biol.* 2019;20(2): 69-84. doi: 10.1038/s41580-018-0080-4

41. Feng D, Gao P, Henley N, et al. SMOC2 promotes an epithelial-mesenchymal transition and a pro-metastatic phenotype in epithelial cells of renal cell carcinoma origin. *Cell Death Dis.* 2022;13(7): 639-654. doi: 10.1038/s41419-022-05059-2

42. Zhong M, Zhu M, Liu Y, et al. TNFAIP8 promotes the migration of clear cell renal cell carcinoma by regulating the EMT. *J Cancer.* 2020;11(10):3061-3071. doi: 10.7150/jca.40191

43. Mikami S, Katsube K, Oya M, et al. Expression of Snail and Slug in renal cell carcinoma: E-cadherin repressor Snail is associated with cancer invasion and prognosis. *Lab Invest.* 2011;91(10):1443-1458. doi: 10.1038/labinvest.2011.111

44. Liu W, Liu Y, Liu H, Zhang W, An H, Xu J. Snail predicts recurrence and survival of patients with localized clear cell

renal cell carcinoma after surgical resection. *Urol Oncol.* 2015;33(2):69e61-10.
doi: 10.1016/j.urolonc.2014.08.003

45. Harada K, Miyake H, Kusuda Y, Fujisawa M. Expression of epithelial-mesenchymal transition markers in renal cell carcinoma: Impact on prognostic outcomes in patients undergoing radical nephrectomy. *BJU Int.* 2012;110 (11 Pt C):E1131-1137.
doi: 10.1111/j.1464-410X.2012.11297.x

46. Rasti A, Madjd Z, Abolhasani M, et al. Cytoplasmic expression of Twist1, an EMT-related transcription factor, is associated with higher grades renal cell carcinomas and worse progression-free survival in clear cell renal cell carcinoma. *Clin Exp Med.* 2018;18(2):177-190.
doi: 10.1007/s10238-017-0481-2

47. Kugler A, Hemmerlein B, Thelen P, Kallerhoff M, Radzun HJ, Ringert RH. Expression of metalloproteinase 2 and 9 and their inhibitors in renal cell carcinoma. *J Urol.* 1998;160(5):1914-1918.
doi: 10.1016/s0022-5347(01)62443-1

48. Chambers AF, Matrisian LM. Changing views of the role of matrix metalloproteinases in metastasis. *J Natl Cancer Inst.* 1997;89(17):1260-1270.
doi: 10.1093/jnci/89.17.1260

49. Xu H, Xu W-H, Ren F, et al. Prognostic value of epithelial-mesenchymal transition markers in clear cell renal cell carcinoma. *Aging.* 2020;12(1):866-883.
doi: 10.18632/aging.102660

50. Sugimoto M, Kohashi K, Itsumi M, et al. Epithelial to mesenchymal transition in clear cell renal cell carcinoma with rhabdoid features. *Pathobiology.* 2016;83(6):277-286.
doi: 10.1159/000445752

51. Li X, Ma X, Chen L, et al. Prognostic value of CD44 expression in renal cell carcinoma: A systematic review and meta-analysis. *Sci Rep.* 2015;5:13157.
doi: 10.1038/srep13157

52. Yao JX, Chen X,. Zhu YJ, Wang H, Hu XY, Guo JM. Prognostic value of vimentin is associated with immunosuppression in metastatic renal cell carcinoma. *Front Oncol.* 2020;10:1181-1190.
doi: 10.3389/fonc.2020.01181

53. Fiedorowicz M, Khan MI, Strzemecki D, et al. Renal carcinoma CD105-/CD44- cells display stem-like properties in vitro and form aggressive tumors in vivo. *Sci Rep.* 2020;10(1):5379.
doi: 10.1038/s41598-020-62205-6

54. Katagiri A, Watanabe R, Tomita Y. E-cadherin expression in renal cell cancer and its significance in metastasis and survival. *Br J Cancer.* 1995;71(2):376-379.
doi: 10.1038/bjc.1995.76

55. Tani T, Laitinen L, Kangas L, Lehto VP, Virtanen I. Expression of E- and N-cadherin in renal cell carcinomas, in renal cell carcinoma cell lines in vitro and in their xenografts. *Int J Cancer.* 1995;64(6):407-414.
doi: 10.1002/ijc.2910640610

56. Gao K, Zhang F, Chen K, et al. Expression patterns and prognostic value of RUNX genes in kidney cancer. *Sci Rep.* 2021;11(1):14934.
doi: 10.1038/s41598-021-94294-2

57. Rooney N, Mason SM, McDonald L, et al. RUNX1 is a driver of renal cell carcinoma correlating with clinical outcome. *Cancer Res.* 2020;80(11):2325-2339.
doi: 10.1158/0008-5472.CAN-19-3870

58. Gong D, Zhang J, Chen Y, et al. The m(6)A-suppressed P2RX6 activation promotes renal cancer cells migration and invasion through ATP-induced Ca(2+) influx modulating ERK1/2 phosphorylation and MMP9 signaling pathway. *J Exp Clin Cancer Res.* 2019;38(1):233-249.
doi: 10.1186/s13046-019-1223-y

59. Ranzuglia V, Lorenzon I, Pellarin I, et al. Serum- and glucocorticoid- inducible kinase 2, SGK2, is a novel autophagy regulator and modulates platinum drugs response in cancer cells. *Oncogene.* 2020;39(40): 6370-6386.
doi: 10.1038/s41388-020-01433-6

60. Pao AC. SGK regulation of renal sodium transport. *Curr Opin Nephrol Hypertens.* 2012;21(5):534-540.
doi: 10.1097/MNH.0b013e32835571be

61. Liu Y, Chen J-B, Zhang M, et al. SGK2 promotes renal cancer progression via enhancing ERK 1-2 and AKT phosphorylation. *Eur Rev Med Pharmacol Sci.* 2019;23(7):2756-2767.
doi: 10.26355/eurrev_201904_17549

62. Baldewijns MM, van Vlodrop IJ, Vermeulen PB, Soetekouw PM, van Engeland M, de Bruine AP. VHL and HIF signalling in renal cell carcinogenesis. *J Pathol.* 2010;221(2):125-138.
doi: 10.1002/path.2689

63. Bostrom AK, Lindgren D, Johansson ME, Axelson H. Effects of TGF-beta signaling in clear cell renal cell carcinoma cells. *Biochem Biophys Res Commun.* 2013;435(1):126-133.
doi: 10.1016/j.bbrc.2013.04.054

64. Ma L, Li Y, Wu Y, et al. The construction of in vitro tumor models based on 3D bioprinting. *Bio-Des Manuf.* 2020;3(3):227-236.
doi: 10.1007/s42242-020-00068-6

65. Xu K, Huang Y, Wu M, Yin J, Wei P. 3D bioprinting of multi-cellular tumor microenvironment for prostate cancer metastasis. *Biofabrication.* 2023;15(3):035020.
doi: 10.1088/1758-5090/acd960

66. Xu K, Han Y, Huang Y, Wei P, Yin J, Jiang J. The application of 3D bioprinting in urological diseases. *Mater Today Bio*. 2022;16:100388.
doi: 10.1016/j.mtbio.2022.100388

67. Mao S, He J, Zhao Y, et al. Bioprinting of patient-derived in vitro intrahepatic cholangiocarcinoma tumor model: Establishment, evaluation and anti-cancer drug testing. *Biofabrication*. 2020;12(4):045014.
doi: 10.1088/1758-5090/aba0c3

68. Xie F, Sun L, Pang Y, et al. Three-dimensional bio-printing of primary human hepatocellular carcinoma for personalized medicine. Biomaterials. 2021;265: 120416.
doi: 10.1016/j.biomaterials.2020.120416

ACCSCIENCE PUBLISHING

International Journal of Bioprinting

RESEARCH ARTICLE

Achieving personalized nutrition for patients with diabetic complications via 3D food printing

Yuanyuan Chen[1], Siwei Bi[2], Jun Gu[3], Qianli Che[4], Ruiqi Liu[2], Wei Li[3], Tingting Dai[5], Dongan Wang[6], Xiaosheng Zhang[1]*, and Yi Zhang[1]*

[1]School of Integrated Circuit Science and Engineering, University of Electronic Science and Technology of China, Chengdu, Sichuan, China

[2]Department of Plastic and Burn Surgery, West China Hospital, Sichuan University, Chengdu, Sichuan, China

[3]Department of Cardiovascular Surgery, West China Hospital, Sichuan University, Chengdu, Sichuan, China

[4]CSCEC SCIMEE Science & Technology Co. Ltd., Chengdu, Sichuan, China

[5]Department of Nutrition, West China Hospital, Sichuan University, Chengdu, Sichuan, China

[6]Department of Biomedical Engineering, City University of Hong Kong, Hong Kong SAR, China

(This article belongs to the *Special Issue: 3D Food Inks: Physicochemical Properties, Product Development, Structure-Functionality and Safety*)

Abstract

The global prevalence of diabetes mellitus is experiencing a notable increase. Diabetic patients need to consistently monitor their fluctuating glucose levels caused by the changing diet. Meanwhile, patients with diabetes face a higher risk of developing oral ulcer than healthy individuals. Fortunately, three-dimensional (3D)-printed food, which is design- and texture-customizable, presents a potential solution to alleviate the discomfort caused by ulcer while providing personalized nutrition for patients with unique dietary requirements. In this study, 3D-printable food inks were created based on four food ingredients with low glycemic index, namely milk powder, wheat bran powder, *Russula alutacea* Fr., (russula mushroom), and *Agaricus bisporus* (button mushroom) content. Rheological testing and texture profile analysis were performed, affirming that the 3D-printed food possesses a soft texture, which minimizes oral mucosal irritation for patients with diabetic ulcers. The effectiveness of 3D-printed food in diabetes management was corroborated by monitoring the blood glucose levels of streptozotocin-induced diabetic rats via gavage. Food with personalized nutritional composition was custom-printed to cater for the protein requirements of patients with diabetic nephropathy. This innovative approach to personalizing nutrition through 3D food printing has the potential to reshape the future of dietary management, ultimately improving the overall health outcomes and quality of life for individuals with diabetes and its complications.

Keywords: 3D food printing; Personalized nutrition; Diabetes; Ulcer; Daily protein intake

***Corresponding authors:**
Xiaosheng Zhang
(zhangxs@uestc.edu.cn)

Yi Zhang
(yi_zhang@uestc.edu.cn)

Citation: Chen Y, Bi S, Gu J, et al. Achieving personalized nutrition for patients with diabetic complications via 3D food printing. *Int J Bioprint*. 2024;10(2):1862.
doi: 10.36922/ijb.1862

Received: September 17, 2023
Accepted: December 11, 2023
Published Online: January 29, 2024

1. Introduction

Diabetes encompasses a cluster of metabolic disorders characterized by hyperglycemia resulting from deficiencies in insulin secretion, insulin action, or both.[1] According to the

International Diabetes Federation (IDF), approximately 451 million adults worldwide were affected by diabetes in 2017, and the figure is projected to rise to 693 million by 2045 if effective prevention measures are not implemented.[2] Diabetes can give rise to long-term complications, such as retinopathy, neuropathy, kidney disease, hypertension, and abnormal lipoprotein metabolism, which, if left unmanaged, potentially lead to life-threatening complications, organ failure, and death.[3]

The American Diabetes Association advocates the Diabetes Plate method as a straightforward way of maintaining a healthy diet to manage blood glucose level.[4,5] This approach has demonstrated effectiveness in improving glycemic control among individuals with diabetes. Moreover, alternative guidelines, such as the European or Canadian recommendations, which suggest the consumption of 45–60% of total energy from carbohydrates, 10–20% from protein, and less than 35% from fat, were also widely practiced.[6]

The aforementioned guidelines are effective and user-friendly. Nevertheless, diabetic patients who suffer from additional complications, such as kidney conditions or oral ulcers, require specific dietary considerations. As one of the most prevalent complications of diabetes, chronic kidney disease (CKD) affects 30% and 40% of patients with types 1 and 2 diabetes, respectively. In light of this, the 2020 National Kidney Foundation Kidney Disease Outcomes Quality Initiative Clinical Practice Guidelines for Nutrition in CKD recommend that daily protein intake (DPI) be adjusted to 0.6–0.8 g/kg of ideal body weight per day for diabetic patients with stages 3–5 CKD.[7] Patients with CKD experience renal function decline, and a low-protein diet has been shown to exert renal protective effects by reducing intraglomerular pressure and improving glomerular hyperfiltration or hypertension.[8] Furthermore, evidence suggests that diabetic patients have more complex oral conditions than non-diabetic individuals and grapple with a higher risk for oral mucosal diseases.[9-12] Recurrent oral ulcer is the most common ulcerative condition among oral mucosal diseases. While the prevalence of recurrent oral ulcer in the general population is approximately 20%,[9,13] it stands at an extremely high level, as high as 45%, in diabetic patients.[14] Although oral ulcers are not life-threatening, pain and discomfort that come with them diminish quality of life and work efficiency among the affected individuals. Therefore, facilitating the healing process of oral ulcers is crucial for improving the quality of life of diabetic patients.[15]

Three-dimensional (3D) printing is considered a prominent digital manufacturing technology within the realm of Industry 4.0, offering the ability to reconstruct food items equipped with improved structural properties, visually appealing presentation, and personalized nutrition.[16] At the same time, 3D-printed food can potentially improve oral intake and nutritional needs of patients, as 3D printing technology is able to create personalized food that meets the dietary need of consumers.[17] For instance, significant efforts have been directed toward the 3D printing of soft-textured and safe-to-swallow food for patients with dysphagia. In addition, the enhanced visual appeal displayed by the 3D-printed food can improve food intake, thereby preventing malnutrition among patients.[18] Additionally, 3D printing has been employed to produce meat substitute, such as a soybean oil-based functional emulsification gel, with the aim of enhancing the lipid profile and reducing saturated fat content in the food.[19] In a similar vein, ground larvae of yellow mealworms (*Tenebrio molitor*) have been 3D-printed into snacks,[20] providing a novel protein source with a high content of total essential amino acid. Other alternative protein sources, such as black soldier fly larva, cricket powder, and sericin, have also been demonstrated to be suitable for 3D food printing.[21]

The 3D printing of food items with a soft texture and personalized nutrition holds promise for improving nutrition intake and alleviating pain among diabetic patients with oral ulcers. This study focuses on formulating 3D-printable food inks using natural ingredients that have established benefits for oral health and diabetes management. We have carefully selected natural food ingredients such as wheat bran, milk powder, and mushrooms. The ample cereal polyphenols found in wheat bran can exert protective effects to enhance diabetes management through multiple pathways. These pathways include reducing oxidative stress and AGEs production, inhibiting inflammation, and regulating gut microbiota.[22-25] Milk powder[26,27] and mushrooms[28,29] are both rich in B vitamins, which promote the healing of canker sores.[15] Additionally, numerous studies have demonstrated the beneficial effects of mushrooms in diabetes control.[30-32] The content of fiber and resistant starch is crucial in food ink formulation.[33,34] The rheological properties, textures, microstructures, and composition of the food inks are subsequently characterized. Customized diets can be created from these raw ingredients utilizing 3D printing technology, incorporating functional compounds that alleviate the symptoms of oral ulcers and other complications of diabetes while providing nutrients in balanced proportions. In this study, animal experiments were conducted to assess the effectiveness of the 3D-printed diet in glycemic control. The utilization of dual-nozzle collaborative 3D printing technology enables precise regulation of the nutritional composition, a crucial aspect for CKD patients requiring protein-restricted diets.

The potential of 3D printing for producing personalized food poses a significant impetus in improving the quality of life and health outcomes of patients with diabetes and other chronic diseases that necessitate tailored nutrition and food with specific texture.

2. Materials and methods

2.1. Formulation of food inks

Powdered *Russula alutacea* (Russula mushroom) and *Agaricus bisporus* (button mushroom) were procured from Xi'an Jinshuo Fruit Industry Co., Ltd. (Xi'an, China), while whole milk powder was obtained from Inner Mongolia Yili Industrial Group Co. Ltd. Both mushroom powders were pulverized by spray drying at a high temperature (>80°C). Edible wheat bran was sourced from Henan Jinyuan Grain and Oil Co., Ltd. (Zhengzhou, China). Xanthan gum (XG) was provided by Yongxin Food Ingredients Co., Ltd. (Guangzhou, China). Vegetable powder was obtained from Xinghua Huatai Food Factory (Taizhou, China), while rice flour was purchased from Beijing Jinhe Luyuan Trade Co., Ltd. (Beijing, China). Natural mineral water from Blu-ray Co. Ltd. (Chengdu, China) was used to formulate the inks. Material-1 was prepared by mixing wheat bran and *Russula alutacea* powder at a 1:1 ratio by weight. Material-2 was prepared by mixing whole milk powder and *Agaricus bisporus* powder at a 1:1 ratio by weight. To prepare the food inks, ingredients in the form of dry powder were weighed in proportion and pre-mixed. Boiling water and XG were then added, and the mixture was stirred again until it became homogeneous. The formulated food ink was then covered with plastic wrap to prevent moisture loss and refrigerated overnight at 4°C for full hydration. The ink was taken out of the refrigerator and left at room temperature for 1 h before use. Two ink formulations based on Material-1 (ink-M1) and Material-2 (ink-M2), respectively, were optimized for best printability (Table 1). For ink-M1, in addition to the optimized formulation (ink-M1-1), two other formulations with higher and lower XG content, respectively, were included for comparison in subsequent analyses. For ink-M2, in addition to the optimized formulation (ink-M2-1), two other formulations with higher and lower water content, respectively, were included for comparison in subsequent analyses.

2.2. 3D food printing

Food inks were 3D-printed by using the FoodBot-D1 extrusion printer (SHINNOVE, FOODBOT-D1, China) equipped with a dual-nozzle feeding system that allowed for the collaborative printing of two different food inks. A nozzle of 0.84 mm in diameter was employed to 3D-print the proposed food inks. The material ratio, filling density, printing speed, and extrusion rate were optimized in preliminary tests. To evaluate the printability of the food inks, a regular hexagon with a side length of 2 cm and a height of 1 cm was printed at a printing speed of 25 mm/s. The ink formulation was considered to possess a good printability if it could be extruded smoothly without any breakage, and the printed specimen was able to maintain structural stability for at least 15 min. Visual evaluation on a scale of 1 (poorest) to 5 (best) was conducted on three replicates of each food ink by assessing factors such as shape fidelity and structural integrity to determine the printability score of the food formulations using the scoring system reported previously.[18,21,35] The ink formulation that received the highest scores among all specimens was considered the optimized formulation.

2.3. Rheological characterization of food inks

The rheological properties of the six food inks shown in Table 1 were characterized using an oscillatory rheometer (Anton Paar, MCR302e, Austria) equipped with stainless steel parallel plates with a diameter of 50 mm and a gap size of 1 mm. To eliminate edge effects, any excess sample was carefully removed. The shear-thinning behavior was evaluated by subjecting the food inks to a stepwise shear rate ramp ranging from 0.1 to 100 s^{-1}. The viscoelastic properties of the ink were studied through amplitude sweep experiments, where a stress ranging from 0.1 to 2000 Pa was applied at a constant frequency of 1 Hz. To mimic the ink's behavior before, during, and after extrusion from the nozzle, recovery tests were conducted. The ink specimen

Table 1. Ink formulations

	Material-1 (%)	XG (%)	Water (%)
Ink-M1-1	45.00	0.45	54.55
Ink-M1-2	48.00	0.07	51.90
Ink-M1-3	45.50	0.00	54.50
	Material-2 (%)	**Water (%)**	
Ink-M2-1	55	45	
Ink-M2-2	45	55	
Ink-M2-3	60	40	

was subjected to an initial shear rate that slowly ramped from 0.1 to 1 s^{-1} in 60 s, followed by a high shear rate of 200 s^{-1} which returned to 0.1 s^{-1} after 6 s. All experiments were performed in triplicates at 25 ± 0.1°C.

2.4. Texture profile analysis

Texture analysis was performed using the Texture Analyzer Universal TA (Shanghai Tengba Instrument Technology Co., Ltd., China) to obtain force–time curves through double-cycle compression tests. To ensure the stability, a 1-cm^3 specimen printed with the FoodBot-D1 was placed at the center of the platform. The test parameters were standardized with a block probe having a trigger load of 5 g, pre-test speed of 2.0 mm/s, and compressive strain of 45%. The test and post-test speeds were also set to 2.0 mm/s. The measured textural properties included the hardness, chewiness, adhesiveness, gumminess, springiness, and stringiness. Each test was repeated three times for each specimen, and the results were averaged and normalized to the highest value obtained in the group.[35]

2.5. Scanning electron microscopy

The microstructure of the food inks was analyzed using scanning electron microscopy (SEM; JSM-7600F, JEOL Ltd., Tokyo, Japan). A small amount of food inks was spread onto a Petri dish, frozen at -20°C for 6 h, and then subjected to vacuum freeze-drying for 72 h. The dried samples were mounted on circular stubs with double-sided adhesive tapes, sputter-coated with gold (7 Pa and 8 W for 40 s), and imaged at magnifications of 500× and 1500× with an excitation voltage of 15 kV.

2.6. International Dysphagia Diet Standardization Initiative tests

International Dysphagia Diet Standardization Initiative (IDDSI) fork pressure test was adopted to qualitatively assess the texture of the 3D-printed food and gauge their suitability for patients with oral ulcer. The framework categorizes texturally modified food into eight levels (0 to 7) and proposes a combination of tests to determine the appropriate level of each food.[36] Food inks for 3D printing usually belong to Level 4 (pureed; extremely thick) or Level 5 (minced and moist), which are suitable for fork pressure test. For the fork pressure test, the 3D-printed specimens were pressed with a fork by thumb until blanching (approximate pressure of 17 kPa), which is equivalent to the tongue pressure used during swallowing.

2.7. Animal experiments

One week before streptozotocin (STZ) injection, male Sprague-Dawley rats (200–250 g) were purchased from Dashuo Co. Ltd. (Chengdu, China) and fed to fully adapt to the environment. The 1% STZ solution dissolved in citrate buffer was injected intraperitoneally into rats at a dose of 65 mg/kg. The glucose level of the blood sample taken from the rat tail vein was measured with a blood glucometer in the following 7 days. The fasting blood glucose level for rats with normal blood glucose was 3.95 ± 1.31 mmol/L, and their blood glucose 120 min after a meal was 5.65 ± 1.63 mmol/L.[37] Rats with the blood glucose level above 16.7 mmol/L for at least 3 consecutive days were used in subsequent gavage experiments. Based on the content for gavage, the rats were divided into three groups—rice group, vegetable group, and 3D-print food powder group. Two parallel experiments were designed, in which either the total mass or the total amount of carbohydrates of the food was controlled. In the equal-mass experiments, 1 g of water was added to every 100 mg of food powder, and the mixture was fully homogenized. Each animal received 1 mL of the homogenized food powder. In the equal-carbohydrate experiments, the total carbohydrate content of each food for gavage was set to 2 g/kg of body weight. The glucose levels at 0 min (the time of oral gavage), 30 min, 60 min, 90 min, and 120 min were measured by using a handheld electrochemical glucose meter and test strip. Both the peak glucose level and the area under the curve (AUC) for glucose were compared for both the equal-mass and equal-carbohydrate scenarios.

2.8. Fourier-transform infrared spectroscopy

The measurement of infrared spectra of food ink formulations using the Spectrum Two (L1600300) Fourier-transform infrared (FT-IR) spectrometer was performed in accordance with the method described by Liu et al.[38] For sample preparation, each food ink formulation was freeze-dried and ground into powder using a mortar. Subsequently, the samples were thoroughly mixed with potassium bromide (KBr) at a 1:100 ratio. The measurements were carried out with the wavenumber range of 4000 cm^{-1} to 400 cm^{-1}, at an ambient temperature of 25°C. The scan speed was set at 0.2 cm/s, and the resolution was set to 4 cm^{-1}.

2.9. Statistical analysis

The data obtained were analyzed using GraphPad Prism software, and the results were expressed as means ± standard error of the mean. Statistical significance was evaluated using analysis of variance (ANOVA). Significance levels were indicated above specific columns, where * denotes $p \leq 0.05$, ** denotes $p \leq 0.01$, *** denotes $p \leq 0.001$, and **** denotes $p \leq 0.0001$. Radar charts for textural profile analysis were generated using Microsoft Excel.

3. Results and discussion

3.1. Printability and rheological properties of food inks

The printability of the food inks was assessed through visual inspection of the hexagons 3D-printed with respective

food inks. Each hexagon was assigned a score from 1 to 5, with 5 representing the one with highest shape fidelity (Table 1). Preliminary tests were conducted to optimize the ink formulation by evaluating the printability of hexagon specimens printed with various food ingredients, XG ratios, nozzle diameters, and fill densities. The compositions and printing parameters of the specimens were planned using the design of experiment methodology. Three specimens of each ink formulation were printed and evaluated using the method described in previous publications,[21,34] and the formulation leading to the highest mean score was considered the optimized formulation in respective groups (**Tables S1** and **S2** in Supplementary File). Three representative inks, including the optimized formulation, were selected from each ink material for further analysis. Among the two types of food inks, Ink-M1-1 and Ink-M2-1 receive the highest scores with a printability score of 4.53 ± 0.13 and 4.46 ± 0.20, respectively. Compared to Ink-M1-1 (Figure 1A), both Ink-M1-2 and Ink-M1-3 exhibited inferior printability, scoring 1.55 ± 0.35 (Figure 1B) and 2.83 ± 0.20 (Figure 1C), respectively. Ink-M1-2 contained a higher proportion of Material-1 and a lower amount of XG compared to Ink-M1-1, resulting in a drier consistency that made it more challenging to extrude from the nozzle during printing. Consequently, the lines extruded with Ink-M1-2 appear segmented and twisted, failing to align well with the toolpath to form the desired shape. XG is a common food thickener used to adjust the rheological properties of food inks. Right amount of XG enhances the extrudability, shear-thinning behavior, and structural stability of the food inks. If the XG content is too high, the food ink is difficult to extrude. If the XG content is too low, the food ink may not be able to maintain the structural stability.[21,39,40] On the other hand, Ink-M1-3 and Ink-M1-1 had similar dryness and water content, except for Ink-M1-1, which contained 0.45 wt% XG. Due to the absence of XG, the hexagon printed with Ink-M1-3 appeared damp, and the extrusion lines tended to spread.[18] The optimized ink based on Material-2 (Ink-M2-1) with a printability score of 4.46 ± 0.20 did not require the addition of XG to maintain the structural integrity of the 3D-printed object, owing to its high starch and fat content known to enhance the printability[41,42] of food inks (Figure 1D). Ink-M2-2 had a higher water content than Ink-M2-1, resulting in post-print spreading, which led to a printability score of 3.97 ± 0.17 (Figure 1E). Conversely, Ink-M2-3 had a lower water content than Ink-M2-1, and the resulting structure 3D-printed with Ink-M2-3 received a printability score of 3.09 ± 0.68. The printout exhibited similar characteristics to that printed with Ink-M1-2, showing segmented and twisted extrusion lines (Figure 1F).

The rheological properties are used to assess the food ink's ability to produce the desired pattern. The rheological properties of all six inks listed in Table 1 were characterized and presented in Figure 2. It was observed that all six inks

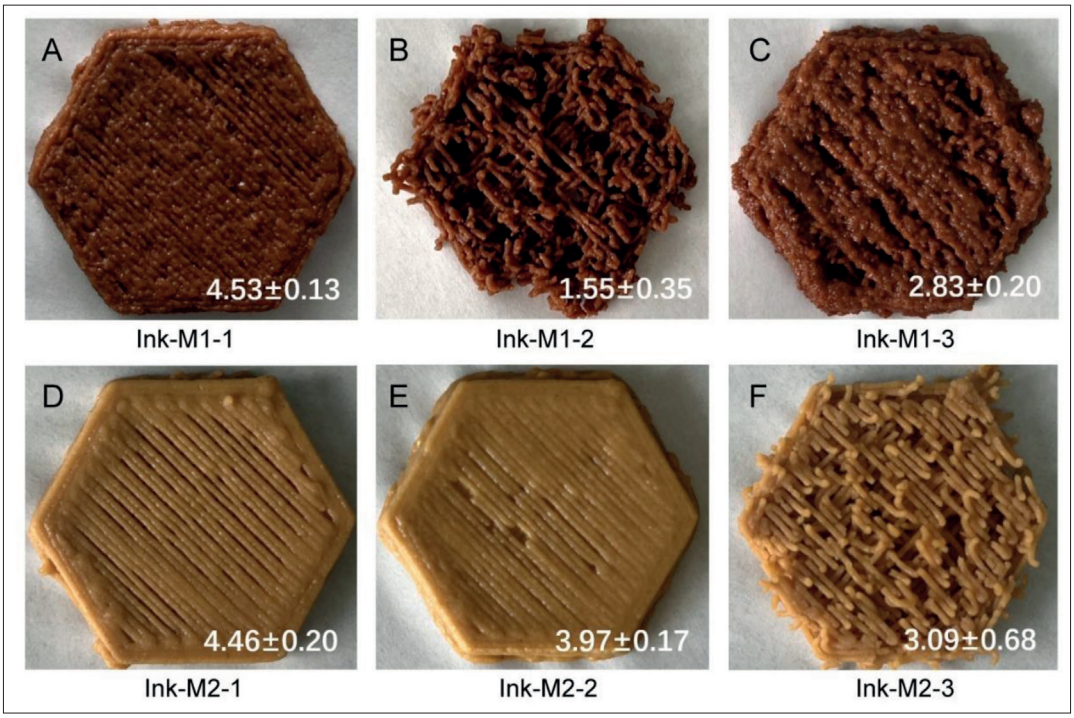

Figure 1. Hexagons 3D-printed with the six food inks using a 0.84-mm nozzle for assessing the printability.

exhibited shear-thinning behavior (Figure 2A and B). There is a significant overlap between the dynamic viscosity versus shear rate curves for the three food inks based on Material-1, with the apparent viscosity dropping from several thousands of Pa·s at a shear rate of 0.1 s^{-1} to close to 10 Pa·s at a shear rate of 100 s^{-1}. On the other hand, the apparent viscosity of the three food inks based on Material-2 exhibited distinct behavior as the shear rate increases. This change in behavior was strongly influenced by the progressive increase in water content of Ink-M2-2, Ink-M2-1, and Ink-M2-3, which has a strong impact on the apparent viscosity. At a low shear rate of 0.1 s^{-1}, the driest formulation (Ink-M2-3) exhibited an apparent viscosity of approximately 10,000 Pa·s, whereas the apparent viscosity of Ink-M2-2 was only around 450 Pa·s. Ink-M2-2-1 showed an intermediate apparent viscosity of about 3500 Pa·s at the same shear rate. As the shear rate increased, the apparent viscosity of the three inks decreased at different rates, and ultimately reached single-digit values at a shear rate of 100 s^{-1}.

The shear modulus of the three food inks based on Material-1 displayed slight differences (Figure 2C),

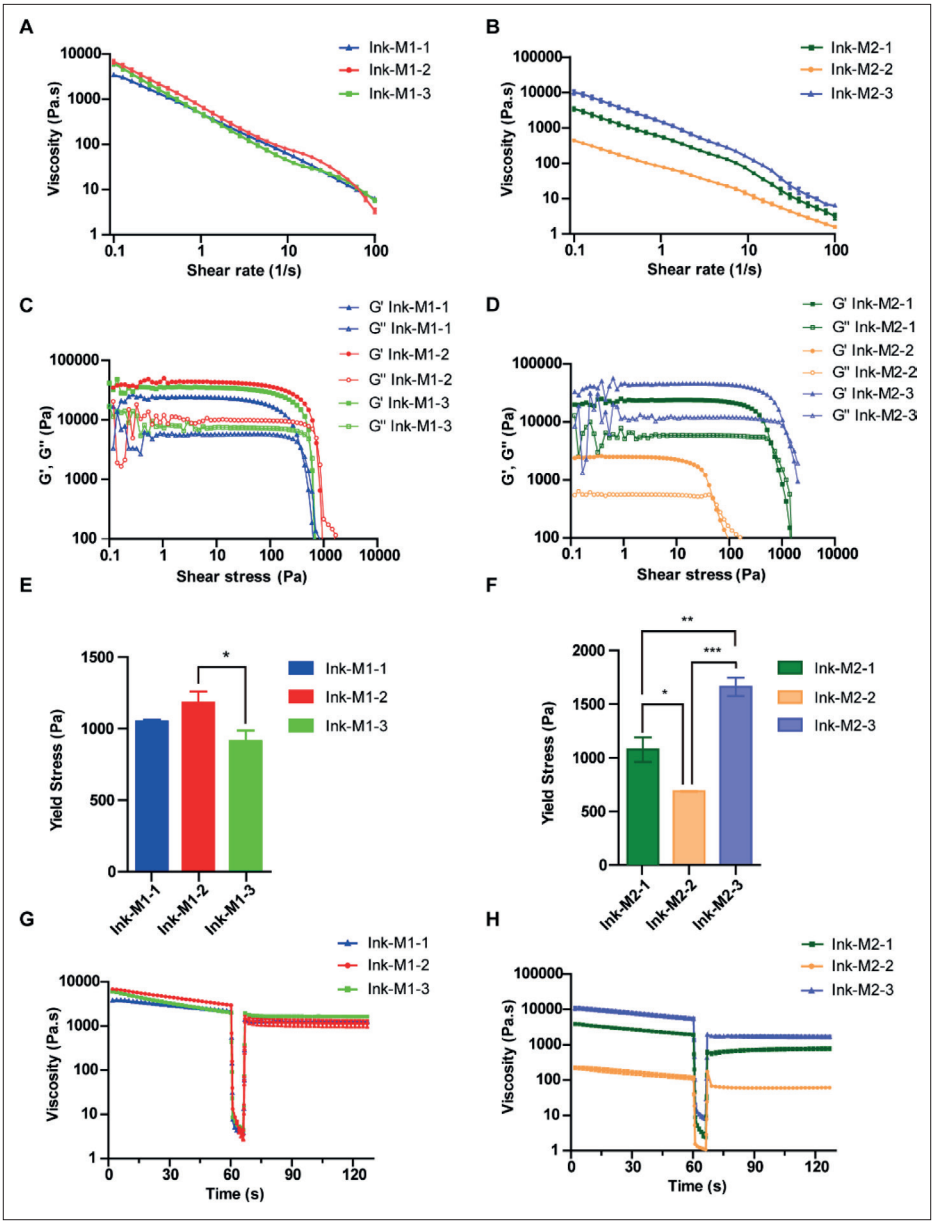

Figure 2. Rheological characteristics of food inks. (A, B) Viscosity versus shear rate for each ink. (C, D) Stress response of the inks as a function of increasing stress. (E, F) Yield stress of the food inks. (G, H) Recovery of food inks over time as measured by changes in viscosity under different shear rates. The data are based on three replicates per sample. *$p < 0.05$, **$p < 0.01$, and ***$p < 0.001$ based on ANOVA.

whereas the three inks based on Material-2 exhibited more distinct variations (Figure 2D). The elastic modulus (G') reflected the ability of the material to store energy against shear deformation, while the viscous modulus (G") characterized its liquid-like behavior, which resulted in energy loss under shear stress. The point at which the G' and G" curves intersected indicated the yield stress of the food ink. The pairwise comparison of the food inks based on Material-1 showed no significant difference in yield stress except for the comparison between Ink-M1-2 and Ink-M1-3 (Figure 2E). However, all three food inks based on Material-2 exhibited significantly different yield stress when compared pairwise (Figure 2F). These observations were consistent with the viscoelastic behaviors displayed by these inks in Figure 2A–D.

To evaluate the extrusion and self-supporting capabilities of the food inks, a thixotropy recovery experiment was conducted. It was observed that all inks exhibited a gradual decrease in viscosity at low shear rates, which aligned with the observed shear-thinning behavior in the flow ramp study (Figure 1G and H). Once the peak shear rate was reached, the apparent viscosity of the food inks drastically dropped, thereby facilitating smooth printing by enabling effortless flow of food inks from the nozzle. Following the printing process, the inks demonstrated rapid recovery of their apparent viscosity, indicating their ability to maintain the structural integrity of the printed objects. The recovery rates for ink-M1-1, ink-M1-2, and ink-M1-3 were 58.02%, 38.59%, and 81.33%, respectively. For ink-M2-1, ink-M2-2, and ink-M2-3, the recovery rates were 40.42%, 52.21%, and 30.77%.

Interestingly, it was noticed that inks with similar viscoelastic behavior did not necessarily exhibit the same level of printability, and *vice versa*. Take Ink-M1-1 and Ink-M1-2 for instance, the two food inks shared comparable apparent viscosity and shear modulus values at a given shear rate. However, their printability differed significantly, as depicted in Figure 1. On the other hand, Ink-M2-1 and Ink-M2-2 displayed similar printability, despite notable differences in apparent viscosity and yield stress.

3.2. Microstructure

In addition to the rheology, the microstructure of food inks plays an important role in their printability. Maintaining the stability of microstructural interactions over a wide frequency range is believed to lead to improved printability.[43] The scanning electron micrographs of all six food inks are depicted in Figure 3A and B. A pronounced fibrous network was observed in Ink-M1-1 (Figure 3A), which had the highest XG content among the three inks based on Material-1. The fibrous network, which is a characteristic microstructure[18] of food inks reinforced with XG, plays a significant role in forming a gel-like matrix. This dense and irregular structural network enhances the mechanical strength of starch-containing gels,[44] providing them with the necessary mechanical stability. In contrast, Ink-M1-3, which did not contain any food hydrocolloids (i.e., XG), displayed numerous micropores of varying sizes in its microstructure, and a high degree of porosity destabilizes the 3D-printed product, leading to deformation and diminished precision.[45] Unlike the densely packed pores formed by starch which enhances the mechanical strength of the food material,[46] the pores in Ink-M1-3 are randomly positioned and loosely packed, bearing a resemblance to a piece of wood damaged by worms. The presence of this type of micropores results in weak support, negatively impacting the printability of the ink. Ink-M1-2 contains a small amount of XG, resulting in the formation of a feeble gel system with a more compact structure.

The microstructure of the three inks based on Material-2 exhibited typical granular structures of milk powder (Figure 3B). As the water content of Ink-M2-2, Ink-M2-1, and Ink-M2-3 gradually decreased, the microstructure of the food ink became progressively more compact, with ink-M2-1 exhibiting a highest degree of porosity and ink-M2-3 showing almost no discernible pores. Notably, Ink-M2-2 displayed a prominent presence of stomata, primarily in the form of lamellar and filamentous structures. This presence of stomata was likely attributed to the gelation of starch when the water content became sufficiently high.[47]

The texture profiles of all six inks are presented in Table 2. The normalized values are presented in Figure 4A, and the original values are presented in **Figure S1** in Supplementary File. The addition of XG to Material-1 resulted in a significant increase in hardness, a key parameter reflecting the potential irritation to the oral mucosa. In the case of the food inks based on Material-2, hardness increased as the moisture content decreased. Specifically, a 15% difference in moisture content led to an approximately 7.3-fold difference in hardness, while a 5% difference led to approximately 2.1-fold difference in hardness. Cohesiveness, which indicated the energy or the number of chewing times required to break down the food until it became palatable and swallowable, and gumminess, which referred to the energy needed to chew a semi-solid food until it was swallowable, followed the same trend as hardness. The chewiness of the three inks based on Material-1 was similar, while the chewiness of the three inks based on Material-2 increased with decreasing water content. Adhesiveness and springiness did not show any significant difference.

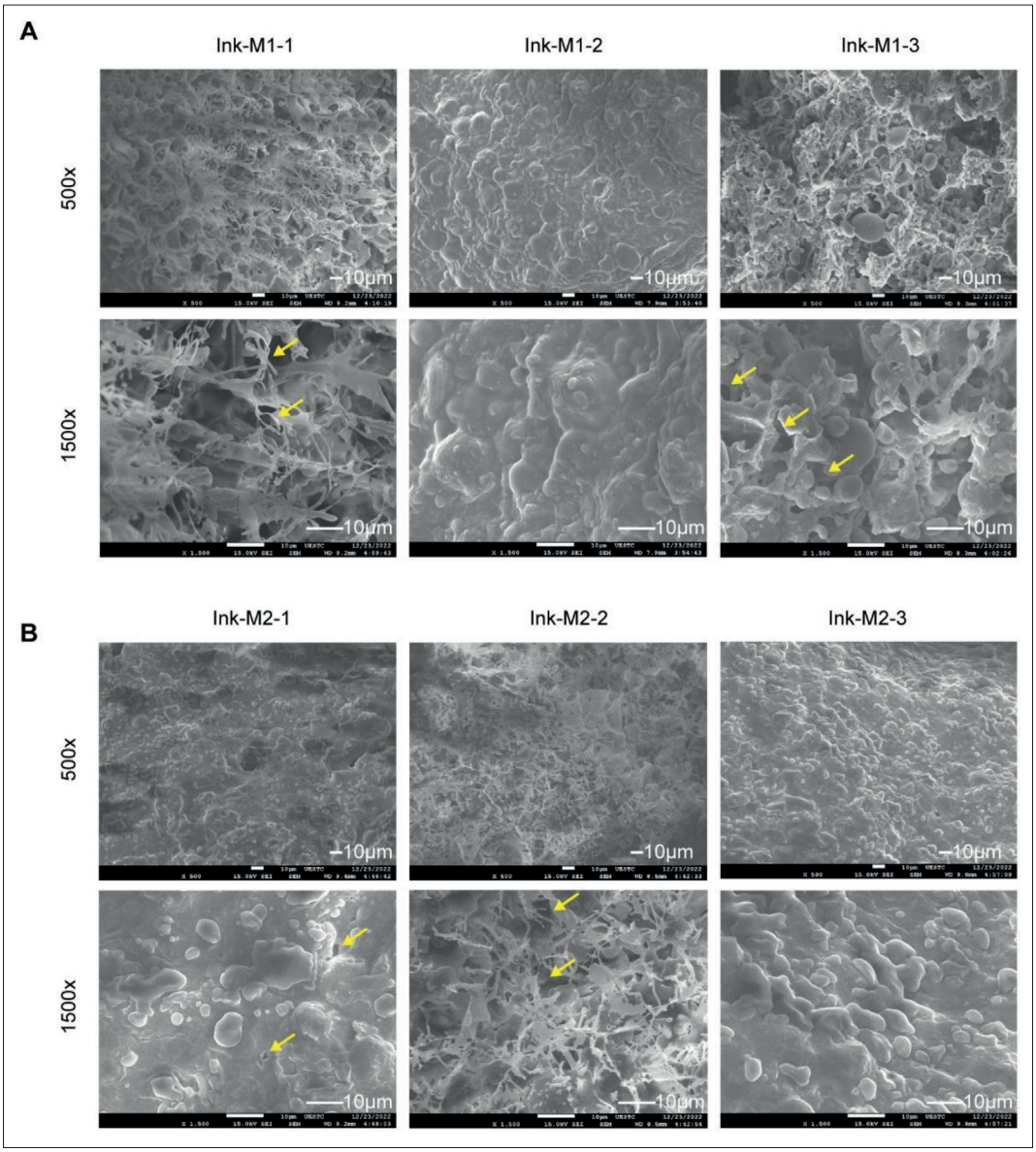

Figure 3. Microstructure of the six food inks at 500× and 1500× magnifications. (A) Ink-M1; (B) Ink-M2.

3.3. Textural analysis

Universal Design Foods (UDF) concept introduced in previous research[48,49] categorizes foods into four groups based on their texture and ease of chewing, as proposed by the Japan Care Food Conference. According to their texture, foods are classified into stage 1 (thin gruel, hardness of 5×10^3 N/m^2), stage 2 (gruel, hardness of 2×10^4 N/m^2), stage 3 (soft-boiled, hardness of 5×10^4 N/m^2), and stage 4 (boiled, hardness of 5×10^5 N/m^2).[50] Based on the literature, the pain threshold of oral ulcer is significantly varied due to the different measurement methods used, lesion severity, lesion location, lesion nature, age of patient, and individual variability. Reported pain thresholds in terms of pressure range from 6.5–7.5 $\times 10^3$ N/m^2 [51] to 11.7–24.2 $\times 10^4$ N/m^2.[52] It is worth noting that the hardness of the optimal inks is 1.89–3.80 N, which corresponds to 1.89–3.80 $\times 10^4$ N/m^2 for the $1 \times 1 \times 1$ cm^3 specimen. Therefore, the 3D-printed food developed in this study causes minimal irritation to patients with diabetic oral ulcers.

The texture profile analysis provides an accurate and quantitative assessment of texture of 3D-printed food items. However, the test is relatively time-consuming and resource-demanding. In comparison, IDDSI tests provide a framework for rapid, convenient, qualitative, and intuitive assessment of food texture. Although the IDDSI framework is developed to evaluate whether the food items

Table 2. Hardness, springiness, cohesiveness, gumminess, chewiness, and adhesiveness of the six food inks

	Hardness (*N*)	Springiness (mm)	Cohesiveness	Gumminess (*N*)	Chewiness (*N*)	Adhesiveness (gf/s)
Ink-M1-1	3.80 ± 0.49	0.15 ± 0.01	0.20 ± 0.00	0.78 ± 0.10	0.11 ± 0.02	-19.79 ± 1.22
Ink-M1-2	4.00 ± 0.14	0.14 ± 0.01	0.20 ± 0.01	0.79 ± 0.02	0.11 ± 0.01	-18.03 ± 0.53
Ink-M1-3	2.64 ± 0.22	0.13 ± 0.00	0.19 ± 0.01	0.49 ± 0.03	0.07 ± 0.01	-18.19 ± 0.68
Ink-M2-1	1.89 ± 0.16	0.12 ± 0.02	0.19 ± 0.01	0.36 ± 0.03	0.04 ± 0.01	-17.65 ± 1.20
Ink-M2-2	0.54 ± 0.03	0.09 ± 0.01	0.18 ± 0.02	0.10 ± 0.01	0.01 ± 0.00	-17.11 ± 1.14
Ink-M2-3	3.99 ± 0.18	0.13 ± 0.00	0.20 ± 0.01	0.80 ± 0.03	0.10 ± 0.00	-18.63 ± 0.57

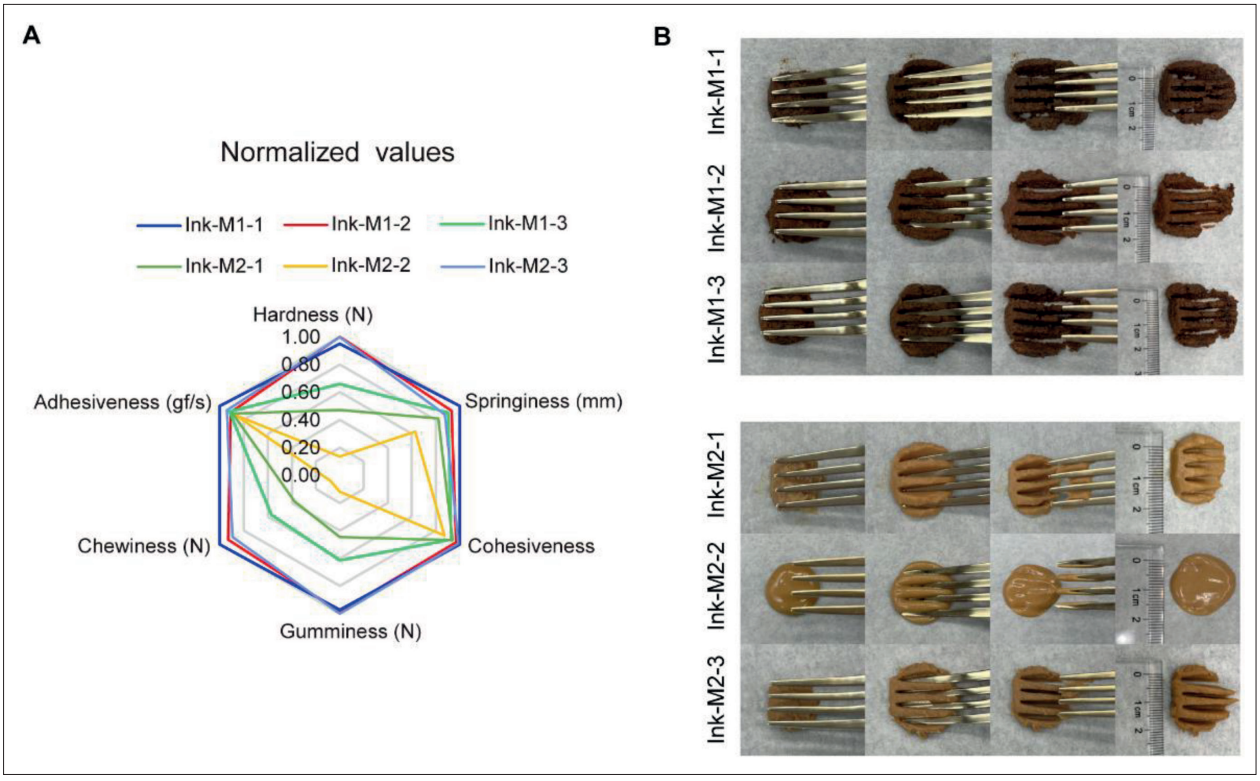

Figure 4. Texture profile analysis of the food inks. (A) Texture profile of the food inks. The values are normalized to the highest value and expressed between 0 and 1. (B) Fork pressure tests of food samples 3D-printed with the six food inks.

are suitable for patients with dysphagia, we believe that the same concept can be adopted to evaluate the suitability of food items for patients with oral ulcer by correlating the quantitative texture analysis with IDDSI tests.

In the fork pressure test, as depicted in Figure 4B, all inks exhibited a smooth texture with almost no lump or granulation. The fork prongs left a distinct pattern on the surface, and all the food inks except Ink-M2-2 retained the indentation from the fork, suggesting these food inks belong to IDDSI Level 5 (minced and moist). Based on the measured hardness of these food inks, it is concluded that foods in IDDSI Level 5 (at ~17 kPa) are soft and suitable for patients with oral ulcers.[53] In comparison, Ink-M2-2 could not retain the indentation from the fork and hence align with IDDSI Level 3 (liquidized/moderately thick food), indicating that IDDSI Level 3 foods are also soft enough for patients with oral ulcers.

Furthermore, the food ingredients, such as *Russula* mushroom and milk powder, are rich in vitamin B[15,54,55] and are believed to possess the capacity to accelerate the healing of oral ulcers.

3.4. FT-IR of food inks

Figure S2A (Supplementary File) depicts the infrared spectrum of the six ink formulations, and **Figure S2B** (Supplementary File) presents the infrared spectrum of

the five raw ingredients. FT-IR analysis provides insight into the micro-molecular interactions of the materials. Between the two groups of inks based on Material-1 and Material-2, the most notable difference is observed in the absorption peak at ~1700 cm^{-1} which corresponds to the C=O stretching of the amide bond. This difference is attributed to the presence of protein-rich milk powder in Material-1. In addition, the peaks for C-H stretching at around 2800 cm^{-1} are more prominent in inks based on Material-1 compared to those based on Material-2. This disparity can be attributed to Material-2, which contains a larger amount of carbohydrates that are rich in OH. The broad OH stretching peak at 3200–3550 cm^{-1} overshadows the C-H peaks. The FT-IR spectra of each individual component are shown in **Figure S2** (Supplementary File). No significant difference was observed between the ink formulation and individual components, indicating a low likelihood of the XG forming new chemical bonds with the food base.

3.5. Regulation of blood glucose by food inks

To evaluate the ability of the 3D-printed food in blood glucose regulation, we performed experiments on male rats aged 8–10 weeks which were induced to develop diabetes via intraperitoneal injection of STZ (Figure 5A). The food ink, obtained by mixing equal mass of Ink-M1-1 and Ink-M2-1, was administered via gavage after an overnight fasting period. In addition to the food ink group, a high-glycemic-index (high GI) group fed with rice powder and a low-glycemic-index (low GI) group fed with vegetable powder (as controls) were included. The blood glucose levels at different time points following gavage were measured (Figure 5B).

The blood glucose levels in diabetic rats following overnight fasting were consistent. After gavage with equal mass of each type of food, the blood glucose level rose in all three groups and peaked at 60 min post-ingestion, after which the blood glucose level declined (Figure 5B). The peak glucose level of the food ink group was significantly

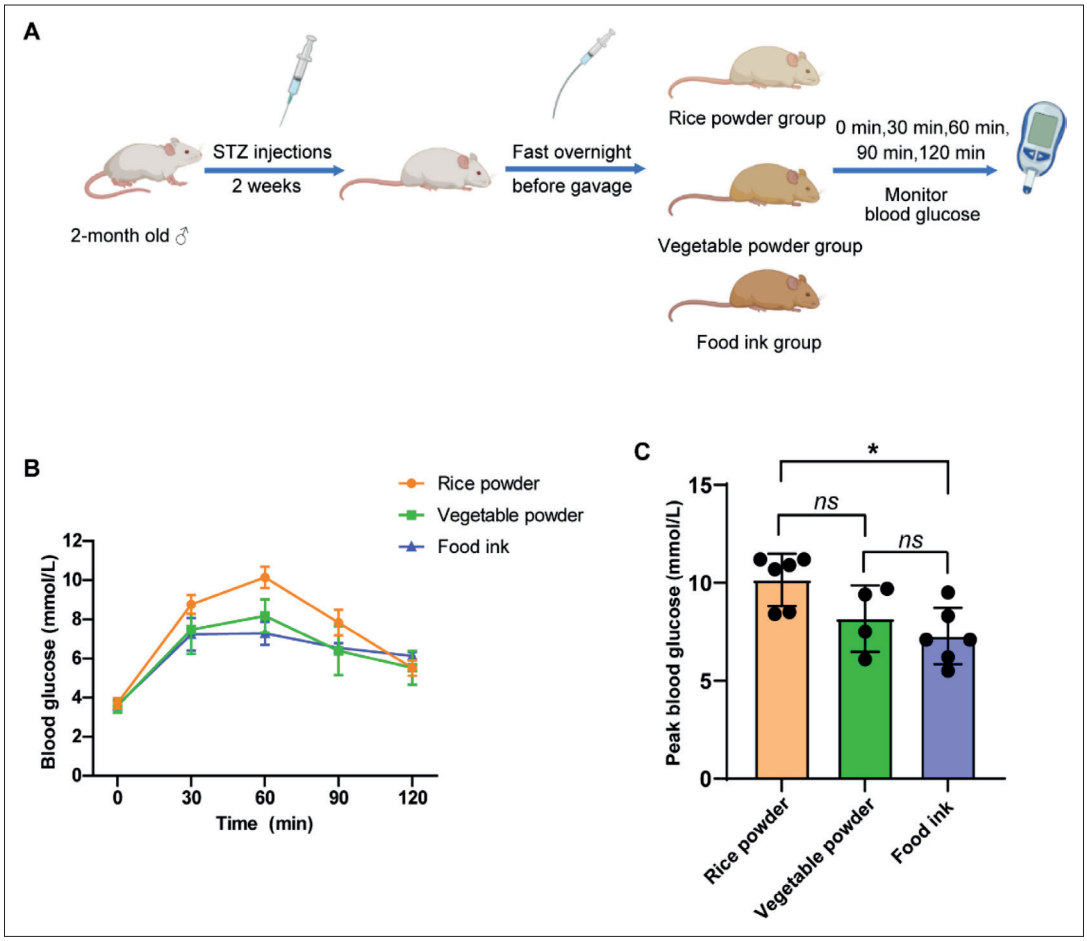

Figure 5. Animal experiments. (A) Schematic illustration of the experiment design. (B) Blood glucose of mice fed with equal mass of rice powder, vegetable powder, and food ink at different time points. (C) Peak blood glucose values in the three groups. *$p < 0.05$ based on ANOVA.

lower ($p < 0.05$) than that of the high GI (rice powder) group (Figure 5C) and showed no significant difference compared to the low GI (vegetable powder) group, suggesting that the 3D food ink is suitable to be used as diabetic diet. The glucose AUC, which is a useful index for evaluating the glucose loading for a specific duration after food ingestion, showed no difference among the three groups (**Figure S3** in Supplementary File).

In another set of experiments, the three groups were fed with each type of food containing equal amount of total carbohydrates, calculated based on the nutritional values on the food label or reported in literature (**Table S3** in Supplementary File). In the case of equal-carbohydrates intake, the glucose AUC of the food ink showed no significant difference compared to that of the rice powder but was larger than that of the vegetable powder (**Figure S4A** and **S4B** in Supplementary File). This difference may be attributed to the 1.51-fold mass increase of the food ink over the rice flour group and a 1.3-fold increase over the vegetable group. Although the total carbohydrate was kept equal in all three groups, the food ink group had a substantially higher total fat content due to the inclusion of milk powder. It has been reported that foods rich in fat may reduce insulin sensitivity and adversely influence glucose metabolism.[56] Although the glucose AUC of the food ink group and the rice powder group shows no statistical difference, the carbohydrate content and the glycemic loading per unit mass in the food ink are significantly lower, which is more well-suited for the glycemic control for patients suffering from diabetes. Therefore, we decided to formulate 3D-printed food items for personalized nutrition based on total mass instead of total carbohydrates in subsequent studies. The peak glucose level (**Figure S4C** in Supplementary File) showed a trend similar to the AUC in the equal-carbohydrate case. The lower blood glucose levels were primarily attributed to the food's formation rather than the 3D printing process. The purpose of 3D printing is twofold. First, 3D food printing is employed to create visually pleasant food items using functional food compositions to control blood glucose levels. Second, 3D food printing can personalize foods, which are tailored to the nutritional needs of patients suffering from diabetes and its complications.

3.6. Achieving personalized nutrition for patients with diabetic complications by 3D food printing

In this study, several dragon-boat-festival-themed items, including dragon boats with a mass of 9.03 g (Figure 6A), arch bridges with a mass of 10.65 g (Figure 6B), bowls with a mass of 3.49 g (Figure 6C), and stuffed *zongzi* (a type of rice dumpling for the dragon boat festival) with a mass of 9.52 g (Figure 6D), were created by collaborative 3D

Figure 6. Food items 3D-printed with Ink-M1-1 and Ink-M2-1. (All items, except for the leave, peddle, and water and quinoa in the bowl, are 3D-printed.) (A) Dragon boat. (B) Arch bridge. (C) Bowl. (D) *Zongzi* (rice dumpling) with filling. (E) A food platter adorned with 3D-printed food items based on the theme of dragon boat festival, a traditional Chinese festival. (F) Dragon boats with various ratios of Ink-M1-1 and Ink-M2-1.

printing of Ink-M1-1 and Ink-M2-1, which are printability-optimized food ink formulation in their respective group, using a dual-nozzle direct ink writing (DIW) printer. All items were plated and served as they were printed (Figure 6E). Each item could be arbitrarily divided into different portions as desired in order to personalize nutritional compositions according to the dietary requirements of diabetic patients with complications.

The focus of 3D food printing has undergone a significant transformation from merely enhancing the visual appeal to controlling and personalizing the nutritional composition of food.[57] Through multi-component collaborative 3D food printing, macro- and micro-nutrients in food items can be tuned to suit individual dietary needs. By slicing the same 3D model into different proportions, the nutrient content can be varied, thereby enabling digital manufacturing of 3D-printed food for achieving personalized nutrition. As shown in Figure 6E, the dragon boat was 3D-printed with Ink-M1-1 and Ink-M2-1 at various ratios. The last figure in the name of each type of dragon boat represents the percentage of Ink-M1-1 in the food item. For instance, the dragon boat labeled as Ink-M1-1-49.0 comprises 49% Ink-M1-1 and 51% Ink-M2-1 by weight. The macronutrient and calorie content of 100 g of the 3D-printed food with various percentage of Ink-M1-1 are shown in Table 3. The macronutrient content of each dragon boat was calculated and listed in **Table S4** (Supplementary File) based on a total weight of 8.2–9.1 g. The difference in weight primarily resulted from the density difference between the two food inks. Notably, the protein content almost doubled as the proportion of Ink-M1-1 changed from 100% to 0%. Meanwhile, the fat content increased by almost 6-folds. However, the content of total carbohydrates showed a declining trend as the proportion of Ink-M1-1 reduced.

Whole milk powder is a significant protein source in daily diets and a major contributor to the production of endogenous advanced glycosylation end-products (AGEs). Excessive endogenous AGEs can increase the risk of conditions such as type 2 diabetes and CKD.[58] CKD affects 30% of patients with type 1 diabetes and 40% of those with type 2 diabetes.[7] A low-protein diet reduces intraglomerular pressure by decreasing afferent arteriolar vasoconstriction, thereby mitigating glomerular hyperfiltration and delaying the progression of CKD toward kidney failure.[59] This study demonstrated that the protein content of food can be tailored to meet the specific DPI needs of patients afflicted with diabetes-induced CKD. For instance, a typical 80 kg adult requires a DPI ranging from 0.8 to 1.3 g/kg of body weight, which translates to 64 to 104 g of protein per day. In contrast, diabetic patients with stage 3–5 CKD are advised to adjust their DPI to 0.6–0.8 g/kg of the body weight per day,[60] amounting to 48 to 64 g of protein for an 80 kg CKD patient. For illustration, individuals without CKD would require approximately 470–760 g of the food item Ink-M1-1-49.0 per day, while CKD patients would have to reduce their food intake to 350–470 g to comply by the DPI requirements if they choose the same food item. Alternatively, CKD patients may opt for 500–670 g of the food item, i.e., Ink-M1-1-100, which offers a lower protein content per unit weight. Among these two food inks, which have similar protein content, Ink-M1-1-100 contains higher carbohydrate and caloric content than Ink-M1-1-49.0, but its fat content is significantly lower. Thus, patients are free to select the food ink that aligns with their unique nutritional and health requirements.

Meanwhile, diabetic patients are at a higher risk of developing oral ulcers compared with the general population. Patients suffering from oral ulcers often opt for liquid or soft foods to avoid the discomfort caused by chewing and swallowing. However, such foods may lack appeal in terms of appearance and texture, which can lead to food refusal and malnutrition.[61,62] Currently, texture-modified food is mainly aimed at elderly patients with dysphagia. Based on international data, the prevalence of oropharyngeal dysphagia in the general population ranges from 2.3% to 16.0%.[63] In contrast, oral ulcers affect up to 25% of the global population.[64] In spite of the high demand

Table 3. Macronutrient and calorie content of 100 g of food 3D-printed with various proportions of Ink-M1-1

	Carbohydrate (g)	Protein (g)	Fat (g)	Energy (kJ)
Ink-M1-1-100	25.88	9.59	1.55	659.93
Ink-M1-1-90.2	25.33	10.37	2.24	689.43
Ink-M1-1-75.2	24.49	11.55	3.29	734.31
Ink-M1-1-49.0	23.01	13.63	5.15	813.09
Ink-M1-1-30.6	21.97	15.09	6.44	868.30
Ink-M1-1-9.8	20.79	16.74	7.91	930.80
Ink-M1-1-0	20.24	17.52	8.61	960.30

spurred by the high prevalence of oral ulcers, to the best of our knowledge, no 3D-printed functional food has been developed prior to this study for patients suffering from this condition.

4. Conclusion

In conclusion, this study presents a novel approach to developing personalized foods for diabetic patients by utilizing 3D printing technology, specifically targeting individuals with complications such as CKD and oral ulcers. By formulating 3D-printable food inks using natural ingredients known for their oral health and diabetes management benefits, customized diets can be created to meet the specific nutritional requirements of these patients.

The rheological properties, textures, microstructures, and composition of the food inks are comprehensively characterized for assessing their suitability for 3D food printing applications. The utilization of dual-nozzle collaborative 3D printing technology allows for precise regulation of the nutritional composition, which helps control protein intake by patients with CKD. Findings from animal experiments confirm the effectiveness of the 3D-printed diet in glycemic control, showcasing the potential of this approach in managing blood glucose levels.

This research highlights the transformative potential of 3D food printing technology in the field of personalized nutrition, offering tailored food options that enhance the quality of life and health outcomes of patients with diabetes and its complications. By combining the benefits of personalized nutrition, improved texture, and targeted functional ingredients, 3D-printed foods have the potential to revolutionize dietary management strategies for individuals with specific dietary requirements.

One major limitation of this study is that we were unable to take into account the pain threshold pressure caused by oral ulcer in designing the food ink due to the lack of relevant literature. Therefore, we can only rely on the pain threshold pressure of diseases of similar nature described in existing literature as a reference. Future studies should be designed to evaluate the pain threshold by means of animal experiments. However, this presents several challenges, such as how to assess pain in the animal model and the potential disparity of pain thresholds between humans and the animal models. Future studies should also explore the optimization of 3D printing parameters, investigate additional functional ingredients, and evaluate the long-term effects of personalized 3D-printed diets on the health and well-being of diabetic patients through clinical trials. With continued advancements in 3D printing technology and a deeper understanding of nutritional science, this innovative approach has the potential to reshape the future of dietary management, ultimately improving the overall health outcomes and quality of life for individuals with diabetes and other chronic conditions.

Acknowledgments

None.

Funding

This work was supported by the National Natural Science Foundation of China (No. 62271107 and 62074029), the National Key Research and Development Program of China (No. 2022YFB3206100), and Key R&D Program of Sichuan Province (No. 2022JDTD0020).

Conflict of interest

The authors declare no conflicts of interest.

Author contributions

Conceptualization: Yi Zhang, Yuanyuan Chen, Jun Gu, Tingting Dai
Data curation: Yuanyuan Chen, Siwei Bi, Ruiqi Liu
Funding acquisition: Xiaosheng Zhang, Yi Zhang
Investigation: Yuanyuan Chen, Siwei Bi,
Methodology: Yuanyuan Chen, Siwei Bi, Jun, Gu, Dongan Wang, Yi Zhang
Project administration: Qianli Che, Wei Li
Writing – original draft: Yuanyuan Chen
Writing – review & editing: Yi Zhang, Siwei Bi, Jun Gu, Dongan Wang, Tingting Dai

Ethics approval and consent to participate

All animal experiments in this study were approved by the Institutional Animal Care and Use Committee of China West Hospital, Sichuan University (No. 20221201007).

Consent for publication

Not applicable.

Availability of data

The data that support the findings of this study are available from the corresponding author upon reasonable request.

Reference

1. American Diabetes Association. Diagnosis and classification of diabetes mellitus. *Diabetes Care.* 2014;37(Supplement_1):S81-S90. doi: 10.2337/dc14-S081

2. Lin X, Xu Y, Pan X, et al. Global, regional, and national burden and trend of diabetes in 195 countries and territories: an analysis from 1990 to 2025. *Sci Rep*. 2020;10(1):14790. doi: 10.1038/s41598-020-71908-9

3. American Diabetes Association. Diagnosis and classification of diabetes mellitus. *Diabetes Care*. 2013;36(Suppl 1): S67-S74. doi: 10.2337/dc13-S067

4. Camelon KM, Hadell K, Jamsen PT, et al. The plate model: a visual method of teaching meal planning. *J Am Diet Assoc*. 1998;98(10):1155-1158. doi: 10.1016/s0002-8223(98)00267-3

5. Zhang Y, Han H, Chu L. Effectiveness of restricted diet with a plate in patients with type 2 diabetes: a randomized controlled trial. *Prim Care Diabetes*. 2022;16(3):368-374. doi: 10.1016/j.pcd.2022.03.007

6. Forouhi NG, Misra A, Mohan V, Taylor R, Yancy W. Dietary and nutritional approaches for prevention and management of type 2 diabetes. *BMJ*. 2018;361:k2234. doi: 10.1136/bmj.k2234

7. Rhee CM, Kalantar-Zadeh K, Moore LW. Medical nutrition therapy for diabetic kidney disease. *J Ren Nutr*. 2021;31(3):229-232. doi: 10.1053/j.jrn.2021.03.004

8. Kitada M, Ogura Y, Monno I, Koya D. A low-protein diet for diabetic kidney disease: its effect and molecular mechanism, an approach from animal studies. *Nutrients*. 2018;10(5):544. doi: 10.3390/nu10050544

9. Dudding T, Haworth S, Lind PA, et al. Genome wide analysis for mouth ulcers identifies associations at immune regulatory loci. *Nat Commun*. 2019;10(1):1052. doi: 10.1038/s41467-019-08923-6

10. Mauri-Obradors E, Estrugo-Devesa A, Jane-Salas E, Viñas M, López-López J. Oral manifestations of diabetes mellitus. A systematic review. *Med Oral Patol Oral Cir Bucal*. 2017;*22*(5):e586-e594. doi: 10.4317/medoral.21655

11. Mohsin SF, Ahmed SA, Fawwad A, Basit A. Prevalence of oral mucosal alterations in type 2 diabetes mellitus patients attending a diabetic center. *Pak J Med Sci*. 2014;30(4): 716-719. doi 10.12669/pjms.304.5220

12. Zeng X, Jin X, Zhong L, et al. Difficult and complicated oral ulceration: an expert consensus guideline for diagnosis. *Int J Oral Sci*. 2022;14(1):28. doi: 10.1038/s41368-022-00178-0

13. Slebioda Z, Szponar E, Kowalska A. Etiopathogenesis of recurrent aphthous stomatitis and the role of immunologic aspects: literature review. *Arch Immunol Ther Exp*. 2014;62(3):205-215. doi: 10.1007/s00005-013-0261-y

14. González-Serrano J, Serrano J, López-Pintor RM, et al. Prevalence of oral mucosal disorders in diabetes mellitus patients compared with a control group. *J Diabetes Res*. 2016;2016:5048967. doi: 10.1155/2016/5048967

15. Gu Y, Huang Y, Qiu Z, et al. Vitamin B(2) functionalized iron oxide nanozymes for mouth ulcer healing. *Sci China Life Sci*. 2020;63(1):68-79. doi: 10.1007/s11427-019-9590-6

16. Kewuyemi YO, Kesa H, Meijboom R, Alimi OA, Adebo OA. 3D food printing improves color profile and structural properties of the derived novel whole-grain sourdough and malt biscuits. *Sci Rep*. 2022;12(1):12347. doi: 10.1038/s41598-022-16659-5

17. Pattarapon P, Zhang M, Mujumdar AS. Application potential of 3D food printing to improve the oral intake for immunocompromised patients: a review. *Food Res Int*. 2022;160:111616. doi: 10.1016/j.foodres.2022.111616

18. Pant A, Lee AY, Karyappa R, et al. 3D food printing of fresh vegetables using food hydrocolloids for dysphagic patients. *Food Hydrocolloids*. 2021;114:106546. doi: 10.1016/j.foodhyd.2020.106546

19. de Souza Paglarini C, de Figueiredo Furtado G, Biachi JP, et al. Functional emulsion gels with potential application in meat products. *J Food Eng*. 2018;222:29-37. doi: 10.1016/j.jfoodeng.2017.10.026

20. Severini C, Azzollini D, Albenzio M, Derossi A. On printability, quality and nutritional properties of 3D printed cereal based snacks enriched with edible insects. *Food Res Int*. 2018;106:666-676. doi: 10.1016/j.foodres.2018.01.034

21. Zhang Y, Lee AY, Pojchanun K, et al. Systematic engineering approach for optimization of multi-component alternative protein-fortified 3D printing food Ink. *Food Hydrocolloids*. 2022;131:107803. doi: 10.1016/j.foodhyd.2022.107803

22. Dong L, Li Y, Chen Q, et al. Cereal polyphenols inhibition mechanisms on advanced glycation end products and regulation on type 2 diabetes. *Crit Rev Food Sci Nutr*. 2023;1-19. doi: 10.1080/10408398.2023.2213768

23. Katileviciute A, Plakys G, Budreviciute A, Onder K, Damiati S, Kodzius R. A sight to wheat bran: high value-added products. *Biomolecules*. 2019;9(12):887. doi: 10.3390/biom9120887

24. Li X-X, Zhang X-X, Zhang R, et al. Gut modulation based anti-diabetic effects of carboxymethylated wheat bran dietary fiber in high-fat diet/streptozotocin-induced diabetic mice and their potential mechanisms. *Food Chem Toxicol*. 2021;152:112235. doi: 10.1016/j.fct.2021.112235

25. Stevenson L, Phillips F, O'Sullivan K, Walton J. Wheat bran: its composition and benefits to health, a European perspective. *Int J Food Sci Nutr*. 2012;63(8):1001-1013. doi: 10.3109/09637486.2012.687366

26. Clarke J, Butler R, Howarth G, Read L, Regester G. Exposure of oral mucosa to bioactive milk factors reduces severity of chemotherapy-induced mucositis in the hamster. *Oral Oncol*. 2002;38(5):478-485. doi: 10.1016/s1368-8375(01)00107-5

27. Sanka K, Munjulury VS, Mohd AB, Diwan PV. Enhancement of solubility, dissolution release profile and reduction in ulcerogenicity of piroxicam by inclusion complex with skimmed milk. *Drug Deliv*. 2014;21(7):560-570. doi: 10.3109/10717544.2013.856964

28. Sharifi-Rad J, Butnariu M, Ezzat SM, et al. Mushrooms-rich preparations on wound healing: from nutritional to medicinal attributes. *Front Pharmacol*. 2020;11:567518. doi: 10.3389/fphar.2020.567518

29. Mao Y, Mao J, Meng X. Extraction optimization and bioactivity of exopolysaccharides from Agaricus bisporus. *Carbohydr Polym*. 2013;92(2):1602-1607. doi: 10.1016/j.carbpol.2012.11.017

30. Khursheed R, Singh SK, Wadhwa S, Gulati M, Awasthi A. Therapeutic potential of mushrooms in diabetes mellitus: role of polysaccharides. *Int J Biol Macromol*. 2020;164: 1194-1205. doi: 10.1016/j.ijbiomac.2020.07.145

31. Dragsted LO. Mushrooms and health. *Am J Clin Nutr*. 2019;110(3):546-547. doi: 10.1093/ajcn/nqz096

32. Shamim MZ, Mishra AK, Kausar T, et al. Exploring edible mushrooms for diabetes: unveiling their role in prevention and treatment. *Molecules*. 2023;28(6). doi: 10.3390/molecules28062837

33. Jiali L, Wu Z, Liu L, et al. The research advance of resistant starch: structural characteristics, modification method, immunomodulatory function, and its delivery systems application. *Crit Rev Food Sci Nutr*. 2023;1-18. doi: 10.1080/10408398.2023.2230287

34. Pant A, Lee AY, Karyappa R, et al. 3D food printing of fresh vegetables using food hydrocolloids for dysphagic patients. *Food Hydrocolloids*. 2021;114:106546. doi: 10.1016/j.foodhyd.2020.106546

35. Lee AY, Pant A, Pojchanun K, et al. Three-dimensional printing of food foams stabilized by hydrocolloids for hydration in dysphagia. *Int J Bioprint*. 2021;7(4):393. doi: 10.18063/ijb.v7i4.393

36. Cichero JA, Lam PT, Chen J, et al. Release of updated international dysphagia diet standardisation initiative framework (IDDSI 2.0). *J Texture Stud*. 2020;51(1):195-196. doi: 10.1111/jtxs.12481

37. Wang Z, Yang Y, Xiang X, Zhu Y, Men J, He M. Estimation of the normal range of blood glucose in rats. *Wei Sheng Yan Jiu*. 2010;39(2):133-137, 142. doi: 10.19813/j.cnki.weishengyanjiu.2010.02.002

38. Liu Z, Bhandari B, Guo C, et al. 3D printing of shiitake mushroom incorporated with gums as dysphagia diet. *Foods*. 2021;10(9). doi: 10.3390/foods10092189

39. Sworn G. Xanthan gum. In: Phillips GO, Williams PA, eds. *Handbook of Hydrocolloids*. 3rd ed. Cambridge, UK:Woodhead Publishing; 2021:833-853. doi: 10.1533/9781845695873.829

40. Habibi H, Khosravi-Darani K. Effective variables on production and structure of xanthan gum and its food applications: a review. *Biocatal Agric Biotechnol*. 2017;10:130-140. doi: 10.1016/j.bcab.2017.02.013

41. Lee C P, Karyappa R, Hashimoto M. 3D printing of milk-based product. *RSC Adv*. 2020;10(50):29821-29828. doi: 10.1039/d0ra05035k

42. Li G, Hu L, Liu J, et al. A review on 3D printable food materials: types and development trends. *Int J Food Sci Technol*. 2022;57(1):164-172. doi: 10.1111/ijfs.15391

43. Nadernezhad A, Groll J. Machine learning reveals a general understanding of printability in formulations based on rheology additives. *Adv Sci*. 2022;9(29):e2202638. doi: 10.1002/advs.202202638

44. Zeng X, Chen H, Chen L, Zheng B. Insights into the relationship between structure and rheological properties of starch gels in hot-extrusion 3D printing. *Food Chem*. 2021;342:128362. doi: 10.1016/j.foodchem.2020.128362

45. Liu Z, Bhandari BR, Prakash S, Mantihal S, Zhang M. Linking rheology and printability of a multicomponent gel system of carrageenan-xanthan-starch in extrusion based additive manufacturing. *Food Hydrocolloids*. 2019;87:413-424. doi: 10.1016/j.foodhyd.2018.08.026.

46. Wu H, Sang S, Weng P, et al. Structural, rheological, and gelling characteristics of starch-based materials in context to 3D food printing applications in precision nutrition. *Compr Rev Food Sci Food Saf*. 2023;22(6):4217-4241. doi: 10.1111/1541-4337.13217

47. Sciarini LS, Rolland-Sabaté A, Guilois S, Decaen P, Leroy E, Le Bail P. Understanding the destructuration of starch in water–ionic liquid mixtures. *Green Chem*. 2015;17(1): 291-299. doi: 10.1039/C4GC01248H

48. Chao C, Hwang JS, Kim IW, Choi RY, Kim HW, Park HY. Coaxial 3D printing of chicken surimi incorporated with mealworm protein isolate as texture-modified food for the elderly. *J Food Eng*. 2022;333:111151. doi: 10.1016/j.jfoodeng.2022.111151

49. Jeong S, Kim H, Lee S. Rheology-based classification of foods for the elderly by machine learning analysis. *Appl Sci*. 2021;11(5):2262.
doi: 10.3390/app11052262

50. Kang AJ, Kim DK, Kang SH, Seo KM, Park HS, Park K-H. EMG activity of masseter muscles in the elderly according to rheological properties of solid food. *Ann Rehabil Med*. 2016;40(3):447-456.
doi: 10.5535/arm.2016.40.3.447

51. List T, Mojir K, Svensson P, Pigg M. A new protocol to evaluate the effect of topical anesthesia. *Anesth Prog*. 2014;61(4):135-144.
doi: 10.2344/0003-3006-61.4.135

52. Ogawa T, Tanaka M, Ogimoto T, Okushi N, Koyano K, Takeuchi K. Mapping, profiling and clustering of pressure pain threshold (PPT) in edentulous oral mucosa. *J Dent*. 2004;32(3):219-228.
doi: 10.1016/j.jdent.2003.11.001

53. Steele CM, Molfenter SM, Péladeau-Pigeon M, Polacco RC, Yee C. Variations in tongue-palate swallowing pressures when swallowing xanthan gum-thickened liquids. *Dysphagia*. 2014;29(6):678-684.
doi: 10.1007/s00455-014-9561-6

54. Hernández-Olivos R, Muñoz M, Núñez E, et al. Salivary proteome of aphthous stomatitis reveals the participation of vitamin metabolism, nutrients, and bacteria. *Sci Rep*. 2021;11(1):15646.
doi: 10.1038/s41598-021-95228-8

55. Raza N, Kim K-H. Quantification techniques for important environmental contaminants in milk and dairy products. *TrAC Trends Anal Chem*. 2018;98:79-94.
doi: 10.1016/j.trac.2017.11.002

56. Lichtenstein AH, Schwab US. Relationship of dietary fat to glucose metabolism. *Atherosclerosis*. 2000;150(2):227-243.
doi: 10.1016/s0021-9150(99)00504-3

57. Pereira T, Barroso S, Gil MM. Food texture design by 3D printing: a review. *Foods*. 2021;10(2):320.
doi: 10.3390/foods10020320.

58. Dong L, Li Y, Chen Q, et al. Research advances of advanced glycation end products in milk and dairy products: formation, determination, control strategy and immunometabolism via gut microbiota. *Food Chem*. 2023;417:135861.
doi: 10.1016/j.foodchem.2023.135861

59. Kitada M, Ogura Y, Monno I, Koya D. A low-protein diet for diabetic kidney disease: its effect and molecular mechanism, an approach from animal studies. *Nutrients*. 2018;10(5):544.
doi: 10.3390/nu10050544

60. Pfeiffer AFH, Pedersen E, Schwab U, et al. The effects of different quantities and qualities of protein intake in people with diabetes mellitus. *Nutrients*. 2020;12(2):365.
doi: 10.3390/nu12020365

61. Zargaraan A, Rastmanesh R, Fadavi G, Zayeri F, Mohammadifar MA. Rheological aspects of dysphagia-oriented food products: a mini review. *Food Sci Hum Wellness*. 2013;2(3-4):173-178.
doi: 10.1016/j.fshw.2013.11.002

62. Aguilera JM, Park DJ. Texture-modified foods for the elderly: status, technology and opportunities. *Trends Food Sci Technol*. 2016;57:156-164.
doi: 10.1016/j.tifs.2016.10.001

63. Rajati F, Ahmadi N, Naghibzadeh ZA, Kazeminia M. The global prevalence of oropharyngeal dysphagia in different populations: a systematic review and meta-analysis. *J Transl Med*. 2022;20(1):175.
doi: 10.1186/s12967-022-03380-0

64. Landová H, Daněk Z, Gajdziok J, Vetchý D, Stembírek J. Oral mucosa and therapy of recurrent aphthous stomatitis. *Ceska Slov Farm*. 2013;62(1):12-18.

ACCSCIENCE PUBLISHING

International Journal of Bioprinting

RESEARCH ARTICLE

Parametric design and performance study of continuous gradient triply periodic minimal surface bone scaffold

Shuangyu Liu[1], Jinlong Feng[1], Fulong Zhang[1]*, Weibo Jiang[2], Tatiana Mikhailovna Vasilieva[3], Ping Lu[4], and Sen Lu[1]

[1]College of Mechanical Engineering, Yancheng Institute of Technology, Yancheng, Jiangsu, China

[2]Department of Orthopaedics, The Second Hospital of Jilin University, Changchun, Jilin, China

[3]Joint Institute for High Temperatures of Russian Academy of Sciences, Izhorskaya str., 13, Bd.2, Moscow, Russia

[4]College of Automotive Engineering, Yancheng Institute of Technology, Yancheng, Jiangsu, China

Abstract

Continuous gradient triply periodic minimal surface (TPMS) porous structure has been proven to be one of the most suitable structures for bone implants due to their excellent mechanical properties and high porosity. This study establishes a parametric modeling method for continuous gradient TPMS structures and optimizes the TPMS porous structure with a continuous gradient change in porosity. Ti-6Al-4V continuous gradient TPMS porous structures were prepared using powder bed fusion (PBF). The mechanical properties and permeability of the continuous gradient TPMS porous structure were studied. The results indicate that the porosity control parameter C for gradient continuous change follows a linear function, with the porosity increasing linearly within the specified range of values. The influence of the periodic parameter ω on the mechanical properties and permeability of different types of TPMS structures varies. The Gyroid continuous gradient structure aligns more closely with the mechanical properties and permeability of bone scaffolds. Furthermore, a TPMS continuous gradient porous structure that is more suitable for trabecular bone implants was obtained through topology optimization design. A bone implant model and object suitable for human trabecular bone were designed and printed, providing technical support for subsequent performance testing and application research of bone implants.

Keywords: Triply periodic minimal surface; Additive manufacturing; Bone scaffold; Mechanical properties and permeability

***Corresponding author:**
Fulong Zhang
(zhangfulong@ycit.edu.cn)

Citation: Liu S, Feng J, Zhang F, et al. Parametric design and performance study of continuous gradient triply periodic minimal surface bone scaffold. *Int J Bioprint.* 2024;10(2):2306.
doi: 10.36922/ijb.2306

Received: November 24, 2023
Accepted: January 19, 2024
Published Online: February 7, 2024

1. Introduction

Bone, the hardest tissue in the human body, serves multiple essential functions, including body support, movement facilitation, hematopoiesis, and effective promotion of blood circulation. Extensive bone injuries are typically caused by trauma, osteomyelitis, or tumors. Medical studies have indicated that bone tissue loses its inherent capacity for repair when the size of the bone defect exceeds 30 mm.[1] Consequently, interventional

therapies involving repair technologies become necessary. Repairing bone tissue has always been a significant challenge in modern medicine. According to research, the global demand for bone substitutes and grafts is projected to reach US$3.4 billion by 2022, with a growth rate of 4.8%.[2] This poses a substantial financial burden on most countries and regions worldwide.

The process of bone remodeling can be divided into four stages: hematoma formation, fibroblast formation, callus formation, and bone remodeling.[3] In this complex process, various cytokines, growth factors, and other signaling molecules are involved in guiding the repair of various cellular defects.[4] This repair process is highly intricate, and in order to enhance repair efficiency and achieve better healing outcomes, it is necessary to create a more stable environment, such as surface folding, to accommodate all signaling molecules and facilitate cell proliferation on its surface.[5] Traditional bone scaffolds generally adopt regular shapes, such as squares, hexagons, and circles. However, these regular shapes are unable to accurately mimic bone structures. With the continuous advancement of three-dimensional (3D) printing technology, the concept of minimal surface structures has emerged. Among them, the triply periodic minimal surface (TPMS) scaffold stands out as an optimal choice.[6] Mathematically speaking, a minimal surface is characterized by zero mean curvature. TPMS structures represent minimal surfaces with complex topological spatial structures. They possess advantageous features, including high surface area, high porosity, and periodic variations. The interconnected interior and smooth surface of TPMS scaffolds make them ideal structures for orthopedic implants.[7] When designing TPMS scaffolds for bone regeneration, one of the crucial factors to consider is pore design.[8,9] This is because the design of pores directly affects the outcome of bone regeneration.[10] Firstly, an interconnected porous structure promotes the diffusion of nutrients to cells, thereby assisting the bone regeneration process. Secondly, natural bone tissues possess porosity, with a range from 30% to 90% in trabecular bone.[11,12] Therefore, when designing a bionic porous scaffold as a bone implant, it is necessary to optimize the pore size and porosity to ensure that the pores are large enough to facilitate nutrient diffusion and tissue growth,[13] while still maintaining a sufficiently large surface area for cell attachment. In addition to directly affecting cell behavior, the pores of the TPMS structure also indirectly impact other important characteristics crucial in the bone regeneration process.[14] For instance, mechanical strength is a vital property of a bone scaffold. The process of bone remodeling depends largely on the ability of bone tissue to perceive and adapt to mechanical load. Consequently, a good mechanical environment is key to the success of bone regeneration. Thus, the scaffold needs to have sufficient mechanical strength to accommodate and stabilize the cells, but not be excessively strong.[15] Sychov et al.[16] used polylactic acid (PLA) as raw material to prepare four TPMS structures of Gyroid, Schwartz diamond, Neovius surface, and D-prime surface by fused deposition modeling (FDM) and studied their compression resistance. The results showed that D-type TPMS structure has the best elastic modulus but with poor energy absorption performance. The G-type TPMS structure has good compressive strength and energy absorption capacity. Yan et al. studied the mechanical properties of Ti-6Al-4V and Al-Si10-Mg Schoen Gyroid (SG) TPMS unit cell structures prepared by powder bed fusion (PBF) under uniaxial compression tests, and fitted the compression test results with the Gibson–Ashy model to guide biological applications and implant matching.[17-19] Furthermore, the structures should have an elastic modulus similar to that of natural bone to prevent the stress shielding effect. The elastic modulus of cortical bone is approximately 1–15 GPa.[20] Therefore, the final bone scaffold should possess a mechanical strength within this range.

The permeability of the bone scaffold is a crucial factor that significantly influences the outcomes of bone regeneration. The permeability is typically quantified using Darcy's law, with the Darcy permeability value (k) being measured.[21,22] Permeability refers to the ability of the scaffold to facilitate fluid flow.[23] Good permeability, indicated by a higher k value while maintaining satisfactory mechanical properties, not only facilitates the diffusion of essential nutrients,[24] but also determines the internal shear force and pressure within the scaffold.[25] Studies have demonstrated that these factors can affect cell differentiation and adaptation by enhancing alkaline phosphatase (ALP) activity and upregulating osteogenic marker genes.[26] Since porosity, pore size, connectivity, curvature, direction, and shape collectively influence the permeability and hydrodynamics of bone scaffolds, it is advantageous to have bone scaffolds with high porosity, sufficient pore connectivity, and appropriate pore size and shape to ensure good permeability, which is beneficial for bone tissue engineering.[27,28] Montazerian et al.[29] analyzed the biological permeability of different TPMS units at different relative densities. The relationship between normalized permeability and volume fraction and the velocity contour of biological fluid were obtained by curve fitting. Varley et al.[30] placed the bone scaffold in different humidity conditions and analyzed its permeability through experimental and theoretical simulation analysis. It is found that the experimental value and the theoretical value are similar in numerical results, providing a theoretical basis for us to use computer simulation to evaluate permeability.

Therefore, when designing bone scaffolds, in addition to ensuring favorable mechanical properties, it is also crucial to consider whether the scaffold structure can maintain high permeability.

In summary, although a high porosity can increase the permeability of the continuous gradient TPMS structure, it also reduces its mechanical properties. Therefore, when considering different application requirements, it is essential to strike a reasonable balance between mechanical properties and permeability. This study aims to optimize and design a continuous gradient TPMS bionic bone structure for bone repair. In this study, we combined experimental and simulation approaches to investigate the parametric design, mechanical properties, permeability, and application of the continuous gradient TPMS bone-like structure. The main purpose of this study is to obtain a bone scaffold structure that matches the performance of human femur and to provide theoretical basis for further realization of human bone tissue repair.

2. Design, performance test, and simulation analysis of continuous gradient TPMS structure

2.1. Parametric design and 3D printing of continuous gradient TPMS structure

The design method plays a crucial role in the quality of generated TPMS models. The geometric characteristics of the minimal surface structure, including parameters such as porosity (or volume ratio), unit cell pore size, and thickness, are key factors that influence its performance. Therefore, geometric design serves as the foundation for effectively controlling the application performance of TPMS structures in different fields. Unlike traditional foam lattice structures, TPMS enables the design of more intricate structural characteristics to mimic natural porous structures.

Compared to other porous structures, TPMS exhibits three significant characteristics. Firstly, TPMS represents an implicit surface, allowing for the complete expression of the geometric structure through algebraic equations, which can be simplified as $f(x, y, z) = C$, where C is a constant. Based on this, TPMS is considered an isosurface. Secondly, TPMS demonstrates periodicity in three independent directions. The parameter function facilitates easy control over the distribution range and period of the model. Lastly, TPMS is characterized as a minimal surface, meaning that the mean curvature of TPMS is zero, resulting in a smooth surface reminiscent of natural phenomena like soap bubbles and leaves.[31]

There are two main approaches to expressing the porous structure of minimal surfaces. According to the Enneper–Weierstrass parameter representation method, TPMS can be accurately calculated[32]:

$$\begin{cases} x = Re\left((e^{i\theta} \int_{(w_0)}^{w} (1-\tau^2) R_{(\tau)} d\tau \right) \\ y = Re\left((e^{i\theta} \int_{(w_0)}^{w} (1+\tau^2) R_{(\tau)} d\tau \right) \end{cases} \quad (I)$$

$$z = Re\left((e^{i\theta} \int_{(w_0)}^{w} 2\tau R_{(\tau)} d\tau \right)$$

In this method, we use the following notation: $i = \pm 1$, τ represents a complex variable, θ is the valve cover angle, Re denotes the real part of the complex variable, and $R(\tau)$ is the Weierstrass function for different types of TPMS units. For example, the Weierstrass functions of G, D, and P surfaces can be expressed as[33]:

$$R(\tau) = \frac{1}{\sqrt{\tau^8 - 14\tau^4 + 1}} \quad (II)$$

However, it is worth noting that this method can only generate a limited number of TPMS units. Currently, several Weierstrass functions for minimal surfaces have been discovered. Just like other mathematical methods, TPMS porous structures can be generated using Equation III[34]:

$$\phi(r) = \sum_{k=1}^{k} A_k \cos\left[\frac{2\pi (h_k \cdot r)}{\lambda_k} + P_k \right] = C \quad (III)$$

Here, A_k represents the amplitude, λ_k is the periodic factor, and P_k is the phase function. Building upon this foundation, the common TPMS units are presented in Table 1. It can be observed from the TPMS implicit function expressions in Table 1 that ω and C are two important parameters that influence the period and curvature of TPMS. In the context of TPMS porous structures, the volume ratio of the two components is solely related to the curvature parameter C. Therefore, by assigning different values to the periodic parameter ω and the curvature parameter C, gradient or non-uniform TPMS porous structures can be generated.

Table 1. Common mathematical expressions of TPMS structure

Unit name	Mathematical expression	3D model
Gyroid (G)	$f(x, y, z) = \sin(\omega_x x)\cos(\omega_y y) + \sin(\omega_z z)\cos(\omega_x x) + \sin(\omega_y y)\cos(\omega_z z) = C$	
Schwarz P(P)	$f(x, y, z) = \cos(\omega_x x) + \cos(\omega_y y) + \cos(\omega_z z) = C$	

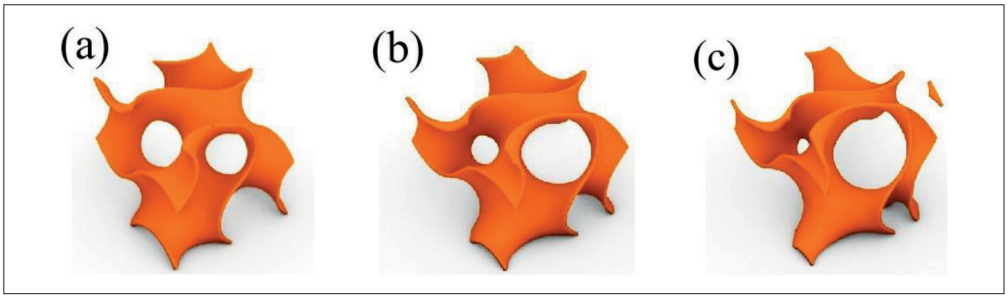

Figure 1. (a) C = 0, G surface; (b) C ≠ 0, G surface; (c) segregation phenomenon.

In this study, G and P cells were utilized as the subjects of research. The grasshopper parametric modeling platform was employed to design a continuous gradient porous structure that is suitable for bone reconstruction.[35] Within the grasshopper environment, the input implicit function can be transformed into a visual grid structure. By iterating through the grid structure multiple times, a grid surface with fewer defects can be obtained, ultimately leading to the development of a TPMS model for additive manufacturing.

Within a given cubic space measuring 20 mm on each side, different TPMS porous structures can be obtained by adjusting the parameter C of the implicit function based on the existing parameters. Taking the G surface as an example, when C is set to 0, the porosity of the unit cell remains the same (refer to Figure 1a). However, when C is not equal to 0, the porosity between adjacent units becomes distinct (as shown in Figure 1b). Similar rules apply to other TPMS structures. Increasing the absolute value of C leads to an increase in porosity, but if the absolute value becomes too large, partition phenomena may occur, resulting in an incomplete TPMS structure (see Figure 1c).

To achieve a tunable pore gradient in the TPMS structure, a linear function is introduced for the parameter C.

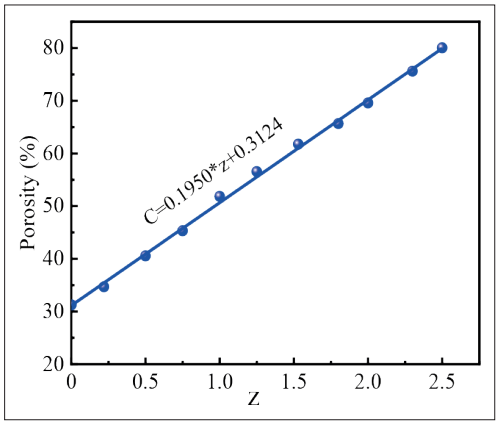

Figure 2. Linear fitting of porosity change

The goal is to obtain a TPMS porous structure with continuously changing porosity. In Equation IV, the linear function for C with respect to the parameter z is defined as:

$$C = \alpha * z + \beta \quad \text{(IV)}$$

In this equation, C is the parameter used to control the porosity, while z represents the Z-direction porosity adjustment value of the TPMS structure. The value range for z is set to be [0,2.5π]. Figure 2 illustrates the variation of porosity and z per unit volume of the porous structure. The porosity changes linearly along the Z-axis as z changes. Similarly, if the parameter C is given a linear function of x or y, the same rule applies to the X-axis or Y-axis.

To obtain a TPMS model with a continuous porosity gradient and good structure, the porosity range is limited to 30–80%. If the porosity is too high, partition phenomena may occur, while a porosity that is too low may result in poor 3D printing quality. Within the limited porosity range, different Z values are selected to determine the corresponding unit cell porosity. A graph of unit cell porosity versus Z values is then plotted. By fitting the data, a functional relationship between the porosity parameter C and z is obtained:

$$C = 0.1954 * z + 0.3124 \quad \text{(V)}$$

In this study, six models of G and P surfaces were designed. The fitting curve in Figure 2 shows that the porosity of the six models is controlled at approximately 65%. The implicit function expressions of the two models are as follows:

$$f(x, y, z) = \sin(\omega x)\cos(\omega y) + \sin(\omega z)\cos(\omega x) + \sin(\omega y)\cos(\omega z) = 0.1954^{*}z + 0.3124 \quad \text{(VI)}$$

$$f(x, y, z) = \cos(\omega x) + \cos(\omega y) + \cos(\omega z) = 0.1954^{*}z + 0.3124 \quad \text{(VII)}$$

The difference between the different models of the two surfaces is achieved by controlling the periodic parameter ω. The periodic parameters for each model are set as

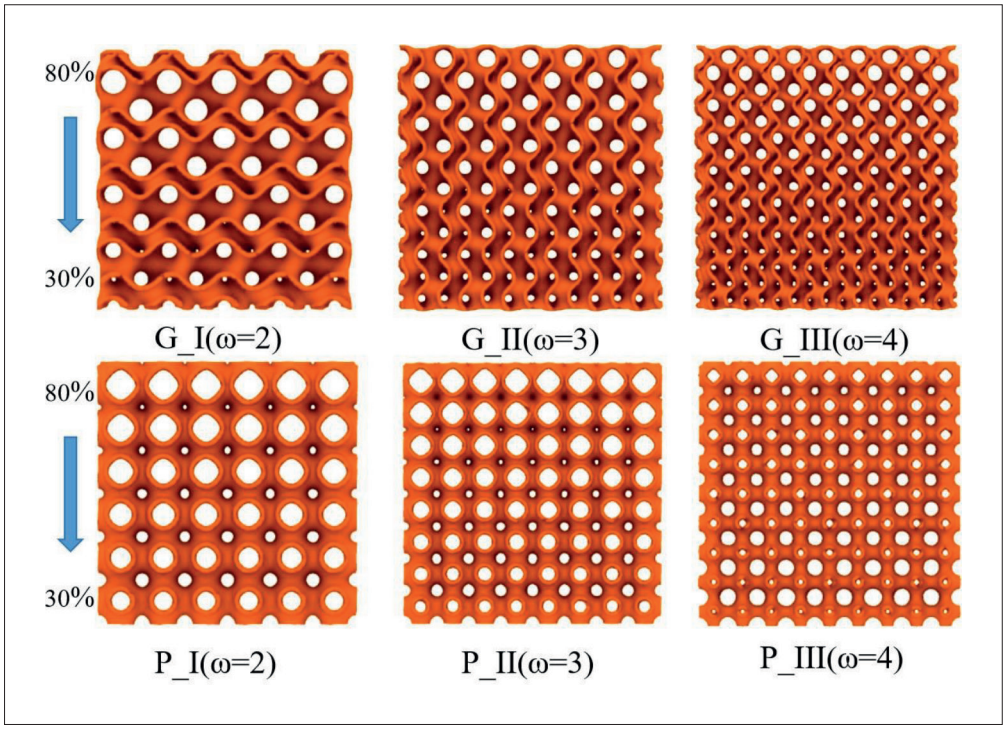

Figure 3. Three-dimensional model of continuous gradient porous structure.

follows: G_I ($\omega = 2$), G_II ($\omega = 3$), G_III ($\omega = 4$), P_I ($\omega = 2$), P_II ($\omega = 3$), and P_III ($\omega = 4$). The thickness of the models is set to 0.4 mm. Figure 3 displays the 3D diagrams of the two sets of models and their specific parameters.

The designed models were manufactured using a metal 3D printing device (L-PBF system CR-PBFM250) with Ti-6Al-4V material having a particle size of 15–45 μm. The printing parameters were optimized prior to printing to ensure high-quality products. The laser power used was 290 W, with a laser spot diameter of 85 μm. The scanning speed was set at 2000 mm/s, and the layer thickness was 40 μm. The printing process was carried out under argon protection at a temperature of 26°C to prevent oxidation. Two samples were made for each model, and the resulting samples were cleaned using compressed air and ultrasound.

2.2. TPMS structure performance test

2.2.1. Porosity test

The total porosity of the samples was determined using the dry weighing method, and the calculation formula used was as follows[36]:

$$Porosity = (1 - m_s / \rho_t * V_d) \quad \text{(VIII)}$$

where m_s is the mass of each sample; ρ_t is the theoretical density of Ti-6Al-4V (4.42 g/cm^3); and V_d is the volume set for printing.

The morphology and manufacturing defects of the samples were observed by means of scanning electron microscopy (SEM; Model FEI200, FEI, USA).

2.2.2. Mechanical properties test

Static compression tests were conducted on a universal testing machine (MTS 809, MTS Systems Corporation, Minnesota, USA) equipped with a 10 kN gravity sensor. The loading rate used was 0.5 mm/min. The elastic modulus of each sample was calculated from the slope of the linear phase observed at the beginning of each curve.

2.3. Finite element analysis of continuous gradient TPMS structure

2.3.1. Finite element analysis of mechanical properties

To establish the initial model, Grasshopper was employed, and the generated STL file was imported into HyperMesh software for topology processing in order to regenerate a refined mesh. The mesh model was then imported into ABAQUS software. The bottom of the *Z*-axis was fixed, and a 40% strain was applied to the upper part of the *Z*-axis. The elastic modulus was set to 110 GPa and the Poisson's ratio to 0.34. After the simulation, the stress distribution of the TPMS structure was visualized.

2.3.2. Finite element simulation of permeability

Six models with varying porosity were selected for the study. These models underwent pretreatment in HyperMesh software before being imported into COMSOL

software for further processing. Since the focus of the study was on the pore space, the porous matrix was not explicitly analyzed. The model has a square cross-section with a dimension of 10 mm by 10 mm and a height of 20 mm. The fluid velocity was defined as u = 0.1 mm/s, and it could freely flow along the normal direction at one end. Although assuming symmetrical boundary conditions for the other boundaries may not align with reality, it was suitable for the TPMS structure modeling. To characterize the flow inside the porous structure, the Reynolds number was estimated using Equation IX[37]:

$$R_e = pul / \mu \quad \text{(IX)}$$

where the blood density ρ = 1080 kg/m^3, and blood viscosity μ = 3.5 x 10^{-3} Pa·s.[38] The side length of the cross-section is used as the characteristic length scale L, and Re = 2 is obtained. The Stokes equation can be used to describe the flow ignoring the inertial term. Finally, the goal of the model is to obtain the average value of porosity and permeability to describe the macroscopic model using Darcy's law or Brinkman equation. Porosity is defined as the ratio of pore space volume V_{fluid} to total volume V_{tot}:

$$\varepsilon = V_{fluid} / V_{tot} \quad \text{(X)}$$

The permeability is calculated using the following relationship[39]:

$$k = u_{out} \mu / \Delta\rho \quad \text{(XI)}$$

3. Results and discussion

3.1. Macro-micro morphology of 3D-printed samples

Figure 4a represents a 3D-printed object showcasing a continuous gradient TPMS porous structure. Upon visual inspection, the printed sample exhibits a smooth surface without any noticeable defects. The internal pores appear unobstructed with good connectivity, resembling the structure of bones. The porosity of the G and P continuous gradient TPMS structures varies layer by layer along the printing direction, following a linear function without any gradient fault phenomena. Figure 4b illustrates the microstructure of the sample. Observing the image, it is evident that there are no particles bonded to the inner wall of the interconnected pores. Additionally, randomly distributed micropores with a diameter smaller than 0.5 mm can be observed. The internal micropore ratio of the manufactured sample is less than 0.5%, and there are no crack defects present.

The actual porosity of the 3D-printed TPMS structure sample is shown in Figure 5. According to the calculation results, it can be observed that the porosity of the manufactured sample is in close agreement with the designed porosity (65%), demonstrating the repeatability of the manufacturing method. The porosity changes layer by layer with the variation of the parameter ω, indicating that adjusting the ω parameter in the trigonometric function allows for effective control over the porosity variation in the continuous gradient TPMS structure. Observation and measurement reveal that the 3D-printed continuous gradient TPMS structure possesses a similar topological structure to the intended 3D model. Additionally, this structure exhibits a porosity change pattern comparable to that of bone structures, thus establishing a foundation for the further design of continuous gradient TPMS artificial bone structures and their mechanical properties.

3.2. Mechanical properties of continuous gradient TPMS structure

Before experimental verification, theoretical research is crucial in order to save costs and optimize experimental procedures. Finite element simulation is considered the optimal method to achieve this goal. A static compression

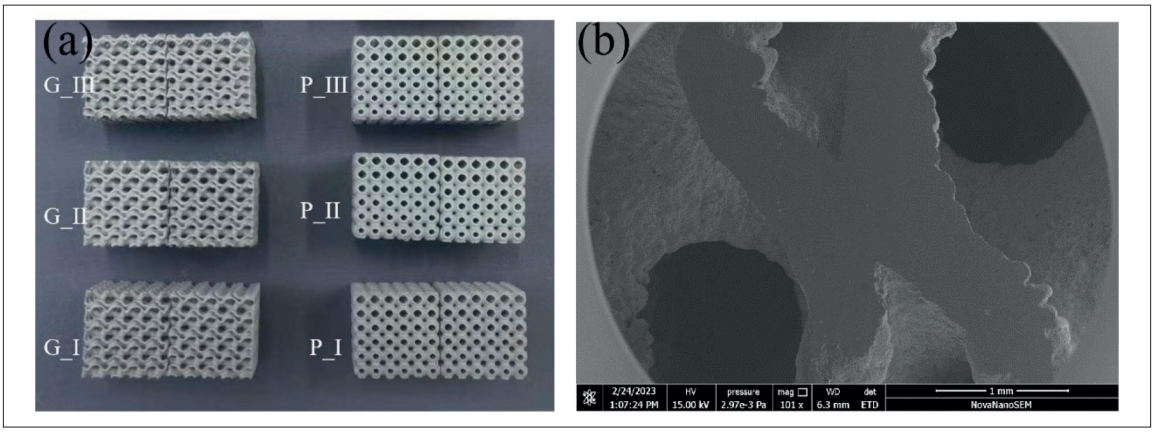

Figure 4. (a) Full picture of the printed sample; (b) the morphology of the G_II sample.

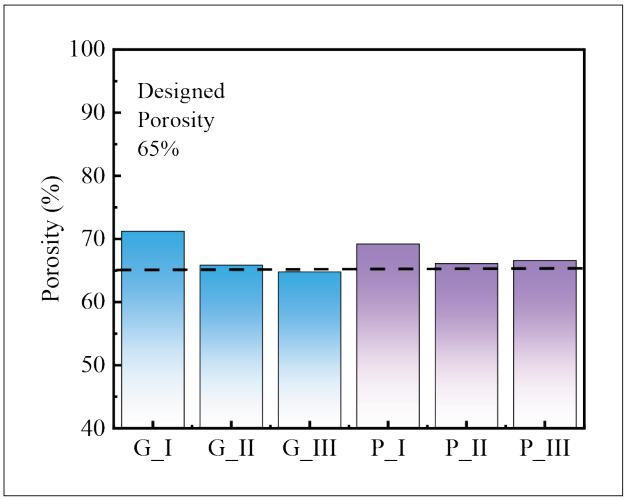

Figure 5. Porosity measurement results of 3D-printed samples.

finite element simulation experiment is conducted on six models, and the stress distribution is analyzed.

Figure 6 illustrates the results of finite element analysis for the G and P continuous gradient porous structures. The stress distribution cloud diagram reveals that the stress conditions vary for the porous structure models with different structures. From the results in Figure 6, it can be observed that the stress of the G continuous gradient porous structure is relatively uniform, with no evident stress concentration. On the other hand, the stress distribution in the P continuous gradient porous structure appears layered, indicating stress concentration. Examining the unit cells of these two structures, the G unit cell exhibits a spiral-like structure, which effectively decomposes pressure. Additionally, the long force transmission path of the spiral structure contributes to the uniform stress distribution within the G structure. On the contrary, the P unit cell resembles a sphere, resulting in force transmission that alternates between concentration and dispersion. The support performance in the middle of the sphere is weakened, making it prone to deformation when subjected to unidirectional force. Figure 7 presents the stress–strain curves obtained from finite element simulation for the two types of porous structures with minimal surfaces. In all structures, the stress experiences a linear increase stage followed by a yielding stage. For the G gradient porous structure, after reaching the yield limit, the stress gradually increases in a wave-like pattern. Conversely, the stress of the P gradient porous structure significantly decreases after reaching the maximum yield stress. As the strain continues to increase, the stress exhibits wave-like fluctuations. These variations in the stress–strain curve correspond to the minimal surface structure. Based on the stress cloud, the G surface experiences uniform stress, resulting in a gradual increase in the stress–strain curve after entering the yield stage. Due to the structural characteristics of the unit cell, the stress curve of the P surface fluctuates after entering the yield stage.

It can be observed from Figure 7c and d that the elastic modulus of the G surface initially increases and then decreases with an increase in periodic parameters. On the other hand, the P surface always shows an increasing trend. Further validation of the mechanical properties difference between the two structures will be conducted through experiments.

Figure 8 represents the stress–strain curve obtained from static compression experiments performed on the two structures. The figure demonstrates that the trend of the stress–strain curve aligns with the simulation results, thus confirming the reliability of the finite element simulation.

Figure 9 displays the fracture mode of the samples used in the compression experiment. It is evident from the figure that the G-type TPMS porous structure exhibits two types of fracture modes: collapse-type fracture and x-type fracture. Specifically, G_I and G_II exhibit collapse fractures, where these structures progressively fragment from the upper part of the sample and disintegrate layer by layer. The two sides of the sample become gradually curved, with no visible cracks. However, G_III demonstrates a different fracture mode. Figure 9 reveals an x-type fracture in G_III, with clear cracks present in the lower part of the sample. The stress cloud depicted in Figure 6 allows us to understand the stress distribution. For G_I and G_II, the stress cloud reveals that stress concentration occurs in the upper part when the strain reaches 15%. Subsequently, the stress propagates uniformly downward, corresponding with the experimental results. Conversely, for G_III, the stress cloud shows a triangular stress concentration in the lower part of the structure, in line with the x-type fracture observed in the experiment. From a structural perspective, the unit cell of the G-type TPMS porous structure exhibits a spiral pattern, resulting in a more uniform force distribution. However, when the structural parameters are increased excessively, internal partitioning may occur. In the case of G_III, the structural parameters are too large, thus generating a gradient structure. Consequently, fine defects manifest in the internal structure due to the significant gradient span, leading to a reduction in mechanical properties. Consequently, G_III possesses lower mechanical properties and may not be suitable for cortical bone tissue engineering applications.

For the P-type porous structure, the fracture mode is a 45° stacking after layer-by-layer fracture, which is consistent with the stress cloud obtained from the simulation. The unit cell of the P-type structure is a hollow sphere slightly

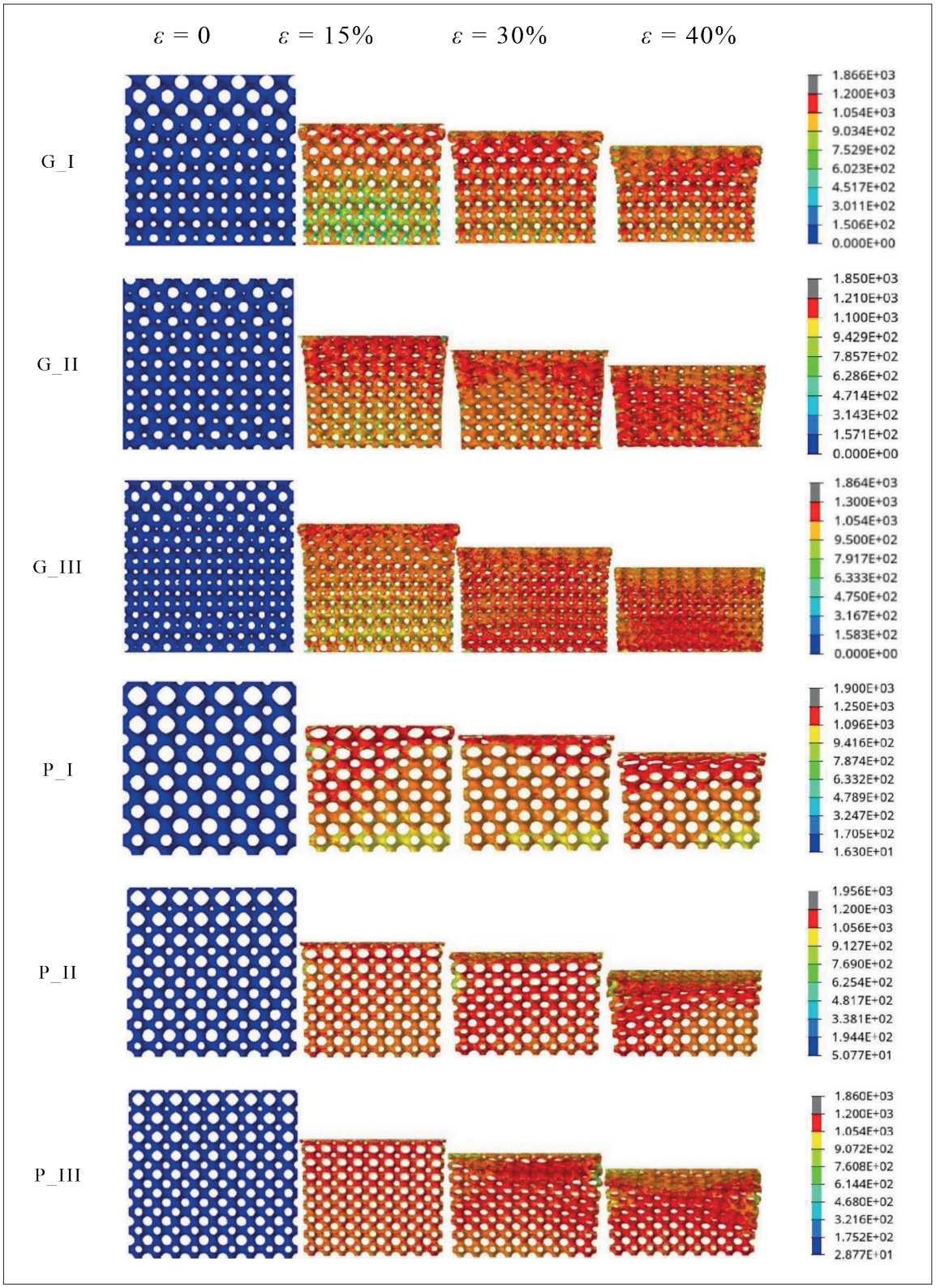

Figure 6. Stress cloud diagram of gradient porous structure.

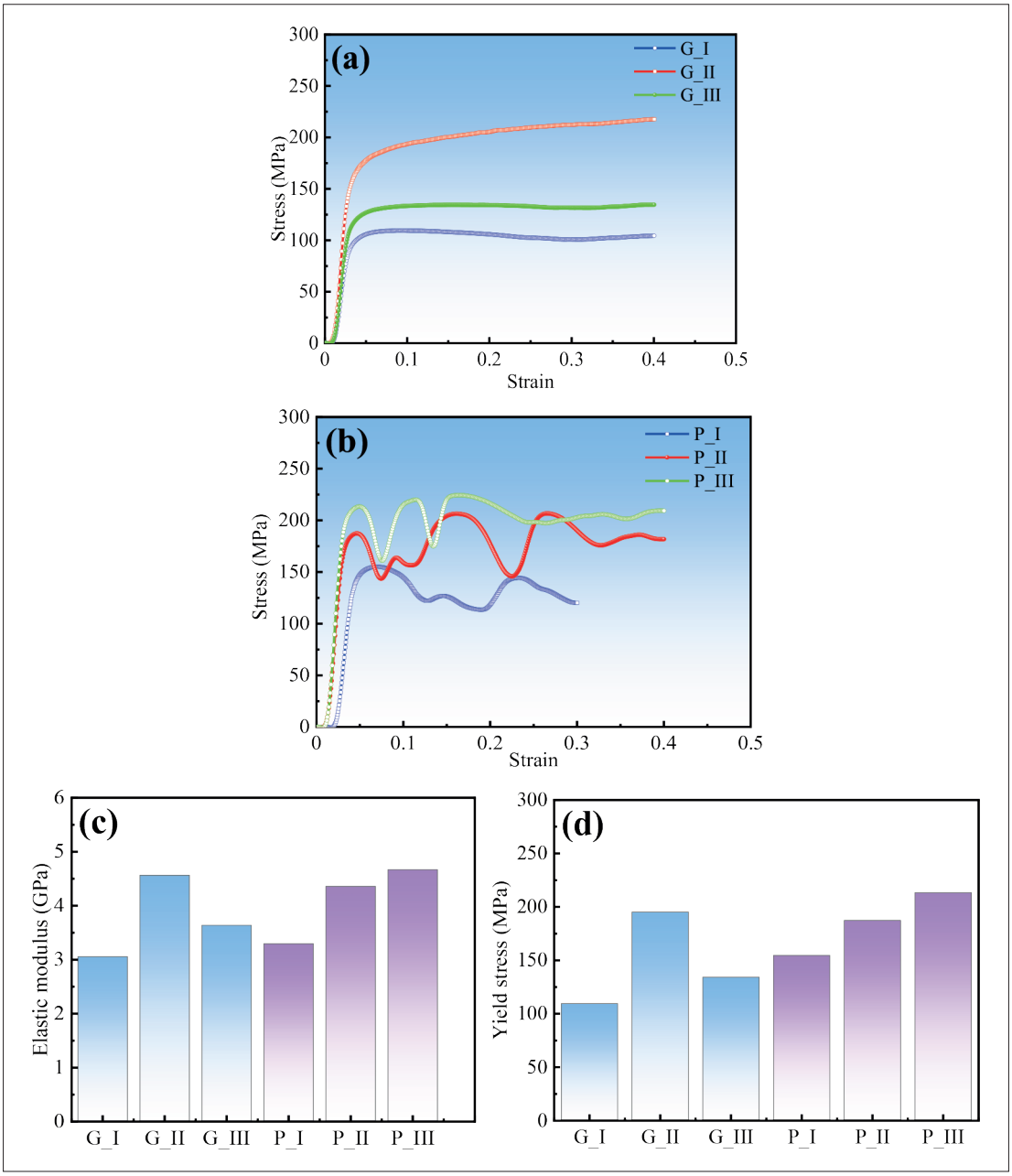

Figure 7. (a) G-type gradient porous structure stress–strain simulation results; (b) P-type gradient porous structure stress–strain simulation results; (c) elastic modulus simulation results; (d) yield stress simulation results.

bulging in the middle. When it is compressed, the stress propagates to the bulging parts on both sides. As the stress on both sides gradually accumulates, fracture occurs after reaching the yield limit. After entering the yield stage, due to its unit cell structure characteristics, it will show a 45° stacking phenomenon. With an increase in periodic parameters, the accumulation phenomenon becomes more obvious, leading to gradually enhanced mechanical properties of the P-type TPMS porous structure.

Figure 10a and b shows the elastic modulus and ultimate fracture strength of G and P structures. The lowest elastic modulus of the G gradient structure is 2.451 GPa, and the lowest yield stress is 98.42 MPa. The minimum elastic modulus of the P gradient structure is 2.936 GPa, and the minimum yield stress is 147.99 MPa. It can be observed that the elastic modulus and yield strength of both G and P gradient structures undergo certain changes with an increase in the periodic parameter ω. Among

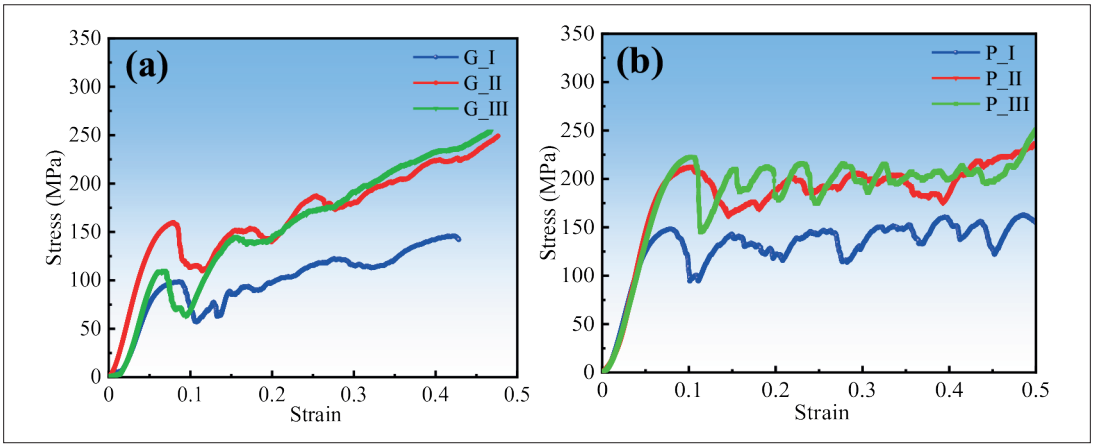

Figure 8. Stress–strain curve of gradient porous structure compression experiment: (a) G structure and (b) P structure.

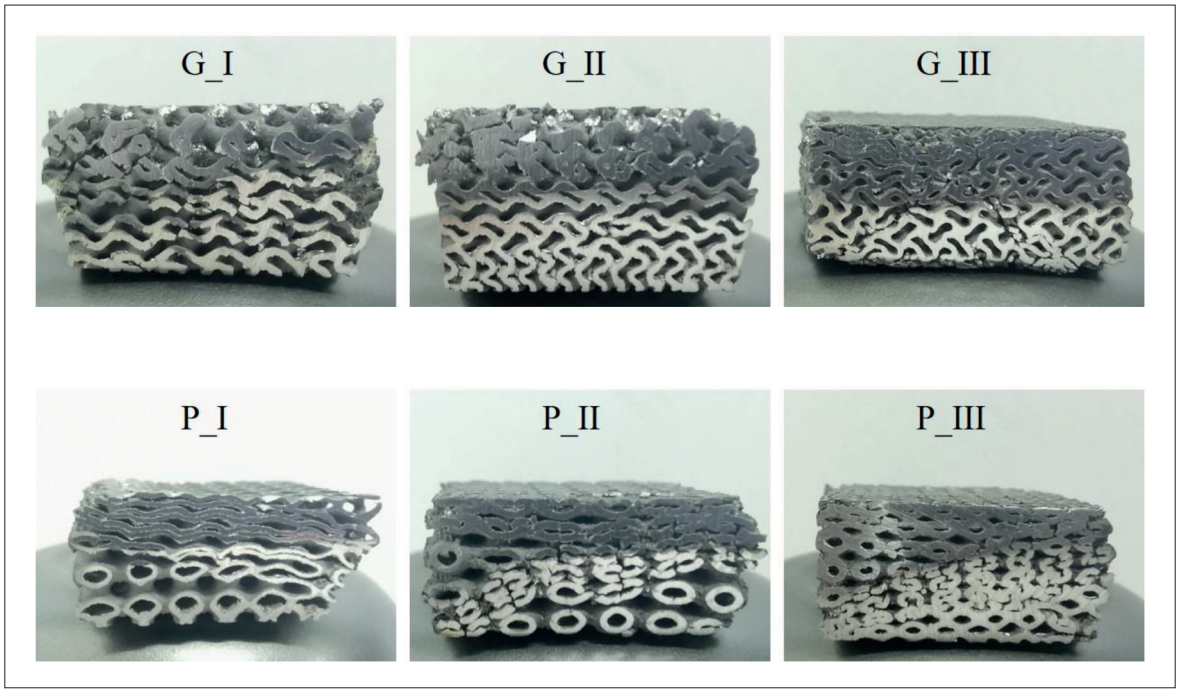

Figure 9. Fracture mode of sample.

them, G_II and P_III exhibit the highest elastic modulus and ultimate strength. This result indicates that the mechanical properties and elastic modulus of the gradient TPMS structure can be improved by adjusting the periodic parameter ω. Specifically, the mechanical properties of the G gradient porous structure increase initially and then decrease as the periodic parameters increase, while the P gradient porous structure shows a continuous increase. Comparing these mechanical properties with those of cancellous bone in the human femoral head, it is found that the designed bone implant models meet the required mechanical properties of human trabecular bone tissue (1–15 GPa).[40-42]

Under the condition of no partition phenomenon, the analysis of Figures 7 and 10 reveals that the mechanical properties of the G structure initially increase and then decrease with an increase in the periodic parameter ω. The mechanical properties reach a maximum value when the periodic parameter ω is approximately 3. On the other hand, the mechanical properties of the P structure increase

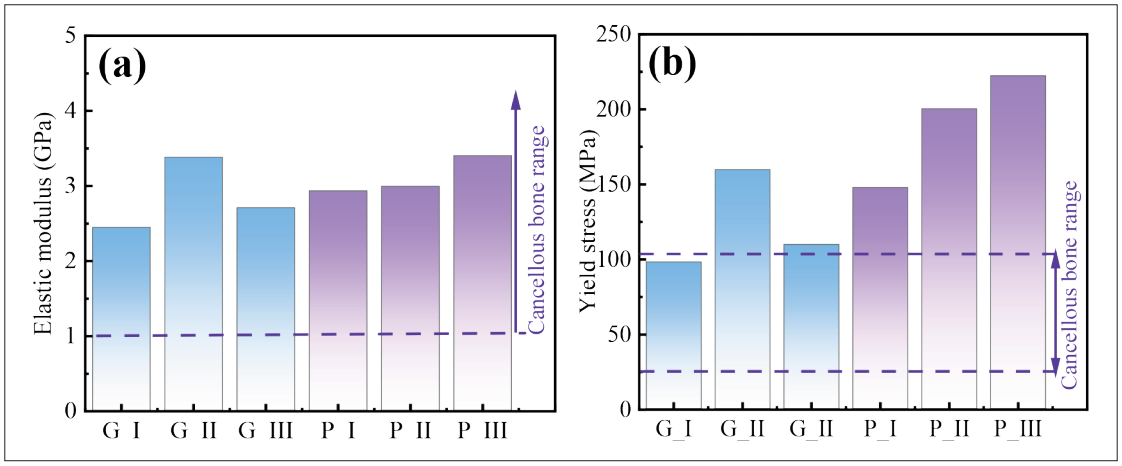

Figure 10. Comparison of mechanical properties of different TPMS structures: (a) elastic modulus and (b) ultimate strength.

with an increase in the periodic parameter ω, and there is no extreme value, making it challenging to determine the range of the periodic parameters.

3.3. Permeability of continuous gradient TPMS structure

To identify a more suitable bone scaffold structure for the human body, the study focused on investigating the permeability of TPMS porous structures with various continuous gradients. Figure 11 displays the flow velocity of different structures and the fluid streamlines from the side of each bracket and the outlet. These streamlines effectively highlight the trajectory of cells or nutrient fluids passing through the bone implant, enabling the analysis of the interaction between the bone implant structure and cells and nutrient fluids that facilitate bone regeneration. From the figure, it is evident that the streamline trajectory in the G gradient structure follows a spiral path, whereas the streamline trajectory in the P gradient structure is almost linear. The spiral trajectory facilitates full contact between cells or nutrient solutions and the bone scaffold, which is beneficial for bone repair. Figure 12 exhibits the permeability of different structural models. The highest permeability is observed in G_II, measuring 2.80×10^{-8} mm^2, while the lowest permeability is found in P_III, measuring 5.20×10^{-9} mm^2.

Based on the analysis of permeability, it is evident that the permeability of G gradient porous structure first increases and then decreases with the increase of periodic parameters. As for the P gradient porous structure, its permeability gradually decreases. In comparison, G_II and P_III possess similar mechanical properties, but G_II boasts the best permeability, aligning well with the characteristics of bone. Consequently, it holds immense potential for practical applications.

4. Optimization of Gyroid bone-like scaffold structure

Through the analysis of mechanical properties and permeability of various continuous gradient TPMS structures, the results indicate that the G-type gradient structure exhibits favorable mechanical properties and permeability, making it more suitable for constructing bone-like structures and promoting bone tissue repair. However, further optimization design is required to ensure a better fit between the continuous gradient TPMS structure and the structure of the human femur. The structure of the human femur is depicted in Figure 13, which shows the continuous change in radial porosity, gradually increasing from the outside to the inside. Additionally, the main force acting on the femur is longitudinal. To achieve a continuous gradient TPMS structure with good permeability and mechanical properties, a function can be assigned to the periodic parameter ω, with a restriction of floating around $\omega = 3$. This enables the realization of parametric control over the continuous gradient TPMS bone-like structure.

To achieve a radial increase in porosity while maintaining a constant relative density, the cell size can be adjusted. This involves changing the parameters of the control period to establish a specific functional relationship. The new functional relation is denoted as Equation XII:

$$\begin{cases} \omega_x = \alpha_{(x,y,z)} * x \\ \omega_y = \alpha_{(x,y,z)} * y \\ \omega_z = \alpha_{(x,y,z)} * z \end{cases} \quad \text{(XII)}$$

In order to create a continuous gradient TPMS structure, the following conditions must be met:

$$d\omega_x = d\omega_y = d\omega_z \quad \text{(XIII)}$$

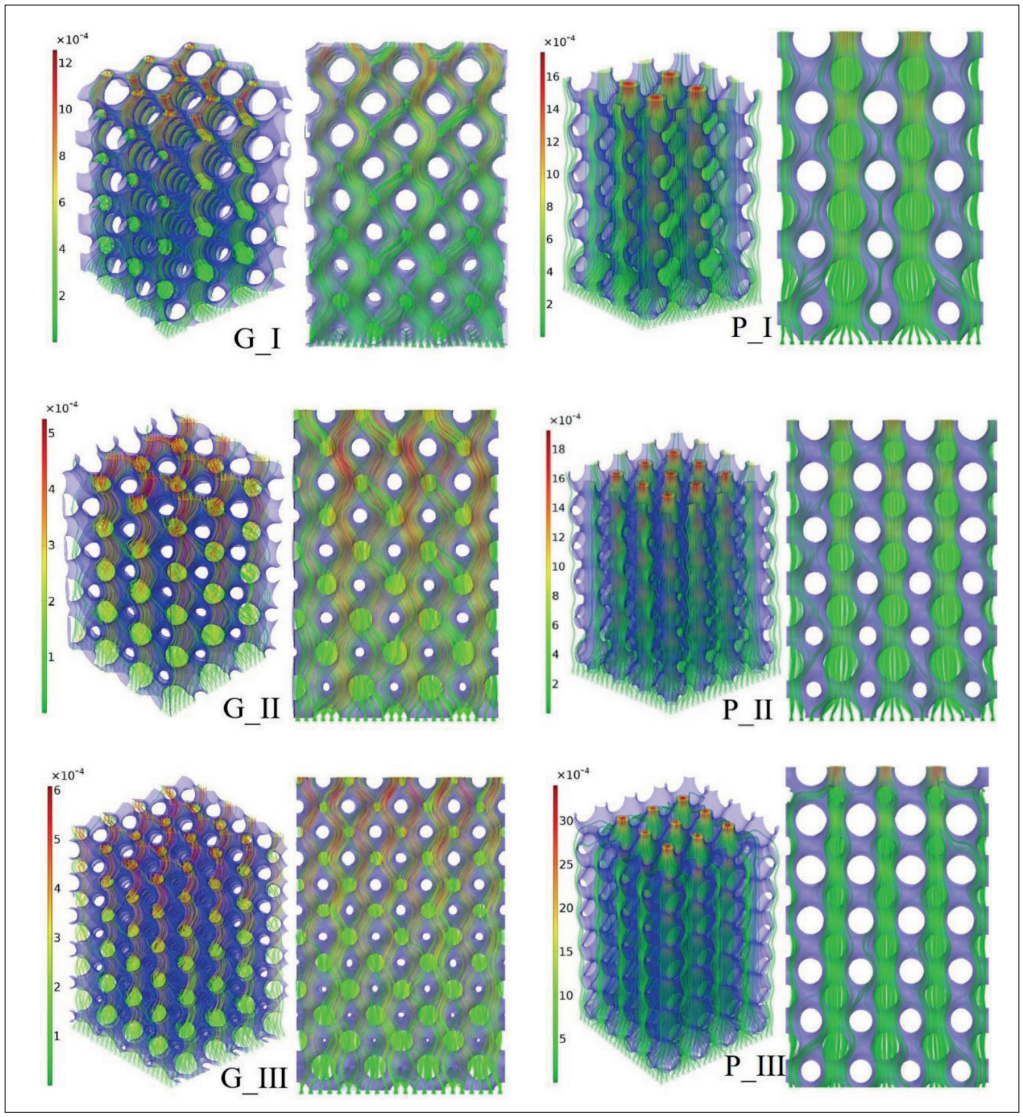

Figure 11. Flow velocity streamline distribution of different structures.

Given the radial variation in porosity in the femur, differential derivation is performed in the *y*-direction:

$$\begin{cases} d\omega_x = \alpha_{(y)} \\ d\omega_y = d\omega_{(y)} * y + \beta_{(y)} \\ d\omega_z = \gamma_{(y)} \end{cases} \quad \text{(XIV)}$$

In order to better describe the influence of the function on the structure forming, a linear function can be defined so that $\alpha_{(y)} = \beta_{(y)} = \gamma_{(y)} k * y + C_1$. Consequently,

$$\alpha_{(y)} = \beta_{(y)} = k * y + C_1 \quad \text{(XV)}$$

$$d\beta_{(y)} * y + \beta_{(y)} = k * y + C_1 \quad \text{(XVI)}$$

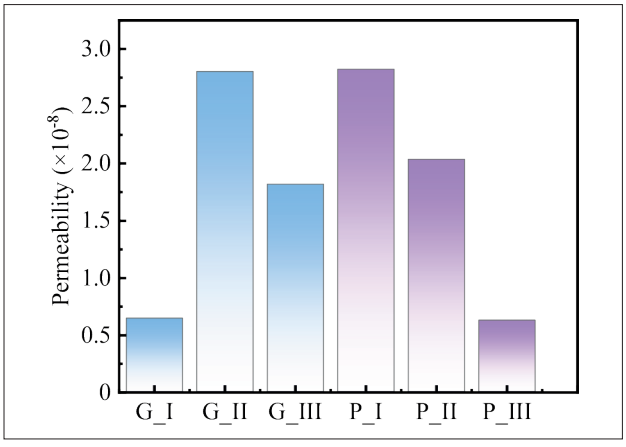

Figure 12. Permeability of different structures.

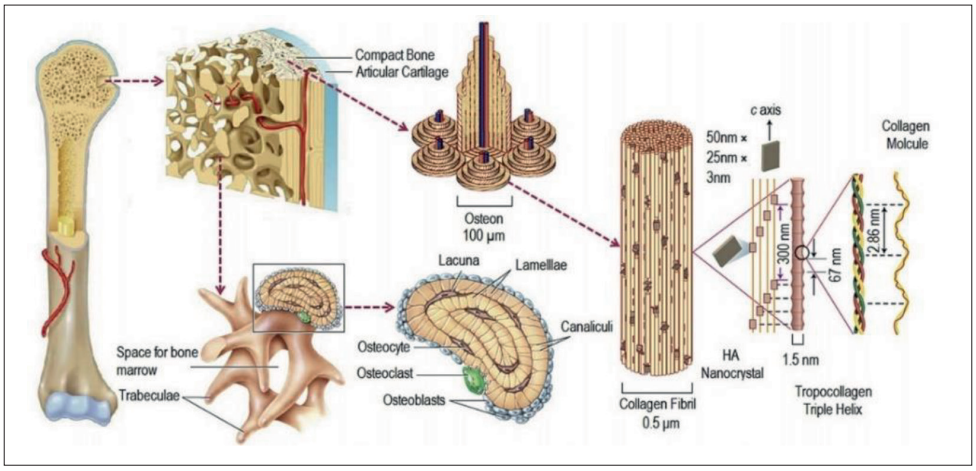

Figure 13. Human femur structure. Adapted with permission from ref.43 (Copyright © 2016, Elsevier).

define two points in a linear function as (Y_{min}, 1), (Y_{max}, e). Using the two-point method, the coefficients in the linear function can be obtained, quorum $k = (n-1)/(Y_{max} - Y_{min})$, $C_1 = -Y_{min} * k + 1$. For $d\beta_{(y)} * y + \beta_{(y)} = k * y + C_1$. It can be obtained by using the solution of the first-order non-homogeneous linear equation $\beta_{(y)} = \frac{k}{2} * y + C_1 + \frac{C_0}{y}$, quorum $C_0 = \frac{1}{2} k Y_{min}^2$. Sorting out the above formula, the following can be obtained:

$$\begin{cases} \omega_x = (ky + C_1) * x \\ \omega_y = (\frac{k}{2} y + C_1 + \frac{C_0}{y}) * y \\ \omega_z = (ky + C_1) * z \end{cases} \quad \text{(XVII)}$$

Therefore, the implicit function expression of the optimized structure is:

$$f(x, y, z) = \sin(\omega_x x)\cos(\omega_y y) + \sin(\omega_z z)\cos(\omega_x x) + \sin(\omega_y y)\cos(\omega_z z) = 0 \quad \text{(XVIII)}$$

The function expression of the periodic parameter is shown in Equation XVII. The unknown number expression in the formula is:

$$\begin{cases} k_1 = (n-1)/(Y_{max} - Y_{min}) \\ C_1 = -Y_{min} * k + 1 \\ C_0 = \frac{1}{2} k * Y_{min}^2 \end{cases} \quad \text{(XIX)}$$

To meet the mechanical requirements of the bone structure, different models were generated by adjusting the input period coefficient (n value) and the minimum (Y_{min}) and maximum (Y_{max}) cell pore sizes. Three suitable models, namely G_2x10, G_2x12, and G_4x12, were selected based on their unit cell sizes. The three models are shown in Figure 14. The specific parameters of each model are displayed in Table 2.

To verify the mechanical properties of these models, compression experiments were conducted using printed samples. To minimize experimental error, each sample

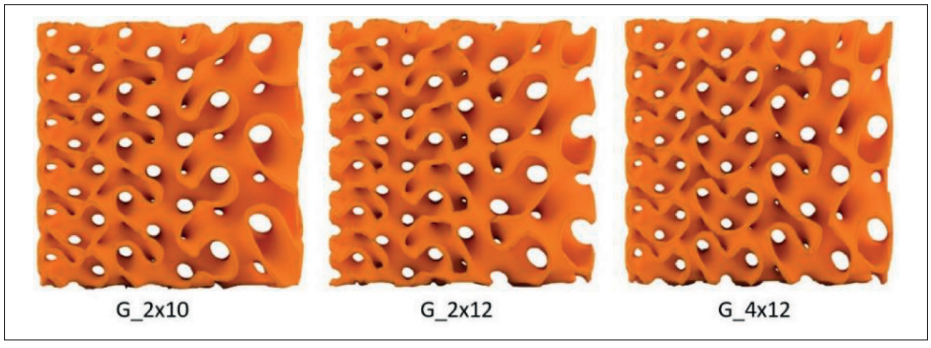

Figure 14. Optimization TPMS gradient structure model.

Table 2. Model parameters.

	n	Y_{min}	Y_{max}
G_2x10	3	2	10
G_2x12	3	2	12
G_4x12	3	4	12

underwent three tests. The stress–strain curve obtained from these experiments is depicted in Figure 15.

Based on Figure 15, it is apparent that, at a constant relative density, the three optimized models exhibit similar ultimate strength to G_II. These models are therefore more

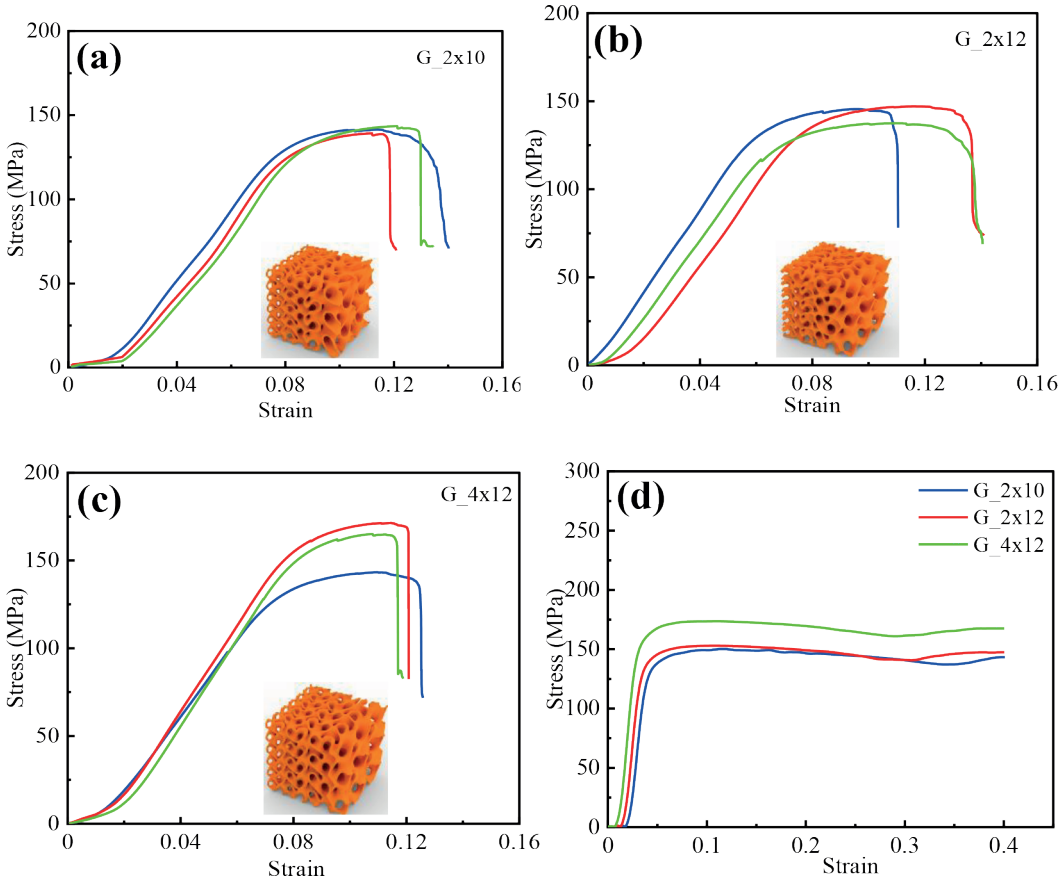

Figure 15. (a) G_2x10 stress–strain curve; (b) G_2x12 stress–strain curve; (c) G_4x12 stress–strain curve; and (d) optimized structural simulation curve.

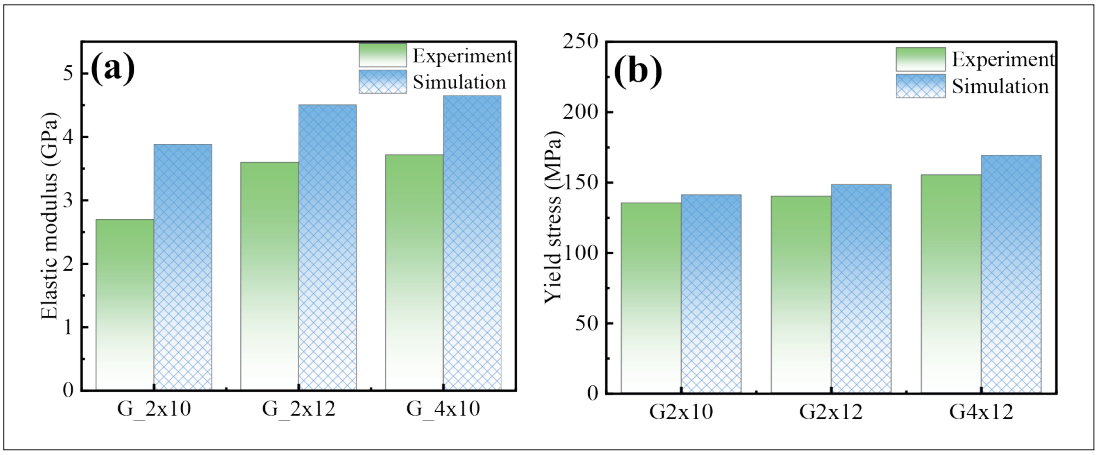

Figure 16. Comparison of experimental and simulated values of optimized structure: (a) elastic modulus and (b) yield stress.

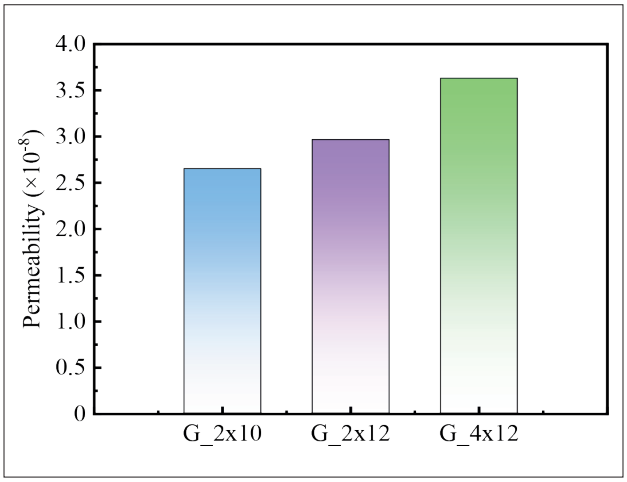

Figure 17. Comparison of optimized structure permeability.

suitable for simulating the structure of the human femur. Furthermore, due to the extensive surface area of the G surface, these models enable full contact between cells or nutrient solution and the bone during bone repair. By controlling the periodic parameters, the obtained topology optimization models replicate the changes in pore size observed in human femoral cancellous bone, thereby better simulating the real human femur and facilitating bone repair.

Comparing the stress–strain curves of the three optimized models, their shapes align with classical plastic deformation curves. The experimental and simulation results for stress–strain comparison demonstrate good agreement. The simulation error for yield strength is found to be 4.2%, verifying the accuracy of the simulation results. Figures 16 and 17 depict a comparison of the mechanical properties and permeability of the three optimized models. Based on these results, it can be concluded that G_4x12 exhibits superior mechanical properties and permeability compared to the other two models. Therefore, it is selected as the bone scaffold structure model.

5. Expected applications

In order to create bone implants suitable for human bone tissue, the G_4x12 model was optimized with good biomechanical properties and permeability. The final bone implant was manufactured using additive manufacturing. The specific process is as follows:

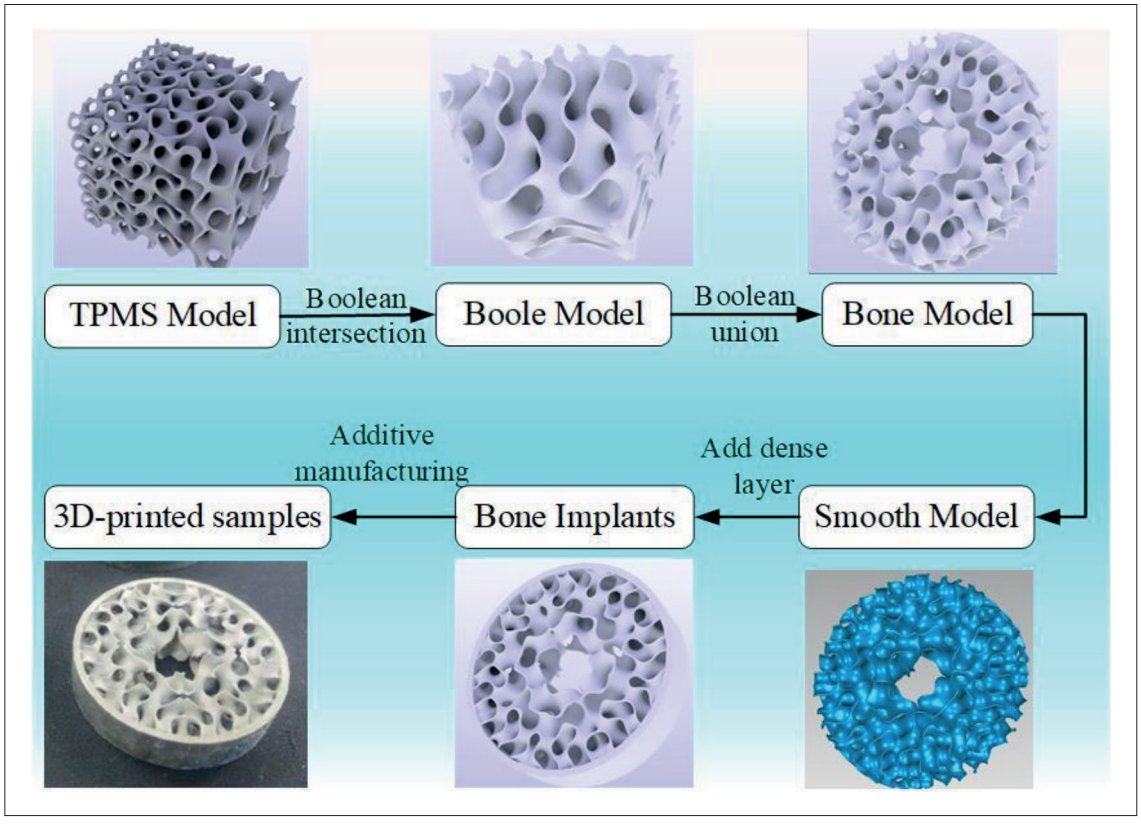

Figure 18. Design and manufacturing process of human femoral implants.

First, a hollow cylindrical space, representing a quarter of the human bone structure, was created. The G_4x12 model was generated within this space, as shown in the Boole Model in Figure 18. Next, a Boolean merge operation was performed on the resulting Boole Model to create an implant that mimics the complete structure of the human bone, as shown in the Bone Model in Figure 18. Then, Laplace smoothing method was used to smooth the joints of the Bone Model, resulting in a smoother transition and tighter connections, as shown in the Smooth Model in Figure 18. A dense bone region was added to the Smooth Model to obtain a bone implant model ready for manufacturing, as shown in the Bone Implants in Figure 18. Finally, the implant was fabricated using a metal 3D printer (L-PBF system CR-PBFM250), and Ti-6Al-4V was used as the material. The 3D-printed sample in Figure 18 showcases the physical bone implant obtained through this process.

This study provides essential information for the rational design of porous orthopedic implants using additive manufacturing. To repair necrotic or broken human femur, Figure 19 presents a personalized bone implant design process using the human femur as an example. The chart is simplified, using a model of a specific shape implant. The front-end-designed human bone implant model possesses mechanical properties that match human bones, and exhibits good permeability, meeting the requirements for bone reconstruction. This research contributes to the evaluation, development, and application of Ti-6Al-4V porous structures for orthopedic purposes.

6. Conclusion

In this study, we conducted bionic structure optimization design for bone implants. The TPMS structure was optimized through a combination of experiments and simulations. We thoroughly discussed the parametric design method, mechanical properties, and permeability of the continuously graded TPMS bionic bone structure. The key conclusions and findings are as follows:

(i) Based on the characteristics of bone structure, we established a linear function $C = 0.1954 * z + 0.3124$ and a range of z to represent the gradient change in porosity of the continuous gradient TPMS structure.

(ii) Under the same porosity change, the mechanical properties of the continuous gradient TPMS structure are significantly affected by the periodic parameter ω. The mechanical properties of the G-type continuous gradient porous structure increase initially and then decrease with increasing ω. However, the mechanical properties of the P-type continuous gradient porous structure consistently increase.

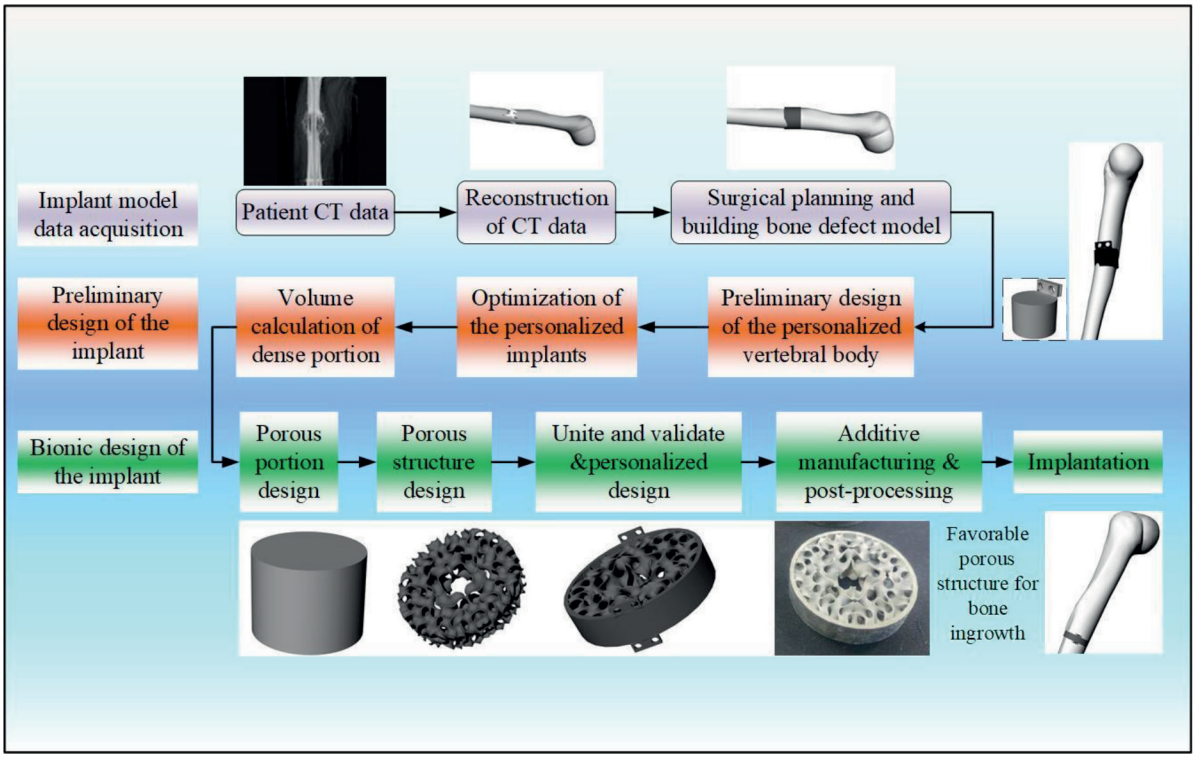

Figure 19. Flow chart of design and optimization process of personalized porous bone implant. Abbreviation: CT, computed tomography.

(iii) The streamline of the G-type continuous gradient porous structure is spiral-shaped, promoting full contact between cells, nutrient solution, and bone, and thus facilitating bone repair. Conversely, the streamline of the P-type continuous gradient porous structure is linear, resulting in insufficient contact between cells, nutrients, and bone, which hinders bone repair.

(iv) In the process of optimizing bone structure, we obtained a function to control the periodic parameter ω of the bone-like structure. The pores within the bone, from the outside to the inside along the radial direction, transition from dense to sparse. The G_4x12 model better fulfills the requirements for human bone reconstruction.

Acknowledgments

None.

Funding

This work was supported by the funding for School-Level Research Projects of the Yancheng Institute of Technology (No. XJR2020033) and the Innovative and Entrepreneurial Talent Foundation of Jiangsu Province (No. JSSCRC2021545).

Conflict of interest

The authors declare no conflicts of interest.

Author contributions

Conceptualization: Shuangyu Liu, Jinlong Feng
Formal analysis: Ping Lu, Sen Lu
Methodology: Weibo Jiang, Tatiana Mikhailovna Vasilieva
Writing – original draft: Jinlong Feng
Writing – review & editing: Shuangyu Liu, Fulong Zhang

Ethics approval and consent to participate

Not applicable.

Consent for publication

Not applicable.

Availability of data

The data that support the findings of this study are available from the corresponding author upon reasonable request.

References

1. Camacho-Alonso F, Tudela-Mulero MR, Buendía AJ, Navarro JA, Pérez-Sayáns M, Mercado-Díaz AM. Bone regeneration in critical-sized mandibular symphysis defects using bioceramics with or without bone marrow mesenchymal stem cells in healthy, diabetic, osteoporotic, and diabetic-osteoporotic rats. *Dent Mater.* 2022;38(8):1283-1300
doi: 10.1016/j.dental.2022.06.019

2. Gao C, Sow WT, Wang Y, et al. Hydrogel composite scaffolds with an attenuated immunogenicity component for bone tissue engineering applications. *J Mater Chem B.* 2021;9(8):2033-2041.
doi: 10.1039/d0tb02588g

3. Cui FZ, Zhang Y, Wen HB, Zhu XD. Microstructural evolution in external callus of human long bone. *Mater Sci Eng C.* 2000;11(1):27-33.
doi: 10.1016/S0928-4931(00)00137-5

4. Yang Y, Xu T, Zhang Q, Piao Y, Bei HP, Zhao X. Biomimetic, stiff, and adhesive periosteum with osteogenic–angiogenic coupling effect for bone regeneration. *Small.* 2021;17(14): 2006598.
doi: 10.1002/smll.202006598

5. Shimoda M, Hikasa M, Ali MA. Micropore shape optimization of porous laminated shell structures. *Addit Manuf.* 2023;69:103530.
doi: 10.1016/j.addma.2023.103530

6. Zheng X, Guo X, Watanabe I. A mathematically defined 3D auxetic metamaterial with tunable mechanical and conduction properties. *Mater Des.* 2021;198:109313.
doi: 10.1016/j.matdes.2020.109313

7. Ma S, Tang Q, Han X, et al. Manufacturability, mechanical properties, mass-transport properties and biocompatibility of triply periodic minimal surface (TPMS) porous scaffolds fabricated by selective laser melting. *Mater Des.* 2020;195:109034.
doi: 10.1016/j.matdes.2020.109034

8. Hu C, Lin H. Heterogeneous porous scaffold generation using trivariate B-spline solids and triply periodic minimal surfaces. *Graph Models.* 2021;115:101105.
doi: 10.1016/j.gmod.2021.101105

9. Li Y, Mao Q, Yin J, Wang Y, Fu J, Huang Y. Theoretical prediction and experimental validation of the digital light processing (DLP) working curve for photocurable materials. *Addit Manuf.* 2021;37:101716.
doi: 10.1016/j.addma.2020.101716

10. Zhang Z-y, Zhang H, Zhang J, Qin S-k, Duan M-d. Study on flow field characteristics of TPMS porous materials. *J Braz Soc Mech Sci Eng.* 2023;45(4):188.
doi: 10.1007/s40430-023-04113-0

11. Qiu N, Wan Y, Shen Y, Fang J. Experimental and numerical studies on mechanical properties of TPMS structures. *Int J Mech Sci.* 2024;261:108657.
doi: 10.1016/j.ijmecsci.2023.108657

12. Chen H, Han Q, Wang C, Liu Y, Chen B, Wang J. Porous scaffold design for additive manufacturing in orthopedics: a review. *Front Bioeng Biotechnol.* 2020;8:609.
doi: 10.3389/fbioe.2020.00609

13. Jones A, Leary M, Bateman S, Easton M. Parametric design and evaluation of TPMS-like cellular solids. *Mater Des.* 2022;221:110908.
doi: 10.1016/j.matdes.2022.110908

14. Yang W, An J, Chua CK, Zhou K. Acoustic absorptions of multifunctional polymeric cellular structures based on triply periodic minimal surfaces fabricated by stereolithography. *Virtual Phys Prototyp*. 2020;15(2):242-249.
doi: 10.1080/17452759.2020.1740747

15. Hu J, Wang S, Li B, Li F, Luo Z, Liu L. Efficient representation and optimization for TPMS-based porous structures. *IEEE Trans Vis Comput Graph*. 2022;28(7):2615-2627.
doi: 10.1109/TVCG.2020.3037697

16. Sychov MM, Lebedev LA, Dyachenko SV, Nefedova LA. Mechanical properties of energy-absorbing structures with triply periodic minimal surface topology. *Acta Astronaut.* 2018;150:81-84.

doi: 10.1016/j.actaastro.2017.12.034

17. Yan C, Hao L, Hussein A, Bubb SL, Young P, Raymont D. Evaluation of light-weight AlSi10Mg periodic cellular lattice structures fabricated via direct metal laser sintering. *J Mater Process Technol.* 2014;214(4):856-864.
doi: 10.1016/j.jmatprotec.2013.12.004

18. Yan C, Hao L, Hussein A, Young P. Ti–6Al–4V triply periodic minimal surface structures for bone implants fabricated via selective laser melting. *J Mech Behav Biomed Mater.* 2015;51:61-73.
doi: 10.1016/j.jmbbm.2015.06.024

19. Yan C, Hao L, Hussein A, Young P, Huang J, Zhu W. Microstructure and mechanical properties of aluminium alloy cellular lattice structures manufactured by direct metal laser sintering. *Mater Sci Eng A*. 2015;628:238-246.
doi: 10.1016/j.msea.2015.01.063

20. Nian Y, Wan S, Avcar M, Yue R, Li M. 3D printing functionally graded metamaterial structure: design, fabrication, reinforcement, optimization. *Int J Mech Sci.* 2023;258:108580.
doi: 10.1016/j.ijmecsci.2023.108580

21. Murshid SA. Bone permeability and mechanotransduction: some current insights into the function of the lacunar-canalicular network. *Tissue Cell.* 2022;75:101730.
doi: 10.1016/j.tice.2022.101730

22. Akbar I, Prakoso A, Astrada Y, et al. Permeability study of functionally graded scaffold based on morphology of cancellous bone. *Malays J Med Health Sci.* 2021;17(SUPP13):60-66.

23. Zhang X, Jiang L, Yan X, Wang Z, Li X, Fang G. Revealing the apparent and local mechanical properties of heterogeneous lattice: a multi-scale study of functionally graded scaffold. *Virtual Phys Prototyp.* 2023;18(1):e2120406.
doi: 10.1080/17452759.2022.2120406

24. Daish C, Blanchard R, Pirogova E, Harvie DJE, Pivonka P. Numerical calculation of permeability of periodic porous materials: application to periodic arrays of spheres and 3D scaffold microstructures. *Int J Numer Methods Eng.* 2019;118(13):783-803.
doi: 10.1002/nme.6037

25. Pennella F, Cerino G, Massai D, et al. A survey of methods for the evaluation of tissue engineering scaffold permeability. *Ann Biomed Eng.* 2013;41(10):2027-2041.
doi: 10.1007/s10439-013-0815-5

26. Montazerian H, Davoodi E, Asadi-Eydivand M, Kadkhodapour J, Solati-Hashjin M. Porous scaffold internal architecture design based on minimal surfaces: a compromise between permeability and elastic properties. *Mater Des.* 2017;126:98-114.
doi: 10.1016/j.matdes.2017.04.009

27. Ma S, Tang Q, Feng Q, Song J, Han X, Guo F. Mechanical behaviours and mass transport properties of bone-mimicking scaffolds consisted of gyroid structures manufactured using selective laser melting. *J Mech Behav Biomed Mater*. 2019;93:158-169
doi: 10.1016/j.jmbbm.2019.01.023

28. Asbai-Ghoudan R, Ruiz de Galarreta S, Rodriguez-Florez N. Analytical model for the prediction of permeability of triply periodic minimal surfaces. *J Mech Behav BiomedMater.* 2021;124:104804.
doi: 10.1016/j.jmbbm.2021.104804

29. Montazerian H, Mohamed MGA, Montazeri MM, et al. Permeability and mechanical properties of gradient porous PDMS scaffolds fabricated by 3D-printed sacrificial templates designed with minimal surfaces. *Acta Biomater.* 2019;96:149-160.
doi: 10.1016/j.actbio.2019.06.040

30. Varley MC, Neelakantan S, Clyne TW, Dean J, Brooks RA, Markaki AE. Cell structure, stiffness and permeability of freeze-dried collagen scaffolds in dry and hydrated states. *Acta Biomater.* 2016;33:166-175.
doi: 10.1016/j.actbio.2016.01.041

31. Al-Ketan O, Abu Al-Rub RK. Multifunctional mechanical metamaterials based on triply periodic minimal surface lattices. *Adv Eng Mater.* 2019;21(10):1900524.
doi: 10.1002/adem.201900524

32. Rajagopalan S, Robb RA. Schwarz meets Schwann: Design and fabrication of biomorphic and durataxic tissue engineering scaffolds. *Med Image Anal.* 2006;10(5):693-712.
doi: 10.1016/j.media.2006.06.001

33. Yan X, Rao C, Lu L, Sharf A, Zhao H, Chen B. Strong 3D printing by TPMS injection. *IEEE Trans Vis Comput Graph*. 2020;26(10):3037-3050.
doi: 10.1109/TVCG.2019.2914044

34. Hu B, Wang Z, Du C, et al. Multi-objective Bayesian optimization accelerated design of TPMS structures. *Int J Mech Sci.* 2023;244:108085.
doi: 10.1016/j.ijmecsci.2022.108085

35. Wang G, Shen L, Zhao J, et al. Design and compressive behavior of controllable irregular porous scaffolds: based on voronoi-tessellation and for additive manufacturing. *ACS Biomater Sci Eng.* 2018;4(2):719-727. doi: 10.1021/acsbiomaterials.7b00916

36. Al-Ketan O, Rowshan R, Abu Al-Rub RK. Topology-mechanical property relationship of 3D printed strut, skeletal, and sheet based periodic metallic cellular materials. *Addit Manuf.* 2018;19:167-183. doi: 10.1016/j.addma.2017.12.006

37. Ali D, Ozalp M, Blanquer SBG, Onel S. Permeability and fluid flow-induced wall shear stress in bone scaffolds with TPMS and lattice architectures: a CFD analysis. *Eur J Mech.* 2020;79:376-385. doi: 10.1016/j.euromechflu.2019.09.015

38. Bezsonov E, Kashirskikh D, Glanz V, Orekhov A. Sialidase-induced desialylation of blood plasma low-density lipoproteins in mice. *Atherosclerosis*. 2023;379:S72. doi: 10.1016/j.atherosclerosis.2023.06.279

39. Pires T, Santos J, Ruben RB, Gouveia BP, Castro APG, Fernandes PR. Numerical-experimental analysis of the permeability-porosity relationship in triply periodic minimal surfaces scaffolds. *J Biomech.* 2021;117:110263. doi: 10.1016/j.jbiomech.2021.110263

40. Ashman RB, Rho JY. Elastic modulus of trabecular bone material. *J Biomech.* 1988;21(3):177-181. doi: 10.1016/0021-9290(88)90167-4

41. Pawlikowski M, Skalski K, Bańczerowski J, Makuch A, Jankowski K. Stress–strain characteristic of human trabecular bone based on depth sensing indentation measurements. *Biocybern Biomed Eng.* 2017;37(2):272-280. doi: 10.1016/j.bbe.2017.01.002

42. Agnelli J, Colombo M, Morroni M, Bignotti F, Baldi F. Mechanical behaviour of cancellous bone tissues used for the manufacturing of heterologous bone grafts. *Biomed Eng Adv.* 2023;5:100073. doi: 10.1016/j.bea.2023.100073

43. Wang X, Xu S, Zhou S, et al. Topological design and additive manufacturing of porous metals for bone scaffolds and orthopaedic implants: a review. *Biomaterials*. 2016;83:127-141. doi: 10.1016/j.biomaterials.2016.01.012

ACCSCIENCE PUBLISHING

International Journal of Bioprinting

RESEARCH ARTICLE

3D-bioprinted cell-laden blood vessel with dual drug delivery nanoparticles for advancing vascular regeneration

Eun Ji Lee[1,2†], Jaewoo Choi[1,2†], Hye Ji Lim[1,2], Deokhyeon Yoon[1,2], Dong Myoung Lee[1,2], Donggu Kang[3], Jeong-Seok Lee[3], Hojun Jeon[3], Kyeong Hyeon Lee[4], Yong-Il Shin[4,5], Sang-Cheol Han[6], Woong Bi Jang[1,2*], and Sang-Mo Kwon[1,2*]

[1]Laboratory for Vascular Medicine and Stem Cell Biology, Department of Physiology, Medical Research Institute, School of Medicine, Pusan National University, Yangsan, Republic of Korea

[2]Convergence Stem Cell Research Center, Pusan National University, Yangsan, Republic of Korea

[3]Research Institute of Additive Manufacturing and Regenerative Medicine, Baobab Healthcare Inc., 55 Hanyangdaehak-Ro, Ansan, Gyeonggi-do, South Korea

[4]Science of Convergence, School of Medicine, Pusan National University, Yangsan, Republic of Korea

[5]Department of Rehabilitation Medicine, Pusan National University Yangsan Hospital, Yangsan, Republic of Korea

[6]CEN Co., Ltd., Nano-Convergence Center, 761 Muan-ro, Miryang, Republic of Korea

(This article belongs to the *Special Issue: Nano-enabled 3D Bioprinting for Various Tissue Engineering*)

Abstract

Vascular regeneration plays a critical role in the treatment of cardiovascular diseases and in tissue engineering applications. In this study, we fabricated and characterized statin/curcumin-loaded nanoparticles for potential applications in vascular regeneration. The nanoparticles exhibited consistent spherical shape and sizes, indicating reproducibility and stability of the fabrication process. The sustained release of the loaded drugs from the nanoparticles indicated their suitability for controlled and prolonged drug delivery. Biocompatibility assessments revealed that the nanoparticles were nontoxic even at high concentrations and over extended periods. Moreover, the incorporation of statin within the nanoparticles enhanced the proliferative capacity and functional abilities of endothelial progenitor cells, thereby promoting angiogenesis and vascular repair. Co-administration of curcumin with statin further augmented the therapeutic effects by reducing intracellular reactive oxygen species levels and providing antioxidant protection against oxidative stress. Furthermore, we successfully integrated these nanoparticles into artificial blood vessels (ABVs) using three-dimensional printing technology, creating customizable constructs capable of supporting vascular regeneration. The viability and proliferative capacity of cells within the ABVs were preserved, which has potential for targeted drug delivery and localized therapy. In *in vivo* models of hindlimb ischemia, transplantation of nanoparticle-loaded ABVs resulted in significant improvements in terms of recovery speed and blood flow. Histological analysis confirmed the enhanced expression of vascular-related markers, indicating improved angiogenesis. Collectively, our findings demonstrate the potential of statin/curcumin-loaded nanoparticles as a promising approach for vascular tissue engineering and regenerative medicine. These nanoparticles offer controlled drug delivery, biocompatibility, and enhanced regenerative properties, suggesting that

†These authors contributed equally to this work.

***Corresponding authors:**
Woong Bi Jang
(jangwoongbi@naver.com)

Sang-Mo Kwon
(smkwon323@pusan.ac.kr)

Citation: Lee EJ, Choi J, Lim HJ, et al. 3D-bioprinted cell-laden blood vessel with dual drug delivery nanoparticles for advancing vascular regeneration. *Int J Bioprint.* 2024;10(2):1857.
doi: 10.36922/ijb.1857

Received: September 18, 2023
Accepted: November 17, 2023
Published Online: January 12, 2024

they are valuable tools for promoting vascular regeneration and advancing therapeutic interventions for cardiovascular diseases. Further research is required to fully elucidate the mechanisms of action and optimize their clinical applications.

Keywords: 3D Bioprinting; Nanoparticles; Artificial blood vessels; Atorvastatin; Curcumin

1. Introduction

Vascular diseases encompass a wide variety of conditions affecting blood vessels and present significant challenges to modern healthcare. From atherosclerosis to peripheral arterial disease, these disorders can lead to severe complications and increase the risk of life-threatening events such as heart attack and stroke.[1-5] Thus, there is a growing need for innovative approaches that can address these conditions more effectively and provide novel methods for treatment and prevention.[6-8] Traditional treatment methods, such as drugs, aim to prevent or manage vascular diseases by strengthening blood vessel function, lowering blood pressure, and preventing blood clot formation. Although these approaches offer preventive benefits, they do not provide a comprehensive treatment strategy for vascular diseases.[9-12] Surgical interventions, including the use of stents, catheters, and artificial blood vessels (ABVs), are often performed in severe cases of vascular diseases. These interventions can deliver immediate therapeutic efficacy by improving the blood flow. However, they have some limitations. Issues such as restenosis (re-narrowing of the blood vessels) after surgery and the challenge of fully restoring non-functional blood vessels limit their long-term effectiveness.[13-16] The emergence of cell therapy products as next-generation treatment strategies holds promise for addressing the limitations of traditional approaches. Cell therapies aim to utilize cells that can repair damaged blood vessels and promote the formation of new blood vessels.[17-20] However, current cell therapies face challenges related to limited cell transplantation ability and the capacity for multipotent angiogenesis (the formation of new blood vessels from pre-existing ones).[21-23]

Among the available approaches, ABVs have been the focal point of research within the medical field, with a primary objective of evaluating and enhancing their performance and safety compared to natural vessels. These ABVs come in various types, including synthetic versions typically composed of thermosensitive polymers and biological constructs crafted from actual tissues. The advantages of ABVs include customization for individual patients, cost-effectiveness in some cases, and compatibility for transplantation. However, the application of ABVs is limited by the risk of infection and potential endothelial cell deficiencies in synthetic variants. Ongoing research strives to overcome these limitations, aiming to improve the utility and safety of artificial blood vessels in medical applications.[24-27] An innovative approach that combines drugs, ABVs, surgical interventions such as stents or catheters, and cell therapies to achieve maximum efficiency by accentuating their respective strengths and while overcoming their weaknesses is garnering increasing attention.[28-30] Prior to the inception of three-dimensional (3D) printing technology, the concept of utilizing combination therapy of drugs and cells in vascular disorder treatments prevailed.[31-33] The technological advancements in 3D printing have led to significant progress in the development of ABVs loaded with cells. Blood vessels consist of various cell types and multiple layers. The transplantation of 3D-printed ABVs alone is fraught with limitations in terms of durability, performance, and regenerative capacity compared to natural blood vessels.[34-36] To address these limitations, cell incorporation is executed during the production of ABVs to heighten their resemblance to native tissue so as to enhance blood vessel regeneration and improve their compatibility.[37-39] For this reason, studies on printing cells loaded with drugs to improve cell functions have been conducted.[40-43] However, maximizing the therapeutic efficacy of transplanted ABVs remains challenging.

Transplantation for ischemic diseases triggers substantial alterations in the surrounding microenvironment. These changes stem from various factors, including diminished oxygen levels resulting from blood loss during the transplantation process under ischemic conditions.[44-46] Additionally, the induction of inflammation and immune responses within the microenvironment occurs as immune cells are recruited to the transplant site, leading to heightened oxidative stress.[45,47,48] These factors collectively impact tissue damage and cellular interactions within the microenvironment. Understanding these intricate microenvironmental alterations is imperative to facilitate the recovery process following transplant surgery in ischemic diseases. Among these dynamic changes, the increased level of reactive oxygen species (ROS) is the prime issue to tackle with. During transplantation, the graft may experience ischemia-reperfusion injury, a condition where the blood supply to the graft is temporarily reduced (ischemia) and then restored when it is connected to the

recipient's circulatory system (reperfusion). This abrupt change in oxygen supply can trigger the production of ROS.[49-51] Additionally, the inflammatory response and immune reactions against the graft contribute to elevated ROS levels, as immune cells generate ROS as part of their defense mechanisms.[48,52,53] Moreover, surgical trauma and tissue manipulation during the transplantation process can disrupt the tissue's natural antioxidant defenses, further promoting oxidative stress. Despite the remarkable effectiveness of ABVs, cells often struggle to adapt to the ROS or hypoxic environment at transplant sites.[54-56] This limitation hinders the translation of their superior efficacy into clinical applications. Therefore, understanding and managing ROS levels during transplantation are of paramount importance to enhance graft survival and overall transplant outcomes.

Curcumin, which enhances the antioxidant and anti-inflammatory responses of cells, has been used to help cells adapt to the microenvironment.[57-59] In this study, we combined curcumin with statin to enhance cell function. Statins, commonly prescribed to lower cholesterol levels, have shown remarkable protective effect on cardiovascular system by reducing plaque formation and inflammation within blood vessels. When statin is applied to endothelial progenitor cells, it enhances nitric oxide production for vasodilation, promotes cell differentiation and maturation, suppresses inflammation, and fosters vascular growth. These mechanisms collectively safeguard vascular health by improving function, promoting restoration, and ensuring endothelial integrity.[60-62]

Cutting-edge nanotechnological techniques have been employed to optimize the delivery and effectiveness of statins and curcumin. While loading two different drugs, the difference in molecular weights and size polarity gives rise to a problem in merging and processing. Encapsulating these substances within nanoparticles has several advantages, including enhanced bioavailability, controlled release, similar characteristics, and targeted delivery. This nanoparticle-based approach not only improves the efficiency of the drug achieved with slow, sustained release of the drug, but also minimizes potential side effects.[63-67] The integration of these advanced techniques seeks to overcome the limitations of the existing treatment methods. Previous investigations were conducted utilizing ABVs and statin-loaded nanoparticles. However, ABVs and statin in isolation present certain limitations. To address these limitations, we encapsulated the drug within nanoparticles and subsequently loaded these nanoparticles into an ABV to validate the efficacy.[68] By combining the benefits of nanoparticle function-enhancing substances, nanoparticles loaded with antioxidant and anti-inflammation substances, stem cells, and 3D printing, it is anticipated that the fundamental challenges of vascular diseases, including the restoration of blood vessel functionality and promotion of angiogenesis, can be addressed more effectively.

2. Materials and methods

2.1. Preparation of nanoparticles, statin-loaded nanoparticles, and curcumin-loaded nanoparticles

Nanoparticles were synthesized using a modified version of a previously reported method.[69] In this procedure, 0.5 g of cetyltrimethylammonium bromide (CTAB) was dissolved in 1000 mL of deionized water, and 2 mL of 1 M NaOH was added with continuous stirring. Next, 1 mL of tetraethyl orthosilicate (TEOS) and 0.1 g of N-(2-aminoethyl)-3-aminopropyltrimethoxy silane (AEAPTMS) were separately dissolved in ethanol in a 1:5 volume ratio and 1:5 weight ratio, respectively, and added to the solution. The resulting mixture formed a white precipitate, which was filtered, washed, and dried at 80°C for 48 h. To remove CTAB, the dried precipitate was dispersed in 100 mL of ethanol, and 0.3 g of NH_4NO_3 was added to the solution. The mixture was stirred at 60°C for several hours, and the precipitate was filtered out and dried at 60°C for 12 h. Subsequently, 0.2 g of $ZnCl_2$ was dissolved in deionized water, and the obtained precipitate was added to the zinc solution. The solution was then dried using a rotary evaporator. The resulting powder was further processed by centrifugation, followed by multiple washes with water and ethanol, drying at 80°C for 12 h, and finally calcination at 55°C for more than 5 h. This product was labeled as nanoparticle (NP). To prepare statin-loaded nanoparticle (NPS) and curcumin-loaded nanoparticle (NPC), 80 mg of NP was dissolved in 80 mL of ethanol and dispersed with ultrasonic waves for 3 min. Simultaneously, 20 mg of statin and curcumin were dissolved in 20 mL of ethanol and mixed at 300 rpm for 3 min. The two solutions were then depressurized under vacuum for 1 h at a pressure of 100 bar. Subsequently, the pressure was lowered to 60 bar and maintained for 30 min before the sample was dried under vacuum at room temperature for 6 h. The resulting products containing statin and curcumin were denoted as NPS and NPC, respectively.

2.2. Characterization of particle size, polydispersity, and composition

Electron microscopy was conducted to qualitatively assess the size and polydispersity of NP, NPS, and NPC. While preparing sample for bio-transmission electron microscope (Bio-TEM; Talos L120C TEM, Thermo Fisher Scientific, Carlsbad, CA, USA), 100 μL of the particles sample in deionized water was dropped on copper grid (FCF200-

CU-50, Electron Microscopy Sciences, USA), and the grid was dried at room temperature at 24 h. All images were recorded using a Gatan 4k × 4k Thermo Scientific Ceta CMOS. The dimensions of the images acquired within each grid were quantified using the ImageJ analysis program and visually represented through a size distribution graph. While preparing sample for transmission electron microscope-energy dispersive spectrometer (TEM-EDS; Talos F200X, Thermo Fisher Scientific, Carlsbad, CA, USA), 100 µL of the particles sample in methanol was dropped on copper grid (FCF200-CU-50, Electron Microscopy Sciences, USA) and washed with deionized water twice. To observe the sample, the grid was dried at room temperature for 24 h. The composition of rapamycin, NP, and NPR was analyzed with Fourier transform infrared (FTIR) spectroscopy. The FTIR spectra of the samples were generated by Nicolet 560 FTIR spectroscope (Nicolet Co., Madison, WI, USA) with 4.0 cm^{-1} resolution and 16 scans ranging from 4000 to 750 cm^{-1}.

2.3. Zeta potential analysis of NP, NPS, and NPC

The zeta potential in NP, NPS, and NPC was measured using Zetasizer Nano ZS (Malvern Instruments). The evaluation of zeta potential was performed based on the principle of electrophotoretic light scattering. A dip cell (zen1002, Malvern Instruments, Malvern, UK) with a pair of parallel palladium electrodes was used to provide electrical trigger on charged particles. The experiments were performed in triplicate, and the data were analyzed using Zetasizer Software.

2.4. Determination of drug release

We prepared calibration standard solutions by diluting NPS and NPC in distilled water, yielding the first standard solution of 10 mg/mL, which was further diluted with methanol to final concentrations of 10, 50, and 100 ppb. The samples were prepared by diluting and soaking NPS and NPC in distilled water, yielding solutions at a concentration of 1 mg/mL, for 7 days prior to releasing. The released samples were filtered with a pore filter (pore size: 0.22 µm). The filtered solution was centrifuged at 10,000 × g for 10 min, and the supernatant was diluted with methanol to a final concentration of 0.01 mg/mL. QTRAP 6500 + low-mass liquid chromatography/mass spectrometry (LC/MS) system (SCIEX, Canada) was used to analyze the cumulative release of NPS and NPC.

2.5. Isolation of endothelial progenitor cells and cell culture

Human endothelial progenitor cells (EPCs) were isolated from human umbilical cord blood as previously described.[70] Briefly, human umbilical cord blood was collected from healthy volunteers after obtaining informed consent according to the protocol approved by the Institutional Review Board of Pusan National University Yangsan Hospital, Republic of Korea (Approval No. PNUYH-05-2017-053). Total mononuclear cells were isolated with Ficoll (GE Healthcare, Buckinghamshire, UK) gradient density centrifugation of human umbilical cord blood. Freshly isolated cells were cultured in endothelial growth medium-2 (EGM-2) supplemented with 5% fetal bovine serum (FBS), human vascular endothelial growth factor (VEGF), human basic fibroblast growth factor, human epidermal growth factor, human insulin-like growth factor 1, ascorbic acid, and GA-1000 (Lonza, Walkersville, MD, USA). The cultures were maintained at 37°C in a 5% CO_2 humidified atmosphere. After 4 days of culture, non-adherent cells were discarded, and the attached cells were further cultured. The cells were subjected to long-term culture to allow the formation of spindle-shaped colonies, and the medium was replenished every 14–21 days. Flow cytometric analysis performed to characterize several surface and pivotal functional markers confirmed that the EPCs were positive for endothelial lineage markers (CD31 and VEGFR2) and hematopoietic stem cell markers (CD34, CXCR4, and c-Kit), and negative for hematopoietic markers such as CD11b, CD14, and CD45.

2.6. Cell viability assay

The viability assay for EPCs was conducted using a cell counting kit-8 (CCK-8) (Dongin, CCK-3000, Seoul, Republic of Korea), according to the manufacturer's instructions. For the analysis of cell toxicity, 5000 cells/well were seeded into each 96-well plate, the medium was replaced with fresh medium containing NP, NPS, and NPC at various concentrations, and the cells were incubated for 24, 48, and 72 h. After incubation, the medium was replaced with 100 µL of 1:10 diluted CCK-8 solution. The plates were then incubated for an additional 1 h. Absorbance was measured at 450 nm using a spectrophotometer (TECAN, Grodig, Austria). Each experiment was repeated at least three times.

2.7. Proliferation assay

To evaluate the proliferation of EPCs, Click-iT® Plus EdU Alexa Fluor® 488 Imaging Kit (C10637; Thermo Fisher Scientific) that uses modified 5-ethynyl-2'-deoxyuridine (a nucleoside analog of thymidine), which can be efficiently incorporated into newly synthesized DNA, was used. For the analysis of cell proliferation, 10,000 cells/well were seeded into each 8-well chamber (154534, Thermo Fisher Scientific, Carlsbad, CA, USA) and pre-conditioned with NP, NPS, and NPC in EGM-2 media for 24 h. The samples were incubated for 2 h in EdU solution and processed according to the manufacturer's instructions. The labeling index was evaluated as EdU-labeled nuclei relative to 4',6-diamidino-2-phenylindole (DAPI)-stained nuclei.

2.8. Tube formation assay

Tube formation assay was performed to assess the function of EPCs in the formation of blood vessel-like structures (tubes). 96-well plates were coated with 65 μL of Matrigel (BD Biosciences, San Diego, CA) and incubated at 37°**C** for 30 min. Afterward, 5000 cells were seeded into each well of a Matrigel-coated 96-well plate. After a 3-h incubation, the plate was examined every hour for tube formation. The total tube length was measured using ImageJ software.

2.9. Migration assay

Migration assay was performed using a 24-well 8.0 μm polycarbonate Transwell chamber consisting of a permeable membrane (Corning Inc., Corning, NY, USA). For the assay, 500 μL of EGM-2 media was added below the cell permeable membrane, while 10,000 cells/100 μL in EBM-2 medium were plated on the upper chamber of the permeable membrane. After 24 h of incubation, the migrated cells were fixed with 4% paraformaldehyde and stained with 0.5% crystal violet at room temperature. The upper chamber was washed, and the top of the membrane was examined for cell migration. The cells were observed under an inverted microscope after mounting, and the number of cells was counted.

2.10. Measurement of intracellular ROS levels

Intracellular ROS levels were measured using the 2′,7′-dichlorodihydrofluorescein diacetate (H_2DCFDA) kit (Thermo Fisher Scientific, Carlsbad, CA, USA). After incubation, the EPCs were harvested and washed with 2% FBS and 200 μM ethylenediaminetetraacetic acid (EDTA) in PBS. After centrifugation at 2000 ×g for 3 min, the pellet was suspended in 10 μM H_2DCFDA in PBS containing 2% FBS and 200 μM EDTA and incubated for 1 h at 37°C in 5% CO_2 atmosphere. Following which, the cells were washed with PBS and analyzed by flow cytometry using the BD Accuri C6 software (BD Biosciences, New Jersey, USA).

2.11. Preparation and mechanical property evaluation of 3D-bioprinted artificial blood vessel

To prepare bioinks, sodium alginate (viscosity >2000 cP, 25°C; Sigma-Aldrich, St. Louis, MO, USA) in Dulbecco's phosphate-buffered saline (DPBS, Gibco, Grand Island, USA) was prepared and stirred for 6 h at 37°C. Next, an atelocollagen solution (pH 4.0; Baobab Healthcare, Gyeonggi-do, Republic of Korea) was mixed with reconstituted buffer (132 mM Na_2HPO_4) at a volume ratio of 1:1 for neutralization.

Vascular printing was performed using a coaxial nozzle (inner needle, 28 G; outer needle, 20 G; Ramé-hart, Succasunna, NJ, USA) equipped with a 3D bioprinter (Root 1; Baobab Healthcare, Gyeonggi-do, Republic of Korea). For the shell material, bioinks were prepared by combining 3% w/v neutralized atelocollagen and 3% w/v alginate at a 4:1 ratio. NPS and NPC (6 mg/500 μL each) were then blended with the shell bioinks (3 mL), resulting in a final concentration of 2 mg/mL for both NPS and NPC in the bioink. Similarly, NP was mixed with the shell bioink as the control group. For the core material, 40% w/v Pluronic F-12 (Sigma-Aldrich) with 100 mM calcium chloride was used as the sacrificial material. For vascular cell printing, the shell material was blended with EPCs (1×10^6 cells/mL). NP, NPS, and NPC without cells were used as controls. The core-shell bioinks were bioprinted at 80 kPa (core) and 60 kPa (shell) using a 200 mM $CaCl_2$ solution to enable *in situ* crosslinking of the alginate solution. Subsequently, the printed vessel was rinsed with DPBS and incubated at 37°C for 1 h. The sacrificial material (core bioink) was removed using ice-cold DPBS. One side of the ABV was set to circulate water with the aid of a circulation pump (MasterFlex L/S, Masterflex, Germany), while the other side was attached to a digital pressure gauge to measure the burst pressure of the ABV. The burst pressure was measured at the point right before ABV rupture, and the burst pressure of cell-laden ABV was measured after 7 days of cultivation.

2.12. Live/dead cell assay

Calcein acetoxy methylester (calcein AM) and ethidium homodimer-2 (InvitrogenTM Life Technologies, Carlsbad, CA, USA) dissolved in 1× PBS, at the concentration of 4 μM and 2 μM, respectively, were used. Calcein AM labels living cells with bright green fluorescence, while ethidium homodimer is a red fluorophore that stains nonviable cells since it cannot penetrate living cells. After 15 min of incubation, the samples were analyzed using a Lionheart FX automated microscope (BioTek, Winooski, VT, USA).

2.13. Fluidity test on artificial blood vessels

To assess the perfusion and patency of a 3D-printed ABV, perfusion test was conducted using pigment ink. The ABV was cut to an appropriate length, and a continuous flow of pigment ink was introduced into the vessel using a 26 G (1/2 inch) syringe. Then, the diffusion of pigment was observed.

2.14. Western blotting

Total protein was isolated from ABV using RIPA Buffer (Thermo Fisher Scientific, Waltham, MA, USA) and a protease inhibitor (Thermo Fisher Scientific, Waltham, MA, USA), according to the manufacturer's specifications. Equal amounts of protein were separated by an 8–15% sodium dodecyl sulfate polyacrylamide gel electrophoresis (SDS-PAGE). The protein bands were then transferred to a polyvinylidene fluoride (PVDF) membrane (Millipore, Billerica, MA, USA). After the membrane was blocked in 5% skim milk for 1 h at room temperature, it was incubated overnight at 4°C with primary antibodies for VE-cadherin,

Ki-67, and β-actin. After incubation with the secondary antibody, i.e., goat anti-rabbit IgG-HRP (ADI-SAB-100-J, Enzo Life Sciences, USA), the bands were visualized using Luminate Crescendo Western HRP Substrate (Millipore, Billerica, MA, USA) and an X-ray film. β-actin was used as the loading control for Western blotting experiment.

2.15. Mouse model of hindlimb ischemia

BALB/c (Nu/Nu) athymic immunodeficient mice unable to produce T cells were used as the animal model of hindlimb ischemia in which transplantation of 3D-printed bio-vessel was performed. BALB/c (Nu/Nu) mice (average weight: 20–24 g) were purchased from Orient Bio (Seongnam, Gyeonggi, Republic of Korea). All animals were housed in an air-conditioned animal room with constant relative humidity and were given access to standard food and water. Animal treatment and maintenance were performed in accordance with the Principles of Laboratory Animal Care, and animal experiments were performed in accordance with the protocols approved by the Pusan National University Institutional Animal Use and Care Committee (Approval No. PNU-2022-0212). All mice were anesthetized by an intraperitoneal injection of 400 mg/kg 2,2,2 tribromoethanol (Avertin; Sigma-Aldrich) prior to the surgical resection of femoral artery and laser Doppler perfusion imaging. The femoral artery was excised from its proximal origin at the branch of the external iliac artery to the distal point, where it bifurcated into the saphenous and popliteal arteries. Immediately after arterial ligation, ischemic hind limbs were transplanted with PBS, EPC, NP@BV (NP-loaded blood vessel), EPC@NP@BV (blood vessel loaded with EPC and NP), and EPC@NPSC@BV (blood vessel loaded with EPC, NPS, and NPC).

2.16. Measurement of blood perfusion and necrosis

Angiogenesis in mouse model with hindlimb ischemia was examined with laser Doppler perfusion imaging (LDPI; Moor Instruments Ltd, Devon, UK) at four time points: 0, 3, 7, 14, and 28 days post-induction of hindlimb ischemia. The blood perfusion levels were measured by comparing the normal right hind limb with the ischemic left hind limb at each time point. The data obtained from LDPI were analyzed using the moorLDI program, a specialized software for assessing blood flow and angiogenesis in preclinical studies. Necrosis was assessed in mice at 0 and 14 days after hindlimb ischemia induction. The extent of necrosis occurring in each animal was quantitatively measured.

2.17. Histological and immunofluorescence analyses

To perform immunostaining, the acquired hindlimb muscles were formalin-fixed, paraffin-embedded, and sectioned at 5 μm. Blood vessels were stained with antibodies for alpha smooth muscle actin (ab5694, 1:100; Abcam plc., Cambridge, UK) and CD31 (ab28364, 1:100; Abcam plc., Cambridge, UK). At first, the paraffin was melted, and the slides were washed using xylan and ethanol. Following antigen retrieval, the tissue was reacted in blocking buffer for 1 h, and the primary antibody was incubated overnight at 4°C. The specimens were incubated with Alexa Fluor 488 secondary antibodies and Alexa Fluor 594 secondary antibodies (Thermo Fisher Scientific, Carlsbad, CA, USA) for 2 h and then washed three times. Nuclei was stained with DAPI using ProLong Diamond Antifade Mountant with DAPI (Invitrogen). Stained sections were visualized using a Lionheart FX automated microscope (BioTek, Winooski, USA).

2.18. Dihydroethidium staining

Before staining with dihydroethidium (DHE; D7008, Sigma-Aldrich, Saint Louis, MO, USA), the tissue sections were rinsed with PBS and incubated with 5 mM DHE for 30 min at 37°C. Stained sections were viewed under Lionheart FX automated microscope (BioTek, Winooski, USA). The percentage of the area exhibiting DHE-positive staining out of the entire stained area was calculated.

2.19. Statistical analysis

Two-tailed unpaired Student's *t*-test and one-way analysis of variance (ANOVA) were conducted for data analyses using GraphPad Prism software (GraphPad, Inc., La Jolla, CA, USA). Data are expressed as mean ± standard deviation. Differences were considered statistically significant at $p < 0.05$.

3. Results

3.1. Fabrication and characterization of NPS and NPC

In this study, we present the design of 3D-printed artificial blood vessels loaded with nanoparticles, each containing two distinct types of drugs. Atorvastatin and curcumin were individually encapsulated within nanoparticles (Figure 1A and B). Subsequently, 3D-printed artificial blood vessels were fabricated by fusing EPCs, bioink, and nanoparticles (Figure 1C). The resulting engineered vessels were then implanted into a mouse model of hindlimb ischemia (Figure 1D).

Statin and curcumin, as a drug for functional enhancement and as an antioxidant drug, respectively, were loaded onto the nanoparticles. Characterization of pure nanoparticles (NP), NPS, or NPC was performed. Morphological analysis revealed that these nanoparticles were round in shape, and the sizes were constant for NP (282.09 nm), NPS (266.56 nm), and NPC (283.25 nm) (Figure 2A and B). Furthermore, for a more detailed characterization of NP structure, a mapping image was obtained through transmission electron microscope-energy dispersive spectrometer analysis (**Figure S1A** in

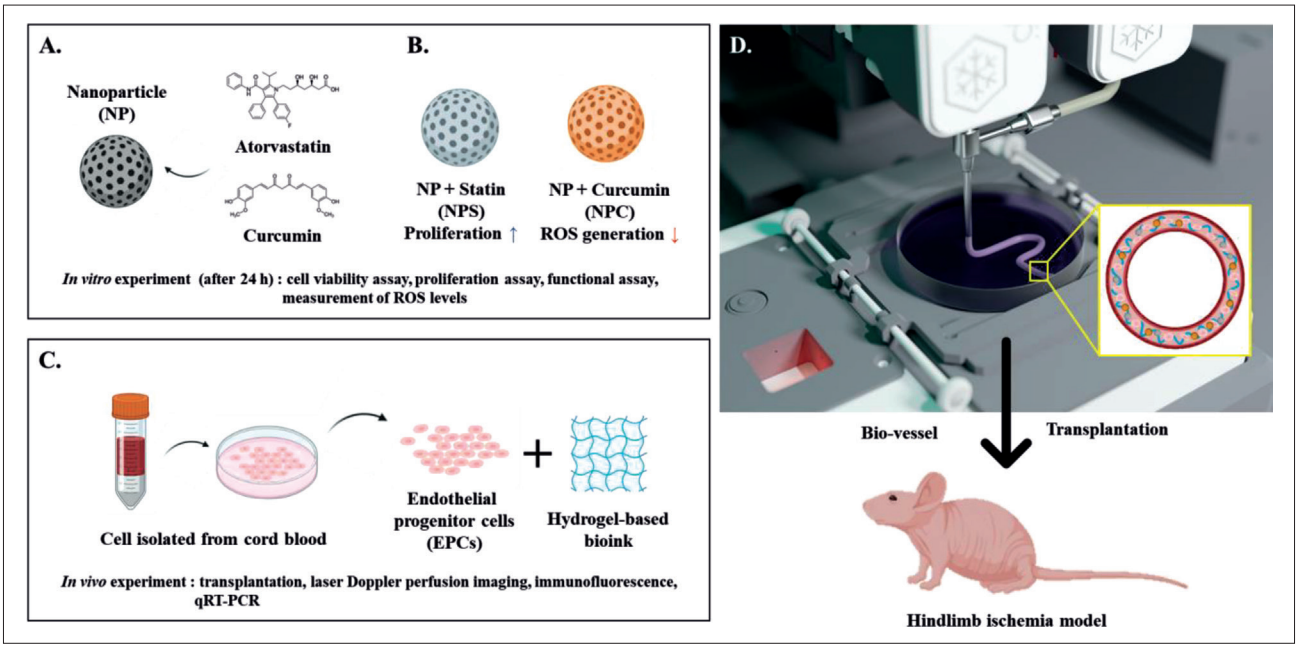

Figure 1. Design of 3D-printed artificial blood vessels (ABVs) loaded with endothelial progenitor cells (EPC) and nanoparticles containing statin and curcumin for treatment in mouse model of hindlimb ischemia. (A) Encapsulation of atorvastatin and curcumin into nanoparticles. (B) Effects of encapsulated NPS and NPC. (C, D) EPCs isolated from umbilical cord blood are combined with bioink to create an ABV, which is transplanted into a mouse model of hindlimb ischemia.

Supplementary File). The analysis confirmed that NP is primarily composed of silicon (Si), oxygen (O), and a trace amount of zinc (Zn). Further quantification of element content revealed approximate weight percentages of 43.9% Si, 53.5% O, and 2.6% Zn, and atomic percentages of 31.6% Si, 67.6% O, and 0.8% Zn (**Figure S1B** and **S1C** in Supplementary File). Based on previous data, NP, NPS, and NPC were individually characterized using FTIR spectroscopy (**Figure S1D** and **S1E** in Supplementary File). In the FTIR spectrum of NP, the presence of a symmetric stretching vibration peak at 1078 cm^{-1} was indicative of the Si-O-Si group, a characteristic feature of SiO_2.[71,72] NPS and NPC exhibited similar characteristics, with Si-O-Si wavelengths observed at 1082 cm^{-1} and 1066 cm^{-1}, respectively. This observation strongly suggests that the primary constituent of NP is SiO_2. NP characterized by this structural configuration demonstrate a loading efficiency of approximately 20% for both statin and curcumin. Zeta potential is often used as an indicator to assess the stability of a sample dispersion. The zeta potential of -16.6 mV for NP, -18.6 mV for NPS, and -20.7 mV for NPC confirmed the stability of the suspension (Figure 2C). To evaluate stability *in vivo*, the degradability of the nanoparticles was evaluated after suspension in PBS, which showed that the shape and size of the nanoparticles were maintained from days 1, 3, and 7 (Figure 2D and E). Subsequently, we performed an experiment to ascertain the quantity of drug released from the NP. Drug release conditions were established with a maximum standard of 7 days (100%), and the daily release rate was then determined. The outcome revealed a slow release of each drug loaded within the nanoparticles (Figure 2F). Overall, it was confirmed that the shape and size of each manufactured nanoparticle were constant and that the content was released from the nanoparticles in a slow but sustained manner.

3.2. *In vitro* biocompatibility assessment of NP

To confirm the cytotoxicity of the nanoparticles, the treatment was performed for each concentration and time period (Figure 3A). No cytotoxicity was observed even when the cells were treated at a high concentration of 1 μg/mL for up to 72 h (Figure 3B). Besides, we found that EPCs treated with NPS demonstrated enhanced proliferation and function. When NPS and NPC (NPSC) were co-administered, a similar tendency was observed (Figure 3C). EdU assay was performed to confirm whether this result was due to an increase in the number of proliferating cells. It was confirmed that the NP was nontoxic, and the number of proliferating cells significantly increased when treated with NPSC (Figure 3D and E). To establish the additional role of statin in enhancing the functions of EPCs, an experiment was conducted to assess blood vessel formation and migration ability. It was confirmed that tube formation (Figure 3F and G) and migration (Figure 3H and I), which are the indicators of angiogenesis, were

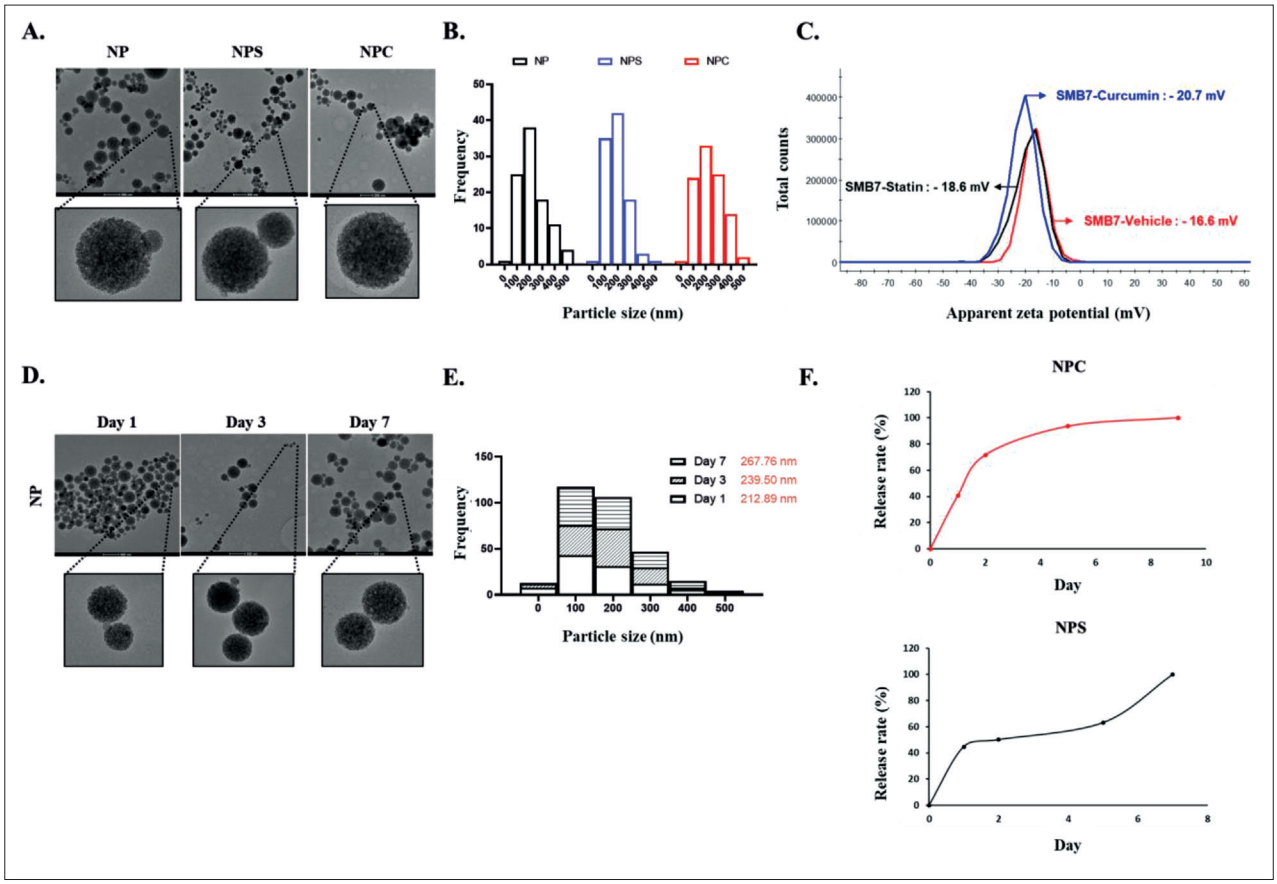

Figure 2. Characterization of statin- and curcumin-loaded nanoparticles. (A) Transmission electron microscopy (TEM) images of blank nanoparticles (NP), statin-loaded nanoparticles (NPS), and curcumin-loaded nanoparticles (NPC). (B) Size distribution graph displaying the measured size of each nanoparticle category. (C) Zeta potential analysis of NP, NPS, and NPC in phosphate-buffered saline (PBS; pH 7.4). (D) Storage stability study of NP, NPS, and NPC; size distribution was analyzed after samples were incubated for 1, 3, and 7 days at 37°C. (E) Size distribution graph displaying the measured size of each nanoparticle type after the samples were incubated for 1, 3, and 7 days at 37°C. (F) Cumulative release of statin and curcumin from nanoparticles assessed using liquid chromatography/mass spectrometry (LC/MS) analysis.

significantly increased upon treatment with NPSC. Curcumin is a type of antioxidant and can antagonize the deleterious effects of ROS. Intracellular ROS staining showed that the increased ROS level induced by hydrogen peroxide (H_2O_2) was suppressed in the NPSC group. To confirm whether the nanoparticles play a role in these effects, nanoparticles without being loaded with any of these drugs (NP) were administered (Figure 3J and K). The resistance to ROS was more pronounced in the NPSC-treated group than in the group treated with statin and curcumin.

3.3. 3D printing-based fabrication and characterization of nanoparticle-loaded artificial blood vessels

To ensure stable transplantation of nanoparticles and cells into the blood vessels, ABVs were fabricated by 3D printing (Figure 4A). The bioinks used in 3D printing (Figure 4B-i), the nozzles (Figure 4B-ii), and the printed ABVs (Figure 4B-iii) are briefly described. Artificial blood vessels, which can be customized in various sizes in terms of their external and internal diameters, can be 3D-printed as described (Figure 4C). Twenty-four hours after the fabrication of ABVs, a live/dead cell staining assay was conducted to verify the presence of cells within the luminal space of the vascular construct. In the case of blood vessels loaded with EPCs and NPS (EPC@NPS@BV), more cells were observed owing to the proliferative ability of the cells compared with the control group (EPC@NP@BV). Blood vessels loaded with EPCs and NPC (EPC@NPC@BV) were found to have a morphology similar to that of the controls. We found that the level of cell proliferation achieved in EPC@NPSC@BV was similar to that observed in NPS@BV (Figure 4D). The fabricated ABV was verified to contain intravascular cells within its internal structure. After we confirmed the presence of a vascular framework in the

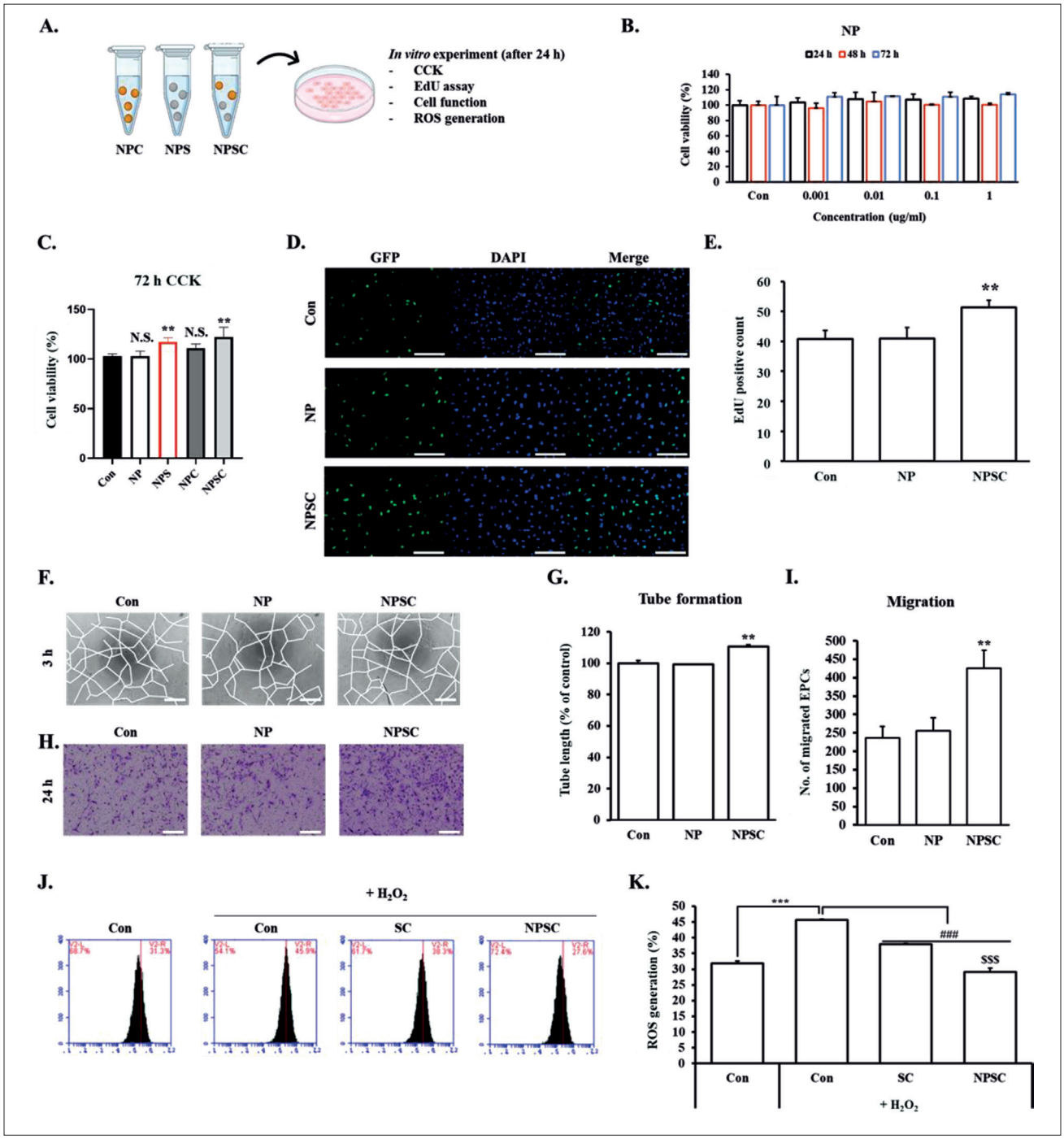

Figure 3. NPS and NPC improve the proliferation and antioxidant effect on EPCs. (A) Schematic illustration of *in vitro* experimental process for curcumin-loaded nanoparticles (NPC), statin-loaded nanoparticles (NPS), and nanoparticles-loaded statin and curcumin (NPSC). (B) EPCs viability in various concentration of blank nanoparticle (NP) ($N = 3$). (C) Cell viability after treatment with NP, NPS, NPC, and NPSC ($N = 3$). (D) Results of EdU cell proliferation assay; 200× magnification images ($N = 3$). Scale bars = 100 μm. (E) Quantification of EdU-positive cells. (F) Investigation of the tube-formation capacity of EPCs treated with NP and NPSC ($N = 3$). Scale bars = 50 μm. (G) Quantification of total tube length. (H) Investigation of the migration capacity of EPCs treated with NP and NPSC using Transwell migration assay. Scale bars = 50 μm. (I) Quantification of migrated cell. (J) ROS generation was measured using fluorescence-activated cell sorting (FACS) and 2′,7′-dichlorodihydrofluorescein diacetate (H_2DCFDA) ($N = 3$). (E) Quantification of the reactive oxygen species (ROS) generation rates using FACS data. Values are expressed as the mean ± standard derivation (SD). $^{*}p < 0.05$, $^{**}p < 0.01$, $^{***}p < 0.001$ as compared to the Con group (untreated group); $^{\#\#\#}p < 0.001$ as compared to the Con group with H_2O_2; $^{\$\$\$}p < 0.001$ as compared to the SC group (a group treated with statin and curcumin); N.S.: not significant.

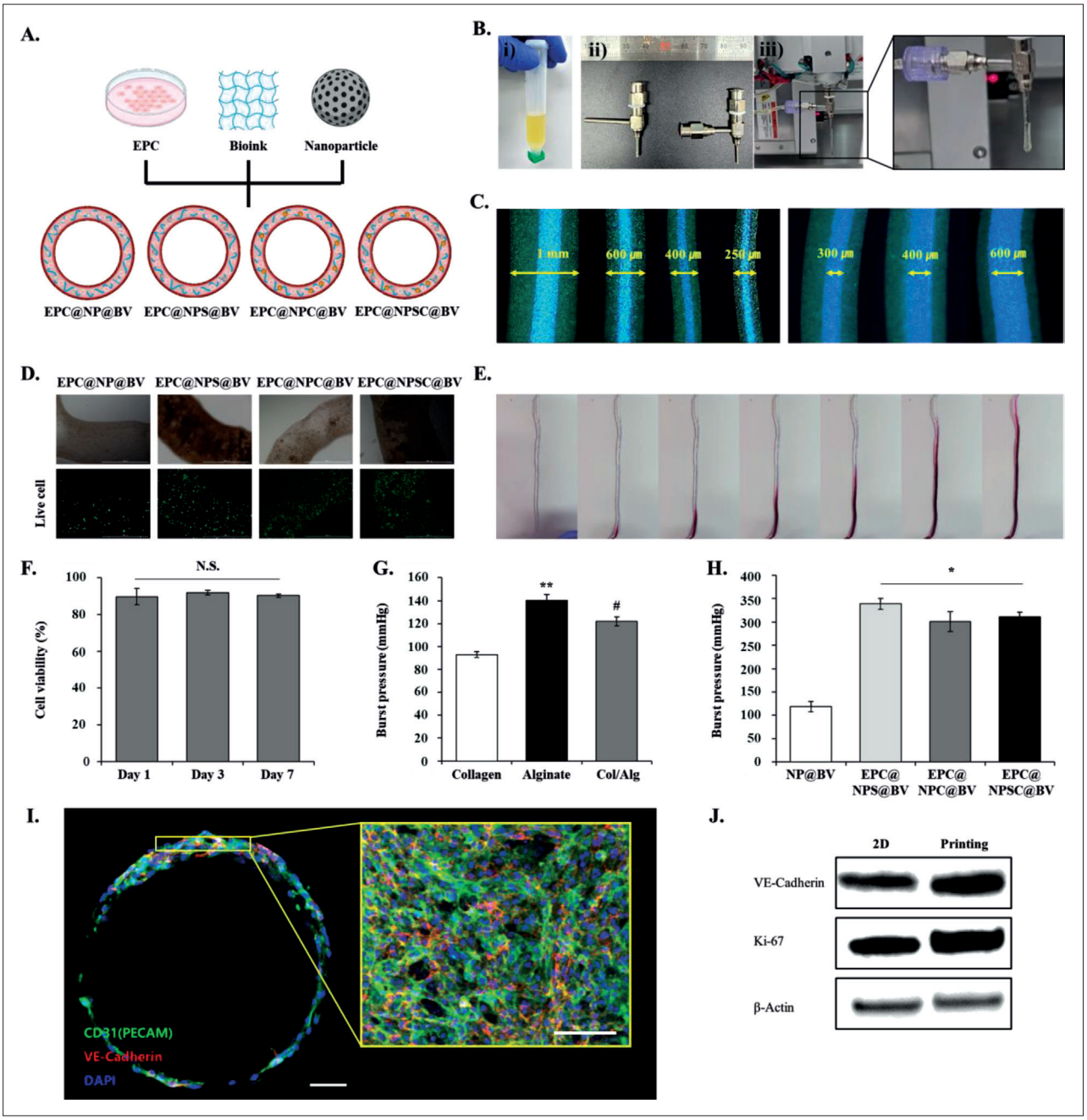

Figure 4. Characterization of 3D-printed artificial blood vessels (ABVs) loaded with endothelial progenitor cells (EPCs), statin-loaded nanoparticles (NPS), and curcumin-loaded nanoparticles (NPC). (A) Schematic illustration of 3D-printed process of ABVs with loaded EPCs and blank nanoparticles (NP), NPS, NPC, or nanoparticles loaded with statin and curcumin (NPSC). (B) Fabricating ABVs using bioink: (i) bioink, a material used in the 3D printing-based manufacture of ABVs; (ii) nozzles in different sizes; (iii) 3D printing of ABVs. (C) Microscopic images of 3D-printed ABVs containing two layers of different thicknesses, which is adjusted by using nozzles of different sizes. (D) Cell viability in groups treated with EPC@NP@BV (blood vessels loaded with EPC and nanoparticle), EPC@NPS@BV (blood vessels loaded with EPC and NPS), EPC@NPC@BV (blood vessels loaded with EPC and NPC), and EPC@NPSC@BV (blood vessels loaded with EPC, NPS, and NPC). (E) Fluidity of the 3D-printed ABVs. (F) Viability of EPCs loaded in ABV by 1, 3, and 7 days. NS indicates not statistically significant ($N = 3$). (G) Burst pressure of ABV fabricated with each bioink. $^{**}p < 0.01$ as compared to the collagen; $^{\#}p < 0.05$ as compared to the collagen ($N = 3$). (H) Burst pressure of ABV in each group NP@BV (NP-loaded blood vessel), EPC@NPS@BV, EPC@NPC@BV, and EPC@NPSC@BV on day 7 of culture. $^{*}p < 0.05$ as compared to the NP@BV ($N = 3$). (I) Expression of markers specific to EPCs, such as CD31 and VE-cadherin, in ABV was confirmed with immunofluorescence staining. (J) Western blotting of Ki-67 and VE-cadherin proteins in 2D-cultured EPCs (as "2D") and ABVs (as "printing").

fabricated ABV, we conducted an experiment to validate the blood flow through ABV, and verified that blood vessels were capable of reliable, sustained blood flow (Figure 4E). In addition to evaluating fluidity, we also investigated the impact of cell viability on blood vessel regeneration during the transplantation of cell-loaded ABV. Cell viability assessments were performed at multiple time points: 1, 3, and 7 days. The results demonstrated consistent and stable cell viability throughout the observation period, indicating the robustness of the cell-loaded ABVs in maintaining cell integrity and supporting potential tissue regeneration (Figure 4F). Further, mechanical properties of the vascular grafts such as burst pressure, compliance, and suture retention were evaluated.[25] In this study, ABVs made from alginate exhibited higher burst pressure values compared with those made solely from atelocollagen. However, due to the absence of cell adhesion ligands,[73] an ABV combining collagen and alginate was created to address the respective drawbacks of both materials (Figure 4G). Subsequently, burst pressure measurements were conducted to assess the burst pressure of cell-laden or cell-free ABVs, which were cultured for 7 days. The groups with cell-laden ABVs (i.e., EPC@NPS@BV, EPC@NPC@BV, EPC@NPSC@BV) exhibited an improvement in burst pressure of more than threefold compared to the cell-free ABV group (i.e., NP@BV) (Figure 4H). Next, to confirm continuous cell growth within the ABVs, fluorescence immunostaining was employed to assess the expression of essential EPC markers, such as CD31 and VE-cadherin (Figure 4I). Additionally, the protein-level expression of CD31 and Ki-67 was compared to that of two-dimensional (2D)-cultured EPCs. It is noteworthy that when transitioning from a 2D culture to a 3D culture environment, we observed a notable increase in the expression of endothelial cell-related markers (Figure 4J). This expression increase of these markers underscores the capacity of 3D culture systems in establishing a more physiologically relevant cellular environment. Unlike traditional 2D cultures, 3D cultures better mimic the natural microenvironment of cells within tissues and organs, allowing for improved cell–cell interactions and the formation of complex cell structures. In this context, the enhanced expression of endothelial cell-related markers suggests that our 3D culture model provides a more suitable platform for studying endothelial cell behavior and function.

3.4. *In vivo* transplantation of artificial blood vessels incorporating drugs-loaded nanoparticles in animal model

Based upon the aforementioned results, we conducted *in vivo* experiments to validate the effects of drugs encapsulated in nanoparticles. Furthermore, the stability of the 3D-printed ABVs incorporating cells and drug-loaded nanoparticles was assessed. The animal model of hindlimb ischemia created in this study was subjected to ABVs transplantation, and functional evaluation was performed (Figure 5A). When only PBS without cells or ABVs were transplanted, all hindlimbs of the treated animals were found to be necrotic. On the 14th day after transplantation, the group transplanted with ABVs without EPC or drug-loaded nanoparticles showed significant limb recovery (Figure 5B). During the follow-up period of up to 28 days, we found that the treatment effect was sustained, similar to that observed on the 14th day. Although the NP@BV group manifested excellent effect, the laser Doppler perfusion imaging results confirmed that the EPC@NPSC@BV group on day 14 showed more profound effect. Most importantly, the group transplanted with ABVs, together with cells and nanoparticles, showed the most pronounced effect from the 7th day after transplantation (Figure 5C). This strong therapeutic effect on the hindlimb was attributed to both the cells and ABVs. The efficacy of vascular endothelial cells is an important factor contributing to the recovery of hindlimb over time; however, EPC@NPSC@BV outperformed other counterparts in terms of the speed of recovery and the amount of blood flow during the recovery period. We also analyzed foot necrosis after transplantation (Figure 5D). Similar to the findings mentioned earlier, the highest incidence of necrosis was observed in the PBS and EPC groups. Notably, however, the EPC@NP@BV and EPC@NPSC@BV groups exhibited the most promising therapeutic outcomes, promoting limb recovery significantly faster than other groups (Figure 5E). This result is supported by the highest expression of α-SMA and CD31, which are vascular-related markers, observed in the EPC@NPSC@BV group (Figure 5F–I). In the final part of the experiment, we determined the presence of ROS generation within the tissue through DHE staining. We observed a significant reduction in DHE-positive staining in the EPC@NPSC@BV group, consistent with the staining results for markers associated with blood vessels (**Figure S2A** and **S2B** in Supplementary File). Taken together, these results collectively suggest the potential utility of ABVs incorporating drug-loaded nanoparticles and EPCs in mitigating the severity of ischemic diseases.

4. Discussion

Despite the advancements in drug therapy and surgical procedures for the treatment of vascular diseases, several notable disadvantages inherent in these approaches limit their long-term effectiveness. Drug therapy, while offering preventive benefits, often requires continuous administration, which may lead to side effects or drug resistance over time. Moreover, drug therapies may not

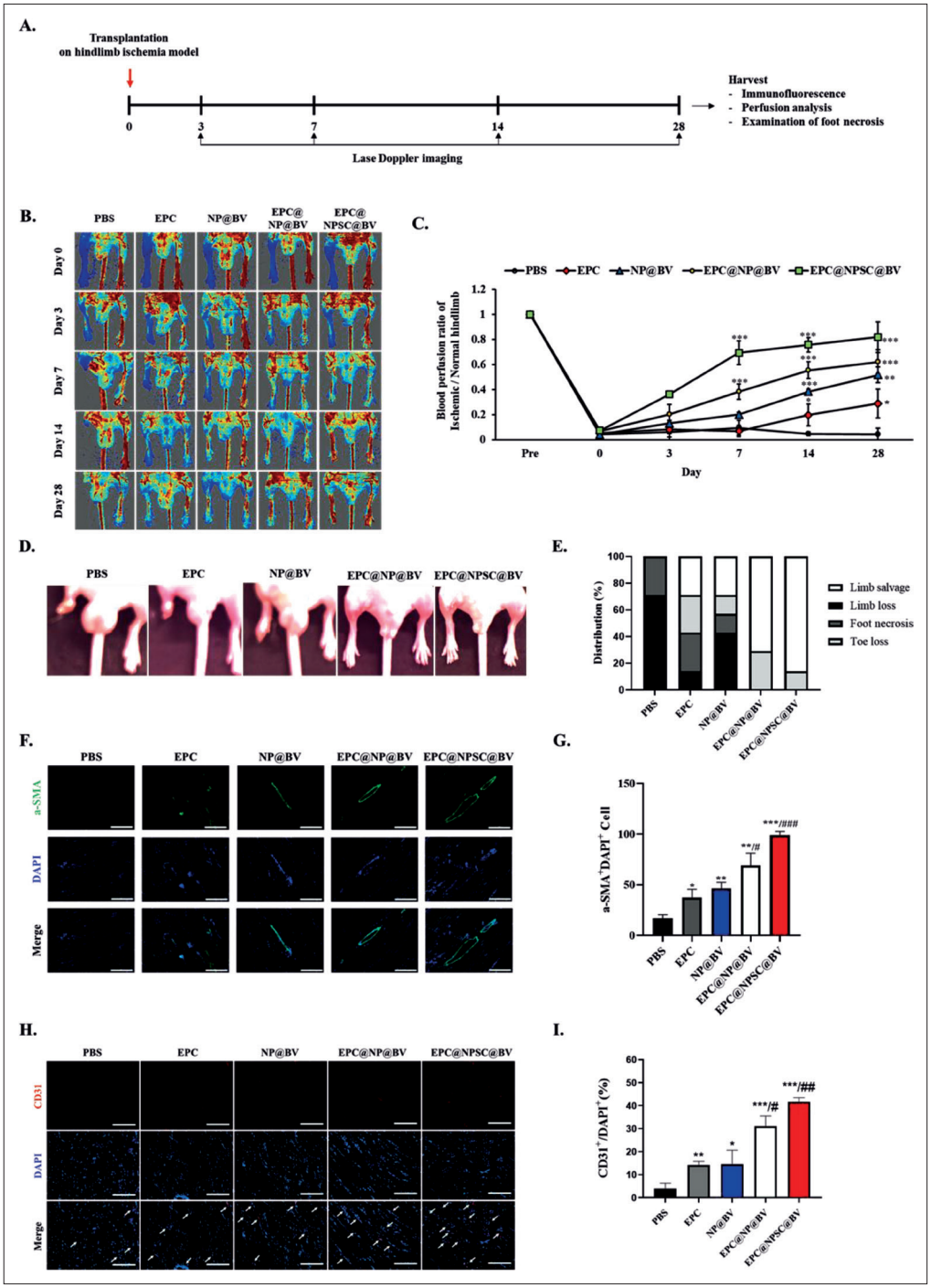

Figure 5. *In vivo* evaluation of 3D-bioprinted artificial blood vessels (ABVs) incorporating nanoparticles loaded with statin and curcumin (NPSC) in mouse model of hindlimb ischemia. (A) Schematic illustration of hindlimb ischemia model construction and ABV implantation. (B) The ratio of blood perfusion by laser Doppler imaging after phosphate-buffered saline (PBS), endothelial progenitor cells (EPC), NP@BV, EPC@NP@BV, and EPC@NPSC@BV transplantation in hindlimb ischemic model, created with BALB/c nude mice, at 0, 3, 7, 14, and 28 days post-transplantation. (C) Quantification of ratio of blood perfusion. (D) Necrosis at day 14 after ABV transplantation in a mouse model of hindlimb ischemia. (E) Quantification of necrosis. (F) Immunostaining with anti-α-smooth muscle actin (SMA) antibody (green) on ischemic limbs subjected to different treatments at 28 days post-transplantation. Scale bars = 200 μm. (G) Quantification of density of α-SMA-positive cells and DAPI-positive cells. (H) Immunostaining with anti-CD31 antibody (red) on ischemic limbs subjected to different treatments at 28 days post-plantation. Scale bars = 200 μm. (I) Quantification of density of CD31-positive cells and DAPI-positive cells. Values are expressed as mean ± standard deviation. $^{*}p < 0.05$; $^{**}p < 0.01$ versus PBS. $^{\#}p < 0.05$, $^{\#\#}p < 0.01$, $^{\#\#\#}p < 0.001$ versus NP.

be able to comprehensively address the underlying causes of vascular diseases, and their efficacy can vary among individuals.[74-76] Contrarily, surgical interventions such as the use of stents or catheters can provide immediate relief by improving blood flow. However, they can be associated with complications, including restenosis or blood clot formation, which may necessitate additional procedures. Additionally, some patients may not be suitable candidates for invasive surgery because of their underlying health conditions or anatomical complexities.[77-79] To overcome the limitations of traditional drug therapy and surgical procedures, this study was designed to leverage innovative approaches combining the strengths of nanotechnology, 3D printing, and cell therapies.

A key aspect addressed in these *in vivo* studies is the microenvironment of the implantation site, which plays a crucial role in determining the success of ABV transplantation. The ROS or hypoxic environment at the transplant site poses a challenge for the transplanted cells to adapt effectively.[54-56] To surmount this limitation, the use of curcumin, known for its antioxidant and anti-inflammatory properties, has been employed to aid cell adaptation to the microenvironment.[57-59] Additionally, the incorporation of statins, renowned for their cardiovascular protective effects, has been explored to enhance cell function and improve treatment efficacy. Nanotechnology plays a pivotal role in optimizing drug delivery.[60-62] Encapsulating statins and curcumin within nanoparticles exhibit several advantages, including enhanced bioavailability, controlled release, and targeted delivery to specific sites.[65-67] This study aimed to improve the efficacy in vascular disease treatment by employing ABVs loaded with nanoparticles and cells. The use of nanoparticles encapsulating therapeutic substances such as statin and curcumin enables controlled and targeted drug delivery, minimizes potential side effects, and ensures sustained drug release over time. The incorporation of stem cells into ABVs promotes angiogenesis and offers a promising avenue to repair damaged blood vessels more effectively. The 3D printing technology allows for precise fabrication of ABVs tailored to individual patient needs, thereby improving the success rate and adaptability of the intervention. By combining these advanced techniques, the experiment sought to optimize treatment delivery and efficacy with the ultimate goal of addressing the fundamental challenges of vascular diseases and enhancing patient outcomes in the long run.

This study demonstrated the successful fabrication and characterization of statin- and curcumin-loaded nanoparticles (NPS and NPC, respectively) and their potential applications in vascular regeneration. These results highlight several important aspects, including the properties of the nanoparticles, their biocompatibility, and their therapeutic effects both *in vitro* and *in vivo*. The fabrication process yielded nanoparticles with consistent spherical shapes and sizes, indicating the reproducibility and stability of the manufacturing method. The sustained release profiles of the loaded drugs from the nanoparticles suggest their potential for use in controlled and prolonged drug delivery, which is crucial for therapeutic interventions (Figure 2). A biocompatibility assessment revealed that the nanoparticles exhibited no cytotoxic effects, even at high concentrations, over an extended period (Figure 3B and C). This finding is crucial for their safe application in biomedical settings. While nanoparticle release is gradual, the resulting biological responses exhibit significant variability, primarily depending on nanoparticle properties and the specific target tissue. We have consistently observed that when cells are directly treated with nanoparticles, cell proliferation, migration, and tube formation are significantly improved due to cellular uptake (Figure 3D–I). However, our study extended beyond this initial timeframe, meticulously examining the sustained and gradual release kinetics of these nanoparticles (Figure 2F). It accomplishes this by ensuring a continuous and steady supply of bioactive agents, which, in turn, supports various aspects of tissue healing and recovery processes over an extended duration. These results suggest that nanoparticles can enhance the regenerative potential of EPCs, which is vital for vascular repair and angiogenesis. The co-administration of NPS and NPC (NPSC) further augmented the therapeutic effects of the nanoparticles (Figure 3J and K). Curcumin, known for its antioxidant properties, reduces the levels of intracellular ROS induced by H_2O_2, thereby providing additional protection against oxidative stress. We have substantiated these effects through additional *in vivo* experiments (**Figure S2A** and **S2B** in Supplementary File). This finding highlights the potential of combining multiple therapeutic agents within a single nanoparticle delivery system to achieve synergistic effects. The controlled release of therapeutic agents, along with the demonstrated biocompatibility, enhanced cell proliferation, and angiogenic properties of the nanoparticles, highlights that combining them with nanoparticles is a compelling approach for applications in tissue engineering and regenerative medicine. Furthermore, this study reveals the plausibility of utilizing dual drugs to enhance the efficacy of vascular regeneration as compared to a single drug, as demonstrated in our previous study.[68] This study showcases the synergistic effect of both statin and curcumin, with the former wielding a prominent influence in regeneration and the latter regulating the microenvironment. This suggests

that the simultaneous administration of multiple drugs, as opposed to the introduction of a single agent, may contribute to a synergistic effect, thereby facilitating the treatment of ischemic diseases. Further research and optimization of nanoparticle delivery systems are warranted to fully understand their mechanisms of action and explore their clinical potential.

The successful fabrication of nanoparticle-laden ABVs using 3D printing technology is a significant advancement in the field of tissue engineering. The ability to create ABVs with customizable sizes and integrated nanoparticles opens new possibilities for targeted drug delivery and localized therapy (Figure 4). The preserved viability and proliferative capacity of cells within ABVs indicate their potential for supporting vascular regeneration. In the *in vivo* transplantation experiment, necrosis was observed in the control group that received ABVs without cells or nanoparticles, highlighting the importance of utilizing combination therapy encompassing cells and drugs. However, the groups that received ABVs loaded with cells and nanoparticles exhibited remarkable recovery from hindlimb ischemia. At 28 days, the EPC@NP@BV group exhibited significantly pronounced vascular recovery ability, whereas the EPC@NPSC@BV group attained the fastest recovery, marked by almost complete recovery within 14 days. The EPC@NPSC@BV group demonstrated the most significant improvements in terms of recovery speed and blood flow, attesting to the synergistic effects of statin and curcumin in cell-based therapy (Figure 5B–E). These findings suggest that EPCs enhance their functionality and proliferative capacity through the uptake of therapeutic agents, thus assuming a critical role in facilitating vascular recovery subsequent to ABV transplantation (Figure 3). Histological analysis revealing enhanced expression of vascular-related markers, such as α-SMA and CD31, in the EPC@NPSC@BV group further supported these outcomes (Figure 5F–I). These findings point to the capability of the combination therapy in facilitating the regeneration of functional blood vessels, which leads to improved angiogenesis.

5. Conclusion

In this study, we successfully prepared NPS and NPC, which were in consistent spherical shape and demonstrate sustained release profiles. The nanoparticles exhibited excellent biocompatibility and promoted the proliferative capacity and functionality of EPC. The integration of these nanoparticles within ABVs using 3D printing technology allows for customizable and functional constructs capable of promoting vascular regeneration. In *in vivo* models, the transplantation of nanoparticle-loaded ABVs resulted in significant improvements in hindlimb ischemia, marked by enhanced recovery speed and blood flow. These findings highlight the potential of statin- and curcumin-loaded nanoparticles as a promising approach for controlled drug delivery and regeneration of functional blood vessels. Further research and optimization are required to fully explore their clinical potential and pave the way for future therapeutic applications.

Acknowledgments

None.

Funding

This work was supported by a grant from the National Research Foundation (NRF2020R1A2C2101297 and 2022R1A5A2027161) funded by the Korean government.

Conflict of interest

The authors declare no conflicts of interest.

Author contributions

Conceptualization: Eun Ji Lee, Jaewoo Choi, Woong Bi Jang, Sang-Mo Kwon

Formal analysis: Eun Ji Lee, Jaewoo Choi, Woong Bi Jang

Investigation: Eun Ji Lee, Jaewoo Choi, Woong Bi Jang, Hye Ji Lim

Methodology: Eun Ji Lee, Jaewoo Choi, Woong Bi Jang, Hye Ji Lim, Deokhyeon Yoon, Dong Myoung Lee, Donggu Kang, Jeong-Seok Lee, Hojun Jeon, Kyeong Hyeon Lee, Yong-Il Shin, Sang-Cheol Han

Writing – original draft: Eun Ji Lee, Jaewoo Choi, Woong Bi Jang

Writing – review & editing: Sang-Mo Kwon

Ethics approval and consent to participate

Human umbilical cord blood was collected from healthy volunteers after obtaining informed consent according to the protocol approved by the Institutional Review Board of Pusan National University Yangsan Hospital, Republic of Korea (Approval No. PNUYH-05-2017-053). Animal treatment and maintenance were performed in accordance with the Principles of Laboratory Animal Care, and animal experiments were performed in accordance with protocols approved by the Pusan National University Institutional Animal Use and Care Committee (Approval No. PNU-2022-0212).

Consent for publication

In accordance with the guidelines for publication involving human subjects, we obtained written consent from

all participants included in our study. Any identifying information has been appropriately masked to protect the privacy of the patients. We have made every effort to adhere to the consent and privacy guidelines set forth. Therefore, this requirement is applicable and has been fulfilled.

Availability of data

The data utilized in this study are available from the corresponding author (Sang-Mo Kwon, Email: smkwon323@pusan.ac.kr) upon reasonable request.

References

1. Pancholy SB, Patel GA, Shah SC, Patel TM. Vascular complications of the wrist: prevention and management. *Interv Cardiol Clin*. 2020;9(1):87-97. doi: 10.1016/j.iccl.2019.08.002
2. Fan J, Watanabe T. Atherosclerosis: known and unknown. *Pathol Int*. 2022;72(3):151-160. doi: 10.1111/pin.13202
3. Libby P. The changing landscape of atherosclerosis. *Nature*. 2021;592(7855):524-533. doi: 10.1038/s41586-021-03392-8
4. Balta S. Endothelial dysfunction and inflammatory markers of vascular disease. *Curr Vasc Pharmacol*. 2021;19(3):243-249. doi: 10.2174/1570161118666200421142542
5. Han Y, Li L, Zhang Y, et al. Phenomics of vascular disease: the systematic approach to the combination therapy. *Curr Vasc Pharmacol*. 2015;13(4):433-440. doi: 10.2174/1570161112666141014144829
6. Horvath L, Nemeth N, Feher G, Kívés Z, Endrei D, Boncz I. Epidemiology of peripheral artery disease: narrative review. *Life (Basel)*. 2022;12(7):1041. doi: 10.3390/life12071041
7. St Hilaire C. Medial arterial calcification: a significant and independent contributor of peripheral artery disease. *Arterioscler Thromb Vasc Biol*. 2022;42(3):253-260. doi: 10.1161/ATVBAHA.121.316252
8. Conte SM, Vale PR. Peripheral arterial disease. *Heart Lung Circ*. 2018;27(4):427-432. doi: 10.1016/j.hlc.2017.10.014
9. Regmi M, Siccardi MA. *Coronary Artery Disease Prevention*. Treasure Island, FL: StatPearls; 2023.
10. Pragodpol P, Ryan C. Critical review of factors predicting health-related quality of life in newly diagnosed coronary artery disease patients. *J Cardiovasc Nurs*. 2013;28(3):277-284. doi: 10.1097/JCN.0b013e31824af56e
11. Lichota A, Szewczyk EM, Gwozdzinski K. Factors affecting the formation and treatment of thrombosis by natural and synthetic compounds. *Int J Mol Sci*. 2020;21(21):7975. doi: 10.3390/ijms21217975
12. Chen H, McGowan EM, Ren N, et al. Nattokinase: a promising alternative in prevention and treatment of cardiovascular diseases. *Biomark Insights*. 2018;13:1177271918785130. doi: 10.1177/1177271918785130
13. Krisnanda C, Menahem S, Lane GK. Intravascular stent implantation for the management of pulmonary artery stenosis. *Heart Lung Circ*. 2013;22(1):56-70. doi: 10.1016/j.hlc.2012.08.008
14. Elens M, Le Fevere de Ten Hove G. In stent re-stenosis after carotid artery stenting. *Eur J Vasc Endovasc Surg*. 2023;65(3):378. doi: 10.1016/j.ejvs.2022.11.026
15. John S, Bain MD, Hui FK, et al. Long-term follow-up of in-stent stenosis after pipeline flow diversion treatment of intracranial aneurysms. *Neurosurgery*. 2016;78(6):862-867. doi: 10.1227/NEU.0000000000001146
16. Chiarito M, Mehran R. Panta rhei, also drug eluting stent technology. *Catheter Cardiovasc Interv*. 2020;95(6):1074-1075. doi: 10.1002/ccd.28918
17. El-Kadiry AE, Rafei M, Shammaa R. Cell therapy: types, regulation, and clinical benefits. *Front Med (Lausanne)*. 2021;8:756029. doi: 10.3389/fmed.2021.756029
18. Zhang L, Xu Q. Stem/progenitor cells in vascular regeneration. *Arterioscler Thromb Vasc Biol*. 2014;34(6):1114-1119. doi: 10.1161/ATVBAHA.114.303809
19. Zakrzewski W, Dobrzynski M, Szymonowicz M, Rybak Z. Stem cells: past, present, and future. *Stem Cell Res Ther*. 2019;10(1):68. doi: 10.1186/s13287-019-1165-5
20. Xie Y, Fan Y, Xu Q. Vascular regeneration by stem/progenitor cells. *Arterioscler Thromb Vasc Biol*. 2016;36(5):e33-40. doi: 10.1161/ATVBAHA.116.307303
21. Leeper NJ, Hunter AL, Cooke JP. Stem cell therapy for vascular regeneration: adult, embryonic, and induced pluripotent stem cells. *Circulation*. 122(5):517-526. doi: 10.1161/CIRCULATIONAHA.109.881441
22. Bashor CJ, Hilton IB, Bandukwala H, Smith DM, Veiseh O. Engineering the next generation of cell-based therapeutics. *Nat Rev Drug Discov*. 2022;21(9):655-675. doi: 10.1038/s41573-022-00476-6
23. Lovell MJ, Mathur A. Cardiac stem cell therapy: progress from the bench to bedside. *Heart*. 2010;96(19):1531-1537. doi: 10.1136/hrt.2009.192385
24. Hou YC, Cui X, Qin Z, et al. Three-dimensional bioprinting of artificial blood vessel: process, bioinks, and challenges. *Int J Bioprint*. 2023;9(4):740. doi: 10.18063/ijb.740
25. Yang GH, Kang D, An S, et al. Advances in the development of tubular structures using extrusion-based 3D cell-printing technology for vascular tissue regenerative applications. *Biomater Res*. 2022;26(1):73. doi: 10.1186/s40824-022-00321-2

26. Moore MJ, Tan RP, Yang N, Rnjak-Kovacina J, Wise SG. Bioengineering artificial blood vessels from natural materials. *Trends Biotechnol*. 2022;40(6):693-707. doi: 10.1016/j.tibtech.2021.11.003

27. Wang D, Xu Y, Li Q, Turng L-S. Artificial small-diameter blood vessels: materials, fabrication, surface modification, mechanical properties, and bioactive functionalities. *J Mater Chem B*. 2020;8(9):1801-1822. doi: 10.1039/c9tb01849b

28. Sun D, Zheng Y, Yin T, et al. Coronary drug-eluting stents: from design optimization to newer strategies. *J Biomed Mater Res A*. 2014;102(5):1625-40. doi: 10.1002/jbm.a.34806

29. Sternberg K, Grabow N, Petersen S, et al. Advances in coronary stent technology--active drug-loaded stent surfaces for prevention of restenosis and improvement of biocompatibility. *Curr Pharm Biotechnol*. 2013;14(1):76-90. doi: 10.2174/138920113804805377

30. Wang Z, Lee SJ, Cheng HJ, Yoo JJ, Atala A. 3D bioprinted functional and contractile cardiac tissue constructs. *Acta Biomater*. 2018;70:48-56. doi: 10.1016/j.actbio.2018.02.007

31. Neumann B, Baror R, Zhao C, et al. Metformin restores CNS remyelination capacity by rejuvenating aged stem cells. *Cell Stem Cell*. 2019;25(4):473-485.e8. doi: 10.1016/j.stem.2019.08.015

32. Jang WB, Park JH, Ji ST, et al. Cytoprotective roles of a novel compound, MHY-1684, against hyperglycemia-induced oxidative stress and mitochondrial dysfunction in human cardiac progenitor cells. *Oxid Med Cell Longev*. 2018;2018:4528184. doi: 10.1155/2018/4528184

33. Mohseni N, Roshan R, Naderi S, Behdani M, Kazemi-Lomedasht F. In vitro combination therapy of pathologic angiogenesis using anti-vascular endothelial growth factor and anti-neuropilin-1 nanobodies. *Iran J Basic Med Sci*. 2020;23(10):1335-1339. doi: 10.22038/ijbms.2020.47782.11000

34. Niklason LE, Lawson JH. Bioengineered human blood vessels. *Science*. 2020;370(6513):eaaw8682. doi: 10.1126/science.aaw8682

35. Papaioannou TG, Manolesou D, Dimakakos E, Tsoucalas G, Vavuranakis M, Tousoulis D. 3D bioprinting methods and techniques: applications on artificial blood vessel fabrication. *Acta Cardiol Sin*. 2019;35(3):284-289. doi: 10.6515/ACS.201905_35(3).20181115A

36. Kakisis JD, Liapis CD, Breuer C, Sumpio BE. Artificial blood vessel: the Holy Grail of peripheral vascular surgery. *J Vasc Surg*. 2005;41(2):349-354. doi: 10.1016/j.jvs.2004.12.026

37. Colosi C, Shin SR, Manoharan V, et al. Microfluidic bioprinting of heterogeneous 3D tissue constructs using low-viscosity bioink. *Adv Mater*. 2016;28(4):677-684. doi: 10.1002/adma.201503310

38. Munisso MC, Yamaoka T. Circulating endothelial progenitor cells in small-diameter artificial blood vessel. *J Artif Organs*. 2020;23(1):6-13. doi: 10.1007/s10047-019-01114-6

39. Zhou X, Nowicki M, Sun H, et al. 3D bioprinting-tunable small-diameter blood vessels with biomimetic biphasic cell layers. *ACS Appl Mater Interfaces*. 2020;12(41):45904-45915. doi: 10.1021/acsami.0c14871

40. Lee A, Hudson AR, Shiwarski DJ, et al. 3D bioprinting of collagen to rebuild components of the human heart. *Science*. 2019;365(6452):482-487. doi: 10.1126/science.aav9051

41. Alonzo M, AnilKumar S, Roman B, Tasnim N, Joddar B. 3D bioprinting of cardiac tissue and cardiac stem cell therapy. *Transl Res*. 2019;211:64-83. doi: 10.1016/j.trsl.2019.04.004

42. Mazzocchi A, Soker S, Skardal A. 3D bioprinting for high-throughput screening: drug screening, disease modeling, and precision medicine applications. *Appl Phys Rev*. 2019;6(1):011302. doi: 10.1063/1.5056188

43. Vanderburgh J, Sterling JA, Guelcher SA. 3D printing of tissue engineered constructs for in vitro modeling of disease progression and drug screening. *Ann Biomed Eng*. 2017;45(1):164-179. doi: 10.1007/s10439-016-1640-4

44. Gonzalez LM, Moeser AJ, Blikslager AT. Animal models of ischemia-reperfusion-induced intestinal injury: progress and promise for translational research. *Am J Physiol Gastrointest Liver Physiol*. 2015;308(2):G63-75. doi: 10.1152/ajpgi.00112.2013

45. Rahbar Saadat Y, Hosseiniyan Khatibi SM, Sani A, Vahed SZ, Ardalan M. Ischemic tubular injury: oxygen-sensitive signals and metabolic reprogramming. *Inflammopharmacology*. 2023;31(4):1657-1669. doi: 10.1007/s10787-023-01232-x

46. Guan Y, Gao N, Niu H, Dang Y, Guan J. Oxygen-release microspheres capable of releasing oxygen in response to environmental oxygen level to improve stem cell survival and tissue regeneration in ischemic hindlimbs. *J Control Release*. 2021;331:376-389. doi: 10.1016/j.jconrel.2021.01.034

47. Dambrova M, Zuurbier CJ, Borutaite V, Liepinsh E, Makrecka-Kuka M. Energy substrate metabolism and mitochondrial oxidative stress in cardiac ischemia/reperfusion injury. *Free Radic Biol Med*. 2021;165:24-37. doi: 10.1016/j.freeradbiomed.2021.01.036

48. Rojas-Morales P, Leon-Contreras JC, Sanchez-Tapia M, et al. A ketogenic diet attenuates acute and chronic ischemic kidney injury and reduces markers of oxidative stress and inflammation. *Life Sci*. 2022;289:120227. doi: 10.1016/j.lfs.2021.120227

49. Mokhtari-Zaer A, Marefati N, Atkin SL, Butler AE, Sahebkar A. The protective role of curcumin in myocardial ischemia-reperfusion injury. *J Cell Physiol*. 2018;234(1):214-222. doi: 10.1002/jcp.26848

50. Malko P, Jiang LH. TRPM2 channel-mediated cell death: an important mechanism linking oxidative stress-inducing pathological factors to associated pathological conditions. *Redox Biol*. 2020;37:101755. doi: 10.1016/j.redox.2020.101755

51. Zhao X, Li S, Mo Y, et al. DCA protects against oxidation injury attributed to cerebral ischemia-reperfusion by regulating glycolysis through PDK2-PDH-Nrf2 axis. *Oxid Med Cell Longev*. 2021;2021:5173035. doi: 10.1155/2021/5173035

52. Rivera JC, Dabouz R, Noueihed B, Omri S, Tahiri H, Chemtob S. Ischemic retinopathies: oxidative stress and inflammation. *Oxid Med Cell Longev*. 2017;2017:3940241. doi: 10.1155/2017/3940241

53. Santos-Zas I, Lemarie J, Tedgui A, Ait-Oufella H. Adaptive immune responses contribute to post-ischemic cardiac remodeling. *Front Cardiovasc Med*. 2018;5:198. doi: 10.3389/fcvm.2018.00198

54. Carlsson PO. Influence of microenvironment on engraftment of transplanted beta-cells. *Ups J Med Sci*. 2011;116(1):1-7. doi: 10.3109/03009734.2010.548609

55. Yan LL, Ye LP, Chen YH, et al. The influence of microenvironment on survival of intraportal transplanted islets. *Front Immunol*. 2022;13:849580. doi: 10.3389/fimmu.2022.849580

56. Zenclussen AC, Hammerling GJ. Cellular regulation of the uterine microenvironment that enables embryo implantation. *Front Immunol*. 2015;6:321. doi: 10.3389/fimmu.2015.00321

57. Yavarpour-Bali H, Ghasemi-Kasman M, Pirzadeh M. Curcumin-loaded nanoparticles: a novel therapeutic strategy in treatment of central nervous system disorders. *Int J Nanomedicine*. 2019;14:4449-4460. doi: 10.2147/IJN.S208332

58. Abrahams S, Haylett WL, Johnson G, Carr JA, Bardien S. Antioxidant effects of curcumin in models of neurodegeneration, aging, oxidative and nitrosative stress: a review. *Neuroscience*. 2019;406:1-21. doi: 10.1016/j.neuroscience.2019.02.020

59. Patel SS, Acharya A, Ray RS, Agrawal R, Raghuwanshi R, Jain P. Cellular and molecular mechanisms of curcumin in prevention and treatment of disease. *Crit Rev Food Sci Nutr*. 2020;60(6):887-939. doi: 10.1080/10408398.2018.1552244

60. Zhao W, Xiao ZJ, Zhao SP. The benefits and risks of statin therapy in ischemic stroke: a review of the literature. *Neurol India*. 2019;67(4):983-992. doi: 10.4103/0028-3886.266274

61. Stancu C, Sima A. Statins: mechanism of action and effects. *J Cell Mol Med*. 2001;5(4):378-387. doi: 10.1111/j.1582-4934.2001.tb00172.x

62. Lee SE, Chang HJ, Sung JM, et al. Effects of statins on coronary atherosclerotic plaques: the PARADIGM Study. *JACC Cardiovasc Imaging*. 2018;11(10):1475-1484. doi: 10.1016/j.jcmg.2018.04.015

63. Hoshyar N, Gray S, Han H, Bao G. The effect of nanoparticle size on in vivo pharmacokinetics and cellular interaction. *Nanomedicine (Lond)*. 2016;11(6):673-692. doi: 10.2217/nnm.16.5

64. Zhang S, Gao H, Bao G. Physical principles of nanoparticle cellular endocytosis. *ACS Nano*. 2015;9(9):8655-8671. doi: 10.1021/acsnano.5b03184

65. Suk JS, Xu Q, Kim N, Hanes J, Ensign LM. PEGylation as a strategy for improving nanoparticle-based drug and gene delivery. *Adv Drug Deliv Rev*. 2016;99(Pt A):28-51. doi: 10.1016/j.addr.2015.09.012

66. Saraiva C, Praca C, Ferreira R, Santos T, Ferreira L, Bernardino L. Nanoparticle-mediated brain drug delivery: overcoming blood-brain barrier to treat neurodegenerative diseases. *J Control Release*. 2016;235:34-47. doi: 10.1016/j.jconrel.2016.05.044

67. Donahue ND, Acar H, Wilhelm S. Concepts of nanoparticle cellular uptake, intracellular trafficking, and kinetics in nanomedicine. *Adv Drug Deliv Rev*. 2019;143:68-96. doi: 10.1016/j.addr.2019.04.008

68. Gao G, Lee JH, Jang J, et al. Tissue engineered bio-blood-vessels constructed using a tissue-specific bioink and 3d coaxial cell printing technique: a novel therapy for ischemic disease. *Adv Funct Mater*. 2017;27(33):1700798. doi: 10.1002/adfm.201770192

69. Kim J, Kim HS, Lee N, et al. Multifunctional uniform nanoparticles composed of a magnetite nanocrystal core and a mesoporous silica shell for magnetic resonance and fluorescence imaging and for drug delivery. *Angew Chem Int Ed Engl*. 2008;47(44):8438-8441. doi: 10.1002/anie.200802469

70. Lee SH, Lee JH, Yoo SY, Hur J, Kim H-S, Kwon SM. Hypoxia inhibits cellular senescence to restore the therapeutic potential of old human endothelial progenitor cells via the hypoxia-inducible factor-1alpha-TWIST-p21 axis. *Arterioscler Thromb Vasc Biol*. 2013;33(10):2407-2414. doi: 10.1161/ATVBAHA.113.301931

71. Guo X, Mao F, Wang W, Yang Y, Bai Z. Sulfhydryl-modified Fe3O4@SiO2 core/shell nanocomposite: synthesis and toxicity assessment in vitro. *ACS Appl Mater Interfaces*. 2015;7(27):14983-14991. doi: 10.1021/acsami.5b03873

72. Shi B, Xie L, Ma B, Zhou Z, Xu B, Qu L. Preparation and properties of highly transparent SiO(2) aerogels for thermal insulation. *Gels*. 2022;8(11):744.
doi: 10.3390/gels8110744

73. Gheorghita Puscaselu R, Lobiuc A, Dimian M, Covasa M. Alginate: from food industry to biomedical applications and management of metabolic disorders. *Polymers (Basel)*. 2020;12(10):2417.
doi: 10.3390/polym12102417

74. Tarbell JM, Cancel LM. The glycocalyx and its significance in human medicine. *J Intern Med*. 2016;280(1):97-113.
doi: 10.1111/joim.12465

75. Schmelzer KP, Liebetrau D, Kammerer W, Meisinger C, Hyhlik-Dürr A. Strategies for avoiding typical drug-drug interactions and drug-related problems in patients with vascular diseases. *Medicina (Kaunas)*. 2023; 59(4):780.
doi: 10.3390/medicina59040780

76. Huynh DTN, Heo KS. Therapeutic targets for endothelial dysfunction in vascular diseases. *Arch Pharm Res*. 2019;42(10):848-861.
doi: 10.1007/s12272-019-01180-7

77. Weiss AJ, Lorente-Ros M, Correa A, Barman N, Tamis-Holland JE. Recent advances in stent technology: do they reduce cardiovascular events? *Curr Atheroscler Rep*. 2022;24(9):731-744.
doi: 10.1007/s11883-022-01049-z

78. Suryawan IGR, Luke K, Agustianto RF, Budi Mulia EP. Coronary stent infection: a systematic review. *Coron Artery Dis*. 2022;33(4):318-326.
doi: 10.1097/MCA.0000000000001098

79. Sanchez-Jimenez E, El-Mokdad R, Chaddad R, Cortese B. Drug-coated balloon for the management of coronary chronic total occlusions. *Rev Cardiovasc Med*. 2022;23(2):42.
doi: 10.31083/j.rcm2302042

ACCSCIENCE PUBLISHING

International Journal of Bioprinting

RESEARCH ARTICLE

Development of 3D-bioprinted artificial blood vessels loaded with rapamycin-nanoparticles for ischemic repair

Jaewoo Choi[1,2†], Eun Ji Lee[1,2†], Hye Ji Lim[1,2], Dong Myoung Lee[1,2], Deokhyeon Yoon[1,2], Gi Hoon Yang[3], Eunjeong Choi[3], Hojun Jeon[3], Kyeong Hyeon Lee[4], Yong-Il Shin[4,5], Sang-Cheol Han[6], Woong Bi Jang[1,2*], and Sang-Mo Kwon[1,2*]

[1]Laboratory for Vascular Medicine and Stem Cell Biology, Department of Physiology, Medical Research Institute, School of Medicine, Pusan National University, Yangsan 50612, Republic of Korea

[2]Convergence Stem Cell Research Center, Pusan National University, Yangsan 50612, Republic of Korea

[3]Research Institute of Additive Manufacturing and Regenerative Medicine, Baobab Healthcare Inc., 55 Hanyangdaehak-Ro, Ansan, Gyeonggi-do 15588, South Korea

[4]Science of Convergence, School of Medicine, Pusan National University, Yangsan 50612, Republic of Korea

[5]Department of Rehabilitation Medicine, Pusan National University Yangsan Hospital, Yangsan 50612, Republic of Korea

[6]CEN Co., Ltd. Nano-Convergence Center, 761 Muan-ro, Miryang 50404, Republic of Korea

(This article belongs to the *Special Issue: 3D Printing of Bioinspired Materials*)

†These authors contributed equally to this work.

***Corresponding author:**
Woong Bi Jang
(jangwoongbi@naver.com)

Sang-Mo Kwon
(smkwon323@pusan.ac.kr)

Citation: Choi J, Lee EJ, Lim HJ, et al. Development of 3D-bioprinted artificial blood vessels loaded with rapamycin-nanoparticles for ischemic repair. *Int J Bioprint*. 2024;10(2):1465.
doi: 10.36922/ijb.1465

Received: August 5, 2023
Accepted: October 3, 2023
Published Online: January 15, 2024

Abstract

Vascular diseases, including ischemic conditions and restenosis, pose significant challenges in clinical practice. Restenosis, the re-narrowing of blood vessels after interventions such as stent placement, remains a major concern despite advances in medical interventions. Addressing these challenges requires innovative approaches that promote vascular regeneration and prevent restenosis. By leveraging the capabilities of three-dimensional (3D) printing technology, artificial blood vessels with lumen can be precisely constructed in customizable sizes, closely mimicking the natural vascular architecture. This approach allows for the incorporation of therapeutic agents and cells to enhance the functionality of the fabricated vessels. In the present study, we investigated the fabrication and characterization of artificial blood vessels using 3D printing technology, with the focus on achieving precise control over the vessel dimensions and architecture to ensure optimal functionality. The use of 3D printing enabled the creation of patient-specific blood vessels with tailored sizes and geometries, providing a personalized solution for vascular treatment. Furthermore, we explored the integration of nanoparticles loaded with therapeutic drugs within the 3D-printed blood vessels. Specifically, rapamycin, a potent drug for preventing restenosis, was encapsulated within the nanoparticles to enable controlled drug release. This approach aimed to address the challenge of restenosis by delivering the drug directly to the affected site and maintaining its therapeutic concentration over an extended period. Additionally, the study investigated the incorporation of endothelial progenitor cells (EPCs), which promote re-endothelialization essential for vascular regeneration and long-term vessel functionality, within the artificial blood vessels. The 3D-printed blood vessels provide an ideal environment for the integration and growth of these cells,

further enhancing their regenerative potential. By combining 3D printing technology, drug-loaded nanoparticles, and EPCs, this study demonstrated the potential of this approach in fabricating functional artificial blood vessels.

Keywords: 3D bioprinting; Tissue engineering; Nanoparticles; Artificial blood vessel; Restenosis; Endothelial progenitor cells

1. Introduction

The human circulatory system heavily relies on an intricate network of blood vessels to ensure the transportation of oxygen, nutrients, and crucial molecules to all organs and tissues.[1,2] However, vascular pathologies, such as atherosclerosis, vascular occlusions, and congenital malformations, present significant challenges to the integrity and functionality of these essential conduits. Consequently, the development of innovative strategies to replace or regenerate damaged blood vessels has become a pivotal area of investigation within the field of regenerative medicine.[3-6]

Recent advances in stem cell research have shown great promise in tissue engineering and regenerative therapies.[5,7,8] Vascular endothelial stem cells, in particular, have emerged as a compelling candidate due to their unique ability to differentiate into mature endothelial cells—the fundamental building blocks of blood vessels.[9-11] Leveraging the regenerative potential of these cells presents a remarkable opportunity to create artificial blood vessels that closely mimic their natural counterparts.

One critical aspect of tissue engineering is the establishment of a functional vascular network within artificial constructs.[12,13] The presence of proper endothelial cells is crucial to maintaining vessel integrity, preventing thrombosis, and facilitating appropriate blood flow. This underscores the significance of vascular endothelial stem cells, as their potential to differentiate into functional endothelial cells offers a viable solution to this challenge.[13-16] By incorporating these stem cells, it becomes feasible to engineer blood vessels with a well-established endothelial lining, thereby enhancing the overall performance and durability of artificial constructs. Furthermore, to ensure the long-term success of artificial blood vessels, it is essential to address issues such as restenosis and thrombosis.[17-19]

Tissue-engineered artificial blood vessels can closely mimic human vascular structures. Recent research efforts have been extensive in replicating complex vascular networks, akin to human blood vessels, using various three-dimensional (3D) bioprinting techniques. Among these, extrusion-based bioprinting, jetting-based bioprinting, and vat photopolymerization-based bioprinting are prominent methods. Extrusion-based bioprinting is the most commonly used method. It typically involves the continuous or layered deposition of bioink composed of living cells and support materials through a nozzle. This technique enables the tissue-specific 3D bioprinting of intricate organ structures. It offers versatility, high speed, and excellent cell viability, making it advantageous for tissue engineering applications.[20-22] Jetting-based bioprinting, on the other hand, employs precise nozzle-based ejection of small droplets of bioink-containing cells and biomaterials. This method boasts high precision and resolution, allowing for the creation of detailed tissue structures. It excels in its ability to deposit droplets with precision, making it suitable for mimicking complex vascular networks and other intricate tissues.[23-25] Vat photopolymerization-based bioprinting relies on selectively curing liquid photopolymer materials layer by layer using ultraviolet light. This technique is capable of achieving high-resolution, intricate tissue structures and offers flexibility in using various biocompatible photopolymer materials.[26-28] These 3D bioprinting techniques hold promise in replicating highly detailed and complex organ structures, similar to those found in the human body. They offer advantages such as precision, high resolution, and material versatility, making them valuable tools in the field of tissue engineering.

In this regard, nanoparticles (NPs) carrying therapeutic agents have emerged as a powerful tool. The NPs utilized in this study are composed of mesoporous silica, characterized by their extremely small size and porous nature, with an average pore diameter of ~5 nm. This porosity allows for efficient drug release in proportion to its size.[29,30] Furthermore, it is feasible to produce these nanoparticles at such a small size in large quantities. When employed within a drug delivery system, the NPs gradually release their contents when introduced into the biological system, highlighting their potential in imposing long-term effects. However, a comprehensive understanding of the biocompatibility of NPs has yet to be established. To address this concern, the study investigated the effects of the NPs through *in vitro* and *in vivo* experiments.

Every drug possesses distinctive molecular structures and characteristics. However, when encapsulated within NPs, these drugs can be transformed into materials with precisely engineered properties. In this study, we engineered NPs with the specific aim of tailoring their

characteristics for 3D printing applications. It is our hypothesis that these specially designed NPs offer distinct advantages, primarily through their unique capability in controlled and sustained drug release. Rapamycin, a potent immunosuppressant and mTOR inhibitor, exhibits immense potential for preventing restenosis.[31-34] By encapsulating rapamycin within NPs, it is possible to precisely deliver the therapeutic agent to targeted areas, facilitating controlled release and sustained effects. This approach offers a unique advantage in maintaining the patency and functionality of engineered blood vessels, further enhancing their therapeutic potential.

2. Materials and methods

2.1. Preparation of nanoparticles and rapamycin-nanoparticles

The NPs were prepared using the previously reported method with a few modifications.[35] First, 0.5 g of cetyltrimethylammonium bromide (CTAB) in 1 L of deionized water was mixed with 2 mL NaOH (1 M) while stirring continuously; 1 mL tetraethyl orthosilicate and 0.1 g N-(2-aminoethyl)-3-aminopropyltrimethoxy silane were then added after separately dissolving them in ethanol at a 1:5 volume ratio and 1:5 weight ratio, respectively. A white precipitate was formed, which was filtered out, washed, and dried at 80°C for 48 h. The CTAB from the precipitate was removed by dispersing the dried precipitate in 100 mL of ethanol solvent; 0.3 g of NH_4NO_3 was added to the solution and stirred at 60°C for several hours, after which the precipitate was collected by filtration, followed by drying at 60°C for 12 h. Thereafter, 0.2 g $ZnCl_2$ was added to deionized water, and the precipitate was added to the zinc solution. The solution was dried using a rotary evaporator; the obtained powder was further centrifuged, washed with water and ethanol several times, dried at 80°C for 12 h, and calcinated at 55°C for >5 h. The resultant products were referred to as NPs. After dissolving 80 mg of NPs in 80 mL ethanol, they were dispersed by ultrasonic waves for 3 min; simultaneously, 20 mg of rapamycin was dissolved in 20 mL ethanol and mixed for 3 min at a speed of 300 rpm. The above solutions were depressurized for 1 h and maintained at 100 BAR in a vacuum state. The pressure was then lowered to 60 BAR, maintained for 30 min, and then dried in a vacuum condition at room temperature for 6 h; this product was termed NP-rapamycin (NP-R).

2.2. Characterization of nanoparticles and rapamycin-nanoparticles

The zeta potential of the NPs and rapamycin-loaded NPs were measured using a Zetasizer Nano ZSP (Malvern Panalytical, Malvern, UK) according to the manufacturer's instructions. Transmission electron microscopy (TEM) imaging analyses of NPs were performed using a Bio-TEM (Talos L120C TEM, Thermo Fisher Scientific, Waltham, USA) operating at 200 kV, and the size distribution was investigated. A diluted NP suspension was dropped onto a carbon-coated mesh transmission electron microscopy (TEM) grid, and the solvent was left to evaporate at room temperature. The NP size distributions were analyzed from the TEM images using ImageJ software (National Institutes of Health, USA).

2.3. Rapamycin release profiling from rapamycin-nanoparticles

The drug release amount of rapamycin in NPs was measured using a liquid chromatography-mass spectrometry system (QTRAP 6500 plus; SCIEX, USA) according to the previously described method.[36,37] NP-R was diluted in distilled water and harvested on indicated days. Rapamycin released from the NPs was centrifuged at 10,000 × g for 10 min, and supernatants were analyzed. The quantification of the data was performed by setting the 5 days as the 100% reference point and relatively quantifying the data for the 1 and 3 days.

2.4. Drug loading efficiency of rapamycin-nanoparticles

Drug loading efficiency of rapamycin in NPs was measured using an ultraviolet-visible spectrometer (Evolution 300, Thermo Fisher Scientific, USA). Rapamycin was dissolved in methanol and added to the NPs at various ratios: 1:2, 1:5, and 1:10. Subsequently, the supernatant was collected, diluted 1/100 in methanol, and placed in a cuvette before measuring its absorbance.

2.5. Preparation of 3D-bioprinted artificial blood vessel

To prepare the bioink, sodium alginate (viscosity, >2,000 cP at 25°C; Sigma-Aldrich; St. Louis, MO, USA) was stirred into Dulbecco's phosphate-buffered saline (DPBS; Gibco, USA) for 6 h at 37°C. Subsequently, an atelocollagen solution (pH 4.0; Baobab Healthcare, Republic of Korea) was combined with reconstituted buffer (132 mM Na_2HPO_4) at a 1:1 volume ratio for neuralization. The 3D bioprinter (Root 1; Baobab Healthcare, Republic of Korea) equipped with a coaxial nozzle (inner needle: 28 G, outer needle: 20 G; Ramé-hart, USA) was used for vascular printing. For the shell material, a mixture of 3% w/v neutralized atelocollagen and 3% w/v alginate was prepared at a 4:1 ratio for the bioink. NP-R or NP only was then incorporated into the shell bioinks to achieve a final concentration of 2 mg/mL. Regarding the core material, a sacrificial material was prepared using 40% w/v Pluronic F-12 (Sigma-Aldrich) with 100 mM calcium chloride. Vascular cell printing was performed by blending the shell material with endothelial progenitor cells

(EPCs; 1×10^6 cells/mL). The core and shell bioinks were bioprinted at 80 kPa (core) and 60 kPa (shell) with a 200 mM $CaCl_2$ solution to enable *in situ* crosslinking of the alginate solution. Subsequently, the printed vessel was rinsed with DPBS and incubated at 37°C for 1 h. The sacrificial material (core bioink) was then removed using ice-cold DPBS. Printed artificial blood vessels were incubated in EGM-2 MV SingleQuot kit Supplement & Growth Factors (CC-4147; Lonza, Basel, Switzerland) with 200 mM of 10% $CaCl_2$ solution. After incubation, the cell viabilities of the artificial blood vessels were analyzed using a Live/Dead Cell Viability/Cytotoxicity Kit (L3224, Invitrogen, USA) according to the manufacturer's instructions. Images were analyzed using a Lionheart FX automated microscope (BioTek).

2.6. Cell cultures

Human EPCs were isolated from human umbilical cord blood as previously reported.[38] Mononuclear cells were isolated via gradient density centrifugation of human umbilical cord blood using Ficoll (Thermo Fisher Scientific, Waltham, USA). Isolated mononuclear cells were cultured in EGM-2 MV SingleQuot kit Supplement & Growth Factors (Lonza) with 1% penicillin/streptomycin (15240062; Thermo Fisher Scientific) at 37°C in a humidified atmosphere containing 5% CO_2. After 4 days in culture, nonadherent cells were aspirated, and culture growth media were added. Subsequently, cells were cultured until spindle-shaped colonies formed and were then replaced with culture media for 14 to 21 days. Human coronary artery smooth muscle cells (HCASMCs) were purchased from ATCC and cultured in vascular cell basal medium (PCS-100-030; ATCC, USA) supplemented with a vascular smooth muscle cell growth kit (PCS-100-042; ATCC) and 1% penicillin/streptomycin at 37°C in a humidified atmosphere containing 5% CO_2.

2.7. Cell proliferation assay

HCASMCs were detached and seeded into an 8-well chamber slide at a density of 1×10^4 cells/well. Rapamycin, NPs, NP-R (low, 10 μg/mL), and NP-R (high, 100 μg/mL) were added to each well. After 24 h, HCASMC proliferation was assessed using the Click-iT™ Plus EdU Cell Proliferation Kit (C10637; Invitrogen) according to the manufacturer's instructions. EdU-positive HCASMCs were analyzed using a Lionheart FX automated microscope (BioTek, VT, USA).

2.8. Immunofluorescent staining

HCASMCs were fixed in their wells using 4% paraformaldehyde in phosphate-buffered saline (PBS) for 10 min. After the fixative was aspirated, cells were permeabilized with 0.25% Triton X-100 in PBS. Cells were then blocked with a solution containing 5% normal goat serum and 1% bovine serum albumin in PBS for 1 h. Next, the cells were incubated overnight at 4°C with Ki-67 antibody (14-5698-82; Invitrogen). Secondary antibody was added to the cells and incubated for 2 h at room temperature. Nuclei were stained with 4',6-diamidino-2-phenylindole (DAPI) using ProLong Diamond Antifade Mountant with DAPI (Invitrogen). The stained samples were observed using a Lionheart FX-automated microscope (BioTek).

2.9. Scratch wound-healing assay

HCASMCs were detached and seeded into 6-well plates at a density of 5×10^5 cells/well. When the cells had reached 100% confluence, they were scratched using a sterile pipette tip. Rapamycin, NP, and NP-R were treated in each well, and the plates were incubated at 37°C in a humidified atmosphere containing 5% CO_2. After 9 h of incubation, HCASMCs were observed under light microscopy, and the wound-healing size was measured using ImageJ software.

2.10. Western blot analysis

Whole cell lysates were extracted from HCASMCs using PRO-PERP Protein extraction buffer (Intron Biotechnology, South Korea). The protein concentration was determined using Pierce BCA assay kit (Thermo Fisher Scientific, USA). Protein samples were separated by sodium dodecyl-sulfate polyacrylamide gel electrophoresis (SDS-PAGE) and transferred onto PVDF membranes (Millipore, USA). Membranes were blocked with 5% skim milk for 1 h and incubated overnight at 4°C with primary antibodies, p-mTOR (5536S, Cell Signaling, USA), mTOR (2983S, Cell Signaling), p-S6K1 (9234S, Cell Signaling), S6K1 (2708S, Cell Signaling), p-AKT (4060S, Cell Signaling), AKT (4691S, Cell Signaling), and GAPDH (SC-47724, Santa Cruz, USA). Horseradish peroxidase-conjugated secondary antibodies were added to the membranes and allowed to stand at room temperature for 2 h. Protein bands were visualized using enhanced chemiluminescence reagents (Millipore, USA).

2.11. Cell viability assay

HCASMC viability was analyzed using a CCK-8 kit (DI1701-01; Dongin, South Korea) according to the manufacturer's instructions. To analyze HCASMC viability, cells were seeded into a 96-well plate at a density of 5×10^3 cells/well and incubated overnight; thereafter, NP and NP-R were added to each well, and the plate was incubated for 24 h. After incubation, the cell viability was determined using the CCK-8 kit. CCK-8 absorbance was measured at 450 nm using a spectrophotometer (Tecan, Mannedorf, Switzerland).

2.12. Murine hind limb ischemia model

Experiments were performed on 8-week-old male BALB/c nude mice (Biogenomics, Seoul, South Korea) maintained under a 12-h light/dark cycle in accordance with the regulations of the Pusan National University. All procedures were performed in accordance with the policies of the Institutional Animal Care and Use Committee of the Pusan National University of Korea. In the murine hind limb ischemia model, ischemia was induced by the ligation of the proximal femoral artery and boundary vessels of the mice. No later than 1 h following surgery, PBS (PBS injection), EPC (EPC injection), NP-R/V (artificial blood vessel loaded with NP-R), EPC@NP/V (artificial blood vessel loaded with NP and EPC), and EPC@NP-R/V (artificial blood vessel loaded with NP-R and EPC) were intramuscularly transplanted into the ischemic thigh area of the experimental group. Blood perfusion was assessed by comparing the ratio of blood flow in the ischemic limb (left) to that in the nonischemic limb (right) using laser Doppler perfusion imaging (LDPI; Moor Instruments Ltd, Devon, UK).

2.13. Measurement of blood flow and tissue necrosis

Blood flow of the ischemic and nonischemic limbs was measured using an LDPI analyzer on days 0, 3, 7, 14, 21, and 28 after the induction of hind limb ischemia. Perfusion of the ischemic and nonischemic limbs was calculated based on colored histogram pixels; red and blue colors indicated high and low perfusion, respectively. Blood perfusion was expressed as the LDPI index, representing the ratio of ischemic to nonischemic limb blood flow. The extent of necrosis in the ischemic hind limb was recorded 28 days postsurgery.

2.14. Histological and immunofluorescence analysis

The ischemic thigh tissues were harvested and fixed with 4% paraformaldehyde (Biosesang, South Korea) 7 and 28 days postsurgery. Each tissue sample was embedded in paraffin. Immunofluorescence staining was performed using primary antibodies against CD31 (ab56299, Abcam, UK), alpha-smooth muscle actin (ab5694, Abcam), CD86 (19589S, Abcam), and CD206 (ab64693, Abcam), as well as secondary antibodies against Alexa-488 and Alexa-594 (Invitrogen; USA). Nuclei were stained with DAPI using ProLong Diamond Antifade Mountant with DAPI (Invitrogen), and stained samples were observed using the Lionheart FX automated microscope.

2.15. Flow cytometry analysis

Raw 264.7 cells were pre-treated with 10 μg/mL of NP-R for 24 h, followed by induction of polarization into M1 and M2 macrophages by treating with lipopolysaccharide (LPS; 100 ng/mL) and interleukin-4 (IL-4; 20 ng/mL) for 24 h. Cells were harvested and centrifuged at 1,500 rpm for 5 min at 4°C. The pellet was re-suspended in 2% fetal bovine serum in PBS and stained with Pacific Blue anti-mouse CD86 (105022, BioLegend, USA), APC anti-mouse CD206 (141408, BioLegend), and FITC anti-mouse F4/80 (130-117-509, Miltenyi Biotec, USA) antibodies for 30 min at 4°C. Cells were analyzed with FACS Canto II (BD Biosciences, USA). Data were analyzed by FlowJo software (BD Biosciences, USA).

2.16. Statistical analysis

Statistical analyses were performed using the GraphPad Prism software (La Jolla, CA, USA). To assess significance, we performed unpaired two-sided Student's *t*-tests. P-values <0.05 were considered statistically significant. Experimental data were presented as the mean ± standard deviation.

3. Results

3.1. Characterization of nanoparticles and rapamycin-nanoparticles

Before the fabrication of artificial blood vessels, NPs were prepared to increase the stability, solubility, and slow down release of drugs to prevent stenosis. To safely load rapamycin into NPs in a manner that was harmless to the human body, the experiment was conducted as follows (Figure 1A): first, the fabricated NPs were prepared as a control without capturing any drug, followed by loading of NPs with rapamycin selected for restenosis prevention (Figure 1A). The fabricated NPs were examined using Bio-TEM, revealing similar sizes (Figure 1B and C). Additionally, the stability of the NPs was determined by measuring the zeta potential, confirming their stability (Figure 1D), and their slow release was verified (Figure 1E). Furthermore, when setting the ratio of rapamycin to NPs at 1:2, 1:5, and 1:10, the measurement of drug loading efficiency yielded results ranging from approximately 10% to 35% (Figure 1F).

3.2. Enhancing drug delivery with nanoparticles: evaluating stability and efficacy for inhibiting smooth muscle cell proliferation and migration

The CCK8 experiment was conducted to evaluate the *in vitro* stability and effect of the fabricated NPs (Figure 2A). It was confirmed that the NPs containing rapamycin were able to inhibit the proliferation of smooth muscle cells (**Figure S1A** in Supplementary File). Furthermore, compared with conventional drugs, the rapamycin contained in NPs demonstrated a higher inhibition of cell proliferation (Figure 2B and C; **Figure S1B** and **C** in Supplementary File). In the case of smooth muscle cells, when a stent or artificial blood vessel was transplanted, they migrated to the graft and induced stenosis. To evaluate the prevention of this migration, the migration ability of smooth muscle cells was evaluated. Rapamycin contained in NPs was found to induce a greater inhibition effect on

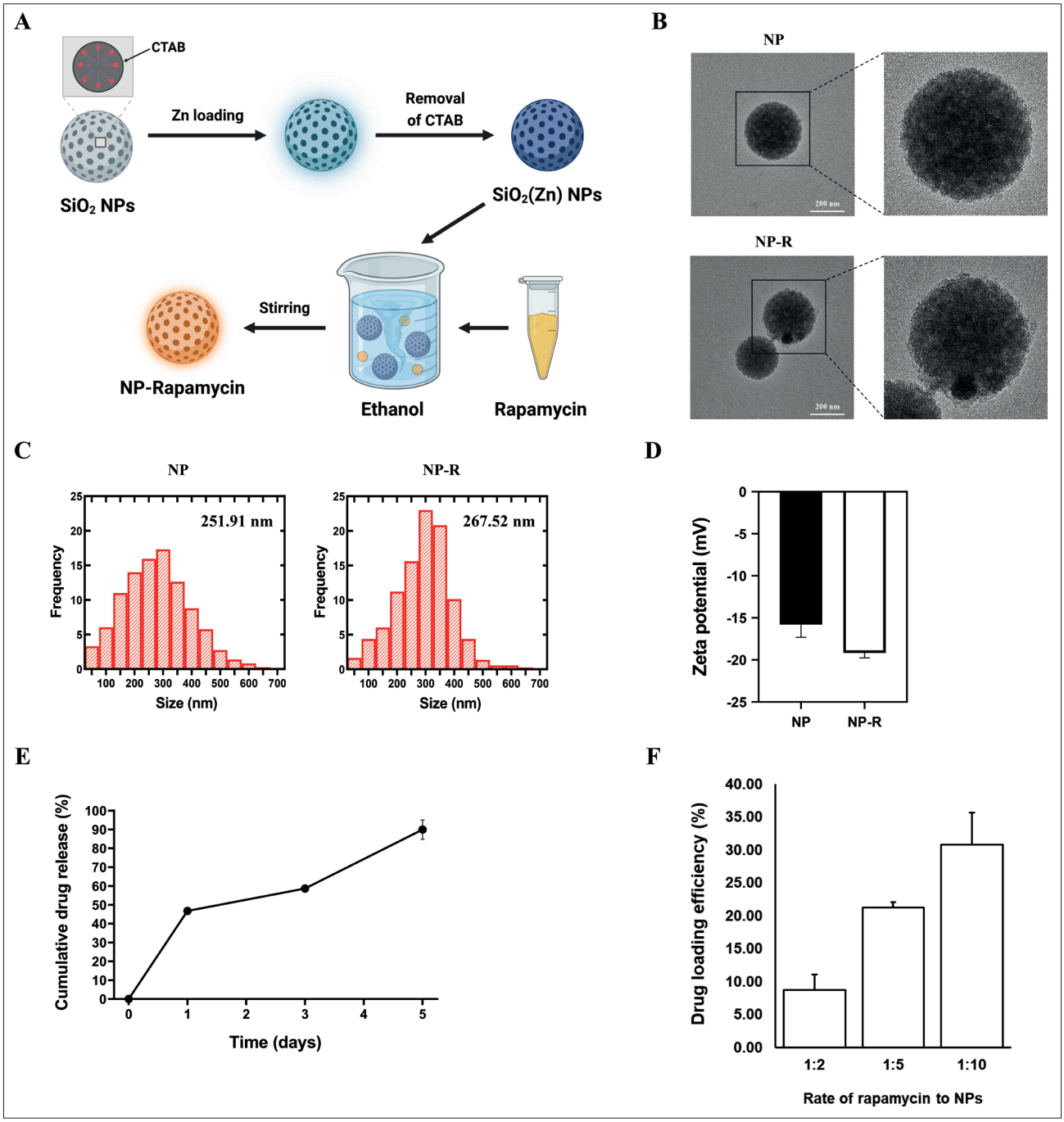

Figure 1. Characterization of nanoparticles and rapamycin-nanoparticles. (A) Schematic illustration of rapamycin-nanoparticles fabrication process. (B) Transmission electron microscopy images of nanoparticles and rapamycin-nanoparticles. Scale bars = 200 μm. (C) The sizes of each nanoparticle are analyzed and expressed as a distribution graph. (D) The zeta potential of the nanoparticles and rapamycin-nanoparticles in phosphate-buffered saline (pH = 7.4). (E) The cumulative release of rapamycin in nanoparticles is analyzed using liquid chromatography-mass spectrometry analysis. (F) Drug loading efficiency of rapamycin in nanoparticles. Abbreviations: CTAB, cetyltrimethylammonium bromide; NP, nanoparticle; Zn, zinc.

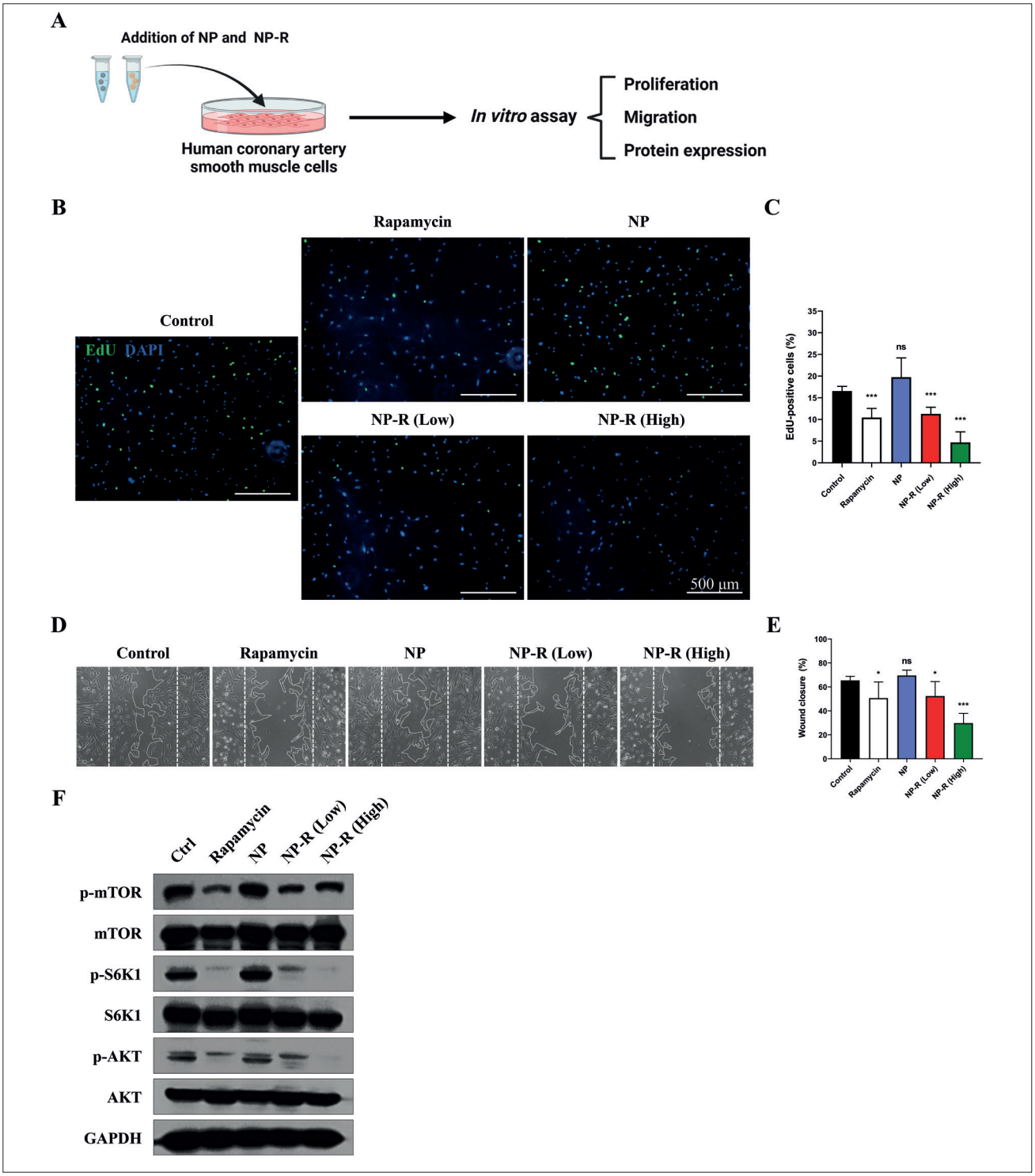

Figure 2. Rapamycin-nanoparticles inhibit smooth muscle cell proliferation and migration. (A) Schematic illustration of the *in vitro* experimental process. (B) EdU cell proliferation assay. Scale bars = 500 μm. (C) Quantification of EdU-positive cells. ***$P < 0.001$; n.s. (not significant), $P > 0.05$ versus control. The values represent the mean ± standard deviation (SD) (n = 5). (D) The migration capacity of human coronary artery smooth muscle cells treated with rapamycin and rapamycin-nanoparticles is investigated using a scratched wound healing assay. (E) Quantification of migrated area. *$P < 0.05$; ***$P < 0.001$; n.s., $P > 0.05$ versus control. The values represent mean ± SD (n = 5). (F) Protein expression of p-mTOR, mTOR, p-S6K1, S6K1, p-AKT, and AKT as evaluated by Western blotting. Abbreviation: NP, nanoparticle.

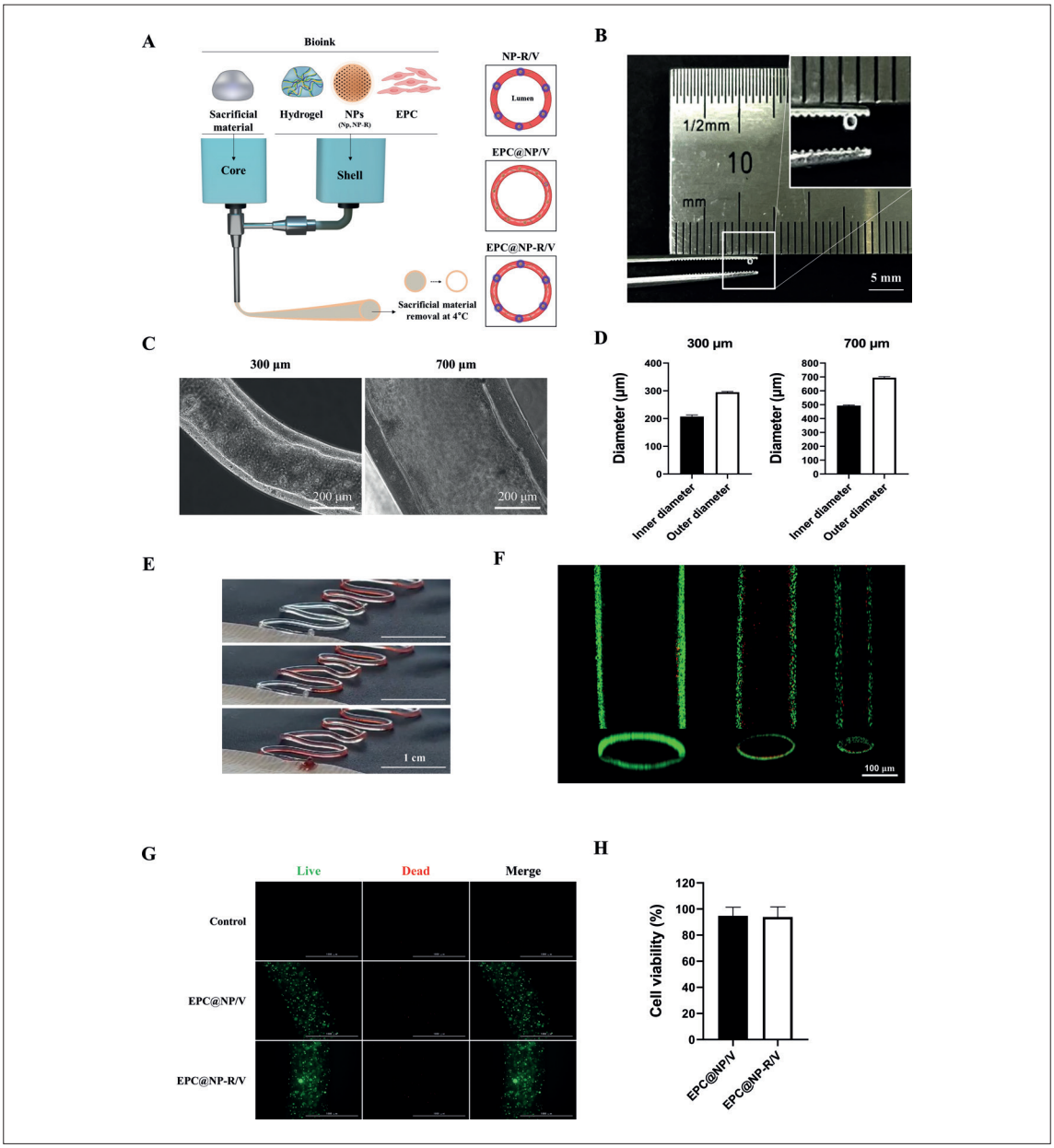

Figure 3. Characterization of 3D-bioprinted artificial blood vessels loaded with rapamycin-nanoparticles and endothelial progenitor cells. (A) Schematic visualization of the nanoparticle and cell-loaded 3D bioprinting process. (B) General image of a 3D-bioprinted artificial blood vessel. Scale bars = 5 mm. (C) Microscopic images of artificial blood vessels with different thicknesses, which were obtained with the adjustment of nozzle size. Scale bars = 200 μm. (D) Inner and outer diameter of artificial blood vessels with different thicknesses, which were obtained with the adjustment of nozzle size. (E) Assessment of flow in the artificial blood vessels. Scale bars = 1 cm. (F) Representative image of live/dead cells in the artificial blood vessels with different thicknesses, which were obtained with the adjustment of nozzle size. Scale bars = 100 μm. (G) Representative image of live/dead cells in the control (NP/V), EPC@NP/V, and EPC@NP-R/V using Live/Dead cell staining assay. Scale bars = 1,000 μm. (H) Cell viability obtained from the Live/Dead cell staining assay. Abbreviations: EPC, endothelial progenitor cell; NP, nanoparticle.

migration ability compared with rapamycin alone, and similar efficacy was observed in NP-R (low) compared with conventional drugs (Figure 2D and E).

In addition to functional evaluation, rapamycin is known to be an mTOR inhibitor; rapamycin contained in NPs exhibited a similar level of inhibitory ability, even in low concentration group, and higher inhibitory ability than the existing concentration in the high concentration group (Figure 2F). These data suggested that NPs produced in this study can prevent restenosis in artificial blood vessel grafts.

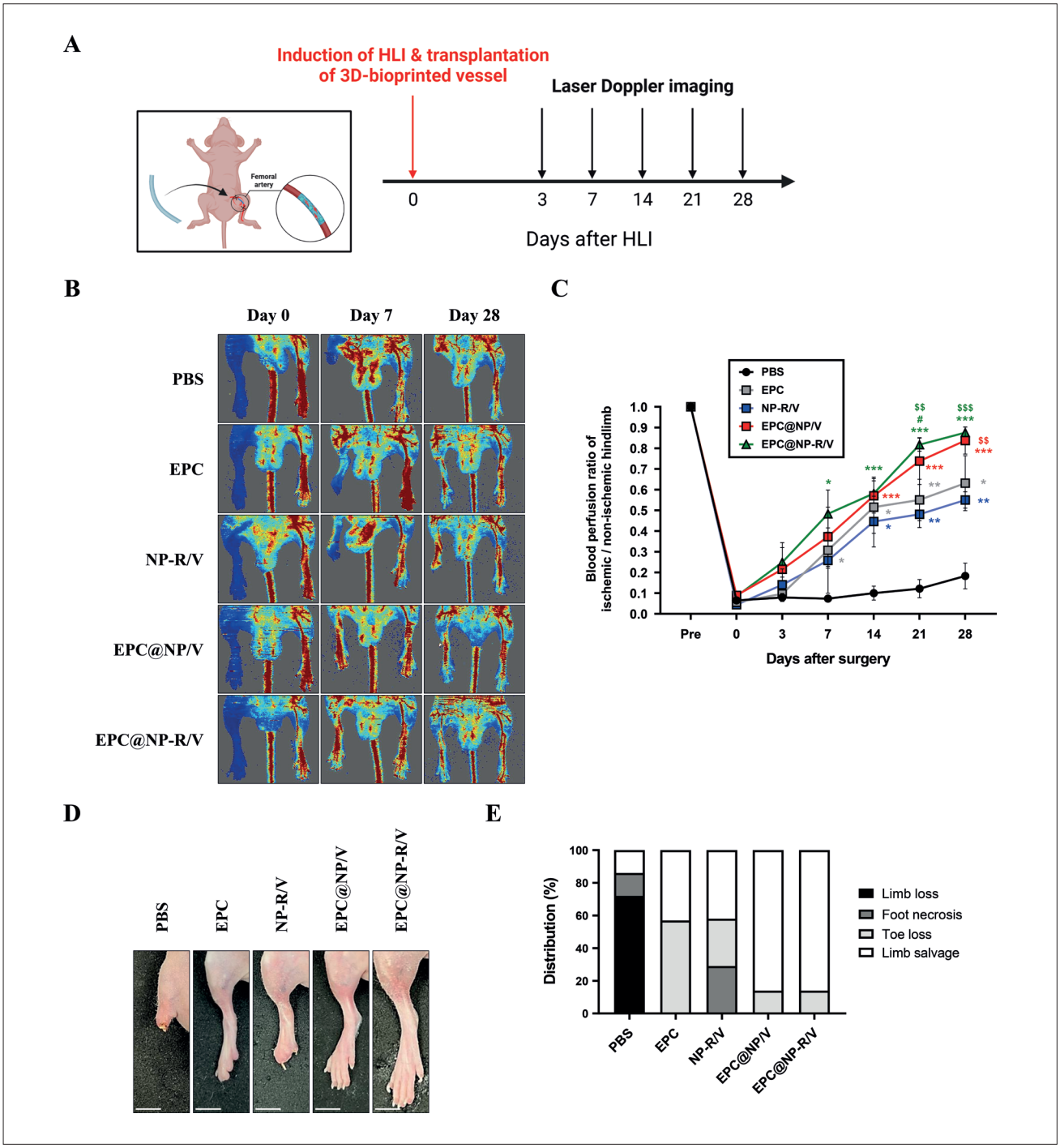

Figure 4. Regenerative effect of 3D-bioprinted artificial blood vessels loaded with rapamycin-nanoparticles and endothelial progenitor cells in a murine hind limb ischemia model. (A) Schematic illustration of the transplantation process of 3D-bioprinted artificial blood vessel in a murine hind limb ischemia model. (B) A murine hind limb ischemia model is established using Balb/c nude mice. The ratio of blood perfusion is evaluated by laser Doppler perfusion imaging analysis in the ischemic limbs of the mice transplanted with phosphate-buffered saline (PBS), endothelial progenitor cells (EPCs), NP-R/V, EPC@NP/V, and EPC@NP-R/V at 0, 7, and 28 days posttransplantation. (C) The ratio of blood perfusion is measured. $^{*}P < 0.05$; $^{**}P < 0.01$; $^{***}P < 0.001$ versus PBS; $^{\#}P < 0.05$ versus EPC, and $^{\$\$}P < 0.01$; $^{\$\$\$}P < 0.001$ versus NP-R/V. The values represent mean ± SEM (n = 5). (D) Representative images of ischemic limbs transplanted with PBS, EPC, NP-R/V, EPC@NP/V, and EPC@NP-R/V at 28 days posttransplantation. Scale bars = 5 mm. (E) Proportions of four states for each group (limb salvage, toe loss, foot necrosis, and limb loss) on postoperative day 28 (n = 7). Abbreviations: EPC, endothelial progenitor cell; HLI, hind limb ischemia; NP, nanoparticle; PBS, phosphate-buffered saline.

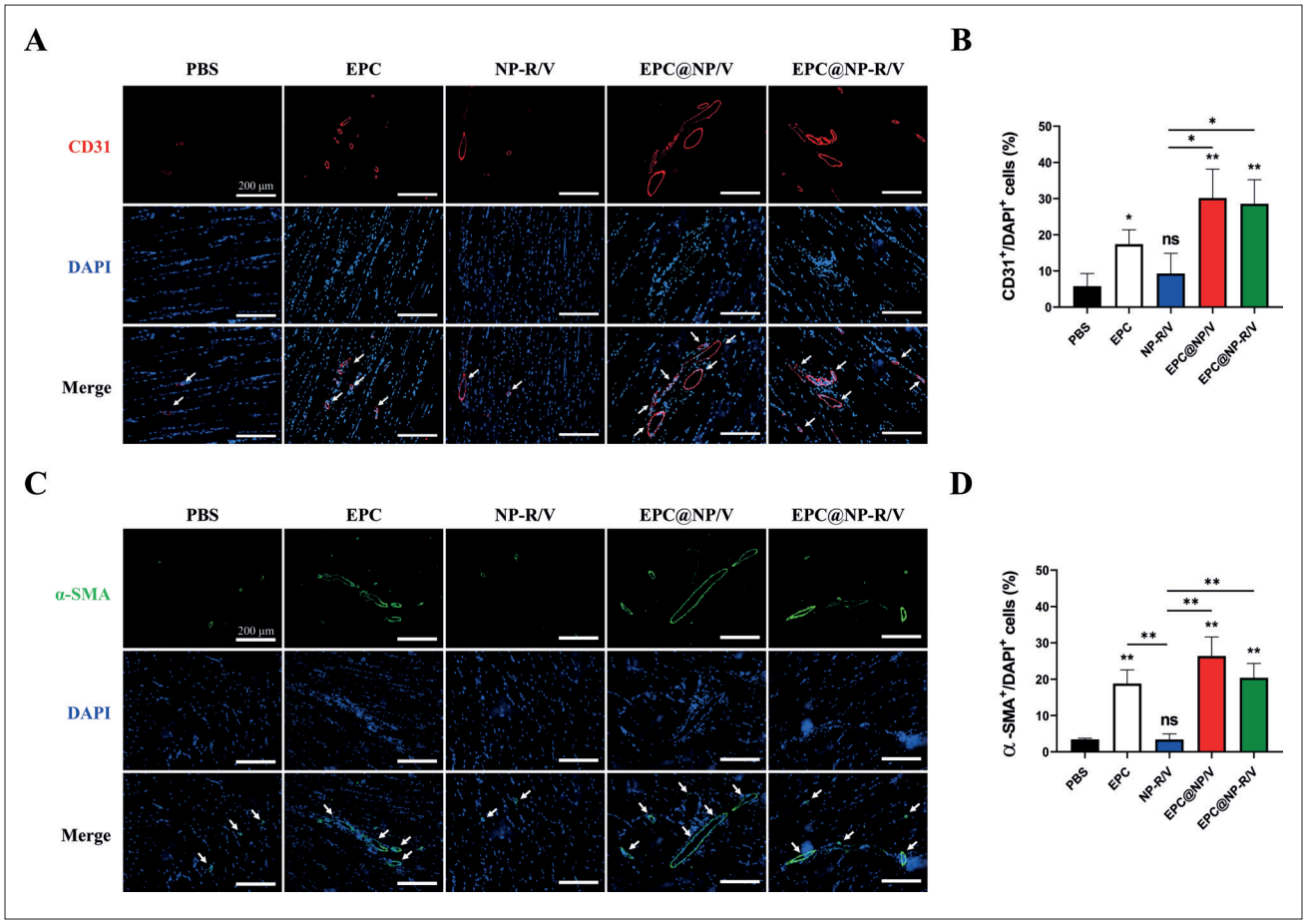

Figure 5. 3D-bioprinted artificial blood vessels with rapamycin-nanoparticles and endothelial progenitor cells improved capillary and arterial blood vessel formation in a murine hind limb ischemia model. (A) Immunostaining with anti-CD31 antibodies (red) for capillary density assessment (white arrows) on postoperative day 28. Scale bar = 200 μm. (B) CD31-positive cell/DAPI density is quantified. *$P < 0.05$; **$P < 0.01$; n.s., $P > 0.05$ versus phosphate-buffered saline (PBS). The values represent mean ± standard deviation (SD) (n = 3). (C) Immunostaining with anti-α-SMA antibody (green) for arteriole density assessment (white arrows) on postoperative day 28. Scale bar = 200 μm. (D) Arteriole density is quantified as the number of α-SMA-positive cells. **$P <$ 0.01; n.s., $P > 0.05$ versus PBS. The values represent mean ± SD (n = 3). Abbreviations: EPC, endothelial progenitor cell; NP, nanoparticle; PBS, phosphate-buffered saline.

3.3. Printing nanoparticle-embedded artificial blood vessels for ischemic disease: assessment of structure, functionality, and drug release

Artificial blood vessels containing NPs and cells were 3D-printed for transplantation into an ischemic disease model, which was the target disease (Figure 3A). The artificial blood vessels with lumen were printed in various sizes (Figure 3B–D). Due to these structural characteristics, it was confirmed that blood flow could successfully flow into the lumen, and the EPCs were properly printed and alive (Figure 3E–G). In addition, the size of the blood vessels can be altered by adjusting the nozzle size and the pressure on the print (Figure 3F). Live/dead cell images confirmed that NP-R did not affect the viability of EPCs (Figure 3G and H). Based on these results, it was confirmed that rapamycin did not affect the proliferation of EPCs, but exhibited strong toxicity in smooth muscle cells. Additionally, the artificial blood vessels exhibited capability to prevent stenosis. The preservation of cellular viability and functionality in response to rapamycin is notably influenced by the distinct cellular morphologies and properties of vascular endothelial stem cells and smooth muscle cells. This study reveals that at an optimal concentration, rapamycin exhibited a dual effect: it did not induce proliferation or cytotoxicity in vascular endothelial stem cells, while inhibiting the proliferation and function of smooth muscle cells (Figures 2 and 3). These findings underscore the potential of rapamycin in preventing restenosis while preserving the vitality and function of vascular endothelial cells, marking it as a promising therapeutic candidate.

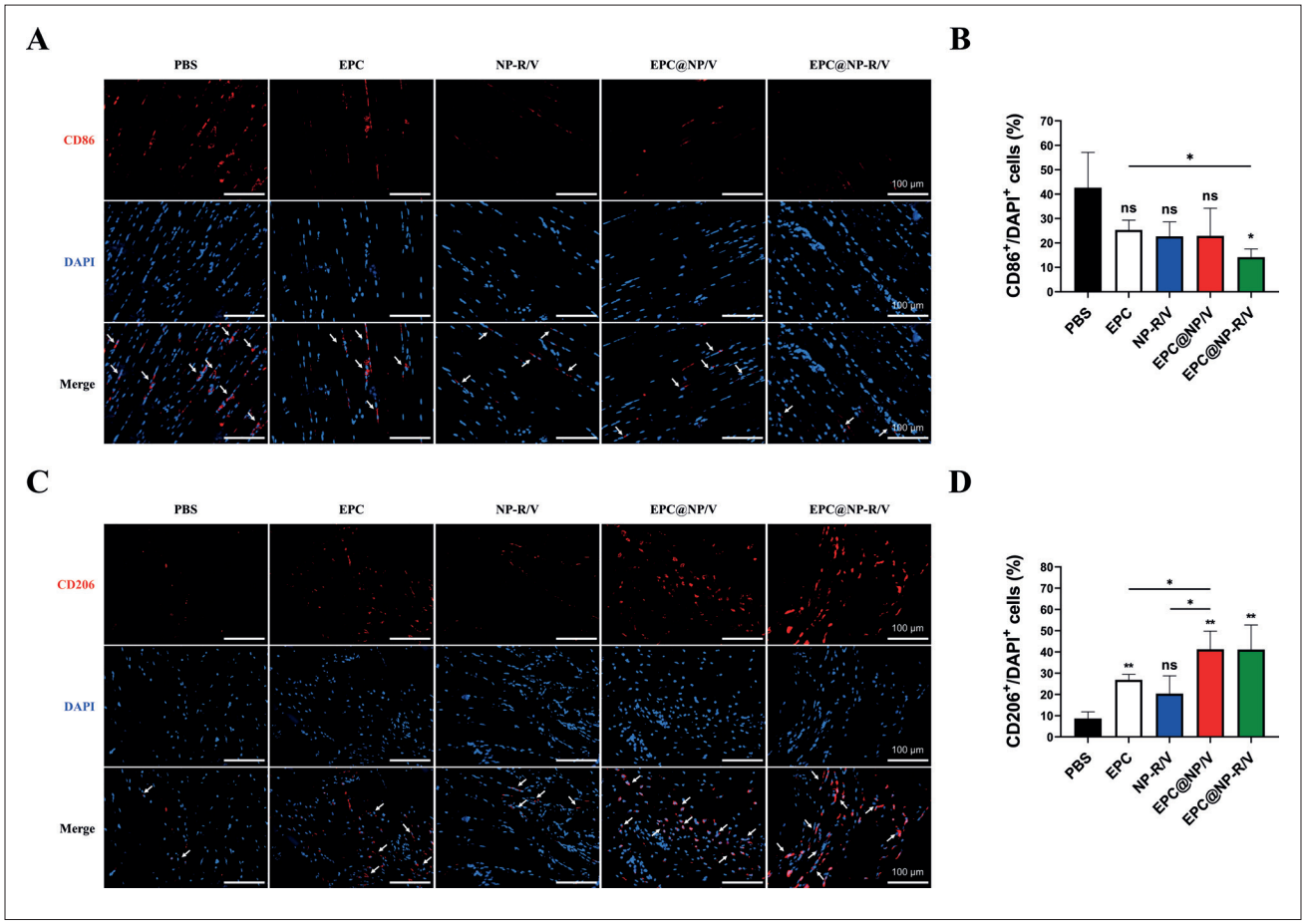

Figure 6. 3D-bioprinted artificial blood vessels with rapamycin-nanoparticles and endothelial progenitor cells reduced M1 and improved M2 macrophage polarization in a murine hind limb ischemia model. (A) Immunostaining with anti-CD86 antibodies (red) for M1 macrophage assessment (white arrows) on postoperative day 7. Scale bar = 100 μm. (B) CD86-positive cell/DAPI density is quantified. *$P < 0.05$; n.s., $P > 0.05$ versus phosphate-buffered saline (PBS). The values represent mean ± standard deviation (SD) (n = 3). (C) Immunostaining with CD206 antibody (red) for M2 macrophage assessment (white arrows) at postoperative day 7. Scale bar = 100 μm. (D) M2 macrophages are quantified as the number of CD206-positive cells. *$P < 0.05$; **$P < 0.01$; n.s., $P > 0.05$ versus PBS. The values represent mean ± SD (n = 3). Abbreviations: EPC, endothelial progenitor cell; NP, nanoparticle; PBS, phosphate-buffered saline.

3.4. Enhancing the therapeutic efficacy of artificial blood vessels in lower extremity ischemia: evaluation of blood flow and recovery ability

To confirm the efficacy of the artificial blood vessels in the lower extremity ischemia model, the following experiment was conducted (Figure 4A): EPC@NP/V or EPC@NP-R/V artificial blood vessels containing EPCs exhibited higher blood flow and recovery ability, demonstrating improved therapeutic efficacy in the group treated with EPC@NP/V or EPC@NP-R/V than the EPC implantation group alone (Figure 4B). The group treated with NP-R/V, which was not loaded with EPCs, demonstrated higher therapeutic efficacy than that treated with PBS; however, its therapeutic efficacy was lower when compared with the group treated with EPCs, and the artificial blood vessel loaded with EPCs. Possibly, this is due to rapid vascular repair using artificial blood vessels as a supportive structure. Ultimately, EPC@NP-R/V manifested efficacy equivalent to that of EPC@NP/V without rapamycin (Figure 4B and C). Additionally, the transplantation of EPC@NP/V and EPC@NP-R/V significantly reduced limb loss, foot necrosis, and toe loss compared with the other groups (Figure 4D and E).

3.5. Comparative histological analysis of efficacy in EPC@NP/V and EPC@NP-R/V

In this animal experiment, it was difficult to compare the efficacy of EPC@NP/V and EPC@NP-R/V; therefore, histological staining was performed. Both groups demonstrated a high efficacy in promoting blood vessel formation, as indicated by the increased expression of CD31 and α-smooth muscle actin (α-SMA), and similar expression

levels were observed in these two groups (Figure 5A–D). Surprisingly, the expression of pro-inflammatory markers was significantly lower in EPC@NP-R/V group compared with that in the EPC@NP/V group (Figure 6A–D). This data was similar to the significant reduction in pro-inflammatory markers observed when treating immune cells with NP-R in *in vitro* experiments (**Figure S2** in Supplementary File). These results suggested that the transplantation of EPC@NP-R/V improves neovascularization and macrophage polarization in ischemic-injured sites.

4. Discussion

Vascular diseases, particularly those related to atherosclerosis and peripheral artery disease, pose significant challenges in current medical treatments.[39,40] Conventional therapies, such as angioplasty and stent implantation, often face limitations, including restenosis, thrombosis, and the lack of endothelialization, leading to recurrent blockages and reduced long-term efficacy. Furthermore, systemic drug administration may result in undesirable side effects and insufficient drug concentrations at the target site.[41-43] These limitations necessitate the exploration of innovative approaches to improve the therapeutic outcomes of vascular diseases given their complex pathophysiology. In addition to the evaluation of NP-R efficacy, the integration of NPs and 3D printing holds immense promise for advancing the field of tissue engineering and regenerative medicine. The combined use of NPs and 3D printing technology offers a myriad of benefits, further enhancing the fabrication and functionality of artificial blood vessels for therapeutic applications.[44-47] First, NPs serve as an efficient drug delivery system by encapsulating therapeutic agents, such as rapamycin. The controlled release of drugs from NPs ensures a sustained and localized delivery, optimizing the therapeutic effect while minimizing systemic side effects.[48-50] This approach allows for precise dosage control and maintains a consistent concentration of the drug within the target site, which is crucial for promoting effective tissue regeneration and preventing restenosis. Second, the careful selection of biocompatible materials for 3D printing and NP formulation ensures minimal adverse reactions when implanted in the human body. By using compatible materials, the risk of inflammation, rejection, or cytotoxicity is significantly reduced, enhancing the overall safety and functionality of the artificial blood vessels.[18,51] To confirm this hypothesis, 3D-printed blood vessels with NP-R were designed, and their effects on anti-restenosis and angiogenesis were tested *in vitro* and *in vivo*.

The artificial blood vessels, each equipped with a lumen, were fabricated in various sizes, mimicking the natural architecture of blood vessels (Figure 3B and C). This structural design enabled the proper flow of blood within the lumen, simulating the functionality of native blood vessels. The successful printing of artificial blood vessels with such complexity and intricacy highlights the potential of 3D printing as a valuable tool for creating tissue-engineered constructs.[18,52,53] Moreover, the incorporation of EPCs within the printed artificial blood vessels facilitated re-endothelialization and promoted vascularization. Live/dead cell imaging confirmed that the viability of EPCs was not compromised by the co-loading of rapamycin within the NPs (Figure 3G and H). This indicated that the printing process and inclusion of NP-R did not adversely affect the survival and functionality of the incorporated cells, further validating the compatibility of this approach for tissue engineering applications. Surprisingly, it was confirmed that NP-R, which did not reduce the cell viability of EPCs (Figure 3G and H), inhibited the migration ability and cell proliferation of smooth muscle cells involved in restenosis (Figure 2); this could potentially prevent restenosis that occurs during artificial blood vessel transplantation.[54-56]

Furthermore, the controlled release of rapamycin from the NPs was assessed. The continuous and slow release of rapamycin over time suggests that the 3D-printed constructs can serve as a sustained drug delivery system, providing prolonged therapeutic effects. This controlled release mechanism ensures a consistent concentration of rapamycin within the local microenvironment, potentially minimizing systemic side effects and improving the efficacy of the treatment.[57-59] To confirm this, animal experiments were performed, and EPC-loaded blood vessels with/without NP-R exhibited excellent recovery ability in the animal models. Precise analysis through histological staining confirmed that the expression of immune-related markers significantly lowers in NP-R-embedded artificial blood vessels than in blood vessels without NP-R.

The combination of 3D printing technology with the integration of NPs and cells in artificial blood vessel fabrication holds significant promise for treating ischemic diseases and preventing restenosis.[58,60-62] The precise control over the structure and composition of the printed constructs, along with the sustained release of rapamycin, contributes to their potential as advanced therapeutic tools.[63-65] Overall, the fabrication and characterization of artificial blood vessels using 3D printing, along with the incorporation of NP-R and EPCs, represent an innovative approach for tissue engineering applications. This study provides valuable insights into the potential of integrating NPs into 3D printing technology and the NPs formulation for improving the efficacy and functionality of artificial blood vessels used in the treatment of ischemic diseases. Furthermore, the use of 3D printing enables the incorporation of various cell types within the artificial blood

vessels, such as EPCs and endothelial cells. This cellular integration could promote re-endothelialization and vascularization, thereby enhancing the overall functionality and biocompatibility of the implanted constructs.

Taken together, the combination of NPs and 3D printing represents a cutting-edge approach for fabricating functional artificial blood vessels. The utilization of NPs for drug delivery and 3D printing for precise fabrication addresses critical challenges in different aspects of tissue engineering, such as drug release control, personalized design, and complex tissue architecture. The continued advancements in 3D printing technology have led to reduced manufacturing costs, making it a more cost-effective approach for producing complex tissue-engineered constructs, such as artificial blood vessels. This affordability increases the accessibility of such treatments, potentially benefiting a larger patient population. With the potential to improve patient outcomes, minimize complications, and revolutionize ischemic disease treatment, this integrated approach paves the way for a new era in regenerative medicine. Further research and clinical validation are required to fully unleash the transformative potential of this innovative technology.

5. Conclusion

This study highlighted the potential of 3D printing technology in the fabrication of artificial blood vessels for tissue engineering applications. The NP-R integrated within the printed constructs demonstrated controlled drug release capabilities, while the inclusion of EPCs promoted re-endothelialization. The 3D-printed artificial blood vessels exhibited a few desirable structural characteristics, including the availability of various sizes and the appearance of lumen, that enable proper blood flow.

The viability of EPCs was maintained within the constructs, even with the inclusion of NP-R. Histological analysis revealed reduced expression of pro-inflammatory markers associated with macrophages in the EPC@NP-R/V group. These findings corroborate the potential of 3D printing technology in the fabrication of functional artificial blood vessels and its compatibility with drug delivery systems. The integration of NPs, rapamycin, and EPCs holds promise for improving the therapeutic outcomes in ischemic diseases.

Acknowledgments

None.

Funding

This research was supported by the Korean Fund for Regenerative Medicine (KFRM) granted by the Korean Government (the Ministry of Science and ICT, the Ministry of Health & Welfare) (21A0101L1).

Conflict of interest

The authors declare no conflicts of interest.

Author contributions

Conceptualization: Jaewoo Choi, Eun Ji Lee, Woong Bi Jang, Sang-Mo Kwon

Investigation: Jaewoo Choi, Eun Ji Lee, Woong Bi Jang, Hye Ji Lim

Methodology: Jaewoo Choi, Eun Ji Lee, Woong Bi Jang, Hye Ji Lim, Dong Myoung Lee, Deokhyeon Yoon, Gi Hoon Yang, Eunjeong Choi, Hojun Jeon, Kyeong Hyeon Lee, Yong-Il Shin, Sang-Cheol Han

Formal analysis: Jaewoo Choi, Eun Ji Lee, Woong Bi Jang

Writing – original draft: Jaewoo Choi, Eun Ji Lee, Woong Bi Jang

Writing – review & editing: Sang-Mo Kwon

Ethics approval and consent to participate

Human umbilical cord blood was obtained from Pusan National University Yangsan Hospital according to the protocol approved by the Institutional Review Board (Approval No. PNUYH-05-2017-053). Informed consent was obtained from human subjects before the use of biological specimens for investigations. Experiments were performed on 8-week-old male BALB/c nude mice (Biogenomics, Seoul, Korea) maintained under a 12 h light/dark cycle in accordance with the regulations of the Pusan National University. All procedures were performed in accordance with the policies of the Institutional Animal Care and Use Committee of the Pusan National University of Korea (Approval No. PNU-2022-0212)

Consent for publication

Not applicable

Availability of data

The data utilized in this study is available from the corresponding author upon reasonable request. Researchers interested in accessing the data may contact Sang-Mo Kwon (smkwon323@pusan.ac.kr) to inquire about data availability, terms of access, and any necessary agreements. We are committed to promoting transparency and collaboration in research.

References

1. Pittman RN, 2011, Regulation of tissue oxygenation, in *Integrated Systems Physiology: From Molecule to Function to Disease*, San Rafael, CA.

2. Tang QR, Xue H, Zhang Q, *et al.*, 2021, Evaluation of the clinical efficacy of stem cell transplantation in the treatment of spinal cord injury: A systematic review and meta-analysis. *Cell Transplant*, 30:9636897211067804. doi: 10.1177/09636897211067804

3. Mao AS, Mooney DJ, 2015, Regenerative medicine: Current therapies and future directions. *Proc Natl Acad Sci U S A*, 112(47):14452-14459. doi: 10.1073/pnas.1508520112

4. Zakrzewski W, Dobrzynski M, Szymonowicz M, *et al.*, 2019, Stem cells: Past, present, and future. *Stem Cell Res Ther*, 10(1):68. doi: 10.1186/s13287-019-1165-5

5. Dzobo K, Thomford NE, Senthebane DA, *et al.*, 2018, Advances in regenerative medicine and tissue engineering: innovation and transformation of medicine. *Stem Cells Int*, 2018:2495848. doi: 10.1155/2018/2495848

6. Serbo JV, Gerecht S, 2013, Vascular tissue engineering: Biodegradable scaffold platforms to promote angiogenesis. *Stem Cell Res Ther*, 4(1):8. doi: 10.1186/scrt156

7. Kwon SG, Kwon YW, Lee TW, *et al.*, 2018, Recent advances in stem cell therapeutics and tissue engineering strategies. *Biomater Res*, 22:36. doi: 10.1186/s40824-018-0148-4

8. Song HG, Rumma RT, Ozaki CK, *et al.*, 2018, Vascular tissue engineering: Progress, challenges, and clinical promise. *Cell Stem Cell*, 22(3):340-354. doi: 10.1016/j.stem.2018.02.009

9. Wakabayashi T, Naito H, 2023, Cellular heterogeneity and stem cells of vascular endothelial cells in blood vessel formation and homeostasis: Insights from single-cell RNA sequencing. *Front Cell Dev Biol*, 11:1146399. doi: 10.3389/fcell.2023.1146399

10. Carmeliet P, Jain RK, 2011, Molecular mechanisms and clinical applications of angiogenesis. *Nature*, 473(7347):298-307. doi: 10.1038/nature10144

11. Majewska A, Wilkus K, Brodaczewska K, *et al.*, 2021, Endothelial cells as tools to model tissue microenvironment in hypoxia-dependent pathologies. *Int J Mol Sci*, 22(2). doi: 10.3390/ijms22020520

12. Phelps EA, Garcia AJ, 2010, Engineering more than a cell: Vascularization strategies in tissue engineering. *Curr Opin Biotechnol*, 21(5):704-709. doi: 10.1016/j.copbio.2010.06.005

13. Munisso MC, Yamaoka T, 2020, Circulating endothelial progenitor cells in small-diameter artificial blood vessel. *J Artif Organs*, 23(1):6-13. doi: 10.1007/s10047-019-01114-6

14. Chambers SEJ, Pathak V, Pedrini E, *et al.*, 2021, Current concepts on endothelial stem cells definition, location, and markers. *Stem Cells Transl Med*, 10(Suppl 2):S54-S61. doi: 10.1002/sctm.21-0022

15. Yoder MC, 2012, Human endothelial progenitor cells. *Cold Spring Harb Perspect Med*, 2(7):a006692. doi: 10.1101/cshperspect.a006692

16. Peters EB, 2018, Endothelial progenitor cells for the vascularization of engineered tissues. *Tissue Eng Part B Rev*, 24(1):1-24. doi: 10.1089/ten.TEB.2017.0127

17. Zhang F, King MW, 2022, Immunomodulation strategies for the successful regeneration of a tissue-engineered vascular graft. *Adv Healthc Mater*, 11(12):e2200045. doi: 10.1002/adhm.202200045

18. Wang D, Xu Y, Li Q, *et al.*, 2020, Artificial small-diameter blood vessels: Materials, fabrication, surface modification, mechanical properties, and bioactive functionalities. *J Mater Chem B*, 8(9):1801-1822. doi: 10.1039/c9tb01849b

19. Hu K, Li Y, Ke Z, *et al.*, 2022, History, progress and future challenges of artificial blood vessels: A narrative review. *Biomater Transl*, 3(1):81-98. doi: 10.12336/biomatertransl.2022.01.008

20. Ozbolat IT, Hospodiuk M, 2016, Current advances and future perspectives in extrusion-based bioprinting. *Biomaterials*, 76:321-343. doi: 10.1016/j.biomaterials.2015.10.076

21. Fu Z, Naghieh S, Xu C, *et al.*, 2021, Printability in extrusion bioprinting. *Biofabrication*, 13(3). doi: 10.1088/1758-5090/abe7ab

22. Yang GH, Kang D, An S, *et al.*, 2022, Advances in the development of tubular structures using extrusion-based 3D cell-printing technology for vascular tissue regenerative applications. *Biomater Res*, 26(1):73. doi: 10.1186/s40824-022-00321-2

23. Angelopoulos I, Allenby MC, Lim M, *et al.*, 2020, Engineering inkjet bioprinting processes toward translational therapies. *Biotechnol Bioeng*, 117(1):272-284. doi: 10.1002/bit.27176

24. Li X, Liu B, Pei B, *et al.*, 2020, Inkjet bioprinting of biomaterials. *Chem Rev*, 120(19):10793-10833. doi: 10.1021/acs.chemrev.0c00008

25. Suntornnond R, Ng WL, Huang X, *et al.*, 2022, Improving printability of hydrogel-based bio-inks for thermal inkjet bioprinting applications via saponification and heat treatment processes. *J Mater Chem B*, 10(31): 5989-6000. doi: 10.1039/d2tb00442a

26. Li W, Mille LS, Robledo JA, *et al.*, 2020, Recent advances in formulating and processing biomaterial inks for vat polymerization-based 3D printing. *Adv Healthc Mater*, 9(15):e2000156. doi: 10.1002/adhm.202000156

27. Yu C, Schimelman J, Wang P, *et al.*, 2020, Photopolymerizable biomaterials and light-based 3D printing strategies for biomedical applications. *Chem Rev*, 120(19): 10695-10743.
doi: 10.1021/acs.chemrev.9b00810

28. Xu X, Awad A, Robles-Martinez P, *et al.*, 2021, Vat photopolymerization 3D printing for advanced drug delivery and medical device applications. *J Control Release*, 329:743-757.
doi: 10.1016/j.jconrel.2020.10.008

29. Ali A, Saeed S, Hussain R, *et al.*, 2023, Synthesis and characterization of silica, silver-silica, and zinc oxide-silica nanoparticles for evaluation of blood biochemistry, oxidative stress, and hepatotoxicity in albino rats. *Acs Omega*, 8(23):20900-20911.
doi: 10.1021/acsomega.3c01674

30. Chen S, Greasley SL, Ong ZY, *et al.*, 2020, Biodegradable zinc-containing mesoporous silica nanoparticles for cancer therapy. *Mater Today Adv*, 6:100066.
doi: 10.1016/j.mtadv.2020.100066

31. Waksman R, Ajani AE, Pichard AD, *et al.*, 2004, Oral rapamycin to inhibit restenosis after stenting of de novo coronary lesions: The Oral rapamune to inhibit restenosis (ORBIT) study. *J Am Coll Cardiol*, 44(7):1386-1392.
doi: 10.1016/j.jacc.2004.06.069

32. Rosner D, McCarthy N, Bennett M, 2005, Rapamycin inhibits human in stent restenosis vascular smooth muscle cells independently of pRB phosphorylation and p53. *Cardiovasc Res*, 66(3):601-610.
doi: 10.1016/j.cardiores.2005.01.006

33. Voisard R, Zellmann S, Muller F, *et al.*, 2007, Sirolimus inhibits key events of restenosis in vitro/ex vivo: Evaluation of the clinical relevance of the data by SI/MPL- and SI/DES-ratios. *BMC Cardiovasc Disord*, 7:15.
doi: 10.1186/1471-2261-7-15

34. Brara PS, Moussavian M, Grise MA, *et al.*, 2003, Pilot trial of oral rapamycin for recalcitrant restenosis. *Circulation*, 107(13):1722-1724.
doi: 10.1161/01.CIR.0000066282.05411.17

35. Kim J, Kim HS, Lee N, *et al.*, 2008, Multifunctional uniform nanoparticles composed of a magnetite nanocrystal core and a mesoporous silica shell for magnetic resonance and fluorescence imaging and for drug delivery. *Angew Chem Int Ed Engl*, 47(44):8438-8441.
doi: 10.1002/anie.200802469

36. Zhou Q, Doherty J, Akk A, *et al.*, 2022, Safety profile of rapamycin perfluorocarbon nanoparticles for preventing cisplatin-induced kidney injury. *Nanomaterials (Basel)*, 12(3).
doi: 10.3390/nano12030336

37. Earla R, Cholkar K, Gunda S, *et al.*, 2012, Bioanalytical method validation of rapamycin in ocular matrix by QTRAP LC-MS/MS: Application to rabbit anterior tissue distribution by topical administration of rapamycin nanomicellar formulation. *J Chromatogr B Analyt Technol Biomed Life Sci*, 908:76-86.
doi: 10.1016/j.jchromb.2012.09.014

38. Lee JH, Lee SH, Choi SH, *et al.*, 2015, The sulfated polysaccharide fucoidan rescues senescence of endothelial colony-forming cells for ischemic repair. *Stem Cells*, 33(6):1939-1951.
doi: 10.1002/stem.1973

39. Bonaca MP, Hamburg NM, Creager MA, 2021, Contemporary medical management of peripheral artery disease. *Circ Res*, 128(12):1868-1884.
doi: 10.1161/CIRCRESAHA.121.318258

40. Gul F, Janzer SF, 2023, *Peripheral Vascular Disease*, StatPearls, Treasure Island (FL).

41. Chin K, 2011, In-stent restenosis: The gold standard has changed. *EuroIntervention*, 7(Suppl K):K43-K46.
doi: 10.4244/EIJV7SKA7

42. Rao J, Pan Bei H, Yang Y, *et al.*, 2020, Nitric oxide-producing cardiovascular stent coatings for prevention of thrombosis and restenosis. *Front Bioeng Biotechnol*, 8:578.
doi: 10.3389/fbioe.2020.00578

43. Perkins LE, 2010, Preclinical models of restenosis and their application in the evaluation of drug-eluting stent systems. *Vet Pathol*, 47(1):58-76.
doi: 10.1177/0300985809352978

44. Nowicki M, Castro NJ, Rao R, *et al.*, 2017, Integrating three-dimensional printing and nanotechnology for musculoskeletal regeneration. *Nanotechnology*,28(38):382001.
doi: 10.1088/1361-6528/aa8351

45. Fischetti T, Borciani G, Avnet S, *et al.*, 2023, Incorporation/enrichment of 3D bioprinted constructs by biomimetic nanoparticles: Tuning printability and cell behavior in bone models. *Nanomaterials (Basel)*, 13(14).
doi: 10.3390/nano13142040

46. Johannesson J, Pathare MM, Johansson M, *et al.*, 2023, Synergistic stabilization of emulsion gel by nanoparticles and surfactant enables 3D printing of lipid-rich solid oral dosage forms. *J Colloid Interface Sci*, 650(Pt B):1253-1264.
doi: 10.1016/j.jcis.2023.07.055

47. Remaggi G, Bergamonti L, Graiff C, *et al.*, 2023, Rapid prototyping of 3D-printed AgNPs- and nano-TiO(2)-embedded hydrogels as novel devices with multiresponsive antimicrobial capability in wound healing. *Antibiotics (Basel)*, 12(7).
doi: 10.3390/antibiotics12071104

48. Liu Y, Li K, Liu B, *et al.*, 2010, A strategy for precision engineering of nanoparticles of biodegradable copolymers for quantitative control of targeted drug delivery. *Biomaterials*, 31(35):9145-9155.
doi: 10.1016/j.biomaterials.2010.08.053

49. Tripathi D, Srivastava M, Rathour K, *et al.*, 2023, A promising approach of dermal targeting of antipsoriatic drugs via engineered nanocarriers drug delivery systems for tackling psoriasis. *Drug Metab Bioanal Lett*.
doi: 10.2174/2949681016666230803150329

50. Mitchell MJ, Billingsley MM, Haley RM, *et al.*, 2021, Engineering precision nanoparticles for drug delivery. *Nat Rev Drug Discov*, 20(2):101-124.
doi: 10.1038/s41573-020-0090-8

51. Kasravi M, Ahmadi A, Babajani A, *et al.*, 2023, Immunogenicity of decellularized extracellular matrix scaffolds: A bottleneck in tissue engineering and regenerative medicine. *Biomater Res*, 27(1):10.
doi: 10.1186/s40824-023-00348-z

52. Pinnock CB, Meier EM, Joshi NN, *et al.*, 2016, Customizable engineered blood vessels using 3D printed inserts. *Methods*, 99:20-27.
doi: 10.1016/j.ymeth.2015.12.015

53. Kakisis JD, Liapis CD, Breuer C, *et al.*, 2005, Artificial blood vessel: The Holy Grail of peripheral vascular surgery. *J Vasc Surg*, 41(2):349-354.
doi: 10.1016/j.jvs.2004.12.026

54. Marx SO, Totary-Jain H, Marks AR, 2011, Vascular smooth muscle cell proliferation in restenosis. *Circ Cardiovasc Interv*, 4(1):104-111.
doi: 10.1161/CIRCINTERVENTIONS.110.957332

55. Huang C, Zhao J, Zhu Y, 2020, Drug-eluting stent targeting Sp-1-attenuated restenosis by engaging YAP-mediated vascular smooth muscle cell phenotypic modulation. *J Am Heart Assoc*, 9(1):e014103.
doi: 10.1161/JAHA.119.014103

56. Huang C, Zhang W, Zhu Y, 2019, Drug-eluting stent specifically designed to target vascular smooth muscle cell phenotypic modulation attenuated restenosis through the YAP pathway. *Am J Physiol Heart Circ Physiol*, 317(3):H541-H551.
doi: 10.1152/ajpheart.00089.2019

57. Yetisgin AA, Cetinel S, Zuvin M, *et al.*, 2020, Therapeutic nanoparticles and their targeted delivery applications. *Molecules*, 25(9).
doi: 10.3390/molecules25092193

58. Falke LL, van Vuuren SH, Kazazi-Hyseni F, *et al.*, 2015, Local therapeutic efficacy with reduced systemic side effects by rapamycin-loaded subcapsular microspheres. *Biomaterials*, 42:151-160.
doi: 10.1016/j.biomaterials.2014.11.042

59. Cheng X, Xie Q, Sun Y, 2023, Advances in nanomaterial-based targeted drug delivery systems. *Front Bioeng Biotechnol*, 11:1177151.
doi: 10.3389/fbioe.2023.1177151

60. Chen EP, Toksoy Z, Davis BA, *et al.*, 2021, 3D bioprinting of vascularized tissues for in vitro and in vivo applications. *Front Bioeng Biotechnol*, 9:664188.
doi: 10.3389/fbioe.2021.664188

61. Papaioannou TG, Manolesou D, Dimakakos E, *et al.*, 2019, 3D bioprinting methods and techniques: Applications on artificial blood vessel fabrication. *Acta Cardiol Sin*, 35(3):284-289.
doi: 10.6515/ACS.201905_35(3).20181115A

62. Tajabadi M, Goran Orimi H, Ramzgouyan MR, *et al.*, 2022, Regenerative strategies for the consequences of myocardial infarction: Chronological indication and upcoming visions. *Biomed Pharmacother*, 146:112584
doi: 10.1016/j.biopha.2021.112584

63. Craparo EF, Cabibbo M, Conigliaro A, *et al.*, 2021, Rapamycin-loaded polymeric nanoparticles as an advanced formulation for macrophage targeting in atherosclerosis. *Pharmaceutics*, 13(4).
doi: 10.3390/pharmaceutics13040503

64. Shi Y, Jiao C, Lu X, *et al.*, 2022, Rapamycin nanoparticles improves drug bioavailability in PLAM treatment by interstitial injection. *Orphanet J Rare Dis*, 17(1):349.
doi: 10.1186/s13023-022-02511-6

65. Chen Y, Zeng Y, Zhu X, *et al.*, 2021, Significant difference between sirolimus and paclitaxel nanoparticles in anti-proliferation effect in normoxia and hypoxia: The basis of better selection of atherosclerosis treatment. *Bioact Mater*, 6(3):880-889.
doi: 10.1016/j.bioactmat.2020.09.005

ACCSCIENCE PUBLISHING

International Journal of Bioprinting

RESEARCH ARTICLE

Manufacturing evaluation of seven medical device companies during the production of a 3D-printed titanium pelvic implant

Alba González Álvarez[1,2]*, Rubén Pérez Mañanes[2,3,4,5], José Antonio Calvo Haro[2,3,4,5], Lydia Mediavilla Santos[2,3,5], and Javier Pascau[1,2]

[1]Departamento de Bioingeniería, Universidad Carlos III de Madrid, Madrid, Spain

[2]Instituto de Investigación Sanitaria Gregorio Marañón (IiSGM), Hospital General Universitario Gregorio Marañón, Madrid, Spain

[3]Servicio de Cirugía Ortopédica y Traumatología, Hospital General Universitario Gregorio Marañón, Madrid, Spain

[4]Departamento de Cirugía, Universidad Complutense de Madrid, Madrid, Spain

[5]Advanced Planning and 3D Manufacturing Unit (UPAM3D), Hospital Gregorio Marañón, Madrid, Spain

Abstract

Powder bed fusion (PBF) technology has become a popular manufacturing method to fabricate custom metallic implants. This trend has generated some regulatory concerns because traditional developing guidelines are not suitable for three-dimensional (3D)-printed implants. This is due to the layered microstructure of additive manufactured parts that produces mechanical properties different than those of traditionally manufactured parts. The inappropriate choice of the process parameters and postprocessing methods can lead to fabrication errors that could negatively affect mechanical properties and dimensional accuracy. The objective of the study was to perform a preliminary evaluation of the quality of manufacturing provided by the medical device industry and identify the best 3D printing practices. We designed a pelvic bone reconstructing implant and asked seven companies to manufacture it in Ti6Al4V with PBF technology. We inspected some important aspects of the manufacturing quality of the prototypes received by evaluating geometrical precision and microstructural integrity in the surface and in the matrix, including a qualitative assessment of voids and grain morphology. Results demonstrated a great difference among the implant prototypes. Two companies proved to be superior and provided defect-free implants. The other five produced evidence of some defects including: geometrical deviations (maximum values of up to 5 mm); heterogeneous acicular grain morphologies; broken sections of lattice structures; and internal and superficial voids and cracks that could potentially compromise functional and clinical performance. To our knowledge, this is the first study analyzing the production of several custom implant additive manufacturers based on a geometrical and microstructural evaluation of the same pelvic implant fabrication. The imperfections found in some prototypes produced by companies certified to commercialize personalized implants highlight the urgent need for technical standards that regulate the safe development of 3D-printed implants. Further analyses are required to determine the actual clinical and mechanical consequences of such imperfections. The results also show that when additive manufacturing is adequately managed, it can be a valid manufacturing method to fabricate defect-free implants.

***Corresponding author:**
Alba González Álvarez
(ms.alba.gonzalez@gmail.com)

Citation: González Álvarez A, Pérez Mañanes R, Calvo Haro JA, Mediavilla Santos L, Pascau J. Manufacturing evaluation of seven medical device companies during the production of a 3D-printed titanium pelvic implant. *Int J Bioprint*. 2024;10(2):0140.
doi: 10.36922/ijb.0140

Received: April 27, 2023
Accepted: July 24, 2023
Published Online: January 31, 2024

Keywords: Custom implants; Ti6Al4V; Powder bed fusion; Implant quality; Defects; Quality control

1. Introduction

In recent years, additive manufacturing (AM) has become a common method to create custom metallic implants with complex shapes and biomimetic features.[1] Its increasing popularity has generated some regulatory concerns because traditional developing guidelines are not suitable for three-dimensional (3D) printing technology.[2] This is due to the layered microstructure of additive manufactured parts that produces mechanical properties different than those of traditionally manufactured parts.[3] The newly released Medical Device Regulation (MDR)[4] based on the EU regulation 2017/745 requires medical device manufacturers to have a quality management system with relevant requirements included in the ISO 13485,[5] which is a formal document that specifies requirements for good management practices. However, its compliance does not guarantee the production of high-quality implants[6] because it does not give explicit requirements to which the medical device should conform. The lack of specific technical requirements[7] and regulatory pathways for 3D-printed implants can lead to manufacturing errors that may possibly affect device performance.[3,8] This is the case when developing bone reconstructing implants that are additively manufactured in Ti6Al4V by powder bed fusion (PBF) technology,[7] including selective laser melting (SLM) or electron beam melting (EBM). The inappropriate choice of postprocesses and printing parameters such as laser diameter and temperature, cooling cycle, or layer thickness (among others) can lead to invisible fabrication errors compromising material properties, dimensional accuracy, and biological function.[9]

The challenges involved in producing defect-free AM implants motivated us to perform a preliminary evaluation of the quality of manufacturing provided by the medical device industry, with a particular focus on companies using Ti6Al4V to develop custom implants. Our study was carried out as a quality control step to select the best companies to co-produce custom implants with and guarantee high quality and safety to patients.

2. Materials and methods

We designed a pelvic bone reconstructing implant (see Figure 1) to be manufactured by as many companies as possible. The objective was to simulate the collaborative process of co-producing a pelvic implant with several manufacturers to achieve the best possible performance and quality. Participation in this study was voluntary. The resulting information is presented anonymously to respect the confidentiality of the participating companies.

2.1. Selection of companies

The companies selected for this study adhered to the criteria as follows: (i) a medical device manufacturer of titanium custom orthopedic implants using AM; (ii) a medical device manufacturer that provides services to Spain (being located in Spain was not required); (iii) a medical device manufacturer that is willing to collaborate for the co-development of custom orthopedic implants for clinical use; and (iv) a medical device manufacturer that is willing to collaborate for the purpose of this study.

A total of 13 companies based in several locations around Europe were identified as potential participants.

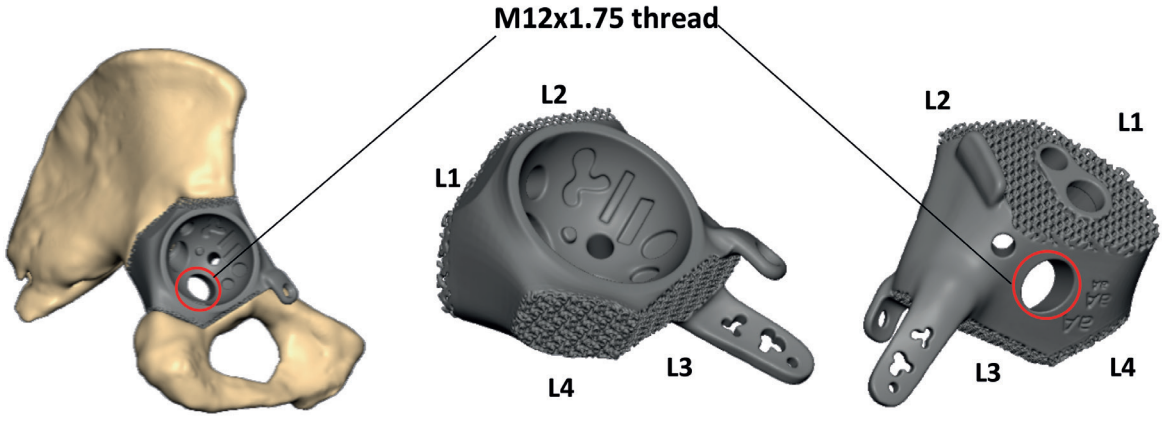

Figure 1. 3D CAD design of the pelvic implant designed to evaluate several manufacturing features including four different surfaces of lattice structures (L), three extracortical plates, some screw holes as well as a threaded hole marked in red.

A first meeting was held individually with all of them. Six companies did not meet the above-mentioned criteria; therefore, they were disqualified for participating in the study. The other seven companies were evaluated.

2.2. Implant test design

The pelvic implant was modeled with Unigraphics NX (Siemens, Texas, US), Geomagic Freeform Plus 2021 (3D Systems, Rock Hill, US), and nTopology software (nTopology, New York, US) simulating a reconstruction to remove a pelvic tumor. A variety of design features were added with the purpose of testing the manufacturing capacity of the companies and not for clinical reasons. These included several screw holes, flanges, and four surfaces of porous structures with different architectures. Several diamond and gyroid structures were chosen with a minimum beam thickness of 0.6 mm for lattices 1, 3, and 4 (L1, L3, and L4) and 0.5 mm for lattice 2 (L2).

2.3. Design transfer for fabrication

2.3.1. Manufacturing specifications proposed

There are no standardized manufacturing requirements for the optimal AM of pelvic custom implants. Therefore, the following general specifications were prepared based on the literature and authors' experience, and communicated to the companies prior to manufacturing. These specifications were defined as general requirements to be discussed with the companies so their manufacturing processes and standards could be identified and noted.

- Material: Ti6Al4V, the gold-standard material to produce pelvic reconstructions and other load-bearing hard tissue due to its biocompatibility, mechanical properties, and corrosion resistance.[10,11]
- AM technology: either SLM or EBM, the most commonly used techniques to fabricate metallic custom implants.[7]
- Maximum density to achieve, 100% if possible, preventing voids as porosity is known to negatively impact the mechanical properties of SLM and EBM parts.[3]
- Avoid residual stresses from non-uniform heat. The cooling rate during additive manufacturing alters the microstructure of the part, affecting mechanical performance.[7]
- Hot isostatic pressing (HIP) to eliminate residual porosity and improve fatigue strength.[2,12]
- Manufacturing of a standard metric thread (M12 x 1.75) in a specific hole (see Figure 1) as per drawings provided.
- Surface finish as per drawings provided, showing several ranges of rugosity from polished surfaces to "as built" surfaces in various areas of the implant. The purpose was to discuss with each manufacturer what different types of surface finishes they were able to perform and apply them to the prototype as a sample. This was requested to account for the variability of surfaces required on metallic implants in different areas and different functions. Surface roughness and controlled topography can facilitate cell attachment and improve osseointegration and bone healing.[13] However, there are areas in implants that are preferred to be smoothly polished to increase soft tissue-to-surface contact, reduce wear debris, and improve dynamic contact for articulating devices.[14]
- General tolerance ranging from 0.1 to 0.2 mm.
- Prototype not for clinical use.
- Maximum quality to achieve: prototype to be evaluated in terms of quality of manufacture.

2.3.2. Manufacturing specifications agreed

A second round of meetings was held with six out of seven companies that requested a discussion about the manufacturing specifications. We will refer to the companies as "Company N" (CN) in the remaining paragraphs. Only company 7 (C7) gave no feedback and sent the manufactured part directly without consultations. For the other six companies, the manufacturing specifications were adapted to each company's capabilities, resources, and standards, after discussion and agreement. The agreed requirements are given in Table 1.

The feedback from companies about the manufacturing specifications was very diverse. C4 and C6 produced with EBM technology, while the rest manufactured with SLM. Most companies were able to offer hybrid manufacturing combining AM with CNC machining except for C7. This company refused to manufacture the thread as they had to subcontract the operation. Only two companies, C5 and C6, agreed to perform the HIP treatment, and both of them had to outsource the process. C5 always perform HIP for orthopedic implants to improve their fatigue performance. C6 did not consider it necessary, but they performed it to follow our indications. The rest of the companies never perform HIP and had no experience about the process. With regard to surface finish, we asked the companies for their preferred surface finish for the pelvic implant. Consequently, the prototypes received present different matte, satin, and mirror finishes.

Table 1. Manufacturing specifications agreed by each company

Company	Manufacturing specifications						Design feedback for AM
	AM technique	Stress relief	HIP	Thread	AM + machining	Main surface finish	
C1	SLM	Yes	No	Yes	Yes	Mirror finish	No
C2	SLM	Yes	No	Yes	Yes	Matte and mirror finish (2 prototypes)	No
C3	SLM	Yes	No	Yes	Yes	Matte finish	No
C4	EBM	No	No	Yes	Yes	Satin finish	Yes
C5	SLM	Yes	Yes	Yes	Yes	Mirror finish	Yes
C6	EBM	No	Yes	Yes	Yes	Matte finish	No
C7	SLM	Yes	No	No	No	Matte finish	No

Abbreviations: AM, additive manufacturing; C, company, EBM, electron beam melting; HIP, hot isostatic pressing; SLM, selective laser melting.

C2 had no preferences and decided to manufacture two prototypes, each one with a different surface finish. Some companies were able to achieve a tolerance of 0.1 mm, whereas others could not manufacture with this level of precision. However, all the companies confirmed they could achieve a manufacturing tolerance of 0.2 mm.

C5 provided feedback about the implant design and requested a modification of L2 to optimize manufacturing, predicting that this area would need support material that, when removed, would break the lattice. Therefore, the architecture for that L2 was thickened to improve manufacturing quality results following their feedback. This was agreed upon and assessed to have no effects on performance. C4 expressed their concerns about the orientation of L2 and mentioned the need to design the lattice in accordance with the orientation of the part in the build. The rest of companies C1, C2, C3, C6, and C7 did not comment on any aspects of the implant design prior to fabrication.

2.3.3. Data preparation

The companies showed a great variety of methods to prepare the CAD data for manufacture. Most of them required only the STL file of the entire implant. Some companies asked for separate STL files of the solid part and the lattice structures. One asked for separate files of the solid and the lattice areas in STEP format. All the data was prepared and provided to each company as requested.

2.4. Prototypes' analyses and criteria for quality assessment

Companies and their respective prototypes were evaluated according to the following criteria: visual inspection, geometrical precision analysis, and microstructural study.

A visual inspection is the first qualitative assessment that helps identify macro defects, important inconsistencies, and large geometrical deviations.

Geometrical precision is crucial to reconstruct a bone defect. An accurate fit between the implant and the remaining bone is required for good performance and to facilitate osseointegration.[13] Dimensional accuracy in lattice structures is also mandatory as they allow for soft tissue adherence and vascularization within the implant and affect the scaffold mechanical properties.[15] Geometrical deviations outside the agreed-upon manufacturing tolerances cannot be allowed because non-compliance could possibly cause some risks to patients.

The internal integrity of the parts was also critical in the evaluation due to the biomechanical functionality of a pelvic implant, considering that microstructural defects could lead to early failure.[16] Ti6Al4V is a dual-phase material composed of α phase and β phase, and the different crystal structures determine the mechanical properties of the parts.[17,18] Pelvic implants are subjected to high patient loading; therefore, the fatigue strength should be optimized. Fatigue strength is extremely sensitive to localized and non-uniform heat, porosity, surface defects, and uncontrolled cooling cycles during fabrication.[19,20] Therefore, we qualitatively inspected the microstructure of each sample by analyzing: (i) integrity of the surface, as irregularities in the surface can lead to crack initiations;[8] (ii) porosity in the periphery of the part as well as internally in the matrix, as the fatigue strength significantly degrades when pores are developed;[3] and (iii) morphology of the grains which will determine the tenacity, elasticity, and mechanical properties of the components.[3]

Communication between designer and manufacturer was also a factor to consider in the assessment. This communication needs to be optimal to guarantee that manufacturing capacities can meet product requirements, so design results are appropriate for the fabrication resources of each company. Furthermore, the Design for Additive Manufacturing (DfAM) discipline should be practiced to improve product performance in all lifecycle stages.[21]

For a complete quality assessment of a pelvic implant production, further analyses should be included, such as porous structures, biocompatibility, adequate cleaning, and mechanical testing. In the current study, as a first step, we focused on geometrical accuracy and microstructural integrity of the parts to identify the best 3D printing practices in the industry.

2.4.1. Visual inspection

The main aspects evaluated were: (i) macro geometrical deviations: the prototypes were assembled to a polylactic anatomical model of the pelvic bone manufactured by fused deposition modeling, assessing their fit; this included an evaluation of the integrity of the lattice structures. Furthermore, a "pass" or "not pass" check was performed for the screw holes in the prototypes with real cortical screws of various sizes; (ii) the prototypes were produced following the specifications agreed before manufacturing; and (iii) the presence of residues from support material or powder that could reveal improper postprocessing and cleaning.

2.4.2. Geometrical precision analysis

The prototypes manufactured were CT scanned with a Nikon XT H 225 scanner (Nikon, Tokyo, Japan) to obtain their digital geometry. The following parameters were used: 150 kVp, 350 μA, 2.5 mm Cu filtration, and 40 μm voxel size. An automatic registration was performed between the scanned digital geometries and the CAD design files for each implant for comparison. Geometrical deviations were mapped and quantified with our own metrical module developed with 3D Slicer software, identifying nonconformities over the 0.2 mm permitted tolerance. The potential consequences these variations could have caused in surgery were explored.

2.4.3. Microstructural analysis

Eight samples were extracted from the longest extracortical plate (flange) of the eight implant prototypes so that the surfaces for analysis were parallel to the building platform for each sample. The specimens were cut with an abrasive wheel, mechanically ground, polished with colloidal suspension, and etched with Kroll's reagent. Microstructures were analyzed using a Zeiss Axio Scope A1 multi-faceted polarized light microscope (Zeiss Industrial Metrology, Oberkochen, Germany) at different stages: after polishing, to study the presence of defects at the periphery as well as in the central area of the samples; and after etching, to identify the material phases of this alpha-beta alloy and the microstructural grain morphology.

Voids were analyzed by micrographic observation. For each sample, one of the side surfaces was ground and polished, but not etched. Then, the metallographic microscope was used to observe the polished surface of each sample with several magnifications. These images were obtained in similar light conditions and were binarized with the same threshold.

2.4.4. Communication

A fluent communication between the implant designer and the manufacturer is crucial to develop defect-free AM parts. This communication was encouraged during all the stages of the study. The feedback from manufacturers assessing the feasibility of fabricating the proposed pelvic design with their manufacturing capacities was expected. When companies proposed modifications to optimize the design, to adapt it to their AM machines and processes, their feedback was considered if such amendments would not compromise implant function.

3. Results

3.1. Prototypes manufactured

The eight prototypes manufactured by the seven companies are displayed in Figure 2. C2 manufactured two prototypes, P2 with mirror finish and P6 with matte finish.

The correspondence between the companies (C) that manufacture each of the prototypes (P) is presented in Table 2.

3.2. Prototypes analysis and quality assessment

3.2.1. Visual inspection

The visual inspection showed important irregularities in five out of the eight prototypes received. The main defects identified are described in Table 3 and displayed in Figure 3.

3.2.2. Geometrical precision analysis

All the prototypes showed values of geometrical deviations over the 0.2 mm of tolerance permitted. However, some deviations were critical, and others could be ignored. The maximum deviation for P4, P5, and P6 was presented in very small and localized areas of lattice structures, and therefore, such deviations could be neglected with no clinical consequences. The mean deviations for these prototypes P4, P5, and P6 were 0.14 mm, 0.15 mm, and 0.14 mm, respectively, therefore within the 0.2 mm allowed. On the other hand, the rest of prototypes P1, P2, P3, P7, and P8 presented large maximum deviations of 3.00, 2.53, 4.94, 4.88, and 3.60 mm, respectively, that could have potentially compromised implant performance.[15,22,23] The most recurrent issue was the inadequate fabrication of large areas of L2. Furthermore, for P2, P3, and P7, the mean deviation was also over 0.2 mm, and these prototypes also presented some deviations in the extracortical plates. The qualitative and quantitative

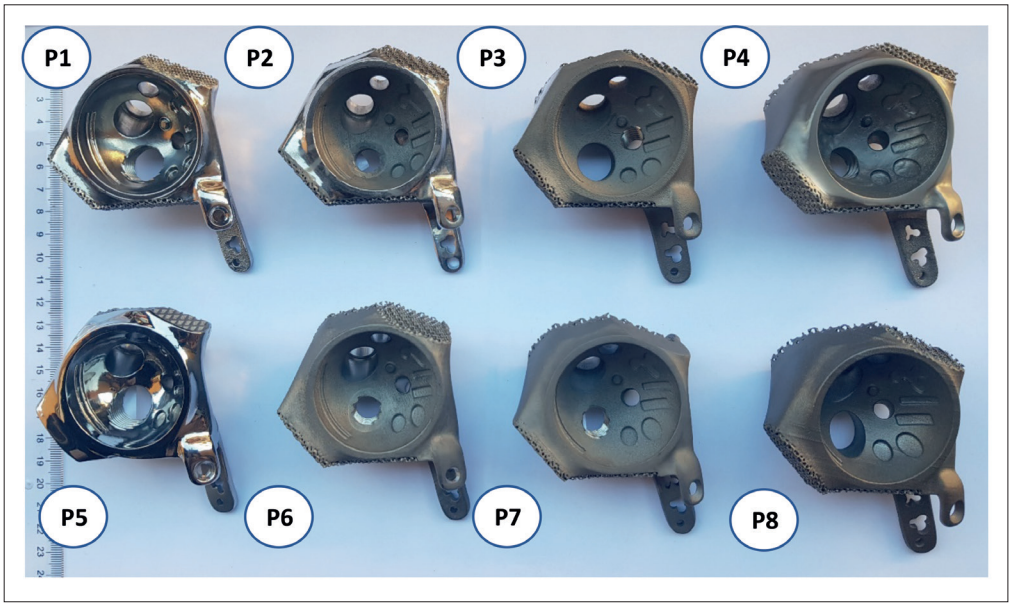

Figure 2. The eight prototypes manufactured by the seven companies that participated in the study. Each company manufactured one prototype (P) except for C2, which manufactured P4 and P6.

Table 2. Correspondence between the seven companies that manufactured the eight prototypes

Prototypes	P1	P2	P3	P4	P5	P6	P7	P8
Manufactured by	C1	C2	C3	C4	C5	C2	C6	C7

Each company manufactured one prototype except for C2, which manufactured P4 and P6. Abbreviations: C, company; P, prototype.

Table 3. Defects identified in each prototype during visual inspection

Prototype (company)	Visual inspection defects
P1 (C1)	• Partially broken L2 (Figure 3a); the issue was communicated before sending the part
P2 (C2)	• Out of tolerance hole's dimensions, wrong diameter and location (Figure 3b)
P3 (C3)	• Partially broken L2 • Visible residues of support material (Figure 3c)
P4 (C4)	• None
P5 (C5)	• None
P6 (C2)	• None
P7 (C6)	• Entire L2 missing (Figure 2) • Mirror surface finish agreed, however matte finish delivered • Sharp edge residue in the thread (Figure 3d) • Cracks in the surface (Figure 3e)
P8 (C7)	• No thread performed and not communicated • Missing corner of the plate (Figure 3f) • Partially broken L2 • Visible residues of support material

results of the geometrical precision analysis are presented in Table 4.

3.2.3. Microstructural analysis

A summary of the results of the microstructural analysis including the morphology of the grains and the observation of porosity (in the periphery and in the center of each sample) are presented in Table 5.

The prototypes demonstrated differences in the microstructural morphology of the grains, and some defects that affected the integrity of the parts were found. The most critical one is P7, which showed a crack that

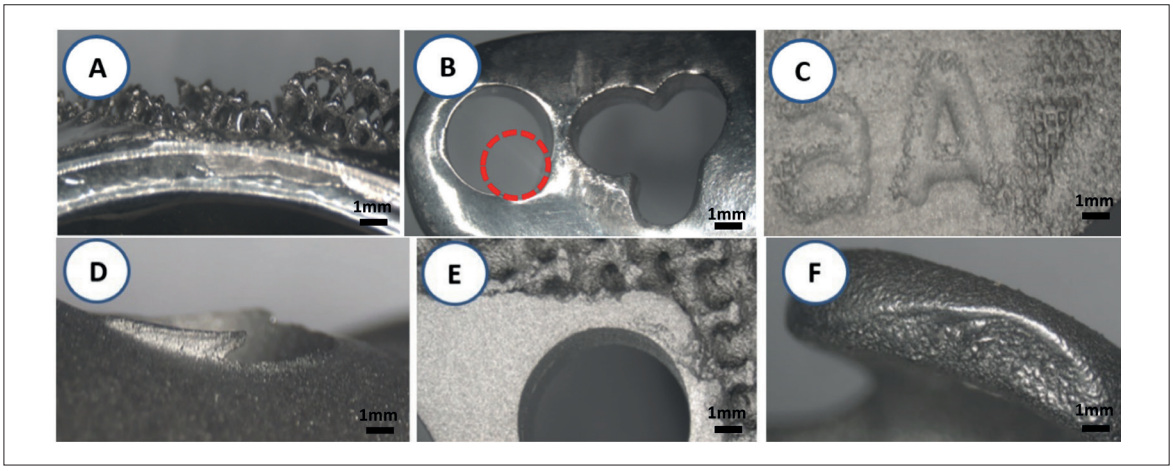

Figure 3. Superficial macrodefects identified during the visual inspection. (A) Lattice structure L2 partially broken in P1. (B) Hole manufactured in the wrong location and with the wrong diameter in P2. The red mark shows what the hole dimension and location should have been. (C) Residues of support material in P3. (D) Sharp edge from incomplete postprocessing in P7. (E) Cracks in the surface in P7. (F) Corner of the extra cortical plate broken in P8.

Table 4. Results of the quantitative geometrical precision analysis and an assessment of the clinical consequences that some deviations could have possibly caused in patients

	Comparison of CAD design (green) and manufactured implant (red)	Numerical deviation color map between the CAD implant design and the scanned manufactured prototypes	Potential clinical consequences of geometrical deviations
P1 (C1) **Max: 3.00 mm** **Mean: 0.16 mm** Std: 0.19 mm	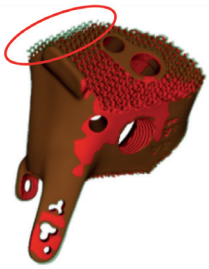	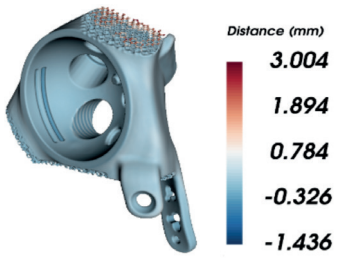	• Most of L2 missing • Potential compromised implant fixation, 3 mm of deviation at tumor resection level, reduced biological and mechanical performance including osseointegration[15,22,23]
P2 (C2) **Max: 2.53 mm** **Mean: 0.22 mm** Std: 0.22 mm		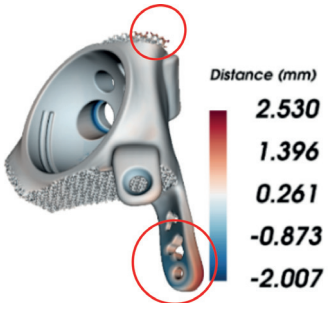	• 2.5 mm deviation in the plate, compromised fit[15] • 2 mm deviation of a hole's diameter in plate, compromised screw fixation at the planned site[15] • 2.3 mm deviation located in only a few cells of L2, no clinical relevance
P3 (C3) **Max: 4.94 mm** **Mean: 0.37 mm** Std: 0.53 mm	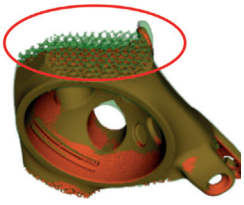	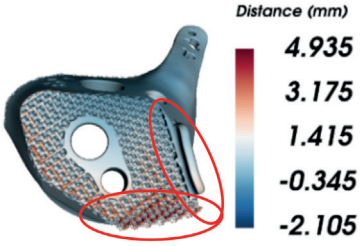	• Most of L2 missing and partially L1 broken, compromised implant fixation, reduced biological and mechanical performance including osseointegration[15,22,23] • 4.9 mm of deviation at tumor resection level • 3 mm deviation of plate geometry, compromised implant fitting on bone[15]

Continued...

Table 4. *Continued...*

P4 (C4) **Max: 2.33 mm** **Mean: 0.14 mm** Std: 0.14 mm	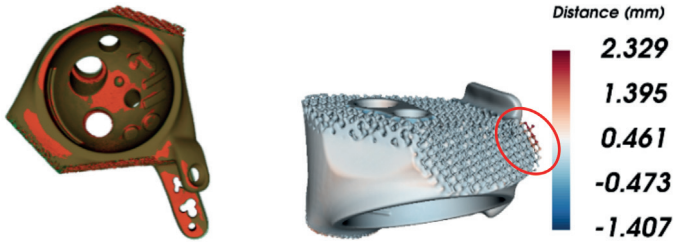	• None; the maximum deviation (2.3 mm) is located in only a few cells of L2 and could be neglected
P5 (C5) **Max: 1.46 mm** **Mean: 0.15 mm** Std: 0.63 mm	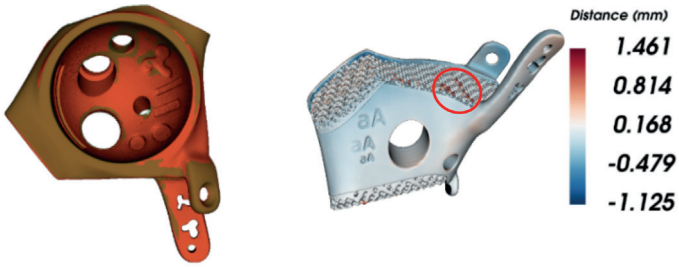	• None; the maximum deviation (1.5 mm) is located in only a few cells of L3 and could be neglected
P6 (C2) **Max: 2.29 mm** **Mean: 0.14 mm** Std: 0.13 mm	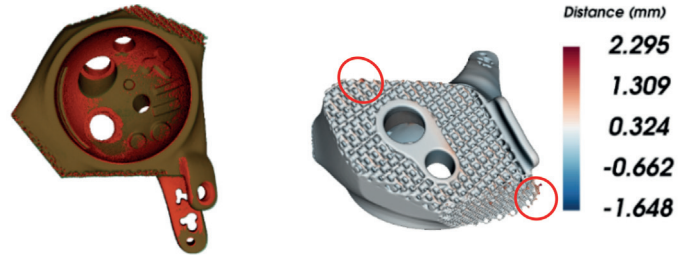	• None; the maximum deviation (2.3 mm) is located in only a few cells of L1 and L2 and could be neglected
P7 (C6) **Max: 4.88 mm** **Mean: 0.37 mm** Std: 0.53 mm	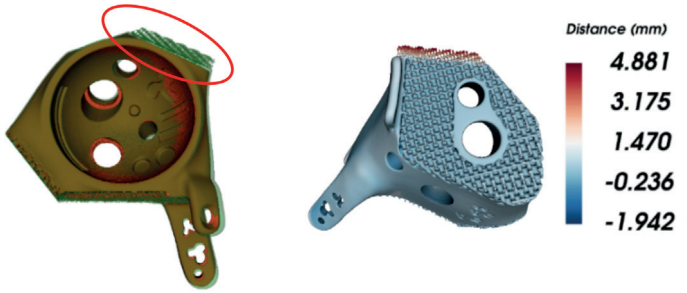	• Entire L2 missing; compromised implant fixation, 4.9 mm of deviation at tumor resection level, reduced biological and mechanical performance including osseointegration[15,22,23] • 1.7 mm deviation of extracortical plates' geometry, compromised implant fitting on bone[15]
P8 (C7) **Max: 3.60 mm** **Mean: 0.14 mm** Std: 0.28 mm	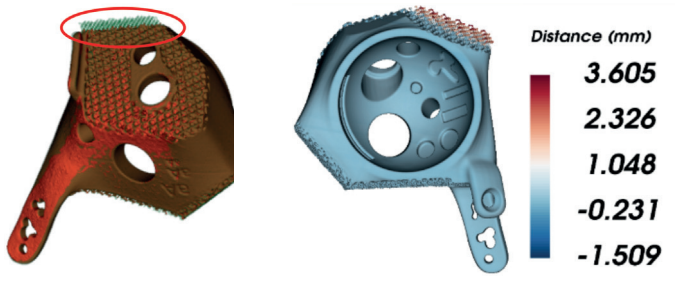	• Most of L2 missing; compromised implant fixation, 3.6 mm of deviation at tumor resection level, reduced biological and mechanical performance including osseointegration[15,22,23]

initiates on the surface and continued toward the center of the component, presenting a potential risk for early failure.[24] P8 showed several discontinuities, such as cracks and large pores, in the surface. P2 and P6 showed the largest voids on the surface and in the center of the part. The morphology and typology of the pores were also varied. Pores with sharp edges (such as the ones in P8) and aligned pores (like in P2) were more damaging than homogeneously dispersed spherical pores (like the ones presented in P3).[25] Pores in the periphery of the part were

Table 5. Summary of the micrographs analysis from the eight samples evaluating porosity in the periphery and the center of the parts as well as grain morphology and phases

	Microstructure		
	Porosity in the periphery	**Porosity in the center**	**Grain morphology and phases**
P1 (C1)	 Discontinuities in the surface that also penetrate toward the center of the part originating cracks. Small voids of spherical morphology around the matrix.	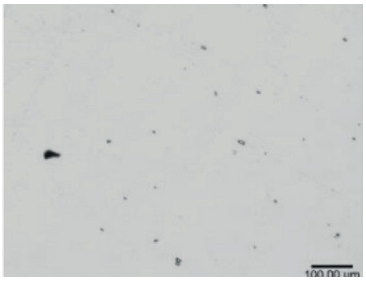 Several discontinuities of small size.	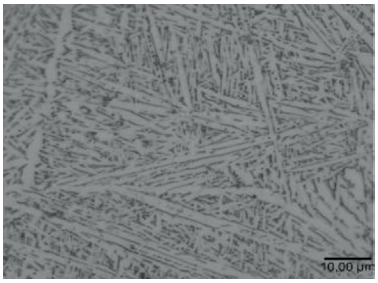 Heterogeneous acicular morphology, dendritic distribution. Columnar grains, α phase alternated with β phase.
P2 (C2)	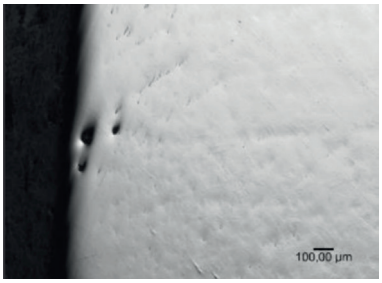 Voluminous discontinuities at the edge of the part with rounded globular shape.	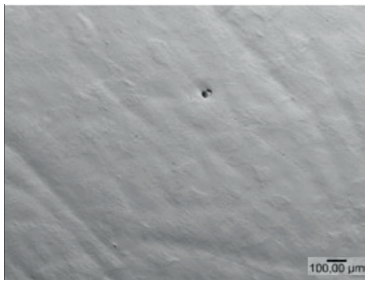 A few discontinuities of small size.	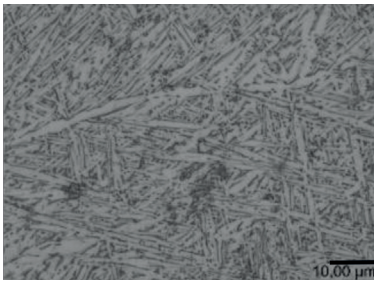 Very heterogeneous acicular morphology, dendritic distribution. Thinner columnar grains, α phase alternated with β phase.
P3 (C3)	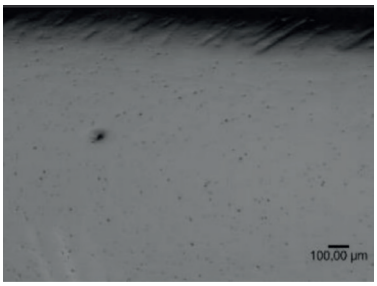 Gas porosity, small voids of spherical morphology.	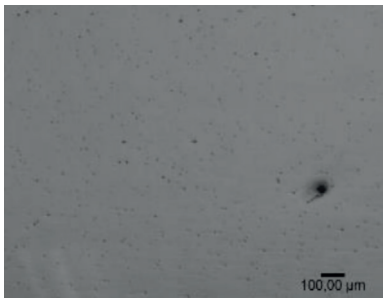 Homogeneous distribution of numerous small discontinuities of globular shape.	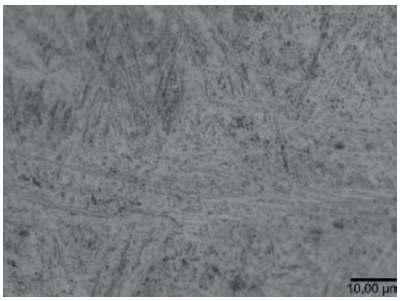 Heterogeneous thinner grain morphology, dendritic distribution. Columnar grains. More homogeneous structure.
P4 (C4)	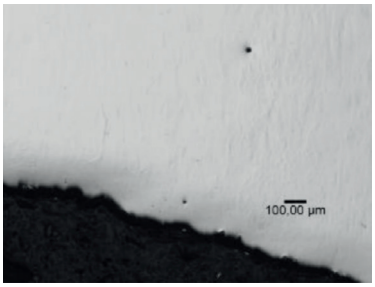 No defects in the surface, spherical discontinuities of small size toward the center.	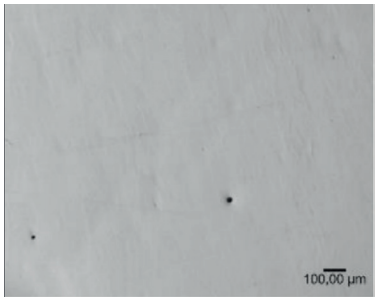 Low content of porosity.	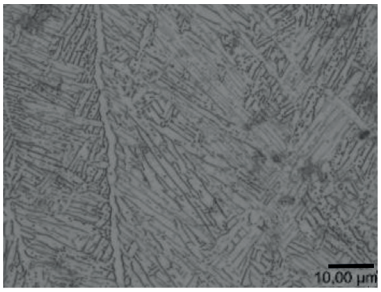 Heterogeneous acicular morphology, dendritic distribution. Columnar grains, α phase alternated with β phase.

Continued...

Table 5. ***Continued...***

P5 (C5)	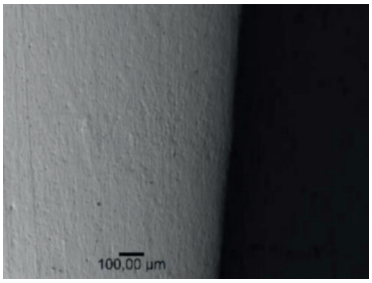 No defects in the surface detected.	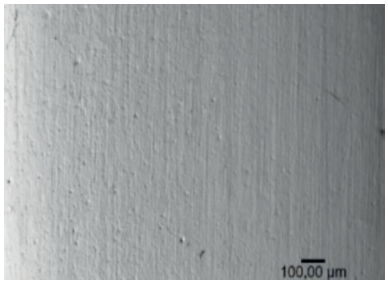 Low content of porosity.	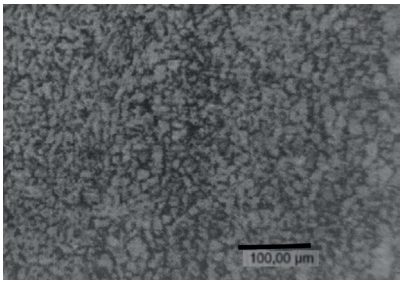 Globular structure. Identifiable and homogeneous α and β phases. Equiaxed and small grains.
P6 (C2)	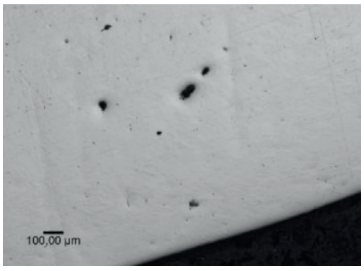 Large inclusions and voids of spherical morphology toward the center of the part.	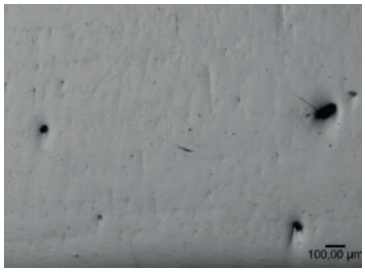 Many small discontinuities and some very large inclusions of spherical morphology.	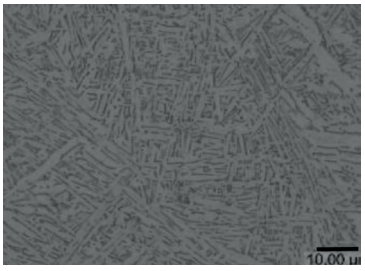 Very heterogeneous acicular morphology, dendritic distribution. Columnar grains, α phase alternated with β phase.
P7 (C6)	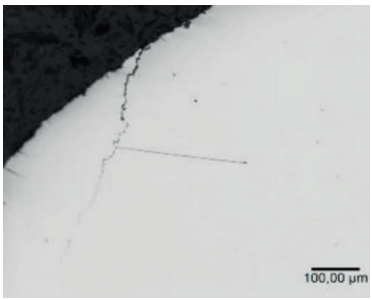 Thin cracks that originate in the surface and expand toward the center of the matrix and less voids than previous samples.	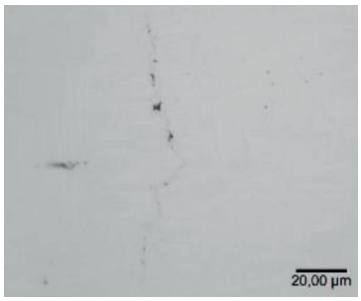 Thin large cracks originated from the surface.	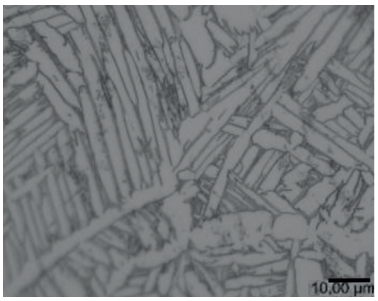 Heterogeneous acicular morphology, dendritic distribution, larger grains. Columnar grains, α phase alternated with β phase.
P8 (C7)	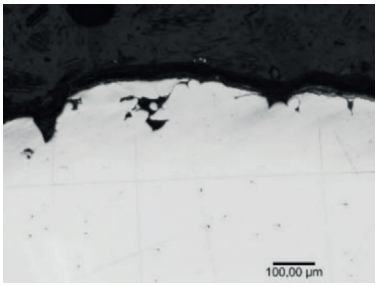 Large voids of irregular morphology that grow toward the center and create some thin cracks. Indications of α case layer.	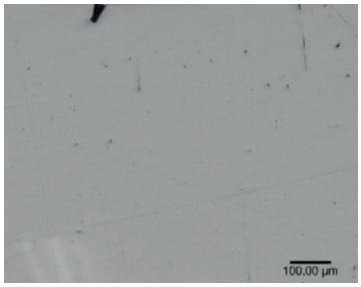 Several small discontinuities of globular shape and a few very large irregular ones.	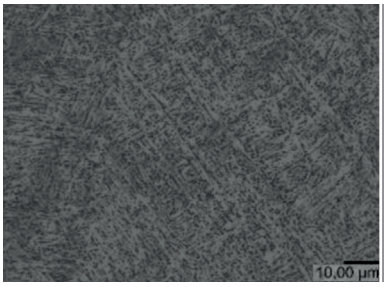 Heterogeneous acicular morphology, dendritic distribution. Columnar grain structure. Thinner grains and heterogeneity

more likely to initiate a crack than those presented in the center of the component.[20] P4 and P5 had no defects on the surface and low presence of voids.

P8 presented a visible layer of alpha-case which showed oxidation and corrosion. This layer could cause a negative effect on mechanical properties, such as ductility, fracture toughness, and fatigue life, of the part especially under dynamic loading.[26]

All the prototypes in this study, except for P5, demonstrated an acicular morphology with a dendritic distribution. The presence of columnar grains implies that the relationship between grain orientation and mechanical anisotropy must be considered, especially for a pelvic implant, subjected to high fatigue loading. In particular, P2, P6, and P8 showed more heterogeneity and thinner grains, which are indicators of an inadequate thermal management during production and least favorable mechanical responses.[26]

Only P5 presented a homogeneous and globular structure with equiaxed and small grains, displaying the best microstructure in this study that theoretically leads to the longest fatigue life.[27] This is highly likely the consequence of applying the optimal thermal processes that achieved appropriate recrystallization from the typical acicular microstructure of PBF technology.[18]

3.2.4. Communication

The way companies managed communication during manufacturing was diverse. Most companies did not provide any feedback about the design of the part, not promoting DfAM practices and manufactured the STL file like a "service bureau" without adapting production process to the design or function of the component. C4 and C5 adapted the production process to the function of the part, providing feedback about the design to optimize manufacturing and results. These two companies were the ones that provided P4 and P5, the best prototypes in terms of geometry and microstructural integrity.

4. Discussion

This study has provided the insights and trends on how some metal additive manufacturers produce custom medical devices in Europe. The analysis has been performed from a neutral perspective as none of the authors have any conflicts of interest with the companies, ensuring that the results are objective and reliable.

Our results show that the current lack of standardization in the AM of metallic implants presents several challenges for the development of consistent and high-quality devices. It has also illustrated the variability among the companies when managing the fabrication of the same implant design. Each company had a tendency toward a preferred 3D printing technology (SLM or EBM), different machines, printing parameters, approaches to orientate the parts in the printing built, postprocessing strategies, communication approaches, etc. We even found variability in the regulatory pathway of the same implant. C3, C4, and C6 commercialize this type of pelvic implant as a class III medical device, while the remaining companies classified it as a class IIB device. Therefore, manufacturers demonstrated different workflows to produce the same implant. Due to these variables, the same implant design implied fabrication problems to some companies and no issues to others. Furthermore, these variations also produced parts with different microstructures and therefore, mechanical properties. Additionally, this study has proved that when the machine settings, process parameters, and postprocesses are not properly chosen, the resulting parts can show imperfections that could affect the integrity of the components.

The manufacturing specifications were defined as general requirements to be discussed with the companies, and they generated a variety of opinions. Firstly, there was a debate about which AM technology, SLM or EBM, is best for implant manufacture. These alternative technologies create distinct microstructures with different mechanical properties.[28] Secondly, the need to perform thermal postprocesses such as HIP was controversial, potentially because adding an HIP procedure considerably increases the cost and time for development. Only two companies, C5 and C6, performed HIP. C5 always incorporates an HIP process to manufacture orthopedic implants. This company provided a complete metallurgy analysis that demonstrated how the HIP process enhanced the microstructure of the part and improved its fatigue strength. The literature supports this opinion for the development of parts that are subject to high fatigue loading.[20] C6, on the other hand, does not apply HIP to their implants but performed it for this study. C4 applies HIP processes to some implants, but not usually to pelvic implants; therefore, they did not perform it for this prototype. The rest of companies believed HIP process is not required for the purpose of this pelvic component.

All the manufacturers knew that the parts were going to be evaluated. However, several imperfections were identified in five out of the eight prototypes received. Further analyses are required to determine the actual clinical and mechanical consequences of such imperfections. In the visual inspection analysis, only three prototypes P4, P5, and P6 did not show any inconsistencies. In the geometrical precision evaluation, the same P4, P5, and P6 showed the lowest values of geometrical deviations with the maximum values located in small areas of lattice structures, which could be neglected. The other five prototypes, P1, P2, P3, P7, and P8, presented large maximum deviations of 3.00, 2.53, 4.94, 4.88, and 3.60 mm, respectively, that could have

potentially risked implant performance.[14] It is important to highlight that all the companies participating in the study are already manufacturing implants that have been used in clinical practice. Most of these companies are ISO 13485 certified, demonstrating that this compliance does not guarantee the high quality of the manufacturing.

P3 and P7 showed maximum deviations of 5 mm. P7 was delivered without the entire L2 and without a warning or feedback about the issue. P1, P3, P7, and P8 were provided with broken lattice structures, and only C1 communicated the issue when shipping the part. Only P4, P5, and P6 produced L2 correctly. This demonstrates that the production workflow and printing parameters can determine whether a design feature is feasible to be manufactured or not. Manufacturers should assess whether they are capable of manufacturing a design with their resources and expertise, and identify potential design issues for optimal printing, applying DfAM practices. In this study, only two companies, C4 and C5, provided feedback about the design before fabrication to optimize it for AM. This highlights the need for improvement in DfAM habits among manufacturers. It is unknown whether the production issue for L2 was caused during printing or postprocessing, but the L2 architecture with a minimum beam thickness of 0.5 mm was confirmed to be achievable by all the companies prior to production. Another nonconformity was found in P2, which had a hole 2 mm bigger in diameter and 2 mm out of the correct location. Interestingly, P6 was manufactured by the same company, but did not present any geometrical deviations, showing the inconsistency of the same company in the quality delivered.

The microstructural analysis also showed some deficiencies such as large pores and cracks in the surfaces, mainly in P8 but also in P1 and P2, that could potentially trigger early fractures. Different grain morphologies were also found between the prototypes. We estimated a potential ranking of microstructures, from the best to the worst, as follows: P5, P3, P4, P1, P6, P2, P8, and P7.

P5 demonstrated to be the most superior prototype for the particular function of the pelvic reconstruction. This is revealed in the accuracy of the geometry, the homogeneity of the implant surfaces, the low content of porosity in the sample analyzed, and the globular morphology of the grain and homogeneous alpha and beta phases. Metal AM parts, especially in PBF, usually show columnar-oriented microstructures.[3] The production of P5 achieved recrystallization and transformed the columnar microstructure to equiaxed microstructure with homogeneous and globular small equiaxed grains. This microstructure has been demonstrated to provide better fatigue strength than heterogeneous morphologies[20] and could have been a consequence of correctly applying thermal methods such as HIP.[12]

The rest of the prototypes present heterogeneous grain morphology with dendritic distributions. P3 could be next in the ranking as it shows the most homogeneous microstructure after P5 and the porosity is of spherical morphology.[29] P4 could be third as it exhibits no defects in the surface and low content of porosity.[30] P1 demonstrated some discontinuities in the surface and in the matrix, but the grain morphology was more favorable than P6, P2, and P8, that showed very heterogeneous grain morphology and thinner grains than the rest of prototypes, indicating the least favorable mechanical responses.[26] P6 and P2 (similarly manufactured by C2) presented similarities with some very large inclusions.[31] The latter was more favorable as it presented less inclusions in the matrix. P8 could be next as it showed a visible layer of alpha-case, which indicates oxidation and corrosion. This layer can cause a negative effect on the mechanical properties of the part such as ductility, fracture toughness, and fatigue life, especially under dynamic loading.[25]

P7 presented the most harmful defect for the integrity of the part. Although the microstructure had favorably large grains, the part showed an internal crack originating in the surface that extended toward the center of the matrix, potentially leading to early failure. Furthermore, the component was delivered with the entire surface of lattice L2 missing, registering deviations of up to 5 mm. It was also sent with a matte finish, although a mirror finish had been agreed before production. Yet, C6, the company that produced P7, is legally certified to commercialize class III custom implants and complies with the ISO 13485.

It is important to find a balance between postprocessing, costs, and functionality during the production of a specific implant. Thermal postprocesses can improve mechanical performance but also have an effect on manufacturing costs. The optimal microstructure required for a maxillofacial cranial plate may be different than for a pelvic reconstruction as the former is not subjected to high fatigue loading, as opposed to the latter. Therefore, they may need different production steps. With the lack of regulatory and standardization guidelines to develop specific implants with AM, engineers must think critically about what production process is required according to the biomechanical requirements of the patient. The different implant requirements are going to determine the characterization of the material and manufacturing steps to achieve a balance between microstructure, mechanical properties, and cost for each individual application.

There also exists a high variability of custom implant prices stipulated by different manufacturers that we must critically analyze. More postprocesses will lead to higher costs. However, high costs are not always a guarantee for good quality but a consequence of several factors, such as process subcontracting, machines barely being used (low volume of production), or marketing decisions. On the other hand, quick and cheap manufacturing may be an indication for an inappropriate production, especially for complex high load-bearing implants, which potentially could require better microstructures. This is an important consideration in a time where we are proving the benefits of AM custom implants,[32-34] but their prices constitute a barrier for a wider clinical application, especially in public healthcare administrations.

Surgeons are usually the decision makers that choose which implants and companies to use for each specific surgery. Their decisions are generally based on company availability and costs rather than quality inspections. When an implant is received for surgery, surgeons assume that it is going to comply with its purposes; therefore, no inspection is carried out. Even if a visual check is performed, the most detrimental defects could be the invisible ones, as shown in this study. Therefore, while regulatory bodies work on creating validation strategies and standards to characterize what a high-quality implant is according to specific functionalities, surgeons should work closely with implant developers to understand the current limitations of AM. Moreover, surgeons and hospitals should choose the companies to collaborate with based on a proven characterization of the manufacturing quality, not only relying on ISO13485 compliance. This paper could be used as a guideline to quickly inspect received parts from manufacturers.

Other decisive aspects to control during the development of 3D-printed implantable devices not included in this study are: the analysis of porous structures; the evaluation of biocompatibility; the performance of fatigue testing; the cleaning of the prototypes after postprocessing, especially in the areas of the porous structures; and the quality of the raw material, which is key to achieving the highest performance in the final part. Parameters of the powder, such as composition, size, surface morphology, shape, and quantity of internal porosity, could influence part performance.[35] Companies usually recycle powder a few times, so controlling that the chemical composition of the powder remains within alloy-specific specifications is vital. Recycled powder could present contamination from powder recovery and reaction with oxygen, nitrogen, or other gases.[36]

There are some limitations in this study. Firstly, the participating companies assumed the manufacturing cost of the part which could have limited the resources dedicated to the implant production. Secondly, the implants were going to be a test and not to be used in clinical practice. However, as companies were fully aware of the objective of this study, they applied their usual production workflows to the manufacturing of the evaluated prototypes. Consequently, the parts were representative of the companies' production standards. Thirdly, the micrographs in our study were taken from a sample of the flange extracted from each prototype, and therefore, the microstructural analysis could not be extrapolated to the entire component. A computed tomography (CT) analysis of each prototype should be performed for an accurate characterization of the prototypes' porosity.

5. Conclusion

To our knowledge, this is the first study evaluating the production process of several custom implant additive manufacturers based on a geometrical and a microstructural inspection of the same pelvic implant fabrication.

The results confirm the lack of standardization in the medical device industry and highlight the urgent need for standards that regulate the safe and consistent development of 3D-printed implants. It has also demonstrated the evidence of geometrical and structural defects in some of the implants analyzed that could potentially compromise implant function and safety. However, further analyses are required to determine the actual clinical and mechanical consequences of such imperfections. Therefore, this study could be used by: (i) regulatory bodies to help control the production and certification of AM implants; and by (ii) surgeons and engineers as a guideline to inspect received parts from manufacturers. The data presented have also revealed that there are some manufacturers developing defect-free titanium components. These results provide evidence that AM can be a valid manufacturing method to fabricate implants when it is adequately operated.

Acknowledgments

We would like to thank all the companies that participated in the study.

Funding

This research was supported by the CONEX-Plus program funded by Universidad Carlos III de Madrid and the European Union's Horizon 2020 research and innovation program under the Marie Sklodowska-Curie grant agreement No. 801538.

Conflict of interest

The authors declare no conflicts of interest.

Author contributions

Conceptualization: Alba González Álvarez, Rubén Pérez Mañanes, José Antonio Calvo Haro, Lydia Mediavilla Santos, Javier Pascau
Formal analysis: Alba González Álvarez
Methodology: Alba González Álvarez
Writing – original draft: Alba González Álvarez
Writing – review & editing: Alba González Álvarez, Rubén Pérez Mañanes, José Antonio Calvo Haro, Lydia Mediavilla Santos, Javier Pascau

Ethics approval and consent to participate

Not applicable.

Consent for publication

Not applicable.

Availability of data

The processed data about this study can be shared upon reasonable request.

References

1. Villapún VM, Carter LN, Avery S, González-Álvarez A, Andrews JW, Cox S. Stakeholder perspectives on the current and future of additive manufacturing in healthcare. *Int J Bioprint*. 2022;8(3):586. doi: 10.18063/ijb.v8i3.586
2. Food and Drug Administration. *Technical Considerations for Additive Manufactured Medical Devices: Guidance for Industry and Food and Drug Administration Staff Document*. Center for Devices and Radiological Health. New Hampshire: USA. 2017;1-30. https://www.fda.gov/regulatory-information/search-fda-guidance-documents/technical-considerations-additive-manufactured-medical-devices (accessed on 16 January 2024).
3. Gong H, Rafi K, Gu H, Janaki Ram GD, Starr T, Stucker B. Influence of defects on mechanical properties of Ti–6Al–4V components produced by selective laser melting and electron beam melting. *Mater Des*. 2015;86:545-554. doi: 10.1016/j.matdes.2015.07.147
4. Regulation (EU) 2017/745 of the European Parliament and of the Council of 5 April 2017 on Medical Devices. https://eur-lex.europa.eu/legal-content/EN/TXT/PDF/?uri=CELEX:32017R0745 (accessed on 6 March 2023).
5. ISO 13485:2016, Quality Management Systems. International Organization for Standardization, Geneva, Switzerland. https://www.iso.org/standard/59752.html (accessed on March 6, 2023).
6. Chiarini A. Effect of ISO 9001 non-conformity process on cost of poor quality in capital-intensive sectors. *Int J Qual Reliab Manag*. 2015;32(2):144-155. doi: 10.1108/IJQRM-03-2013-0041
7. Wong K-C, Scheinemann P. Additive manufactured metallic implants for orthopaedic applications. *Sci China Mater*. 2018;61(4):440-454. doi: 10.1007/s40843-017-9243-9
8. Hothi H, Henckel J, Bergiers S, Laura AD, Schlueter-Brust K, Hart A. The analysis of defects in custom 3D-printed acetabular cups: A comparative study of commercially available implants from six manufacturers. *J Orthop Res*. 2022;(October):1-12. doi: 10.1002/jor.25483
9. Martinez-Marquez D, Delmar Y, Sun S, Stewart RA. Exploring macroporosity of additively manufactured titanium metamaterials for bone regeneration with quality by design: A systematic literature review. *Materials (Basel)*. 2020;13(21):1-44. doi: 10.3390/ma13214794
10. Liu X, Chu PK, Ding C. Surface modification of titanium, titanium alloys, and related materials for biomedical applications. *Mater Sci Eng R Rep*. 2004;47(3): 49-121. doi: 10.1016/j.mser.2004.11.001
11. Gonzalez Alvarez A, Dearn KD, Lawless BM, et al. Design and mechanical evaluation of a novel dynamic growing rod to improve the surgical treatment of early onset scoliosis. *Mater Des*. 2018;155:334-345. doi: 10.1016/j.matdes.2018.06.008
12. Tammas-Williams S, Withers PJ, Todd I, Prangnell PB. The effectiveness of hot isostatic pressing for closing porosity in titanium parts manufactured by selective electron beam melting. *Metall Mater Trans A Phys Metall Mater Sci*. 2016;47(5):1939-1946. doi: 10.1007/s11661-016-3429-3
13. Barrère F, Mahmood TA, de Groot K, van Blitterswijk CA. Advanced biomaterials for skeletal tissue regeneration: Instructive and smart functions. *Mater Sci Eng R Rep*. 2008;59(1):38-71. doi: 10.1016/j.mser.2007.12.001
14. Suska F, Kjeller G, Tarnow P, et al. Electron beam melting manufacturing technology for individually manufactured jaw prosthesis: A case report. *J Oral Maxillofac Surg*. 2016;74(8):1706.e1-1706.e15. doi: 10.1016/j.joms.2016.03.046
15. Martinez-Marquez D, Mirnajafizadeh A, Carty CP, Stewart RA. Application of quality by design for 3D printed bone prostheses and scaffolds. *PLoS ONE*. 2018;13(4):1-47. doi: 10.1371/journal.pone.0195291
16. Van Hooreweder B, Moens D, Boonen R, Kruth JP, Sas P. Analysis of fracture toughness and crack propagation of

Ti6Al4V produced by selective laser melting. *Adv Eng Mater*. 2012;14(1–2):92-97.
doi: 10.1002/adem.201100233

17. Vrancken B, Thijs L, Kruth JP, Humbeeck JV. Heat treatment of Ti6Al4V produced by selective laser melting: microstructure and mechanical properties. *J Alloys Compd*. 2012;541:177-185.
doi: 10.1016/j.jallcom.2012.07.022

18. Vilaro T, Colin C, Bartout D. As-fabricated and heat-treated microstructures of the Ti-6Al-4V alloy processed by selective laser melting. *Metall Mater Trans A*. 2011;42(10):3190-3199.
doi: 10.1007/s11661-011-0731-y

19. Li SJ, Murr LE, Cheng XY, et al. Compression fatigue behavior of Ti-6Al-4V mesh arrays fabricated by electron beam melting. *Acta Mater*. 2012;60(3):793-802.
doi: 10.1016/j.actamat.2011.10.051

20. Fotovvati B, Namdari N, Dehghanghadikolaei A. Fatigue performance of selective laser melted Ti6Al4V components: State of the art. *Mater Res Express*. 2019;6(1):012002.
doi: 10.1088/2053-1591/aae10e

21. Vaneker T, Bernard A, Moroni G, Gibson I, Zhang Y. Design for additive manufacturing: Framework and methodology. *CIRP Ann*. 2020;69(2):578-599.
doi: 10.1016/j.cirp.2020.05.006

22. Coelho PG, Hollister SJ, Flanagan CL, Fernandes PR. Bioresorbable scaffolds for bone tissue engineering: Optimal design, fabrication, mechanical testing and scale-size effects analysis. *Med Eng Phys*. 2015;37(3):287-296.
doi: 10.1016/j.medengphy.2015.01.004

23. Kingsak M, Maturavongsadit P, Jiang H, Wang Q. Cellular responses to nanoscale substrate topography of TiO2 nanotube arrays: cell morphology and adhesion. *Biomater Transl*. 2022;3(3):221-233.
doi: 10.12336/biomatertransl.2022.03.006

24. Liu QC, Elambasseril J, Sun SJ, Leary M, Brandt M, Sharp PK. The effect of manufacturing defects on the fatigue behaviour of Ti-6Al-4V specimens fabricated using selective laser melting. *Adv Mater Res*. 2014;891–892:1519-1524.
doi: 10.4028/www.scientific.net/AMR.891-892.1519

25. Seth P, Jha JS, Alankar A, Mishra SK. Alpha-case formation in Ti–6Al–4V in a different oxidizing environment and its effect on tensile and fatigue crack growth behavior. *Oxid Met*. 2022;97(1–2):77-95.
doi: 10.1007/s11085-021-10079-y

26. Lee YS, Cho S, Ji C, Jo I, Choi M. Impact of morphology on the high cycle fatigue behavior of Ti-6Al-4V for aerospace. *Metals (Basel)*. 2022;12(10):1722.
doi: 10.3390/met12101722

27. Xu W, Sun S, Elambasseril J, Liu Q, Brandt M, Qian M. Ti-6Al-4V additively manufactured by selective laser melting with superior mechanical properties. *JOM*. 2015;67(3):668-673.
doi: 10.1007/s11837-015-1297-8

28. Bertsch KM, Voisin T, Forien JB, et al. Critical differences between electron beam melted and selective laser melted Ti-6Al-4 V. *Mater Des*. 2022;216:110533.
doi: 10.1016/j.matdes.2022.110533

29. Wu GQ, Shi CL, Sha W, Sha AX, Jiang HR. Effect of microstructure on the fatigue properties of Ti-6Al-4V titanium alloys. *Mater Des*. 2013;46:668-674.
doi: 10.1016/j.matdes.2012.10.059

30. Frkan M, Konecna R, Nicoletto G, Kunz L. Microstructure and fatigue performance of SLM-fabricated Ti6Al4V alloy after different stress-relief heat treatments. *Transp Res Procedia*. 2019;40(1):24-29.
doi: 10.1016/j.trpro.2019.07.005

31. Ran J, Jiang F, Sun X, Chen Z, Tian C, Zhao H. Microstructure and mechanical properties of ti-6al-4v fabricated by electron beam melting. *Crystals*. 2020;10(11):1-18.
doi: 10.3390/cryst10110972

32. Gonzalez Alvarez A, Dovgalski L, Evans PL, Key S. Development and surgical application of a custom implant that enables a vertical vector of mandibular distraction. *Proc Inst Mech Eng H*. 2020;234(10):1172-1180.
doi: 10.1177/0954411920940848

33. Gonzalez Alvarez A, Evans PL, Dovgalski L, Goldsmith I. Design, additive manufacture and clinical application of a patient-specific titanium implant to anatomically reconstruct a large chest wall defect. *Rapid Prototyp J*. 2021;27(2):304-310.
doi: 10.1108/RPJ-08-2019-0208

34. Gonzalez Alvarez A, Ananth S, Dovgalski L, Evans PL. Custom three-dimensional printed orbital plate composed of two joined parts with variable thickness for a large orbital floor reconstruction after post-traumatic zygomatic fixation. *Br J Oral Maxillofac Surg*. 2020;58(10):e341-e342.
doi: 10.1016/j.bjoms.2020.08.082

35. Contaldi V, Corrado P, Del Re F, et al. Direct metal laser sintering of Ti-6Al-4V parts with reused powder. *Int J Adv Manuf Technol*. 2022;120(1–2):1013-1021.
doi: 10.1007/s00170-022-08807-y

36. Emminghaus N, Bernhard R, Hermsdorf J, Kaierle S. Residual oxygen content and powder recycling: Effects on microstructure and mechanical properties of additively manufactured Ti-6Al-4V parts. *Int J Adv Manuf Technol*. 2022; 121(5–6):3685-3701.
doi: 10.1007/s00170-022-09503-7

ACCSCIENCE PUBLISHING

International Journal of Bioprinting

RESEARCH ARTICLE

Man vs. machine: Automated bioink mixing device improves reliability and reproducibility of bioprinting results compared to human operators

Dongwei Wu[1], Shumin Pang[2], Viola Röhrs[1], Johanna Berg[1], Ahmed S. M. Ali[1], Yikun Mei[1], Mathias Ziersch[1], Beatrice Tolksdorf[1], and Jens Kurreck[1]*

[1]Chair of Applied Biochemistry, Institute of Biotechnology, Technische Universität Berlin, Berlin, Germany

[2]Chair of Advanced Ceramic Materials, Institute of Material Science and Technology, Technische Universität Berlin, Berlin, Germany

Abstract

The bioink mixing process is highly relevant to the bioink quality, which is the basis for reproducible extrusion-based three-dimensional (3D) bioprinting (EBB). Currently, most bioinks mixed by skilled human operators show variations in terms of cell homogeneity and biological properties as well as other properties. For preparation of many types of bioinks, striking the balance between homogeneity and cell viability remains a major challenge. This study investigates the relationship between bioink homogeneity and mixing parameters, particularly mixing speed and number of exchanges, utilizing a customized automated device. We found that up to a certain point, increasing the rate of mixing led to a better distribution of cells within the bioink, but beyond that point, there was a detrimental effect on cell viability. In contrast, the mixing number had less impact on the physiological properties of the cells in the bioink. Furthermore, a comparison between skilled human and machine bioink mixing revealed that the machine consistently provided better outcomes in terms of bioink homogeneity, cell distribution, and cell viability, highlighting the advantages and importance of standardizing the bioink mixing process. The methodology and approaches in this study can improve the reproducibility and reliability of EBB bioink and may thereby advance the field of 3D bioprinting in various applications.

Keywords: Bioink; Hydrogel mixing; Mixing device; Bioprinting; Homogeneity; Cell viability

***Corresponding author:**
Jens Kurreck
(jens.kurreck@tu-berlin.de)

Citation: Wu D, Pang S, Röhrs V, et al. Man vs. machine: Automated bioink mixing device improves reliability and reproducibility of bioprinting results compared to human operators. *Int J Bioprint*. 2024;10(2):1974.
doi: 10.36922/ijb.1974

Received: October 5, 2023
Accepted: December 14, 2023
Published Online: February 12, 2024

1. Introduction

Bioprinting has become a widely used technology in various fields of biomedical research.[1-3] Among the different methodologies, extrusion-based bioprinting (EBB) has become the most widely used approach.[4,5] This is primarily attributed to its affordability and maneuverability, which allow for the creation of intricate three-dimensional (3D) structures that closely resemble the architecture and microenvironment of native tissues.

By enabling the direct spatial deposition of living cells and biomaterials, EBB offers great potential for advancing tissue engineering and regenerative medicine.[6,7] A critical component of the EBB process is the bioink, which is extruded as a continuous strand and can be stacked to fabricate 3D objects. Consequently, the properties of the bioink significantly influence printability, structural stability, cell growth, and differentiation by acting as essential physical support. However, current bioinks still face numerous limitations, with one of the major challenges being the preparation of the bioinks in a reproducible and cell-friendly manner. Achieving consistency would ensure a precise and consistent bioprinting process that maintains high cell biocompatibility.[8]

The preparation of bioinks dictates the success of EBB technology, as it directly impacts the quality of the printed constructs and the biological properties of the encapsulated cells.[9] Inhomogeneous bioink can lead to nozzle clogging, structural collapse, uneven cell distribution, and variations at different stages of bioprinting.[10] The inconsistency of the matrix components can cause an unstable viscosity of the bioink, while the uneven distribution of cells can result in cell aggregation and cell vacancy. This can negatively affect the printability and resolution of the bioprinted constructs and hamper the accuracy of the experimental outcomes.

For the sake of clarity, we define homogeneity as the uniformity of the bioink mixture, which significantly influences the printability, structural integrity, and cell distribution of the printed constructs. Conversely, cell viability refers to the ability of the encapsulated cells to survive and maintain their biological function during and after the printing process. However, these two factors, homogeneity and cell viability, often pose a challenge during bioink preparation, and one factor generally works against the other. Thorough and unstinted mixing is a common approach to obtain a homogeneous mixture, but it can potentially harm the encapsulated cells. A high rate of mixing and/or too long a duration may even irreversibly disrupt the interactions among hydrogel molecules, such as entangled structures, as well as covalent or non-covalent bonds.[11] Compared to other bioprinting methods such as stereolithography and inkjet bioprinting, this issue is particularly pronounced in EBB, which requires a higher viscosity bioink than the other techniques.

To achieve a homogeneous bioink for EBB, several techniques have been developed for blending the components. The pipetting method and spatula mixing are simple approaches that involve placing the materials in a container and either pipetting them up and down or stirring them manually. However, both methods introduce air bubbles during the mixing process. Many companies provide two-in-one-out mixing kits, which enable rapid bioink mixing.[12] These kits, however, have design limitations such as constraining the volume ratio between the cell suspension and bioink. Additionally, these devices suffer from an inherently big loss of material due to the dead volume of the mixing chamber. In some laboratories, a planetary mixer is utilized to prepare viscous mixtures.[13,14] This method is good for reproducibility, but it still presents difficulties in cartridge loading for EBB purposes. One widely used approach is the syringe coupler method, which involves mixing the materials using two syringes by repeatedly pushing the plungers back and forth. This method has gained significant popularity in EBB bioink preparation due to its cost-effectiveness, reduced waste, avoidance of air entrapment, and low risk of contamination.[15-19] When using a syringe coupler to mix bioinks, two crucial parameters are the speed at which the plungers are pushed and the number of pushes performed, referred to as mixing speed and mixing exchanges, respectively.

Like other mixing methods, the syringe coupler method also faces the challenge of balancing between bioink homogeneity and cell viability, particularly when dealing with viscous bioinks. To address this issue, Dani et al. made improvements by exploring customized couplers with different inner geometries.[20] They discovered that a screw-like mixing coupler yielded a homogeneous bioink with high cell viability after a lower number of exchanges. However, the relationship between mixing parameters (such as mixing speed and mixing exchanges) and bioink homogeneity/cell viability remains unclear. Further research is needed to better understand this relationship and achieve a balance between bioink homogeneity and cell viability, for ultimately improving the physical and biological quality of the fabricated constructs. This is crucial for enhancing the reliability of the bioprinting process. Additionally, it is worth noting that in most of the current studies, the researchers' handling and experience in the bioink mixing process can lead to significant differences between individuals. This factor decreases the reproducibility of the bioprinting process, thereby influencing the subsequent experimental results. Thus, standardized protocols in bioink mixing to ensure consistent and reproducible outcomes in bioprinting are highly desirable.

In light of these challenges, the primary objective of this study is to establish a standardized approach for the bioink mixing process, thereby enabling precise control over bioink properties for EBB (Figure 1). This research comprehensively investigated the influence of various mixing parameters on bioink homogeneity and cell viability. A dedicated mixing device was developed to ensure reliable and reproducible operations of the desired

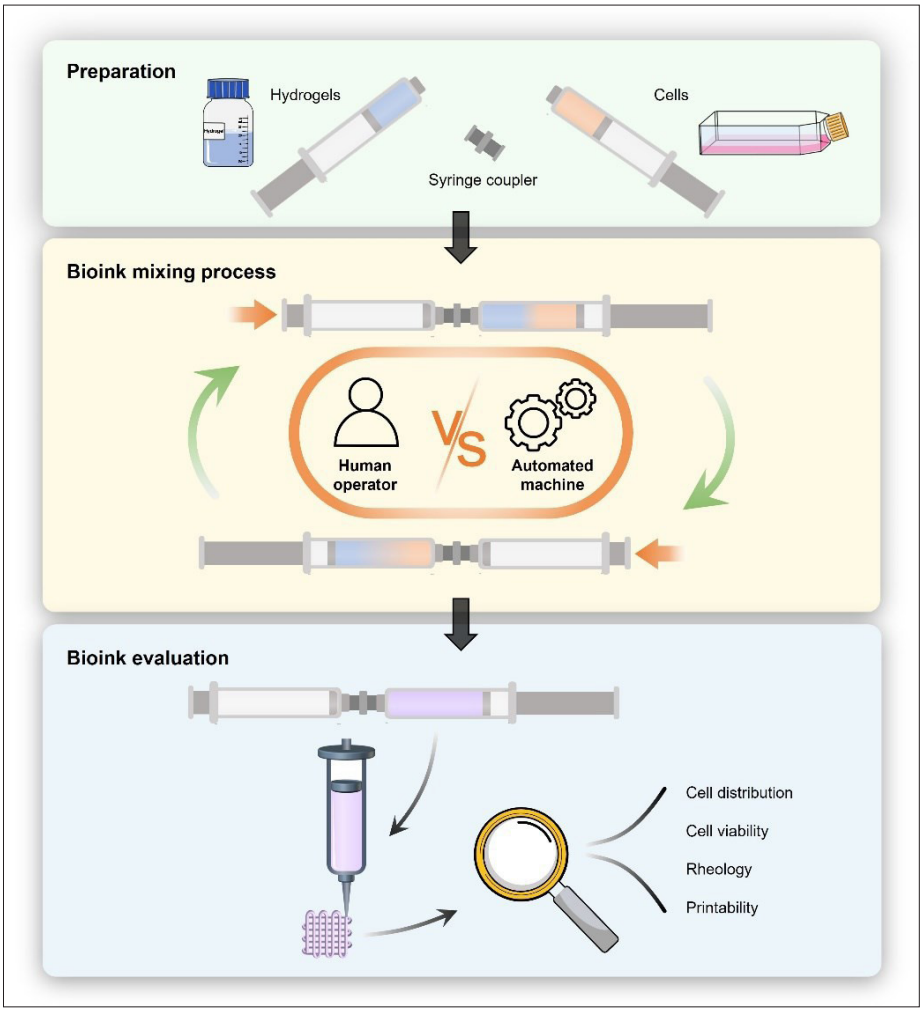

Figure 1. Schematic diagram of the experiment design in this study. Two syringes were loaded with a hydrogel and a cell suspension, respectively, before connecting with a coupler. The bioink mixing process was then performed manually by human operators or automatically by the machine. The mixed bioinks were evaluated and bioprinted.

mixing parameters. By evaluating bioink homogeneity and cell viability under different mixing conditions, we sought to identify the optimal combination of parameters. Furthermore, a comparison was conducted between human mixing and machine mixing to assess the effects on cell distribution, cell viability, and rheological properties. This study demonstrates the critical importance of standardizing the bioink mixing process for bioprinting applications. The developed methodology provides valuable guidance for future research on bioink preparation, ultimately enhancing the quality and reliability of bioprinted constructs.

2. Materials and methods

2.1. Design and use of the mixing device

To ensure a controlled and consistent bioink mixing process, we developed an electronic mixing device, as depicted in Figure 2A and B. This device consists of a linear sliding table (Oumefarnfc9v7rz8m, Oumefar, Shenzhen, China), four endstops (JY-3DP-084, Jopto, Shenzhen, China), a stepper motor (42BYGH48, Oubang Transmission, Jiangsu, China), a stepper driver (TMC2100, Trinamic, Hamburg, Germany), a microcontroller unit (MCU; UNO R3, Arduino, Ivrea, Italy), and a touchscreen interface (starbun-776, Starbun, Shenzhen, China). In addition, all other plastic parts were designed on Creo Parametric (Parametric Technology Corporation, MA, USA) software and produced by fused deposition modeling (FDM; Monoprice Select Mini, Boston, CA, USA) and liquid crystal display (LCD; Original Prusa SL1S SPEED, Prague, Czech Republic) 3D printers, with white polylactic acid (PLA; PLA175bk1000, Amazon Basics, Munich, Germany) and transparent resin (tough clear VALUE resin; PrimaCreator, Malmö, Sweden), respectively.

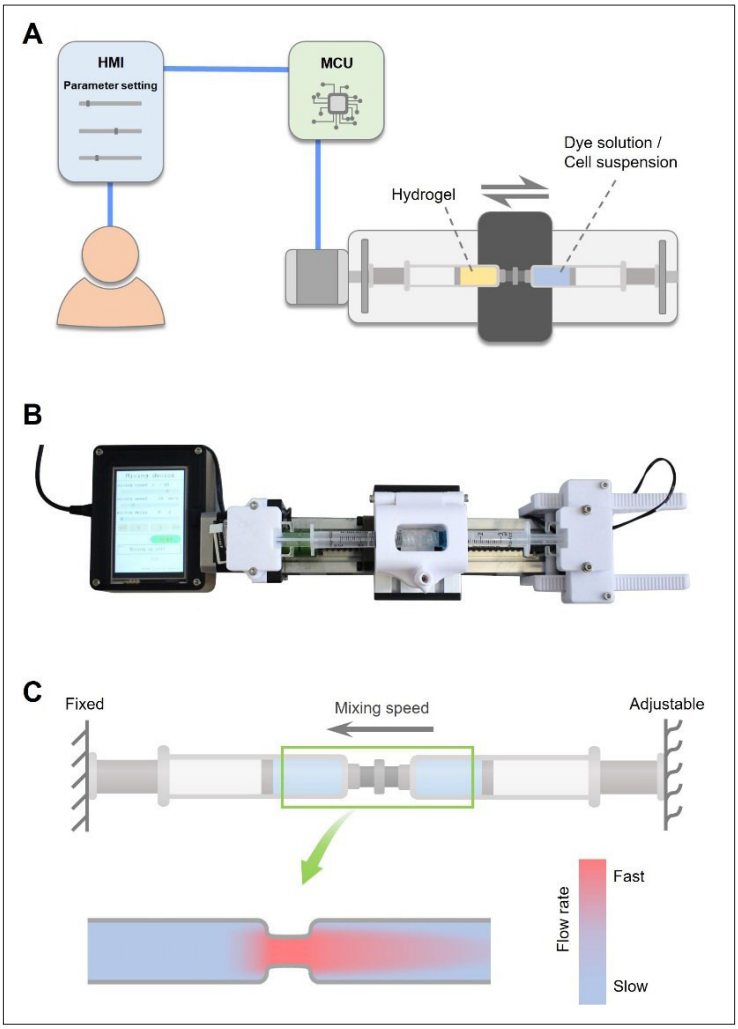

Figure 2. Design of the bioink mixing device and hydrogel mixing at different conditions. (A) The user determines the input parameters through the human–machine interface (HMI), which is connected to a microcontroller unit (MCU) that transmits the settings to the stepper motor. The motor finally drives the sliding table and thereby mediates mixing of the bioink. (B) A picture of the automated bioink mixing device. (C) Schematic of the working principle of the automated mixing device and hydrogel mixing in connected syringes.

The components were optimized and assembled prior to program design, structural modeling, motion validation, and stability test. Parameters such as mixing speed, number of exchanges, and delay time can be set directly via the control unit on the mixing machine. These settings regulate the stepper motor, thereby controlling the movement of the sliding table. For hydrogel mixing, the loaded syringes (Omnifix Luer-Lock Solo 3 mL, B. Braun Melsungen AG, Melsungen, Germany) were introduced into the mixing unit, and the mixing process was carried out according to the settings.

2.2. Preliminary hydrogel mixing test

Sodium alginate solutions of varying concentrations (2%, 4%, 6%, 8%, 10% (w/v)) were prepared by dissolving sodium alginate powder (W201502-1KG, Sigma, Shanghai, China) in deionized water with magnetic stirring at 37°C overnight. To mimic the cell suspension and determine the blending state, an aqueous solution with 0.001% (w/v) methylene blue (M9140, Sigma, Munich, Germany) was used. For hydrogel mixing, the alginate solution and the methylene blue solution were loaded into separate syringes, which were then coupled and subjected to mixing process on the developed automated mixing device. Throughout the process, the mixing effect was observed and recorded using a digital camera (EOS 700D, Canon, Tokyo, Japan). The photos were subsequently evaluated by examining the distribution of the blue color and scored from 0 to 10 points.

2.3. Cell culture

HEK293-GFP cells (human embryonic kidney cells that express green fluorescence protein [GFP]) were purchased

from GenTarget (GenTarget Inc., San Diego, CA, USA). These cells were cultured in low-glucose Dulbecco's Modified Eagle Medium (DMEM; Biowest, Nuaillé, France) containing 10% fetal calf serum (FCS; c.c.pro, Oberdorla, Germany), 4.5 mg/mL glucose (Sigma), 2 mM L-glutamine (Biowest), and 1× non-essential amino acid (NEAA; Biowest). The HepaRG cell line was purchased from Biopredic International (Saint Gregoiré, France) and cultured in William's E medium (Gibco, Paisley, UK) supplemented with 10% FCS, 2 mM L-glutamine, 5 µg/mL Insulin (Sigma), and 50 µM Hydrocortisone (Sigma). The human non-small lung cancer cell line A549 (ACC 107; DSMZ, Braunschweig, Germany) was cultured in high-glucose DMEM (Biowest) with 10% FCS and 2 mM L-glutamine (Biowest). All cell lines were cultured in a 37°C incubator with 5% CO_2. Upon reaching 75% confluence, the cells were washed with phosphate-buffered saline (PBS; Biowest) prior to harvesting using trypsin-EDTA (Biowest) for either passaging or bioink mixing.

2.4. Bioink mixing process

Three different hydrogels were prepared according to the specifications outlined in Table 1: Alginate and the blend of gelatin/alginate are widely used natural hydrogels for bioink preparation. Gelatin (G2500-500G) used in this experiment was obtained from Sigma (St. Louis, MO, USA). Poly(acrylic acid) (PAA; Carbopol 940, Acros Organics, Belgium) is a synthetic component with high biocompatibility. The respective powder components were dissolved in complete medium and stirred overnight at 37°C. Subsequently, 1 mL of the resulting hydrogel was loaded into a syringe, while 0.9 mL cell suspension (2×10^7 cells) and 0.1 mL 1 M $CaSO_4$ suspension were combined in a separate syringe. In the case of PAA bioink mixing, 0.1 mL $CaSO_4$ suspension was replaced by 0.1 mL complete medium.

For mixing of the bioink, two syringes were loaded with materials and carefully connected using a female Luer thread style coupler (Masterflex, Gelsenkirchen, Germany) without introducing air bubbles. The connected syringes were then placed on the sliding platform with the syringe barrels secured, while the thumb rests were appropriately positioned at both ends. Once the parameters were set, the program executed the predetermined settings, causing the sliding platform to move the syringe barrels back and forth in a highly controllable manner. The mixing process was terminated according to the specified parameters. For comparison, the mixing process was also carried out manually by human operators.

2.5. Bioink characterization

Following the mixing process, the bioink was transferred into a cartridge for further evaluation of cell distribution and viability. A sample of 0.5 mL bioink was taken from three different positions (start, middle, and end) within the cartridge and placed onto a glass slide. As illustrated in **Figure S1A** (Supplementary File), the bioink sample was compressed into a thin layer by a cover slide held up by two 100-µm-thick spacers. The resulting bioink layer was observed under a fluorescence microscope (Observer Z1, Zeiss, Jena, Germany) to assess the distribution of cells within the bioink.

Metabolic activity of the cells was also quantified after bioprinting using the tetrazolium hydroxide salt (XTT, (2,3-Bis-(2-Methoxy-4-Nitro-5-Sulfophenyl)-2H-Tetrazolium-5-Carboxanilide) assay according to the manufacturer's instructions (Thermo Fisher, Kandel, Germany). The mixed bioink from the aforementioned positions was printed as single-layer disc constructs into a 48-well plate using an extrusion-based printhead equipped with a 22G nozzle on a regenHU bioprinter (3D discovery, regenHU, Switzerland). After printing, 300 µL of complete medium supplemented with 20 mM $CaCl_2$ (Roth, Karlsruhe, Germany) were added to each well. The XTT assay was performed 1 day after bioprinting by adding 150 µL of XTT working solution, which is a mixture of 1 mg/mL XTT solution and 3.83 mg/mL phenazine methosulfate (PMS, AppliChem, Darmstadt, Germany) at a volume ratio of 500:1. Following a 4-h incubation period, 100 µL supernatant from each well was transferred to a 96-well plate for absorbance measurement at 450 nm (with 620 nm as the reference wavelength) in a microplate reader (Sunrise, Tecan, Männedorf, Switzerland). Cell-free constructs were included as background control, and all absorbance values were corrected by subtracting the corresponding background value.

Table 1. Formula of hydrogels for bioink mixing in this study

Hydrogel	Solute	Solvent	Note
6% alginate	3 g sodium alginate	50 mL complete medium	N/A
6% gelatin + 4% alginate	3 g gelatin 2 g sodium alginate	50 mL complete medium	N/A
2% PAA	1 g PAA	50 mL complete medium	pH neutralized using 10 M NaOH solution after dissolving

Cell viability assays were also performed using a viability/cytotoxicity kit (Thermo Fisher Scientific, Waltham, MA, USA). After 1 day in culture, the bioprinted constructs were incubated with phenol red-free RPMI (Biowest) containing 2 μM calcein acetoxymethyl ester (calcein AM) and 2 μM ethidium homodimer-1 for 30 min after supernatant removal and PBS washing. The green (live) and red (dead) signals were then analyzed by the fluorescence microscopy. For the constructs with HEK293-GFP cells, calcein AM was not used due to the existing green fluorescence signal from the cells.

To examine the entire content of the cartridge, the bioink was printed in a zigzag pattern on a petri dish (Standard tissue culture dish 100; Sarstedt, Nümbrecht, Germany) and visualized using a universal imaging system (ChemiDoc™ MP, Bio-Rad, Hercules, CA, USA). The Alexa 488 mode with an exposure time of 0.5 s was utilized to excite GFP in stably transfected HEK293 cells and to capture the images. The images were further processed using ImageJ software (ImageJ 1.53e, National Institutes of Health, Bethesda, MD, USA).

2.6. Rheological measurement

The rheological properties of the bioink were characterized using a rotational rheometer (Anton Paar, Physics MCR 301, Graz, Austria) equipped with a steel parallel plate (25 mm diameter) at a temperature of 25°C. A frequency sweep test was conducted over a range of 0.1 to 100 Hz at a constant shear strain of 0.1%. This test provided information on the viscoelastic behavior of the bioink over a range of frequencies. In addition, a shear rate sweep mode was performed to assess the flow behavior of the bioink between 0.01 s^{-1} and 300 s^{-1}. To evaluate the thixotropic behavior of the bioinks, a three-step shear amplitude switching test (0.01%, 200%, and 0.01%) was employed at 1 Hz. This testing allowed characterizing the bioink's ability to recover its viscosity and structural properties after shearing and thus distinguished between permanent and reversible damage.

2.7. Printability evaluation

To assess the printability of the bioinks, different evaluation methods have been reported.[21,22] Similarly, various constructs were printed on a glass slide using a syringe pump printhead equipped with a 22G nozzle on a regenHU 3D discovery bioprinter. After printing, the constructs were imaged by a digital camera to evaluate the uniformity of the bioinks deposition and assess the quality of the printed structures, providing insights into the homogeneity and printability of the bioinks.

2.8. Statistical analysis

All experiments were performed in triplicate, and the data are presented as mean ± standard deviation (SD), unless otherwise stated. One-way ANOVA in Prism 9 (GraphPad, Boston, MA, USA) was used to analyze the results, which were considered to be statistically significant at levels of $^{*}p < 0.05$, $^{**}p < 0.01$, $^{***}p < 0.001$, and $^{****}p < 0.0001$.

3. Results

3.1. Bioink mixing by human operators

Generally, bioinks can be mixed manually using two connected syringes. To assess the inter-individual variability of manual mixing, three human operators with different levels of experience were selected to perform bioink mixing to compare their bioink preparation. The test operators mixed an ink of two components, a 6% alginate hydrogel and a HEK293-GFP cell suspension. The obtained mixture contained 3% alginate and 10^7 HEK293-GFP cells/mL, the alginate concentration and cell density of which were reported to be suitable for bioprinting.[23-26] The GFP expressed by HEK293-GFP cells allows easy observation of cell distribution under a fluorescence microscope.

We found substantial differences in both cell distribution and cell viability between the bioinks mixed by different operators(Figure 3). When operator 1 mixed the bioink, the cells were distributed relatively evenly in different positions within the cartridge, but some small cell aggregates were present, and the cell viability was extremely low (Figure 3A and B). Although the viability was higher after mixing by operator 2, cells aggregated in numerous clusters, indicating a high level of inhomogeneity in the bioink. Bioink preparation by operator 3 resulted in even higher cell viability and a better cell distribution, but variations were found to be high among different positions. Interestingly, the variation caused by mixing by different operators was much more pronounced than that caused by different mixing by a certain operator.

To improve the bioink quality and reduce experience-dependent variability, all operators were introduced to use conditions which were identified to give good mixing results in our preliminary experiments, i.e., initial mixing at an intermediate speed of approximately 2 s/repetition for 80 repetitions, followed by slow mixing for 4 repetitions every 3 min, so that the total incubation time was approximately 15 min. These guidelines improved the bioink quality somewhat with respect to homogeneity and cell viability. However, substantial differences in bioink quality still remained, even though all operators were tasked with using the same criteria. This is probably attributed to the inherent limitations of human operators in consistently and precisely implementing predetermined conditions. These initial experiments demonstrate that bioinks prepared by different individuals exhibit considerable differences. We therefore sought to improve

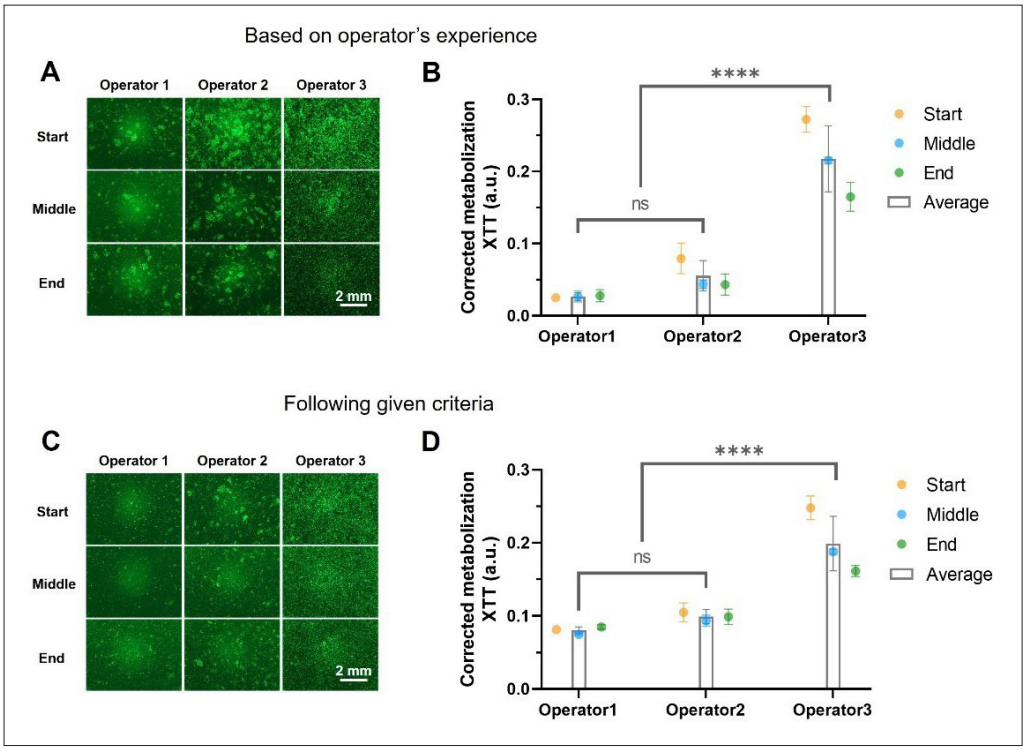

Figure 3. Bioink mixing by human operators. The operators mixed the bioink manually based on their experience (A, B) or following given criteria (C, D). A hydrogel of 6% alginate and a suspension of HEK293-GFP were used for the mixing experiment. After bioink mixing, the cell distribution was analyzed under a fluorescence microscope, and the cell viability was evaluated using the XTT method. $n = 3$; data are expressed as mean ± SD; ****$p < 0.0001$ by one-way ANOVA.

the bioink quality and the reproducibility of cell printing by using an automated, adjustable mixing device.

3.2. Hydrogel preparation by an automated machine

For the first optimization steps of the mixing device, sodium alginate was used to prepare a hydrogel, and an aqueous solution of 0.001% methylene blue represented the cell suspension with generally low viscosity. The mixing effect was evaluated by assessing the distribution of the blue color. Various concentrations of alginate hydrogels were prepared to obtain different viscosities. The alginate hydrogel and the methylene blue solution were filled into separate syringes. Mixing was performed using a fixed coupling of the syringes on the mixing device, where the components were extruded from one syringe into another by moving the syringe barrels (Figure 2C). Initially, alginate hydrogels of different concentrations were supplemented with methylene blue and mixed at a rate of 10 mm/s. As depicted in Figure 4A, homogeneity of the mixture was achieved in approximately 40–50 mixing exchanges at alginate concentrations of 4% or less. In contrast, for alginate concentrations of 6% and more, the required number of mixing exchanges increased substantially. At very high alginate concentrations exceeding 8%, even 100 exchanges were insufficient to obtain a homogeneous hydrogel at 10 mm/s.

The mixing speed is a critical factor influencing the mixing process and the quality of the bioink, including its viscoelastic properties and biological performance. The higher flow rates can induce turbulence with eddies and swirls, facilitating homogeneous mixing,[27,28] but can also be detrimental to the hydrogel components and cells. Therefore, we investigated the minimum number of exchanges required to obtain a homogeneous mixture of 6% alginate and methylene blue solution at different mixing speeds. The results (Figure 4B) reveal that an extremely slow mixing speed of 1 mm/s did not yield a homogeneous bioink even after 100 exchanges, as the components were transferred between the two syringes in a steady manner of laminar flow (**Figure S2** in Supplementary File). Mixing speeds above 5 mm/s proved to be more efficient, as more turbulent flow occurred and gradually dominated the flow behavior at higher exchange rates, requiring less than 100 exchanges to reach homogeneity. At a speed of 50 mm/s, only 50 exchanges were required to obtain a homogenous solution.

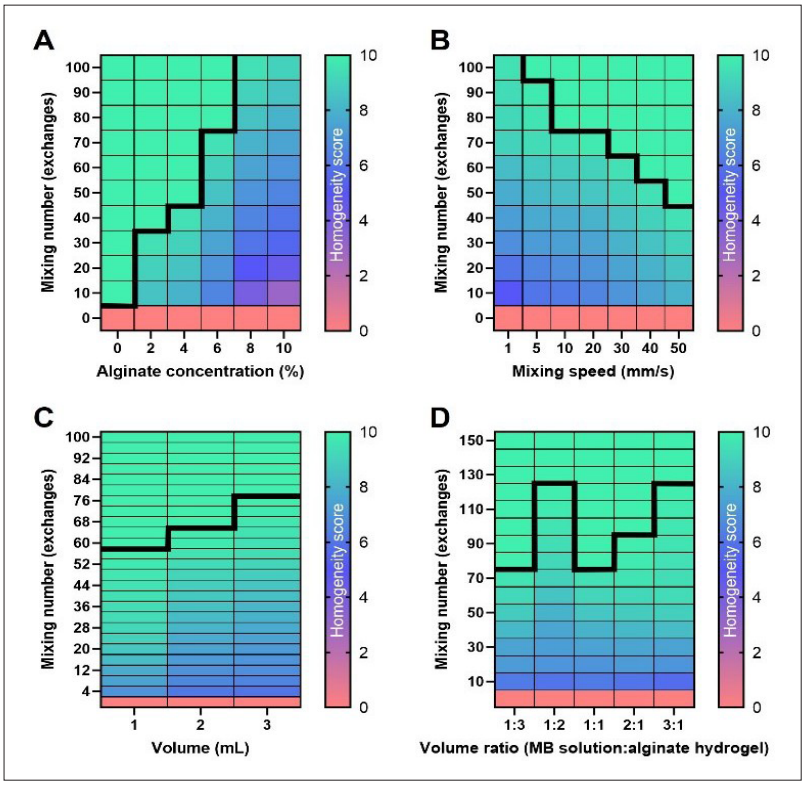

Figure 4. Hydrogel mixing at different conditions using the automated device. Hydrogel mixing was preliminarily explored for different alginate concentrations (A), mixing speeds (B), mixture volume (C), and volume ratios (methylene blue (MB) solution volume : alginate hydrogel volume) (D). Alginate concentration of 6% was tested (B, C), while various concentrations were used (D; **Table S1** in Supplementary File). The mixing effect was assessed at regular intervals of exchanges during the process. The larger numbers indicate the better blending effect, and the black thick lines mark the critical point where the hydrogel reached a homogeneous state under the given conditions.

The volumes of the different components are also likely to make a difference for the mixing behavior. Therefore, the mixing process was further examined using different total volumes ranging from 1 mL to 3 mL at a speed of 10 mm/s. As illustrated in Figure 4C, the number of exchanges required to achieve homogeneity increased with the volume of the mixed components due to their increased longitudinal dimensions.

Additionally, experiments were conducted with different volume ratios (methylene blue volume to alginate hydrogel volume) with a final alginate concentration of 3% at 10 mm/s. As shown in Figure 4D, ratios of 1:3 and 1:1 required the fewest number of exchanges to obtain homogeneous mixtures. For the case of 1:3 ratio, a lower initial alginate concentration of 4% was required to obtain a final value of 3%. This is lower than other ratios, with initial concentrations ranging from 4.5% to 12%, and therefore, the initial viscosity of the hydrogel component was the lowest. When methylene blue solution and hydrogel were mixed in equal volumes, both components had the maximum probability of overall distribution in the system before mixing. Both of them can facilitate the mixing effect.

3.3. Impact of mixing conditions on cell distribution and viability

Cell distribution and viability are greatly influenced by the mixing process, in addition to the bioprinting conditions. To investigate how the mixing process impacts bioink homogeneity and cell status, a systematic exploration was carried out with different mixing parameters. The two fundamental parameters for mixing bioink using a syringe coupler are the mixing speed and the number of exchanges. As described for the manual mixing experiments outlined above, a hydrogel consisting of 6% alginate and a suspension of HEK293-GFP cells were used.

Initially, the components were mixed for 100 exchanges at different speeds ranging from 5 mm/s to 50 mm/s. As can be seen in the fluorescence microscopy images shown in Figure 5A, no substantial differences of cell distribution in samples from different positions were observed after 100 exchanges for any of the tested

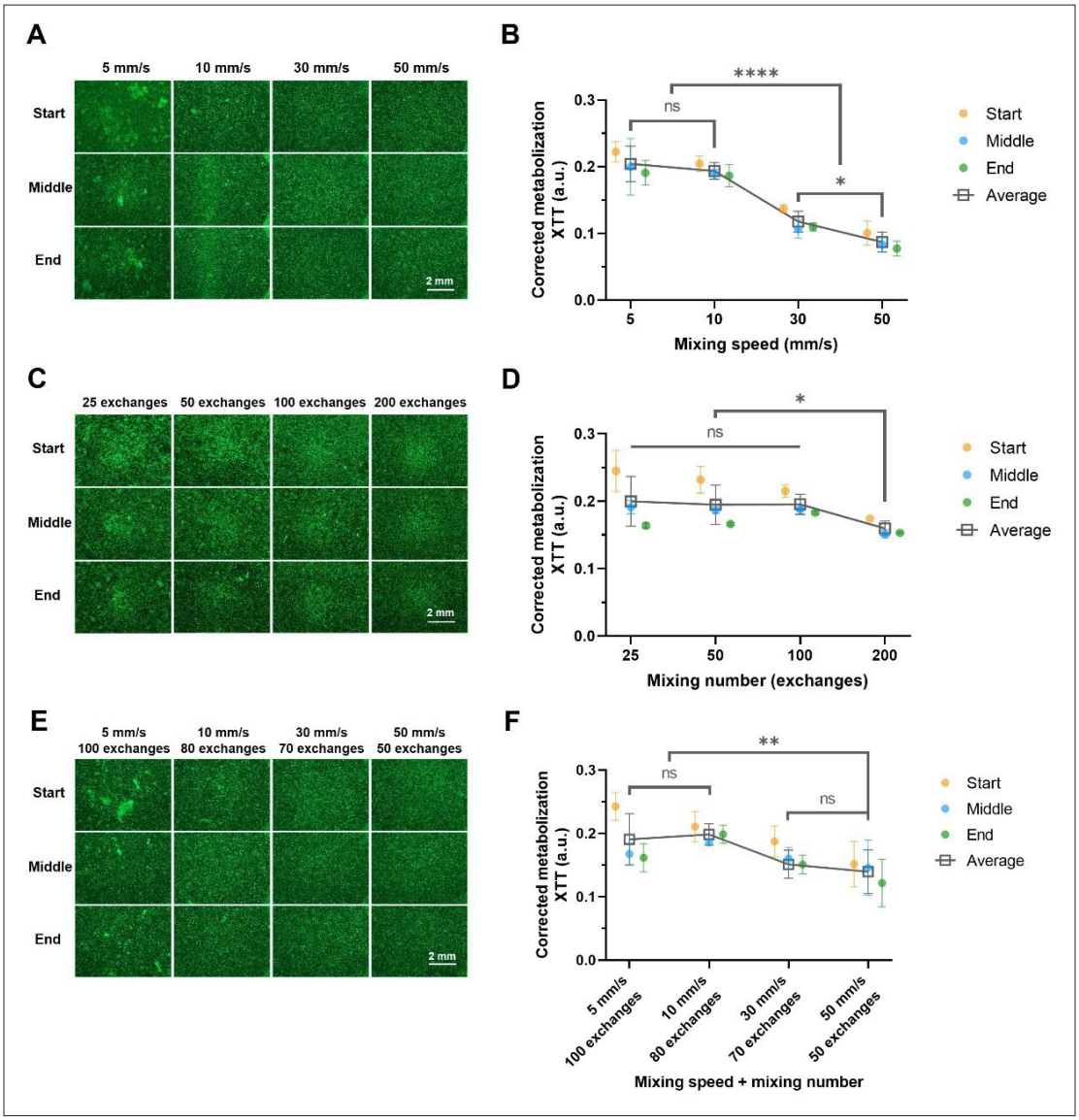

Figure 5. Influence of mixing condition on cell distribution and viability. A 6% alginate hydrogel and a HEK293-GFP cell suspension were mixed by the automated mixing device. The final bioink contained 3% alginate and had a cell density of 10^7 cells/mL. Fluorescence microscopy images show the cell distribution after mixing (A, C, E), and the absorbance in the XTT assays represents the metabolic activity of the cells 1 day after mixing and bioprinting (B, D, F). Influence of mixing speed (fixed exchange number of 100 times, referring to how many times the mixture was transferred from one syringe to another) (A, B), number of exchanges (fixed mixing speed of 10 mm/s) (C, D), and various combinations of mixing speed/mixing number (E, F). $n = 3$; data are expressed as mean ± SD; $^*p < 0.05$, $^{**}p < 0.01$, and $^{****}p < 0.0001$ by one-way ANOVA.

speeds. In contrast, considerable formation of cell clusters was observed when using a lower mixing speed of 5 mm/s, indicating uneven mixing in microscale level. This observation was further conformed by the zigzag extrusion of the bioink, which contained numerous cell aggregates (**Figure S1B** in Supplementary File, white dots indicate a strong signal reflecting high local cell density, which is much greater than other areas displayed in dark purple). Cell distribution was substantially improved when the mixing speed increased to 10 mm/s, and the clustering was completely gone at speeds of 30 and 50 mm/s. However, data from XTT assay revealed that the cell viability was significantly lower at speeds of 30 and 50 mm/s (Figure 5B). In particular, a 50% decrease in viability was detected in cells subjected to a mixing speed of 50 mm/s, which caused severe shearing during the process. This strong shearing can be attributed to the extremely high flow rate (calculated to be around 16 times the mixing speed) in the coupler area within a constrained shape (Figure 2C).

The mixing process was further evaluated by varying the number of exchanges between 25 and 200 times at mixing speed of 10 mm/s. Again, cell distribution and viability were assessed following the mixing process (Figure 5C and D). Predictably, the analysis indicated that the homogeneity of the bioinks improved with increasing numbers of exchanges. Unexpectedly, however, the metabolic activity was almost unaffected by the number of exchanges, and even after 200 exchanges, only a slight decrease in metabolic activity was observed. Furthermore, the standard deviation between different experiments decreased at higher numbers of exchanges. Staining of dead cells with ethidium homodimer-1 did not indicate a substantially higher number of dead cells after 200 exchanges compared to fewer exchanges (**Figure S3** in Supplementary File).

Next, we tested various combinations of mixing speed and numbers of exchanges, as higher speeds tend to achieve homogenous bioinks at lower numbers of exchanges. As can be seen in Figure 5E and F, the combination of a low speed of 5 mm/s with a high number of exchanges (100 times) failed to achieve homogeneity, consistent with the above-described results of the mixing speed test (Figure 5A). The high-speed combinations of 30 mm/s and 70 exchanges and of 50 mm/s with 50 exchanges resulted in homogeneous bioink mixtures with well-dispersed cells. However, cell viability was substantially reduced, with the difference for 50 mm/s with 50 exchanges reaching statistical significance. In contrast, the combination of a mixing speed of 10 mm/s and a mixing number of 80 exchanges achieved comparatively good cell homogeneity, while maintaining high cell viability. To further improve the cell distribution in the bioink, the mixing speed was slightly increased to 15 mm/s at a mixing number of 80 exchanges. Compared to the speed of 10 mm/s, homogeneity was improved further without a decrease in cell viability (**Figure S4** in Supplementary File). Thus, a speed of 15 mm/s and a mixing number of 80 exchanges gave the best overall performance, and the parameter combination was used for all subsequent experiments. The mixing process of an alginate hydrogel (6%) and methylene blue solution (0.001%) under these conditions is shown in **Video S1** (Supplementary File).

3.4. Reproducibility of bioink mixing by machine

As described above, we found that bioinks produced by different human operators had inconsistent properties. We therefore assessed the bioink mixing by the automated device and compared its reproducibility to that of a relatively experienced human operator (No. 3 in the experiments above). Both man and machine mixed the 6% alginate hydrogel with the HEK293-GFP cell suspension. Subsequently, the cell distribution and viability were examined. As depicted in Figure 6A and B, the cell distribution and cell viability were considered generally satisfactory after mixing by the human operator. The cells were well-dispersed in the bioink, and the average cell viability was relatively high. However, cell viability had comparatively high variability in cells taken from either adjacent sites or different positions within the cartridge (Figure 6B). This can be attributed to insufficient mixing in the local regions and the longitudinal distribution of the cells by a poorly controllable mixing process. As a result, the average cell viability varied by more than 40% in some experiments.

In comparison, the machine had a substantially superior mixing performance in terms of both the cell homogeneity and cell viability (Figure 6C and 6D). The cells were distributed more evenly across different positions within the cartridge. The average cell viability was found to be slightly higher than that of human mixing. Importantly, the deviations of cell viability were lower for different positions in the cartridge and between independent experiments. Similar results were also found and confirmed in zigzag bioprinting of the bioinks (Figure 6E and F). The favorable capability of the automated device was also validated using another cell line without GFP expression (HepaRG) immediately after bioink mixing and bioprinting process (**Figure S5** in Supplementary File). The automated device thus produced bioinks with higher homogeneity, comparable cell viability, and superior reproducibility between multiple experiments compared to bioinks produced by a skilled human operator, who has rich experience in bioink mixing in the long-term practice. To investigate the influence on cell functions, the albumin secretion and cytochrome P450 3A4 (CYP3A4) activity were evaluated using HepaRG cell line, both of which are important liver function markers. The results indicate that HepaRG cells maintained the secretion level of albumin for both mixing groups from day 1 to day 7, while the values for CYP3A4 activity increased substantially (**Figure S6** in Supplementary File). No significant difference was detected for the two mixing groups during the testing period. Therefore, bioink mixing executed by automated machine did not negatively impact cell functions compared to that by experienced human operator.

In addition, to evaluate cell distribution and viability, we also measured the rheological properties of the bioinks produced by the human operator or the automated mixing device. The rheological properties are of utmost importance for extrusion-based 3D bioprinting. The analysis revealed that all the bioinks after either human or machine mixing exhibited stability under the testing frequency ranging from 0.1 to 100 Hz (Figure 7A and B) and demonstrated

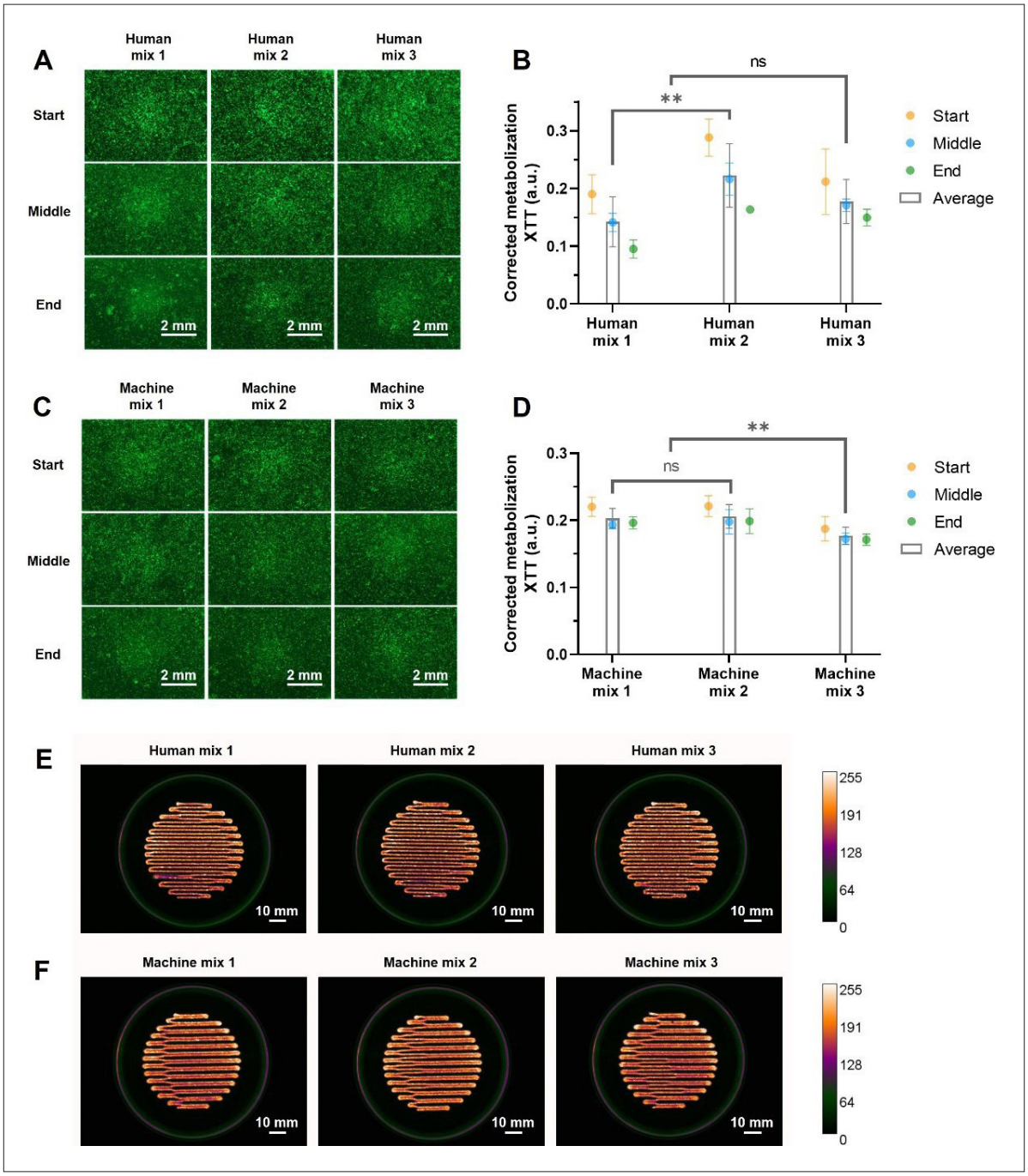

Figure 6. Reproducibility of bioink mixing performed by man or the automated mixing device. The alginate hydrogel of 6% and HEK293-GFP cells were mixed by a skilled operator or the machine. Cell distribution was observed right after mixing under the fluorescence microscope (A, C), and cell viability was measured 1 day after printing by XTT assays (B, D). The zigzag shapes were also extruded on the petri dishes to evaluate the homogeneity of the whole bioink in the cartridge (E, F). $n = 3$; data are expressed as mean ± SD; $^{**}p < 0.01$ by one-way ANOVA.

shear-thinning behaviors (Figure 7C and D). Similarly, both bioinks transitioned into the liquid-like state (G' < G") under shearing and recovered quickly into the solid-like state (G' > G") when shearing stopped (Figure 7E and F). However, the bioinks produced by the automated mixing device showed smaller deviations in modulus and viscosity compared to those mixed by the human operators. Furthermore, the recovery rate of the storage modulus reached a higher level in machine-mixed bioinks than human-mixed ones. These rheological findings

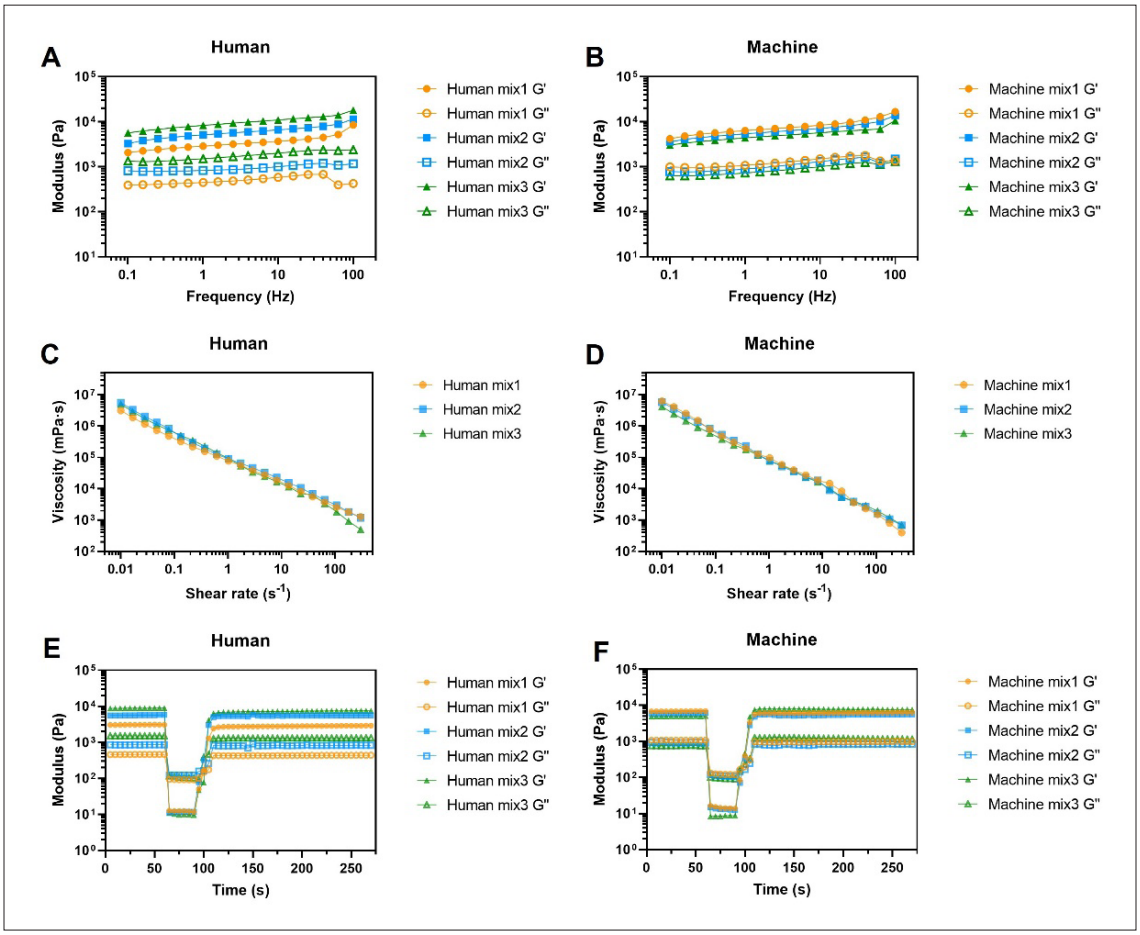

Figure 7. Rheological properties of bioinks after mixing by a human operator or the automated mixing device. The rheological behaviors of the bioinks after manual or machine mixing were measured by modes of frequency sweep (A, B), shear rate sweep (C, D), and 3-step shear strain switching test (E, F).

further support the results obtained by fluorescence microscopy and XTT assessment, indicating that machine mixing offers advantages with respect to properties and reproducibility of bioinks prepared for extrusion-based 3D bioprinting applications.

3.5. Bioink preparation by mixing device with different cell types and different hydrogels

For the experiments described so far, the optimized hydrogel was mixed with 6% alginate and HEK293-GFP cells. To investigate whether the mixing device has a general applicability, different cell types from various organs and different hydrogels were used for further experiments. In addition to the HEK293-GFP (kidney) cells, HepaRG (liver) and A549 (lung) cells were used for further experiments. Following mixing with the automated device, cell viability, as determined by XTT assays, was high and had very small deviations for all cell types used (Figure 8A). The result of live/dead staining as shown in Figure 8B confirmed the favorable mixing effect regarding both cell distribution and physiological properties. Note that for HEK293-GFP cells, only dead cells were stained to fluoresce red with ethidium homodimer-1, as the inherent green fluorescence of GFP outshone green fluorescence from calcein AM after conversion by viable cells.

In the next step, extra hydrogels such as a blend of gelatin/alginate and the synthetic polymer PAA were also used in addition to the alginate hydrogel. Again, the automated mixing device produced bioinks with highly viable cells and low deviations (Figure 8C). Importantly, the cells were homogeneously distributed in the bioinks (Figure 8D). It is therefore reasonable to assume that the mixing device works with high reproducibility and performance for many cell types and hydrogels.

3.6. Printability of bioinks after mixing with the automated device

In addition to the previously discussed properties, printability is another crucial feature of bioinks, as it directly impacts the physiological properties of printed

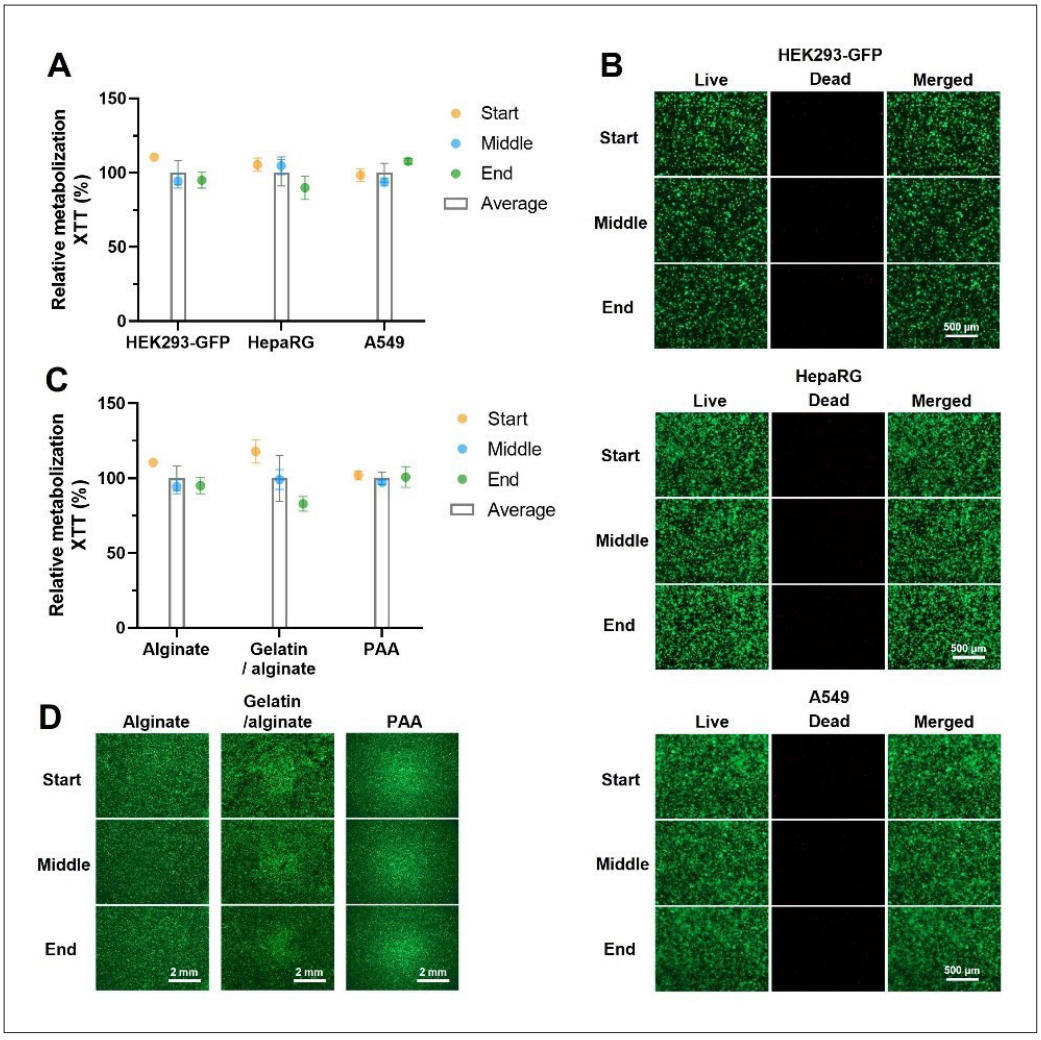

Figure 8. Machine mixing of bioinks using different cell types and hydrogels. (A) Metabolic activity of different cell types after automated mixing with 6% alginate as evaluated by XTT assays 1 day after bioprinting. The values were normalized to the respective average for each cell type. Cell viability determined by live/dead staining. Cells were treated with calcein AM and ethidium homodimer-1 to stain living cells green and dead cells red. (C) Metabolic activity of HEK293-GFP cells in different hydrogels (alginate, alginate/gelatin, and PAA). The values were normalized to the respective average for each cell type. (D) Cell distribution as determined by fluorescence microscopy directly after mixing. $n = 3$; data are expressed as mean ± SD.

constructs. To assess this aspect, we tested three different hydrogels: alginate, gelatin/alginate, and PAA, using the regenHU 3DDiscovery bioprinter to print various models on glass slides. As shown in **Figure S7** (Supplementary File), all three bioinks can be extruded into continuous hydrogel filaments during printing, which is the fundamental requirement for extrusion-based bioprinting. We specifically tested the production of a waffle structure, as it is a popular model in 3D bioprinting research due to its simple and stable architecture, as well as its porosity which ensures a desirable level of cell survival.[29-33] All bioinks mixed with the automated device were found to be suitable for printing the waffle model. Furthermore, the bioinks were also successfully used to print a pyramid model, which requires both high homogeneity and stiffness of the bioink. These results highlight the good printability of the bioinks after machine mixing.

4. Discussion

Hydrogels have been demonstrated to be highly effective matrices for 3D cell culture.[34-36] Viscous hydrogels, in particular, have been extensively utilized as bioinks in EBB.[37,38] These hydrogels not only create a suitable aqueous 3D environment for cells, but also enable the fabrication of complex architectures with excellent printability and fidelity by preventing deformation driven by gravity or surface tension.[7,39] The preparation of viscous bioinks, however, presents challenges. While vigorous methods

ensure homogeneity of the bioinks, the shear force generated during the process may damage living cells.[40]

The syringe coupler method has been extensively used to prepare the EBB bioinks, which is a favorable technique for handling viscous hydrogels and components.[15,20,41-44] After filling the material and expelling the air, the syringes were connected with a coupling piece (Luer coupler) to isolate the mixing components from the environment so that air bubbles and contamination risks can be largely avoided during the mixing process. Mixing speed and mixing exchanges are crucial parameters when using a syringe coupler to mix bioinks. We noticed that researchers in the field of 3D bioprinting rely on their individual experiences when preparing bioinks. These experiences can vary significantly between beginners and experienced operators. Typically, researchers acquire relevant knowledge through daily practice, education, and training.[45,46] While not given sufficient attention in the past, bioink mixing is clearly an important parameter which, going forward, needs to be carefully documented and controlled. In this study, we simulated this scenario and found that different human operators produce bioink mixes that vary quite a little in quality, even when all other conditions remained the same.

This inconsistency can result in variations in research outcomes across different researchers and laboratories, and severely jeopardize the reproducibility of the experiments. The variability in manual movements can also result in cell damage or prevent the generation of a homogeneous bioink mixture. An appropriate approach to improve the experimental quality is to provide clear and detailed information for the bioink mixing procedure, based on which the experimenter might improve the performance and the experimental outcomes. However, this might still be insufficient to ensure the reproducibility of bioinks. Our findings indicate that bioinks can still exhibit significant variations depending on the mixing operator, even though the same instructions were followed. This can be attributed to factors such as physical strength, manual dexterity, prior experience, and attention to detail, which are difficult to change or control.[47]

To overcome the problem of inconsistent bioink preparation, we propose replacing human actions with machine motions of automated technology. This methodology can achieve a higher level of control and reproducibility. In our study, we developed a customized automated device for bioink mixing, which has a compact structure, convenient operation features, high compatibility, and a reliable control program. The machine can provide precise and repeatable movements during the mixing process, enabling exact setting of different parameters for bioink mixing in a highly controllable and effective manner.

When the mixing speed was very low, the system inside the syringes and the coupler exhibited laminar flow. Under these conditions, the components were transported along the longitudinal direction within the individual flow layer, and mixing of the layers of different density was almost entirely absent. Conversely, a high mixing speed induced turbulent flow, where the components were randomly moved across different layers by eddies.[48] Consequently, the cell suspension can be effectively spread out and dispersed into the hydrogel phase, resulting in a homogeneous bioink. However, speeds above a certain threshold caused substantial shear stress, which negatively affected the cells and even the hydrogel molecules. According to our systematic evaluation, a mixing speed at 15 mm/s is sufficient for effectively blending the mixture of 6% alginate and cell suspension without causing significant cell damage. In contrast to mixing speed, the mixing number was found to be a minor factor, exerting a minor influence on homogeneity and cell viability. Thus, the harsh shear stress induced by rapid and jerky movements of plungers is more detrimental to living cells than the cumulative impact of a higher mixing number.

In the next step, we compared the performance of the bioink mixing machine to that of a human operator. This assessment demonstrated a clear advantage of the automated system, which mixed bioinks with higher homogeneity and reproducibility than the human operator. To assess the general applicability of the standardized bioink mixing process by the automated device, we conducted experiments using different cell lines and hydrogel formulations. These experiments confirmed that the machine mixing approach could consistently produce homogeneous bioinks with high cell viability using various common bioink compositions, regardless of the specific cell line or hydrogel formulation used.

Although overall outcomes were positive, it is important to acknowledge that the applied parameters might be not optimal for all scenarios. Different cell lines have distinct features in terms of cell dimensions and tolerance to shear force, which lead to variations in both homogeneity and cell viability. Additionally, hydrogels exhibit diverse density, viscosity, and rheological behaviors, causing different flow state within the system and subsequently affecting the uniformity of the bioinks.

Overall, we found that the developed automated bioink mixing device results in bioinks with better homogeneity and favorable cell viability compared to human operators, which can further contribute to more reliable and reproducible outcomes for 3D bioprinting research. Generally, these kinds of automated devices are highly parameter-sensitive such as time, speed, and distance, and

it is possible to make adjustments according to the prior experiment result. Conversely, more precise and accurate control of these parameters can bring more reproducible results and greatly simplify the optimization process. Finally, a positive feedback loop, which is very effective for the optimization of experimental conditions, is formed. Once the parameters have been determined, the conditions can be precisely reproduced in subsequent experiments. Hence, this is considered an effective step to enhance the consistency and repeatability of the 3D bioprinting results.

Importantly, the strategy and methodology of this study is readily scalable and popularized for relevant applications in this field. Li et al.[49] built an automated active mixing platform adapted from syringe pumps that can prepare homogeneous hydrogel bioinks automatically, yielding results consistent with ours. Nonetheless, the developed platform still exhibits some limitations, especially regarding the different syringe compatibility, convenience on changing mixture volume, and large-space occupation. Here, we provide a rational design of the automated device, which is more compatible, maneuverable, reliable, and compact in size. Various volumes/volume ratios and standard/customized couplers can be easily handled due to the readily adjustable rack structure and barrel-moving design. Syringes from different manufacturers can also be used by simply switching the endstop adaptors. The involved hardware is easily accessible and ordinary in common automation equipment, such as 3D printers, automatic loading devices, and robotics.[50-53] Therefore, we believe that this strategy can not only effectively improve the cell status and bioink homogeneity, but also contribute to the situations of mixing spheroids,[54] growth factors,[55] drugs,[56] pigment,[57] nanoparticles,[58,59] etc. This could facilitate the 3D bioprinting research and also benefit the related areas.

Future research should focus on exploring additional mixing parameters to further optimize the bioink mixing process. These parameters may include temperature control, motion acceleration and deceleration control, and more complex mixing programs with varying mixing periods. Exploring various cell densities, additional hydrogel candidates, and different bioink forms (e.g., microgels, cell aggregates) is also of interest. This comprehensive approach would contribute to enhancing the reproducibility and quality of bioink preparation in various applications of 3D bioprinting.

5. Conclusion

In conclusion, this study systematically investigated the effects of various mixing parameters, particularly the mixing speed and the mixing number, on bioink homogeneity and cell viability. The results reveal that the mixing speed has a more pronounced impact on these parameters than the mixing number. The study also highlighted the importance of standardizing the bioink mixing process for 3D bioprinting. By using a machine for bioink mixing, notable improvements were observed in bioink homogeneity, cell distribution, cell viability, and rheological properties compared to human mixing, which was characterized by strong inter-individual variations, as well as variability among independent experiments carried out by the same operator. These findings strongly suggest that the standardization of bioink mixing process using an automated device is instrumental for substantially enhancing the reproducibility and reliability of 3D bioprinting experiments. Furthermore, automated mixing of hydrogels will also contribute to improvements of the experimental outcome in related areas such as 3D cell culture, organoid research, and stem cell cultivation. The American folk hero John Henry won the contest against the steam-powered rock drilling machine with his hammer but died doing so. Just a few years later, no one called into question whether machines were faster. Nowadays, it is obvious that automatization is necessary to improve the quality of precision research.

Acknowledgments

We are thankful to Erik Wade for proofreading and valuable discussion.

Funding

This research was supported by the Chinese Scholarship Council (CSC; fellowship No. 201906780024 to D.W., and fellowship No. 201906780023 to S.P.). Financial support from the Einstein Foundation Berlin (Einstein Center 3R, EZ-2020-597-2) is gratefully acknowledged.

Conflict of interest

The authors declare no conflicts of interest.

Author contributions

Conceptualization: Jens Kurreck, Dongwei Wu, Shumin Pang, Ahmed S. M. Ali

Data curation: Dongwei Wu, Shumin Pang, Ahmed S. M. Ali, Yikun Mei, Viola Röhrs

Formal analysis: Jens Kurreck, Dongwei Wu, Shumin Pang, Viola Röhrs, Johanna Berg, Ahmed S. M. Ali, Yikun Mei, Mathias Ziersch, Beatrice Tolksdorf

Funding acquisition: Jens Kurreck, Johanna Berg

Methodology: Jens Kurreck, Dongwei Wu, Shumin Pang, Ahmed S. M. Ali

Resources: Jens Kurreck, Johanna Berg

Writing – original draft: Jens Kurreck, Dongwei Wu, Shumin Pang

Writing – review & editing: Jens Kurreck, Dongwei Wu, Shumin Pang, Viola Röhrs, Johanna Berg, Ahmed S. M. Ali, Yikun Mei, Mathias Ziersch, Beatrice Tolksdorf

Ethics approval and consent to participate

Not applicable.

Consent for publication

Not applicable.

Availability of data

Data are available from the corresponding author upon reasonable request.

References

1. Assad H, Assad A, Kumar A. Recent developments in 3D bio-printing and its biomedical applications. *Pharmaceutics*. 2023;15(1):255. doi: 10.3390/pharmaceutics15010255
2. Hagenbuchner J, Nothdurfter D, Ausserlechner MJ. 3D bioprinting: novel approaches for engineering complex human tissue equivalents and drug testing. *Essays Biochem*. 2021;65(3):417-427. doi: 10.1042/ebc20200153
3. Berg J, Kurreck J. Clean bioprinting - fabrication of 3D organ models devoid of animal components. *ALTEX*. 2021;38(2):269-288. doi: 10.14573/altex.2009151
4. Bhattacharyya A, Janarthanan G, Tran HN, Ham HJ, Yoon J, Noh I. Bioink homogeneity control during 3D bioprinting of multicomponent micro/nanocomposite hydrogel for even tissue regeneration using novel twin screw extrusion system. *Chem Eng J*. 2021;415:128971. doi: 10.1016/j.cej.2021.128971
5. Wang Y, Yuan X, Yao B, Zhu S, Zhu P, Huang S. Tailoring bioinks of extrusion-based bioprinting for cutaneous wound healing. *Bioact. Mater.* 2022;17:178-194. doi: 10.1016/j.bioactmat.2022.01.024
6. Ainsworth MJ, Chirico N, de Ruijter M, et al. Convergence of melt electrowriting and extrusion-based bioprinting for vascular patterning of a myocardial construct. *Biofabrication*. 2023;15(3):035025. doi: 10.1088/1758-5090/ace07f
7. Ozbolat IT, Hospodiuk M. Current advances and future perspectives in extrusion-based bioprinting. *Biomaterials*. 2016;76:321-343. doi: 10.1016/j.biomaterials.2015.10.076
8. Kessel B, Lee M, Bonato A, Tinguely Y, Tosoratti E, Zenobi-Wong M. 3D bioprinting of macroporous materials based on entangled hydrogel microstrands. *Adv Sci*. 2016;7(18):2001419. doi: 10.1002/advs.202001419
9. Karvinen J, Kellomäki M. Design aspects and characterization of hydrogel-based bioinks for extrusion-based bioprinting. *Bioprinting*. 2023;32:e00274. doi: 10.1016/j.bprint.2023.e00274
10. Vu M, Pramanik A, Basak AK, Prakash C, Shankar S. Progress and challenges on extrusion based three dimensional (3D) printing of biomaterials. *Bioprinting*. 2022; 27:e00223. doi: 10.1016/j.bprint.2022.e00223
11. Jia R, Zhang M, Yang T, Ma M, Sun Q, Li M. Evolution of the morphological, structural, and molecular properties of gluten protein in dough with different hydration levels during mixing. *Food Chem: X*. 2022;15:100448. doi: 10.1016/j.fochx.2022.100448
12. Thayer PS, Orrhult LS, Martínez H. Bioprinting of cartilage and skin tissue analogs utilizing a novel passive mixing unit technique for bioink precellularization. *JoVE*. 2018;131(131):e56372. doi: 10.3791/56372
13. Li G, Huang K, Deng J, et al. Highly conducting and stretchable double-network hydrogel for soft bioelectronics. *Adv Mater*. 2022;34(15):2200261. doi: 10.1002/adma.202200261
14. Raja N, Park H, Gal CW, Sung A, Choi Y-J, Yun H-s. Support-less ceramic 3D printing of bioceramic structures using a hydrogel bath. *Biofabrication*. 2023; 15(3):035006. doi: 10.1088/1758-5090/acc903
15. Zheng Z, Wu J, Liu M, et al. 3D bioprinting of self-standing silk-based bioink. *Adv Healthc Mater*. 2018;7(6):1701026. doi: 10.1002/adhm.201701026
16. Guagliano G, Volpini C, Sardelli L, et al. Hep3Gel: a shape-shifting extracellular matrix- based, three-dimensional liver model adaptable to different culture systems. *ACS Biomater Sci Eng*. 2023;9(1):211-229. doi: 10.1021/acsbiomaterials.2c01226
17. Dou Z, Tang H, Chen K, et al. Highly elastic and self-healing nanostructured gelatin/clay colloidal gels with osteogenic capacity for minimally invasive and customized bone regeneration. *Biofabrication*. 2023;15(2):025001. doi: 10.1088/1758-5090/acab36
18. Berg J, Hiller T, Kissner MS, et al. Optimization of cell-laden bioinks for 3D bioprinting and efficient infection with influenza A virus. *Sci Rep*. 2018;8(1):13877. doi: 10.1038/s41598-018-31880-x
19. Wu D, Berg J, Arlt B, et al. Bioprinted cancer model of neuroblastoma in a renal microenvironment as an efficiently applicable drug testing platform. *Int J Mol Sci*. 2022;23(1):122. doi: 10.3390/ijms23010122

20. Dani S, Ahlfeld T, Albrecht F, et al. Homogeneous and reproducible mixing of highly viscous biomaterial inks and cell suspensions to create bioinks. *Gels.* 72021;(4):227. doi: 10.3390/gels7040227

21. Cavallo A, Al Kayal T, Mero A, et al. Marine collagen-based bioink for 3D bioprinting of a bilayered skin model. *Pharmaceutics.* 2023;15(5):1331. doi: 10.3390/pharmaceutics15051331

22. Gillispie G, Prim P, Copus J, et al. Assessment methodologies for extrusion-based bioink printability. *Biofabrication.* 2020;12(2):022003. doi: 10.1088/1758-5090/ab6f0d

23. Kang D, Liu Z, Qian C, et al. 3D bioprinting of a gelatin-alginate hydrogel for tissue-engineered hair follicle regeneration. *Acta Biomater*. 2023;165:19-30. doi: 10.1016/j.actbio.2022.03.011

24. Isaacson A, Swioklo S, Connon CJ. 3D bioprinting of a corneal stroma equivalent. *Exp Eye Res*. 2018;173:188-193. doi: 10.1016/j.exer.2018.05.010

25. Cadena M, Ning L, King A, et al. 3D bioprinting of neural tissues. *Adv Healthc Mater.* 2021;10(15):2001600. doi: 10.1002/adhm.202001600

26. Graham AD, Olof SN, Burke MJ, et al. High-resolution patterned cellular constructs by droplet-based 3D printing. *Sci Rep.* 2017;7(1):7004. doi: 10.1038/s41598-017-06358-x

27. Pretorius V, Smuts TW. Turbulent flow chromatography. A new approach to faster analysis. *Anal Chem.* 1966;38(2):274-281. doi: 10.1021/ac60234a030

28. Dimotakis PE. Turbulent mixing. *Annu Rev Fluid Mech.* 2005;37(1):329-356. doi: 10.1146/annurev.fluid.36.050802.122015

29. Hiller T, Berg J, Elomaa L, et al. Generation of a 3D liver model comprising human extracellular matrix in an alginate/gelatin-based bioink by extrusion bioprinting for infection and transduction studies. *Int J Mol Sci.* 2018;19(10):3129. doi: 10.3390/ijms19103129

30. Berg J, Weber Z, Fechler-Bitteti M, et al. Bioprinted multi-cell type lung model for the study of viral inhibitors. *Viruses.* 2021;13(8):1590. doi: 10.3390/v13081590

31. Al-Zeer MA, Prehn F, Fiedler S, et al. Evaluating the suitability of 3D bioprinted samples for experimental radiotherapy: a pilot study. *Int J Mol Sci*. 2022;23(17):9951. doi: 10.3390/ijms23179951

32. Senturk E, Bilici C, Afghah F, et al. 3D bioprinting of tyramine modified hydrogels under visible light for osteochondral interface. *Biofabrication*. 2023;15(3):034102. doi: 10.1088/1758-5090/acd6bf

33. Xin S, Deo KA, Dai J, et al. Generalizing hydrogel microparticles into a new class of bioinks for extrusion bioprinting. *Sci Adv.* 2021;7(42):eabk3087. doi: 10.1126/sciadv.abk3087

34. Tibbitt MW, Anseth KS. Hydrogels as extracellular matrix mimics for 3D cell culture. *Biotechnol Bioeng.* 2009;103(4):655-663. doi: 10.1002/bit.22361

35. Nam S, Stowers R, Lou J, Xia Y, Chaudhuri O. Varying PEG density to control stress relaxation in alginate-PEG hydrogels for 3D cell culture studies. *Biomaterials.* 2019;200:15-24. doi: 10.1016/j.biomaterials.2019.02.004

36. Pasturel A, Strale P-O, Studer V. Tailoring common hydrogels into 3D cell culture templates. *Adv Healthc Mater.* 2020;9(18):2000519. doi: 10.1002/adhm.202000519

37. Cui X, Li J, Hartanto Y, et al. Advances in extrusion 3D bioprinting: a focus on multicomponent hydrogel-based bioinks. *Adv Healthc Mater.* 2020;9(15):1901648. doi: 10.1002/adhm.201901648

38. Unagolla JM, Jayasuriya AC. Hydrogel-based 3D bioprinting: a comprehensive review on cell-laden hydrogels, bioink formulations, and future perspectives. *Appl Mater Today.* 2020;18:100479. doi: 10.1016/j.apmt.2019.100479

39. Ho T-C, Chang C-C, Chan H-P, et al. Hydrogels: properties and applications in biomedicine. *Molecules*. 2022;27(9):2902. doi: 10.3390/molecules27092902

40. Puertas-Bartolomé M, Włodarczyk-Biegun MK, del Campo A, Vázquez-Lasa B, San Román J. 3D printing of a reactive hydrogel bio-ink using a static mixing tool. *Polymers.* 2020;12(9):1986. doi: 10.3390/polym12091986

41. Jeon O, Lee YB, Lee SJ, Guliyeva N, Lee J, Alsberg E. Stem cell-laden hydrogel bioink for generation of high resolution and fidelity engineered tissues with complex geometries. *Bioact Mater.* 2022;15:185-193. doi: 10.1016/j.bioactmat.2021.11.025

42. Semba JA, Mieloch AA, Tomaszewska E, Cywoniuk P, Rybka JD. Formulation and evaluation of a bioink composed of alginate, gelatin, and nanocellulose for meniscal tissue engineering. *Int J Bioprint.* 2023;9(1):621. doi: 10.18063/ijb.v9i1.621

43. Pagan E, Stefanek E, Seyfoori A, et al. A handheld bioprinter for multi-material printing of complex constructs. *Biofabrication*. 2023;15(3):035012. doi: 10.1088/1758-5090/acc42c

44. Mörö A, Samanta S, Honkamäki L, et al. Hyaluronic acid based next generation bioink for 3D bioprinting of human stem cell derived corneal stromal model with innervation. *Biofabrication*. 2023;15(1):015020. doi: 10.1088/1758-5090/acab34

45. Hunsberger J, Simon C, Zylberberg C, et al. Improving patient outcomes with regenerative medicine: how the Regenerative Medicine Manufacturing Society plans to move the needle

forward in cell manufacturing, standards, 3D bioprinting, artificial intelligence-enabled automation, education, and training. *Stem Cells Transl Med.* 2020;9(7):728-733.
doi: 10.1002/sctm.19-0389

46. Brown A. 3D printing in instructional settings: identifying a curricular hierarchy of activities. *TechTrends*. 2015; 59(5):16-24.
doi: 10.1007/s11528-015-0887-1

47. Boogert NJ, Madden JR, Morand-Ferron J, Thornton A. Measuring and understanding individual differences in cognition. *Philos Trans R Soc Lond B Biol Sci.* 2018;373(1756):20170280.
doi: 10.1098/rstb.2017.0280

48. Spurk JH, Aksel N, eds. *Fluid Mechanics*. Cham: Springer International Publishing; 2020: 223-249.
doi: 10.1007/978-3-030-30259-7_7

49. Li J, Shelby T, Alizadeh HV, Shelby H, Yang YP. Development and characterization of an automated active mixing platform for hydrogel bioink preparation. *Int J Bioprint.* 2023;9(4):4.
doi: 10.18063/ijb.705

50. Samokhin AS. Syringe pump created using 3D printing technology and arduino platform. *J Anal Chem.* 2020;75(3):416-421.
doi: 10.1134/S1061934820030156

51. Campbell T, Jones JFX. Design and implementation of a low cost, modular, adaptable and open-source XYZ positioning system for neurophysiology. *HardwareX*. 2020; 7:e00098.
doi: 10.1016/j.ohx.2020.e00098

52. Hadisujoto B, Wijaya R. Development and accuracy test of a fused deposition modeling (FDM) 3D printing using H-Bot mechanism. *IJoCED*. 2021;3(1):46-53.
doi: 10.35806/ijoced.v3i1.148

53. Manolescu VD, Secco EL. Design of an assistive low-cost 6 d.o.f. robotic arm with gripper. In: Yang XS, Sherratt S, Dey N, Joshi A, eds. *Proceedings of Seventh International Congress on Information and Communication Technology.* Singapore: Springer Nature Singapore; 2023: 39-55.

54. Othman SA, Soon CF, Ma NL, et al. Alginate-gelatin bioink for bioprinting of hela spheroids in alginate-gelatin hexagon shaped scaffolds. *Polym Bull.* 2021;78(11):6115-6135.
doi: 10.1007/s00289-020-03421-y

55. Freeman FE, Pitacco P, van Dommelen LHA, et al. 3D bioprinting spatiotemporally defined patterns of growth factors to tightly control tissue regeneration. *Sci Adv.* 2020;6(33):eabb5093.
doi: 10.1126/sciadv.abb5093

56. Mirek A, Belaid H, Bartkowiak A, et al. Gelatin methacrylate hydrogel with drug-loaded polymer microspheres as a new bioink for 3D bioprinting. *Biomater Adv.* 2023;150:213436.
doi: 10.1016/j.bioadv.2023.213436

57. Seo JW, Kim GM, Choi Y, Cha JM, Bae H. Improving printability of digital-light-processing 3D bioprinting via photoabsorber pigment adjustment. *Int J Mol Sci.* 2022;23(10):5428.
doi: 10.3390/ijms23105428

58. Ding Y-W, Zhang X-W, Mi C-H, Qi X-Y, Zhou J, Wei D-X. Recent advances in hyaluronic acid-based hydrogels for 3D bioprinting in tissue engineering applications. *Smart Mater Med.* 2023;4:59-68.
doi: 10.1016/j.smaim.2022.07.003

59. Serafin A, Culebras M, Oliveira JM, Koffler J, Collins MN. 3D printable electroconductive gelatin-hyaluronic acid materials containing polypyrrole nanoparticles for electroactive tissue engineering. *Adv Compos Hybrid Mater.* 2023;6(3):109.
doi: 10.1007/s42114-023-00665-w

ACCSCIENCE PUBLISHING

International Journal of Bioprinting

RESEARCH ARTICLE

Modeling inflammatory response using 3D bioprinting of polarized macrophages

Nimal Raveendran, Kanchan Vaswani, Pingping Han, Saraswat Basu, Corey S. Moran, and Sašo Ivanovski*

Centre for Orofacial Regeneration, Reconstruction and Rehabilitation, The School of Dentistry, The University of Queensland, Queensland, Australia

Abstract

The field of drug discovery has seen the rise of three-dimensional (3D) bioprinting as a promising tool for disease modeling. The focus to date has been on tissue engineering and cancer modeling, although the application of 3D-bioprinted models for the study of inflammation using macrophages is still in its infancy. This study explores the potential of bioprinting technology in the development of a 3D macrophage model and macrophage response to inflammatory stimuli using this platform. To this end, we established a 3D-bioprinted macrophage model and assessed the inflammatory and anti-inflammatory response to bacterial endotoxin (lipopolysaccharide, LPS) and the drug ibuprofen (Ibu), respectively. Optimal conditions for macrophage differentiation of the human monocytic cell line, THP-1, in the 3D environment were studied, as well as the effect of the 3D microenvironment on macrophage polarization. Viability of THP-1 cells following the 3D bioprinting process was demonstrated and maintained, allowing successful macrophage differentiation of the cells. The developed 3D-bioprinted macrophage model exhibited elevated expression of selected pro-inflammatory gene and protein markers following exposure to LPS, consistent with polarization from M0 to M1 phenotype. Additionally, the model was responsive to the anti-inflammatory properties of Ibu, demonstrating its potential in drug screening and discovery. The current study highlights the potential of bioprinting in the investigation of inflammatory cell response and behavior in a 3D environment *ex vivo*, opening new avenues for research in modeling inflammatory responses to various stimuli.

Keywords: Macrophages; 3D culture; 3D bioprinting; Drug discovery

***Corresponding author:**
Saso Ivanovski
(s.ivanovski@uq.edu.au)

Citation: Raveendran N, Vaswani K, Han P, Basu S, Moran CS, Ivanovski S. Modeling inflammatory response using 3D bioprinting of polarized macrophages. *Int J Bioprint*. 2024;10(2):2116. doi: 10.36922/ijb.2116

Received: October 26, 2023
Accepted: December 20, 2023
Published Online: February 21, 2024

1. Introduction

The macrophage is an important immune cell that plays a key role in host defense. Elie Metchnikoff, awarded the Nobel Prize in 1908 for his work on phagocytosis, proposed that the key to immunity was to "stimulate the phagocytes."[1,2] Since then, immunologists have been studying macrophages and their role in the immune system. Inflammatory and immune complications are an indicator of an impaired immune system. Researchers can use models of inflammatory response to study disease progression and the efficacy of anti-inflammatory drugs and other interventions.

There are currently several techniques available for *in vitro* disease modeling, including three-dimensional (2D) and three-dimensional (3D) culture models. 2D culture is the most utilized model, although poor cell differentiation, unrealistic cell proliferation, decreased drug resistance, and inaccurate response to stimuli remain the significant challenges.[3-5] 2D culture also limits the number of cell types that can be co-cultured and cannot accurately represent the complex microenvironment of human tissues.[6] 3D culture is a more complex model that facilitates better cell-to-cell contact and intercellular signaling. 3D culture provides a more native cell environment and is becoming increasingly important in drug development and preclinical testing. Protein expression patterns and intracellular junctions more closely resemble *in vivo* conditions compared to 2D monolayer cultures. Moreover, 3D models play a valuable role in the clinical development process, allowing for better characterization of cells and their microenvironments, as well as drug response, efficacy, and toxicity. Comparatively, 2D culture is a less complex and less expensive option, but 3D models provide more robust and relevant results, gradually becoming essential for advancing our understanding of cellular and molecular mechanisms in health and disease.

In the field of drug testing, there exist three distinct 3D models: scaffold-based cultures, non-scaffold-based cultures such as organoids and cellular spheroids, and tissue-engineered models utilizing bioprinting technology.[7-9] Tissue-engineered models present several benefits compared to their scaffold-based and non-scaffold-based counterparts. First, tissue-engineered models more accurately replicate the natural organization (cellular niche) and function of human tissues through cell culture techniques, providing a more physiologically relevant representation of human anatomy.[10,11] Second, these models facilitate the formation of complex and functional cell–cell interactions, which play a critical role in proper tissue function and may not be attainable in scaffold-based or non-scaffold-based cultures.[11] Third, tissue-engineered models afford a more realistic representation of drug response in human tissues, leading to improved predictions of drug efficacy and toxicity.[12,13] Finally, tissue-engineered models can be tailored to specific disease states or therapeutic targets, enabling more targeted drug testing.[14] Thus, tissue-engineered models offer a more accurate representation of human tissues and are a valuable tool for drug discovery and testing as they enable tissue-like structures to be created *in vitro*.[15,16] The pre-eminence of 3D bioprinting as a tissue engineering method for disease modeling is underscored by its aptitude for accurate reproduction of intricate tissue structures, enabling precise customization and the integration of diverse cell types within a unified model. The capability to generate patient-specific tissues enhances its applicability in comprehensively investigating disease mechanisms and devising personalized therapeutic strategies. Furthermore, 3D bioprinting plays a pivotal role in diminishing dependence on animal testing and furnishes a realistic platform for drug evaluation, thereby positioning itself as a forefront technology in the progression of disease research and therapeutic advancement.[9] Several human cell types are currently being researched using 3D-bioprinted models.[17,18]

Recent studies have established the feasibility of 3D-bioprinted constructs of anti-inflammatory (M2) macrophages as a novel approach for disease modeling[19] and tissue engineering applications.[20] There is, however, a paucity of data related to modeling pro-inflammatory (M1) macrophages. Recently, a bioprinted lung tissue model was developed to study inflammation and the use of viral inhibitors.[21] At the time of writing, this is the only study that incorporated M1 macrophage polarization and investigated pathogenic biology while shedding light on the development of new therapeutic anti-inflammatory drugs. The objective of the present study was to establish a 3D-bioprinted inflammation model using the macrophage cell line THP-1, and within this model, evaluate the efficacy of ibuprofen (Ibu) as an anti-inflammatory agent. The outcomes of this study will contribute to the advancement of knowledge in the field of 3D-bioprinted macrophage models and their application in the study of inflammation.

2. Materials and methods

2.1. Cell culture

The human leukemia monocytic cell line THP-1 (courtesy of Prof. K. Schroder, Institute for Molecular Biosciences, University of Queensland, Australia) was cultured in basal medium (BM) made of RPMI 1640 Medium (Life Technologies, Australia) supplemented with 10% (v/v) heat-inactivated fetal bovine serum (FBS; Gibco®, Australia) and 1% (v/v) antibiotic-antimycotic (Gibco®, Australia) at 37°C under 5% CO_2. The cells were differentiated into macrophages (M0) using phorbol 12-myristate 13-acetate (PMA; Sigma-Aldrich, USA). M0 were polarized into classically activated macrophages (M1) with lipopolysaccharides produced from *Escherichia coli* (LPS; Sigma-Aldrich, USA).

2.2. Optimization of 3D bioprinting of THP-1 and evaluation of printability (Pr)

The optimal concentration of gelatin methacryloyl (GelMA; Gelomics Pty Ltd., Australia) was determined with a 55 ± 3% degree of functionalization for 3D

bioprinting. Different concentrations of GelMA (2.5, 5, 7.5, 10, 12.5, 15% (w/v)) containing 0.15% (w/v) photoinitiator lithium phenyl (2,4,6-trimethyl benzoyl) phosphinate (LAP; Sigma-Aldrich, USA) were mixed at 37°C, loaded in sterile 3D bioprinting cartridges and incubated at 23°C for 20 min for thermal crosslinking. 25 G (inner diameter of 260 μm) sterile tapered dispensing tips were connected to the cartridges and loaded in a BIOX 3D bioprinter (CELLINK, Sweden) to optimize 3D bioprinting parameters (printing pressure and speed). The 3D-bioprinted constructs were photo-crosslinked using a custom-made 15 × 12 cm^2 LED panel (wavelength 405 nm and total power 20 W) at 1 cm curing offset for 1 min. The constructs were immediately transferred to Dulbecco's phosphate-buffered saline (DPBS) for imaging to calculate the printability (Pr) as described below.

The 3D-bioprinted constructs with 0–90° alignment were imaged using a stereomicroscope (Leica EZ4E), and the square grids' geometry (area A and perimeter L) was measured with ImageJ software. The printability (Pr) of the constructs was quantified using Equation I. A Pr value between 0.9 and 1.1 is considered to be an acceptable printability range.[22]

$$\mathrm{Pr} = \frac{L \times L}{16A} \quad \text{(I)}$$

Based on the printability evaluation, 7.5% and 10% (w/v) GelMA was used for THP-1 3D bioprinting. THP-1 (2×10^6) were pelleted from the suspension culture by centrifugation at 200 × g for 3 min, washed twice with DPBS, and redispersed in 7.5% and 10% (w/v) GelMA containing 0.15% (w/v) LAP. The prepared bioinks were loaded into a BIOX 3D bioprinter (CELLINK, Sweden) and bioprinted using the optimized printing conditions (Figure 1).

2.3. Assessment of 3D-bioprinted THP-1 viability through live/dead staining

The viability of THP-1 immediately (day 0) and 1 and 3 days post-printing was assessed using fluorescent live/dead staining ($n = 3$) as previously reported.[23] The 3D-bioprinted constructs were stained using 5 μg/mL fluorescein diacetate (FDA; Sigma-Aldrich, Australia) and 2 μg/mL propidium iodide (PI; Sigma-Aldrich, Australia) for 30 min, then imaged using Nikon Eclipse Ti confocal microscope for FDA-bound live (green) THP-1 (excitation [Exc] 488 nm/ emission [Ems] 500–550 nm), and PI-bound dead (red) THP-1 (Exc 561 nm / Ems 570–1000 nm). The number of green and red THP-1 cells was determined using ImageJ software, and the viability was calculated as the percentage of FDA-bound cells within the total cell population (both FDA and PI-strained cells).

$$\mathit{Cell\ viability}\,(\%) = \frac{\mathit{Total\ number\ of\ FDA\ bound\ live\ cells\,(green)}}{\mathit{Total\ number\ of\ cells\ with\ green\ and\ red\ signals}} \times 100$$

2.4. Optimization of macrophage (M0) differentiation in 3D-bioprinted THP-1

The 3D-bioprinted THP-1 constructs were treated with different doses of PMA, and evaluation of macrophage differentiation was carried out by quantifying the number of cells expressing the known M0 marker, CD11b.[24-26] The bioprinted and photo-crosslinked constructs ($10 \times 10 \times 0.8$ mm^3) were transferred to 12-well plates and equilibrated overnight in BM. A comparative 2D culture for macrophage differentiation was prepared by seeding 5×10^5 THP-1 cells into the wells of 12-well culture plates in 1 mL of BM. After equilibration, the 3D-bioprinted constructs and the 2D controls were incubated with 0, 10, 25, 50, 100, and 200 ng/mL PMA in BM for 2 days and then equilibrated again in BM (no PMA) for another day ($n = 3$). The PMA-treated cells in 2D were harvested for flow cytometry by treating with TrypLE™ Express Enzyme (Gibco®, Australia) for 10 min at 37°C. The macrophages were retrieved from the 3D-bioprinted constructs by completely digesting the GelMA constructs ($10 \times 10 \times 0.8$ mm^3) 200 μL of 1 mg/mL (285 U/mL) collagenase (Thermo Fisher Scientific, Australia) for 10 min at 37°C. The optimization of collagenase digestion parameters (concentration/treatment time) is described in Figure S1 (Supplementary File).

The harvested cells were washed with DPBS and stained with Fixable Viability Stain 510 (BD Biosciences, USA) for 20 min at room temperature (23°C). Cells were incubated with Human BD Fc Block™ (BD Biosciences, USA) for 10 min and stained with a panel of surface markers. CD90, CD11b, and CD80 were used as negative marker, macrophage (M0 and M1) marker, and M1 marker, respectively. Data were acquired using a BD LSRFortessa™ Cell Analyzer supported by BD FACS Diva software. Cell populations were identified on FlowJo (Tree Star, Ashland, OR).

2.5. Role of 3D microenvironment in macrophage polarization

The polarization of M0 in 3D-bioprinted constructs in the absence of stimulatory factors such as LPS was assessed by investigating gene expression. Bioprinted THP-1 within the 3D constructs ($n = 3$) were differentiated to M0 using PMA and equilibrated in BM. Cells were harvested at 6 h, and 1, 2, and 4 days after collagenase digestion and stored at -80°C for future assay. Total RNA from was isolated

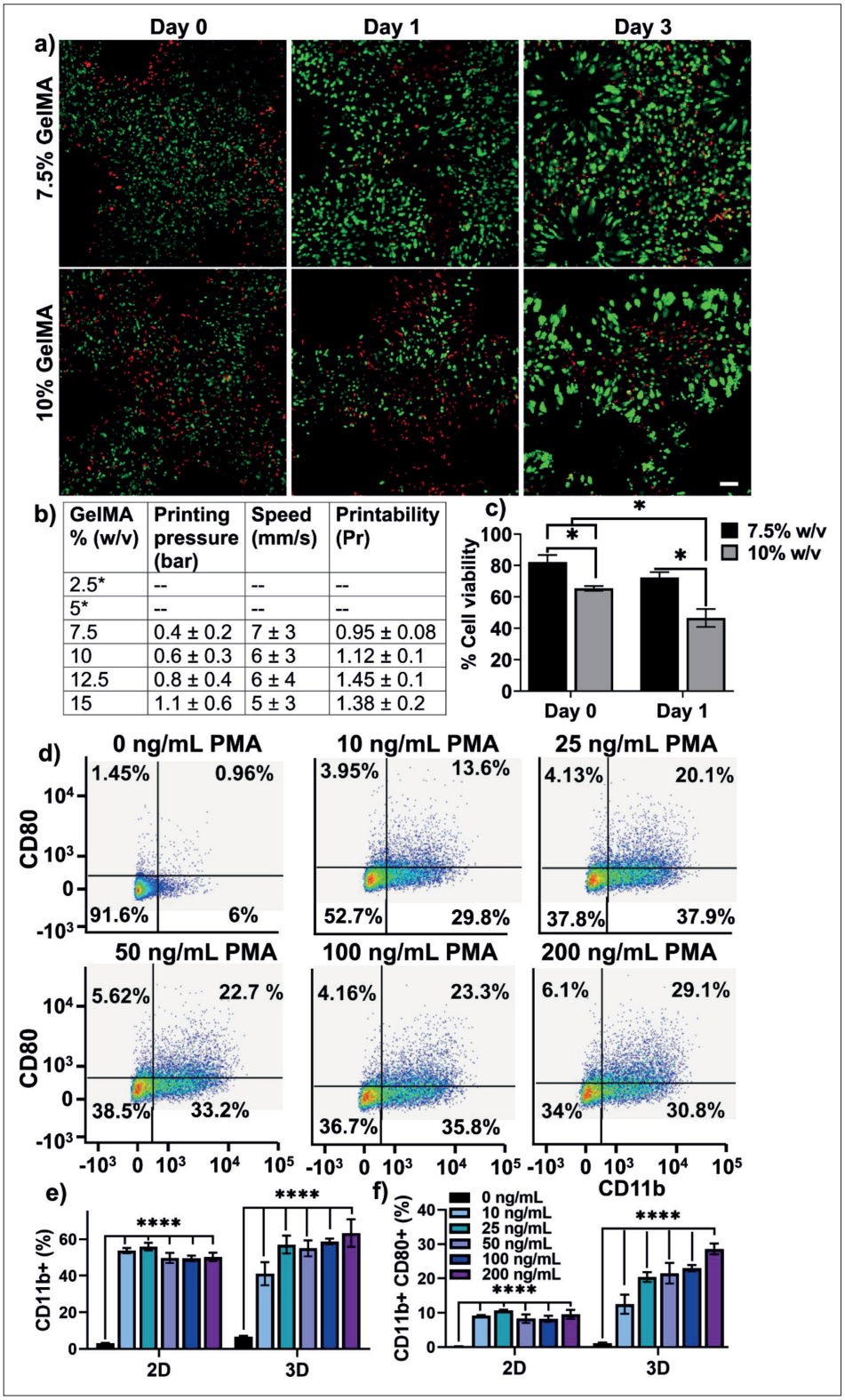

Figure 1. (**a**) Confocal microscopy images of live/dead staining of 3D-bioprinted THP-1 using 7.5% and 10% GelMA on days 0, 1, and 3; (**b**) optimized 3D-bioprinted parameters for different concentrations of GelMA; * bioink extruded as droplets and was not printable; (**c**) percentage of THP-1 viability calculated from the live/dead images; (**d**) flow cytometry dot plots for CD11b expression in 3D-bioprinted THP-1 cells treated with different concentrations of PMA; quantified (%) $CD11b^+$ (**e**) and $CD11b^+$ $CD80^+$ cells (**f**) in the presence of increasing concentrations of PMA.

from harvested cells using ISOLATE II RNA Mini Kit (Meridian Life Science, Australia) and quantified using Thermo Fisher Scientific NanoDrop ONE^c (Australia). Complementary DNA (cDNA) for the isolated RNA was prepared using SuperScript III First-Strand Synthesis kit (Invitrogen) in SimpliAmp™ Thermal Cycler (Applied Biosystems by Thermo Fisher Scientific, Australia). Real-time quantitative polymerase chain reaction (RT-qPCR) for M1 (IL-1β, IL-6, iNOS, and TNF-α) and M2a (CD206 and DC-SIGN) markers was performed with StepOnePlus™ Real-Time PCR System (Applied Biosystems) using SYBR® Green master mix (Invitrogen). The forward and reverse primers used for the RT-qPCR are listed in Table S1 (Supplementary File). The recorded cycle threshold (C_t) values were used to calculate the fold change using the Livak method (ΔΔCt method).[27] The fold change ($2^{-\Delta\Delta Ct}$) is the relative gene expression ($2^{-\Delta Ct}$) in the 3D-bioprinted constructs divided by the $2^{-\Delta Ct}$ of the 2D-cultured M0.

2.6. Optimization of LPS dose

Activation of M1 macrophages within the 3D-bioprinted constructs in the presence of increasing doses of *Ec*-LPS was investigated. Bioprinted THP-1 were differentiated to M0 using the optimized PMA dose of 25 ng/mL for 2 days. After 1 day of rest, the culture media (1 mL/construct) were replaced with BM in the presence of increasing doses of *Ec*-LPS (0, 50, 100, 200, 500, 1000, 5000, and 10,000 ng/mL; $n = 3$) and incubated for 3 days. The conditioned media were collected and replenished with fresh media and respective *Ec*-LPS doses at 1, 2, and 3 days. The release of M1-specific cytokine (IL-6) in the conditioned media was quantified using ELISA (Thermo Fisher Scientific, Australia) as per the manufacturer's instructions and normalized to the wet weight of each construct measured at day 3. Cells retrieved from collagenase-digested constructs were assessed for expression of the M1-specific surface marker CD80 by flow cytometry (section 2.4).

2.7. iNOS expression

The expression of iNOS in M1-polarized cells within 3D bioprinted constructs was visualized using immunofluorescence. At day 3, non-polarized M0 constructs and M1-polarized (using optimal *Ec*-LPS dose 1000 ng/mL) constructs were fixed in 4% (w/v) PFA for 20 min and permeabilized using 0.2% (v/v) Triton X-100 for 30 min. Afterward, the constructs were incubated in blocking buffer (1% (w/v) bovine serum albumin and 10% (v/v) normal goat serum in DPBS) for 2 h at room temperature, then 200 ng/μL of anti-iNOS primary antibody (Abcam, UK) in blocking buffer for 24 h at 4°C. Thereafter, the constructs were incubated with 5 ng/μL secondary antibody Alexa Fluor® 488-conjugated-anti mouse antibody (Abcam, UK), 5 μg/mL DAPI (4', 6-diamidino-2-phenylindole; Sigma-Aldrich, Australia), and 0.8 U/mL TRITC-Ph (tetramethylrhodamine-conjugated phalloidin; Sigma-Aldrich, Australia) in PBS for 1 h at room temperature. The final constructs were imaged using Nikon Eclipse Ti confocal microscope. Excitation/emission wavelengths used for the secondary antibody (for iNOS in green color), DAPI (for nucleus in blue color), and TRITC-Ph (for actin filaments in red color) were 488 nm/500–550 nm, 405 nm/417–477 nm, and 561 nm/570–1000 nm, respectively.

2.8. Action of Ibu in the 3D-bioprinted inflammation model

THP-1 were 3D-bioprinted, differentiated to M0 (PMA, 25 ng/mL for 2 days and resting for 1 day), and polarized to M1 (LPS, 1000 ng/mL for 2 days). The concentrations of 10 and 15 μg/mL Ibu (Sigma-Aldrich, Australia) were selected for the study based on Ibu pharmacokinetics.[28] The M1-polarized constructs were incubated with 10 μg/mL (Ibu1) and 15 μg/mL Ibu (Ibu2) in BM for 3 days, with M1-polarized constructs without Ibu and M0-differentiated constructs as negative and positive control, respectively.

Test, negative control, and positive control constructs ($n = 3$) were collected on days 1 and 3 for gene expression analysis (described in section 2.5). Relative gene expression was normalized to the relative gene expression of positive control (M0) to calculate fold change. Phenotypic characterization of M1 macrophages after 3 days of Ibu treatment was performed via flow cytometry ($n = 3$) for M0 markers (CD11b and CD33) and M1 marker (CD80). Conditioned media from each group were collected on days 1, 2, and 3 of culture, and ELISA was used to measure levels of secreted IL-6, IL-1β, TNF-α (Thermo Fisher Scientific, Australia), and prostaglandin E2 (PGE_2; Cayman Chemical, USA). The cumulative quantity of released protein was normalized with the wet weight of the constructs. The effect of Ibu on the polarized 3D-bioprinted M1 cells was also evaluated by measuring the secretion of TNF-α and IL-1β using ELISA.

2.9. Statistical analysis

All the data are presented as mean ± SD and were analyzed using GraphPad Prism Version 8. One-way and two-way analyses of variance (ANOVA) with a Tukey post-hoc analysis were used to test for differences between experimental and control groups. Statistical significance was set at $p \leq 0.05$.

3. Results and discussion

3D bioprinting is an innovative additive manufacturing technology that enables the construction of tissue- or organ-like structures through a layer-by-layer

assembly of cells, growth factors, and/or other bioactive components.[29] This groundbreaking technology has found application in cancer modeling and served as a robust and reproducible approach for investigating novel anticancer drugs.[9,30,31] However, the exploration of 3D-bioprinted macrophages for simulating inflammatory conditions and responses is still in its infancy.[32] Recent research has demonstrated the practicality of 3D-bioprinted structures consisting of polarized (M2) macrophages as a fresh approach for disease modeling[19] and various applications in tissue engineering.[20] However, there is a significant scarcity of data when it comes to modeling inflammation using pro-inflammatory (M1) macrophages. Recent advancements include the development of a bioprinted lung tissue model aimed at studying inflammation and assessing the effectiveness of viral inhibitors.[21] The researchers integrated THP-1 cells into a multicellular model and measured the release of pro-inflammatory cytokines, specifically IL-1β and IL-8, following LPS stimulation. Nevertheless, the study falls short of providing a comprehensive exploration of macrophage polarization and does not address the model's capability to respond to external stimuli, such as anti-inflammatory drugs. The current study developed a 3D-bioprinted macrophage model and assessed its inflammatory response to bacterial endotoxin (LPS). Additionally, the effectiveness of an anti-inflammatory drug (Ibu) in inhibiting the inflammatory response of the 3D-bioprinted macrophages was investigated.

3.1. Viability of 3D-bioprinted THP-1

The printing pressure and speed for different concentrations of GelMA are presented in Figure 1b. Macrophages are tissue resident cells, and most inflammatory conditions impact connective tissues and resident organs, and as such, it is relevant that macrophages are tested for their ability to model inflammatory responses in an environment that resembles the native extracellular matrix, as is the case with GelMA. Based on the optimal printability of the constructs (Pr = 0.9 to 1.1; Figure 1b), 7.5% and 10% (w/v) GelMA was used for cell printing. The viability of THP-1 cells was quantified using live/dead imaging, as shown in Figure 1a and c. Immediately after bioprinting with 7.5% (w/v) GelMA, THP-1 viability remained comparable with the viability of cells before mixing with the GelMA bioink (82 ± 5%). However, the higher concentration of bioink resulted in increased printing pressure and a significant decrease in THP-1 viability, as observed in the bioprinting of other cell types.[23,33] Cell viability at day 3 could not be quantified as the proliferating cells formed aggregates, and individual cells could not be identified.

3.2. Optimization of macrophage (M0) differentiation in 3D-bioprinted THP-1

PMA is commonly used to differentiate THP-1 cells into cells that mimic human monocyte-derived macrophages, with characteristics of decreased proliferation and increased cell attachment, phagocytosis, and expression of multiple macrophage markers and cytokines.[25,34-36] Since small differences in culture conditions, including PMA concentration, can affect the differentiation and polarization of THP-1 cells,[37-39] it is essential to determine the most appropriate conditions for differentiation when using these cells as a model.

The PMA dose response toward the M0 differentiation of THP-1 cells cultured in a 2D environment has been extensively investigated.[38-40] However, the PMA dose response of THP-1 cells in a 3D environment is not well explored, as most of the research has focused on using a fixed PMA concentration between 100 and 300 nM.[41-46] A previous research—the only study on the M1 polarization of 3D-bioprinted THP-1 cells—also used a fixed concentration of PMA (200 ng/mL= 324.2 nM).[21]

Here, M0 differentiation of THP-1 cells in 2D culture and 3D construct was quantified using different concentrations of PMA using flow cytometry (Figure 1d). The expression level of M0 marker, CD11b, and M1 marker and CD80 was determined from live single cells retrieved from 3D or 2D culture (Figure 1e and f). All PMA concentrations tested stimulated similar levels of CD11b expression in 2D culture. The 3D-bioprinted cells also responded to all PMA concentrations tested with similar CD11b expression to that observed in 2D culture (Figure 1e). Maeß et al. showed that PMA concentrations higher than 25 ng/mL resulted in higher expression of M1-related genes (*IL-1β*, *TNF-α*, and *IL-8*) in 2D-cultured THP-1 cells and might mask the effect of subsequent stimuli.[38,39] Therefore, the influence of PMA on M1 polarization of 3D-bioprinted THP-1 cells was tested by quantifying the expression of the M1 surface marker CD80 (Figure 1f). The exposure of THP-1 cells with the higher dose of PMA resulted in increased expression of CD80, and as such, 25 ng/mL PMA was used for M0 differentiation of 3D-bioprinted THP-1 cells.

3.3. Role of 3D microenvironment in macrophage polarization

Macrophages (M0) are equipped with a wide range of surface receptors that detect their environment and undergo polarization.[47] Studies have shown that different properties of biomaterials and hydrogels, such as surface chemistry,[48]

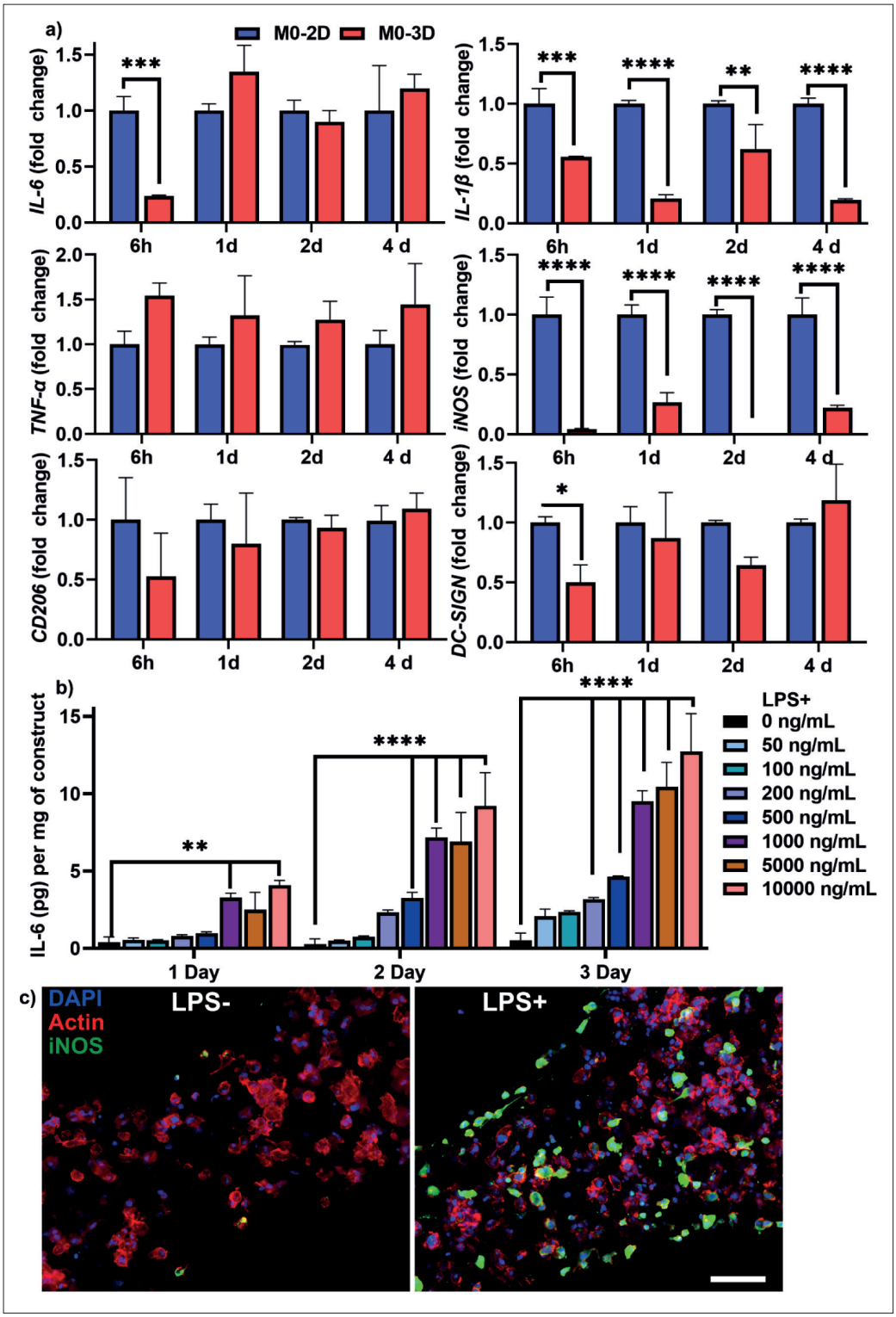

Figure 2. (**a**) Relative gene expression of *IL-1β*, *IL-6*, *iNOS*, *TNF-α*, *CD206*, and *DC-SIGN* in the M0 cells embedded in the 3D-bioprinted constructs presented as fold change, normalized with the respective gene expression in 2D culture; (**b**) the amount of IL-6 protein released by the M0 macrophages upon the exposure to different concentrations of LPS; (**c**) immunofluorescence imaging for iNOS in the 3D-bioprinted macrophages with and without LPS treatment.

stiffness,[44] mechanical force,[49] pore size,[50] availability of oxygen[51] (related to the diffusion coefficient of hydrogel), and cell-binding motifs,[52] can stimulate M1 or M2 polarization. Therefore, the influence of the 3D-bioprinted microenvironment toward the M1/M2 polarization of M0 macrophages was examined. Gene expression of M1 markers (*IL-1β*, *IL-6*, *iNOS,* and *TNF-α*) and M2 markers (CD206 and DC-SIGN) in M0 cells present in the 3D-bioprinted constructs at 6 h, and days 1, 2, and 4 post-printing was compared with the gene expression of M0 cells in 2D culture (Figure 2a). The expression of *IL-1*β and *iNOS* in 3D-bioprinted macrophages was downregulated compared to 2D culture, while *IL-6*, *TNF-α*, *CD206*, and *DC-SIGN* expression remained comparable to that in 2D cultures, indicating that neither the bioprinting process nor the 3D construct microenvironment stimulates macrophage polarization. As such, the findings show that M0 macrophage retains this phenotype, and the model is suitable for activation studies.

3.4. Optimization of LPS dose for M1 polarization

LPS has been shown to stimulate M1 polarization of THP-1 cells in 2D and 3D environments.[35,38,42] However, data on the influence of LPS on 3D-bioprinted macrophages are limited.[21] Here, polarization of M0 cells to the M1 phenotype within 3D-bioprinted constructs was assessed by measuring secreted levels of the pro-inflammatory marker IL-6 in the presence of increasing concentrations of LPS over 3 days in culture (Figure 2b). The increase in LPS dose resulted in an increased IL-6 release. LPS (1000 ng/mL) treatment resulted in a sharp increase in the release of IL-6 compared to the lower concentrations (0–500 ng/mL). Secreted IL-6 levels in constructs exposed to LPS concentrations over 1000 ng/mL were not significantly different statistically compared to constructs in the presence of 1000 ng/mL. The expression of iNOS by polarized cells was visualized using immunostaining, with constructs treated with 1000 ng/mL comprising more iNOS-expressing cells (green color in Figure 2c), confirming the successful polarization of cells toward the M1 phenotype at this LPS dose, within the 3D construct.

The expression of M1 surface marker CD80 was quantified using flow cytometry (Figure 3). An increase in LPS dose saw an associated increase in the percentage of $CD80^+$ cells (Figure 3a and b). The highest concentrations of 5 *μ*g/mL and 10 *μ*g/mL showed a similar CD80 expression as that of 1000 ng/mL; therefore, the lower dose was selected for M1 polarization in the subsequent 3D construct study.

The effect of the selected LPS dose (1000 ng/mL) on the expression of M1 phenotype-associated genes at selected time points is shown in Figure 3c–g. Expression of M1-specific genes, namely *IL-1*β, *IL-6*, *TNF*-α, *iNOS*, and *IL10*, was significantly increased compared to that of untreated M0 cells. Based on gene expression, cytokine and surface marker profile, and an optimized LPS dose of 1000 ng/mL, a 3D-bioprinted model for the activation and polarization of THP-1 cells toward the M1 phenotype was demonstrated, with potential application to the study of pro-inflammatory systems and anti-inflammatory interventions.

3.5. Anti-inflammatory properties of Ibu on 3D-bioprinted model

Ibu is a non-steroidal anti-inflammatory drug that decreases cyclooxygenase activity and inhibits prostaglandins, such as PGE_2, and other pro-inflammatory cytokines.[53-55] The efficacy of Ibu in reducing inflammation in the optimized 3D-bioprinted "inflammatory M1" model was evaluated using qPCR, cytokine, and surface marker analyses described above. The M1-polarized constructs were incubated with 10 μg/mL (Ibu1) and 15 μg/mL Ibu (Ibu2) (Figure 4). While no significant change in *IL-1β* and *TNF-α* gene expression was observed in the first 24 h, both concentrations of Ibu significantly reduced *iNOS*, *IL-6*, *IL-1β*, and *TNF-α* gene expression by day 3 of culture (Figure 4a–d). Notably, downregulated gene expression of iNOS at this time point was comparable to iNOS expression in M0 controls (Figure 4c). The anti-inflammatory action of Ibu on bioprinted M1 cells was further demonstrated by flow cytometry targeting the cell surface marker CD80, with the percentage of $CD80^+$ cells in the $CD11b^+CD33^+CD80^+$ (M1) population reduced approximately 2-fold in the presence of Ibu, compared to M1 controls (Figure 4e and f).

Conditioned media from 3D-bioprinted constructs cultured in the presence or absence of Ibu were assayed by ELISA to determine the concentration of PGE_2 and cytokines (IL-6, IL-1β, and TNF-α) released by 3D-bioprinted M0/M1 cells (Figure 5b–d). The presence of Ibu in the culture medium significantly reduced PGE_2 expression to levels lower than the M0 control at all three time points (Figure 5a). A similar effect of both Ibu concentrations was observed for TNF-α and IL-6 release, although levels of these cytokines remained above that of M0 controls (Figure 5b and d). Levels of IL-1β in conditioned media from M1 constructs exposed to Ibu after 2 and 3 days were significantly lower than M1 without Ibu, although IL-1β release remained markedly higher than M0 control constructs (Figure 5c).

The efficacy of Ibu against inflammation stimulated by the LPS produced by a different pathogenic bacterium was also evaluated. *P. gingivalis*, an anaerobic gram-

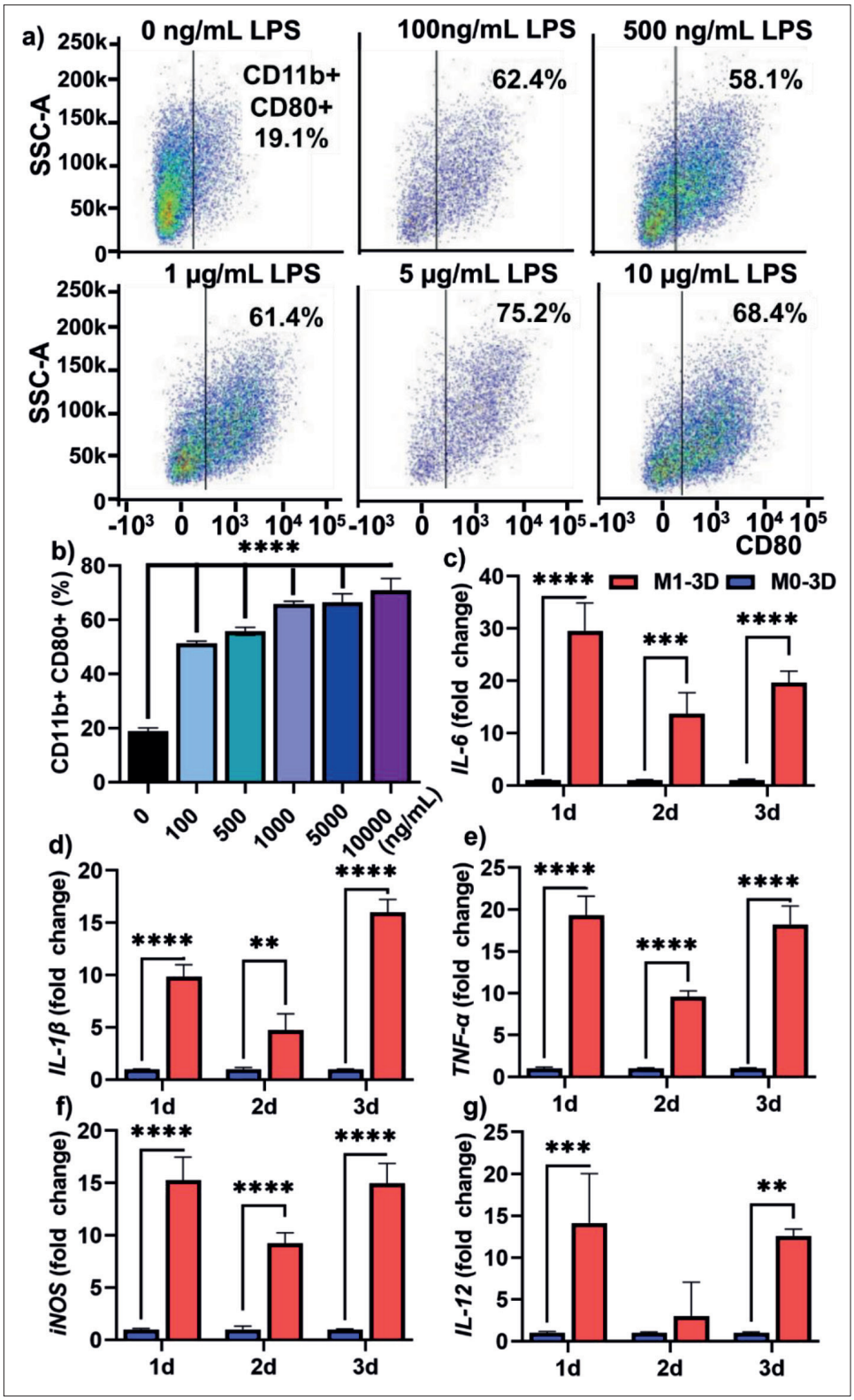

Figure 3. (**a**) The flow cytometry dot plot for CD80 expression in the 3D-bioprinted macrophages after different LPS dose treatments; (**b**) quantified CD80 expression from the flow cytometry results; (**c**–**g**) gene expression of different M1 markers after the LPS treatment (1 μg/mL): (**c**) *IL-6*, (**d**) *IL-1β*, (**e**) *TNF-α*, (**f**) *iNOS*, and (**g**) *IL-12*.

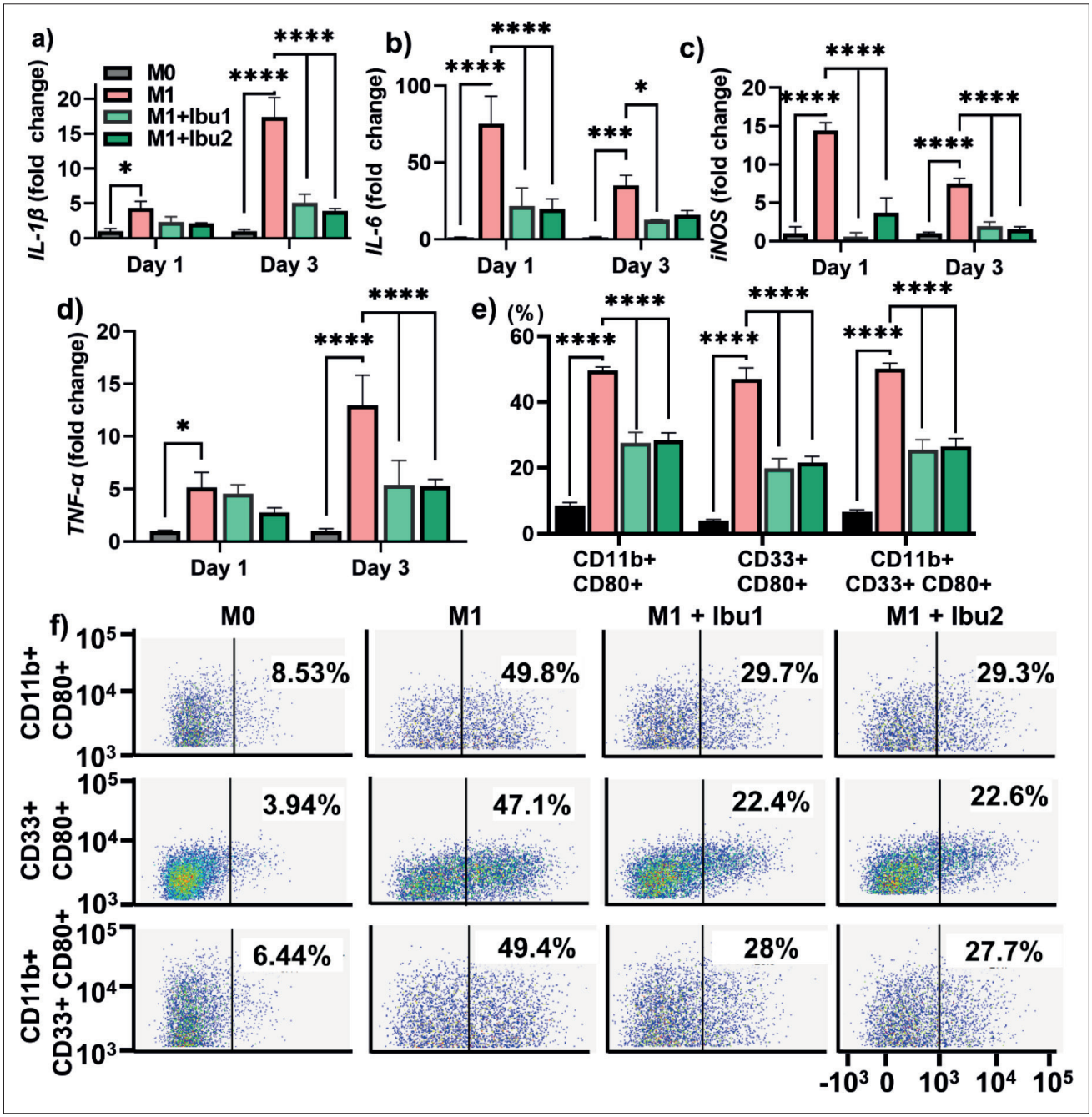

Figure 4. (**a**–**d**) Gene expression of different M1 markers: (**a**) *IL-1β*, (**b**) *IL-6*, (**c**) *iNOS*, and (**d**) *TNF-α* after the Ibu treatment; (**e**) quantified CD80 expression from the flow cytometry results; (**f**) flow cytometry dot plot for macrophage markers CD11b and CD33 and M1 marker CD80 expression in the M1-polarized (LPS) 3D-bioprinted macrophages after Ibu treatment. Notes: Ibu1, 10 μg/mL; Ibu2, 15 μg/mL.

negative bacterium, is recognized as a key causative agent in the widely prevalent chronic inflammatory disease periodontitis.[56] The LPS produced by *P. gingivalis* is commonly employed to evaluate chronic inflammatory disease.[57,58] Treatment of *P. gingivalis* LPS-stimulated M1 cells in the 3D bioprint model with Ibu resulted in a significant decrease in the release of TNF-α and IL-1β (Figure 5e and f). These data showed that the model was responsive to different inductive environments, and hence may be useful in modeling different inflammatory disease states.

The present study establishes an *in vitro* 3D-bioprinted construct comprising viable THP-1-

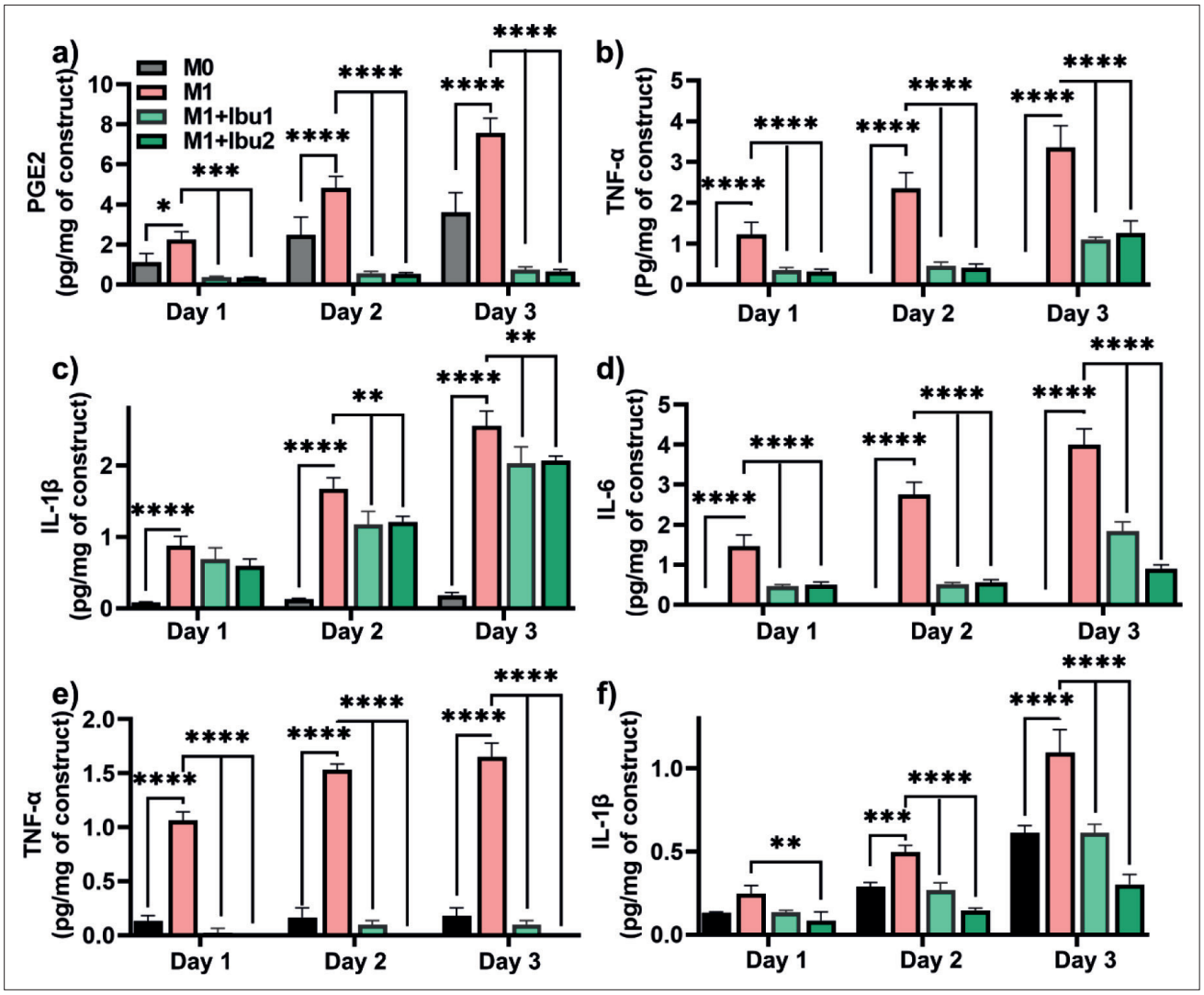

Figure 5. The amount of (**a**) PGE2, (**b**) TNF-α, (**c**) IL-1β, and (**d**) IL-6 released was quantified using ELISA after the Ibu treatment of LPS (*E. coli*)-polarized M1 cells in the 3D-bioprinted construct, and the amount of (**e**) TNF-α and (**f**) IL-1β released after the Ibu treatment of LPS (*P. gingivalis*)-polarized M1 cells in the 3D-bioprinted construct.

derived LPS-stimulated (inflammatory) macrophages that are responsive to the anti-inflammatory action of Ibu, validated by protein production, gene expression, and phenotypic marker endpoint assessments. Future investigations hold the potential to broaden the scope by integrating diverse cell types within a multicellular framework, thus creating an environment more representative of *in vivo* conditions. Exploring the intricate interplay between macrophages and other relevant cell types in the context of inflammatory responses and tissue remodeling is a promising avenue. The spatial configuration of cells within the model can unveil critical insights, paving the way for the development of targeted and efficacious treatments across a spectrum of acute and chronic inflammatory conditions.

The successful demonstration of Ibu efficacy within our model serves as a stepping stone for extending the applicability to evaluate the effectiveness of various therapeutic molecules and drugs. This knowledge is instrumental in refining treatment strategies, without the need to use costly and ethically challenging animal models. Further, there are important implications for developing precise interventions tailored to individual patient needs. The advent of patient-specific models offers a groundbreaking opportunity to tailor treatment approaches and assess unique patient responses to

therapeutic interventions, marking a significant stride toward personalized medicine.

The established model can be further expanded and modified, allowing for exploration of the multifaceted, dynamic processes of wound healing and regeneration, including tissue mimicry, macrophage behavior, and intricate cell–cell interactions. This opens avenues for a more comprehensive understanding of physiological processes and pathophysiological conditions, providing a robust foundation for advancements in regenerative medicine, drug development, and personalized healthcare. The versatility of the developed model positions it as a valuable tool for unraveling the complexities of biological systems and holds promise for diverse applications in biomedical research and clinical practice.

In terms of future directions, a comprehensive study of all cells contributing to the inflammatory milieu would be important to model the entire inflammatory process. To this end, the current model requires further optimization to accurately mimic the *in vivo* tissue inflammatory process by characterization of a 3D construct carrying the myriad of different cells found in native tissues.

4. Conclusion

This study aimed to optimize the 3D bioprinting method for THP-1 cells and evaluate macrophage differentiation and polarization within the bioprinted construct under culture conditions. Optimal concentration of PMA and LPS for M0 differentiation and M1 polarization within the 3D-bioprinted model were determined, and the anti-inflammatory action of Ibu against these cells within the construct was demonstrated. However, further model validation is required using different pro-inflammatory stimuli and anti-inflammatory drugs. The 3D constructs developed in this study are limited in their ability to replicate human tissues or organs due to the sole inclusion of only a single cell type (macrophages). As such, this research serves as an important step toward establishing clinically relevant inflamed tissue models, and there is a need for future studies to incorporate diverse cell types in multicellular constructs to achieve more comprehensive replication of target tissues.

Acknowledgments

The authors would like to thank Colgate-Palmolive, NY, USA for their financial support.

Funding

This research was funded by Colgate-Palmolive industrial grant.

Conflict of interest

The authors declare no conflicts of interest.

Author contributions

Conceptualization: Nimal Raveendran, Kanchan Vaswani, Pingping Han, Corey S. Moran, Sašo Ivanovski
Formal analysis: Nimal Raveendran, Pingping Han, Corey S. Moran, Sašo Ivanovski
Funding acquisition: Sašo Ivanovski
Investigation: Nimal Raveendran, Kanchan Vaswani, Saraswat Basu
Methodology: Nimal Raveendran, Kanchan Vaswani, Saraswat Basu, Sašo Ivanovski
Project administration: Nimal Raveendran, Corey S. Moran, Sašo Ivanovski
Supervision: Sašo Ivanovski
Validation: Nimal Raveendran, Pingping Han, Corey S. Moran
Visualization: Nimal Raveendran, Pingping Han
Writing – original draft: Nimal Raveendran, Kanchan Vaswani
Writing – review & editing: Corey S. Moran, Sašo Ivanovski

Ethics approval and consent to participate

Not applicable.

Consent for publication

Not applicable.

Availability of data

Data is available from the corresponding author upon reasonable request.

References

1. Merien F. A journey with Elie Metchnikoff: from innate cell mechanisms in infectious diseases to quantum biology. *Front Public Health*. 2016;4:125. doi: 10.3389/fpubh.2016.00125
2. Lokaj J, John C. Ilya Ilich Metchnikov and Paul Ehrlich: 1908 Nobel Prize winners for their research on immunity. *Epidemiol Mikrobiol Imunol*. 2008;57(4):119-124.
3. Wrzesinski K, Fey SJ. From 2D to 3D--a new dimension for modelling the effect of natural products on human tissue. *Curr Pharm Des*. 2015;21(38):5605-5616. doi: 10.2174/1381612821666151002114227
4. Kapalczynska M, Kolenda T, Przybyla W, et al. 2D and 3D cell cultures - a comparison of different types of cancer cell cultures. *Arch Med Sci*. 2018;14(4):910-919. doi: 10.5114/aoms.2016.63743
5. Jensen C, Teng Y. Is it time to start transitioning from 2D to 3D cell culture? *Front Mol Biosci*. 2020;7:33.

doi: 10.3389/fmolb.2020.00033

6. Malindisa S, Josephs JS, Ntwasa M. Two-dimensional (2D) and three-dimensional (3D) cell culturing in drug discovery. In: Radwa Ali M, ed. *Cell Culture*. IntechOpen; 2018.

7. Gunti S, Hoke ATK, Vu KP, London NR, Jr. Organoid and spheroid tumor models: techniques and applications. *Cancers (Basel)*. 2021;13(4). doi: 10.3390/cancers13040874

8. Dini S, Binder BJ, Fischer SC, et al. Identifying the necrotic zone boundary in tumour spheroids with pair-correlation functions. *J R Soc Interface*. 2016;13(123). doi: 10.1098/rsif.2016.0649

9. Germain N, Dhayer M, Dekiouk S, Marchetti P. Current advances in 3D bioprinting for cancer modeling and personalized medicine. *Int J Mol Sci*. 2022;23(7). doi: 10.3390/ijms23073432

10. Agarwal S, Saha S, Balla VK, Pal A, Barui A, Bodhak S. Current developments in 3D bioprinting for tissue and organ regeneration–a review. *Front Mech Eng*. 2020;6. doi: 10.3389/fmech.2020.589171

11. Bose S, Roy M, Bandyopadhyay A. Recent advances in bone tissue engineering scaffolds. *Trends Biotechnol*. 2012;30(10):546-554. doi: 10.1016/j.tibtech.2012.07.005

12. Satpathy A, Datta P, Wu Y, Ayan B, Bayram E, Ozbolat IT. Developments with 3D bioprinting for novel drug discovery. *Expert Opin Drug Discov*. 2018;13(12):1115-1129. doi: 10.1080/17460441.2018.1542427

13. Sun T, Jackson S, Haycock JW, MacNeil S. Culture of skin cells in 3D rather than 2D improves their ability to survive exposure to cytotoxic agents. *J Biotechnol*. 2006;122(3):372-381. doi: 10.1016/j.jbiotec.2005.12.021

14. Li Y, Kilian KA. Bridging the gap: from 2D cell culture to 3D microengineered extracellular matrices. *Adv Healthc Mater*. 2015;4(18):2780-2796. doi: 10.1002/adhm.201500427

15. Langer R, Vacanti J. Advances in tissue engineering. *J Pediatr Surg*. 2016;51(1):8-12. doi: 10.1016/j.jpedsurg.2015.10.022

16. Knight E, Przyborski S. Advances in 3D cell culture technologies enabling tissue-like structures to be created in vitro. *J Anat*. 2015;227(6):746-756. doi: 10.1111/joa.12257

17. Potyondy T, Uquillas JA, Tebon PJ, et al. Recent advances in 3D bioprinting of musculoskeletal tissues. *Biofabrication*. 2021;13(2). doi: 10.1088/1758-5090/abc8de

18. Barreiro Carpio M, Dabaghi M, Ungureanu J, Kolb MR, Hirota JA, Moran-Mirabal JM. 3D bioprinting strategies, challenges, and opportunities to model the lung tissue microenvironment and its function. *Front Bioeng Biotechnol*. 2021;9:773511. doi: 10.3389/fbioe.2021.773511

19. Zhong Z, Wang J, Tian J, et al. Rapid 3D bioprinting of a multicellular model recapitulating pterygium microenvironment. *Biomaterials*. 2022;282:121391. doi: 10.1016/j.biomaterials.2022.121391

20. Sun X, Ma Z, Zhao X, et al. Three-dimensional bioprinting of multicell-laden scaffolds containing bone morphogenic protein-4 for promoting M2 macrophage polarization and accelerating bone defect repair in diabetes mellitus. *Bioact Mater*. 2021;6(3):757-769. doi: 10.1016/j.bioactmat.2020.08.030

21. Berg J, Weber Z, Fechler-Bitteti M, et al. Bioprinted multi-cell type lung model for the study of viral inhibitors. *Viruses*. 2021;13(8). doi: 10.3390/v13081590

22. Ouyang L, Yao R, Zhao Y, Sun W. Effect of bioink properties on printability and cell viability for 3D bioplotting of embryonic stem cells. *Biofabrication*. 2016;8(3):035020. doi: 10.1088/1758-5090/8/3/035020

23. Thattaruparambil Raveendran N, Vaquette C, Meinert C, Samuel Ipe D, Ivanovski S. Optimization of 3D bioprinting of periodontal ligament cells. *Dent Mater*. 2019;35(12):1683-1694. doi: 10.1016/j.dental.2019.08.114

24. Haloul M, Oliveira ERA, Kader M, et al. mTORC1-mediated polarization of M1 macrophages and their accumulation in the liver correlate with immunopathology in fatal ehrlichiosis. *Sci Rep*. 2019;9(1):14050. doi: 10.1038/s41598-019-50320-y

25. Starr T, Bauler TJ, Malik-Kale P, Steele-Mortimer O. The phorbol 12-myristate-13-acetate differentiation protocol is critical to the interaction of THP-1 macrophages with Salmonella Typhimurium. *PLOS ONE*. 2018;13(3): e0193601. doi: 10.1371/journal.pone.0193601

26. Surdziel E, Clay I, Nigsch F, et al. Multidimensional pooled shRNA screens in human THP-1 cells identify candidate modulators of macrophage polarization. *PLOS ONE*. 2017;12(8):e0183679. doi: 10.1371/journal.pone.0183679

27. Schmittgen TD, Livak KJ. Analyzing real-time PCR data by the comparative CT method. *Nat Protoc*. 2008;3(6):1101-1108. doi: 10.1038/nprot.2008.73

28. Kale P. Pharmacokinetics and bioavailability of single dose ibuprofen and pseudoephedrine alone or in combination: a randomized three-period, cross-over trial in healthy Indian volunteers. *Front Pharmacol*. 2014;5:98. doi: 10.3389/fphar.2014.00098

29. Dey M, Ozbolat IT. 3D bioprinting of cells, tissues and organs. *Sci Rep*. 2020;10(1):14023.

doi: 10.1038/s41598-020-70086-y

30. Almela T, Tayebi L, Moharamzadeh K. 3D bioprinting for in vitro models of oral cancer: toward development and validation. *Bioprinting*. 2021;22:e00132. doi: 10.1016/j.bprint.2021.e00132

31. Neufeld L, Yeini E, Pozzi S, Satchi-Fainaro R. 3D bioprinted cancer models: from basic biology to drug development. *Nat Rev Cancer*. 2022;22(12):679-692. doi: 10.1038/s41568-022-00514-w

32. Aldrich A, Kuss MA, Duan B, Kielian T. 3D bioprinted scaffolds containing viable macrophages and antibiotics promote clearance of Staphylococcus aureus craniotomy-associated biofilm infection. *ACS Appl Mater Interfaces*. 2019;11(13):12298-12307. doi: 10.1021/acsami.9b00264

33. Raveendran N, Ivanovski S, Vaquette C. The effect of culture conditions on the bone regeneration potential of osteoblast-laden 3D bioprinted constructs. *Acta Biomater*. 2023;156:190-201. doi: 10.1016/j.actbio.2022.09.042

34. Auwerx J, Staels B, Van Vaeck F, Ceuppens JL. Changes in IgG Fc receptor expression induced by phorbol 12-myristate 13-acetate treatment of THP-1 monocytic leukemia cells. *Leuk Res*. 1992;16(3):317-327. doi: 10.1016/0145-2126(92)90070-n

35. Schwende H, Fitzke E, Ambs P, Dieter P. Differences in the state of differentiation of THP-1 cells induced by phorbol ester and 1,25-dihydroxyvitamin D3. *J Leukoc Biol*. 1996;59(4):555-561.

36. Qin Z. The use of THP-1 cells as a model for mimicking the function and regulation of monocytes and macrophages in the vasculature. *Atherosclerosis*. 2012;221(1):2-11. doi: 10.1016/j.atherosclerosis.2011.09.003

37. Aldo PB, Craveiro V, Guller S, Mor G. Effect of culture conditions on the phenotype of THP-1 monocyte cell line. *Am J Reprod Immunol*. 2013;70(1):80-86. doi: 10.1111/aji.12129

38. Park EK, Jung HS, Yang HI, Yoo MC, Kim C, Kim KS. Optimized THP-1 differentiation is required for the detection of responses to weak stimuli. *Inflamm Res*. 2007;56(1):45-50. doi: 10.1007/s00011-007-6115-5

39. Maeß MB, Wittig B, Cignarella A, Lorkowski S. Reduced PMA enhances the responsiveness of transfected THP-1 macrophages to polarizing stimuli. *J Immunol Methods*. 2014;402(1-2):76-81. doi: 10.1016/j.jim.2013.11.006

40. Wang L, Zhu L, Duan C, Li L, Chen G. Total saponin of Dioscorea collettii attenuates MSU crystal-induced inflammation via inhibiting the activation of the NALP3 inflammasome and caspase-1 in THP-1 macrophages. *Mol Med Rep*. 2020;21(6):2466-2474. doi: 10.3892/mmr.2020.11035

41. Sapudom J, Karaman S, Mohamed WKE, Garcia-Sabaté A, Quartey BC, Teo JCM. 3D in vitro M2 macrophage model to mimic modulation of tissue repair. *NPJ Regen Med*. 2021;6(1):83. doi: 10.1038/s41536-021-00193-5

42. Garcia-Sabaté A, Mohamed WKE, Sapudom J, Alatoom A, Al Safadi L, Teo JCM. Biomimetic 3D models for investigating the role of monocytes and macrophages in atherosclerosis. *Bioengineering*. 2020;7(3). doi: 10.3390/bioengineering7030113

43. Sapudom J, Mohamed WKE, Garcia-Sabaté A, et al. Collagen fibril density modulates macrophage activation and cellular functions during tissue repair. *Bioengineering (Basel)*. 2020;7(2). doi: 10.3390/bioengineering7020033

44. Bystroňová J, Ščigalková I, Wolfová L, Pravda M, Vrana NE, Velebný V. Creating a 3D microenvironment for monocyte cultivation: ECM-mimicking hydrogels based on gelatine and hyaluronic acid derivatives. *RSC Adv*. 2018;8(14):7606-7614. doi: 10.1039/c7ra13739g

45. Barthes J, Dollinger C, Muller CB, et al. Immune assisted tissue engineering via incorporation of macrophages in cell-laden hydrogels under cytokine stimulation. *Front Bioeng Biotechnol*. 2018;6. doi: 10.3389/fbioe.2018.00108

46. Wodzanowski KA, Caplan JL, Kloxin AM, Grimes CL. Multiscale invasion assay for probing macrophage response to gram-negative bacteria. *Front Chem*. 2022;10. doi: 10.3389/fchem.2022.842602

47. Mantovani A, Sica A, Sozzani S, Allavena P, Vecchi A, Locati M. The chemokine system in diverse forms of macrophage activation and polarization. *Trends Immunol*. 2004;25(12):677-686. doi: 10.1016/j.it.2004.09.015

48. Rostam HM, Singh S, Vrana NE, Alexander MR, Ghaemmaghami AM. Impact of surface chemistry and topography on the function of antigen presenting cells. *Biomater Sci*. 2015;3(3):424-441. doi: 10.1039/c4bm00375f

49. Wong VW, Rustad KC, Akaishi S, et al. Focal adhesion kinase links mechanical force to skin fibrosis via inflammatory signaling. *Nat Med*. 2011;18(1):148-152. doi: 10.1038/nm.2574

50. Madden LR, Mortisen DJ, Sussman EM, et al. Proangiogenic scaffolds as functional templates for cardiac tissue engineering. *Proc Natl Acad Sci USA*. 2010;107(34):15211-15216. doi: 10.1073/pnas.1006442107

51. Zhou J, Bai W, Liu Q, Cui J, Zhang W. Intermittent hypoxia enhances THP-1 monocyte adhesion and chemotaxis and promotes M1 macrophage polarization via RAGE. *Biomed Res Int*. 2018;2018:1650456.

doi: 10.1155/2018/1650456

52. Sicari BM, Dziki JL, Siu BF, Medberry CJ, Dearth CL, Badylak SF. The promotion of a constructive macrophage phenotype by solubilized extracellular matrix. *Biomaterials*. 2014;35(30):8605-8612.
doi: 10.1016/j.biomaterials.2014.06.060

53. Shackelford RE, Alford PB, Xue Y, Thai S-F, Adams DO, Pizzo S. Aspirin inhibits tumor necrosis factorα gene expression in murine tissue macrophages. *Mol Pharmacol*. 1997;52(3):421-429.
doi: 10.1124/mol.52.3.421

54. Lee YJ, Chuang YC. Ibuprofen augments pro-inflammatory cytokine release in a mouse model of Vibrio vulnificus infection. *Microbiol Immunol*. 2010;54(9):542-550.
doi: 10.1111/j.1348-0421.2010.00249.x

55. Uematsu S, Matsumoto M, Takeda K, Akira S. Lipopolysaccharide-dependent prostaglandin E(2) production is regulated by the glutathione-dependent prostaglandin E(2) synthase gene induced by the Toll-like receptor 4/MyD88/NF-IL6 pathway. *J Immunol*. 2002;168(11):5811-5816.
doi: 10.4049/jimmunol.168.11.5811

56. Rafiei M, Kiani F, Sayehmiri F, Sayehmiri K, Sheikhi A, Zamanian Azodi M. Study of Porphyromonas gingivalis in periodontal diseases: a systematic review and meta-analysis. *Med J Islam Repub Iran*. 2017;31:62.
doi: 10.18869/mjiri.31.62

57. Ko Y-J, Kwon K-Y, Kum K-Y, et al. The anti-inflammatory effect of human telomerase-derived peptide on P. gingivalis lipopolysaccharide-induced inflammatory cytokine production and its mechanism in human dental pulp cells. *Mediators Inflammation*. 2015;2015:385127.
doi: 10.1155/2015/385127

58. Darveau RP, Pham TT, Lemley K, et al. Porphyromonas gingivalis lipopolysaccharide contains multiple lipid A species that functionally interact with both toll-like receptors 2 and 4. *Infect Immun*. 2004;72(9):5041-5051.
doi: 10.1128/iai.72.9.5041-5051.2004

ACCSCIENCE PUBLISHING

International Journal of Bioprinting

RESEARCH ARTICLE

Melt-electrowriting of 3D anatomically relevant scaffolds to recreate a pancreatic acinar unit *in vitro*

Viola Sgarminato[1,2,3], Michela Licciardello[1,2,3], Gianluca Ciardelli[1,2,3,4†], and Chiara Tonda-Turo[1,2,3*†]

[1]Department of Mechanical and Aerospace Engineering, Politecnico di Torino, Turin, Italy

[2]POLITO BIOMedLAB, Politecnico di Torino, Turin, Italy

[3]Interuniversity Center for the Promotion of the 3Rs Principles in Teaching and Research, Pisa, Italy

[4]CNR-IPCF, National Research Council-Institute for Chemical and Physical Processes, Pisa, Italy

(This article belongs to the *Special Issue: 3D Bioprinting for Tumor Modeling*)

Abstract

Melt-electrowriting (MEW) belongs to the group of advanced additive manufacturing techniques and consists of computer-aided design (CAD)-assisted polymer extrusion combined with a high-voltage supply to achieve deposition of polymeric fibers with diameters in the micrometric range (1 to 20 μm) similar to the size of natural extracellular matrix fibers. In this work, we exploit MEW to design and fabricate a three-dimensional (3D) model that resembles the morphology of the exocrine pancreatic functional unit without the need of supports, mandrels, or sacrificial materials. Optimized process parameters resulted in a MEW scaffold having regular fibers (19 ± 5 μm size) and an acinar cavity showing high shape fidelity. Then, human foreskin fibroblasts (HFF1) and human pancreatic ductal epithelial cells (HPDE), wild-type HPDE, and HPDE overexpressing *KRAS* oncogene were allowed to colonize the entire 3D structure and the acinar cavity. Thus, a physiologically relevant 3D model was created *in vitro* after 24 days using a co-culture protocol (14 days of HFF1 alone plus 10 days of HPDE and HFF1 co-culture). The effect of cell crosstalk within the MEW scaffolds was also assessed by monitoring HFF1 secretion of interleukin (IL)-6, a pro-inflammatory cytokine responsible for the inflammatory cascade occurring in pancreatic cancer. High levels of IL-6 were detected only when fibroblasts were co-cultured with the HPDE overexpressing *KRAS*. These findings confirmed that the MEW 3D *in vitro* model is able to recreate the characteristic hallmark of the pathological condition where cancer oncogenes mediate fibroblast activities.

Keywords: Melt-electrowriting; Exocrine pancreas; *In vitro* models; 3D scaffolds; Pancreatic ductal adenocarcinoma

†These authors contributed equally to this work.

***Corresponding author:**
Chiara Tonda-Turo
(chiara.tondaturo@polito.it)

Citation: Sgarminato V, Licciardello M, Ciardelli G, Tonda-Turo C. Melt-electrowriting of 3D anatomically relevant scaffolds to recreate a pancreatic acinar unit *in vitro*. *Int J Bioprint*. 2024;10(2):1975.
doi: 10.36922/ijb.1975

Received: October 6, 2023
Accepted: November 17, 2023
Published Online: February 23, 2024

1. Introduction

Pancreatic adenomeres secreting the digestive enzymes are the functional units of exocrine pancreas and are the sites where the first lesions of pancreatic ductal adenocarcinoma (PDAC) develop. In pancreas, an adenomere is constituted by acinar and ductal

epithelial cells surrounded by a thin basal lamina, stromal tissue, and pancreatic stellate cells (PSCs).[1,2] The PSCs are stromal cells responsible for the intense desmoplastic reaction occurring during the PDAC development.[3,4] Indeed, in healthy tissue, PSCs are characterized by high expression of both ectodermal and mesenchymal markers and significant amount of retinoids such as vitamin A in lipid droplets.[5]

Under the influence of inflammatory cues and cancer cells-derived factors, PSCs become active and assume a myofibroblast-like phenotype capable of deregulating extracellular matrix (ECM) homeostasis.[6] Typically, activated PSCs surround the cancer cells and communicate with them via different cytokines and factors (i.e., interleukin [IL]-6, IL-1β, and transforming growth factor beta [TGF-β]), through complex autocrine and paracrine signaling pathways.[7-9] Therefore, the interplay between cancer and stromal cells plays a key role in tumor evolution, promoting the pancreatic cancer progression by significantly affecting gene expression patterns, metabolic activities, invasion/metastasis phenomena, and resistance mechanisms.[10] However, the mechanisms implicated in the early stages of PDAC evolution, as well as the complex and dynamic phenomena involved in the crosstalk between cancer epithelial and stromal cells, still remain unclear.[11] This lack of knowledge limits the possibilities of early PDAC diagnosis, thereby resulting in a poor clinical prognosis. Indeed, the number of patients undergoing surgical resection is below 10%, as most of clinical cases have spread metastases at diagnosis.[12,13] Furthermore, the extremely complex bioarchitecture of the pancreatic tumor microenvironment (TME) affects the efficacy of drugs and causes the failure of current therapeutic strategies that are inadequate to treat this extremely aggressive cancer.[12,14] To improve the knowledge of the disease with the ultimate goal of performing early diagnoses and designing effective therapies for enhancing patients' prognosis, functional and reliable *in vitro* models need to be designed and fabricated.[15-20]

For many years, cancer research has been conducted using two-dimensional cell cultures and animal models, which poorly recapitulate the biological complexity of the disease in humans. Recent efforts in creating more representative preclinical *in vitro* models have led to the development of experimental replica of human tissues in a 3D environment or inside a microfluidic chip (organ-on-chip). PDAC-on-chip permits the recapitulation of the physiological crosstalk between different cell phenotypes and the high-throughput analysis,[21] but it is unable to mimic the 3D complex gland morphology of the functional unit of exocrine pancreas. Nevertheless, it remains a challenge to reproduce the microanatomy of the exocrine pancreas (intended as 3D architecture and cellular composition) in 3D biomimetic platforms, which fail to fully recapitulate the native compartmentalized architecture of tumor microenvironment, which is known to affect cell activity and cancer-cell response to drugs.[5,22,23] Specifically, the glandular morphology has been mimicked by using different techniques,[24-27] which however have limitations such as low reproducibility, throughput, and shape fidelity.

The present work focuses on the development of a 3D *in vitro* model that resembles the functional unit of exocrine pancreas through melt-electrowriting (MEW). MEW technology combines principles of conventional electrospinning (solution electrospinning) with melt extrusion-based methods,[28,29] and it can be defined as a contactless 3D printing technique due to the longer distance between needle and print bed. Indeed, like solution electrospinning, a high voltage (HV) is applied between the nozzle and the collector to exert an electrostatic attraction on the molten material, and a so-called Taylor cone forms at the nozzle tip. The electrical field forces the formation of a microscale polymer filament from the Taylor cone, which is deposited into a micrometer fiber on the collector.[28,29] Due to the distance between nozzle and platform and the fiber stretching induced by the electric field, the size of the extruded filament in MEW is about ten times lower than the filament diameter obtained by fused deposition modeling (FDM) where the distance between nozzle and collector is minimal (i.e., a few hundreds of microns),[30] thus resulting in a better resolution of the printed structures.[31] Compared to other extrusion-based techniques, such as 3D bioprinting, MEW allows to achieve better resolutions, in terms of minimum feature width, and higher geometrical accuracy due to the use of thermoplastic polymers instead of cell-laden hydrogels.[32,33]

For these reasons, MEW was adopted in this work to obtain microscale polycaprolactone (PCL) scaffolds mimicking the half structure of the pancreatic acinus (Figure 1a and b) having a resolution and size not achievable with the 3D printing technologies available so far. The use of this synthetic thermoplastic polymer (PCL) has been widely adopted in the fabrication of scaffolds as it is highly processable by electrospinning[34-36] and additive manufacturing,[37-40] and it is recognized to support cell attachment, migration, growth, and long-term cultures. Then, MEW scaffolds were seeded with stromal cells (human fibroblasts) (Figure 1c$_i$) and HPDE (both healthy HPDE and HPDE overexpressing *KRAS* oncogene) to develop the 3D models (Figure 1c$_{ii}$) having a biomimetic geometry and cell distribution.

2. Materials and methods

2.1. Cell culture

Human pancreatic ductal epithelial cells (HPDE)—both wild-type HPDE (HPDE-WT) and HPDE stably expressing

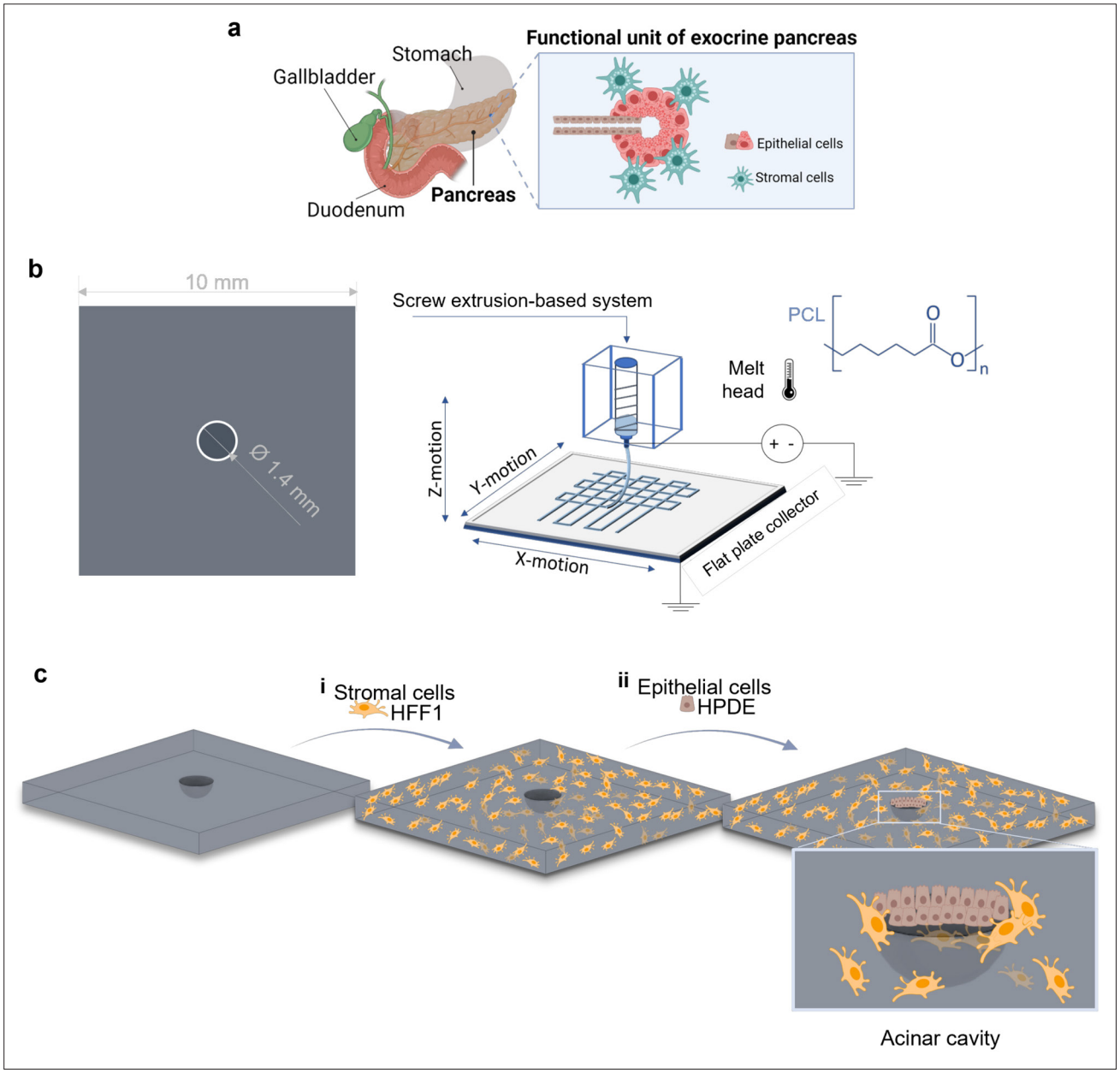

Figure 1. 3D layer-by-layer *in vitro* model. (a) Illustration of the functional unit of exocrine pancreas, composed by epithelial cells surrounded by stromal cells. (b) Melt-electrowriting (MEW) was employed: CAD drawings, processing of polycaprolactone (PCL), and production of a microscopic *in vitro* model. (c) The MEW scaffolds were then cellularized by seeding human fibroblasts (i) and epithelial cells (ii). Figure drawn using Biorender.com.

activated *KRAS* (HPDE-KRAS)—were kindly provided by Prof. F. Bussolino (Candiolo Cancer Institute-IRCCS-FPO, Candiolo, Italy). The cells were cultured in RPMI-1640 medium (Gibco, Jenks, USA) supplemented with 1% penicillin–streptomycin (Gibco), 1% L-glutamine (Gibco), and 10% fetal bovine serum (FBS; Gibco). Human foreskin fibroblasts (HFF1) cells were obtained from ATCC® and cultured in Dulbecco's Modified Eagle's Medium (DMEM) supplemented with 1% penicillin–streptomycin (Gibco), 2% L-glutamine (Gibco), and 15% FBS (Gibco). Cell lines were maintained in a humidified CO_2 incubator at 37°C and 5% CO_2.

2.2. Scaffold design and fabrication by MEW

The 3D MEW models were designed through SolidWorks® CAD software. The CAD models consist of a square-based 3D structure with a central cavity (Figure 1c). The cuboid had a final dimension of 10 mm (length) × 10 mm

(width) × 2.5 mm (thickness), while the central cavity was designed with a diameter of 1.4 mm. CAD models were discretized into triangles, and .stl files were thus generated. Then, the g-codes were obtained using the Ultimaker Cura 4.8.0 software by setting the parameters needed to perform the slicing and later optimized using the Repetier-Host and NC Viewer v1.1.3 software. Specifically, the automated g-codes, generated by the .stl files slicing, were further edited to (i) prevent the needle from passing over the scaffold between one layer and the next, so as to avoid depositing undesired fibers; and (ii) implement an additional extrusion step at the initial phase of the printing process, in order to stabilize the jet. Then, NovaSpider v5 instrument (CIC nanoGUNE) was employed to fabricate PCL (Mw ~ 43,000 Da; 19561-500, Polysciences Inc., Warrington, USA) scaffolds by MEW. To achieve a printed structure with proper filament diameter, pore size, and shape fidelity, several process parameters were tested, by varying their values in the ranges shown in Table 1. Ambient parameters (i.e., chamber temperature and humidity) were set at 27.5°C ± 3°C and 44% ± 2%, respectively. In detail, the humidity was monitored and controlled by an external humidifier (miniClima Humidity Control, miniClima Schönbauer GmbH, Wien, Austria) connected to the NovaSpider apparatus.

2.3. Dimensional analyses

The effect of parameters on printed scaffold resolution was evaluated by scanning electron microscopy (SEM; Tescan Vega, Brno-Kohoutovice, Czech Republic) of MEW scaffolds. Before analysis, all the samples were coated with a thin platinum layer. SEM images were then analyzed using ImageJ[41] to quantify the average size of fibers. In detail, two scaffolds per condition were examined, and 40 values for each scaffold were measured.

2.4. Seeding of stromal cells in MEW constructs

At first, the MEW constructs were incubated in a solution containing 70% ethanol and 30% water overnight and then irradiated with ultraviolet light for 1 h (30 min on each side) for sterilization purposes before cell seeding.

Table 1. Process parameters used to fabricate the MEW scaffolds

Scaffold type	i	ii	iii	iv
Nozzle size (mm)	0.5	0.5	0.5	0.3
Flow (%)	20	40	40	20
Infill line distance (μm)	80	110	110	80
Infill rotate angle (°)	45	45	90	90
Speed (mm/s)	70	60	60	40
Distance (mm)	7	6	6	12
Printing temperature (°C)	130	100	100	90
Voltage (kV)	5	7	5	5

Human fibroblasts were seeded in sterile MEW scaffolds placed in a 48-well plate. In particular, HFF1 were seeded on MEW constructs by pipetting 40 μL of a 1.6 × 10^6 cells/mL cell suspension on the top of the scaffolds. The constructs were maintained at 37°C and 5% CO_2 for 1 h before 600 μL of medium was added to each well.

2.5. Viability assay

The viability of human fibroblasts (HFF1) cultured in MEW constructs was evaluated through the fluorimetric resazurin reduction method (CellTiter-Blue, G8080, Promega, Milano, Italy) 3, 7, 14, 21, and 28 days after seeding. The assay was carried out according to the manufacturers' protocols. Briefly, culture medium was removed, and constructs were washed with 1× phosphate-buffered saline (PBS; Gibco). A solution of 16% CellTiter-Blue in complete cell culture medium was prepared and added to the constructs. After an incubation period of 3–4 h at 37°C, 100 μL of the medium was pipetted into different wells of a 96-well plate, and fluorescence was measured using a plate reader (Synergy HTX Multi-Mode Reader, BioTek) at 530 nm excitation wavelength and 590 nm emission wavelength. All the obtained data were then exported and elaborated using GraphPad Prism 9.3.1.

2.6. Stromal cells distribution within MEW scaffolds: confocal microscopy and scanning electron microscopy analyses

Fluorescence imaging was performed to monitor the distribution of stromal cells (HFF1) seeded within the 3D scaffolds. The constructs were washed once with 1× PBS and fixed with 4% paraformaldehyde (PFA; Sigma Aldrich) for 30 min at room temperature, after 72 h of culture. They were then washed twice with 1× PBS, permeabilized in 0.5% Triton X-100 (Sigma Aldrich) in 1× PBS for 10 min, and incubated with 1% bovine serum albumin (BSA; Invitrogen, Carlsbad, CA, USA) for 30 min to enhance the quality of the staining. The cytoskeletons of fibroblasts in MEW scaffolds were stained with Alexa Fluor™ 488 Phalloidin (A12379, Invitrogen) at 1:60 concentration in a solution of 1× PBS with 1% BSA. Nuclei were stained with DAPI reagent (4',6-diamidino-2-phenylindole, Dihydrochloride; D1306, Invitrogen) at 1:1000 concentration in 1× PBS solution. All samples were then imaged by confocal microscopy (Eclipse Ti2, Nikon, Konan Minato-ku, Japan). The resulting images were post-processed with ImageJ software.

Furthermore, SEM analyses were performed upon dehydration of fixed fibroblasts within the scaffolds to observe both HFF1 cells and the MEW filaments. Samples were dehydrated by soaking them into ethanol/

water solutions starting from 30/70 up to 100/0. Before analysis, all the samples were coated with a thin platinum layer.

2.7. Epithelization of the cavity

HPDE-KRAS and HPDE-WT cells were detached from the culture flask, counted, and resuspended to a 10 µL volume to obtain a 2.1 × 10^6 cells/mL concentration. Then, cells were seeded into the cavity of cellularized MEW scaffold, where HFF1 were allowed to grow for 2 weeks. The co-cultured constructs were placed in a 48-well plate.

The HPDE cells/HFF1 cell ratio was set at 1:3, according to studies demonstrating the relevancy that ratios of 1:1 to 1:3 have *in vivo*.[42-44] Cells were co-cultured in DMEM/F-12 supplemented with 15% FBS (Gibco), 1% penicillin–streptomycin (Gibco), and 2% L-glutamine (Gibco) since previous experiments had proven the efficacy of this culture medium composition in promoting cell viability.[21] The constructs were then fully covered with 600 µL of medium after 60 min. The cellularized structures were maintained in a humidified CO_2 incubator at 37°C and 5% CO_2.

2.8. Immunocytochemistry and confocal microscopy

The co-cultured MEW constructs were fixed with 4% paraformaldehyde (PFA; Sigma Aldrich) for 30 min at room temperature, after 3, 7, 10, and 14 days of co-culture. They were then rinsed with PBS twice and kept at 4°C. Each sample was then permeabilized with 0.2% Triton X-100 in PBS for 10 min at room temperature and successively washed 3 times for 5 minutes with PBS + 0.1% Tween 20 (PBST) at room temperature. Then, samples were blocked with 2% BSA in PBST for 60 min and rinsed three times with PBST. The samples were incubated with primary antibodies—alpha-smooth muscle actin recombinant rabbit monoclonal antibody (1:200; 701457 100 µg, Invitrogen) and E-cadherin monoclonal antibody (HECD-1; 1:2000; 13-1700, Invitrogen)—in PBST + 1% BSA for 24 h at 4°C. Samples were then rinsed 3 times with PBST at room temperature for 5 min. Then, the samples were incubated with secondary antibodies—Cyanine5-conjugated goat anti-mouse secondary antibody (1:200; A10524, Invitrogen) and Alexa Fluor™ 555-conjugated goat anti-rabbit secondary antibody (1:500; A27017, Invitrogen)—in PBST + 1% BSA for 2 h at room temperature. Samples were rinsed with PBST for 5 min at room temperature thrice. The cytoskeletons of HFF1 and HPDE cells seeded in MEW scaffolds were then stained with Alexa Fluor™ 488 Phalloidin (A12379, Invitrogen) at 1:60 concentration in a solution of 1× PBS with 1% BSA. Samples were rinsed with PBS for 5 min at room temperature thrice, before the staining with DAPI (D1306, Invitrogen) in PBS (1:1000) for 5 min at room temperature. They were then washed once with PBS, and finally mounted on glass coverslips using Fluoromount™ Aqueous Mounting Medium (00-4958-02, Invitrogen) for imaging. All samples were then imaged by confocal microscopy (Eclipse Ti2, Nikon). The resulting images were post-processed and analyzed with ImageJ software. In particular, the fluorescence intensity (mean gray values along the *z*-axis) corresponding to the E-cadherin signal was analyzed in z-stack acquisitions and plotted to compare the epithelial cell distributions within the cavity of the MEW scaffold at different time points of culture period. The fluorescence intensity values were normalized to the minimum value measured by the software for each sample.

2.9. Interleukin-6 cytokines release

The concentration of cytokines was determined in cell supernatants collected, after 2, 3, 10, and 14 days from HPDE cells seeding, from the wells containing the MEW scaffolds co-cultured with HFF1, HFF1 + HPDE-KRAS, and HFF1 + HPDE-WT cells. IL-6 cytokines were quantified with the IL-6 Human ELISA Kit (BMS213-2, Invitrogen). The concentrations were calculated using the standard curve generated by plotting the absorbance values of each standard sample on the ordinate and the human IL-6 standard concentrations on the abscissa.

2.10. Statistical analysis

All bar graph data are presented as the mean ± standard deviation (SD) from at least three independent experiments per condition or time point. Significance was measured as indicated for each experiment, with two-way or one-way analysis of variance (ANOVA) followed by pairwise comparison with Tukey's multiple comparisons test using GraphPad Prism 9.3.1; $^{*}p < 0.05$, $^{**}p < 0.01$, $^{***}p < 0.001$, $^{****}p < 0.0001$.

3. Results

3.1. Fabrication of acinar structures

The effect of the process parameters on the resulted MEW scaffolds was evaluated qualitatively by observing the print shape fidelity with respect to the CAD design at the macroscopic and microscopic levels, and quantitatively by measuring the diameter of fibers. The SEM images in Figure 2a show representative images of MEW scaffolds produced by varying the process parameters in the ranges reported in Table 1. Specifically, the structures were obtained with: 0.5 mm (i–iii) and 0.3 mm (iv) nozzle size; 20% (i, iv) and 40% (ii, iii) flow; 80 µm (i, iv) and 110 µm (ii, iii) infill line distance; 45° (i, ii) and 90° (iii, iv) infill rotate angle; 70 mm/s (i), 60 mm/s (ii, iii), and 40 mm/s (iv) speed; 7 mm (i), 6 mm (ii, iii), and 12 mm (iv) distance; 130°C (i), 100°C (ii, iii), and 90°C (iv) printing temperature; and 5 kV (i, iii, iv) and 7 kV (ii) voltage.

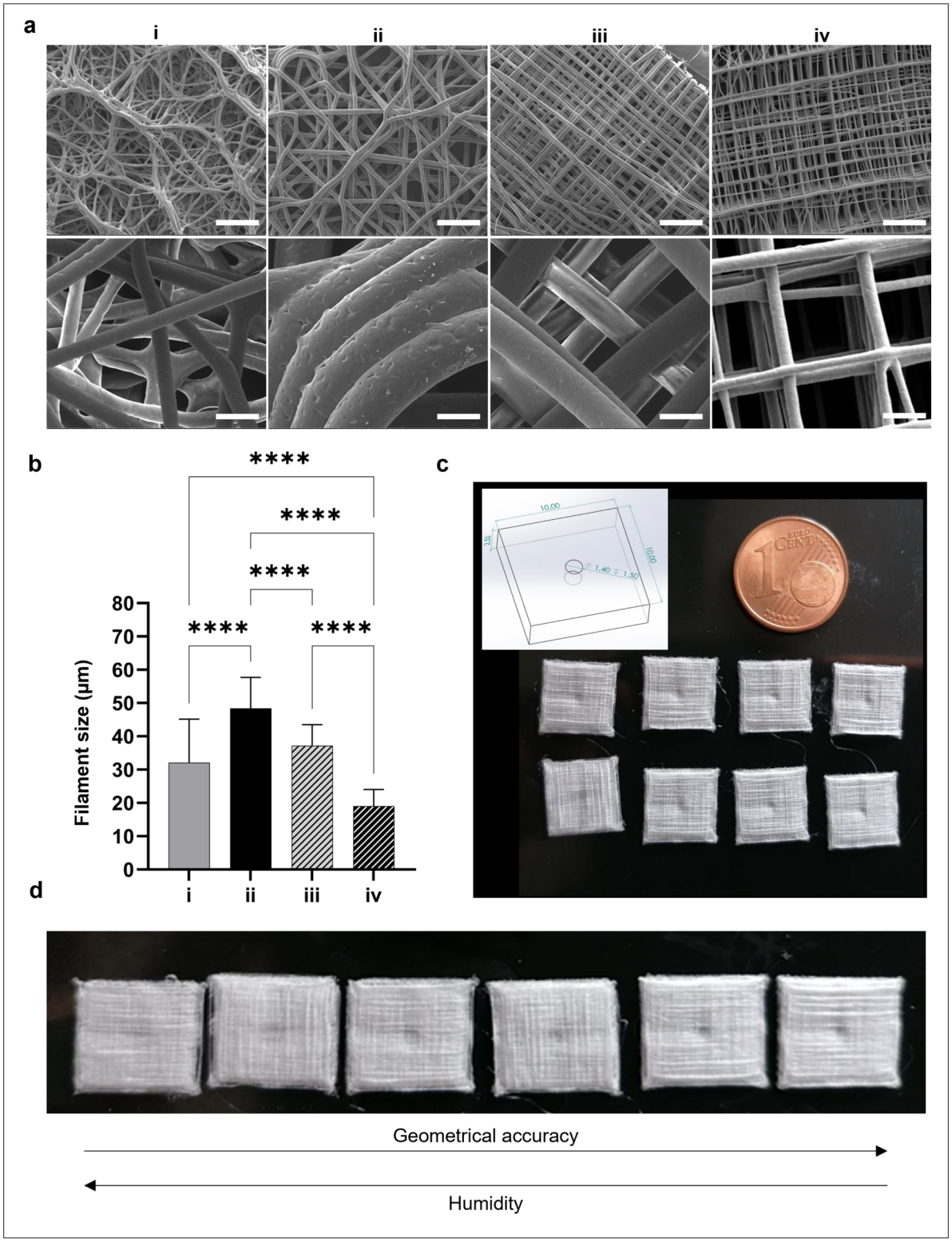

Figure 2. Fabrication of acinar structures by melt-electrowriting (MEW). (a) Scanning electron microscopy (SEM) images of scaffolds obtained by setting different process parameters, according to Table 1. Scale bars: 500 µm (first row) and 100 µm (second row). (b) Bar plots reporting the dimensional analysis (filament size) on the different scaffold types (n = 2; 40 images per scaffold). Tukey's multiple comparisons test: *p < 0.05, **p < 0.01, ***p < 0.001, ****p < 0.0001. (c) CAD drawing and photographs of the printed structures corresponding to scaffold type iv. (d) Photographs showing the relationship between geometrical accuracy and humidity, which varies between 44% and 54%.

The differences in terms of precision in filament deposition, pore interconnectivity, and fiber size in MEW scaffolds were observed. In general, the constructs obtained with the highest printing temperature (130°C) had randomly deposited fibers (Figure 2a$_{i}$), while the pores of scaffolds produced with an infill deposition angle of 45° were poorly interconnected (Figure 2a$_{ii}$). Decreasing the flow and the nozzle diameter and increasing the distance between needle and platform improve the accuracy of filament deposition and the structure resolution as the filament size also decreases (Figure 2a$_{iii–iv}$ and b). The scaffolds with the best resolution and pore interconnectivity (scaffold type iv) were chosen as optimal constructs for cell culture. Several replicas as shown in Figure 2c show high reproducibility of the manufacturing process.

Geometrical accuracy and shape fidelity were found to be affected by ambient parameters rather than the process parameters as shown in Figure 2d. Specifically, by decreasing the humidity from 54% to 44%, the geometry accuracy of printed constructs visibly improves.

3.2. Viability and distribution of stromal cells in MEW model

Figure 3a shows the viability of stromal cells, measured by a fluorometric/colorimetric assay, in which the metabolic capacity of live cells is quantified. The results demonstrate the ability of MEW constructs in supporting the growth of human fibroblasts for a period of up to 28 days. In particular, a statistically significant ($p < 0.0001$) increment in cell viability occurred from 3 days, 7 days, and 14 days to 28 days. On the contrary, the increment from 21 days to 28 days was minimal.

The distribution of cells inside the 3D scaffolds was evaluated by fluorescence microscopy and SEM analyses on the cellularized structures. Representative confocal and SEM images of MEW scaffolds seeded with HFF1 are depicted in Figures 3b and 4. An increment in stromal cells proliferation within the 3D MEW structures can be qualitatively observed from 14 days to 21 days and 28 days (Figure 4). Starting from 3 weeks of culture, the formation of a stromal matrix occurred, and the developed new tissue covered much of the scaffold surface after 28 days in culture. Indeed, the presence of granular corpuscles on the fibers at 21 days and 28 days after seeding could be ascribed to the ECM deposited by HFF1. The fiber dimension comparable to the cell size allowed an optimal colonization by fibroblasts that were able to adhere to different fibers, creating bridges across the pores, and to grow with support by the polymeric grid, indicating that a biomimetic process is in progress.

3.3. Crosstalk between epithelial and stromal cells in MEW model

The ability of the developed MEW model in reproducing the natural compartmentalization typical of the exocrine pancreatic microenvironment was analyzed (Figure 5). In particular, the interactions between epithelial and stromal cells were evaluated by quantifying the release of pro-inflammatory cues through the ELISA test and by observing the cell distribution (Figure 5a). Interleukin-6 release was measured in serum collected by MEW models seeded with HFF1 (monoculture), HFF1 + HPDE-KRAS cells or HFF1 + HPDE-WT cells at different time points of the culture period. As shown in Figure 5b, the level of IL-6 was higher for fibroblasts co-cultured with HPDE-KRAS cells at 2 days and 3 days, as compared with other conditions (HFF1 and HFF1 + HPDE-WT). This finding points to the augmented inflammation caused by the presence of HPDE-KRAS cells in co-culture with stromal cells. However, at later time points (10 days and 14 days), the IL-6 release decreased, suggesting that inflammation mediated by pro-inflammatory cytokines such as IL-6 mainly occurred in the initial phase of tumor–stroma crosstalk. Figure 5c shows the plots relative to E-cadherin signal from epithelial cells measured in the z-stack acquisitions from the top of the model to the bottom of the cavity (Figure 5d). The z-stack videos (**Videos S1–S3** in Supplementary File) and the confocal images in Figure 6 demonstrate the presence of HPDE-KRAS cells predominantly inside the cavity of the MEW scaffolds, thus confirming the success of the seeding procedure. The epithelial cells remained collimated in the biomimetic cavity for 10 days, while they were also visible in the portion around the cavity 14 days after seeding. Indeed, the plots of the signal corresponding to 7 and 10 days after seeding are characterized by a peak of fluorescence intensity in correspondence to the cavity's bottom ($z \approx 700$ μm), while the fluorescence intensity of epithelial cells co-cultured for 14 days with HFF1 resulted highest for the focal planes proximal to the upper surface of the model ($z = 0$ μm). Moreover, the intensity values measured in models after 10 days from HPDE-KRAS cells seeding are two-fold higher than those quantified after 7 days. Therefore, a culture period of 10 days seems to be optimal to guarantee the collimation of epithelial cells inside the cavity while maintaining a good level of proliferation.

The interactions between stromal and HPDE-KRAS cells within the cavity have been also qualitatively analyzed in confocal images at higher magnifications (Figure 7). Interestingly, the images relative to 3 and 7 days of co-culture show the tendency of epithelial cells to form 3D clusters between fibroblasts interconnections, reassembling the cell organization similar to the physiological exocrine

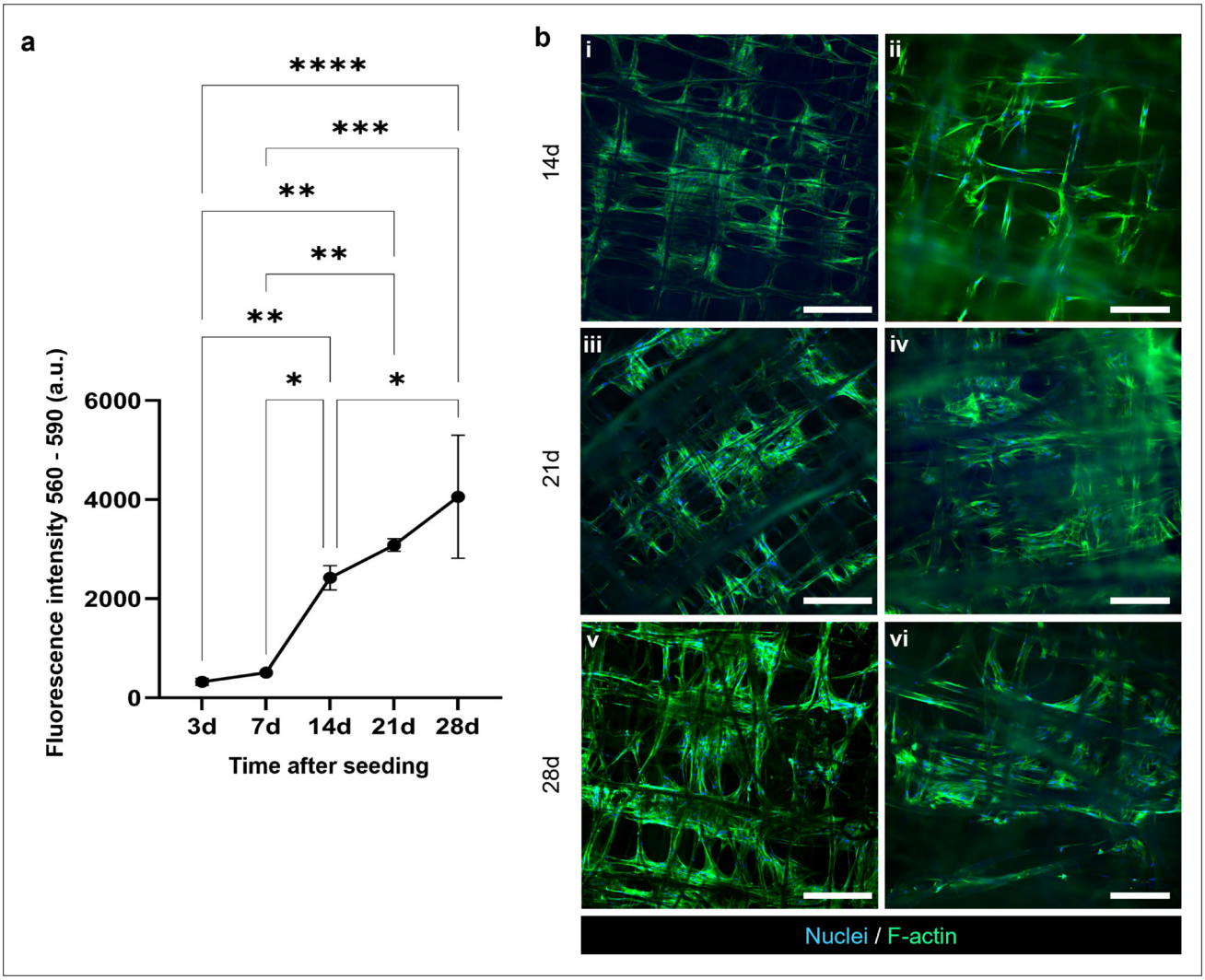

Figure 3. Viability and distribution of stromal cells in 3D MEW scaffolds. (a) Metabolic activity of fibroblasts seeded on MEW scaffolds as a function of time, measured from the reduction of resazurin (n = 3). Tukey's multiple comparisons test: *p < 0.05, **p < 0.01, ***p < 0.001, ****p < 0.0001. (b) Representative confocal images at 10× (i, iii, v) and 20× (ii, iv, vi) magnifications of HFF1 at 14, 21, and 28 days after seeding. Scale bars: 100 µm (i) and 50 µm (ii). (c) Scanning electron microscopy (SEM) images at different magnifications showing the HFF1 colonization within the MEW constructs. Scale bars: 500 µm (i, iv, vii), 100 µm (ii, v, viii), and 20 µm (iii, vi, ix).

pancreatic unit (epithelial cells surrounded by stromal cells). After 7, 10, and 14 days in co-culture, HPDE-KRAS cells visibly proliferated within the MEW model, growing on fibers and on the stromal tissue and colonizing most of the cavity's bottom.

4. Discussion

Two-dimensional models are valuable low-cost systems that can be easily applied in *in vitro* experiments,[45] but they are unable to recapitulate the biological and biophysical complexity of human tumor microenvironment.[46] Indeed, several studies have largely proved that pancreatic cancer and stromal cells grown in a 3D bioengineered environment respond to drugs differently than cells in two-dimensional models and show features more similar to the ones typical of PDAC components (e.g., chemoresistance, biochemical gradients, tumor–stroma cytoarchitecture).[47-51] For this reason, pancreatic cancer research has been oriented in recent years toward the development of novel *in vitro* models such as organ-on-chip and 3D models that better mimic the human tumor for *in vivo* conditions, for addressing ethical concerns in animal experiments, and to deepen our understanding of PDAC physiopathology.[52,53] So far, only few studies focused on replicating the 3D gland geometry of the functional unit of exocrine pancreas,[23-25,54,55] but they

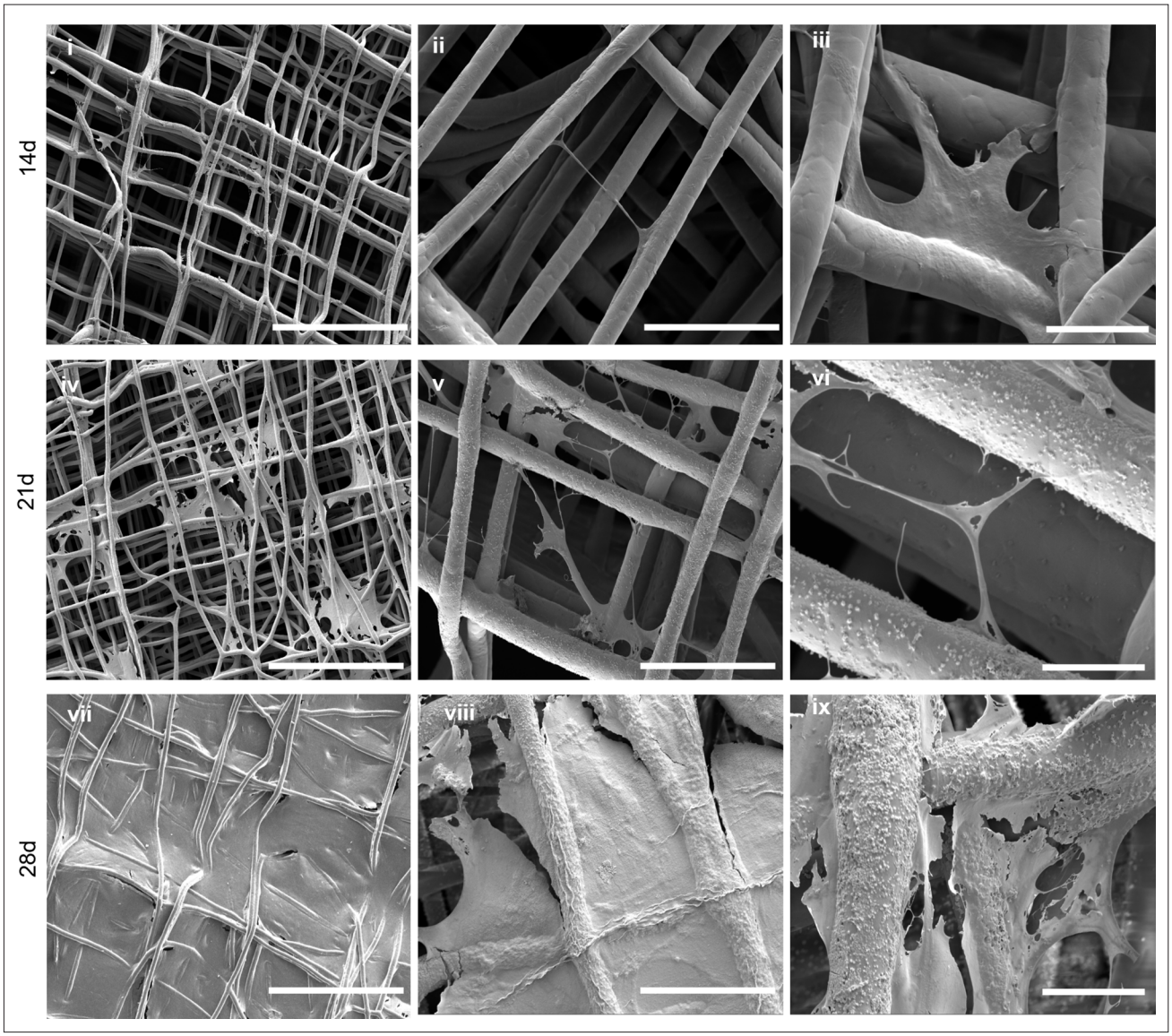

Figure 4. Distribution of stromal cells in 3D MEW scaffolds. Scanning electron microscopy (SEM) images at different magnifications showing the HFF1 colonization within the MEW constructs. Scale bars: 500 μm (i, iv, vii), 100 μm (ii, v, viii), and 20 μm (iii, vi, ix).

failed to reproduce the acino-ductal morphology[24,54] or incorporate the stromal components.[25,56] In this work, we designed and fabricated a 3D model, a layer-by-layer PCL scaffold, that recapitulates the morphology and composition of the exocrine pancreatic functional unit. In particular, we used MEW to obtain microscale constructs, which support cells' growth and provide physiological stimuli, since the MEW fibers are similar in size to natural ECM fibers that have diameters ranging from 1 to 20 μm[57] (Figure 2).

Although the accuracy in obtaining 3D complex geometries is lower in MEW compared with other layer-by-layer techniques (e.g., fused deposition modeling), where the polymer extrusion is discontinuous and the ambient parameters (e.g., humidity and ambient temperature) poorly affect the jet stability and the filament deposition,[30,58,59] the work described in this paper goes beyond the state of the art in the MEW field[28,31] and can be considered a pioneer study creating such a complex geometry of the gland (at a millimeter scale) without the need of any supports and/or cylindrical rotary mandrels. Thus, our approach bypasses the technical difficulties in separating the printed scaffolds from the supports and permits to fabricate morphologies other than mandrels shape and dimensions.[60-65] It has recently been shown that complex tubular structures can

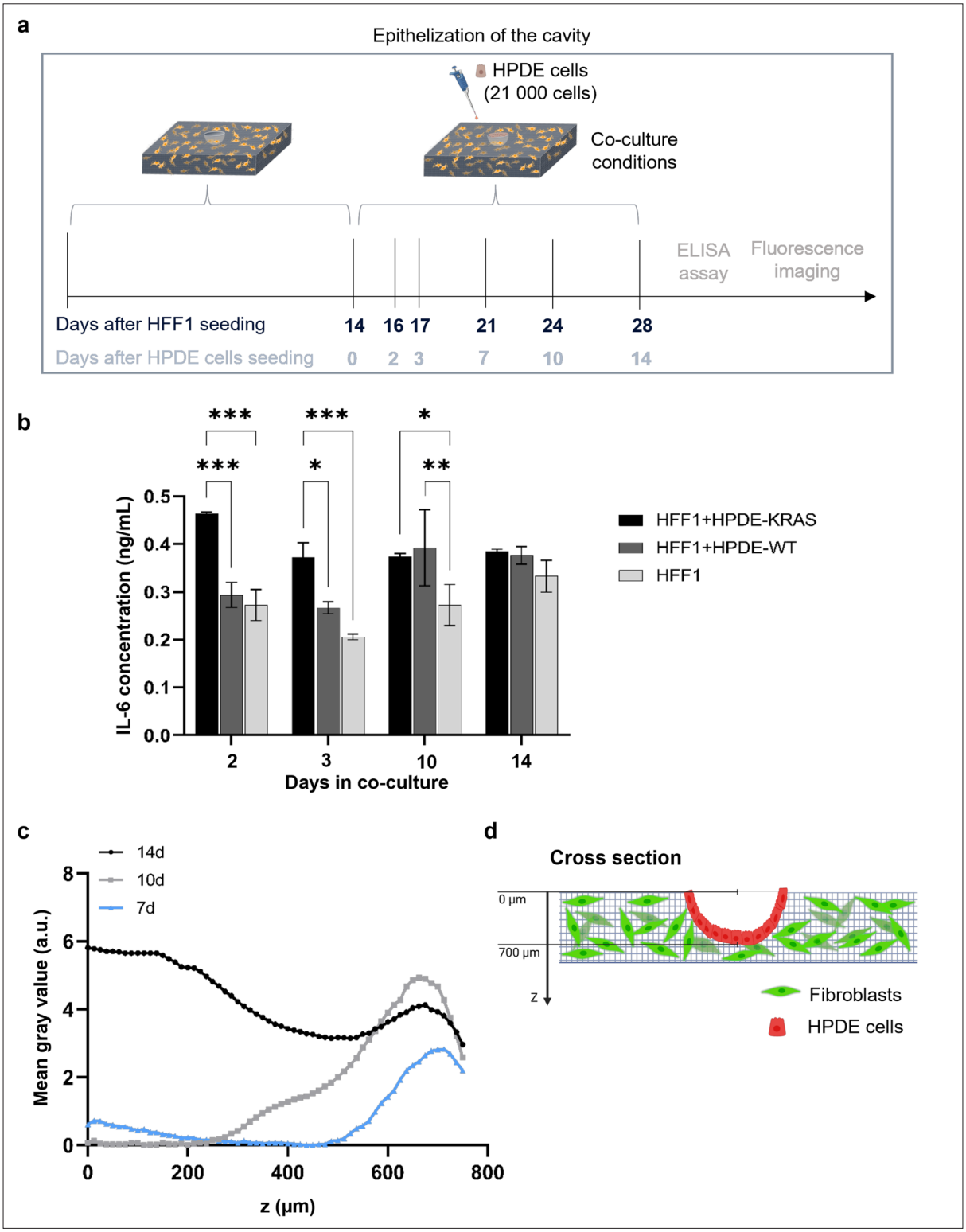

Figure 5. Epithelization of the cavity in the fibroblast-laden MEW scaffold. (a) Schematic illustration of the experiments pipeline. (b) Bar plots of the data obtained from ELISA test for IL-6 level for each culture condition (HFF1, HFF1 + HPDE-WT, and HFF1 + HPDE-KRAS) grouped per time step (n = 3). Each condition has been assayed in duplicate following the manufacturer's instructions. Tukey's multiple comparisons test: *p < 0.05, **p < 0.01, ***p < 0.001, ****p < 0.0001. (c) Plots reporting the intensity values of E-cadherin signal along the z-axis in constructs co-cultured with HFF1 and HPDE-KRAS cells for 7, 10, and 14 days. (d) Drawing showing the region where the z-stack images were acquired.

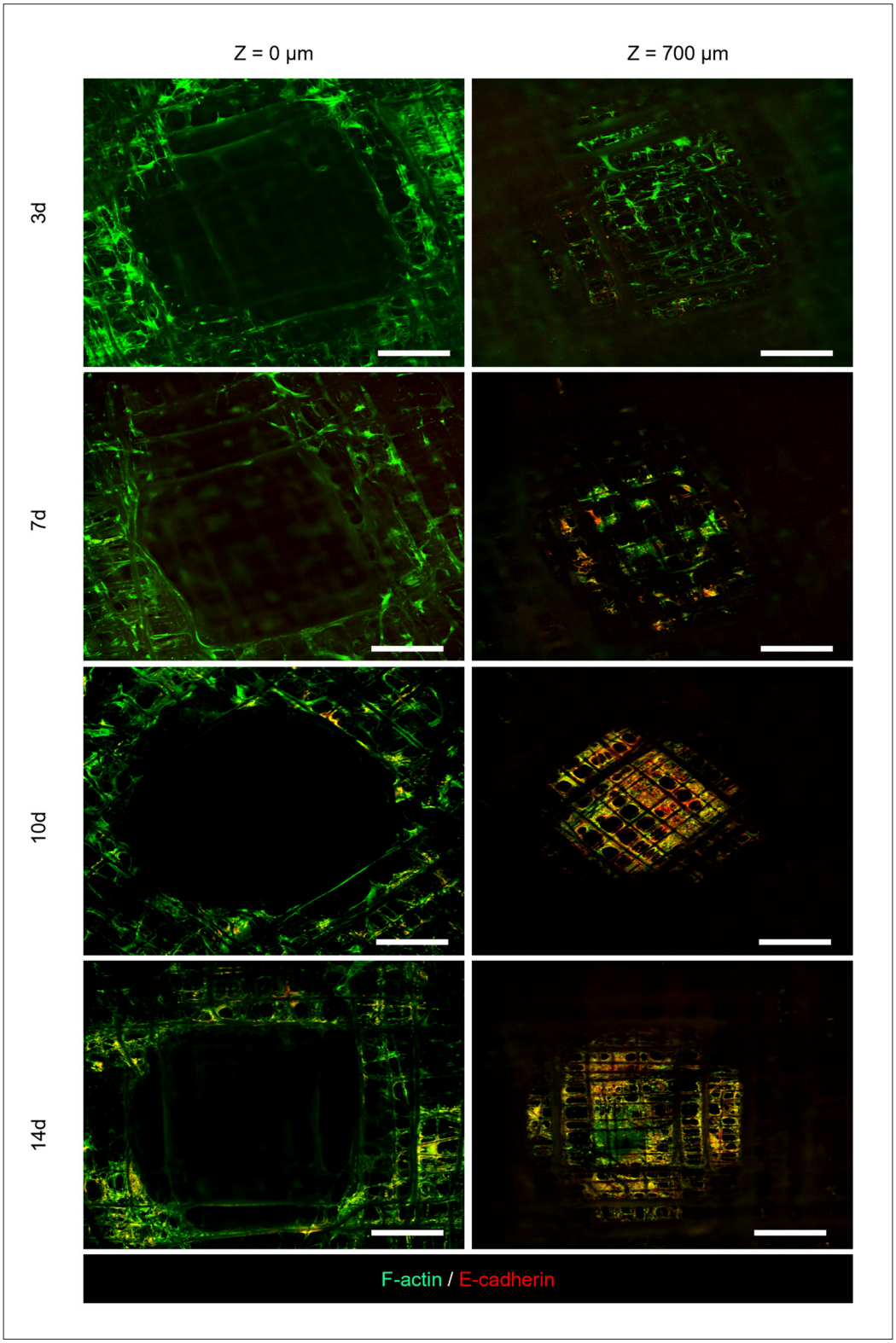

Figure 6. Distribution of epithelial cells co-cultured with fibroblasts in 3D MEW scaffolds. Representative confocal images at 4× magnification showing constructs slices at different depths, after 3 days, 7 days, 10 days, and 14 days from HPDE-KRAS cells seeding. Scale bars: 500 µm.

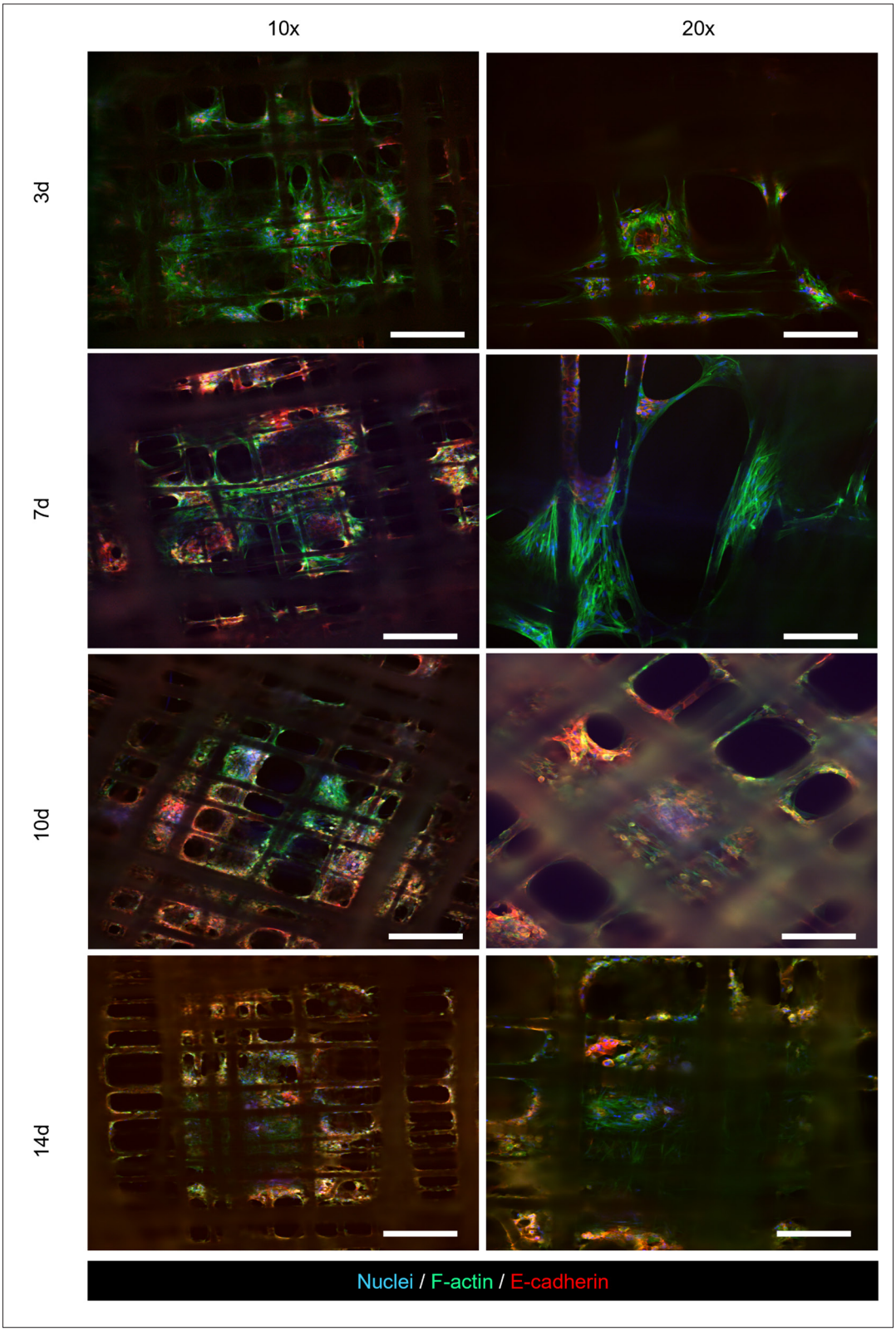

Figure 7. Interactions between stromal and HPDE-KRAS cells within the cavity of MEW model. Representative confocal images at 10× and 20× magnifications showing HFF1 and HPDE-KRAS cells co-cultured within the cavity, after 3 days, 7 days, 10 days, and 14 days from HPDE-KRAS cells seeding. Scale bars: 200 μm (left column) and 100 μm (right column).

be obtained by incorporating the method of layer shifting in the programmed toolpath, using planar collectors.[66,67] However, these scaffolds were poorly interconnected as fibers tend to adhere to each other. In contrast, we showed that the printing of complex biomimetic structures have high shape fidelity and interconnected porosity, which are key features for biological studies as confirmed by adhesion and proliferation assays using stromal cells (HFF1) that remained viable and active for at least 4 weeks in MEW constructs (Figure 3). These results are supported by other studies in literature, showing the culture of cells on PCL scaffolds obtained by MEW for several weeks.[61,68] Therefore, our results confirm the ability of these biomimetic scaffolds in promoting cell growth and tissue formation, in line with the numerous studies reporting the large use of PCL in additive manufacturing approaches for biomedical applications.[37-40]

The model developed in this study was able to maintain long-term culture of human fibroblasts, which adhered to different fibers to create bridges across the pores and grew with the support of polymeric grid, imitating the natural process. The surface of MEW scaffolds was almost covered by a thin layer of stromal matrix after 28 days in culture (Figure 4).

Moreover, we detected the presence of granular corpuscles on fibers of MEW models, at 21 days and 28 days after HFF1 seeding. Evidence in literature seems to confirm our hypothesis that correlates the presence of such corpuscles with the deposition of ECM by fibroblasts.[69,70] However, further analyses are needed to confirm this statement.

Human pancreatic ductal epithelial cells were seeded in the cavity of the structures, where HFF1 were allowed to grow for 2 weeks (Figure 5). The epithelial–stromal cells crosstalk occurring in the MEW model was studied in terms of fibroblasts inflammation mediated by IL-6 (Figure 5b). Indeed, the release of IL-6 by inflamed tumor-associated fibroblasts plays a key role in PDAC–stroma interplay and regulates a wide range of mechanisms involved in pancreatic cancer, such as angiogenesis, epithelial-to-mesenchymal transition, and immunosuppression.[71-73] It has been demonstrated previously that the release of IL-6 by HPDE-KRAS cells under monoculture on artificial substrates was minimal and negligible compared to HFF1.[21] Our results indicate a higher IL-6 release by fibroblasts in co-culture with HPDE-KRAS cells for 2 days and 3 days, in comparison with HFF1 alone or HFF1 under co-culture with healthy HPDE cells (HPDE-WT). This is in line with studies in literature reporting the role of the *KRAS* oncogene as a driver for the IL-6 production by stromal cells.[74,75]

The MEW model developed in this study recapitulates the *in vivo* pathological condition, accompanied by IL-6 secretion by fibroblasts during the inflammation of cancer cells.[76] The ability of this model in reproducing the inflammatory cascade occurring in pancreatic cancer is further confirmed by numerous studies showing notable differences in serum IL-6 levels between PDAC patients and healthy individuals.[77-83]

However, the differences in IL-6 levels of fibroblasts co-cultured with either healthy epithelial cells or epithelial cells overexpressing *KRAS* were statistically significant only at early stages of the experiment, suggesting that the IL-6-mediated inflammation occurred mainly during the first few hours (up to 72 h). At later phases of the experiment, inflammation might be mediated by other proteins.[84]

The ability of the human MEW model in reproducing the natural compartmentalization typical of the exocrine pancreatic microenvironment was demonstrated, as the epithelial cells were localized within the cavity while fibroblasts colonized the 3D structure. Indeed, HPDE-KRAS cells colonized the acino-like structure and remained collimated in the cavity up to 10 days of co-culture period and then started to migrate within the scaffold and on the scaffold upper surface (Figure 5c and d, and Figure 6; and **Videos S1–S3** in Supplementary File). Therefore, the optimal protocol for co-culture implementation within the MEW structure was set: 14 days of fibroblasts culture alone plus 10 days of fibroblasts and epithelial cells co-culture. Indeed, these time points permit the creation of a cellularized MEW model that mimics the native compartmentalized 3D tumor architecture, which is widely recognized to significantly influence behavior of cancer cells.[22,85,86] Moreover, the crosstalk between stromal and epithelial cells can also be easily monitored in this model, as the open structure allows the observation of the epithelial cell organization within the cavity, between the fibroblast interconnections (Figure 7). Although these results demonstrate the possibility to model the functional unit of the exocrine pancreas *in vitro* and to study the interactions between PDAC and stromal cells occurring at different stages of pancreatic cancer progression in a very controlled and biomimetic way, additional works are warranted to improve this model. For instance, advanced bioprinting systems can be employed in combination with MEW[87] to print the epithelial cells into a monolayer on the previously obtained MEW model, within the acinar-like cavity in a precise and software-guided way.

5. Conclusion

This work describes the engineering approach adopted to fabricate a layer-by-layer microscale model resembling the half structure of the functional unit of the exocrine pancreas, for the study of pancreatic cancer. MEW was employed to obtain the complex 3D structure without the

need for supports, mandrels, or sacrificial materials. The constructed PCL scaffold represents, at the microscale, a biomimetic porous network able to support the growth and proliferation of stromal cells over several weeks. In particular, human fibroblasts and HPDE overexpressing the *KRAS* oncogene were used to replicate the stromal and cancer epithelial components, respectively. The ability of this model in promoting the formation of a stromal tissue after 28 days of culture, as well as the capability in replicating the compartmentalized architecture typical of the pancreatic cancer microenvironment by hosting both stromal cells and epithelial cells, was assessed. Indeed, the specific localization of the epithelial cells within the acinar cavity was achieved and maintained up to 10 days. Moreover, the MEW model features the crosstalk between stromal and PDAC cells on IL-6 release, mirroring the pathological condition *in vivo*.

Therefore, the successful realization of the biomimetic construct described in this paper provides an important step toward a fully human 3D *in vitro* model of the pancreatic gland capable of recapitulating acinar morphology, allowing long-term analyses of pancreatic cancer progression from the very early stages and facilitating the design of effective treatments against this cancer.

Acknowledgments

We thank Prof. F. Bussolino for the support in cell culturing.

Funding

This project was carried out with the support of Fondazione Compagnia di San Paolo - Trapezio Call for Proposals -Target 1 project "ExocRine glAndular Tissue mOdelS TExocRine glandular Tissue mOdelS Through precisely designed biomimetic EnviroNmEntS: an engineering tools to improve understanding and treatment for pancreatic cancer (ERATOSTHENES)".

Conflict of interest

The authors declare no conflicts of interest.

Author Contributions

Conceptualization: Gianluca Ciardelli, Chiara Tonda-Turo
Data curation: Viola Sgarminato, Michela Licciardello
Formal analysis: Viola Sgarminato, Chiara Tonda-Turo
Funding acquisition: Gianluca Ciardelli, Chiara Tonda-Turo
Investigation: Viola Sgarminato, Michela Licciardello, Chiara Tonda-Turo
Methodology: Michela Licciardello, Chiara Tonda-Turo
Writing – original draft: Viola Sgarminato, Chiara Tonda-Turo
Writing – review & editing: Gianluca Ciardelli

Ethics approval and consent to participate

Not applicable.

Consent for publication

Not applicable.

Availability of data

Data are available from the corresponding author upon reasonable request.

References

1. Hegyi P, Petersen OH. The exocrine pancreas: the acinar-ductal tango in physiology and pathophysiology. *Rev Physiol Biochem Pharmacol*. 2013;165:1-30. doi: 10.1007/112_2013_14
2. Shih HP, Wang A, Sander M. Pancreas organogenesis: from lineage determination to morphogenesis. *Annu Rev Cell Dev Biol*. 2013;29:81-105. doi: 10.1146/annurev-cellbio-101512-122405
3. Weniger M, Honselmann KC, Liss AS. The extracellular matrix and pancreatic cancer: a complex relationship. *Cancers*. 2018;10(9):316. doi: 10.3390/cancers10090316
4. Fu Y, Liu S, Zeng S, Shen H. The critical roles of activated stellate cells-mediated paracrine signaling, metabolism and onco-immunology in pancreatic ductal adenocarcinoma. *Mol Cancer*. 2018;17:62. doi: 10.1186/s12943-018-0815-z
5. Pothula SP, Pirola RC, Wilson JS, Apte MV. Pancreatic stellate cells: aiding and abetting pancreatic cancer progression. *Pancreatology*. 2020;20:409-418. doi: 10.1016/j.pan.2020.01.003
6. Wang S, Li Y, Xing C, et al. Tumor microenvironment in chemoresistance, metastasis and immunotherapy of pancreatic cancer. *Am J Cancer Res*. 2020;10:1937-1953.
7. Bynigeri RR, Jakkampudi A, Jangala R, et al. Pancreatic stellate cell: Pandora's box for pancreatic disease biology. *World J Gastroenterol*. 2017;23:382. doi: 10.3748/wjg.v23.i3.382
8. Apte MV, Wilson JS, Lugea A, Pandol SJ. A starring role for stellate cells in the pancreatic cancer microenvironment. *Gastroenterology*. 2013;144:1210-1219. doi: 10.1053/j.gastro.2012.11.037
9. Wu Y, Zhang C, Jiang K, Werner J, Bazhin AV, D'Haese JG. The role of stellate cells in pancreatic ductal adenocarcinoma: targeting perspectives. *Front Oncol*. 2021;10. doi: 10.3389/fonc.2020.621937
10. Zhan HX, Zhou B, Cheng Y, et al. Crosstalk between stromal cells and cancer cells in pancreatic cancer: new insights into stromal biology. *Cancer Lett*. 2017;392:83-93. doi: 10.1016/j.canlet.2017.01.041

11. Cui SJ, Tang TY, Zou XW, Su Q-M, Feng L, Gong X-Y. Role of imaging biomarkers for prognostic prediction in patients with pancreatic ductal adenocarcinoma. *Clin Radiol*. 2020;75:478.e1-478.e11. doi: 10.1016/j.crad.2019.12.023
12. Orth M, Metzger P, Gerum S, et al. Pancreatic ductal adenocarcinoma: Biological hallmarks, current status, and future perspectives of combined modality treatment approaches. *Radiat Oncol.* 2019;14(1):141. doi: 10.1186/s13014-019-1345-6
13. Porciuncula A, Hajdu C, David G. The dual role of senescence in pancreatic ductal adenocarcinoma. *Adv Cancer Res*. 2016;131:1-20. doi: 10.1016/bs.acr.2016.05.006
14. Brunet LR, Hagemann T, Andrew G, Mudan S, Marabelle A. Have lessons from past failures brought us closer to the success of immunotherapy in metastatic pancreatic cancer? *Oncoimmunology.* 2016;5(4). doi: 10.1080/2162402X.2015.1112942
15. Cave DD, Rizzo R, Sainz B, Gigli G, Del Mercato LL, Lonardo E. The revolutionary roads to study cell–cell interactions in 3d in vitro pancreatic cancer models. *Cancers (Basel).* 2021;13(4):930. doi: 10.3390/cancers13040930
16. Osuna de la Peña D, Trabulo S, Collin E, et al. Bioengineered 3D models of human pancreatic cancer recapitulate in vivo tumour biology. *Nat Commun*. 2021;12:5623. doi: 10.1038/s41467-021-25921-9
17. Haque MR, Rempert TH, Al-Hilal TA, Wang C, Bhushan A, Bishehsari F. Organ-chip models: opportunities for precision medicine in pancreatic cancer. *Cancers (Basel).* 2021;13(17):4487. doi: 10.3390/cancers13174487
18. Mollica H, Teo YJ, Tan DZ, et al. A 3D pancreatic tumor model to study T cell infiltration. *Biomater Sci.* 2021;9:7420-7431. doi: 10.1039/D1BM00210D
19. Schuster B, Junkin M, Kashaf SS, et al. Automated microfluidic platform for dynamic and combinatorial drug screening of tumor organoids. *Nat Commun*. 2020;11:1-12. doi: 10.1038/s41467-020-19058-4
20. Nguyen, DHT, Lee E, Alimperti S, et al. A biomimetic pancreatic cancer on-chip reveals endothelial ablation via ALK7 signaling. *Sci Adv*. 2019;5(8):eaav6789. doi: 10.1126/sciadv.aav6789
21. Sgarminato V, Marasso SL, Cocuzza M, et al. PDAC-on-chip for in vitro modeling of stromal and pancreatic cancer cell crosstalk. *Biomater Sci.* 2022;11:208-224. doi: 10.1039/D2BM00881E
22. Kota J, Hancock J, Kwon J, Korc M. Pancreatic cancer: stroma and its current and emerging targeted therapies. *Cancer Lett*. 2017;391:38-49. doi: 10.1016/j.canlet.2016.12.035
23. Hajiabbas M, D'Agostino C, Simińska-Stanny J, Tran SD, Shavandi A, Delporte C. Bioengineering in salivary gland regeneration. *J Biomed Sci*. 2022;291(29):1-24. doi: 10.1186/s12929-022-00819-w
24. Gupta P, Pérez-Mancera PA, Kocher H, Nisbet A, Schettino G, Velliou EG. A novel scaffold-based hybrid multicellular model for pancreatic ductal adenocarcinoma—toward a better mimicry of the in vivo tumor microenvironment. *Front Bioeng Biotechnol*. 2020;8:290. doi: 10.3389/fbioe.2020.00290
25. Venis SM, Moon HR, Yang Y, Utturkar SM, Konieczny SF, Han B. Engineering of a functional pancreatic acinus with reprogrammed cancer cells by induced: PTF1a expression. *Lab Chip*. 2021;21:3675-3685. doi: 10.1039/d1lc00350j
26. Charbonneau AM, Kinsella JM, Tran SD. 3D cultures of salivary gland cells in native or gelled egg yolk plasma, combined with egg white and 3D-printing of gelled egg yolk plasma. *Materials (Basel).* 2019;12(21):3480. doi: 10.3390/ma12213480
27. Jain P, Kathuria H, Dubey N. Advances in 3D bioprinting of tissues/organs for regenerative medicine and in-vitro models. *Biomaterials*. 2022;287:121639. doi: 10.1016/j.biomaterials.2022.121639
28. Loewner S, Heene S, Baroth T, et al. Recent advances in melt electro writing for tissue engineering for 3D printing of microporous scaffolds for tissue engineering. *Front Bioeng Biotechnol*. 2022;10. doi: 10.3389/fbioe.2022.896719
29. Hutmacher DW, Dalton PD. Melt electrospinning. *Chem Asian J*. 2011;6:44-56. doi: 10.1002/asia.201000436
30. Kade JC, Dalton PD. Polymers for melt electrowriting. *Adv Healthc Mater.* 2021;10(1):2001232. doi: 10.1002/adhm.202001232
31. Cao K, Zhang F, Zaeri A, et al. Advances in design and quality of melt electrowritten scaffolds. *Mater Des*. 2023;1;226. doi: 10.1016/j.matdes.2023.111618
32. Moroni L, Boland T, Burdick JA, et al. Biofabrication: a guide to technology and terminology. *Trends Biotechnol.* 2018;36:384-402. doi: 10.1016/j.tibtech.2017.10.015
33. Fu Z, Naghieh S, Xu C, Wang C, Sun W, Chen X. Printability in extrusion bioprinting. *Biofabrication*. 2021;13(3): 033001. doi: 10.1088/1758-5090/abe7ab
34. Licciardello M, Ciardelli G, Tonda-Turo C. Biocompatible electrospun polycaprolactone-polyaniline scaffold treated with atmospheric plasma to improve hydrophilicity. *Bioengineering*. 2021;8(2):24. doi: 10.3390/bioengineering8020024

35. Mancuso E, Tonda-Turo C, Ceresa C, et al. Potential of Manuka honey as a natural polyelectrolyte to develop biomimetic nanostructured meshes with antimicrobial properties. *Front Bioeng Biotechnol.* 2019;7:344. doi: 10.3389/fbioe.2019.00344

36. Giuntoli G, Muzio G, Actis C, et al. In-vitro characterization of a hernia mesh featuring a nanostructured coating. *Front Bioeng Biotechnol*. 2021;8:589223. doi: 10.3389/fbioe.2020.589223

37. Backes, EH, Harb SV, Beatrice CA, et al. Polycaprolactone usage in additive manufacturing strategies for tissue engineering applications: a review. *J Biomed Mater Res B Appl Biomater*. 2022;110:1479-1503. doi: 10.1002/jbm.b.34997

38. Großhaus C, Bakirci E, Berthel M, et al. Melt electrospinning of nanofibers from medical-grade poly(ε-caprolactone) with a modified nozzle. *Small*. 2020;16:2003471. doi: 10.1002/smll.202003471

39. Kumar N, Joisher H, Ganguly A. Polymeric scaffolds for pancreatic tissue engineering: a review. *Rev Diabet Stud.* 2017;14:334-353. doi: 10.1900/RDS.2017.14.334

40. Yang X, Wang Y, Zhou Y, Chen J, Wan Q. The application of polycaprolactone in three-dimensional printing scaffolds for bone tissue engineering. *Polymers (Basel)*. 2021;13:2754. doi: 10.3390/polym13162754

41. Abràmoff MD, Magalhães PJ, Ram SJ. Image processing with ImageJ. *Biophotonics Int*. 2004;11:36-42.

42. Lee JH, Kim SK, Khawar IA, Jeong S-Y, Chung S, Kuh H-J. Microfluidic co-culture of pancreatic tumor spheroids with stellate cells as a novel 3D model for investigation of stroma-mediated cell motility and drug resistance. *J Exp Clin Cancer Res.* 2018;37:1-12. doi: 10.1186/s13046-017-0654-6

43. Jeong SY, Lee JH, Shin Y, Chung S, Kuh H-J. Co-culture of tumor spheroids and fibroblasts in a collagen matrix-incorporated microfluidic chip mimics reciprocal activation in solid tumor microenvironment. *PLoS One*. 2016;11:e0159013. doi: 10.1371/journal.pone.0159013

44. Fujiwara M, Kanayama K, Hirokawa YS, Shiraishi T. ASF-4-1 fibroblast-rich culture increases chemoresistance and mTOR expression of pancreatic cancer BxPC-3 cells at the invasive front in vitro, and promotes tumor growth and invasion in vivo. *Oncol Lett.* 2016;11:2773. doi: 10.3892/ol.2016.4289

45. Weeber F, Ooft SN, Dijkstra KK, Voest EE. Tumor organoids as a pre-clinical cancer model for drug discovery. *Cell Chem Biol.* 2017;24:1092-1100. doi: 10.1016/j.chembiol.2017.06.012

46. Kapałczyńska M, Kolenda T, Przybyła W, et al. 2D and 3D cell cultures - a comparison of different types of cancer cell cultures. *Arch Med Sci.* 2018;14:910-919. doi: 10.5114/aoms.2016.63743

47. Desoize B, Jardillier J. Multicellular resistance: a paradigm for clinical resistance? *Crit Rev Oncol Hematol.* 2000;36:193-207. doi: 10.1016/s1040-8428(00)00086-x

48. Brancato V, Oliveira JM, Correlo VM, Reis RL, Kundu SC. Could 3D models of cancer enhance drug screening? *Biomaterials*. 2020;232:119744. doi: 10.1016/j.biomaterials.2019.119744

49. Shichi Y, Norihiko S, Masaki M, et al. Enhanced morphological and functional differences of pancreatic cancer with epithelial or mesenchymal characteristics in 3D culture. *Sci Rep.* 2019;9:10871. doi: 10.1038/s41598-019-47416-w

50. Fang Y, Eglen RM. Three-dimensional cell cultures in drug discovery and development. *SLAS Discov*. 2017;22:456-472. doi: 10.1177/1087057117696795

51. Laschke MW, Menger MD. Life is 3D: boosting spheroid function for tissue engineering. *Trends Biotechnol.* 2017;35:133-144. doi: 10.1016/j.tibtech.2016.08.004

52. Tomás-Bort E, Kieler M, Sharma S, Candido JB, Loessner D. 3D approaches to model the tumor microenvironment of pancreatic cancer. *Theranostics*. 2020;10:5074-5089. doi: 10.7150/thno.42441

53. Monteiro MV, Ferreira LP, Rocha M, Gaspar VM, Mano JF. Advances in bioengineering pancreatic tumor-stroma physiomimetic biomodels. *Biomaterials*. 2022;287:121653. doi: 10.1016/j.biomaterials.2022.121653

54. Bradney MJ, Venis SM, Yang Y, Konieczny SF, Han B. A biomimetic tumor model of heterogeneous invasion in pancreatic ductal adenocarcinoma. *Small*. 2020;16(10):e1905500. doi: 10.1002/smll.201905500

55. Sung JH, Shuler ML. Microtechnology for mimicking in vivo tissue environment. *Ann Biomed Eng.* 2012;40:1289-1300. doi: 10.1007/s10439-011-0491-2

56. Randriamanantsoa S, Papargyriou A, Maurer HC, et al. Spatiotemporal dynamics of self-organized branching in pancreas-derived organoids. *Nat Commun*. 2022;13:1-15. doi: 10.1038/s41467-022-32806-y

57. Ushiki T. Collagen fibers, reticular fibers and elastic fibers. A comprehensive understanding from a morphological viewpoint. *Arch Histol Cytol.* 2002;65:109-126. doi: 10.1679/aohc.65.109

58. Rajan K, Samykano M, Kadirgama K, Harun WSW, Rahman MM. Fused deposition modeling: process, materials, parameters, properties, and applications. *Int J Adv Manuf Technol*. 2022;120:1531-1570. doi: 10.1007/s00170-022-08860-7

59. Bachs-Herrera A, Yousefzade O, Del Valle LJ, Puiggali J. Melt electrospinning of polymers: blends, nanocomposites, additives and applications. *Appl Sci.* 2021;11(4):1808. doi: 10.3390/app11041808

60. Saidy NT, Shabab T, Bas O, et al. Melt electrowriting of complex 3D anatomically relevant scaffolds. *Front Bioeng Biotechnol*. 2020;8:793. doi: 10.3389/fbioe.2020.00793

61. Peiffer QC, de Ruijter M, van Duijn J, et al. Melt electrowriting onto anatomically relevant biodegradable substrates: resurfacing a diarthrodial joint. *Mater Des*. 2020;195:109025. doi: 10.1016/j.matdes.2020.109025

62. Brooks-Richards TL, Paxton NC, Allenby MC, Woodruff MA. Dissolvable 3D printed PVA moulds for melt electrowriting tubular scaffolds with patient-specific geometry. *Mater Des*. 2022;215:110466. doi: 10.1016/j.matdes.2022.110466

63. Saha U, Nairn R, Keenan O, Monaghan MG. A deeper insight into the influence of the electric field strength when melt-electrowriting on non-planar surfaces. *Macromol Mater Eng*. 2021;306:2100496. doi: 10.1002/mame.202100496

64. Constante, G, Apsite I, Alkhamis H, et al. 4D biofabrication using a combination of 3D printing and melt-electrowriting of shape-morphing polymers. *ACS Appl Mater Interfaces*. 2021;13:12767-12776. doi: 10.1021/acsami.0c18608

65. Van Genderen AM, Jansen K, Kristen M, et al. Topographic guidance in melt-electrowritten tubular scaffolds enhances engineered kidney tubule performance. *Front Bioeng Biotechnol*. 2021;8:617364. doi: 10.3389/fbioe.2020.617364

66. Liashenko I, Hrynevich A, Dalton PD. Designing outside the box: unlocking the geometric freedom of melt electrowriting using microscale layer shifting. *Adv Mater*. 2020;32:2001874. doi: 10.1002/adma.202001874

67. Bakirci E, Schaefer N, Dahri O, et al. Melt electrowritten in vitro radial device to study cell growth and migration. *Adv Biosyst*. 2020;4:2000077. doi: 10.1002/adbi.202000077

68. Korpershoek, JV, Korpershoek JV, Ruijter M, et al. Potential of melt electrowritten scaffolds seeded with meniscus cells and mesenchymal stromal cells. *Int J Mol Sci*. 2021;22:11200. doi: 10.3390/ijms222011200

69. Neves SC, Moreira Teixeira LS, Moroni L, et al. Chitosan/poly(ε-caprolactone) blend scaffolds for cartilage repair. *Biomaterials*. 2011;32:1068-1079. doi: 10.1016/j.biomaterials.2010.09.073

70. Malakpour Permlid A, Roci P, Fredlund E, et al. Unique animal friendly 3D culturing of human cancer and normal cells. *Toxicol In Vitro*. 2019;60:51-60. doi: 10.1016/j.tiv.2019.04.022

71. Kuen J, Darowski D, Kluge T, Majety M. Pancreatic cancer cell/fibroblast co-culture induces M2 like macrophages that influence therapeutic response in a 3D model. *PLoS One*. 2017;12:e0182039. doi: 10.1371/journal.pone.0182039

72. van Duijneveldt G, Griffin MDW, Putoczki TL. Emerging roles for the IL-6 family of cytokines in pancreatic cancer. *Clin Sci*. 2020;134:2091-2115. doi: 10.1042/CS20191211

73. Öhlund D, Handly-Santana A, Biffi G, et al. Distinct populations of inflammatory fibroblasts and myofibroblasts in pancreatic cancer. *J Exp Med*. 2017;214:579-596. doi: 10.1084/jem.20162024

74. Feurino LW, Zhang Y, Bharadwaj U, et al. IL-6 stimulates Th2 type cytokine secretion and upregulates VEGF and NRP-1 expression in pancreatic cancer cells. *Cancer Biol Ther*. 2007;6:1096-1100. doi: 10.4161/cbt.6.7.4328

75. Ancrile B, Lim KH, Counter CM. Oncogenic Ras-induced secretion of IL6 is required for tumorigenesis. *Genes Dev*. 2007;21:1714-1719. doi: 10.1101/gad.1549407

76. Nagasaki T, Hara M, Nakanishi H, Takahashi H, Sato M, Takeyama H. Interleukin-6 released by colon cancer-associated fibroblasts is critical for tumour angiogenesis: anti-interleukin-6 receptor antibody suppressed angiogenesis and inhibited tumour–stroma interaction. *Br J Cancer*. 2014;110:469-478. doi: 10.1038/bjc.2013.748

77. Ebrahimi B, Tucker SL, Li D, Abbruzzese JL, Kurzrock R. Cytokines in pancreatic carcinoma. *Cancer*. 2004;101:2727-2736. doi: 10.1002/cncr.20672

78. Wigmore SJ, Fearon KC, Sangster K, Maingay JP, Garden OJ, Ross JA. Cytokine regulation of constitutive production of interleukin-8 and -6 by human pancreatic cancer cell lines and serum cytokine concentrations in patients with pancreatic cancer. *Int J Oncol*. 2002;21:881-886. doi: 10.3892/ijo.21.4.881

79. Talar-Wojnarowska, R, Gasiorowska A, Smolarz B, Romanowicz-Makowska H, Kulig A, Malecka-Panas E. Clinical significance of interleukin-6 (Il-6) gene polymorphism and Il-6 serum level in pancreatic adenocarcinoma and chronic pancreatitis. *Dig Dis Sci*. 2009;54:683-689. doi: 10.1007/s10620-008-0390-z

80. Barber MD, Fearon KCH, Ross JA. Relationship of serum levels of interleukin-6, soluble interleukin-6 receptor and tumour necrosis factor receptors to the acute-phase protein response in advanced pancreatic cancer. *Clin Sci*. 1999;96:83-87.

81. Okada S, Okusaka T, Ishii H, et al. Elevated serum interleukin-6 levels in patients with pancreatic cancer. *Jpn J Clin Oncol*. 1998;28:12-15. doi: 10.1093/jjco/28.1.12

82. Błogowski W, Deskur A, Budkowska M, et al. Selected cytokines in patients with pancreatic cancer: a preliminary report. *PLoS One*. 2014;9:e97613.
doi: 10.1371/journal.pone.0097613

83. Mroczko B, Groblewska M, Gryko M, Kędra B, Szmitkowski M. Diagnostic usefulness of serum interleukin 6 (IL-6) and C-reactive protein (CRP) in the differentiation between pancreatic cancer and chronic pancreatitis. *J Clin Lab Anal*. 2010;24:256-261.
doi: 10.1002/jcla.20395

84. Chen K, Wang Q, Li M, et al. Single-cell RNA-seq reveals dynamic change in tumor microenvironment during pancreatic ductal adenocarcinoma malignant progression. *EBioMedicine*. 2021;66:103315.
doi: 10.1016/j.ebiom.2021.103315

85. Pothula SP, Pirola RC, Wilson JS, Apte MV. Pancreatic stellate cells: aiding and abetting pancreatic cancer progression. *Pancreatology*. 2020;20:409-418.
doi: 10.1016/j.pan.2020.01.003

86. Koikawa K, Ohuchida K, Ando Y, et al. Basement membrane destruction by pancreatic stellate cells leads to local invasion in pancreatic ductal adenocarcinoma. *Cancer Lett*. 2018;425:65-77.
doi: 10.1016/j.canlet.2018.03.031

87. Dufour A, Gallostra XB, O'Keeffe C, et al. Integrating melt electrowriting and inkjet bioprinting for engineering structurally organized articular cartilage. *Biomaterials*. 2022;283:121405.
doi: 10.1016/j.biomaterials.2022.121405

ACCSCIENCE PUBLISHING

International Journal of Bioprinting

RESEARCH ARTICLE

Exploring the mechanical strength, antimicrobial performance, and bioactivity of 3D-printed silicon nitride-PEEK composites in cervical spinal cages

Cemile Basgul[1]*, Paul DeSantis[1], Tabitha Derr[1], Noreen J. Hickok[2], Ryan M. Bock[3], and Steven M. Kurtz[1]

[1]Implant Research Core, School of Biomedical Science, Engineering, and Health Systems, Drexel University, Philadelphia, United States of America

[2]Department of Orthopedics, Sidney Kimmel Medical College, Thomas Jefferson University, Philadelphia, United States of America

[3]SINTX Technologies, Inc., Salt Lake City, Utah, United States of America

Abstract

In this study, our goal was to assess the suitability of a polyether-ether-ketone (PEEK) and silicon nitride (Si_3N_4) polymer composite for antimicrobial three-dimensional (3D)-printed cervical cages. Generic cage designs (PEEK and 15 vol.% Si_3N_4-PEEK) were 3D-printed, including solid and porous cage designs. Cages were tested in static compression, compression shear, and torsion per ASTM F2077. For antibacterial testing, virgin and composite filament samples were inoculated with *Staphylococcus epidermidis* and *Escherichia coli*. *In vitro* cell testing was conducted using MC3T3-E1 mouse preosteoblasts, where cell proliferation, cumulative mineralization, and osteogenic activity were measured. The 3D-printed PEEK and Si_3N_4-PEEK cages exhibited adequate mechanical strength for all designs, exceeding 14.7 kN in compression and 6.9 kN in compression shear. Si_3N_4-PEEK exhibited significantly lower bacterial adhesion levels, with a 93.9% reduction (1.21 log), and enhanced cell proliferation when compared to PEEK. Si_3N_4-PEEK would allow for custom fabrication of 3D-printed spinal implants that reduce the risk of infection compared to unfilled PEEK or metallic alloys.

Keywords: Cervical fusion cage; Anti-infection; Polyether-ether-ketone; Silicon nitride; 3D printing; ASTM F2077

***Corresponding author:**
Cemile Basgul
(cb997@drexel.edu)

Citation: Basgul C, DeSantis P, Derr T, Hickok NJ, Bock RM, Kurtz SM. Exploring the mechanical strength, antimicrobial performance, and bioactivity of 3D-printed silicon nitride-PEEK composites in cervical spinal cages. *Int J Bioprint*. 2024;10(2):2124.
doi: 10.36922/ijb.2124

Received: October 27, 2023
Accepted: December 26, 2023
Published Online: February 26, 2024

1. Introduction

Spinal fusion is the gold-standard treatment[1] when back pain becomes intractable, but up to 35% of patients experience failed fusions.[2-4] These failures can result from poor osseointegration that critically depends on surface and mechanical properties of the spinal cage[5-7] and biological factors. Among these factors, low level of bacterial contamination localized to the bone–implant interface may inhibit bone growth.[8,9] Currently, traditionally molded or machined polyether-ether-ketone (PEEK) cages are

the most common cages, which are endowed with PEEK's strength, elastic modulus comparable to that of the bone, biocompatibility, and radiolucency.[10,11]

Earlier investigations have affirmed the robust mechanical strength of three-dimensional (3D)-printed PEEK in different implant applications.[12] Subsequent studies have explored ways to enhance PEEK's bioactivity by adding bioactive fillers into PEEK to allow the utilization of novel materials in 3D printing technology without compromising inherent strengths of PEEK.[13] This pragmatic approach seeks to optimize PEEK for implants, aiming for a balanced performance that integrates strong mechanical properties with improved bioactivity.[14] These efforts contribute to the material's adaptability across diverse medical applications.[15]

However, enhancing cellular attraction on implant surfaces inherently increases the susceptibility to bacterial adhesion. Consequently, the imperative consideration of incorporating antimicrobial features into implant surfaces is crucial, especially when fostering osseointegration.[1,16] Improved osteoblast adhesion and maturation have been achieved with additively manufactured solid and mesoporous PEEK materials for spinal cage applications[17,18]—currently, there are no cages that exhibit antibacterial properties. Moreover, there is a continuing unmet clinical need for biomaterials employed in spinal cages that promote osseointegration, prevent bacterial growth, withstand *in vivo* loading, and facilitate efficient medical imaging—factors that are crucial for the performance of the implant.

Among spinal cages, the ceramic silicon nitride (Si_3N_4), also known as as-fired-silicon-nitride (AFSN), has shown very few infections in the clinical arena.[19] *In vitro,* Si_3N_4 shows decreased bacterial colonization compared to other commonly used materials and supports osteoblast maturation and mineralization.[20] Si_3N_4 is radiolucent and exhibits longevity, but like all ceramic materials, it exhibits high elastic modulus, raising concerns about possible stress shielding and brittle fracture in cases where the device experiences significant non-compressive loading.[21] To overcome these concerns, we explored the use of PEEK/Si_3N_4 composites. We hypothesize that this composite material will possess the osseointegrative and antimicrobial properties of Si_3N_4 while maintaining the mechanical properties and ductility of PEEK. Accordingly, we assessed the potential suitability of composite Si_3N_4-PEEK materials for fabricating 3D-printed cervical cages. Specifically, we sought to address the following questions: (i) Will 3D-printed Si_3N_4-PEEK cervical cages have the strength of conventional cages? (ii) Will 3D-printed Si_3N_4-PEEK composites exhibit antimicrobial properties? (3) How 3D-printed Si_3N_4-PEEK composites affect the *in vitro* cell response for osseointegration?

2. Methods

2.1. Si_3N_4-PEEK cages and 3D printing

Cervical spinal cages utilized in this study were initially designed using Solidworks (2021, Dassault Systèmes, France) (see **Figure S1** in Supplementary File). Subsequently, porous sections were designed and incorporated using nTopology (2021, Dassault Systèmes, France) with pore size ranging between 700 and 800 microns. Cages were created using fused filament fabrication (FFF) technology by a third-generation medical 3D printer (Kumovis R1, Munich, Germany) (Figure 1; **Table S1** in Supplementary File). The PEEK and Si_3N_4-PEEK filaments (1.75 mm) used in 3D printing of cervical cages were produced by Orthoplastics (Lancashire, UK). PEEK resin was provided by Solvay (Zeniva®, Brussels, Belgium), and 15% volume submicron sintered β-Si_3N_4 powder (Flex-SN, SINTX Technologies, Salt Lake City, UT, USA) was compounded (Foster Corp., Putnam, CT, USA) with the PEEK resin to produce the composite resin used for the Si_3N_4-PEEK filament. The cages were printed in the upright position (Figure 1) to demonstrate the worst-case scenario, emphasizing the weakest layer adhesion for mechanical testing.

2.2. Mechanical testing

2.2.1. Compression and compression shear

Tests were conducted on an Instron 5567 system (Instron, Norwood, MA) equipped with calibrated load and displacement sensors, with a load cell capacity of 30 kN for both compression and compression shear tests. A strain rate of 25 mm/min was chosen as per ASTM F2077,[22] and load–displacement curves were plotted using the data (**Figure S2** in Supplementary File). Stiffness values were calculated from the curves using a custom script in MATLAB 2021b, using the recommendations in ASTM F2077[22] as a guide.

2.2.2. Torsion

Prior to and after mechanical testing, each cage underwent imaging using a digital microscope (VHX-7000, Keyence). The experiments were performed utilizing an Instron 8874 system (Instron, Norwood, MA) fitted with calibrated load and displacement sensors, with a load cell capacity of 100 N·m for torque tests. Torsion tests were carried out at 60°/min, as per the ASTM 2077[22] recommendations, with a preloading force of 500 N applied to the cages (**Figure S3** in Supplementary File).

Torque–angle curves were plotted from the data. Stiffness, yield moment, and ultimate moment values

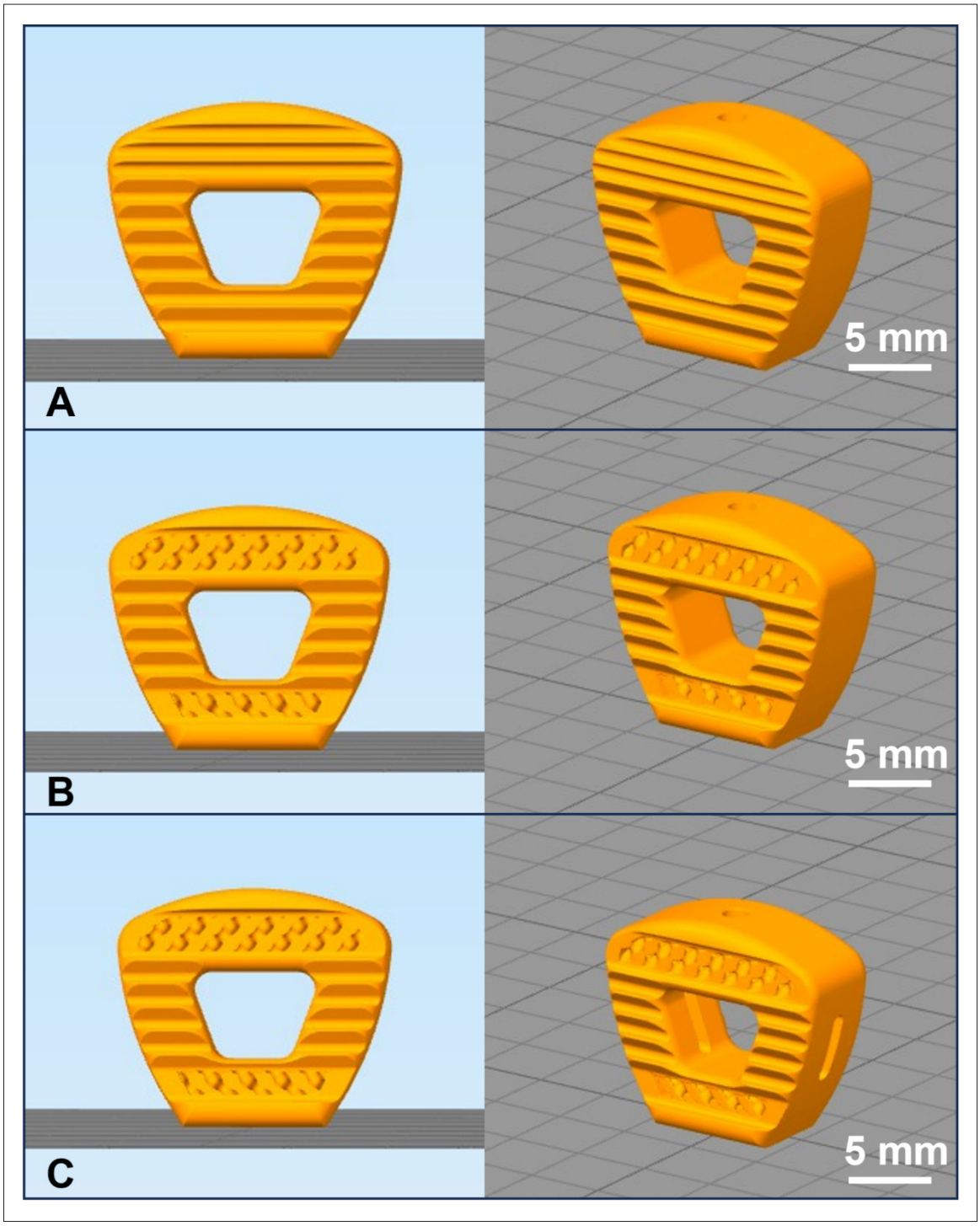

Figure 1. Design of 3D-printed cervical cages: solid (A), porous where top and bottom sections have porous structures (B), and porous window design with an additional window on the sides (C). Front views are shown on the left and isometric views on the right.

were calculated from the curves using a custom script in MATLAB 2021b, using the recommendations in ASTM F2077[22] as a guide. To calculate the yield moment, offset angular displacement (OAD) was calculated as "3.02°" in Equation I, defined by the standard. The offset on the angular displacement axis is calculated as 10% of the intradiscal height ($H_{intradiscal}$) divided by the implant height ($H_{implant}$), multiplied by a constant.

$$OAD = \frac{H_{intradiscal} \times 0.1 \times 180^{\circ}}{H_{implant} \times \pi}$$

The normality of the data distributions was assessed by applying the Shapiro–Wilk test. Groups were compared via analysis of variance (ANOVA), followed by a post-hoc Tukey Honest Significant Difference Test. Furthermore, a 2 × 3 factorial ANOVA was conducted to evaluate the primary effects of material (PEEK vs. Si_3N_4-PEEK) and design (Solid, Porous, and Porous Window). All statistical analyses were performed with a commercially available software program (SPSS version 28), using an alpha level of 0.05.

2.3. Antibacterial testing

2.3.1. Antibacterial adhesion

PEEK, Si_3N_4-PEEK, and AFSN rods (1.75 × 12 mm) were prepared, with AFSN acting as a positive control due to its demonstrated antimicrobial effect *in vivo* and it being the pure form of the antimicrobial component of the Si_3N_4-PEEK composite material.[21] Rods were placed in 10% human serum, 1 × phosphate-buffered saline (PBS), and 7 mg/mL dextrose (48-well plate, n = 6/condition) and inoculated with 10^3, 10^4, or 10^5 colony-forming units per milliliter (CFU/mL) of *Staphylococcus epidermidis* (ATCC 14990). Samples were incubated at 37°C and 95 rpm for 24 h, aseptically removed, gently rinsed 3 times in PBS, and placed in 10% trypsin[23] to release adherent bacteria from the material surface. Serial dilutions were plated on 3M™ Petrifilms™, and colonies were then counted (countable range 20–300 CFU). Each antimicrobial experiment was independently performed 3 times and also repeated under the same conditions for *Escherichia coli* (ATCC 25922). Statistical significance was tested using a Kruskal–Wallis test (Prism v9, GraphPad, 2020).

2.3.2. Scanning electron microscopy

Scanning electron microscopy (SEM) samples were prepared by aseptic removal of samples, gentle rinsing in PBS, fixing with 4% paraformaldehyde for 20 min, followed by serial dehydrations (10 min in PBS, 20% ethanol, 40% ethanol, 60% ethanol, 80% ethanol, and 100% ethanol). Samples were dried overnight, sputter-coated in 80/20 Pt/Pd, and imaged by SEM (Zeiss Supra 50VP).

2.4. Cell culture

PEEK, Si_3N_4-PEEK, AFSN, and Ti6Al4V samples (10 × 10 × 1 mm^3) were prepared, with Ti6Al4V acting as a positive control due to its interaction with osteoblast-like cells being well-studied, and it is known to support osseointegration *in vivo*.[24] Samples were sterilized by sonicating in 70% ethanol for 30 min, transferred to a sterile environment, soaked 3 times in 70% ethanol for 30 min, and dried overnight in the biological safety cabinet. Samples were pre-incubated for 24 h in Minimum Essential Medium α (MEM α, Gibco) supplemented with 10% fetal bovine serum (FBS; Gibco) and 1% penicillin–streptomycin (Gibco) in ultra-low attachment plates (Corning) followed by seeding with 30,000 MC3T3-E1 mouse preosteoblasts (ATCC CRL-2593); tissue culture plastic (Corning) served as a positive control. Mouse preosteoblasts were chosen because they faithfully recapitulate the molecular events that occur during osteoblast maturation and can be compared to existing work due to their immortalized nature.[25,26] After 7 days of incubation, cell culture media were supplemented with 5 mM β-glycerophosphate (Sigma-Aldrich) and 50 μg/mL L-ascorbic acid (Sigma-Aldrich) to promote mineralization. To evaluate short-term cell attachment and proliferation, BioVision's MTT Cell Proliferation Assay Kit was used after 24 and 72 h. To evaluate osteogenic activity, a combined approach described by Wilkesmann, Westhauser, and Fellenberg was used to simultaneously determine cell number with fluorescein-diacetate (FDA) and alkaline phosphatase activity with 4-methylumbelliferone-phosphate (4-MUP) after 7, 14, and 21 days.[27] Mineralization was measured by staining with 2% alizarin red stain after 21 and 28 days and visualized, and then the stain was dissolved in 20% methanol and 10% acetic acid in deionized water, followed by spectrophotometric quantitation (λ = 405 nm, TECAN Infinite M200).

Statistical significances for each set of results were evaluated by ANOVA, followed by a post-hoc Tukey's multiple comparisons test (n = 6, α = 0.05, Prism v9, GraphPad, 2020).

3. Results

3.1. Si_3N_4-PEEK cages and 3D printing

A total of five cages per group of solid, porous, and porous window designs for PEEK and Si_3N_4-PEEK were 3D-printed and examined for structural integrity (Figure 2). Furthermore, weight measurements were conducted for each group of cages to identify outliers, addressing the possibility of any infill/extrusion issues (**Table S2** in Supplementary File).

3.2. Mechanical testing

3.2.1. Compression and compression shear

For compression, force–displacement curves of the cages that were tested above the 5th percentile ultimate force (6236 N)[28] were plotted. For each group, the first linear regions were defined separately, and the stiffness (Table 1) was computed by determining the slope of the linear region for each sample.

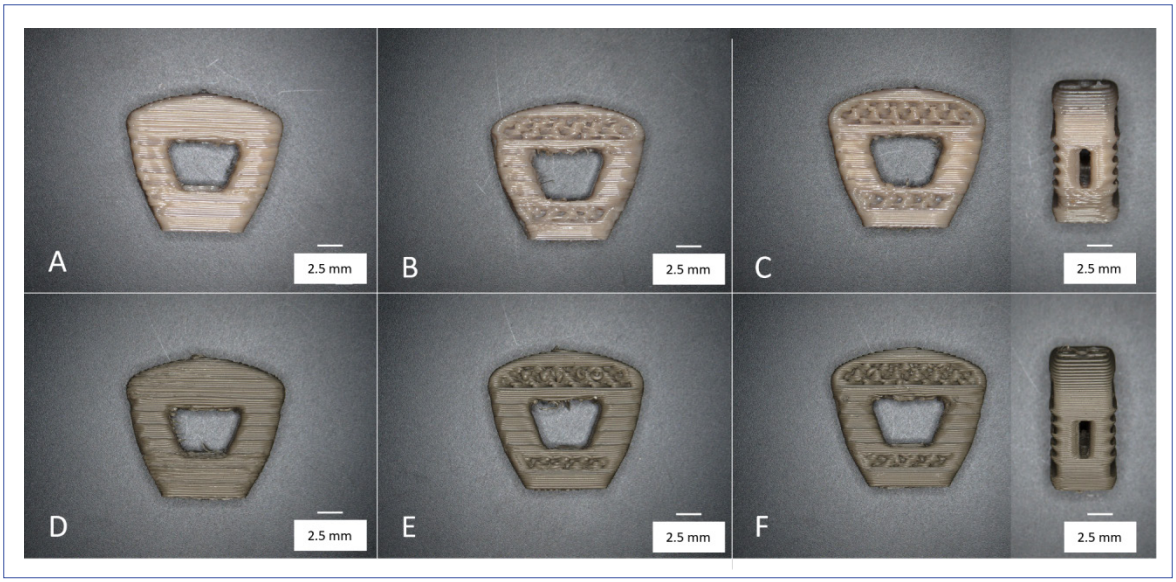

Figure 2. Sample cages that were 3D-printed for mechanical testing. Solid (A, D), porous (B, E), and porous window (front and side views) (C, F) designs for PEEK (A, B, C) and Si_3N_4-PEEK (D, E, F) materials.

The data demonstrated a normal distribution for the majority of the groups (four out of six). According to 2 × 3 factorial ANOVA, design was significantly affecting the stiffness under compression ($p < 0.001$). The stiffness of the porous design was significantly higher than the solid design (mean difference = 6185 N/mm, $p < 0.001$) and the porous window design (mean difference = 1606 N/mm, $p = 0.01$). The stiffness of the porous window design was also significantly higher than the solid design (mean difference = 4579 N/mm, $p < 0.001$). When stiffness was examined as a function of material, the main effect was not significant in stiffness of the cages as well as the interaction between material and design.

In addition to the main effects, the group comparisons between PEEK and Si_3N_4-PEEK and the designs were analyzed (Figure 3).

There was no significant difference in stiffness between PEEK and Si_3N_4-PEEK per design (Figure 3A). The compression stiffness of PEEK porous and porous window designs was significantly higher than that of the solid design (mean difference = 5622 and 4277 N/mm respectively, $p < 0.001$ for both). Similarly, for Si_3N_4-PEEK, porous and porous window designs achieved higher compression stiffness than solid design (mean difference = 6748 and 4881 N/mm respectively, $p < 0.001$ for both) (Figure 3B). In addition to surpassing the 5th percentile of ultimate strength loading,[28] porous window designs for both PEEK and Si_3N_4-PEEK materials were tested above 50th percentile of ultimate compression strength defined by Peck et al.[28] (10,800 N) (**Table S3** in Supplementary File). Furthermore, solid and porous designs for both PEEK and Si_3N_4-PEEK materials were tested above 75th

Table 1. Mechanical testing metrics calculated for cages

	PEEK solid	PEEK porous	PEEK porous window	Si_3N_4-PEEK solid	Si_3N_4-PEEK porous	Si_3N_4-PEEK porous window
Compression stiffness (N/mm)	7886 ± 1771	13508 ± 918	12163 ± 388	6911 ± 1053	13659 ± 997	11791 ± 2032
Shear stiffness (N/mm)	3171 ± 580	4052 ± 1291	3793 ± 1011	4482 ± 235	5501 ± 517	4587 ± 816
Torsional stiffness (Nm/deg)	0.48 ± 0.08	0.36 ± 0.05	0.36 ± 0.04	0.60 ± 0.11	0.47 ± 0.09	0.45 ± 0.07
Yield moment (N·m)	8.27 ± 0.45	5.29 ± 0.52	4.77 ± 0.26	10.5 ± 0.60	6.90 ± 0.65	5.49 ± 1.07
Ultimate moment (N·m)	8.86 ± 0.60	5.82 ± 0.28	5.45 ± 0.13	11.4 ± 0.37	7.76 ± 0.21	6.49 ± 1.05

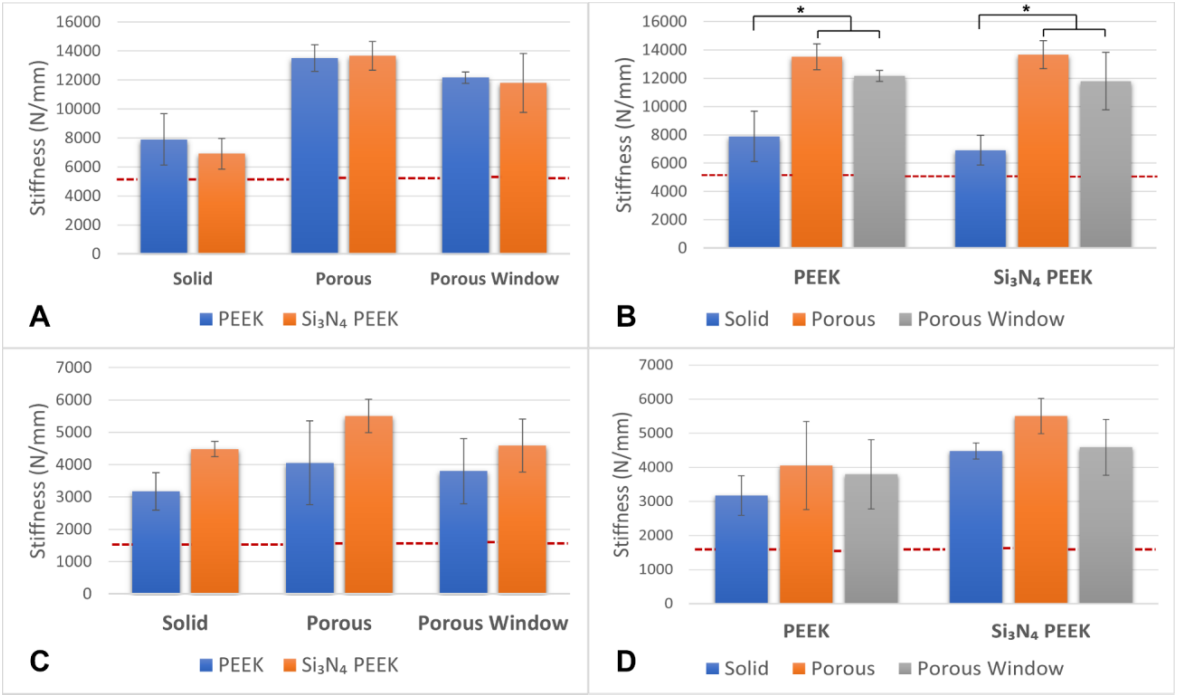

Figure 3. Comparison in stiffness between PEEK and Si_3N_4-PEEK per solid, porous, and porous window designs: compression (A, B) and compression shear (C, D). Dotted line indicates the 5th percentile stiffness as per Peck et al.[28] without shear in the beginning.

percentile of ultimate compression strength defined by Peck et al.[28] (14,728 N) (**Table S3** in Supplementary File).

For compression shear tests, the cages were tested above the 5th percentile ultimate shear force (1515 N).[28] The force–displacement curves were plotted for each sample. Data were normally distributed for all groups. According to 2 × 3 factorial ANOVA, the main effect of material was significantly affecting the shear stiffness ($p < 0.001$). Si_3N_4-PEEK cages had significantly higher stiffness than PEEK cages (mean difference = 1185 N/mm, $p < 0.001$). The main effect of the design was observed within the borderline significance level ($p = 0.049$). The porous design's shear stiffness was slightly higher than the solid design's stiffness (mean difference = 950 N/mm, $p = 0.04$). Finally, the interaction between the main effects (material and design) was not significant.

In addition to the main effects, the group comparisons between PEEK and Si_3N_4-PEEK and the designs were analyzed (Figure 3). There was no significant difference in shear stiffness between PEEK and Si_3N_4-PEEK per design (Figure 3C). Similarly, the shear stiffness between the designs for both PEEK and Si_3N_4-PEEK was not significantly different (Figure 3D). In addition to 5th percentile of ultimate shear strength loading,[28] porous window designs for PEEK were tested above 50th percentile of ultimate shear strength defined by Peck et al.[28] (4626 N) (**Table S3** in Supplementary File). Furthermore, solid and porous designs for both PEEK and Si_3N_4-PEEK materials and porous window design of Si_3N_4-PEEK were tested above 75th percentile of ultimate shear strength defined by Peck et al. (6868 N) (**Table S3** in Supplementary File).

3.2.2. Torsion

For torsion tests, the cages were tested until failure according to ASTM F2077[22] (Figure 4).

The torque–angle curves were plotted for each sample. For each sample, ultimate moment, yield moment, and stiffness values were calculated from the graphs (Table 1).

Torsional stiffness data were normally distributed for all the groups. According to 2 × 3 factorial ANOVA, both main effects (material and design) significantly affected the torsional stiffness of cages ($p = 0.001$ and $p < 0.001$, respectively). Si_3N_4-PEEK cages had significantly higher torsional stiffness than PEEK cages (mean difference = 0.10 Nm/deg, $p = 0.001$). Cages with the solid design achieved the highest torsional stiffness and that was significantly higher than the cages with the porous and porous window design (mean difference = 0.13 and 0.14 Nm/deg, $p = 0.004$ and $p = 0.002$, respectively). Finally, the interaction between the main effects (material and design) was not significant.

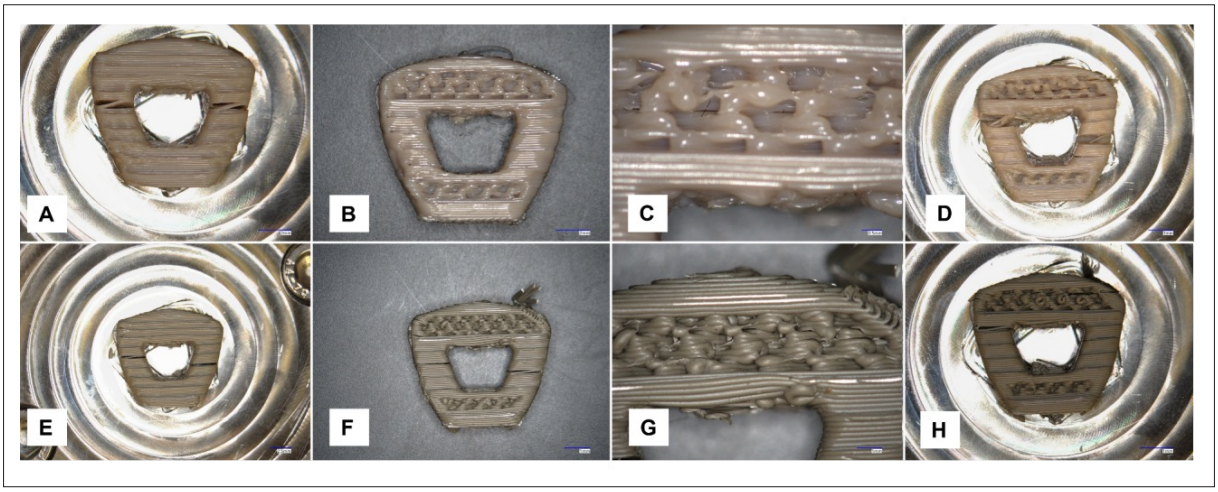

Figure 4. Samples after torsion testing: PEEK solid (A), porous (B, C), and porous window (D) designs, Si_3N_4-PEEK solid (E), porous (F, G), and porous window (H) designs. Close-up views of porous sections are shown in (C) and (G).

In addition to the main effects, the group comparisons between PEEK and Si_3N_4-PEEK and the designs were analyzed. The difference between PEEK and Si_3N_4-PEEK cages' stiffness was not significant per design (Figure 5A). In the comparison of designs, it was observed that the stiffness of Si_3N_4-PEEK solid cages was slightly greater than that of Si_3N_4-PEEK porous window cages (mean difference = 0.16 Nm/deg and $p = 0.04$) (Figure 5B).

Yield moment data were normally distributed for all the groups. According to 2 × 3 factorial ANOVA, both main effects (material and design) significantly affected the yield moment of cages ($p = 0.001$ and $p < 0.001$, respectively). Si_3N_4-PEEK cages had significantly higher yield moment than PEEK cages (mean difference = 1.52 N·m, $p < 0.001$). Cages with the solid design achieved the highest yield moment and that was significantly higher than that of the cages with porous and porous window design (mean difference = 3.29 and 4.26 N·m, respectively, $p < 0.001$ for both). In addition, porous design's yield torque was significantly higher than the porous window design (mean difference = 0.97 N·m, $p = 0.002$). Finally, the interaction between the main effects (material and design) was small but significant ($p = 0.04$).

In addition to the main effects, the group comparisons between PEEK and Si_3N_4-PEEK and their designs were analyzed (Figure 5C and D). Si_3N_4-PEEK cages demonstrated higher yield moment than PEEK cages both for solid and porous designs (mean difference = 2.24 and 1.61, $p < 0.001$ and $p = 0.007$, respectively) (Figure 5C). For PEEK, solid cages, yield moment was higher than both porous and porous window cages (mean difference = 2.97 and 3.49 N·m, respectively, $p < 0.001$). Similarly, Si_3N_4-PEEK solid cages demonstrated higher yield torque than both Si_3N_4-PEEK porous and porous window cages (mean difference = 3.60 and 5.02, respectively, $p < 0.001$). Additionally, porous window design had lower yield torque compared to porous design of Si_3N_4-PEEK cages (mean difference = 1.42 N·m, $p = 0.02$) (Figure 5D).

Ultimate moment data were normally distributed for the majority of the groups (five out of six). According to 2 × 3 factorial ANOVA, both main effects (material and design) significantly affected the ultimate moment of cages ($p < 0.001$). Si_3N_4-PEEK cages had significantly higher ultimate moment than PEEK cages (mean difference = 1.83 N·m, $p < 0.001$). Cages with the solid design achieved the highest ultimate torque and that was significantly higher than that of the cages with the porous and porous window design (mean difference = 3.32 and 4.14 N·m respectively, $p < 0.001$ for both). In addition, porous design's ultimate torque was significantly higher than that of the porous window design (mean difference = 0.82 N·m, $p = 0.002$). Finally, the interaction between the main effects (material and design) was small but significant ($p = 0.02$).

In addition to the main effects, the group comparisons between PEEK and Si_3N_4-PEEK and the designs were analyzed (Figure 5E and F). Si_3N_4-PEEK cages of both solid and porous designs showed significantly higher ultimate moment than PEEK cages (mean difference = 2.49 and 1.95 N·m, $p < 0.001$) (Figure 5E). For PEEK, solid cages' ultimate moment was higher than both porous and porous window design cages (mean difference = 3.05 and 3.41, respectively, $p < 0.001$ for both). Similarly, Si_3N_4-PEEK solid cages demonstrated higher ultimate torque than both Si_3N_4-PEEK porous and porous window cages (mean difference = 3.59 and 4.87, respectively, $p < 0.001$ for both). Additionally, porous window design caused lower ultimate

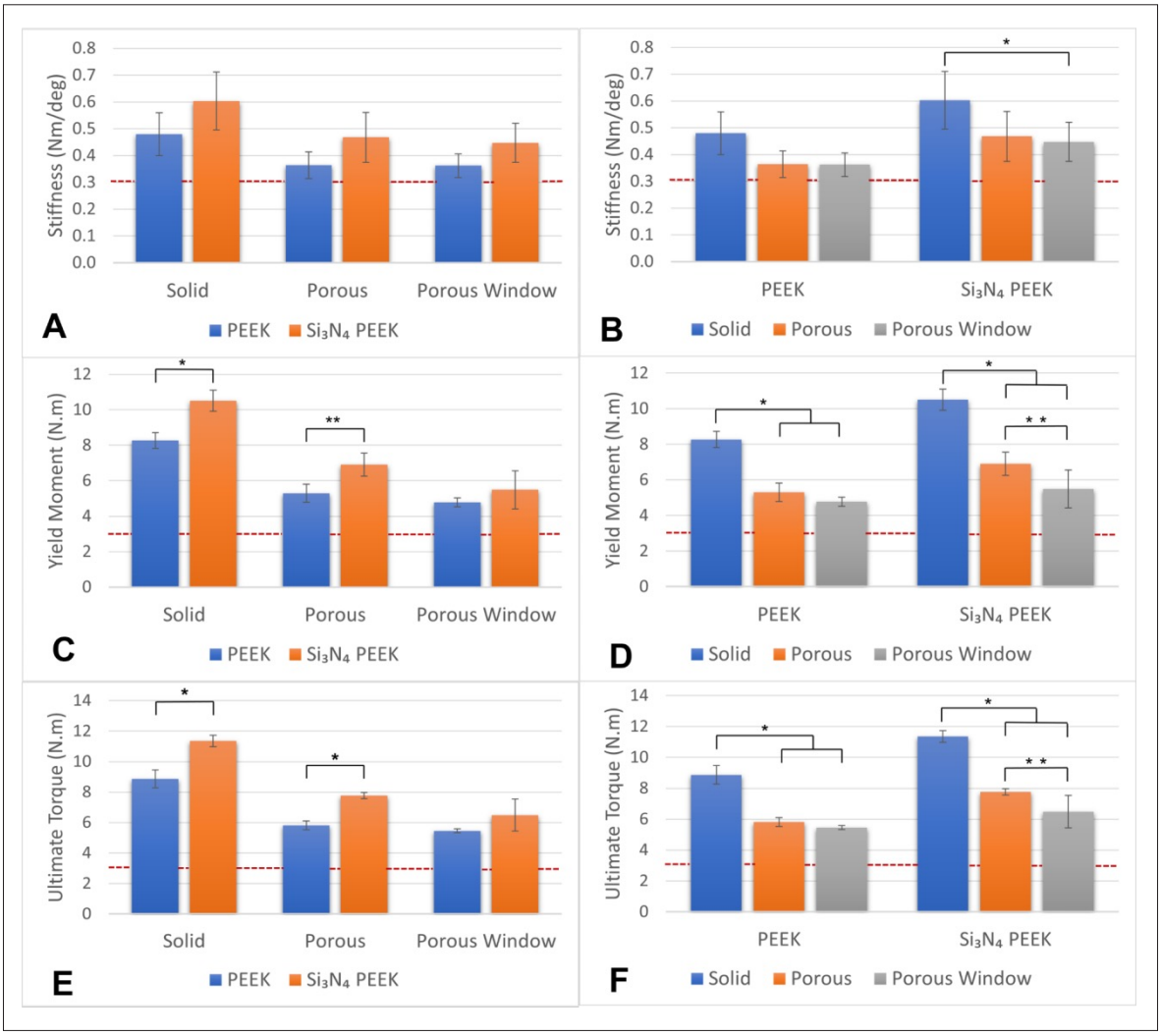

Figure 5. Comparison between PEEK and Si_3N_4-PEEK designs: torsional stiffness (A, B), yield moment (C, D), and ultimate torque (E, F). (A, C, E) Comparison based on the material. (B, D, F) Comparison based on the designs across the same material. Dotted line indicates the 5th percentile as per Peck et al.[28]

torque compared to porous design for Si_3N_4-PEEK cages (mean difference = 1.26 Nm, $p = 0.01$) (Figure 5F).

3.3. Antibacterial testing

Because Si_3N_4 has been reported to possess antibacterial activity, we tested the ability of the different materials to inhibit bacterial adhesion, expressed as colony-forming units per milliliter (CFU/mL). For each level of inoculum and for both *S. epidermidis* and *E. coli*, AFSN samples consistently had the lowest numbers of adherent bacteria, indicating the greatest overall antimicrobial effect (Figure 6). Si_3N_4-PEEK consistently showed greater antibacterial activity than pure PEEK samples ($p < 0.05$), but less antibacterial activity when compared to pure Si_3N_4 ($p < 0.05$).

When incubated with *S. epidermidis*, Si_3N_4-PEEK samples showed a 1.02, 1.21, and 1.22 log reduction for starting inocula of 10^3, 10^4, and 10^5 CFU/mL, respectively, as compared to PEEK samples. For *E. coli*, mean log reductions were 1.10, 1.45, and 1.66. When all groups were pooled, the average mean log reduction for Si_3N_4-PEEK compared to PEEK was 1.28. Representative SEM micrographs of *S. epidermidis* and *E. coli* on Si_3N_4-PEEK samples are shown in Figure 6C and D.

3.4. Osteogenic activity of cells cultured on different substrates

MTT assay was used to quantify short-term cell proliferation of the mouse preosteoblasts on each surface (Figure 7). Absorbance results for each group were normalized to a known number of cells to determine the approximate number of cells on each surface. The number of cells for each group was significantly different

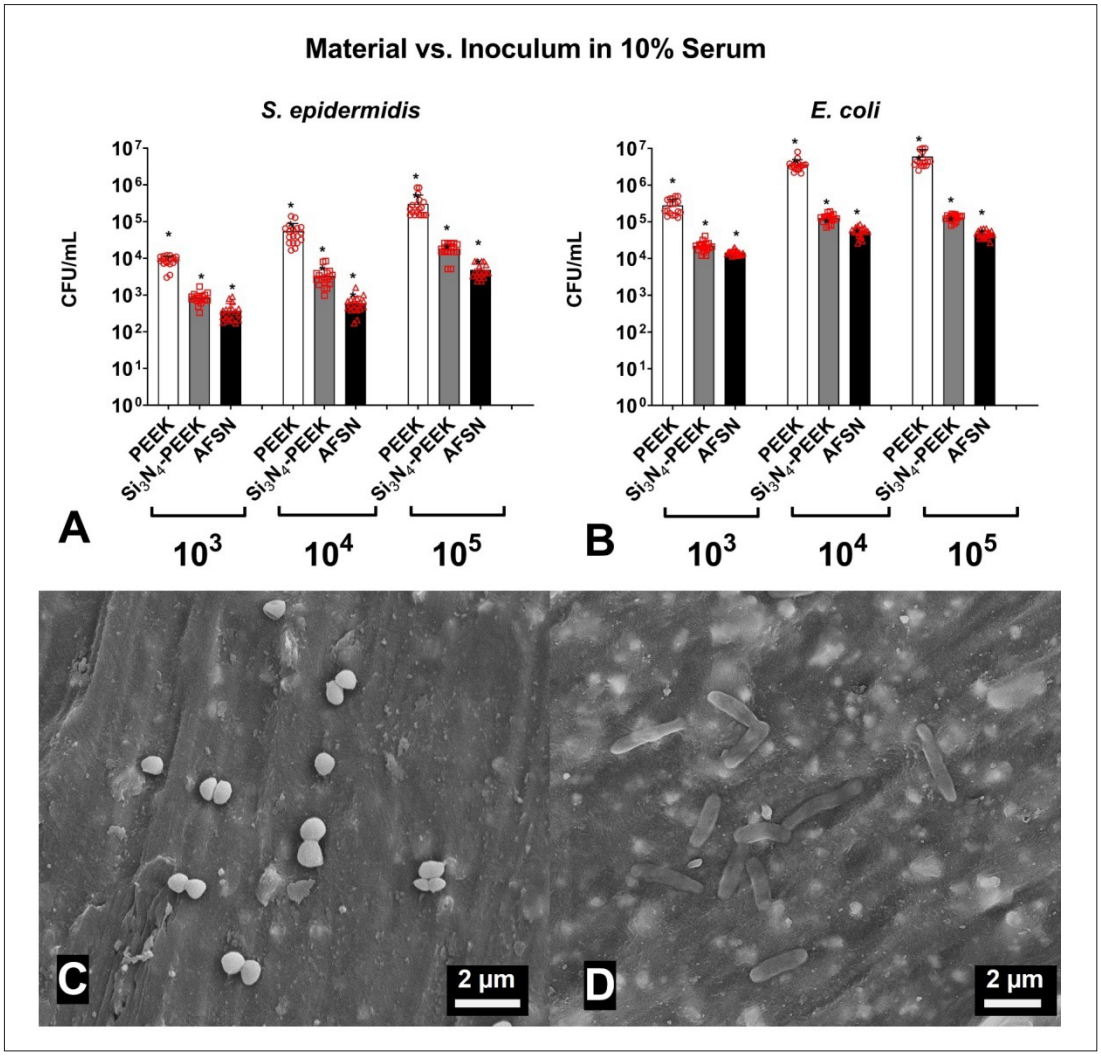

Figure 6. Effects of inoculum and material on bacterial colonization. Number of colony-forming units per milliliter for *S. epidermidis* (A) and *E. coli* (B) for PEEK, Si_3N_4-PEEK, and AFSN materials. Scanning electron micrographs of *S. epidermidis* (a gram-positive bacterium that grows in grape-like clusters) (C) and *E. coli* (a gram-negative bacterium with a rod-like structure) (D) on Si_3N_4-PEEK samples after 24 h.

from each other at both 24 h ($p < 0.01$) and 72 h ($p < 0.05$). At both time points, Si_3N_4-PEEK surfaces showed higher cell proliferation when compared to PEEK and AFSN (Figure 7A and B). Ti6Al4V (control group), a titanium alloy commonly used in orthopedic implants, had the highest average number of cells overall at both time points.

Normalized osteogenic activity was determined by dividing the alkaline phosphatase activity determined with 4-MUP, by cell number determined by an FDA stain assay. After 7 days, there was no significant difference in osteogenic activity between any surfaces; however, this result was expected due to the mineralization media not being introduced until after this time point. On day 14, the PEEK group had significantly less osteogenic activity when compared to all other groups at this time point, and Si_3N_4-PEEK performed similarly to AFSN. The Ti group had the highest overall average osteogenic activity at this time point. On day 21, PEEK was not significantly different from tissue culture plastic (TCP), the group with the lowest average normalized osteogenic activity. Normalized osteogenic activity was significantly increased for Si_3N_4-PEEK when compared to PEEK, and significantly increased for AFSN when compared to Si_3N_4-PEEK. The Ti had significantly more osteogenic activity than all other groups at this time point (Figure 7C).

Alizarin Red binds to calcium and can be used to quantify cumulative mineralization of cell culture samples. After 21 days, Si_3N_4-PEEK had significantly more Alizarin Red stain than all other groups ($p < 0.05$), indicating the

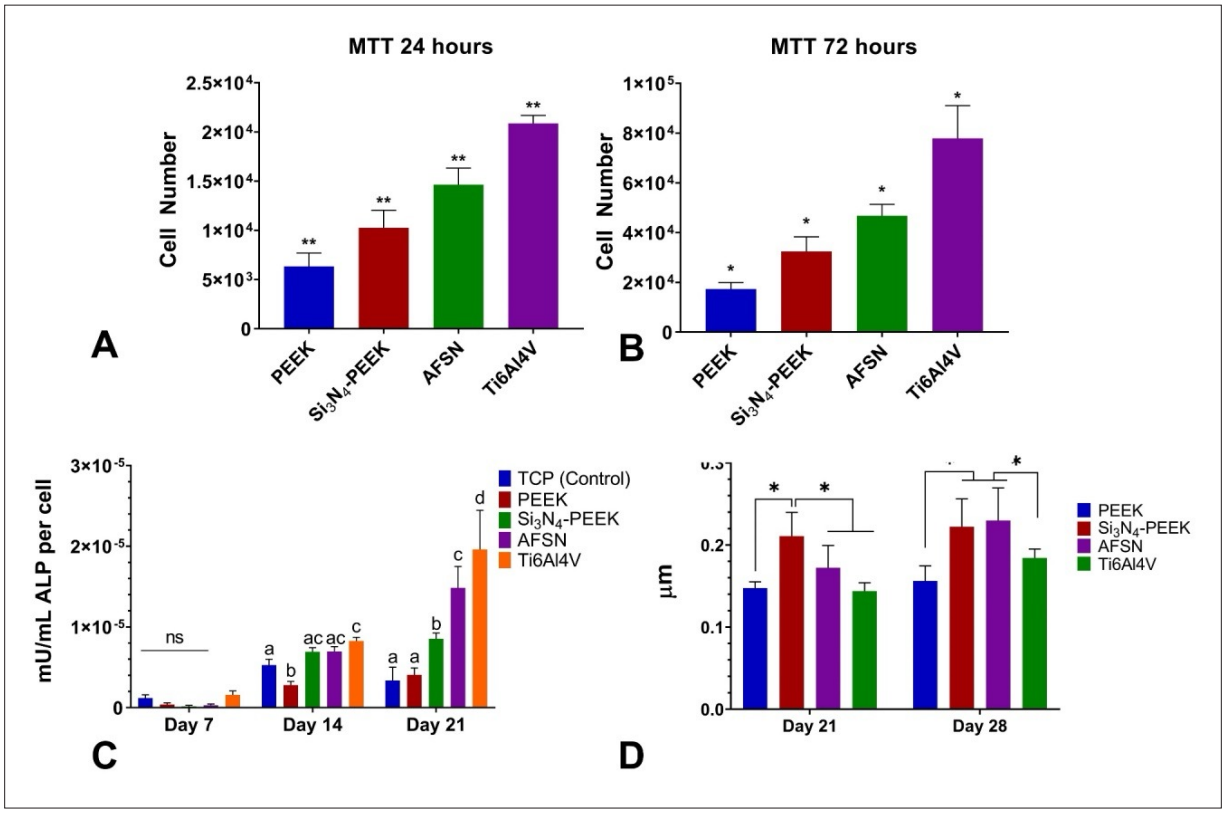

Figure 7. Comparison of cell number via MTT assay at 24 h (A) and 72 h (B) on PEEK, Si_3N_4-PEEK (SN-PEEK), as-fired silicon nitride (AFSN), and Titanium (Ti) alloy (Ti6Al4V). (C) Comparison of normalized osteogenic activity between control group, PEEK, Si_3N_4-PEEK, AFSN, and Ti for each time point; groups sharing the same letter are not significantly different from each other ($p < 0.05$). (D) Cumulative mineralization on PEEK, Si_3N_4-PEEK, AFSN, and Ti surfaces at days 21 and 28.

highest amount of cumulative mineralization. After 28 days, there was no significant difference between the Si_3N_4-PEEK and AFSN groups, but both of these groups had significantly more Alizarin Red stain than the PEEK and Ti groups ($p < 0.05$) (Figure 7D).

4. Discussion

Infection represents a significant risk factor contributing to spinal implant failures, underscoring the critical need for biomedical materials possessing not only excellent mechanical and pro-osteogenic characteristics but also robust antimicrobial properties. A composite material comprising Si_3N_4-PEEK holds the potential to allow fabrication of customized 3D-printed spinal implants, with the additional benefit of being mildly antimicrobial, a property that contemporary implant materials like unfilled PEEK and metal alloys do not possess. Mechanically, the 3D-printed PEEK and Si_3N_4-PEEK cages exhibited a gradual yielding behavior across all designs. Notably, the mean strength of the generic 3D-printed cage designs exceeded the 75th percentile benchmarks established by Peck et al.,[28] registering at 14.7 kN in compression and 6.9 kN in compression shear. In terms of biological activity, the Si_3N_4-PEEK material demonstrated a 93.9% reduction (~1.2 log or 12-fold) in bacterial adhesion when compared to PEEK ($p < 0.01$). Significantly higher cell proliferation was observed on Si_3N_4-PEEK as compared with PEEK, indicating its bio- and osteocompatibility of Si_3N_4-PEEK. In keeping with osteocompatibility, the cumulative mineralization of cell culture samples was higher on Si_3N_4-PEEK samples than on PEEK.

Several limitations to the current study should be recognized. The mechanical results obtained in this study are linked to the specific setup of the printer and the consistent temperature conditions utilized during the research. It is reasonable to anticipate that alterations in the printer's setup or adjustments in its configurations, as well as variations in temperature conditions, could lead to different effects on the mechanical properties and porosity of 3D-printed PEEK cages, which might differ from those observed in this study. The incorporation of Si_3N_4 into PEEK was constrained by the extrusion capabilities and filament condition required for successful fused filament fabrication of the cages and specimens utilized

in this study. Another limitation was that our antibacterial testing concentrated on *S. epidermidis* and *E. coli*, which might not encompass the full spectrum of potentially relevant pathogens. Furthermore, although we assessed cell proliferation and osteogenic activity using mouse preosteoblasts, these cells show only weak osteoblastic cell activity, and the interactions will best be determined in studies that place the implants into bone defects.

Previously, Peck et al.[28] investigated the mechanical performance of cervical cages that were submitted to the Food and Drug Administration (FDA), and they included unique materials other than metal and PEEK. Using these data as benchmarks, our results showed that all the designs with both materials (Si_3N_4-PEEK and PEEK) achieved more than 5th percentile stiffness under all three forces. In addition, cages were tested above 50th percentile of ultimate compression and compression shear strength defined by Peck et al.[28] Furthermore, the cervical cages examined in this study surpassed 104% of the ultimate load capacity in compression and exhibited over 3 times the shear strength compared to machined cages previously reported in the literature.[17] While the primary goal of incorporating Si_3N_4 into PEEK was to enhance its antibacterial properties, it was notable that this process resulted in an increased torsional strength of the cages.

Contrastingly, the stiffness of solid cages was found to be lower than that of porous designs under compression and shear. This unexpected result may be attributed to varying loading mechanisms, which necessitate testing in compression, shear, and torsion, as mandated by ASTM standards for cages.[22] The current study focused on the worst-case scenario, emphasizing the critical role of layer bonding in interpreting results. The lower stiffness observed in solid cages under compression and shear forces was unforeseen. The 3D printer used in the study employed an additional cooling setting, partially activated to facilitate inter-layer cooling for subsequent layers. Excessive cooling, however, could compromise layer adhesion. The porous sections, having less material and shorter cooling times, may have exhibited better adherence under similar cooling conditions than their solid counterparts. This phenomenon is less pronounced in torsion testing, where the unique loading conditions involve layer compression up to 500 N, followed by layer twisting, favoring solid layers. This underscores the significance of carefully controlling printing conditions when working with PEEK implants.

There exist differing opinions regarding the incorporation of ceramics into PEEK. Some studies suggest an increase[29,30] while others have demonstrated a decrease in strength.[31,32] Research indicating increased strength implies the ability of polymer–ceramic matrix to endure higher loads, effectively transferring some stress from polymer to ceramic and leveraging on the ceramic's higher strength.[33] Conversely, discussions on strength reduction highlight concerns about the limited interfacial interaction between the polymer and ceramic.[34] It is crucial to acknowledge that factors such as volume content, microstructure, chemical composition, ceramic properties, and the bonding between PEEK and ceramic play pivotal roles in simultaneously enhancing mechanical strength.[29] In our study, Si_3N_4-PEEK cages showed higher torsional strength than PEEK cages. Regarding the designs, solid cages achieved the highest torsional strength, and porous cages were stronger than porous cages with windows. In a similar manner, Fogel et al.[35] investigated the design influence on mechanical performance of spinal cages and indicated higher stiffness for solid design.

Previous studies investigated Si_3N_4[19,20,36] and Si_3N_4-PEEK[37-39] for their ability to enhance the biological activities of PEEK-based implants—including maturation of osteoblasts and antimicrobial activity.[20,39] Gorth et al. found decreased biofilm formation as well as fewer live bacteria on both the as-fired (AFSN) and polished Si_3N_4 compared with PEEK and titanium surfaces.[20] In a companion *in vivo* study, Webster et al.[19] observed improved osseointegration for Si_3N_4 samples relative to PEEK and Ti6Al4V implanted into rat calvaria wound sites contaminated with *S. epidermidis*. Bock et al.[36] showed similar results *in vitro* using a human plasma-based inoculum with *S. epidermidis* and *E. coli* exposed to a range of surface-modified Si_3N_4 materials. Pezzotti et al.[37] found that incorporating 15 vol.% coarse (approx. 50–250 μm) Si_3N_4 into PEEK led to improved proliferation and mineralization of SaOS2 cells in addition to a 1-$\log_{10}$ reduction in adherent *S. epidermidis* relative to monolithic PEEK following a 24-h exposure *in vitro*. Marin et al.[38] observed increased alkaline phosphatase activity and mineralization of KUSA-A1 mesenchymal stem cells exposed to the same coarse, 15 vol.% Si_3N_4-PEEK composite relative to monolithic PEEK, but cell proliferation was not improved. It was hypothesized that the large regions of PEEK between the coarse silicon nitride particles were responsible for this lack of improvement since Si_3N_4 is thought to act at short distances, very near its surface, through the products of hydrolysis reactions. This observation, along with 3D printing requirements, led to the modification of the powder feedstock used for the composite in this study to obtain a submicron size distribution. Hu et al.[39] demonstrated the potential of Si_3N_4-PEEK in biomedical applications as it exhibited osteogenic and antibacterial activities. Our findings clearly showed that a 3D-printed Si_3N_4-PEEK composite was able to achieve a significant reduction in numbers of adherent bacteria, with slightly greater activity against gram-negative bacteria. This latter finding is of importance as these microorganisms are

the most common causes of deep infections.[40] It is probable that increased antimicrobial properties could be achieved with higher concentrations of Si_3N_4, but these increases will need to be balanced with the composite material's ability to be 3D-printed and the effects on mechanical properties as the Si_3N_4 concentration probes or exceeds the percolation threshold.

In addition to reduced bacteria activity, Si_3N_4 coating onto PEEK surfaces was shown to promote cell responses *in vitro* and improve osseointegration *in vivo.*[41,42] The application of Si_3N_4 coating led to increased adhesion, proliferation, differentiation, and osteoblast gene expression using MC3T3-E1 cells *in vitro*. Moreover, the bioactive Si_3N_4 coating on PEEK facilitated bone regeneration and enhanced osseointegration *in vivo.*[41] Hu et al.[42] found that Si_3N_4-coated PEEK significantly enhanced the adhesion, proliferation, differentiation, and expression of osteogenesis-related genes in rat bone marrow stromal cells (rBMSCs) when compared to PEEK. In our research, Si_3N_4-PEEK enhanced cell proliferation and also increased the normalized osteogenic activity in comparison to PEEK; AFSN showed greater proliferation and osteogenic maturation than either Si_3N_4-PEEK or PEEK itself. Importantly, cumulative mineralization at 28 days showed no differences between the Si_3N_4-PEEK and AFSN groups, and perhaps more importantly, both were greater than that measured for the PEEK and Ti6Al4V groups.

5. Conclusion

Various designs of Si_3N_4-PEEK spinal cages fabricated using fused filament fabrication were assessed for mechanical strength. The findings revealed that Si_3N_4-PEEK cages exhibited satisfactory mechanical strength across all designs tested in this study. Further, the Si_3N_4 additive concentration was sufficiently low to maintain the plastic properties of the PEEK matrix. Antimicrobial activity and osseocompatibility were compared on Si_3N_4-PEEK with virgin PEEK, AFSN, and titanium surfaces. Compared to PEEK, Si_3N_4-PEEK surfaces demonstrated reduced bacterial adhesion, and increased osteoblast-like cell proliferation and mineralization. These results suggest that Si_3N_4-PEEK holds promise as a viable biomaterial for spinal implant applications.

Acknowledgments

The authors acknowledge the contributions of Mr. Sean Ronayne, formerly of SINTX Technologies, along with Mr. Douglas Hoxworth and Ms. Nicole Martoccio of SINTX Technologies, for their efforts in filament production, sample preparation, and testing. We would also like to acknowledge the contributions of Dr. Hannah Spece, IRC professor, during the early stages of the project, particularly for her invaluable work in designing and printing activities for the cages used in this study.

Funding

This research was supported, in part, by the National Institute of General Medical Sciences of the National Institutes of Health under award number R41GM146268.

Conflict of interest

Dr. Ryan M. Bock is currently employed by SINTX, a company specializing in the production of silicon nitride powder. As our research pertains to silicon nitride-based materials, there is a potential conflict of interest that arises due to Dr. Bock's affiliation with SINTX. Dr. Noreen Hickok and Dr. Steven Kurtz are paid consultants for SINTX and also have a conflict of interest. However, we want to emphasize that the research presented in this paper has been conducted independently and without any undue influence from the company. Dr. Kurtz also reports that he is a member of Gyroid LLC, a scientific and technical consulting firm. Unrelated to the present work, Dr. Kurtz reports institutional funding from 3Spine; Celanese; Ceramtec; DJO Global; Invibio; Lima Corporate; Mitsubishi Chemical Advanced Materials; Orthoplastics; SINTX Technologies; Stryker; Wright Medical Technology; and Zimmer Biomet. Dr. Kurtz is a board member of Formae, Inc., and receives book royalties from Elsevier, Inc. We have taken necessary measures to ensure the integrity and objectivity of the present study, adhering to the highest standards of scientific rigor and ethics. We are committed to transparency and have disclosed Dr. Bock's, Dr. Hickok's, and Dr. Kurtz's conflicts of interest to ensure that the journal's readers can evaluate our work within this context.

Author contributions

Conceptualization: Ryan M. Bock, Steven M. Kurtz, Noreen J. Hickok

Formal analysis: Cemile Basgul, Paul DeSantis, Tabitha Derr

Investigation: Cemile Basgul, Paul DeSantis, Tabitha Derr

Methodology: Cemile Basgul, Paul DeSantis, Ryan M. Bock, Steven M. Kurtz, Noreen J. Hickok

Writing – original draft: Cemile Basgul, Paul DeSantis

Writing – review & editing: Cemile Basgul, Paul DeSantis, Tabitha Derr, Noreen J. Hickok, Ryan M. Bock, Steven M. Kurtz

Ethics approval and consent to participate

Not applicable.

Consent for publication

Not applicable.

Availability of data

Data are available from the corresponding author upon reasonable request.

References

1. Seaman S, Kerezoudis P, Bydon M, Torner JC, Hitchon PW. Titanium vs. polyetheretherketone (PEEK) interbody fusion: meta-analysis and review of the literature. *J Clin Neurosci*. 2017;44:23-29. doi: 10.1016/j.jocn.2017.06.062
2. Bydon M, De la Garza-Ramos R, Abt NB, et al. Impact of smoking on complication and pseudarthrosis rates after single- and 2-level posterolateral fusion of the lumbar spine. *Spine*. 2014;39(21):1765-1770. doi: 10.1097/BRS.0000000000000527
3. Shriver MF, Lewis DJ, Kshettry VR, Rosenbaum BP, Benzel EC, Mroz TE. Pseudoarthrosis rates in anterior cervical discectomy and fusion: a meta-analysis. *Spine J*. 2015;15(9):2016-2027. doi: 10.1016/j.spinee.2015.05.010
4. Dede O, Thuillier D, Pekmezci M, et al. Revision surgery for lumbar pseudarthrosis. *Spine J*. 2015;15(5):977-982. doi: 10.1016/j.spinee.2013.05.039
5. Jain S, Eltorai AE, Ruttiman R, Daniels AH. Advances in spinal interbody cages. *Orthop Surg*. 2016;8(3): 278-284. doi: 10.1111/os.12264
6. Tan ET, Ling JM, Dinesh SK. The feasibility of producing patient-specific acrylic cranioplasty implants with a low-cost 3D printer. *J Neurosurg*. 2016;124(5):1531-1537. doi: 10.3171/2015.5.JNS15119
7. Wilcox B, Mobbs RJ, Wu AM, Phan K. Systematic review of 3D printing in spinal surgery: the current state of play. *J Spine Surg*. 2017;3(3):433-443. doi: 10.21037/jss.2017.09.01
8. Bose S, Tarafder S. Calcium phosphate ceramic systems in growth factor and drug delivery for bone tissue engineering: a review. *Acta Biomater*. 2012;8(4):1401-1421. doi: 10.1016/j.actbio.2011.11.017
9. Oosterbos CJ, Vogely H, Nijhof MW, et al. Osseointegration of hydroxyapatite-coated and noncoated Ti6Al4V implants in the presence of local infection: a comparative histomorphometrical study in rabbits. *J Biomed Mater Res*. 2002;60(3):339-347. doi: 10.1002/jbm.1288
10. Kurtz SM. Development and clinical performance of PEEK intervertebral cages. In: Kurtz S, ed. *PEEK Biomaterials Handbook*. 2nd ed. Norwich, NY; 2019: William Andrew Publishing: 263-280. doi: 10.1016/B978-0-12-812524-3.00015-6
11. Mendenhall S. 2017 Profile of hospital spine programs. *Orthop Network News*. 2017;28(4):7-10.
12. Basgul C, Spece H, Sharma N, Thieringer FM, Kurtz SM. Structure, properties, and bioactivity of 3D printed PAEKs for implant applications: a systematic review. *J Biomed Mater Res B Appl Biomater*. 2021;109(11):1924-1941. doi: 10.1002/jbm.b.34845
13. Rendas P, Figueiredo L, Machado C, Mourão A, Vidal C, Soares B. Mechanical performance and bioactivation of 3D-printed PEEK for high-performance implant manufacture: a review. *Prog Biomater*. 2023;12(2):89-111. doi: 10.1007/s40204-022-00214-6
14. Zheng Z, Liu P, Zhang X, et al. Strategies to improve bioactive and antibacterial properties of polyetheretherketone (PEEK) for use as orthopedic implants. *Mater Today Bio*. 2022;16:100402. doi: 10.1016/j.mtbio.2022.100402
15. Roskies M, Jordan JO, Fang D, et al. Improving PEEK bioactivity for craniofacial reconstruction using a 3D printed scaffold embedded with mesenchymal stem cells. *J Biomater Appl*. 2016;31(1):132-139. doi: 10.1177/0885328216638636
16. Hickok N, Rochfort ETJ, Jaekel DJ, Richards RG, Moriarty TF, Poulsson AHC. Bacterial interactions with PEEK. In: Kurtz SM, ed. *PEEK Biomaterials Handbook*. 2nd ed. Norwich, NY: William Andrew Publishing; 2019: 121-146. doi: 10.1016/B978-0-12-812524-3.00009-0
17. Basgul C, Yu T, MacDonald DW, Siskey R, Marcolongo M, Kurtz SM. Structure-property relationships for 3D printed PEEK intervertebral lumbar cages produced using fused filament fabrication. *J Mater Res*. 2018;33(14):2040-2051. doi: 10.1557/jmr.2018.178
18. Spece H, Yu T, Law A, Marcolongo M, Kurtz SM. 3D printed porous PEEK created via fused filament fabrication for osteoconductive orthopaedic surfaces. *J Mech Behav Biomed Mater*. 2020:103850. doi: 10.1016/j.jmbbm.2020.103850
19. Webster TJ, Patel AA, Rahaman MN, Bal BS. Anti-infective and osteointegration properties of silicon nitride, poly(ether ether ketone), and titanium implants. *Acta Biomater*. 2012;8(12):4447-4454. doi: 10.1016/j.actbio.2012.07.038
20. Gorth DJ, Puckett S, Ercan B, Webster TJ, Rahaman M, Bal BS. Decreased bacteria activity on Si3N4 surfaces compared with PEEK or titanium. *Int J Nanomed*. 2012:4829-4840. doi: 10.2147/IJN.S35190
21. Du X, Lee SS, Blugan G, Ferguson SJ. Silicon nitride as a biomedical material: an overview. *Int J Mol Sci*. 2022;23(12). doi: 10.3390/ijms23126551

22. ASTM International. *Standard Test Methods for Intervertebral Body Fusion Devices*. PA, USA: ASTM; 2022. doi: 10.1520/F2077-22

23. Knott S, Curry D, Zhao N, et al. Staphylococcus aureus floating biofilm formation and phenotype in synovial fluid depends on albumin, fibrinogen, and hyaluronic acid. *Front Microbiol*. 2021;12:655873. doi: 10.3389/fmicb.2021.655873

24. Wu S-H, Li Y, Zhang Y-Q, et al. Porous titanium-6 aluminum-4 vanadium cage has better osseointegration and less micromotion than a poly-ether-ether-ketone cage in sheep vertebral fusion. *Artif Organs*. 2013;37(12):E191-E201. doi: 10.1111/aor.12153

25. Quarles LD, Yohay DA, Lever LW, Caton R, Wenstrup RJ. Distinct proliferative and differentiated stages of murine MC3T3-E1 cells in culture: an in vitro model of osteoblast development. *J Bone Miner Res*. 1992;7(6):683-692. doi: 10.1002/jbmr.5650070613

26. Chen YH, Connelly JP, Florian C, Cui X, Pruett-Miller SM. Short tandem repeat profiling via next-generation sequencing for cell line authentication. *Dis Model Mech*. 2023;16(10). doi: 10.1242/dmm.050150

27. Wilkesmann S, Westhauser F, Fellenberg J. Combined fluorescence-based in vitro assay for the simultaneous detection of cell viability and alkaline phosphatase activity during osteogenic differentiation of osteoblast precursor cells. *Methods Protoc*. 2020;3(2). doi: 10.3390/mps3020030

28. Peck JH, Sing DC, Nagaraja S, Peck DG, Lotz JC, Dmitriev AE. Mechanical performance of cervical intervertebral body fusion devices: a systematic analysis of data submitted to the Food and Drug Administration. *J Biomech*. 2017;54:26-32. doi: 10.1016/j.jbiomech.2017.01.032

29. Monich PR, Henriques B, Novaes de Oliveira AP, Souza JCM, Fredel MC. Mechanical and biological behavior of biomedical PEEK matrix composites: A focused review. *Mater Lett*. 2016;185:593-597. doi: 10.1016/j.matlet.2016.09.005

30. Luo C, Liu Y, Peng B, et al. PEEK for oral applications: recent advances in mechanical and adhesive properties. *Polymers*. 2023;15(2):386. doi: 10.3390/polym15020386

31. Manzoor F, Golbang A, Jindal S, et al. 3D printed PEEK/HA composites for bone tissue engineering applications: effect of material formulation on mechanical performance and bioactive potential. *J Mech Behav Biomed Mater*. 2021;121:104601. doi: 10.1016/j.jmbbm.2021.104601

32. Javaid S, Dey M, Matzke C, Gupta S. Synthesis and characterization of engineered PEEK-based composites for enhanced tribological and mechanical performance. *J Appl Polym Sci*. 2022;139(39):e52886. doi: 10.1002/app.52886

33. Ill Yong K, Sugino A, Kikuta K, Ohtsuki C, Cho SB. Bioactive composites consisting of PEEK and calcium silicate powders. *J Biomater Appl*. 2008;24(2):105-118. doi: 10.1177/0885328208094557

34. Petrovic L, Pohle D, Münstedt H, Rechtenwald T, Schlegel KA, Rupprecht S. Effect of βTCP filled polyetheretherketone on osteoblast cell proliferationin vitro. *J Biomed Sci*. 2006;13(1):41-46. doi: 10.1007/s11373-005-9032-z

35. Fogel G, Martin N, Williams GM, et al. Choice of spinal interbody fusion cage material and design influences subsidence and osseointegration performance. *World Neurosurg*. 2022;162:e626-e634. doi: 10.1016/j.wneu.2022.03.087

36. Bock RM, Jones EN, Ray DA, Bal BS, Pezzotti G, McEntire BJ. Bacteriostatic behavior of surface modulated silicon nitride in comparison to polyetheretherketone and titanium. *J Biomed Mater Res A*. 2017;105(5):1521-1534. doi: 10.1002/jbm.a.35987

37. Pezzotti G, Marin E, Adachi T, et al. Incorporating Si3N4 into PEEK to produce antibacterial, osteocondutive, and radiolucent spinal implants. *Macromolecular Bioscience*. 2018;18(6):1800033. doi: 10.1002/mabi.201800033

38. Marin E, Boschetto F, Zanocco M, et al. KUSA-A1 mesenchymal stem cells response to PEEK-Si3N4 composites. *Mater Today Chem*. 2020;17:100316. doi: 10.1016/j.mtchem.2020.100316

39. Hu G, Zhu Y, Xu F, et al. Comparison of surface properties, cell behaviors, bone regeneration and osseointegration between nano tantalum/PEEK composite and nano silicon nitride/PEEK composite. *J Biomater Sci Polym Ed*. 2022;33(1):35-56. doi: 10.1080/09205063.2021.1974812

40. Breijyeh Z, Jubeh B, Karaman R. Resistance of gram-negative bacteria to current antibacterial agents and approaches to resolve it. *Molecules*. 2020;25(6). doi: 10.3390/molecules25061340

41. Dai Y, Guo H, Chu L, et al. Promoting osteoblasts responses in vitro and improving osteointegration in vivo through bioactive coating of nanosilicon nitride on polyetheretherketone. *J Orthop Translat*. 2020;24:198-208. doi: 10.1016/j.jot.2019.10.011

42. Xu Z, Wu H, Wang F, et al. A hierarchical nanostructural coating of amorphous silicon nitride on polyetheretherketone with antibacterial activity and promoting responses of rBMSCs for orthopedic applications. *J Mater Chem B*. 2019;7(39):6035-6047. doi: 10.1039/C9TB01565E

ACCSCIENCE PUBLISHING

International Journal of Bioprinting

RESEARCH ARTICLE

Roles of pore architecture of artificial bone grafts in invasion competition between bone and fibrous tissue and orientation of regenerated bone

Keigo Shibahara,[1,2] Koichiro Hayashi,[1]* Yasuharu Nakashima,[2] and Kunio Ishikawa[1]

[1]Department of Biomaterials Faculty of Dental Science, Kyushu University, Maidashi, Higashi-ku, Fukuoka, Japan

[2]Department of Orthopaedic Surgery, Graduate School of Medical Sciences, Kyushu University, Maidashi, Higashi-ku, Fukuoka, Japan

(This article belongs to the *Special Issue: Advanced Biomaterials for 3D Printing and Healthcare Application*)

Abstract

In the reconstruction of bone defects close to soft tissue, preventing the invasion of fibrous tissue into the bone defect is key to successful bone reconstruction. In this study, we clarified the effects of the pore architecture of artificial bone grafts on the penetration of bone and fibrous tissue, and the orientation of regenerated bone. Carbonate apatite grafts with uniaxial pores along the long- (L-graft) or short-axis (S-graft) direction of the graft and biaxial pores along the long- and short-axes (LS-graft) were used. These grafts were implanted in bone defects created by rabbit ulnae amputation. The pores of the L-, S-, and LS-grafts opened into the bone stumps, muscles, and bone stumps and muscles together, respectively. In the L-graft, the graft pores developed bone from the bone stump to the graft center, while preventing excessive invasion of fibrous tissue. In S- and LS-grafts, the graft pores along the short axis allowed the invasion of fibrous tissue into the grafts. Consequently, although the bone grew to the edge regions in these grafts, further bone ingrowth was inhibited by the fibrous tissue. Furthermore, the pore architecture of the grafts affected the orientation of the regenerated bone. The degree of orientation of the bone formed in the L- and S-grafts was 1.6-fold higher than that formed in the LS-grafts. Thus, controlling the pore architecture allowed the growth of bone to predominate over that of fibrous tissue and induced the formation of bone with an ordered orientation.

Keywords: Pore architecture; Bone; Apatite; Tissue regeneration; Graft

***Corresponding author:**
Koichiro Hayashi
(khayashi@dent.kyushu-u.ac.jp)

Citation: Shibahara K, Hayashi K, Nakashima Y, Ishikawa K. Roles of pore architecture of artificial bone grafts in invasion competition between bone and fibrous tissue and orientation of regenerated bone. *Int J Bioprint*. 2024;10(2):2323. doi: 10.36922/ijb.2323

Received: November 28, 2023
Accepted: January 22, 2024
Published Online: March 1, 2024

1. Introduction

Owing to the aging global population, the incidence of non-union bone fractures is increasing.[1-4] Non-union bone fractures reduce quality of life and impose an economic burden on patients.[3,4] In terms of the pathology of non-unions, fibrous tissue is always present in the defective region and prevents bone regeneration.[5,6] Notably, in bone defects close to the soft tissue, such as fractures of long bones with segmental bone loss, fibrous

tissue easily invades the bone defect and forms scars, resulting in an increased risk of non-union fractures.[5-7] Thus, the risk of non-union can be reduced by preventing the invasion of excess fibrous tissue into the bone defects, during bone regeneration.[5,6]

Remarkably, fibrous tissue grows faster than bone and occupies more space than newly formed bone.[8] Therefore, although several researchers have attempted to reconstruct bone after segmental bone loss using artificial bone grafts,[9-13] the pores of the grafts were occupied by fibrous tissue prior to new bone formation, resulting in the failure of bone regeneration. In implant dentistry, to avoid the rapid invasion of fibrous tissue into the graft, the bone is augmented by reserving space for bone formation using a barrier membrane to prevent the invasion of fibrous tissue. This process is known as guided bone regeneration.[14] However, barrier membranes are difficult to handle; when not handled properly, they do not prevent soft tissue penetration and can cause infection.[15] Ideally, an artificial bone graft alone should realize both bone ingrowth and prevention of fibrous tissue invasion into bone defects.

Therefore, bone grafts should allow enhanced bone ingrowth to predominate over soft tissue penetration. Furthermore, when a bone graft is resorbed before bone formation, soft tissue invades the space created by bone graft resorption. Therefore, the bone graft should be maintained until bone formation, and then gradually resorbed. Bone ingrowth, osteoconductivity, and bioresorption are affected by the chemical components of bone grafts.[16-20] Calcium sulfate and beta-tricalcium phosphate (β-TCP) are resorbed spontaneously, leading to the excessive formation of fibrous tissue in the resorbed region.[16,17] In contrast, sintered hydroxyapatite (HAp) is resorbed and remains intact in the human body,[18] and carbonate apatite (CAp), an analog of bone minerals, is resorbed by osteoclasts and subsequently forms bone in the resorption region.[19,20] Furthermore, the osteoconductivity of CAp is higher than that of β-TCP and HAp.[19,20] Therefore, CAp is a potential candidate for bone regeneration, as it can inhibit fibrous tissue invasion.

Furthermore, pore architecture is known to have a crucial impact on both bone formation and inhibition of fibrous tissue invasion. Based on previous findings obtained using rabbit calvaria models, CAp grafts with uniaxial pores can promote bone ingrowth within the pores while preventing the invasion of fibrous tissue.[21-23] The direction of graft pores also affects bone regeneration.[24,25] Using a rabbit radius segmental bone defect model Feng et al. revealed that tubular β-TCP grafts were more favorable for bone ingrowth and vascularization than those with multidirectional pores, in a rabbit radius segmental bone defect model.[24] Petersen et al. reported that in a rat femoral segmental bone defect model, the pore orientations in porcine collagen grafts affected cell migration and alignment of collagen fibers in the defect.[25] Porcine collagen grafts with pores parallel to the bone axis formed bones faster than those with pores oriented perpendicular to the bone axis or in random directions.[25] Furthermore, the collagen fibers in the bone matrix were parallel to the bone axis, similar to those in the original long bone.[25]

Thus, CAp grafts with unidirectional pores, whose orientations are parallel to the bone axis and whose apertures open only onto the bone stumps, are expected to preferentially allow bone ingrowth and prevent the invasion of fibrous tissue for bone regeneration in the case of segmental bone loss in long bones. Based on this hypothesis, we clarified the effects of pore direction on the amount and orientation of newly formed bone and the prevention of fibrous tissue invasion in a rabbit ulnar segmental bone loss model using rectangular CAp grafts with different pore directions. The pores were oriented along the long, short, or both long and short axes of the grafts, which were oriented parallel, perpendicular, or both parallel and perpendicular to the bone axis, respectively.

2. Methods

2.1. Fabrication of L-, S-, and LS-grafts using 3D-printing techniques

Three types of L-, S-, and LS-grafts were fabricated as described previously.[26] Briefly, the graft structures were designed using Fusion 360 (Autodesk, San Rafael, CA, USA), resulting in a stereolithography (STL) file. A mixture of calcium carbonate powder (50% volume; Sakai Chemical, Sakai, Japan) and a photosensitive resin (50% volume; SPR302, SK Fine, Kusatsu, Japan) was prepared using a planetary centrifugal mixer (SK-350TV; Shashin Kagaku, Kyoto, Japan) to form a precursor slurry. An SLA-based 3D printer (SZ-1100, SK Fine) was used to polymerize and crosslink the precursor slurry based on STL files. The laser of the printer had a diameter of 12 μm, power of 6 mW, scan speed of 1000 mm/s, and a wavelength of 355 nm. The printed green bodies were subjected to ultrasonic cleaning in ethanol for 60 s to remove uncured resin. Subsequently, the green bodies were debound following the heating process, which began at 232°C for 0.25°C/min, followed by an increase to 412°C at 0.21°C/min, another increase to 600°C at 2.3°C/min, and finally an increase to 650°C at 0.4°C/min, before being maintained at 650°C for 24 h. At 550°C, the atmosphere in the heating box changed from air to carbon dioxide. Pure $CaCO_3$ grafts were obtained via heating. After heating, the $CaCO_3$ grafts were immersed in a 1 mol/L Na_2HPO_4 solution at 80°C for 7 days to convert the chemical composition from $CaCO_3$ to CAp.

2.2. Characterization of L-, S-, and LS-grafts

The X-ray diffraction (XRD) patterns of L-, S-, and LS-grafts were recorded to observe the apatite crystalline phase using a diffractometer (D8 Advance, Bruker AXS GmbH, Karlsruhe, Germany). Fourier-transform infrared (FTIR) spectra of the L-, S-, and LS-grafts were recorded to evaluate the compositions using an FT/IR-6200 spectrometer (JASCO, Tokyo, Japan). The morphologies of the L-, S-, and LS-grafts were confirmed using micro-computed tomography (μ-CT; ScanXmate-L080T/L090T, Comscan Techno Co., Ltd., Kanagawa, Japan) and scanning electron microscopy (SEM; S3400N, Hitachi High-Technologies Corporation, Tokyo, Japan). The lengths on the side of the pore aperture and the strut thickness for each graft were estimated from the SEM images. At least ten pores and struts in each graft were used to estimate the pore aperture size and strut thickness, respectively. The porosities of the macro-pores, in other words, macro-porosities, in L-, S-, and LS-grafts were analyzed using μ-CT software (TRI/3D-BON-FCS64, RATOC System Engineering Co., Ltd, Tokyo, Japan). The total porosities of the L-, S-, and LS-grafts were measured using the theoretical density of HAp (3.16 g/cm^3, five samples in each graft). The compressive strengths of the L-, S-, and LS-grafts were measured using a universal testing machine (Autograph AGS-J; Shimadzu, Kyoto, Japan) by loading parallel to the long (10-mm length direction) and short (6-mm length direction) axes of the graft at a crosshead speed of 1 mm/min until fracture. One sample of each graft was used to measure the compressive strength in each direction.

2.3. Surgery

The animal experiments were approved by the Animal Care and Use Committee of Kyushu University (Approval No. A23-007-0). We used 12 Japanese white rabbits (18-week-old, male, 2.9–3.4 kg, Japan SLC, Co., Ltd., Shizuoka, Japan) in this study. A critical-sized (10 mm length) rabbit ulnar segmental bone defect model was used to evaluate the effect of pore architecture on tissue ingrowth (**Figure S1** in Supplementary File).[27] To achieve analgesic and sedative effects, ketamine (30 mg/kg) and xylazine (5.0 mg/kg) were administered intramuscularly to the thighs of rabbits to achieve analgesic and sedative effects. Prior to skin incision, lidocaine (6 mg/kg) was injected subcutaneously. Gentamicin (4 mg/kg) was intraperitoneally administered to prevent infection. The diaphyseal ulna was exposed by separating the intermuscular space between the extensor digitorum communis and extensor digitorum lateralis. The muscles were treated carefully to minimize damage because excessive damage to the muscles can induce abnormal accumulation of fibrotic tissue within the new bone.[28] The ulna was amputated along both sides of a 10-mm width guide block using a sagittal blade bone saw (Zimmer Biomet Co., Ltd., Tokyo, Japan). The graft was implanted into the defect and fixed with a stainless steel plate and four screws. A polyethylene terephthalate (PET) sheet was placed between the graft and the radius. Finally, the graft was fixed to the plate using a single loop–4-0 nylon suture loop (MANI Co., Ltd., Tochigi, Japan). After irrigation with saline, the muscles and skin were repaired using 4-0 nylon suture. The aforementioned surgery was performed on both forearms. The forearms were not immobilized after surgery. At 4 and 12 weeks postoperative (PO), the rabbits were sacrificed using an overdose of ketamine and xylazine (n = 4 per group). After sacrifice, both forearms were harvested and immersed in 10% formalin solution to fix the tissues.

2.4. Gross and radiographical analyses

The images of the specimens were obtained by photography, a radiographic system (HA-60, HITEX Co., Ltd, Osaka, Japan), and a μ-CT system (ScanXmate-L080T/L090T). Photographs were captured immediately after the surgery to demonstrate the orientation of the uniaxial pores in the defects and the types of tissue in contact with the pore apertures. Radiographs were obtained to observe temporal changes in the exterior of the grafts. The μ-CT images were taken to observe temporal changes in the graft interior. The μ-CT images were reconstructed using μ-CT software (TRI/3D-BON-FCS64). The new bone volume-to-total volume (BV/TV) and material volume-to-total volume (MV/TV) ratios were measured according to previously published methods.[29] The total volume is defined as the volume enclosed by the graft perimeter.

2.5. Histological analyses

The hematoxylin–eosin (HE)-stained images were prepared after scanning the photographs, radiographs, and μ-CT images. The new bone area-to-total area (BA/TA) and material area-to-total area (MA/TA) were measured using a BZ-X digital analyzer (Keyence Co., Ltd., Osaka, Japan). The total area was defined as the area enclosed by the graft perimeter. To clarify the effects of graft pore direction on vascularization, the thicknesses and angles of the blood vessels formed in each graft were analyzed using HE-stained sections. The angles of the blood vessels were estimated using an ImageJ plug-in, called FibrilTool.[30] The directions parallel and perpendicular to the bone axis were defined as 0° and 90°, respectively. Twenty regions of interest (ROIs) per section were used for the analysis. The orientation of the new bone was analyzed from the HE-stained images using the ImageJ plug-in FibrilTool.[30] The orientation of new bone was determined from that of the collagen fibers in the new bone. Acidic eosin stains the collagen fibers light pink and accentuates their structures.[31]

Therefore, HE-stained images are suitable for evaluating the orientation of collagen fibers in tissues. A 10-fold magnified HE-stained image was obtained for evaluation using a BZ-X digital analyzer. At least three areas were selected for the analysis. ROIs which were squares of approximately 100 μm side were manually created. At least 50 ROIs were analyzed in each group during each observation period. FibrilTool provided the orientation angles and anisotropy scores of the new bone within the ROI. The reference angles were determined using the same method employed for measuring the blood vessel angles. The degree of anisotropy was represented by the length of the lines, quantified using values ranging from 0 (indicating no order) to 1 (indicating perfect order), and calculated using FibrilTool.

2.6. Statistical analyses

All analyses were conducted using EZR, version 1.61 (Saitama Medical Center, Jichi Medical University, Saitama, Japan), which is a graphical user interface for R version 4.2.0.[32] One-way analyses of variance (ANOVA) and Tukey's test were used for statistical analyses, and a significance level of $p < 0.05$ was employed to determine the statistical significance.

3. Results and discussion

3.1. Fabrication and characterization of L-, S-, and LS-grafts

The L-, S-, and LS-grafts were 10 mm long, 6 mm wide, and 3 mm thick (Figure 1A–C). The uniaxial pores in the L-, S-, and LS-grafts run along the long, short, and along both the long and short axial directions of the graft, respectively (Figure 1D–F). The pore apertures were square, and the lengths were ~538 ± 39 μm from the side (**Table S1** in Supplementary File). The thickness of the struts was ~325 ± 17 μm (**Table S1** in Supplementary File). Pores of less than 2 μm in diameter in the short direction were observed between the crystals in the high-magnification SEM images of the struts (Figure 1G–I).

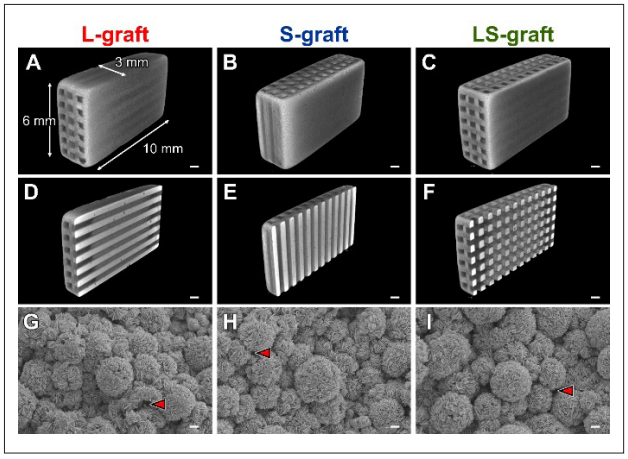

Figure 1. (A–C) Three-dimensional μ-CT images, (D–F) cross-sectional μ-CT images, and (G–I) high-magnified SEM images of outer surfaces of L-, S-, and LS-grafts. Red arrows indicate micropores. Scale bars: 1 mm (A–F), and 2 μm (G–I).

The XRD patterns revealed that the diffraction patterns of the L-, S-, and LS-grafts coincided with those of CAp (Figure 2A).[33,34] In the FTIR spectra of the L-, S-, and LS-grafts and CAp, phosphate absorption bands were observed at 566–605 and 959–1128 cm^{-1} (Figure 2B). The doublet carbonate absorption bands were observed at 1477 and 1416 cm^{-1} in the carbonate ν3 region and were due to the presence of carbonates of A- and B-type, respectively.[33,34] The XRD and FTIR results indicate that the L-, S-, and LS-grafts were composed of AB-type CAp.

The macro-porosities of the L-, S-, and LS-grafts were 30.7, 31.8, and 36.6%, respectively (**Table S1** in Supplementary File). The total porosities of the L-, S-, and LS-grafts were 53.6, 53.9, and 59.1%, respectively (**Table S1** in Supplementary File). The average compressive strengths of L- and S-grafts parallel and perpendicular to the pore direction were 26 and 13 MPa, respectively (**Figure S2** and **Table S1** in Supplementary File). The average compressive strength of the LS-graft was 8 MPa (**Figure S2** and **Table S1** in Supplementary File). Thus, the total porosity and compressive strength of L-grafts were similar to those of the S-grafts. Furthermore, LS-grafts possessed higher total porosity and lower compressive strength than the L- and S-grafts. The correlation between the porosity and strength coincided with that of typical ceramics.[35]

3.2. Gross and radiographical evaluations

Photographs taken immediately after surgery revealed that the pore apertures in the L-, S-, and LS-grafts opened onto the bone stumps, muscles, and both bone stumps and muscles (Figure 3A–C). The pore apertures in the L- and S-grafts did not open into the muscle or bone stumps (Figure 3A and B). On radiographs of the L-graft at 4 weeks PO, both edges of the graft were filled with new bone, and gaps between the bone stumps and grafts were not observed (Figure 3D). In contrast, gaps were observed between the graft and the bone stumps on the radiographs of the S- (Figure 3E) and LS-grafts (Figure 3F). At 12 weeks PO, the radiographic density within the uniaxial pore spaces of the L-graft was similar to that of the struts (Figure 3G). Furthermore, the boundaries between the uniaxial pores and struts were unclear. These findings were attributed to bone ingrowth and graft resorption. In the radiographs of the S- (Figure 3H) and LS-grafts (Figure 3I) at 12 weeks PO, the gaps between the bone stumps and grafts disappeared and were filled with new bone. Although the pore sizes in

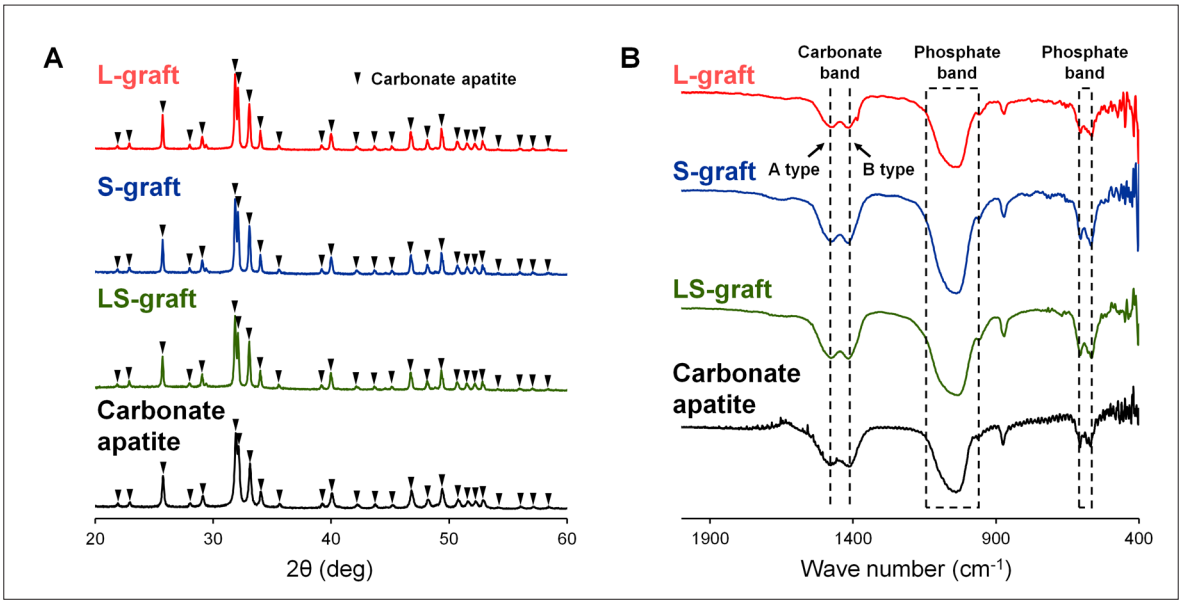

Figure 2. (A) XRD patterns and (B) FTIR spectra of L-, S-, LS-grafts, and carbonate apatite.

the edge regions were larger than those at 4 weeks PO, they changed little in the central regions. These findings suggest that bone ingrowth did not reach the central regions of these grafts even at 12 weeks PO.

The μ-CT images reveal that new bone penetrated the L-graft through the pores and grew parallel to the bone axis at 4 weeks PO (Figure 4A). In contrast, only a small quantity of bone penetrated the S-graft because of the lack of pore apertures in contact with the host bone (Figure 4B). In the LS graft, although the new bone penetrated the graft edge regions, it grew in different directions (Figure 4C). At 12 weeks PO, new bone grew into the center of the L-graft, and a portion of the L-graft was replaced with new bone (Figure 4D). In contrast, a small quantity of bone penetrated the S-graft (Figure 4E). The S-graft partially resorbed without bone ingrowth (Figure 4E). In the LS graft, the bone stagnated at the graft edge regions and obstructed the bone marrow cavities (Figure 4F), marking the beginning of non-union.[35] Although the BV/TVs at 4 weeks PO revealed no significant difference between the L- (3.9 ± 1.9%), S- (1.0 ± 1.1%), and LS-grafts (2.7 ± 1.7%), a significant difference was detected at 12 weeks PO between the L- (17.1 ± 1.5%), LS- (12.9 ± 2.0%), and S-grafts (6.5 ± 0.7%) (Figure 4G). No significant difference in MV/TV was observed between the L- and S-grafts at 4 and 12 weeks PO (L-graft: 74.8 ± 1.4% at 4 weeks and 49.3 ± 3.7% at 12 weeks, S-graft: 71.7 ± 2.8% at 4 weeks and 51.8 ± 4.3% at 12 weeks). The MV/TV of LS-graft was the lowest by far at 4 (61.2 ± 2.0%) and 12 weeks PO (40.1 ± 4.3%) due to the higher total porosity than those of L- and S-grafts (Figure 4H). The average resorption rate of L-grafts from 4 to 12 weeks (25.5%) was higher than that of S- (19.9%) and LS-grafts (21.1%). Thus, the L-graft was extensively replaced with new bone during the 12-week period. In contrast, bone formation in the S- and LS-grafts was limited to the graft edge regions.

3.3. Histological analyses for bone amount and orientation

Abundant bone formed in the pores of the L-graft at 4 weeks PO, and a portion of the struts was replaced with new bone (Figure 5A). Although thin bone was formed on the strut surface of the S-graft, fibrous tissue occupied the pore center (Figure 5B). The fibrous tissue invaded the pores from the muscle side of the LS-graft, preventing bone ingrowth (Figure 5C). At 12 weeks PO, abundant bone still dominated the pores of the L-graft, and a portion of the graft struts was replaced with new bone (Figure 5D). In the S-graft, although bone formed on the strut surface, fibrous tissue occupied the pore center (Figure 5E). In the LS graft, fibrous tissue invaded the pores from the muscle side, preventing bone ingrowth in the direction of the bone axis (Figure 5F). Furthermore, blood vessels formed along the pore directions of the L- and S-grafts (**Figure S3A**, **B**, **D**, and **E** in Supplementary File) at 4 and 12 weeks PO, whereas blood vessels ran in multiple directions within the LS-grafts (**Figure S3C** and **F** in Supplementary File). The orientation of the tissue formed in the L-, S-, and LS-grafts was analyzed using histological images. At 4 weeks PO, new bone was oriented in the pore direction of the L- and S-grafts (Figure 5G and H). Thus, the orientation of new

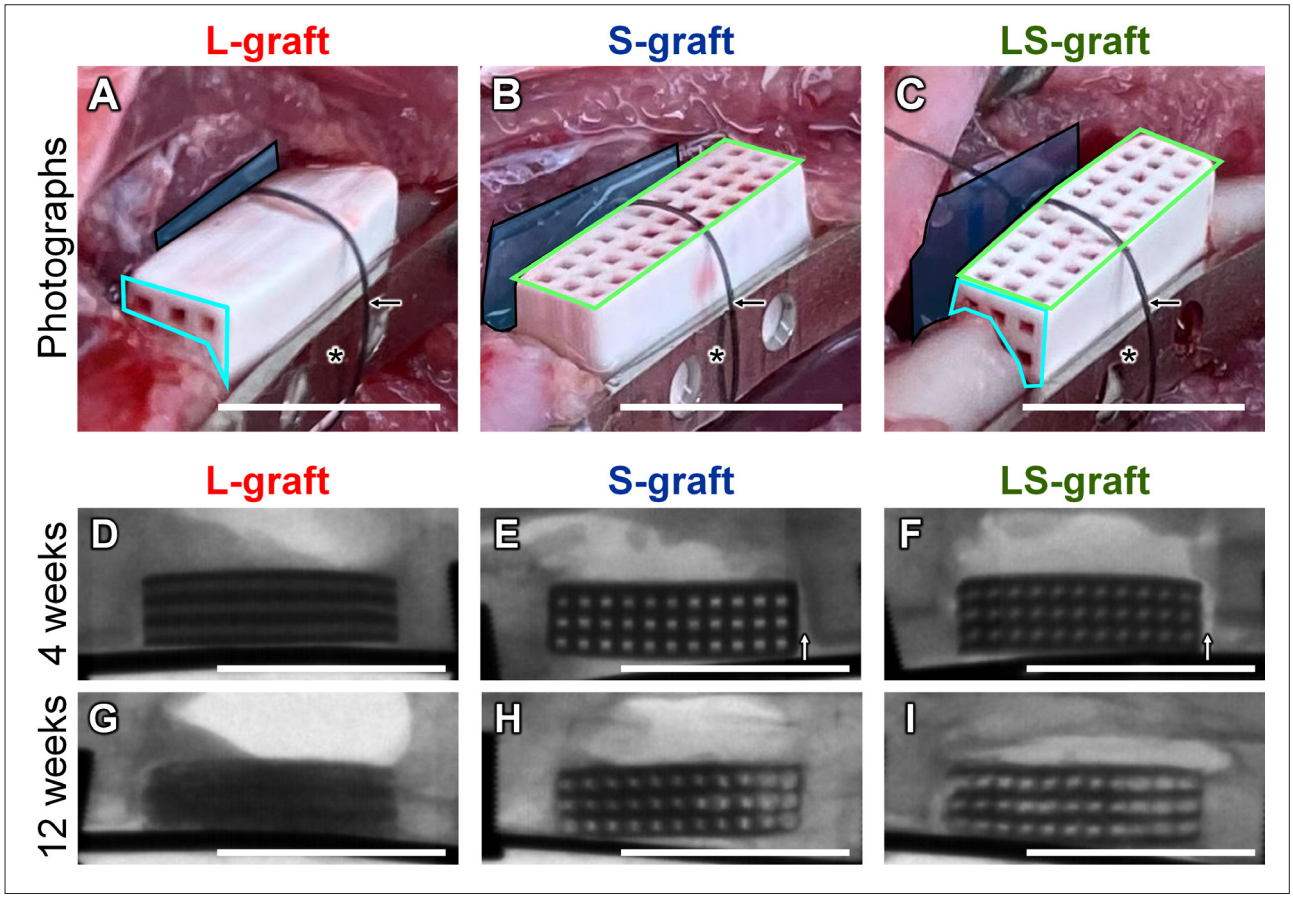

Figure 3. Photographs immediately after implantation of (A) L-, (B) S-, and (C) LS-grafts. Radiographs of the grafts at (D–F) 4 weeks and (G–I) 12 weeks PO. The channel apertures (long-axis channel apertures) in the regions surrounded by cyan lines make contact with the bone edge. The channel apertures (short-axis channel apertures) in the regions surrounded by green lines make contact with the skeletal muscles. The PET sheets are highlighted in blue. Black arrows indicate the single-looped nylon thread. Asterisks (*) indicate stainless-steel plates. White arrows indicate gaps regions without abundant new bones. Scale bars: 10 mm.

bone in the L- and S-grafts was parallel and perpendicular to the bone axis, respectively. The new bone in the LS-graft did not exhibit consistent orientation (Figure 5I). In the L- and S-grafts at 12 weeks PO, the bone was still oriented in the pore direction for each graft (Figure 5J and K). In the LS-graft at 12 weeks PO, the new bone showed no orientation (Figure 5L).

The results for BA/TA (Figure 6A) and MA/TA (Figure 6B) coincide with those for BV/TV (Figure 4G) and MV/TV (Figure 4H), respectively. The blood vessel thicknesses at 4 and 12 weeks PO in the L-graft (59.7 ± 6.0 μm at 4 weeks PO and 56.1 ± 8.9 μm at 12 weeks PO) were significantly greater than those of S- (34.7 ± 6.3 μm at 4 weeks PO and 33.8 ± 7.3 μm at 12 weeks PO) and LS-grafts (38.6 ± 3.4 μm at 4 weeks PO and 38.3 ± 4.2 μm at 12 weeks PO, $p > 0.001$, Figure 6C). No significant difference was observed between the S- and LS-grafts in terms of blood vessel thickness. The angles of the blood vessels in the L-graft were 8.4 ± 8.7° and 9.4 ± 7.0° at 4 and 12 weeks PO, respectively (Figure 6D). The angles of the blood vessels in the S-graft were 82.0 ± 8.1° and 74.7 ± 11.4° at 4 and 12 weeks PO, respectively. Therefore, the blood vessels within the uniaxial pores of the L- and S-grafts ran along each pore direction. The angles of the blood vessels in the LS-grafts were 46.8 ± 28.6° and 38.2 ± 29.1° at 4 and 12 weeks PO, respectively (Figure 6D). Thus, the blood vessel angles in the LS-grafts coincided with the intermediate values of the blood vessel angles in the L- and S- grafts, and the standard deviation was large, indicating that the blood vessels in the LS-graft ran in multiple directions. These findings demonstrate that the uniaxial pore openings onto only the bone stumps were necessary to form well-developed blood vessels oriented in the direction of the bone axis. The orientation angle of new bone in the L-graft was 10.4 ± 8.3° and 15.3 ± 15.8° at 4 and 12 weeks PO, respectively (Figure 6E). The orientation angle of new bone in the S-graft was 84.0 ± 6.5° and 75.1

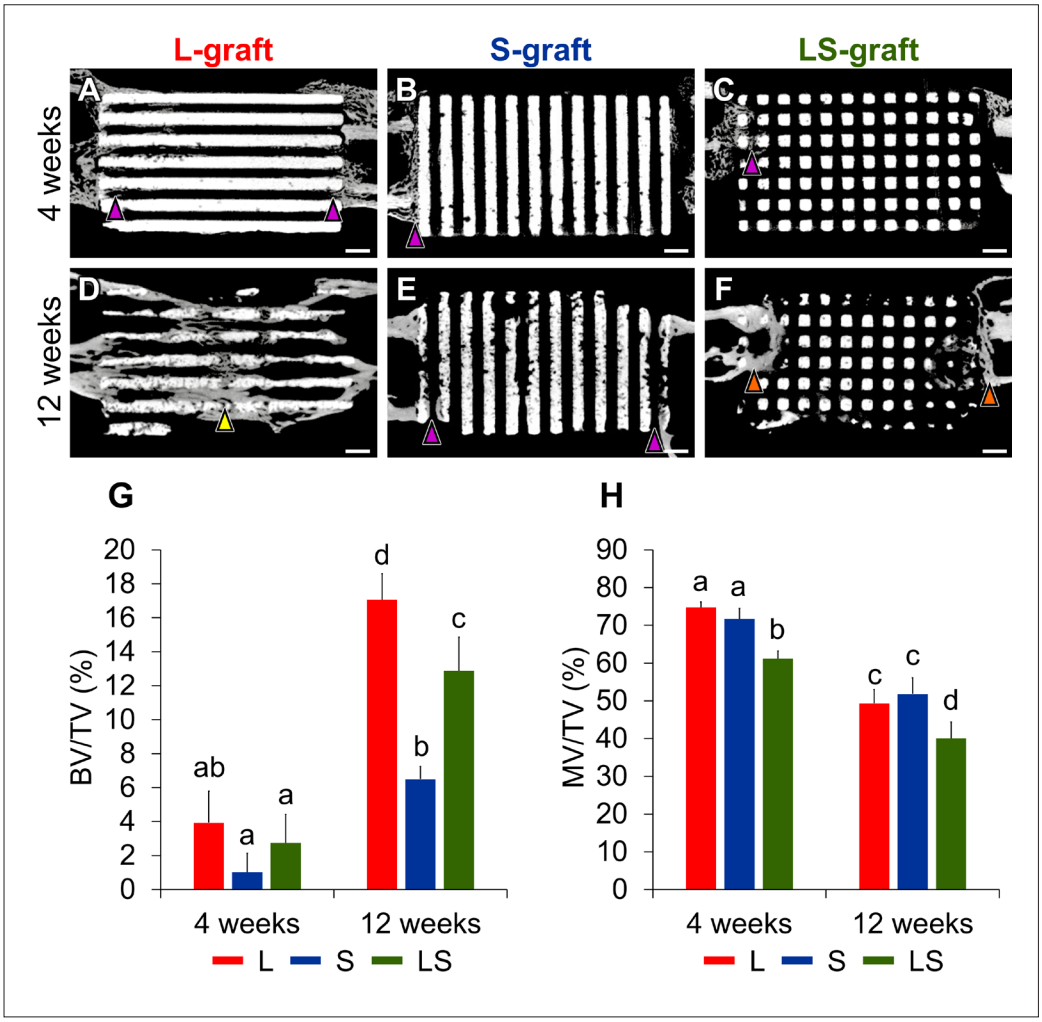

Figure 4. Cross sectional μ-CT images at (A–C) 4 weeks and (D–F) 12 weeks PO, respectively. Purple, yellow, and brown arrowheads indicate new bone at the edge of the graft, new bone in the center of the graft, and the obstruction of the bone marrow cavity, respectively. Scale bars: 1 mm. (G) BV/TV, and (H) MV/TV; significant differences are indicated by different letters ($p < 0.05$).

± 14.8° at 4 and 12 weeks PO, respectively. Therefore, new bones within the uniaxial pores of the L- and S-grafts were oriented along each pore direction. Meanwhile, the angles in the LS-grafts were 48.4 ± 29.0° and 61.1 ± 23.5° at 4 and 12 weeks PO, respectively; these values fell in between those of the L- and S-grafts. Although the bone formed in the L-graft revealed no statistically significant difference in the orientation angle between 4 and 12 weeks PO, those in the S- and LS-grafts revealed significant differences. For the anisotropic degree of new bone, no significant difference was detected among the L-, S-, and LS-grafts at 4 weeks PO (L-graft: 0.14 ± 0.07, S-graft: 0.15 ± 0.04, LS-graft: 0.13 ± 0.07) (Figure 6F). At 12 weeks PO, however, the anisotropic degree of new bone in the LS-graft was 30–36% lower than those of L- and S-grafts (L-graft: 0.11 ± 0.08, S-graft: 0.10 ± 0.06, LS-graft: 0.07 ± 0.05). In all grafts, the degree of anisotropy of the new bone significantly decreased from 4 to 12 weeks PO. The significant differences in orientation angles and anisotropic degrees between 4 and 12 weeks PO were attributed to the maturation of bone within the grafts, which changed from spindle to lamellar structures with maturation between 4 (**Figure S4A** and **B** in Supplementary File) and 12 weeks PO (**Figure S4C** and **D** in Supplementary File). The lamellar lines were not as straight as the spindle-shaped collagen fibers, which decreased the degree of bone orientation.

Thus, the hypothesis that grafts with uniaxial pores whose directions are parallel to the bone axis and apertures open onto only the bone stumps preferentially promotes bone ingrowth and prevents the invasion of fibrous tissue has been validated. Furthermore, the uniaxial pores restored bone orientation earlier than the biaxial pores.

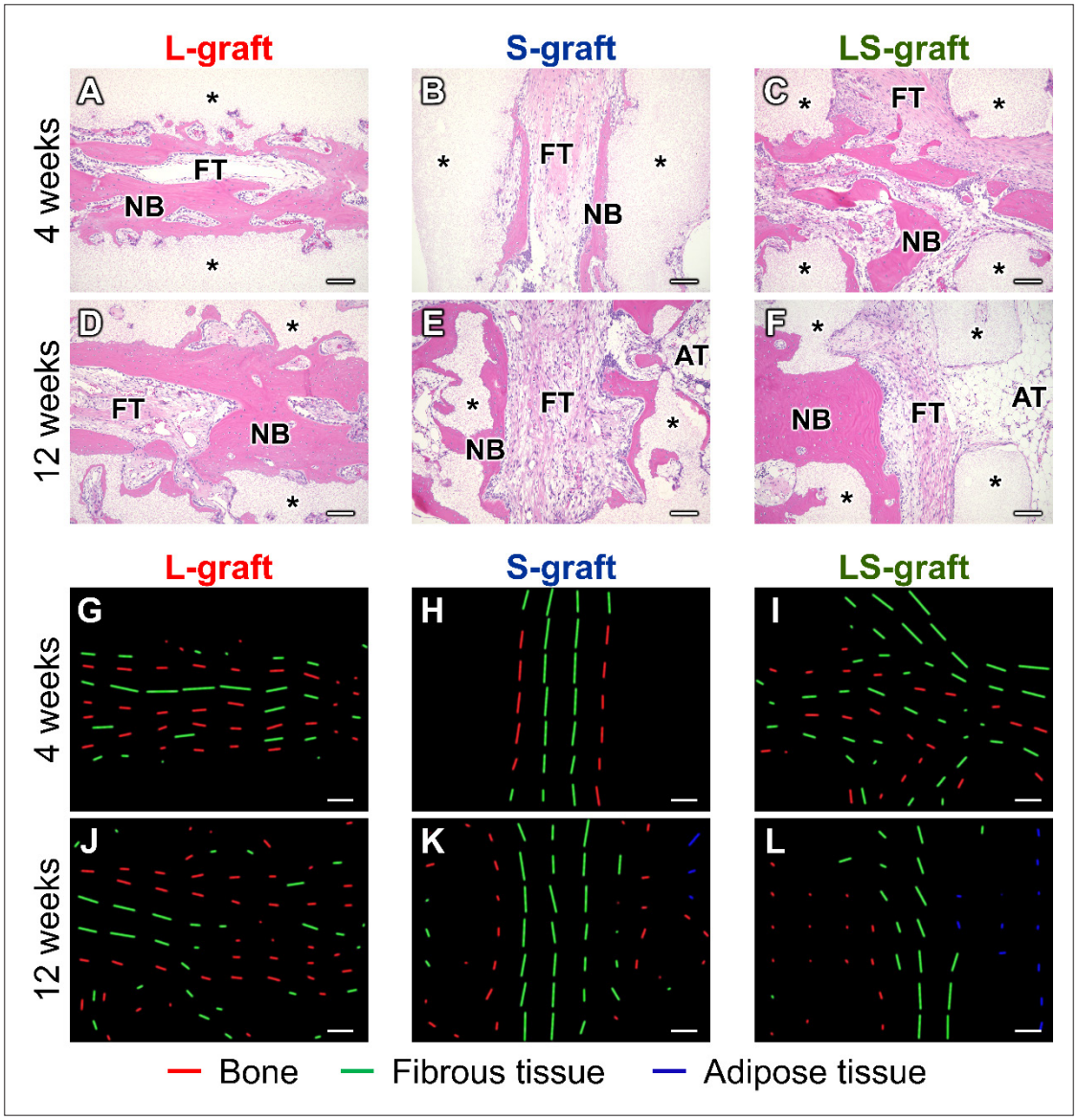

Figure 5. HE-stained images in the new bone area at (A–C) 4 weeks and (D–F) 12 weeks PO. Analyzed images of bone orientations within pores at (G–I) 4 weeks and (J–L) 12 weeks PO. Asterisks (*) indicate material. NB, FT, and AT denote new bone, fibrous tissue, and adipose tissue, respectively. The right and left sides of images are the bone stump sides. The top and bottom sides of the images show the muscle sides. The highlighted red, green, and blue lines indicate the orientations of new bones, fibrous tissues, and adipose tissue, respectively. Scale bars: 100 μm.

To the best of our knowledge, this is the first study to demonstrate that the pore direction and type of tissue in contact with the pore aperture affect the tissue invasion behavior and bone orientation.

Cipitria et al. attempted to reconstruct critical-sized ovine tibial defects using 3D porous grafts composed of polycaprolactone (PCL) and TCP, which had a total porosity of 70%, pore size of 1200 μm, strut diameter of 300 μm, and inter-strut gap of about 100 μm.[10] The pores and inter-strut gaps opened onto the bone stumps and soft tissues, respectively. Three months after implantation, a fibrous network was formed throughout the graft via the pores and gaps, and subsequent mineralization occurred along the fibrous network. Therefore, a portion of the new bone formed across the struts, and eventually, the graft alone was unable to form a bone that bridged the defect, even after 12 months of implantation. Hara et al. compared bone formation in rat femoral segmental bone defects between two types of 3D porous poly (L-lactide-co-ε-caprolactone) grafts with 300–500 μm pores: one was

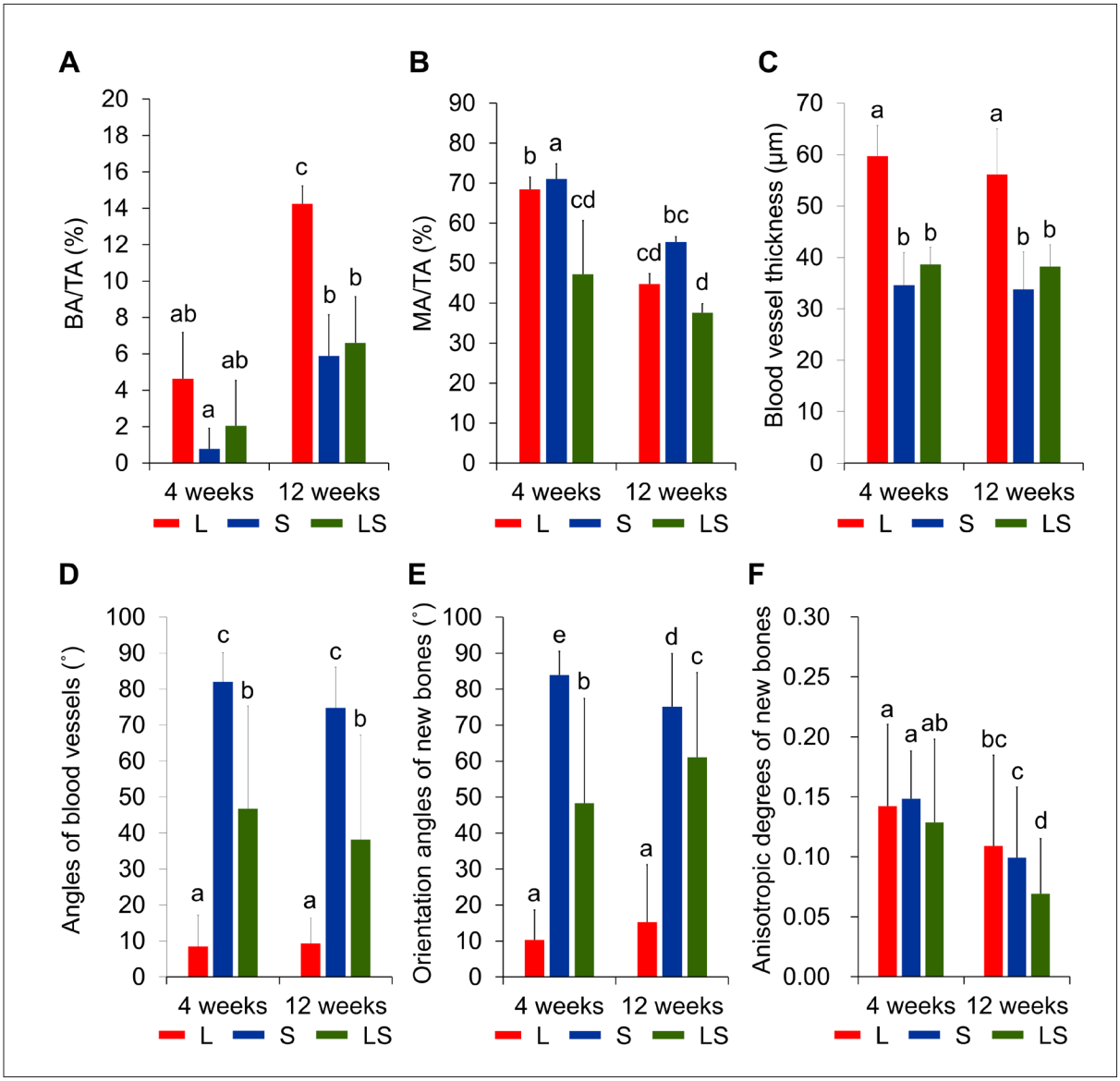

Figure 6. (A) BA/TA, (B) MA/TA, (C) blood vessel thickness, (D) angles of blood vessels relative to the pore direction, (E) orientation angles of new bones, and (D) anisotropic degrees of new bones. Significant differences are indicated by different letters ($p < 0.05$).

tubular grafts with pores on the wall (66.3% of porosity), and the other was cylindrical grafts with 0/90 lay-down pattern (53.1% of porosity).[36] Although implantation of these grafts promoted bone formation better compared to non-implantation of grafts, these grafts did not form bone to bridge the defects even at 15 weeks PO. Conversely, Feng et al. reported that one-dimensional porous β-TCP grafts with a tubular pore opening only onto the bone stamps promoted bone ingrowth in rabbit radius segmental bone defects.[24] Furthermore, Pan et al. implanted one-dimensional porous β-TCP graft with single tubular pore and multi-tubular pores, which were parallel to the bone axis, into rabbit tibial segmental bone defects. The β-TCP graft with multi-tubular pores promoted bone formation and restored bone bending strength faster than that with single-tubular pore.[37] These previous findings support our finding that uniaxial pores should open only onto the bone stumps to effectively reconstruct segmental bone defects.

Conventionally, the high porosity of the graft contributes to bone formation while reducing the mechanical strength.[38] Thus, merely adjusting porosity is not sufficient to achieve graft strength and bone formation. However, in this study, we overcame this challenge: Although the total porosity of the L-graft was lower than that of the

LS-graft, the L-graft formed a larger quantity of bone and demonstrated higher mechanical strength than the LS-graft. These findings demonstrate that porosity can be reduced without sacrificing bone formation by controlling the pore structure based on the bone defect morphology, thereby avoiding a reduction in graft strength. Moreover, we found that the L-graft formed a bone oriented in the direction of the bone axis, whereas the LS-graft formed bone that was not oriented in an orderly fashion, resulting in obstruction of the bone marrow. Thus, the formation of oriented bone and the avoidance of bone marrow obstruction are other benefits of pore structure control based on the consideration of bone defect morphology.

In clinical practice, grafts should be used differently, depending on the site and morphology of the bone defect.[39] When bone should be formed along one axis, for example, bone reconstruction in segmental bone defects as in this study and vertical bone augmentation in dentistry, grafts with a uniaxial porous structure, such as a honeycomb and tube, including the L-graft, are considered suitable.[21-24,27,37,40] In bone defects where surrounding bone is present, 3D porous grafts and grafts with biaxial pores, such as the LS-graft, may be useful.[41,42] However, despite this type of bone defect, when the host bone is oriented, grafts with a uniaxial porous structure seem more suitable than 3D porous grafts for regenerating bone along the bone axis.

In future studies, optimization of the pore size and shape is required because previous studies have demonstrated that these characteristics affect tissue invasion and bone formation.[43,44] Zhao et al. reported that calcium phosphate cement graft with 200–300 μm pores promoted bone formation compared to those with 300–450 μm and 450–600 μm pores in radius segmental bone defects in rabbits.[43] Van Bael et al. reported the effects of pore size (500 and 1000 μm) and pore shape (triangular, hexagonal, and rectangular) on the *in vitro* proliferation and differentiation of 3D human periosteum-derived cell cultures using Ti6Al4V bone grafts.[44] They reported that the smaller pore (500 μm) was more beneficial for cell growth than larger pores (1000 μm), and the triangular pore exhibited higher alkaline phosphatase activity of cells than hexagonal and rectangular pores. In this study, the graft possessed square pores of ~500 μm on a side; however, changing the pores to 200–300-μm pores in triangular shape may improve the bone formation.

This study showed that soft tissues occupied the graft when the pores were oriented toward the soft tissues, whereas bone was preferentially formed in the graft when the pores were oriented only toward the bone. However, this study did not elucidate the underlying mechanism in detail. *In vitro* studies are useful for elucidating the mechanism by which this system can be made simpler. However, the simple two-dimensional cell culture was quite different from the dynamic and complex system of segmental bone defects in this study, and it seems inefficient for elucidating the mechanism of pore orientation effects. Although the 3D dynamic culture of several types of cells may mimic segmental bone defects and be effective for the elucidation of the mechanism, the establishment of a 3D culture system requires considerable time and effort, and that alone is one research project. We intend to elucidate this mechanism in future studies.

Longer-term observations may reveal more pronounced effects of the graft pore structure on bone regeneration because obstruction of the bone marrow is the beginning of non-union.[45] Therefore, we plan to conduct long-term animal experiments in future.

4. Conclusion

CAp grafts with uniaxial pores parallel, perpendicular, or both parallel and perpendicular to the bone axis were fabricated. The pores of these grafts opened onto the bone stumps, muscles, and both bone stumps and muscles. These grafts were implanted into segmental bone defects of rabbit ulnae to evaluate the effects of pore architecture on bone ingrowth and orientation. In CAp grafts with uniaxial pores perpendicular and both parallel and perpendicular to the bone axis, fibrous tissue invaded the pores faster than the new bone, preventing bone formation and resulting in disordered bone ingrowth orientation. In contrast, in CAp grafts with uniaxial pores parallel to the bone axis, the pores preferentially allow the invasion of new bone. Consequently, the bone oriented along the direction of the bone axis was abundantly formed. The findings of this study provide an understanding of the effect of graft pore structure on the amount and orientation of formed bone and contribute to the development of grafts with optimal pore structures for the reconstruction of segmental bone defects.

Acknowledgments

None.

Funding

This study was supported in part by Japan Agency for Medical Research and Development under grant no. JP22ym0126098h and Japan Society for the Promotion of Science KAKENHI under grant nos. JP23K18593 and JP22H03954.

Conflict of interest

The authors declare no conflicts of interest.

Author contributions

Conceptualization: Koichiro Hayashi
Data curation: Koichiro Hayashi and Keigo Shibahara
Formal analysis: Koichiro Hayashi and Keigo Shibahara
Funding acquisition: Koichiro Hayashi
Investigation: Koichiro Hayashi and Keigo Shibahara
Methodology: Koichiro Hayashi
Project administration: Koichiro Hayashi, Yasuharu Nakashima, Kunio Ishikawa
Supervision: Koichiro Hayashi
Validation: Koichiro Hayashi and Keigo Shibahara
Visualization: Koichiro Hayashi and Keigo Shibahara
Writing – original draft: Keigo Shibahara
Writing – review & editing: Koichiro Hayashi

Ethics approval and consent to participate

Animal experiments were approved by the Animal Care and Use Committee of Kyushu University (approval no. A23-007-0).

Consent for publication

Not applicable.

Availability of data

The data that support the findings of this study are available from the corresponding author upon reasonable request.

References

1. GBD 2019 Fracture Collaborators. Global, regional, and national burden of bone fractures in 204 countries and territories, 1990–2019: a systematic analysis from the Global Burden of Disease Study 2019. *Lancet Healthy Longev*. 2021;2:e580-e592. doi: 10.1016/S2666-7568(21)00172-0
2. Shen Y, Huang X, Wu J, et al. The global burden of osteoporosis, low bone mass, and its related fracture in 204 countries and territories, 1990-2019. *Front Endocrinol*. 2022;13. doi: 10.3389/fendo.2022.882241
3. Stewart SK. Fracture non-union: a review of clinical challenges and future research needs. *Malays Orthop J*. 2019;13:1-10. doi: 10.5704/MOJ.1907.001
4. Wildemann B, Ignatius A, Leung F, et al. Non-union bone fractures. *Nat Rev Dis Primers*. 2021;7:57. doi: 10.1038/s41572-021-00289-8
5. Leng Y, Yang F, Wang Q, et al. Material-based therapy for bone nonunion. *Mater Des*. 2019;183:108161. doi: 10.1016/j.matdes.2019.108161
6. Dahl MT, Morrison S. Segmental bone defects and the history of bone transport. *J Orthop Trauma*. 2021;35:S1-7. doi: 10.1097/BOT.0000000000002124
7. Sparks DS, Saifzadeh S, Savi FM, et al. A preclinical large-animal model for the assessment of critical-size load-bearing bone defect reconstruction. *Nat Protoc*. 2020;15:877-924. doi: 10.1038/s41596-019-0271-2
8. Schenk RK, Buser D, Hardwick WR, Dahlin C. Healing pattern of bone regeneration in membrane-protected defects: a histologic study in the canine mandible. *Int J Oral Maxillofac*. 1994;9:13-29. https://www.researchgate.net/publication/15047765
9. Reichert JC, Wullschleger ME, Cipitria A, et al. Custom-made composite scaffolds for segmental defect repair in long bones. *Int Ortho*. 2011;35:1229-1236. doi: 10.1007/s00264-010-1146-x
10. Cipitria A, Lange C, Schell H, et al. Porous scaffold architecture guides tissue formation. *J Bone Miner Res*. 2012;27:1275-1288. doi: 10.1002/jbmr.1589
11. Berner A, Reichert JC, Woodruff MA, et al. Autologous vs. allogenic mesenchymal progenitor cells for the reconstruction of critical sized segmental tibial bone defects in aged sheep. *Acta Biomater*. 2013;9:7874-7884. doi: 10.1016/j.actbio.2013.04.035
12. Akagi H, Ochi H, Soeta S, et al. A comparison of the process of remodeling of hydroxyapatite/Poly-D/L-lactide and beta-tricalcium phosphate in a loading site. *Biomed Res Int*. 2015;2015:730105. doi: 10.1155/2015/730105
13. Song J, Kim J, Woo HM, et al. Repair of rabbit radial bone defects using bone morphogenetic protein-2 combined with 3D porous silk fibroin/β-tricalcium phosphate hybrid scaffolds. *J Biomater Sci Polym Ed*. 2018;29:716-729. doi: 10.1080/09205063.2018.1438126
14. Abtahi S, Chen X, Shahabi S, Nasiri N. Resorbable membranes for guided bone regeneration: critical features, potentials, and limitations. *ACS Mater Au*. 2023;3:394-417. doi: 10.1021/acsmaterialsau.3c00013
15. Lee FH, Shen PC, Jou IM, Li C-Y, Hsieh J-L. A population-based 16-year study on the risk factors of surgical site infection in patients after bone grafting. *Medicine*. 2015;94:e2034. doi: 10.1097/MD.0000000000002034
16. Rodham PL, Giannoudis VP, Kanakaris NK, Giannoudis PV. Biological aspects to enhance fracture healing. *EFORT Open Rev*. 2023;8:264-282. doi: 10.1530/EOR-23-0047
17. Barba A, Diez-Escudero A, Maazouz Y, et al. Osteoinduction by foamed and 3D-printed calcium phosphate scaffolds: effect of nanostructure and pore architecture. *ACS Appl Mater Interfaces*. 2017;9:41722-41736.

doi: 10.1021/acsami.7b14175

18. Nakamura T, Matsumine A, Asanuma K, Matsubara T, Sudo A. Treatment of bone defect with calcium phosphate cement subsequent to tumor curettage in pediatric patients. *Oncol Lett*. 2016;11:247-252.
doi: 10.3892/ol.2015.3855

19. Hayashi K, Kishida R, Tsuchiya A, Ishikawa K. Honeycomb blocks composed of carbonate apatite, β-tricalcium phosphate, and hydroxyapatite for bone regeneration: effects of composition on biological responses. *Mater Today Bio*. 2019;4:100031.
doi: 10.1016/j.mtbio.2019.100031

20. Hayashi K, Kishida R, Tsuchiya A, Ishikawa K. Granular honeycombs composed of carbonate apatite, hydroxyapatite, and β-tricalcium phosphate as bone graft substitutes: effects of composition on bone formation and maturation. *ACS Appl Bio Mater*. 2020;3:1787-1795.
doi: 10.1021/acsabm.0c00060

21. Hayashi K, Shimabukuro M, Kishida R, Tsuchiya A, Ishikawa K. Honeycomb scaffolds capable of achieving barrier membrane-free guided bone regeneration. *Mater Adv*. 2021;2:7638-7649.
doi: 10.1039/d1ma00698c

22. Hayashi K, Shimabukuro M, Kishida R, Tsuchiya A, Ishikawa K. Structurally optimized honeycomb scaffolds with outstanding ability for vertical bone augmentation. *J Adv Res*. 2022;41:101-112.
doi: 10.1016/j.jare.2021.12.010

23. Hayashi K, Kishida R, Tsuchiya A, Ishikawa K. Channel aperture characteristics of carbonate apatite honeycomb scaffolds affect ingrowths of bone and fibrous tissues in vertical bone augmentation. *Bioengineering*. 2022;9(11):627.
doi: 10.3390/bioengineering9110627

24. Feng YF, Wang L, Li X, et al. Influence of architecture of β-tricalcium phosphate scaffolds on biological performance in repairing segmental bone defects. *PLoS One*. 2012;7:e49955.
doi: 10.1371/journal.pone.0049955

25. Petersen A, Princ A, Korus G, et al. A biomaterial with a channel-like pore architecture induces endochondral healing of bone defects. *Nat Commun*. 2018;9:4430.
doi: 10.1038/s41467-018-06504-7

26. Hayashi K, Kishida R, Tsuchiya A, Ishikawa K. Supporting information superiority of triply periodic minimal surface gyroid structure to strut-based grid structure in both strength and bone regeneration. *ACS Appl Mater Interfaces*. 2023;15:34570-34577.
doi: 10.1021/acsami.3c06263

27. Shibahara K, Hayashi K, Nakashima Y, Ishikawa K. Honeycomb scaffold-guided bone reconstruction of critical-sized defects in rabbit ulnar shafts. *ACS Appl Bio Mater*. 2021;4:6821-6831.
doi: 10.1021/acsabm.1c00533

28. Julien A, Kanagalingam A, Martínez-Sarrà E, et al. Direct contribution of skeletal muscle mesenchymal progenitors to bone repair. *Nat Commun*. 2021;12:2860.
doi: 10.1038/s41467-021-22842-5

29. Hayashi K, Yanagisawa T, Kishida R, Ishikawa K. Effects of scaffold shape on bone regeneration: tiny shape differences affect the entire system. *ACS Nano*. 2022;16:11755-11768.
doi: 10.1021/acsnano.2c03776

30. Boudaoud A, Burian A, Borowska-Wykręt D, et al. FibrilTool, an ImageJ plug-in to quantify fibrillar structures in raw microscopy images. *Nat Protoc*. 2014;9:457-463.
doi: 10.1038/nprot.2014.024

31. Gurcan MN, Boucheron LE, Can A, Madabhushi A, Rajpoot NM, Yener B. Histopathological image analysis: a review. *IEEE Rev Biomed Eng*. 2009;2:147-171.
https://doi.org /10.1109/RBME.2009.2034865

32. Kanda Y. Investigation of the freely available easy-to-use software "EZR" for medical statistics. *Bone Marrow Transplant*. 2013;48:452-458.
doi: 10.1038/bmt.2012.244

33. Ren F, Ding Y, Leng Y. Infrared spectroscopic characterization of carbonated apatite: a combined experimental and computational study. *J Biomed Mater Res A*. 2014;102:496-505.
doi: 10.1002/jbm.a.34720

34. Madupalli H, Pavan B, Tecklenburg MMJ. Carbonate substitution in the mineral component of bone: discriminating the structural changes, simultaneously imposed by carbonate in A and B sites of apatite. *J Solid State Chem*. 2017;255:27-35.
doi: 10.1016/j.jssc.2017.07.025

35. Jodati H, Yılmaz B, Evis Z. A review of bioceramic porous scaffolds for hard tissue applications: effects of structural features. *Ceram Int*. 2020;46:15725-15739.
doi: 10.1016/j.ceramint.2020.03.192

36. Hara K, Hellem E, Yamada S, et al. Efficacy of treating segmental bone defects through endochondral ossification: 3D printed designs and bone metabolic activities. *Mater Today Bio*. 2022;14:100237.
doi: 10.1016/j.mtbio.2022.100237

37. Pan Q, Li Y, Xu J, et al. The effects of tubular structure on biomaterial aided bone regeneration in distraction osteogenesis. *J Orthop Transl*. 2020;25:80-86.
doi: 10.1016/j.jot.2020.09.009

38. Al-Maharma AY, Patil SP, Markert B. Effects of porosity on the mechanical properties of additively manufactured components: a critical review. *Mater Res Express*. 2020;7:122001.
doi: 10.1088/2053-1591/abcc5d

39. Hannink G, Arts JJC. Bioresorbability, porosity and mechanical strength of bone substitutes: what is optimal for bone regeneration? *Injury*. 2011;42:S22-S25.

doi: 10.1016/j.injury.2011.06.008

40. Shibahara K, Hayashi K, Nakashima Y, Ishikawa K. Reconstruction of load-bearing segmental bone defects using carbonate apatite honeycomb blocks. *ACS Mater Au*. 2023;3:321-336.
doi: 10.1021/acsmaterialsau.3c00008

41. Lu T, Feng S, He F, Ye J. Enhanced osteogenesis of honeycomb β-tricalcium phosphate scaffold by construction of interconnected pore structure: an in vivo study. *J Biomed Mater Res A*. 2020;108:645-653.
doi: 10.1002/jbm.a.36844

42. He F, Lu T, Fang X, et al. Novel extrusion-microdrilling approach to fabricate calcium phosphate-based bioceramic scaffolds enabling fast bone regeneration. *ACS Appl Mater Interfaces*. 2020;12:32340-32351.
doi: 10.1021/acsami.0c07304

43. Zhao YN, Fan JJ, Li ZQ, Liu YW, Wu YP, Liu J. Effects of pore size on the osteoconductivity and mechanical properties of calcium phosphate cement in a rabbit model. *Artif Organs*. 2017;41:199-204.
doi: 10.1111/aor.12742

44. Van Bael S, Chai YC, Truscello S, et al. The effect of pore geometry on the in vitro biological behavior of human periosteum-derived cells seeded on selective laser-melted Ti6Al4V bone scaffolds. *Acta Biomater*. 2012;8:2824-2834.
doi: 10.1016/j.actbio.2012.04.001

45. Hoerth RM, Seidt BM, Shah M, et al. Mechanical and structural properties of bone in non-critical and critical healing in rat. *Acta Biomater*. 2014;10:4009-4019.
doi: 10.1016/j.actbio.2014.06.003

ACCSCIENCE PUBLISHING

International Journal of Bioprinting

RESEARCH ARTICLE

Bioprinting with adipose stem cells and hydrogel modified with bioactive glass

Krishna C.R. Kolan[1], Apurv Saxena[2], Bradley A. Bromet[3], Lesa B. Steen[4], August T. Bindbeutel[1], Julie A. Semon[3]*, Delbert E. Day[4], and Ming C. Leu[1]

[1]Department of Mechanical and Aerospace Engineering, Missouri University of Science and Technology, Rolla, Missouri, United States of America

[2]Department of Chemistry, Missouri University of Science and Technology, Rolla, Missouri, United States of America

[3]Department of Biological Sciences, Missouri University of Science and Technology, Rolla, Missouri, United States of America

[4]Department of Material Science and Engineering, Missouri University of Science and Technology, Rolla, Missouri, United States of America

Abstract

Bioprinting research is focused on utilizing growth factors and multiple cell types to create clinically relevant three-dimensional (3D) tissue models using hydrogels. Rheological and biological challenges are two main factors that limit the creation of extrudable bioactive hydrogels. In this study, we investigate incorporation of fast dissolving and bioactive borate glass in different weight to volume percentages (0.075 to 0.6%) to alginate-gelatin (1:1) hydrogel to improve rheological properties and enable bioprinting with bioactive glass. The addition of glass improved the stiffness of the hydrogel. Human adipose-derived mesenchymal stem cells (ASCs) were uniformly mixed in this bioink at 1×10^6 cells/mL concentration, and spheroid specimens were cultured in both static and dynamic culture conditions. Grid-shaped scaffolds measuring ~$18 \times 18 \times 1$ mm^3 were fabricated with the viable glass concentrations, and ASC viability was evaluated using Live/Dead assay. Despite immediate toxicity, an increased viability after 7 days with 0.15 w/v % or less borate glass content demonstrated the potential in utilizing highly resorbable calcium-releasing biomaterials such as bioactive glasses to modify hydrogels suitable for bioprinting cellularized 3D structures.

Keywords: Bioink; Bioactive glass; Ceramics; Adipose stem cells; Alginate; Gelatin

***Corresponding author:**
Julie A. Semon
(semonja@mst.edu)

Citation: Kolan KCR, Saxena A, Bromet BA, et al. Bioprinting with adipose stem cells and hydrogel modified with bioactive glass. *Int J Bioprint*. 2024;10(2):2057. doi: 10.36922/ijb.2057

Received: October 18, 2023
Accepted: January 31, 2024
Published Online: March 1, 2024

1. Introduction

Extrusion-based bioprinting is gaining in popularity because its versatility enables the fabrication of materials over a wide range of viscosities.[1] A majority of the current generation commercial bioprinters are all based on extrusion three-dimensional (3D) printing techniques.[2] The success of extrusion-based bioprinting depends largely on the proper selection of an extrudable hydrogel precursor and the proper selection of cell type. Hydrogels such as alginate, chitosan, hyaluronic acid, gelatin, collagen, fibrin, Matrigel, Pluronic® F127, and polyethylene glycol are commonly used to encapsulate

cells for extrusion-based bioprinting techniques.[3] No one material offers both the required rheological and biological properties, and therefore, it is a common practice to create a composite hydrogel to suit specific bioprinting application.

Alginate has been extensively used as synthetic extracellular matrix (ECM) that mimics native human tissues for more than three decades.[4,5] Alginate is derived from algae that crosslinks in the presence of divalent cations such as Ca^{2+} and Mg^{2+} and is suitable for bioprinting applications.[6] As alginate exhibits poor cell adhesion and proliferation due to the lack of arginine-glycine-aspartate (RGD) tripeptide sequences, it is functionalized to include RGD peptide sequence in its molecular structure.[7,8] An alternative approach is to add gelatin to alginate to prepare a composite hydrogel to enhance the hydrogel's ability to support cell adhesion and rheological properties for extrusion-based bioprinting techniques.[9-14] Despite being unstable at physiological temperatures, gelatin improves the printability of the composite alginate+gelatin (AG) hydrogel at room temperature due to the thermoreversible gel–sol transition behavior of gelatin.[9] AG hydrogels have been evaluated by researchers in different weight ratios to improve rheological properties at room temperature to facilitate printability without affecting the cell viability.[10,14] Researchers have also pursued media ionic strength modification and deposition at ~10°C, instead of room temperature, to improve printability.[13] Despite good viability (~90%) with epidermal stem cells, sheep stem cells, and aortic smooth muscle cells in the above studies, the main challenges that remain for AG hydrogel are to achieve: (i) printability at room temperature, (ii) controlled degradation of alginate, and (iii) slower dissolution of gelatin for improved viability over time.

Until the late 2000s, a material was considered bioactive upon formation of a hydroxyapatite-like layer on its surface to bond with hard tissue (bone) upon implantation.[15,16] Recently, the definition of "bioactive" has expanded, and the bioactive glass dissolution products have been increasingly investigated for vascularization, wound healing, cardiac, lung, and nerve tissue engineering applications in addition to traditional bone repair and teeth applications.[17] The research on bioactive glasses has evolved to produce glass compositions that are highly resorbable based on borate (B_2O_3) network instead of traditional silicate (SiO_2) network.[18-20] The dissolution of bioactive glasses depends not only on the durability of the main glass-forming network (e.g., SiO_2 or B_2O_3) and the overall glass composition, but it also depends on several other factors such as residual stresses during heat treatment and surface roughness.[21] It is known that borate glass dissolves at a faster rate compared to Bioglass®, and the calcium (Ca^{2+}) ions released during glass dissolution could initiate the crosslinking of alginate-based hydrogels.[22] Recently, investigators added copper or niobium to bioactive glass and then printed with hydrogel in order to fabricate a fast-recovering and printable construct.[23,24] Other researchers used borate-based bioactive glass to improve the printability of AG hydrogels by increasing the stiffness of the printed construct.[25]

Previously, we investigated cell viability in a 3D-bioprinted AG-glass composite hydrogel, using a recently FDA-approved borate-based bioactive glass (13-93B3 glass, referred to as B3) and human adipose stem cells (ASCs).[26] The B3 glass is particularly attractive due to its high dissolution rate and angiogenic ability.[27-29] This specific glass composition has demonstrated an ability to heal difficult-to-treat diabetic wounds, a capability thought to stem from their angiogenic properties. However, the exact reasons for their effectiveness and the underlying mechanisms involved are still not entirely clear. One recent study showed that an increased collagen III/collagen I ratio for ASCs with B3 glass exposure could establish one possible mechanism for wound-healing behavior with B3 glass.[30]

ASCs are extracted from the stromal vascular fraction of subcutaneous fat, which is more accessible and involving a less invasive procedure than acquiring their bone marrow counterpart, the more commonly studied bone-derived mesenchymal stem cells.[31-33] Additionally, they yield a greater number of cells after isolation than bone-derived mesenchymal stem cells and have a higher proliferative capacity. For these reasons, in addition to their differentiation, angiogenic, and therapeutic abilities, they are increasingly used in tissue engineering strategies.

In this study, we: (i) examined how the rheological characteristics of AG hydrogel are enhanced by adding B3 microparticles, (ii) identified the optimal range of B3 glass in bioprinting AG hydrogels and ASC viability, and (iii) evaluated the stability of AG hydrogel and the dissolution of gelatin under these conditions.

2. Materials and methods

2.1. Cell culture

Frozen vials of human ASCs were thawed and plated in complete cell culture media (CCM) and incubated at 37°C with 5% humidified CO_2. To ensure that the findings were universal and not unique to a single donor, ASCs from three different unrelated donors (LaCell, New Orleans, LA, USA) were tested in all experiments. More details about the ASC culture conditions and media requirements can be found in our previous work.[34,35] CCM was prepared with alpha minimum essential media (α-MEM) by adding 10% fetal bovine serum, 1% 100× L-glutamine, and

1% 100× antibiotic/antimycotic. On the second day of culture, ASCs were washed with phosphate-buffered saline (PBS), viable ASCs were harvested with 0.25% trypsin/1 mM ethylenediaminetetraacetic acid (EDTA), and re-plated at a concentration of no more than 15,000 ASCs per dish. ASCs that reached ≤70% confluency were lifted between the second and sixth passages for suspension in AG hydrogels for all experiments. ASCs from subsequent passages were not utilized for experiments as they could affect pluripotent properties of ASCs.

2.2. Bioink preparation

Gelatin (Type B, Sigma-Aldrich, St. Louis, MO, USA) in 3 w/v % (0.3 g in 10 mL) was dissolved in Dulbecco's Modified Eagle Medium (DMEM; Gibco, Thermo Fisher Scientific, MA, USA) in a glass beaker at ~40°C while being magnetically stirred at 150 rpm. After gelatin dissolution, sodium alginate (Sigma-Aldrich, St. Louis, MO, USA) in 3 w/v % (0.3 g in 10 mL) was added to the gelatin solution and mixed overnight to obtain the AG hydrogel. B3 glass powder particles (less than 20 μm with ~3 μm d_{50} particle size; chemical composition in wt.%: 53% B_2O_3, 20% CaO, 12% K_2O, 6% Na_2O, 5% MgO, 4% P_2O_5) were added to the solution in four different weight ratios (0.075, 0.15, 0.3, and 0.6 w/v %) after gelatin dissolution and allowed to dissolve for ~10 min before the addition of alginate powder. For example, 0.075 w/v % B3 glass corresponds to 1.25% of total combined weight of alginate and gelatin in the solution. Therefore, AG hydrogels made with 0.075, 0.15, 0.3, and 0.6 w/v % B3 glass are referred as 1.25G, 2.5G, 5G, and 10G, respectively, in this paper. All powders including gelatin, sodium alginate, and B3 glass powder particles were ultraviolet-sterilized before being added to the DMEM solution. ASCs pellet (4×10^6) was re-suspended in 0.2 mL CCM and pipetted into AG hydrogel and magnetically stirred for no more than 3 min to obtain a uniform cell distribution and a final ASC concentration of 1.0×10^6 cells per 1 mL of bioink. The bioink was transferred to 3 mL Loctite® Henkel syringe barrel, centrifuged to remove air bubbles, and attached with 22G (410 μm) or 25G (250 μm) tips (SmoothFlow Tapered, Nordson EFD, Westlake, OH, USA) for 3D bioprinting.

2.3. Rheological characterization

For rheological characterization, hydrogels were prepared in deionized (DI) water with gelatin (3 w/v %), alginate (3 w/v %), and AG (6 w/v %), and with the addition of B3 glass in different weight concentrations. AG hydrogels with and without B3 glass were tested for viscosity using a Kinexus rheometer (Malvern Panalytical, Westborough, MA, USA) with a parallel plate set-up. A gap of 0.5 mm was set between plates, and the measurements were conducted at room temperature. A fresh scoop of gel was loaded each time to test viscosity, recovery, yield strength, etc. Three different tests were conducted on the gels: (i) viscosity vs. shear rate (to measure viscosity with increasing shear rate from 0.1 to 100 s^{-1}), (ii) oscillation amplitude sweep, and (iii) recovery tests (changing shear rate from steady state to a predetermined rate for a certain amount of time). In oscillation amplitude sweeps, percentage strain was considered input, and machine output data of loss vs. storage modulus components were plotted. Data points below 0.1 s^{-1} shear rate were not reported because of the instability at low shear rates. Although one set of data was reported for each gel type, measurements were repeated to confirm the validity of the data. Statistical analysis of the rheological data was not performed because of the significant differences between the samples prepared with several orders of magnitudes difference in results.

2.4. Scaffold fabrication

A custom-modified tabletop cartesian 3D printer to include syringes connected through digital syringe dispenser (Loctite®, Rocky Hill, CT, USA) was used to fabricate scaffolds. The 3D printer and printing schema are illustrated in Figure 1a and b, and the 3D printer is shown in Figure 1c. Scaffold dimensions were set to 15 mm length, 15 mm width, and ~ 1 mm thickness (6 layers) and printed with 0–90° filament orientation in alternate layers. A customized software was written for G-code generation and syringe dispenser control. Sterile practices were followed for scaffold fabrication with ASCs, bioink syringes were maintained at room temperature, and the scaffolds were bioprinted in less than an hour inside the laminar flow hood.

2.5. Physical assessment

Test specimens with overall dimensions of $40 \times 20 \times 5$ mm^3 were fabricated to have a 20 mm gauge length and 10 mm section width for tensile tests. Dense specimens without any designed pores were used for these tests, and specimens were crosslinked with 0.1 M $CaCl_2$ solution for 10 min before tensile tests. Specimens were tested on Instron machine (Instron 5969, Norwood, MA, USA) at a crosshead speed of 5 mm/min. The swelling properties of the hydrogel were assessed on scaffolds with dimensions of $15 \times 15 \times 1$ mm^3. Swelling percentage (S) was calculated using the formula, $S = [(S_t - S_c)/S] \times 100$, where S_t is scaffold weight after 24 h soak in DI water, and S_c is scaffold weight immediately after crosslinking.

2.6. Scanning electron microscopy

Hydrogel in bulk (~2–3 mL in a centrifuge tube) was freeze-dried to porous foam-like pellets. The pellets were coated with Au-Pd for about ~60 s by mounting the samples on a rotating platform using a Hummer Sputter Coater. The

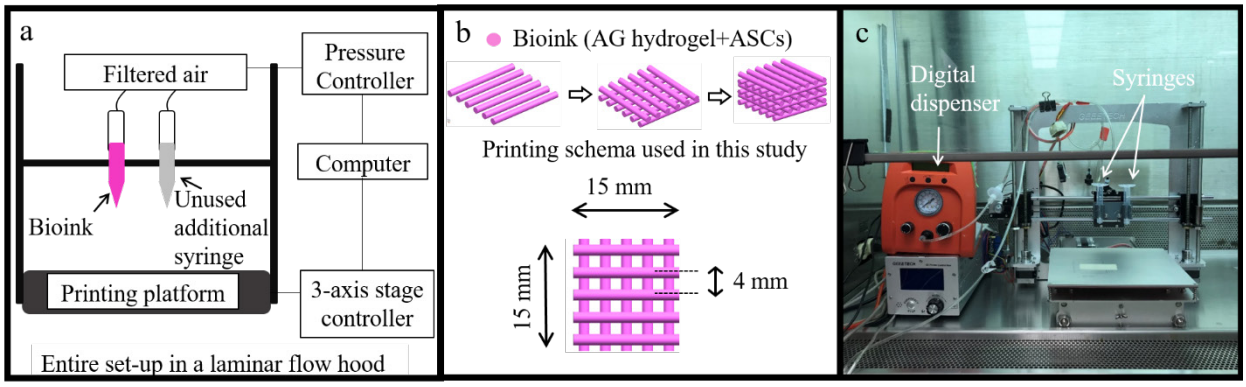

Figure 1. Extrusion-based 3D printing. (a) Schematic of printer used in this study; (b) the printing process and scaffold dimensions; (c) bioprinter in the laminar flow hood with a syringe dispenser.

samples were observed under a field emission scanning electron microscope (FE-SEM, S-4700, Hitachi, Japan) to analyze the microstructure by capturing the images at 5 kV accelerating voltage at various magnifications.

2.7. X-ray diffraction analysis

X-ray diffraction (XRD) analysis (Philips X-Pert, Westborough, MA, USA) was performed on the powdered freeze-dried sample to test for any crystalline hydroxyapatite-like formations in the material. Scans were run from 2θ values ranging from 10° to 80° using Cu Kα radiation (λ = 0.154056 nm).

2.8. ^{1}H-NMR spectroscopy analysis

In this work, gelatin was physically blended with alginate to form a composite gel and not chemically crosslinked. It was expected that with time as bioprinted scaffold is incubated at 37°C, gelatin present in the scaffold could potentially be separated and leached into the media. In order to study the release of gelatin from the AG hydrogel used in this study, AG, 1.25G, and 2.5G scaffolds measuring 15 × 15 × 1 mm^3 were fabricated without cells, crosslinked with 0.1 M $CaCl_2$ solution for 10 min, and washed twice with DI water. The samples were soaked in DI water in airtight containers under standard culture conditions for up to 7 days. The surrounding DI water collected after 1 day and 7 days including the $CaCl_2$ solution used for crosslinking were all analyzed for presence of gelatin using proton nuclear magnetic resonance (^{1}H-NMR) spectroscopy (Bruker 400 MHz Avance™ III HD, Billerica, MA, USA). First, known quantities of gelatin were dissolved in DI water, and 0.2 mL of gelatin solution was mixed with 0.6 mL of deuterium oxide (99.9 atom %, Sigma Aldrich, St. Louis, MO, USA), and the solution was transferred to NMR tube (Colorspec®, Sigma Aldrich, St. Louis, MO, USA) and analyzed for 10 min. The area under a unique characteristic gelatin peak at ~1.9 ppm (Figure 2a) on the horizontal axis was calculated

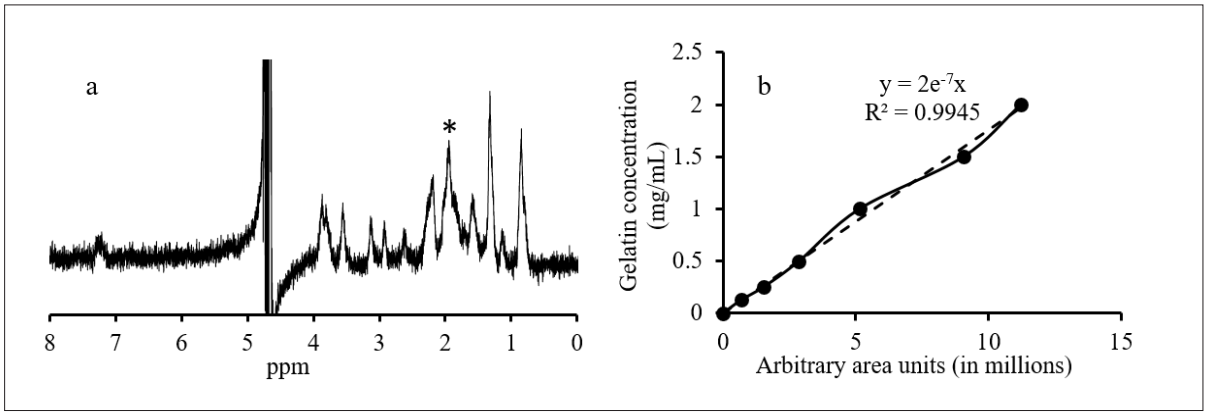

Figure 2. (a) NMR spectra of gelatin with characteristic peak at ~1.9 ppm (indicated by *) that was considered for area; (b) gelatin standard curve plotted based on the area corresponding to the gelatin concentration.

and averaged for known quantity of gelatin concentration to obtain a gelatin standard curve as shown in Figure 2b.

2.9. Cell viability

The ASC viability was evaluated using a Live/Dead viability kit (ref. L3224, Carlsbad, CA, USA). Briefly, 20 µL of ethidium homodimer-1 and 5 µL of calcein were pipetted into 10 mL of PBS to create the Live/Dead reagent. At specific time points, scaffolds were washed twice with PBS and soaked in 1 mL of reagent solution for at least 30 min under dark conditions at room temperature before imaging under a confocal microscope (Nikon A1R-HD Eclipse Ti2, Melville, NY, USA). A random 5 × 5 mm^2 area was imaged with a 40 µm step for each of the three scaffolds at different time points. To quantify the viability results, a maximum intensity projection image was created with red, green, and blue channels using ImageJ software. The red and green channels of the image provided the dead cell and live cell counts. ASC viability in percentage was calculated using this formula: [live cells/(live cells + dead cells)] × 100%.

2.10. Statistical analysis

Six samples in each set were used for tensile tests, and three samples in each set were used for cell viability quantification. The results were reported as average ± standard deviation. Minitab® software was used to analyze the difference in means of different groups using one-way analysis of variance (ANOVA). The means were considered significantly different if the *P*-value is less than 0.05.

3. Results and discussion

3.1. Rheological assessment of hydrogels

One of the objectives of the study was to evaluate the extent of rheological modification of the AG hydrogel with the addition of B3 glass. Hydrogel viscosity and its shear-thinning behavior are crucial in extrusion-based 3D printing processes as such behavior allows the material to flow through the nozzle at low air pressure without causing severe damage to cells. DI water was used to investigate the rheological behavior of B3 glass-mixed gels instead of complete culture media. The reason for this choice is to analyze the true nature of the effect of the dissolved glass and released ions (Ca^{2+}, Mg^{2+}, and others from the glass) without having any interactions with other salts present in the culture media. It was hypothesized that the effect of B3 glass amount on rheological behavior would serve as a realistic indicator while using gels made with culture media. Despite the evidence in literature demonstrating a significant difference in the swelling of gels made with DI water compared to that of gels made with culture media, the difference is insignificant for viscosity of gels made with DI water or culture media with highly resorbable B3 glass.[36] It was noticed in our experiments that B3 glass dissolves in a few minutes during the gel mixing process to significantly affect gel viscosity irrespective of the media (DI water or culture media). Figure 3 shows the change in viscosity of all hydrogels considered in this study with increasing shear rate. The viscosity of alginate (Alg),

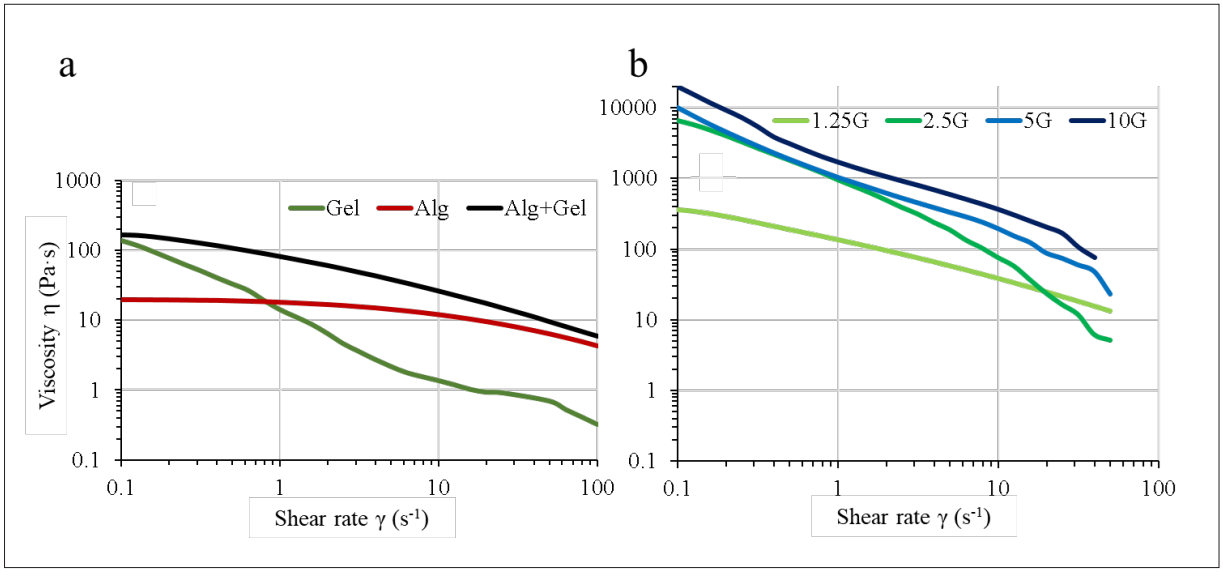

Figure 3. Hydrogel viscosity as a function of shear rate at room temperature before crosslinking with $CaCl_2$. (a) Alginate, gelatin, and alginate+gelatin (AG) without glass; (b) effect of B3 glass addition on AG hydrogels in different weight concentrations.

gelatin (Gel), and alginate+gelatin (Alg+Gel or AG) is shown in Figure 3a, and the viscosity of B3 glass-modified AG hydrogels with 1.25 wt.% (1.25G), 2.5 wt.% (2.5G), 5 wt.% (5G), and 10 wt.% (10G) glass content is shown in Figure 3b. The viscosity for all hydrogels was measured at room temperature and before crosslinking with 0.1 M $CaCl_2$ solution. At higher shear rates, modified hydrogels with B3 glass slipped out of the plates (especially, 5G and 10G) of the rheometer, and the test was stopped before the programmed shear rate of 100 s^{-1}. Overall, all AG hydrogels irrespective of B3 glass addition showed a shear-thinning behavior with decreased viscosity at increasing shear rates.

As B3 glass is a fast-dissolving bioactive glass, it quickly starts to release Ca^{2+} and Mg^{2+} ions, which are divalent, and other ions including K^+, PO_4^{3-}, Na^+, and B^{3+} to the surrounding aqueous media. As the divalent ions initiate the crosslinking with alginate in the hydrogel, the viscosity of hydrogels with B3 glass was significantly increased by several orders of magnitude (Figure 3b). The addition of 2.5 wt.% B3 glass resulted in a significant and sharp increase in hydrogel viscosity from 1.25 wt.% B3 glass addition (from ~350 Pa·s to ~7000 Pa·s at 100 s^{-1}). The differences in viscosity at $t = 0$ s observed for 2.5G, 5G, and 10G hydrogels (~7000 Pa·s, ~10,000 Pa·s, and ~11,000 Pa·s at 100 s^{-1}, respectively) were not as significant as viscosity differences between 1.25G and 2.5G hydrogels. These findings suggest the likelihood of an optimal B3 glass concentration, ranging between 1.25 and 2.5 wt.%, for AG hydrogels composed of 3 w/v % alginate and 3 w/v % gelatin.

Amplitude sweep oscillatory tests were conducted on all samples to determine the viscoelastic behavior of AG hydrogels modified with B3 glass. Figure 4 shows the variation of G' and G" with strain percentage and the linear viscoelastic region for each hydrogel. At low concentrations of glass (1.25%), there is no significant difference in the storage modulus (G') in comparison to AG hydrogel (Figure 4b), whereas with the increase in glass concentration to 2.5% made a significant difference. Figure 4c shows the variation in loss modulus (G") for all gels investigated in this study. The transition from G">G' to G'>G" was more prominent in 2.5G, 5G (shown in Figure 4d and e), and 10G hydrogels clearly showing a viscoelastic solid-like behavior with a consistent behavior of G'>G", indicating the increased stiffness of the modified AG hydrogels with B3 glass. This is observed with a clearly defined yield point (cross-over point of G' and G"). The shear stress values around the yield point for gels were recorded as ~3400 Pa for 2.5G, ~3000 Pa for 5G, and ~1300 Pa for 10G. It is also observed that the yield point occurs at lower strain for gels made with higher glass percentage. This seems to be consistent with the lower shear stress values. This could be because of the non-uniformity of the composite AG gels made with higher glass percentages. Figure 4a shows the physical behavior of gels prepared with increasing glass content. It can be clearly seen that gel made with the most glass content behaves like a large piece of crosslinked gel. For example, extruding or manual separation of 10G gel resulted in pockets of crosslinked gel (pockets of gel chunks) being extruded or separated from the hydrogel rather than a single continuous filament extrusion. This non-uniformity is believed to arise during the gel preparation process as pockets of alginate could be crosslinked in a localized manner even before the complete uniform mixing of hydrogel. As a result, during the oscillatory sweep tests, chunks of gels were noticed to break apart and come out of the plates at higher strain.

In addition to shear-thinning and solid-like behavior of hydrogels, the viscosity recovery of the hydrogel after removal of shear force is crucial in extrusion-based 3D bioprinting applications. As hydrogel is extruded through the nozzle, it suffers from higher shear stress and flows through the tip because of a shear-thinning behavior. After deposition of a filament, the hydrogel should recover its molecular structure and viscosity to avoid spreading on the substrate and withstand the weight of successive filaments that would be deposited on top of the current filament. To determine the recovery behavior of B3 glass-modified AG hydrogels in a rheometer, hydrogels were initially maintained under a steady-state shear rate of 0.1 s^{-1} to obtain a stabilized viscosity value. After reaching a steady-state viscosity, the shear rate was increased to higher shear rates (10 s^{-1} and 100 s^{-1}) in two separate tests for a specific amount of time (30 s and 10 s, respectively), immediately followed by a cooling period of 0.1 s^{-1} shear rate. Viscosity of hydrogels recorded at different shear rates with time is shown in Figure 5. The recovery data of two tests (at 10 s^{-1} and at 100 s^{-1} shear rates) were combined, and the time scale was adjusted for a simplified representation. A significant drop in viscosity for all hydrogels at increased shear rates can be clearly observed in Figure 5. Recovery time is defined as the time taken for a hydrogel to attain its original steady-state viscosity value from the reduced values at higher shear rates. The shear rate of 100 s^{-1} was used to mimic the behavior of the hydrogel passing through the nozzle tip during extrusion. The results indicated a "near-zero" recovery time for 2.5G and 5G hydrogels after application of 100 s^{-1} shear rate, which was evident from their step-function-like recovery to attain a constant viscosity at 160 s, as shown in Figure 5. 1.25G and AG hydrogels required 60 s and 90 s, respectively, to recover and attain a constant viscosity, as can be observed from the curvature indicated by arrows in Figure 5. It was also observed that hydrogels never truly recovered to 100% of their original steady-state viscosity values (at $t = 0$ s) after the removal

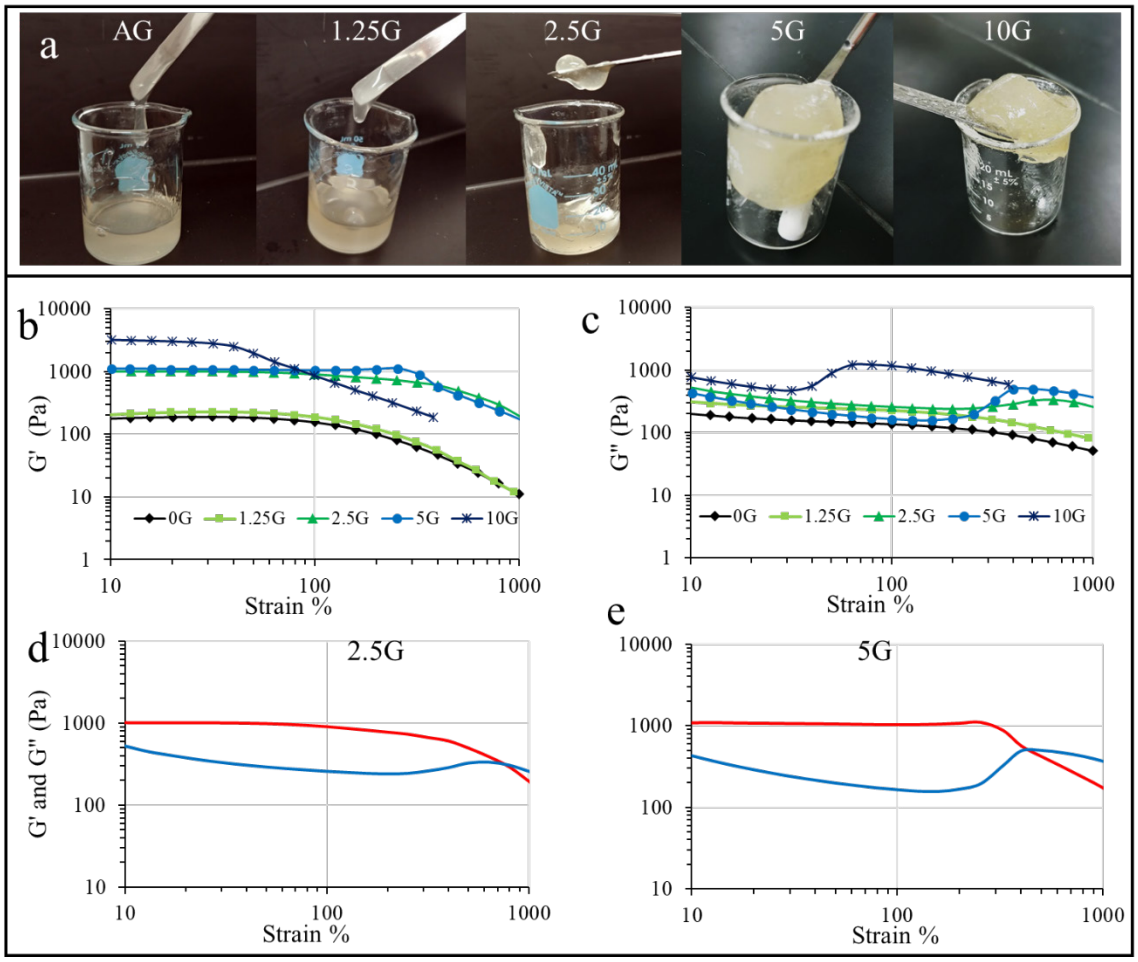

Figure 4. Viscoelastic behavior of AG hydrogels. (a) The physical behavior of hydrogels immediately after overnight stirring in a beaker kept on a 40°C hot plate. Flowability of hydrogels stopped with increased B3 glass content (at 2.5G). 2.5G, 5G, and 10G hydrogels exhibit a solid-like behavior. (b) Storage modulus (G') and (c) loss modulus (G") as a function of Strain percentage at room temperature before crosslinking with $CaCl_2$ for alginate-gelatin gels without glass and with different B3 glass weight percentages. (d) G' and G" for 2.5G, and (e) G' and G" for 5G.

of 100 s^{-1} shear rate. For example, steady-state viscosity of 2.5G hydrogel at t = 0 s was ~7000 Pa·s, and its recovered viscosity value between 160 and 220 s was at ~2000 Pa·s. This behavior was noticed in hydrogels with high B3 glass content (>2.5 wt.%) and believed to have occurred due to the loss of material between plates during tests at shear rate of 100 s^{-1}. The recovery time results provided a satisfactory representation of the recovery behavior as they confirmed the printability of all hydrogels with and without B3 glass addition. The recovery behavior of 10G hydrogel is not shown in Figure 5 because of its inhomogeneity and high material loss during recovery tests even at low shear rates.

3.2. Fabrication, swelling, and mechanical property assessment

The determination of viscosity and material recovery times enabled scaffold fabrication with AG, 1.25G, and 2.5G hydrogels. Six-layered scaffolds measuring 15 × 15 × 1 mm^3 were fabricated. The printing parameters used to fabricate scaffolds along with the printability matrix for different hydrogels are shown in Table 1. Hydrogels were first tested for their extrudability through a syringe at different air pressures with different nozzle tips. Although all hydrogel types were extrudable using different tip sizes ranging from internal diameter of 250 μm to 580 μm, the extrusion of highly viscous 5G and 10G hydrogels required high air pressures, extrudate was uneven, and consistent filament formation was not feasible. In part, this could be due to inhomogeneous mixture of alginate and gelatin components in 5G and 10G hydrogels. Addition of more glass meant availability of more Ca^{2+} ions to initiate alginate crosslinking before achieving a homogeneous composite hydrogel. Moreover, utilizing higher air pressures would damage the cells in the hydrogel, and large

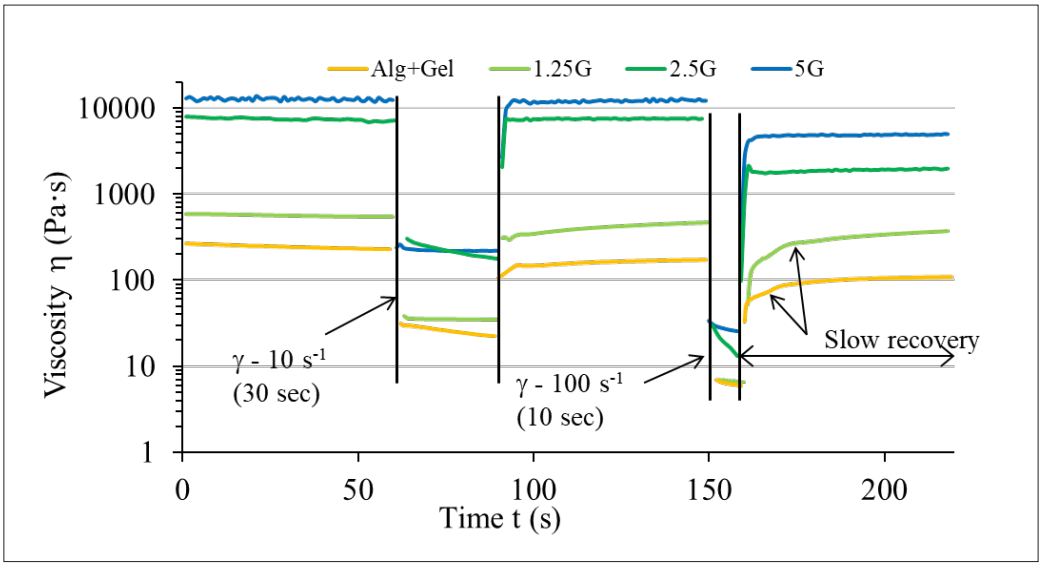

Figure 5. Effect of B3 glass addition on the recovery behavior of hydrogels. AG hydrogel and 1.25G required 90 s and 60 s, respectively, to recover to their original viscosity values, whereas 2.5G and 5G show immediate recovery.

tip sizes would compromise the resolution of the fabricated parts. Therefore, by considering the above, scaffolds were fabricated only with AG, 1.25G, and 2.5G hydrogels. Both 22G (410 μm inner diameter) and 25G (250 μm inner diameter) conical-shaped nozzle tips were considered for printing the AG, 1.25G, and 2.5G hydrogels. Specifically, 25G tips were used for AG and 1.25G gels, whereas 22G tip was used for 2.5G gels due to viscosity differences (orders of magnitude different). Despite using a larger tip, the air pressure required to extrude 2.5G gel was four times that of 1.25G, and the extrudate was thinner than that of 1.25G gel. Therefore, the layer height had to be reduced to 0.12 mm from 0.14 mm for AG and 1.25G gels. For AG and 1.25 gels, the extrudate requires time to recover, and therefore despite using a smaller nozzle tip (25G–250 μm), the extrudate spreads immediately after printing and a ~1 mm extrudate was obtained. This spreading behavior is expected based on the viscosity and poor recovery of the AG and 1.25 gels as discussed in our rheological study. A similar sized extrudate (~1 mm) width was obtained for 2.5G gel printed with a larger tip (22G–410 μm) and a much higher air pressure. The recovery time determined by recovery tests was implemented as dwell (wait) time between successive layers during scaffold fabrication. Figure 6 shows scaffolds fabricated before and after dwell time implementation. Before dwell time implementation, fabrication of a designed porous scaffold resulted in solid part formation after six layers of deposition as shown in Figure 6. This happened as the initially deposited layers merged on the substrate unable to recover and carry the weight of successive layers that were deposited during part fabrication. However, dwell time implementation allowed

Table 1. Scaffold fabrication parameters and printability matrix

Fabrication parameters				Printability matrix		
Hydrogel	AG	1.25G	2.5G	Hydrogel	3D part printability	Filament formation
P (psi)	4	5	20	AG	✓	✓
S (mm/s)	15	15	15	1.25G	✓	✓
h (mm)	0.14	0.14	0.12	2.5G	✓	✓
t (s)	90	60	0	5G	×	~
φ (μm)	250	250	410	10G	×	~

Abbreviations: P—air pressure; S—table speed; h—layer height; t—wait time between layers; φ—nozzle tip internal diameter; ✓—feasible; ×—not feasible; ~—irregular and inconsistent filament formation.

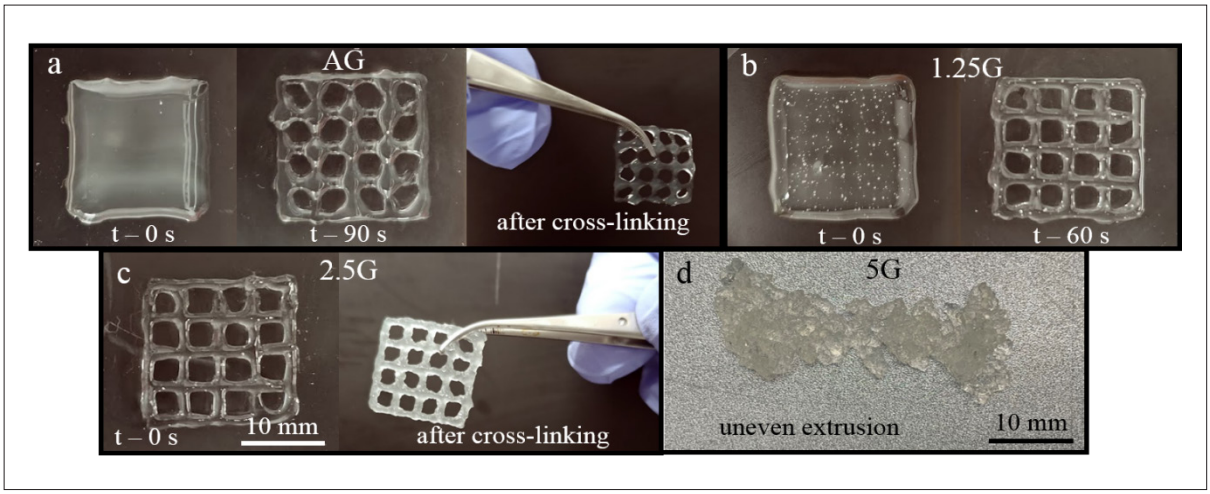

Figure 6. Scaffold fabrication with (a) AG, (b) 1.25G, (c) 2.5G, and (d) 5G hydrogels. Implementation of dwell time (t) between successive layer depositions aided in hydrogel recovery and made it feasible to fabricate AG and 1.25G scaffolds. Increasing the B3 glass content reduced the dwell time from 90 s to 0 s as 2.5G hydrogel scaffold could be fabricated with no dwell time. Failure to fabricate parts (dog-bone like specimen) with 5G hydrogel is also shown.

the filament recovery and thus enabled the designed scaffold fabrication. This was further tested in a complex 3D structure with internal channels mimicking a vascular network (Figure 7).

Scaffolds were crosslinked with 0.1 M $CaCl_2$ solution for 10 min immediately after fabrication, washed, and soaked in DI water for 24 h to measure the swelling percentage. Swelling of hydrogels indirectly represents the capacity of the material to absorb media and allow cell growth and proliferation. Swelling of AG hydrogel was increased after 24 h with the addition of B3 glass. The swelling of AG scaffolds was ~36%, whereas it increased to ~44% for 1.25G scaffolds and further to ~51% for 2.5G scaffolds. The release of Ca^{2+} and Mg^{2+} ions with B3 glass dissolution initiates alginate crosslinking during hydrogel preparation (overnight stirring), and the molecular structure was further condensed after crosslinking with $CaCl_2$ solution. Therefore, 2.5G scaffolds have a highly defined and consolidated molecular structure among the three scaffolds, and this was evident from the shrinkage of 2.5G scaffolds (~18%) after crosslinking. After scaffolds were soaked in DI water, they relaxed and absorbed DI water driven by the ionic concentration gradient with high number of ions present inside the scaffold structure (because of glass dissolution), and no ions present in the soaked media (DI water). Hydrogel swelling depends on the ionic concentration of the soaking solution and the number of ionic groups present in the hydrogel. It was reported that increased ionic groups in hydrogel increased its swelling ratio because of the osmotic pressure created by the increased counterions in the hydrogel.[37] This could be the reason for the high swelling percentage observed for 2.5G scaffolds. Higher swelling ratio for AG hydrogels prepared with high ionic strength PBS was also reported in a recent work and was consistent with our results.[13]

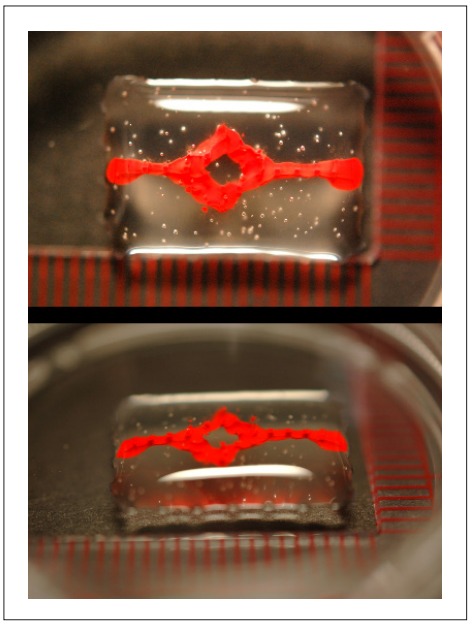

Figure 7. A superior (top picture) and anterior (bottom picture) view of a complex structure fabricated by 3D extrusion printing of AG hydrogel-B3 glass composite. A second nozzle was used to extrude red dye to view the internal channel. This construct demonstrates our technique of 3D printing with two different inks.

In this study, small amounts of B3 glass (7.5 mg/10 mL of DI water for 1.25G and 15 mg/10 mL of DI water

for 2.5G) were added to modify the AG hydrogel. The dissolution rate of borate-based glasses including B3 glass in different forms such as glass microspheres, large particles (>200 μm), and scaffolds in DI water, PBS, and simulated body fluid (SBF) have been investigated in the past.[38-41] These studies reported that the majority of B3 glass dissolution occurred during the first 24-h soak period after which the dissolution rate slowed due to the ionic concentration gradient and other factors. In comparison, the glass particles used in the current study are significantly smaller with an average particle size of 3 μm (20 μm mesh sieved) that could have dissolved within 24 h. Therefore, it could be safely assumed that the rheological, swelling, and mechanical properties of the modified AG hydrogels are mostly dependent on the ionic dissolution products of B3 glass and not the physical presence of glass particulates. Figure 8a shows the microstructure of the 2.5G hydrogel, indicating a highly porous and honeycomb-like structure with interconnected porosity. B3 glass particles were not detected in the microstructure, and the characteristic amorphous peaks of the glasses were also absent in the XRD analysis of the 2.5G hydrogel.

Figure 8b shows the dog-bone-shaped specimens utilized for evaluating the tensile strength of hydrogels immediately after crosslinking. A typical load vs. deflection curve for all three specimens is shown in Figure 8c, which indicates the increase in scaffold stiffness with the addition of B3 glass. The elastic modulus of AG, 1.25G, and 2.5G specimens was 33 ± 17 kPa, 62 ± 7 kPa, and 73 ± 13 kPa, respectively, and the ultimate tensile strength of specimens was 26 ± 5 kPa, 21 ± 4 kPa, and 34 ± 9 kPa. 2.5G specimens had highest ultimate tensile strength and were significantly stiffer ($p < 0.05$) in comparison to AG specimens. The increased stiffness was in agreement with the rheological data that showed increased viscosity, decreased recovery time, and a viscoelastic solid-like behavior for 2.5G hydrogels. As the added B3 glass dissolves, the dissolution ions crosslink more alginate polymer chains in the AG hydrogel that causes increased stiffness. Researchers have previously reported that human mesenchymal stem cells (MSCs) encapsulated in ionically crosslinked alginate hydrogels show adipogenic differentiation at moduli of <10 kPa and show osteogenic differentiation at moduli of 11–30 kPa.[42,43] The authors also suggest that osteogenic differentiation of MSCs could be enhanced in hydrogels with faster stress relaxation. AG hydrogels modified with B3 glass (2.5G and 1.25G) have elastic moduli in similar range, and the stress relaxation occurs through breakage and subsequent forming of ionic crosslinks. In addition, stress relaxation could also occur because of the fast swelling of B3 glass modified AG hydrogels (especially, 2.5G). Therefore, the addition of B3 glass to modify AG hydrogels could be useful to tune the human stem cells activity.

An important factor to consider is the retention of scaffold mechanical properties (or scaffold integrity and structure) in culture conditions with time. AG hydrogel strength greatly depends on the w/v % of the alginate and gelatin used in the preparation and the ionic strength of the crosslinking solution. For example, Duan et al. used 6 w/v % of alginate and gelatin (compared to 3 w/v % used in our study), and the crosslinked samples with 0.3 M $CaCl_2$ (compared to 0.1 M $CaCl_2$ in our study) reported improved mechanical properties that were able to sustain for up to 7 days in culture conditions.[14] Our attempts to test specimens after soaking them in DMEM for 7 days at culture conditions were not successful as specimens were broken in the grips of the Instron machine, and insignificant elastic modulus and strength values were recorded. Our results indicated a rapid loss of modulus and strength to a point where they were not suitable for any load-bearing applications, which is in agreement with results reported by Giuseppe et al.[10] However, it must be noted that 1.25G and 2.5G scaffolds had sufficient integrity

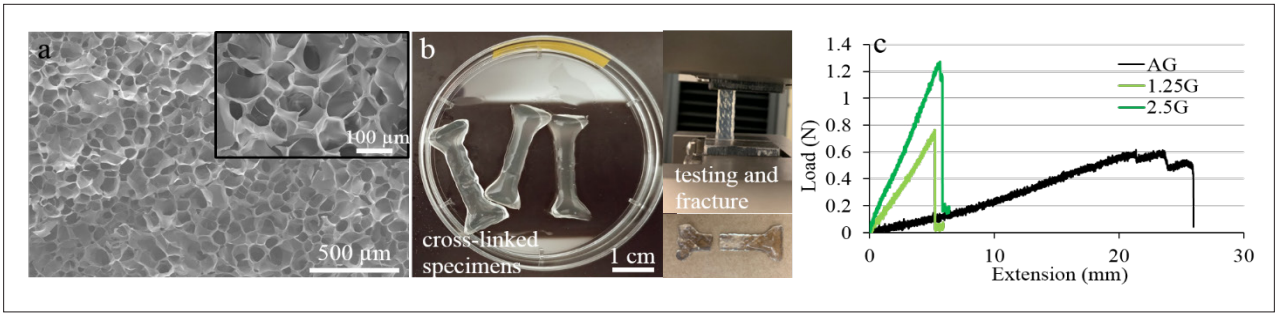

Figure 8. (a) SEM image of 2.5G hydrogel with ~100 μm interconnected pores shown in the magnified inlet picture; b) dog-bone specimens used for tensile tests; (c) typical load vs. extension graphs of AG, 1.25G, and 2.5G specimens.

after 14 days in culture to handle and perform biological assays. In general, hydrogel degradation depends on the soaking media composition and enzymes present in it. In our study, DI water was utilized to prepare all hydrogels and to investigate the scaffold swelling characteristics, which are different from other studies where PBS or DMEM was utilized. Nevertheless, samples used for mechanical tests were stored in DMEM to mimic the *in vitro* environment. In addition, we also investigated the structural integrity of 2.5G scaffolds in the CCM at culture conditions without crosslinking with $CaCl_2$ solution. This test was performed to examine if the divalent cations (Ca^{2+} and Mg^{2+}) that are released from B3 glass into the hydrogel, which helps initiate the hydrogel crosslinking, would be sufficient to sustain the scaffold structural integrity in culture conditions. Figure 9 shows a collapsed 2.5G scaffold that was not crosslinked after a 2-h incubation in CCM at 37°C, whereas a scaffold crosslinked with 0.1 M $CaCl_2$ retained its structural fidelity after 7 days in culture. This result demonstrates that despite the improvement achieved with B3 glass addition in terms of printability of AG hydrogel, rheological characteristics, and initial mechanical properties, addition of glass alone would not be sufficient to fabricate a 3D scaffold without the chemical crosslinking using $CaCl_2$ solution.

3.3. Effect of B3 glass on ASCs viability

One important objective of this study was to evaluate the amount of B3 glass that is acceptable to add to the AG hydrogel to provide viable human ASCs. As B3 glass dissolves much faster than traditional silicate-based bioactive glasses and faster than 45S5 glass, it was important to establish that the resultant concentration of ionic dissolution products has no toxic effects on ASCs *in vitro*. The toxicity could be resulted due to pH increase as alkali ions are released to CCM with B3 glass dissolution. Recently, B3 glass was added to ASCs in two different approaches: directly being added as particles during cell culture, and indirectly (glass dissolution products) exposing cells to two-dimensional (2D) cell culture environment at a B3 glass concentrations that are less than 10 mg/mL.[30,35] These studies reported that a high concentration of B3 glass exposure (>10 mg/mL) could be toxic to ASCs, whereas low concentrations alter ASC protein secretions that may regulate wound healing. Several studies have investigated the toxicity of silicate-based bioactive glasses toward stem cells in a 2D environment, reporting that an optimum concentration of ionic dissolution products could exist upon which the treatment that could be toxic to cells was administered.[44-46] To establish a baseline, we first investigated the B3 glass toxicity to ASCs in 3D environment by adding glass in different weight percentages to AG hydrogel. First, ASCs were encapsulated in AG, 1.25G, 2.5G, 5G, and 10G hydrogels, and 3D-bioprinted as spheroids. To investigate the cell viability, spheroids were cultured in both static (6-well plates under standard culture conditions) and dynamic (6-well plates kept on a rocker) conditions. Figure 10 shows the live/dead assay images of the spheroids on day 0 (2 to 4 h after extrusion and crosslinking), day 1, and day 4 after culture. Spheroids made with 5G and 10G spheroids were irregular in shape because of the high viscosity, and difficulties were encountered to uniformly mix ASCs in these hydrogels. Patches of the hydrogel with empty pockets (without cells) and irregular shapes could be observed in the live/dead images of 5G and 10G hydrogels (Figure 10d, e, i, and n). Also, significant number of dead cells (red spots) can be observed in the live/dead images of 5G and 10G spheroids at all time points which was not the case with other spheroids, whereas more viable ASCs than dead cells were noticed in AG, 1.25G, and 2.5G spheroids.

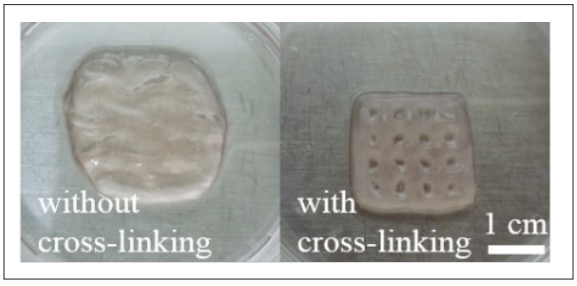

Figure 9. 2.5G scaffold in CCM at 37°C after 2 h (left) and after 7 days (right).

Figure 11 shows the quantification of the live/dead assay results. The results clearly indicate that increasing the percentage of B3 glass could be toxic to ASCs in the hydrogel. The viability of ASCs in AG spheroids without B3 glass was significantly higher than ASC viability in 10G, 5G, and 2.5G spheroids immediately after extrusion and crosslinking with $CaCl_2$. ASC viability in spheroids cultured under dynamic conditions was also higher in comparison to viability in spheroids cultured under static conditions after 24 h. This could be due to efficient nutrient transfer to ASCs under dynamic conditions than static conditions. In addition, for spheroids containing B3 glass, Ca^{2+}, B^{3+}, and other ions released after glass dissolution in the spheroid could diffuse more freely to the media under dynamic conditions than static culture conditions. This could cause the pH of the spheroid to go basic in static conditions and negatively affect ASCs. Addition of B3 glass increased the pH of hydrogels from neutral for AG to pH 8 for 1.25G, pH 8.5 for 2.5G, and up to pH 9 for 10G hydrogel. This could be the reason for high toxicity of B3 glass to ASCs, especially in 2.5G, 5G, and 10G spheroids on day 0, i.e., immediately after mixing ASCs. Though the inside of spheroid maintained relatively high pH, the pH of the surrounding CCM remained neutral during culture

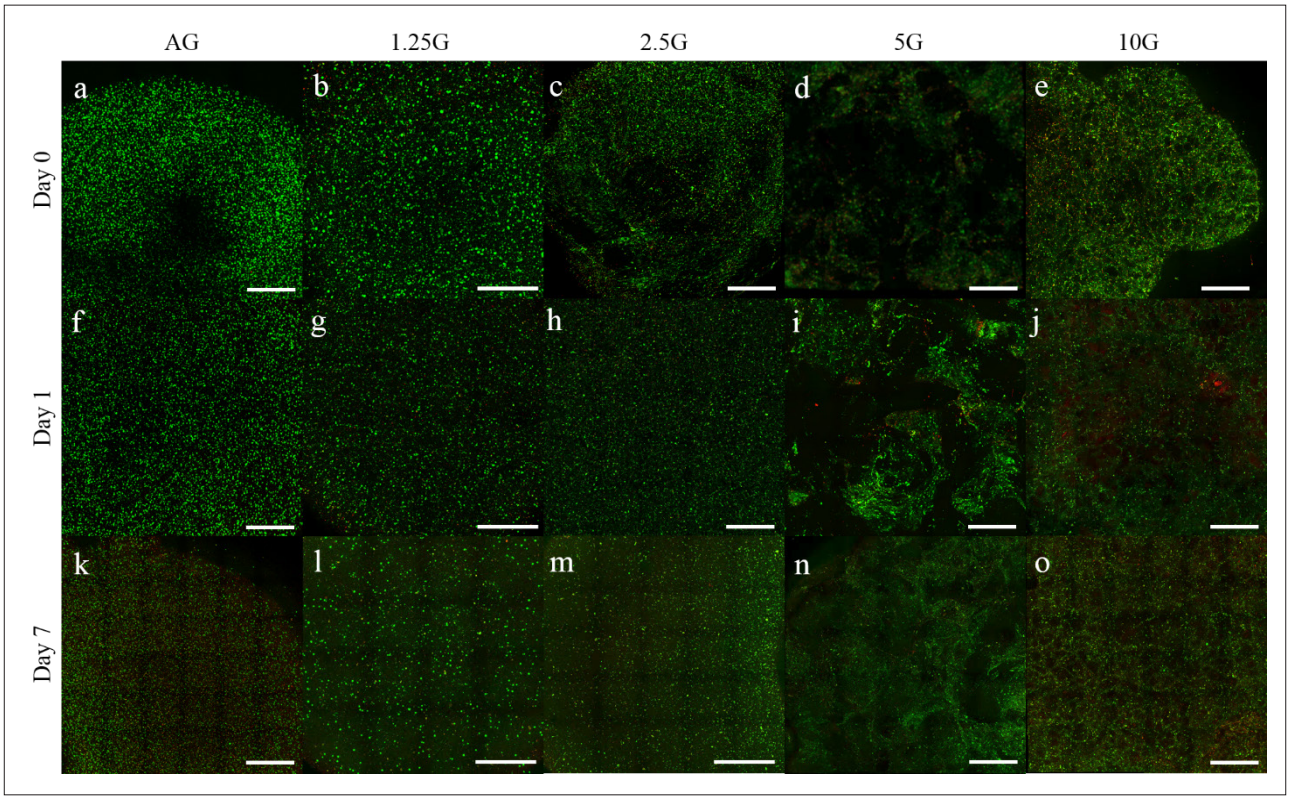

Figure 10. Live/Dead assay images of AG, 1.25G, 2.5G, 5G, and 10G spheroids cultured in dynamic conditions for up to 7 days. (a–e) Viability on day 0 (within 2 to 4 h after extrusion), (f–j) viability after 24 h, (k–o) viability after 7 days. Scale bars: 1 mm. Green dots in images represent live cells, and red dots represent dead cells. Undissolved borate glass particles could react with assay reagents and potentially cause green background fluorescence for samples with higher percentage glass (5G and 10G).[26] The background was ignored during cell quantification with ImageJ software.

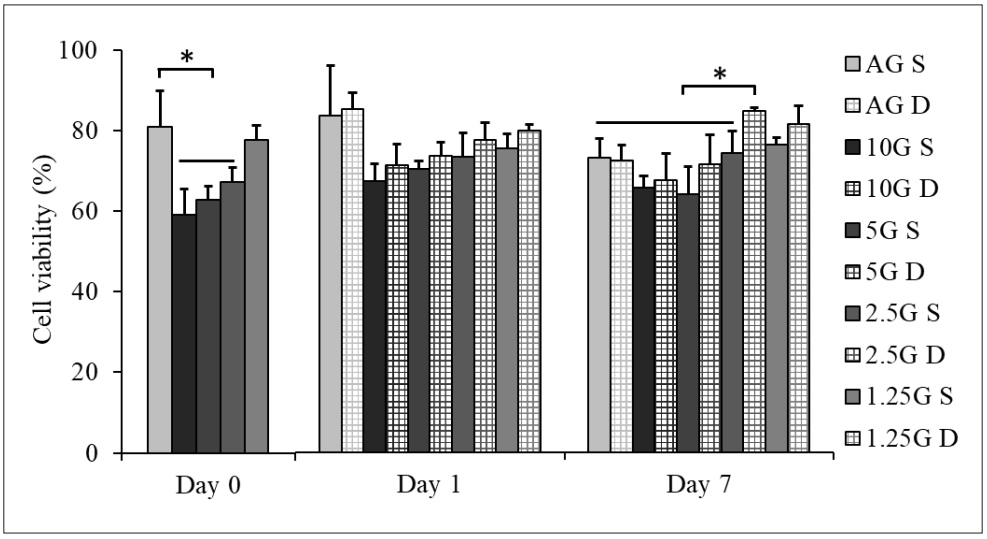

Figure 11. ASCs viability in AG, 1.25G, 2.5G, 5G, and 10G spheroids cultured in both static (S; solid columns) and dynamic conditions (D; checkered pattern columns). ASCs viability significantly decreased ($p < 0.05$) with increase in borate glass content (increasing dark shade represents increasing glass content) in less than 4 h after glass addition. ASCs in borate glass-modified hydrogel, which were recovered with time, showed significantly higher viability in hydrogel modified with lower glass percentages ($p < 0.05$).

conditions. This could be attributed to two reasons: (i) the increase in pH due to release of ions from B3 glass to a larger extent could be limited to inside of the hydrogel matrix, and (ii) the release of gelatin from hydrogel matrix to surrounding media could neutralize the increase in pH because of any ions released from B3 glass, thereby causing the pH of the media to remain in the neutral range (7–7.6) for all gel types (1.25G to 10G). In any case, with the regular change in media and presence of dynamic culture conditions, pH of the spheroids and neutralized media as well as ASC viability eventually improved after 7 days in culture, and 2.5G spheroids had significantly higher viability than AG spheroids.

The ASC viability in spheroidal culture helped determine the range of viable B3 glass percentages that could be added to AG hydrogel (0.075 and 0.15 w/v % or 1.25G and 2.5G gels) and the suitable culture conditions (dynamic better than static). Nonetheless, it is important to validate the established B3 glass concentrations and culture conditions with the 3D-printed constructs. Therefore, AG, 1.25G and 2.5G lattice structures containing ASCs and measuring 15 × 15 × 1 mm^3 were bioprinted and cultured for up to 7 days under dynamic conditions. Figure 12 shows the live/dead assay images of the scaffolds. A higher percentage of viable ASCs (green spots) than dead cells can be clearly seen in all images. A higher percentage of dead cells in the edges of the pores, possibly caused by the crosslinking with $CaCl_2$ solution, is a notable observation. Figure 13 shows the results of quantified live/dead assay images of bioprinted scaffolds. The ASC viability in scaffolds was similar to the viability of AG, 1.25G, and 2.5G spheroids, with ASC viability in AG scaffold being significantly higher than 2.5G scaffold. However, after 7 days in culture, despite possessing a higher percentage of viable ASC populations, both 1.25G and 2.5G scaffolds were not significantly different than AG scaffolds in terms of cell viability. In addition, a significant decline in ASC viability in AG hydrogel was observed in both bioprinted scaffolds and spheroids from day 1 to day 7 under culture conditions. The decline in ASC viability could be attributed to the release of gelatin from AG hydrogel scaffold. In this study, gelatin was mainly added for cell adhesion and proliferation as alginate alone does not contain the necessary RGD tripeptide to support cell adhesion. In AG

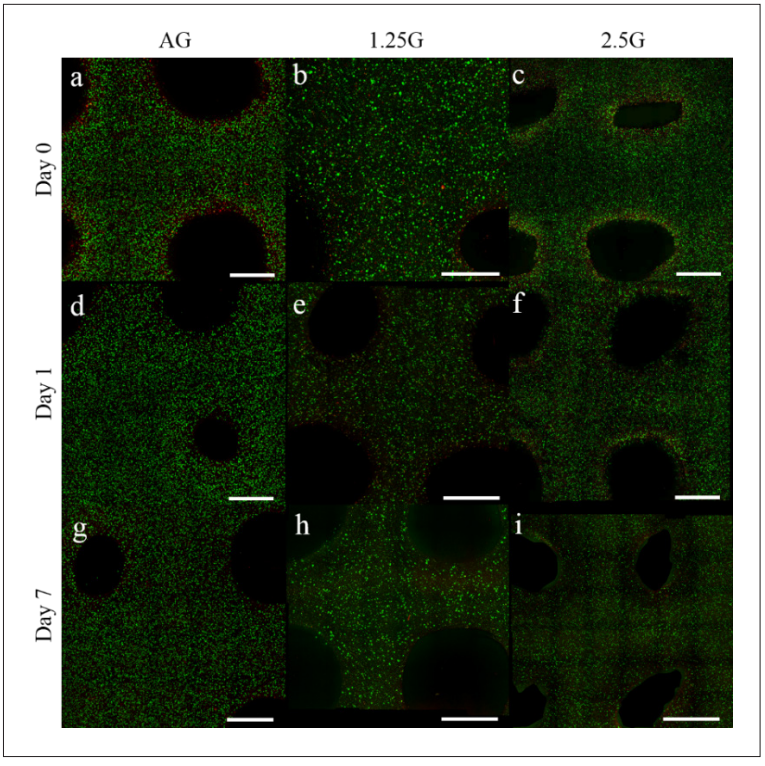

Figure 12. Live/Dead assay images of bioprinted AG, 1.25G, and 2.5G scaffolds cultured in dynamic conditions for up to 7 days. (a–c) viability on day 0 (within 2 to 4 h after bioprinting and crosslinking), (d–f) viability after 24 h, and (g–i) viability after 7 days. Scale bars: 1 mm. A higher percentage of dead cells (red spots) were observed near pore edges in comparison with the scaffold interior, indicating cell death due to exposure to $CaCl_2$ solution during crosslinking and the overall presence of low cell numbers at edges.

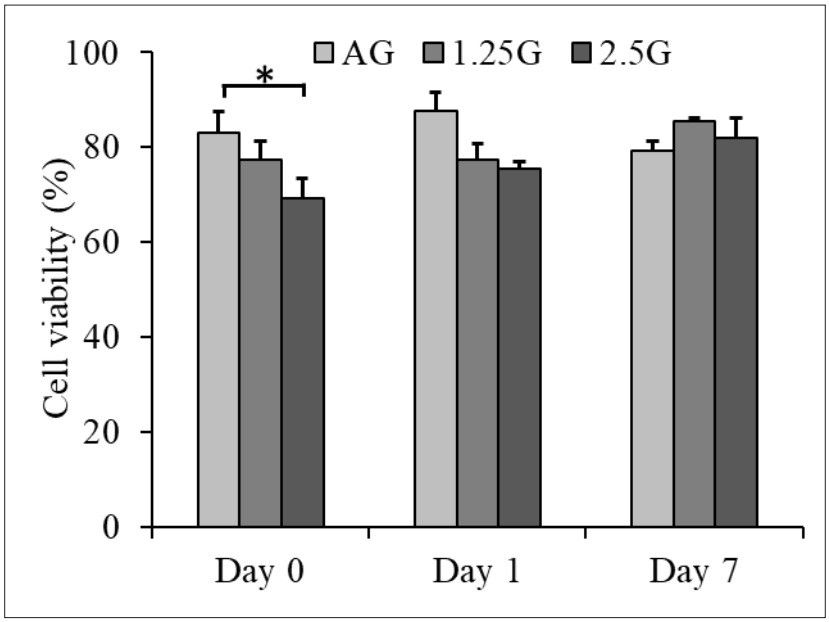

Figure 13. ASCs viability in AG, 1.25G, and 2.5G bioprinted scaffolds cultured in dynamic conditions. ASCs viability significantly decreased ($p < 0.05$) with the addition of 2.5 wt.% borate glass content in bioprinted scaffolds in less than 4 h after glass addition. After 7 days in culture, ASCs, which were recovered in modified hydrogels, exhibited higher cell viability in scaffolds bioprinted with modified hydrogels in comparison with AG hydrogel, although the difference was not statistically significant ($p < 0.05$).

hydrogel preparation, gelatin and alginate hydrogels were physically blended together to form a composite hydrogel. In order to study the release of gelatin from the AG hydrogel used in this study, AG, 1.25G and 2.5G scaffolds measuring $15 \times 15 \times 1$ mm^3 were fabricated without cells, crosslinked with $CaCl_2$ solution, and soaked in DI water under standard culture conditions for up to 7 days. The surrounding DI water was collected after 24 h and on day 7 and checked for gelatin presence using proton nuclear magnetic resonance (^{1}H-NMR) spectroscopy (Figure 2). The results indicated that gelatin release started immediately after crosslinking and continued as scaffolds incubated in DI water (Figure 14). This loss of ~70% of gelatin from the scaffold could possibly explain the decline in ASC viability after 7 days in culture in AG scaffolds. The release of gelatin from 1.25G and 2.5G scaffolds was ~40% and ~50%, respectively, which could explain the modest improvement in cell viability in these scaffolds in comparison to AG scaffolds after 7 days. A more appropriate possibility in future could be to covalently crosslink the gelatin and alginate molecular chains for prolonged culture conditions and slow down the release of gelatin from the structure (limited to no more than ~25% after 7 days) as proposed in one study.[47]

Studies that have previously investigated the hydrogel+bioactive glass composite focused on creating a 3D porous matrix or scaffolds for cell seeding and injectable matrix for bone repair, as well as applications mostly limited to bone tissue engineering.[48-54] To date, very few studies have investigated the addition of bioactive glass to hydrogel to regulate hydrogel viscosity and incorporate cells in the hydrogel+bioactive glass matrix for bioprinting tissue models or 3D cell culture applications.[55-58] Addition of silicate-based bioactive glass nanoparticles to alginate dialdehyde-gelatin promoted bone-like apatite layer formation and showed no toxicity to the bioprinted human osteosarcoma cells (MG-63).[55] Results from experimenting with human dental pulp stem cells (DPSCs) encapsulated in a bioactive glass containing alginate/Matrigel composite hydrogel indicated higher levels of osteogenic expression by DPSCs in the presence of both Matrigel and bioactive glass.[57] Although bioactive glass composition was not reported in the aforementioned study, the minimal effects on mechanical properties of composite hydrogels could perhaps indicate a slow dissolving silicate-based bioactive glass. In another study, ionic dissolution products of a silicate-based bioactive glass were used to prepare an osteogenic media to culture and crosslink gellan gum or collagen type I hydrogels containing ASCs. Another study reported osteogenesis of ASCs in hydrogels modified with bioactive glass.[58] One common aspect in the above studies is the use of silicate-based bioactive glass. The dissolution rates of silicate-based glasses are several times slower in comparison to borate-based glasses.[15] Therefore, nanoparticles of silicate-based glass are often used to fasten

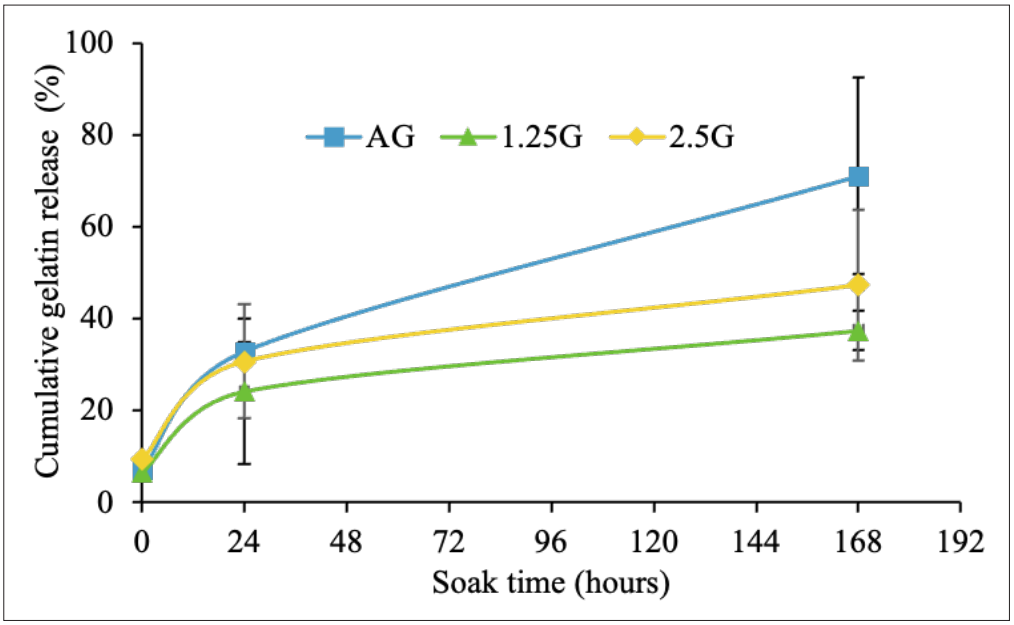

Figure 14. Gelatin release profiles from AG, 1.25G, and 2.5G scaffolds.

the glass particle dissolution and release ions to control the hydrogel viscosity and establish a window of printable time for the composite hydrogel.[55] However, borate-based bioactive glasses dissolve rapidly and supply the dissolution products (including Ca^{2+} ions) to control the hydrogels viscosity for 3D printing without affecting their shear-thinning behavior. The mechanisms that are currently adopted during bioprinting with alginate-based hydrogels include filament exposure to $CaCl_2$ solution to initiate crosslinking and fabrication under temperature-controlled environment by modifying the solvent ionic strength.[13,59] In this study, we successfully demonstrated bioprinting with borate glass-modified hydrogels at room temperature. This study is the first to report the use of borate-based bioactive glass to improve the extrudability of alginate-based hydrogels with consideration of human ASC viability.

4. Conclusion

Our research showcased the capability of B3 glass to facilitate printing using AG hydrogel at room temperature, eliminating the requirement for a temperature-controlled setting. This improvement was analyzed not just in terms of the hydrogel's printability at room temperature, but also regarding its impact on cell viability. Rheological properties of an AG hydrogel were modified with the addition of 0.075 to 0.6 w/v % of highly resorbable B3 glass, and scaffolds were successfully fabricated. The addition of B3 glass (0.075 and 0.15 w/v %) increased the viscosity (from 0.2 kPa·s to 7 kPa·s) and made the AG hydrogel exhibit a viscoelastic solid-like behavior (G'> G") that improved the hydrogel recovery and enabled effortless extrusion 3D printing of scaffolds. AG scaffold stiffness increased with the addition of B3 (from 33 kPa to 73 kPa), and the mechanical properties showed the potential of the modified AG hydrogel to serve as a viable matrix for human ASCs. Despite the toxicity of B3 to ASCs when added in quantities higher than 0.3 w/v % to hydrogel (<70% viable ASCs), lower quantities of B3 have increased the viability in comparison to AG hydrogels without B3 after 7 days in culture (>80% viable ASCs). Overall, the rheological modification of alginate-based hydrogels with B3 glass showed the potential for future applications in extrusion-based bioprinting with human ASCs.

Acknowledgments

The authors thank Austin Martin and Jeremy Watts for their help with rheological assessment of hydrogels and freeze-drying hydrogels. The glass used in this study was provided by Mo-Sci Corporation, Rolla, MO, USA.

Funding

This research was funded by the Intelligent Systems Center and the Center for Biomedical Research at the Missouri University of Science and Technology.

Conflict of interest

The authors declare no conflicts of interest.

Author contributions

Conceptualization: Krishna C.R. Kolan, Julie A. Semon
Investigation: Krishna C.R. Kolan, Lesa B. Steen, August T. Bindbeutel, Apurv Saxena, Bradley A. Bromet
Methodology: Krishna C.R. Kolan, Julie A. Semon, Apurv Saxena
Formal analysis: Krishna C.R. Kolan, Julie A. Semon
Writing – original draft: Krishna C.R. Kolan
Writing – review & editing: Apurv Saxena, Delbert E. Day, Julie A. Semon, Ming C. Leu

Ethics approval and consent to participate

Not applicable.

Consent for publication

Not applicable.

Availability of data

The datasets generated during the current study are available from the corresponding author upon reasonable request.

References

1. Ozbolat IT, Hospodiuk M. Current advances and future perspectives in extrusion-based bioprinting. *Biomaterials*. 2016;76:321-343. doi: 10.1016/j.biomaterials.2015.10.076
2. Choudhury D, Anand S, Naing M. The arrival of commercial bioprinters – towards 3D bioprinting revolution! *Int J Bioprint*. 2018;4(2). doi: 10.18063/IJB.v4i2.139
3. Gungor-Ozkerim PS, Inci I, Zhang YS, Khademhosseini A, Dokmeci MR. Bioinks for 3D bioprinting: an overview. *Biomater Sci*. 2018;6(5):915-946. doi: 10.1039/c7bm00765e
4. Rowley JA, Madlambayan G, Mooney DJ. Alginate hydrogels as synthetic extracellular matrix materials. *Biomaterials*. 1999;20(1):45-53. doi: 10.1016/S0142-9612(98)00107-0
5. Smidsrød O, Skjåk-Braek G. Alginate as immobilization matrix for cells. *Trends Biotechnol*. 1990;8(3):71-78. doi: 10.1016/0167-7799(90)90139-O
6. Reakasame S, Boccaccini AR. Oxidized alginate-based hydrogels for tissue engineering applications: a review. *Biomacromolecules*. 2018;19(1):3-21. doi: 10.1021/acs.biomac.7b01331
7. Jeon O, Alsberg E. Photofunctionalization of alginate hydrogels to promote adhesion and proliferation of human mesenchymal stem cells. *Tissue Eng Part A*. 2013;19(11-12):1424-1432. doi: 10.1089/ten.TEA.2012.0581
8. Alsberg E, Anderson KW, Albeiruti A, Franceschi RT, Mooney DJ. Cell-interactive alginate hydrogels for bone tissue engineering. *J Dent Res*. 2001;80(11):2025-2029. doi: 10.1177/00220345010800111501
9. Rastogi P, Kandasubramanian B. Review of alginate-based hydrogel bioprinting for application in tissue engineering. *Biofabrication*. 2019;11(4):042001. doi: 10.1088/1758-5090/ab331e
10. Giuseppe M Di, Law N, Webb B, et al. Mechanical behaviour of alginate-gelatin hydrogels for 3D bioprinting. *J Mech Behav Biomed Mater*. 2018;79:150-157. doi: 10.1016/J.JMBBM.2017.12.018
11. Chung JHY, Naficy S, Yue Z, et al. Bio-ink properties and printability for extrusion printing living cells. *Biomater Sci*. 2013;1(7):763. doi: 10.1039/c3bm00012e
12. Jiang T, Munguia-Lopez J, Flores-Torres S, et al. Bioprintable alginate/gelatin hydrogel 3D in vitro model systems induce cell spheroid formation. *J Vis Exp*. 2018;(137):e57826. doi: 10.3791/57826
13. Li Z, Huang S, Liu Y, et al. Tuning alginate-gelatin bioink properties by varying solvent and their impact on stem cell behavior. *Sci Rep*. 2018;8(1):8020. doi: 10.1038/s41598-018-26407-3
14. Duan B, Hockaday LA, Kang KH, Butcher JT. 3D Bioprinting of heterogeneous aortic valve conduits with alginate/gelatin hydrogels. *J Biomed Mater Res Part A*. 2013;101A(5):1255-1264. doi: 10.1002/jbm.a.34420
15. Rahaman MN, Day DE, Sonny Bal B, et al. Bioactive glass in tissue engineering. *Acta Biomater*. 2011;7(6):2355-2373. doi: 10.1016/j.actbio.2011.03.016
16. Kokubo T, Takadama H. How useful is SBF in predicting in vivo bone bioactivity? *Biomaterials*. 2006;27(15):2907-2915. doi: 10.1016/j.biomaterials.2006.01.017
17. Miguez-Pacheco V, Hench LL, Boccaccini AR. Bioactive glasses beyond bone and teeth: emerging applications in contact with soft tissues. *Acta Biomater*. 2015;13:1-15. doi: 10.1016/J.ACTBIO.2014.11.004
18. Richard M. *Bioactive Behavior of a Borate Glass*. Master's Theses. Missouri University of Science and Technology; 2000.
19. Jung S. *Borate Based Bioactive Glass Scaffolds for Hard and Soft Tissue Engineering*. Dissertation. Missouri University of Science and Technology; 2010.
20. George J. *Dissolution of Borate Glasses and Precipitation of Phosphate Compounds*. Dissertation. Missouri University of Science and Technology; 2015.
21. Nychka JA, Mazur SLR, Kashyap S, Li D, Yang F. Dissolution of bioactive glasses: the effects of crystallinity coupled with stress. *JOM*. 2009;61(9):45-51.

doi: 10.1007/s11837-009-0132-5

22. Liu X, Rahaman MN, Day DE. Conversion of melt-derived microfibrous borate (13-93B3) and silicate (45S5) bioactive glass in a simulated body fluid. *J Mater Sci Mater Med*. 2013;24(3):583-595. doi: 10.1007/s10856-012-4831-z

23. Zhao F, Yang Z, Xiong H, Yan Y, Chen X, Shao L. A bioactive glass functional hydrogel enhances bone augmentation via synergistic angiogenesis, self-swelling and osteogenesis. *Bioact Mater*. 2023;22:201-210. doi: 10.1016/j.bioactmat.2022.09.007

24. Zhu H, Monavari M, Zheng K, et al. 3D bioprinting of multifunctional dynamic nanocomposite bioinks incorporating Cu-doped mesoporous bioactive glass nanoparticles for bone tissue engineering. *Small*. 2022;18(12):2104996. doi: 10.1002/smll.202104996

25. Monavari M, Homaeigohar S, Medhekar R, et al. A 3D-printed wound-healing material composed of alginate dialdehyde-gelatin incorporating astaxanthin and borate bioactive glass microparticles. *ACS Appl Mater Interfaces*. 2023;15(44):50626-50637. doi: 10.1021/acsami.2c23252

26. Kolan KCR, Semon JA, Bromet B, Day DE, Leu MC. Bioprinting with human stem cells-laden alginate-gelatin bioink and bioactive glass for tissue engineering. *Int J Bioprint*. 2019;5(2.2):3. doi: 10.18063/ijb.v5i2.2.204

27. Jung SB. Borate based bioactive glass scaffolds for hard and soft tissue engineering. *Zhurnal Eksp i Teor Fiz*. 2010;389.

28. Watters R, Brown R, Day D. Angiogenic effect of bioactive borate glass microfibers and beads in the hairless mouse. *Bioact Glas*. 2015;1(1). doi: 10.1515/bglass-2015-0017

29. Lin Y, Brown RF, Jung SB, Day DE. Angiogenic effects of borate glass microfibers in a rodent model. *J Biomed Mater Res Part A*. 2014;102(12):4491-4499. doi: 10.1002/jbm.a.35120

30. Thyparambil N, Gutgesell L, Bromet B, et al. Bioactive borate glass triggers phenotypic changes in adipose stem cells. *J Mater Sci Mater Med*. 2020;31(4):35. doi: 10.1007/s10856-020-06366-w

31. Dykstra JA, Facile T, Patrick RJ, et al. Concise review: fat and furious: harnessing the full potential of adipose-derived stromal vascular fraction. *Stem Cells Transl Med*. 2017;6(4):1096-1108. doi: 10.1002/sctm.16-0337

32. Gimble JM, Guilak F, Bunnell BA. Clinical and preclinical translation of cell-based therapies using adipose tissue-derived cells. *Stem Cell Res Ther*. 2010;1(2):19. doi: 10.1186/scrt19

33. Bourin P, Bunnell BA, Casteilla L, et al. Stromal cells from the adipose tissue-derived stromal vascular fraction and culture expanded adipose tissue-derived stromal/stem cells: a joint statement of the International Federation for Adipose Therapeutics and Science (IFATS) and the International Society for Cellular Therapy (ISCT). *Cytotherapy*. 2013;15(6):641-648. doi: 10.1016/j.jcyt.2013.02.006

34. Kolan KCR, Semon JA, Bindbeutel AT, Day DE, Leu MC. Bioprinting with bioactive glass loaded polylactic acid composite and human adipose stem cells. *Bioprinting*. 2020;18:e00075. doi: 10.1016/j.bprint.2020.e00075

35. Thyparambil NJ, Gutgesell LC, Hurley CC, Flowers LE, Day DE, Semon JA. Adult stem cell response to doped bioactive borate glass. *J Mater Sci Mater Med*. 2020;31(2):1-8. doi: 10.1007/s10856-019-6353-4

36. Suvarnapathaki S, Nguyen MA, Wu X, Nukavarapu SP, Camci-Unal G. Synthesis and characterization of photocrosslinkable hydrogels from bovine skin gelatin. *RSC Adv*. 2019;9:13016-13025. doi: 10.1039/c9ra00655a

37. Okay O. *General Properties of Hydrogels*. Berlin, Heidelberg: Springer; 2009:1-14. doi: 10.1007/978-3-540-75645-3_1

38. Jung S, Day D. Conversion kinetics of silicate, borosilicate, and borate bioactive glasses to hydroxyapatite. *Phys Chem Glas*. 2009;50(2):85-88.

39. Liu X, Pan H, Fu H, Fu Q, Rahaman MN, Huang W. Conversion of borate-based glass scaffold to hydroxyapatite in a dilute phosphate solution. *Biomed Mater*. 2010;5(1):015005. doi: 10.1088/1748-6041/5/1/015005

40. George JL, Brow RK. In-situ characterization of borate glass dissolution kinetics by μ-Raman spectroscopy. *J Non Cryst Solids*. 2015;426:116-124. doi: 10.1016/J.JNONCRYSOL.2015.07.003

41. Fu Q, Rahaman MN, Fu H, Liu X. Silicate, borosilicate, and borate bioactive glass scaffolds with controllable degradation rate for bone tissue engineering applications. I. Preparation and in vitro degradation. *J Biomed Mater Res Part A*. 2010;95A(1):164-171. doi: 10.1002/jbm.a.32824

42. Huebsch N, Arany PR, Mao AS, et al. Harnessing traction-mediated manipulation of the cell/matrix interface to control stem-cell fate. *Nat Mater*. 2010;9(6):518-526. doi: 10.1038/nmat2732

43. Chaudhuri O, Gu L, Klumpers D, et al. Hydrogels with tunable stress relaxation regulate stem cell fate and activity. *Nat Mater*. 2016;15(3):326-334. doi: 10.1038/nmat4489

44. Qazi TH, Hafeez S, Schmidt J, Duda GN, Boccaccini AR, Lippens E. Comparison of the effects of 45S5 and 1393 bioactive glass microparticles on hMSC behavior. *J Biomed Mater Res A*. 2017;105(10):2772-2782. doi: 10.1002/jbm.a.36131

45. Hoppe A, Boccaccini AR. Biological impact of bioactive glasses and their dissolution products. *Front Oral Biol*. 2015;17:22-32. doi: 10.1159/000381690

46. Wang X, Tolba E, Schröder HC, et al. Effect of bioglass on growth and biomineralization of SaOS-2 cells in hydrogel after 3D cell bioprinting. *PLoS One*. 2014;9(11):e112497. doi: 10.1371/journal.pone.0112497

47. Sarker B, Singh R, Silva R, et al. Evaluation of fibroblasts adhesion and proliferation on alginate-gelatin crosslinked hydrogel. *PLoS One*. 2014;9(9):e107952. doi: 10.1371/journal.pone.0107952

48. Couto DS, Hong Z, Mano JF. Development of bioactive and biodegradable chitosan-based injectable systems containing bioactive glass nanoparticles. *Acta Biomater*. 2009;5(1): 115-123. doi: 10.1016/j.actbio.2008.08.006

49. Nikpour P, Salimi-Kenari H, Fahimipour F, et al. Dextran hydrogels incorporated with bioactive glass-ceramic: nanocomposite scaffolds for bone tissue engineering. *Carbohydr Polym*. 2018;190:281-294. doi: 10.1016/j.carbpol.2018.02.083

50. Killion JA, Kehoe S, Geever LM, et al. Hydrogel/bioactive glass composites for bone regeneration applications: synthesis and characterisation. *Mater Sci Eng C*. 2013;33(7):4203-4212. doi: 10.1016/j.msec.2013.06.013

51. Moreira CDF, Carvalho SM, Sousa RG, Mansur HS, Pereira MM. Nanostructured chitosan/gelatin/bioactive glass in situ forming hydrogel composites as a potential injectable matrix for bone tissue engineering. *Mater Chem Phys*. 2018;218:304-316. doi: 10.1016/j.matchemphys.2018.07.039

52. Gantar A, Drnovšek N, Casuso P, et al. Injectable and self-healing dynamic hydrogel containing bioactive glass nanoparticles as a potential biomaterial for bone regeneration. *RSC Adv*. 2016;6(73):69156-69166. doi: 10.1039/C6RA17327F

53. Zhu N, Chatzistavrou X, Papagerakis P, Ge L, Qin M, Wang Y. Silver-doped bioactive glass/chitosan hydrogel with potential application in dental pulp repair. *ACS Biomater Sci Eng*. 2019;5(9):4624-4633. doi: 10.1021/acsbiomaterials.9b00811

54. Washio A, Teshima H, Yokota K, Kitamura C, Tabata Y. Preparation of gelatin hydrogel sponges incorporating bioactive glasses capable for the controlled release of fibroblast growth factor-2. *J Biomater Sci Polym Ed*. 2019;30(1):49-63. doi: 10.1080/09205063.2018.1544474

55. Leite ÁJ, Sarker B, Zehnder T, Silva R, Mano JF, Boccaccini AR. Bioplotting of a bioactive alginate dialdehyde-gelatin composite hydrogel containing bioactive glass nanoparticles. *Biofabrication*. 2016;8(3):035005. doi: 10.1088/1758-5090/8/3/035005

56. Douglas TEL, Dziadek M, Gorodzha S, et al. Novel injectable gellan gum hydrogel composites incorporating Zn- and Sr-enriched bioactive glass microparticles: High-resolution X-ray microcomputed tomography, antibacterial and in vitro testing. *J Tissue Eng Regen Med*. 2018;12(6): 1313-1326. doi: 10.1002/term.2654

57. Sevari SP, Shahnazi F, Chen C, Mitchell JC, Ansari S, Moshaverinia A. Bioactive glass-containing hydrogel delivery system for osteogenic differentiation of human dental pulp stem cells. *J Biomed Mater Res Part A*. 2020;108(3):557-564. doi: 10.1002/jbm.a.36836

58. Vuornos K, Ojansivu M, Koivisto JT, et al. Bioactive glass ions induce efficient osteogenic differentiation of human adipose stem cells encapsulated in gellan gum and collagen type I hydrogels. *Mater Sci Eng C*. 2019;99:905-918. doi: 10.1016/j.msec.2019.02.035

59. Sun W, Starly B, Daly AC, et al. The bioprinting roadmap. *Biofabrication*. 2020;12(2):022002. doi: 10.1088/1758-5090/ab5158

ACCSCIENCE PUBLISHING

International Journal of Bioprinting

RESEARCH ARTICLE

Bioprinted autologous human skin equivalents for *in vitro* testing of therapeutic antibodies

Mahid Ahmed[1,2], David Hill[3,4], Shaheda Ahmed[2], Stefan Przyborski[5,6], Kenneth Dalgarno[1]*, and Anne Dickinson[2,4]

[1]School of Engineering, Newcastle University, Newcastle upon Tyne, NE3 1PS, United Kingdom

[2]Alcyomics Ltd., The Biosphere, Draymans Way, Newcastle Helix, Newcastle upon Tyne, NE4 5BX, United Kingdom

[3]Faculty of Health Sciences and Wellbeing, Sunderland University, Sunderland, SR1 3SD, United Kingdom

[4]Translational & Clinical Research Institute, Faculty of Medical Science, Medical School, Newcastle University, Newcastle upon Tyne, NE2 4HH, United Kingdom

[5]Department of Bioscience, Durham University, South Road, Durham, DH1 3LE, United Kingdom

[6]Reprocell Europe Ltd., NETPark Plexus, Thomas Wright Way, Sedgefield, Co. Durham, TS21 3FD, United Kingdom

Abstract

In recent years, advances in tissue engineering have brought forward the accessibility of human skin equivalents for *in vitro* applications; however, the availability of human-based engineered tissue models suitable for high-throughput screening of biologics remains limited. Here, we report a method of manufacturing fully autologous (with both fibroblasts and keratinocytes from the same donor) human skin equivalents for determining preclinical therapeutic antibody adverse immune reactions *in vitro*. Using a combination of precise solenoid microvalve-based bioprinting and 96-well scale Alvetex inserts, autologous skin cells were bioprinted and cultured to develop a scalable approach to manufacturing skin equivalents. We demonstrated that fibroblasts and keratinocytes can be bioprinted with a high degree of precision while maintaining viability post printing. Histological staining showed that the bioprinted 96-well based skin equivalents were comparable to human skin. The fully autologous human skin equivalents were co-cultured *in vitro* with autologous peripheral blood monocytes with and without muromonab-CD3 (OKT3) and natalizumab (Tysabri), biologics which are known to cause and inhibit adverse immune reactions (type IV hypersensitivity), respectively. Analysis of supernatants from skin-equivalent monocyte co-cultures revealed significant proinflammatory cytokine responses (such as interferon gamma) in co-cultures treated with OKT3 when compared to Tysabri and negative controls. Consequently, this study provides proof of concept that through a combination of bioprinting and Alvetex scaffold-based culture systems, scalable human skin equivalents can be manufactured for high-throughput identification of adverse immune reactions during preclinical stages of the drug development process.

Keywords: Autologous tissue models; Skin-equivalent models; Microvalve bioprinting; Transwell culture

***Corresponding author:**
Kenneth Dalgarno
(kenny.dalgarno@newcastle.ac.uk)

Citation: Ahmed M, Hill D, Ahmed S, Przyborski S, Dalgarno K, Dickinson A. Bioprinted autologous human skin equivalents for *in vitro* testing of therapeutic antibodies. *Int J Bioprint*. 2024;10(2):1851. doi: 10.36922/ijb.1851

Received: September 17, 2023
Accepted: January 10, 2024
Published Online: March 11, 2024

1. Introduction

The limited availability of human tissue for preclinical assays compounds the need for the use of animal-based studies during the drug development process. In addition to the ethical concerns associated with the use of animal models, such studies may not be representative of the outcome of subsequent first in human studies.[1] This contributes to the high failure rate that the pharmaceutical industry experiences when taking drugs to human clinical trials.[2] *In vivo* animal models ultimately differ in physiology to humans.[3] Even in the case of larger animal models such as non-human primates, many underlying differences remain, influencing the efficacy of animal models as pre-clinical tools.[3] When adverse immune reactions (which may cause type IV hypersensitivity reactions) of a drug are not identified in preclinical studies but become apparent during clinical trials, the consequences for participants can be seriously life-threatening.[1,4] Furthermore, the financial burden resulted from clinical trial failure may further hinder drug developers.[5] With high rates of failure at clinic and a reported decline in both pharmaceutical research and development productivity and investment,[6] the mantra of "fail early, fail fast" is becoming increasingly important to drug developers.

Following the signing of the FDA Modernization Act 2.0, drug developers are under increasing pressure to investigate the use of non-animal-based assays. While *in vitro* and *ex vivo* assays are used during the preclinical development process,[7] there is a growing need for tools that can provide greater physiologically relevant complexity and interactions. *Ex vivo* assays can be used to determine adverse immune responses to systemic therapies.[8] However, human-based *ex vivo* assays that seek to bridge the gap between preclinical animal studies and human clinical trials are challenging to scale up. Looking beyond the scope of drug development, access to human tissue remains a barrier even for medical and biological research.[9] With an overall movement toward the 3Rs (Reduction, Refinement, and Replacement), there is growing interest, however, in human *in vitro* three-dimensional (3D) models.

In recent years, the fields of *in vitro* tissue engineering and 3D cell culture have benefited from the growth of biofabrication techniques.[10,11] Within the tissue engineering community, biofabrication is considered to be the intersection of additive manufacturing, the layer-by-layer process of manufacturing a 3D construct, and tissue engineering.[12] To biofabricate tissue constructs, bioprinting is commonly used to organize and print cells or cell aggregates to create a 3D tissue model.[11] Bioprinting itself can be categorized into four commonly used methods: extrusion-based bioprinting and three drop-on-demand (DoD) processes inkjet printing, microvalve bioprinting, and laser-based bioprinting. Extrusion-based bioprinting uses pneumatic or mechanical mechanisms, allowing close control of bioink[13] material flow, making the process ideal for the deposition of pre-mixed hydrogels.[14,15] Inkjet bioprinting is DoD process, which typically uses thermal actuators[16] or piezoelectric actuators[17] to dispense individual droplets of bioink in the picoliter range.[18] This makes inkjet printing ideal for low-viscosity bioinks with lower cell densities.[15] Laser-based systems use the principle of laser-induced forward transfer to dispense individual droplets of material, which are typically cell-laden hydrogels.[13] Like inkjet bioprinters, microvalve bioprinters dispense low-viscosity bioinks, but it has also been demonstrated that microvalves can be arranged in a print-head such that they can print materials such as hydrogel precursors laden with a high density of cells.[19] For low-viscosity bioinks, microvalve can deposit high droplets of high-cell-concentration solutions in the nanoliter range,[20] and so for the development of micro-tissue models offers an efficient way of depositing the numbers of cells that such models require.

The bottom-up nature of biofabrication has led to the production of a range of engineered tissue-like constructs or scaffolds suitable for tissue engineering such as skin equivalents, constructs for bone repair, cartilage-like tissue, and cardiac models.[21-24] However, these examples typically rely on allogeneic materials to create 3D tissue constructs. Examples of bioprinted tissues where autologous cells and autologous materials are applied largely fall within the scope of regenerative medicine.[25,26] In contrast, it has been demonstrated that using traditional top-down approaches to tissue engineering can produce fully humanized constructs, which may be adapted to autologous settings.[27] In particular, the use of inert permeable plastic scaffolds with porous substrates, such as Transwell® and Alvetex® scaffolds, has become almost ubiquitous as the method of creating bi-layered keratinocyte-fibroblast co-cultures for skin equivalents.[28] However, traditional approaches to tissue engineering lack the benefit of automation and therefore the scalability offered by biofabrication. In considering scalability, the use of standard well-plate formats is a key enabler as it allows for scale up and scale out in a format familiar in most microbiology labs and which is easy to interface with many downstream processes. As such, there is limited availability of scalable, fully humanized and autologous tissue available for preclinical *in vitro* drug screening.

Here, we demonstrate how the permeable scaffold approach can be combined with microvalve-based biofabrication to develop a fully human, autologous skin equivalent which can be co-cultured with autologous immune cells in a 96-well format. This approach provides

proof-of-concept that human skin equivalents produced, using scalable, automated biofabrication techniques can be used as a preclinical tool to predict potential adverse immune responses of therapeutic antibodies.

2. Materials and methods

2.1. Cell culture

Full Local Research Ethics Committee (LREC) approval was obtained before sourcing healthy volunteer samples for this study. After obtaining informed consent, two 4 mm skin biopsies and 60 mL of whole blood were collected from healthy volunteers. Skin biopsies were rinsed in phosphate-buffered saline (PBS; Sigma-Aldrich, UK), then excess adipose tissue was removed from the skin biopsies, and the biopsies were incubated in 1.0 U/mL dispase solution (Scientific Laboratory Supplies, UK) for 18 h at 4°C to allow separation of the epidermis from the dermis. Once separated, the dermis and epidermis were processed independently. To isolate dermal fibroblasts, the separated dermal samples were dissected, placed into 6-well plates, and covered with 100 µL of fetal bovine serum (FBS; Thermo Fisher Scientific, UK). The dermal samples were incubated using standard culture conditions (37°C with 5% CO_2) for 24 h. After 24 h, wells were topped up with 5 mL of Media A (Table 1). Dermal dissects were observed for fibroblast outgrowth with media changed twice weekly. Once significant outgrowth was observed, fibroblasts were dissociated using trypsin/EDTA (Sigma-Aldrich) using standard culture conditions for 5 min. The dissociated fibroblasts were further cultured for up to 7 passages. Keratinocytes were dissociated from epidermal samples using trypsin/EDTA using standard cell culture conditions. The resulting cells were further cultured in Media B (Table 1) for up to 3 passages with media changed twice weekly. Lymphoprep™ density gradient medium (STEMCELL Technologies, UK) was used to isolate human peripheral blood monocytes (PBMCs) from whole blood sourced from healthy volunteers as previously described.[8]

2.2. Bioprinting equipment and process

For this study, a Microfab Jetlab 4 XL (Microfab Technologies Inc., US) printer was retrofitted to accommodate solenoid VHS series microvalves (Lee Products Ltd., US)

Table 1. Media formulations and working concentrations

Media	Components	Supplier	Final concentration
A	Dulbecco's Modified Eagles Medium	Sigma-Aldrich, UK	-
	Fetal calf serum	Fisher Scientific, UK	10%
	Penicillin/Streptomycin/Amphotericin	Sigma-Aldrich, UK	1%
	L-glutamine	Sigma-Aldrich, UK	1%
B	Epilife	Fisher Scientific, UK	-
	Human Keratinocyte Growth Supplement	Fisher Scientific, UK	1%
	Penicillin/Streptomycin/Amphotericin	Sigma-Aldrich, UK	1%
	L-glutamine	Sigma-Aldrich, UK	1%
C	3 Part Dulbecco's Modified Eagles Medium	Sigma-Aldrich, UK	-
	1 Part Ham's F12 Nutrient Mixture	Sigma-Aldrich, UK	-
	Chelex-treated fetal calf serum	Fisher Scientific, UK	5%
	Penicillin/Streptomycin/Amphotericin	Sigma-Aldrich, UK	1%
	L-glutamine	Sigma-Aldrich, UK	1%
	Cholera toxin	Sigma-Aldrich, UK	8.5 ng/mL
	Hydrocortisone	Sigma-Aldrich, UK	0.4 µg/mL
	Human insulin	Sigma-Aldrich, UK	5 µg/mL
	Adenine	Sigma-Aldrich, UK	24 µg/mL
	Human epidermal growth factor	PeproTech, US	20 ng/mL
D	3 Part Dulbecco's Modified Eagles Medium	Sigma-Aldrich, UK	-
	1 Part Ham's F12 Nutrient Mixture	Sigma-Aldrich, UK	-
	Fetal calf serum	Fisher Scientific, UK	10%
	Penicillin/Streptomycin/Amphotericin	Sigma-Aldrich, UK	1%
	Cholera toxin	Sigma-Aldrich, UK	8.5 ng/mL
	Hydrocortisone	Sigma-Aldrich, UK	0.4 µg/mL
	Human epidermal growth factor	PeproTech, US	20 ng/mL
	Human transferrin	PeproTech, US	5 µg/mL
	L-ascorbic acid	Sigma-Aldrich, UK	100 µg/mL
F	RPMI-1640	Sigma-Aldrich, UK	-
	Autologous serum	-	20%
	Penicillin/Streptomycin/Amphotericin	Sigma-Aldrich, UK	1%

to create a high-throughput bioprinting platform. The inkjet printhead of the Jetlab 4 printer was replaced with a microvalve printhead (Figure 1), which could accommodate four individual custom-built ink reservoirs, each with an ink capacity of 2.5 mL. Inkjet printing is very effective for small volumes and can offer single-cell resolution, but the development of skin-equivalent models requires higher volume deposition rates, and so, for this reason, microvalve printing was preferred. The outlets of the reservoirs were threaded to contain a male–male 062 MINSTAC threaded connector (Lee Products Ltd.); one side of which was fixed into the reservoir (Figure 1). The other end of the male–male connector was used to attach the solenoid VHS series. The valve configuration used in this study had female 062 MINSTAC threaded inlets and outlets and was used alongside 062 MINSTAC jeweled orifice nozzles (Lee Products Ltd., US) with orifice diameters of 190 µm. To generate actuation signals for the microvalves, spike and hold electrical drivers (Lee Products Ltd.) were connected to both the Jetlab 4 device signal output channels and the signal connections of the Individual valves. This allowed signals produced by the waveform printed circuit board (PCB) of the Jetlab to be converted to a 24 V spike voltage and a 5 V dwell voltage. The optimal parameters for reliable microdispensing of low viscosity inks were investigated by exploring the impact on adjusting the operating dwell time (time that the microvalve remains open during one actuation cycle) and pneumatic backpressure used to eject droplets from the reservoir. The custom-designed reservoir housed a gold-plated neodymium magnet, which was suspended within the bioink and was used to agitate cells within the bioink. The magnet within the reservoir was rotated by an additional rotating magnet located perpendicular to the external wall of the reservoir. The external magnet was connected to a 24 V DC motor via drive belt, which was operated at 18 V for printing of cells. To measure the volume dispensed, 200 droplets of media D (Table 1) were printed into 1.5 mL Eppendorf tubes (Fisher Scientific), which was weighed using a microbalance (Mettler Toledo). The volume per droplet was calculated from this data. Dwell times of 100–1000 µs and backpressures of 50–500 mmHg were investigated at increments of 50 µs and 50 mmHg. To further ensure consistency of output, a microvalve purge step was used between print events.

2.3. Cell viability post printing

To ensure that the correct number of dermal fibroblasts and epidermal keratinocytes were dispensed when printing skin equivalents, fibroblast suspensions were prepared at a concentration of 25×10^6 cells/mL in Media A and keratinocytes were prepared at a concentration of 20×10^6 cells/mL in Media B and loaded into reservoirs. Following a 60 µL purge of the bioink through the microvalves, 20 µL of each cell suspension was printed in three separate wells of a 96-well plate. Cells were printed with a backpressure of 150 mmHg and a dwell time of 1000 µs. As described above, a 10 µL aliquot of each printed suspension was then mixed 1:1 with trypan blue, and cell number and viability were quantified using a hemocytometer.

2.4. Bioprinting of cells for the development of autologous skin equivalents

Figure 2 illustrates the 96-well Alvetex® (Reprocell, UK) culture system, and the general approach to developing

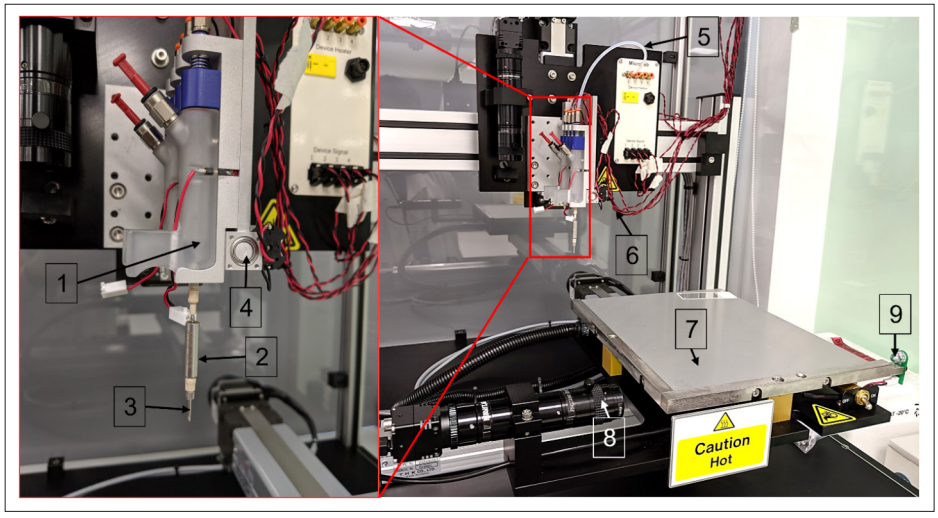

Figure 1. Customized Jetlab bioprinter. (1) Ink reservoir which holds the bioink and magnet to agitate cell suspension. (2) Solenoid valve. (3) Removable nozzle. (4) Magnetic agitator to rotate the gold-plated magnet present within the reservoir. (5) Backpressure tubing. (6) Valve actuation signal wiring. (7) XY printing platform. (8) Drop analysis camera. (9) Stroboscopic LED.

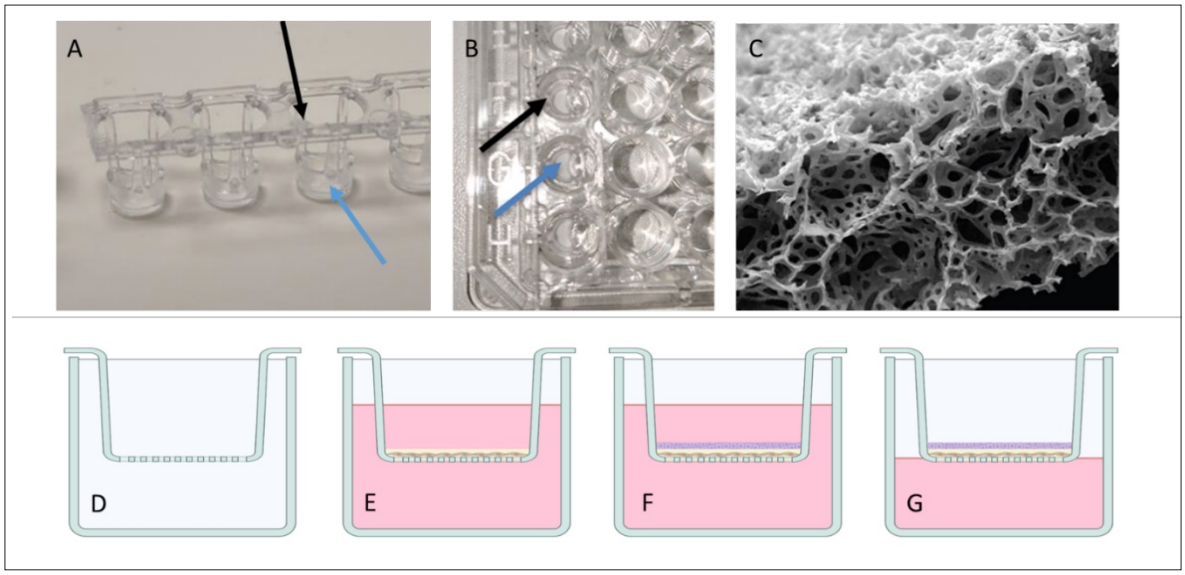

Figure 2. Development of skin equivalent models. (A, B) 96-well Alvetex® scaffold system; black arrows show inserts, blue arrows porous membrane. (C) 200 µm thick Alvetex® porous membrane. (D–G) Stages in model development. (D) Schematic of scaffold insert. (E) Dermal incubation of fibroblasts only for up to 28 days. (F) Basal incubation of keratinocytes for 3 days. (G) Incubation of model at air–liquid interface for 14 days. Panels D–G were created using Biorender.com.

skin equivalents. Prior to printing of cells, the 96-well Alvetex® (Reprocell, UK) scaffolds were washed in 70% ethanol and rinsed in two changes of PBS. A fibroblast cell suspension was prepared in Media A at a concentration of 25×10^6 cells/mL. The Suspension (20 µL) was directly printed onto the Alvetex® scaffolds within the Transwells to create dermal equivalents, which were then incubated at standard culture conditions for 3 h. Following the 3-h incubation, the cell-laden scaffolds were submerged in Media A overnight. After 24 h, the scaffolds were cultured using Media A supplemented with 100 µg/mL of L-ascorbic acid. The dermal equivalents were cultured for 18 days with media changed daily. After 18 days, the dermal equivalents were gently rinsed in PBS to remove excess media prior to directly printing the autologous epidermal keratinocytes on top of the dermal equivalents. Keratinocytes were suspended in Media C (Table 1) at a concentration of 20×10^6 cells/mL with 20 µL of the keratinocyte cell suspension printed onto each dermal equivalent. The co-cultures were then incubated for 90 min at standard culture conditions and then gently submerged in Media C for 3 days with media changed daily. Skin equivalents were then raised to the air–liquid interface (ALI) by aspirating Media C and adding sufficient Media D (Table 1) to the wells to cover the underside of each dermis, without submerging the epidermis region of the tissue. The co-cultures were cultured at the ALI at standard conditions for 14 days with media changed daily. After day 14 of ALI culture, the skin equivalents were harvested for histological evaluation or further cultured with autologous immune cells and monoclonal antibodies.

2.5. Histological evaluation of skin equivalents

Mature skin equivalents were harvested, formalin-fixed, paraffin-embedded, and sectioned. Sections (4 µm) were stained with hematoxylin and eosin (H&E; Fisher Scientific, UK) and Picrosirius red (Abcam, UK). Skin equivalents were analyzed for specific biomarkers, cytokeratin, involucrin, and loricrin via immunofluorescence. Sections were taken to water, washed in pH 7.4 tris-buffered saline (TBS), and antigen retrieval was conducted using pH 6 citrate buffer for 10 min. Sections were washed in TBS and then permeabilized with 0.2% Triton-X for 10 min followed by blocking with 10% goat serum (Sigma-Aldrich, UK) for 1 h. Sections were washed in TBS and then incubated with primary antibodies prepared in 10% goat serum for 1 h. Primary antibodies used were mouse anti-cytokeratin 14 (1:250, ab7800, Abcam), rabbit anti-involucrin (1:400, ab181980, Abcam), rabbit anti-cytokeratin 10 (1:500, ab76318, Abcam), and rabbit anti-loricrin (1:125, ab198994, Abcam). After 1 h, sections were washed in TBS and then incubated with secondary antibodies goat anti-mouse Alexa Fluor-488 (AF-488; Thermo Fisher Scientific) and goat anti-rabbit Alexa Fluor-647 (AF-647; Thermo Fisher Scientific); dilution of 1:400 was used for both. Slides were rinsed in a final wash of TBS, and then coverslips were mounted with Vectashield® mounting medium with DAPI (Vector Laboratories, US). Slides were imaged using an Axioimager microscope (Carl Zeiss AG, Germany).

2.6. Assessment of adverse immune reactions of monoclonal antibodies

Fully developed and autologous bioprinted skin equivalents were washed twice with PBS before co-culture with autologous PBMCs in 96-well plates with 1×10^6 cells per well in Media E (Table 1). Skin equivalents were treated with 1 μg/mL of OKT3 (Jannsen-Cilag, UK) or Tysabri (Biogen Idec Inc., US). Negative controls were skin equivalents cultured in Media E with and without autologous PBMCs and without biologics. The co-cultures were incubated at standard culture conditions for 3 days when 100 μL of supernatant was aspirated to analyze proinflammatory cytokine release.

2.7. Multiplex proinflammatory cytokine detection assay

To quantify cytokine secretion in supernatants of autologous skin-equivalent PBMC co-cultures, a multiplex human proinflammatory cytokine panel kit (Meso Scale Discovery, US) for identification of interferon gamma (IFN-γ), interleukin-10 (IL-10), interleukin-12 p70 (IL-12p70A), interleukin-13 (IL-13), interleukin-1 beta (IL-1β), interleukin-2 (IL-2), interleukin-4 (IL-4), interleukin-6 (IL6), and tumor necrosis factor alpha (TNFα) was used as per manufacturer instructions with the omission of IL-8 detection antibodies. Plates were analyzed using a QuickPlex multiplex plate reader (MSD). Supernatants were analyzed in biological triplicates.

2.8. Statistical analysis

Data are presented as mean ± standard deviation. Statistical analyses for the quantified cytokine levels were conducted using one-way analysis of variance (ANOVA) with Tukey HSD. Parameters for statistical significance were defined as $p \leq 0.05$ (*) and $p \leq 0.0001$ (****).

3. Results

3.1. Printing parameter optimization and printing of skin cells

Optimal printing parameters were established by characterizing changes in printing dwell time and backpressure and measuring the dispensed volumes, as shown in Figure 3. Figure 3 shows that a minimum dwell time of 200 μs and backpressure of 50 mmHg could

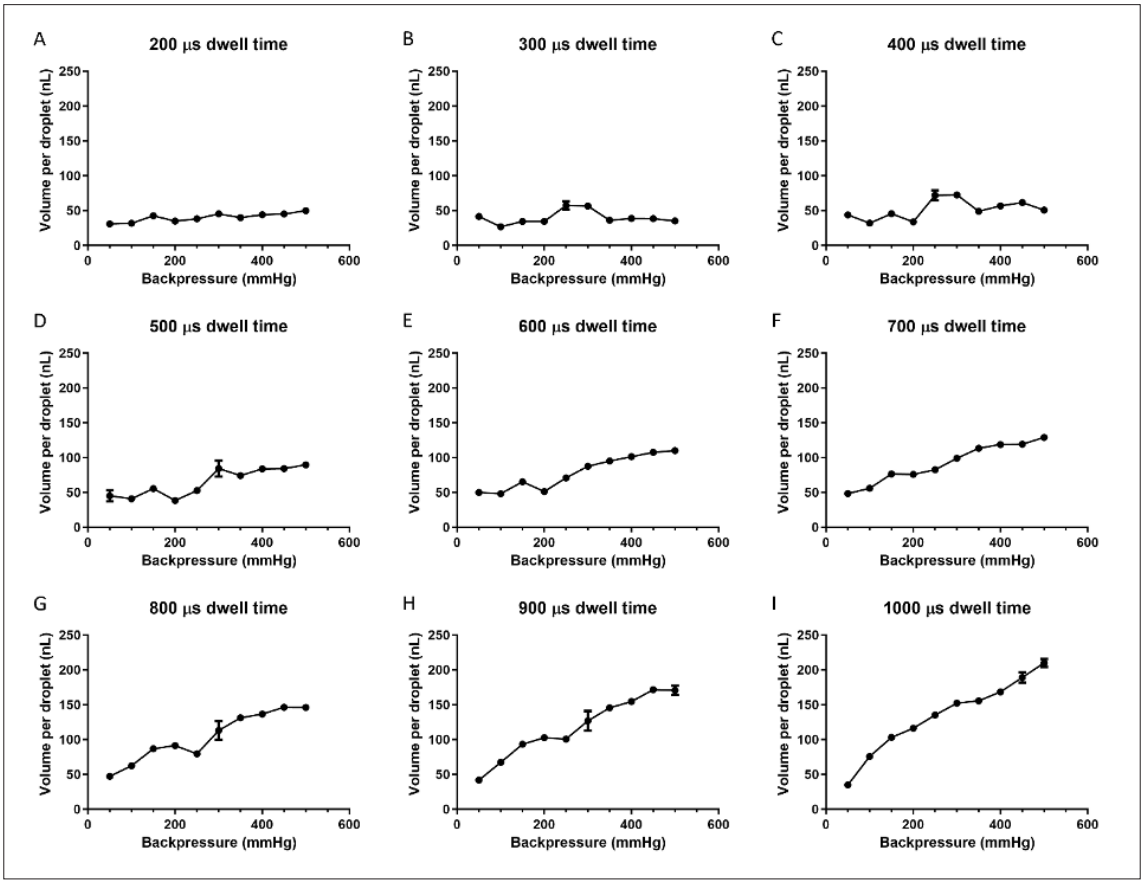

Figure 3. Mean volume of media dispensed per droplet at varying dwell times and positive pneumatic pressures. Data are presented as mean ± one standard deviation. $N = 3$.

successfully deposit material, and attempting to print with parameters below these values did not yield successful droplet deposition. At lower dwell times (Figure 3A–D), a variance in the volume per droplet was demonstrated across the range of backpressures tested. Higher dwell times (Figure 3E–I) resulted in a more linear increase in the volume per droplet dispensed across the pressure range. Peak output was 210 ± 6 nL per droplet, produced at a dwell time of 1000 µs with a backpressure of 500 mmHg. A dwell time of 1000 µs and a backpressure of 150 mmHg with a volume per droplet of 103 ± 1 nL were used to print cells and produce skin equivalents, giving good balance between productivity and consistency of output.

To print the skin-equivalent models, fibroblasts were suspended at 25 × 10^6 cells/mL and keratinocytes were suspended at 20 × 10^6 cells/mL with 20 µL of each suspension per well into 3 wells. The cell counts and viability from bioprinting of both fibroblasts and keratinocytes are presented in Figure 4. Both the number and viability of printed cells were stable and consistent across both cell types, demonstrating that the bioprinter was robust and reproducible in dispensing high number of cells within a small volume.

3.2. Histology of bioprinted skin

Representative images of H&E-stained bioprinted dermal and full-thickness skin equivalents are shown in Figure 5, with human skin shown in Figure 5D for reference. Figure 5A shows a good distribution of cells throughout the scaffold, with a consistent layer of dermal fibroblasts seen lining the top surface of the scaffold. Within the scaffold, clusters of cells could be seen near the upper surface of the scaffold, but the number of cells within the scaffold increased toward the bottom of the scaffold. Underneath the scaffold, a thick fibroblast layer was visible. Fibers of eosin-stained extracellular matrix (ECM) produced by the fibroblasts were also observed. An H&E-stained full-thickness skin equivalent can be seen in Figure 5B. The dermis of the full-thickness human skin equivalent (HSE) was well populated with a layer of fibroblasts on top of the scaffold supporting the epidermis. The epidermis of the HSE contained visible basal, spinous, and granular layers and a very thin stratum corneum. The differentiating and superficially migrating keratinocytes formed a spinous layer. The layer of granular cells indicated by the darker and slightly speckled hematoxylin-stained nuclei (which separated during sectioning) was located above the spinous keratinocytes. Picrosirius red staining of bioprinted full-thickness skin equivalents showed that the dermis was heavily loaded with collagen (Figure 5C). Large thick crosslinked collagen layers could be seen directly beneath the epidermis at the dermal–epidermal junction. This layer of collagen could be seen across the dermis, supporting the formation of an epidermis.

Immunofluorescence staining was used to stain markers present throughout the different layers in the epidermis of both healthy human skin and bioprinted full-thickness skin equivalents (Figure 6). Cytokeratin 14 (CK14) was detected directly above the dermal–epidermal junction (white dotted line), indicating the presence of basal keratinocytes at the dermal epidermal junction. The basal keratinocytes superficially migrated, stratified, and expressed cytokeratin 10 (CK10) when undergoing differentiation. CK10 was positively detected above basal keratinocytes indicating stratification and the formation of a spinous strata. Involucrin was expressed in the same regions as CK10, and loricrin was present in the corneal envelope of the epidermis. Overall, the bioprinted full-thickness skin equivalents featured the relevant epidermal differentiation markers within the correct regions of the epidermis showing that the skin equivalents were comparable to healthy human skin.

Quantified levels of proinflammatory cytokines are presented in Figure 7. The elevated IL-2 levels in specimens treated with OKT3 (muromonab) were significant when

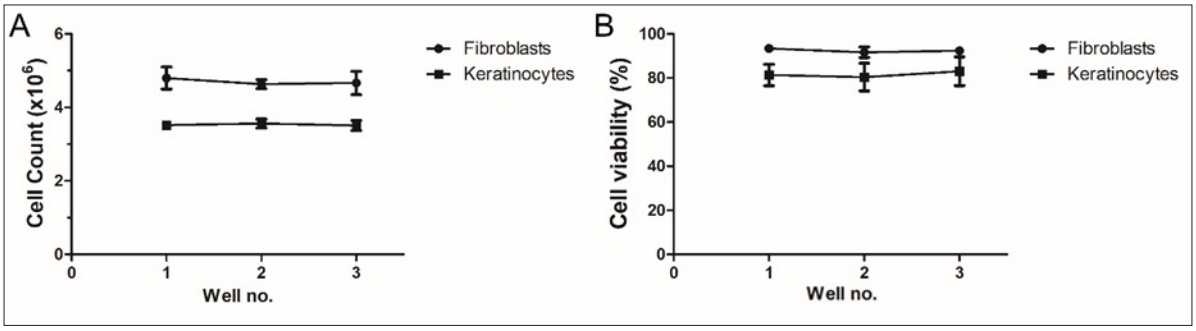

Figure 4. Cell counts and viability of both bioprinted fibroblasts and keratinocytes under a dwell time 1000 µs and backpressure of 150 mmHg. (A) Cell counts of bioprinted fibroblasts and keratinocytes. (B) Cell viability of fibroblasts and keratinocytes. Data are presented as mean ± one standard deviation. $N = 3$.

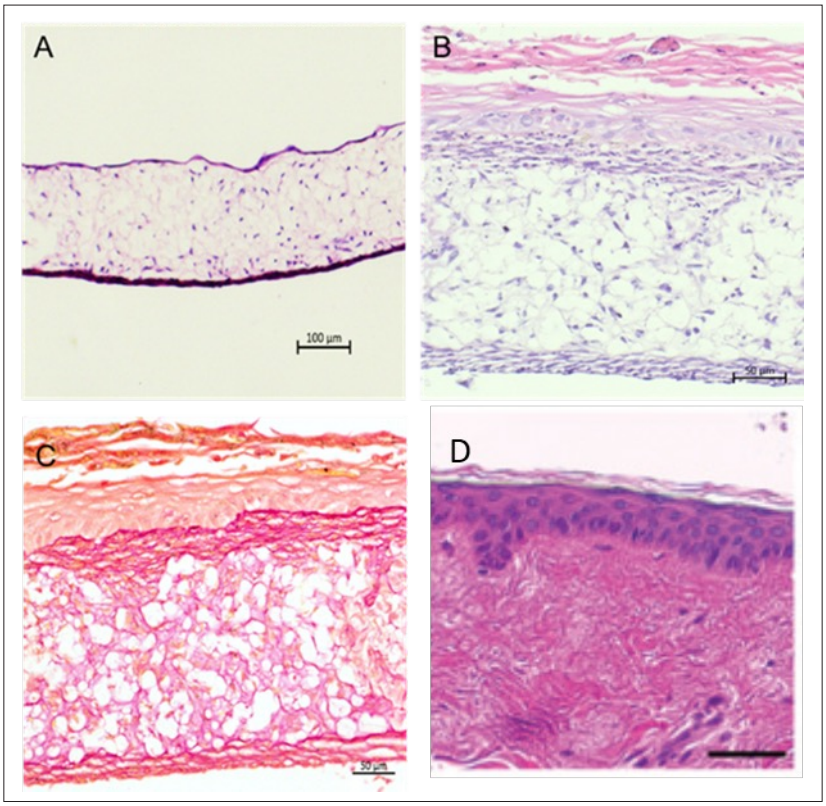

Figure 5. Representative staining of bioprinted dermal and full-thickness skin equivalents. (A) Representative H&E staining of dermal equivalent (day 14); scale bar: 100 µm. (B) Representative H&E staining of full-thickness skin equivalent (day 35); scale bar: 50 µm. (C) Representative Picrosirius red staining of full-thickness skin equivalents (day 35); scale bar: 50 µm. (D) H&E staining of human skin, scale bar 25 µm.

compared to the media and isotype controls, suggesting an OKT3-induced T-cell response. This links to IFN-γ expression in OKT3-treated co-cultures, where T cells activated by IL-2 could then increase expression of IFN-γ. There was no statistical significance in secretion of both IL-4 and IL-13. IL-4 and IL-13 are both associated with a Th2 type response,[29,30] and the lack of expression of IL-4 and IL-13 also suggests that a Th2 immune response was not induced. The elevated expression of TNF-α is comparable to the use of OKT3 *in vivo* while the levels of TNFα, IFN-γ, and IL-2 are similar to cytokine profiles generated *in vitro*.[31,32] All models show high levels of expression of IL-6, which is not unexpected, as it is constitutively produced by keratinocytes,[33] but no significant differences are seen for this marker across the experimental conditions. This data indicates that it is feasible to use fully humanized full-thickness bioprinted HSEs to identify the immunotoxicity of monoclonal antibodies *in vitro* by multiplex quantification of cytokines to create a cytokine profile of the potential immune response.

4. Discussion

The successful bioprinting of fully autologous skin equivalents in a 96-well format as reported in this work provides a foundation for future work to manufacture skin equivalents on an industrial scale. There have been many examples of bioprinted human skin; however, no previous studies have demonstrated that printed skin equivalents could be used for *in vitro* testing of therapeutic antibodies.[34] This novel application of a fully human bioprinted tissue suitable for *in vitro* testing of therapeutic antibodies may be highly beneficial to the drug development process of the pharmaceutical industry.[34] The proof of concept demonstrated here could be utilized during the different stages of the drug development pipeline for safety testing of drug candidates, allowing early elimination or modification of problem candidates, as well as at the preclinical stage to prevent "late failure" prior to the clinical testing phase. There have been many publications in the field of biofabrication exploring the use of DoD printing processes such as ink jetting, solenoid microvalves, and laser-assisted printing.[13,19,35] Such studies focus on the biofabrication of constructs using the deposition of high-viscosity bioinks consisting of cell-laden crosslinked gels or gel precursors.[14,20,36,37] As a result, few studies investigate the use of cell-laden low-viscosity bioinks; therefore, little information is reported on the reproducibility of the printing process. Figure 3 indicates

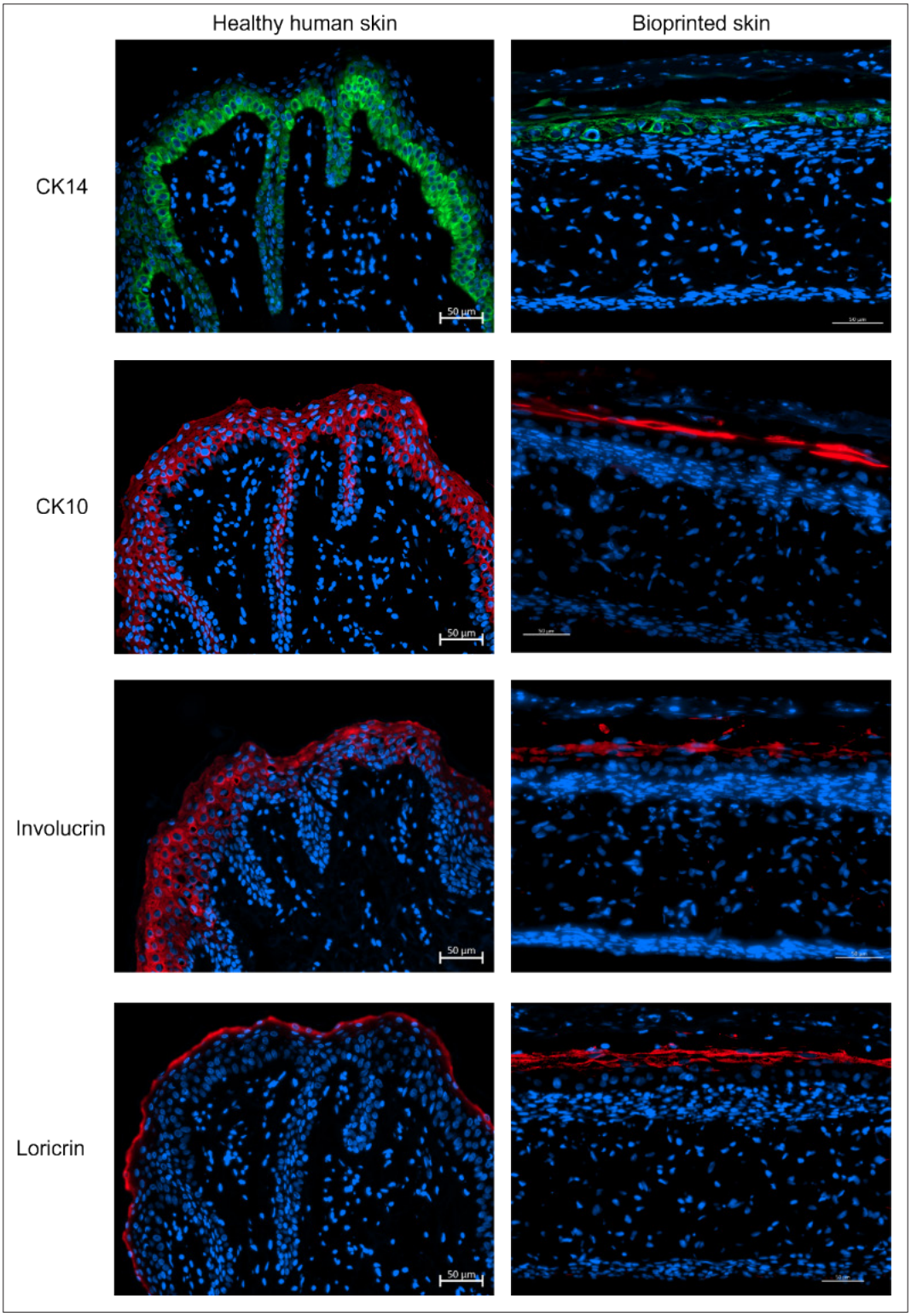

Figure 6. Representative staining of healthy human skin and bioprinted skin equivalents (at day 35). Healthy human skin and skin equivalents were stained for CK14 (green), CK10 (red), involucrin (red), and loricrin (red). Cell nuclei were stained blue with Hoechst 33342. Scale bars: 50 µm.

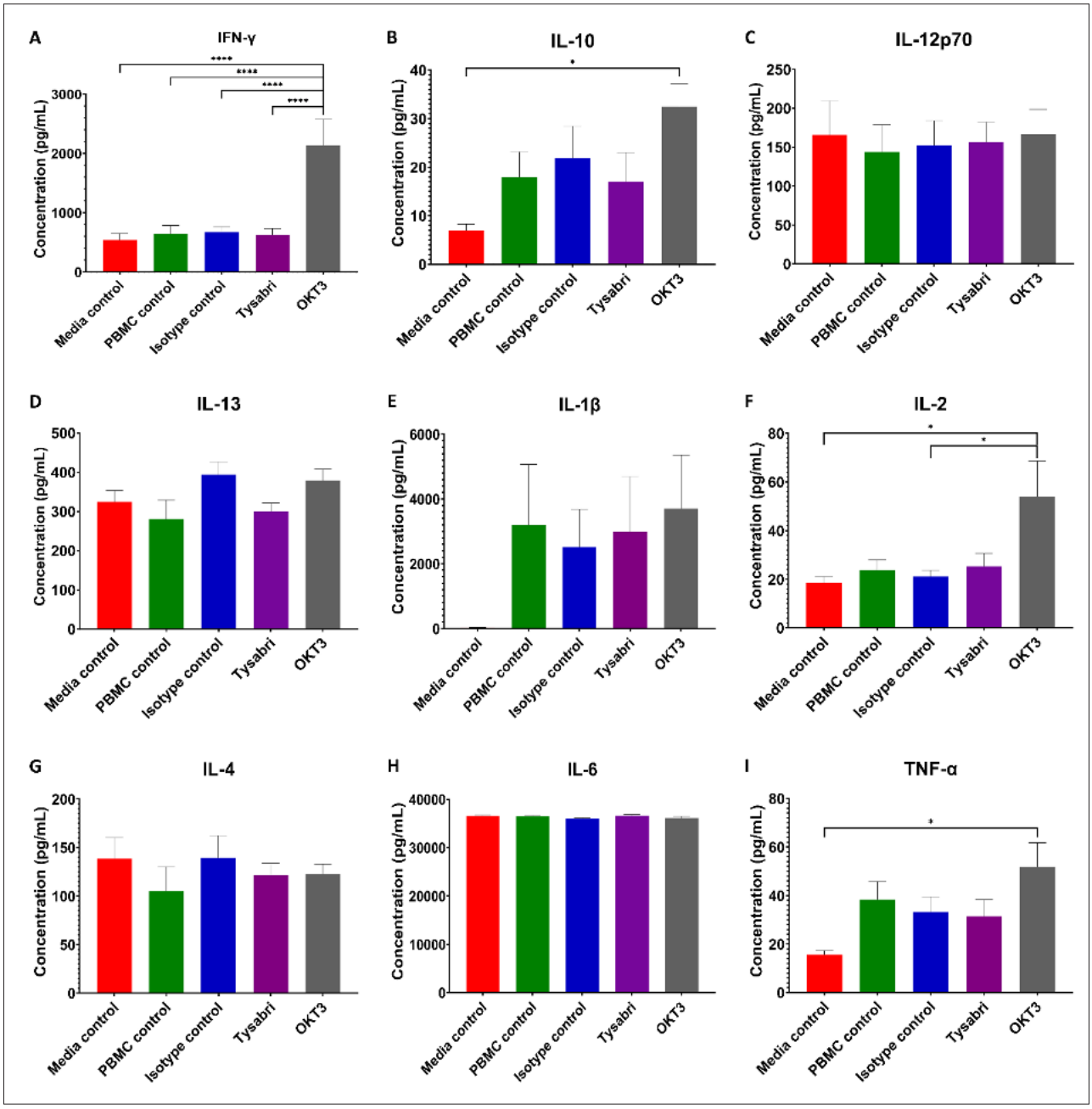

Figure 7. Mean proinflammatory cytokine concentrations from autologous co-cultures. The concentrations of cytokines detected from the supernatants of autologous co-cultures. Statistically significant differences between conditions are indicated by * and ****, which represent $p < 0.05$ and $p < 0.0001$, respectively.

that with reservoir agitation and microvalve purging, the process can offer a consistent and automatable approach in the development of tissue models.

Traditionally, commercially available skin equivalents are manufactured using top-down tissue engineering techniques. Therefore, such skin equivalents typically rely on non-human or human allogeneic ECM, as is the case for many studies which have bioprinted equivalents.[38] Therefore, currently available skin equivalents are not compatible with assays that require fully autologous systems. This work has demonstrated a hybridized approach to tissue engineering, combining top-down and bottom-up methodologies to create fully human skin equivalents. As demonstrated in this work, bioprinted skin cells can populate inert scaffolds and

produce their own ECM (Figure 5) in an autologous setting. The resulting skin equivalents were comparable to healthy human skin (Figure 6) and could be co-cultured with PBMCs to produce a fully autologous assay with automated deposition of cells, which is scalable to commercial demand. The biologically inert scaffold-based approach allows the formation of a fully autologous human skin equivalent. The bioprinting of viable and functional human cells using solenoid microvalves circumvents the labor-intensive aspect of creating 96-well tissue constructs on a large scale. This method enables the production of biologically representative and functional HSEs that may be developed in a scalable manner. This approach could potentially be applied to wider applications such as disease modeling and modeling of wound healing, and one specific aspect of future work will involve innervating the 3D skin model using neuronal and Swann cells lines in order to further validate the model and assess pain-relieving drugs. In terms of development and use of human skin equivalents, this method of biofabrication produces a human skin equivalent that provides a potential alternative to non-animal testing and avoids cross-species reactivity, which can impact data interpretation.

5. Conclusion

This study successfully demonstrated that solenoid microvalve-based bioprinting of autologous skin equivalents in a 96-well format could be used to determine adverse immune responses of monoclonal antibodies in the human setting. Primary human skin cells were shown to be viable post printing and were shown to retain the functional capabilities required of the cells to generate human skin equivalents. The co-culture of autologous bioprinted skin equivalents with autologous PBMCs successfully identified adverse immune reactions of positive and negative therapeutic antibodies, respectively. Overall, this study has demonstrated that bioprinted human tissue can identify *in vitro* adverse immune responses triggered by therapeutic antibodies. The scalability of both the Alvetex inserts and the bioprinting approach means that in combination these technologies are able to produce human skin equivalents at high-throughput rates, enhancing pre-clinical evaluation of novel biologics prior to clinical testing.

Acknowledgments

None.

Funding

This research was supported by the EPSRC Centre for Doctoral Training in Additive Manufacturing and 3D Printing (EP/L01534X/1), and by Innovate UK through Project 103597 (Novel manufacture and commercialization of a 96-well 3D skin model for drug and toxicology testing).

Conflict of interest

The authors declare no conflicts of interest.

Author contributions

Conceptualization: Kenneth Dalgarno, Anne Dickinson, Stefan Przyborski
Investigation: Mahid Ahmed
Methodology: David Hill, Shaheda Ahmed
Formal analysis: Mahid Ahmed, David Hill, Shaheda Ahmed
Writing – original draft: Mahid Ahmed, Kenneth Dalgarno, Anne Dickinson
Writing – review & editing: David Hill, Kenneth Dalgarno, Anne Dickinson, Stefan Przyborski

Ethics approval and consent to participate

Skin cells were obtained from healthy volunteers, with ethical approval for the procedure from Newcastle and North Tyne 1 Research Ethics Committee, REC 10/H0906/58.

Consent for publication

Not applicable.

Availability of data

Data can be obtained from the Newcastle University Open Data Archive (https://doi.org/10.25405/data.ncl.24566740.v1).

References

1. Stebbings R, Findlay L, Edwards C, et al. "Cytokine storm" in the phase I trial of monoclonal antibody TGN1412: better understanding the causes to improve preclinical testing of immunotherapeutics. *J Immunol.* 2007;179(5):3325-3331. doi: 10.4049/jimmunol.179.5.3325

2. Hay M, Thomas D, Craighead J, Economides C, Rosenthal J. Clinical development success rates for investigational drugs. *Nat Biotechnol.* 2014;32:40-51. doi: 10.1038/nbt.2786

3. Pound P, Ritskes-Hoitinga M. Is it possible to overcome issues of external validity in preclinical animal research? Why most animal models are bound to fail. *J Transl Med.* 2018;16:304. doi: 10.1186/s12967-018-1678-1

4. Panoskaltsis N, McCarthy NE, Knight SC. Myelopoiesis of acute inflammation: lessons from TGN1412-induced cytokine storm. *Cancer Immunol Immunother.* 2021;70:1155-1160.

doi: 10.1007/s00262-020-02702-9

5. DiMasi JA, Grabowski HG, Hansen RW. Innovation in the pharmaceutical industry: new estimates of R&D costs. *J Health Econ*. 2016;47:20-33. doi: 10.1016/j.jhealeco.2016.01.012
6. Mahlich J, Bartol A, Dheban S. Can adaptive clinical trials help to solve the productivity crisis of the pharmaceutical industry? - a scenario analysis. *Health Econ Rev.* 2021;11:4. doi: 10.1186/s13561-021-00302-6
7. Hughes JP, Rees S, Kalindjian SB, Philpott KL. Principles of early drug discovery. *Br J Pharmacol.* 2011;162(6):1239-1249. doi: 10.1111/j.1476-5381.2010.01127.x
8. Ahmed SS, Whritenour J, Ahmed MM, et al. Evaluation of a human *in vitro* skin test for predicting drug hypersensitivity reactions. *Toxicol Appl Pharmacol.* 2019;369:39-48. doi: 10.1016/j.taap.2019.02.005
9. Lawrence E, Sims J, Gander A, et al. The barriers and motivators to using human tissues for research: the views of UK-based biomedical researchers. *Biopreserv Biobank*. 2020;18(4):266-273. doi: 10.1089/bio.2019.0138
10. Harley WS, Li CC, Toombs J, et al. Advances in biofabrication techniques towards functional bioprinted heterogeneous engineered tissues: a comprehensive review. *Bioprinting.* 2021;23:e00147. doi: 10.1016/j.bprint.2021.e00147
11. di Marzio N, Eglin D, Serra T, Moroni L. Bio-Fabrication: convergence of 3D bioprinting and nano-biomaterials in tissue engineering and regenerative medicine. *Front Bioeng Biotechnol.* 2020;8. doi: 10.3389/fbioe.2020.00326
12. Groll J, Boland T, Blunk T, et al. Biofabrication: reappraising the definition of an evolving field. *Biofabrication.* 2016;8(1):013001. doi: 10.1088/1758-5090/8/1/013001
13. Koch L, Deiwick A, Franke A, et al. Laser bioprinting of human induced pluripotent stem cells-the effect of printing and biomaterials on cell survival, pluripotency, and differentiation. *Biofabrication*. 2018;10(3):035005. doi: 10.1088/1758-5090/aab981
14. Cubo N, Garcia M, Del Cañizo JF, Velasco D, Jorcano JL. 3D bioprinting of functional human skin: production and *in vivo* analysis. *Biofabrication*. 2016;9(1):015006. doi: 10.1088/1758-5090/9/1/015006
15. Murphy S, Atala A. 3D bioprinting of tissues and organs. *Nat Biotechnol.* 2014;32:773-785. doi: 10.1038/nbt.2958
16. Solis LH, Ayala Y, Portillo S, Varela-Ramirez A, Aguilera R, Boland T. Thermal inkjet bioprinting triggers the activation of the VEGF pathway in human microvascular endothelial cells *in vitro*. *Biofabrication*. 2019;11(4):045005. doi: 10.1088/1758-5090/ab25f9
17. Dudman JPR, Ferreira AM, Gentile P, et al. Reliable inkjet printing of chondrocytes and MSCs using reservoir agitation. *Biofabrication.* 2020;12(4):045024. doi: 10.1088/1758-5090/aba2f8
18. Li X, Liu B, Pei B, et al. Inkjet bioprinting of biomaterials. *Chem Rev.* 2020;120(19):10793-10833. doi: 10.1021/acs.chemrev.0c00008
19. Faulkner-Jones A, Fyfe C, Cornelissen DJ, et al. Bioprinting of human pluripotent stem cells and their directed differentiation into hepatocyte-like cells for the generation of mini-livers in 3D. *Biofabrication*. 2015;7(4):044102. doi: 10.1088/1758-5090/7/4/044102
20. Dudman J, Ferreira AM, Gentile P, Wang X, Dalgarno K. Microvalve bioprinting of MSC-chondrocyte co-cultures. *Cells*. 2021;10(12):3329. doi: 10.3390/cells10123329
21. Ng WL, Qi JTZ, Yeong WY, Naing MW. Proof-of-concept: 3D bioprinting of pigmented human skin constructs. *Biofabrication.* 2018;10(2):025005. doi: 10.1088/1758-5090/aa9e1e
22. Yang X, Lu Z, Wu H, Li W, Zheng L, Zhao J. Collagen-alginate as bioink for three-dimensional (3D) cell printing based cartilage tissue engineering. *Mater Sci Eng C*. 2018;83:195-201. doi: 10.1016/j.msec.2017.09.002
23. Fedorovich NE, Kuipers E, Gawlitta D, Dhert WJA, Alblas J. Scaffold porosity and oxygenation of printed hydrogel constructs affect functionality of embedded osteogenic progenitors. *Tissue Eng Part A*. 2011;17(19-20):2473-2486. doi: 10.1089/ten.TEA.2011.0001
24. Alonzo M, AnilKumar S, Roman B, Tasnim N, Joddar B. 3D bioprinting of cardiac tissue and cardiac stem cell therapy. *Transl Res.* 2019;211:64-83. doi: 10.1016/j.trsl.2019.04.004
25. Albanna M, Binder KW, Murphy SV, et al. In situ bioprinting of autologous skin cells accelerates wound healing of extensive excisional full-thickness wounds. *Sci Rep.* 2019;9(1):1856. doi: 10.1038/s41598-018-38366-w
26. Zhou Y, Qin R, Chen T, Zhang K, Gui J. 3D bioprinting modified autologous matrix-induced chondrogenesis (AMIC) technique for repair of cartilage defects. *Mater Des.* 2021;203. doi: 10.1016/j.matdes.2021.109621
27. Hill DS, Robinson ND, Caley MP, et al. A novel fully humanized 3D skin equivalent to model early melanoma invasion. *Mol Cancer Ther.* 2015;14(11):2665-2673. doi: 10.1158/1535-7163.MCT-15-0394
28. Choudhury S, Das A. Advances in generation of three-dimensional skin equivalents: pre-clinical studies to clinical therapies. *Cytotherapy.* 2021;23(1):P1-9. doi: 10.1016/j.jcyt.2020.10.001
29. Berger A. Th1 and Th2 responses: what are they? *BMJ*. 2000;321:424.

doi: 10.1136/bmj.321.7258.424

30. Swain SL, Weinberg AD, English M, Huston G. IL-4 directs the development of Th2-like helper effectors. *J Immunol.* 1990;145(11):3796-3806.

31. Gaston RS, Deierhoi MH, Patterson T, et al. OKT3 first-dose reaction: association with T cell subsets and cytokine release. *Kidney Int.* 1991;39(1):141-148. doi: 10.1038/ki.1991.18

32. Römer PS, Berr S, Avota E, et al. Preculture of PBMCs at high cell density increases sensitivity of T-cell responses, revealing cytokine release by CD28 superagonist TGN1412. *Blood*. 2011;118(26):6772-6782. doi: 10.1182/blood-2010-12-319780

33. Yoshizaki, K, Nishimoto N, Matsumoto K, et al. Interleukin 6 and expression of its receptor on epidermal keratinocytes. *Cytokine*. 1990;2(5):381-387. doi: 10.1016/1043-4666(90)90069-6

34. Mazzocchi A, Soker S, Skardal A. 3D bioprinting for high-throughput screening: drug screening, disease modeling, and precision medicine applications. *Appl Phys Rev.* 2019;6(1):011302. doi: 10.1063/1.5056188

35. Mandrycky C, Wang Z, Kim K, Kim DH. 3D bioprinting for engineering complex tissues. *Biotechnol Adv.* 2016;34(4): 422-434. doi: 10.1016/j.biotechadv.2015.12.011

36. Lee V, Singh G, Trasatti JP, et al. Design and fabrication of human skin by three-dimensional bioprinting. *Tissue Eng Part C*. 2014;20(6):473-484. doi: 10.1089/ten.TEC.2013.0335

37. Michael S, Sorg H, Peck CT, et al. Tissue engineered skin substitutes created by laser-assisted bioprinting form skin-like structures in the dorsal skin fold chamber in mice. *PLoS One*. 2013;8(3):e57741. doi: 10.1371/journal.pone.0057741

38. Weng T, Zhang W, Xia Y, et al. 3D bioprinting for skin tissue engineering: current status and perspectives. *J Tissue Eng.* 2021;12:20417314211028574. doi: 10.1177/20417314211028574

ACCSCIENCE PUBLISHING

International Journal of Bioprinting

RESEARCH ARTICLE

Biomimetic mineralization of 3D-printed polyhydroxyalkanoate-based microbial scaffolds for bone tissue engineering

Dahong Kim[1,2], Su Jeong Lee[3], Dongjin Lee[1], Ji Min Seok[1,2], Seon Ju Yeo[1], Hyungjun Lim[1], Jae Jong Lee[1], Jae Hwang Song[4], Kangwon Lee[2,5], Won Ho Park[6], and Su A Park[1]*

[1]Nano-Convergence Manufacturing Systems Research Division, Korea Institute of Machinery and Materials (KIMM), Daejeon, Republic of Korea

[2]Department of Applied Bioengineering, Graduate School of Convergence Science and Technology, Seoul National University, Seoul, Republic of Korea

[3]Department of Microbiology, CHA University, Seongnam, Republic of Korea

[4]Department of Orthopaedic Surgery, Konyang University Hospital, Daejeon, Republic of Korea

[5]Research Institute for Convergence Science, Seoul National University, Seoul, Republic of Korea

[6]Department of Organic Materials Engineering, Chungnam National University, Daejeon, Republic of Korea

(This article belongs to the *Special Issue: Advancements in 3D Printing, Microfluidics, and Their Integrated Applications*)

Abstract

Polyhydroxyalkanoates (PHAs) have gained much attention as a potential alternative to conventional plastic bone scaffolds due to their biocompatibility and biodegradability, among a diverse range of advantageous properties. However, the water resistance of PHA creates an environment that can interfere with cell interactions. In this study, a three-dimensional-printed PHA scaffold was fabricated through fused deposition modeling printing considering the physical properties of PHA. The PHA bone scaffolds were then coated with polydopamine (pDA) and/or hydroxyapatite (HA) in various configurations using a relatively simple and rapid process involving only immersion. The PHA–pDA–HA scaffold showed enhanced cell viability, proliferation, and differentiation, and could thus serve as a versatile platform for bone tissue engineering applications.

Keywords: Polyhydroxyalkanoate; Biomineralization; Biopolymer; Bone scaffold; Polydopamine; Bioprinting

*** Corresponding author:**
Su A Park
(psa@kimm.re.kr)

Citation: Kim D, Lee SJ, Lee D, et al. Biomimetic mineralization of 3D-printed polyhydroxyalkanoate-based microbial scaffolds for bone tissue engineering. *Int J Bioprint*. 2024;10(2):1806. doi: 10.36922/ijb.1806

Received: September 12, 2023
Accepted: November 2, 2023
Published Online: January 16, 2024

1. Introduction

There has been growing interest in biodegradable polymers as a substitute for traditional petrochemical-based polymers, with a focus on green alternative.[1–3] The use of biopolymers is necessary in certain circumstances, such as for biomedical applications, due to their biodegradability, biocompatibility, and non-toxicity.[4–6] Polyhydroxyalkanoates (PHAs) are biodegradable polymers that are naturally produced in bacterial fermentation. PHAs are composed of monomers derived from carboxylic acids, such as fatty acids, and their physical and chemical properties can vary depending on the specific types of monomers

present in the polymer.[2] By virtue of its biocompatibility and biodegradability, PHA has been increasingly used in medical applications, such as those involving bone scaffolds and implants.[4,7] Notably, PHA exhibits lower acidity and generates fewer inflammatory degradation products than existing degradable polymers, such as polylactic acid (PLA), indicating its potential in mitigating cytotoxicity issues.

Three-dimensional (3D) bioprinting facilitates new bone formation by enabling the fabrication of complex 3D scaffold structures that offer mechanical support and utilize a wide range of materials, including biocompatible polymers.[1–3] 3D printing techniques comprise various categories, including extrusion-based, jetting-based, and vat photopolymerization-based printing. Depending on the material characteristics and the desired structure, different types of 3D bioprinting technologies can be applied in tissue engineering or the medical field.[8-11] In particular, extrusion-based printing involves the fused filament fabrication (FFF) method, which utilizes thermoplastic materials. The material is heated and melted within the 3D printer, then systematically layered to create a 3D structure. Extrusion-based printing is widely used for shaping various thermoplastic polymers due to its ease of use and the lack of solvent requirements. PHA is known to be highly suitable for fabricating scaffolds through 3D printing, owing to its thermoplastic property, excellent processability, and ability to provide appropriate physical properties.[12,13] However, PHAs are naturally resistant to moisture (i.e., are water-insoluble), which can interfere with host cell attachment, growth, and differentiation in the context of bone regeneration.[4,13]

In this study, 3D-printed PHA scaffolds were functionalized with bioactive molecules to enhance their biological performance. The surface of a 3D-printed PHA scaffold was coated with polydopamine (pDA) and hydroxyapatite (HA) using a straightforward technique. Immersion was the only step required for creating the pDA and HA coatings, thus providing a simple and rapid process. pDA supports cell adhesion and enhances calcination for bone remodeling. Biomineralization with HA, which is compositionally similar to the mineral phase of bone, enhances the osteogenic differentiation of osteoblast-like cells. Thus, the pDA and HA coatings further advance the potential applications of PHA scaffolds in osteogenesis.

2. Materials and methods

2.1. Biopolymer scaffold fabrication

PHA (molecular weight: 257 kDa; CJ CHEILJEDANG, Seoul, Korea) was fabricated using an extrusion-based printing approach with a 3D bioprinter (Korea Institute of Machinery and Materials, Daejeon, Korea). The PHA scaffold was printed using a nozzle size of 400 μm, printing speed of around 500 mm/min, pneumatic pressure of 80 kPa, and temperature of 180°C. The printing process was completed in <40 min to prevent thermal denaturation (**Figure S1** in Supplementary File).

2.2. Surface functionalization of the PHA scaffold with pDA and a mineralized PHA scaffold with HA

The PHA scaffold was coated with pDA and HA. pDA was dissolved in 10 mM Tris-HCl buffer at a concentration of 2 mg/mL and stirred for 1 h. The printed PHA scaffold was soaked in a solution containing pDA and stirred for 24 h at room temperature. The scaffold coated with pDA was washed at least three times in deionized water and then dried in vacuum at 40°C for 24 h.

HA was produced using a 5× simulated body fluid (SBF) solution (Biosesang, Korea). The composition of the 5× SBF solution is as follows: Na^+, 710 mM; K^+, 25 mM; Mg^{2+}, 7.7 mM; Cl^-, 739.7 mM; HCO^{3-}, 21 mM; HPO_4^{2-}, 5 mM; and SO_4^{2-}, 2.5 mM. The PHA scaffolds with pDA were soaked in the SBF solution, which was stirred at room temperature for 72 h. The biopolymers with pDA and HA were rinsed at least three times to remove the residue and then dried (Figure 1).

2.3. Surface characterization of functionalized biopolymer scaffold

The surface morphology of the printed biopolymer with pDA and HA coatings was investigated using scanning electron microscopy (SEM; Sirion, FEI, USA). The wettability of the biopolymers was evaluated based on the contact angle (Contact Angle Meter DM 210; Kyowa Kirin, Inc., Tokyo, Japan). A 4 μL droplet was placed on the surface of the samples, and the contact angle was measured after 30 s.

2.4. Physiochemical characterization of the biopolymer scaffold

Attenuated reflectance-infrared (ATR-IR) spectroscopy was used to measure the chemical composition of PHA and pDA at a resolution of 4 cm^{-1}. The chemical composition of the samples was determined using X-ray photoelectron spectroscopy (XPS) for the identification of specific chemical elements (C, O, N, Ca), using a monochromatic Al-Kα radiation source with an X-ray beam spot size of 400 μm. The phase of the calcium phosphate of HA that formed on the scaffold surface was identified using X-ray diffraction (XRD) over the 2θ range of 25–50°. Thermogravimetric analysis (TGA) was used to investigate the influence of pDA and HA on the degradation temperature and thermal stability of the biopolymer. The samples were heated from 25°C to 850°C at a rate of 10°C/min.

2.5. Mechanical properties

Compression test was evaluated on a universal testing machine (RB301 UNITECH-M; RnD, Korea) with a 500 kN load cells and a 5 mm/min crosshead speed. The sample size was 5 × 5 × 3 mm, and the strand size was 400 μm.

2.5. Cell culture

MG63, which is an osteoblast-like cell line, was cultured in Dulbecco's modified Eagle's medium (DMEM; Gibco/Thermo Fisher Scientific, Waltham, MA, USA) with 10% fetal bovine serum and 1% penicillin (Gibco). The cells were cultured at 37°C under 5% CO_2 conditions.

2.6. Cell viability, proliferation, and differentiation on a functionalized PHA biopolymer scaffold

The cells were seeded on the PHA biopolymer scaffolds, and the scaffolds were evaluated for cell survival, proliferation, and differentiation. The scaffold was sterilized for 1 min using 70% ethanol, followed by a phosphate-buffered saline wash. MG63 cells (5 × 10^5 cells/mL) were seeded on each sample and cultured for 7 days for viability and proliferation, and for 10 days for differentiation.

Viability was investigated using a live/dead assay kit (Live and Dead Kit, Invitrogen, USA) containing calcein AM and ethidium homodimer-1. Live cells were stained with calcium AM (green), and dead cells were labeled with ethidium homodimer (red). The cells on the scaffolds were stained for 1 h in an incubator. Cell proliferation was evaluated using the WST-1 assay (Premix WST-1 Cell Proliferation Assay System; Takara Bio, Shiga, Japan). The cells on the scaffolds were immersed in WST-1 solution for 30 min, and the supernatant was measured at 440 nm with a microplate reader (SpectraMax iD3; Molecular Devices, San Jose, CA, USA). A radioimmunoprecipitation assay (RIPA) buffer (Pierce RIPA buffer; Thermo Fisher Scientific) was used to lyse the cells of the scaffold for *alkaline phosphatase* (ALP) extraction, and the cells were preserved at -80°C. The ALP kit was utilized according to the manufacturer's instructions. Picogreen dsDNA assay (Quant-iT™ PicoGreen™ dsDNA Assay Kit; Invitrogen/Thermo Fisher Scientific, Waltham, MA, USA) was used to normalize the ALP activity.

2.7. Statistical analysis

All quantitative data are presented as mean ± standard deviation. One-way analysis of variance (ANOVA) was used to analyze the results, followed by Tukey's post-hoc test. Asterisks in the figures denote significant values ($p < 0.05$). Statistical analysis was performed using Origin software (ver. 8.6; OriginLab Corporation, Northampton, MA, USA).

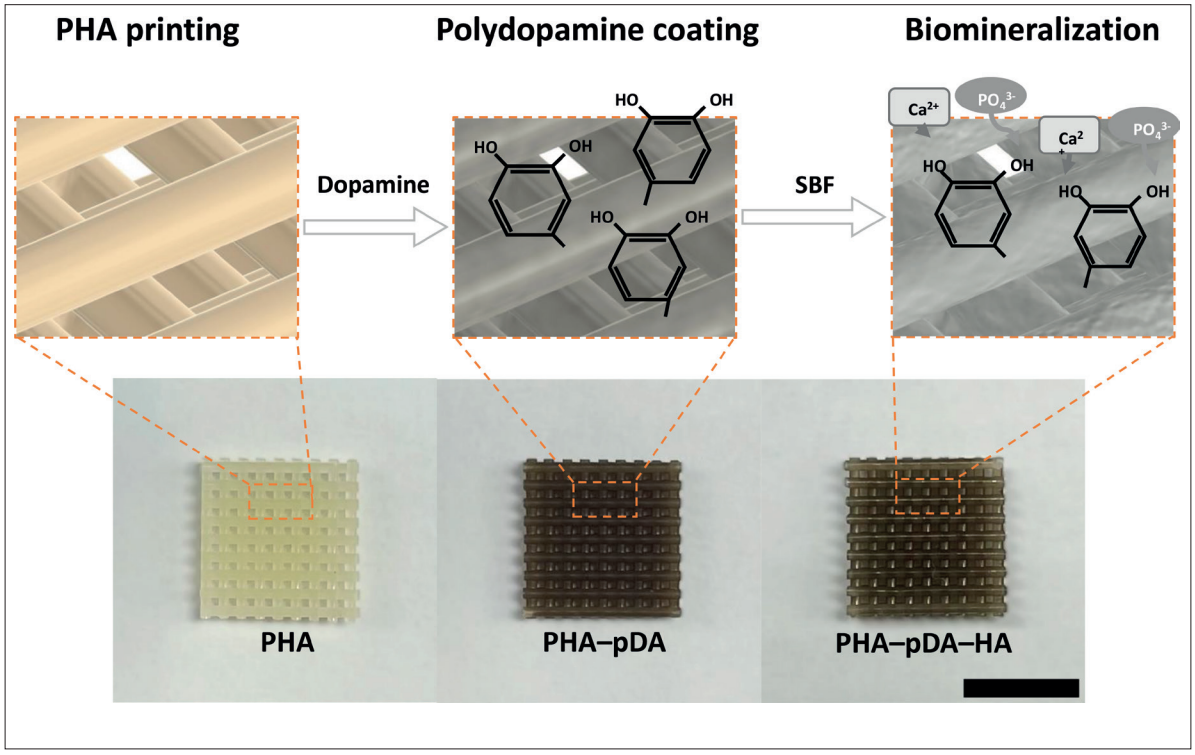

Figure 1. Schematic illustrations of 3D-printed polyhydroxyalkanoate (PHA) and other modified scaffolds, and biomimetic mineralization on their surfaces for osteogenesis. Abbreviations: HA, hydroxyapatite; pDA, polydopamine; PHA, polyhydroxyalkanoate; SBF: simulated body fluid.

3. Results and discussion

3.1. Surface characterization of PHA biopolymer scaffold with pDA and HA

PHA has been identified as a promising material for use in biopolymer scaffolds due to its biocompatibility and biodegradability. PHA is also a promising biopolyester for extrusion-based printing due to its comparatively low glass transition temperature.[12]

When using 3D bioprinting to fabricate scaffolds, it is essential to meet the required conditions such as structure, mechanical properties, and osteoconductivity to fulfill the role of a bone scaffold. In particular, it is crucial for the scaffold to possess a structure that precisely matches the bone defect, enabling the reconstruction of the original bone shape and effectively responding to dynamic forces. Precise printability with excellent spatial capabilities is required to ensure that the printed structures accurately replicate virtual models. The printing state of the PHA was verified by adjusting the pressure and printing speed, which are the speeds of the print head. To identify conditions with strand sizes similar to the size of the nozzle, the strand sizes at pneumatic pressures of 60, 80, and 100 kPa, and printing speed of 400, 500, and 600 mm/min were compared (Figure 2a). The dots in Figure 2a represent the strand sizes obtained when printing PHA under various pressure and printing speed conditions. Additionally, the red-shaded region denotes an error margin of approximately 10%, determined based on a nozzle size of 400 μm. This region was considered indicative of suitable printability. A higher pressure and a slower printing speed resulted in an increasing trend in strand size. As the printing speed increased and the pressure decreased, the strand tended to become thinner in size. At the condition of 80 kPa and 500 mm/min, a strand size of 405.47 ± 3.98 μm was observed, which closely matched the nozzle size of 400 μm (**Figure S2** in Supplementary File). Therefore, all the scaffolds for subsequent experiments were fabricated under these conditions.

The surface morphology of the printed PHA scaffold, pDA-coated PHA scaffold, and pDA-HA-coated PHA scaffold were evaluated. The results showed that the printed PHA scaffold had a smooth surface (Figure 2b). The pDA-coated PHA scaffold surface was covered by agglomerates after 24 h. HA, in the form of a large plate, covered the surface of the biomineralized scaffold through SBF treatment for 72 h. It is well known that pDA coating facilitates rapid CaP nucleation due to the availability of free catechols not involved in substrate adhesion, which is important for CaP nucleation.[14–16]

These surface treatments led to differences in wettability (Figure 3a). The water contact angle of the PHA scaffold was 81.025° ± 2.25, whereas the contact angle for the PHA–pDA and PHA–pDA–HA scaffolds was 0° within 1 min. Water droplets rapidly penetrated the surface when pDA was present. Thus, the hydrophilicity of the surface increased sharply with the pDA coating. Surface wettability has a significant influence on the interactions between the scaffold surface and the cells. A hydrophilic surface provides for better adsorption of proteins (e.g., fibronectin) and growth factors compared with a hydrophobic surface.[17,18]

A compression test was conducted to measure the mechanical properties of PHA and functionalized PHA scaffolds (Figure 3b). Pressure was applied up to a stain of 0.6 mm/mm, and stress–strain graphs for all groups exhibited a similar trend.

Furthermore, the results also indicated that there was not a significant difference in Young's modulus (Figure 3c). It was confirmed that the physical properties were not greatly altered by the reactions of pDA and HA.

3.2. Physicochemical characterization of the PHA scaffold with pDA and HA

The formation of pDA and HA on the PHA scaffold was verified through examination of the physicochemical characteristics (Figure 4). Before the growth of HA, ATR-IR spectroscopy was conducted to confirm pDA formation (Figure 4a). The broad absorption band at 3360 cm^{-1} corresponds to the stretching vibrations of catechol–OH in pDA. The peak at 1615 cm^{-1} is associated with the stretching vibration of the C=O bond, and the peak at 1500 cm^{-1} indicates aromatic C=C stretching and N-H bending. The presence of a pDA coating was confirmed on the PHA–pDA and PHA–pDA–HA scaffolds.[19–21]

After confirming pDA formation on the PHA scaffold, HA formation was subsequently verified using XPS analysis (Figure 4b). The presence of an N1s peak was confirmed in both the PHA–pDA and PHA–pDA–HA groups, but not in the PHA group.[22] Furthermore, the Ca2p peak was observed only for the PHA–pDA–HA group (Figure 4c). These results indicate the formation of biominerals and pDA on the PHA surface. It is widely recognized that pDA contains numerous catecholamine groups that play a significant role in biomineral formation. The catecholamine groups not involved in substrate adhesion are capable of binding with Ca^{2+} ions.[14]

The formation of HA was confirmed by XRD with reference to the JCPDS 9-432 standard.[23,24] Peaks corresponding to HA were detected only in the PHA–pDA–HA group (Figure 4d). The peak of HA appeared to be relatively broad, indicating that the formed HA has low crystallinity and an irregular orientation, as confirmed in SEM images.[25]

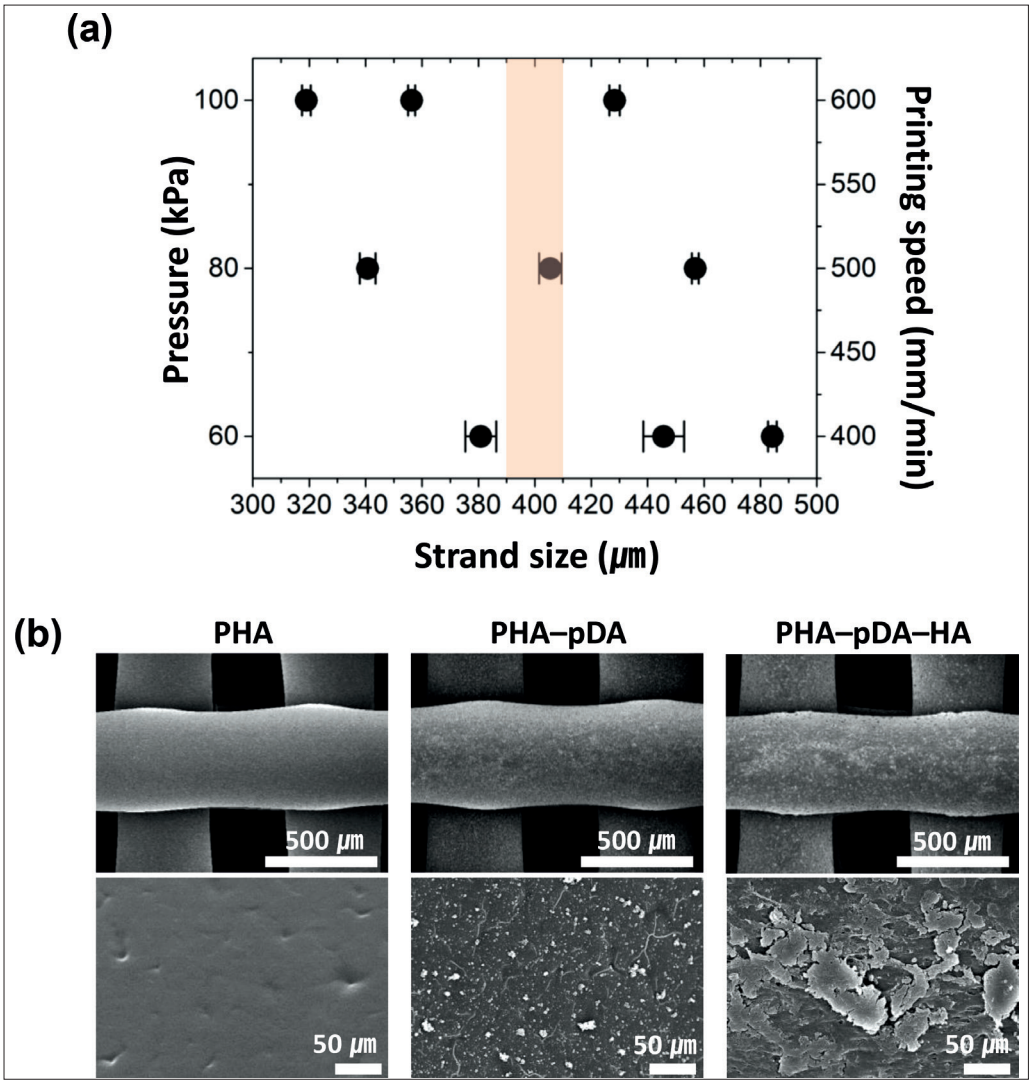

Figure 2. Surface characterization of the PHA, PHA–pDA, and PHA–pDA–HA scaffolds. (a) Printability of PHA in various printing conditions. (b) Scanning electron microscopy images of PHA, PHA–pDA, and PHA–pDA–HA scaffolds. Abbreviations: HA, hydroxyapatite; pDA, polydopamine; PHA, polyhydroxyalkanoate.

The thermal stability of both the PHA and surface-modified PHA scaffolds was evaluated using TGA (Figure 4e). PHA has a thermal decomposition temperature of 291.8°C. PHA–pDA and PHA–pDA–HA showed thermal decomposition peaks at 296.0°C and 297.7°C, respectively. One of the challenges of PHAs is their low thermal stability.[12,26] The TGA results indicated that thermal stability could be enhanced by using pDA and HA coatings.

3.3. *In vitro* osteogenic ability of the functionalized 3D-printed PHA scaffolds

A biomaterial scaffold for bone tissue engineering should facilitate cell activity to guide the formation of new bone and promote functional restoration at defect sites.[22,27,28] Biomaterials used for bone recovery are expected to possess bioactive functions and to be biocompatible for bone regeneration purposes. PHA is widely used in biomedical engineering, including tissue engineering, due to its mechanical properties, biocompatibility, biodegradability, and reduced inflammation. However, PHA lacks sufficient bioactive functionality to promote osteogenesis.[22,29,30] To compensate for this, both pDA and HA were introduced to the surface of PHA scaffold. It is well known that pDA not only makes the surface hydrophilic due to the –OH group, but also enhances the interfacial properties of bone implants.[31-33] Due to the presence of substantial amount of catechol group, pDA exhibits antioxidant and antibacterial properties. Moreover, it is recognized for its ability to promote initial cell adhesion and proliferation, as well as to stimulate the expression of osteogenesis-

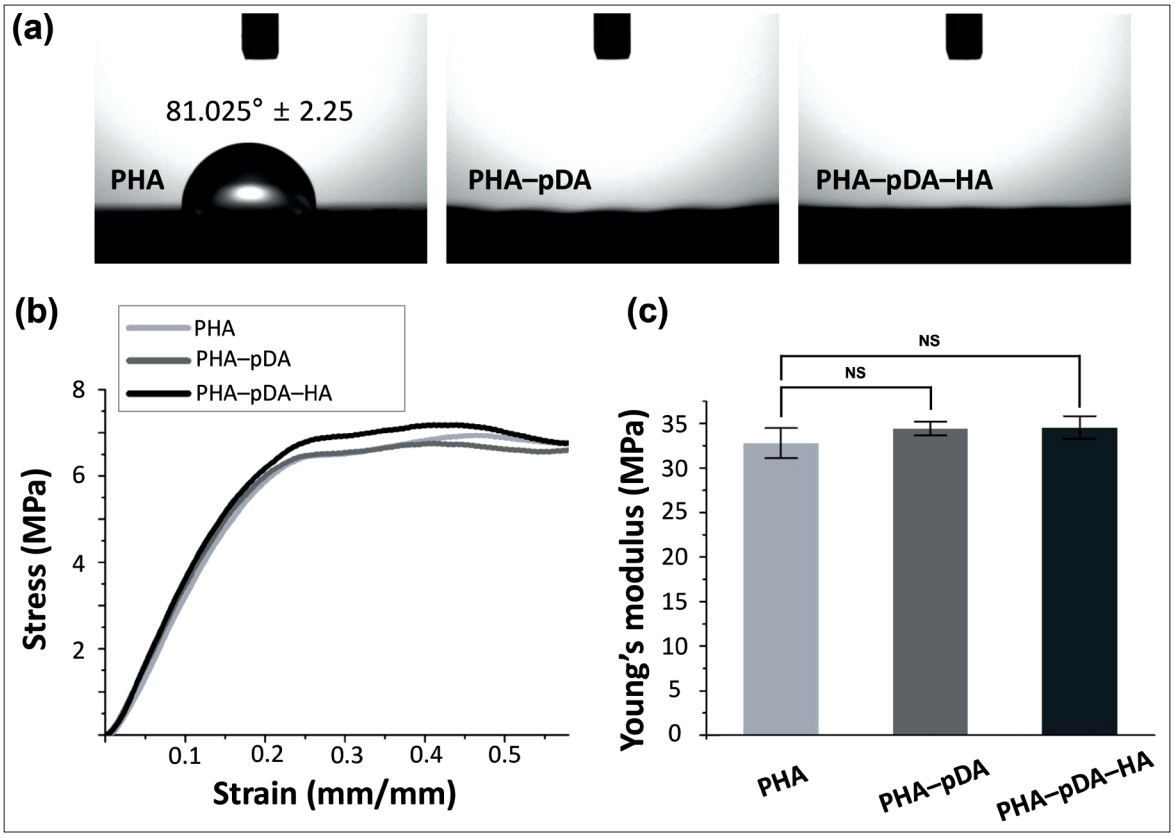

Figure 3. Physical properties of the PHA, PHA–pDA, and PHA–pDA–HA scaffolds. (a) Representative images of water contact angle. (b) Stress–strain curve of compression test. (c) Young's modulus. Abbreviations: HA, hydroxyapatite; pDA, polydopamine; PHA, polyhydroxyalkanoate.

related genes. Importantly, pDA is known to offer a versatile biomineralization, including the integration of hydroxyapatite.

In this study, biocompatibility was confirmed using MG63, which is an osteoblast-like cell (Figure 5a). The cells adhered to all groups using PHA biomaterials and proliferated well. The group functionalized with pDA and HA showed relatively higher cell adhesion compared to the PHA group. Cell viability was assessed on both days 4 and 7 (Figure 5c). It was observed that, except for the PHA group on day 4, which exhibited a viability of 86.67% ± 1.29, all other groups consistently maintained a viability exceeding 97% every day. Furthermore, PHA also exhibited cell viability exceeding 97% on day 7. The high viability indicated that the PHA and functionalized PHA scaffolds did not have a negative impact on the cells. Especially, the functionalized PHA scaffold group showed apparent enrichment, and spindle-shaped cells had attached to the scaffold surface by day 7 (Figure 5b).

Scaffolds for osteogenesis have been studied extensively in terms of their surface properties, such as hydrophilicity. Hydrophilicity can promote the adsorption of protein, which can lead to improved cell–substrate adhesion (e.g., integrin).[17,18]

The effects of PHA and the functionalized scaffold on osteoblast proliferation were confirmed by WST-1 on days 1, 4, and 7 (Figure 6a). Cell proliferation was enhanced significantly for the functionalized PHA groups. The highest proliferation rate was seen in the PHA–pDA–HA group on days 1, 4, and 7. To investigate osteogenic differentiation, the ALP activity of the osteoblasts was measured (Figure 6b). ALP is considered an initial marker of osteoblast differentiation and new bone formation. ALP activity increased in all PHA groups. In particular, significantly higher ALP activity was observed for the PHA–pDA–HA scaffold compared with the PHA and PHA–pDA scaffolds. The PHA–pDA scaffold exhibited significant differences compared to the PHA group after 10 days.

Surface modification involving pDA, which is a qualified bone biosubstitute, was employed in this study because it possesses high biocompatibility and functionality, and can be prepared easily. pDA also enhances cell proliferation and calcium deposition, leading to mineralization.[32,34] Its impact can be further increased by combining it with

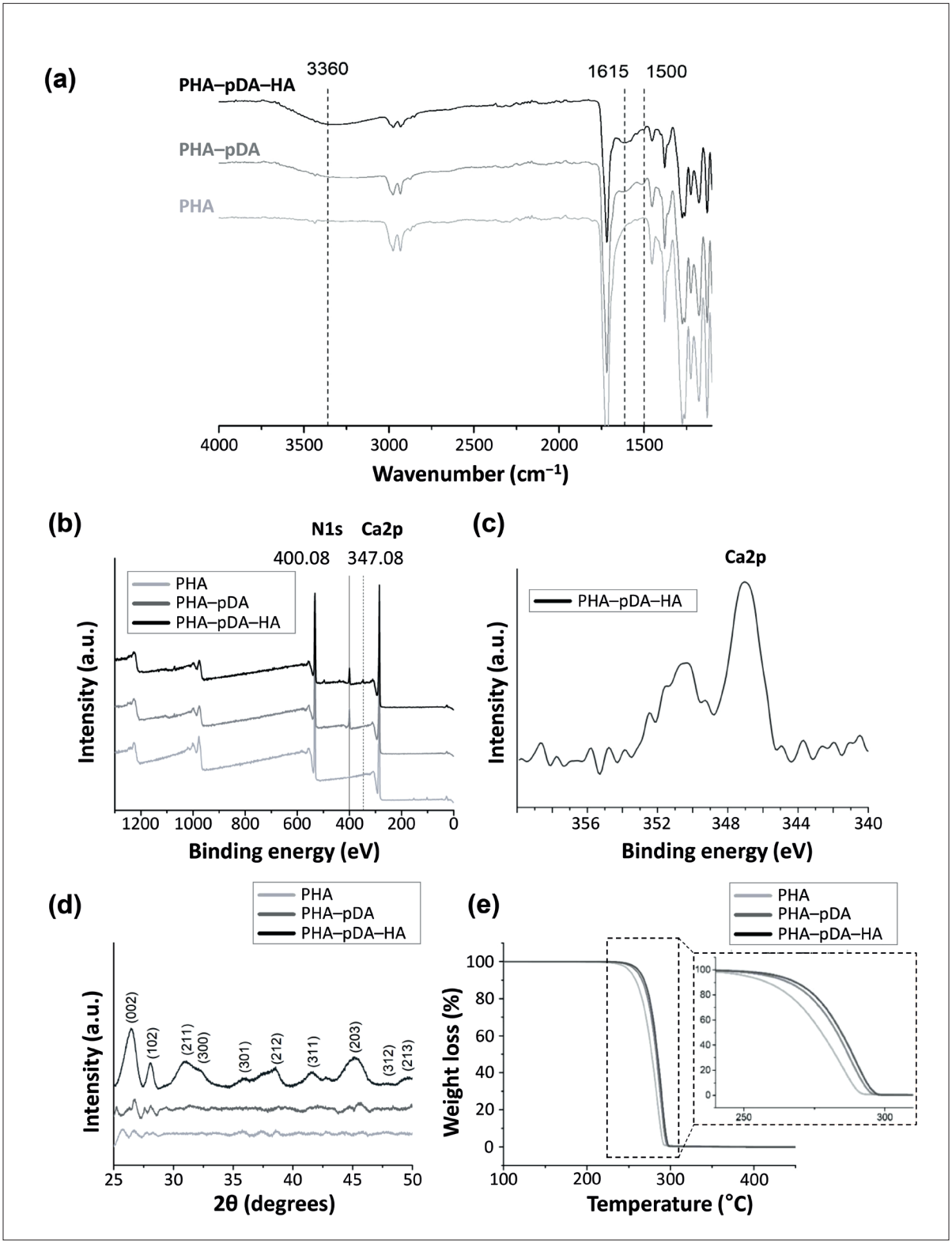

Figure 4. Physiochemical characterization of the PHA, PHA–pDA, and PHA–pDA–HA scaffolds. (a) Fourier-transform infrared spectrum showing pDA coating on the PHA surface. (b, c) X-ray photoelectron spectroscopy confirming pDA and calcium phosphate mineral formation via the N1s and Ca2p peaks (b) or Ca2p peak (c). (d) X-ray diffraction pattern of HA grown on the 3D-printed PHA surface. (e) Thermogravimetric analysis showing changes in thermal stability. Abbreviations: HA, hydroxyapatite; pDA, polydopamine; PHA, polyhydroxyalkanoate.

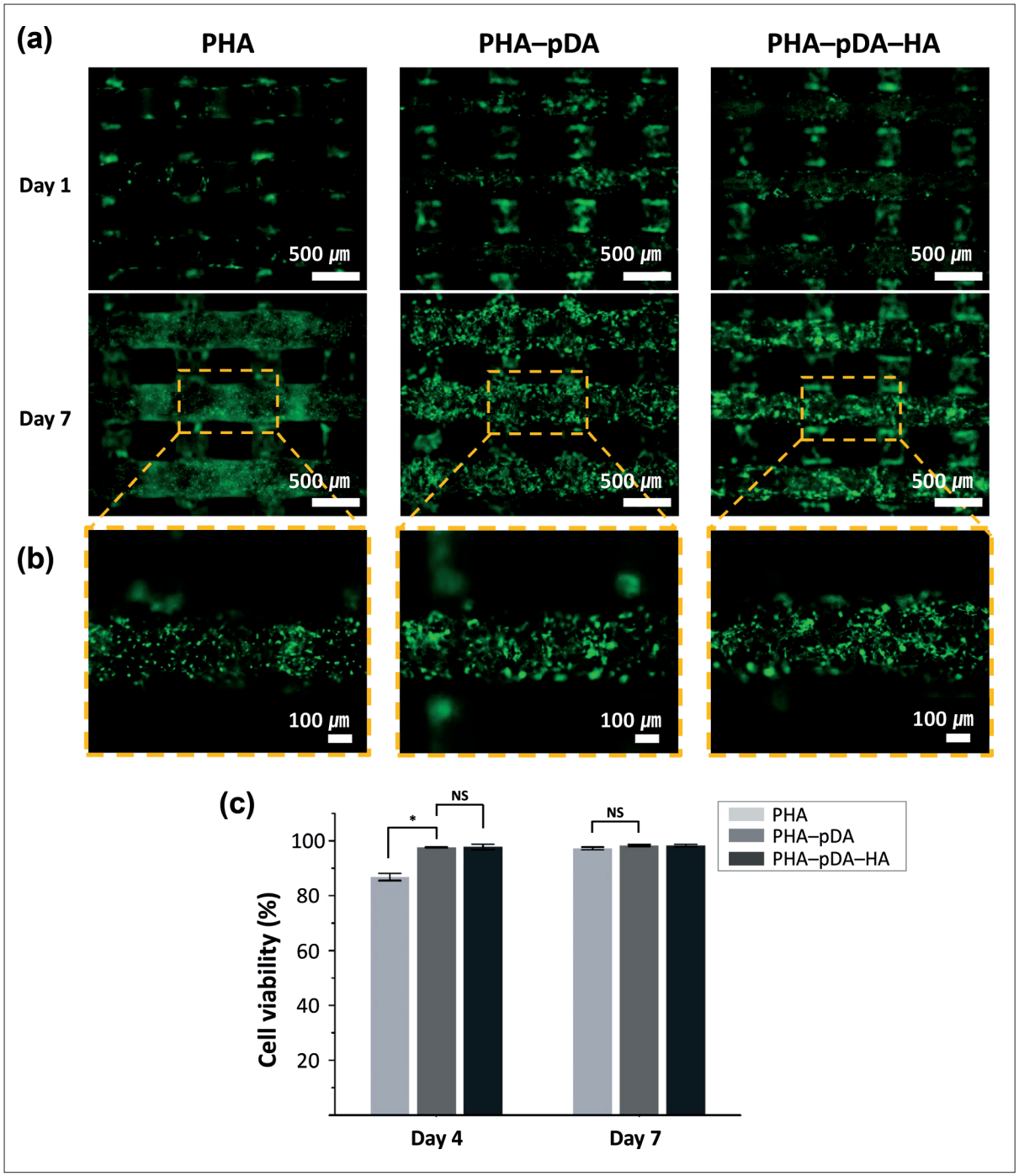

Figure 5. Viability of osteoblast-like cells on the PHA, PHA–pDA, and PHA–pDA–HA scaffolds. (a) Live and dead assays of MG63 cells on days 1, 4, and 7. (b) Representative magnified images depicting cell adhesion on the scaffold on day 7. (c) Cell viability of the polyhydroxyalkanoate (PHA) and surface-modified scaffolds on day 4 and day 7. $n = 4$; NS, no significant difference; $^{*}p < 0.05$; $^{**}p < 0.01$; $^{***}p < 0.001$. Abbreviations: HA, hydroxyapatite; pDA, polydopamine; PHA, polyhydroxyalkanoate.

growth factors.[35] Therefore, coating the PHA surface with pDA facilitates osteoconductivity by enhancing cell proliferation and differentiation. Also, biocompatible HA is generally used for bone scaffolds, as its composition is similar to the mineral phase of bone.[16,36] Thus, HA-based bone scaffolds enhance the osteogenic differentiation of osteoblast-like cells and promote bone repair both *in vitro* and *in vivo*.[33,37-39] The results of this study confirmed

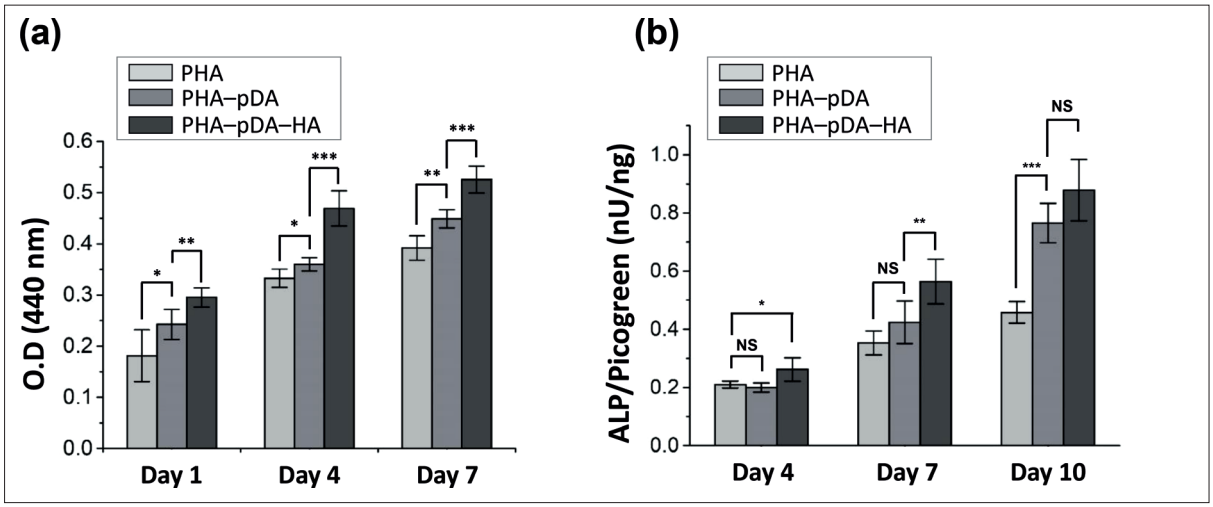

Figure 6. Proliferation and differentiation of osteoblast-like cells on the PHA, PHA–pDA, and PHA–pDA–HA scaffolds. (a) Cell proliferation on days 1, 4, and 7. (b) *Alkaline phosphatase* (ALP) activity confirming the differentiation of osteoblast-like cells. $n = 5$; NS, no significant difference; $^{*}p < 0.05$; $^{**}p < 0.01$; $^{***}p < 0.001$. Abbreviations: ALP, alkaline phosphatase; HA, hydroxyapatite; pDA, polydopamine; PHA, polyhydroxyalkanoate.

that osteoconductivity can be enhanced through simple functionalization of pDA and HA on the surface of the PHA scaffold.

4. Conclusion

PHA has gained much attention as a potential alternative to conventional plastics, because its physical and chemical properties can be adjusted by altering the types of monomers in the polymer. It is highly likely to be utilized in various biomedical applications due to its biocompatibility and biodegradability. However, the application of PHA as a bone scaffold material presents challenges due to its resistance to moisture and water insolubility, which makes cell adhesion or growth factor infiltration difficult to occur. In this study, a simple method was used to functionalize the surface of a 3D-printed PHA scaffold with pDA and HA, with the aim of utilizing it as a bone scaffold. The PHA scaffold was successfully fabricated using an extrusion-based printing approach for bone scaffolds. The 3D-printed PHA scaffold was then coated with pDA via a simple immersion process and subjected to biomineralization, during which the free-catechol group of pDA aided calcination of CaP, resulting in HA formation. The pDA coating enhanced the hydrophilicity of the scaffold, thus creating a cell-friendly environment. The pDA coating was confirmed by ATR-IR spectroscopy and XPS analyses, while the formation of HA was verified through XPS and XRD. TGA analysis indicated that the thermal stability of the functionalized PHA scaffolds was higher than that of the PHA scaffold. Osteogenic ability of the scaffolds was verified by means of the *in vitro* osteoblast-like cell culture. Compared to 3D-printed PHA scaffolds, the functionalized PHA scaffolds with pDA and HA exhibited superior cell viability, proliferation, and differentiation, and the biomineralized PHA scaffolds displayed strong osteogenic properties. Thus, the 3D-printed PHA scaffolds functionalized with pDA and HA show great promise as versatile platforms for bone tissue engineering.

Acknowledgments

None.

Funding

This research was supported by the National Research Foundation (NRF; No. NRF-2019M3A9E2066348 and NRF-2021M3H4A4079292) and the National Research Council of Science & Technology (CRC22021-200) funded by the Korean government.

Conflict of interest

The authors declare no conflicts of interest.

Author contributions

Conceptualization: Dahong Kim, Su A Park
Data curation: Su Jeong Lee, Ji Min Seok
Formal analysis: Dongjin Lee, Seon Ju Yeo
Investigation: Kangwon Lee, Won Ho Park
Methodology: Hyungjun Lim, Jae Jong Lee, Jae Hwang Song
Supervision: Su A Park
Writing – original draft: Dahong Kim
Writing – review & editing: Dahong Kim, Su A Park

Ethics approval and consent to participate

Not applicable.

Consent for publication

Not applicable.

Availability of data

All data associated with this study are present in the paper or the Supplementary File. All relevant data are available from the authors.

References

1. Lee JM, Yeong WY. Design and printing strategies in 3D bioprinting of cell-hydrogels: a review. *Adv Healthc Mater*. 2016;5(22):2856-2865. doi: 10.1002/adhm.201600435
2. Naser AZ, Deiab I, Darras BM. Poly(lactic acid) (PLA) and polyhydroxyalkanoates (PHAs), green alternatives to petroleum-based plastics: a review. *RSC Adv*. 2021;11(28):17151-17196. doi: 10.1039/d1ra02390j
3. Tomietto P, Russo F, Galiano F, et al. Sustainable fabrication and pervaporation application of bio-based membranes: combining a polyhydroxyalkanoate (PHA) as biopolymer and Cyrene™ as green solvent. *J Memb Sci*. 2022;643:120061. doi: 10.1016/j.memsci.2021.120061
4. Dwivedi R, Pandey R, Kumar S, Mehrotra D. Poly hydroxyalkanoates (PHA): role in bone scaffolds. *J Oral Biol Craniofacial Res*. 2020;10(1):389-392. doi: 10.1016/j.jobcr.2019.10.004
5. Misra SK, Ansari TI, Valappil SP, et al. Poly(3-hydroxybutyrate) multifunctional composite scaffolds for tissue engineering applications. *Biomaterials*. 2010;31(10):2806-2815. doi: 10.1016/j.biomaterials.2009.12.045
6. Guo W, Wang X, Yang C, Huang R, Wang H, Zhao Y. Microfluidic 3D printing polyhydroxyalkanoates-based bionic skin for wound healing. *Mater Futur*. 2022;1(1):015401. doi: 10.1088/2752-5724/ac446b
7. Bao G, Jiang T, Ravanbakhsh H, et al. Triggered micropore-forming bioprinting of porous viscoelastic hydrogels. *Mater Horiz*. 2020;7(9):2336-2347. doi: 10.1039/d0mh00813c
8. Gu BK, Choi DJ, Park SJ, Kim MS, Kang CM, Kim CH. 3-Dimensional bioprinting for tissue engineering applications. *Biomater Res*. 2016;20(1):1-8. doi: 10.1186/s40824-016-0058-2
9. Li W, Mille LS, Robledo JA, Uribe T, Huerta V, Zhang YS. Recent advances in formulating and processing biomaterial inks for vat polymerization-based 3D printing. *Adv Healthc Mater*. 2020;9(15):2000156. doi: 10.1002/adhm.202000156
10. Ng WL, Huang X, Shkolnikov V, Suntornnond R, Yeong WY. Polyvinylpyrrolidone-based bioink: influence of bioink properties on printing performance and cell proliferation during inkjet-based bioprinting. *Bio-Design Manuf*. 2023;6:676-690. doi: 10.1007/s42242-023-00245-3
11. Fu Z, Naghieh S, Xu C, Wang C, Sun W, Chen X. Printability in extrusion bioprinting. *Biofabrication*. 2021;13(3). doi: 10.1088/1758-5090/abe7ab
12. Mehrpouya M, Vahabi H, Barletta M, Laheurte P, Langlois V. Additive manufacturing of polyhydroxyalkanoates (PHAs) biopolymers: materials, printing techniques, and applications. *Mater Sci Eng C*. 2021;127:112216. doi: 10.1016/j.msec.2021.112216
13. Tarrahi R, Fathi Z, Seydibeyoğlu MÖ, Doustkhah E, Khataee A. Polyhydroxyalkanoates (PHA): from production to nanoarchitecture. *Int J Biol Macromol*. 2020;146:596-619. doi: 10.1016/j.ijbiomac.2019.12.181
14. Ryu J, Ku SH, Lee H, Park CB. Mussel-inspired polydopamine coating as a universal route to hydroxyapatite crystallization. *Adv Funct Mater*. 2010;20(13):2132-2139. doi: 10.1002/adfm.200902347
15. Wang N, Yu X, Kong Q, et al. Nisin-loaded polydopamine/hydroxyapatite composites: biomimetic synthesis, and in vitro bioactivity and antibacterial activity evaluations. *Colloids Surf A Physicochem Eng Asp*. 2020;602:125101. doi: 10.1016/j.colsurfa.2020.125101
16. Liu Z, Qu S, Zheng X, et al. Effect of polydopamine on the biomimetic mineralization of mussel-inspired calcium phosphate cement in vitro. *Mater Sci Eng C*. 2014;44:44-51. doi: 10.1016/j.msec.2014.07.063
17. Tseng SJ, Cheng CH, Lee TM, Lin JC. Studies of osteoblast-like MG-63 cellular proliferation and differentiation with cyclic stretching cell culture system on biomimetic hydrophilic layers modified polydimethylsiloxane substrate. *Biochem Eng J*. 2021;168:107946. doi: 10.1016/j.bej.2021.107946
18. Zhang Y, Andrukhov O, Berner S, et al. Osteogenic properties of hydrophilic and hydrophobic titanium surfaces evaluated with osteoblast-like cells (MG63) in coculture with human umbilical vein endothelial cells (HUVEC). *Dent Mater*. 2010;26(11):1043-1051. doi: 10.1016/j.dental.2010.07.003
19. Owji N, Mandakhbayar N, Gregory DA, et al. Mussel inspired chemistry and bacteria derived polymers for oral mucosal adhesion and drug delivery. *Front Bioeng Biotechnol*. 2021;9:1-13. doi: 10.3389/fbioe.2021.663764
20. Luo H, Gu C, Zheng W, Dai F, Wang X, Zheng Z. Facile synthesis of novel size-controlled antibacterial hybrid

spheres using silver nanoparticles loaded with polydopamine spheres. *RSC Adv*. 2015;5(18):13470-13477. doi: 10.1039/c4ra16469e

21. Kim H, Lee K, Ko CY, et al. The role of nacreous factors in preventing osteoporotic bone loss through both osteoblast activation and osteoclast inactivation. *Biomaterials*. 2012;33(30):7489-7496. doi: 10.1016/j.biomaterials.2012.06.098
22. Zhang X, Li J, Chen J, et al. Enhanced bone regeneration via PHA scaffolds coated with polydopamine-captured BMP2. *J Mater Chem B*. 2022;10(32):6214-6227. doi: 10.1039/d2tb01122k
23. Auclair-Daigle C, Bureau MN, Legoux JG, Yahia L. Bioactive hydroxyapatite coatings on polymer composites for orthopedic implants. *J Biomed Mater Res A*. 2005;73(4):398-408. doi: 10.1002/jbm.a.30284
24. Múzquiz-Ramos EM, Cortés-Hernández DA, Escobedo-Bocardo J. Biomimetic apatite coating on magnetite particles. *Mater Lett*. 2010;64(9):1117-1119. doi: 10.1016/j.matlet.2010.02.025
25. Park JH, Lee DY, Oh KT, Lee YK, Kim KM, Kim KN. Bioactivity of calcium phosphate coatings prepared by electrodeposition in a modified simulated body fluid. *Mater Lett*. 2006;60(21-22):2573-2577. doi: 10.1016/j.matlet.2005.07.091
26. Guo W, Yang K, Qin X, Luo R, Wang H, Huang R. Polyhydroxyalkanoates in tissue repair and regeneration. *Eng Regen*. 2022;3(1):24-40. doi: 10.1016/j.engreg.2022.01.003
27. Garot C, Bettega G, Picart C. Additive manufacturing of material scaffolds for bone regeneration: toward application in the clinics. *Adv Funct Mater*. 2021;31(5):2006967. doi: 10.1002/adfm.202006967
28. Lichte P, Pape HC, Pufe T, Kobbe P, Fischer H. Scaffolds for bone healing: concepts, materials and evidence. *Injury*. 2011;42(6):569-573. doi: 10.1016/j.injury.2011.03.033
29. Dhania S, Bernela M, Rani R, et al. Scaffolds the backbone of tissue engineering: advancements in use of polyhydroxyalkanoates (PHA). *Int J Biol Macromol*. 2022;208:243-259. doi: 10.1016/j.ijbiomac.2022.03.030
30. Elmowafy E, Abdal-Hay A, Skouras A, Tiboni M, Casettari L, Guarino V. Polyhydroxyalkanoate (PHA): applications in drug delivery and tissue engineering. *Exp Rev Med Dev*. 2019;16(6):467-482. doi: 10.1080/17434440.2019.1615439
31. Li L, Li Y, Yang L, et al. Polydopamine coating promotes early osteogenesis in 3D printing porous Ti6Al4V scaffolds. *Ann Transl Med*. 2019;7(11):240-240. doi: 10.21037/atm.2019.04.79
32. Kao CT, Lin CC, Chen YW, Yeh CH, Fang HY, Shie MY. Poly(dopamine) coating of 3D printed poly(lactic acid) scaffolds for bone tissue engineering. *Mater Sci Eng C*. 2015;56:165-173. doi: 10.1016/j.msec.2015.06.028
33. Jo S, Kang SM, Park SA, Kim WD, Kwak J, Lee H. Enhanced adhesion of preosteoblasts inside 3D PCL scaffolds by polydopamine coating and mineralization. *Macromol Biosci*. 2013;13(10):1389-1395. doi: 10.1002/mabi.201300203
34. Im S, Choe G, Seok JM, et al. An osteogenic bioink composed of alginate, cellulose nanofibrils, and polydopamine nanoparticles for 3D bioprinting and bone tissue engineering. *Int J Biol Macromol*. 2022;205:520-529. doi: 10.1016/j.ijbiomac.2022.02.012
35. Park J, Lee SJ, Jung TG, et al. Surface modification of a three-dimensional polycaprolactone scaffold by polydopamine, biomineralization, and BMP-2 immobilization for potential bone tissue applications. *Colloids Surf B Biointerfaces*. 2021;199:111528. doi: 10.1016/j.colsurfb.2020.111528
36. Loty C, Sautier JM, Boulekbache H, Kokubo T, Kim HM, Forest N. In vitro bone formation on a bone-like apatite layer prepared by a biomimetic process on a bioactive glass-ceramic. *J Biomed Mater Res*. 2000;49(4):423-434. doi: 10.1002/(sici)1097-4636(20000315)49:4<423::aid-jbm1>3.0.co;2-7
37. Konka J, Buxadera-Palomero J, Espanol M, Ginebra MP. 3D printing of hierarchical porous biomimetic hydroxyapatite scaffolds: adding concavities to the convex filaments. *Acta Biomater*. 2021;134:744-759. doi: 10.1016/j.actbio.2021.07.071
38. Avanzi IR, Parisi JR, Souza A, et al. 3D-printed hydroxyapatite scaffolds for bone tissue engineering: a systematic review in experimental animal studies. *J Biomed Mater Res B Appl Biomater*. 2023;111(1):203-219. doi: 10.1002/jbm.b.35134
39. Barba A, Maazouz Y, Diez-Escudero A, et al. Osteogenesis by foamed and 3D-printed nanostructured calcium phosphate scaffolds: effect of pore architecture. *Acta Biomater*. 2018;79:135-147. doi: 10.1016/j.actbio.2018.09.003

ACCSCIENCE PUBLISHING

International Journal of Bioprinting

RESEARCH ARTICLE

Oozing: An accessible technique to create 3D-printed scaffolds suitable for tissue engineering

Juan Crespo-Santiago[1,2*], Luis M. Delgado[3], Rafa Madariaga[4], Laia Millan[1], Oriol Chico[1], Pau Oliver[1], Román Pérez[3], and Marta Otero-Viñas[2,5*]

[1]Elisava Barcelona School of Design and Engineering, University of Vic-Central University of Catalonia (UVIC-UCC), La Rambla 30, 08002, Barcelona, Spain

[2]Tissue Repair and Regeneration Laboratory (TR2Lab), Institute for Research and Innovation in Life and Health Sciences in Central Catalonia (IrisCC), Ctra. de Roda, 70 08500, Vic, Barcelona, Spain

[3]Bioengineering Institute of Technology, International University of Catalonia (UIC), Immaculada 22, 08017, Barcelona, Spain

[4]Data Analysis and Modeling Research Group (DAM), Department of Economics and Business, University of Vic-Central University of Catalonia (UVIC-UCC), Sagrada Família 7, 08500, Vic, Spain

[5]Faculty of Science, Technology, and Engineering. University of Vic – Central University of Catalonia (UVIC-UCC), C. de la Laura, 13, 08500, Vic, Barcelona, Spain

Abstract

Tissue-engineered constructs require mimicking the extracellular matrix microenvironment of native tissue for better promoting cell growth. Commercial three-dimensional (3D) printers provide a versatile platform to fabricate tissue models, but they possess certain constraints regarding the reproduction of natural tissue structures due to the limited functionality of current slicing strategies and hardware. In this study, we present a new approach to 3D-printing polylactic acid (PLA) constructs with fibers in the range of microns by combining the oozing effect and algorithm-aided design (AAD) with a conventional fused deposition modeling printer. Three different oozing geometries were compared with two controls to explore their mechanical behavior and their cellular culture growth potential. Microscopic analysis revealed that oozing groups possessed higher porosity and statistically significantly thinner fibers than controls. Sodium hydroxide treatment reversibly increased the hydrophilicity of PLA without affecting the scaffolds' mechanical properties in the compression tests. In addition, cell culture assays showed that oozing specimens exhibited a greater capacity of promoting SaOs-2 osteoblastic cell proliferation after 7 days in comparison with controls. We demonstrated that randomly distributed microfibered environments can be fabricated with an ordinary 3D printer utilizing the oozing effect and advanced AAD, resulting in improved biomimetic 3D constructs for tissue-engineering strategies.

Keywords: Oozing; 3D printing; Tissue engineering; Cell cultures; Polylactic acid

***Corresponding authors:**
Juan Crespo-Santiago
(jcrespo@elisava.net)

Marta Otero-Viñas
(marta.otero@uvic.cat)

Citation: Crespo-Santiago J, Delgado LM, Madariaga R, et al. Oozing: an accessible technique to create 3D-printed scaffolds suitable for tissue engineering. *Int J Bioprint*. 2024;10(2):2337.
doi: 10.36922/ijb.2337

Received: November 29, 2023
Accepted: January 22, 2024
Published Online: March 12, 2024

1. Introduction

The demand for new tissues in regenerative medicine therapies has led to an increase in new tissue-engineering strategies to fabricate synthetic constructs for damaged

tissue replacement.[1,2] Tissue-engineered constructs or scaffolds require mimicking the microenvironment of the biological extracellular matrix (ECM) niche, composed of a microfibered complex that contributes to the mechanical support of the tissue.[3,4] The morphology and microstructure of scaffolds must satisfy specific mechanical and biological requirements including structure material organization, surface morphology, and proper porosity (pore size, distribution, and interconnectivity) to promote cell adhesion and proliferation, and subsequent ECM remodeling.[5,6]

Additive manufacturing technologies (three-dimensional [3D] printing) have become a promising approach to personalized regenerative treatments. These techniques are characterized by their design potential, high speed, and low cost, which allow the fabrication of tissue constructs from the micro- to the macro-scale, providing suitable structural and mechanical support for 3D cell cultures, thereby producing new, enhanced tissue.[7-12] Numerous types of constructs have been developed for several tissues using 3D printing for regenerative medicine: composites and polymers for bone tissue engineering,[13,14] cartilage for the meniscus,[15] or polylactic acid for vascular grafts,[16] among others.[17]

There are several sorts of additive manufacturing technologies that generate scaffolds for biomedical applications. Traditional modalities, such as fused deposition modeling (FDM), selective laser sintering (SLS), or stereolithography (SLA), among others,[18] allow the creation of components with micro-scaled geometries in various materials, such as polymers, composites, and metals with high accuracy and reproducibility.[19,20] Despite these advantages, many of these printing conditions are lethal to cells, such as high temperature or toxic chemicals. Hence, these techniques commonly generate acellular scaffolds that can be utilized for tissue-engineering purposes by seeding cells after fabrication.[21]

In contrast, recent techniques such as 3D bioprinting, in which a suspension of living cells together with suitable biomaterials and growing factors (bioink) is directly deposited to create 3D living tissue,[22] create interesting soft-tissue constructs, such as composites for ear regeneration,[23] or collagen for the human heart, in addition to many others.[24-26] 3D bioprinting can be classified according to American Society for Testing and Materials (ASTM) into: extrusion-based,[27] jetting-based,[28] and vat photopolymerization-based.[29] Although these techniques have a variety of applications, including trauma treatment, whole tissue creation, and *in vitro* drug testing, several drawbacks including bioink's dimensional stability, limited speed, or cell viability during printing process remain unsolved; therefore, soft materials like hydrogels are generally utilized for fabrication.[21,27,30]

FDM is one of the most widely utilized 3D printing technologies due to its versatility, simple maintenance, and low cost.[31,32] In comparison to others, this technique possesses many advantages, including availability of a wide range of biodegradable and biocompatible materials that can be printed, and compatibility with different CAD software. FDM has a simple working principle: A preformed polymeric thermoplastic filament is heated to a semiliquid state and then extruded through a nozzle directly onto the building platform following a programmed model, with thin layers being deposited on top of one another.[33-35] Moreover, no toxic solvents are needed to dissolve the polymeric filaments for printing, thus avoiding cell mortality when working with cell cultures.[36,37] Nevertheless, FDM has certain major constraints such as limited accuracy due to the thickness of the final extruded filament, the relationship between viscosity and nozzle diameter, or the high temperature applied during the melt-extrusion process that may change inherent material properties.[38]

Limited resolution is, particularly, one of the main disadvantages in FDM as the accurate impression is limited by the nozzle diameter.[39,40] Commonly, these nozzle diameters range from 0.8 mm to 0.2 mm, being unusual to find smaller diameters due to their easy clogging tendency and subsequent incapacity to ensure proper flow settings.[41,42] Furthermore, another well-known drawback of FDM printing occurs when the nozzle deposits a small amount of molten material and immediately moves to the next position. This movement creates the "stringing" effect or oozing: a very thin "hair" of molten material that extends across the direction of travel of the nozzle.[43,44] The oozing effect can be caused by a slow retraction speed, overheating in the extruder, high printing speed, or very long movements over open spaces, among others.[45-47]

The achievement of a microfiber-like environment represents a major feature to better mimic the tissue ECM niche. Several techniques such as electro direct writing,[48] electrospinning,[49,50] or melt-blowing[51] can create micro-scaled fibers, but FDM lacks the capacity to generate the thin required fibers due to the technique's own limitations. However, recent studies have successfully fabricated various arrays of microfibers leveraging the oozing effect, by the manipulation and implementation of certain parameters of the printing process, such as the printing speed or the feed rate, and combined them with algorithm-aided design (AAD).[44,52] Generally, these approaches can be found as a stack of parallel-like patterns with fibers in the range of hundreds of microns,[42] or as a combination of parallel-like

structures with layers of randomly distributed microfibers created by another technique (such as melt-spinning or electrospinning).[53,54] Although the fundamentals of this methodology have been similarly reported elsewhere,[44,52] AAD-controlled random distributions remain unexplored. These advances point to the direction of overcoming one of the fundamental architectural flaws of FDM, which is the macroscopic geometry of the fibers and subsequent macro-porosity of the scaffolds.

Several thermoplastic materials used in FDM printing include polylactic acid (PLA), acrylonitrile butadiene styrene (ABS), polycaprolactone (PCL), polyether ether ketone (PEEK), and nylon,[20,55] or other natural biopolymers.[56] PLA is a promising biopolymer in biomedical applications due to its properties such as biocompatibility, biodegradability, mechanical strength, process ability, and non-toxicity.[57] PLA scaffolds have been extensively utilized in bone tissue,[58] cartilage,[59] meniscus,[60] vascular tissue,[61] and other biomedical applications.[62] However, PLA has certain limitations concerning its use, such as a slow degradation rate and hydrophobicity, which affect cell adhesion to scaffold, rendering new tissue formation difficult.[61]

In this study, we developed algorithm-designed 3D constructs utilizing the oozing effect, employing both parallel and random distributions of the fibers (ranging from 30 μm up to a few hundred). In addition, we compared these constructs with ordinary FDM-printed scaffolds to analyze their cell growth potential. A selection of three different oozing-like geometries and two commonly manufactured controls were 3D-printed and fully characterized to better understand their architectural and mechanical properties together with their biological potential. The algorithm-controlled 3D random distribution of the microfibers in the oozing specimens in cell cultures represents a novel approach to developing a better biomimetic scaffold to be used in tissue-engineering repairing strategies.

2. Materials and methods

The research methodology employed to evaluate the scaffolds design and microstructure was based in 3 stages shown in Figure 1 and described in detail below in this section. A total of five experimental groups with five different infill geometries were selected for the study: Three groups were printed with oozing technique, and two controls were printed following standard procedure.

2.1. Design of the experimental infills

The three oozing specimens were designed following three different sequences: two of them with a parallel-fiber pattern, differentiated by a low-density knitting and a high-density knitting, respectively, and the third one with a random fiber pattern. In addition, two controls were designed with standard architectures: a waffle-like geometry and a gyroid (Figure 2). The five experimental groups, namely random oozing (Or), simple oozing (Os), complex oozing (Oc), gyroid (Gy), and waffle (Gof), were all designed cubic-shaped with an outer volume of 10 × 10 × 10 mm. All oozing groups, Os, Or, and Oc, were developed using the Silkworm (v0.0.1) plugin for Grasshopper3d

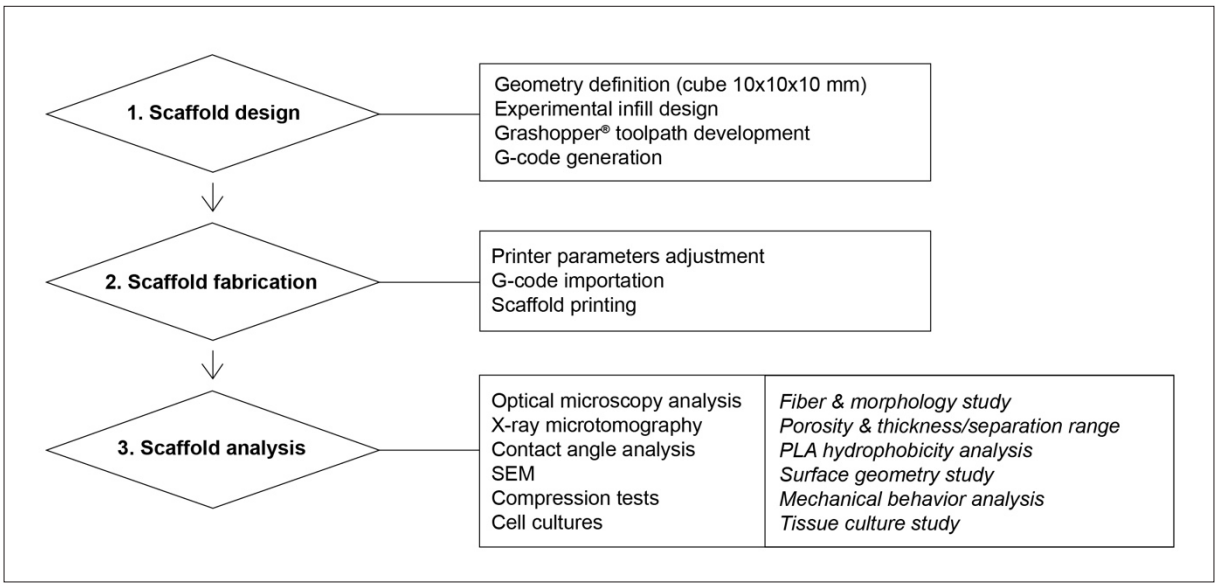

Figure 1. Stages of experimental methodology. Abbreviations: PLA, polylactic acid; SEM, scanning electron microscopy.

(Rhinoceros). Control group (Gof) was designed with CAD software, and Gy group was designed with Ultimaker Cura (v4.8.0, Ultimaker) slicer. All specimens were prepared for 3D printing with Ultimaker Cura (v4.8.0, Ultimaker) (**Figure S1** in Supplementary File).

The oozing print methodology was based on depositing a small drop of extruded material on a certain coordinate, then moving the nozzle to the next coordinate without extruding any material between both points. This method allows the generation of oozing fiber. The Or specimen was designed by distributing a random population of 60 points in each of the 4 lateral façades of a 10 × 10 × 10 mm cube, with a total of 240 points (Figure 2A1 and A2). The resulting lattice was created by assigning several random displacements of the nozzle on an *X*–*Y* plane, and then iterating different patterns at every layer of the *Z* axis. These displacements were generated and developed in Silkworm plugin by designing different tool paths (Figure 2C and D). The Os specimen was designed by creating a grid of 8 × 8 square spaces on a 10 × 10 mm *X*–*Y* plane (Figure 2B1 and B2). The *X*–*Y* planes were stacked along the *Z* axis, and each layer was rotated 90° from the previous one enabling the creation of the whole volume. The specimen was printed using the identical oozing methodology as with the Or specimen. Figure 2D shows the Grasshopper tool paths used for this specimen. The Oc specimen was designed following the same procedure as with the Os specimen by creating a grid of 12 × 12 square spaces on a 10 × 10 mm *X*–*Y* plane. Two commonly used infill patterns were selected as

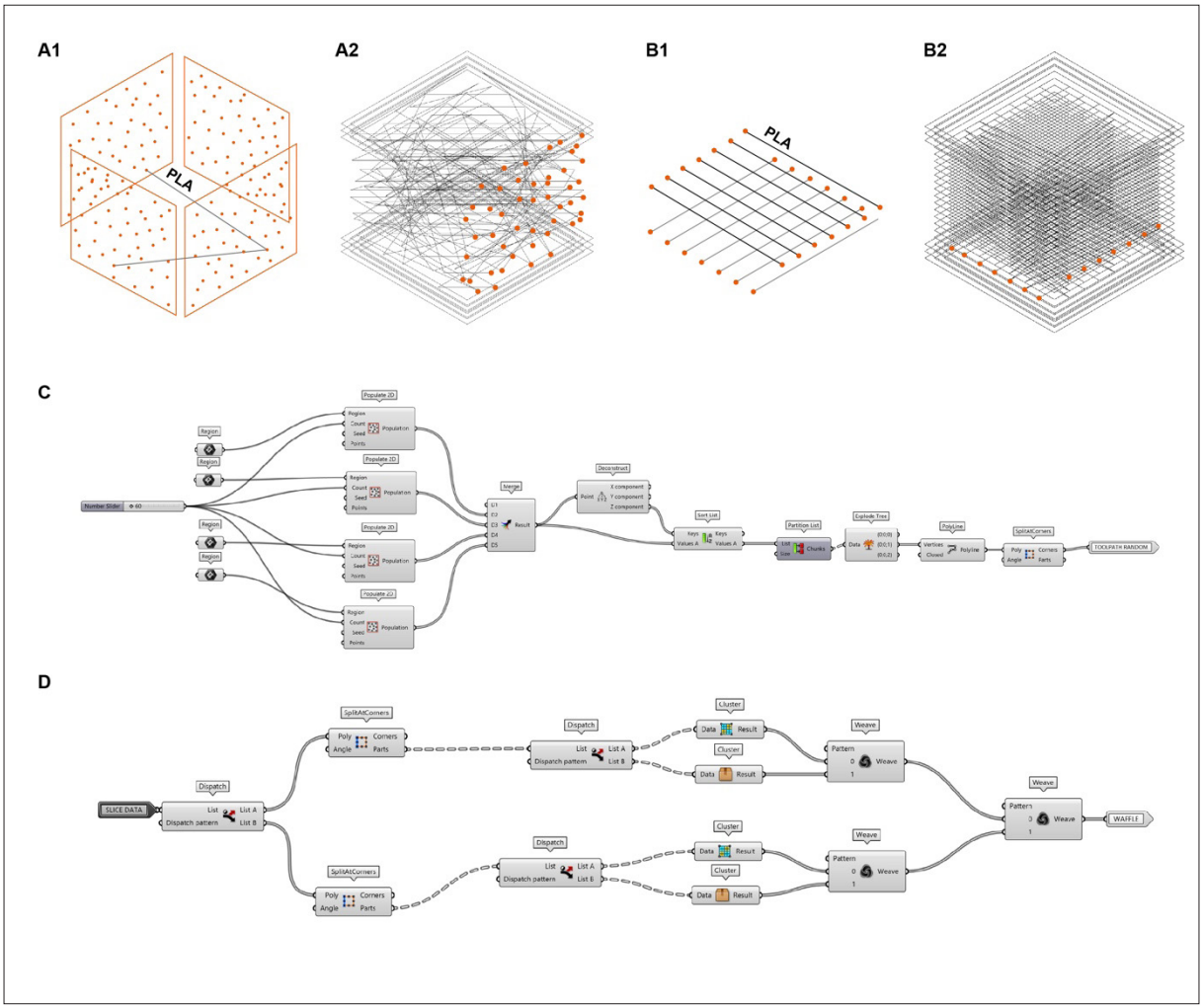

Figure 2. Schemes and toolpaths for scaffold design. Orange dots represent the nozzle stop, and black lines show the deposited material in form of oozing fibers. (A1) Planes showing the random distribution of 60 points created for Or specimen. (A2) Schematic of nozzle displacement path for Or specimen. (B1) Parallel pathways and planes created for Os specimen. (B2) Schematic of nozzle displacement path for Os specimen. (C) Grasshopper toolpath for Or specimen. (D) Grasshopper toolpath for Os specimen.

control groups: a gyroid geometry (Gy) and waffle-like geometry (Gof). The Gy specimen was generated using the gyroid infill form in Ultimaker Cura software creating four iterations in a 10 × 10 × 10 mm cube. The Gof sample was designed in SolidWorks (Dassault Systemes) as a 10 × 10 × 10 mm cube with an internal matrix of 5 × 5 equidistant holes of 1 × 1 mm.

2.2 Three-dimensional printing of scaffolds

All scaffolds were 3D-printed using an Ender-5 Pro printer (Creality 3D) equipped with a 0.4 mm nozzle and using 1.75 mm diameter PLA filament (Smartfil, Smartmaterials 3D), 210°C extrusion temperature, 60°C bed temperature, and 0.2 mm layer height. The printing speed was 80 mm/s for the control groups, with a feed rate of 1200 and constant flow rate. For the oozing groups, the printing speed was 59 mm/s, whereas the feed rate and the flow rate were set by Silkworm plugin (see Figure S2 for G-codes). For controls (Gy and Gof), G-codes were generated with Ultimaker Cura, with the .STL files imported beforehand. For experimental groups (Or, Os, and Oc), the G-codes were directly obtained and exported from Silkworm plugin (Grasshopper3d). After printing, all specimens were characterized, with the volume (x, y, and z) measured using a vernier caliper and the weight determined on a digital scale (Figure 3).

2.3. Porosity determination by X-ray microtomography

Porosity was measured using a Skyscan 1272 micro-CT (Bruker) at a 10 mm resolution. The X-ray source peak voltage was 50 kV with an intensity of 200 μA, 180° scanning, and a 0.2° step. The porosity was obtained using the CTAn software provided by Bruker. Ranges of thickness and separation distributions were also analyzed within this study (Figures 4 and 5).

2.4. Fiber thickness analysis

Fiber thickness was measured using a stereomicroscope (StereoBlue SB 1903, Euromex) with a digital camera (CMEX DC5000f, Euromex). Measurements were performed using the software ImageFocus Plus V2 (Euromex). For each experimental group, three samples were fabricated at five different heights (2 mm, 4 mm, 6 mm, 8 mm, and 10 mm) by directly stopping the 3D printer when the height of the sample reached the desired value. A total of three fibers were randomly selected at these five different heights per specimen. The thickness was measured at five points along each fiber: start (at the very beginning of the fiber), mid1 (an equidistant point from the middle and the start), center (at the middle point of the fiber), mid2 (an equidistant point from the middle and the end), and end (a point very close to the end of the fiber). However, regarding Gy and

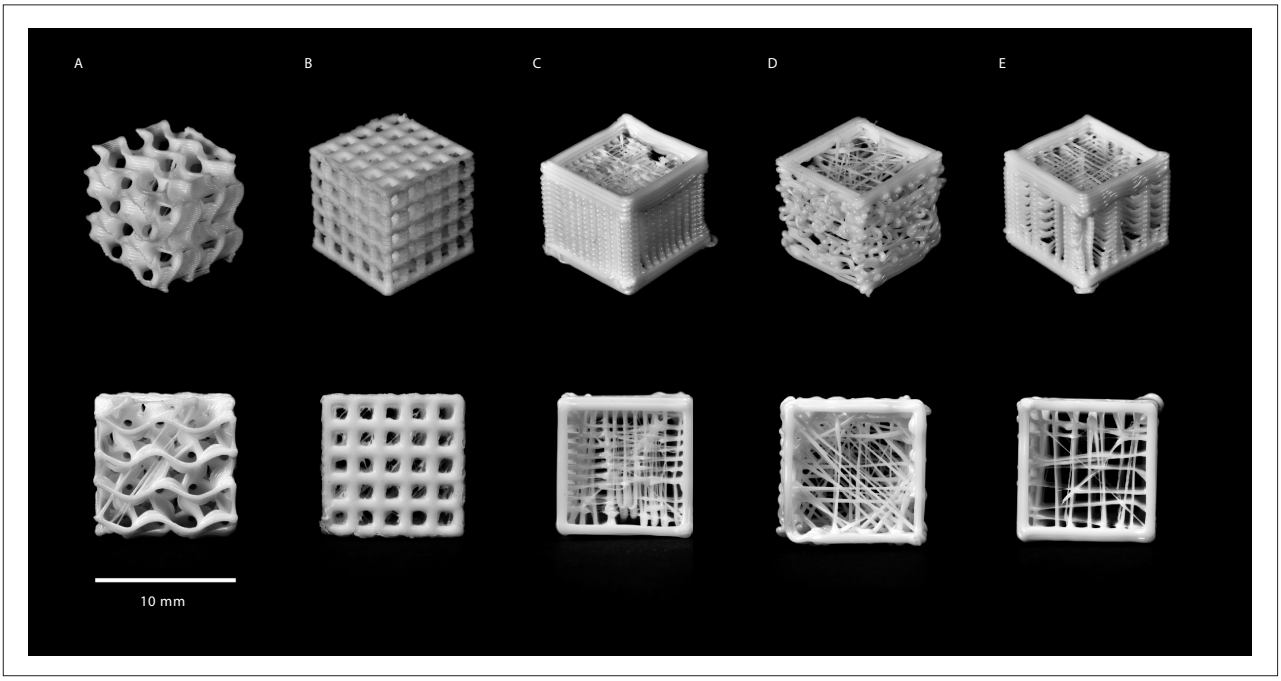

Figure 3. 3D-printed PLA experimental groups with different knitting patterns. (A) Gy: gyroid architecture; (B) Gof: waffle-like architecture; (C) Oc: oozing with parallel dense knitting; (D) Or: oozing with random knitting; and (E) Os: oozing with parallel low-dense knitting. Images in the top row present perspective view of the specimens, and the bottom row shows top-view images of the specimens.

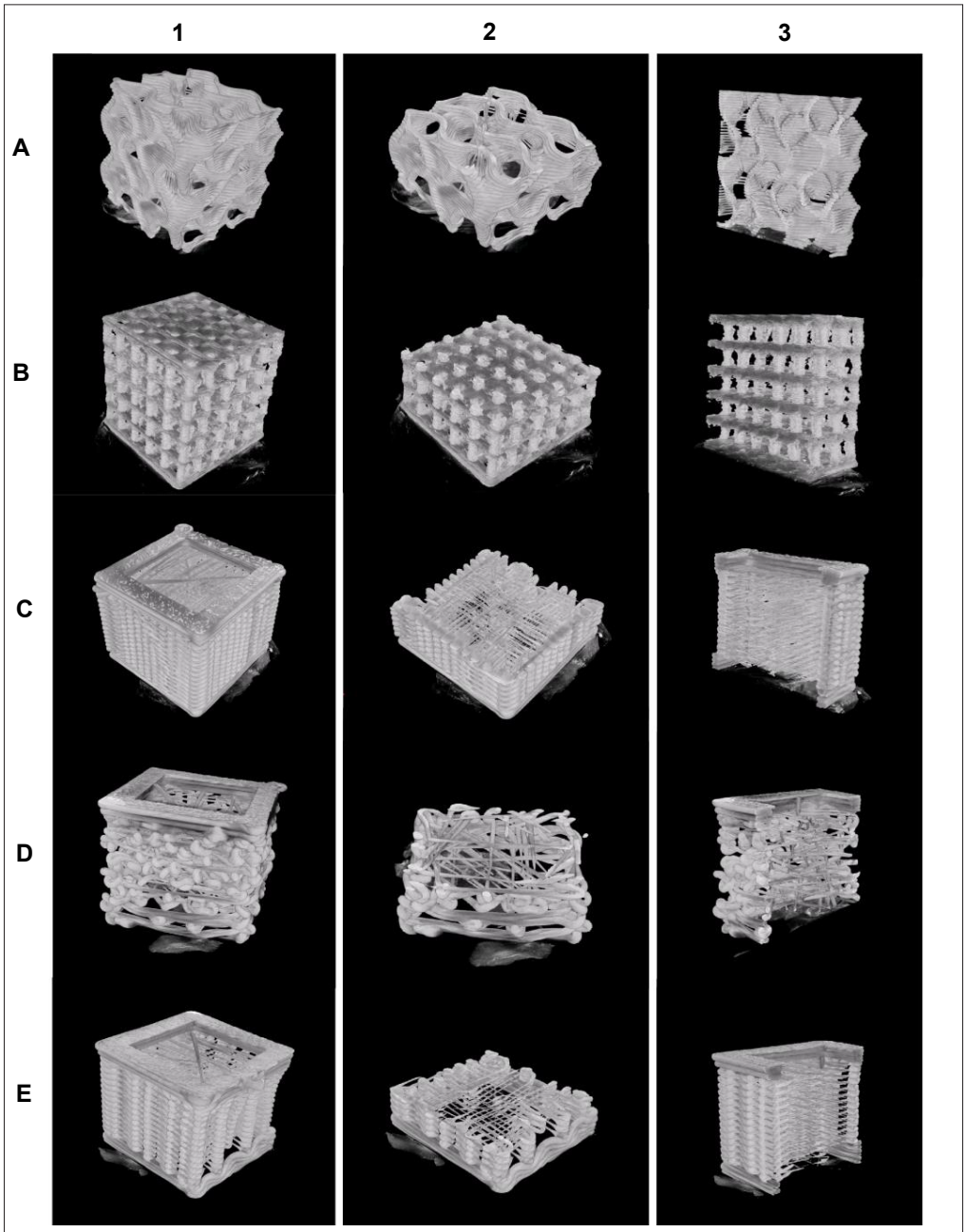

Specimen	Volume (mm^3)	SD	Mass (g)	SD	Porosity (%)
Or	1213	11.97	0.319	0.011	83.66
Oc	1188	27.09	0.413	0.010	77.78
Os	1200	25.47	0.327	0.003	86.58
Gy	1071	20.69	0.329	0.007	76.04
Gof	1227	22.38	0.486	0.017	67.83

Figure 4. X-ray microtomography reconstructions of the five specimens. (A) Gy, (B) Gof, (C) Oc, (D) Or, and (E) Os. Column 1 shows perspective views of the specimens, column 2 shows the top views, and column 3 shows the lateral views of the specimens. (F) Physical characteristics (volumes, masses, and total porosity) of the specimens (n = 10).

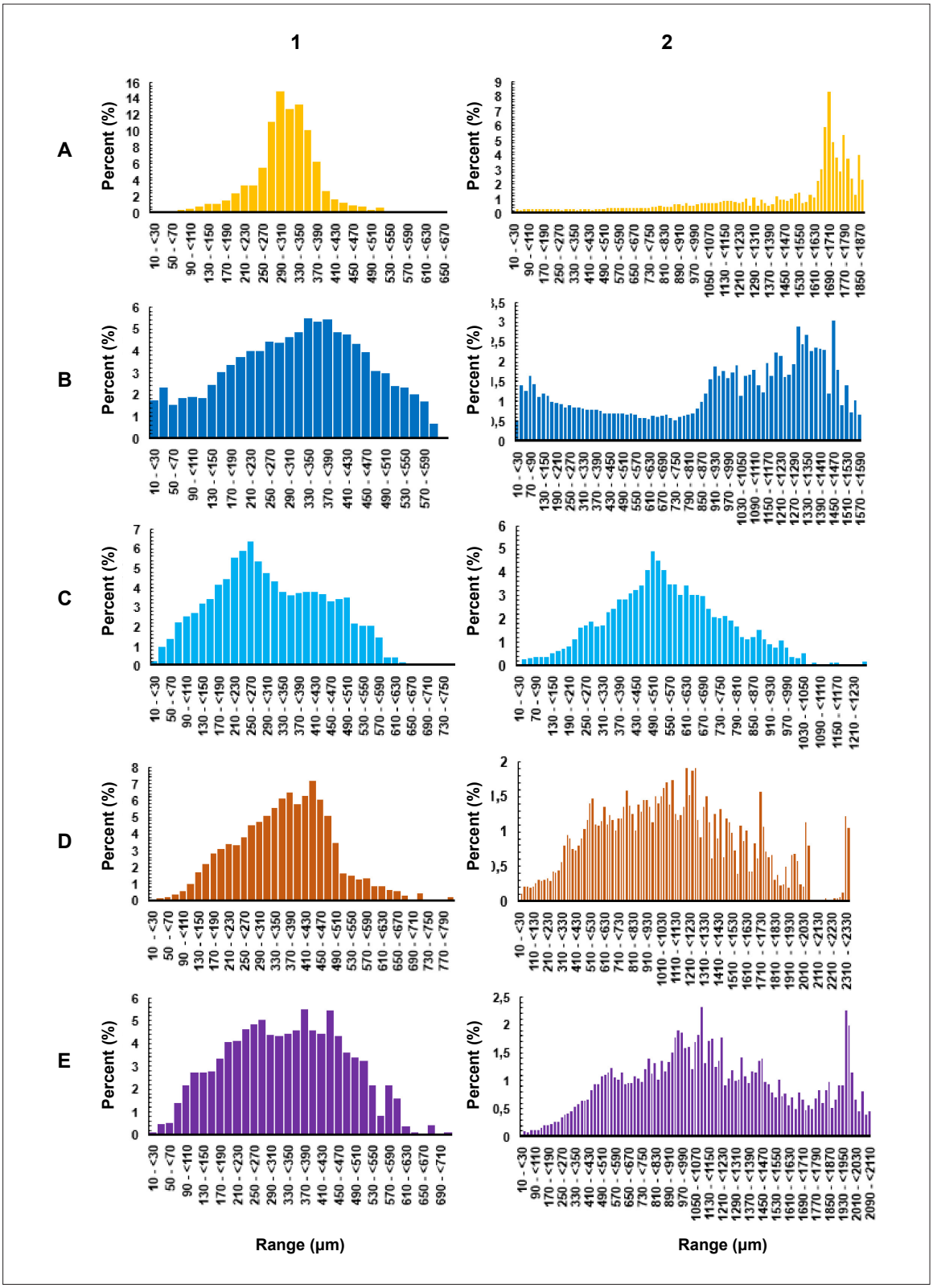

Figure 5. Range distributions for (A) Gy, (B) Gof, (C) Oc, (D) Or, and (E) Os. Column 1 shows thickness distribution, and column 2 shows fiber separation distribution.

Gof, geometries we measured the grid thickness instead of shred thickness, as they do not possess proper fibers as the oozing groups (Figure 6).

2.5. Effect of sodium hydroxide treatment

Scaffolds were submerged in a sodium hydroxide solution (NaOH, 2 M solution, Sigma-Aldrich) for 15 min at room temperature. Then, the samples were washed for 5 min in distilled water three times.

2.6. Scaffold surface analysis

The specimens were coated with a gold layer using an agar sputter coater (AGB 7340, AgarScientific) and analyzed with a scanning electron microscope (SEM, JSM 5410, JEOL) operated at 10 kV. A total of four regions per scaffold were studied (Figure 7).

2.7. Contact angle assays

Water contact angle was assessed using PLA discs with a contact angle measuring system (OCA 15, Dataphysics) using the sessile drop method. For these assays, six PLA discs (10 mm in diameter and 2 mm in height) were 3D-printed using the same parameters described above with a 100% infill. A distilled water drop (3 µL) was generated at 1 µL/s, and photographs were captured for posterior analysis using SCA 20 software (Dataphysics) (Figure 8).

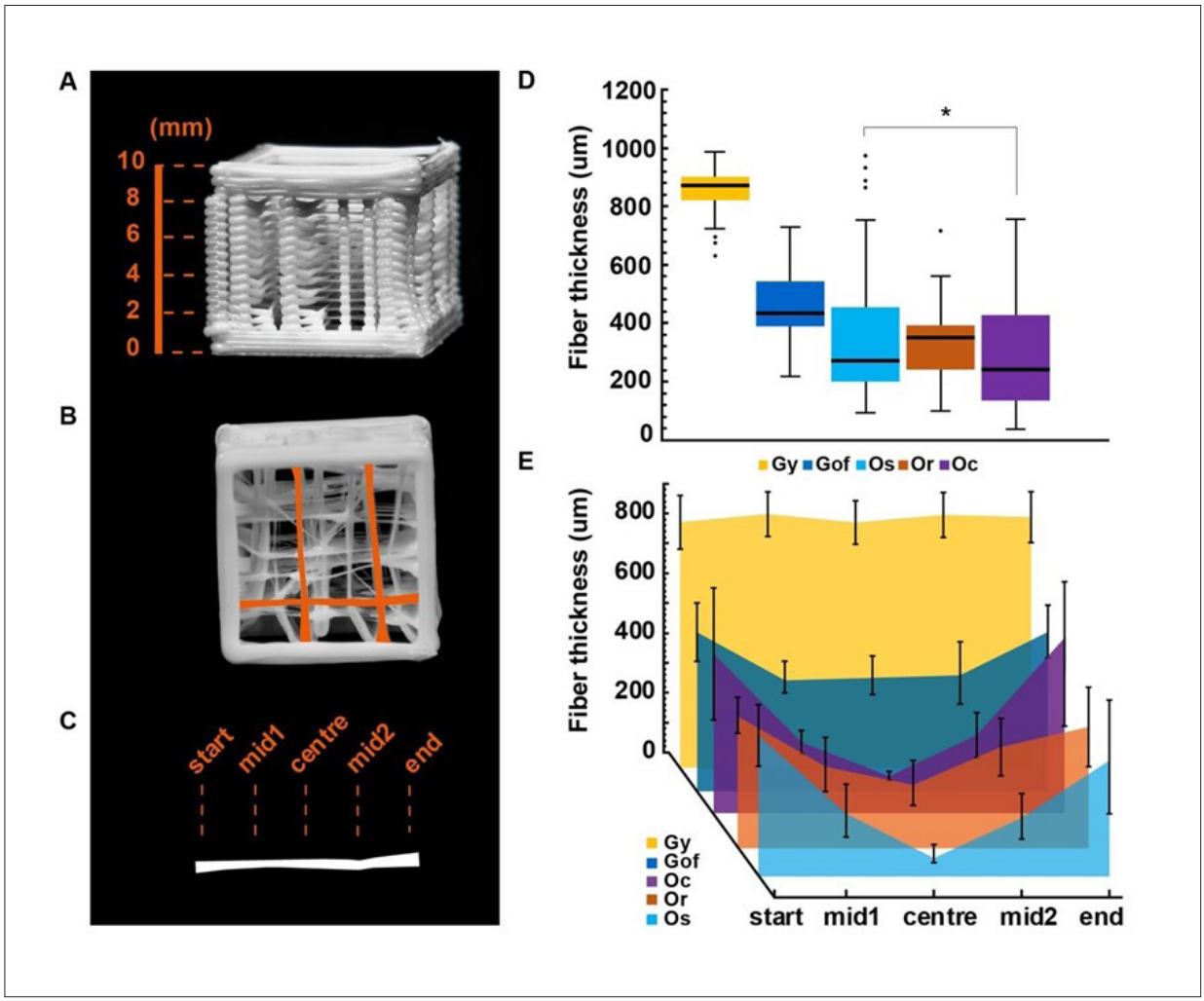

Figure 6. Fiber thickness analysis. (A–C) Scheme of the fiber thickness measuring setup. (A) Scheme of the five different heights (2, 4, 6, 8, and 10 mm) for performing fiber measurements. (B) Example of three randomly selected fibers at each height of the sample to perform the fiber thickness analysis. (C) Representation of five selected points to measure thickness along the fiber (start, mid1, center, and end). (D) Fiber thickness means measurements per specimen ($n = 45$, * $p < 0.05$ by Kruskal–Wallis test). (E) Thickness measurements across the fiber per specimen.

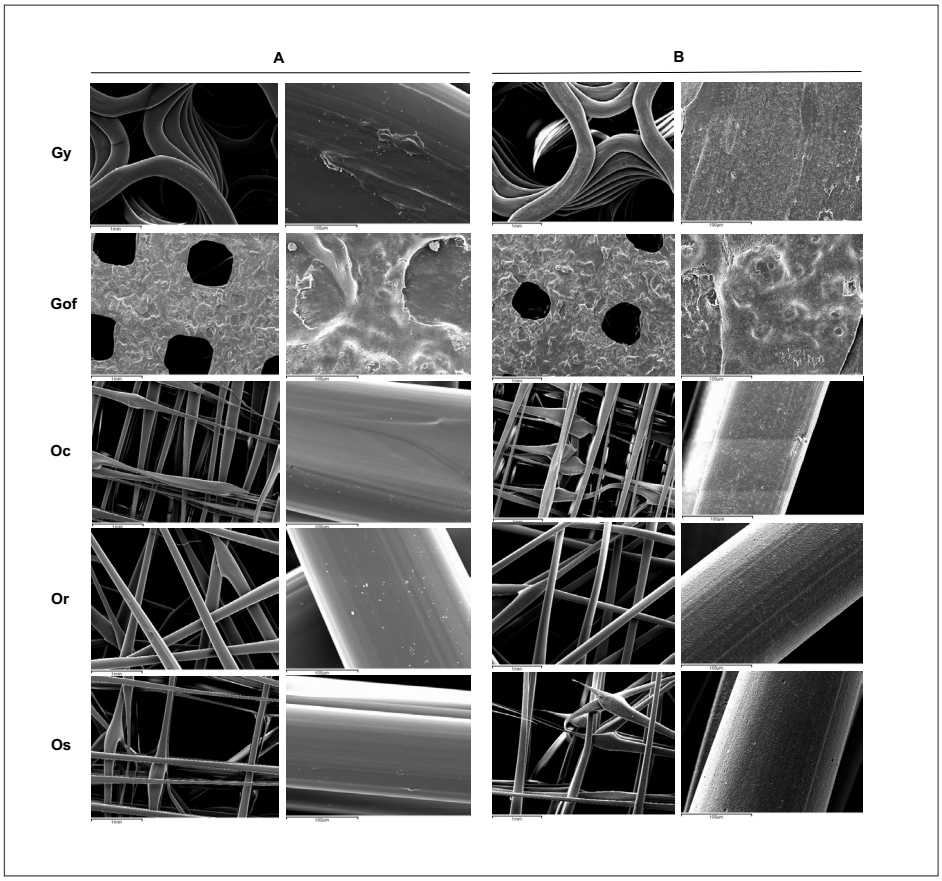

Figure 7. Specimens surface analysis by scanning electron microscopy. (A) Control specimens' images (prior to treatment) and (B) specimens images after NaOH treatment. Scale bar: 100 μm.

2.8. Compression tests

A total of five specimens per condition (control and treated with NaOH) for each experimental group were tested on a universal testing machine (Z005, Zwick) equipped with a 2.5 kN load cell and compression plates. The load and displacement values of the tested specimens were recorded, and the compression stress and strain were calculated according to the obtained load and displacement after the experiments. The loading rate was at 5 mm/min (Figure 9). E modulus was calculated at the linear elastic deformation region using a linear regression included in TestXpert II (Zwick).

2.9. Cell cultures

SaOs-2 cell line (Sigma-Aldrich) was cultured in McCoy's 5A medium (Fisher Scientific), supplemented with 10% fetal bovine serum (FBS, Sigma) and 1% penicillin–streptomycin (Fisher Scientific). A total of 300,000 cells were seeded per scaffold. Cells were incubated for 1, 3, and 7 days at 37°C, under a condition of 5% CO_2 and 95% humidified air. Metabolic activity was assessed by performing a resazurin reduction assay. Briefly, seeded cells were incubated with cell culture medium (600 μL) containing resazurin (10 μg/mL) sodium salt (Sigma) for 2 h at 37°C, under a condition of 5% CO_2 and 95% humidified air. Then, 100 μL of cell culture medium were transferred to a 96-well plate, and absorbance was measured at 570 nm and 600 nm using a microplate reader (Synergy HT Multi-detection Microplate Reader, Bio-Tek). Cell metabolic activity was expressed in terms of percentage reduction of resazurin and normalized to control values obtained from tissue culture plastic (TCP) of the same day.

Immunological assays to observe cell adhesion to the scaffolds were performed and observed using a confocal microscope (CLSM, TCS SP8, Leica Microsystems). Briefly, after 7 days of seeding, scaffolds were washed with phosphate-buffered saline (PBS) to remove dead cells. Then, the scaffolds were fixed using 4% paraformaldehyde (PFA) for 30 min and washed with PBS three times. Acti-Stain 488 phalloidin antibody (Cytoskeleton, Inc.) was used for cytoskeleton staining by diluting it in PBS (7 μL per mL), and scaffolds were

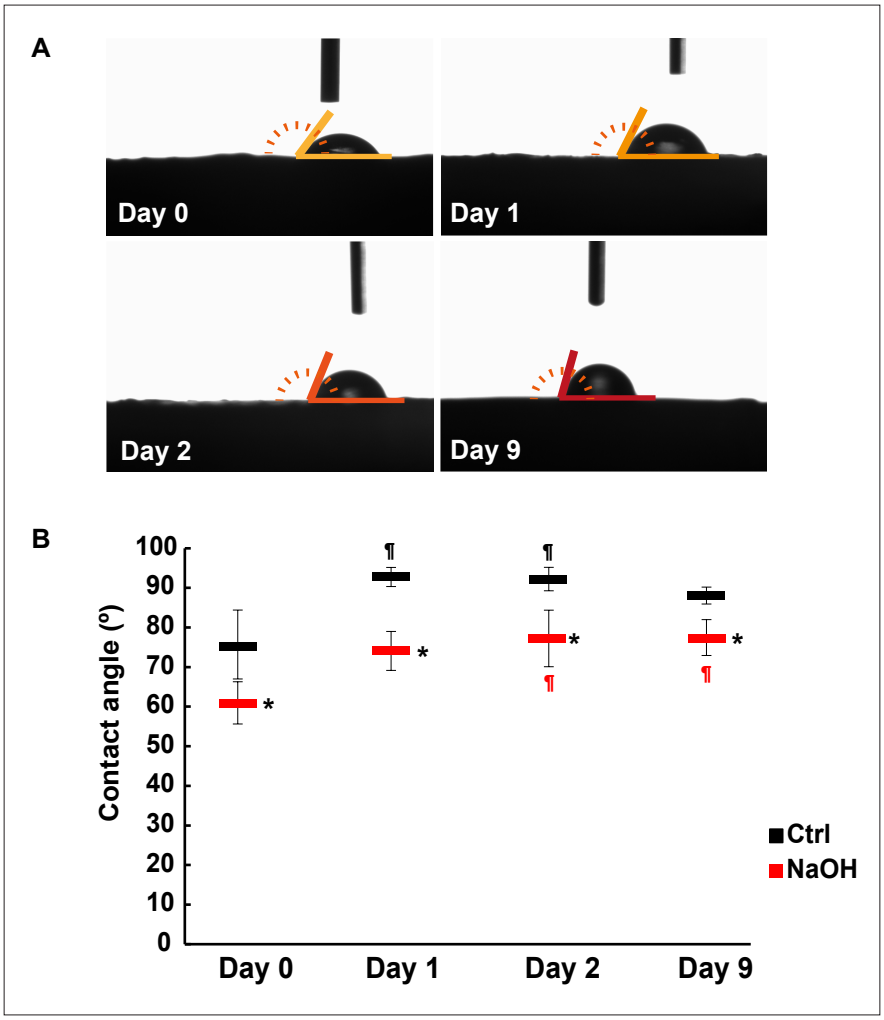

Figure 8. Water drop contact angle assays. (A) Scheme of water drop contact angle determination at different tested times. (B) Contact angle measurements at day 0, day 1, day 2, and day 9 in control groups and NaOH-treated groups. (n = 6, * and ¶ $p < 0.05$ by Kruskal–Wallis test)

incubated for 45 min with the solution (500 µL). Then, scaffolds were washed three times with PBS. Cell nuclei were stained using DAPI ready-made solution (Sigma-Aldrich) diluted at 1:1000 in PBS and incubated for 30 s. Finally, the scaffolds were washed with PBS and were observed in the confocal microscope using the Alexa 488 and DAPI filters and z-stacking. All assays were performed in triplicate (Figure 10).

2.10 Statistical analysis

All results are expressed as means ± standard deviation (SD). All data were analyzed using different tests of equality of means, with a confidence level of 95% ($p < 0.05$). First, Kolmogorov–Smirnov test was deployed to assess data normality. The results of normality tests dictate the different methods used for testing: in cases where the data were normally distributed, an analysis of variance (ANOVA) test was used to compare means of samples, or else, Kruskal–Wallis tests were used.

3. Results

3.1. Observations of the scaffolds

The five experimental groups—Gy, Gof, Oc, Or, and Os—are presented in Figure 3, captured in perspective (top) and top views (bottom), respectively. The unique features of each scaffold were clearly displayed, and the different knitting patterns could be observed. Figure 3A shows the gyroid geometry (Gy), and Figure 3B shows the waffle-like geometry of (Gof). Figure 3C and E show the predominant parallel pattern created using the oozing technique, in a dense grid (Oc) and in a lesser dense grid (Os), respectively. Figure 3D shows the aleatory pattern of Or, where fibers do not follow any predominant direction. A very important

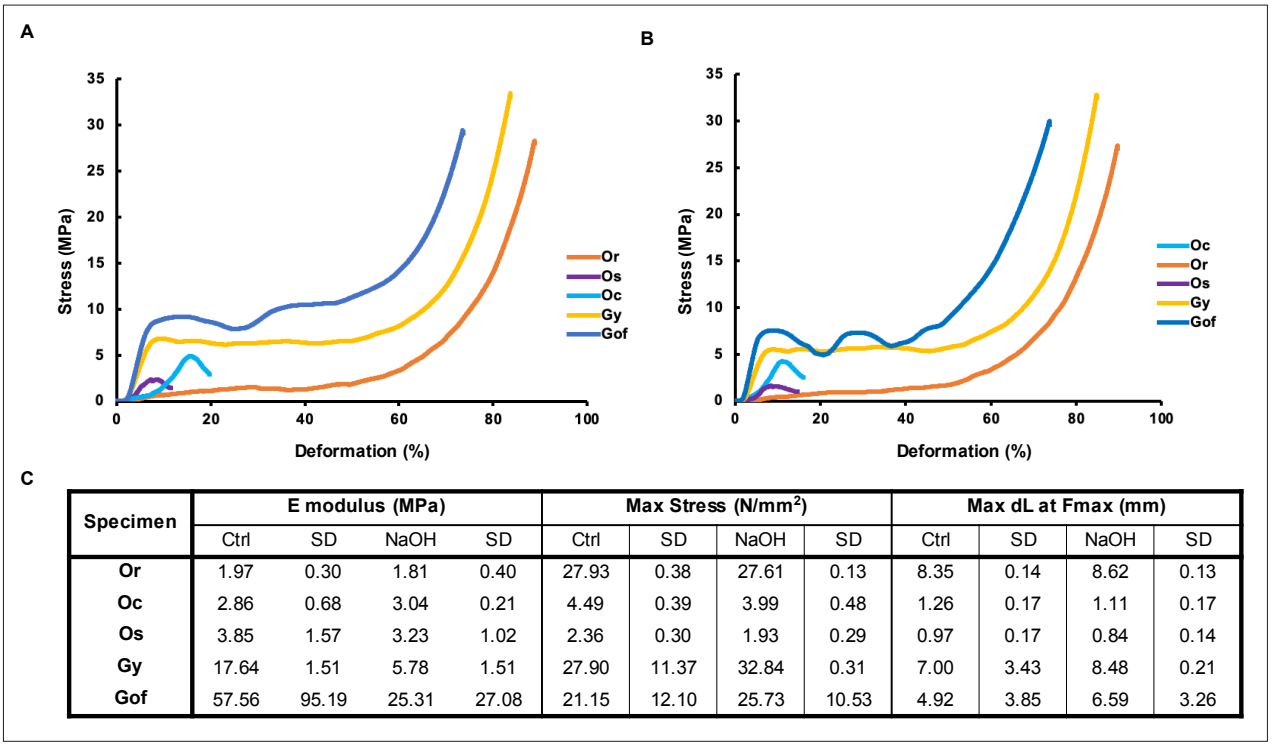

Specimen	E modulus (MPa)				Max Stress (N/mm^2)				Max dL at Fmax (mm)			
	Ctrl	SD	NaOH	SD	Ctrl	SD	NaOH	SD	Ctrl	SD	NaOH	SD
Or	1.97	0.30	1.81	0.40	27.93	0.38	27.61	0.13	8.35	0.14	8.62	0.13
Oc	2.86	0.68	3.04	0.21	4.49	0.39	3.99	0.48	1.26	0.17	1.11	0.17
Os	3.85	1.57	3.23	1.02	2.36	0.30	1.93	0.29	0.97	0.17	0.84	0.14
Gy	17.64	1.51	5.78	1.51	27.90	11.37	32.84	0.31	7.00	3.43	8.48	0.21
Gof	57.56	95.19	25.31	27.08	21.15	12.10	25.73	10.53	4.92	3.85	6.59	3.26

Figure 9. Stress–strain curve for compression tests. (A) Representative curves for compression assay in control samples (prior to treatment). (B) Representative curves for compression assays in samples after NaOH treatment. (C) Results for E modulus, maximum stress, and maximum elongation at maximum stress per each specimen group ($n = 5$ per experimental group and per condition, $p < 0.05$).

fact that we observed in the oozing groups is that fibers never touch each other in the interior knitting.

3.2. Volume and mass measurements

The outer volumes determination showed similar values between Gy and Oc, and both have statistical differences ($p < 0.05$) with Or, Os, and Gof (Figure 4F). In the case of Gy, this difference may be attributed to the design of the geometry of Gy itself, as this specimen does not possess a supporting frame like the others. This lack of structural support for the (Gy) specimen may have led to a certain shrinkage of the structure after printing (**Figure S1** in Supplementary File). Masses were found to differ between specimens, with Gof being the heaviest of them all, followed by Oc, then Gy and Os with similar weights, and Or was the lightest (Figure 3F). Our results demonstrated that the density of the inner knitting pattern varies considerably from one specimen to another and therefore the amount of extruded material in each specimen.

3.3. X-Ray microtomography porosity

The X-ray scanning and reconstruction analysis of all the specimens' geometry allowed the appreciation of the actual inner geometry of the scaffolds and performing their physical characterization (Figure 4A–E). The mass and total porosity analysis of the specimens demonstrated a direct correlation with the amount of extruded material, with the oozing specimens—Oc, Or, and Os—being the most porous and, hence, the lightest ones, in contrast with control groups (Gy and Gof). The thickness distribution determination showed a very similar profile in all oozing groups (Oc, Or, and Os) and in control groups (Gof and Gy), with the majority ranging from ~30 μm to ~630 μm (Figure 5). However, the thickness distribution was much more concentrated in the range of ~310 μm to ~390 μm in Gy specimen. In terms of the separation distribution, our results showed many similarities between groups, but with different pattern distributions: a marked skew right pattern for Gy specimen, a tendency to a uniform distribution in Gof, Oc, and Or displaying a symmetric unimodal pattern, and a multimodal distribution in Os group. In addition, Gof, Or, and Os showed a more scattered separation pattern. The biggest separation distribution and the most concentrated were found in Gy group, as the values range from 1630 μm to 1830 μm. In contrast, the smallest separations were found in Oc group, as it possessed the densest knitting pattern.

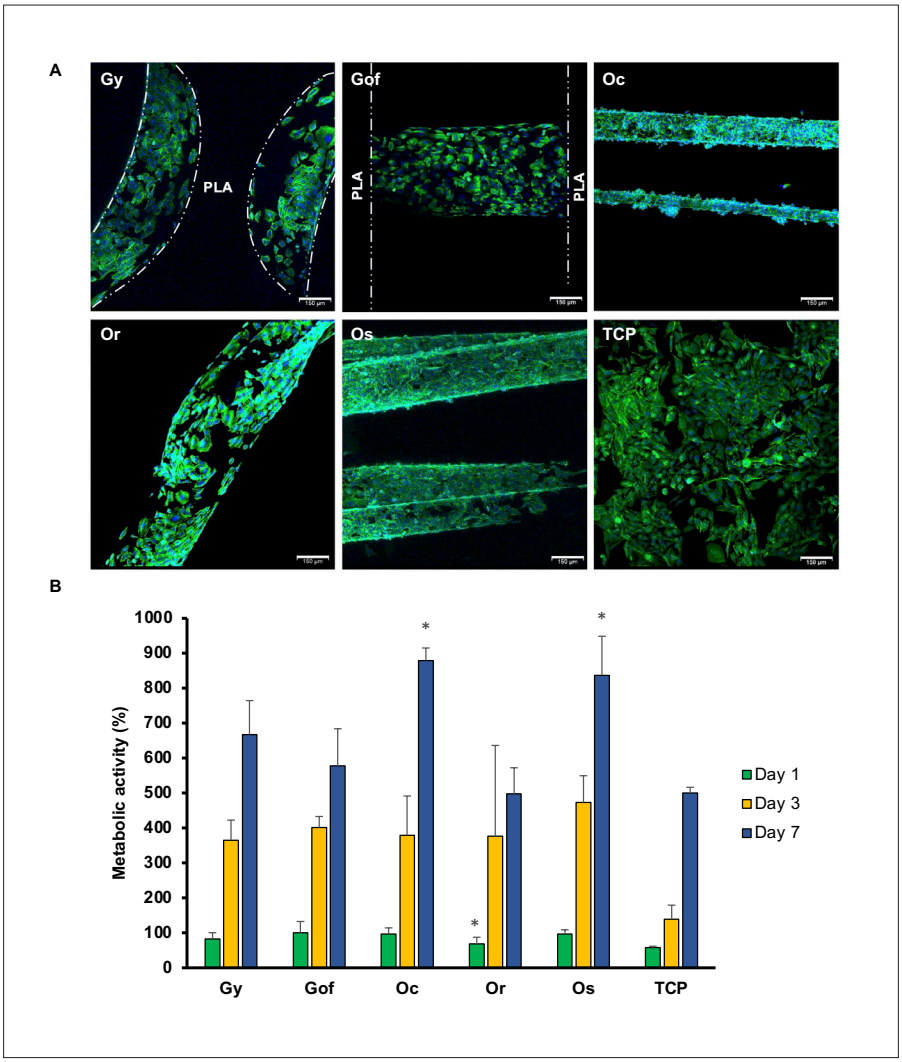

Figure 10. Cell culture assays in the scaffolds. (A) Representative immunofluorescence images of confocal microscopy of cell culture onto the different scaffolds (Gy, Gof, Oc, Or, and Os) and in control (TCP) at day 7 after seeding. Nuclei were stained with DAPI and cytoskeleton with phalloidin. Scale bar: 150 µm. (B) Metabolic activity at days 1, 3, and 7 ($n = 3$, $p < 0.05$ Mann–Whitney test).

3.4. Fiber thickness

The results of fiber thickness measurements at five different selected points in each fiber (Figure 6A–C) demonstrated statistically significant differences ($p < 0.05$) between the oozing groups (Or, Oc, and Os) and the control groups (Gy and Gof), with the fibers in the oozing group relevantly thinner than in the controls (Figure 6D).

All oozing specimens showed greater thickness at the end of the fibers and a progressive narrowing as it reached the center of the fiber. This characteristic was common to all samples. Specimen Gof showed more constant values, and specimen Gy displayed almost equal values in every measured point. Although the mean values of fiber thickness were found to be similar at the beginning (start) and at the end (end) of the fibers, measurements in the center of the fiber (center) varied depending on the specimen, and were narrower in the oozing groups (Os, Oc, and Or), ranging from ~70 µm to ~240 µm, than in the (Gof) or (Gy) groups, which displayed less difference in thickness. These results may be related to the fact that the control groups were not properly fabricated with oozing techniques but with regular FDM nozzle deposition (Figure 6E).

3.5. NaOH treatment

With scanning electron microscopy (SEM) analysis, we studied several images of regions of interest (ROI) on the surface of the scaffolds to compare the surface aspect prior to and after NaOH treatment (Figure 7A–B). Our results

demonstrated that NaOH solution erodes the surface of the fibers. In addition, the hydrophilicity assay showed statistically significant differences (* $p < 0.05$) between controls and NaOH-treated groups at each measuring point (day 0, day 1, day 2, and day 9), with a constant shift of ~9° to 15° observed between conditions. Similarly, statistically significant differences in contact angle within time were separately found in both conditions. Additionally, the contact angle in the controls was statistically significant ($'p < 0.05$) between day 0 and day 1, and between day 0 and day 2. However, the NaOH-treated group showed differences between day 0 and day 2, and between day 0 and day 9 (Figure 8).

3.6 Compression study

Our results from the determination of elastic modulus (E), maximum stress (Max stress), and maximum elongation at maximum force (Max dL at F_{max}) for all scaffolds in both experimental conditions (NaOH treatment and control) demonstrated no statistically significant differences ($p < 0.05$) between conditions for any studied parameter, indicating that treatment does not affect mechanical properties (Figure 9). Interestingly, Gy and Gof specimens' data showed a higher E modulus in both conditions (NaOH treatment and control) compared to the oozing groups, with Gof's being three or four times higher than that of Gy. Maximum stress values showed similar behavior in both experimental conditions for all specimens, except for Oc and Os, which were found to be considerably lower. Maximum elongation at maximum force showed similar results in both conditions for all specimens with a lower value in Oc and Os specimens (Figure 9C).

3.7. Cell culture studies

To assess how the morphology or accuracy of the 3D-printed structure could affect the cell response, SaOs-2 cells were seeded and cultured within the scaffolds. Metabolic activity was determined using a resazurin salt reduction assay, and cytoskeleton staining was observed with a confocal microscope (Figure 10A). Tissue culture plastic (TCP) was used as a control for cell behavior while Gof, commonly used in tissue-engineering applications, was used as a control of the infill structure. As shown in Figure 10B, there was no difference in the initial adhesion (day 1) of cells to the different scaffolds, except for Or, which displayed a significantly lower cell adhesion ($p < 0.05$). However, this lower metabolic activity was not statistically significant at days 3 and 7. Moreover, the metabolic activity was gradually increased during the culture time, being comparable to that of Gof and normal TCP, and was significantly higher for Os and Oc at day 7 ($p < 0.05$). These results correlated with higher density of fibers per volume in the Os and Oc scaffolds. The immunofluorescence results (Figure 10B) were consistent with the metabolic activity, showing that scaffold walls of Gy and Gof were mostly covered by spread cells at day 7. Similarly, fibers of Os, Or, and Oc were also completely covered by spread cells.

4. Discussion

Oozing or stringing effect has been generally described as a non-desirable drawback in FDM.[38,62] Despite these considerations, some recent studies have developed interesting approaches utilizing this effect to design environments with fibers in the range of microns (from a few tens up to hundreds). Various geometries have been studied by means of this technique, such as planar parallel arrangements,[44,63] 3D parallel distributions,[51,59,64] and also hybrid constructions, combining FDM with another technique, such as airbrushing[54] or electrospinning,[65] in order to create a stack of alternate layers. Nevertheless, these approaches still fail to produce an improved biomimetic 3D environment with randomly distributed fibers, as they all remain gridded.[66-68]

Our study focused on developing a set of novel FDM-printed constructs with random and gridded distributions of microfibers that may better mimic those of the native ECM niche. In addition, we analyzed the potential of these constructs, which support cell culture growth, as bone tissue-engineering strategies. This may represent an important progress, as we introduced for the first time the potential of using the oozing or stringing phenomenon to enhance the 3D-printed scaffolds characteristics for better promoting cell attachment and growth, as the created fiber dimensions better matched the ECM natural niche.[69,70]

We demonstrated that design is a fundamental tool to overcome FDM printing limitations when using conventional printing machines. Our results showed that it is possible to surpass the constraints of an accessible FDM ordinary printer by using AAD to improve the architecture of the scaffolds, corroborating similar algorithm-based methodology previously described in the literature.[65] Moreover, our scaffolds' design algorithms were especially designed to create random distributions of the fibers, providing an innovative framework that enhances the FDM printing application to an improved biomimetic-like approach in the tissue-engineering field.[70-72]

Our results demonstrated the oozing effect is a repeatable technique that can be controlled considering a certain degree of tolerance within fiber geometry. An accurate setting of the printing parameters, such as feeding speed and printing speed, among others, and other intrinsic

variables like temperature and relative humidity of the ambience have been reported to reduce fiber geometrical variability.[44] Despite these considerations, a certain degree of heterogeneity can be expected when working with the oozing technique.[51]

Our results showed that the scaffolds of the oozing groups exhibited an enhanced cell attachment and proliferation within 7 days of culture in comparison with controls. These results are possibly attributed to the microscale of the fibers together with an increased porosity of the whole construct, as suggested elsewhere.[42,73] These data increase the knowledge about the utility of FDM oozing-created constructs as scaffolds for growing cells, in concordance with other previous publications. Nevertheless, further culture assays should be performed to confirm and improve the understanding of their biological potential as a tissue-engineering strategy.[57]

Regarding fiber geometry, we found that oozing groups possessed dispersed fiber thickness depending on the point they were measured, with the lowest measurement found in the middle of the fiber in every case, in agreement with other studies.[73] In contrast, controls (Gy and Gof) presented notably more homogeneous fiber thickness, due to the fact that their infill cannot be considered a proper fiber but a regular FDM deposition.[5,54] Oozing groups exhibited statistically significant thinner fibers than controls, corroborating that the oozing effect can achieve considerably narrower fibers than standard FDM printing as it has been proven in the literature.[44,51] Acquiring a better control over the range of thicknesses for every printed fiber with the oozing technique would represent a major advance for creating tissues with different fiber arrangements. Printing speed together with flow rate and feed rate are fundamental variables to be mastered in future works as pointed elsewhere.[41,45,73]

As observed, a scaffold's porosity grade was directly related to mechanical behavior as an increase in the inner voids led to a lower compressive strength. These results are in agreement with other reported publications, which described the scaffold porosity being inversely proportional to mechanical strength, resulting in a less dense construct that can only withstand lower stress.[56,74] Interestingly, it has been described that mechanical strength is geometry-dependent. Fernandez-Vicente et al.[35] described a series of constructs with different infill patterns and the same mass that showed different mechanical behavior as certain specimens supported greater mechanical loading depending on their pattern design. Despite these observations, the influence of the geometry pattern caused a variation of less than 5%.

Polylactic acid is a well-known biocompatible polymer extensively used in biomedical applications. However, it has certain limitations concerning its use such as a slow degradation rate and strong hydrophobicity that can interfere with cell adhesion.[56,60] Alternatively, our results demonstrated that the NaOH treatment can increase the hydrophilicity characteristics of the PLA scaffold and maintain them nearly 9 days, enhancing the potential of PLA in bioengineering tissue applications. Furthermore, our data demonstrated that control specimens showed a similar behavior to NaOH-treated specimens, suggesting that FDM printing itself (melting and extruding process) modifies PLA's hydrophilic superficial properties. This temporally increased hydrophilicity proposes a certain reversibility of the process when PLA is 3D-printed, corroborating other published studies.[75] Interestingly, NaOH treatment of the constructs did not affect their mechanical behavior, probably due to the treatment only affecting the surface of the scaffolds, as previously described.[57]

With good cell adhesion and proliferation activity on the scaffolds in all tested specimens, our data support the application of this new set of scaffolds in tissue engineering. In addition, in the cases of Oc and Os specimens, the cell activity observed was higher than in the other specimens. These results may be justified by the smaller fiber separation in these two specimens in comparison with Or and controls (Gof and Gy) that could allow increased cell density in the scaffold pores. This cell density could promote greater cellular proliferation and occupancy in these constructs, as it has been noted in other reports.[67,76] Nevertheless, these results may be confirmed with ulterior studies in the field.

5. Conclusion

The oozing technique together with our AAD-controlled random distribution provides an interesting platform to create 3D-printed scaffolds with fibers in the range of microns that may better mimic the ECM niche than those fabricated by conventional FDM without advanced programming. The benefits of this technical approach are reliant on its capacity to overcome the limitation of the extruded filament's diameter, and the typical parallel-like distribution of the scaffolds. Nonetheless, we are cognizant of the necessity to better control the oozing process to improve the mastering of the thickness and geometry of fibers. Our strategy to combine AAD with an accessible 3D printer together with cell culture assays represents a powerful approach to creating novel biomimetic constructs with great potential suitable for tissue engineering.

Acknowledgments

None.

Funding

The authors would like to thank the Government of Catalonia [2017 SGR 708 and 2021 XARDI 00002]; the Spanish Ministry of Science and Innovation Ramón y Cajal fellowship [RYC2018-025977-I]; MINECO/FEDER Project [RTI2018-096088-J-100]; and the PO FEDER of Catalonia 2014ᴐ32020 [project PECT Osona Transformació Social, Ref. 001-P-000382].

Conflict of interest

The authors declare no conflicts of interest.

Author contributions

Conceptualization: Juan Crespo-Santiago
Data curation: Laia Millan, Oriol Chico, Pau Oliver
Formal analysis: Juan Crespo-Santiago, Rafa Madariaga
Funding acquisition: Marta Otero-Viñas, Roman Perez
Investigation: Juan Crespo-Santiago, Luis M. Delgado, Laia Millan, Oriol Chico, Pau Oliver
Methodology: Juan Crespo-Santiago
Resources: Luis M. Delgado
Validation: Juan Crespo-Santiago
Visualization: Juan Crespo-Santiago
Writing – original draft: Juan Crespo-Santiago
Writing – review & editing: Marta Otero-Viñas, Luis M Delgado

Ethics approval and consent to participate

Not applicable.

Consent for publication

Not applicable.

Availability of data

G-codes can be downloaded directly from: https://github.com/JuanCrespoSantiago/Oozing-Gcodes.git

References

1. Langer R, Vacanti JP. Tissue engineering. *Science*. 1993;260(5110):920-926. doi: 10.1126/science.8493529
2. Ikada Y. Challenges in tissue engineering. *J R Soc Interface*. 2006;3(10):589-601. doi: 10.1098/rsif.2006.0124
3. Shin H, Jo S, Mikos AG. Biomimetic materials for tissue engineering. *Biomaterials*. 2003;24(24):4353-4364. doi: 10.1016/S0142-9612(03)00339-9
4. Yue B. Biology of the extracellular matrix: an overview. *J Glaucoma*. 2014;23(8):S20-S23. doi: 10.1097/IJG.0000000000000108
5. Ceretti E, Ginestra P, Neto PI, Fiorentino A, da Silva JVL. Multi-layered scaffolds production via fused deposition modeling (FDM) using an open source 3D printer: process parameters optimization for dimensional accuracy and design reproducibility. *Procedia CIRP*. 2017;65:13-18. doi: 10.1016/j.procir.2017.04.042
6. Jiang X, Zheng W, Takayama S, Chapman RG, Kane RS, Whitesides GM. Micro-scale patterning of cells and their environment. In: Lanza R, Langer R, Vacanti JP, eds. *Principles of Tissue Engineering*. 4th ed. Cambridge, Massachusetts: Elsevier Inc.; 2013: 359-384. doi: 10.1016/B978-0-12-398358-9.00019-7
7. Richards DJ, Tan Y, Jia J, Yao H, Mei Y. 3D printing for tissue engineering. *ISR J Chem*. 2013;53(9-10):805-814. doi: 10.1002/ijch.201300086
8. Lee M, Wu BM. Recent advances in 3D printing of tissue engineering scaffolds. *Methods Mol Biol*. 2012;868:257-267. doi: 10.1007/978-1-61779-764-4_15
9. Choi JW, Kim N. Clinical application of three-dimensional printing technology in craniofacial plastic surgery. *Arch Plast Surg*. 2015;42(3):267-277. doi: 10.5999/aps.2015.42.3.267
10. Jakus AE, Secor EB, Rutz AL, Jordan SW, Hersam MC, Shah RN. Three-dimensional printing of high-content graphene scaffolds for electronic and biomedical applications. *ACS Nano*. 2015;9(4):4636-4648. doi: 10.1021/acsnano.5b01179
11. Huang H, Zhang B, Zhong J, et al. The behavior between fluid and structure from coupling system of bile, bile duct, and polydioxanone biliary stent: a numerical method. *Med Eng Phys*. 2023;113:103966. doi: 10.1016/J.MEDENGPHY.2023.103966
12. Xu Y, Zhang F, Zhai W, Cheng S, Li J, Wang Y. Unraveling of advances in 3D-printed polymer-based bone scaffolds. *Polymers*. 2022;14(3). doi: 10.3390/polym14030566
13. Valashani SMM, Barrett CJ, Barthelat F. Self-assembly of microscopic tablets within polymeric thin films: a possible pathway towards new hybrid materials. *RSC Adv*. 2015;5(7):4780-4787. doi: 10.1039/c4ra15166f
14. Turnbull G, Clarke J, Picard F, et al. 3D bioactive composite scaffolds for bone tissue engineering. *Bioact Mater*. 2018;3(3):278-314. doi: 10.1016/j.bioactmat.2017.10.001

15. Szojka A, Lalh K, Andrews SHJ, Jomha NM, Osswald M, Adesida AB. Biomimetic 3D printed scaffolds for meniscus tissue engineering. *Bioprinting*. 2017;8:1-7. doi: 10.1016/j.bprint.2017.08.001

16. Kabirian F, Ditkowski B, Zamanian A, Heying R, Mozafari M. An innovative approach towards 3D-printed scaffolds for the next generation of tissue-engineered vascular grafts. *Mater Today Proc*. 2018;5(7):15586-15594. doi: 10.1016/j.matpr.2018.04.167

17. DeStefano V, Khan S, Tabada A. Applications of PLA in modern medicine. *Eng Regen*. 2020;1:76-87. doi: 10.1016/j.engreg.2020.08.002

18. Mota C, Puppi D, Chiellini F, Chiellini E. Additive manufacturing techniques for the production of tissue engineering constructs. *J Tissue Eng Regen Med*. 2015;9(3):174-190. doi: 10.1002/term.1635

19. Chung JJ, Im H, Kim SH, Park JW, Jung Y. Toward biomimetic scaffolds for tissue engineering: 3D printing techniques in regenerative medicine. *Front Bioeng Biotechnol*. 2020;8. doi: 10.3389/fbioe.2020.586406

20. Alagoz AS, Hasirci V. 3D printing of polymeric tissue engineering scaffolds using open-source fused deposition modeling. *Emergent Mater*. 2020;3(4):429-439. doi: 10.1007/s42247-019-00048-2

21. Gillispie G, Prim P, Copus J, et al. Assessment methodologies for extrusion-based bioink printability. *Biofabrication*. 2020;12(2). doi: 10.1088/1758-5090/ab6f0d

22. Papaioannou TG, Manolesou D, Dimakakos E, Tsoucalas G, Vavuranakis M, Tousoulis D. 3D bioprinting methods and techniques: applications on artificial blood vessel fabrication. *Acta Cardiol Sin*. 2019;35(3):284-289. doi: 10.6515/ACS.201905_35(3).20181115A

23. Lee JS, Hong JM, Jung JW, Shim JH, Oh JH, Cho DW. 3D printing of composite tissue with complex shape applied to ear regeneration. *Biofabrication*. 2014;6(2). doi: 10.1088/1758-5082/6/2/024103

24. Lee A, Hudson AR, Shiwarski DJ, et al. 3D bioprinting of collagen to rebuild components of the human heart. *Science*. 2019;365(6452):482-487. doi: 10.1126/science.aav9051

25. Jung JW, Lee JS, Cho DW. Computer-aided multiple-head 3D printing system for printing of heterogeneous organ/tissue constructs. *Sci Rep*. 2016;6. doi: 10.1038/srep21685

26. Liu J, Zhou Y, Lu J, et al. Injectable, tough and adhesive zwitterionic hydrogels for 3D-printed wearable strain sensors. *Chem Eng J*. 2023;475:146340. doi: 10.1016/J.CEJ.2023.146340

27. Ramesh S, Harrysson OLA, Rao PK, et al. Extrusion bioprinting: recent progress, challenges, and future opportunities. *Bioprinting*. 2021;21. doi: 10.1016/j.bprint.2020.e00116

28. Ng WL, Huang X, Shkolnikov V, Suntornnond R, Yeong WY. Polyvinylpyrrolidone-based bioink: influence of bioink properties on printing performance and cell proliferation during inkjet-based bioprinting. *Bio-Des Manuf*. 2023;6(6):676-690. doi: 10.1007/s42242-023-00245-3

29. Chartrain NA, Williams CB, Whittington AR. A review on fabricating tissue scaffolds using vat photopolymerization. *Acta Biomater*. 2018;74:90-111. doi: 10.1016/j.actbio.2018.05.010

30. Moroni L, Boland T, Burdick JA, et al. Biofabrication: a guide to technology and terminology. *Trends Biotechnol*. 2018;36(4):384-402. doi: 10.1016/j.tibtech.2017.10.015

31. Mwema FM, Akinlabi ET. Basics of fused deposition modelling (FDM). In: Castro M, eds. *SpringerBriefs in Applied Sciences and Technology*. Cham, Switzerland: Springer; 2020: 1-15. doi: 10.1007/978-3-030-48259-6_1

32. Hoque ME, Chuan YL, Pashby I. Extrusion based rapid prototyping technique: an advanced platform for tissue engineering scaffold fabrication. *Biopolymers*. 2012;97(2):83-93. doi: 10.1002/bip.21701

33. Gross BC, Erkal JL, Lockwood SY, Chen C, Spence DM. Evaluation of 3D printing and its potential impact on biotechnology and the chemical sciences. *Anal Chem*. 2014;86(7):3240-3253. doi: 10.1021/ac403397r

34. Yazar A, Top N, Bülbül R, Şahin I. Effect of infill density and infill pattern on mechanical properties in fused deposition modeling (FDM). In: *Proceedings of the Innovative Approaches in Additive Manufacturing Congress (IA4AM). Gazi University;* 2021.

35. Fernandez-Vicente M, Calle W, Ferrandiz S, Conejero A. Effect of infill parameters on tensile mechanical behavior in desktop 3D printing. *3D Print Addit Manuf*. 2016;3(3):183-192. doi: 10.1089/3dp.2015.0036

36. Zein I, Hutmacher DW, Cheng Tan K, Hin Teoh S. Fused deposition modeling of novel scaffold architectures for tissue engineering applications. *Biomaterials*. 2002;23(4):1169-1185. doi: 10.1016/S0142-9612(01)00232-0

37. Boparai KS, Singh R, Singh H. Development of rapid tooling using fused deposition modeling: a review. *Rapid Prototyp J*. 2016;22(2):281-299. doi: 10.1108/RPJ-04-2014-0048

38. Günaydın K, Türkmen HS. Common FDM 3D printing defects. In: *Proceedings of the International Congress on 3D Printing (Additive Manufacturing) Technologies and Digital Industry*; 2018.

39. Gupta S, Bissoyi A, Bit A. A review on 3D printable techniques for tissue engineering. *Bionanoscience*. 2018;8(3):868-883. doi: 10.1007/s12668-018-0525-4

40. Yang S, Leong KF, Du ZME, Chua CK. The design of scaffolds for use in tissue engineering. Part II. Rapid prototyping techniques. *Tissue Eng*. 2002;8(1):1-11. doi: 10.1089/107632702753503009

41. Sukindar NA, Ariffin MKA, Baharudin BTHT, Jaafar CNA, Ismail MIS. Analyzing the effect of nozzle diameter in fused deposition modeling for extruding polylactic acid using open source 3D printing. *J Teknol*. 2016;78(10):7-15. doi: 10.11113/jt.v78.6265

42. del Barrio Cortés E, Matutano Molina C, Rodríguez-Lorenzo L, Cubo-Mateo N. Generation of controlled micrometric fibers inside printed scaffolds using standard FDM 3D printers. *Polymers*. 2023;15(1). doi: 10.3390/polym15010096

43. Zhang Y, Harrison C. Tomo: wearable, low-cost, electrical impedance tomography for hand gesture recognition. In: *Proceedings of the 28th Annual ACM Symposium on User Interface Software and Technology*. Association for Computing Machinery, Inc.; 2015:167-173. doi: 10.1145/2642918.2647356

44. Lu Q, Song KY, Feng Y, Xie J. Fabrication of suspended uniform polymer microfibers by FDM 3D printing. *CIRP J Manuf Sci Technol*. 2021;32:179-187. doi: 10.1016/j.cirpj.2020.11.005

45. Paraskevoudis K, Karayannis P, Koumoulos EP. Real-time 3d printing remote defect detection (Stringing) with computer vision and artificial intelligence. *Processes*. 2020;8(11):1-15. doi: 10.3390/pr8111464

46. Visscher DO, Bos EJ, Peeters M, et al. Cartilage tissue engineering: preventing tissue scaffold contraction using a 3D-printed polymeric cage. *Tissue Eng Part C Methods*. 2016;22(6):573-584. doi: 10.1089/ten.tec.2016.0073

47. Zhang Z, He H, Fu W, Ji D, Ramakrishna S. Electrohydrodynamic direct-writing technology toward patterned ultra-thin fibers: advances, materials and applications. *Nano Today*. 2020;35. doi: 10.1016/j.nantod.2020.100942

48. Lannutti J, Reneker D, Ma T, Tomasko D, Farson D. Electrospinning for tissue engineering scaffolds. *Mater Sci Eng C*. 2007;27(3):504-509. doi: 10.1016/j.msec.2006.05.019

49. Chlanda A, Kijeńska E, Święszkowski W. Microscopic methods for characterization of selected surface properties of biodegradable, nanofibrous tissue engineering scaffolds. In: *Proceedings of the Materials Science Forum*. Trans Tech Publications Ltd; 2017:213-216. doi: 10.4028/www.scientific.net/MSF.890.213

50. Kara Y, Kovács NK, Nagy-György P, Boros R, Molnár K. A novel method and printhead for 3D printing combined nano-/microfiber solid structures. *Addit Manuf*. 2023;61. doi: 10.1016/j.addma.2022.103315

51. Gleadall A. FullControl GCode designer: open-source software for unconstrained design in additive manufacturing. *Addit Manuf*. 2021;46. doi: 10.1016/j.addma.2021.102109

52. Naghieh S, Badrossamay M, Foroozmehr E, Kharaziha M. Combination of PLA micro-fibers and PCL-gelatin nanofibers for development of bone tissue engineering scaffolds. *IJSIEC*. 2017;6(1):1-4. doi: 10.4172/2090-4908.1000150

53. Molde J, Steele JAM, Pastino AK, Mahat A, Murthy NS, Kohn J. A step toward engineering thick tissues: distributing microfibers within 3D printed frames. *J Biomed Mater Res A*. 2020;108(3):581-591. doi: 10.1002/jbm.a.36838

54. Corapi D, Morettini G, Pascoletti G, Zitelli C. Characterization of a polylactic acid (PLA) produced by fused deposition modeling (FDM) technology. *Procedia Struct Integr*. 2019;24:289-295. doi: 10.1016/j.prostr.2020.02.026

55. Nagarajan S, Radhakrishnan S, Kalkura SN, Balme S, Miele P, Bechelany M. Overview of protein-based biopolymers for biomedical application. *Macromol Chem Phys*. 2019;220(14). doi: 10.1002/macp.201900126

56. Ebrahimi F, Ramezani Dana H. Poly lactic acid (PLA) polymers: from properties to biomedical applications. *Int J Polym Mater Polym Biomater*. 2022;71(15):1117-1130. doi: 10.1080/00914037.2021.1944140

57. Gregor A, Filová E, Novák M, et al. Designing of PLA scaffolds for bone tissue replacement fabricated by ordinary commercial 3D printer. *J Biol Eng*. 2017;11(1). doi: 10.1186/s13036-017-0074-3

58. Wasyłeczko M, Sikorska W, Chwojnowski A. Review of synthetic and hybrid scaffolds in cartilage tissue engineering. *Membranes*. 2020;10(11):1-28. doi: 10.3390/membranes10110348

59. Szojka A, Lalh K, Andrews SHJ, Jomha NM, Osswald M, Adesida AB. Biomimetic 3D printed scaffolds for meniscus tissue engineering. *Bioprinting*. 2017;8:1-7. doi: 10.1016/j.bprint.2017.08.001

60. Singhvi MS, Zinjarde SS, Gokhale DV. Polylactic acid: synthesis and biomedical applications. *J Appl Microbiol*. 2019;127(6):1612-1626. doi: 10.1111/jam.14290

61. Lasprilla AJR, Martinez GAR, Lunelli BH, Jardini AL, Filho RM. Poly-lactic acid synthesis for application in biomedical devices - a review. *Biotechnol Adv*. 2012;30(1):321-328. doi: 10.1016/j.biotechadv.2011.06.019

62. Alafaghani A, Qattawi A, Ablat MA. Design consideration for additive manufacturing: fused deposition modelling. *Open J Appl Sci*. 2017;7(6):291-318. doi: 10.4236/ojapps.2017.76024

63. Zhang B, Seong B, Nguyen VD, Byun D. 3D printing of high-resolution PLA-based structures by hybrid electrohydrodynamic and fused deposition modeling techniques. *J Micromech Microeng*. 2016;26(2). doi: 10.1088/0960-1317/26/2/025015

64. Heljak MK, Kurzydlowski KJ, Swieszkowski W. Computer aided design of architecture of degradable tissue engineering scaffolds. *Comput Methods Biomech Biomed Engin*. 2017;20(15):1623-1632. doi: 10.1080/10255842.2017.1399263

65. Chen S, McCarthy A, John JV, Su Y, Xie J. Converting 2D nanofiber membranes to 3D hierarchical assemblies with structural and compositional gradients regulates cell behavior. *Adv Mater*. 2020;32(43). doi: 10.1002/adma.202003754

66. Collins MN, Ren G, Young K, Pina S, Reis RL, Oliveira JM. Scaffold fabrication technologies and structure/function properties in bone tissue engineering. *Adv Funct Mater*. 2021;31(21). doi: 10.1002/adfm.202010609

67. Choi WJ, Hwang KS, Kwon HJ, et al. Rapid development of dual porous poly(lactic acid) foam using fused deposition modeling (FDM) 3D printing for medical scaffold application. *Mater Sci Eng C*. 2020;110. doi: 10.1016/j.msec.2020.110693

68. Söhling N, Neijhoft J, Nienhaus V, et al. 3D-printing of hierarchically designed and osteoconductive bone tissue engineering scaffolds. *Materials*. 2020;13(8). doi: 10.3390/MA13081836

69. Sankaravel SG, Syed RB, Manivachakan V. In vitro and mechanical characterization of PLA/egg shell biocomposite scaffold manufactured using fused deposition modeling technology for tissue engineering applications. *Polym Compos*. 2022;43(1):1-638. doi: 10.1002/pc.26365

70. da Silva K, Kumar P, Choonara YE, du Toit LC, Pillay V. Three-dimensional printing of extracellular matrix (ECM)-mimicking scaffolds: a critical review of the current ECM materials. *J Biomed Mater Res A*. 2020;108(12): 2324-2350. doi: 10.1002/jbm.a.36981

71. Zaszczyńska A, Moczulska-Heljak M, Gradys A, Sajkiewicz P. Advances in 3D printing for tissue engineering. *Materials*. 2021;14(12). doi: 10.3390/ma14123149

72. Tamay DG, Usal TD, Alagoz AS, Yucel D, Hasirci N, Hasirci V. 3D and 4D printing of polymers for tissue engineering applications. *Front Bioeng Biotechnol*. 2019;7(JUL). doi: 10.3389/fbioe.2019.00164

73. Gleadall A, Visscher D, Yang J, Thomas D, Segal J. Review of additive manufactured tissue engineering scaffolds: relationship between geometry and performance. *Burns Trauma*. 2018;6. doi: 10.1186/s41038-018-0121-4

74. Baptista R, Guedes M, Pereira MFC, Maurício A, Carrelo H, Cidade T. On the effect of design and fabrication parameters on mechanical performance of 3D printed PLA scaffolds. *Bioprinting*. 2020;20. doi: 10.1016/j.bprint.2020.e00096

75. Schneider M, Fritzsche N, Puciul-Malinowska A, et al. Surface etching of 3D printed poly(lactic acid) with NaOH: a systematic approach. *Polymers*. 2020;12(8). doi: 10.3390/POLYM12081711

76. Guduric V, Metz C, Siadous R, et al. Layer-by-layer bioassembly of cellularized polylactic acid porous membranes for bone tissue engineering. *J Mater Sci Mater Med*. 2017;28(5). doi: 10.1007/s10856-017-5887-6

ACCSCIENCE PUBLISHING

International Journal of Bioprinting

RESEARCH ARTICLE

Evaluating the clinical benefit and acceptance of a bespoke 3D-printed splint for the treatment of mallet finger injury: A pilot study in a cohort of patients

Una M. Cronin[1], Aidan O'Sullivan[1], Margo Sheerin[2], Kevin J. O'Sullivan[1], Niamh M. Cummins[3,4,5], Damien Ryan[6], and Leonard W. O'Sullivan[1]*

[1]Rapid Innovation Unit, Confirm Smart Manufacturing Centre & Health Research Institute, University of Limerick, Limerick, Ireland

[2]Occupational Therapy Department, University Hospital Limerick Group, Nenagh General Hospital, Co., Tipperary, Ireland

[3]School of Medicine, SLÁINTE Research and Education Alliance in General Practice, Primary Healthcare and Public Health, Faculty of Education and Health Sciences, University of Limerick, Limerick, Ireland

[4]Ageing Research Centre, Health Research Institute, University of Limerick, Limerick, Ireland

[5]Department of Paramedicine, School of Primary and Allied Health Care, Monash University, Melbourne, Australia

[6]Emergency Department, ALERT Limerick EM Education Research Training, University Hospital Limerick, Limerick, Ireland

***Corresponding author:**
Leonard W. O'Sullivan
(leonard.osullivan@ul.ie)

Citation: Cronin UM, O'Sullivan A, Sheerin M, et al. Evaluating the clinical benefit and acceptance of a bespoke 3D-printed splint for the treatment of mallet finger injury: A pilot study in a cohort of patients. *Int J Bioprint*. 2024;10(2):1963. doi: 10.36922/ijb.1963

Received: October 3, 2023
Accepted: November 3, 2023
Published Online: March 8, 2024

Abstract

Mallet finger injuries due to forced flexion of the distal interphalangeal joint represent a common reason for hospitalization. These injuries are primarily managed using generic Stack splints. The gold standard of care is custom splinting by a specialized hand therapist. However, this is not widely available due to staffing constraints. The aims of this study are to: (i) evaluate whether treating mallet finger injuries with a custom three-dimensional (3D)-printed splint is clinically beneficial, and (ii) assess patient and healthcare professional (HCP) acceptance and experience of bespoke 3D-printed mallet splints over generic splints. Ten adult patients with closed mallet finger injury were recruited in this study, which was conducted across three Injury Units in the University of Limerick Hospital Group (ULHG). Each patient's injured finger was measured using calipers and subsequently fitted with a bespoke 3D-printed splint. Clinical benefit and acceptance of bespoke 3D-printed splints for the treatment of mallet finger injury was assessed. The results indicate that it is clinically advantageous to use a custom 3D-printed splint over a premolded generic splint. Out of the ten patients recruited, eight had successful outcomes based on the occupational therapist (OT) measurements using the Crawford classification scale. The results showed that 40% of patients scored excellent, 30% good, 30% fair, and 0% poor. In addition, in terms of patient and HCP acceptance of the splint, nine of the ten patients stated that they would use the 3D-printed custom splint again, if needed, in the future. In conclusion, a high level of patient and HCP acceptance signifies the clinical advantage of using 3D-printed splints. This pilot study shows that advances in 3D printing could make custom splinting a viable option for use in personalized healthcare.

Keywords: Mallet finger; Mallet Injury; 3D printing; Additive Manufacturing

1. Introduction

An epidemiologic study of soft tissue musculoskeletal injuries found that mallet fingers were the fifth most common bodily injury.[1] Thus, mallet finger injuries are common in Emergency Departments (ED) and Injury Units (IUs) of hospitals.[2] Mallet finger injuries result from forced flexion or hyperextension of the distal interphalangeal joint (DIPj). The overextension of the DIPj tears the extensor tendon where it inserts into the distal phalanx. This injury may occur with or without an associated fracture, resulting in the loss of extensor mechanism. If not managed appropriately, a permanent extension lag and a possible swan neck deformity may occur.[3] These injuries commonly occur across all demographic groups as a result of work or sports activities.[4] Another less common presentation is spontaneous mallet injury, whereby no external trauma has occurred to cause the injury. This form of injury, though less common, is associated with other underlying illnesses, such as rheumatoid arthritis or osteoarthritis.[5]

Mallet finger injuries should be treated with immobilization or "static" splinting in extension or slight hyperextension for up to 8 weeks, which includes 2 weeks of night splinting at the end of treatment. This mode of treatment, when supported by effective discharge advice and strong patient compliance, allows healing by maintaining an upward force on the injured finger until the tendon injury or fracture heals.[6] The splint must be worn continuously, and the proximal interphalangeal joint (PIPj) must have enough clearance to bend to ensure the patient does not lose range of movement. If the splint is removed and the injured finger is allowed to bend, the extensor tendon may re-rupture, requiring the splinting process to be repeated. This can delay healing by several weeks and can lead to a swan neck deformity.[7] An unhealed mallet finger injury may not function properly, resulting in pain and, in time, arthritis.[8]

There are several splinting options that follow similar modes of treatment. Some splints are provided by companies directly to hospitals, an example being prefabricated generic Stack splints. Other splints are custom-made for patients, with the most notable example being the thermoplastic splint, which is molded, typically by a skilled hand therapist, to fit the patient's finger. Of these splinting methods, custom splinting is the preferred treatment option.[9,10] However, prefabricated generic Stack splints remain the most common treatment provided by healthcare facilities.[11] A study that investigated the conservative management of mallet splinting in Irish hospitals found that ED teams are restricted in their choice of splint due to stock availability.[12] Being readily available in the ED, generic Stack splints appear to be the most used in that department.

Generic Stack splints are not without limitations. Due to variability in finger size and shape between patients, and swelling of the injured finger, a correct or optimal fit may not be achieved. This can then affect patient compliance.[13] Stack splints typically come in eight sizes, but perfect fit may not be realized for every patient. In addition, generic Stack splints do not consider the finger length of the individual patient, so the PIPj may not be free to move if the splint is too long. There is no proven benefit to recovery when both the PIPj and DIPj are immobilized. Therefore, patients need to be able to continue to move their PIPj while the DIPj is immobilized.[14] The generic Stack splint also needs to be secured in place. This typically involves taping around the injured finger. However, this can be challenging for patients who are trying to manage the injury by themselves. In addition, generic Stack splints have been found to increase the risk of skin complications compared to custom-made orthoses. Skin complications such as mechanical dermatitis from tape placement and adhesive sensitivity have been documented for many years.[15]

The numerous challenges faced by hospital staffing systems make provision of personalized healthcare difficult. Custom-made splints require a specialized hand therapist to provide individualized care. Hand therapists apply the required splint to the patients, based on their anatomy. They also factor in their daily activities to help optimize recovery. These custom splints take approximately 30 min to create. Unfortunately, the low availability of specialist hand therapists in Irish hospitals indicates that custom splinting for mallet injuries is generally not available.[12]

Three-dimensional (3D) printing offers tremendous opportunities in the development of patient-centered bespoke care. The use of 3D printing to create bespoke devices to directly treat patients has been increasing in recent years.[16] Advances in materials, printing technology, and experience have led to increased clinical use, moving away from the one-size-fits-all model. 3D printing is now beginning to harness medical imaging data to optimize patient-specific devices such as splints and casts. Initially, 3D printing was used primarily for anatomical modeling, to aid in education and planning.[17] However, its application has been expanded to the creation of patient-specific devices in the realm of point of care (POC). 3D printing can enable the production of anatomically

matched and patient-specific devices with high tunability, and can provide an innovative approach to individualized healthcare, thus expanding the manufacturing of custom devices within the healthcare settings.[18]

Previous studies have assessed the feasibility of treating mallet fingers with 3D printing technology. Among these studies, five tested 3D-printed devices on non-injured volunteers.[19-23] Wong et al. assessed the feasibility of 3D printing a customized mallet splint on site for 13 non-injured Mars Desert Research Station mission crew members.[18] Choi et al. compared custom casts comprising plaster of Paris, evaluated their use against a 3D-printed splint, and conducted a wearability assessment in an unreported number of non-injured participants.[19] Zolfagharian et al. designed and 3D-printed a custom mallet splint for one healthy volunteer.[20] Papavasiliou et al. compared custom 3D-printed splints to conventional custom-made thermoplastic splints and assessed patient comfort and satisfaction for hand injuries.[21] Gupta et al. assessed a 3D-printed mallet splint on 20 non-injured volunteers.[24] Nam et al. aimed to treat an injured patient with a mallet injury using a 3D-printed device.[23] These six studies did not assess bespoke 3D-printed mallet splints in the treatment of mallet injury for multiple patients. Also, none assessed patient and healthcare professional (HCP) acceptance of the 3D-printed mallet splint.

The primary aim of this study is to evaluate the clinical benefit of applying a custom 3D-printed mallet splint to multiple patients requiring splinting for mallet injury. The secondary aim is to explore patient and HCP acceptance of 3D-printed mallet splints, in relation to fit, comfort, and appropriateness. The customization of the 3D-printed splint, where the anthropometrics of each patient guided the design, was key to providing comfort while providing clinical benefit. This is the first prospective, multi-site study offering custom 3D-printed devices to a cohort of patients (n = 10) for treating mallet finger injury.

2. Materials and methods

This study was approved by the Research Ethics Committee of ULHG (reference 087/2022). Written informed consent was obtained from all participants before beginning the study.

2.1. Materials

The bespoke splints were printed on a Figure 4 (3D printer make) standalone 3D Printer (3D Systems, South Carolina, United States of America) using the PRO-BLK material from the same manufacturer.

2.2. Study design

This was a multi-site study conducted in three hospitals across ULHG. This hospital group saw approximately 71,315 attendances at their ED and IUs in 2019.[25] To that end, the inclusion of three units provided a representative group for study recruitment. The time frame for recruitment for the study was 6 months, commencing in January 2023 and ending in June 2023.

The inclusion criteria were adult patients presenting to the ED or IU with a Type 1 or Type 2 closed mallet finger injury based on the Doyle Classification System.[26] The exclusion criteria were injuries with obvious abnormal anatomy or skin complications. There was no randomization of participants. All patients that met the inclusion criteria were invited to participate in the study by their treating HCP.

2.3. Design and production of 3D-printed splints

Measurements at eight discrete points of the injured finger were recorded (Figure 1) using a vernier calipers (Mitutoyo brand) with a resolution of 0.01 mm.

Calipers were the chosen measuring device because they were available to the research team at the beginning of the study. They were also more practical because they did not require specialist equipment (3D scanner, dedicated computer) or specialist training on a new technology.

A 3D CAD model of the custom splint was designed in SolidWorks® (Dassault Systems, France) using the dimensions recorded from the patient. A design table was used to automatically modify a standard base model using the unique dimensions of the patient, creating a bespoke splint for every patient with no additional design effort or engineering required (Figure 2).

2.4. Study process

2.4.1. Initial presentation

At their initial presentation (t = 0 days), patients who met the inclusion criteria and consented to participate in the study were allocated four follow-up appointments (t = 7, t = 9, t = 21, and t = 56 days; Table 1).

The patients were fitted with a generic Stack splint at their initial presentation and were instructed to wear this temporarily until the 3D-printed splint was ready approximately 7 days later. This was to ensure immediate commencement of a treatment and to allow for any swelling to reduce before being measured and fitted for the 3D-printed splint. The Stack splint was, therefore, worn during the period when the patient's finger was most swollen. The logistics of the study did not allow deviation from this.

Each patient was given discharge advice consistent with the normal standard of care in each unit. The discharge

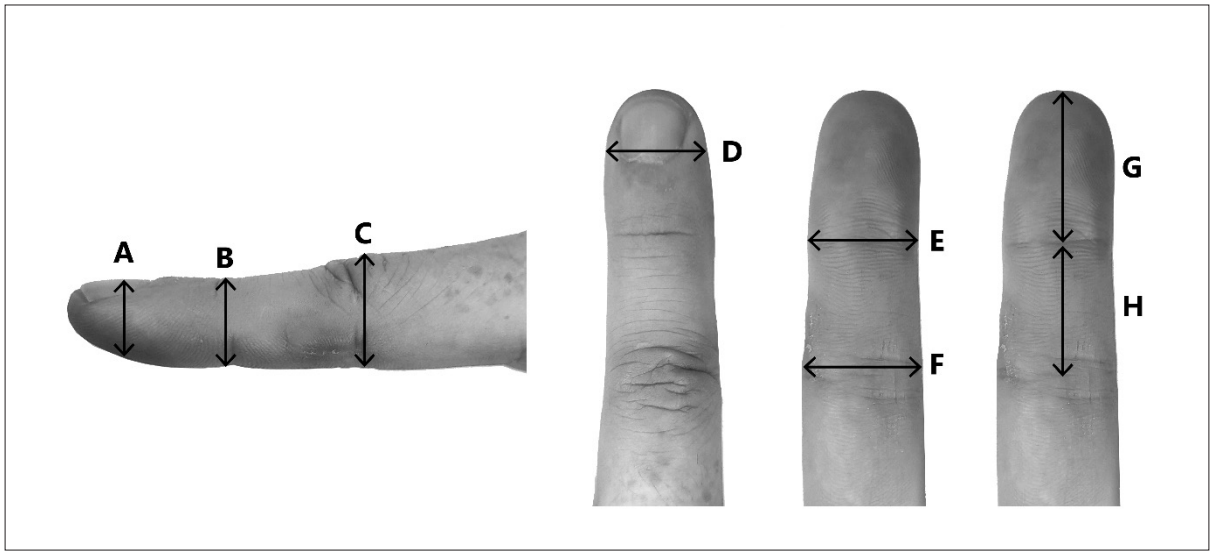

Figure 1. Points of measurement for injured finger. Original picture based on Wong.[18]

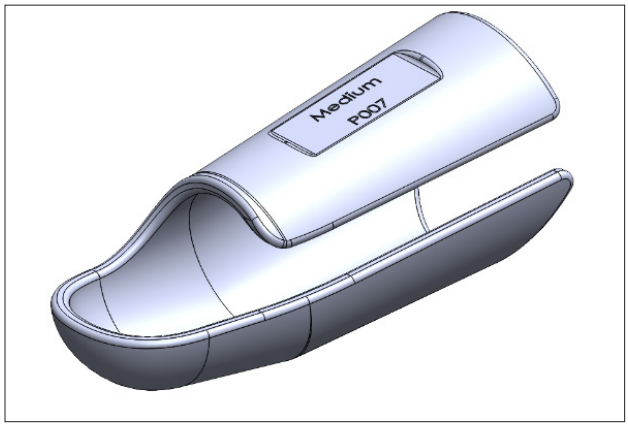

Figure 2. Image of custom 3D-printed splint.

advice was the same for the Stack splint and the 3D-printed splint.

2.4.2. Measuring (t = 7 days)

Each measuring appointment was conducted with a single member of the research team (A.O.'S) to control for inter-individual differences in measurement skills or approaches. An HCP (nurse, advanced nurse practitioner, or doctor) was also present to ensure the finger was kept straight to avoid re-injury.

2.4.3. Fitting (t = 9 days)

A 3D-printed splint was manufactured using the measurements of the patient's finger. The splint was delivered and fitted to the patient in the hospital. An HCP oversaw the fitting to evaluate the injured finger for skin integrity or other complications that could preclude the patient from further participation in the study.

2.4.4. Mid-trial review (t = 21 days)

A consultant in emergency medicine reviewed each patient after wearing the 3D-printed splint for 21 days to evaluate skin integrity and general progress. If any concerns were noted regarding compliance or comfort, the patient was changed to an alternative treatment method and removed from the study.

2.4.5. Final review (t = 56 days)

A final review appointment including an interview was conducted at 56 days by an OT with expertise in the

Table 1. Patient appointments and study stages

Initial presentation (day 0)	Measuring (day 7)	Fitting (day 9)	Midtrial review (day 21)	Final review (day 56)
Patient presented to hospital. Standard treatment commenced	Finger measured	3D-printed splint fitted	Review by consultant in emergency medicine (skin, pain, progress)	Final interviews with researcher and OT

provision of hand therapy assessments and intervention (M.S.). The lead researcher (U.C.) was also present.

2.5. Patient interview

Initially, the patient was interviewed regarding their perception and acceptance of the 3D-printed splint using a modified form of the Quebec User Evaluation of Satisfaction with assistive Technology QUEST (Version 2.0).[27] The questionnaires were validated by an external group of experts before commencing the study (a consultant in emergency medicine, an advanced nurse practitioner, a research nurse, and an OT).

The patient's satisfaction with the Stack splint and the 3D-printed splint was assessed using a Likert scale and free-text answers. It was explained to each patient that the initial splint was applied when the finger was likely to be most swollen. Patients were encouraged to be cognizant of this when answering the questionnaire to avoid bias against their initial splint.

The second part of the interview was conducted by the OT with a focus on clinical outcomes and acceptance.

2.6. Measurements

The OT removed the splint and assessed the range of movement of the DIPj using a Rolyon® finger goniometer (Smith and Nephew, London, UK). The patient's measurement was compared to the Crawford classification scale. This is the most commonly used outcome classification tool for mallet finger treatment.[28]

- Excellent: No pain with full range of motion at the DIPj
- Good: Less than 10-degree extension deficit
- Fair: 10–25 degrees of extension deficit with no pain
- Poor: More than 25 degrees of extension deficit or persistent pain

If there was an extension deficit of more than 10 degrees or poor active extension, the splint was continued for a further 2 weeks, followed by night splinting for a further 2 weeks, as directed by the OT.

2.7. Acceptance

Patient feedback was collected in the free-form section of each questionnaire to capture each patient's detailed experience of both splints. Both the patient and the OT were asked if they would use the 3D-printed splint again.

2.8. Data analysis

Data from the questionnaires were tabulated and analyzed using Microsoft Office Excel, and descriptive statistics were used to describe the data.

3. Results

3.1. Participation and study completion rate

Over a 6-month period, 16 patients were recruited, with 10 completing the study. There were eight males and two females, and their average age was 58. All patients sustained their injury through trauma. Two patients withdrew from the study due to an inability to attend all scheduled appointments as required. One patient failed to attend any follow-up appointments after the bespoke splint was fitted, despite attempts to contact the patient and rearrange appointments.

The intention was that all patients would wear a generic Stack splint before being fitted with the 3D-printed splint. However, one patient could not tolerate the generic Stack splint because a close fit could not be obtained. In that case, a dorsal aluminum splint was applied. This patient's data are not included in the results.

On mid-trial review with the consultant in emergency medicine, two patients were found to have osteoarthritic changes to their finger joints. After review by the OT and consultant in emergency medicine, it was decided that these were more complicated injuries. Consequently, these patients were removed from the study and prescribed custom thermoplastic splinting and regular reviews by the OT. The ten patients who completed the study wearing the 3D-printed splint attended the final interview with the lead researcher and OT.

3.2. Clinical outcome

Out of the ten patients recruited, eight had successful outcomes based on the OT measurements while using the Crawford classification scale. The results showed that 40% of the patients scored excellent, 30% good, 30% fair, and 0% poor.

Of the two patients with unsuccessful outcomes, one abandoned the use of the splint within the first 6 weeks and returned to participation in sporting activities; the other repeatedly bent the injured finger during hand washing due to a misunderstanding of discharge advice.

3.3. Clinician acceptance

The OT was asked the following question: "Based on your experience with this patient, would you consider a 3D-printed splint such as this to be potentially suitable for other patients with closed hand injuries?"

In all ten cases, the OT indicated they would be happy to use a 3D-printed splint in future in place of Stack splints. However, they noted the need to improve aeration and durability to ensure the effectiveness of the splint.

3.4. Patient acceptance

Analysis of the questionnaires revealed a clear patient acceptance of the 3D-printed splint (Table 2). All but one

Table 2. Percentage satisfaction of Stack vs. 3D-printed splint qualities

	% Not satisfied at all		% Not very satisfied		% More or less satisfied		% Quite satisfied		% Very satisfied	
	Stack	3D-printed	Stack	3D-printed	Stack	3D-printed	Stack	3D-printed	Stack	3D-printed
Dimensions	0	0	20	0	50	10	20	40	10	50
Weight	0	0	10	0	40	0	40	50	10	50
Ease in adjusting	0	0	40	0	20	10	20	40	20	50
Safe and secure	0	10	30	10	40	20	20	10	10	60
Durability	10	0	10	0	10	10	20	60	50	30
Easy to use	10	0	20	0	40	10	20	40	10	50
Comfort	10	0	20	0	20	0	20	40	30	60
Effective	0	0	10	10	60	10	20	10	10	70
Easy to remove for hand washing	10	0	10	0	30	10	30	20	20	70
Easy to reapply after hand washing	10	0	0	0	50	0	30	30	10	70

patient said they would choose the 3D-printed splint again if they had reason to use it (90%).

(i) In relation to dimensions, 50% of patients rated the 3D-printed splint as being very satisfactory compared to 10% for the Stack splint.

(ii) In relation to the weight of the splint, 50% of patients rated the 3D-printed splint as very satisfactory compared to 10% for the Stack splint.

(iii) In relation to ease in adjusting, 50% of patients rated the 3D-printed splint as being very satisfactory compared to 20% for the Stack splint.

(iv) In relation to how safe and secure the splint felt, 60% of patients rated the 3D-printed splint as very satisfactory compared to 10% for the Stack splint.

(v) In relation to durability, 30% of patients rated the 3D-printed splint as very satisfactory in comparison to 50% for the Stack splint.

(vi) In relation to ease of use, 50% of patients rated the 3D-printed splint as very satisfactory compared to 10% for the Stack splint.

(vii) In relation to comfort, 60% of patients rated the 3D-printed splint as very satisfactory compared to 30% for the Stack splint.

(viii) In relation to effectiveness, 70% of patients rated the 3D-printed splint as very satisfactory compared to 10% for the Stack splint.

(ix) In relation to ease of removing for hand washing, 70% of patients rated the 3D-printed splint as very satisfactory compared to 20% for the Stack splint.

(x) In relation to ease of reapplying after hand washing, 70% of patients rated the 3D-printed splint as very satisfactory compared to 10% for the Stack splint.

3.5. Patient feedback

Most patients commented on how much lighter the 3D-printed splint was. They also commented that the 3D-printed splint was at times more difficult to remove for hand hygiene because it had a tighter fit than the generic Stack splint (Figures 3 and 4). This was contrary to the original belief that the Stack splint would be tighter because it was applied for the first 7 days post injury when the finger would most likely be swollen. Patients cited this tightness as a positive during the questionnaire. They felt the splint was more comfortable because it fit neatly. Patients commented that they felt immediate relief when the 3D-printed splint was applied after the generic Stack splint.

Patients reported their injured finger swelling and decreasing at times throughout the study. Some patients developed skin complications when wearing the generic Stack splint. The lack of a custom fit caused the splint to rub against the skin, leading to blisters and discomfort. Figure 5A shows an example of an ill-fitting generic Stack splint, and Figure 5B shows skin maceration secondary to an ill-fitting generic Stack splint.

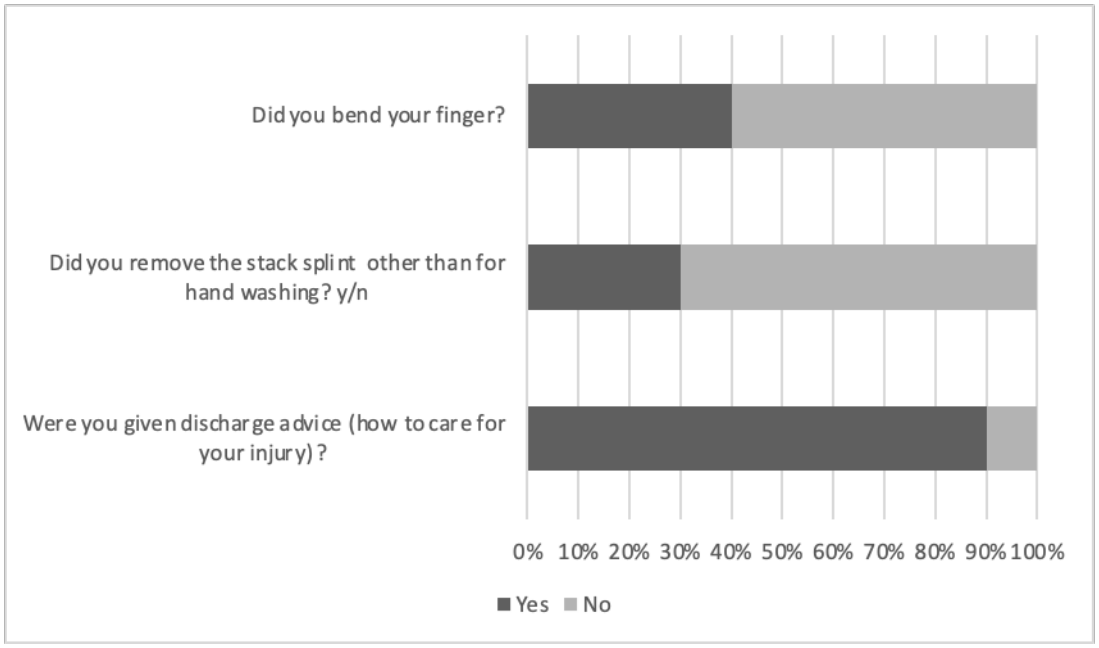

Figure 3. Stack splint foundational questions.

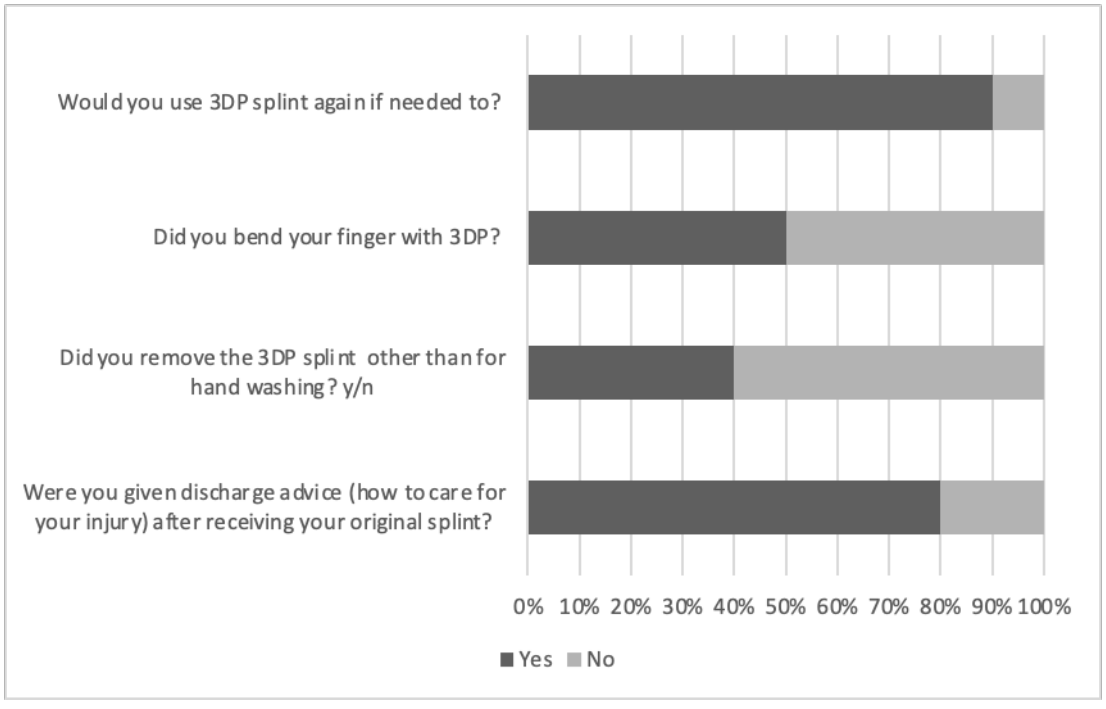

Figure 4. 3D-printed splint foundational questions. Abbreviation: 3DP, 3D-printed.

Patients were asked if they were given discharge advice (how to care for your injury) after receiving their original splint; 90% of them answered yes. Patients were then asked if they bent their finger at any point throughout their treatment; 40% of patients reported that they did not bend their finger at any time throughout their treatment.

Nine of the ten patients reported that the 3D-printed splint began to warp and lose its structure from week 4

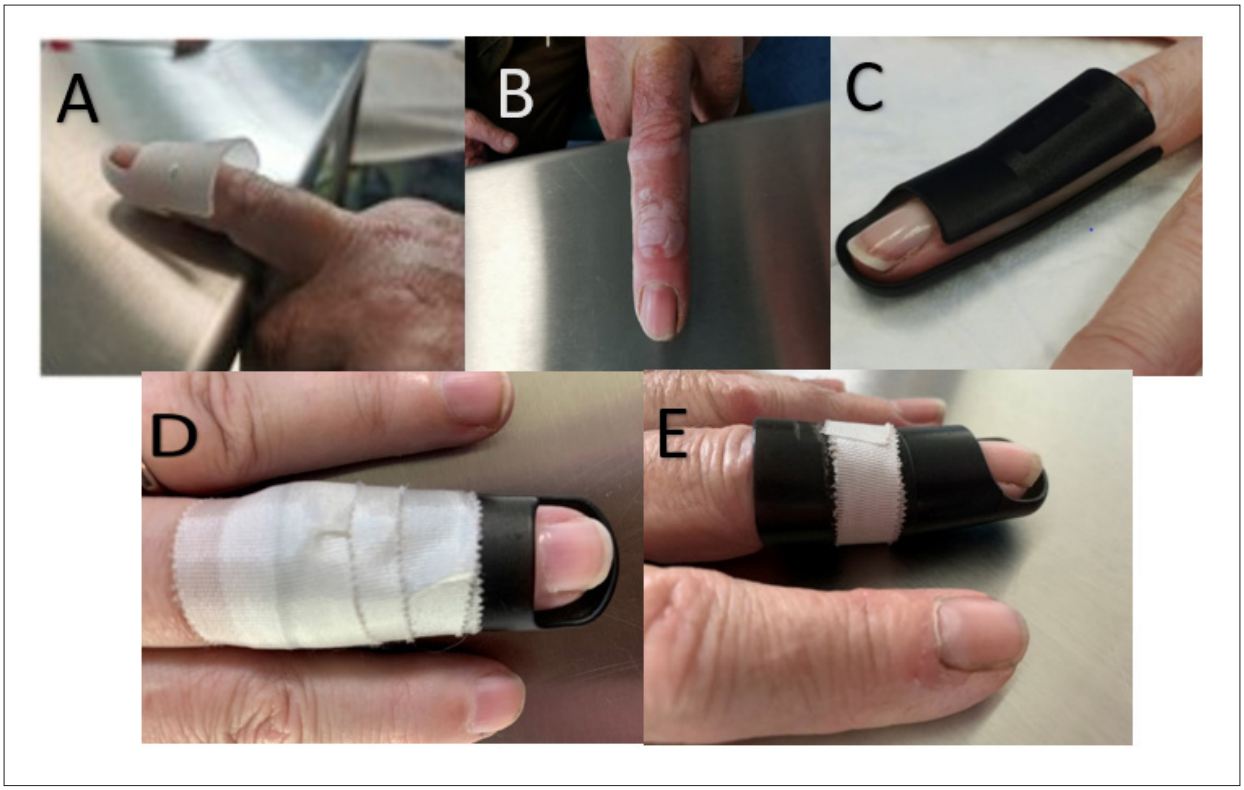

Figure 5. Selected patient photos showing generic versus 3D-printed custom splint. (A) Ill-fitting Stack splint; (B) skin maceration from ill-fitting Stack splint; (C) air-vent opening displayed along the side of the 3D-printed splint; (D) over-taping, which causes blocking of the airflow in a 3D-printed splint; (E) light taping, which secures the splint and allows airflow in the 3D-printed splint.

onward. This is an important finding because this decline in the mechanical properties of a 3D-printed material has been reported previously and needs to be addressed in future research.[29] This may explain why the Stack splint was rated higher than the 3D-printed splint in relation to durability (30% of patients rated the 3D splint as very satisfactory in comparison to 50% for the Stack splint for durability).

Patients also reported that the 3D-printed splint was at times warm and commented that better air flow could increase comfort. This is again an important finding as improving airflow, thus comfort, will be a key focus on the next iteration. On analyzing how patients were taping the 3D-printed splint, those who mentioned the splint was too hot at times and required improved air flow had over-taped the splint. Figure 5C shows the air vent along the side of the 3D-printed splint. Figure 5D displays over-taping causing a blockage of air flow through the 3D-printed splint, and Figure 5E shows light taping to secure the splint and allow airflow. Despite over-taping being a possible cause to the 3D-printed splint feeling hot at times, the material used for 3D printing of mallet splints needs addressing in relation to warping and airflow.

Patients commented that not having to use tape to secure the 3D-printed splint would have been an added bonus as trying to secure the splint alone can be cumbersome. One patient did not wear tape throughout the study and did not experience the splint falling off. However, nine out of ten patients wore tape throughout to secure the splint.

3.6. Patient quotes

Regarding the generic Stack splint, one patient commented that it "*wasn't much good*" to them. The patient found it "*clumsy, too big*" and that it got "*caught in clothes and bed clothes*" while performing activities of daily living (ADLs). The patient also reported that the 3D-printed splint, although much improved and being a better fit, was "*sweaty*" and "*needed more ventilation.*" Patients commented that the Stack splint seemed "*better ventilated as [sic] had holes*" and "*felt more airy.*"

Patients commented that wearing either splint throughout the day was difficult in relation to performing ADLs. Many found wearing a glove useful to keep the splints dry. However, they noted the need for *"extra care removing the glove as [sic] can pull the splint away.*" They also noted that it "*increases sweating.*"

Some patients commented that on hot days, or when busy using their hands, their injured finger could swell at times. In relation to the generic Stack splint, they said "*as this didn't fit well, I had space to swell.*" Conversely, in relation to the custom-fit 3D-printed splint, they said "*there was less space to swell so it could feel tight at times.*"

Part of the recovery for mallet injury involves flexing the PIPj. Allowing and encouraging flexion of the PIPj reduces difficulty with range of movement and recovery when the splint is removed. It also improves functional use of the hand during the DIPj immobilization period. Patients commented that they felt a much better range of movement with the 3D-printed splint than the Stack splint. Patients also commented that they "*couldn't bend the finger at all*" with the generic Stack splint because "*it was too long*" and covered the joint.

4. Discussion

This research uncovers a clinical benefit, albeit in a small cohort. This was a pilot study involving ten patients. Future studies assessing statistical aspects should consider the power of such study to ascertain the number of patients. Patients successfully recovered using the 3D-printed splint as evidenced by the Crawford classification scale used by the OT. The findings—40% of patients made an excellent recovery and 40% made a good recovery—are promising. This is the first study to show a clinical benefit by supporting multiple patients in their recovery from mallet injury using a 3D-printed mallet splint.

The study also shows an acceptance of a 3D-printed mallet splint. Both patients and an OT confirmed they would use the splint again if needed, with modifications. These findings are encouraging and are helpful to expand research in the use of 3D printing for mallet finger injuries going forward. However, it is important to note that mallet finger injuries tend to swell mostly during the first week of injury, thus a generic Stack splint was used during that period in the current study. Patients may have reported relief on the fitting of the 3D-printed mallet splint due to a reduction of swelling and not solely due to the bespoke fit.

Key areas of focus in this study were measuring finger dimensions, patient requirements, design of the 3D-printed splint, patient discharge advice and compliance, and process. These are discussed in the following section along with key findings and recommendations for further research.

4.1. Measurements of finger dimensions

Calipers were used to measure each patient's finger anthropometrics because they were available to the research team and are an accurate measuring method. Moreover, they do not require specialized computer equipment, which would have been impractical in this clinical setting at least.[24] Patients were recruited from three different hospital sites, and this would have necessitated three scanning devices and associated computing requirements. 3D scanning could certainly have a role in bespoke splint design, and further studies should consider this.

4.2. Patient requirements

Mallet injuries require patients to be highly involved and dedicated to their recovery. A splint immobilizes the area to promote healing; however, patients must follow strict discharge guidelines, adhere to hand hygiene, and complete the treatment time. In this study, every patient had experience of both a generic Stack splint and the 3D-printed splint within the same treatment period. Therefore, the ratings of both splints are not just accurate, and they are immediate when the generic Stack is changed to the 3D-printed splint. The 3D-printed splint was applied approximately 7 days after the initial injury. Because the injured finger typically swells during the first 7 days post-injury, it could be argued that the 3D-printed splint was applied at a less swollen and painful time in the patient's recovery. However, the custom fit was a welcome change, affording more comfort, and reducing skin maceration and blistering experienced with the generic Stack splint. Once the 3D-printed splint was fitted, incidence of maceration and blistering was reduced. Patient feedback highlighted some modifications to improve the 3D-printed splint.

4.2.1. Design of splint

The design of the 3D-printed splint aimed to support the healing of the mallet injury while ensuring comfort of using and clinical soundness of the splint. The outcomes of the study are positive clinically, but the following areas were highlighted for improvement: (i) air flow, (ii) securing to the finger, (iii) giving clearance to the PIPj, and (iv) material used.

Modern Stack splints are regularly perforated to allow air flow and increase comfort. Perforations were not included in the 3D-printed splint for this study at the request of the clinical expert who, based on their experience, felt perforations in the splint encourage swelling through the small perforations and can add to skin complications. Instead, a gap was left along the length of the splint to allow for airflow. Patients who found the 3D-printed splint too hot had placed tape around the circumference of the splint and over this gap. Patients who placed a thin layer of tape at the base of the splint reported no issues with airflow. Ventilation is a key element for comfort and to protect the skin. The design therefore needs to evolve to best facilitate

airflow. In addition, discharge advice on how best to secure the 3D-printed splint is essential and needs more focus.

4.2.2. Securing to the finger

Although one of the goals of the initial design was to minimize the use of adhesive tape to secure the splint, patients generally preferred the additional security provided by tape. Patients had been securing the generic Stack splint with tape for several days before wearing the 3D-printed splint and felt more secure continuing with tape. However, the amount of tape required to secure the 3D-printed splint was notably less than that required for the generic splint. It is important to consider designing a splint that does not require any extra taping to make it easier to remove and reapply.

4.2.3. Materials

Patients also reported that the 3D-printed splint fit well on initial application. However, over the 8 weeks, some patients reported that the splint began to change shape, losing its form and distorting. This led to increased use of tape to ensure the splint stayed in place. The distortion can be attributed to the mechanical properties of the 3D printing material and is an important finding for future design iterations. The material needs to be robust and durable enough to last the duration of the treatment. Further research is needed to determine what material to use.

4.2.4. PIPj

It is necessary to keep the PIPj free to flex during mallet finger treatment.[12] Only the DIPj needs to be immobilized. Therefore, when designing a splint for mallet finger treatment, it is essential to allow enough clearance between the base of the splint to the PIPj. Focusing on each patient's anthropometrics as the study progressed ensured the PIPj had adequate clearance to move freely.

In addition to some modifications needed for the 3D-printed splint, the process used for this study worked well as a research study but needs careful consideration to be made logistically possible in healthcare facilities. Currently, generic Stack splints are the most common offering for treatment of mallet finger injuries. One unit in the ULHG provides custom splinting from the OT team on a limited basis. Although the 3D-printed splint was found to be more acceptable to patients in this study, there are barriers to the roll out of this service across healthcare units.

4.3. Process challenges

Based on the findings of this small pilot study, the introduction of 3D-printed mallet splints for patients in hospitals would appear to be a welcome treatment option. Patterson et al. report that the use of 3D printing in hand therapy is still very much in its infancy.[30] They attribute this to the absence of purpose-built software programs for splint design. There is, therefore, a considerable learning curve for healthcare practitioners to become proficient in designing splints.

There are many steps required to bring this 3D-printed splint option to patients. The development of 3D printing technologies has progressed at a rapid pace since its introduction in the late 1980s. Regulation on the use of 3D printing for healthcare applications is often unclear.[31] However, some guidance is forming; ISO 52910 outlines guidelines on the use of additive manufacturing in product design and is applicable to all products fabricated by any type of additive manufacturing.[32] Until this guidance is clear and appropriate for medical applications, the use of 3D printing outside of research studies will be curtailed. Nonetheless, it is important to discuss key steps in the process to help visualize a future for 3D printing for mallet finger injuries in hospitals.

One area this study highlighted as challenging is the immediate need for a custom 3D-printed splint to treat a patient. Patients presenting at hospital with a mallet injury require timely treatment. The procedure in this study involved first applying the generic Stack splint to each patient for a number of days to allow the research team time to coordinate the measuring, printing, and fitting of the 3D-printed splint. As a measuring technician is not based in each unit, and the appropriate 3D printer is not present in each unit, some additional steps would be needed to offer an immediate 3D-printed mallet splint.

4.4. Discharge advice and compliance

There are many studies detailing how patients are often discharged without a clear understanding of their discharge advice.[33-35] This can lead to confusion, frustration, poor compliance, and clinical complications for patients.

Mallet injuries require patients to closely follow their discharge advice to support their recovery. It is therefore essential to provide clear, concise discharge advice to ensure patients can care for their injury while at home. It is equally important to ensure patients understand the advice given.

A study conducted by Groth et al. looked at the impact of compliance on the rehabilitation of patients with mallet finger injuries.[36] They revealed that compliant patients have excellent outcomes more often than non-compliant patients (61.5% and 9.1%, respectively). Two of the patients enrolled in this study did not comply with discharge advice. One removed the splint before completing their treatment,

and the other bent the finger throughout the course of the study. This was an unfortunate misunderstanding and one that reinforces the importance of ensuring patients fully understand how to care for their injury before being discharged.

4.5. Implications of findings

This pilot study has shown a clinical benefit of 3D printing splints to treat mallet injuries, albeit in a small cohort. Within the Irish healthcare system, custom splinting is not widely available because specialist roles are not broadly in place. This leads to delays in custom splinting, or patients being provided with a generic Stack splint for the duration of their treatment.

This study provides initial evidence to support custom splinting for hand injuries, emphasizing that patients deserve custom splinting to support healing, comfort, and recovery from their injuries.[37] Using 3D-printed bespoke mallet splints provides a custom fit and therefore improves access to custom care that is otherwise currently limited. To that end, offering 3D-printed mallet splints in EDs and IUs should be considered. By expanding research beyond the current offering of feasibility and pilot studies, a focus on clinical outcomes of 3D-printed mallet splints on a wider scale could provide the data-driven evidence needed to change the current healthcare splinting options.

4.6. Future work

There are some further research considerations arising from this study. Patient and clinician acceptance along with clinical efficacy were the key areas of focus for this pilot study. One consideration is the cost implications of 3D-printed mallet splints versus generic Stack splints. A health economics review of the resources, equipment, and infrastructure required to implement 3D printing of mallet splints is beyond the scope of this current study, but future studies should consider this. Other areas for further consideration include:

- An optimal method to measure mallet fingers for 3D printing
- The ventilation of 3D-printed mallet splints
- Methods of securing the splint
- Finding the optimum 3D printing material for use in the printing of mallet splints
- Defining the process for providing 3D-printed mallet splints outside the research realm

5. Conclusions

This study aimed to evaluate the clinical outcome along with patient and HCP acceptance of bespoke 3D-printed mallet splints for the treatment of mallet finger injury. The patients and a specialist hand OT felt that they would use the 3D-printed splint over the generic Stack splint if needed again. 3D printing has been demonstrated as a viable method for producing bespoke devices for patients with mallet injury, albeit on a small scale. There is potential for 3D printing to produce mallet injury splints, which could provide an enhanced clinical offering over traditional splinting methods. By using patient-centered, bespoke 3D printing capabilities, the management of mallet injuries can be improved and custom splinting offered to a wider population.

Acknowledgments

None.

Funding

This publication has emanated from research supported by Science Foundation Ireland (SFI) under Grant Numbers SFI 16/RC/3918 co-funded by the European Regional Development Fund.

Conflict of interest

The authors declare no conflicts of interest.

Author contributions

Conceptualization: Damien Ryan
Formal analysis: Kevin J. O'Sullivan
Funding acquisition: Leonard W. O'Sullivan
Investigation: Una M. Cronin, Aidan O'Sullivan, Margo Sheerin
Project administration: Una M. Cronin
Resources: Aidan O'Sullivan
Supervision: Niamh Cummins, Damien Ryan, Leonard W. O'Sullivan
Validation: Kevin J. O'Sullivan
Visualization: Una M. Cronin
Writing – original draft: Una M. Cronin
Writing – review and editing: Una M. Cronin, Aidan O'Sullivan, Kevin J. O'Sullivan, Niamh Cummins, Damien Ryan, Leonard W. O'Sullivan

Ethics approval and consent to participate

This study was approved by the Research Ethics Committee of ULHG (Reference 087/2022). Written informed consent was obtained from all participants prior to the study.

Consent for publication

Patients were given and requested to read Patient Information Leaflets before signing consent forms.

Permission was obtained from each of the subjects to *publish* their data and images.

Availability of data

The data that support the findings of this study are not openly available but are available from the corresponding author upon reasonable request. Data are located in controlled access data storage at the University of Limerick.

References

1. Clayton RA, Court-Brown CM. The epidemiology of musculoskeletal tendinous and ligamentous injuries. *Injury*. 2008;39(12):1338-1344. doi: 10.1016/j.injury.2008.06.021
2. Xiao M, Yao Y, Fan C, et al. Multiple H-bonding chain extender-based polyurethane: ultrastiffness, hot-melt adhesion, and 3D printing finger orthosis. *Chem Eng J*. 2022;433:133260. doi: 10.1016/j.cej.2021.133260
3. Bendre AA, Hartigan BJ, Kalainov DM. Mallet finger. *J Am Acad Orthop Surg*. 2005;13(5):336-344. doi: 10.5435/00124635-200509000-00007
4. Khera BH, Chang C, Bhat W. An overview of mallet finger injuries. *Acta Biomed*. 2021;92(5):e2021246. doi: 10.23750/abm.v92i5.11731
5. Kleinbaum Y, Heyman Z, Ganel A, Blankstein A. Sonographic imaging of mallet finger. *Ultraschall Med*. 2005;26(03):223-226. doi: 10.1055/s-2005-858165
6. Griffin M, Hindocha S, Jordan D, Saleh M, Khan W. Management of extensor tendon injuries. *Open Orthop J*. 2012;6:36-42. doi: 10.2174/1874325001206010036
7. Alla SR, Deal ND, Dempsey IJ. Current concepts: mallet finger. *Hand*. 2014;9(2):138-144. doi: 10.1007/s11552-014-9609-y
8. Garberman SF, Diao E, Peimer CA. Mallet finger: results of early versus delayed closed treatment. *J Hand Surg*. 1994;19(5):850-852. doi: 10.1016/0363-5023(94)90200-3
9. Güven E, Suner-Keklik S. Custom-made finger splint versus prefabricated finger splint: finger flexion stabilization. *Rev Assoc Med Bras*. 2022;68(7):935-938. doi: 10.1590/1806-9282.20220093
10. Pike J, Mulpuri K, Metzger M, Ng G, Wells N, Goetz T. Blinded, prospective, randomized clinical trial comparing volar, dorsal, and custom thermoplastic splinting in treatment of acute mallet finger. *J Hand Surg Am*. 2010;35(4):580-588. doi: 10.1016/j.jhsa.2010.01.005
11. O'Brien LJ, Bailey MJ. Single blind, prospective, randomized controlled trial comparing dorsal aluminum and custom thermoplastic splints to stack splint for acute mallet finger. *Arch Phys Med Rehabil*. 2011;92(2):191-198. doi: 10.1016/j.apmr.2010.10.035
12. Minchin P, Spirtos M. Investigation of the conservative management of mallet injury in Irish acute hospitals. *Hand Ther*. 2012;17(2):28-36. doi: 10.1258/ht.2012.012004
13. Valdes K, Naughton N, Algar L. Conservative treatment of mallet finger: a systematic review. *J Hand Ther*. 2015;28(3):237-246. doi: 10.1016/j.jht.2015.03.001
14. Katzman B, Klein D, Mesa J, Geller J, Caligiuri D. Immobilization of the mallet finger: effects on the extensor tendon. *J Hand Surg*. 1999;24(1):80-84. doi: 10.1016/s0266-7681(99)90041-4
15. Rayan GM, Mullins PT. Skin necrosis complicating mallet finger splinting and vascularity of the distal interphalangeal joint overlying skin. *J Hand Surg Am*. 1987;12(4):548-552. doi: 10.1016/s0363-5023(87)80206-x
16. Vaz VM, Kumar L. 3D printing as a promising tool in personalized medicine. *AAPS PharmSciTech*. 2021;22:1-20. doi: 10.1208/s12249-020-01905-8
17. Kermavnar T, Shannon A, O'Sullivan KJ, McCarthy C, Dunne CP, O'Sullivan LW. Three-dimensional printing of medical devices used directly to treat patients: a systematic review. *3D Print Addit Manuf*. 2021;8(6):366-408. doi: 10.1089/3dp.2020.0324
18. Wong JY. On-site 3D printing of functional custom mallet splints for Mars analogue crewmembers. *Aerosp Med Hum Perform*. 2015;86(10):911-914. doi: 10.3357/AMHP.4259.2015
19. Choi H, Seo A, Lee J. Mallet finger lattice casts using 3D printing. *J Healthc Eng*. 2019;2019:4765043. doi: 10.1155/2019/4765043
20. Zolfagharian A, Gregory TM, Bodaghi M, Gharaie S, Fay P. Patient-specific 3D-printed splint for mallet finger injury. *Int J Bioprint*. 2020;6(2):259. doi: 10.18063/ijb.v6i2.259
21. Papavasiliou T, Shah RK, Chatzimichail S, Uppal L, Chan JC. Three-dimensional printed customized adjustable mallet finger splint: a cheap, effective, and comfortable alternative. *Plast Reconstr Surg Glob Open*. 2021;9(3):e3500. doi: 10.1097/GOX.0000000000003500
22. Chhikara K, Gupta S, Saharawat S, Sarkar S, Chanda A. Design, manufacturing, and trial of a 3D printed customized finger splint for patients with rheumatoid arthritis. *Rheumato*. 2023;3(1):51-62. doi: 10.3390/rheumato3010004
23. Nam H-S, Seo CH, Joo S-Y, Kim DH, Park D-S. The application of three-dimensional printed finger splints for

post hand burn patients: a case series investigation. *Ann Rehabil Med*. 2018;42(4):634-638.
doi: 10.5535/arm.2018.42.4.634

24. Gupta A, Chaturvedi S, Bhat AK, Samheel M. Design and manufacture of customizable finger immobilizer and mallet finger splints. In: *Proceedings of the 2019 International Conference on Biomedical Innovations and Applications (BIA)*. IEEE; 2019:1-4.
doi: 10.1109/BIA48344.2019.8967477

25. Teoh T, Powell J, Kelly J, et al. Outcomes of point-of-care testing for influenza in the emergency department of a tertiary referral hospital in Ireland. *J Hosp Infect*. 2021;110:45-51.
doi: 10.1016/j.jhin.2021.01.004

26. Lamaris GA, Matthew MK. The diagnosis and management of mallet finger injuries. *Hand*. 2017;12(3):223-228.
doi: 10.1177/1558944716642763

27. Mezzio AJ, Valdes K. Determining patient satisfaction with an upper and lower extremity orthotic intervention using the QUEST 2.0: a systematic review. *Technol Disabil*. 2019;31(4):141-151.
doi: 10.3233/TAD-190247

28. Altan E, Alp NB, Baser R, Yalçın L. Soft-tissue mallet injuries: a comparison of early and delayed treatment. *J Hand Surg*. 2014;39(10):1982-1985.
doi: 10.1016/j.jhsa.2014.06.140

29. Shahrubudin N, Koshy P, Alipal J, Kadir M, Lee T. Challenges of 3D printing technology for manufacturing biomedical products: a case study of Malaysian manufacturing firms. *Heliyon*. 2020;6(4):e03734.
doi: 10.1016/j.heliyon.2020.e03734

30. Patterson RM, Salatin B, Janson R, Salinas SP, Mullins MJS. A current snapshot of the state of 3D printing in hand rehabilitation. *J Hand Ther*. 2020;33(2):156-163.
doi: 10.1016/j.jht.2019.12.018

31. Willemsen K, Nizak R, Noordmans HJ, Castelein RM, Weinans H, Kruyt MC. Challenges in the design and regulatory approval of 3D-printed surgical implants: a two-case series. *Lancet Digit Health*. 2019;1(4): e163-e171.
doi: 10.1016/S2589-7500(19)30067-6

32. Kawalkar R, Dubey HK, Lokhande SP. A review for advancements in standardization for additive manufacturing. *Mater Today Proc*. 2022;50:1983-1990.
doi: 10.1016/j.matpr.2021.09.333

33. Clarke C, Friedman SM, Shi K, Arenovich T, Monzon J, Culligan C. Emergency department discharge instructions comprehension and compliance study. *CJEM*. 2005;7(1):5-11.
doi: 10.1017/s1481803500012860

34. Engel KG, Buckley BA, Forth VE, et al. Patient understanding of emergency department discharge instructions: where are knowledge deficits greatest? *Acad Emerg Med*. 2012;19(9):E1035-E1044.
doi: 10.1111/j.1553-2712.2012.01425.x

35. Hastings SN, Barrett A, Weinberger M, et al. Older patients' understanding of emergency department discharge information and its relationship with adverse outcomes. *J Patient Saf*. 2011;7(1):19-25.
doi: 10.1097/PTS.0b013e31820c7678

36. Groth GN, Wilder DM, Young VL. The impact of cormpliance on the rehabilitation of patients with mallet finger injuries. *J Hand Ther*. 1994;7(1):21-24.
doi: 10.1016/S0894-1130(12)80037-8

37. Waldburger L, Schaller R, Furthmüller C, Schrepfer L, Schaefer DJ, Kaempfen A. 3D-printed hand splints versus thermoplastic splints: a randomized controlled pilot feasibility trial. *Int J Bioprint*. 2022;8(1):474.
doi: 10.18063/ijb.v8i1.474

ACCSCIENCE PUBLISHING

International Journal of Bioprinting

RESEARCH ARTICLE

Bottom-up and top-down VAT photopolymerization bioprinting for rapid fabrication of multi-material microtissues

Daniel Nieto[1]*, Alberto Jorge de Mora[2], Maria Kalogeropoulou[1], Anant Bhusal[3], Amir K. Miri[4], and Lorenzo Moroni[1]

[1]Complex Tissue Regeneration Department, MERLN Institute for Technology Inspired Regenerative Medicine, Universiteitssingel 40, 6229ER Maastricht, The Netherlands

[2]University Hospital of Santaigo de Compostela, Galicia, Spain

[3]Department of Mechanical Engineering, Rowan University, NJ 08028, USA

[4]Department of Biomedical Engineering, New Jersey Institute of Technology, Newark, NJ 07102, USA

(This article belongs to the *Special Issue: Advanced light-based bioprinting*)

Abstract

Over the years, three-dimensional (3D) bioprinting has attracted attention for being a highly automated manufacturing system that allows for the precise design of living constructs where cells and biomaterials are displaced in predefined positions to recreate cell–matrix and cell–cell interactions similar to native tissues. Such technologies rarely offer multi-material features. In this paper, we present a new approach for bioprinting of multi-material tissue constructs using VAT photopolymerization at high resolution and fidelity. We developed a versatile dual-mode bioprinter that can easily be modulated to print in both top-down and bottom-up approaches. The custom-built platform was then used to fabricate microtissues and hydrogel microfluidic models. Combining bottom-up and top-down biofabrication tools can offer an optimal solution for hard–soft multi-material composites and for bioprinting tissue–tissue interface models. We demonstrated the possibility for hard–soft multi-material bioprinting by generating musculoskeletal tissue with integrated microvasculature. Combining multiple material bioprinting and microfluidic chips shows advantages in two aspects: precise regulation of microenvironment and accurate emulation of multi-tissue interfaces.

Keywords: VAT photopolymerization; Digital light processing; Multi-material bioprinting; Microtissues; Bottom-up and top-down bioprinting; Musculoskeletal tissue

***Corresponding author:**
Daniel Nieto
(daniel.nieto@udc.es)

Citation: Nieto D, Jorge de Mora A, Kalogeropoulou M, Bhusal A, Miri AK, Moroni L. Bottom-up and top-down VAT photopolymerization bioprinting for rapid fabrication of multi-material microtissues. *Int J Bioprint*. 2024;10(2):1017. doi: 10.36922/ijb.1017

Received: May 30, 2023
Accepted: July 18, 2023
Published Online: April 2, 2024

1. Introduction

Three-dimensional (3D) bioprinting has been benchmarked as a promising technology for creating disease models and microtissues for drug screening applications[1-4]. The main working principle of this technology, and its ultimate goal, is the fabrication of 3D artificial tissues that can closely replicate the natural biological microenvironments of native tissues, using a wide range of biomaterials laden with living cells[5]. Such microtissue models can be further integrated into microfluidic encasements containing chambers

and channels, in which cells can expand and grow, and finally, build functional organ parts *in vitro*[6-8]. However, native tissues and organs possess inherent heterogeneity in physical, mechanical, and biological properties[9]. In order to capture this heterogeneity, the combination of multiple materials with distinct mechanical properties as well as different cell types is necessary. Recent advancements in tissue engineering evidenced the fabrication of multi-tissue models, which can closely imitate organ-to-organ interfaces, in order to investigate the complex interactions and monitor the dynamic responses of multiple organs to pharmaceutical compounds. Multi-tissue microfluidic platforms have been developed to model lung[10], liver[11], intestine[12], kidney[13], brain[14], and heart[15]. Thus, it becomes apparent that the use of 3D bioprinting for the recreation of microphysiological systems of tissue–tissue interfaces can expand the capabilities of the existing tissue models[16-18].

The bioprinting technologies currently used for the fabrication of living tissue models can be divided into three broad categories, namely extrusion- and jetting-based bioprinting as well as VAT photopolymerization. Extrusion bioprinting uses pressure generated by a pneumatic or mechanical system, or a combination of both, to deposit cell-loaded bioinks[19]. It is a relatively inexpensive process that allows high printing speeds and provides precise control over the porosity and mechanical properties of the final constructs, making it an attractive method for producing harder tissue scaffolds. Extrusion has been used at high cell densities, but the choice of available biomaterials is relatively limited, as the rheological properties of the biotins are critical to cell viability. Apart from the properties of the bioinks, the printing speed directly affects the shear stress to which the cells are subjected during printing. Therefore, the resolution of the final scaffold may need to be limited to avoid cell apoptosis[20]. On the other hand, inkjet bioprinting is based on continuous (continuous inkjet, CI) or discrete (drop-on-demand, DOD) deposition of a liquid biomaterial onto a substrate. This bioprinting method has been used to produce cell-loaded scaffolds with high resolution and good shape fidelity, which are good candidates for soft tissue bioprinting[21]. However, the major disadvantage of inkjet bioprinting is the risk of needle clogging, which can interrupt the printing process and expose the cells to high shear stress, negatively affecting cell viability.

VAT photopolymerization bioprinting technologies include light-based methods, namely laser-based bioprinting, stereolithography (SLA), and digital light processing (DLP)[22]. Laser-based printing offers good resolution and high fabrication speeds but has not been successfully combined with cells because of the problems associated with using laser light with living material[23]. SLA generally uses ultraviolet (UV) light to selectively solidify a light-sensitive bioink layer by layer. It can produce 3D structures with good resolution and can be combined with hydrogel-based bioinks, allowing significant control over the resulting matrix properties[24,25]. Similar to SLA, DLP is a technology based on the layer-by-layer crosslinking of photosensitive inks by exposure to a projection mask[26]. The projection of light can be achieved via liquid crystal displays (LCDs) and digital micromirror devices (DMDs), which focus the light as square voxel patterns on the surface of the ink[27]. Due to the non-contact nature of light, SLA and DLP are attractive bioprinting methods because they do not have the problems associated with contact-based bioprinting (e.g., clogging, shear stress)[22,28].

Current bioprinting methodologies are mostly limited by printing single material tissue models[29], and the available multi-material are less cost-effective and time-consuming[30]. Additionally, they are not able to bioprint cell-laden constructs with multi-material components in relevant clinical dimensions. Extrusion bioprinting was demonstrated for multi-material human umbilical vein endothelial cells (HUVECs)[31]. Likewise, 3D human renal proximal tubules were printed for replicating a human kidney-on-a-chip and retained viable for 8 weeks[32]. The bioprinting time of the methodologies is in the range of a few hours, indicating that extrusion 3D bioprinting lacks acceptable printing time and resolution of microtissue material fabrication; therefore, multi-material methodologies able of using multiple bioinks for the rapid manufacture of hydrogel-based constructs are still required.

More recently, it has been demonstrated that a multi-material DLP-based bioprinter was developed to fabricate high-resolution microtissues[26]. In addition, Miri *et al.* used a multi-material DLP bioprinting of hydrogel-based microfluidic chips[28], while Zhu *et al.* applied a similar DLP bioprinting for making a pre-vascularized (channels seeded by HUVECs) tissue models[33]. These studies suggest the capacity of DLP-based bioprinting for creating multi-material microtissues[34,35].

Most light-based bioprinters are based on a "top-down" printing approach, where a UV light source located below the bath of the photosensitive biomaterial is used to selectively polymerize it to generate a 3D structure in a layer-by-layer fashion[36]. The "top-down" configuration has been shown to work well with hard materials, resulting in scaffolds with enhanced mechanical properties that can provide sufficient support[37]. However, processing softer materials with this method is still challenging. Recent studies reported an alternative approach, by placing the light source for the projection of the printing pattern above the photosensitive material[38,39], introducing a "bottom-

up" bioprinting method. Using the bottom-up principle, complex soft tissues can be generated from microscale modules as opposed to the top-down approach, which is mostly used for the fabrication of conventional scaffolds. Commercial light-based systems are almost entirely designed to print hard materials and do not offer multi-material features, which, in combination with the challenge of adapting such systems for the use of soft biomaterials (e.g., hydrogels), has hampered their wide implementation in the biofabrication community.

Therefore, although much progress has been made with the above-mentioned bioprinting systems, they fail to recreate multi-material tissue models with different mechanical properties during a single printing session and at relevant clinical printing timeframes. To address this gap, we have developed a versatile dual-mode bioprinter that can easily be modulated to print in both top-down and bottom-up approaches. Combining bottom-up and top-down biofabrication can offer an optimal solution for hard–soft multi-materials composites and for bioprinting tissue–tissue interface models. We have demonstrated the possibility for hard–soft multi-material bioprinting in a single construct by generating a musculoskeletal tissue model. This new system can be implemented to enable the biofabrication of multi-material microtissues.

2. Materials and methods

2.1. Bioprinting system

A custom-made DLP multi-material bioprinter was designed and fabricated as shown in Figure 1a. The DLP bioprinter consists of a digital light projector (Wintech Digital Light Projector DLP6500), a UV light source (385 nm), UV optical lenses (212 mm focal length), and a high-resolution (20 nm) *z*-axis platform (Figure 1b and c). The *z*-axis platform was controlled by a microcontroller (Arduino UNO; Arduino, Italy). A UV mirror was mounted on a rotating platform to allow for switching between the bottom-up and top-down printing configurations, as shown in Figure 1b. The mirror and DLP were horizontally aligned on the same axis, and rotation of 45° in each direction changes the path of the light upward and downward direction in the bioprinter. The bioprinting approach requires positioning of *z*-axis platform along the direction of light. For top-down approach, the biomaterial reservoir is lowered, and the mirror is directed, so the light source is from the top; for bottom-up approach, the reservoir is lifted, and light source is targeted from the bottom of reservoir. In these approaches, the UV light is projected onto the bioink. The 3D models were designed using AutoCAD, converted to two-dimensional (2D) bitmap slices, and converted to dynamic micromirror patterns using a digital micromirror device (DMD) (DLP® LightCrafter™ 6500; Texas Instruments). In the DMD panel, an array of reflective-coated micromirrors generates light patterns with high resolution (1050 × 920) and speed (10 kHz switching rate) (Figure 1c). When the bioink is introduced into the focal plane of the projected image, the digital state of each micromirror can be controlled as either 0 (dark) or 1 (light reflective), resulting in its layer-by-layer photocrosslinking. The lateral resolution of the fabricated object is theoretically limited by the physical size of the DMD mirrors (7.6 μm); however, the lateral experimental print resolution was set to 10 μm. A stage controller (Thorlabs MTS25-Z8 (MTS25/M-Z8) Motorized Translation Stage) was programmed for vertical stage movement, while the UV light source was directed to the DMD panel via an optical path to facilitate light reflection through the optical lenses onto the stage. For microfluidics bioprinting, delivery of different bioinks into the crosslinking area was achieved using a microfluidics chip with a polydimethylsiloxane (PDMS) chamber and a syringe pump (Figure 1d and f). To thoroughly wash away the non-crosslinked bioink, we used phosphate-buffered saline (PBS), and the same process was repeated for the second and the following bioinks. The thickness of the flowing pre-polymer was designed to be around 200 μm. Each bioprinting methodology configuration (bottom-up and top-down) needs some specific adjustment, which is described in sections 3.1 and 3.2, respectively.

For microfluidics bioprinting, the delivery of biomaterial into the crosslinking chamber was regulated by sequential injection of the biomaterial in a PDMS microfluidic chip designed to act as a crosslinking chamber. The microfluidics chamber has diameter of 7 mm. To enhance the adhesion of PEGDA-and GelMA-based bioinks on the platform, the bottom glass substrate of the chip was coated with 3-(trimethoxysilyl)-propyl methacrylate (TMSPMA) Sigma-Aldrich, St. Louis, MO)[17]. Switching from one material to another requires washing steps when printing multi-material structures. Thus, while changing from one material to another, we introduced the DPBS in the culture chamber and dipped the model for washing. The bioink flow is controlled by injecting it into the PDMS chamber consecutively. Subsequently, the non-crosslinked material was removed by PBS washing, and the bioprinting process was repeated using a second bioink.

2.2. Reagents and materials

For the bottom-up biofabrication strategy, poly (caprolactone-co-trimethylene carbonate) urethane acrylate (PCT 50:50) (Mw = 3 kDa) was used. The Photopolymer was synthesized as previously described[33]. For top-down and microfluidics bioprinting, a

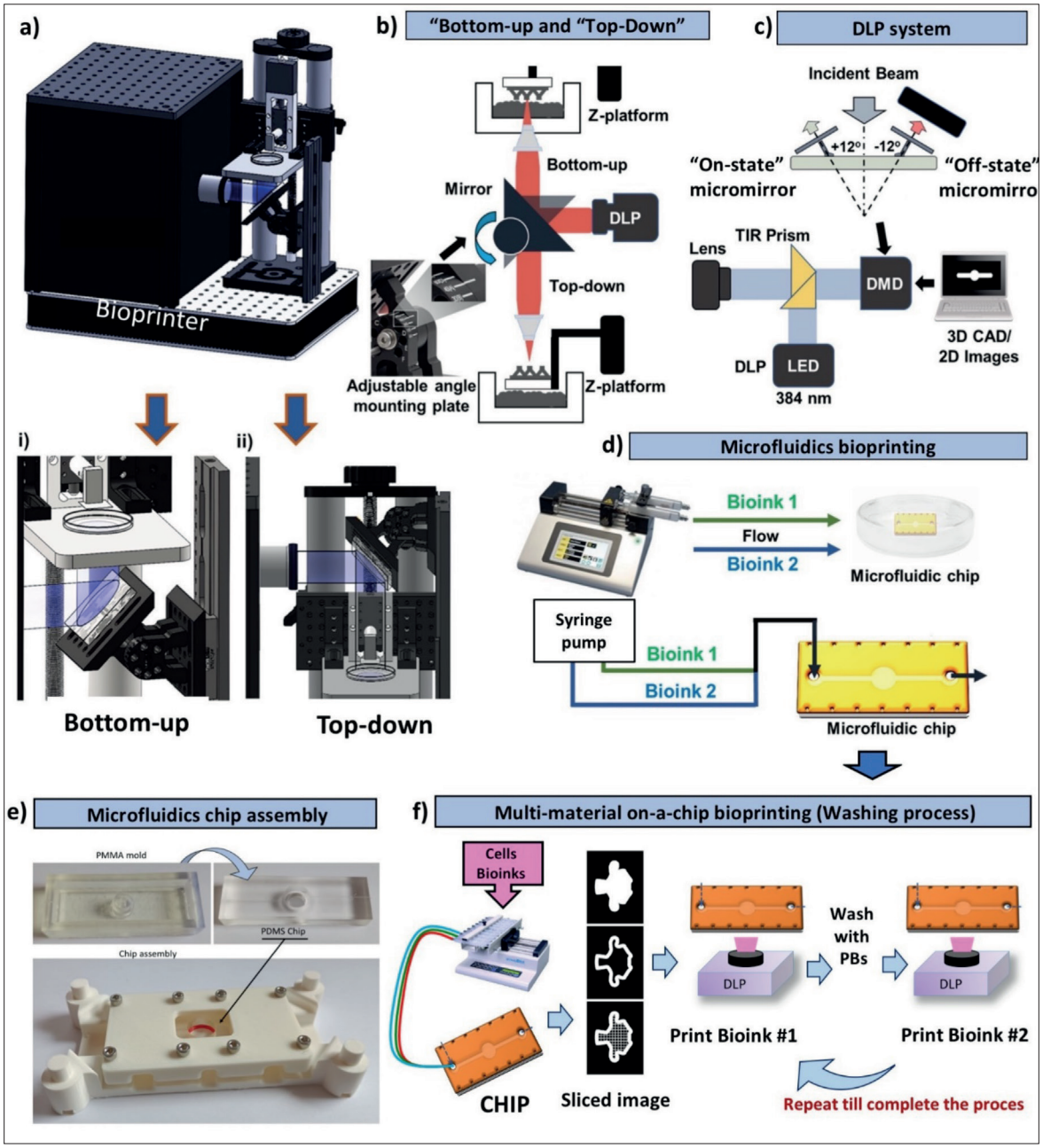

Figure 1. (a) CAD images of the bioprinter showing the (i) bottom-up and (ii) top-down configurations. (b) Schematics showing the setup for selecting top-down and bottom-up configurations. (c) Schematics showing the bioprinter projection setup. (d) Microfluidics setup for on-a-chip bioprinting. (e) Images of the PMMA mold, the casted PDMS chip, and the chip assembly. (f) Illustration of the bioprinting and the washing process between different biomaterials.

photocrosslinkable solution of (poly (ethylene glycol) diacrylate (PEGDA); Mn = 700; Sigma-Aldrich, St. Louis, MO, USA) along with gelatin methacryloyl (GelMA) were used. GelMA was prepared by dissolving porcine skin gelatin (CAS number 9000-70-8; Sigma-Aldrich, St. Louis, MO, USA) and methacrylic anhydride (MA) (CAS number 760-93-0; Sigma-Aldrich, St. Louis, MO, USA) in Dulbecco's phosphate-buffered saline (DPBS). GelMA and PEGDA were used with different concentrations and different photoinitiator (PI) concentrations. For evaluating cell printability, we used GelMA, which has been widely used in various biomedical applications due to its suitable biological properties and tunable physical characteristics. Lithium phenyl-2,4,6-trimethylbenzoylphosphinate (LAP)

(ApolloScientific) was used as a photoinitiator, due to its sensitivity to blue light (absorption peak around 385 nm), which corresponds to the wavelength of the printer's UV light source[22].

2.3. Mechanical testing

Mechanical stiffness of 3D-bioprinted samples was determined by compression testing. Cylindrical samples with diameter (8 mm) and height (4 mm) were printed and tested with a universal testing machine (Shimadzu EZ-SX, Columbia, MD). Displacement-controlled tests were performed at a strain rate of 10% per min. UV exposure time was set up at 0.2 s (for each layer sized ~100 µm). Three tests were performed for each group to achieve statistical significance. The linear slopes of stress–train curves were used as the elastic modulus.

2.4. Microfluidic device design and fabrication

The microfluidic chip was fabricated from polydimethylsiloxane (PDMS) precursor (Sylgard 184; Dow Corning). The chip mold was designed using Autodesk Inventor, and the resulting 3D model was imported to a 3D SLA printer (Formlabs 3). Subsequently, a solution of elastomer and curing agent at a ratio of 10:1 was poured onto the mold, cured at 85°C for 2 h, and peeled off. The resulting microfluidic device consisted of a perforated PDMS brick (75 mm × 25 mm × 8 mm), with one inlet and one outlet at the sides (both 500 µm in diameter). In the middle part of the construct, a circular chamber (Ø 7 mm) was included that also served as the bioprinting site. Stainless steel adaptors (20G) were connected to the inlets/outlets to deliver or remove different bioinks to and from the printing chamber (Figure 1f).

2.5. Cell bioprinting

2.5.1. Cell preparation

To evaluate cell bioprinting, we used mesenchymal stem cells (MSCs), and muscle cells (C2C12). Cell lines were cultured with Dulbecco's Modified Eagle Medium (DMEM; Sigma Aldrich) supplemented with 10% fetal bovine serum (FBS) (Gibco) and 1% penicillin/streptomycin (Sigma) in culture flask under controlled conditions (37°C, 5% CO_2). At 80% of confluence, cells were subcultured using trypsin at 0.25% v/v (Sigma).

Human umbilical endothelial cells (HUVECs) were cultured in DMEM with low sugar, 10% FBS, and 1% penicillin/streptomycin to include the vascular component in our models.

2.5.2. Preparation of bioinks

GelMa (3% w/v)/PEGDA (15% w/v) solution was prepared by dissolving the biomaterials in PBS and then adding lithium phenyl-2,4,6-(LAP). The bioink was mixed, using a syringe, with the cells to a concentration of 1.5×10^6 cells/mL and then loaded into the biomaterial reservoir. Cell-loaded, non-printed hydrogel samples were prepared as a control. Both the printed hydrogels and the controls were placed in P12 well plates with media and cultured under controlled conditions (37°C, 5% CO_2) for 7 days.

2.5.3. Cell proliferation assay

The proliferation rate was evaluated by encapsulating the cells within the hydrogel (n = 3) and growing them in monolayer and was measured by colorimetric AlamarBlue® assay (Bio-Rad Laboratories, Inc., manufactured by Trek Diagnostic Systems, USA). Hydrogels and controls were incubated with 10 µL/100 µL of AlamarBlue® solution for 1 h at 37°C. Subsequently, fluorescence intensity was measured at an excitation wavelength of 530 nm and emission of 590 nm (microplate reader MB-580/530, Heales).

2.5.4. Cell viability assay

The viability of cells in the hydrogel and controls was evaluated by the live/dead assay (Thermo Fisher™) at days 1, 3, and 7 after bioprinting. Briefly, samples were washed twice in PBS, stained with calcein AM and ethidium homodimer-1 (EthD-1) at the concentration indicated by the manufacturer, and incubated for 30 min at room temperature protected by light. Images were taken using a confocal microscope (Nikon Eclipse Ti-E A1, USA) and analyzed with ImageJ (NIH).

2.5.5. Cell migration assays

To visualize the migration inside, the chip HUVECs, MSCs, and C2C12 cell were stained separately with different cell trackers: HUVECs with Cell Tracker Red (CTR; Thermo Fisher), and C2C12 and MSCs with Cell Tracker Green (CTG; Thermo Fisher). After being isolated and added to the 3D construct, all the cell types were incubated for 30 min in PBS with 1 µL/mL of their respective fluorescent dye. They were then washed with PBS. Images were acquired using a confocal microscope (Nikon Eclipse Ti-E A1, USA and Zeiss LSM 710, Germany) equipped with two filters, namely Alexa 594 (CTR) and FITC (CTG).

2.5.6. Statistical analysis

Analysis of variance (ANOVA) and two-tailed Student's t-test were used to determine the statistical significance between different conditions. Cell viability and proliferation results are represented as mean ± standard deviation (SD) from three replicates. A difference between the mean values for each group was considered statistically significant when the p value was less than 0.05.

3. Results

The dual-mode DLP system presented in this study was used for the fabrication of various complex constructs in order to showcase its potential as a novel biofabrication method.

3.1. Complex scaffold printing

In the proposed bottom-up biofabrication strategy for hard tissue bioprinting (Figure 1a(i)), the desired pattern was created by reflecting UV illumination from the DMD array focused on the specific focal plane to crosslink the pre-polymer solutions. The light beam was projected from the bottom of the platform to the polymer solution. As the UV mask was projected, the material stuck to the glass holder mounted onto the *z*-axis platform. The gap between the glass holder and resin platform defines the layer thickness, which is maintained by controlling the movement of *z*-axis based on the fabrication stage. During the fabrication of first layer, the stage was lowered to the pre-defined height, and as the velocity reached zero, the UV mask was projected to fabricate the first layer. For the succeeding layer, the velocity of stage was increased to move the stage in the upward direction, and the new layer was polymerized by a dynamic photomask. The supply of pre-polymer solution was maintained by injecting the polymer into the chamber through a microfluidic chip setup. Fabrication parameters including the depth of pre-polymer stream, curing depth, curing uniformity, and spatial resolution in *X*, *Y*, and *Z* directions were previously optimized for PCT using a range of UV exposure times and intensities using a stereolithography system[33]. To demonstrate the bottom-up bioprinting approach capability, we engineered 3D scaffolds using PCT (Figure 2a(i) and (ii)).

The top-down bioprinting mode (Figure 1a(ii)) was used for the fabrication of soft material constructs. The printing chamber containing a pre-polymer solution was lowered below the adjustable rotational mirror, so the light beam was projected from the top of the platform. The glass

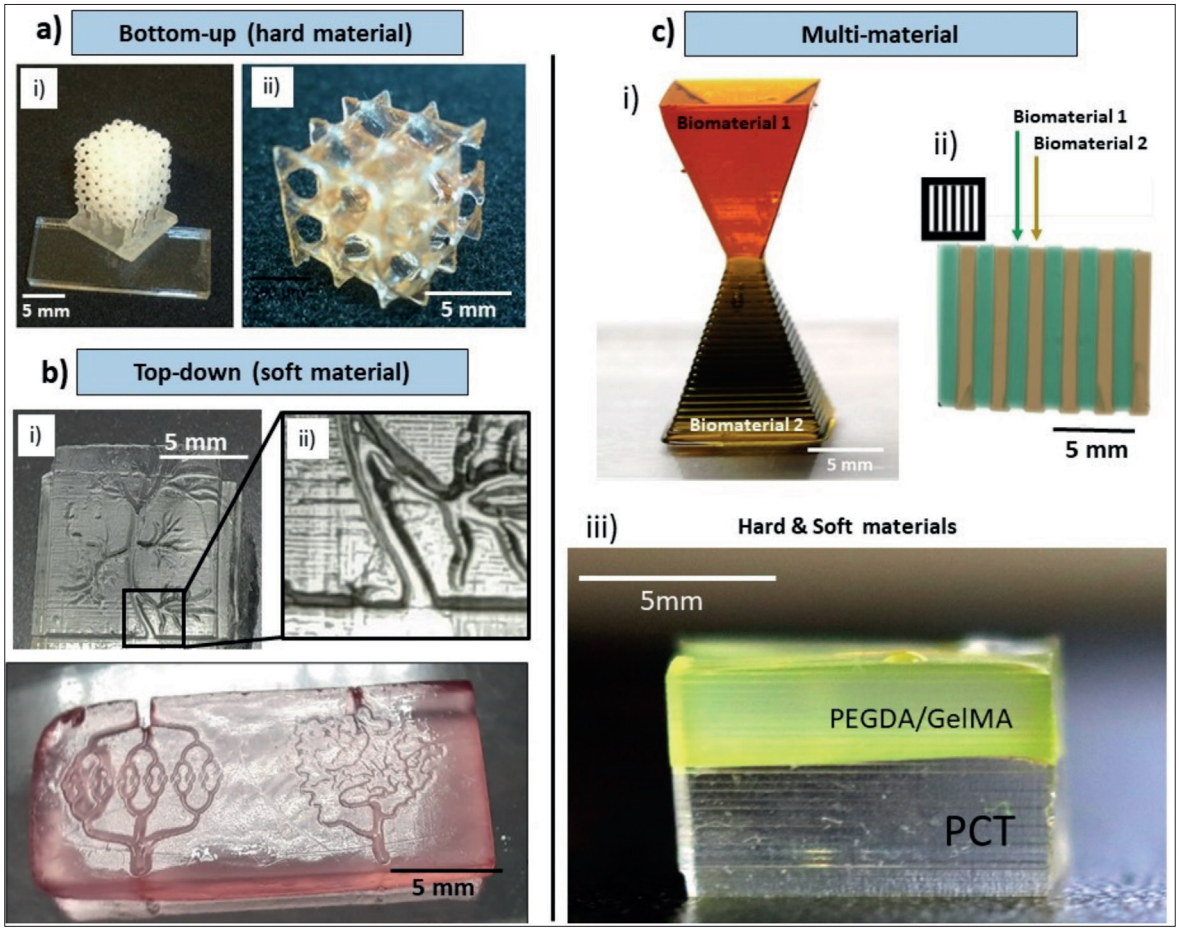

Figure 2. Printability data. (a) Bottom-up: (i, ii) 3D PCT scaffold patterns. (b) Top-down: (i) microvasculature-like shape structures using 60% v/v PEGDA, (ii) sliced and magnified area showing no clogging of channels during printing, (iii) multichannel shapes structures, (c) Multi-material: (i) pyramid-like structure, (ii) multichannel multi-material structure using 5% v/v GelMA and PEGDA 60% v/v, and (iii) hard (PCT) and soft (PEGDA-GelMA) multi-material printed structure.

holder mounted onto the *z*-axis platform was set to a specific focal plane corresponding to the desired layer thickness. The UV mask for the first layer was projected, and the first layer was printed on the glass holder. The stage was then moved downward to print the succeeding layer and so on. To demonstrate the fabrication potential of the top-down approach, a microvascular architecture was printed (Figure 2b) using 60% v/v PEGDA (Figure 2b(i)), and GelMA 5% w/v and PEGDA 15% v/v (Figure 2b(iii)) which highlighted the *XY* resolution of the system, in the order of 10 to 25 μm.

3.2. Dual-mode multi-material bioprinting

The capacity of the bioprinter for multi-material printing was assessed via the fabrication of different 3D structures, such as double pyramid-like structures (Figure 2c(i)) and multi-channel structures (GelMA and PEGDA) (Figure 2c(ii)) and hard (PCT)/soft (PEGDA-GelMA) composite materials (Figure 2c(iii)).

3.3. Mechanical characterization

A key biomimicry feature in tissue engineering is the fabrication of scaffolds with similar mechanical properties to those of native tissues. We tested the stiffness of 3D-bioprinted constructs by PEGDA/GelMA composition, PI mass concentration, and degree of photocrosslinking. The results show tunable stiffness values for the proposed bioink formulations: GelMA/PEGDA/PI (Figure 3a). By increasing the GelMA concentration from 0% to 3% w/v, an increase in the stiffness of PEGDA/GelMA samples was observed. A further increase in GelMA concentration from 3% to 5% w/v had a combined increasing and decreasing effect on the stiffness of PEGDA/GelMA samples. The minimum average elastic modulus obtained was 22 ± 1.0 kPa for 3% w/v GelMA and 15% v/v PEGDA with 0.05% w/v PI, and the maximum modulus was 870 ± 8 kPa for 5% w/v GelMA and 35% v/v PEGDA concentration with 0.1% PI. An increase in the PI concentration increased the final construct stiffness (Figure 3a). The stiffness properties of vascular (~10–100 kPa)[46-47] and muscle tissues (~10–150

a)

GelMA (%)	PEGDA (15%)	PEGDA (25%)	PEGDA (35%)
0.05 % LAP PI – Exposure time 0.2 s (Modulus kPa)			
0	25.0±0.8	43.0±2.0	420±6.0
3	22.0±1.0	44.0±3.0	530±10
5	53.0±2.0	67.0±9.0	650±8.0
0.1 % LAP PI – Exposure time 0.2 s (Modulus kPa)			
0	75.0±2.0	87.0±5.0	870±12.0
3	80.0±3.0	100±7.0	630±5.0
5	54.0±0.8	106±3.0	580±7.0

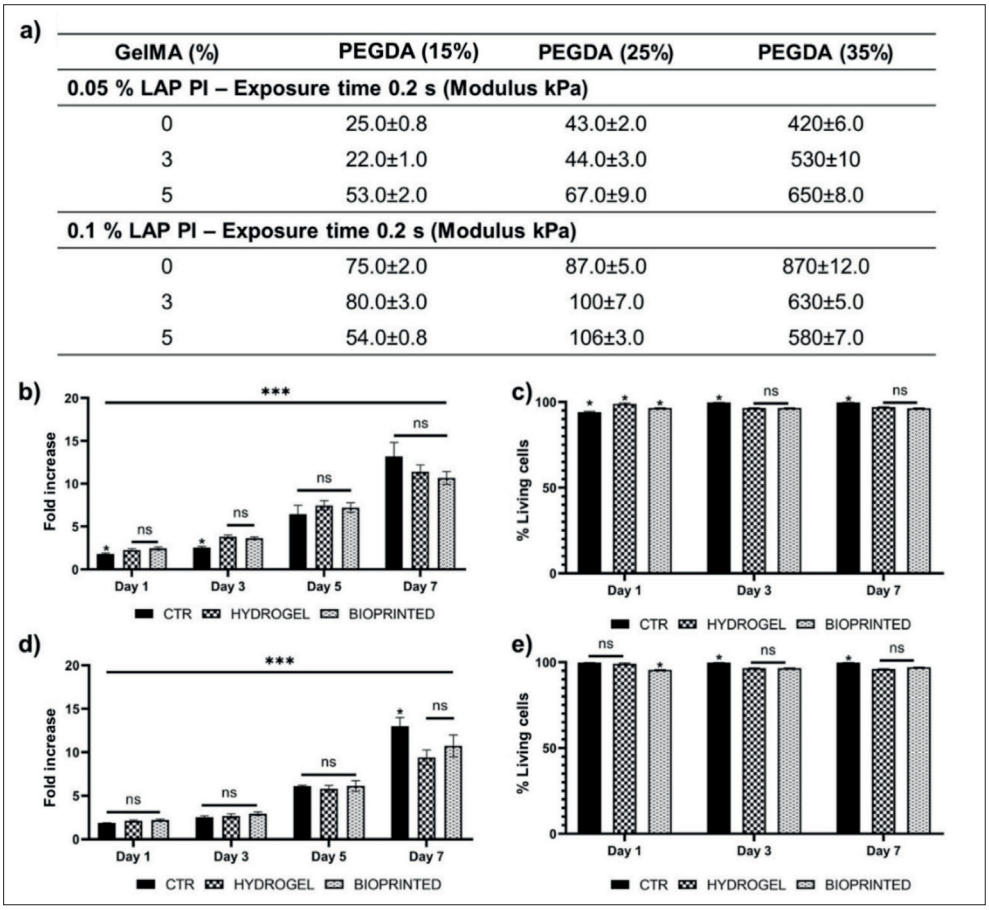

Figure 3. (a) Stiffness values for the proposed bioink formulations: GelMA/PEGDA/PI. (b) Proliferation assay readings for HUVECs encapsulated in GelMA/PEGDA up to day 7. (c) HUVECs viability up to day 7. (d) Proliferation assay readings for C2C12 encapsulated in GelMA/PEGDA up to day 7. (e) C2C12 viability up to day 7. *$p < 0.05$; ***$p < 0.005$; ns: not significant.

kPa)[48] can be imitated by tuning the bioink composition and crosslinking parameters.

3.4. Cell viability and proliferation

The initial results highlight the potential of this new bioprinting approach to create multi-material heterogeneous architectures for tissue engineering applications. In addition, the bioprinter can regulate the structure's stiffness by controlling printing parameters, such as hydrogel concentration, PI concentration, and light exposure time. As a proof of concept, cell viability and proliferation rate in 5% w/v GelMA was assessed. Two GelMA-based bioinks, containing HUVECs and C2C12 cells, respectively, were used, and viability and proliferation assays were analyzed (Figure 3b–e). The tests were performed on days 1, 3, and 7 post-printing. The absorbance data were represented as fold increase to day 0. The absorbance value represented as fold increase for HUVECs in bioprinted system showed similar change compared to control until day 7 after bioprinting (n = 3). However, on day 7, cells grown in monolayer showed a higher growth rate (n = 3). The viability of encapsulated cells was observed until day 7 in hydrogel post-printing and quantified. The cell viability in case of both HUVECs and C2C12 until day 7 was more than 89% with no significant difference. A slight difference at days 3 and 7 was observed when compared to gel-free control (n = 3).

3.5. Multi-material musculoskeletal model

Using the microfluidics configuration described in section 2 (Figure 1d), we developed a multi-material bioprinting approach for generating a musculoskeletal tissue model with integrated vasculature. We combined two different cell types, i.e., HUVECs and MSCs, for the vasculature, and used C2C12 cells for the muscle tissue, in the same construct (Figure 4d). To bioprint the musculoskeletal model (Figure 4a), a co-planar printed pattern depicting a vascular and muscle structure was bioprinted using the selected biomaterial

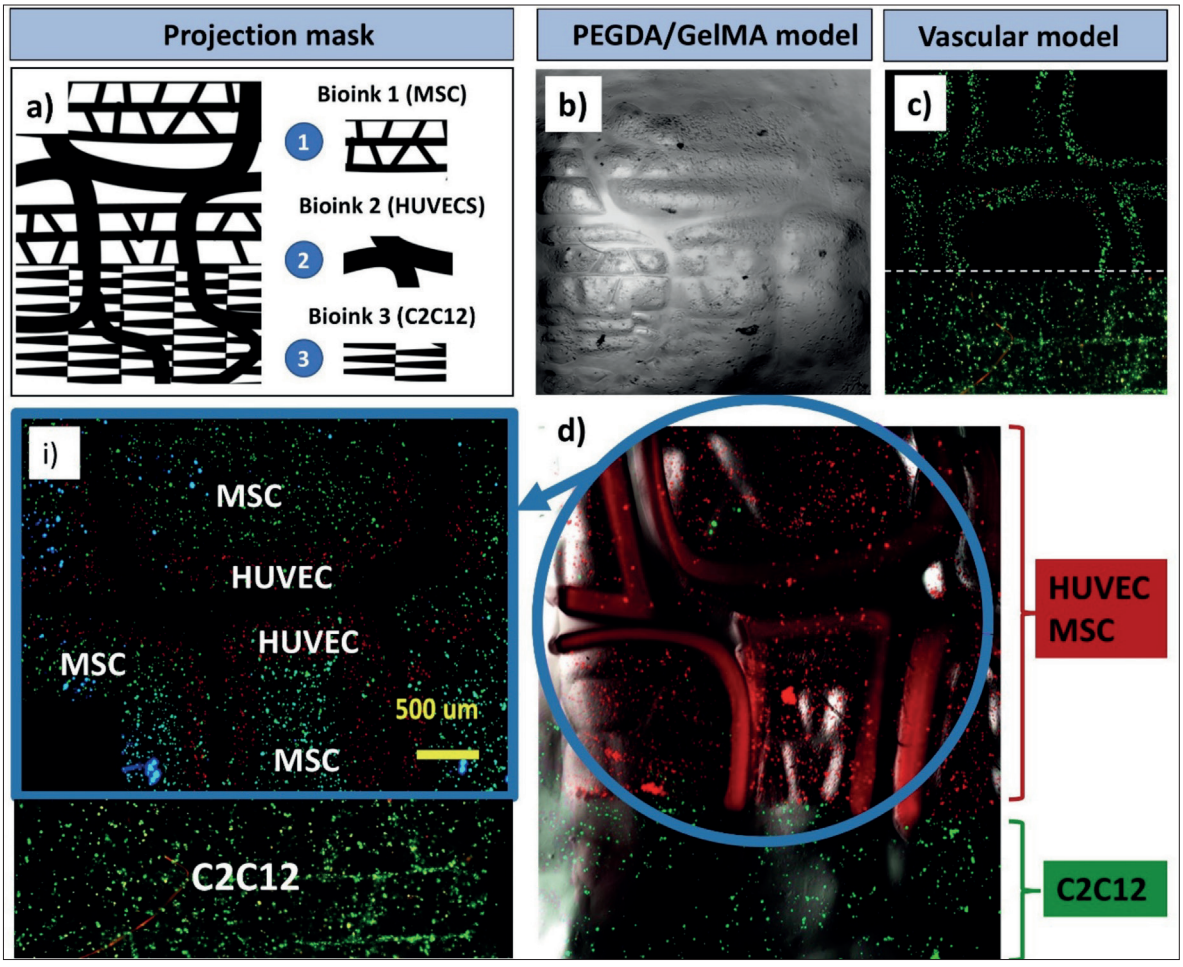

Figure 4. Demonstration of multi-material bioprinting musculoskeletal junction. (a) DLP projection pattern showing the bioinks locations. (b) Initial model made by PEGDA/GelMA. (c) Stacked 3D structure depicting the interface of two bioinks containing HUVECs and C2C12 cells. (d) Bioprinted muscle and vascular junction comprising three bioinks.

concentration: C2C12 and MSCs were mixed with (GelMA 3% w/v and PEGDA 15% w/v), while HUVECs were mixed with (GelMA 5% w/v and PEGDA 15% w/v).

As illustrated in Figure 4, the fluorescence image revealed the capability of the system to print the spatially distributed cell-laden bioinks, laying down the basis for future fabrication of functional multi-material musculoskeletal tissues. The addition of more PEGDA could result in more mechanical stability. It will make it easier to handle the tissue microenvironment fabrication. Still, PEGDA led to more encapsulated cell toxicity; indeed, 30%–40% v/v concentrations of PEGDA might be inappropriate for biological components. The GelMA/PEGDA bioink used in the microfluidics fabrication processes of the musculoskeletal environment, the proposed PI concentration, and the UV exposure were found to be safe for the proposed cell bioink application.

4. Discussion

Herein, we presented a novel bioprinting system, which facilitates the fabrication of multi-material constructs laden with three different cell types, as a proof of concept for a musculoskeletal tissue model on-a-chip. The incorporation of a rotating mirror to the printing system allowed the fast switch between the bottom-up and top-down printing modes and the combination of both approaches on a single musculoskeletal junction model. As a future upgrade of the dual printer, a fully automated system could be developed, in order to couple the movement of the stage with the mirror rotation, thus further optimizing the fabrication time and limiting the manual steps of the process. This modification could facilitate the implementation of the dual printer in the mass production of a wide range of organs-on-chips using the bottom-up, top-down, or combined processes.

The wide range of constructs that can be fabricated using the dual-printing approach was highlighted by the different geometries (Figure 2). Scaffolds with interconnected pores and intricate patterns can be generated using the bottom-up approach, providing mechanical support as well as a suitable environment for cells to grow[40]. The top-down approach was used for the fabrication of complex microvasculature patterns from GelMA and PEGDA. On their own, these constructs can be used as a soft support for vascularized tissue models, and the generated channels can be used for the perfusion of medium or other fluids. The maximum printing volume, which depends on the biomaterial container used, was determined for each bioprinting configuration. The DLP can project over an area of 7 × 12 cm. Nevertheless, for the case of bottom-up and top-down approaches and for the proposed biomaterial container configuration, the printing volume was determined to be around 3 × 3 × 3 cm. In the case of microfluidics bioprinting, the microfluidics working chamber has a diameter of 8 mm. The lateral resolution (*XY*) of the DLP is in the order of 10 microns, and the Z resolution of 20 nm can be achieved by the Thorlabs Z platform. To avoid cross-contamination issues during the bioprinting process, we added a washing bath in between each material selection (the washing process is illustrated on Figure 1f). The process can easily be adapted for work with more than two materials by flowing different biomaterials into the chip or by using more biomaterials containers in the bottom-up and top-down approaches. However, it should be noted here that careful selection of the final mechanical properties of the soft support is necessary, in order to avoid flow-induced delamination that could result in accelerated degradation as well as channel clogging. Examples of multi-material printing were also presented showing structures made with two discrete hard–soft parts, respectively (Figure 2c(i) and (iii)). Furthermore, a construct consisting of six soft and six hard alternating regions was fabricated (Figure 2c(ii)). Those soft–hard material combinations could be used in order to model bone-to-soft tissue interfaces[41,42]. Especially by combining more regions in one construct and controlling the mechanical properties of each region, tissue models consisting of more than two materials can be fabricated, allowing the study of complex systems such as the intervertebral disc regeneration[43].

The prepared bioinks were made from GelMA and PEGDA, due to their wide use in biofabrication applications as well as their light responsiveness[44]. By combining the two materials in different concentrations while also changing the concentration of the photoinitiator, we could get a compression modulus range from ~22 kPa to ~870 kPa. The measured moduli showed an increase with both the GelMA and PEGDA concentrations when using 0.05% LAP. Interestingly, this trend was not the same when the concentration of the photoinitiator was increased. More precisely, PEGDA 15% mixed with 3% of GelMA showed an increased modulus when compared to the PEGDA 15%/GelMA 0% formulation. However, when the concentration of GelMA was increased to 5%, the modulus showed a decrease of approximately 32.5%. Furthermore, the concentration increases of GelMA from 0% to 3% and subsequently to 5% resulted in a 27.6% and a further 8% modulus decrease when mixing with 35% PEGDA.

Most musculoskeletal diseases do not have a curative treatment yet. Some pathologies, such as amyotrophic lateral sclerosis, Duchenne's disease, or Lou Gehrig's disease, still do not have real treatment[45,46]. Some treatments for more common chronic diseases, such as cholesterolemia and diabetes, also have unwanted muscle

effects. In this sense, musculoskeletal on-a-chip is a novel and promising technology that can be used to evaluate the safety and effectiveness of drug and therapeutic development, enlightening the execution of clinical trials. Considering the number of new cases diagnosed and the direct and indirect costs associated with their treatment, the economic impact of on-a-chip models on the biomedical field is very high since this new technology allows for the screening of new, more effective drugs against these diseases, and the application of personalized medicine can shorten the treatment times and reduce the different problems associated with the use of generalized drugs. In this study, we present a multi-material musculoskeletal model made using three different cell types incorporated in a GelMA 3%/PEGDA 15%/LAP 0.1% bioink formulation. The concentration of PEGDA was kept at the lowest experimental value presented, in order to avoid cell toxicity associated with higher PEGDA concentrations[36]. Based on the results of the mechanical tests, a sufficiently stiff bioink (between ~20 kPa and ~870 kPa) could be obtained with this bioink formulation (PEGDA/GelMA/LAP) whose stiffness values are comparable to that reported for vascular[47] and muscle tissues[48-49].

Despite of the potential of organ-on-chip models in imitating various tissues and organs[50,51], musculoskeletal on-a-chip platforms have been evolving slowly compared with on-a-chip platforms for other tissue types[52,53]. The slow adoption of musculoskeletal on-a-chip platforms in studies of musculoskeletal pathologies can be associated with the conceptual and practical challenges in modeling the different cell types, extracellular matrix (ECM) interactions and *in vivo* mechanical loadings; the lack of innervation and vascularization; and the effective recapitulation of complex soft-to-hard tissue interfaces. 3D collagen scaffolds have been reported as a candidate model; however, they typically include a single cell type and fail to closely recapitulate the heterogeneity of the musculoskeletal tissue[54]. The major challenges associated with mimicking the physiology of the musculoskeletal on-a-chip have been identified, including incorporation of biological barriers and simulation of joint compartments and heterogeneous tissue interfaces. Overcoming these challenges will revolutionize musculoskeletal research by enabling physiologically relevant, predictive models of human tissues and joint diseases to accelerate and de-risk therapeutic discovery and translation to the clinic[55].

Additionally, to address the challenges of creating (clinically relevant) disease model on-a-chip with the associated biomarkers that can recapitulate the dynamic nature of tissue and chronic pathologies in the musculoskeletal system, new engineering innovations are still required on various features of the musculoskeletal on-a-chip model. For example, complex joint on-a-chip systems must be able to recreate the joint cartilage and the subchondral bone, synovial fluid, and associated vascularized tissues to simulate transport of nutrients, *in vivo* loading, and inflammation[56-57]. Highly organized muscle fibers are another example of the complex microarchitectural engineering required to model innervated tissues. Biological interfaces and ECM gradients are essential for recreating mechanical and cellular functions and signaling. For example, migration of immune cells from the bone marrow into the vasculature (the infiltration of platelets, neutrophils, macrophages), migration of various immune cells to sites of tissue injury, and cancer metastases underline the importance of engineering vascular barriers[58,59].

Without new technologies contributing to the reduction of investment risks associated with new drug development, these challenges will not be overcome, and new applications will deviate from translational efforts. Recent advances in 3D bioprinting have allowed the fabrication of complex structures and tissues with controlled architectures. As a result, there is growing interest in adopting these technologies in emerging areas that need a highly organized construct of biofabrication, such as tissue engineering and, in particular, more realistic modeling of the musculoskeletal tissue microenvironment[60,61]. Such bioprinted musculoskeletal on-a-chip approaches are ideal due to the following advantages: (i) the use of the patient's cells; (ii) the small size of the system; (iii) the small amount of tissue required for analysis; (iv) short development time (1–2 weeks); (v) low-cost manufacturing; (vi) scalability for high-throughput screening (HTS) testing; and (vii) the decrease in the use of experimental animals.

5. Conclusion

In this work, we developed a dual bottom-up and top-down bioprinter, which was demonstrated to be a versatile and powerful tool for 3D bioprinting soft and hard biomaterials, independently or simultaneously. The new bioprinter also allowed to manufacture of high-resolution tissue models, showing potential for the biofabrication of 3D multi-material and tissue interface structures.

Such biofabrication workstation offers several innovations. First, a dual-printer configuration allows for greater control of the mechanical and physical properties, such as density, viscosity, or permeability. Second, having control over the complete process, it was possible to bioprint multi-material tissue structures using different hydrogels, allowing for greater precision in achieving tissue interface constructs and hard scaffolds that can be incorporated into

soft tissue bioprinting. The unique characteristic of our dual bottom-up and top-down bioprinter can significantly upgrade the current level of control for multi-material bioprinting of existing bioprinting techniques. This dual concept is also expandable to other tissue interfaces, as many tissue bioinks as needed, by simply increasing the number of biomaterial chambers. In addition, the combination with the microfluidic chip for bioprinting can expand its applicability to multi-material bioprinting of complex tissue interfaces and emerges as a promising technology for both clinical precision medicine and industrial-scale drug discovery, thanks to its capability of handling small samples and highly multiplexed operations for high-throughput assays.

Acknowledgments

A.K.M. acknowledges the NJIT start-up fund and the National Institutes of Health (NIH, R21DC018818).. D.N. acknowledges "EAPA_384/2016 Atlantic KET Med Project, co-financed by the Interreg Atlantic Area Programme through the European Regional Development Fund". L.M. acknowledges the Dutch Province of Limburg and the Brightlands Materials Center for support that made this research project possible.

Funding

EAPA_384/2016 Atlantic KET Med Project is co-financed by the Interreg Atlantic Area Programme through the European Regional Development Fund.

Conflict of interest

The authors declare no conflicts of interest.

Author contributions

Conceptualization: Daniel Nieto
Investigation: Daniel Nieto
Methodology: Daniel Nieto, Alberto Jorge de Mora
Writing – original draft: Daniel Nieto, Anant Bhusal, Maria Kalogeropoulou
Writing – review & editing: Daniel Nieto, Amir K. Miri, Lorenzo Moroni
Funding Acquisition: Daniel Nieto, Lorenzo Moroni

Consent for publication

Not applicable.

Availability of data

Raw data used in this work are available from the corresponding author upon reasonable request.

References

1. Wu Q, Liu J, Wang X, et al. Organ-on-a-chip: Recent breakthroughs and future prospects. *Biomed Eng Online.* 2020;19:1-19.
2. Bhatia SN, Ingber DE. Microfluidic organs-on-chips. *Nat Biotechnol.* 2014;32(8): 760-772.
3. Mathur A, Loskill P, Shao K, et al. Human iPSC-based cardiac microphysiological system for drug screening applications. *Sci Rep.* 2015;5:1-7.
4. Neužil P, Giselbrecht S, Länge K, Huang TJ, Manz A. Revisiting lab-on-a-chip technology for drug discovery. *Nat Rev Drug Discov.* 2012;11(8):620-632.
5. Ribas J, Sadeghi H, Manbachi A, et al. Cardiovascular organ-on-a-chip platforms for drug discovery and development. *Appl In Vitro Toxicol.* 2016;2:82-96.
6. Ho CT, Lin RZ, Chen RJ, et al. Liver-cell patterning lab chip: Mimicking the morphology of liver lobule tissue. *Lab Chip.* 2013;13:3578-3587.
7. Booth R, Kim H. Characterization of a microfluidic in vitro model of the blood-brain barrier (μBBB). *Lab Chip.* 2012;12(10):1784-1792.
8. Lee SH, Jun B-H. Advances in dynamic microphysiological organ-on-a-chip: Design principle and its biomedical application. *J Indus Eng Chem.* 2019;(71):65-77.
9. Huh D, Matthews BD, Mammoto A, et al. Reconstituting organ-level lung functions on a chip. *Science.* 2010;328(5986):1662-1668.
10. Beckwitt CH, Clark AM, Wheeler S, et al. Liver 'organ on a chip'. *Exp Cell Res.* 2018;63(1):15-25.
11. Kim HJ, Huh D, Hamilton G, Ingber DE. Human gut-on-a-chip inhabited by microbial flora that experiences intestinal peristalsis-like motions and flow. *Lab Chip.* 2012;12: 2165-2174.
12. Wilmer MJ, Ng CP, Lanz HL, Vulto P, Suter-Dick L, Masereeuw R. Kidney-on-a-chip technology for drug-induced nephrotoxicity screening. *Trends Biotechnol.* 2016;34(2):156-170.
13. Phan DT, Bender RHF, Andrejecsk JW, et al. Blood–brain barrier-on-a-chip: Microphysiological systems that capture the complexity of the blood–central nervous system interface. *Exp Biol Med.* 2017;242(17):1669-1678.
14. Huebsch N, Loskill P, Deveshwar N, et al. Miniaturized iPS-cell-derived cardiac muscles for physiologically relevant drug response analyses. *Sci Rep.* 2016;(6):1-12.
15. Mandrycky C, Wang Z, Kim K, Kim D-H. 3D bioprinting for engineering complex tissues. *Biotechnol Adv.* 2016;34(4): 422-434.
16. Arrigoni C, Lopa S, Candrian C, Moretti M. Organs-on-a-chip as model systems for multifactorial musculoskeletal diseases. *Curr Opin Biotechnol.* 2020;63:79-88.

17. Datta P, Dey M, Ataie Z, Unutmaz D, Ozbolat IT. 3D bioprinting for reconstituting the cancer microenvironment. *NPJ Precis Oncol.* 2020;4:1-13.
18. Xiang Y, Miller K, Guan J, Kiratitanaporn W, Tang M, Chen S. 3D bioprinting of complex tissues in vitro: State-of-the-art and future perspectives. *Arch Toxicol.* 2022;96(3):691-710 .
19. Jiang T, Munguia-Lopez JG, Flores-Torres S, Kort-Mascort J, Kinsella JM. Extrusion bioprinting of soft materials: An emerging technique for biological model fabrication. *Appl Phys Rev*. 2019;l6(1):011310.
20. Ozbolat IT, Hospodiuk M. Current advances and future perspectives in extrusion-based bioprinting. *Biomaterials*. 2016;76:76321-76343.
21. Li X, Liu B, Pei B, et al. Inkjet Bioprinting of Biomaterials. *Chem Rev*. 2020;120(19):10793-10833.
22. Ng WL, Lee JM, Zhou M, et al. Vat polymerization-based bioprinting-process, materials, applications and regulatory challenges. *Biofabrication*. 2020;12(2):022001.
23. Antoshin AA, Churbanov SN, Minaev NV, et al. LIFT-bioprinting, is it worth it? *Biofabrication*. 2019;15:e00052.
24. Grigoryan B, Sazer DW, Avila A, et al. Development, characterization, and applications of multi-material stereolithography bioprinting. *Sci Rep*. 2021;11(1):3171.
25. Zhang R, Larsen NB. Stereolithographic hydrogel printing of 3D culture chips with biofunctionalized complex 3D perfusion networks. *Lab Chip*. 2017;17(24):4273-4282.
26. Miri AK, Nieto D, Iglesias L, et al. Microfluidics-enabled multimaterial maskless stereolithographic bioprinting. *Adv Mater.* 2018;30:1800242.
27. Grogan SP, Chung PH, Soman P, et al. Digital micromirror device projection printing system for meniscus tissue engineering. *Acta Biomater*. 2013;9(7):7218-7226.
28. Bhusal A, Dogan E, Nguyen HA, et al. Multi-material digital light processing bioprinting of hydrogel-based microfluidic chips. *Biofabrication*. 2021;14:014103.
29. Dogan E, Bhusal A, Cecen B, Miri AK. Miri. 3D printing metamaterials towards tissue engineering. *Appl Mater Today*. 2020;20:100752.
30. Mobaraki M, Ghaffari M, Yazdanpanah A, Luo Y, Mills DK. Bioinks and bioprinting: A focused review. *Bioprinting*. 2020;18:e00080.
31. Kolesky DB, Homan KA, Skylar-Scott MA, Lewis JA. Three-dimensional bioprinting of thick vascularized tissues. *Proc Natl Acad Sci.* 2016;113(12):3179-3184.
32. Homan KA, Kolesky DB, Skylar-Scott MA, et al. Bioprinting of 3D convoluted renal proximal tubules on perfusable chips. *Sci Rep.* 2016;6:34845.
33. Zhu W, Qu X, Zhu J, et al. Direct 3D bioprinting of prevascularized tissue constructs with complex microarchitecture. *Biomaterials*. 2017;124:106–115.
34. Miri AK, Mirzaee I, Hassan S, et al. Effective bioprinting resolution in tissue model fabrication. *Lab Chip*. 2019;19(11):2019-2037.
35. Miri AK, Mostafavi E, Khorsandi D, Hu S-K, Malpica M, Khademhosseini A. Bioprinters for organs-on-chips. *Biofabrication*. 2019;11(4):042002.
36. Zheng Z, Eiglin D, Alini M, Richards GR, Qin L, Lai Y. Visible light-induced 3D bioprinting technologies and corresponding bioink materials for tissue engineering: A review. *Engineering*. 2021;7:966-978.
37. Cook AB, Clemons TD. Bottom-up versus top-down strategies for morphology control in polymer-based biomedical materials. *Adv NanoBiomed Res.* 2022;2(1): 2100087.
38. Kumar H, Kim K. Stereolithography 3D bioprinting. *Methods Mol Biol*. 2020;2140:93-108.
39. Li W, Wang M, Ma H, Chapa-Villarreal abiola A, Lobo AO, Zhang YS. Stereolithography apparatus and digital light processing-based 3D bioprinting for tissue fabrication. *iScience*. 2023;26(2):106039.
40. Kuhnt T, Marroquín R, Camarero-Espinosa S, et al. Poly (caprolactone-co-trimethylenecarbonate) urethane acrylate resins for digital light processing of bioresorbable tissue engineering implants. *Biomater Sci*, 2019;7(12):4984-4989.
41. Nieto D, Jiménez G, Moroni L, López-Ruiz E, Gálvez-Martín P, Marchal JA. Biofabrication approaches and regulatory framework of metastatic tumor-on-a-chip models for precision oncology. *Med Res Rev*. 2021;42(5):1978-2001.
42. Hu Y, Zhang H, Wang S, et al. Bone/cartilage organoid on-chip: Construction strategy and application. *Bioact Mater*. 2023;25:29-41.
43. Bowles RD, Setton LA. Biomaterials for intervertebral disc regeneration and repair. *Biomaterials*. 2017;129:54-67.
44. Hosseinabadi HG, Nieto D, Yousefinejad A, Fattel H, Ionov L, Miri AK. Ink material selection and optical design considerations in DLP 3D printing. *Appl Mater Today*. 2023;30:101721.
45. Scaricamazza S, Salvatori I, Ferri A, Valle C. Skeletal muscle in ALS: An unappreciated therapeutic opportunity? *Cells*. 2021;10(3):525. https://doi.org/10.3390/cells10030525
46. Paganoni S, Karam C, Joyce N, Bedlack R, Carter GT. Comprehensive rehabilitative care across the spectrum of amyotrophic lateral sclerosis. *NeuroRehabilitation*. 2015;37(1):53-68. https://doi.org/10.3233/nre-151240
47. Zhou SW, Wang J, Chen SY, Ren K-F, Wang Y-X, Ji J. The substrate stiffness at physiological range significantly modulates vascular cell behavior. *Colloids Surf B Biointerfaces*. 2022;(214):112483.

48. Lee Y, Kim M, Lee H. The measurement of stiffness for major muscles with shear wave elastography and myoton: A quantitative analysis study. *Diagnostics*. 2021;11(3):524.

49. Singh G, Chanda A. Mechanical properties of whole-body soft human tissues: A review. *Biomed Mater*. 2021;16(6):062004.

50. Huh D, Hamilton GA, Ingber DE. From 3D cell culture to organs-on-chips. *Trends Cell Biol.* 2011;21(12):745-754.

51. Low LA, Mummery C, Berridge BR, Austin CP, Tagle DA. Organs-on-chips: Into the next decade. *Nat Rev Drug Discov,* 2021;20(5):345-361.

52. Ajalik RE, Alenchery RG, Cognetti JS, et al. Human organ-on-a-chip microphysiological systems to model musculoskeletal pathologies and accelerate therapeutic discovery. *Front Bioeng Biotechnol.* 2022;(10):846230.

53. Scaricamazza S, Salvatori I, Ferri A, Valle C. Skeletal muscle in ALS: An unappreciated therapeutic opportunity? *Cells*. 2021;10(3):525.
doi: 10.3390/cells10030525

54. Ma J, Holden K, Zhu J, Pan H, Li Y. The application of three-dimensional collagen-scaffolds seeded with myoblasts to repair skeletal muscle defects. *J Biomed Biotechnol*. 2011;2011: 812135.
doi: 10.1155/2011/812135

55. Pan C-C, Bruyas A, Yang YP. Bioprinting for tissue engineering and regenerative medicine. *Mater Matt Aldrich.* 2016;(11):49-52.

56. Rainbow R, Ren W, Zeng L. Inflammation and joint tissue interactions in OA: Implications for potential therapeutic approaches. *Arthritis*. 2012;741582.

57. Pirosa A, Gottardi R, Alexander PG, Tuan RS. Engineering in-vitro stem cell-based vascularized bone models for drug screening and predictive toxicology. *Stem Cell Res Ther.* 2018;9: 112.
doi: 10.1186/s13287-018-0847-8

58. McDowell SAC, Quail DF. Immunological regulation of vascular inflammation during cancer metastasis. *Front Immunol.* 2019;10:1984.

59. Goel S, Duda DG, Xu L, et al. Normalization of the vasculature for treatment of cancer and other diseases. *Physiol Rev.* 2011;91(3):1071-1121.
https://doi.org/10.1152/physrev.00038.2010

60. Naghieh S, Lindberg G, Tamaddon M, Liu C. Biofabrication strategies for musculoskeletal disorders: Evolution towards clinical applications. *Bioengineering (Basel)*. 2021;8(9):123.

61. Volpi M, Paradiso A, Costantini M, Święszkowski W. Hydrogel-based fiber biofabrication techniques for skeletal muscle tissue engineering. *ACS Biomater Sci Eng.* 2022;8:379-405.

ACCSCIENCE PUBLISHING

International Journal of Bioprinting

RESEARCH ARTICLE

Optimizing implant lattice design for large distal femur defects: Stimulating interface bone growth to enhance osseointegration

Chun-Ming Chang[1], Pei-Chun Wong[2], Sin-Liang Ou[3], Chih-En Ko[4], and Yu-Tzu Wang[4]*

[1]Taiwan Instrument Research Institute, National Applied Research Laboratories, Hsinchu, Taiwan

[2]Graduate Institute of Biomedical Optomechatronics, College of Biomedical Engineering, Taipei Medical University, Taipei, Taiwan

[3]Department of Biomedical Engineering, Da-Yeh University, Changhua, Taiwan

[4]Department of Mechanical and Electro-Mechanical Engineering, TamKang University, New Taipei City, Taiwan

Abstract

Large bone defects in the distal femur present a significant challenge due to the lack of inherent self-healing capabilities. Traditional approaches, such as utilizing polymethyl methacrylate (PMMA) in conjunction with a plate for distal femur reconstruction, have shown unsatisfactory osseointegration outcome, which leads to complications. To address this challenge, this study focuses on developing a lattice-structured implant for reconstructing distal femoral bone defects. The lattice geometry is based on the cuboctahedron lattice, with its design optimized through the adjustment of pillar diameter and arrangement angle. The lattice structure is designed to stimulate the surrounding bone, ultimately enhancing osseointegration in distal femur reconstruction. Finite element analysis revealed that for promoting bone ingrowth toward the implant, setting the optimal lattice structure parameters, i.e., a 45° arrangement angle and a 0.8 mm pillar diameter, is required. Fabricated using state-of-the-art metal three-dimensional printing, the implant underwent rigorous validation through biomechanical testing, *in vitro* biological assays, and animal experiments. The comprehensive results affirmed the bioactivity of the lattice-structured implant, underscoring its capability to improve osseointegration in distal femoral defect reconstruction.

Keywords: Lattice; Osseointegration; Bone strain; Osteoconductive; Distal femur; Mechanical behavior

***Corresponding author:**
Yu-Tzu Wang
(YTLWH@mail.tku.edu.tw)

Citation: Chang C-M, Wong P-C, Ou S-L, Ko C-E, Wang Y-T. Optimizing implant lattice design for large distal femur defects: Stimulating interface bone growth to enhance osseointegration. *Int J Bioprint*. 2024;10(2):2590. doi: 10.36922/ijb.2590

Received: December 20, 2023
Accepted: February 20, 2024
Published Online: March 21, 2024

1. Introduction

Bone defects in the distal femur can arise from accidental injuries or tumor resection.[1] Regrettably, complete self-healing in the case of large bone defects remains unattainable.[2-3] A commonly employed approach for reconstructing and stabilizing larger distal femur defects involves using polymethyl methacrylate (PMMA) in combination with a plate.[4-5] However, the exothermic polymerization process of PMMA has the potential to induce

necrosis in the surrounding bone.[6-7] This necrosis weakens the mechanical bond between PMMA and the bone, resulting in early loosening known as aseptic loosening.[8] Furthermore, owing to its smooth surface and structure, PMMA lacks osteoconductive properties, thereby impeding favorable osseointegration.[8] Related studies have indicated that loosening of the interface between PMMA and bone constitutes a prevalent cause for re-operation in distal femoral defects, leading to complications such as fractures (14%) and nonunions (12%).[9] Therefore, it becomes evident that PMMA is not an optimal option for reconstructing large bone defects in the distal femur.

Implants featuring lattice structure that conforms to the profile of the bone defect have emerged as a potential alternative for reconstructing large bone defects.[3,10] In the case of solid metal implants, the material properties of metals can lead to stress-shielding effects due to a mismatch with the bone's elastic modulus (for instance, Ti6Al4V has an elastic modulus of 110–120 GPa, while cortical bone ranges from 10 to 40 GPa).[11-13] However, designing the lattice structure and modifying its alignment allow for variation in the elastic modulus of the lattice to significantly improve the mechanical compatibility between the implant and the bone.[13,14] This approach effectively circumvents the stress-shielding effect and enhances the implant's osteoconductive properties,[15] facilitating bone ingrowth into the implant.[16] Moreover, the loading applied to the bone plays a critical role in stimulating bone growth within the implant.[16] Several studies have demonstrated that applying an appropriate load to the bone through the lattice on the implant, which generates strains near but not exceeding 4000 μ, effectively stimulates bone growth into the implant and enhances osseointegration.[17,18]

In the past decade, various lattice structures had been extensively studied.[16,19-21] One notable lattice structure is the cuboctahedron lattice, which is recognized for its simple appearance.[22] The internal space within the lattice facilitates efficient nutrient transportation and waste removal, and the multi-corner design of the lattice structure makes it conducive for the attachment and clustered growth of osteoblasts.[15,23] Although the cuboctahedron lattice demonstrates favorable conditions for osteoblast differentiation and growth, further investigation is warranted to evaluate its applicability for distal femur reconstruction. Specifically, it is crucial to determine whether the cuboctahedron lattice structure can mitigate the stress-shielding effect and enhance osteoconductivity. Finite element method (FEM) can be employed to analyze the stress fields within the metallic implant and strain fields in the soft evolving tissue.[24] This analysis assists in designing the structural parameters of the cuboctahedron lattice to align with the mechanical conditions of the distal femur.[25]

Currently, metal three-dimensional (3D) printing using Ti6Al4V as a material through selective laser melting (SLM) has become a commonly adopted technique for fabricating complex metal implants,[26,27] and numerous studies have demonstrated its applicability.[16,21,24,28] Accordingly, in this study, metal 3D printing was employed to fabricate implants with complex lattice structures.

Designing lattice-optimized implants for the target anatomical region currently represents a prevailing trend in lattice development. Scholars have designed lattice variations in types and sizes tailored for distinct regions, including craniofacial,[29] dental implants,[30] hip,[4,20] tibial,[24] and spinal implants.[31-33] This optimization aims to align the lattice with the biomechanical conditions of the target area, fostering the growth of surrounding bone. The design of this study critically incorporated considerations related to mechanical, structural, and cell growth aspects. This study aimed to integrate finite element analysis, parameter optimization, biomechanical test, *in vitro* biological test, and animal experiment to develop a lattice design specifically tailored for distal femur defect reconstruction implants, with the primary objective of refining the lattice structures within the implant for improved overall performance. Through the design of cuboctahedron lattice variations, incorporating different arrangements and lattice pillar diameters, and utilizing finite element analysis to explore material properties under various parameters, we sought to identify an optimal lattice. This lattice was intended to generate an appropriate bone strain (4000 μ) at the bone interface, ultimately improving the osseointegration effect of the implant. The bone interface strain behavior around the implant was verified using the biomechanical test, and *in vitro* biological tests were used to assess whether the optimal lattice structure (OLS) was conducive to cell growth and proliferation. Additionally, animal experiments were employed to simulate *in vivo* responses of the implant, providing a comprehensive evaluation of the biological activity of the lattice and confirming its utility in assessing osseointegration ability.

2. Materials and methods

2.1. Cuboctahedron lattice-parametric design of unit lattice

A cuboctahedron lattice is a polyhedral structure composed of eight triangular faces and six square faces, featuring a total of 12 vertices and 24 edges.[22] This lattice structure possesses a unit volume of $2 \times 2 \times 2$ mm^3. The lattice alignment angle and the lattice pillar diameter are two primary structural parameters of the cuboctahedron lattice. The lattice alignment angle was classified into two categories: 0° and 45°. The lattice pillars were designed with a circular cross-section, and the diameter parameter was

intentionally varied across five levels, ranging from 0.6 mm to 1.0 mm (0.6/0.7/0.8/0.9/1.0 mm) (Figure 1a). Given the micro-scale nature of lattice structures, any modifications to the lattice geometry can profoundly impact the inherent material properties of the metal (Ti6Al4V). In this study, the Material Designer module of the Ansys Workbench software (ANSYS Workbench 2022R2, ANSYS Inc., PA, USA) was utilized to precisely define the material properties of various lattices with different structural parameters.

2.2. Material properties of the lattice analysis

In the Material Designer module, the orthotropic elasticity constants for a periodic unit cell are computed using the following equations. The analysis involved considering six load cases: three tensile tests (X, Y, Z) and three shear tests (XY, YZ, XZ). Each case applies a corresponding macroscopic strain, and reaction forces in the boundary faces of the representative volume elements (RVE) are employed to assemble the stiffness matrix, from which engineering constants are extracted. Consider the tensile test in the X-direction. For an orthotropic material, Equation I is applicable:

$$\begin{bmatrix}\sigma_x\\ \sigma_y\\ \sigma_z\\ \sigma_{xy}\\ \sigma_{yz}\\ \sigma_{zx}\end{bmatrix}=\begin{bmatrix}D_{11} & D_{12} & D_{13} & 0 & 0 & 0\\ D_{21} & D_{22} & D_{23} & 0 & 0 & 0\\ D_{31} & D_{32} & D_{33} & 0 & 0 & 0\\ 0 & 0 & 0 & D_{44} & 0 & 0\\ 0 & 0 & 0 & 0 & D_{55} & 0\\ 0 & 0 & 0 & 0 & 0 & D_{66}\end{bmatrix}\begin{bmatrix}\varepsilon_x\\ \varepsilon_y\\ \varepsilon_z\\ \varepsilon_{xy}\\ \varepsilon_{yz}\\ \varepsilon_{zx}\end{bmatrix} \quad \text{(I)}$$

Fixing the strain in the X-direction to 0.001 and setting all other strains to zero yield the first column of the stiffness matrix (Equation II). Assuming RVE volume as $[0, L_x] \times [0, L_y] \times [0, L_z]$, deformations are represented along the X-direction (Equation III), Y-direction (Equation IV), and Z-direction (Equation V). In addition to these periodicity conditions, rigid body motions must also be prevented (Equation VI).

$$\begin{bmatrix}D_{11}\\ D_{21}\\ D_{31}\\ 0\\ 0\\ 0\end{bmatrix}=\frac{1}{0.001}\begin{bmatrix}\sigma_x\\ \sigma_y\\ \sigma_z\\ \sigma_{xy}\\ \sigma_{yz}\\ \sigma_{zx}\end{bmatrix} \quad \text{(II)}$$

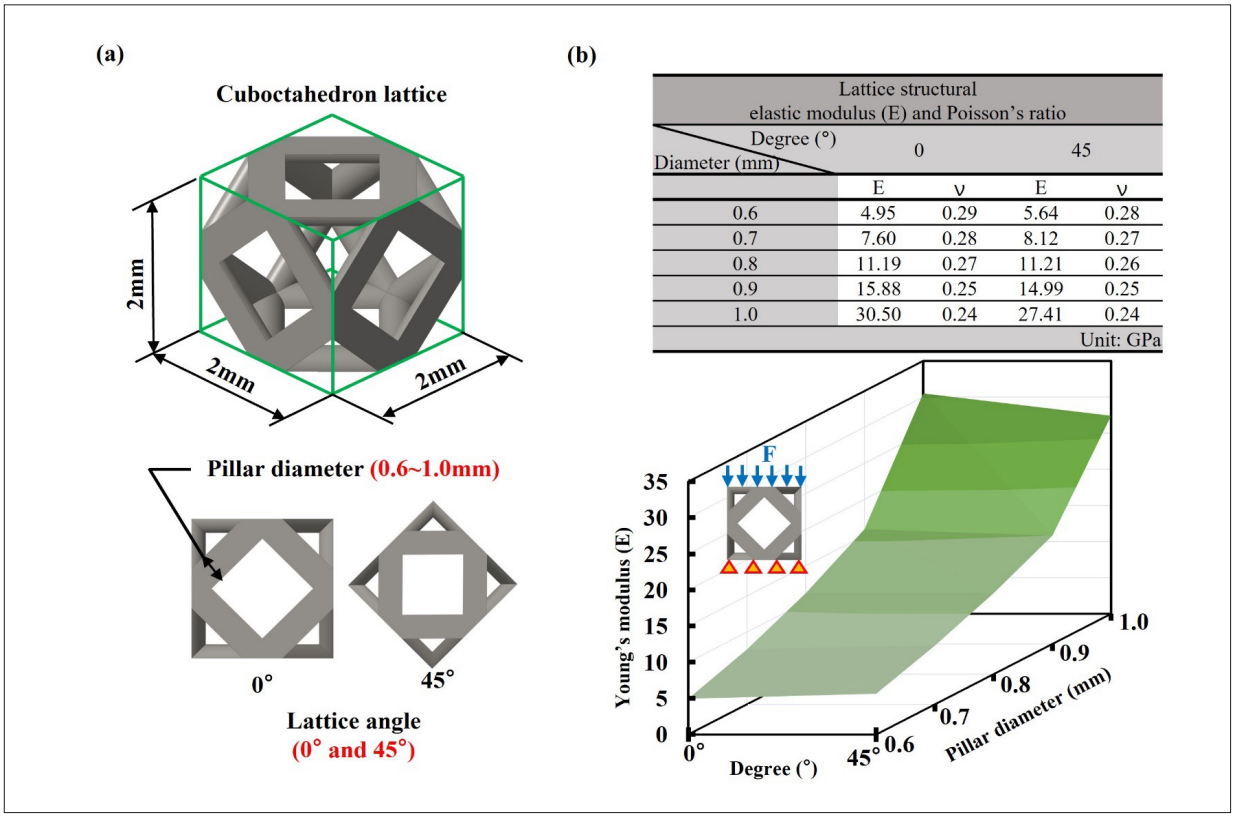

Figure 1. Cuboctahedron lattice. (a) Unit size and structure of cuboctahedron lattice; (b) elastic modulus and Poisson's ratio of each lattice.

$$\begin{aligned} u_x(L_x,y,z) &= u_x(0,y,z) + \varepsilon L_x \\ u_y(L_x,y,z) &= u_y(0,y,z) \\ u_z(L_x,y,z) &= u_z(0,y,z) \end{aligned} \quad \text{(III)}$$

$$\begin{aligned} u_x(x,L_y,z) &= u_x(x,0,z) \\ u_y(x,L_y,z) &= u_y(x,0,z) \\ u_z(x,L_y,z) &= u_z(x,0,z) \end{aligned} \quad \text{(IV)}$$

$$\begin{aligned} u_x(x,y,L_z) &= u_z(x,y,0) \\ u_y(x,y,L_z) &= u_y(x,y,0) \\ u_z(x,y,L_z) &= u_z(x,y,0) \end{aligned} \quad \text{(V)}$$

$$\begin{aligned} u_x(a\ point\ with\ x=0) \\ u_y(a\ point\ with\ y=0) \\ u_z(a\ point\ with\ z=0) \end{aligned} \quad \text{(VI)}$$

To compute macroscopic stresses, the forces on the top faces are integrated. For instance, for σ_x, the force in the X-direction at the face $x = L_x$ is integrated and normalized with the face area. Similar procedures are followed for σ_y and σ_z. The entries for D_{11}, D_{21}, and D_{31} in the stiffness matrix are easily obtained. By repeating the steps for all the other load case, all the entries for the stiffness matrix, including D_{11}, D_{21}, and D_{31}, are determined. The stiffness matrix is inverted to obtain the compliance matrix following Equation VII. Finally, the engineering constants (E_x, E_y, E_z, G_{xy}, G_{yz}, G_{xz}, ν_{xy}, ν_{yz}, and ν_{xz}) are computed using the relationships outlined in Equation VIII.[34]

$$[C] = [D^{-1}] \quad \text{(VII)}$$

$$[C] = \begin{bmatrix} \frac{1}{E_x} & \frac{-\nu_{yx}}{E_y} & \frac{-\nu_{zx}}{E_z} & 0 & 0 & 0 \\ \frac{-\nu_{xy}}{E_x} & \frac{1}{E_y} & \frac{-\nu_{zy}}{E_z} & 0 & 0 & 0 \\ \frac{-\nu_{xz}}{E_x} & \frac{-\nu_{yz}}{E_y} & \frac{1}{E_z} & 0 & 0 & 0 \\ 0 & 0 & 0 & \frac{1}{G_{xy}} & 0 & 0 \\ 0 & 0 & 0 & 0 & \frac{1}{G_{yz}} & 0 \\ 0 & 0 & 0 & 0 & 0 & \frac{1}{G_{xz}} \end{bmatrix} \quad \text{(VIII)}$$

In the Material Designer module, various unit lattice structures were defined as RVE. The material properties of Ti6Al4V were assigned to the lattice model within the module, followed by meshing and computational analysis to predict the stresses and strains experienced by the different lattice structures. Finally, the elastic modulus and Poisson's ratios of the various lattice structures were computed (Figure 1b).[34] These lattice structures can be regarded as innovative, each exhibiting distinct material properties and characteristics stemming from their unique structural parameters.

2.3. Creating a geometry model for distal femur defect reconstruction

The femur (ENOVO-186, ENOVO, Shanghai, China) was modeled using computed tomography (CT) image, and the plate (Tandry Locking Plate System, thickness 5.0 mm, All Micro Precision Co., Ltd., Taiwan) and reconstruction screws were designed through computer-aided design (CAD) software (Creo Parametric v5.0, PTC, Needham, MA, USA), allowing for precise customization and adaptation to the patient's specific needs. To simulate a common defect in the distal femur, a 25 mm height defect was created 55 mm from the knee joint surface.[35,36] The geometry of the femur defect served as the foundation for the contour of the implant. The implant was conceived as a hollow structure for lightweight design, with a 2 mm thickness to ensure adequate structural strength. A lattice structure, 4 mm thick, was incorporated on the top and bottom (proximal and distal layers) of the implant in contact with the bone. Different lattice designs can be substituted during analysis to investigate the mechanical behavior of these varied lattice structures. The implant was securely fixed to the distal femur defect with a reconstruction plate and screws (Tandry Locking screw and Cortex screw, All Micro Precision Co., Ltd., Taiwan) on the lateral side of the femur. One of the screws was anchored to both the implant and the reconstruction plate, ensuring stable fixation of the implant, plate, and bone. The overall model for distal femur defect reconstruction encompasses the cortical bone, cancellous bone, reconstructed plate, screws, and implant components (Figure 2).

2.4. Analysis of lattice structure parameters through finite element analysis

In this study, a distal femur defect reconstruction model was established to analyze the biomechanical behavior of a parametric lattice implant. The aim was to identify the OLS by determining the structural parameters that effectively stimulate bone interface growth. The relevant material properties for the analysis are presented in Table 1. To construct the mesh model, a free-mesh approach with 10-node tetrahedral elements was used (Figure 3). The number and density of the mesh were determined through convergence tests, as shown in Table 1, to ensure the accuracy of the analysis. During a typical gait cycle,

it is commonly assumed that the loading on the femur is approximately four times the body weight.[37] A downward force of 2800 N was applied to the femoral head in the analyzed model, considering a patient's body weight to be 70 kg. Fixed support was provided on the lateral and medial condyle surfaces of the distal femur. The contact settings between the components were set to "frictional" to govern the interactions among the bone and screw, plate and screw, as well as the lattice and bone. This frictional setting incorporated the sliding resistance based on the friction coefficient, allowing these components to move relative to each other. This simulation represented the state of the implant and bone before osseointegration occurred following surgery (Figure 3).

During the analysis, different lattice structures were substituted for the lattice layers on the implant to assess the compression of the third principal strain on the surrounding bones. The goal was to identify lattice structures that induced a strain close to, but not exceeding, 4000 μ, indicating that the OLS exhibits osteoconductive properties and accelerates bone growth, thereby enhancing the osseointegration effect.

2.5. Biomechanical testing of implants and bone cement for distal femur reconstruction

Biomechanical tests were conducted to assess the efficacy of lattice structure on the distal femur reconstruction implant in stimulating bone growth and enabling the production of appropriate strain in the surrounding area. These tests were conducted to investigate the differences in surrounding bone growth (osteoconductive) among an implant with OLS (OLS implant), an implant without lattice structure (NLS implant), and bone cement (Radiopaque Bone Cement, Stryker Corporation, Michigan, USA). The OLS implant and the NLS implant were manufactured

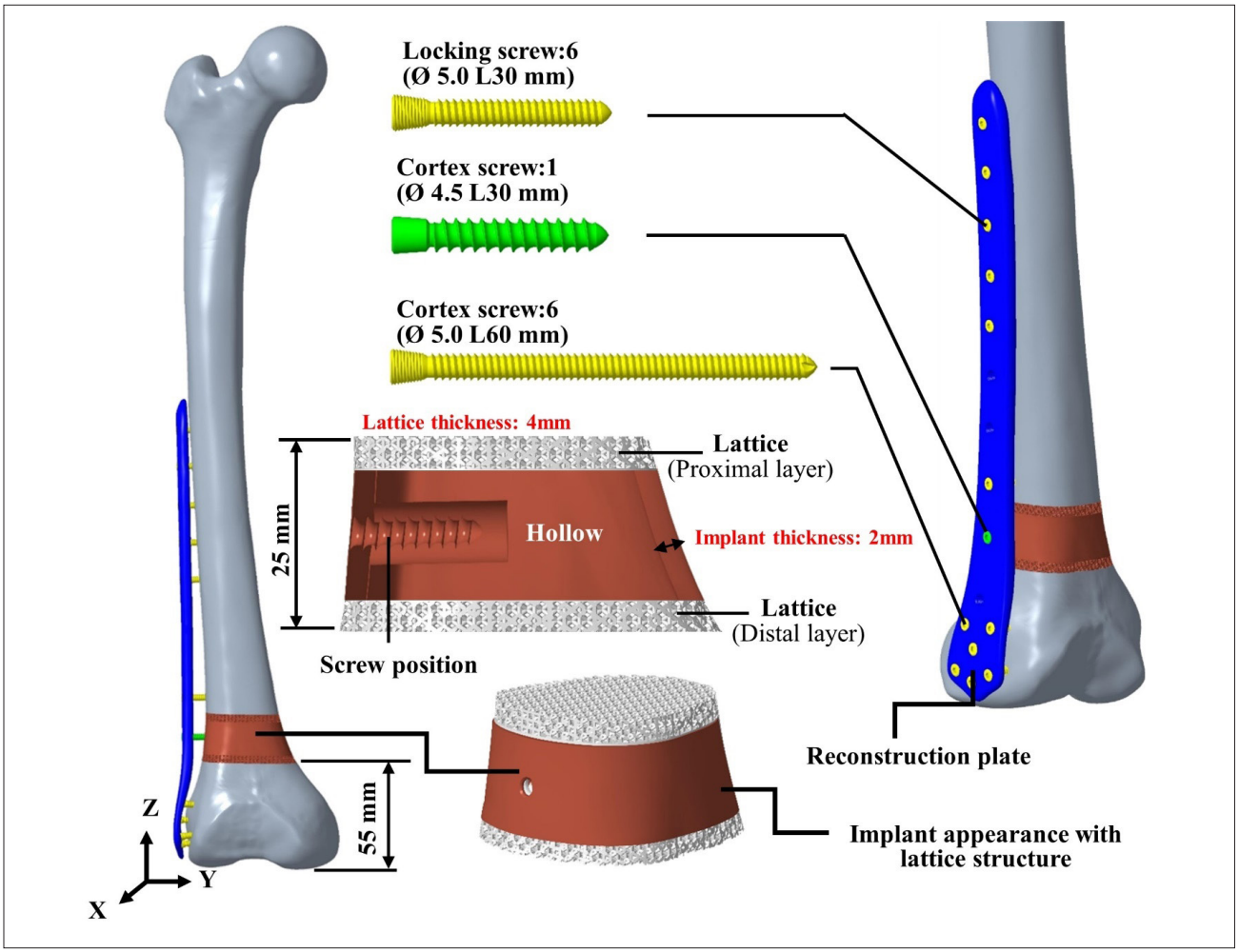

Figure 2. Overall model for distal femur defect reconstruction (modeling for finite element analysis).

Table 1. Material properties and number of elements/nodes for each model used in the finite element analysis

Material		Elastic modulus (GPa)	Poisson's ratio	Reference
Cortical bone		17	0.3	[38,39,40]
Cancellous bone		0.52	0.29	[39,41]
Reconstruction plate and screws	**(Ti6Al4V)**	110	0.37	[42,43]
Implant body				
Number of nodes/elements		**Elements**		**Nodes**
Cortical bone		185,123		310,457
Cancellous bone		397,580		581,592
Reconstruction plate		216,784		330,754
Screws		100,720		108,200
Implant (with lattice)		138,394		205,286

using metal 3D printing (AM250, Renishaw plc, Woton-under-Edge, Gloucestershire, UK). The process parameters included layer thickness of 30 μm, laser power of 100 W, laser exposure time of 60 μs, laser focus of 75 μm, point distance of 75 μm, and hatch distance of 20 μm. The femur model was fabricated using FDM polymer 3D printing (Fortus 250MC, Stratasys Ltd., Reḥovot, Israel). Subsequently, the implants (OLS and NLS implants) and bone cement were attached to the femur model using a reconstruction plate and screws, respectively. This assembled model was utilized as the test subject for biomechanical testing, with a sample size of $n = 3$.

In the biomechanical testing process, the test model was secured within a universal testing machine (HT-2402 Universal material testing machine, Hung Ta Instrument Co., Ltd., Taichung, Taiwan). A strain gauge was attached near the interface between the femoral head and the implant. A downward force was then applied to the femoral head at a controlled loading speed of 2 mm/min,[42] and the strain gauge's value was recorded when the loading reached 2800 N. This

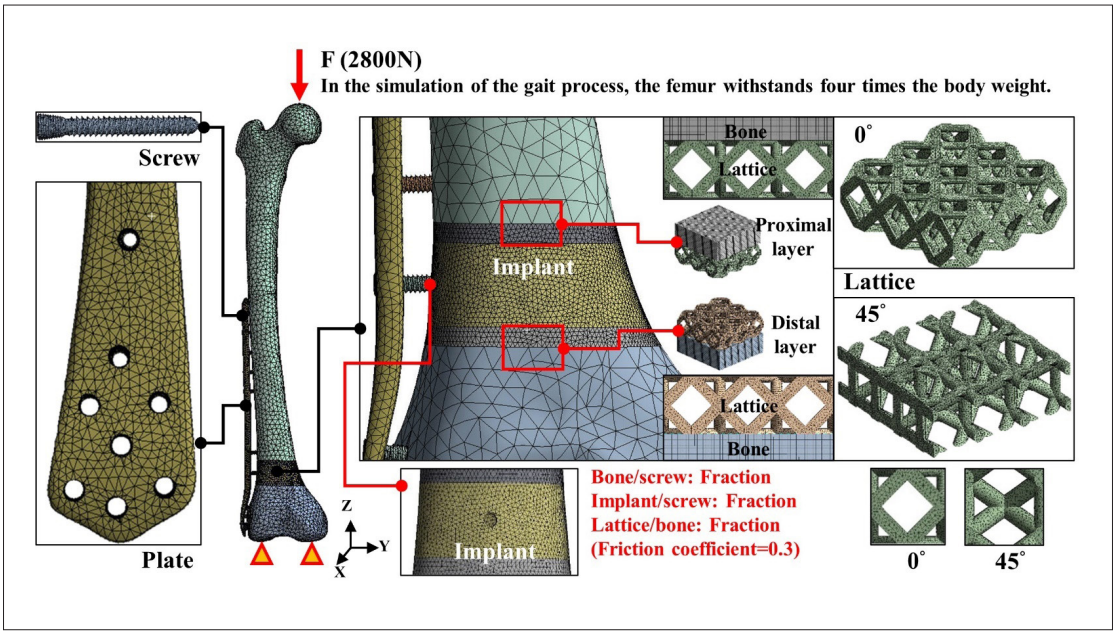

Figure 3. Demonstration of the mesh model for the finite element analysis.

procedure simulated the strain experienced in the bone surrounding the OLS implant, NLS implant, and bone cement during gait (Figure 4). The strain data obtained through biomechanical testing were compared with the values derived from finite element analysis to validate the accuracy of the analytical results.

2.6. *In vitro* biological tests of lattice structures

In vitro biological experiments were performed to observe the impact of a specific lattice structure on essential aspects of the behaviors of MG-63 cells, an osteoblast-like cell line, including growth, differentiation, and migration. The culture medium for cultivating MG-63 cells contains 10% fetal bovine serum. MG-63 cells were first cultured in an environment maintained at 37°C, 5% CO_2, 95% air, and 100% relative humidity for 48 h. A mixture of MG-63 cells and culture medium was quantitatively added to both smooth discs and discs featuring the OLS structure (n = 3). These specimens were then placed in a cell culture incubator for 24, 48, and 72 h. Following the completion of cell growth, a quantitative MTT solution (3-(4,5-dimethylthiazol-2-yl)-2,5-diphenyltetrazolium bromide) was added to each specimen. This solution reacts with the mitochondria in the cells, producing formazan. Subsequently, dimethyl sulfoxide (DMSO) solution was added to dissolve the formazan in the surviving MG-63 cells. The optical density value (OD value) of the solution was then measured using a full-wavelength spectrometer. Through a full-wavelength spectrometer, the transmittance and absorbance of the solution can be measured to evaluate the OD value. Higher OD values, resulting from lower transmittance, indicate a greater number of surviving MG-63 cells.

2.7. Animal experiments for simulating the efficacy of lattice osseointegration

Surgical procedures for animal experiments were approved by the Animal Use Protocol National Laboratory Animal Center (NARLabs) (IACUC Approval No.: TIRI-IACUC-2023-009). The experiments were conducted on Lanyu pigs, which were divided into two groups based on the type of implants: solid and optimized lattice structure. Each group consisted of three specimens (n = 3). These implant specimens, designed as cylinders (Ø 4.2 mm/L 10 mm), were fabricated using metal 3D printing, following the same parameters as described in the previous section for biomechanical specimens. The animal experiments were conducted in stages: preoperative, intraoperative, post-operative, and sacrifice. In the preoperative stage, a mixture of Zoletil/Telazol and xylazine was administered via intramuscular injection as premedication anesthesia, followed by penicillin G and meloxicam to prevent infections and alleviate pain. During the operation, a hole with a diameter of 4.2 mm and a depth of 10 mm was created in the distal lateral femur using a bone drill for the individual implantation of specimens. A plate (approximately 120 mm in length, 3 mm in thickness) and a screw (3 mm in diameter, 10 mm in length) were secured to the distal lateral femur to enhance strength. Post-surgery, C-arm fluoroscopy X-ray confirmed the position of implants and any abnormalities. Post-operative care included the oral administration of meloxicam and the antibiotic cephalexin

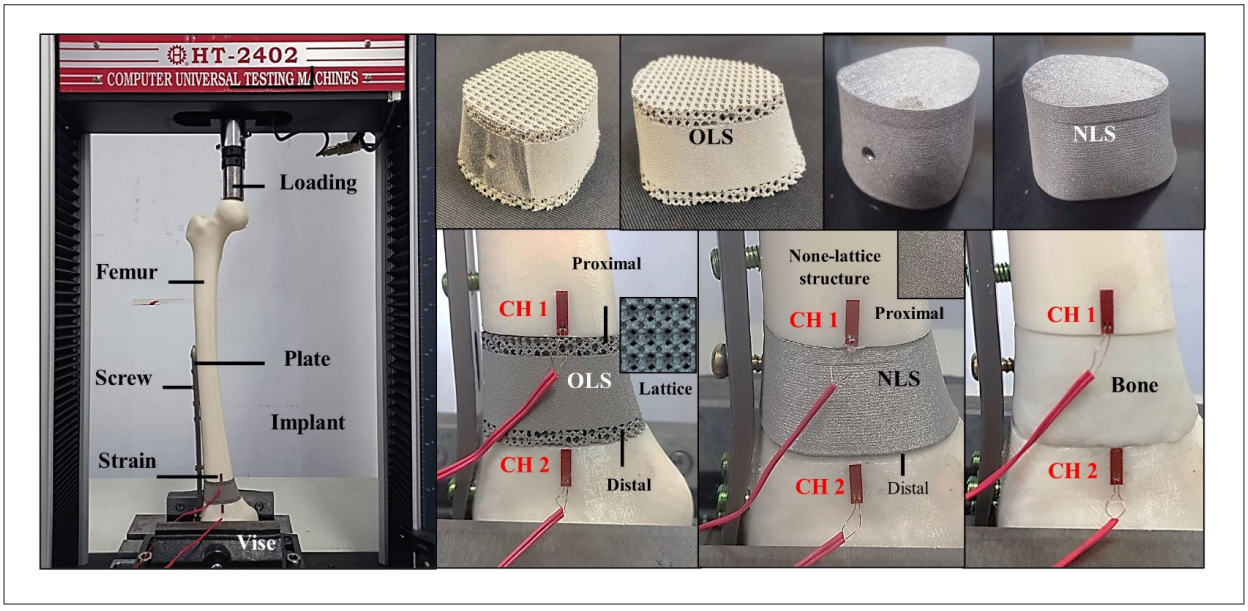

Figure 4. Biomechanical tests on the OLS implant, NLS implant, and bone cement for evaluating the strain in the bone surrounding the implant.

for 1 week, along with intramuscular meloxicam injection for pain management. Post-operative CT imaging at fixed intervals (2 weeks, 4 weeks, 8 weeks, and 12 weeks) assessed implant displacement or femur fractures. The animals were sacrificed 12 weeks post-surgery; after being deeply anesthetized, the animals were euthanized with intravenous KCl. After extracting femur segments, micro-CT (with a 9 μm resolution) employed for CT scan was performed for assessment of the density and area of the surrounding bone. This allowed for the evaluation of the osseointegration status of the specimens (Figure 5).

3. Results

3.1. Determination of lattice structure parameters for distal femur reconstruction

In the context of finite element analysis for distal femur reconstruction, the lattice structure within the proximal and distal layers of the implant was carefully designed. This lattice structure was characterized by an alignment angle of 45° and a pillar diameter of 0.8 mm. The analysis revealed that the bone in contact with this lattice structure displayed a maximum bone strain of no more than 4000 μ (proximal layer: -3840.0 μ/distal layer: -3528.3 μ). This lattice structure, referred to as the OLS, demonstrated a remarkable ability to promote bone growth within the implant (Table 2).

3.2. Biomechanical test results of OLS implant, NLS implant, and bone cement

To validate the accuracy of the analyzed values, the results of biomechanical tests were compared with those obtained from finite element analysis (Figure 6). In the proximal layer of the OLS implant, the analyzed strain around the bone was 1752.6 μ. Biomechanical testing using a strain gauge at the same location produced an average strain of 2046.4 μ, resulting in a 16.8% difference between the analyzed and tested results. In the distal layer of the OLS implant, the analyzed strain was 1966.8 μ. The average strain value obtained from the tests was 2252.6 μ, yielding a difference of 14.5%. The comparison between the analytical and test data strongly indicates that the finite element analysis results align with the findings, showing high level of reliability.

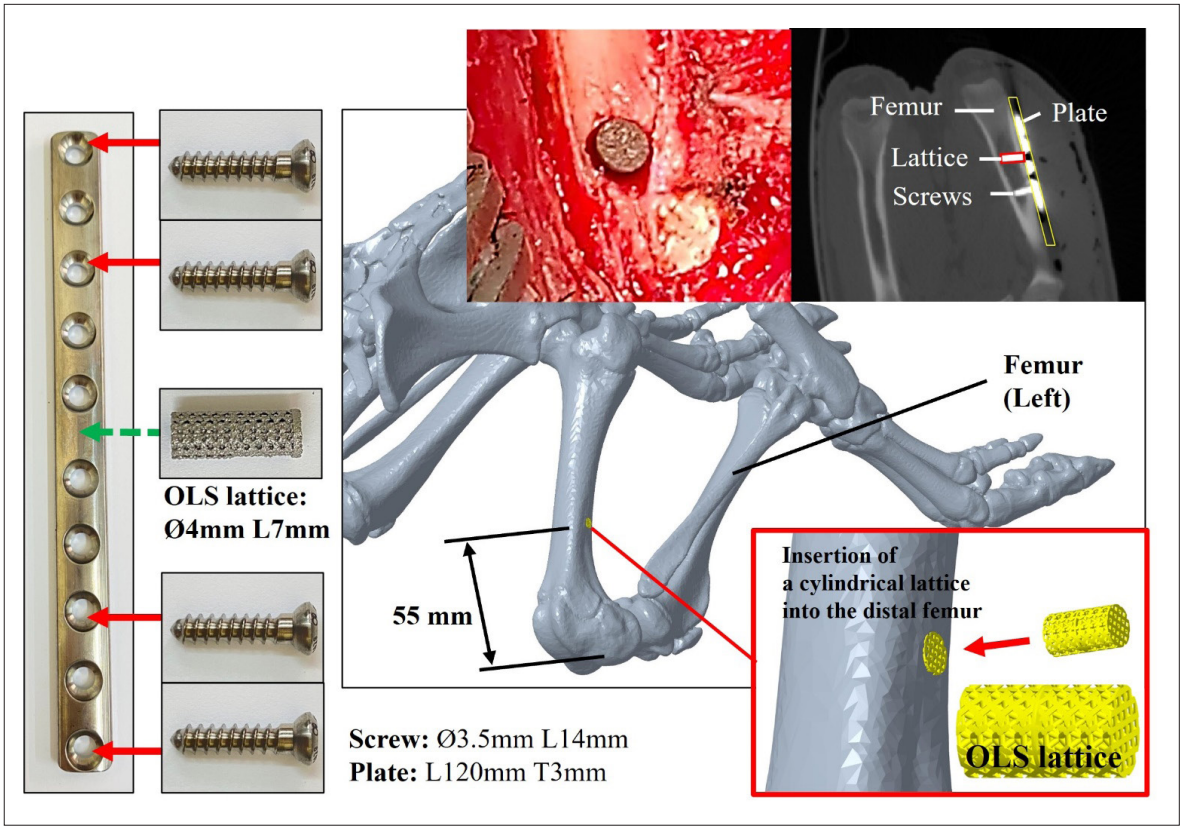

Figure 5. Animal experimental procedures and applications of implants.

Biomechanical tests revealed that the average bone strain around the proximal and distal layers of the OLS implant ranged from 2046.4 to 2252.57 μ. In contrast, the NLS implant exhibited a significant difference in bone strain between the proximal and distal layers, likely due to structural limitations hindering force transmission from the proximal to the distal layer, resulting in a bone strain of 994.37 μ in the distal layer. Conversely, the biomechanical test results of bone cement revealed a consistent issue, i.e., a significant difference in bone strain between the proximal and distal layers, which reach levels of 1483.15–4043.87 μ. Notably, the bone strain exceeded 4000 μ in the proximal layer, indicating that the bone cement had the least capacity for stimulating bone growth (Table 3).

Figure 7 illustrates the results of the *in vitro* biological test, with the transmittance wavelengths ranging approximately from 300 to 1000 nm. After 24 h of testing, the OLS disc exhibits significantly lower solution transmittance than the smooth disc, indicating higher OD values for the OLS disc group. This confirms a superior cell survival rate in the OLS disc group. Comparing different test times and their corresponding results reveals that the OLS structure indeed accelerates cell growth, while cell growth on the smooth disc is comparatively slow. This suggests that the structure of the OLS disc is better suited for facilitating both cell growth and proliferation.

3.3. Outcomes of the animal experiments

The results of the animal experiment revealed consistent stability, with no instances of implant displacement or dislodgement observed throughout the entire observation period. After a 12-week duration, the animals were sacrificed, and computerized tomography was utilized to capture images of the implants. The area encompassing both the implants and immature bone was reconstructed utilizing reverse engineering reconstruction software (Dragonfly, Object Research Systems (ORS), Montreal, Canada). In all three groups of implants, the percentage of intracavity growth exceeded 79.80%, underscoring

Table 2. Evaluation of bone strain around the proximal and distal layers of the implant's lattice

Third principal strain on the surrounding bones (Compression)							
Z, X, Y	Lattice angle (°)		Pillar diameter (mm)				
			0.6	0.7	0.8	0.9	1.0
Proximal layer, Distal layer	0°	Proximal	-1637.2 μ	-2304.4 μ	-2763.5 μ	-3422.0 μ	-2966.7 μ
		Distal	-738.7 μ	-1012.8 μ	-2420.4 μ	-3073.9 μ	-1493.4 μ
	45°	Proximal	-2135.3 μ	-2729.5 μ	-3840.0 μ	-5733.8 μ	-4317.7 μ
		Distal	-1787.9 μ	-2222.9 μ	-3528.3 μ	- 4518.1μ	-1726.6 μ

X, Y; Max., -650, -700, -750, -800, -900, -1100, -1300, -1500, Min.

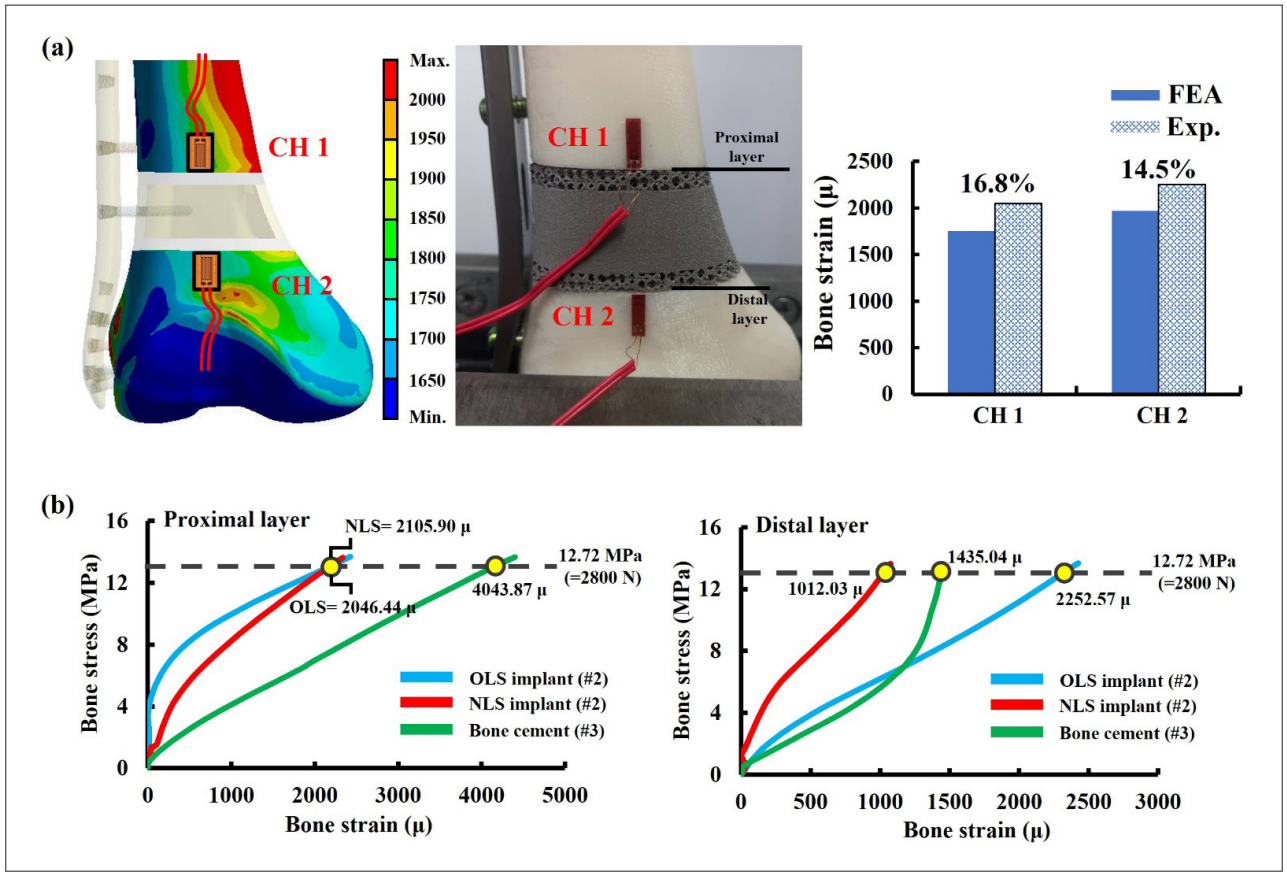

Figure 6. Biomechanical test results of OLS implant, NLS implant, and bone cement. (a) Validation of finite element analysis results; (b) biomechanical test results.

Table 3. Biomechanical test results of OLS implant, NLS implant, and bone cement

		Biomechanical test		
Bone strain (μ)		OLS implant	NLS implant	Bone cement
Proximal layer	Analysis value	1752.6	N/A	N/A
	Test #1	1977.82	2087.82	4035.33
	Test #2	2056.69	2116.69	4056.53
	Test #3	2104.81	2113.185	4039.75
	Average	2046.44	2105.90	4043.87
	sd.	64.11	15.75	11.18
	Differences (%)	16.77	N/A	N/A
Distal layer	Analysis value	1966.8	N/A	N/A
	Test #1	2193.40	1000.77	1535.85
	Test #2	2262.82	1012.03	1478.54
	Test #3	2301.48	970.31	1435.04
	Average	2252.57	994.37	1483.15
	sd.	54.76	21.58	50.56
	Differences (%)	14.53	N/A	N/A

the efficacy of the lattice design in guiding bone growth and achieving favorable osseointegration. Conversely, the solid implants, characterized by the non-porous structure, restricted immature bone growth to the external periphery of the implant, impeding penetration into the implant itself. This limitation significantly compromised the implant's ability to integrate with the surrounding bone. Notably, the volume of immature bone within the OLS surpassed the original implant cavity volume. This observation suggests that immature bone smoothly grows not only into the lattice structure but also along the implant's periphery. The immature bone effectively encompasses the implant, thereby augmenting the implant's osseointegration capability (Table 4).

4. Discussion

4.1. Optimal lattice structure design for implants in distal femur mechanical conditions

From a macroscopic perspective, it is crucial to examine the implant's structure to ensure its capability to withstand the body's weight and the daily-life force loading, such as those during walking, without suffering damage. In this study, the implant structure was designed to be hollow, with a thickness of 2 mm. The primary objective of this design was to allow for potential future incorporation of growth factors known to enhance osteoconductive properties.[43,44] The 2 mm thickness for the implant was based on relevant literature, which suggests that such a design could maintain adequate mechanical strength.[45]

Various structures, positions, and movement patterns within the body experience varying forms and magnitudes of loading. While walking, the hip bears an average load of 238% of body weight.[46] In a sitting position, the lumbar spine undergoes a pressure load of approximately 1698 N, contrasting with 1076 N in a standing position.[47] Throughout the gait cycle, the tibial and ankle regions can bear loads up to 3.5 times the body weight.[48] The craniofacial region frequently experiences masticatory forces, with molars bearing a load of around 250 N.[29] Comparing the loads in each area reveals significant differences, emphasizing the necessity to design implant lattices differently to accommodate various loading conditions and expedite implant osseointegration.

4.2. Correlation between lattice structure parameters and material properties

From a microcosmic perspective, it is essential for the lattice structure on the implant surface to possess an appropriate elastic modulus and favorable osteoconductive properties to facilitate bone growth into it. A crucial design criterion for distal femur defect reconstruction implant is selecting lattice structure parameters whose elastic modulus aligned that of nature bone,[10] while avoiding the stress shielding effect.[49-52] Upon further exploration of the relationship between lattice pillar diameter and material properties (Figure 8), it becomes evident that the bone strain around the lattice increases as the pillar diameter increases. The elastic modulus of the lattice shows significant growth as the pillar diameter increases, up to 0.9 mm, reaching elastic moduli of 14.99 GPa and 15.88 GPa. However, this leads to strains on the surrounding bones exceeding 4000 μ.[17] To prevent the lattice from having an excessively high elastic modulus, it is essential to avoid selecting a pillar diameter above 0.9 mm. The excessive modulus could adversely

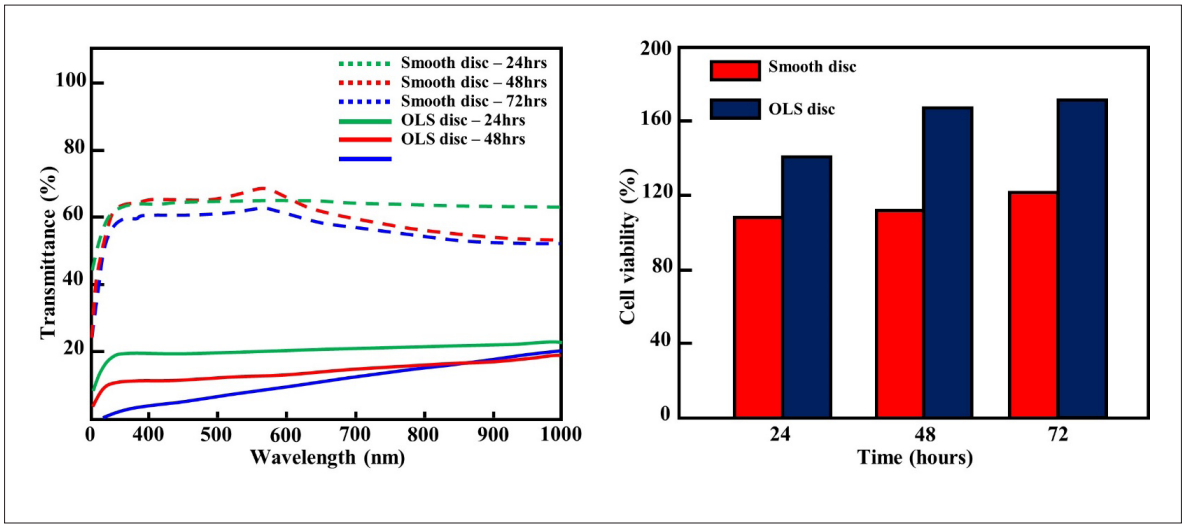

Figure 7. *In vitro* biological test results (solution transmittance and cell survival rate) for the smooth disc and OLS disc.

Table 4. Animal experiment results, including computed tomography images and volume of the models and bone

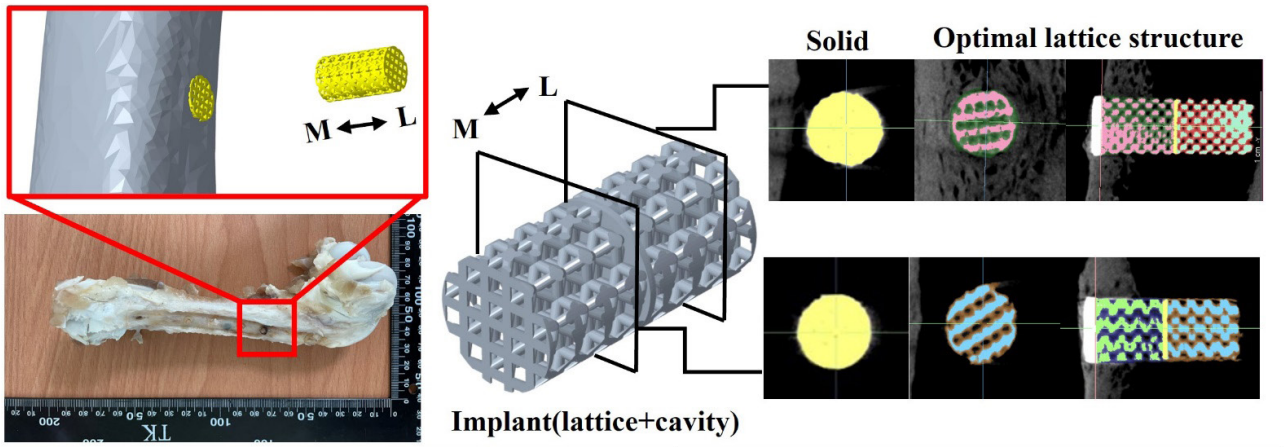

Implant(lattice+cavity) (mm^3)	138.474		
Lattice (mm^3)	50.94		
Implant cavity (mm^3)	87.534		
Volume calculation after testing	Test 1	Test 2	Test 3
Immature bone (mm^3)	89.49	63.72	78.69
Cavity (mm^3)	14.37	15.54	17.68
The proportion of immature bone growth (%) (within the implant)	83.58	82.25	79.80

impact strain distribution in the surrounding bone and reduce the lattice's osteoconductive properties.

Interestingly, when the lattice's pillar diameter was set to 1.0 mm, the strain generated by the lattice in contact with the bone decreased significantly, contrary to the expected increase, even though the elastic modulus increased to 27.41 and 30.50 GPa. The change from a 0.9 mm to a 1.0 mm pillar diameter resulted in the closure of quadrangular holes within the lattice structure (Figure 8). This alteration significantly increased the elastic modulus but also altered the strain patterns and tendencies within the bones. The surrounding bone strain did not reach the desired value with the altered lattice configuration. In this study, cuboctahedron lattices with pillar diameters greater than 0.9 mm were categorized as different lattice types (different lattice families) and were not taken into consideration.

On the other hand, the alignment angles of the lattice also play a significant role in influencing bone strain. The analysis results indicated that a lattice alignment angle of 45° led to greater variations in bone strain when compared to a lattice arrangement angle of 0°. Intriguingly, while considering the different arrangement angles, it was noted that the changes in the elastic modulus of the lattice were not particularly substantial. This suggests that there might be additional factors contributing to the analytical outcomes. In this study, the surface area of the lattice (the area in contact with the bone) was calculated for various alignment angles. The results revealed that the lattice with 0° alignment exhibited a larger surface area, approximately 1.25 to 2.88 times larger than that of the lattice with 45° alignment. According to the stress calculation equation ($\sigma = P/A$), stress is inversely proportional to the area.[16] This implies that, for a constant force (P), a smaller lattice surface area leads to higher stress on the bone in contact with the lattice, consequently increasing the bone strain[53] (Figure 9). Therefore, the lattice was designed with parameters of 0.8 mm diameter and 45° alignment angle, which allow for generating bone strain close to, but not exceeding, 4000 μ, in the contacted bone. This design offers improved osteoconductive properties and enhances the osseointegration effect of the implant.

Diverse lattice alignment angles not only yield different contact areas but also influence the stress distribution within the lattice. The bone strain in contact with the lattice structure increases as the lattice becomes stronger (exhibiting higher lattice stress, specifically von Mises

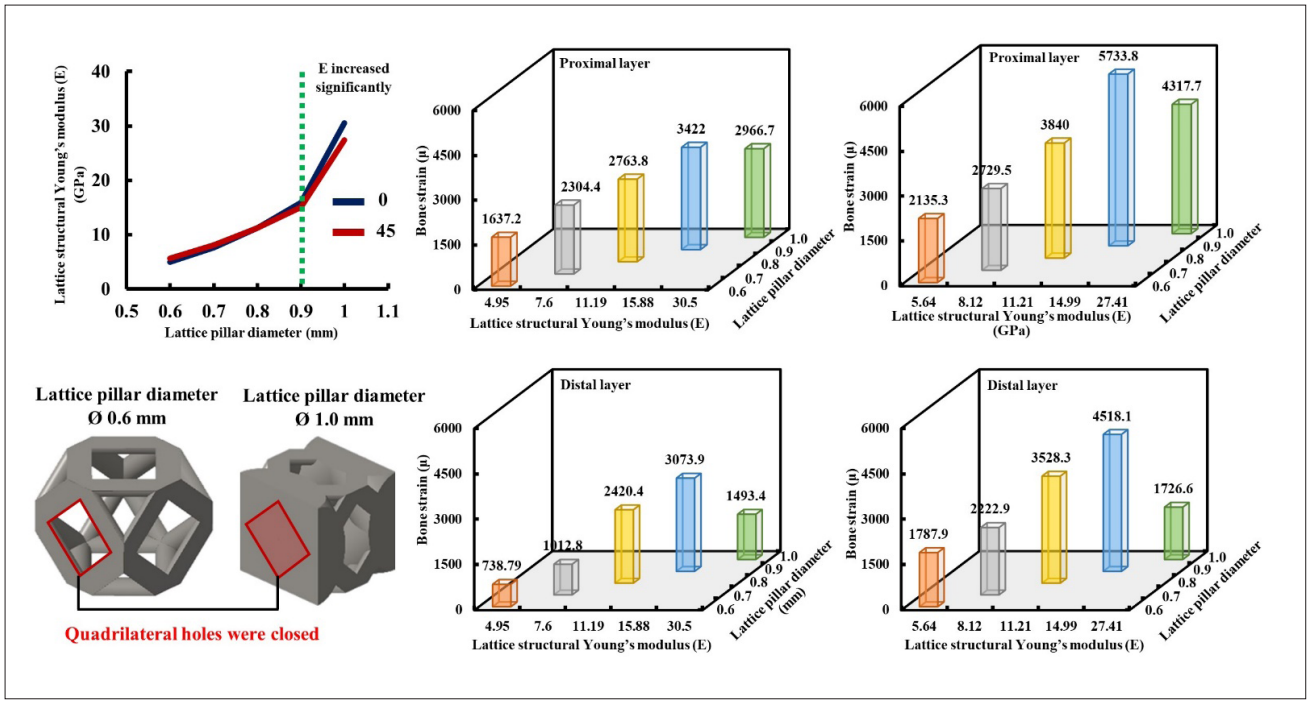

Figure 8. Relationship between lattice pillar diameter/elastic modulus and bone strain.

stress).[54] The lattice structural stress was measured at 0° and 45° alignment angles (proximal layer lattice with a 0.8 mm diameter), and the results showed that the stress in the 0° lattice structure was 1954.5 MPa, approximately 16% lower than the stress in the 45° lattice structure (2272.8 MPa) (Figure 10). The stress distribution in the 45° lattice structure allowed for more effective transmission of forces from the bone-contact surface to the interior of the implant. Such efficient transmission facilitated continuous stimulation of bone cells as they grew deeper into the lattice structure, thereby enhancing cell attachment, migration, growth, and differentiation.

4.3. Sensitivity analysis of lattice diameter and alignment angle parameters

One main objective of this study was to identify which lattice structural parameter, either lattice strut diameter or lattice alignment angle, plays a more pivotal role in the design of distal femur reconstruction implants. Both parameters influence osteoconductive capacity and osseointegration, but the importance of their effects remained uncertain. To address this, sensitivity analysis was employed to identify the key factor among these lattice parameters. The sensitivity parameters, lattice pillar diameter (0.6/0.7/0.8/0.9 mm), and lattice alignment angle (0° and 45°) were calculated and analyzed using the sensitivity analysis module in Ansys software. The response variable in this analysis was bone strain in contact with the lattice. The sensitivity analysis utilizes the space-filling Latin hypercube sampling method of adaptive metamodel of optimal prognosis (AMOP) for point sampling. Response surface method (RSM) was applied to fit dataset and generate a response surface. The sensitivity value of the parameter was determined by calculating the slope of the response surface.[55]

The results of the sensitivity analysis showed that the lattice pillar diameter has a substantial influence on the response, accounting for 65.9%, while the lattice alignment angle contributes to 27% (Figure 11). These findings indicate that varying the lattice pillar diameter parameter has the most significant impact on bone strain. Notably, the results align with the findings obtained from the finite element analysis. The findings suggest that when altering the cuboctahedron lattice, emphasizing the design of the lattice diameter can effectively address various mechanical conditions and achieve the desired strain in the surrounding bone. This approach facilitates the application of various lattices for different patients with distal femur defect.

4.4. Bioactivity of the lattice-structured implant

In vitro biological test assessments have revealed the OLS implant's structural compatibility with cell growth, indicating its suitability for cellular proliferation. Notably, even in the absence of mechanical loading, the observed

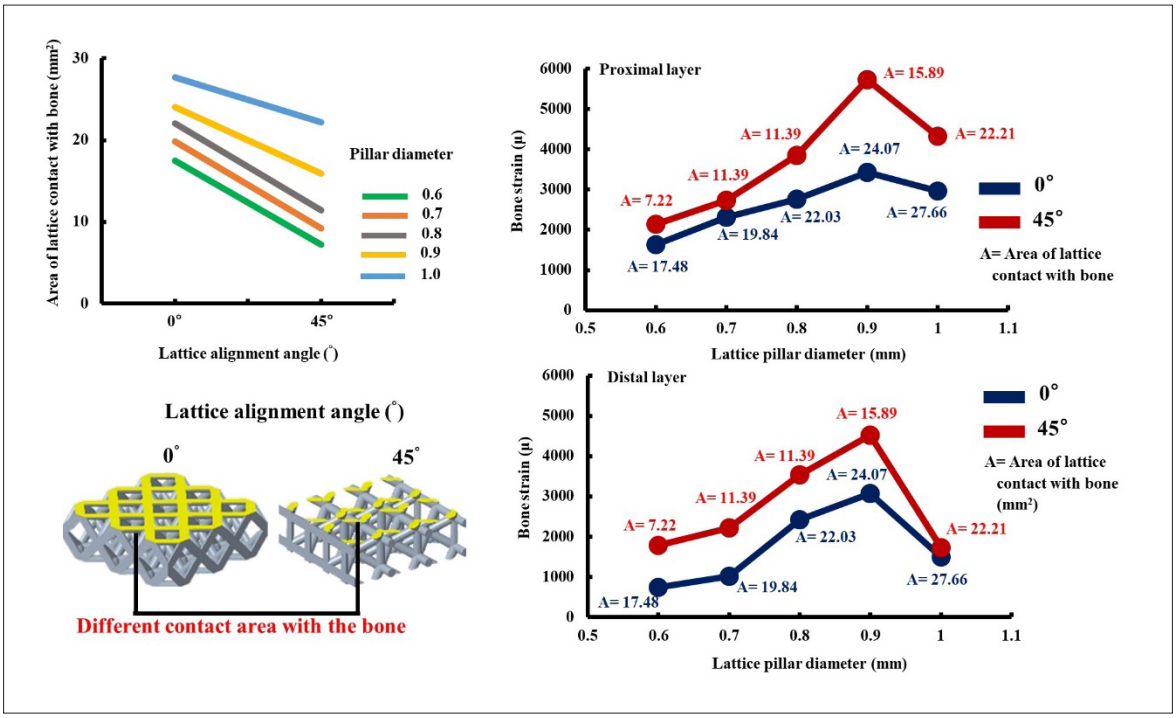

Figure 9. Relationship between lattice alignment angle/surface area and bone strain.

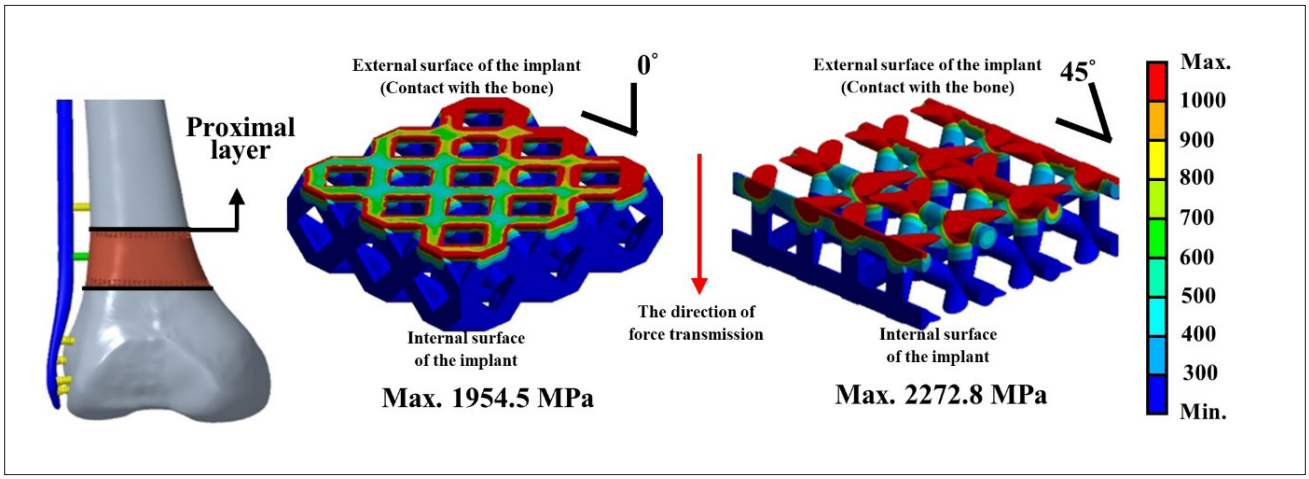

Figure 10. von Mises stress distribution for 0° and 45° lattice alignment angle.

outcome may be attributed to the porosity and structure of the lattice. The OLS implant's surface features flat areas that offer a favorable environment for initial cell adhesion, promoting cell stabilization and survival. As cells grow into the lattice's internal void, the OLS implant's varied corner features facilitate cell clustering, inducing differentiation and proliferation. Consequently, the OLS implant demonstrated superior biological activity compared to the smooth disc in *in vitro* biological tests.

Additionally, literature suggests that a lattice porosity ranging from 60% to 70% is deemed optimal for cell growth.[56] In alignment with this, the OLS implant exhibited a porosity of 69.8% in this study. This affirms that, for favorable bone growth characteristics, the lattice must not only undergo mechanical stimulation but also possess a structure conducive to cellular growth. Such attributes are crucial for facilitating the implant to achieve favorable osseointegration.

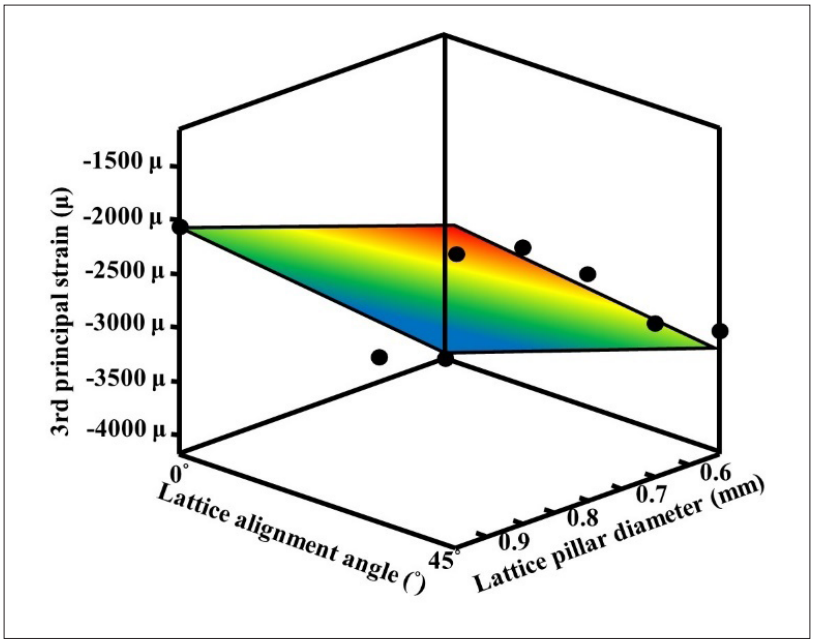

Figure 11. Sensitivity analysis results for the diameter of lattice pillars and lattice alignment angles.

In future studies, enhancing lattice bone growth could involve filling the lattice voids with growth factors, potentially inducing and accelerating osteoblasts to grow into the voids.[57-60] The present study introduces a lattice structure designed to stimulate the bone interface. Moreover, its capability to carry growth factors or drugs within the void accelerates osteoblast differentiation and proliferation.

4.5. Implications of biomechanical test results for clinical applications

Variations in implant structures and strengths impact the stress distribution between the femur and the implant, as well as the strain distribution in the surrounding bone. The absence of microstructure on the exterior of the implant (NLS implant) leads to an overall increase in the elastic modulus of the implant. This increase may result in stress shielding in the proximal layer of the implant, which has been well-documented in previous studies.[49-52] Additionally, this effect causes a decrease in the strain on the bone in contact with the implant, leading to surrounding bone loss and affecting the strain in the distal layer of the bone. Bone cement exhibited results opposite to those of NLS implant, primarily due to its lower modulus of elasticity (2.65 GPa).[61] The strain on the bone head in contact with the proximal layer of the implant exceeded 4000 μ, hindering bone growth stimulation and reducing osseointegration efficiency. From a structural perspective, neither the NLS implant nor the bone cement provides an ideal environment for osteoblast attachment, differentiation, and growth. In contrast, the lattice structure design of the implant offers distinct advantages in this regard. By modifying the lattice design, adjusting the implant's elastic modulus, and optimizing the bone contact area, a more favorable environment for osteoblast attachment, differentiation, and growth can be created. This, in turn, allows for early osseointegration in the weight-bearing area of the reconstructed femur.[62] Such early osseointegration is vital for the restoration of strength loading, ultimately enabling the patient to regain their daily mobility.

The lattice structure serves as a specialized design to foster an environment conducive to osseointegration, with its structural strength tailored to align with the specific biomechanical conditions of distinct body regions. To assess the suitability of the lattice structure for cell attachment, growth, and reproduction in a static environment, an *in vitro* biological test was conducted. The *in vivo* osseointegration capability of the implant was verified through the animal experiment, in which the implant was inserted into the pig femur, mimicking the biomechanical conditions and responses in the human body. Results from both tests demonstrated that the lattice structure provided increased 3D space on the implant's surface, effectively promoting osseointegration. Existing literature suggests that femur bone healing typically spans 8 to 14 weeks.[63] In comparison, our animal experiment revealed that the OLS implant achieved nearly full cavity volume growth (approximately 80%) within 12 weeks.

This confirms that the osseointegration time between the defective bone and the implant is comparable to the bone-to-bone osseointegration time.

4.6. Limitations of the study

In this study, the OLS implant was designed specifically for a distinct region of the distal femur. Future considerations should involve gathering cases of distal femur tumors or fractures, segmenting the femur into sections, and designing varied optimal microstructures based on the diverse biomechanical conditions of each section. This approach aims to comply with the clinical requirements of osseointegration.

5. Conclusion

This study aimed to develop an innovative implant for reconstructing large bone defects in the distal femur, focusing on optimizing the lattice design at the bone interface to effectively stimulate surrounding bone growth. By utilizing the biomechanical conditions specific to the distal femur and employing finite element analysis, we determined that a lattice design featuring a 0.8 mm pillar diameter and a 45° alignment angle would induce the appropriate strain in the surrounding bone for bone growth (approximating 4000 μ). Biomechanical tests further confirmed that the OLS implant efficiently stimulates the surrounding bone, generating a strain ranging from 2046.4 μ to 2252.57 μ, conducive to bone growth. *In vitro* biological tests have substantiated that the conductivity of the OLS implant is conducive to promoting cell growth and proliferation. Additionally, animal studies have demonstrated that the material and structural characteristics of the OLS implant effectively induce osseointegration, with the percentage of intraluminal growth exceeding 79.8%. The implant's notable bioactivity also enhances its osseointegration capability.

Acknowledgments

None

Funding

This work was supported by the National Science and Technology Council (Project NSTC 112-2221-E-032-004-MY3).

Conflict of interest

The authors declare no conflicts of interest.

Author contributions

Conceptualization: Chun-Ming Chang, Pei-Chun Wong, Yu-Tzu Wang

Formal analysis: Chih-En Ko, Yu-Tzu Wang

Investigation: Chun-Ming Chang, Yu-Tzu Wang

Methodology: Chun-Ming Chang, Pei-Chun Wong, Yu-Tzu Wang

Writing – original draft: Chun-Ming Chang, Sin-Liang Ou, Yu-Tzu Wang

Writing – review & editing: Yu-Tzu Wang

Ethics approval and consent to participate

Surgical procedures for animal experiments were approved by the Animal Use Protocol National Laboratory Animal Center (NARLabs) (Protocol Title: Long-term Stability of lattice Implant, IACUC Approval No.: TIRI-IACUC-2023-009).

Consent for publication

Not applicable.

Availability of data

Data are available from the corresponding author upon reasonable request.

Reference

1. Wiese A, Pape HC. Bone defects caused by high-energy injuries, bone loss, infected nonunions, and nonunions. *Orthop Clin North Am.* 2010;41(1):1-4. doi: 10.1016/j.ocl.2009.07.003

2. Seitz H, Rieder W, Irsen S, Leukers B, Tille C. Three-dimensional printing of porous ceramic scaffolds for bone tissue engineering. *J Biomed Mater Res B Appl Biomater.* 2005;74(4):782-788. doi: 10.1002/jbm.b.30291

3. Jones AC, Arns CH, Sheppard AP, Hutmacher DW, Milthorpe BK, Knackstedt MA. Assessment of bone ingrowth into porous biomaterials using MICRO-CT. *Biomaterials.* 2007;28(15):2491-2504. doi: 10.1016/j.biomaterials.2007.01.046

4. Eil Bakhtiari SS, Bakhsheshi-Rad HR, Karbasi S, et al. Polymethyl methacrylate-based bone cements containing carbon nanotubes and graphene oxide: an overview of physical, mechanical, and biological properties. *Polymers.* 2020;12(7):1469. doi: 10.3390/polym12071469

5. Vaishya R, Chauhan M, Vaish A. Bone cement. *J Clin Orthop Trauma.* 2013;4(4):157-163. doi: 10.1016/j.jcot.2013.11.005

6. Gundapaneni D, Goswami T. Thermal isotherms in PMMA and cell necrosis during total hip arthroplasty. *J Appl Biomater Funct Mater.* 2014;12(3):193-202. doi: 10.5301/jabfm.5000196

7. Revie IC, Wallace ME, Orr JF. The effect of PMMA thickness on thermal bone necrosis around acetabular sockets. *Proc Inst Mech Eng H.* 1994;208(1):45-51. doi: 10.1177/095441199420800106

8. Hasandoost L, Rodriguez O, Alhalawani A, et al. The role of poly(methyl methacrylate) in management of bone loss and infection in revision total knee arthroplasty: a review. *J Funct Biomater.* 2020;11(2):25. doi: 10.3390/jfb11020025

9. Mnaymneh W, Malinin TI, Lackman RD, Hornicek FJ, Ghandur-Mnaymneh L. Massive distal femoral osteoarticular allografts after resection of bone tumors. *Clin Orthop Relat Res.* 1994;303:103-115. doi: 10.1097/00003086-199406000-00013

10. Kim T, See CW, Li X, Zhu D. Orthopedic implants and devices for bone fractures and defects: past, present and perspective. *Eng Regen*. 2020;1:6-18. doi: 10.1016/j.engreg.2020.05.003

11. Song Y, Xu DS, Yang R, Li D, Wu WT, Guo ZX. Theoretical study of the effects of alloying elements on the strength and modulus of β-type bio-titanium alloys. *Mater Sci Eng A*. 1999;260(1):269-274. doi: 10.1016/S0921-5093(98)00886-7

12. Velasco MA, Narváez-Tovar CA, Garzón-Alvarado DA. Design, materials, and mechanobiology of biodegradable scaffolds for bone tissue engineering. *Biomed Res Int.* 2015;2015:729076. doi: 10.1155/2015/729076

13. Geetha M, Singh AK, Asokamani R, Gogia AK. Ti based biomaterials, the ultimate choice for orthopaedic implants – a review. *Prog Mater Sci.* 2009;54(3):397-425. doi: 10.1016/j.pmatsci.2008.06.004

14. Liu Y, Li K, Wu H, et al. Synthesis of Ti-Ta alloys with dual structure by incomplete diffusion between elemental powders. *J Mech Behav Biomed Mater.* 2015;51:302-312. doi: 10.1016/j.jmbbm.2015.07.004

15. Arabnejad S, Burnett Johnston R, Pura JA, Singh B, Tanzer M, Pasini D. High-strength porous biomaterials for bone replacement: a strategy to assess the interplay between cell morphology, mechanical properties, bone ingrowth and manufacturing constraints. *Acta Biomater.* 2016;30:345-356. doi: 10.1016/j.actbio.2015.10.048

16. Hsieh MT, Begley MR, Valdevit L. Architected implant designs for long bones: advantages of minimal surface-based topologies. *Mater Des.* 2021;207:109838. doi: 10.1016/j.matdes.2021.109838

17. Mikuni-Takagaki Y, Suzuki Y, Kawase T, Saito S. Distinct responses of different populations of bone cells to mechanical stress. *Endocrinology.* 1996;137(5):2028-2035. doi: 10.1210/endo.137.5.8612544

18. Ehrlich PJ, Lanyon LE. Mechanical strain and bone cell function: a review. *Osteoporos Int.* 2002;13(9):688-700. doi: 10.1007/s001980200095

19. Al-Tamimi AA, Almeida H, Bartolo P. Structural optimization for medical implants through additive manufacturing. *Prog Addit Manuf.* 2020;5(2):95-110. doi: 10.1007/s40964-020-00109-7

20. Burton HE, Eisenstein NM, Lawless BM, et al. The design of additively manufactured lattices to increase the functionality of medical implants. *Mater Sci Eng C Mater Biol Appl.* 2019;94:901-908. doi: 10.1016/j.msec.2018.10.052

21. Wang P, Li X, Luo S, Nai MLS, Ding J, Wei J. Additively manufactured heterogeneously porous metallic bone with biostructural functions and bone-like mechanical properties. *J Mater Sci Technol.* 2021;62:173-179. doi: 10.1016/j.jmst.2020.05.056

22. Bucklen BS, Wettergreen WA, Yuksel E, Liebschner MAK. Bone-derived CAD library for assembly of scaffolds in computer-aided tissue engineering. *Virtual Phys Prototyp.* 2008;3(1):13-23. doi: 10.1080/17452750801911352

23. Van Bael S, Chai YC, Truscello S, et al. The effect of pore geometry on the in vitro biological behavior of human periosteum-derived cells seeded on selective laser-melted Ti6Al4V bone scaffolds. *Acta Biomater.* 2012;8(7):2824-2834. doi: 10.1016/j.actbio.2012.04.001

24. Guoqing Z, Junxin L, Chengguang Z, Juanjuan X, Xiaoyu Z, Anmin W. Design optimization and manufacturing of bio-fixed tibial implants using 3D printing technology. *J Mech Behav Biomed Mater.* 2021;117:104415. doi: 10.1016/j.jmbbm.2021.104415

25. Mishra RN, Singh MK, Kumar V. Biomechanical analysis of human femur using finite element method: a review study. *Mater Today: Proc.* 2022;56(1):384-389. doi: 10.1016/j.matpr.2022.01.222

26. Alabort E, Barba D, Reed RC. Design of metallic bone by additive manufacturing. *Scr Mater.* 2019;164:110-114. doi: 10.1016/j.scriptamat.2019.01.022

27. Lozanovski B, Leary M, Tran P, et al. Computational modelling of strut defects in SLM manufactured lattice structures. *Mater Des.* 2019;171:107671. doi: 10.1016/j.matdes.2019.107671

28. Ejnisman L, Gobbato B, de França Camargo AF, Zancul E. Three-dimensional printing in orthopedics: from the basics to surgical applications. *Curr Rev Musculoskelet Med*. 2021;14(1):1-8. doi: 10.1007/s12178-020-09691-3

29. Wang YT, Hsu CK. Novel parameter optimization lattice design for improving osseointegration in hypo-loading regions – a case study of maxillary tumor reconstruction implant. *Mater Des.* 2023;233(2023):112274. doi: 10.1016/j.matdes.2023.112274

30. Lee KS, Lee WC, Kim PG, et al. Biomechanical evaluation of initial stability of a root analogue implant design with

drilling protocol: a 3D finite element analysis. *Appl Sci*. 2020;10:4104.
doi: 10.3390/app10124104

31. Delikanli YE, Kayacan MC. Design, manufacture, and fatigue analysis of lightweight hip implants. *J Appl Biomater Funct Mater.* 2019;17(2):2280800019836830.
doi: 10.1177/2280800019836830

32. Kang J, Dong E, Li X, et al. Topological design and biomechanical evaluation for 3D printed multi-segment artificial vertebral implants. *Biomater Adv*. 2021;127: 112250.
doi: 10.1016/j.msec.2021.112250

33. Kang H, Lin CY, Hollister SJ. Topology optimization of three dimensional tissue engineering scaffold architectures for prescribed bulk modulus and diffusivity. *Struct Multidiscipl Optim*. 2010;42(4):633-644.
doi: 10.1007/s00158-010-0508-8

34. Rayhan SB, Rahman M. Modeling elastic properties of unidirectional composite materials using Ansys material designer. *Int J Struct Integr.* 2020;28:1892-1900.
doi: 10.1016/j.prostr.2020.11.012

35. Raja BK, Arun KC, Dheenadayalan J. Classification of distal femur fractures and their clinical relevance. *Trauma Int*. 2016;2(1):3-6.
doi: 10.13107/ti.2016.v02i01.012

36. Schmidt U, Penzkofer R, Bachmaier S, Augat P. Implant material and design alter construct stiffness in distal femur locking plate fixation: a pilot study. *Clin Orthop Relat Res.* 2013;471(9):2808-2814.
doi: 10.1007/s11999-013-2867-0

37. Ahirwar H, Gupta VK, Nanda HS. Finite element analysis of fixed bone plates over fractured femur model. *Comput Methods Biomech Biomed Engin.* 2021;24(15): 1742-1751.
doi: 10.1080/10255842.2021.1918123

38. Chethan KN, Bhat SN, Shenoy SB. Biomechanics of hip joint: a systematic review. *Int J Eng Technol.* 2018;7(3): 1672-1676.
doi: 10.14419/ijet.v7i3.15231

39. Darwish SM, Al-Samhan AM. Optimization of artificial hip joint parameters. *Materwiss Werksttech*. 2009;40(3):218-223.
doi: 10.1002/mawe.200900430

40. Niinomi M. Mechanical properties of biomedical titanium alloys. *Mater Sci Eng A*. 1998;243(1):231-236.
doi: 10.1016/S0921-5093(97)00806-X

41. Reina-Romo E, Sampietro-Fuentes A, Gómez-Benito MJ, Domínguez J, Doblaré M, García-Aznar JM. Biomechanical response of a mandible in a patient affected with hemifacial microsomia before and after distraction osteogenesis. *Med Eng Phys.* 2010;32(8):860-866.
doi: 10.1016/j.medengphy.2010.05.012

42. Zhang Y, Yan C, Zhang L, Zhang W, Wang G. Comparison of ordinary cannulated compression screw and double-head cannulated compression screw fixation in vertical femoral neck fractures. *Biomed Res Int.* 2020;2020:2814548.
doi: 10.1155/2020/2814548

43. Maia PW, Teixeira ML, Scavone de Macedo LG, et al. Use of platelet-rich fibrin associated with xenograft in critical bone defects: histomorphometric study in rabbits. *Symmetry.* 2019;11(10):1293.
doi: 10.3390/sym11101293

44. Bai MY, Wang CW, Wang JY, Lin MF, Chan WP. Three-dimensional structure and cytokine distribution of platelet-rich fibrin. *Clinics (Sao Paulo)*. 2017;72(2):116-124.
doi: 10.6061/clinics/2017(02)09

45. Wu PK, Lee CW, Sun WH, Lin CL. Biomechanical analysis and design method for patient-specific reconstructive implants for large bone defects of the distal lateral femur. *Biosensors.* 2022;12(1):4.
doi: 10.3390/bios12010004

46. Bergmann G, Deuretzbacher G, Heller M, et al. Hip contact forces and gait patterns from routine activities. *J Biomech.* 2001;34(7):859-871.
doi: 10.1016/s0021-9290(01)00040-9

47. Callaghan JP, McGill SM. Low back joint loading and kinematics during standing and unsupported sitting. *Ergonomics*. 2001;44(3):280-294.
doi: 10.1080/00140130118276

48. Hamandi F, Laughlin R, Goswami T. Failure analysis of PHILOS plate construct used for pantalar arthrodesis paper II—screws and FEM simulations. *Metals.* 2018;8(4):279.
doi: 10.3390/met8040279

49. Arabnejad S, Burnett Johnston R, Pura JA, Singh B, Tanzer M, Pasini D. High-strength porous biomaterials for bone replacement: a strategy to assess the interplay between cell morphology, mechanical properties, bone ingrowth and manufacturing constraints. *Acta Biomater.* 2016;30: 345-356.
doi: 10.1016/j.actbio.2015.10.048

50. Park JY, Park SH, Kim MG, Park SH, Yoo TH, Kim MS. Biomimetic scaffolds for bone tissue engineering. *Adv Exp Med Biol.* 2018;1064:109-121.
doi: 10.1007/978-981-13-0445-3_7

51. Boyle C, Kim IY. Comparison of different hip prosthesis shapes considering micro-level bone remodeling and stress-shielding criteria using three-dimensional design space topology optimization. *J Biomech.* 2011;44(9):1722-1728.
doi: 10.1016/j.jbiomech.2011.03.038

52. Rahmanian R, Moghaddam NS, Haberland C, Dean D, Miller M, Elahinia M. Load bearing and stiffness tailored NiTi implants produced by additive manufacturing: a simulation study. *Proc SPIE*. 2014;9058:905814.
doi: 10.1117/12.2048948

53. Alghamdi HS. Methods to improve osseointegration of

dental implants in low quality (type-IV) bone: an overview. *J Funct Biomater.* 2018;9(1):7.
doi: 10.3390/jfb9010007

54. Maskery I, Aremu AO, Parry L, Wildman RD, Tuck CJ, Ashcroft IA. Effective design and simulation of surface-based lattice structures featuring volume fraction and cell type grading. *Mater Des.* 2018;155:220-232.
doi: 10.1016/j.matdes.2018.05.058

55. Sahu NK, Andhare AB. Multiobjective optimization for improving machinability of Ti-6Al-4V using RSM and advanced algorithms. *J Comput Des Eng.* 2019;6(1):1-12.
doi: 10.1016/j.jcde.2018.04.004

56. Taniguchi N, Fujibayashi S, Takemoto M, et al. Effect of pore size on bone ingrowth into porous titanium implants fabricated by additive manufacturing: an in vivo experiment. *Mater Sci Eng C Mater Biol Appl.* 2016;59:690-701.
doi: 10.1016/j.jmst.2020.05.056

57. Roberts TT, Rosenbaum AJ. Bone grafts, bone substitutes and orthobiologics: the bridge between basic science and clinical advancements in fracture healing. *Organogenesis.* 2012;8(4):114-124.
doi: 10.4161/org.23306

58. Bhatt RA, Rozental TD. Bone graft substitutes. *Hand Clin.* 2012;28(4):457-468.
doi: 10.1016/j.hcl.2012.08.001

59. Harwood PJ, Ferguson DO, Michael ALR. An update on fracture healing and non-union. *Orthop Trauma.* 2010;24(1):9-23.
doi: 10.1016/j.mporth.2009.12.004

60. Fisher DM, Wong JM, Crowley C, Khan WS. Preclinical and clinical studies on the use of growth factors for bone repair: a systematic review. *Curr Stem Cell Res Ther.* 2013;8(3):260-268.
doi: 10.2174/1574888x11308030011

61. Kharmanda G. Integration of multi-objective structural optimization into cementless hip prosthesis design: improved Austin-Moore model. *Comput Methods Biomech Biomed Engin.* 2016;19(14):1557-1566.
doi: 10.1080/10255842.2016.1170121

62. Xiong YZ, Gao RN, Zhang H, Dong LL, Li JT, Li X. Rationally designed functionally graded porous Ti6Al4V scaffolds with high strength and toughness built via selective laser melting for load-bearing orthopedic applications. *J Mech Behav Biomed Mater.* 2020;104:103673.
doi: 10.1016/j.jmbbm.2020.103673

63. Ding W. Opportunities and challenges for the biodegradable magnesium alloys as next-generation biomaterials. *Regen Biomater.* 2016;3(2):79-86.
doi: 10.1093/rb/rbw003

Our Journals

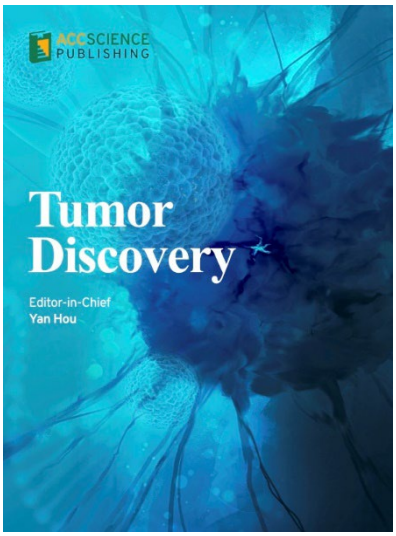

Tumor Discovery is a peer-reviewed and open-access journal that aims to present new cancer research with strong emphasis on fundamental and translational studies. *Tumor Discovery* covers topics, including but not limited to the following:

- Etiology and pathogenesis of cancer
- Mechanisms and molecular pathways underlying cancer initiation and progression
- Tumor metastasis
- Tumor evolution and heterogeneity
- Tumor microenvironment and tumor-host interactions
- Cancer genetics and genomics
- Cancer characterization using omics approaches
- Discovery and validation of cancer biomarker
- Discovery of new therapeutic targets
- New approaches of diagnostic and treatment modalities
- Statistical methods in cancer research

Global Translational Medicine is a quarterly journal that focuses on medicine, biological sciences, and biomaterials engineering. The goal of *Global Translational Medicine* is to provide a platform to researchers for showcasing their latest research works in translational medicine so as to advance the field towards the betterment of human health. Despite the advancement of omics and new technologies, the process of transforming these technologies and scientific research results into effective therapies and putting them into clinical use still has a long way to go. *Global Translational Medicine* provides a platform to fill the gaps in preclinical and inter-disciplinary research, to promote clinical translation of scientific research results, and to contribute to the conception of new and improved preventive measures as well as diagnostic and therapeutic techniques of diseases.

Global Translational Medicine covers the following themes: cardiovascular disease, metabolism/diabetes/obesity, neuroscience/neurology, cancer, biomaterials and their applications in medicine, proteomics/metabolomics, pharmacogenomics, biomarkers, bioinformatics and data mining, animal and clinical research, and medical methods arising from interdisciplinary crossover.

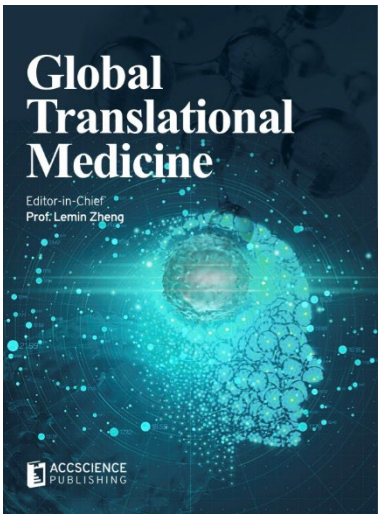

Start a new journal

Write to us via email if you are interested to start a new journal with AccScience Publishing. Please attach your CV, professional profile page and a brief pitch proposal in your email. We shall inform you of our decision whether we are interested to collaborate in starting a new journal.

Contact: info@accscience.com

ACCSCIENCE PUBLISHING

ACCSCIENCE PUBLISHING

Publishing Office:
8 Burn Road, #15-03 Trivex, Singapore 369977.
Editorial Office:
30-2, Jalan BS 1/2, Olive Hill Business Park, 43300 Seri Kembangan, Selangor. Malaysia.

Editorial Office: editor.ijb@accscience.com
General Inquires: info@accscience.com

https://accscience.com/journal/IJB